Springer Proceedings in Physics 207

Ivan A. Parinov · Shun-Hsyung Chang
Vijay K. Gupta *Editors*

Advanced Materials

Proceedings of the International Conference on "Physics and Mechanics of New Materials and Their Applications", PHENMA 2017

Springer

Springer Proceedings in Physics

Volume 207

The series Springer Proceedings in Physics, founded in 1984, is devoted to timely reports of state-of-the-art developments in physics and related sciences. Typically based on material presented at conferences, workshops and similar scientific meetings, volumes published in this series will constitute a comprehensive up-to-date source of reference on a field or subfield of relevance in contemporary physics. Proposals must include the following:

- name, place and date of the scientific meeting
- a link to the committees (local organization, international advisors etc.)
- scientific description of the meeting
- list of invited/plenary speakers
- an estimate of the planned proceedings book parameters (number of pages/articles, requested number of bulk copies, submission deadline).

More information about this series at http://www.springer.com/series/361

Ivan A. Parinov · Shun-Hsyung Chang
Vijay K. Gupta
Editors

Advanced Materials

Proceedings of the International Conference on "Physics and Mechanics of New Materials and Their Applications", PHENMA 2017

Springer

Editors
Ivan A. Parinov
I. I. Vorovich Mathematics, Mechanics and Computer Sciences Institute
Southern Federal University
Rostov-on-Don
Russia

Shun-Hsyung Chang
Department of Microelectronics Engineering
National Kaohsiung University of Science and Technology
Kaohsiung
Taiwan

Vijay K. Gupta
Indian Institute of Information Technology, Design and Manufacturing, Jabalpur
Jabalpur, Madhya Pradesh
India

ISSN 0930-8989 ISSN 1867-4941 (electronic)
Springer Proceedings in Physics
ISBN 978-3-319-78918-7 ISBN 978-3-319-78919-4 (eBook)
https://doi.org/10.1007/978-3-319-78919-4

Library of Congress Control Number: 2018937704

Printed on acid-free paper

This Springer imprint is published by the registered company Springer International Publishing AG part of Springer Nature
The registered company address is: Gewerbestrasse 11, 6330 Cham, Switzerland

Preface

Accelerated development of theoretical, experimental, and computational methods, intended for researching and designing various technologies for obtaining promising materials, composites, and structures, determines modern trends in materials science and related scientific and technical fields. Modern requirements bring to the fore huge attention to the development of environmentally friendly materials. Industrial technologies need the creation of devices and goods, with very high measurement accuracy, reliability, durability, which are able to function under conditions of temperature and pressure that vary widely, as well as in the aggressive environment. At the same time, the high characteristics of the developed devices and technologies directly depend on the properties of the materials used. The study of modern physical processes and technologies is also impossible to imagine without creating materials and devices with optimal and outstanding properties.

This collection of 50 papers presents selected reports of the 2017 International Conference on "Physics, Mechanics of New Materials and Their Applications" (PHENMA 2017), which has been taken place in Jabalpur, India, October 14–16, 2017 (http://phenma2017.math.sfedu.ru). The conference was sponsored by the Council of Scientific and Industrial Research (India), Ministry of Education and Science of the Russian Federation, South Scientific Center of the Russian Academy of Science, Russian Foundation for Basic Research, Ministry of Science and Technology of Taiwan, New Century Education Foundation (Taiwan), Ocean & Underwater Technology Association (Taiwan), Unity Opto Technology Co., Ltd. (Taiwan), Fair Well Fishery Co., Ltd. (Taiwan), Woen Jinn Harbor Engineering Co., Ltd. (Taiwan), Lorom Group (Taiwan), Longwell Co., (Taiwan), University of 17 Agustus 1945 Surabaya (Indonesia), University of 45, Surabaya (Indonesia), University of Islam Kadiri (Indonesia), Khon Kaen University (Thailand), Don State Technical University (Russia), South Russian Regional Centre for Preparation and Implementation of International Projects.

The thematic of the PHENMA 2017 continued ideas of previous international symposia and conferences: PMNM 2012 (http://pmnm.math.rsu.ru), PHENMA 2013 (http://phenma.math.sfedu.ru), PHENMA 2014 (http://phenma2014.math.sfedu.ru), PHENMA 2015 (http://phenma2015.math.sfedu.ru), and PHENMA

2016 (http://phenma2016.math.sfedu.ru), whose results have been published in the following edited books "Physics and Mechanics of New Materials and Their Applications", Ivan A. Parinov, Shun Hsyung-Chang (Eds.), Nova Science Publishers, New York, 2013, 444 p. ISBN: 978-1-62618-535-7; "Advanced Materials—Physics, Mechanics and Applications", Springer Proceedings in Physics. Vol. 152. Shun-Hsyung Chang, Ivan A. Parinov, Vitaly Yu. Topolov (Eds.), Springer, Heidelberg, New York, Dordrecht, London, 2014, 380 p. ISBN: 978-3319037486; "Advanced Materials—Studies and Applications", Ivan A. Parinov, Shun-Hsyung Chang, Somnuk Theerakulpisut (Eds.), Nova Science Publishers, New York, 2015, 527 p. ISBN: 978-1-63463-749-7; "Advanced Materials—Manufacturing, Physics, Mechanics and Applications", Springer Proceedings in Physics, Vol. 175, Ivan A. Parinov, Shun-Hsyung Chang, Vitaly Yu. Topolov (Eds.). Heidelberg, New York, Dordrecht, London: Springer Cham. 2016, 707 p. ISBN: 978-3319263229 and Advanced Materials—Techniques, Physics, Mechanics and Applications, Springer Proceedings in Physics, Vol. 193, Ivan A. Parinov, Shun-Hsyung Chang, Muaffaq A. Jani (Eds.). Heidelberg, New York, Dordrecht, London: Springer Cham. 2017, 627 p. ISBN: 978-3-319-56062-5, respectively.

The papers of the PHENMA 2017 are divided into four scientific directions: (i) processing techniques of advanced materials, (ii) physics of advanced materials, (iii) mechanics of advanced materials, and (iv) applications of advanced materials.

Into framework of the first topic are considered, in particular, binary-, ternary-, and four-component systems on the base of sodium niobate, porous, and composite materials based on lead-free ferroelectric ceramics. Then there are present the techniques of the growth of zinc oxide nanorod arrays on piezoelectric substrates and the synthesis of titanate nanotubes. Moreover, the evolution of structure and its activity at the distribution of metals in nanoparticles are studied. The first section is finished by considering the goods, fabricated by 3D printing process, and designing novel solvents for deep desulfurization using methods of molecular dynamics.

The physical direction is opened by the investigations of the surface structures and properties of oxygen-adsorbed TiC(111) surface and also the presentation of density matrix method in atom theory. Novel results are present for electric response to bending vibrations and pyroelectric effect in unpolarized ferroelectric ceramics. Then new data on a broad set of structural, dielectric, magnetic, and elastic properties and also effects of doping are discussed for solid solutions of different ferroelectrics and multiferroics. Other papers are devoted to investigations of photoelectrical and optoacoustic properties of ZnO–ferroelectric structure and lithium niobate crystals. The study of interfacial microstructures and characterization of the titanium–stainless steel friction welds finishes this section.

In the section of mechanics are present new mathematical and finite element models with dissipations for multiferroic media with voids, and nonlocal nonlinear analysis of composites is performed. Then studies of carbon nanotube systems and applied theory of the vibration of inhomogeneously polarized piezo elements are discussed. Elastic-guided waves in laminate fiber-reinforced composite plates, in particular, at wave propagation through damaged interface and estimation of wave

energy are studied, which are continued by 3D boundary-element modeling of transversal vibrations of poroelastic plates. This section also includes damage models for composites and crack initiation in surface-hardened titanium alloys. Moreover, contact interactions for bodies of complex shape taking into account wear are treated as well as physical, mechanical, and tribological properties of nanocomposites. Finally, mechanical properties of two-layer coating using nanoindentation are discussed.

The presented applications are touched to set of modern devices, manufactured on the base of novel approaches and reprocessing of slag and wastes for the development of environmentally friendly materials and goods. First, it is analyzed Helmholtz resonator for estimating acoustic metamaterial properties. Then new thermoelectric converter based on "metal—dielectric—semiconductor—metal" structures is discussed. Finite element analysis is applied to development of cymbal transducer from porous piezoceramics, and mathematical modeling of stepped beam energy harvesting is performed on the base of Euler–Bernoulli's theory. Moreover, there are evaluated performance of piezoelectric micropump and treated coded control of piezo actuator nano- and microdisplacements for mechatronics systems. Detailed consideration is devoted to mineral additives from technogenic raw materials and treatment of dioxin-contaminated soil by organic waste co-composting system. Biocomposites are characterized as suitable materials for human and bottom ash-reinforced aluminum metal matrix composite is proposed for motorcycle detail manufacture.

The book will be very useful for students, graduate students, scientists, and engineers who research and develop nanomaterials and structures, ferro–piezo-electrics, pyroelectrics, magnetic and environmentally friendly materials and composites. The book also discusses theoretical and experimental problems, related to research and mathematical modeling of modern devices using new promising materials that are suitable for wide application in various scientific, technological, and technical fields. The book includes new research results in the field of materials science, condensed matter physics, physicalmechanical theory, modeling and experiment, methods of processing and developing advanced materials and composites, numerical methods, and different applications.

Rostov-on-Don, Russia — Ivan A. Parinov
Kaohsiung, Taiwan — Shun-Hsyung Chang
Jabalpur, India — Vijay K. Gupta

Contents

Contributors

A. G. Abubakarov Research Institute of Physics, Southern Federal University, Rostov-on-Don, Russia

Sergey M. Afonin Department of Intellectual Technical Systems, National Research University of Electronic Technology (MIET), Moscow, Russia

Swati Agrawal Machine Dynamics and Vibrations Laboratory, Mechanical Engineering Discipline, PDPMIIITDM, Jabalpur, India

S. M. Aizikovich Don State Technical University, Rostov-on-Don, Russia; Southern Federal University, Rostov-on-Don, Russia

Anastasia A. Alekseenko Chemistry Faculty, Southern Federal University, Rostov-on-Don, Russia

Nataliya E. Anashkina N.V. Mel'nikov Institute of Comprehensive Exploitation of Mineral Resources, Russian Academy of Science, Moscow, Russia

K. P. Andryushin Research Institute of Physics, Southern Federal University, Rostov-on-Don, Russia

I. N. Andryushina Research Institute of Physics, Southern Federal University, Rostov-on-Don, Russia

V. P. Bagmutov Department of Strength of Materials, Volgograd State Technical University, Volgograd, Russia

Ekaterina M. Bayan Southern Federal University, Rostov-on-Don, Russia

Vansh Bedi Department of Mechanical Engineering, Thapar Institute of Engineering & Technology, Patiala, Punjab, India

Sergey V. Belenov Chemistry Faculty, Southern Federal University, Rostov-on-Don, Russia

A. V. Blazhevich Research Institute of Physics and Faculty of Physics, Southern Federal University, Rostov-on-Don, Russia

Boris V. Bondarev Moscow Aviation Institute, Moscow, Russia

Anders E. Boström Division of Dynamics, Department of Applied Mechanics, Chalmers University of Technology, Göteborg, Sweden

Igor Zh. Bunin N.V. Mel'nikov Institute of Comprehensive Exploitation of Mineral Resources, Russian Academy of Science, Moscow, Russia

O. A. Bunina Research Institute of Physics and Faculty of Physics, Southern Federal University, Rostov-on-Don, Russia

N. I. Buravchuk I. I. Vorovich Mathematics, Mechanics and Computer Sciences Institute, Southern Federal University, Rostov-on-Don, Russia

Shun-Hsyung Chang National Kaohsiung Marine University, Kaohsiung, Taiwan

Valentine A. Chanturiya N.V. Melâ€™nikov Institute of Comprehensive Exploitation of Mineral Resources, Russian Academy of Science, Moscow, Russia

Woo-Seong Che Department of Mechatronics Engineering, Kyungsung University, Busan, Republic of Korea

M. I. Chebakov Southern Federal University, Rostov-on-Don, Russia

V. A. Chebanenko Southern Scientific Center of RAS, Rostov-on-Don, Russia

Muralimohan Cheepu Department of Mechatronics Engineering, Kyungsung University, Busan, Republic of Korea

H. Chen University of Macau, Macau, China

C.-C. Chou National Taiwan University of Science and Technology, Taipei, Taiwan, China

S. A. Danilchenko Rostov State Transport University, Rostov-on-Don, Russia; Southern Federal University, Rostov-on-Don, Russia

D. S. Denisevich Department of Strength of Materials, Volgograd State Technical University, Volgograd, Russia

Olga V. Doroshenko Institute for Mathematics, Mechanics and Informatics, Kuban State University, Krasnodar, Russian Federation

S. I. Dudkina Research Institute of Physics, Southern Federal University, Rostov-on-Don, Russia

Le Van Duong Department of Mechanical Engineering and Energy, Transportation Le Quy Don Technical University, Ha Noi, Vietnam

Artem Eremin Institute for Mathematics, Mechanics and Informatics, Kuban State University, Krasnodar, Russia; Institute of Mechanics, Helmut-Schmidt-University/University of the Federal Armed Forces, Hamburg, Germany

I. V. Ershov Don State Technical University, Rostov-on-Don, Russia

Aleksey G. Fedorenko Southern Scientific Center of Russian Academy of Sciences, Rostov-on-Don, Russia

N. S. Filatova Physics Research Institute, Southern Federal University, Rostov-on-Don, Russia

Amit Gahlaut Mechanical Engineering Department, Rajasthan Technical University, Kota, Rajasthan, India

Dinara Gapeyenko School of Engineering, Nazarbayev University, Astana, Kazakhstan

Leonid V. Grigoryev Optoinformatic Technologies and Materials Department, ITMO University, St. Petersburg, Russia; Radioelectronics and Optoelectronics System Department, Saint-Petersburg State University of Aerospace Instrumentation, St. Petersburg, Russia

E. V. Glushkov Institute for Mathematics, Mechanics and Informatics, Kuban State University, Krasnodar, Russia

N. V. Glushkova Institute for Mathematics, Mechanics and Informatics, Kuban State University, Krasnodar, Russia

Mikhail V. Golub Institute for Mathematics, Mechanics and Informatics, Kuban State University, Krasnodar, Russian Federation

Ievgen Ie. Gorbenko Lugansk Taras Shevchenko National University, Lugansk, Ukraine

R. U. Gruzdev Southern Federal University, Rostov-on-Don, Russia

V. K. Gupta Machine Dynamics and Vibrations Laboratory, Mechanical Engineering Discipline, PDPMIIITDM, Jabalpur, India

Vipul Gupta Machine Dynamics and Vibrations Laboratory, Mechanical Engineering Discipline, PDPMIIITDM, Jabalpur, India

O. V. Guryanova I. I. Vorovich Mathematics, Mechanics and Computer Sciences Institute, Southern Federal University, Rostov-on-Don, Russia

A. A. Gusev Institute of Solid State Chemistry and Mechanochemistry, SB RAS, Novosibirsk, Russia

Vladimir E. Guterman Chemistry Faculty, Southern Federal University, Rostov-on-Don, Russia

Rakesh Kumar Haldkar Mechanical Engineering Displine, PDPM Indian Institute of Information Technology Design and Manufacturing, Jabalpur, India

Retno Hastijanti University of 17 Agustus 1945, Surabaya, Indonesia

O. M. Holodova Don State Technical University, Rostov-on-Don, Russia

W. Y. Huang Department of Marine Environmental Engineering, National Kaohsiung Marine University, Kaohsiung, Taiwan

Leonid Igumnov Research Institute for Mechanics, National Research Lobachevsky State University of Nizhni Novgorod, Nizhni Novgorod, Russia

V. V. Ilyasov Don State Technical University, Rostov-on-Don, Russia

Gerardo Iovane Department of Computer Science, University of Salerno, Fisciano, SA, Italy

V. P. Isupov Institute of Solid State Chemistry and Mechanochemistry, SB RAS, Novosibirsk, Russia

P. G. Ivanochkin Rostov State Transport University, Rostov-on-Don, Russia

Prashant Jamwal School of Engineering, Nazarbayev University, Astana, Kazakhstan

M. A. Jani University of 17 Agustus 1945 Surabaya, Surabaya, Indonesia

D. P. Jena Industrial Acoustics Laboratory, Department of Industrial Design, National Institute of Technology, Rourkela, India

C.-Y. Jenny Lee Department of Microelectronics Engineering, National Kaohsiung Marine University, Kaohsiung, Taiwan

Yu. V. Kabirov Department of Physics, Southern Federal University, Rostov-on-Don, Russia

A. Kaewlaoyoong Department of Safety Health and Environmental Engineering, National Kaohsiung First University of Science and Technology, Kaohsiung, Taiwan

E. M. Kaidashev Southern Federal University, Rostov-on-Don, Russia

P. K. Kankar Machine Dynamics and Vibrations Laboratory, Mechanical Engineering Discipline, PDPMIIITDM, Jabalpur, India

G. Ya. Karapetyan I. I. Vorovich Institute of Mathematics, Mechanics and Computer Sciences, Southern Federal University, Rostov-on-Don, Russia

Galina K. Khachatryan Central Research Institute of Geological Exploration for Base and Precious Metals, Moscow, Russia

Yun Hae Kim Department of Material Engineering, Korea Maritime and Ocean University, Busan, Korea

Sergey A. Kirakosyan Chemistry Faculty, Southern Federal University, Rostov-on-Don, Russia

Evgenia V. Kirillova RheinMain University of Applied Sciences, Wiesbaden, Germany

L. I. Kiseleva Southern Scientific Center of RAS, Rostov-on-Don, Russia

N. B. Kofanova Department of Physics, Southern Federal University, Rostov-on-Don, Russia

I. V. Kolesnikov Rostov State Transport University, Rostov-on-Don, Russia

Vladimir I. Kolesnikov Rostov State Transport University, Rostov-on-Don, Russia

Elizaveta V. Koporulina N.V. Mel'nikov Institute of Comprehensive Exploitation of Mineral Resources, Russian Academy of Science, Moscow, Russia

Anna S. Kostenikova Southern Federal University, Rostov-on-Don, Russia

T. V. Krasnyakova Institute of Physical Organic and Coal Chemistry, Donetsk, Ukraine; Lugansk Taras Shevchenko National University, Lugansk, Ukraine

Alex F. Kraychko Radioelectronics and Optoelectronics System Department, Saint-Petersburg State University of Aerospace Instrumentation, St. Petersburg, Russia

L. I. Krenev Don State Technical University, Rostov-on-Don, Russia

S. P. Kubrin Research Institute of Physics and Faculty of Physics, Southern Federal University, Rostov-on-Don, Russia

Yu. A. Kuprina Research Institute of Physics and Faculty of Physics, Southern Federal University, Rostov-on-Don, Russia; Institute of Solid State Chemistry and Mechanochemistry, SB RAS, Novosibirsk, Russia

M. F. Kupriyanov Department of Physics, Southern Federal University, Rostov-on-Don, Russia

M. E. Kutepov Southern Federal University, Rostov-on-Don, Russia

Rolf Lammering Institute of Mechanics, Helmut-Schmidt-University/University of the Federal Armed Forces, Hamburg, Germany

Olga Lesnjak Department of Theoretical and Applied Mechanics, Don State Technical University, Rostov-on-Don, Russia

C. Lin Department of Marine Environmental Engineering, National Kaohsiung Marine University, Kaohsiung, Taiwan

M. A. Lugovaya Southern Federal University, Rostov-on-Don, Russia

Timofey G. Lupeiko Southern Federal University, Rostov-on-Don, Russia

A. G. Lutokhin Physics Research Institute, Southern Federal University, Rostov-on-Don, Russia

A. A. Lyapin Southern Federal University, Rostov-on-Don, Russia

M. A. Malitskaya Research Institute of Physics and Faculty of Physics, Southern Federal University, Rostov-on-Don, Russia

D. S. Manturov Rostov State Transport University, Rostov-on-Don, Russia

Vladislav S. Menshchikov Chemistry Faculty, Southern Federal University, Rostov-on-Don, Russia

B. C. Meshi Don State Technical University, Rostov-on-Don, Russia

O. A. Miakisheva Institute for Mathematics, Mechanics and Informatics, Kuban State University, Krasnodar, Russia

Yuri F. Migal Rostov State Transport University, Rostov-on-Don, Russia

Anatoly V. Mikhailov Optical Technology Department, Optical Research Institute, St.Petersburg, Russia

T. A. Minasyan Southern Federal University, Rostov-on-Don, Russia

B. I. Mitrin Don State Technical University, Rostov-on-Don, Russia

Karisma Mohapatra Industrial Acoustics Laboratory, Department of Industrial Design, National Institute of Technology, Rourkela, India

S. Mukherjee PDPM Indian Institute of Information Technology, Design and Manufacturing, Jabalpur, India

Ph. V. Myasnikov Rostov State Transport University, Rostov-on-Don, Russia

N. A. Myasnikova Rostov State Transport University, Rostov-on-Don, Russia

Maula Nafi University of 17 Agustus 1945, Surabaya, Indonesia

Andrey V. Nasedkin I.I. Vorovich Institute of Mathematics, Mechanics and Computer Science, Southern Federal University, Rostov-on-Don, Russia

Anna A. Nasedkina I.I. Vorovich Institute of Mathematics, Mechanics and Computer Science, Southern Federal University, Rostov-on-Don, Russia

A. V. Nazarenko Southern Scientific Centre of Russian Academy of Science, Rostov-on-Don, Russia

Vachyslav G. Nefedov Radioelectronics and Optoelectronics System Department, Saint-Petersburg State University of Aerospace Instrumentation, St. Petersburg, Russia

Alina K. Nevelskaya Chemistry Faculty, Southern Federal University, Rostov-on-Don, Russia

Ch. V. Nguyen School of Mechanical Engineering, Le Quy Don Technical University, Hanoi, Vietnam

A. L. Nikolaev Southern Federal University, Rostov-on-Don, Russia

E. S. Novikov Rostov State Transport University, Rostov-on-Don, Russia

N. M. Novikovsky Research Institute of Physics, Southern Federal University, Rostov-on-Don, Russia

Pavel Oganesyan I. I. Vorovich Mathematics, Mechanics and Computer Sciences Institute, Southern Federal University, Rostov-on-Don, Russia

N. M. Olekhnovich Scientific-Practical Materials Research Centre of NAS of Belarus, Minsk, Belarus

S. V. Orlov Research Institute of Physics and Faculty of Physics, Southern Federal University, Rostov-on-Don, Russia

Mikhail N. Palatnikov I.V. Tananaev Institute of Chemistry and Technology of Rare Elements and Mineral Raw Materials of the Kola Science Center of the Russian Academy of Sciences, Murmansk, Russia

Sandeep Kumar Parashar Mechanical Engineering Department, Rajasthan Technical University, Kota, Rajasthan, India

I. A. Parinov I. I. Vorovich Institute of Mathematics, Mechanics and Computer Sciences, Southern Federal University, Rostov-on-Don, Russia

Chang Wook Park Department of Material Engineering, Korea Maritime and Ocean University, Busan, Korea

A. V. Pavlenko Research Institute of Physics, Southern Federal University, Rostov-on-Don, Russia; Southern Scientific Centre of Russian Academy of Science, Rostov-on-Don, Russia

Andrey Petrov Research Institute for Mechanics, National Research Lobachevsky State University of Nizhni Novgorod, Nizhni Novgorod, Russia

E. I. Petrova Southern Federal University, Rostov-on-Don, Russia

D. K. Pham Don State Technical University, Rostov-on-Don, Russia

Ekaterina A. Pilipenko Donetsk A.A. Galkin Physics and Technology Institute, Donetsk, Ukraine

I. G. Popova Don State Technical University, Rostov-on-Don, Russia

S. K. Prajapati PDPM Indian Institute of Information Technology, Design and Manufacturing, Jabalpur, India

N. V. Prutsakova Don State Technical University, Rostov-on-Don, Russia

Vasiliy V. Pryadchenko Physical Faculty, Southern Federal University, Rostov-on-Don, Russia

A. V. Pushkarev Scientific-Practical Materials Research Centre of NAS of Belarus, Minsk, Belarus

Larisa E. Pustovaya Don State Technical University, Rostov-on-Don, Russia

E. P. Putri University of 17 Agustus 1945 Surabaya, Surabaya, Indonesia; Khon Kaen University, Khon Kaen, Thailand

Y. V. Radyush Scientific-Practical Materials Research Centre of NAS of Belarus, Minsk, Belarus

S. I. Raevskaya Research Institute of Physics and Faculty of Physics, Southern Federal University, Rostov-on-Don, Russia

I. P. Raevski Research Institute of Physics and Faculty of Physics, Southern Federal University, Rostov-on-Don, Russia

P. Raghu Civil Engineering Department, Indian Institute of Technology Hyderabad, Sangareddy, India

Amirtham Rajagopal Department of Civil Engineering, Indian Institute of Technology, Hyderabad, India

Rituraj Rajpoot Department of Mechanical Engineering, Thapar Institute of Engineering & Technology, Patiala, Punjab, India

K. S. S. Reddy Department of Civil Engineering, Indian Institute of Technology Hyderabad, Hyderabad, India

A. N. Reznichenko Southern Federal University, Rostov-on-Don, Russia

L. A. Reznichenko Research Institute of Physics, Southern Federal University, Rostov-on-Don, Russia

E. S. Rodinin Physics Research Institute, Southern Federal University, Rostov-on-Don, Russia

Pavel Romanenko I. I. Vorovich Mathematics, Mechanics and Computer Sciences Institute, Southern Federal University, Rostov-on-Don, Russia

Elsen Ronando University of 17 Agustus 1945, Surabaya, Indonesia

E. V. Rozhkov I. I. Vorovich Mathematics, Mechanics and Computer Science Institute, Southern Federal University, Rostov-on-Don, Russia

A. G. Rudskaya Department of Physics, Southern Federal University, Rostov-on-Don, Russia

D. I. Rudsky Department of Physics, Southern Federal University, Rostov-on-Don, Russia

Mariya V. Ryazantseva N.V. Mel'nikov Institute of Comprehensive Exploitation of Mineral Resources, Russian Academy of Science, Moscow, Russia

A. N. Rybyanets Southern Federal University, Rostov-on-Don, Russia

Ery Sadewa University of 17 Agustus 1945, Surabaya, Indonesia

E. V. Sadyrin Don State Technical University, Rostov-on-Don, Russia

V. P. Sakhnenko Physics Research Institute, Southern Federal University, Rostov-on-Don, Russia

D. A. Sarychev Research Institute of Physics and Faculty of Physics, Southern Federal University, Rostov-on-Don, Russia

B. Saswata Department of Materials Science and Metallurgical Engineering, Indian Institute of Technology Hyderabad, Hyderabad, India

A. N. Savkin Department of Strength of Materials, Volgograd State Technical University, Volgograd, Russia

S. A. Shcherbinin Southern Federal University, Rostov on Don, Russia

A. A. Sedov Department of Strength of Materials, Volgograd State Technical University, Volgograd, Russia

Wolfgang Seemann Karlsruhe Institute of Technology, Karlsruhe, Germany

Dhawal Shah School of Engineering, Nazarbayev University, Astana, Kazakhstan

Oleg V. Shakin Radioelectronics and Optoelectronics System Department, Saint-Petersburg State University of Aerospace Instrumentation, St. Petersburg, Russia

Daria B. Shemet Physical Faculty, Southern Federal University, Rostov-on-Don, Russia

Tanuja Sheorey Mechanical Engineering Displine, PDPM Indian Institute of Information Technology Design and Manufacturing, Jabalpur, India

A. V. Shevchuk Department of Physics, Southern Federal University, Rostov-on-Don, Russia

Maria S. Shevtsova RheinMain University of Applied Sciences, Wiesbaden, Germany

L. A. Shilkina Research Institute of Physics, Southern Federal University, Rostov-on-Don, Russia

Alexey Shpenev A. Yu. Ishlinsky Institute for Problems in Mechanics RAS, Moscow, Russia

Dmitry S. Shtarev Far Eastern State Transport University, Khabarovsk, Russia; Y.A. Kosygin Institute of Tectonics and Geophysics of Far East Department of Russian Academy of Science, Khabarovsk, Russia

I. A. Shvetsov Southern Federal University, Rostov-on-Don, Russia

N. A. Shvetsova Southern Federal University, Rostov-on-Don, Russia

Nikolay V. Sidorov I.V. Tananaev Institute of Chemistry and Technology of Rare Elements and Mineral Raw Materials of the Kola Science Center of the Russian Academy of Sciences, Murmansk, Russia

Brijesh Kumar Singh Machine Dynamics and Vibrations Laboratory, Mechanical Engineering Discipline, PDPMIIITDM, Jabalpur, India

Sukhdeep Singh Department of Mechanical Engineering, Thapar Institute of Engineering & Technology, Patiala, Punjab, India

E. I. Sitalo Research Institute of Physics and Faculty of Physics, Southern Federal University, Rostov-on-Don, Russia

A. N. Soloviev Don State University, Rostov-on-Don, Russia; Southern Federal University, Rostov-on-Don, Russia

Arkadiy Soloviev Department of Theoretical and Applied Mechanics, Don State Technical University, Rostov-on-Don, Russia

Vasiliy V. Srabionyan Physical Faculty, Southern Federal University, Rostov-on-Don, Russia

B. Srinivas Department of Mechanical Engineering, MVGR College of Engineering, Vizianagaram, Andhra Pradesh, India

Vineet Srivastava Department of Mechanical Engineering, Thapar Institute of Engineering & Technology, Patiala, Punjab, India

V. V. Stashenko Research Institute of Physics and Faculty of Physics, Southern Federal University, Rostov-on-Don, Russia

Alexander V. Syuy Far Eastern State Transport University, Khabarovsk, Russia

Natalya A. Teplyakova I.V. Tananaev Institute of Chemistry and Technology of Rare Elements and Mineral Raw Materials of the Kola Science Center of the Russian Academy of Sciences, Murmansk, Russia

N. M. Teslenko Research Institute of Physics, Southern Federal University, Rostov-on-Don, Russia

Hsiao-Wen Tin National Kaohsiung Marine University, Kaohsiung, Taiwan

V. V. Titov Research Institute of Physics and Faculty of Physics, Southern Federal University, Rostov-on-Don, Russia

Elena P. Troitskaya Donetsk A.A. Galkin Physics and Technology Institute, Donetsk, Ukraine

Sandeep Vats Department of Mechanical Engineering, Thapar Institute of Engineering & Technology, Patiala, Punjab, India

D. Venkateswarlu Department of Mechanical Engineering, Marri Laxman Reddy Institute of Technology and Management, Hyderabad, Telangana, India

I. A. Verbenko Research Institute of Physics, Southern Federal University, Rostov-on-Don, Russia

Maria G. Volkova Southern Federal University, Rostov-on-Don, Russia

Igor Vorobtsov Research Institute for Mechanics, National Research Lobachevsky State University of Nizhni Novgorod, Nizhni Novgorod, Russia

C. T. Vu Department of Marine Environmental Engineering, National Kaohsiung Marine University, Kaohsiung, Taiwan

Yudha Wrahatnala University of 17 Agustus 1945, Surabaya, Indonesia

C.-C. Yang Department of Microelectronics Engineering, National Kaohsiung Marine University, Kaohsiung, Taiwan

V. I. Yatsenko Southern Federal University, Rostov-on-Don, Russia

Yuriy I. Yurasov Research Institute of Physics, Southern Federal University, Rostov-on-Don, Russia; Southern Scientific Centre RAS, Rostov-on-Don, Russia

I. N. Zakharchenko Research Institute of Physics and Faculty of Physics, Southern Federal University, Rostov-on-Don, Russia

I. N. Zakharov Department of Strength of Materials, Volgograd State Technical University, Volgograd, Russia

Yu. N. Zakharov Physics Research Institute, Southern Federal University, Rostov-on-Don, Russia

T. P. Zhdanova Don State Technical University, Rostov-on-Don, Russia

D. A. Zhilin Southern Federal University, Rostov-on-Don, Russia

Eugen Zimmermann Institute of Mechanics, Helmut-Schmidt-University/ University of the Federal Armed Forces, Hamburg, Germany

Sergei V. Zubkov Scientific Research Institute of Physics, Southern Federal University, Rostov-on-Don, Russia

Part I
Processing Techniques of Advanced Materials

Chapter 1
Binary, Ternary and Four-Component Systems Based on Sodium Niobate: Phase Diagrams of States, the Role of the Number of Components and Defectiveness in the Formation of the Properties

L. A. Reznichenko, I. A. Verbenko, L. A. Shilkina, A. V. Pavlenko, S. I. Dudkina, I. N. Andryushina, K. P. Andryushin, A. G. Abubakarov and T. V. Krasnyakova

Complex systems are a challenge to the art of a researcher.
Haken [1]

Abstract According to the results of the analysis of the solid solutions in the multicomponent systems, based on lead titanate zirconate (PZT), there have been defined the search stages for the new functional materials for various purposes. The role of the number of components in the formation of the electrophysical properties has been shown. It has been defined that the 5-component systems, based on the PZT, provide the optimal combinations of basic electrical parameters. The phase diagrams of the two-, three- and four-component systems, based on sodium niobate, have been considered. The complexity of phase diagrams has been shown, which are distinguished by a large number of structural transitions, and by a variety of phase transformations in comparison with the systems, based on the PZT. It has been defined that in niobate systems, a considerable growth of electrophysical parameters during the transition to the four-component system was observed. The

L. A. Reznichenko · I. A. Verbenko · L. A. Shilkina · A. V. Pavlenko · S. I. Dudkina · I. N. Andryushina (✉) · K. P. Andryushin · A. G. Abubakarov
Research Institute of Physics, Southern Federal University, Rostov-on-Don, Russia
e-mail: futur6@mail.ru

A. V. Pavlenko
Southern Scientific Centre of Russian Academy of Science, Rostov-on-Don, Russia

T. V. Krasnyakova
Lugansk Taras Shevchenko National University, Lugansk, Ukraine

T. V. Krasnyakova
Institute of Physical Organic and Coal Chemistry, Donetsk, Ukraine

I. A. Parinov et al. (eds.), *Advanced Materials*, Springer Proceedings in Physics 207, https://doi.org/10.1007/978-3-319-78919-4_1

influence of the defectiveness of solid solutions on the formation of their macro-properties has been revealed. It has been defined that in one multicomponent system, the materials with different totality of the parameters can be obtained on the base of the compounds with fundamentally different macro-responses, which will allow using them in the combined equipment complexes, functioning in a sufficiently wide operating frequency range.

1.1 Introduction

The creation of functional ferroelectric materials (FFEMs) with optimal properties for various applications remains an important material science task, and unless it has been solved it is impossible to satisfy the growing demands of electronics, the space industry, nuclear power engineering, and medical equipment.

Since the beginning of the FFEMs study (1940–50s), four main groups of the materials can be distinguished: those based (i) on barium titanate, (ii) on lead titanate zirconate (PZT), (iii) on lead niobate, (iv) on potassium niobate. Among them, the most widely used materials are based on the PZT [2–4], which can be explained by the existence of the morphotropic region (MR) in this system. It is a region of a structural phase transition, accompanied by extremes of electrophysical parameters, in particular, by high piezoelectric parameters, and it is also accompanied by the possibility of changing them in wide limits. The latter is substantially determined by the broad isomorphism inherent to the solid solutions (SSs) of PZT. The attempts to find the groups of highly effective materials with the perovskite structure in the study of other two-component systems did not yield the desired results. The components of these two-component systems with the ABO_3 composition have Pb^{2+}, Bi^{2+}, Cd^{2+} in the *A* positions, and Ti^{4+}, Zr^{4+}, Sn^{4+}, Hf^{4+} in the *B* positions, i.e. the cations providing ferroelectric properties and an increase in the Curie temperature. Among the studied systems, it has not been found any system equivalent to PZT, which, apart from the high piezoelectric characteristics, is distinguished by a broad isomorphism.

During the first period of the industrial materials creation on the base of PZT in the 1950–60s, the PZT system was modified with mono-oxides of various metals. Among them, the best materials for various purposes are those of the PZT type of the company "Vernitron" USA [5].

In the late sixties and early seventies of the last century, Japanese researchers performed the transition from the PZT system to three-component systems based on it, which made it possible to increase the piezoelectric parameters of ferroelectric SSs and improve their sinterability [6]. Subsequent modification of SSs of the $PbTiO_3$–$PbZrO_3$–$PbNb_{2/3}Mg_{1/3}O_3$ system with various oxides led to a significant improvement in their characteristics and to the creation of industrial materials such as of the PCM type of the company Matsushita Electric, Japan [7].

During the same years (at the end of the 1960s and at the beginning of the 1970s) the researches on three-component systems, based on the PZT [8], was started in the Research Institute of Physics of the Rostov State University (RSU). Almost immediately, it led to the intensive study of four-, five-component SSs, and at the end 1990s to the study of the based on PZT six-component systems of the type: $PbTiO_3-PbZrO_3-\sum_1^n PbB'_{1-\alpha}B''_{\alpha}O_3 (n = 2, 3, 4)$. Here there are 5-, 6-valence cations; 1-, 2-, 3-valence cations; α = 1/2, 1/3, 1/4 depending on the valence. The results of these studies are present in papers [9–25] and are generalized in monographs [26–28].

It should be noted that with the increase in the number of the components, the regions of compositions with the optimal combinations of parameters for various fields expand, a variety of properties grows, the most important electrophysical parameters [9, 10, 16, 17] increase. These results witness on the significant advantages of multicomponent systems over the simpler systems, which serves the base for them. These advantages will be reflected in detail below.

In the above-mentioned periods of time, studies of another group of materials were carried out, namely, SSs, based on alkali metal niobates (AMN). The latter possess unique combinations of parameters (low specific gravity, high sound velocity, wide range of permittivity and mechanical Q values at sufficiently high values of piezoelectric parameters) that cannot be implemented in SSs, based on PZT [4, 29–44]. However, they have not been widely used in technology for a long time because of the difficulties in obtaining them by traditional methods, which is due to the complexity of their crystal structure, the presence of a large number of phase transitions and due to the strong dependence of the properties on the conditions of structure formation. Intensive research of these SSs has been carried out after the European Union adopted the Legislative Initiative [45], limiting the use of lead containing materials in electronic and electrical equipment, which, being a toxic and volatile element, poses a threat to the environment and to human health [46–54].

In Russia, the ecological situation is characterized by both a high level of current anthropogenic impact on the environment and a significant amount of accumulated environmental damage. In this regard, the adoption of a number of laws in Russia, based on the paradigm of the best available technologies [55] and a genuine breakthrough on the environmental legislative front, make it necessary to perform the transition in all electrotechnical sectors to non-toxic (first of all, lead-free) intellectual materials. The only alternative to already existing materials science brands are ferroactive compositions and their solid solutions (SSs), based on alkali and alkaline earth metal niobates (NAM, NAEM).

In the result of researches, about 200 types of functional materials and methods for their production were created in the Research Institute of Physics of the SFedU (RSU), protected by more than 250 security documents: author's certificates, Russian and foreign patents, and *know-how*. These materials belong to the following 10 groups, which differ in the totality of their electrophysical parameters and, as consequence, in the fields of application that "cover" practically all known piezo-technical areas:

(1) materials with high dielectric permittivity for low-frequency converters in systems of microspaces;
(2) materials with high anisotropy of piezoelectric parameters, intended for ultrasonic flaw detection, thickness measurement and other devices for non-destructive testing;
(3) materials with high stability of resonance frequency, used in frequency-selective filter devices;
(4) highly-sensitive materials for work in accelerometers, in devices for ultrasonic testing of products and equipment;
(5) high-temperature materials for transducers that keep working capacity at elevated temperatures;
(6) materials with low dielectric permittivity, high pyrocoefficient, high speed of sound, intended for use in high-frequency acoustoelectric transducers on surface and bulk waves, as well as in pyroelectric receivers;
(7) materials resistant to electrical and mechanical influences, promising for ultrasonic radiators, piezoelectric motors, reducing piezotransformers, generators of high voltage, etc.;
(8) materials with low coercive force for use in memory devices;
(9) pistol materials for working as temperature sensors, auto-heat stabilizing heaters;
(10) electrostrictive materials, fixing the change in the linear dimensions of the objects.

The material parameters of some groups are presented in Table 1.1.

Table 1.1 Basic electro-physical parameters of the materials, developed in the Research Institute of Physics

Materials	Parameters				
	$\varepsilon_{33}^T/\varepsilon_0$	$\mathrm{tg}\delta \times 10^2$	K_p	$\lvert d_{31}\rvert$, pC/N	Q_M
With high dielectric permittivity (group 1)	2800–6000	1.2–2.9	0.68-0.71	245–380	35–80
With high anisotropy of the piezoelectric parameters (group 2)	120–180	1.0–2.2	0–0.10	0–5	8–2000
With high resonance frequency stability (group 3)	180–1400	0.2–2.0	0.10–0.53	6–100	300–12000
High-sensitive (group 4)	650–1400	1.6–2.0	0.62–0.68	95–170	90–105
High-temperature (group 5)	48–455	0.1–1.9	0.015–0.32	0.5–35	100–4000
With low dielectric permittivity (group 6)	120–510	0.3–1.0	0.20–0.54	12–70	150–4500
Resistant to electrical and mechanical influences (group 7)	900–2300	0.30–0.85	0.57–0.66	85–195	1000–2000

The aspiration to the universality of science-intensive products leads to the need of combining several different options in one chemical composition, the diversity of which cannot be achieved within monobjects. In piezomaterial science, this leads to the transition to multifunctional compositions, in particular, to multicomponent systems, based on the compounds with fundamentally different macro responses.

Our purpose was to establish the general nature of the change of electrical properties due to the change of the number of SSs components in the systems, based on PZT and NAM. Moreover, we studied transition from solid solutions (SSs), which are the base of one group of materials (alkali metal niobates) to the SSs, which are the base of another group of materials (with the participation of the Pb(Ti, Zr)O_3 system). On the base of the formation of a new set of parameters, combining the advantages of both groups of ferroelectric piezoceramics, we studied two-, three-component systems, based on AMN, as well as a four-component system $(1 - x)$(Na, Li)NbO_3–xPb(Ti, Zr)O_3.

1.2 Objects: Methods of Their Obtaining and Research

The objects of the study were SSs of multicomponent systems, based on PZT: Pb(Zr, Ti)O_3–Pb(B', B'')$_n$$O_3$ (where B' = Nb, W, B'' = Zn, Mg, Cd, Bi, Co, Ni, n = 2, 3, 4); SSs of binary, ternary and four-component systems, based on sodium niobate: $(Na_{1-x}Li_x)NbO_3$ $(0 \leq x \leq 0.145)$, $(Na_{1-x}K_x)NbO_3$ $(0 \leq x \leq 1.0)$, $(Na_{1-x}Pb_x)(Nb_{1-x}Ti_x)O_3$ $(0 \leq x \leq 1.0)$, (Na, Li, Pb)(Nb, Ti)O_3, $(1 - x)(Na_{0.875}Li_{0.125})NbO_3$–$xPb(Ti_{0.5}Zr_{0.5})O_3$ (quasi-binary section of the four-component system $NaNbO_3$–$LiNbO_3$–$PbTiO_3$–$PbZrO_3$ with a step $\Delta x = 0.05$ in the range $0 < x$ 0.20 and $0.90 < x \leq 1.00$, $\Delta x = 0.10$ in the range $0.20 < x \leq 0.70$, $\Delta x = 0.025$ in the range $0.70 < x \leq 0.90$). SSs were obtained by double solid-phase synthesis at T_1 = 800 °C, T_2 = 850 °C, $\tau_1 = \tau_2$ = 5 h followed by sintering with the use of hot pressing (HP) method [56] at T_C = 950–1250 °C (depending on composition), under pressure P = 19.6 MPa, τ_{sin} = 40 min. We used monoxides and carbonates of the qualifications: PbO, TiO_2–"ec", $Li_2(Na, K)_2CO_3$–"cc", Nb_2O_5–"Nbo-Pt".

X-ray diffraction studies of the objects were carried out by the method of powder diffraction on a DRON-3 diffractometer using $Co_{K\alpha}$ radiation (Bragg-Brentano focusing scheme). We investigated the crushed objects, which made it possible to exclude the influence of surface effects, stresses and textures, appearing during the preparation of ceramics. The cell parameters were calculated using the standard procedure [57], the measurement error was $\Delta a = \Delta b = \Delta c = \pm 0.003$ Å, $\Delta V = \pm 0.05$ Å^3, where a, b, c are the parameters, V is the volume of the perovskite cell. The homogeneous deformation parameter δ, characterizing the spontaneous deformation as the relative elongation of the reduced perovskite cell along the polar axis, was calculated by the formulae: $\delta_T = 2/3\ (c/a - 1)$, for the tetragonal (T) phase and $\delta_{Rh} = \cos \alpha$, for the rhombohedral (Rh) phase [57].

The relative permittivity after the polarization of the samples $\left(\varepsilon_{33}^{T}/\varepsilon_0\right)$, the dielectric loss tangent (tan δ), the piezomodule $(|d_{31}|)$, the electromechanical coupling coefficient of the planar vibration mode (K_p), the mechanical quality factor (Q_M), the sound velocity were determined at room temperature in according to [58]. Relative errors in determining the parameters of solid solutions were for $\left(\varepsilon_{33}^{T}/\varepsilon_0\right) \leq \pm 1.5\%$, $\tan\delta \leq \pm 5.0\%$, $K_p \leq \pm 2.0\%$, $|d_{31}| \leq \pm 4.0\%$, $Q_M = \leq \pm 12\%$, $V_1^E \leq \pm 0.3\%$.

1.3 Advantages of Multicomponent Systems and the Role of the Number of Components in the Formation of the Macroproperties of Solid Solutions on the Base of PZT

Above, we mentioned the significant advantages of multicomponent systems over the simpler systems, which serve their base. These advantages of the SSs systems, based on PZT, are considered in detail in [10, 13, 26]:

(i) with the increasing number of the system components, MR dimensionality increases (the isothermal section of the phase diagram of the *k*-component system has $(k - 1)$-dimensional MR in the case of a two-phase transition), and it also increases in adjacent phase diagrams (PDs) regions, which greatly extends the choice of SSs with a given combination of parameters;

(ii) the introduction of new components, forming SSs with the components of the initial system, allows one to change widely the composition of SSs and, consequently, their parameters and to obtain a wide variety of materials properties;

(iii) with the increasing number of components of the system, the effectiveness of SSs increases;

(iv) with the increase in the number of components up to 4, 5, as a rule, the manufacturability of the systems is improving. This is probably due to the heterovalent substitutions with an increase in the number of ions, entering into the SSs, lead to the formation of an additional concentration of point defects, ensuring intensive diffusion processes, and consequently, the sintering process, the formation of an optimal microstructure and physical properties of the ceramic.

The authors, adopted the method [26] of creating new materials, based on the study of phase diagrams of multicomponent systems, which, unlike the modification, greatly facilitates the search and prediction of SSs with given properties, since it allows establishing a direct connection between the structure of SSs, their properties and application areas [11, 15, 19, 21]. There are three stages of search:

(i) the choice of cationic composition of the components;
(ii) the definition of the MR and its position on the PDs;
(iii) the determination of the number of the components.

The choice of the cation composition is based on the stated direct dependence of the ferroelectricity degree of SSs on the electronegativity (EN) of the B'' elements in the corresponding oxidation degree and, consequently, on the degree of covalence of the B''–O bond. As a measure of the ferroelectricity of SSs, there can be used a homogeneous strain parameter δ [57], since the magnitude of the stresses that arise when domain reorientation depends on it (the ferroelectricity is understood as the stability of the domain structure to external influences).

The determination of the MR and its position on the PDs are performed by studying the concentration dependences of the most important electrophysical parameters of SSs, which allow us to distinguish the regions of their extreme values or favorable combinations for various applications on the PDs.

The choice of the number of the components is based on the analysis of the change in the electrophysical and structural parameters of SSs during the transition from the two-component system of the PZT to three- and four-component systems, based on it [10] (Fig. 1.1), and from the three-component system $Pb(Ti, Zr)O_3-PbNb_{2/3}Zn_{1/3}O_3$ to four-and five-component on its base [13] (Fig. 1.2). Figure 1.1 shows the dependence of the structural and electrical parameters on the number of the components (N). For comparison, there were chosen SSs with a close content of the corresponding components, located near the tetragonal boundary of the MR. It is seen that with increasing of N (Fig. 1.1) the permittivity $\left(\varepsilon_{33}^T/\varepsilon_0\right)$ increases. A particularly noticeable increase of $\varepsilon_{33}^T/\varepsilon_0$ occurs, when there are introduced $PbNb_{2/3}Co_{1/3}O_3$ и $PbW_{1/2}Co_{1/2}O_3$ ferroelectric oxides as fourth components and to a lesser extent, when there are introduced $PbNb_{2/3}Co_{1/3}O_3$ и $PbW_{1/2}Co_{1/2}O_3$ ferroelectric oxides. The change of the piezomodule d_{31} is similar to the change of $\varepsilon_{33}^T/\varepsilon_0$, and the coefficient of electromechanical coupling K_p increases with growth of N to a lesser extent than $\varepsilon_{33}^T/\varepsilon_0$ and d_{31}. In the transition from three-component system $Pb(Ti, Zr)O_3$–$PbNb_{2/3}Zn_{1/3}O_3$ to four- and five-component systems on its base, changes of its electrophysical and structural parameters are similar to those described above (Fig. 1.2).

In all cases with an increase of N, there is observed a noticeable decrease of the parameter c of the perovskite cell due to an insignificant decrease or constancy of the parameter a. This reduces the spontaneous deformation, characterized by a homogeneous parameter of deformation δ [57], which may be due to the disordering of the structure during the introduction of the foreign ions into the crystal lattice.

The determination of the MR and its position on the PDs is performed by studying the concentration dependences of the most important electrophysical parameters of SSs, which allows us to distinguish the regions of their extreme values or favorable combinations for various applications on the PDs.

The choice of the number of the components is based on the analysis of the change in the electrophysical and structural parameters of SSs during the transition

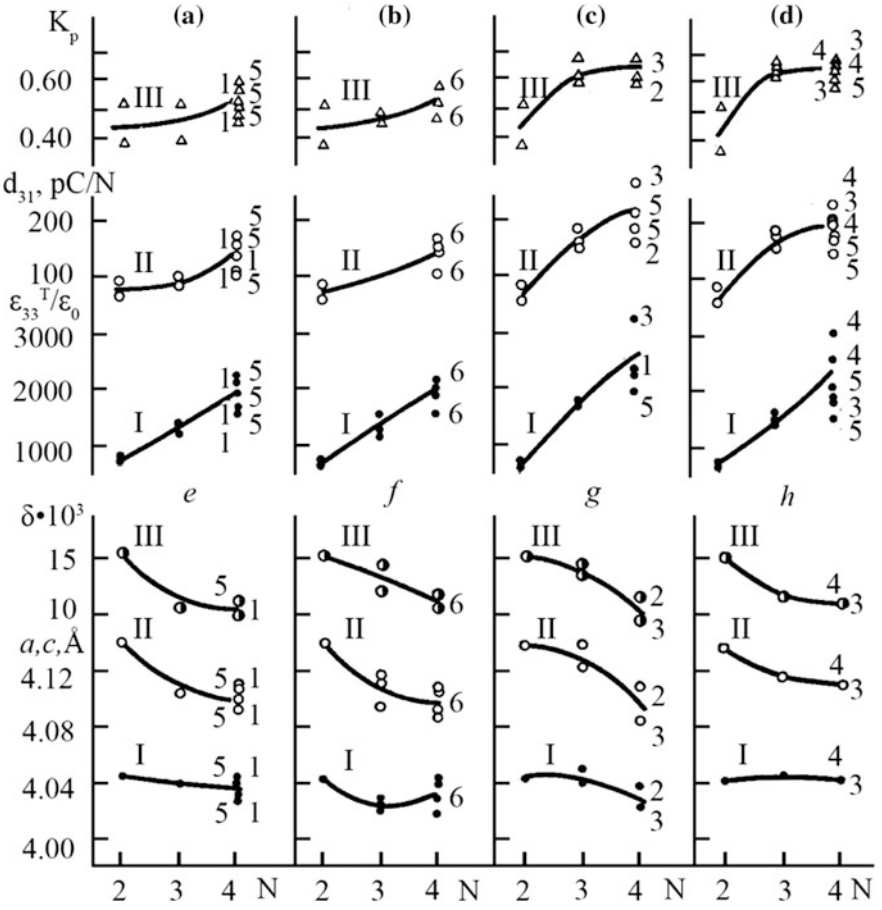

Fig. 1.1 Dependences of the electrophysical parameters $\varepsilon_{33}^T/\varepsilon_0$ (I), d_{31} (*II*), K_p (*III*) (**a**–**d**), as well as parameters of the perovskite unit cell a (I), c (II) and homogeneous deformation parameter δ (III) (**e**–**h**) from the number of components N in the samples, based on the double system $PbTiO_3$–$PbZrO_3$, in which the third component is $PbNb_{2/3}Zn_{1/3}O_3$ (**a**, **e**); $PbNb_{2/3}Mg_{1/3}O_3$ (**b**, **f**); $PbW_{1/2}Cd_{1/2}O_3$ (**c**, **g**); $PbW_{1/3}Bi_{2/3}O_3$ (**d**, **h**); and the fourth is $PbNb_{2/3}Co_{1/3}O_3$ (1), $PbW_{1/2}Co_{1/2}O_3$ (2), $PbW_{1/2}Ni_{1/2}O_3$ (3), $PbW_{1/2}Mg_{1/2}O_3$ (4), $PbNb_{2/3}Mg_{1/3}O_3$ (5), $PbNb_{2/3}Zn_{1/3}O_3$ (6); samples of the binary system were prepared according to conventional technology, triple and quadruple, according to ceramic technology (**a**, **b**, **e**, **f**) and hot pressing method (**c**, **d**, **g**, **h**) [10]

from the two-component system of PZT to three- and four-component systems, based on it [10] (Fig. 1.1) and from the three-component system Pb(Ti, Zr)O_3–$PbNb_{2/3}Zn_{1/3}O_3$ to four- and five-component on its base [13] (Fig. 1.2). Figure 1.1 shows the dependences of the structural and electrical parameters on the number of the components N. For comparison, there were chosen SSs with a close content of the corresponding components, located near the tetragonal boundary of the MR. It is seen that with increasing of N (Fig. 1.1) the permittivity $\varepsilon_{33}^T/\varepsilon_0$ increases.

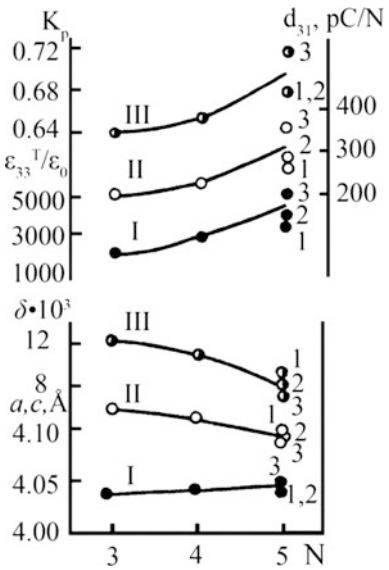

Fig. 1.2 The electrophysical parameters $\varepsilon_{33}^{T}/\varepsilon_0$ (I), d_{31}(II), K_p(III) and the structural parameters a (I), c(II), δ(III) as functions of the number N of components in solid-solution systems based on $PbTiO_3$–$PbZrO_3$–$PbNb_{2/3}Zn_{1/3}O_3$; data points 1, 2, 3 refer to three distinct five-component systems [13]

This suggestion was confirmed in the paper [18], in which we studied a number of SSs of the four-component system (Pb, Sr)NiO_3–$PbZrO_3$–$PbW_{1/2}Mg_{1/2}O_3$–$PbNb_{2/3}Zn_{1/3}O_3$ and two 5-component systems based on it. The content of the first three components of the 4-component system remained unchanged during the transition to 5-component systems, while the fourth part of the $PbNb_{2/3}Zn_{1/3}O_3$ component was substituted by the complex oxide $PbNb_{2/3}B''_{1/3}O_3$ ($B'' = Mg^{2+}$, Ni^{2+}) (there were substituted the ions of approximately one ionic radius). It follows from general statements [59] that the higher translational parameter a corresponds to higher degrees of the short-range order in the arrangement of different atoms along the sites of the sublattice.

The introduction of disorder into such an arrangement (alongside with different disordered displacements of the atoms) should lead to the increase of a.

The results of the precision X-ray diffraction studies have shown that during the transition from 4-component system to 5-component systems, parameter a increases due to the simultaneous decrease in the homogeneous strain parameter in the tetragonal phase of δ_T (Fig. 1.3). This agrees with the data of the papers [10, 13].

The transition to 6-component systems, as shown by the results of the analysis [28] (Fig. 1.4), leads to the decrease of δ, but K_p also decreases, and the growth of $\varepsilon_{33}^{T}/\varepsilon_0$ and d_{31} slows down. Thus, it can be concluded that the 5-component systems, based on the PZT, provide the optimal combinations of the electrophysical parameters of SSs.

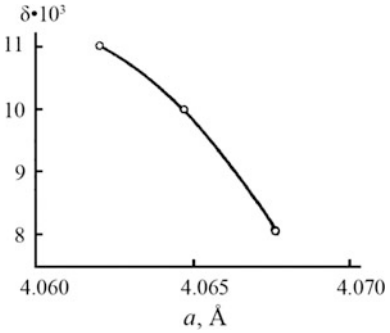

Fig. 1.3 Dependence of the homogeneous strain parameter δ on the parameter a for the systems of solid solutions (Pb,Sr)TiO_3–$PbZrO_3$–$PbW_{1/2}Mg_{1/2}O_3$–$PbNb_{2/3}Zn_{1/3}O_3$–$PbNb_{2/3}B''_{1/3}O_3$ [18]

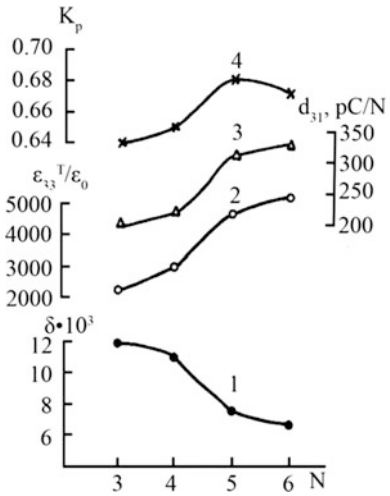

Fig. 1.4 Dependence of the parameters on the number of components N in solid solutions of three-, four-, five- and six-component systems on the same basis $PbTiO_3$–$PbZrO_3$–$PbNb_{2/3}Zn_{1/3}O_3$–$PbW_{1/2}Mg_{1/2}O_3$: *1*—δ; *2*—$\varepsilon_{33}^T/\varepsilon_0$; *3*—$d_{31}$; *4*—$K_p$ [28]

1.4 Multicomponent Systems and the Role of the Number of Components in the Formation of Macroproperties of Solid Solutions, Based on NAM

1.4.1 PDs of Two and Three-Component Systems, Based on Niobate

The information, accumulated to the present time, indicates that the only real alternative to the PZT-composition are niobium-containing systems. Moreover, they are the most complex, and among them, there are those, based on the compounds involving alkali metals.

On the one hand, the discrepancy between the radii of alkali cations and the parameters of the inter-octahedral voids, which they occupy in the perovskite structure, determines its "looseness". As a result, there is ease of stability loss,

which leads to the appearance of a series of successive phase transformations and the formation of the states, which "respond" differently on the external impact. It is, to a certain extent, the reason of the manifestation of three qualities of complex niobium oxides: (i) polymorphism of compounds, (ii) morphotropy and (iii) non-stoichiometry of the composition [60].

On the other hand, crystal-chemical structural features contribute to the hydrolysis of the initial niobium substances during the synthesis and to narrowing of the interval of its optimum temperatures. They also contribute to increased reactivity of the reagents and high volatility of alkali metals at relatively low temperatures, excessive anisotropic growth of giant ideomorphic grains during recrystallization, self-destruction of ceramics and their polarization electrolysis. All these causes (and many other things) lead to the critical dependences of the properties of niobate materials on the thermodynamic background (the conditions of obtaining).

Finally, the known determining influence on the macroproperties of niobate media of the phase, granulometric, defective, and rheological state of niobium pentoxide, the main initial reagent, involved in the synthesis of alkali niobates, and the problems, associated with the variable valence of niobium, make the interpretation of many scientific results ambiguous. Moreover, there are grounds to consider the formation kinetics of this class of substances from the standpoint of self-organization effects, which we noted earlier in [39].

The illustrations of the above-mentioned features are the PDs of two- and three-component systems, based on sodium niobate (Figs. 1.5 and 1.6), which are distinguished by a great variety of phase transformations in comparison with systems, based on PZT. In the system $(Na_{1-x}Li_x)NbO_3$ (Fig. 1.5a), 13 states are observed at room temperature, in the solubility range of the components ($\sim$14.5 mol% $LiNbO_3$), including 7 areas of coexistence of the phases of different nature. X-ray methods established the location of 3 MRs, in which the symmetry of the cell and regions with a change in the isomorphic type of SSs vary in different ways. The resulting Rh-phase in the interval $0.1075 \leq x \leq 0.1310$ is similar to the phase of N sodium niobate at $T < 170$ K [61]. This is supported by the same type of crystal structure of SSs and $NaNbO_3$ data (perovskite type), by the presence in both cases of a superstructure, associated with doubling of the axial vectors of the perovskite cell (in $NaNbO_3$ at $T < 170$ K). Due to the "crushing" of oxygen octahedral, it is supported by the closeness of the parameters of the perovskite Rh-cell of SSs with $0.1075 \leq x \leq 0.1310$ (at $T = T_{room}$) and $NaNbO_3$ (at $T < 170$ K): $a = 3.902$ Å, $\alpha = 89°\ 6'$ and $a = 3.908$ Å, $\alpha = 89°\ 13'$, respectively.

In the system (Na, Pb)(Nb, Ti)O_3 (Fig. 1.5b), SSs with a perovskite-type structure are formed throughout the concentration range of the components ($0 \leq x \leq 1.0$). The presence of 19 phase states, including 9 MRs, separates the phases with different symmetry and multiplicity of the perovskite subcell, with the different electrical, isomorphic type of SSs. In the (Na, K)NbO_3 system (Fig. 1.5c), a continuous series of SS is formed. Radiographic and dielectric methods revealed 13 phase states, including 7 MRs, separating regions with different types of SSs, electrical ordering, superstructure. The appearance of phase transition in these

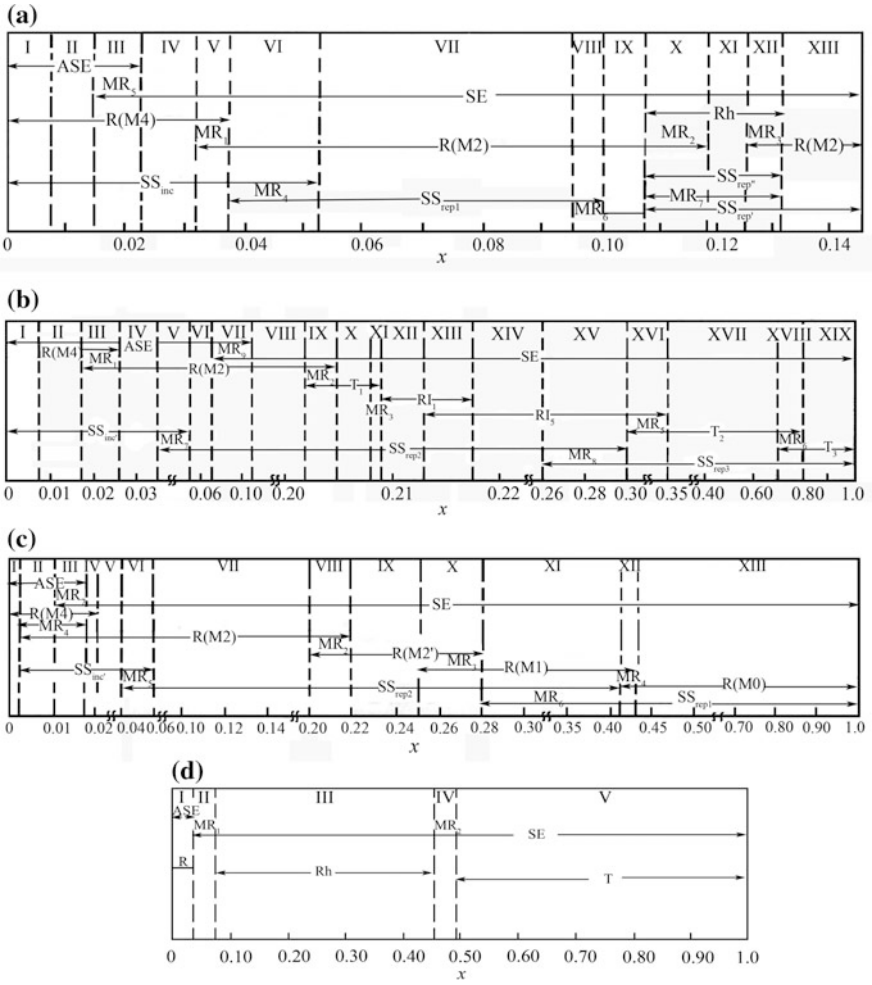

Fig. 1.5 **a** Phase diagram of the SSs system (Na, Li)NbO_3. **b** Phase diagram of the SSs system (Na, Pb)(Nb, Ti)O_3. **c** Phase diagram of the SSs system (Na, K)NbO_3. **d** Phase diagram of the SSs system $PbZr_{1-x}Ti_xO_3$ [62]

systems is connected with a change in the type of dipole ordering (ASE, SE, PT), the multiplicity of the perovskite subcell (multiplicative phase transition), isomorphic SSs species (configurational phase transitions).

In the PZT system (Fig. 1.5d), a continuous series of SS is formed in the entire concentration range ($0 \leq x \leq 1.0$). X-ray diffraction revealed 5 phase states, including 2 MRs separating regions with different types of SSs and 3 phases: rhombic, rhombohedral, and tetragonal [62]. In [63] the authors established the

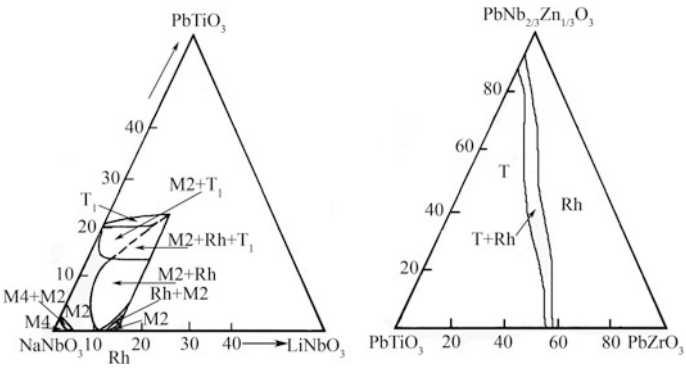

Fig. 1.6 Phase diagrams of three-component systems

presence of a monoclinic phase in the concentration range $0.453 \leq x \leq 0.477$ at room temperature. Unlike the above-mentioned two-component systems, based on sodium niobate, PD of the PZT system is much simpler.

In Fig. 1.6 for comparison, there are given PDs of two three-component systems: based on PZT ($PbTiO_3$–$PbZrO_3$–$PbNb_{2/3}Zn_{1/3}O_3$) and on the base of sodium niobate ($NaNbO_3$–$LiNbO_3$–$PbTiO_3$). If the diagram of the first system is divided into two regions: tetragonal and rhombohedral with the MR between them (T + Rh), then on the second PD there is a whole set of MRs between the tetragonal, rhombohedral and rhombic (monoclinic) phases (for example, M2 + T, M2 + R).

The dependencies between the structural and electrophysical parameters, established for the systems, based on the PZT [28], can be also distributed to a certain extent of the niobate systems. The main structural SSs characteristics of the considered type are the homogeneous strain parameter δ [57] and the associated degree of domain reorientations made during the η [64] polarization. However, it is necessary to take into account the "collapse of the structure" in niobate systems. For example, in the system (Na, Pb)(Nb, Ti)O_3 in a wide concentration range ($\sim$23 mol% $PbTiO_3$), superstructural lines are observed due to the "structure collapse", and their intensity decreases with increasing of $PbTiO_3$ concentration. The measured values of δ can be represented as a sum: $\delta_{meas} = \delta + \delta_{crump}$, where δ is the homogeneous strain parameter associated with spontaneous polarization, δ_{crump} is the deformation parameter due to "crumpling". To establish the correct relationship between structural and electrophysical parameters in niobate systems, it is necessary to isolate the true value of δ from the total by comparing the residual macroscopic deformation of the samples ($\Delta L/L_0$) with the degree of domain reorientations η.

1.4.2 *Four-Component System (1 − x)(Na, Li)NbO_3–x$Pb(Ti, Zr)O_3$ and the Role of the Number of Components in the Formation of Macroproperty of SSs*

In the general case, in the study of four-component systems, the main problem (as in the case of triple and double systems) is reduced to the search for MR, the, compositions of which have extreme properties. The method of searching for the MR in the four-component system consists of preliminary approximation of its boundary surfaces by planes, further refinement of the shape and extent, and the identification of the optimum composition zone inside it [28]. In this case, the approximation reflects the position of the MR in the system more accurately and the more informative data on the components (compounds) exist, as well as the double and triple systems that make up the four-component system.

There has been considered the system $(1 - x)(Na_{0.875}Li_{0.125})NbO_3$–$xPb(Ti_{0.5}Zr_{0.5})O_3$ (quasi-binary section of the four-component system $NaNbO_3$–$LiNbO_3$–$PbTiO_3$–$PbZrO_3$ with a step $\Delta x = 0.05$ in the range $0 < x \leq 0.20$ and $0.90 < x \leq 1.00$, $\Delta x = 0.10$ in the range $0.20 < x \leq 0.70$, $\Delta x = 0.025$ in the range $0.70 < x \leq 0.90$).

We performed the analysis of the properties of components and the nature of the phase transformations in the double (Fig. 1.5a, b, d) and ternary (Fig. 1.6) SSs systems, forming the investigated system. The results lead to the conclusion that PDs of the latter must be very complex, with a large number of structural transitions, "crumpling" of the structure, defect in both cation sublattices, etc. This makes it extremely difficult to obtain both the samples of the given composition and the subsequent interpretation of the obtained data. Take into account the presence of the information about MR in only two binary systems (Na, Li)NbO_3 and (Na, Pb)(Nb, Ti)O_3 with the common component of $NaNbO_3$, as well as the different character of the symmetry change in MR in (Na, Li)NbO_3–Pb(Ti, Zr)O_3 and Pb(Ti, Zr)O_3. Then the uncertainty of MR position (and the planes approximating it) becomes obvious in the studied system.

Due to this, we have obtained and investigated the samples of SSs of only one line, connecting the compositions of SSs with extremal properties, belonging to the (Na, Li)NbO_3 and Pb(Ti, Zr)O_3 systems, in the tetrahedron. This way of investigating the four-component system in this case seems to be the most rational, since it makes it possible to obtain a general characterization of the system by a minimum number of experiments.

Figure 1.7 shows a tetrahedron of compositions with isolated sections of the system (dot-dash line) and experimental points. The choice of the extreme components of the quasibinary section of the investigated four-component system is caused by the extreme nature of the electrophysical parameters in them [65–68]. The analysis of the obtained X-ray diffraction data make it possible to establish the formation of a continuous series of SS, crystallizing (i) in the Rh modification at

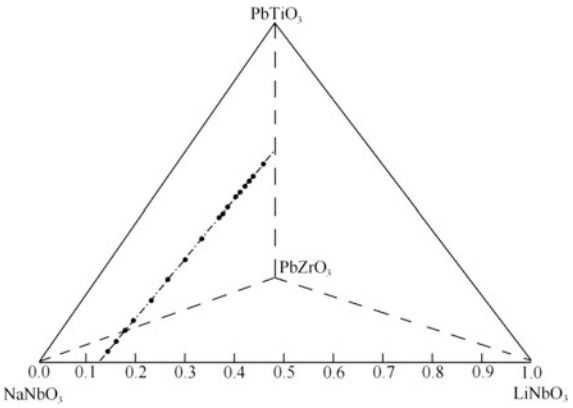

Fig. 1.7 Tetrahedron of the compositions of the (Na, Li) NbO_3–Pb(Ti, Zr)O_3 system with the allotted cut (dash-dot line) and experimental points

$0.00 < x < 0.05$, (ii) with a mixture of Rh- and R-phases (MR) at $0.05 \leq x$ 0.10, (iii) in *R*-modifications at $0.10 < x < 0.25$, (iv) with a tetragonal (T) distorted perovskite cell at $0.70 < x \leq 1.00$. The parameters of latter vary non-monotonously, experiencing anomalies at $x = 0.80$–0.90. The small values of the SS cell deformations with $0.25 < x \leq 0.70$ do not make it possible to clearly determine the type of symmetry in this region (presented as the pseudocubic (Psc)) and to establish the position of the second morphotropic transition into the T-phase. Presumably, a series of rhombic phases with close structural parameters form here.

Examination of the relationships "composition—structure—properties" in niobate systems shows that, due to the variety of combinations of parameters, they are significantly inferior to the systems, based on PZT [26]. This is facilitated, in particular, by a smaller difference in spontaneous deformation in different phases, a change in one direction of the dielectric constant during the polarization of the ceramic and structural features of the systems, based on sodium niobate [69–71].

Figure 1.8 shows the dependence of structural (δ) and electrophysical parameters ($\varepsilon_{33}^{T}/\varepsilon_0$, K_p, d_{31}) on the number of components (N) in SSs of two-, three-, four-component systems, based on sodium niobate.

For comparison, we selected SSs with a close content of the corresponding components, located near the rhombohedral (or tetragonal) boundary of the MR. It is seen that with increasing N, $\varepsilon_{33}^{T}/\varepsilon_0$ increases. A particularly noticeable increase of $\varepsilon_{33}^{T}/\varepsilon_0$ occurs with the transition to the four-component system. The piezomodule d_{31} also increases, practically repeating the course of $\varepsilon_{33}^{T}/\varepsilon_0$. The coefficient of electromechanical coupling K_p in the transition to the three-component system varies insignificantly, and it increases sharply at $N = 4$. The homogeneous deformation parameter δ, like multicomponent systems, based on PZT, decreases during the transition from two-component system to three-component one. This parameter increases slightly with the increasing of N when the transition to the 4-component system increases. It is apparently due to the large content of $PbTiO_3$ in SSs of the 4-component system. The analysis of the dependencies of the electrophysical

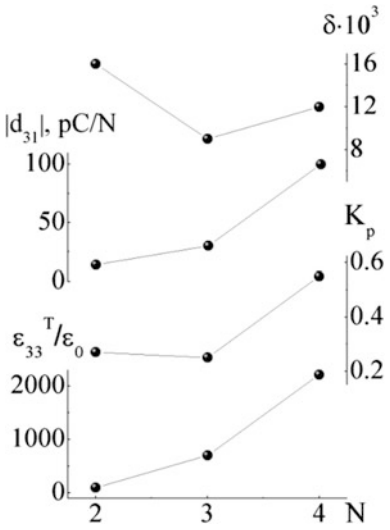

Fig. 1.8 Dependences on the number of components of the electrophysical parameters: $\varepsilon_{33}^{T}/\varepsilon_0$, K_p, $|d_{31}|$, δ in the SS $(1-x)NaNbO_3$–$xLiNbO_3$ (2); $xNaNbO_3$–$yLiNbO_3$–$zPbTiO_3$ (3); $(1-x)$ $[0.875NaNbO_3$–$0.125LiNbO_3]$–$xPb(Ti_{0.5}Zr_{0.5})O_3$ (4)

characteristics on N in both cases (systems, based on PZT and sodium niobate) testifies the effectiveness of the multicomponent systems building.

It should be noted that, materials in the systems, based on PZT, can be obtained within a single system by changing the concentration of the components (due to the sharp difference in the characteristics of the structure) [28]. At the same time, the selection of the materials within a separate niobate of the system is very limited (in particular, it is connected with the low K_p values outside its maximum). Here properties change mainly due to the transition from one system to another, that is, by replacing or introducing new components [72]. The study of the present multicomponent system on the base of the compounds with fundamentally different macro-responses makes it possible to obtain materials with a different set of parameters in one system. It allows one to use them in combined instrumentation complexes working in a fairly wide operating frequency range. Thus, SSs of the system with a low content of x is characterized by a combination of the characteristic parameters of niobate materials. So they demonstrate relatively low values of $\varepsilon_{33}^{T}/\varepsilon_0$ with sufficiently high values of V_1^E, which allows their using as the base materials of microwave devices. Compositions with $0.70 < x < 0.85$, which have high values of $\varepsilon_{33}^{T}/\varepsilon_0$ = (2000–2300), K_p = (0.550–0.569) and $|d_{31}|$ = (85.6–170.0) pC/N can be effectively used in LF-electromechanical converters.

Taking into account the obtained results, we plan further investigation of the multicomponent systems, based on the binary system $xNaNbO_3$–$yKNbO_3$: $xNaNbO_3$–$yKNbO_3$–$zPbTiO_3$; $xNaNbO_3$–$yKNbO_3$–$zPbTiO_3$–$mPbZrO_3$; $xNaNbO_3$–$yKNbO_3$–$zLiNbO_3$; $xNaNbO_3$–$yKNbO_3$–$zLiNbO_3$–$mPbTiO_3$; $xNaNbO_3$–$yKNbO_3$–$zLiNbO_3$–$mPbTiO_3$–$nPbZrO_3$.

1.4.3 The Role of Defectiveness in the Frmation of the Properties of Alkali Metal Niobates

We have revealed the role of the intrinsic (determined by the cation–anionic composition and the structure of SSs), the biographical (related to the thermodynamic prehistory of the objects), and the deformation (generated by external conditions) defects and their interactions in the appearance of new phase states, determining the features of the electrophysical properties of AM.

We have shown the possibility of inhibition of the interruption processes of the "polarization chains" by the vacancies populating them with superionic stochiometric ions. In this case, spontaneous deformation increases substantially and $\varepsilon_{33}^{T}/\varepsilon_0$. decreases. The simultaneous increase in K_p of such SSs is a consequence of their shift in the phase diagram towards the MR. Based on these results, we have proposed the method for crystal-chemical modeling of Nb-containing ferroelectric piezoceramics with a low dielectric constant.

We have shown that in the systems with morphotropic phase transitions, non-monotonous changes are observed in their vicinity, namely: changes of $T_{\text{sin } t}$, ρ_v, the activation energies of the formation reactions E_a, the width of the forbidden band E_d, and the degrees of reproducibility of the electrophysical properties. All SSs, which locate in the neighborhood or inside the MR have minimal $T_{\text{sin } t}$. The pressing rate of powder samples is determined by diffusion processes and depends on the degree of perfection of the crystal structure of the powder particles. Then the decrease of $T_{\text{sin } t}$ can take place due to the increased defectiveness of the MR compositions, in particular, with an increased concentration of lattice vacancies, the motion of which is facilitated along the extended defects (interphase boundaries). Because of the given value of the vacancy diffusion coefficient, the diffusion coefficient of atoms is proportional to the concentration of vacancies, and the diffusion processes in the MR are substantially activated. This is the reason for the intensification of sintering of the corresponding SSs. The high values of v and the light color of the SSs samples from the MR confirm absence of significant defect in oxygen, owing to which departure from the lattice of volatile ions (V_A) is assumed. The increase of V_A, which are acceptors in the NN-based SSs with the n-type conductivity, should lead to the increase of ρ_v. It is confirmed experimentally (we observed minimum in the $\rho_v - x$ dependence in PZT with the p-type conductivity in SSs from the MR).

A decrease of E_a in the region of the morphotropic phase transition indicates an increased reactivity of the initial mixtures of corresponding SSs. It is also a consequence of the non-phase MR and the resulting increased defectiveness of the SSs. The characteristic changes of E_a in the systems indicate that the composition peculiarities, associated with their belonging to MR, are already manifested at low calcination temperatures (670–970 K), when in the mixtures of the initial reagents, instead of SSs with a given composition, the clusters mainly formed, corresponding to all intermediate and final states of the mixtures.

It has been stated that the greatest dispersion of dielectric and piezoelectric parameters exists in the MR ($\varepsilon_{33}^{T}/\varepsilon_0$, K_p, d_{31}, Q_M, etc.). This is explained by the following. In the MR, there is a rapid change in parameters with insignificant variations in the composition. Due to this any violation of the prescribed stoichiometry (facilitated by the solid-phase synthesis) leads to significant change in the phase state, the structure, and, as a consequence, in the electrophysical properties of the SSs.

We have studied the processes of formation and development of bulk crystallochemical defects of the mesoscopic scale (clusters), presenting themselves the embryos of new phases in the systems with concentration PT. It is shown that their stepwise evolution in the process of approaching by SSs to MR passes through several stages, which find a response in the change in the macroscopic properties. An assumption has been made about the role of clusters in the formation of extreme electrophysical parameters of the objects.

Thus, the role of defectiveness in the formation of the properties of alkali metal niobates is manifested in the following: (i) stabilization of the ASE state; (ii) an anomalous change in the dielectric properties with the frequency of the measuring field at low concentrations of the secondary components in binary SS; (iii) the elimination of anion deficiency by crystallographic shear; (iv) the relationship between the "hard work" phase and the change in the type of isomorphic solid solution; (v) the non-monotonous behavior in the vicinity of the morphotropic region of the sintering temperature of SS, their specific electric resistance, the activation energy of the solid-state interaction, the width of the forbidden band, the magnitude of the Curie temperature shift due to the pressure at hot pressing, the degree of "dispersion" of the electrophysical properties; (vi) clustering of the structure, preceding the concentration PT.

1.5 Conclusion

We have performed the analysis of the SSs of multicomponent systems, based on lead titanate zirconate (PZT) and established the stages of the search for new functional materials for various applications. We have show the role of the number of components in the formation of electrophysical properties of SSs on the example of the study of 2-6-component systems, based on the PZT. It has been stated that 5-component systems provide optimal combinations of basic electrophysical parameters for most fields of applications.

We have considered phase diagrams of two-, three- and four-component systems, based on sodium niobate. It has been shown the complexity of phase diagrams, which are distinguished by a large number of structural transitions, by a variety of phase transformations in comparison with the systems, based on PZT. It has been stated that a significant increase in the electrophysical parameters in niobate systems is observed during the transition to 4-component system. We

revealed the effect of the defectiveness of solid solutions on the formation of their macroproperties. It is manifested, among other features, (i) in an anomalous change in the dielectric properties with the frequency of the measuring field at small concentrations of the second components in binary SSs; (ii) in the non-monotonous behavior near the MR of the sintering temperature of SSs, in their specific electric resistance. It has been stated that in one multicomponent system, materials with different sets of parameters can be obtained on the base of the compounds with fundamentally different macro-responses, which will allow using them in combined equipment complexes, working in a sufficiently wide operating frequency range.

Acknowledgements The results are obtained within the framework of the state task of the Ministry of Education and Science of the Russian Federation: Projects Nos. 3.6371.2017/8.9, 3.6439.2017/8.9; grant of the Russian Foundation for Basic Research No. 16-32-60095; Presidential Scholarships PS-3197.2016.3; PS-3330.2016.3. The equipment of the Center for Collective Use "Electromagnetic, Electromechanical and Thermal Properties of Solids" of the Research Institute of Physics, Southern Federal University was used in the research.

References

1. T. Haken, *Information and Self-Organization. A Macroscopic Approach to Complex Systems*, 3 edn. (Springer, Berlin, 2006), 258p
2. G. Shirane, K. Suzuki, J. Phys. Soc. Japan **7**, 333 (1952)
3. E. Sawaguchi, J. Phys. Soc. Japan **8**, 615 (1953)
4. B. Jaffe, W.R. Cook Jr., H. Jaffe, *Piezoelectric Ceramics* (Academic Press, London, 1971)
5. H. Jaffe, D.A. Berlincourt, Proc. IEEE **53**(10), 1372 (1965)
6. H. Ouchi, K. Nagano, S. Hayakawa, J. Am. Ceram. Soc. **48**, 630 (1965)
7. *Electronic Components Catalog 1974–75*. Matsushita Electric. Co., Ltd., Kadoma, Osaka, Japan, 624 (1975)
8. A.Y. Danciger, R.U. Devlikanova, S.I. Dudkina, B.P. Mordanov, T.V. Rogach, M.F. Kupriyanov, E.G. Fesenko, Izv. AS USSR. Ser. Phys. **35**(9), 1983 (1971) (in Russian)
9. E.G. Fesenko, A.Y. Danciger, O.N. Razumovskaya, R.U. Devlikanova, A.N. Klevcov, M.F. Kupriyanov, S.I. Dudkina, Izv. AS USSR. Ser. Phys. **39**(5), 1090 (1975) (in Russian)
10. E.G. Fesenko, A.Y. Danciger, O.N. Razumovskaya, S.I. Dudkina, Izv. AS USSR. Ser. Nonorg. Mater. **21**(7), 1235 (1985) (in Russian)
11. A.Y. Danciger, N.V. Dergunova, S.I. Dudkina, O.N. Razumovskaya, L.A. Shilkina, Izv. AS USSR. Ser. Phys. **54**(4), 717 (1990) (in Russian)
12. E.G. Fesenko, A.Y. Danciger, S.I. Dudkina, N.V. Dergunova, O.N. Razumovskaya, L.A. Reznichenko, L.A. Shilkina, Izv. AS USSR. Ser. Nonorg. Mater. **27**, 424 (1991) (in Russian)
13. A.Y. Danciger, N.V. Dergunova, S.I. Dudkina, E.G. Fesenko, Ferroelectrics **132**, 213 (1992)
14. A.Y. Danciger, N.V. Dergunova, S.I. Dudkina, O.N. Razumovskaya, L.A. Shilkina, V.A. Servuli, Ferroelectrics **132**, 207 (1992)
15. A.Y. Danciger, O.N. Razumovskaya, L.A. Reznichenko, S.I. Dudkina, AS USSR. Ser. Phys. **57**(6), 103 (1993) (in Russian)
16. A.Y. Danciger, O.N. Razumovskaya, L.A. Reznichenko, L.D. Grineva, R.U. Devlikanova, S. I. Dudkina, S.V. Gavrilyachenko, N.V. Dergunova, Nonorg. Mater. **29**(9), 1288 (1993) (in Russian)
17. A.Y. Danciger, S.I. Dudkina, L.A. Reznichenko, O.N. Razumovskaya, N.V. Dergunova, A.N. Klevcov, Nonorg. Mater. **31**(6), 831 (1995) (in Russian)

18. A.Y. Danciger, S.I. Dudkina, M.F. Kupriyanov, O.N. Razumovskaya, L.A. Reznichenko, AS USSR. Ser. Phys. **59**(9), 104 (1995) (in Russian)
19. A.Y. Danciger, L.A. Reznichenko, O.N. Razumovskaya, A.N. Klevcov, S.I. Dudkina, S.V. Gavrilyachenko, N.V. Dergunova, V.A. Servuli, AS USSR. Ser. Phys. **61**(2), 350 (1997) (in Russian)
20. L.A. Reznichenko, S.I. Dudkina, A.Y. Danciger, O.N. Razumovskaya, L.A. Shilkina, Nonorg. Mater. **37**(10), 1250 (2001) (in Russian)
21. L.A. Reznichenko, A.Y. Danciger, O.N. Razumovskaya, S.I. Dudkina, I.P. Raevskij, L.A. Shilkina, A.N. Klevcov, Nonorg. Mater. **37**(12), 1510 (2001) (in Russian)
22. A.Y. Danciger, O.N. Razumovskaya, L.A. Reznichenko, S.I. Dudkina, L.A. Shilkina, A.N. Klevcov, Nonorg. Mater. **37**(12), 1516 (2001) (in Russian)
23. A.Y. Danciger, O.N. Razumovskaya, L.A. Reznichenko, S.I. Dudkina, L.A. Shilkina, A.N. Klevcov, Nonorg. Mater. **38**(1), 84 (2002) (in Russian)
24. L.A. Reznichenko, L.A. Shilkina, O.N. Razumovskaya, E.A. Yaroslavceva, S.I. Dudkina, I.A. Verbenko, O.A. Demchenko, Y.I. Yurasov, I.N. Andryushina, A.A. Esis, Nonorg. Mater. **45** (2), 210 (2009) (in Russian)
25. L.A. Reznichenko, L.A. Shilkina, O.N. Razumovskaya, E.A. Yaroslavceva, S.I. Dudkina, I.A. Verbenko, O.A. Demchenko, I.N. Andryushina, Y.I. Yurasov, A.A. Esis, Nonorg. Mater. **45** (1), 69 (2009) (in Russian)
26. E.G. Fesenko, A.Y. Danciger, O.N. Razumovskaya, *New Piezoceramic Materials* (Rostov State University Press, Rostov-on-Don, 1983) (in Russian)
27. A.Y. Danciger, O.N. Razumovskaya, L.A. Reznichenko, L.D. Grineva, R.U. Devlikanova, S. I. Dudkina, S.V. Gavrilyachenko, N.V. Dergunova, A.N. Klevcov, *High-Efficient Piezoceramic Materials (Handbook)* (Kniga, Rostov-on-Don, 1994)
28. A.Y. Danciger, O.N. Razumovskaya, L.A. Reznichenko, V.P. Sahnenko, A.N. Klevcov, S.I. Dudkina, L.A. Shilkina, N.V. Dergunova, A.N. Rybyanec, *Multicomponent Systems Ferroelectric Complex Oxides: Physics, Crystallography, Technology. Design Aspects of Ferro-piezoelectric Materials* (Rostov State University Press, Rostov-on-Don, 2001) (in Russian)
29. L.A. Reznichenko, L.A. Shilkina, AS USSR Ser. Phys. **39**(5), 1118 (1975) (in Russian)
30. L.A. Reznichenko, L.A. Shilkina, JTP **47**(2), 453 (1977) (In Russian)
31. L.A. Shilkina, L.A. Reznichenko, M.F. Kupriyanov, E.G. Fesenko, JTP **47**(10), 2173 (1977) (in Russian)
32. I.P. Raevskij, L.A. Reznichenko, O.I. Prokopalo, E.G. Fesenko, Izv. AS USSR. Ser. Nonorg. Mater. **15**(5), 872 (1979) (in Russian)
33. O.N. Razumovskaya, L.A. Shilkina, L.A. Reznichenko, L.M. Rudkovskaya, Izv. AS USSR. Ser. Nonorg. Mater. **15**(12), 2207 (1979) (in Russian)
34. L.A. Reznichenko, A.V. Turik, L.A. Shilkina, V.A. Tais'eva, M.F. Kupriyanov, Izv. AS USSR. Ser. Nonorg. Mater. **16**(11), 2002 (1980) (in Russian)
35. L.A. Reznichenko, N.V. Dergunova, G.A. Geguzina, O.N. Razumovskaya, L.A. Shilkina, AS USSR Ser. Phys. **60**(10), 120 (1996) (in Russian)
36. L.A. Reznichenko, G.A. Geguzina, N.V. Dergunova, Nonorg. Mater. **34**(2), 222 (1998) (in Russian)
37. L.A. Reznichenko, O.N. Razumovskaya, L.A. Shilkina, A.Y. Danciger, S.I. Dudkina, I.V. Pozdnyakova, V.A. Servuli, JTP **70**(11), 58 (2000) (in Russian)
38. L.A. Reznichenko, A.Y. Danciger, O.N. Razumovskaya, S.I. Dudkina, L.A. Shilkina, I.V. Pozdnyakova, V.A. Servuli, JTP **70**(11), 63 (2000) (in Russian)
39. L.A. Reznitchenko, V.A. Alyoshin, A.N. Klevtsov, O.N. Razumovskaya, L.A. Shilkina, Ferroelectrics **247**(1–3), 95 (2000)
40. I.V. Pozdnyakova, L.A. Reznitchenko, V.G. Gavrilyatchenko, Ferroelectrics **247**(1–3), 89 (2000)
41. N.V. Dergunova, L.A. Reznitchenko, V.P. Sakhnenko, O.N. Razumovskaya, G.A. Gegusina, Ferroelectrics **247**(1–3), 107 (2000)

42. L.A. Reznitchenko, O.N. Razumovskaya, L.A. Shilkina, Y.A. Danciger, S.I. Dudkina, I.V. Pozdnyakova, V.A. Servuli, Ferroelectrics **247**(1–3), 125 (2000)
43. I.A. Verbenko, O.N. Razumovskaya, L.A. Shilkina, L.A. Reznichenko, K.P. Andryushin, Nonorg. Mater. **45**(6), 762 (2009) (in Russian)
44. I.A. Verbenko, O.N. Razumovskaya, L.A. Shilkina, L.A. Reznichenko, K.P. Andryushin, V. V. Kilessa, Nonorg. Mater. **45**(7), 877 (2009) (in Russian)
45. Off. J. Eur. Union **37**, 19 (2003); Off. J. Eur. Union **54**, 88 (2011)
46. Y. Saito, H. Takao, T. Tani et al., Nature **432**, 84 (2004)
47. Y. Guo, K. Kakimoto, H. Ohsato, Mater. Let. **59**, 241 (2005)
48. J.-F. Li, J.K. Wang, B.-P. Zhang, L.-M. Zhang, J. Am. Ceram. Soc. **89**, 706 (2006)
49. H. Du, F. Tang, F. Luo, D. Zhu, S. Qu, Z. Pei, W. Zhou, Mater. Res. Bul. **42**, 1594 (2007)
50. M.-R. Yang, S.-Y. Chu, C.-C. Tsai, J. Alloy Compd. **507**, 433 (2010)
51. R. Rai, I. Coondoo, R. Rani, I. Bdikin, S. Sharma, A.L. Kholkin, Curr. Appl. Phys. **13**, 430 (2013)
52. R. Rai, R. Rani, S. Sharma, A.L. Kholkin, J. Alloy Compd. **577**, 575 (2013)
53. Ch-S Chen, ChCh. Chou, Y-Sh Lin, P.-Y. Chen, H. Chen, Ceram. Int. **39**, 125 (2013)
54. S.-U. Park, J.-H. Koh, Mater. Res. Bull. **58**, 69 (2014)
55. On Strategy of National Security of Russian Federation up to 2020. RF Presidential Decree No. 537, 12 May 2009 (revision 01 July 2014) (in Russian)
56. K. Okadzaki, *Technology of Technical Dielectrics* (Ehnergy, Moscow, 1976) (in Russian)
57. E.G. Fesenko, *Perovskite Famity and Ferroelectricity* (Atomizdat, Moscow, 1972) (in Russian)
58. IEEE Standard on Piezoelectricity ANSI/IEEE Std 176–1987, New-York (1988). https://doi.org/10.1109/ieeestd.1988.79638
59. M.A. Krivoglaz, A.A. Smirnov, *Theory of Ordering Alloys* (FizMatLit, Moscow, 1958) (in Russian)
60. A.V. Voloshin, *Tantalum-Niobates: Systematics, Crystallochemistry and Evolution of Mineral Formation in Granite Pegmatites* (Nauka, Saint-Petersburg, 1993) (in Russian)
61. H.D. Megaw, Ferroelectrics **7**(1–4), 87 (1974)
62. I.N. Andryushina, L.A. Reznichenko, L.A. Shilkina, K.P. Andryushin, S.I. Dudkina, Ceram. Int. **39**(2), 1285 (2013)
63. B. Noheda, D.E. Cox, G. Shirane, J.A. Gonzalo, L.E. Cross, S.-E. Park, Appl. Phys. Lett. **74** (14), 2059 (1999)
64. Y.A. Kvapulin'skij, Z. Surov'yak, M.F. Kupriyanov, S.M. Zajcev, A.Y. Danciger, E.G. Fesenko, JTP **49**(3), 1049 (1979) (in Russian)
65. L.A. Reznichenko, L.A. Shilkina, O.N. Razumovskaya, S.I. Dudkina, E.S. Gagarina, A.V. Borodin, Nonorg. Mater. **39**(2), 187 (2003) (in Russian)
66. L.A. Reznichenko, L.A. Shilkina, O.N. Razumovskaya, E.A. Yaroslavceva, S.I. Dudkina, O. A. Demchenko, YuI Yurasov, A.A. Esis, I.N. Andryushina, Sov. Phys. Solids **51**(5), 958 (2009) (in Russian)
67. I.N. Andryushina, L.A. Reznichenko, L.A. Shilkina, K.P. Andrushin, YuI Yurasov, S.I. Dudkina, Ceram. Int. **39**(7), 7635 (2013)
68. L.A. Shilkina, S.I. Dudkina, I.N. Andryushina, L.A. Reznichenko, K.P. Andryushin, S.V. Titov, V.M. Shabanov, O.N. Razumovskaya, Sov. Phys. Solids **57**(4), 712 (2015) (in Russian)
69. L.A. Reznichenko, O.N. Razumovskaya, L.S. Ivanova, A.Y. Danciger, L.A. Shilkina, E.G. Fesenko, Nonorg. Mater. **21**(2), 282 (1985) (in Russian)
70. E.G. Fesenko, L.A. Reznichenko, L.S. Ivanova, O.N. Razumovskaya, A.Y. Danciger, L.A. Shilkina, N.V. Dergunova, JTP **55**(3), 601 (1985) (in Russian)
71. E.G. Fesenko, A.Y. Danciger, L.A. Reznichenko, M.F. Kupriyanov, L.A. Shilkina, M.B. Bogush, JTP **52**(2), 362 (1982) (in Russian)
72. E.G. Fesenko, A.Y. Danciger, L.A. Reznichenko, L.A. Shilkina, O.N. Razumovskaya, JTP **52** (11), 2262 (1982) (in Russian)

Chapter 2
Growth and Study of Zinc Oxide Nanorods Arrays on Piezoelectric Substrates

D. A. Zhilin, G. Y. Karapetyan, M. E. Kutepov, T. A. Minasyan, V. I. Yatsenko and E. M. Kaidashev

Abstract Our studies have shown the possibility of using the thermal synthesis method from Zn vapors to obtain ZnO nanorods arrays as a sensitive element for UV radiation SAW sensors. The piezoelectric properties of the $LiNbO_3$ substrate typically degrade upon nanorods growth at elevated temperature. This limitation is solved by using additional annealing of prepared structure at 550 °C in an oxygen atmosphere. The obtained ZnO NRs were investigated by scanning electron microscopy and photoluminescence.

2.1 Introduction

ZnO nanostructures have a wide range of applications in various devices. ZnO nanorods (ZnO NRs) are interesting due to electronic and optoelectronic properties [1, 2] and are often the functional elements of such devices as: ultraviolet (UV) nanolasers [3], LED [4, 5], chemical sensors [6], solar elements [7], sensors of UV radiation [8], nanogenerators [9]. The design of UV surface acoustic waves (SAW), based on zinc oxide nanostructures [10–13] as sensitive elements, is highly topical problem. SAW sensors are promising for cost effective wireless and battery-free devices.

A highly efficient SAW oscillator based photodetector with UV light sensitive ZnO film on the surface of a piezoelectric $LiNbO_3$ substrate was designed recently [14]. More specifically, the sensor is able to detect UV radiation with intensity as low as 1.8 μW cm^{-2}. UV SAW photodetector with ZnO NRs as light harvesting element shows even greater sensitivity, due to much larger surface area and better scattering properties of ZnO NRs, compared to ZnO film [15].

D. A. Zhilin (✉) · G. Y. Karapetyan · M. E. Kutepov · T. A. Minasyan · V. I. Yatsenko · E. M. Kaidashev
Southern Federal University, 200/1, Stachki Ave, Rostov-on-Don 344090, Russia
e-mail: d.a.zhilin@mail.ru

I. A. Parinov et al. (eds.), *Advanced Materials*, Springer Proceedings in Physics 207, https://doi.org/10.1007/978-3-319-78919-4_2

$LiNbO_3$ has a high electromechanical coupling coefficient. In contrast to other piezoelectric materials, such as $La_3Ga_5SiO_{14}$ (langasite) and $GaPO_4$, $LiNbO_3$ has a wide range of acceptable frequencies, and low acoustic losses [16].

However, heat-treated $LiNbO_3$ suffers from degradation due to the loss of oxygen [17]. Therefore, the design of $LiNbO_3$ based SAW devices, where high-temperature synthesis of zinc oxide nanostructures is needed such as carbothermic synthesis ($\sim$950 °C) is limited [18]. ZnO nanostructures are also widely designed by chemical methods, such as hydrothermal and electrochemical deposition [16, 19]. However, ZnO nanorods, grown using such methods, often create structural defects, which limit the performance of UV SAW photodetectors.

In our previous reports [20, 21], we designed arrays of ZnO NRs with great optical quality by using lower-temperature thermal evaporation methods of growth from Zn vapor at 550–600 °C. We also showed that, depending on the method of synthesis, i.e. the thermal or carbothermal method, the designed ZnO nanostructures show different concentrations of oxygen vacancies related defects. In particular, the photoresponse of ZnO structures with high/low concentration of oxygen vacancies reveal preferable green/UV spectral sensitivity [21].

In this chapter, we study the growth of ZnO NRs arrays on the piezoelectric lithium niobate substrate at reduced temperature by the thermal evaporation method and properties of designed UV SAW photodetector.

2.2 Experimental

A 128°-*YX* $LiNbO_3$ substrate was chemically cleaned. Thin ($\sim$100 nm) buffer ZnO layer was deposited on the $LiNbO_3$ substrate to relax the surface strains, induced by lattices parameters misfit and, thus, to reduce the ZnO nucleation barrier and improve the vertical orientation of nanorods. ZnO layer was prepared using pulsed laser deposition (PLD) method at 500 °C in oxygen ambient pressure of 2×10^{-2} mbar. Laser ablation was performed by focusing KrF (248 nm, 10 Hz) laser beam on rotating ceramic ZnO target to give a fluence of $\sim$2 J/cm^2. ZnO layer was deposited on the central part (5 mm) of the 9 × 20 mm substrate using shadow mask as shown in Fig. 2.1.

Vertically oriented ZnO nanorods were grown on the ZnO buffer layer by thermal evaporation method from Zn vapor in reactor shown in Fig. 2.2. The reactor consists of a pumped quartz tube, which temperature is maintained by

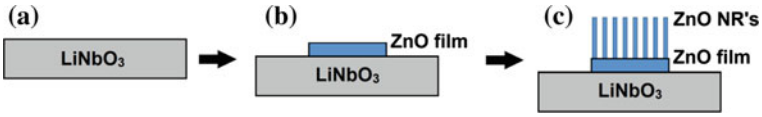

Fig. 2.1 **a** $LiNbO_3$ substrate; **b** $LiNbO_3$ substrate with the ZnO film; **c** final structure $LiNbO_3$/ZnO(film)/ZnO(NRs)

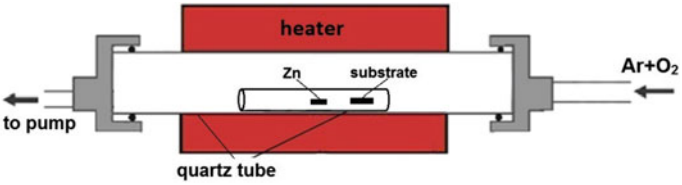

Fig. 2.2 Experimental setup, used for thermal evaporation method

horizontal furnace. Pressure and flow rate of Ar and oxygen gasses was controlled by 647C (MKS Instruments) mass-flow controller.

In contrast to [13], our reactor was equipped by a small quartz tube (with a length of 8.5 cm, an outer diameter of 1.3 cm, an inner diameter of 1.0 cm), open on both sides. The precursor (99.9999% Zn metal granule) and the substrate were placed in a small quartz tube, which was in a larger 32 mm tube of reactor, as shown in Fig. 2.2. A small reactor volume enables localization of Zn vapor and makes the optimization of synthesis parameters more flexible. The center of the ZnO NRs growth region was 3.5 cm downstream from the Zn metal granule. Reactor was evacuated to $\sim$1 mbar and filled with Ar gas to atmospheric pressure and again pumped down to $\sim$1 mbar. This procedure was carried out twice to remove the residual atmospheric oxygen from the volume. The gas mixture pressure was maintained at 11 mbar during reactor heating and synthesis. The reactor was heated to the working temperature for 20 min and continuous argon flow of 240 sccm was maintained at this stage. Upon reaching the working temperature of 550 °C an oxygen flow of 6 sccm was also introduced to reactor. The ZnO nanorods were grown for 30 min.

The temperature of a substrate in thermal evaporation method is almost two times lower, compared to 900–950 °C in carbothermal synthesis. However, the piezoelectric properties of the $LiNbO_3$ substrate also become slightly worse due to the loss of oxygen. To compensate the lost oxygen, the sample was annealed during 30 min at 550 °C immediately after the synthesis. The Ar flow was stopped and pure oxygen of 500 sccm was introduced to reactor. The oxygen pressure was maintained at 400 mbar. The sample was cooled down in this oxygen flow. We found that such annealing in oxygen flow nearly completely restores the piezoelectric properties of a $LiNbO_3$ substrate.

The surface morphology of obtained ZnO NRs is shown in Fig. 2.3.

The UV SAW photodetector was examined by using a made experimental setup shown in Fig. 2.4 and used earlier elsewhere [22]. Briefly, the sample is positioned on top of two perfectly aligned 128°-*YX* $LiNbO_3$ polished substrates with unidirectional interdigital transducer (IDT) with an internal reflectors on each piece. The central frequency of the IDTs is equal to 120.7 MHz. The edges of the substrates are rounded and covered with an SAW absorber to avoid reflection on the edges. The acoustic wave may easily propagate back and forward in all three $LiNbO_3$ pieces with minimal losses. The samples were illuminated by HeCd laser with

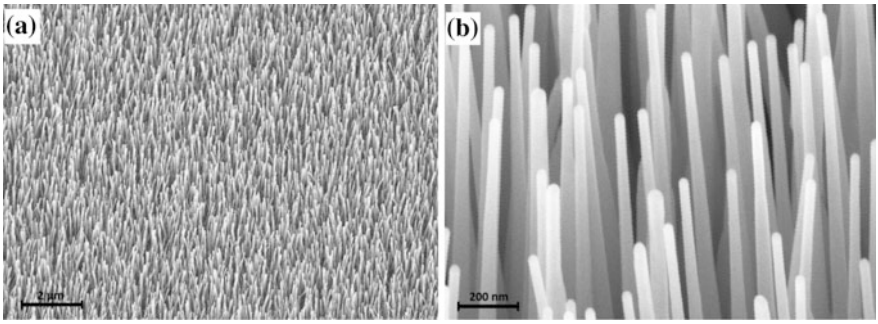

Fig. 2.3 **a**, **b** SEM images of ZnO NRs arrays, obtained by thermal evaporation method

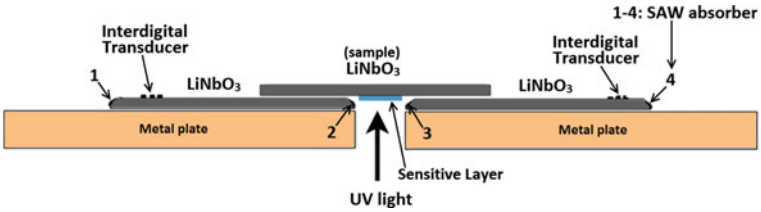

Fig. 2.4 Experimental setup for studying UV SAW detectors

325 nm wavelength. The laser beam was focused by using a lens on the surface of a sample with light emission power density of 3.2 mW cm^{-2}.

Both passed and reflected SAWs were analyzed by using Network Analyzer Obzor-304, Planar.

2.3 Results and Discussion

The photoluminescence spectra of ZnO NRs, shown in Fig. 2.5, reveal intense exciton, related emission near 380 nm and a broad by $\sim$5 times lower emission band, related to oxygen vacancies and other structural defects. The UV/green PL emission ratio of nanorods, prepared by present thermal evaporation method, is much higher, compared to those, observed for similar nanorods, obtained at elevated temperature by carbothermal method. The ZnO nanorods, obtained by the thermal evaporation method, have lower concentration of defects, associated with an oxygen vacancies, compared to those, grown by carbothermal method. A more detailed comparison of properties of ZnO NRs, obtained by these two methods, was reported by us elsewhere [21]. In particular, it was concluded that ZnO NRs, obtained by thermal evaporation method, have higher UV sensitivity than ZnO NRs, obtained by carbothermal method.

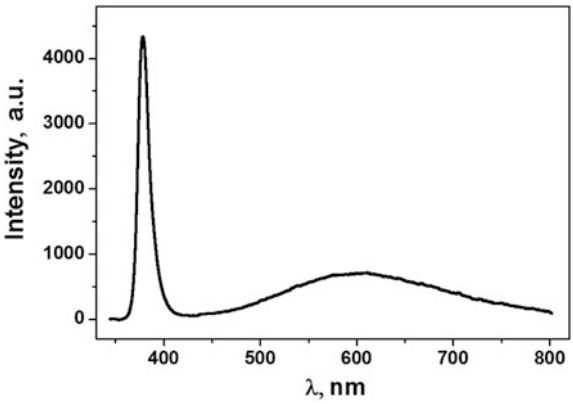

Fig. 2.5 Photoluminescence spectrum of ZnO NRs obtained by thermal evaporation method

Extra charge carriers are generated in ZnO NRs upon the exposure by UV radiation. Acoustic-electronic interaction results in attenuation of SAW and a reduction of the surface wave velocity. Both effects can be used to detect UV radiation.

The attenuation (Γ) and the velocity change (Δυ) of SAW can be described as

$$\frac{\Delta\upsilon}{\upsilon_0} = \frac{K^2}{2}\frac{1}{1+\left(\sigma/\sigma_m\right)^2}, \tag{2.1}$$

$$\Gamma = K^2\frac{\pi}{\lambda}\frac{\sigma/\sigma_m}{1+\left(\sigma/\sigma_m\right)^2} \tag{2.2}$$

where $K^2 = e_0^2/\varepsilon c$ is the effective electromechanical coupling coefficient, σ is the conductivity of the ZnO film (film sheet conductivity), $\sigma_m = \omega_m \varepsilon \varepsilon_0$ is the material constant, λ is the wavelength of SAW.

SAW is found to be gradually attenuated/reflected by prepared ZnO(NRs)/ZnO (film) structure and does not pass through it. The SAW, reflected from the photosensitive region, returns to ITD, which excites SAW. Therefore, we studied UV sensitivity of ZnO NRs via SAW reflection.

The S_{11} frequency response of a SAW, reflected from ZnO (NRs)/ZnO (film) structure is shown in Fig. 2.6. The reflected wave is time-shifted to the generated wave, which causes an interference effect due to the superposition of the generated and reflected SAW and leads to oscillations on the frequency response.

Under exposure by UV light, the oscillations on the S_{11} curve become much lower evidencing that the reflected SAW is attenuated because of the acoustic-electronic interaction of the electric field of the SAW with light generated carriers (Fig. 2.6b).

The Fourier transforms of the S_{11} characteristics, which represent time SAW response are shown in Fig. 2.7a, b for the cases with and without UV illumination,

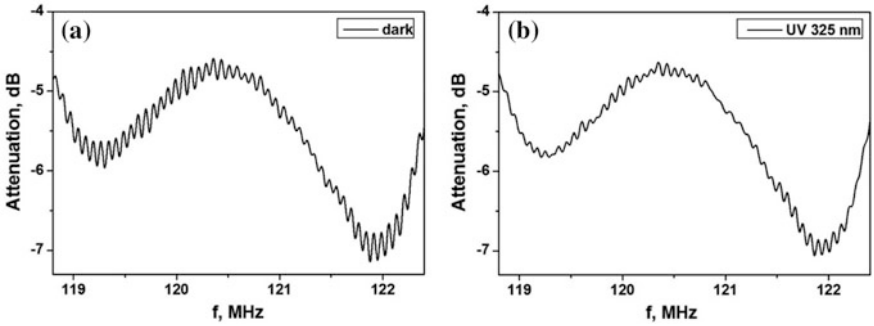

Fig. 2.6 Frequency characteristic of the sample ZnO (NRs)/ZnO (film)/$LiNbO_3$: **a** without UV radiation, **b** with UV radiation (325 nm)

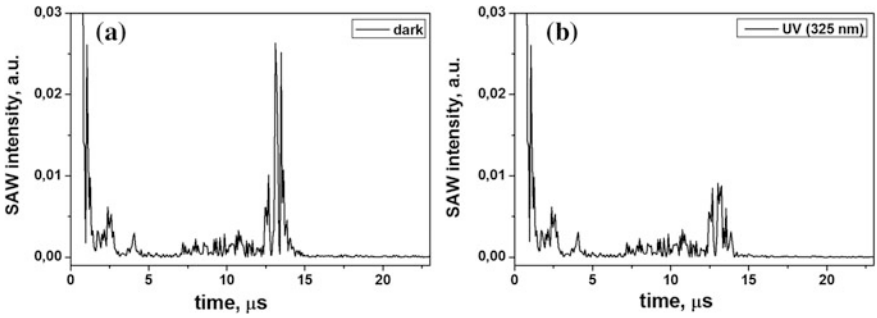

Fig. 2.7 Fourier transformation of the amplitude-frequency characteristic: **a** without exposure, **b** with exposure to UV light (325 nm)

respectively. The amplitude of the reflected wave is decreased by $\sim 70\%$ under applied UV irradiation.

2.4 Conclusion

In this paper, we demonstrate a possibility to use the thermal evaporation method to grow ZnO nanorod array from Zn at 550 °C to obtain a UV-sensitive element on the $LiNbO_3$ substrate without degrading the $LiNbO_3$ piezoelectric properties. We found that a relight SAW is gradually attenuated by ZnO nanorod array. However, a SAW reflection from the photo-sensitive ZnO nanorod array can be used for UV light detection. We believe that the concept to use SAW reflection from ZnO nanorod array may be used for remote control of UV light sensitive SAW-based RF-ID tags.

Acknowledgements This research work is supported by the Russian Education and Science Ministry, the project No. 16.5405.2017/8.9 and Grant RFBR-MOST № 16-58-52013 MNT_a.

References

1. A.B. Djurišić, Y.H. Leung, Small **2**, 944 (2006)
2. C.-Y. Chen, M.-W. Chen, J.-J. Ke, C.-A. Lin, J.R.D. Retamal, J.-H. He, Surface effects on optical and electrical properties of ZnO nanostructures. Pure Appl. Chem. **82**, 2055 (2010)
3. M.H. Huang, S. Mao, H. Feick, H. Yan, Y. Wu, H. Kind, E. Weber, R. Russo, P. Yang, Science **292**, 1897 (2001)
4. A. Nadarajah, R.C. Word, J. Meiss, R. Könenkamp, Nano Lett. **8**, 534 (2008)
5. X.W. Sun, J.Z. Huang, J.X. Wang, Z. Xu, Nano Lett. **8**, 1219 (2008)
6. J.Y. Park, D.E. Song, S.S. Kim, Nanotechnology **19**, 105503 (2008)
7. M. Law, L.E. Greene, J.C. Johnson, R. Saykally, P. Yang, Nat. Mater. **4**, 455 (2005)
8. S.P. Ghosh, K.C. Das, N. Tripathy, G. Bose, D.H. Kim, T.I. Lee, J.M. Myoung, J.P. Kar, IOP Conf. Ser. Mater. Sci. Eng. **115**, 012035 (2016)
9. Y. Qin, X. Wang, Z.L. Wang, Nature **451**, 809 (2008)
10. A.S. Bagdasarian, V.G. Dneprovski, G.Y. Karapetyan, S.A. Bagdasaryan, in *Piezoelectric and Related Materials: Research and Applications*, ed. by I.A. Parinov (Nova Science Publishers, New York, 2012), p. 189
11. P. Sharma, K. Sreenivas, Appl. Phys. Lett. **83**, 3617 (2003)
12. P. Sharma, S. Kumar, K. Sreenivas, J. Mater. Res. **18**, 545 (2003)
13. A.A. Mohanan, R. Parthiban, N. Ramakrishnan, J. Micromech. Microeng. **26**, 025017 (2016)
14. D.-L. Chenga, K.-S. Kaoa, C.-H. Loa, C.-H. Liangb, L.-P. Chanc, C.-W. Tsung, Y.-Y. Li, Ultraviolet sensing system using ZnO based surface acoustic wave oscillator. *Proceedings of the 3rd International Conference on Industrial Application Engineering*. vol. 435 (2015)
15. W.-S. Wang, T.-T. Wu, T.-H. Chou, Y.-Y. Chen. A, ZnO nanorod-based SAW oscillator system for ultraviolet detection. Nanotechnology **20**, 135503 (2009)
16. R. Fachberger, G. Bruckner, G. Knoll, R. Hauser, J. Biniasch, L. Reindl, IEEE Trans. Ultrason. Ferroelectr. Freq. Control **51**, 1427 (2004)
17. J. Hornsteiner, E. Born, G. Fischerauer, E. Riha, in *Proceedings 1998 IEEE International Frequency Control Symposium* (1998), p. 615
18. N.V. Lyanguzov, E.M. Kaydashev, I.N. Zakharchenko, O.A. Bunina, Tech. Phys. Lett. **39**, 767 (2013)
19. P.K. Samanta, A.K. Bandyopadhyay, Appl. Nanosci. **2**, 111 (2012)
20. V.I. Pushkariov, A.L. Nikolaev, E.M. Kaidashev, in *Advanced Materials—Studies and Applications*, ed. by I.A. Parinov, S.-H. Chang, S. Theerakulpisut (Nova Science Publishers, New York, 2015), p. 51
21. D.A. Zhilin, N.V. Lyanguzov, V.I. Pushkariov, L.A. Nikolaev, V.E. Kaydashev, E. M. Kaidashev, in *Advanced Materials—Studies and Applications*, ed. by I.A. Parinov, S.-H. Chang, S. Theerakulpisut (Nova Science Publishers, New York, 2015), p. 57
22. G.Y. Karapetyan, V.E. Kaydashev, D.A. Zhilin, T.A. Minasyan, K.G. Abdulvakhidov, E.M. Kaidashev, Use of multiple acoustic reflections to enhance SAW UV photo-detector sensitivity. Smart Mater. Struct. **26**, 035029 (2017)

Chapter 3
Ferroelectrically Hard Porous Ceramics: Fabrication, Properties and Ultrasonic Transducer Applications

I. A. Shvetsov, E. I. Petrova, M. A. Lugovaya, N. A. Shvetsova, S. A. Shcherbinin and A. N. Rybyanets

Abstract New family of porous ceramics, based on ferroelectrically hard PZT compositions with properties, combining better parameters of PZT ceramics and 1–3 composites for high intensity ultrasonic applications, are developed. The fabrication methods, measurement techniques, and the results of experimental study of ferroelectrically hard porous piezoceramics are described. The physical justification of the applicability of porous ceramics for high intensity focused ultrasound applications (HIFU), as well as HIFU transducers designs, the results of acoustics field measurements, and the results of ex vivo experiments on biological tissues are also presented. Developed ferroelectrically hard porous piezoceramics are characterized by increased values of piezoelectric and electromechanical coupling factors, reduced values of acoustic impedance and lateral parasitic modes of vibration, as well as better resonance characteristics compared to dense piezoceramic elements. Moreover, porous piezoceramics elements are easily processed, more stable against thermal and mechanical influences and provide higher adhesion of electrodes in comparison with standard dense piezoceramic and composite elements that makes it prospective materials for high power ultrasonic applications. It was shown that the use of ferroelectrically hard porous ceramics simplifies the manufacturing process, allows one to increase the main operational characteristics of HIFU transducers and makes them competitive in comparison with the standard ultrasonic transducers for promising applications in the field of medical therapy.

3.1 Introduction

Limited piezoceramic materials are currently available for use in ultrasonic transducer designs for medical diagnostics equipment, non-destructive testing (NDT), level-and flowmetry, and underwater acoustics [1], taking into account combina-

I. A. Shvetsov · E. I. Petrova · M. A. Lugovaya · N. A. Shvetsova
S. A. Shcherbinin · A. N. Rybyanets (✉)
Southern Federal University, 194, Stachky Ave, Rostov on Don, Russia
e-mail: arybyanets@gmail.com

I. A. Parinov et al. (eds.), *Advanced Materials*, Springer Proceedings in Physics 207, https://doi.org/10.1007/978-3-319-78919-4_3

tions of high efficiency (sensitivity), resolution (bandwidth) and operational requirements (working pressure, temperature etc.). The market of piezoelectric ceramics is currently characterized by a wide use of piezoceramic compositions, based on lead zirconate titanate (PZT), lead magnesium niobate (PMN), lead metaniobate (PN) and lead titanate (PT) [2, 3]. To date, practically all broadband ultrasonic transducers were built using strongly externally damped PZT or PN ceramics. Despite high Curie temperature, low mechanical quality factor, and low acoustic impedance, PN ceramics demonstrate weak piezoelectric properties. In addition, PN is very difficult in manufacture that is reflected in its high production cost [4].

Therefore, efforts have been made to replace PN ceramics by piezocomposites with 1–3 connectivity type [5, 6]. However, there are considerable operational limitations with this type of material, in particular, with respect to the maximum pressure and allowable working temperature [7]. Moreover, to date the production costs of 1–3 composite elements well exceeds the price of standard ultrasonic transducers.

Porous piezoelectric ceramics based on PZT compositions were proposed as a promising candidate for the replacement of PN ceramics in wide-band ultrasonic transducers for medical diagnostic and nondestructive testing equipment [8–11]. The use of piezoelectric porous ceramics simplifies the manufacturing process, allows one to increase the main operational characteristics of ultrasonic transducers and makes them competitive in comparison with the traditional designs. Intensive technological and research works as well as improvement of manufacture methods have allowed large-scale production of porous piezoelectric ceramics with controllable and reproducible properties and porosity [12–16]. To date, ferroelectrically soft PZT-type compositions were mainly used as initial materials for 1–3 composites and porous piezoelectric ceramics fabrication [12].

Meanwhile, the requirements for the characteristics of medical ultrasonic transducers have changed drastically in recent years because of the emergence of new fields of application, primarily, focusing ultrasound transducers of high intensity (HIFU) for ultrasonic ablation and therapy systems [17–19]. The emergence of new applications and meeting their specific demands stimulates the development and improvement of piezoelectric materials and technologies for their manufacture. At the same time, the main emphasis is shifted to improving the functional properties, miniaturization, compatibility with modern microelectronic technologies, durability and reliability of products, as well as reducing their costs [20].

With growing demand for piezoceramic properties for advanced piezoelectric and ultrasonic applications alongside with increasing operational requirements [21], porous piezoelectric ceramics based on ferroelectrically hard PZT compositions with specific characteristics (high durability, resistance to mechanical shocks, low acoustic impedance and high electromechanical characteristics) are of considerable interest from both scientific and practical point of view [22].

This chapter describes the fabrication method, measurement technique, and systematical experimental data for ferroelectrically hard porous piezoceramics.

The physical justification of the use of porous ceramics in HIFU applications, as well as HIFU transducers designs, results of acoustics field measurements, as well as the results of ex vivo experiments on biological tissues are also presented.

3.2 Experimental Results

As the starting piezoceramic materials, standard powders of the ferroelectric PZT compositions PCR-78, PCR-8, ZTSSt-3 were used [23]. Porous ceramics was fabricated by modified method of burning out of porophore agents. Complexes of organic compounds with various rheological (dispersity, particle shape and size) and physical (decomposition temperature) characteristics were used as the porophores. The use of special treatment regimes at the stages of powders grinding, burning out of the porophores and sintering the ceramics ensured the fabrication of a high-quality homogeneous porous ceramics with controlled parameters (porosity up to 70% and an average pore size $\sim$25 μm).

Measurements of elastic, dielectric, and piezoelectric parameters of the porous piezoceramic elements were performed on standard samples using the Agilent 4294A impedance analyzer according IEEE Standard [24] and the PRAP resonance spectra analysis program [25]. The PRAP program [26] analyzes the impedance spectra for determining the complex properties of the piezoelectric material and taking into account the features of measuring low-quality inhomogeneous materials. The character of porosity dependencies of elastic, dielectric, and piezoelectric parameters for all studied ferroeletrically hard porous PZT piezoceramics was practically similar taking into account the measurements accuracy.

Figures 3.1, 3.2, 3.3, 3.4 and 3.5 show dependences of main parameters of porous piezoceramics PCR-78 on relative porosity p, typical for ferroelectrically hard PZT compositions.

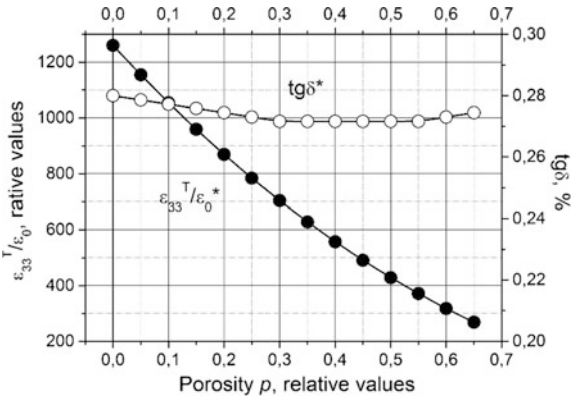

Fig. 3.1 Dependences of dielectric constant $\varepsilon_{33}^T/\varepsilon_0^*$ and dielectric loss tangent tgδ^* on relative porosity p for ferroelectrically hard porous piezoceramics PCR-78

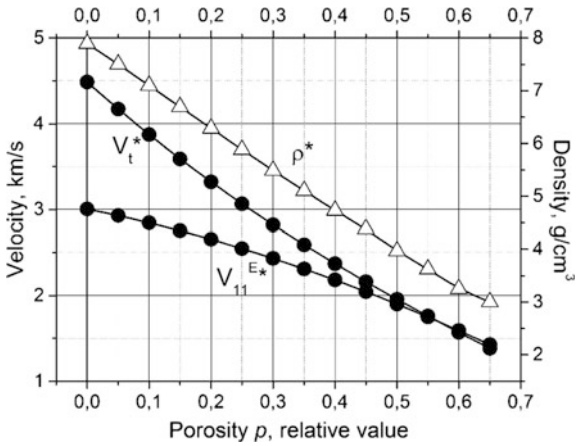

Fig. 3.2 Dependences of density ρ^* and sound velocity of thickness V_t^* and longitudinal V_{11}^{E*} modes of vibrations on relative porosity p for ferroelectrically hard porous piezoceramics PCR-78

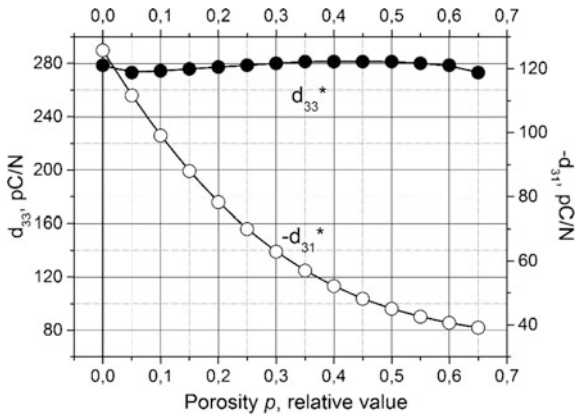

Fig. 3.3 Dependences of the piezoelectric moduli d_{33}^* and d_{33}^* on relative porosity p for ferroelectrically hard porous piezoceramics PCR-78

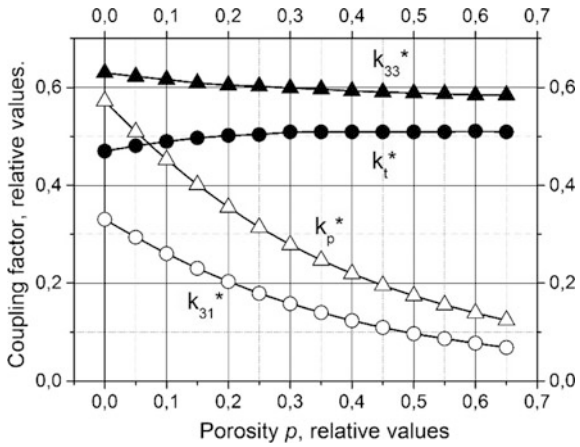

Fig. 3.4 Dependences of electromechanical coupling coefficients k_{33}^*, k_{31}^*, k_t^* and k_p^* on relative porosity p for ferroelectrically hard porous piezoceramics PCR-78

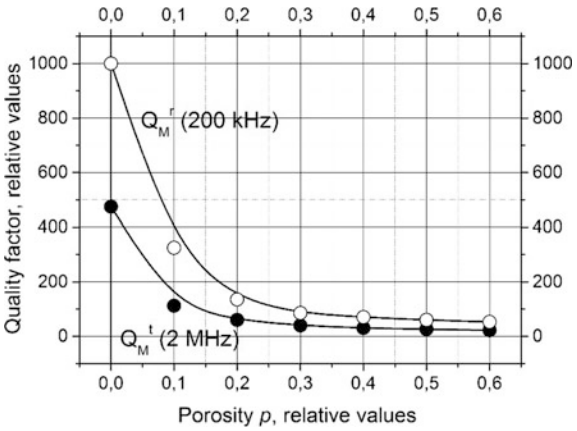

Fig. 3.5 Experimental dependences of mechanical quality factors of radial Q_M^{r*} and thickness Q_M^{t*} oscillation modes on relative porosity p for ferroelectrically hard porous piezoceramics PCR-78

The dielectric constant $\varepsilon_{33}^T/\varepsilon_0^*$ of ferroelectrically hard porous piezoceramics decreases practically linearly with increase in the porosity p (Fig. 3.1), which is due to a significant difference in dielectric permeabilities of piezoceramics and air. The dielectric loss tangent $\mathrm{tg}\delta^*$ of ferroelectrically hard porous ceramics decreases insignificantly with p grows in the entire range of porosity values (Fig. 3.1) and approaches the initial value only at $p > 0.65$. This is due to changes in the character of the domain structure and the mobility of the domain walls of piezoelectric ceramics. The more developed specific surface and the "defective" structure of ferroelectrically hard porous piezoceramics contribute to the fixation of domain walls and prevents different from the 180° rotations of the domains, which leads to decrease in $\mathrm{tg}\delta^*$.

The density ρ^* of the ferroelectrically hard porous piezoceramics decreases linearly with increasing p (Fig. 3.2), in accordance with the expression $\rho^* = \rho(1-\rho)$, where ρ is the theoretical density of dense piezoceramics.

The behavior of the velocity $V_{11}^{E*} = \sqrt{\frac{1}{\rho^* S_{11}^{E*}}}$ with increasing p (Fig. 3.2) is determined by the competing effect of changes in density ρ^* and elastic compliance S_{11}^{E*}, which increases rapidly due to the decrease in the elastic rigidity of the porous ceramic frame. The velocity $V_t^* = \sqrt{\frac{C_{33}^{D*}}{\rho^*}}$ decreases rapidly with increasing p (Fig. 3.2), which is also due to a faster decrease in the elastic rigidity $\left(C_{33}^{D*}\right)$ of the porous ceramic frame, as compared with the decrease in density ρ^*.

The piezoelectric modulus d_{33}^* of ferroelectrically hard porous piezoceramics changes insignificantly in the range $0 < p < 0.6$ (Fig. 3.3), which is due to the continuity of the ceramic quasi-rod structure of the porous piezoceramics in the direction of residual polarization (thickness of the element). Reduction in relative area of piezoactive phase, as in the case of 1–3 composites, is compensated by an increase in the specific pressure on the ceramic frame.

An increase in d_{33}^* are due to the more complete polarization of porous ceramics as compared to the dense material. Ferroelectrically hard porous piezoceramics are

capable of withstanding higher polarizing voltages without breakdown of the element. In addition, more developed surface and defective structure of porous ceramics contribute to the fixation of different from the 180° reversible rotations of domains, realized under polarizing field.

The decrease of $\left|d_{31}^{*}\right|$ with increasing p for ferroelectrically hard porous piezoceramics (Fig. 3.3) is obvious and is caused by violation of continuity of piezoceramic frame in lateral direction.

The electromechanical coupling coefficient k_{33}^{*} of ferroelectrically hard porous piezoceramics decreases insignificantly with an increase in porosity p (Fig. 3.4), which is due to the invariance of electro-mechanical coupling in the direction of residual polarization of the quasi-rod structure and absence of mechanical clamping in porous ceramic frame. A slight decrease in k_{33}^{*} is connected with increase in elastic compliance S_{33}^{E*} of the porous ceramic frame $\left(k_{33}^{*2}=d_{33}^{*2}/\left(\varepsilon_{33}^{T*}S_{33}^{E*}\right)\right)$. The behavior of electromechanical coupling coefficients k_p and k_{31} with increasing porosity p (Fig. 3.4) is determined by the competing effect of decrease in piezoelectric modulus d_{31}^{*} and dielectric constant ε_{33}^{T*} and increase in elastic compliance S_{11}^{E*} and S_{12}^{E*} in accordance with the relations $k_p^{*2}=2d_{31}^{*2}/\left(\varepsilon_{33}^{T*}\left(S_{11}^{E*}+S_{12}^{E*}\right)\right)$ and $k_{31}^{*2}=d_{31}^{*2}/\left(\varepsilon_{33}^{T*}S_{11}^{E*}\right)$. The main reason for the decrease in k_p and k_{31} is the above mentioned violation of the continuity of piezoceramics frame in lateral direction and, as a consequence, corresponding growth in elastic compliance of ferroelectrically hard porous piezoceramics.

The electromechanical coupling coefficient k_t^{*} of the thickness mode of vibration increases with increasing porosity, approaching the value of k_{33}^{*} (Fig. 3.4). This is due to the removal of the mechanical clamping of the porous piezoceramics frame in the lateral direction typical for dense ceramics. At further increase in p, the coefficient k_t^{*} decreases as a result of decrease in piezoconstant $e_{33}^{*}\left(k_t^{*2}=e_{33}^{*2}/\left(\varepsilon_{33}^{S*}C_{33}^{D*}\right)\right)$. The relationship between the resulting values of the considered electromechanical coupling coefficients for any porosity is described quite well by an approximate relation: $k_t^{*2}\approx\left(k_{33}^{*2}+k_p^{*2}\right)/\left(1-k_p^{*2}\right)$.

The character of the Q_M^{*} dependence on porosity p for ferroelectrically hard piezoceramics with high initial Q_M^{*} values differs significantly from the corresponding dependences for ferroelectrically soft PZT type piezoceramics [3]. In the low porosity region, the mechanical quality factors for thickness Q_M^{t*} and radial Q_M^{r*} vibrational modes decrease with increasing porosity much more rapidly than in the case of ferroelectrically soft PZT piezoceramics (Fig. 3.5). It occurs due to the peculiarities of the frequency dependences of elastic waves attenuation [5]. In the region of low porosity, pores are isolated, backscattering is absent and mechanical quality factors decreases rapidly enough in proportion to the number of pores. At further porosity increase, decrease in Q_M^{*} slows down due to backscattering.

It should be noted that the scattering losses that cause a reduction in mechanical quality factors of porous ceramics are not true dissipative losses, that is, scattering

Table 3.1 Piezoelectric parameters of the developed ferroelectrically hard porous piezoceramics

Material/ parameter	$\varepsilon_{33}^T/\varepsilon_0$	$tg\delta$ (%)	d_{33} (pC/N)	$\lvert d_{31}\rvert$ (pC/N)	k_t	k_p	V_t (m/s)	Q_M^t	Z_A (Mrayl)
PCR-78[a]	575	0.3	280	55	0.52	0.22	2385	25	12
PCR-78[b]	890	0.33	270	85	0.51	0.32	3340	42	21
ZTSSt-3[a]	650	0.6	300	50	0.53	0.2	2500	20	12
ZTSSt-3[b]	1015	0.7	290	75	0.52	0.3	3500	35	20

Note [a]is the relative content of the ceramic phase = 0.4; [b]is the relative content of the ceramic phase = 0.2

losses do not lead to direct conversion of acoustic energy into thermal energy, which is essential for applications in high power ultrasonic transducers.

Ferroelectrically hard porous piezoceramics, similarly to the 1–3 composites, are characterized by the increased values of k_t^* and d_{33}^*, the lowered values of d_{31}^*, k_p^*, k_{31}^*, V_t^*, Q_M^{t*}, Z_A^*, as well as the better resonance characteristics of the porous piezoelements, compared to dense ones. In addition, ferroelectrically hard porous piezoceramics are easily processed, more resistant to thermal and mechanical impacts and provide a higher adhesion of electrodes compared to standard dense piezoceramics that makes these materials prospective for high power ultrasonic applications. Table 3.1 shows elastic, dielectric, and piezoelectric parameters of the developed ferroelectrically hard porous piezoceramics.

3.3 The Physical Justification of the Using of Porous Ceramics in HIFU Applications

Let us consider ultrasonic transducer with acoustic impedance Z_C loaded on a medium with impedance Z_W (for example, water). The transmission coefficients for the displacement amplitude, pressure and power for a plane acoustic wave, propagating along the interface between two media with different impedances, are determined by the following expressions [27]:

$$K_U = \frac{2Z_C}{Z_W + Z_C},\ K_P = \frac{2Z_W}{Z_W + Z_C}\ \text{and}\ K_J = 1 - \left|\frac{Z_W - Z_C}{Z_W + Z_C}\right|^2, \tag{3.1}$$

were Z_C and Z_W are the acoustic impedances of two media.

The approximate value of the acoustic quality factor of a loaded piezoceramic resonator at a level of 3 dB is determined as [27]:

$$Q_A \approx \frac{\pi}{2}\frac{Z_C}{(Z_D + Z_W)}, \tag{3.2}$$

were Z_C, Z_D and Z_W are the acoustic impedances of ceramics, damper and load, respectively (in the continuous high-power mode, acoustic damping is impractical, therefore usually $Z_D = 0$).

It is obvious that for materials with high mechanical quality factor, the main parameter, limiting the acoustic Q-factor of a loaded transducer, is the difference between the acoustic impedances of piezoceramics and medium. The intrinsic mechanical quality factor of piezoceramics determines only internal losses in the material.

The amplitude of vibrations of working surface U_C and acoustic pressure in piezoelectric element P_C in the resonance regime increase by a factor of Q_A, compared with the static deformation, determined by the piezomodulus and the applied voltage. Thus, for the amplitude of vibrations and pressure in water, we can write the following expressions:

$$U_W = U_C K_U = U_C^0 Q_A K_U,\ P_W = P_C K_P = P_C^0 Q_A K_P \tag{2.3}$$

At the same time, it is quite obvious that resonance increase in U_C and P_C, especially, when focusing transducer work in high power mode, has some significant limitations, related both to internal losses in the material, bindings and leads, and to the loading of the working surface by reflected waves, as well as tensile strength of the ceramics. In real conditions, at excitation levels close to the limiting ones, U_C and P_C exceed U_C^0 and P_C^0 not more than 3–5 times (an increase of 10 times can be considered as limiting).

Figures 3.6 and 3.7 show the qualitative dependences of U_W/U_C^0 and P_W/P_C^0 on Z_C, calculated from (2.3) for different maximum values of Q_A. It is obvious from Fig. 3.6, that the decrease in the acoustic impedance of piezoceramics Z_C, even at inevitable for porous piezoceramics decrease in the acoustic quality factor, under real operating conditions of the HIFU transducer (limitation of U_C and P_C i.e. Q_A)

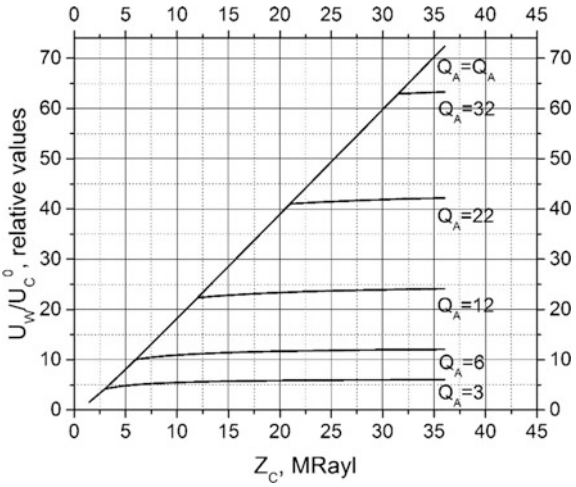

Fig. 3.6 Dependences of the normalized vibration amplitude U_W/U_C^0 in water on the acoustic impedance of the ceramics Z_C, calculated from (2.3) for different maximum values of Q_A

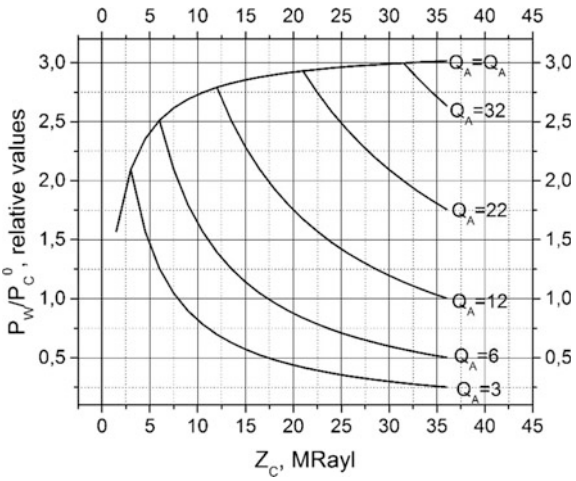

Fig. 3.7 Dependences of the normalized pressure P_W/P_C^0 in water on acoustic impedance of ceramics Z_C, calculated from (2.3) at various maximum values Q_A

does not lead to any decrease in the radiation efficiency (sound pressure and the sound intensity). The both sound parameters are related to the displacement amplitude due to the relations: $P = Z\omega U$ and $J = 1/2(Z\omega^2 U^2)$, where Z is the acoustic impedance of the medium, U is the displacement of the particles, and ω is the circular frequency.

The calculated dependences make it possible to choose the optimum porosity (acoustical impedance) of porous ceramics for obtaining the maximum acoustic output of HIFU transducer. The matching of the impedances of piezoceramics and water can also be achieved with the help of intermediate quarter-wavelengths layers, but in a continuous or quasi-continuous high power regime, this is very difficult for technological reasons. In the impulse high power mode, where acoustic matching is possible, porous piezoceramic is more easily matched with water or tissue load and provide the necessary adhesion of the quarter wavelength layers.

Take into account the advantages of ferroelectrically hard porous piezoceramics, mentioned in the previous section (high resistance to thermal and mechanical shocks, high adhesion of electrodes, high values of k_t^*, reduced values of $\mathrm{tg}\delta^*$, Z_A^*, k_p^*, and k_{31}^*, and, as a consequence, the better resonance characteristics and surface displacement profile). Then it can be concluded that the developed porous piezoceramics are a promising material for high intensity ultrasonic applications.

The obtained results made it possible to realize the original concept of designing high-intensity ultrasonic transducers, based on ferroelectrically hard porous piezoceramics for promising applications in the field of medical therapy (lithotripsy. liposuction, ablation systems etc.).

3.4 HIFU Transducers, Based on Ferroelectrically Hard Porous Piezoceramics, for Medical Applications

3.4.1 HIFU Transducers Design

On the base of developed ferroelectrically hard porous piezoceramics, HIFU transducers with diameter up to 100 mm at frequencies of 200 kHz–2 MHz, operating at electric input power up to 500 W in continuous and burst modes and providing acoustic intensity in focus up to 20 kW/cm^2, were developed and tested. Some examples of developed HIFU transducers are described below.

Figure 3.8 show ferroelectrically hard porous piezoceramic elements on different stages of fabrication process.

Figure 3.9 show the elements of HIFU transducer design and assembled HIFU transducer, designed for medical ablation system [28].

HIFU transducer (Fig. 3.9), comprising 2 MHz spherical element, having radius of curvature 65 mm, was made from ferroelectrically hard porous piezoceramics with 85 mm aperture and 40 mm center hole. The piezoelement was sealed in custom-designed cylindrical housing filled with the mineral oil providing acoustic contact and cooling of the porous ceramic element. The housing had an acoustic window made of very thin (0.15 mm) concave PVC membrane. Center opening was intended for ultrasonic imaging transducer mounting (Fig. 3.8).

Figure 3.10 show spherical focusing element and assembled HIFU transducer, designed for medical blood coagulation system [29].

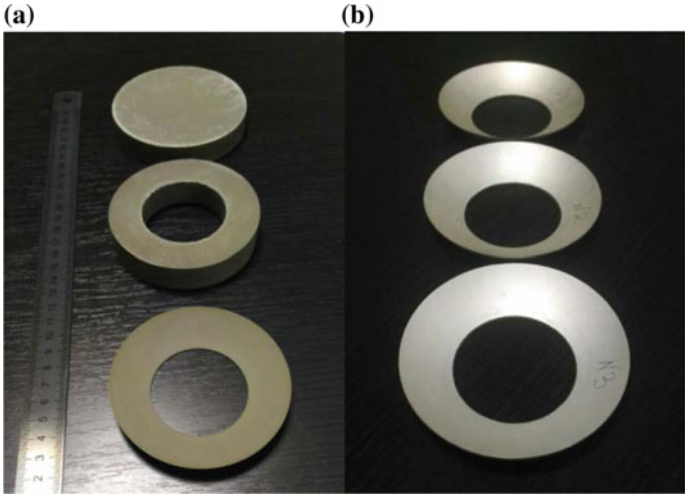

Fig. 3.8 Porous piezoceramic elements on different stages of fabrication process: **a** piezoceramic block, blank and grinded spherical element; **b** silvered spherical elements

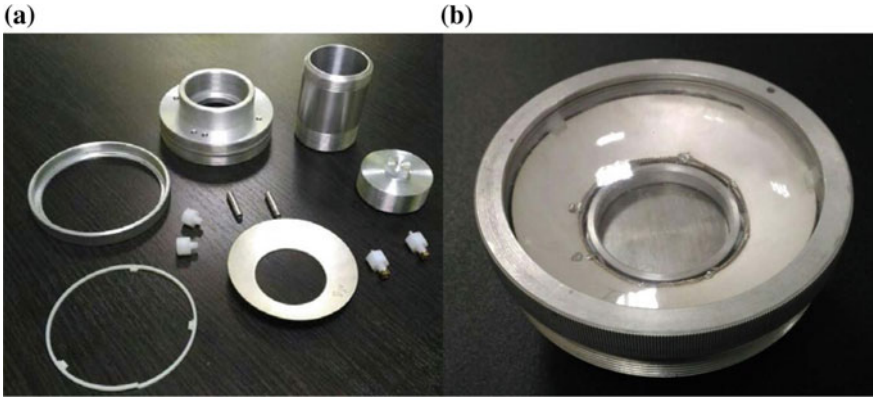

Fig. 3.9 HIFU transducer design on different stages of assembling: **a** elements of HIFU transducer design; **b** assembled HIFU transducer

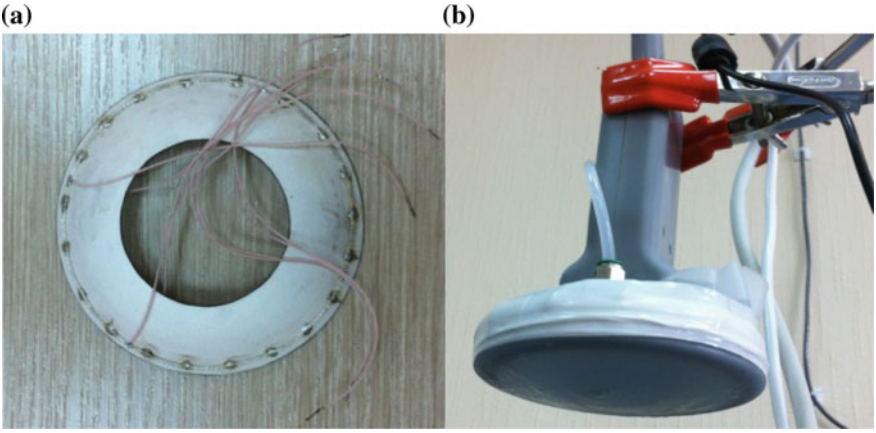

Fig. 3.10 Focusing piezoelement (**a**) and assembled HIFU ultrasonic transducer (**b**)

HIFU transducer (Fig. 3.10), comprising 1.6 MHz spherical element, having radius of curvature 54 mm, was made from ferroelectrically hard porous piezoceramics with 80 mm aperture and 40 mm center hole. The piezoelement was sealed in custom-designed housing, filled with the mineral oil, providing acoustic contact and cooling of the element. The front surface of the housing was covered by very thin (0.1 mm) flexible latex membrane, providing acoustic contact with a tissue. Ultrasonic imaging transducer was inserted and sealed in the center opening (Fig. 3.10).

3.4.2 Ex Vivo Experiments on Biological Tissues

Fresh muscle tissues, adipose and porcine liver were obtained from a butcher within 24 h of slaughter. HIFU transducer, made from ferroelectrically hard piezoceramics and shown in Fig. 3.9 (with central frequency of 2 MHz, aperture 85 mm, focusing distance 65, and 40 mm center hole) has been used for ex vivo experiments [28].

The acoustic intensity in the focus of HIFU transducer was kept equal to 750 W/cm^2 (ISAL). The samples of biological tissues were placed in oil bath and positioned under HIFU transducer so that acoustic focus was placed inside the sample of tissue. The samples were sonicated by CW or burst mode focused ultrasound with the frequency of 2 MHz during 3–60 s at different burst lengths (from 10 to 200 cycles) and duty cycles (from 1/2 to 1/100). After ultrasound exposure the tissues samples were sectioned along the ultrasound beam axis, respectively to visualize and compare the dimensions of tissues lesions [29, 30].

The photographs of ultrasound (thermal and cavitational) lesions in the porcine, muscle, and liver samples induced by HIFU are shown in Fig. 3.11.

It is obvious from Fig. 3.11 that developed HIFU transducer, based on ferroelectrically hard porous piezoceramics, is characterized by high efficiency and selectivity and can provide thermal and cavitational lesions in biological tissues.

3.4.3 In Vivo Experiments on Blood Vessels

The experiments were made on lamb's femoral artery in vivo at a standard hemostasis protocol. The main problem of HIFU application for hemostasis is low ultrasound absorption ability of blood and, as a result, low coagulation rate and heating at real arterial blood flow. For this reason, during ultrasound exposure, arterial blood flow was stopped temporarily using intravascular balloon. HIFU

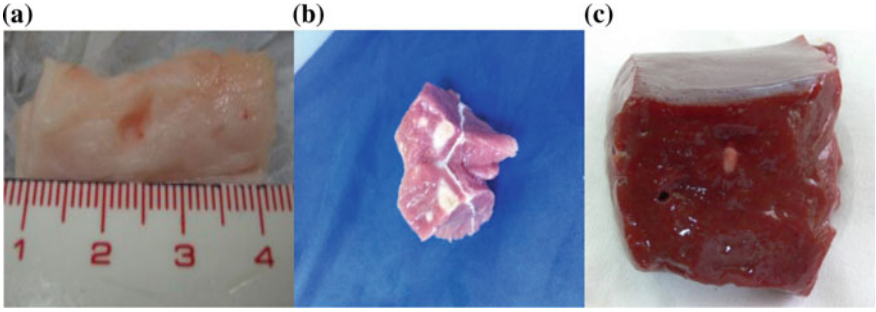

Fig. 3.11 Cavitational (**a**), and thermal (**b**, **c**) lesions in the porcine, muscle, and liver samples induced by HIFU transducers, fabricated from ferroelectrically hard porous piezoceramics; treatment protocols: **a** burst mode—burst length = 10 cycles, duty cycle = 1/20, exposure time = 9 s; **b** CW mode—exposure time = 3 and 30 s; **c** CW mode—exposure time = 9 s

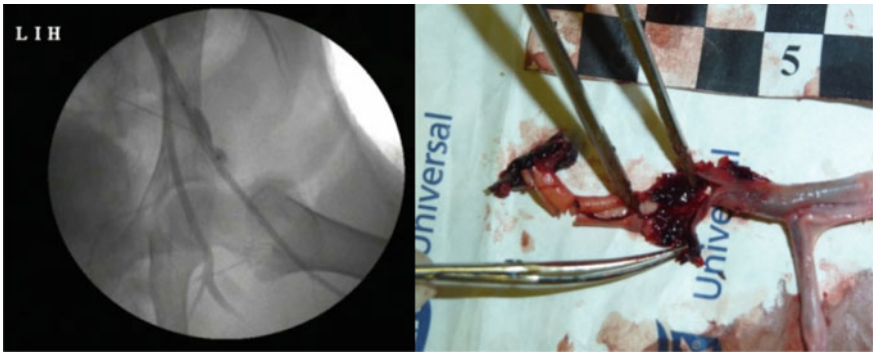

Fig. 3.12 X-ray image of blood vessels, showing ultrasound hemostasis and photograph of vessel clots in dissected lamb's femoral artery

transducer with 1.6 MHz frequency, described in previous sections (Fig. 3.10), was used for experiments [31].

For the driving of HIFU transducer, linear RF amplifier E&I model 2400L RF and function generator Agilent 33521B operating in CW mode were used. The acoustic intensity in the focus, preliminary measured in water tank, was maintained at 5000 W/cm^2 (ISAL) for the lamb's femoral artery treatment. To adjust the focus of HIFU transducer on the target, an ultrasonic imaging system, combined with HIFU transducer, was used [32].

After HIFU treatment and angiography study, the samples of lamb's femoral artery were extracted to disclose vessel clots and confirm hemostasis.

Figure 3.12 shows angiography image, obtained using contrast agents and photograph of dissected femoral artery.

Figure 3.13 show lamb's femoral artery in situ and dissected part of the artery with vessel clot, formed as result of postponed hemostasis.

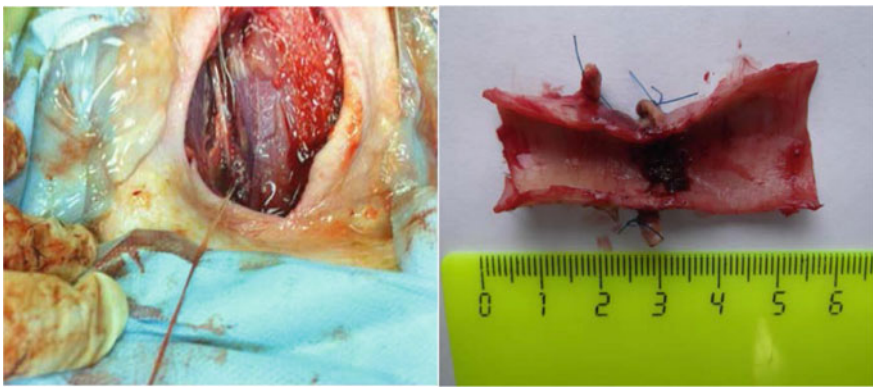

Fig. 3.13 Photographs of lamb's femoral artery in situ and dissected part of the artery with vessel clot, formed as result of postponed hemostasis

The results of in vivo experiments on blood vessels confirm the applicability of HIFU therapy for hemostasis treatments and provide additional confirmation of high efficiency and selectivity of developed HIFU transducers.

3.5 Conclusion

The results of systematic studies allowed us to develop a new family of porous ceramics, based on ferroelectrically hard PZT compositions with properties, combining better parameters of PZT ceramics and 1–3 composites for high intensity ultrasonic applications.

Ferroelectrically hard porous piezoceramics are characterized by increased values of piezoelectric and electromechanical coupling factors, reduced values of acoustic impedance and lateral parasitic modes of vibration, as well as better resonance characteristics, compared to dense piezoceramic elements. Moreover, the porous piezoceramic elements are easily processed, more stable against thermal and mechanical influences and provide higher adhesion of electrodes in comparison with standard dense piezoceramic and composite elements that makes them prospective materials for high power ultrasonic applications. It was shown that the use of ferroelectrically hard porous ceramics simplifies the manufacturing process, allows one to increase the main operational characteristics of HIFU transducers and makes them competitive in comparison with the standard ultrasonic transducers for promising applications in the field of medical therapy and surgery.

The obtained results made it possible to realize the original concept of designing HIFU transducers on the base of ferroelectrically hard porous piezoceramics for promising applications in the field of medical therapy (lithotripsy. liposuction, ablation systems etc.).

The results of ex vivo experiments on tissues (fresh porcine adipose tissue, bovine liver) and in vivo experiments on blood vessels confirm the applicability of ferroelectrically hard porous piezoceramics for HIFU transducers design and prove the efficacy, safety, and selectivity of the developed HIFU transducers.

Acknowledgements This work was financially supported by the Ministry of Education and Science of the Russian Federation: the basic parts of the state task, themes No. BP0110-11/2017-44 (12.5425.2017/8.9), No. 3.8863.2017/ITW (3.8863.2017/7.8) and Russian Foundation for Basic Research (RFBR № 16-58-48009-Ind-omi).

References

1. W. Wersing, N. Setter, in *Piezoelectric Materials in Devices* (Swiss Federal Institute of Technology, Lausanne, 2002), p. 29
2. W.A. Smith, IEEE Ultrason. Symp. Proc. (1989), p. 755
3. T.R. Shrout, W.A. Shulze, J.V. Biggers, Mater. Res. Bull **14**(12), 1553 (1979)

4. K. Rillenmyer, T. Shrout, W.A. Schulze, R.E. Newnham, Ferroelectrics **41**, 189 (1982)
5. Andrey Rybyanets, Anastasia Rybyanets, IEEE Trans. UFFC **58**(9), 1757 (2011)
6. R.E. Newnham, D.P. Skinner, L.E. Cross, Mater. Res. Bull. **13**(5), 525 (1978)
7. V.Y. Topolov, C.R. Bowen, *Electromechanical Properties in Composites Based on Ferroelectrics* (Springer, London, 2009), 202pp
8. W.A. Smith, A.A. Shaulov, Ferroelectrics **87**, 309 (1988)
9. S.S. Lopatin, T.G. Lupeiko, Izv. AN USSR. Ser. Neorg. Mat. **27**, 1948 (1991)
10. W. Wersing, K. Lubitz, J. Moliaupt, Ferroelectrics **68**, 77 (1986)
11. R. Ramesh, H. Kara, C.R. Bowen, Ultrasonic **43**, 173 (2005)
12. A.N. Rybyanets, I.E.E.E. Trans, UFFC **58**, 1492 (2011)
13. A.N. Rybjanets, A.V. Nasedkin, A.V. Turik, Integr. Ferroelectrics **63**, 179 (2004)
14. A. Rybianets, A.V. Nasedkin, Ferroelectrics **360**, 57 (2007)
15. A.N. Rybjanets, O.N. Razumovskaja, L.A. Reznitchenko, V.D. Komarov, A.V. Turik, Integr. Ferroelectrics **63**, 197 (2004)
16. A.N. Rybianets, Ferroelectrics **360**, 84 (2007)
17. A. Rybianets, Y. Eshel, L. Kushkuley, Proc. IEEE Ultrason. Symp. **1**(4152336), 1911 (2006)
18. A.N. Rybyanets, in *Advanced Materials—Manufacturing, Physics, Mechanics and Applications*, ed. by I.A. Parinov, S.-H. Chang, V.Y. Topolov. Springer Proceedings in Physics, vol. 175 (Springer, Cham , 2016), p. 211
19. A.N. Rybyanets, in *Piezoelectrics and Related Materials: Investigations and Applications*, ed. by I.A. Parinov (Nova Science Publishers, New York, 2012), p. 143
20. I.A. Shvetsov, N.A. Shvetsova, A.N. Reznitchenko, A.N. Rybyanets, in *Advanced Materials —Techniques, Physics, Mechanics and Applications*, ed. by I.A. Parinov, S.-H. Chang, M.A. Jani. Springer Proceedings in Physics, vol. 193 (Springer, Cham, 2017), p. 489
21. V. Goland, L. Kushkuley, S. Mirman, Y. Zadok, S. Ben-Ezra, A. Shalgi, A. Rybyanets, in *Proceedings of the 2007 IEEE Ultrasonic Symposium IUS* (2007), p. 1305
22. A.N. Rybyanets, in *Advanced Materials—Manufacturing, Physics, Mechanics and Applications*, ed. by I.A. Parinov, S.-H. Chang, V.Y. Topolov. Springer Proceedings in Physics, vol. 175 (Springer, Cham, 2016), p. 603
23. A.J. Dantziger et al., *Multicomponent Systems of Ferroelectric Solid Solutions: Physics, Crystallochemistry, Technology. Design Aspects of Piezoelectric Materials*, vol. 1–2 (Rostov State University Press, Rostov-on-Don, 2001), 800pp
24. *IEEE Standard on Piezoelectricity* (ANSI/IEEE Std., 1987), p. 176
25. PRAP (Piezoelectric Resonance Analysis Programme). *TASITechnicalSoftwareInc* (www.tasitechnical.com)
26. A. Rybianets, L. Kushkuley, Y. Eshel, A. Nasedkin, in *Proceedings—IEEE Ultrasonics Symposium*, vol. 1 (2006), p. 4152245, 1533
27. G.S. Kino, *Acoustic Waves: Devices, Imaging, and Analog Signal Processing* (Prentice Hall, Englewood Cliffs, 1987), 601pp
28. A.N. Rybyanets, A.A. Naumenko, Phys. Procedia **70**, 1148 (2015)
29. A.N. Rybyanets, AIP Conf. Proc. **1215**, 287 (2010)
30. A.N. Rybyanets, M.A. Lugovaya, A.A. Rybyanets, AIP Conf. Proc. **1215**, 291 (2010)
31. A.N. Rybyanets, A.A. Naumenko, O.A. Sapozhnikov, V.A. Khokhlova, Phys. Procedia **70**, 1152 (2015)
32. A.N. Rybyanets, A.A. Naumenko, N.A. Shvetsova, V.A. Khokhlova, O.A. Sapozhnikov, A.E. Berkovich, in *Advanced Materials—Manufacturing, Physics, Mechanics and Applications*, ed. by I.A. Parinov, S.-H. Chang, V.Y. Topolov. Springer Proceedings in Physics, vol. 175 (Springer, Cham, 2016), p. 621

Chapter 4
Porous and Composite Materials Based on Lead-Free Ferroelectric Ceramics for Ultrasonic Transducers Applications

E. I. Petrova, M. A. Lugovaya, I. A. Shvetsov, N. A. Shvetsova, A. N. Reznichenko and A. N. Rybyanets

Abstract This chapter describes the fabrication technology, as well as the results of systematic studies of the properties of "ceramics-polymer" composites with 1-3 connectivity type, ceramic matrix composites "ceramics/crystal", and porous ceramics based on lead-free sodium-lithium niobates (Na, Li)NbO_3 and sodium-potassium niobates (Na, K)NbO_3 compositions. Experimental samples of lead-free porous piezoelectric ceramics and composites were fabricated, and measurements of elastic, dielectric and piezoelectric parameters, as well as microstructural studies of experimental samples were performed. It was shown that the use of alkali metal niobates in the form of 1-3 composites, ceramic matrix composites, and porous ceramics allows one to increase the main functional parameters of these materials and makes them competitive with piezoceramics of the PZT system. The developed lead-free porous and composite materials have a unique combination of parameters and can be used in the manufacture of ultrasonic transducers and devices for a wide range of applications, including medical and nondestructive testing equipment.

4.1 Introduction

Piezocomposite materials are currently occupied a negligible on volume, but a very important part of the piezoelectric materials market—materials for medical ultrasonic equipment, non-destructive testing and underwater acoustics. Composite and porous systems have a smaller acoustic impedance than the original piezoelectric ceramics, they are more plastic and are better adapted to mechanical impact loads, have a lower mechanical quality factor, higher piezoelectric sensitivity $(g = d/\varepsilon)$, and electromechanical activity (k_t) etc. Thus, composites and porous ceramics expand the field of application of piezoelectrics and are often developed as an

E. I. Petrova · M. A. Lugovaya · I. A. Shvetsov · N. A. Shvetsova
A. N. Reznichenko · A. N. Rybyanets (✉)
Southern Federal University, 194, Stachki Ave, Rostov-on-Don 344090, Russia
e-mail: arybyanets@gmail.com

I. A. Parinov et al. (eds.), *Advanced Materials*, Springer Proceedings in Physics 207, https://doi.org/10.1007/978-3-319-78919-4_4

alternative to piezoceramics. A detailed description of the properties, application fields and fabrication methods of various composite piezoelectrics and porous ceramics can be found in the reviews and original articles [1–14].

Currently, piezoceramic materials of the PZT system are mainly used as raw materials for the fabrication of composites with 1-3 connectivity type and porous piezoceramics [8, 9]. This is due to the high piezoactivity and proven fabrication technology of PZT materials. Other ceramic compositions in the form of 1-3 composites and porous ceramics have not been studied practically because of inherent initial anisotropy, low piezoelectric activity, and technological difficulties.

Lead-free ferroelectric ceramics is of great interest mainly due to the growing attention to environmental problems [15]. Studies on lead-free piezoelectrics [16, 17] made it possible to determine useful piezoelectric compositions in the system $(Na_{1-x}Bi_x)TiO_3$. Other candidates among the lead-free systems are perovskites based on alkali metal niobates, layered bismuth-containing compounds $Bi_4Ti_3O_{12}$, $SrBi_2Nb_2O_9$ and tungsten bronzes (Sr, Ba)Nb_2O_6 [18, 19]. Among the known lead-free ceramics based on alkali metal niobates [20], ferroelectric ceramics based on solid solutions (Na, Li)NbO_3 and (Na, K)NbO_3 are of greatest practical interest [9, 15]. However, it seems very doubtful that any new lead-free piezoceramic system with piezoelectric properties close to the properties of the PZT system will be found in the nearest future. Therefore, the interest is currently concentrated on the known lead-free compositions in attempts to improve their properties and adapt to various applications. Thus, the study of composites and porous ceramics based on lead-free compounds, is interesting both from scientific and practical points of view. The use of alkali metal niobates in the form of 1-3 composites, ceramic matrix composites, and porous ceramics allows one to increase the main functional parameters of these materials and makes them competitive with piezoceramics of the PZT system.

This chapter describes the fabrication technology, as well as the results of systematic studies of the properties of “ceramics-polymer” composites with 1-3 connectivity type, ceramic matrix composites “ceramics/crystal” and porous ceramics based on lead-free alkali metal niobates [9, 15]. Special attention is paid to an accurate measurement of the parameters of porous piezoceramics and composites, which is a difficult task for dissipative materials with low mechanical quality factor an inhomogeneous structure.

4.2 Experimental Results

4.2.1 Lead-Free Piezoceramics Based on Alkali Metal Niobates

Lead-free compositions based on solid solutions of the (Na, Li)NbO_3 (PCR-35) and (Na, K)NbO_3 (PCR-34) systems [9] were chosen as the initial materials for fabrication of porous ceramics and composites. Experimental samples of piezoceramics

were fabricated by the hot-pressing method. Microstructural studies were carried out on polished and etched surfaces of the samples using the NeoPhot-21 optical microscope. Measurements of the complex elastic, dielectric, and piezoelectric parameters of the piezoelectric elements were performed on standard samples using an Agilent 4294A impedance analyzer and a PRAP resonance spectra analysis program [21]. The PRAP program [21] analyzes the impedance spectra for determining the complex properties of the piezoelectric material. This program uses the generalized form of the Smith method to determine the material properties for any standard resonance mode and the generalized relation method for the radial mode, valid for materials with an arbitrary Q-factor [22, 23]. To obtain a complete set of complex constants, standard one-dimensional vibration modes, typical for the symmetry class of 6 mm, and corresponding piezoceramic samples of various shapes and sizes were used.

Figure 4.1 shows optical micrographs of polished and etched surfaces of piezoceramic samples PCR-35. It is obvious from Fig. 4.1, that hot-pressed piezoceramics PCR-35 have a low porosity $P \approx 1\%$, a chaotic packing of crystallites with straight and curved crystallite boundaries and an average grain size of $R \approx 7$ μm.

The basic dielectric, piezoelectric and physical parameters for hot-pressed lead-free piezoceramics are listed in Table 4.1.

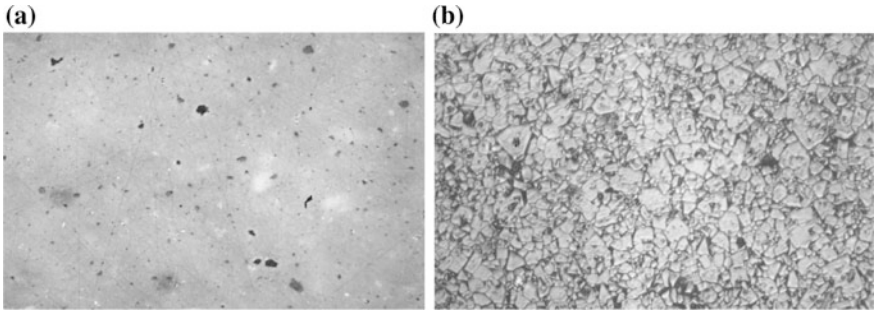

Fig. 4.1 Polished surface of the piezoceramic element PCR-35 (**a**) and microstructure detected by thermal etching (**b**)

Table 4.1 Parameters of lead-free hot-pressed piezoceramics

Material/ parameter	$\varepsilon_{33}^T/\varepsilon_0$	$tg\delta$ (%)	d_{33} (pC/N)	$\lvert d_{31}\rvert$ (pC/N)	k_t	k_p	V_t (m/s)	Q_M^p	ρ (g/cm^3)	Z_A (Mrayl)
PCR-34	460	2.5	102	45	0.46	0.42	6100	150	4.1	25
PCR-35	120	1.6	40	12	0.4	0.2	6200	1000	4.45	20

Table 4.2 Full set of complex constants of hot-pressed piezoceramics PCR-35

Parameter	Real part	Imaginary part
S_{11}^E (m^2/N)	6.81×10^{-12}	-1.34×10^{-14}
S_{12}^E (m^2/N)	-1.38×10^{-12}	3.49×10^{-15}
S_{13}^E (m^2/N)	-1.04×10^{-12}	–
S_{33}^E (m^2/N)	7.02×10^{-12}	-9.73×10^{-14}
S_{55}^E (m^2/N)	1.58×10^{-11}	-6.56×10^{-14}
S_{66}^E (m^2/N)	1.64×10^{-11}	-3.37×10^{-14}
d_{15} (C/N)	3.04×10^{-11}	-1.98×10^{-12}
d_{31} (C/N)	-1.01×10^{-11}	1.1×10^{-13}
d_{33} (C/N)	3.19×10^{-11}	-2.02×10^{-12}
ε_{11}^T (F/m)	1.32×10^{-9}	-1.18×10^{-10}
ε_{33}^T (F/m)	1.12×10^{-9}	-1.94×10^{-11}

The complete set of complex constants of PCR-35 piezoceramics measured for shear, longitudinal, radial and thickness modes of piezoceramic elements is shown in Table 4.2.

4.2.2 *Composites with 1-3 Connectivity Based on Lead-Free Piezoceramics*

For composites fabrication we used the standard method of "cutting and filling". Hot-pressed piezoceramics PCR-35 and PCR-34, possessing a unique combination of parameters [9], were used as a ceramic base. Two different types of polymer matrixes were used: plasticized epoxy resin ED-20 and polyurethane composition PDI-3AK. To obtain a high-quality polymer phase, we used vacuum casting of polymer compositions with the appropriate solvents. The best results were obtained for the PCR-34 piezoceramic material. The lower piezoelectric activity and the initial anisotropy of the PCR-35 composition did not allow us to obtain the desired parameters.

Figures 4.2, 4.3, 4.4 and 4.5 show the dependences of the main elastic, dielectric and piezoelectric parameters of PCR-34/polyurethane PDI-3AK composites with 1-3 connectivity type on the relative content of piezoceramics.

The dielectric constant of 1-3 composites $\varepsilon_{33}^T/\varepsilon_0^*$ decreases practically linearly with a decrease in the content of the ceramic phase v (Fig. 4.2), which is due to a significant difference in dielectric permittivities of piezoceramics and polymer.

The behavior of the sound velocity for a thickness mode of vibration $V_t^* = \sqrt{\frac{C_{33}^{D*}}{\rho^*}}$ with a change in v is determined by the competing effect of changes in the modulus of elasticity C_{33}^{D*} and density ρ^* (Fig. 4.2). In the ranges $0.7 < v < 1$ and $0 < v < 0.3$, the decrease in V_t^* is determined by the rapid decrease of C_{33}^{D*} due to the

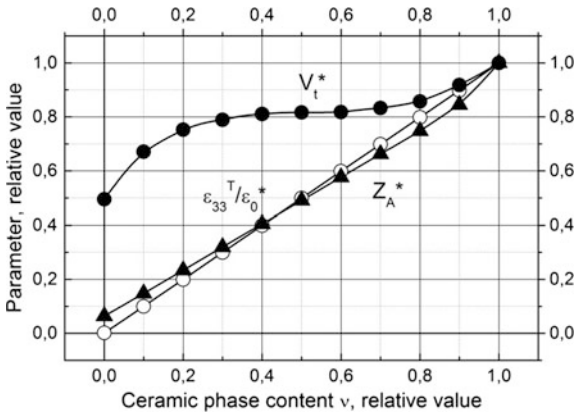

Fig. 4.2 Dependences of the permittivity $\varepsilon_{33}^T/\varepsilon_0^*$, the sound velocity for the thickness mode of vibration V_t^* and acoustic impedance Z_A^* on the relative content of the ceramic phase v for 1-3 composites of PCR-34/polyurethane PDI-3AK. The values of the parameters are normalized to the corresponding values of the hot-pressed ceramic PCR-34 ($\varepsilon_{33}^T/\varepsilon_0 = 460$, $V_t = 6100$ м/с, $Z_A = 25$ Mrayl)

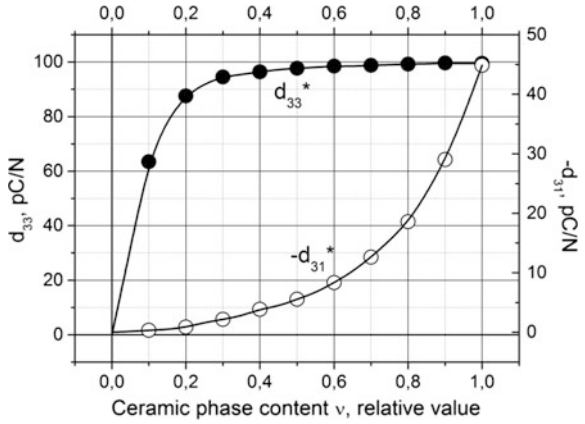

Fig. 4.3 Dependences of piezoelectric modulus d_{33}^* and d_{31}^* on the relative content of the ceramic phase v for 1-3 composites of PCR-34/polyurethane PDI-3AK

contribution of the elastic moduli of the polymer phase. In the interval $0.3 < v < 0.7$, V_t^* practically does not change, which is caused by the predominant contribution of the linear decrease in density ρ^*.

The acoustic impedance Z_A^* decreases with decreasing v practically linearly (Fig. 4.2) in accordance with the expression: $Z_A^* = \rho^* V_t^*$.

The piezoelectric modulus d_{33}^* for 1-3 composites in the interval of the ceramic phase content $0.3 < v < 1$ decreases insignificantly (Fig. 4.3), which is caused by the continuity of the ceramic rods structure of 1-3 composites in the direction of residual polarization. The decrease in the relative area of the piezoactive phase is

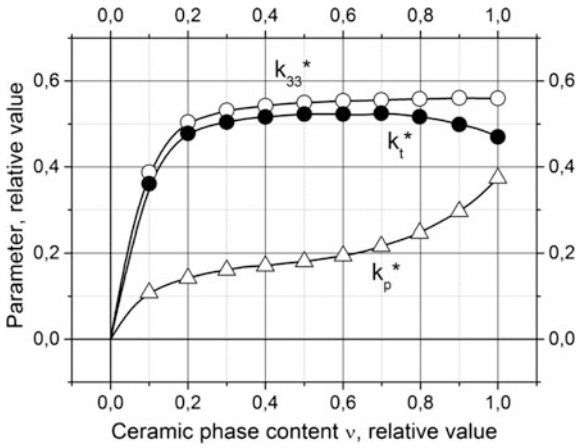

Fig. 4.4 Dependences of the electromechanical coupling coefficients k_{33}^*, k_t^* and k_p^* on the relative content of the ceramic phase v for 1-3 composites of PCR-34/polyurethane PDI-3AK

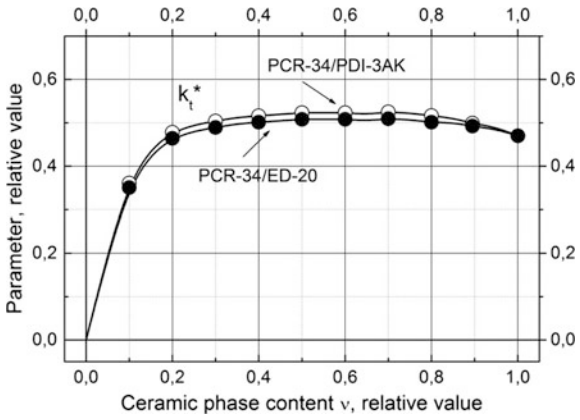

Fig. 4.5 Dependences of the electromechanical coupling factor k_t^* on the relative content of the ceramic phase v for 1-3 composites with different polymer phase: RCP-34/polyurethane PDI-3AK, PCR-34/plasticized epoxy ED-20. The values of k_t^* are normalized to the value of k_t for hot pressed ceramic PCR-34

compensated by an increase in the specific pressure on the ceramic rods due to the substantially lower elastic stiffness of the polymer as compared with the ceramic. With further decrease in v, d_{33}^* decreases rapidly due to a significant increase in the relative area of the non-piezoactive polymer phase. Increasing the elastic stiffness of the polymer leads to a decrease in d_{33}^* for any v, since the non-piezoactive polymer perceives a part of the load applied to the composite element.

The rapid decrease of $\left|d_{31}^*\right|$ with decreasing v (Fig. 4.3) is obvious and is caused by a violation of the continuity of the ceramic phase in the lateral direction. Polymer interlayer between the ceramic rods prevents mechanical deformation of the composite element in the lateral direction.

The coefficient of electromechanical coupling k_{33}^* for 1-3 composites in the interval of the ceramic phase content $0.3 < v < 1$ decreases insignificantly (Fig. 4.4), which is due to the invariance of the electromechanical coupling in the direction of residual polarization of the rod structure of 1-3 composites and an insignificant

mechanical clamping of ceramic rods by a polymer matrix. At further decrease in v, k_{33}^* decreases sharply, because of the rapid growth of the elastic compliance of S_{33}^{E*}, $k_{33}^{*2} = d_{33}^{*2}/\left(\varepsilon_{33}^{T*} S_{33}^{E*}\right)$ due to the increase in the contribution of the elastic compliance of the polymer S_{11}^{p} and the decrease of the piezoelectric modulus d_{33}^*.

The behavior of the planar coupling coefficient k_p^* (Fig. 4.4) with decreasing v is determined by the competing effect of decreasing piezoelectric modulus d_{31}^* and dielectric constant ε_{33}^{T*}, and increasing the elastic compliances S_{11}^{E*} and S_{12}^{E*} in accordance with the relation $k_p^{*2} = 2d_{31}^{*2}/\left[\varepsilon_{33}^{T*}\left(S_{11}^{E*} + S_{12}^{E*}\right)\right]$. The main reason for the decrease in k_p^* is the violation of the continuity of the ceramic phase in the lateral direction, caused by the presence of a polymer interlayer between the ceramic rods.

The coefficient of electromechanical coupling of the thickness mode of vibrations k_t^* increases with decreasing the content of the ceramic phase in the interval $0.4 < v < 1$, approaching the value k_{33}^* (Fig. 4.4). This is due to the removal of the mechanical clamping of the composite element in the lateral direction, typical for dense ceramics (the coefficient of electromechanical coupling for the ceramic rod is k_{33}, and the mechanical clamping of the ceramic by the polymer is insignificant). With further decrease in v, the coefficient k_t^* decreases rapidly due to the increasing influence of the polymer phase and the rapid decay of the piezoelectric constant e_{33}^*, $k_t^{*2} = e_{33}^{*2}/\left(\varepsilon_{33}^{S} C_{33}^{D}\right)$. The relationship between the resultant values of the considered electromechanical coupling coefficients for any v is described fairly well by an approximate relation: $k_t^{*2} \approx \left(k_{33}^{*2} + k_p^{*2}\right)/\left(1 - k_p^{*2}\right)$.

The elastic properties of the polymer phase significantly affect the piezoelectric parameters of 1-3 composites. The "softer" the polymer (less degree of clamping of the rods by the polymer matrix), the higher the values of k_t^*, k_{33}^* and d_{33}^*. Figure 4.5 illustrates the effect of the elastic properties of the polymer phase on the electromechanical coupling coefficient k_t^*. The use of softer polymers (polyurethane, plasticized epoxy resin) can significantly increase k_t^* of the composite. The influence of the polymer phase significantly affects not only the piezoelectric parameters, but also substantially determines acoustic impedance, dielectric and mechanical losses, aging characteristics, and mechanical properties of 1-3 composites.

The structure of 1-3 composite materials not only leads to an increase in the piezoelectric parameters, but also to a qualitative improvement in the resonance characteristics of piezoelectric elements. The impedance and phase characteristics of the composite elements are smoother and do not contain parasitic resonances, the resonance gap $(f_a - f_r)/f_r$ is wider, and the characteristic impedance ratio Z_a/Z_r is smaller compared to a conventional ceramic element of comparable dimensions.

The obtained experimental dependences (Figs. 4.2, 4.3, 4.4 and 4.5) are in good agreement with the literature data and the results of modeling for 1-3 composites based on PZT ceramics [10, 11].

Table 4.3 shows the main parameters of the developed 1-3 composites based on lead-free ceramics.

Table 4.3 Dielectric, piezoelectric and physical parameters of the developed 1-3 composites based on lead-free ceramics

Material/ parameter	$\varepsilon_{33}^T/\varepsilon_0$	tgδ (%)	d_{33} (pC/N)	$\lvert d_{31}\rvert$ (pC/N)	k_t	k_p	V_t (m/s)	Q_M^p	Z_A (Mrayl)
PCR-34/ PDI-3AK[a]	180	0.03	98	5	0.53	0.18	4880	16	11.2
PCR-34/ PDI-3AK[b]	100	0.03	95	3	0.51	0.15	4630	12	5.6

Note [a]Is the relative content of the ceramic phase = 0.4; [b]is the relative content of the ceramic phase = 0.2

4.2.3 Porous Lead-Free Piezoelectric Ceramics

For porous ceramics fabrication we used a modified method of burning out of porophore agents. Complexes of organic compounds with various rheological (dispersity, particle shape and size) and physical (decomposition temperature) characteristics were used as the porophores. The main difference between this method and those commonly used in the preparation of porous structures [12–14] consists in the use of finely dispersed organic powders (10–20 μm) and special processing regimes in grinding, porophore burning out, and sintering stages of the ceramics fabrication. It provides obtaining a qualitative homogeneous ceramics with controlled parameters (porosity up to 70% and average pore size ≈ 20 μm). The developed technology allows obtaining porous ceramics with anisotropic and gradient porosity, as well as the fabrication of thick porous films using the tape casting process [24, 25].

As raw ceramic materials, standard synthesized powders of piezoceramics PCR-34 and PCR-35 were used [9]. The best results were obtained for the PCR-34 material. The lower piezoelectric activity and initial anisotropy, typical for the composition of PCR-35, as in the case of 1-3 composites, did not allow obtaining the desired parameters.

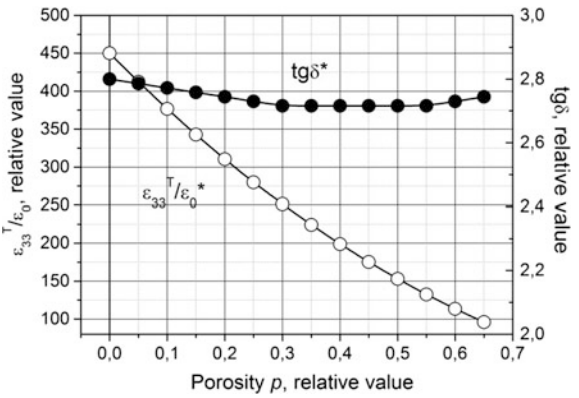

Fig. 4.6 Dependences of the permittivity $\varepsilon_{33}^T/\varepsilon_0$ and the dielectric loss tangent on the relative porosity p for porous piezoceramics PCR-34

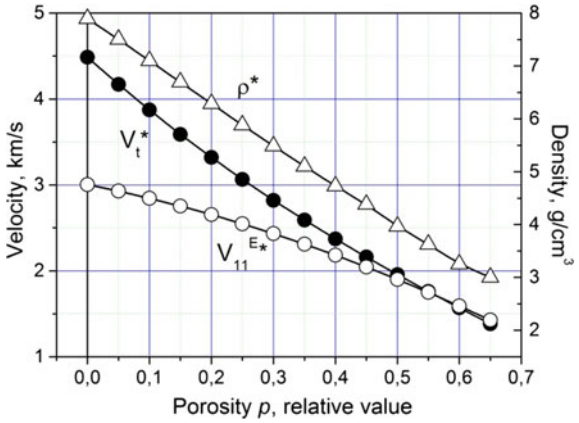

Fig. 4.7 Dependences of the density ρ^* and sound velocity of thickness V_t^* and longitudinal V_{11}^{E*} modes of vibrations on the relative porosity p for porous piezoceramics PCR-34

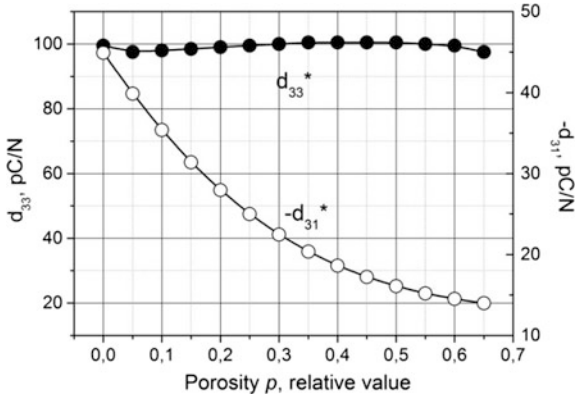

Fig. 4.8 Dependences of the piezoelectric moduli d_{33}^* and d_{31}^* on the relative porosity p for porous piezoceramics PCR-34

Figures 4.6, 4.7, 4.8, 4.9 and 4.10 show the dependences of the main parameters of the porous piezoceramics PCR-34 on the relative porosity, p.

The dielectric constant $\varepsilon_{33}^T/\varepsilon_0$ of the lead-free porous ceramics decreases practically linearly with increase in the porosity, p (Fig. 4.6), which is due to a significant difference in dielectric permeabilities of piezoceramics and air. The dielectric loss tangent tgδ decreases insignificantly with p grows in the entire range of porosity values (Fig. 4.6) and approaches the initial value only at $p > 0.65$. This is due to changes in the character of the domain structure and the mobility of the domain walls of piezoelectric ceramics. The more developed specific surface and the "defective" structure of the porous ceramics contribute to the fixation of domain walls and prevents different from the 180° rotations of the domains, which leads to decrease in tgδ. It should be noted that highly porous piezoceramics are hygroscopic and the correct measurements of $\varepsilon_{33}^T/\varepsilon_0$ and tgδ can be obtained only at controlled humidity of the atmosphere.

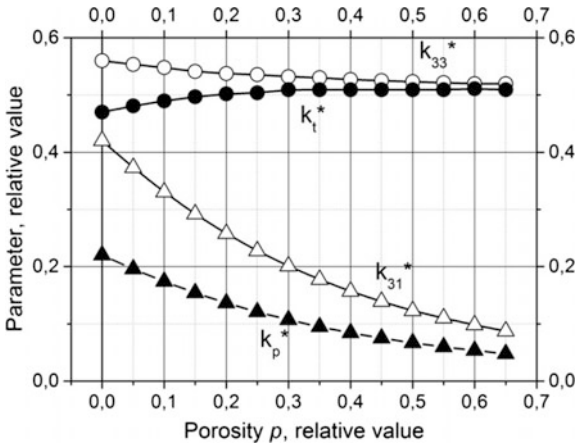

Fig. 4.9 Dependences of the electromechanical coupling coefficients k_{33}^*, k_{31}^*, k_t^* and k_p^* on the relative porosity p for porous piezoceramics PCR-34

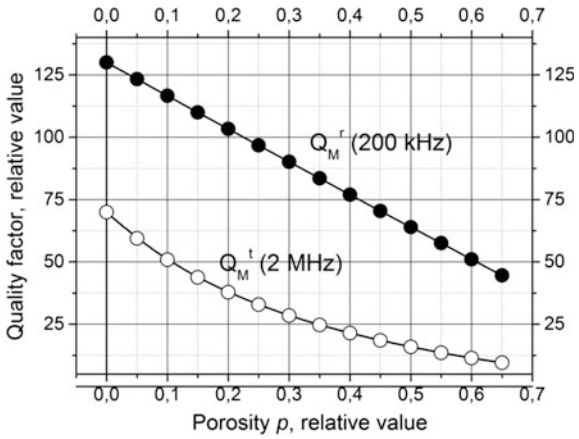

Fig. 4.10 Experimental dependences of the mechanical quality factors of the radial Q_M^{r*} and thickness Q_M^{t*} vibrations modes on the relative porosity p for porous piezoceramics PCR-34

The density ρ^* of the lead-free porous ceramics decreases linearly with increasing p (Fig. 4.7), in accordance with the expression: $\rho^* = \rho(1-p)$, where ρ is the theoretical density of piezoceramics.

The behavior of the velocity $V_{11}^{E*} = \sqrt{\frac{1}{\rho^* S_{11}^{E*}}}$ with increasing p (Fig. 4.7) is determined by the competing effect of changes in density $\rho*$ and elastic compliance S_{11}^{E*}, which increases rapidly due to the decrease in the elastic rigidity of the porous ceramic frame. The velocity $V_t^* = \sqrt{\frac{C_{33}^{D*}}{\rho^*}}$ decreases rapidly with an increase in p (Fig. 4.7), which is also due to a faster decrease in the elastic rigidity $\left(C_{33}^{D*}\right)$ of the porous ceramic frame, as compared with the decrease in density ρ^*.

The piezoelectric modulus $d_{33}*$ of lead-free porous ceramics in the range $0 < p < 0.6$ changes insignificantly (Fig. 4.8), which is due to the continuity of the ceramic quasi-rod structure of the porous ceramics in the direction of residual polarization (thickness of the element). Reduction of the relative area of the

piezoactive phase, as in the case of 1-3 composites, is compensated by an increase in the specific pressure on the ceramic frame (the elastic stiffness of the air can be neglected in comparison with ceramics).

At correctly performed measurements, an insignificant increase in d_{33}^* can be only due to the better polarization of porous ceramics as compared to the dense material. The porous piezoceramics are capable of withstanding large polarizing voltages without breakdown in the body of the element. In addition, the more developed surface and the defective structure of porous ceramics contribute to the fixation of different from the 180° reversible rotations of domains realized under the action of the polarizing field. The results of the studies reporting a significant increase or decrease in the piezoelectric modulus d_{33}^* [14, 26, 27] appear to be erroneous for the following reasons:

(i) different regimes of sintering and polarization of piezoceramic elements with different porosity were used;
(ii) measurements of d_{33}^* by quasi-static method were performed with a large error (the measured value depends on the indenter size and location of the pressure application).

The decrease of $\left|d_{31}^*\right|$ for lead-free porous ceramics with increasing p (Fig. 4.8) is obvious and is caused by the violation of the continuity of the ceramic frame in the lateral direction (the lateral dimensions of the element are an order of magnitude greater than its thickness, which makes it unlikely to preserve a continuous quasi-rod ceramic frame in this direction).

The coefficient of electromechanical coupling k_{33}^* of lead-free porous ceramics decreases insignificantly with the increase in the porosity p (Fig. 4.9), which is due to the invariance of the electro-mechanical coupling in the direction of residual polarization of the quasi-rod structure and the absence of mechanical clamping in the porous ceramic frame. A slight decrease in k_{33}^* is associated with an increase in the elastic compliance S_{33}^{E*} of the porous ceramic frame: $k_{33}^{*2} = d_{33}^{*2}/\left(\varepsilon_{33}^{T*} S_{33}^{E*}\right)$.

The behavior of the electromechanical coupling coefficients k_p and k_{31} with increasing porosity p (Fig. 4.9) is determined by the competing effect of decreasing piezoelectric modulus d_{31}^* and dielectric constant ε_{33}^{T*} and increasing elastic compliance S_{11}^{E*} and S_{12}^{E*} in accordance with the relations $k_p^{*2} = 2d_{31}^{*2}/\left[\varepsilon_{33}^{T*}\left(S_{11}^{E*} + S_{12}^{E*}\right)\right]$ and $k_{31}^{*2} = d_{31}^{*2}/\left(\varepsilon_{33}^{T*} S_{11}^{E*}\right)$. The main reason for the decrease in k_p and k_{31} is the above mentioned violation of the continuity of the ceramic frame in the lateral direction and, as a consequence, the corresponding growth in the elastic compliance of lead-free porous ceramics.

The electromechanical coupling coefficient for the thickness mode of vibration k_t^* increases with increasing porosity, approaching the value of k_{33}^* (Fig. 4.9). This is due to the removal of the mechanical clamping of the porous frame in the lateral direction typical for dense ceramics (the coefficient of electromechanical coupling

for the ceramic rod is k_{33}^*, and there is no mechanical clamping of the ceramics frame by air). With a further increase in p, the coefficient k_t^* decreases as a result of the drop in the piezoconstant e_{33}^* : $k_t^{*2} = e_{33}^{*2}/\left(\varepsilon_{33}^{S*} C_{33}^{D*}\right)$ The relationship between the resulting values of the considered coefficients of the electromechanical coupling for any porosity is described quite well by an approximate relation: $k_t^{*2} \approx \left(k_{33}^{*2} + k_p^{*2}\right)\Big/\left(1 - k_p^{*2}\right)$.

The mechanical quality factor of the thickness mode vibrations Q_M^{t*} decreases with increasing porosity much faster than the mechanical quality factor of the radial mode Q_M^{r*} (Fig. 4.10), which is caused by the frequency dependence of the attenuation of elastic waves. The nature of the changes of mechanical quality factor of lead-free porous ceramics is determined by the scattering of elastic wave at the pores. The attenuation coefficient (reverse of Q_M) of an elastic wave depends on the size and shape of the scattering centers, their number and the frequency of the wave. The main mechanism determining the mechanical quality factor of dense piezoceramics (internal friction caused by the interaction of an elastic wave with a domain structure and defects [18]), in our case plays a secondary role. In the case of spherical pores, the frequency dependence of the damping coefficient (Rayleigh scattering, $\lambda \gg D$) is determined by the approximate relation $\alpha \approx kD^3 f^4$, where D is the average pore diameter, and f is frequency. Respectively, the Q_M factor decreases as $1/f^3$. In the region of low porosity, the pores are isolated, backscattering is absent and the mechanical quality factors decreases rapidly enough in proportion to the number of pores. As the porosity increases, the decrease in Q_M^* slows down due to backscattering.

Porous lead-free piezoceramics similarly to the 1-3 composites are characterized by the increased values of k_t^* and d_{33}^*, the lowered values of d_{31}, k_p, k_{31}, V_t, Q_M^t, Z_A, as well as the better resonance characteristics of the porous piezoelements. In addition, porous lead-free piezoceramic elements are easily processed, resist to thermal and mechanical influences and provide a higher adhesion of electrodes, compared to conventional piezoceramics. Table 4.4 shows the main parameters of the developed lead-free porous piezoceramics.

Table 4.4 Dielectric, piezoelectric and physical parameters of lead-free porous ceramics PCR-34

Material/ parameter	$\varepsilon_{33}^T/\varepsilon_0$	tgδ (%)	d_{33} (pC/N)	$\lvert d_{31}\rvert$ (pC/N)	k_t	k_p	V_t (m/s)	Q_M^p	ρ (g/cm^3)	Z_A (Mrayl)
PCR-34[a]	310	2.5	102	32	0.52	0.09	3250	20	2.75	8.93
PCR-34[b]	200	2.75	98	56	0.51	0.13	4500	35	3.5	15.75

Note [a]Is the relative content of the ceramic phase = 0.4; [b]is the relative content of the ceramic phase = 0.2

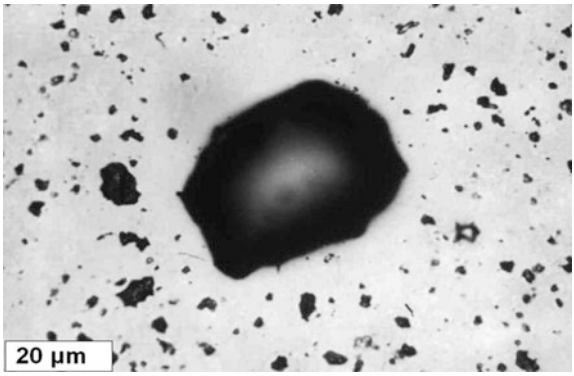

Fig. 4.11 Optical micrographs of polished surfaces of PCR-34/20% $LiNbO_3$ ceramic/crystal piezocomposite

4.2.4 *Lead-Free Ceramic Matrix Piezocomposites*

Lead-free ceramic matrix piezocomposites, composed by the PCR-34 ceramics matrix with randomly distributed $LiNbO_3$ monocrystal particles were fabricated and tested. Piezoceramic powders composed of synthesized (Na, K)NbO_3 solid solutions (PCR-34) and milled $LiNbO_3$ monocrystal particles (20 µm average size) were used as matrix and filling components, respectively. Sintering of the green bodies was carried out at special thermal profiles to prevent cracking, caused by difference in shrinkage and thermal expansion coefficients of the composite components [28, 29]. Samples of ceramic matrix composites "ceramics/crystal" with the volume fraction of crystalline filler 0–20% were fabricated and tested. Figure 4.11 shows an example of ceramic matrix piezocomposite microstructure.

It is readily seen in Fig. 4.11 that inclusion of the unshrinkable phase ($LiNbO_3$ monocrystal particles) into ceramic matrix, prevents shrinkage of ceramic matrix and leads to microporosity appearance. Dielectric, piezoelectric and physical parameters of experimental samples of lead-free ceramic matrix composites are listed in Table 4.5.

New lead-free ceramic matrix piezocomposites composed by $LiNbO_3$ monocrystal particles, embedded in porous (Na, K)NbO_3 piezoceramic matrix are characterized by a unique spectrum of the electrophysical properties unachievable for standard PZT ceramic compositions fabricated by standard methods and can be useful for wide-band ultrasonic transducer applications [30–32].

Table 4.5 Parameters of PCR-34/20%$LiNbO_3$ ceramic/crystal piezocomposite

Material/ parameter	$\varepsilon_{33}^T/\varepsilon_0$	tgδ (%)	d_{33} (pC/N)	$\lvert d_{31}\rvert$ (pC/N)	k_t	k_p	V_t (m/s)	Q_M^p	ρ (g/cm^3)	Z_A (Mrayl)
PCR-34/ $LiNbO_3$	120	2	100	22	0.58	0.2	5000	30	4.5	22.5

4.3 Conclusion

The results of systematic studies allowed us to develop manufacture technology of lead-free "ceramics-polymer" composites with 1-3 connectivity type, ceramic matrix composites "ceramics/crystal", and porous ceramics, based on lead-free sodium-lithium niobates (Na, Li)NbO_3 and sodium-potassium niobates (Na, K) NbO_3 compositions. The developed lead-free porous and composite materials have a unique combination of parameters unachievable for standard PZT ceramic compositions, fabricated by standard methods. They can be used in the manufacture of ultrasonic transducers and devices for a wide range of applications, including medical diagnostic equipment, nondestructive testing, level and flow-metry, underwater acoustics, as well as power ultrasonic systems for medical and technological purposes.

Acknowledgements This work was financially supported by the Ministry of Education and Science of the Russian Federation: the basic parts of the state task, themes № BP0110-11/2017-44 (12.5425.2017/8.9), № 3.8863.2017/ITW (3.8863.2017/7.8).

References

1. W.A. Smith, A.A. Shaulov, Ferroelectrics **87**, 309 (1988)
2. W.A. Smith, in *IEEE Ultrasonics Symposium Proceedings* (1989), p. 755
3. J. Mendola, B. Jimenez, Ferroelectrics **53**, 159 (1984)
4. T.R. Shrout, W.A. Shulze, J.V. Biggers, Mat. Res. Bull. **14**(12), 1553 (1979)
5. K. Rillenmyer, T. Shrout, W.A. Schulze, R.E. Newnham, Ferroelectrics **41**, 189 (1982)
6. R.Y. Ting, Ferroelectrics **49**, 251 (1983)
7. Andrey N. Rybyanets, Ferroelectrics **419**(1), 90 (2011)
8. A.N. Rybyanets, in *Advanced Materials—Manufacturing, Physics, Mechanics and Applications*, vol. 175, Springer Proceedings in Physics, ed. by I.A. Parinov, C. Shun-Hsyung, V.Y. Topolov (Springer, Cham, Heidelberg, New York, Dordrecht, London, 2016), p. 211
9. A.J. Dantziger et al., *Multicomponent Systems of Ferroelectric Solid Solutions: Physics, Crystallochemistry, Technology. Design Aspects of Piezoelectric Materials* (Rostov State University Press, Rostov on Don, 2001), pp. 1–2
10. T.R. Gururaja, W.A. Schulze, L.E. Cross, B.A. Auld, Y.A. Shui, Y. Wang, Ferroelectrics **54**, 183 (1984)
11. B.A. Auld, Y.A. Shui, Y. Wang, J. de Physique **45**, 159 (1984)
12. D.-M. Liu, Porous ceramic materials: fabrication, characterization, applications. Key Eng. Mater. **115** (1986)
13. S.S. Lopatin, T.G. Lupeiko, Izv. AN USSR. Ser. Neorg. Mat. **27**, 1948 (1991)
14. W. Wersing, K. Lubitz, J. Moliaupt, Ferroelectrics **68**(1/4), 77 (1986)
15. I.P. Raevskii, M.P. Ivliev, L.A. Reznitchenko, M.N. Palatnikov, L.E. Balyunis, M.A. Malitskaya, Tech. Phys. **47**(6), 772 (2002)
16. T.R. Shrout, S.J. Zhang, J. Electr. **19**, 113 (2007)
17. P.K. Panda, J. Mater. Sci. **44**, 5049 (2009)
18. J. Rodel, W. Jo, K.T.P. Seifert, E.M. Anton, T. Granzow, D. Damjanovic, J. Am. Ceram. Soc. **92**, 1153 (2009)

19. J. Rodel, K.G. Webber, R. Dittmer, W. Jo, M. Kimura, D. Damjanovic, J. Eur. Ceram. Soc. **35**, 1659 (2015)
20. J.G. Wu, D.Q. Xiao, J.G. Zhu, Chem. Rev. **115**, 2559 (2015)
21. PRAP (Piezoelectric Resonance Analysis Programme). TASl Technical Software Inc. (www.tasitechnical.com)
22. A.N. Rybianets, R. Tasker, Ferroelectrics **360**(1), 90 (2007)
23. A. Rybianets, L. Kushkuley, Y. Eshel, A. Nasedkin, in *2006 IEEE Ultrasonics Symposium IUS*, acc. no. 9474463 (Vancouver, BC, Canada, 2006), p. 1533
24. A.N. Rybyanets, IEEE Trans. UFFC **58**(7), 1492 (2011)
25. A.N. Rybjanets, O.N. Razumovskaja, L.A. Reznitchenko, V.D. Komarov, A.V. Turik, Integr. Ferroelectr. **63**, 197 (2004)
26. M. Kahn, J. Amer. Ceram. Soc. **68**(11), 623 (1985)
27. K.H. Hikita, K. Jamada, M. Nishioka, M. Ono, Ferroelectrics **49**(1/4), 265 (1983)
28. A.N. Rybianets, Ferroelectrics **360**(1), 84 (2007)
29. A. Rybianets, Y. Eshel, L. Kushkuley, in *Proceedings 2006 IEEE Ultrasonics Symposium IUS*, (2006), p. 1911
30. Andrey Rybyanets, Anastasia Rybyanets, IEEE Trans. UFFC **58**(9), 1757 (2011)
31. A.N. Rybyanets, A.A. Naumenko, G.M. Konstantinov, N.A. Shvetsova, M.A. Lugovaya, Phys. Solid State **57**(3), 558 (2015)
32. A.N. Rybyanets, G.M. Konstantinov, A.A. Naumenko, N.A. Shvetsova, D.I. Makar'ev, M.A. Lugovaya, Phys. Solid State **57**(3), 527 (2015)

Chapter 5
Post-treatment of Pt-*M* (*M* = Cu, Co, Ni)/C Electrocatalysts with Different Distribution of Metals in Nanoparticles: Evolution of Structure and Activity

Sergey V. Belenov, Vladislav S. Menshchikov, Alina K. Nevelskaya, Vasiliy V. Pryadchenko, Daria B. Shemet, Vasiliy V. Srabionyan, Anastasia A. Alekseenko, Sergey A. Kirakosyan and Vladimir E. Guterman

Abstract The article discusses a wide range of issues related to the relationship between the composition and fine structure (architecture) of bimetallic nanoparticles and electrochemical performance of Pt-*M*/C (*M* = Cu, Co, Ni) electrocatalysts. Among these questions are: evolution of nanoparticles during thermo-treatment, catalytic activity in the oxygen reduction and methanol electro-oxidation reactions, corrosion-morphological stability of the catalysts, selective dissolution of alloying component.

5.1 Introduction

The problem of obtaining an efficient catalyst with low platinum content, high specific activity and increased operating life is very important for the creation of competitive electrochemical power sources [1–4]. The cost of the catalytic layer in low-temperature fuel cells (FC) makes up a significant proportion (up to 40%) of the membrane-electrode assembly cost, which, in combination with a short service life of the fuel cells, determines the high cost of electricity produced. The reduction in the cost of produced electricity and the fuel cells themselves can be achieved

S. V. Belenov (✉) · V. S. Menshchikov · A. K. Nevelskaya · A. A. Alekseenko
S. A. Kirakosyan · V. E. Guterman
Chemistry Faculty, Southern Federal University, Zorge St. 7,
Rostov-on-Don 344090, Russia
e-mail: sbelenov@sfedu.ru

V. V. Pryadchenko · D. B. Shemet · V. V. Srabionyan
Physical Faculty, Southern Federal University, Zorge St. 5,
Rostov-on-Don 344090, Russia

I. A. Parinov et al. (eds.), *Advanced Materials*, Springer Proceedings
in Physics 207, https://doi.org/10.1007/978-3-319-78919-4_5

both by the reducing of platinum content in the catalytic layer (in the catalyst) thanks to its high activity, and by increasing stability of the catalyst and entire catalytic layer [1–4]. One of the possible solutions of this problem is the obtaining of platinum-based electrocatalysts, which contain bimetallic nanoparticles with predominant segregation of platinum atoms on the surface and, in the optimal case, with "*M*-core—Pt-shell" architecture [4–8].

The results of theoretical calculations and experimental studies show that Pt-*M* nanoparticles can be classified into several types according to the character of components distribution: a uniform distribution of metals (solid solution), an ordered distribution of metals (intermetallide), nanoparticles with "core-shell structure", where one of the metals is located in the center of the nanoparticle (the core), and the other metal (shell) covers this core. Segregation of platinum atoms in the surface layers of nanoparticles, as a rule, leads to the increase in the activity and, sometimes, to the growth of electrocatalysts stability [9–11]. That is the reason why the interest in bimetallic nanoparticles of core—shell architecture grows recently.

Thus, attention to such nanostructured objects is due to a complex of reasons, the main of which are the desire to reduce the content of precious metal in the catalyst, to increase stability of FC and catalytic activity of platinum in current-producing electrochemical reactions due to the promoting effect of metal core on the shell [2, 4, 9, 12, 13].

The synthesis of such materials is a difficult problem because of the need to form a solid shell of platinum, able to reliably protect the core from the effects of the external environment. In according with the results of analysis of numerous publications devoted to methods for synthesizing catalysts containing nanoparticles with a core-shell structure, these methods can be conditionally divided into two types: (i) sequential formation of the core and shell of the nanoparticle [3] and (ii) obtaining core-shell structure by the post-treatment of solid solution nanoparticles [14, 15]. The use of the first approach, could produce nanoparticles with different shell thicknesses, while using the second approach is better for obtaining a thin platinum shell of 1–2 atomic layers in combination with a significant concentration of platinum atoms in the nanoparticle core.

Note that the mixture of nanoparticles of different sizes, some of which have a defective shell, is obtained after the real synthesis. The presence of particles with a non-uniform shell negatively affects on the functioning of FC, since the dissolution of unprotected core metal results in membrane contamination and failure of the FC. That is why various methods of catalysts post-treatment are widely used to increase their stability and functional characteristics of FC.

A thermal treatment and treatment in various acids are the most widely used among the methods of catalysts post-treatment [14, 16]. In the case of materials containing nanoparticles with a non-uniform platinum shell, the treatment in acid solutions leads to the selective dissolution of the core metal. On the one hand that could increase stability of the material, but on the other hand it can lead to the reduction in the specific characteristics, because of detaching of individual nanoparticles from carbon surface. In addition, under certain conditions, a treatment of such materials in the acids leads to the formation of so-called hollow

nanoparticles, in which only the platinum shell remains due to the dissolution of the core metal.

Typically, thermo-treatment is used to form bimetallic nanoparticles with high degree of alloying, since the co-precipitation of platinum and a less noble metal does not always lead to the formation of a uniform solid solution [16, 17]. Since an atmosphere of inert gases with a small addition of hydrogen are used in the heat treatment process, it leads to the reduction of the oxide of less noble metal, formed at the stage of synthesis.

Thermo-treatment of materials containing nanoparticles with a core-shell structure produces its own effects [10, 11]. A more perfect shell can be obtained from the defective platinum shell, by filling defects in the shells due to the diffusion of platinum atoms. On the other hand, during the thermo-treatment nanoparticles could grow due to agglomeration and the core-shell structure may be destroyed due to interdiffusion of the Pt and *M* atoms. Therefore, the optimization of thermo-treatment conditions: temperature regime, duration, composition of the atmosphere, etc. is an important issue.

In our opinion, despite a large number of articles devoted to the thermo-treatment of bimetallic nanoparticles deposited on disperse carbon carrier, the processes occurring during the treatment of bimetallic nanoparticles with a core-shell structure, including a change in the architecture of nanoparticles upon heating, are not sufficiently studied. At the same time, it is obvious that the architecture of nanoparticles determines their functional characteristics, and it is necessary to control the microstructure of the materials to obtain high-performance catalysts.

The purpose of the research is to study the effect of thermo-treatment on the structure of bimetallic nanoparticles of different architectures and catalytic activity of Pt-*M* (*M* = Cu, Co, Ni)/C materials in the oxygen reduction and methanol oxidation reactions.

5.2 Experimental

Carbon supported Pt-*M* (*M* = Cu, Co, Ni) nanoparticles were synthesized by wet-synthesis using $NaBH_4$ as a reducing agent, this technique is described in detail in [13]. Briefly, in water—ethylene glycol suspension of carbon powder (Vulcan XC72, Cabot) and metal precursors at pH = 10 (an excess of NH_3) was added excess a freshly prepared 0.5 M $NaBH_4$. Synthesis was carried out in one and two stages to obtain alloy materials [18] and materials with core-shell structure [13, 19], respectively, Pt-*M* (*M* = Cu, Co, Ni)/C materials obtained by wet-synthesis in one and two stages and marked, respectively, as Pt-*M*1 and Pt-*M*2.

The temperature treatment was carried out using a PTC-1.2-40 furnace (NPP Teplopribor) in an argon atmosphere in the temperature range 250–350 °C according to the following scheme: rapid (about 10 min) heating to the set temperature, holding at the set temperature for 1 h, slow spontaneous cooling after

switching off the heating for 4–5 h to room temperature. Materials after heat treatment were marked by adding a numerical value of the treatment temperature as an index to the name of the material, for example the material after treatment at 350 °C–Pt-Cu1_350.

The composition of the synthesized Pt-*M*/C nanocatalysts corresponds to mass fraction of the metallic component of 35% by weight. The chemical composition of prepared materials was determined by X-ray fluorescence analysis using the X-ray spectrometer ARL OPTIM'X.

Synchrotron X-ray powder diffraction patterns were collected at μSpot beam-line Synchrotron Radiation Facility (Berlin, Germany). The monochromatic beam with the wavelength λ = 0.69489 Å was used. The sample-to-detector distance, the tilt angles of the detector and the wavelength were calibrated using LaB_6 NIST standard sample.

Pt L3- and Cu K-edge EXAFS spectra for the studied materials were measured at the μSpot beam-line [20, 21], of the BESSY-II Synchrotron Radiation Facility (Berlin, Germany). Mean electron current of a storage ring was maintained during experiment at 250 mA in Top-Up mode. The measurements were performed in the transmission mode utilizing a Si (111) channel-cut monochromator and two ionization chambers and diode for reference channel.

The TEM analysis was performed using a JEM-2100 (JEOL, Japan) microscope. Electrocatalyst powders (0.5 mg) were placed in 1 ml of heptane to prepare the samples for the TEM analysis. The suspension was then ultrasonically dispersed, and one drop of the suspension was deposited onto a copper grid sputter-coated with carbon.

The electrochemical characteristic was measured at rotating disc electrode on standard tree electrode cell [22]. As a reference electrode, a saturated silver chloride electrode was used and as a counter electrode was used platinum wire. The values of the potentials in the work are given relative to the reversible hydrogen electrode.

Catalysts dropped at electrode using prepared «catalytic inks», containing 0.006 g catalyst, 900 μl isopropanol and 100 μl 0.5% Nafion [23].

The 6 μl resulting suspension was dropped on the glass-graphite electrode (with diameter of 5 mm) via pipette, then after the drying of the drop, 7 μl of a 0.05% solution of Nafion were applied to fix the catalytic layer.

For the electrodes standardization before further measurements, 100 CV cycles were recorded in the range from 0.03 to 1.26 V with a potential sweep rate of 200 mV/s. After standardization, 2 CVs were registered to determine the electrochemically active area (ESA) of the catalyst in the same potential range with a sweep rate of 20 mV/s. The calculation of the ESA value was based on the amount of electricity spent for adsorption/desorption of atomic hydrogen [22, 24].

To measure the activity of the catalysts, a series of potentio-dynamic curves were recorded on a rotating disk electrode in the potential range 0.1–1.2 V with a potential sweep rate of 20 mV/s at different electrode rotation speeds (400, 900, 1600, 2500 rpm). The measured curves were normalized to cell resistance (24 Ω) and the background curve measured in the saturation with Arelectrolyte was subtracted, as described in [25].

5.3 Results and Discussion

5.3.1 *Effect of Thermo-Treatment on Structure of Pt-M (M = Cu, Co, Ni)/C Materials*

Powder diffractograms of Pt-*M* (*M* = Cu, Co, Ni)/C materials, shown in Fig. 5.1, are typical for platinum-containing catalysts on a carbon carrier and contain metal phase reflections corresponding to a face-centered cubic lattice of the space group Fm-3 m [26]. Note that on all presented powder diffractograms, there are not reflections corresponding to the phases of pure metals or their oxides (Fig. 5.1).

The significant broadening of reflections on X-ray diffraction patterns is due to the presence of the phase in the form of nanoscale crystallites whose size (D_{aver}) was estimated using the Scherrer equation [27–29] (Table 5.1). According to results of XRD analysis (Fig. 5.1), average nanoparticles size increased during thermo-treatment from 250 to 350 °C (Table 5.1). This fact agrees well with the literature data [17, 30, 31]. Observed increase in the average size of nanoparticles is most expressed for Pt-Cu/C materials: from 1.8–2.4 nm to 10.7–11.5 nm. For Pt-Ni/C and Pt-Co/C materials the average particle size coarsening occurs to a lesser extent, about 1.5–2 times.

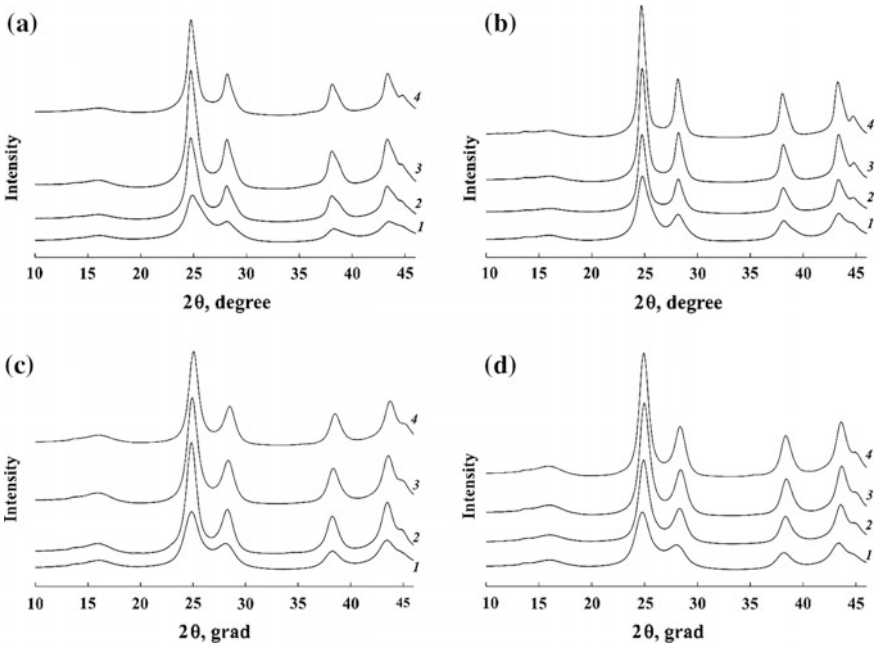

Fig. 5.1 XDR patterns for **a** Pt-Ni1, **b** Pt-Ni2, **c** Pt-Co1, **d** Pt-Co2 catalysts as prepared (1) and after thermal treatment at 250 °C (2), 300 °C (3), 350 °C (4)

Table 5.1 Some characteristics of Pt-*M* (*M* = Cu, Co, Ni)/C materials prepared by the wet-synthesis

Sample	Composition	ω Pt (%)	ω *M* (%)	D_{aver} (XRD) (nm)	*S* (H_{ads}) (m^2/g)
Pt-Cu1	$Pt_{1.1}Cu$	27	35	1.9	44 ± 4
Pt-Cu1_350	$Pt_{1.1}Cu$	27	35	10.7	30 ± 3
Pt-Cu2	$Pt_{0.8}Cu$	21	26	2.3	50 ± 5
Pt-Cu2_350	$Pt_{0.8}Cu$	21	26	11.5	32 ± 3
Pt-Co1	$Pt_{0.7}Co$	16.8	26.4	2.1	70 ± 7
Pt-Co1_350	$Pt_{0.7}Co$	16.8	26.4	3.5	60 ± 6
Pt-Co2	$Pt_{1.0}Co$	17.5	24.8	2.1	73 ± 7
Pt-Co2_350	$Pt_{1.0}Co$	17.5	24.8	4.1	65 ± 6
Pt-Ni1	$Pt_{2.7}Ni$	15.9	27.6	1.8	85 ± 9
Pt-Ni1_350	$Pt_{2.7}Ni$	15.9	27.6	3.7	85 ± 8
Pt-Ni2	$Pt_{3.7}Ni$	19.0	29.2	2.4	68 ± 7
Pt-Ni2_350	$Pt_{3.7}Ni$	19.0	29.2	4.9	72 ± 7

The chemical composition of the electrocatalysts, determined by the X-ray fluorescent analysis (XFA), was somewhat different from the composition calculated by the precursors loading (Table 5.1): the relative content of copper atoms in the Pt-Cu2 material was slightly higher than the calculated one, and Co and Ni concentrations were higher than the calculated values for all materials.

It is known that high-resolution transmission electron microscopy (TEM) allows one to determine the average size of nanoparticles, deposited on the carbon carrier surface, and study a fine structure of the nanoparticles, to reveal the presence of defects, etc. The TEM investigation of the Pt-Cu/C catalysts (Fig. 5.2a, c) confirmed the formation of bimetallic nanoparticles of size range of 2 ± 10 nm: dark metallic nanoparticles, uniformly distributed over the surface of the carbon carrier, are visible in photos. The results of TEM give a larger size of the nanoparticles in comparison with the calculation using the Scherrer equation (Table 5.1). This fact can be related both to the presence of X-ray amorphous shells on the surface of nanoparticles and to the complex composition of bimetallic nanoparticles consisting of 2–3 domains.

The results of the TEM for Pt-Cu/C materials after thermo-treatment at 300 °C (Fig. 5.2b, d) indicate some enlargement of the nanoparticle size, which well agrees with the XRD data. It is possible that during the thermo-treatment at these temperatures both agglomeration of individual particles occurs, and a rearrangement of the internal structure of nanoparticles [19], resulted to transformation of 2–3 domains in single crystallite of big size.

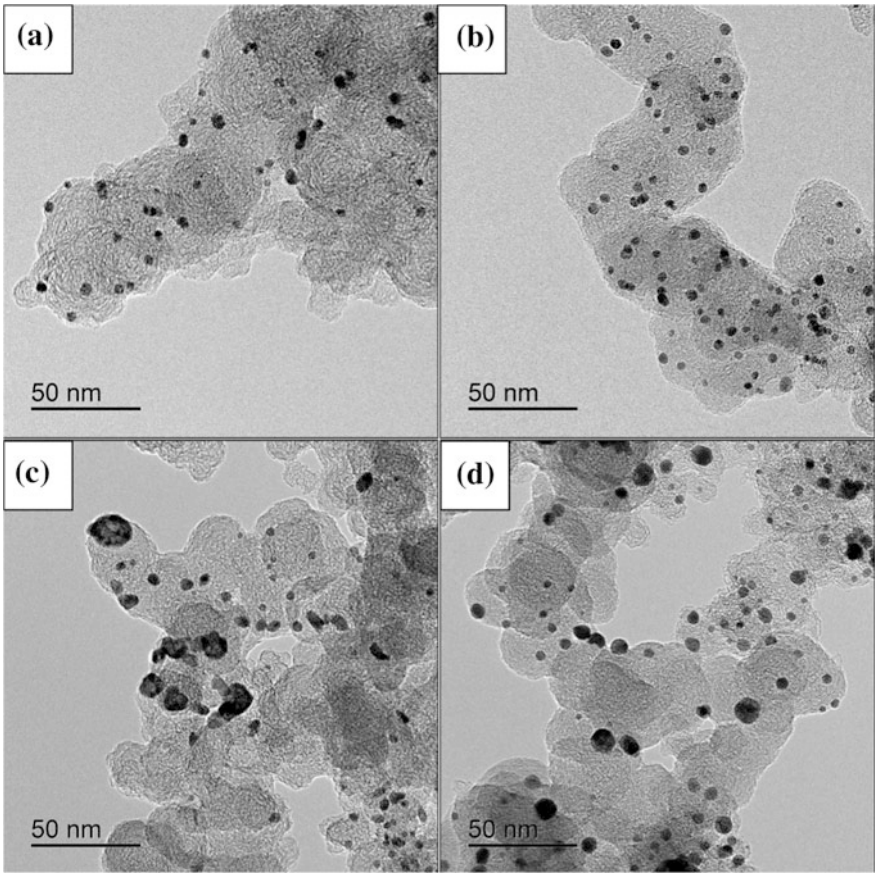

Fig. 5.2 TEM images of Pt-Cu1 before **a** and after **b** thermo-treatment at 300 °C; Pt-Cu2 before **c** and after **d** thermo-treatment at 300 °C

5.3.2 *Effect of Thermo-Treatment on Atomic Structure of Pt-M (M = Cu, Co, Ni) Nanoparticles*

The magnitudes of the Fourier-transforms of experimental Pt L3-edge EXAFS of Pt-*M* (*M* = Co, Ni) materials before and after thermo-treatment at different temperatures are compared in Fig. 5.3a. Detailed analysis of the local atomic structure of bimetallic particles by EXAFS-spectroscopy was not a purpose of this paper, since this is the subject of a separate study. However, even a qualitative analysis of the spectra obtained can provide useful information about changes in the structure of bimetallic nanoparticles during thermo-treatment. For nickel-containing materials Pt-Ni1 and Pt-Ni2 (Fig. 5.3a, b), the analysis shows a significant change in the character of the spectrum during the transition from “as prepared” state to the

material after treatment at 250 °C. Further increase in the treatment temperature practically does not affect the character of the spectrum. So, the change in the structure of bimetallic Pt-Ni nanoparticles took place at 250 °C. In the case of Pt-Co materials, the character of the changes in the spectra is much more complicated and several temperature transitions were observed (Fig. 5.3c, d).

5.3.3 *Effect of Thermo-Treatment on Electrochemical Surface Area of Pt-M (M = Cu, Co, Ni)/C Materials*

Figure 5.4 shows cyclic voltammograms (CVs) of studied Pt-*M* (*M* = Cu, Co, Ni)/C materials before and after thermo-treatment in inert atmosphere. It can be seen from CVs data that all characteristic regions (hydrogen, double layer, oxygen) are clearly expressed for materials both before and after treatment. ESA values, determined for different Pt-*M* (*M* = Cu, Co, Ni)/C materials, were in the range from 44 m^2/g (Pt) for Pt-Cu1 to 85 m^2/g (Pt) for Pt-Ni1 (Table 5.1). According to obtained results, an increase of the temperature of the treatment leads to the decrease in the electrochemically active surface area for all samples. That is associated with an

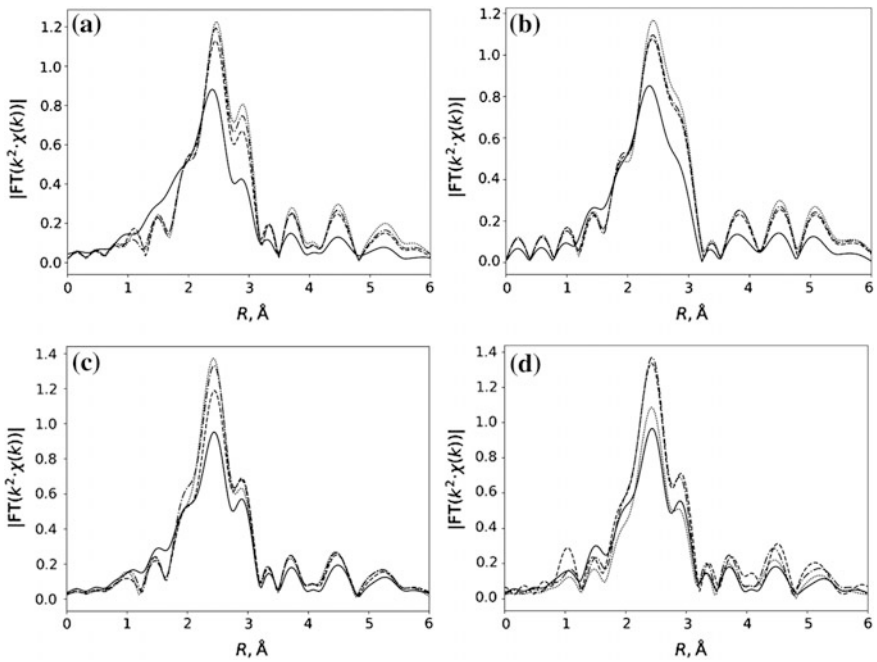

Fig. 5.3 EXAFS for **a** Pt-Ni1, **b** Pt-Ni2, **c** Pt-Co1, **d** Pt-Co2 as prepared catalyst (solid line) and after treatment at 250 °C (dashed line), 300 °C (cross-hatching line) and 350 °C (dotted line)

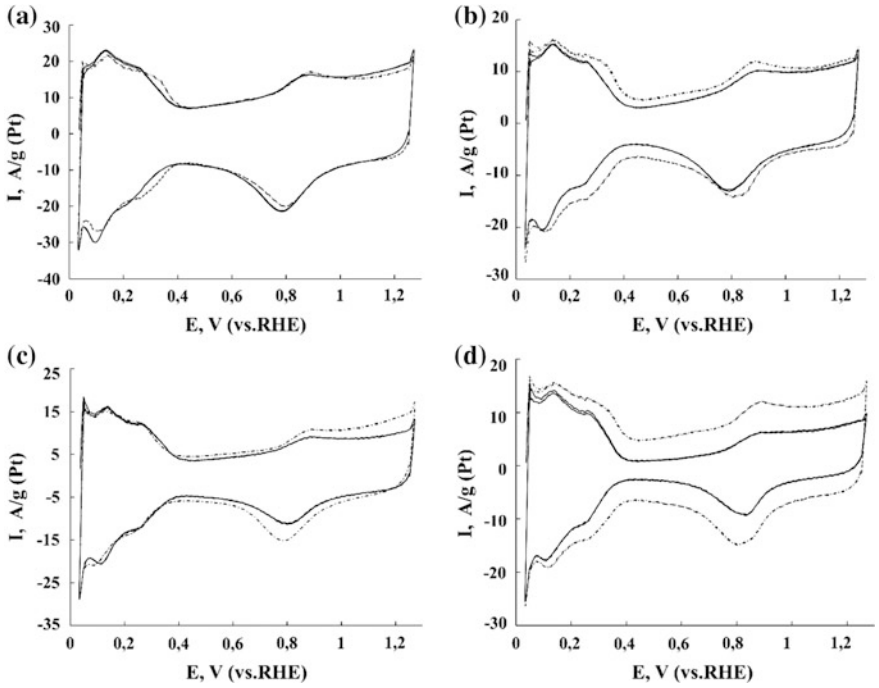

Fig. 5.4 CV for **a** Pt-Ni1, **b** Pt-Ni2, **c** Pt-Co1, **d** Pt-Co2 as prepared catalyst (solid line) and after treatment at 350 °C (dotted line); electrolyte—Ar-saturated 0.1 M $HClO_4$, room temperature, sweep rate: 20 mV s^{-1}

increase in the particle size. This effect was most pronounced for two samples: $Pt_{0.7}Co/C$ (Pt-Co1) [from 70 m^2/g (Pt) to 60 m^2/g (Pt)] and $Pt_{0.8}Cu$ (Pt-Cu2) [from 50 m^2/g (Pt) to 32 m^2/g (Pt)].

5.3.4 *Effect of Thermo-Treatment on Catalytic Activity of Pt-M (M = Cu, Co, Ni)/C Materials in Oxygen Redaction Reaction*

The activity of Pt-*M* (*M* = Cu, Co, Ni)/C catalysts in oxygen reduction reaction (ORR) in acid media was investigated by the linear sweep voltammetry (LSV) (Fig. 5.5). Pt-Cu1 material had demonstrated the greatest mass-activity 301 A/g (Pt) and half-wave potential value ($E_{1/2}$) among all studied catalysts (Table 5.2) in the "as prepared" state.

The mass-activity of catalysts after thermo-treatment at 350 °C increased from 168 A/g (Pt) to 344 A/g (Pt) for $Pt_{1.0}Co/C$ (Pt-Co2) and from 136 A/g(Pt) to 331 A/g(Pt) for $Pt_{2.7}Ni/C$ (Pt-Ni1) (Table 5.2).

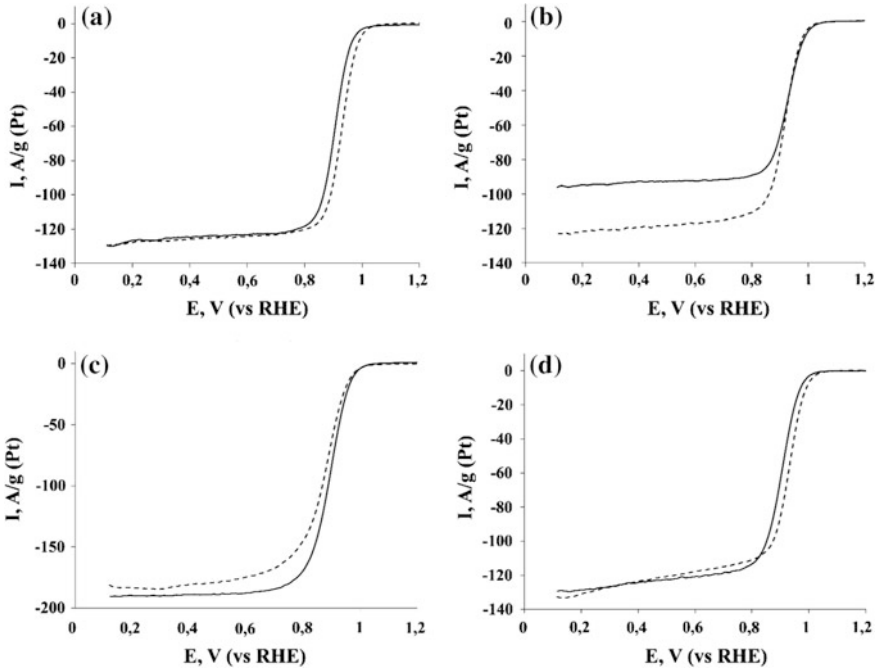

Fig. 5.5 Liner sweep voltammetry for **a** Pt-Ni1, **b** Pt-Ni2, **c** Pt-Co1, **d** Pt-Co2 "as prepared" catalysts (solid line) and after treatment at 350 °C (dotted line); electrolyte—O_2-saturated 0.1 M $HClO_4$, room temperature, sweep rate: 20 mV s^{-1}, rotation speed is 1600 rpm

Table 5.2 Composition and activity of Pt-*M* (*M* = Cu, Co, Ni)/C catalysts prepared by the wet-synthesis

Sample	Composition		I_k, A/g (Pt)	I_k, A/m^2	$E_{1/2}$, V
	As prepared	After CV			
Pt-Cu1	$Pt_{1.1}Cu$	$Pt_{1.8}Cu$	301	7.08	0.92
Pt-Cu1_350	$Pt_{1.1}Cu$	$Pt_{1.5}Cu$	164	5.21	0.92
Pt-Cu2	$Pt_{0.8}Cu$	$Pt_{1.7}Cu$	134	2.82	0.90
Pt-Cu2_350	$Pt_{0.8}Cu$	$Pt_{1.7}Cu$	44	1.37	0.87
Pt-Co1	$Pt_{0.7}Co$	$Pt_{7.0}Co$	139	1.98	0.90
Pt-Co1_350	$Pt_{0.7}Co$	$Pt_{4.2}Co$	95	1.60	0.89
Pt-Co2	$Pt_{1.0}Co$	$Pt_{6.2}Co$	168	2.32	0.92
Pt-Co2_350	$Pt_{1.0}Co$	$Pt_{4.7}Co$	344	5.32	0.92
Pt-Ni1	$Pt_{2.7}Ni$	$Pt_{6.8}Ni$	136	1.61	0.91
Pt-Ni1_350	$Pt_{2.7}Ni$	$Pt_{6.7}Ni$	331	3.87	0.93
Pt-Ni2	$Pt_{3.7}Ni$	$Pt_{8.7}Ni$	204	3.00	0.93
Pt-Ni2_350	$Pt_{3.7}Ni$	$Pt_{8.7}Ni$	225	3.14	0.92

The study of the catalysts composition before and after CV measurement showed that in some cases heat treatment reduced the amount of the non-noble component dissolved. For example, for $Pt_{1.0}Co$/C (Pt-Co2) material, the amount of dissolved cobalt decreases from $Pt_{6.2}Co$ to $Pt_{4.7}Co$ and for $Pt_{0.7}Co$/C (Pt-Co1) material—from $Pt_{7.0}Co$ to $Pt_{4.2}Co$ after thermo-treatment at 350 °C (Table 5.2). At the same time, the thermo-treatment had no effect on the amount of alloying component dissolved for nickel-containing materials $Pt_{3.7}Ni$ and $Pt_{2.7}Ni$.

5.3.5 *Effect of Thermo-Treatment on Catalytic Activity of Pt-M (M = Cu, Co, Ni)/C Materials in Methanol Oxidation Reaction*

To study the activity of obtained Pt-*M* (*M* = Cu, Co, Ni)/C materials in the methanol electro-oxidation reaction (MOR) we used the method of cyclic voltammetry (Fig. 5.6). The survey was carried out on a stationary electrode in 0.1 M $HClO_4$ + 0.5 M CH_3OH electrolyte, saturated with argon at atmospheric pressure. Figure 5.6a shows CVs for Pt-*M* (*M* = Cu, Co, Ni)/C catalysts, obtained by two different synthesis techniques—in one and in two steps. Among these materials, Pt-Ni2 catalyst was more active in MOR (Fig. 5.6). In according with authors [32, 33] the thermo-treatment can increase a catalytic activity of bimetallic materials in MOR. This may be due to the ordering of atoms in a bimetallic nanoparticle. For Pt-Co1_350 and Pt-Ni1_350 catalysts, activity in MOR significantly increased (Fig. 5.6b). When comparing the characteristics of Pt-Ni2 and heat-treated Pt-Co1 and Pt-Ni1 catalysts, the most activity in MOR shows the Pt-Ni2 material.

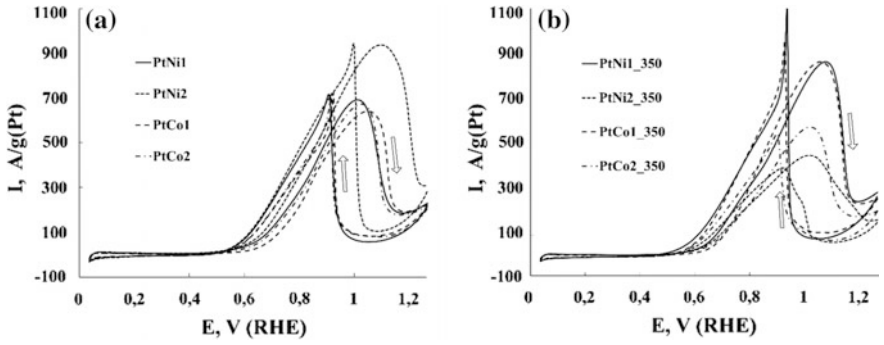

Fig. 5.6 **a** CV for as prepared catalysts and **b** catalysts after thermo-treatment at 350 °C; Electrolyte—Ar-saturated 0.1 M $HClO_4$ + 0.5 M CH_3OH, room temperature, sweep rate: 20 mV/s

5.4 Conclusions

Based on the results of the study a number of Pt-*M* (*M* = Cu, Co, Ni)/C materials, obtained by wet-synthesis, it was found that Pt-Cu1 catalyst, obtained in one stage of synthesis, is the most active material in ORR, and Pt-Ni2 material, obtained by a two-step synthesis method, is the most active in MOR. It was found that the thermo-treatment in optimal conditions led to an increase in the catalytic activity of materials. For example, the mass-activity of the $Pt_{1.0}Co/C$ and $Pt_{2.7}Ni/C$ catalysts in ORR increased by 2–2.5 times after thermo-treatment at 350 °C. For Pt-Co1 and Pt-Ni1 catalysts, an activity in MOR significantly increased after thermo-treatment at 350 °C, too.

Acknowledgements This research was supported by the Russian Science Foundation (grant No 16-19-10115). Experimental EXAFS and XRD study was performed at the Syncrotron Radiation Facility BESSY II (Berlin, Germany).

References

1. V.R. Stamenkovic, B.S. Mun, M. Arenz, K.J.J. Mayrhofer, C.A. Lucas, G. Wang, P.N. Ross, N.M. Markovic, Nat. Mater. **6**, 241 (2007)
2. A.B. Yaroslavtsev, YuA Dobrovolsky, N.S. Shaglaeva, L.A. Frolova, E.V. Gerasimova, E.A. Sanginov, Russ. Chem. Rev. **81**, 191 (2012)
3. Z. Peng, H. Yang, Nano Today **4**, 143 (2009)
4. X. Ge, L. Chen, J. Kang, T. Fujita, A. Hirata, W. Zhang, J. Jiang, M. Chen, Adv. Funct. Mater. **23**, 4156 (2013)
5. M. Ammam, E.B. Easton, J. Power Sources **222**, 79 (2013)
6. M. Luo, L. Wei, F. Wang, K. Han, H. Zhu, J. Power Sources **270**, 34 (2014)
7. D. Thompsett, *Technology and Applications* (2003)
8. Q. Lv, J. Chang, W. Xing, Ch. Liu, RSC Adv **4**, 32997 (2014)
9. N. Jung, Y. Sohn, H.J. Park, K.S. Nahm, P. Kim, S.J. Yoo, Appl. Catal. B **196**, 199 (2016)
10. D. Wang, Y. Yu, H.L. Xin, R. Hovden, P. Ercius et al., Nano Lett. **12**, 5230 (2012)
11. D. Wang, H.L. Xin, R. Hovden, H. Wang, Y. Yu, D.A. Muller, F.J. Disalvo, H.D. Abruña, Nat. Mater. **12**, 81 (2013)
12. R.N. Singh, R. Awasthi, C.S. Sharma, Int. J. Electrochem. Sci. **9**, 5607 (2014)
13. V.E. Guterman, S.V. Belenov, AYu. Pakharev, M. Min, NYu. Tabachkova, E.B. Mikheykina, L.L. Vysochina, T.A. Lastovina, Int. J. Hydrogen Energy **41**, 1609 (2016)
14. T. Travitsky, D. Ripenbein, Y. Golodnitsky, L. Rosenberg, E. Burshtein, J. Power Sources **161**, 782 (2006)
15. C. Wang, M. Chi, D. Li, D. Strmcnik, D. van der Vliet, G. Wang, V. Komanicky, K. Chang, A.P. Paulikas, D. Tripkovic, J. Pearson, K.L. More, N.M. Markovic, V.R. Stamenkovic, J. Am. Chem. Soc. **133**, 14396 (2011)
16. C.W.B. Bezerra, L. Zhang, H. Liu, K. Lee, A.L.B. Marques, E.P. Marques, H. Wang, J. Zhang, Journal of Power Sources **173**, 891 (2007)
17. L. Xiong, A. Manthiram, J. Electrochem. Soc. **152**, 697 (2005)
18. V.E. Guterman, T.A. Lastovina, S.V. Belenov, N.Y. Tabachkova, V.G. Vlasenko et al., J. Solid State Electrochemistry. **18**, 1307 (2014)
19. S.V. Belenov, V.A. Volochaev, V.V. Pryadchenko, V.V. Srabionyan, D.B. Shemet, N.Y. Tabachkova, V.E. Guterman, Nanotechnol. Russ. **12**, 147 (2017)

20. V.V. Srabionyan, V.V. Pryadchenko, A.A. Kurzin, S.V. Belenov, L.A. Avakyan, V.E. Guterman, L.A. Bugaev, Physics of the Solid State **58**, 752 (2016)
21. V.V. Pryadchenko, S.V. Belenov, D.B. Shemet, V.A. Volochaev, V.V. Srabionyan, L.A. Avakyan, N.Y. Tabachkova, V.E. Guterman, L.A. Bugaev, Phys. Solid State **59**, 1666 (2017)
22. U.A. Paulus, A. Wokaun, G.G. Scherer, T.J. Schmidt, V. Stamenkovic, V. Radmilovic, N.M. Markovic, P.N. Ross, J. Phys. Chem. B **106**, 4181 (2002)
23. V.E. Guterman, S.V. Belenov, A.A. Alekseenko, NYu. Tabachkova, V.A. Volochaev, Russ. J. Electrochem. **53**, 531 (2017)
24. A. Pozio, M. Francesco, Cemmi A. De, F. Cardellini, J. Power Sources **105**, 13 (2002)
25. K. Shinozaki, J.W. Zack, S. Pylypenko, B.S. Pivovar, S.S. Kocha, J. Electrochem. Soc. **162**, 1384 (2015)
26. R.W.G. Wyckoff, *Cubic Closest Packed, CCP, Structure. Crystal Structures,* vol. **1**, 7. 2nd edition (Interscience Publishers, New York, 1963)
27. J.I. Langford, A.J.C. Wilson, J. Appl. Crystallogr. **11**, 102 (1978)
28. I.N. Leontyev, S.V. Belenov, V.E. Guterman, P. Haghi-Ashtiani, A.P.J. Shaganov, Phys. Chem. C. **115**, 5429 (2011)
29. A.A. Alekseenko, V.E. Guterman, V.A. Volochaev, S.V. Belenov, Inorg. Mater. **51**, 1258 (2015)
30. B.N. Wanjala, R. Loukrakpam, J. Luo, P.N. Njoki, D. Mott, C.J. Zhong, M. Shao, L. Protsailo, T. Kawamura, J. Phys. Chem. C **114**, 17580 (2010)
31. A.N. Valisi, T. Maiyalagan, L. Khotseng, V. Linkov, S. Pasupathi, Electrocatalysis **3**, 108 (2012)
32. R. Rahul, R.K. Singh, M. Neergat, J. Electroanal. Chem. **712**, 223 (2014)
33. A. Stassi, I. Gatto, G. Monforte, V. Bagilo, E. Passalacqua, V. Antonucci, A.S. Arico, J. Power Sources **208**, 35 (2012)

Chapter 6
Hydrothermal Two-Step Synthesis of Titanate Nanotubes

Ekaterina M. Bayan, Timofey G. Lupeiko, Maria G. Volkova, Anna S. Kostenikova, Larisa E. Pustovaya and Aleksey G. Fedorenko

Abstract In this paper, we describe the synthesis of titanium dioxide nanotubes via hydrothermal method. We have examined the obtained materials using TEM, XRD analysis. The samples were prepared from titanium chloride via a two-step hydrothermal process. The synthesized samples are composed of regularly shaped nanotubes with the outer diameter being about 5–8 nm and length of about 50–70 nm. The hydrothermal treatment technology was used in the experiment to obtain nanomaterials containing nanotubes with smooth surfaces. We have found out that titanium dioxide nanotubes demonstrate an increased photo-catalytic activity, which can be as high as that of the best commercial crystalline powders or even higher.

6.1 Introduction

Titanium dioxide (TiO_2) is one of the most important semiconductor materials. It is relatively cheap and demonstrates chemical and biological stability, low toxicity and high efficiency in the oxidation of organic and biological objects [1, 2]. Properties of TiO_2 materials depend on specific surface area, its type and the ratio of the crystalline phase (anatase, rutile, brookite), dimensions of structure units, morphology and composition. A number of authors suggested that anatase phase provides the highest photoactivity, others claimed that synergetic effects on the photoactivity of anatase were observed during rutile mixed phases [2].

TiO_2 nanomaterials in the form of various structures are synthesized to improve the properties of materials, such as nanoparticles [3, 4], nanotubes [5, 6], nanowires

E. M. Bayan (✉) · T. G. Lupeiko · M. G. Volkova · A. S. Kostenikova
Southern Federal University, Rostov-on-Don, Russia
e-mail: ekbayan@sfedu.ru

L. E. Pustovaya
Don State Technical University, Rostov-on-Don, Russia

A. G. Fedorenko
Southern Scientific Center of Russian Academy of Sciences, Rostov-on-Don, Russia

I. A. Parinov et al. (eds.), *Advanced Materials*, Springer Proceedings in Physics 207, https://doi.org/10.1007/978-3-319-78919-4_6

[7, 8], nanorods, layered materials [9, 10] etc. One-dimensional TiO_2 structures, such as nanotubes, possess a large concentration of exposed active facets and exceptional electronic, optical and mechanical properties. These characteristics make them viable candidates for a wide range of applications [11]. Titanium dioxide nanotubes are important materials for the modern chemical industry. They can be used in a wide range of applications and industries including photocatalysis, energy storage, gas sensors production, etc. One-dimensional protonated TiO_2 nanostructures have been also proposed as potential solid acid catalysts [12].

At present time, there are various methods of TiO_2 nanomaterials synthesis. Hydrothermal synthesis, template method and electrochemical method are the most popular. The optimum method should be chosen taking into account the anticipated results. The electrochemical method [13] of synthesis is rather simple; it implies anode oxidation of titanium metal in etching acidic solution. This method is useful for receiving TiO_2 in the rutile crystalline phase: anode films of titanium dioxide can be applied as photoelectrodes [14].

Another interesting method is template method [15, 16]. It consists of hydrolysis of titanium alcoholates in the presence of micelles (the latter are formed by surface-active substance). Template method of synthesis can be used to receive materials, which are good carriers for the catalyst [17].

Despite the large number of scientific publications on TiO_2 synthesis, focused on different crystal phases, particle size or surface area, the relationship between morphology, structural properties and catalytic behavior needs in further investigation. Titanium dioxide in various phase compositions with controlled dimensions can be produced using various methods of synthesis, varying its parameters (precursor concentration, temperature, duration of process etc.)

A hydrothermal approach is considered as the best method for TiO_2 nanotubes synthesis due to its simplicity and high production [18, 19]. The effect of hydrothermal treatment on the morphological and acid catalytic properties of titanium dioxide nanomaterials were examined in the work [20].

In the present study, we have made an attempt to examine the properties of TiO_2 nanotubes prepared via a two-step hydrothermal process. We have paid attention to the structure of obtained titanium dioxide nanomaterials, their crystalline phase and photocatalytic activity.

6.2 Research Method

6.2.1 Material Synthesis

All reagents were obtained commercially and used without any further purification. All solutions were prepared using deionized water. The samples were prepared from titanium chloride via a two-step hydrothermal process.

First, a titanium hydroxide was obtained from titanium chloride according to previously described methods [16]. Then, obtained TiO_2 powder was suspended in distilled water in a Teflon tube, filling volume was 80%. The reaction mixture was hydrothermally treated for 24 h at 170 °C (sample 1), 200 °C (sample 2), after that the substance was dried at 100 °C. Thus, we obtained an intermediate TiO_2 product.

The second step was hydrothermal synthesis of nanotubes. In this experiment, intermediate TiO_2 products and 10 M NaOH (1 g TiO_2/10 ml of 10 M NaOH) were placed into a Teflon tube with a filling volume of 80%. Hydrothermal treatment was continued for 48 h at 160 °C. Then, obtained TiO_2 nanotubes were washed with the hydrochloric acid to pH = 7 and then were washed with deionized water until chlorine ions were not detected. Finally, the samples were dried at 80 °C.

6.2.2 Materials Characterization

The phase composition of the samples was studied by X-ray powder diffraction (XRD) analysis, carried out using an ARL X'TRA, Thermo ARL (Switzerland), diffractometer equipped with a high-intensity Cu-Kα1 irradiation (λ = 1.540562 Å) operated at 40 kV and 30 mA in the range of 20°–60°.

Thermogravimetric (TGA) and Differential Thermal Analysis (DTA) were carried out using a thermal analyzer (STA 449°S/4G Jupiter Jupted) at a heating rate of 10 °C/min.

The morphological characteristics were analyzed with transmission electron microscopy (TEM) utilizing a TEM Tecnai G2 Spirit Bio TWIN microscope operating at 120 kV.

6.2.3 Photocatalyst Preparation

The photocatalytic activity of obtained materials was studied on a photodegradation reaction model of a cation type organic azo dye methylene blue (MB, $C_{16}H_{18}N_3SCl$, C_o = 20 mg/l) in aqueous solution as described in the paper [21]. Experiments were carried out at room temperature with UV radiation (low-pressure mercury lamp, 10 W).

After purification, the MB concentration (C) was determined spectrophotometrically (spectrophotometer UNICO 1201). Each experiment was repeated at least three times. In addition, the decomposition of MB (complete dye mineralization) was also controlled analytically by determining the content of nitrate and sulfate anions in the filtrate after photocatalytic purification by using the Capel-105M capillary electrophoresis system.

Commercial catalyst Degussa P25 was used as a comparative sample.

6.3 Result and Discussion

6.3.1 DTA/TGA Measurements

The synthesized titanium hydroxide (first-step) was examined by TG-DTA (Fig. 6.1). We can identify several stages of sample change on the thermogravimetric curve (Fig. 6.1). It has been fixed that at temperatures below 120 °C, the endothermic peak arises and the weight of the material decreases mainly due to the removal of adsorbed water. At temperatures of 120–400 °C, weight loss is observed due to the decomposition of titanium hydroxide to titanium dioxide. In the temperature range 400–800 °C, the weight of material is stable, and furthermore, high thermal effects are observed. A small exothermic effect at 430 °C can be explained by the formation of the anatase phase.

6.3.2 TEM Images

We have synthesized titanium dioxide nanotubes using hydrothermal two-step synthesis. At all stages of the synthesis process, the TiO_2 materials are of nanosize, but the morphology is different.

The transmission electron microscopy demonstrated that TiO_2 materials, synthesized by the hydrothermal method, were composed of nanosize particles with a shape close to an oval (Fig. 6.2b). These characteristics distinguished them from previously spherical powders (Fig. 6.2a), obtained by sol-gel technology [22]. The

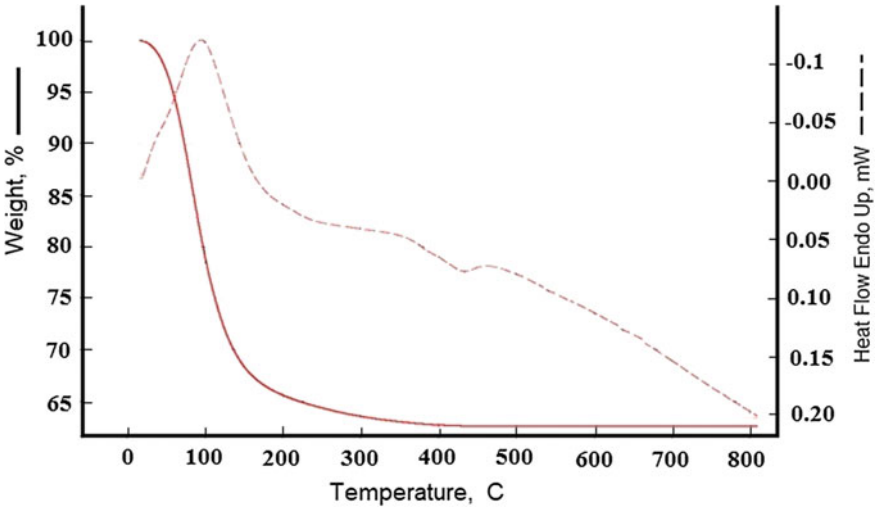

Fig. 6.1 Results of DTA–TG analysis of the titanium hydroxide

morphology of the hydrothermal synthesized particles is homogeneous. In the sol-gel method, particles tend to aggregate; it follows from the presence of conglomerates of several microns in size. It can decrease the total surface area of materials and reduce their catalytic activity. It is important to notice that in the hydrothermal synthesized materials the degree of aggregation is lower.

As can be seen on the TEM microphotographs, the synthesized nanotubes are open-ended hollow tubular objects of 7–10 nm in outer diameter and about 50–70 nm in length (Fig. 6.2c, d). The typical diameter of their inner channel is 5 nm. The hydrothermal treatment technology was used in the experiment to obtain nanomaterials, containing nanotubes with smooth surfaces. Note the fact that particle-like morphology of the precursor does not exist anymore, indicating that the efficiency of hydrothermal reaction is high.

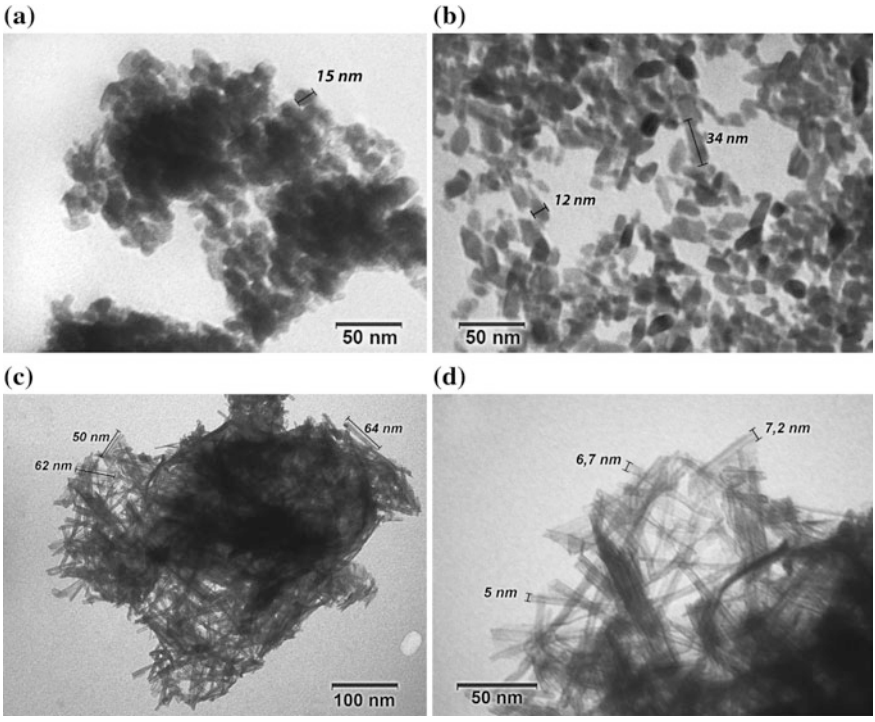

Fig. 6.2 TEM microphotographs of TiO_2 nanoparticles synthesized by sol-gel (**a**) [22], hydrothermally treated at 200 °C (**b**) and TiO_2 nanotubes (**c**, **d**)

6.3.3 XRD Patterns

According to the XRD data, the powders synthesized from titanium chloride and dried at a temperature lower than 100 °C are X-ray amorphous; it indicates that crystalline phases are absent. Figure 6.3 shows the XRD patterns of intermediate TiO_2 products, which were hydrothermally treated at different temperatures 170 and 200 °C. The XRD analysis revealed the sole formation of anatase polymorph. The experiment showed that with increasing temperature of hydrothermal synthesis, the peak intensity in XRD patterns increases. This suggests that the samples are characterized by increased particles size of crystal.

XRD analysis of the final product was used to demonstrate phase structure of obtained TiO_2 nanotubes.

Significant expansion of the peak shape may be observed in the experiment due to the formation of nanostructured objects and the twisting of atomic layers.

As described in [23–25], the generally accepted TiO_2 nanotubes formation mechanism of hydrothermal synthesis consists of four stages:

(i) dissolution of titanium dioxide TiO_2 precursors and breaking of Ti–O–Ti bonds in the concentrated alkaline solution $TiO_2 + 2NaOH = 2Na^+ + TiO_3^{2-} + H_2O$;
(ii) the formation of layered nanosheets $2Na^+ + TiO_3^{2-} = [Na_2TiO_3]_{nanosheets}$;
(iii) exfoliation of nanosheets,
(iv) growing nanosheets with the increasing tendency of curling, which leads to the formation of nanotubes $[Na_2TiO_3]_{nanosheets} = [Na_2TiO_3]_{nanotubes}$.

The final stage of titanium dioxide nanotubes formation can be described schematically by the equation: $[Na_2TiO_3]_{nanotubes} + H_2O = [H_2TiO_3]_{nanotubes} + 2NaOH$.

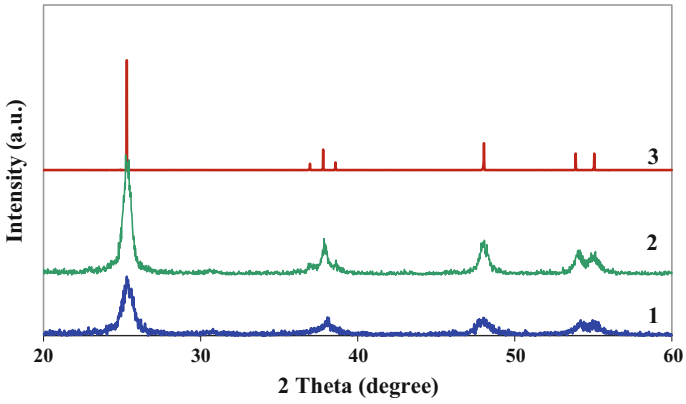

Fig. 6.3 XRD patterns of intermediate TiO_2 products: hydrothermally treated at 170 °C (1), 200 °C (2) and of anatase (3)

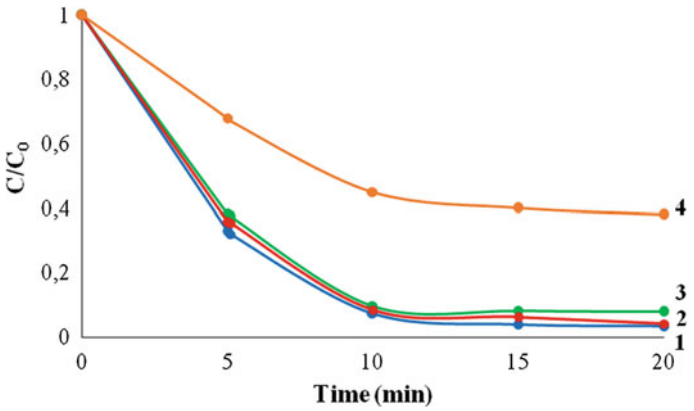

Fig. 6.4 Degradation profiles for intermediate products, treated at 170 °C (1), 200 °C (2), nanotubes (3) and Degussa P25 (4) with respect to methylene blue

6.3.4 Photocatalytic Activities of TiO_2 Nanotubes

Figure 6.4 exhibits the photocatalytic activity of obtained materials on the degradation of methylene blue, a heterocyclic aromatic chemical compound. After 10 min of UV-light irradiation, the MB residual concentrations were less than 10% for all the synthesized materials. It should be noted that the particles intermediate products and nanotubes demonstrate very similar photocatalytic activity. All synthesized materials exhibit better photocatalytic activity than commercial catalyst Degussa P25.

6.4 Conclusion

In this study, we have successfully synthesized anatase TiO_2 nanotubes using two-step hydrothermal method. We have demonstrated that the first-step hydrothermal synthesized materials are composed of nanosized particles with an oval shape and characterized by low aggregation. The obtained nanotubes are characterized by optimized structure integrity (with diameter of 5–8 nm and length of 50–70 nm) and uniformity of the morphology. The obtained materials demonstrate improved photocatalytic activity and could be recommended for wider applications.

References

1. A. Nada, Y. Moustafa, A. Hamdy, S. Abd El-Wahab, D. Yahea, Chem. Mater. Res. **6**, 40 (2014)
2. R. Scotti, M. D'Arienzo, A. Testino, F. Morazzoni, G. Liu, K. Wangn, N. Hoivik, H. Jakobsen, Appl. Catal. B **88**, 497 (2009)
3. E.M. Bayan, T.G. Lupeiko, L.E. Pustovaya, A.G. Fedorenko, in *Advanced Materials—Techniques, Physics, Mechanics and Applications*, ed. by I.A. Parinov, S.-H. Chang, M.A. Jani. Springer Proceedings in Physics, vol. 193 (Springer, Cham, 2017), p. 17
4. E.M. Bayan, T.G. Lupeiko, E.V. Kolupaeva, L.E. Pustovaya, A.G. Fedorenko, Russ. J. Phys. Chem. B **11**(4), 600 (2017)
5. N. Jasmeen, Visakhapatnam India Open J. Nano **2**, 2 (2013)
6. M. Boehme, G. Fu, E. Ionescu, W. Ensinger, Nano-Micro Lett. **2**(1), 26 (2010)
7. A. Hua, X. Zhang, K.D. Oakes, P. Peng, Y. Norman Zhou, M.R. Servos, J. Hazard. Mater. **189**, 278 (2011)
8. P. Yang, D.F. Zeigler, K.C. Bryant, T.R. Martin, D.R. Gamelinb, C.K. Luscombe, J. Mater. Chem. C **2**, 4922 (2014)
9. M.F. Vildanova, S.S. Kozlov, A.B. Nikolskaia, O.I. Shevaleevskiy, N.A. Tsvetkov, O.V. Alexeeva, L.L. Larina, Nanosyst. Phys. Chem. Math. **8**(4), 540 (2017)
10. L.M.P. Garcia, G.H.M. Gurgel, L.X. Lovisa, R.M. Nascimento, C.A. Paskocimas, M.R.D. Bomio, F.V. Motta, Mater. Sci. Eng. Int. J. **1**(1), 7pp (2017)
11. V. Etacheri, C. Di Valentin, J. Schneider, D. Bahnemann, S.C. Pilla, J. Photochem. Photobiol. C Photochem. Rev. **25**, 1 (2015)
12. M. Sluban, B. Cojocaru, V.I. Parvulescu, J. Iskra, R.C. Korošec, P. Umek, J. Catal. **346**, 161 (2017)
13. Z.D. Gao, Q.L. Zhuang, Y.Y. Song, K. Lee, P. Schmuki, Chemistryopen **2**(3), 93 (2013)
14. R. Kumar, J. Rashid, M.A. Barakat, Colloids Interface Sci. Commun. **5**, 1 (2015)
15. G.Y. Teo, M.P. Ryan, D.J. Riley, Electrochem. Commun. **47**, 13 (2014)
16. L.S. Semko, L.P. Storozhuk, S.V. Khutornoi, N.V. Abramov, P.P. Gorbik, Inorg. Mater. **51** (5), 430 (2015)
17. G.G. Bessegato, T.T. Guaraldo, J.F. de Brito, M.V.B. Zanoni, M.F. Brugnera, Electrocatalysis **6**(5), 415 (2015)
18. T. Kasuga, M. Hiramatsu, A. Hoson, T. Sekino, K. Niihara, Langmuir **14**, 3160 (1998)
19. E. Horvth, A. Kukovecz, Y. Konya, I. Kiricsi, Chem. Mater. **19**(4), 927 (2007)
20. E. Wada, M. Kitano, K. Nakajimaa, M. Hara, J. Mater. Chem. A **41**(1), 12768 (2013)
21. E.M. Bayan, T.G. Lupeiko, L.E. Pustovaya, A.G. Fedorenko, in *Advanced Materials—Manufacture, Physics, Mechanics and Applications*, ed. by I.A. Parinov, S.-H. Chang, V.Y. Topolov. Springer Proceedings in Physics, vol. 175 (Springer, Cham, 2016), p. 51
22. E.M. Bayan, T.G. Lupeiko, L.E. Pustovaya, A.G. Fedorenko, Nanotechnol. Russ. **12**(5–6), 269 (2017)
23. C. Chao, Z. Ren, S. Yin et al., Adv. Powder Technol. **25**, 745 (2014)
24. L.Q. Weng, S.H. Song, S. Hodgson et al., J. Eur. Ceram. Soc. **26**, 1405 (2006)
25. M. Shahrezaei, S. Habibzadeh, A.A. Babaluo et al., J. Exp. Nanosci. **12**(1), 45 (2017)

Chapter 7
Influence of Nanosecond Electromagnetic Pulses on the Structural Characteristics, Physico-Chemical and Technological Properties of Diamonds

Igor Zh. Bunin, Valentine A. Chanturiya, Nataliya E. Anashkina, Galina K. Khachatryan, Mariya V. Ryazantseva and Elizaveta V. Koporulina

Abstract To improve the existing diamond recovery process, the effect of high-power (high-voltage) nanosecond electromagnetic pulses (HPEMP) on the physical and technological properties of diamond crystals was studied. Infrared Fourier spectroscopy (FTIR), X-ray photoelectron spectroscopy (XPS), microscopy, electroosmosis, and other methods were employed to examine the structural, chemical, electrical and physico-chemical changes in the surface properties of natural and synthetic diamonds as a result of pulsed energy impacts. The mechanism, stages (phases) of the composition changes in the functional surface layer, electrical, physico-chemical, and flotation properties of diamond crystals were identified. For the first time ever, it was experimentally demonstrated that the non-thermal action of high-voltage nanosecond pulses on natural diamonds causes the formation of microshift defects in the B2 crystalline lattice (platelets), whose elevated content, apparently, contributes to the higher strength of diamond crystals.

I. Zh. Bunin (✉) · V. A. Chanturiya · N. E. Anashkina · M. V. Ryazantseva
E. V. Koporulina
N.V. Mel'nikov Institute of Comprehensive Exploitation of Mineral Resources, Russian Academy of Science, 4, Kryukovsky Tupik, Moscow 111020, Russia
e-mail: bunin_i@mail.ru

G. K. Khachatryan
Central Research Institute of Geological Exploration for Base and Precious Metals, Moscow 117545, Russia

I. A. Parinov et al. (eds.), *Advanced Materials*, Springer Proceedings in Physics 207, https://doi.org/10.1007/978-3-319-78919-4_7

7.1 Introduction

In recent years, there has been extensive research, both in Russia and globally, on the application of non-conventional (non-mechanical) physical and physicochemical impacts on minerals and mineral suspensions to enhance the physicochemical and process contrast of the minerals and, as a consequence, the separation performance of mineral components in the concentration of complex ores [1–5].

In the concentration of diamond kimberlites, one of the highly relevant problems is the development of novel high-performance methods for improving the concentrate grade by enhancing the contrast of the hydrophobic, lipophobic, luminescent properties of diamonds and rock-forming minerals [6, 7].

In [5, 8–12], the prerequisites were identified and the possible mechanisms examined the process of disintegrating and modifying the properties contrast of fine mineral media (geomaterials) by short (nanosecond, $\sim$1–10 ns) electromagnetic pulses with a high electrical field intensity E ($\sim 10^7$ V/m). This type of energy impacts is classified as the so-called non-thermal, since the energy of an individual pulse is insufficient to significantly alter the temperature of the object as a whole [13, 14].

In [14, 15], we found that the action of high-voltage pulsed fields causes a reduction in the microhardness of the rock-forming minerals of kimberlites (olivine, serpentine, and calcite) by 40–66% as a result of disruption in the microstructure of the surface layers, formation of defects at different structural scales (dislocations, microcracks, incomplete surface microfaults), disordering and amorphization of the surface of natural dielectric minerals. The findings supported the theoretical possibility of using pulsed energy impacts to improve the efficiency of softening the rock-forming minerals of diamond kimberlites, to ensure the integrity of diamond crystals in ore diminution processes by reducing the residence time of the kimberlite rock in autogenous mills.

In this paper, we present the findings of a comprehensive study of the action of high-voltage nanosecond pulses on the chemical-structural, physico-chemical, and process (technological) properties of natural and synthetic diamonds for assessing the performance of HPEMP methods in the processing (concentration) of diamond ores.

7.2 Experimental

7.2.1 Materials and Research Technique

The studies were conducted on crystals of natural industrial diamonds with a grain size of $-2 \cdots +1$ mm from the Triassic placers of the Bulkur site in Nizhne-Lensky District (northeastern part of the Siberian Platform, Yu. M. Sibirtsev's collection,

VANPO Aerogeology). Some of the experiments were conducted on samples of synthetic diamonds, grade AC-120, with a particle size of $-50 \cdots +40$ μm.

For the electric pulse treatment of the diamond crystals, the high-voltage nanosecond video pulse generator (UEIRM-1 by NPP Fon, Ryazan) was used with the following electrophysical pulse parameters: τ (pulse front) ~1–5 ns, τ (pulse duration) ~50 ns, U(pulse amplitude) ~25 kV, electric field strength between the pulse generator electrodes $E \sim 10^7$ V/m, pulse repetition frequency 100 Hz, pulse energy ~0.1 J, treatment (processing) time range t_{treat} = 10–150 s (electromagnetic pulsed irradiation dose—number of pulses $N_{imp} = 10^3$–1.5×10^4). The experiments were carried out in standard atmospheric conditions without an ohmic contact between the mineral particles and the high voltage source, which enabled a pulsed nanosecond dielectric barrier discharge of atmospheric pressure, and in some cases a spark discharge between the surface of the crystals and the active electrode (anode) of the generator.

The phase and structural impurities of the natural industrial diamond crystals were examined using IR Fourier spectroscopy (FTIR) with a Nicolet-380 spectrometer with a Carl Zeiss micro-lighting attachment in the range 400–4000 cm^{-1}. The luminescent properties (luminiscence color and level) of the natural diamonds were studied in UV rays with a Wood-OLDD-01 lamp (wavelength 365 and 254 nm).

Changes in the morphological and chemostructural properties of the surfaces of diamond crystals caused by the electromagnetic pulse treatment were examined by analytical electron microscopy (SEM-EDX, scanning electron microscope LEO 1420VP—EDX Oxford INCA Energy 350, low-vacuum microscope JEOL JSM-6610LV) and optical microscopy (optical microscope, digital optical stereomicroscope Olympus SZ61 using the Grenu layout).

The micromorphological features of the diamond surface were thoroughly studied by atomic force microscopy (AFM, modular scanning probe microscope Ntegra Prima, NT-MDT, Zelenograd, Russia) in semi-contact mode in air under standard conditions. Simultaneously with the AFM images of the surface topography of the samples (Height, nm), images were taken of the surface phase contrast caused by the phase change of the cantilever oscillations upon needle contact with surface areas with different mechanical properties. The distribution and magnitude of the electrostatic potential of the diamond crystal's surface (V, mV) relative to the probe potential were examined by the Kelvin probe force microscopy (KPFM). For scanning, silicon AFM cantilevers of the series NSG10/TiN with conductive TiN coating on the needle side. The scanning step was determined by the linear dimensions of the scan area and the number of steps 256 × 256. On each sample, 2–3 characteristic regions were identified, on which a series of consecutive scans was conducted with a reduction in the scale of the scan area (scan size) from 10–20 to 1–2 μm.

The wettability of the diamond surfaces was determined using the contact apparatus KP-CK5 by V.A. Glembotsky. Industrial diamond crystals were placed in a 20 ml cuvette filled with distilled water, a 3 mm air bubble was introduced with a custom plunger, and for a given contact time, the adherence of the air bubble to the diamond crystal was measured. Based on the wettability of the mineral surface, the

crystals were classified as either hydrophobic or hydrophilic diamonds [16]. Crystals adhering to the air bubble upon contact of <50 ms were classified as hydrophobic, crystals that did not adhere after >5 s were classified as hydrophilic. Diamonds that attached to the bubble in the time interval between 50 ms and 5 s were classified as mixed.

Flotation activity of natural diamonds of different classification types before and after electromagnetic pulse treatment was studied by non-frothing flotation in distilled water without reagents in the Hollimond tube. Air was fed into the tube by a minicompressor via a Schott filter for 5 min.

Additional studies were carried out on synthetic diamonds. X-ray photoelectron spectroscopy (XPS, Kratos Axis Ultra DLD spectrometer with monochromatic X-ray generator Al$K\alpha$) was used to study the surface phase composition of synthetic diamond particles. The electrokinetic (zeta) potential of synthetic diamonds before and after HPEMP treatment was measured by electroosmosis with a Perrin apparatus in distilled water with pH 5.5–6.5 on weighed mineral samples of 1 g. Measurement error of ζ-potential did not exceed 5%.

7.3 Results and Discussions

7.3.1 Crystallomorphological Analysis of Natural Diamonds

Crystallomorphological analysis of natural industrial diamonds demonstrated the predominance of typical rounded varieties (50%), mostly with cryptic layering and sheaf striation, less frequently with shagreen and plastic deformation bands, with the predominance of crystals of varieties I (60%), V (20%), and VII (15%) according to the mineralogical classification by Orlov [17]. Diamonds of variety I are mainly represented by rounded dodecahedroids (Fig. 7.1a) and octahedra (Fig. 7.1b), making up more than 50% of all crystals. The share of laminar crystals of the octahedron-rhombododecahedron series (Fig. 7.1c) and of the transitional type (Fig. 7.1d) was 35%. A characteristic feature of the collection was a large number of damaged and broken crystals ($\sim$75%) (Fig. 7.1e). A high share of crystals with signs of natural etching ($\sim$45%) was found with widespread scars and caverns; individual crystals had traces of corrosion and matting of the surface. The share of diamonds with twins and intergrowths was 40%; these mainly were crystals of the varieties V–VII. Microinclusions of graphite and sulphides were found in 35% of the collection's diamonds. The share of colored diamonds was 70%. Mainly, these are gray-colored crystals due to multiple graphite inclusions (Fig. 7.1c, d), 20% of the crystals have a gray-brown hue due to the presence of plastic deformation bands. In general, the diamonds from the Bulkur site are characterized by a higher than normal share of crystals with low to medium iron content and a significant share of fractured crystals [18].

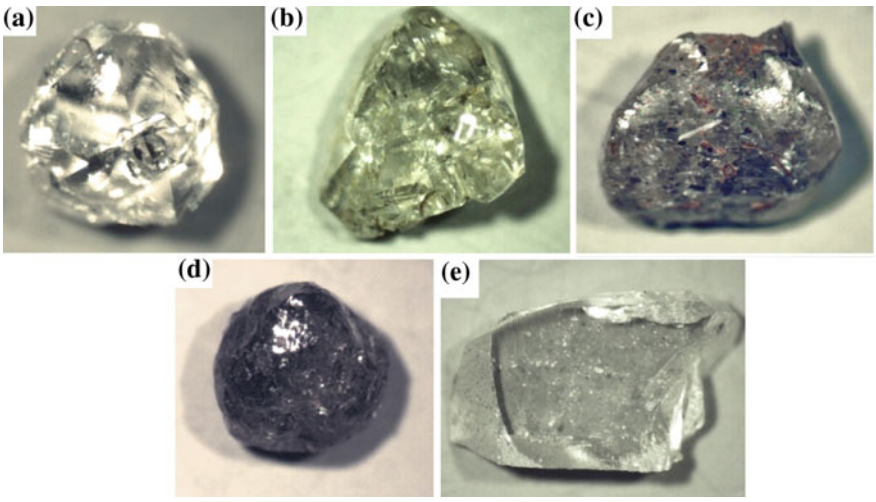

Fig. 7.1 Morphology of diamond crystals of the Late Triassic placers of the Lower-Lensky District: **a** dodecahedroid; **b** octahedr; **c** transitional type octahedron-rhombododecahedron; **d** transitional type octahedron-pseudorhombododecahedron; **e** broken crystal

The share of luminescent diamonds in the collection is only 15%. The most common luminescence hue is blue-azure. The absence of photoluminescence in the examined crystals is apparently due to a special impurity composition characterized by an increased content of structurally bound aggregated nitrogen, inclusions of graphite and iron oxides, as well as mineral films on the surface of diamonds.

7.3.2 Effect of HPEMP Treatment on the Structural and Chemical Properties of the Surface and Structural Defects of Diamonds

7.3.2.1 Fourier-Transform Infrared Spectroscopy (FTIR)

Based on the nature of the IR spectra, the examined natural industrial diamonds belong exclusively to Type Ia; nitrogen-free varieties (Type IIa) were not detected. IR spectra of the diamonds included several systems of spectral lines. Absorption bands in the 1900–2600 cm^{-1} region are due to the natural vibrations of the diamond's crystalline lattice [19]. As suggested in [20], the system of lines 2860, 2930, and 2960 cm^{-1} is associated with the oscillations of the CH_3 and CH_2 groups of aliphatic structures (saturated hydrocarbons or their fragments). Since these lines can also be seen in the spectrum of a colorless transparent crystal fragment without visible surface contamination (Fig. 7.1d), we can assume the presence of hydrocarbon phases inside the crystal. A wide diffuse band with a maximum of

$\sim$3400 cm^{-1} and the related line $\sim$1650 cm^{-1} are associated with the absorption of OH groups apparently contained in the adsorbed water [20]. Water molecules can be both part of the mineral phases filling caverns and cracks on the surface of diamond crystals and, similarly to hydrocarbons, be locked inside the crystal. The group of lines in the 3700–3600 cm^{-1} region is probably associated with impurities of clay minerals [21] filling, together with iron oxides, caverns, cracks, and other depressions on the surface of crystals.

IR spectra of the examined diamond crystals indicate the presence of nitrogen in forms A (lines 480 and 1282 cm^{-1}) and B (lines 1010 and 1175 cm^{-1}), microshift B2 defects (line $\sim$1365 cm^{-1} from the wave number range 1368–1374 cm^{-1}), structural hydrogen impurity manifesting itself as narrow peaks at 1405 and 3107 cm^{-1}. As noted earlier [22], the crystals are classified in two groups. The first group are mainly dark-colored (Fig. 7.1c, d) high-nitrogen crystals with a total content of structurally bound nitrogen of >1100 at. ppm and a content of aggregated nitrogen of %N(B) <30 of the total impurity concentration. The other group is mainly colorless (Fig. 7.1a, b, e) crystals with a moderate nitrogen content with a total impurity content of 200–980 at. ppm and a relatively high share of aggregated nitrogen (an average of 48 $\pm$ 16% of the total impurity concentration).

As a result of the exposure of natural diamond samples to high-voltage nanosecond pulses with an increasing treatment time, the IR spectra of the crystals changed markedly. First of all, this applies to crystals having on their surfaces mineral films of iron oxides, clay minerals, and other impurities caused by the prolonged residence of the diamond in an exogenous geological setting. Almost all studied samples with phase impurities containing the hydrocarbon and OH groups described above were found to have lost these impurities as a result of the electromagnetic pulse treatment. For instance, at $t_{treat} \geq$ 50 s, the intensities of the spectral lines 2918 cm^{-1} and 2849 cm^{-1} and bands $\sim$3400 cm^{-1}, caused by impurities of hydrocarbons and H_2O, respectively, reduced markedly in the IR spectrum of one of the crystals from the collection (B-17) (Fig. 7.2a).

Based on FTIR, there was no deep structural rearrangement of the diamond crystals under the influence of electromagnetic pulses, but the absorption coefficient of the line $\sim$1365 cm^{-1} grew consistently, which indicated an increase in the concentration of platelet defects B2 (platelets, i.e. small plates) (Fig. 7.2b), represented by interstitial carbon atoms [23]. Of the 15 natural diamond samples, treated by HPEMP, a small increase in the occurrence of the defect B2 was recorded in seven crystals. It is characteristic that all these crystals belong to the group with moderate nitrogen content and a higher than normal degree of nitrogen aggregation %N(B). Five samples from the collection belonged to the group with high nitrogen content and a reduced %N(B). In the IR spectra of these diamonds, no increase in the B2 concentration was found after the treatment.

The observed changes in the IR spectra of natural diamonds do not contradict the available information on the nature of B2-platelet defects [23]. Earlier, Sobolev [24] demonstrated a general trend toward a higher content of platelets in crystals with an increasing concentration of B-nitrogen. However, B-centers in crystals can exist independently from defects such as platelets. One of the studies [25] showed that

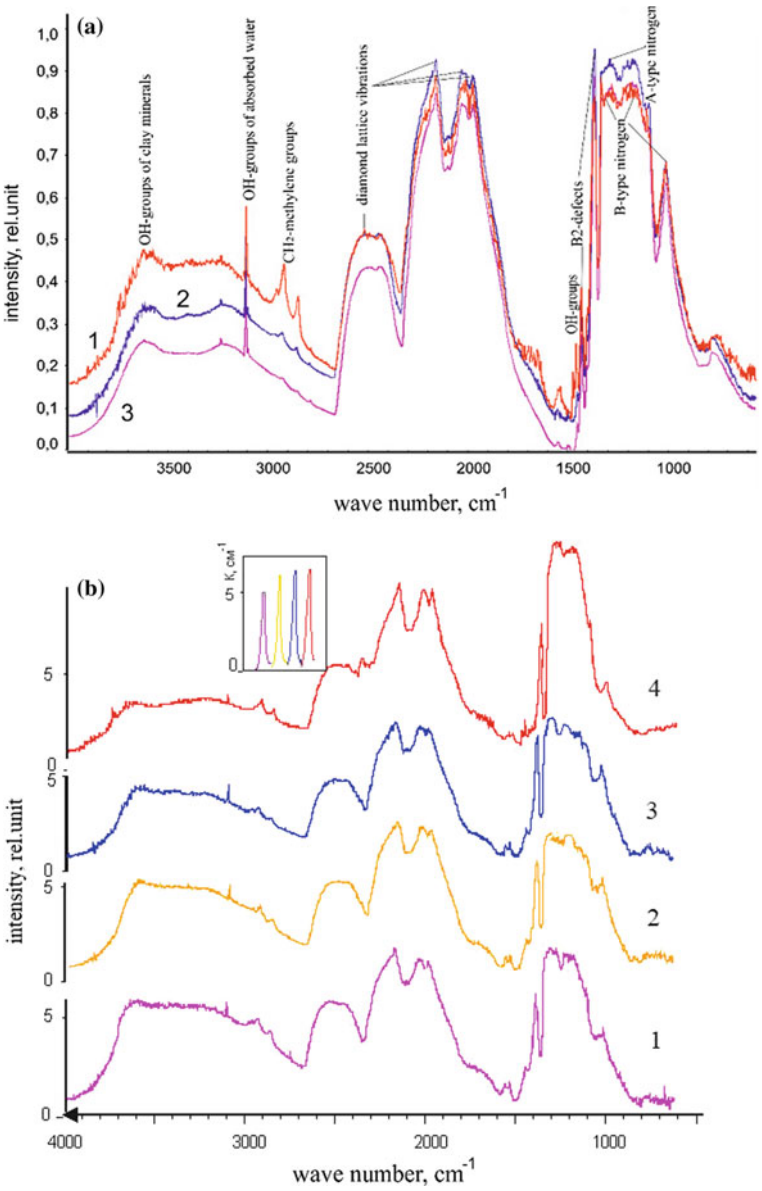

Fig. 7.2 **a** IR-spectra of diamond crystals B-17: *1* before and *2*, *3* after HPEMP processing for 50 s (*2*) and 150 s (*3*); **b** enlarged fragment of the IR-spectra with wave number 1365 cm^{-1}: *1* before and *2–4* after electropulse processing for 30 s (*2*), 50 s (*3*), 150 s (*4*)

platelets are most common in diamonds with a layered octahedral inner structure and are virtually absent in crystals with a fibrous internal structure. Given this, platelets are defined as microshift defects in layered octahedral diamond crystals, whose formation is facilitated by the presence of nitrogen B-centers in the crystal.

Thus, it can be assumed that nanosecond electromagnetic pulses lead to the formation of new B2-centers in diamond crystals with moderate nitrogen content, predominantly with a layered octahedral internal structure and an increased share of nitrogen B-defects in the structure. As a result of the study of microhardness of diamond crystals exposed to deformation in a natural setting, in [19] it was found that B-centers increase the dispersion strength of natural diamonds compared to the original state by a factor of 1.7.

7.3.2.2 X-ray Photoelectron Spectroscopy Findings

The examination of XPS data demonstrated that the surface of synthetic diamond particles contained ~87% C, ~12% O, and ~1% N. Figure 7.3 shows the X-ray photoelectron survey (general) spectrum and XPS spectra of electron levels of carbon atoms C1*s* and oxygen atoms O1*s*. The main line of the XPS spectrum of 1*s*-electrons of carbon C1*s* atoms was decomposed into components corresponding to the following chemical forms of carbon: C–C—graphite phase with sp^2-hybridization of valence electronic states of the carbon atom with a bond (binding) energy of E_{BE} = 284.0 eV, allotropic modification of carbon of the diamond type with sp^3-hybridization and E_{BE} = 285.0 eV [26]; C–Met carbon bonded to metal atoms, E_{BE} = 283.0 eV; contribution by the various carbon groups in the surface with E_{BE} = 286.2, 287.4, 288.5 eV [27].

Photoelectron peak of the O1*s* level of oxygen was decomposed into individual components with the following four lines identified in the spectrum: E_{BE} = 529.7 eV (O–Met) [28], surface adsorbed oxygen [29]; E_{BE} = 530.9 eV (HO–Met, C=O) [30]; E_{BE} = 532.0 eV (OH–C) [31]; E_{BE} = 533.0 eV, surface adsorbed water (C–O–C, C–O) [32].

Structural-phase transformations of the surface layer of diamond crystals as a result of the HPEMP treatment are mainly caused by a change in the chemical state of oxygen atoms. In the spectrum of O1*s*-level of oxygen, the share (at.,%) of the peak with E_{BE} = 530.9 eV, increased by 3.2–4.3%, related to the oxygen of hydroxyl groups, bonded to the surface atoms of metals (hydroxylation of the surface) or to the oxygen of the C=O surface carbonyl groups (oxidation of the diamond surface).

7.3.2.3 Analytical Electron and Atomic–Force Microscopy

According to scanning electron microscopy (SEM–EDX) data, as a result of the electromagnetic pulse treatment of diamond crystals of $t_{treat} \cong 30$ s, fragments of

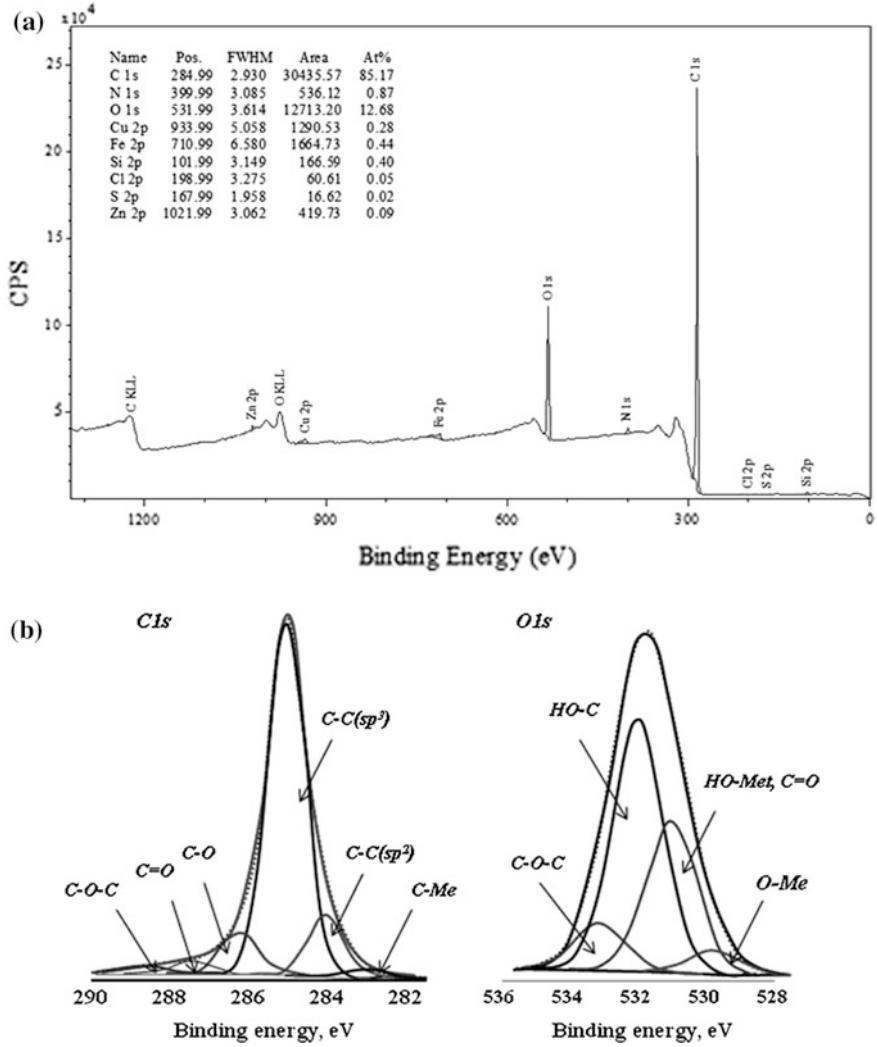

Fig. 7.3 **a** XPS survey spectrum of synthetic diamonds; **b** higher resolution C1*s* of carbon and O1*s* of oxygen photoelectron spectra of surface of diamond crystals

secondary mineral phases sized from 40 to 100 μm, presumably calcium sulfate and iron oxides (hydroxides), separated from the diamond surface.

Examination of the morphological features of the surface of a diamond crystal at the nanometer level (*Z*) using an atomic force microscope (AFM) showed the presence of narrow protracted bands, separated by characteristic secondary cracks (scars, ruptures) (Fig. 7.4a, d, e). According to AFM data, the main changes in the micromorphology of the diamond crystal surface as a result of the exposure to HPEMP were the deepening and widening of the sides of secondary cracks

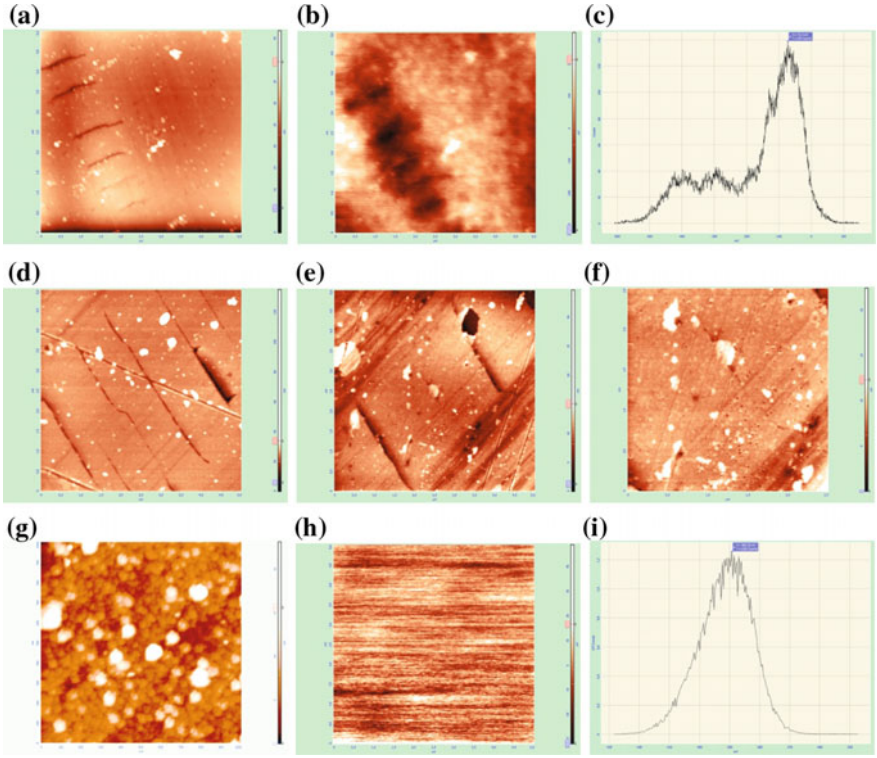

Fig. 7.4 AFM images (**a**, **d**, **e**, **f**, **g**) of the relief, and (**b**, **h**) surface potential for the diamond broken crystal (**a**, **b**) before and (**d**, **e**, **f**, **g**, **h**) after HPEMP processing for (**d**, **e**) 30 s, and (**g**, **h**) 50 s. Surface potential distributions (**c**, **i**) for the 5 × 5 μm area of the diamond surface. Scanning fields: 5 × 5 μm^2 (**a**, **b**, **d**, **e**, **h**), 2.5 × 2.5 μm^2 (**f**), and 1 × 1 μm^2 (**g**)

(Fig. 7.4d, e) and neocrystallization in the form of rounded particles (neoformations) of different sizes—from tens to 100 nm (Fig. 7.4f, g).

7.3.3 Electrophysical, Physicochemical, and Flotation Properties of Diamonds

7.3.3.1 HPEMP Effects on the Electrical Properties of Diamonds

As a result of a $t_{treat} \cong 10 - 150$ s electropulse treatment of synthetic diamond samples, the electrokinetic potential of the particles increased monotonically in the negative values range of ζ-potential due to the oxidation of the surface layer of the crystals and changes in the functional cover of their surface with the formation of hydroxyl and/or carbonyl groups (see XPS data). The value of the ζ-potential

changed from −9.3 mV in the original state (before HPEMP treatment) to −14.0 mV ($t_{treat} \cong 50$ s) and −20.8 mV ($t_{treat} \cong 150$ s).

Using the Kelvin probe, it was shown that, as a result of the electromagnetic pulse treatment of natural technical (industrial) diamond crystals, the maxima of the distribution of the electrostatic potential of the surface (V_{max}, mV; Fig. 7.4b, h) shifted to the negative range by 230–320 mV: from −70 mV in the original state to −300 mV ($t_{treat} \cong 10$ s) and −390 mV ($t_{treat} \cong 50$ s) (Fig. 7.4c, i). The findings do not contradict the available information on the change in the electrokinetic potential of synthetic diamond particles when exposed to HPEMP. Apparently, the increase in the negative values of the electrostatic potential of the diamond surface is due to the injection of charge carriers (electrons) from the electrodes into the surface layer of the mineral when exposed to strong electric fields (10^7–10^9 V/m) [33].

7.3.3.2 Changes in the Surface Hydrophobicity and Flotation Activity of Diamonds When Exposed to HPEMP

As a result of the experiments to assess the effect of HPEMP on the hydrophobic-hydrophilic state of the surface of natural diamonds, three conventional types of diamond crystals were identified among the samples in the original state: diamonds with a hydrophobic surface, diamonds with a hydrophilic surface, and diamonds with mixed properties. Under the electropulse treatment, the number of hydrophilic diamonds decreased by 22% (from 45 to 23%), reaching the minimum at $t_{treat} \cong 150$ s (Fig. 7.5a), while the number of crystals with mixed properties increased (Fig. 7.5c). The maximum share of hydrophobic diamonds was recorded as a result of an impulse treatment of $t_{treat} \cong 50$ s (Fig. 7.5b), and with increasing treatment time the number of hydrophobic crystals decreased.

The increase in the hydrophobicity of diamond samples as a result of the HPEMP treatment appears due to the detachment and partial destruction of mineral films on the surface of the crystals, which indicate the advisability of using high-voltage nanosecond pulses to effectively destroy and remove surface hydrophilic mineral micro- and nanophases from diamond crystals and to increase the contrast of the physicochemical and process properties of kimberlite minerals [14]. At the same time, prolonged electroimpulse treatment led to the oxidation of the surface of purified crystals (confirmed by XPS in synthetic diamonds), causing the hydrophilization of hydrophobic diamonds and development of mixed properties.

As a result of the conducted flotation trials, a nonlinear dependence was found between the floatability (recovery) of diamonds and the electropulse treatment time $\varepsilon(t_{treat})$ with a maximum at $t_{treat} \sim 150$ s ($\varepsilon_{max} = 61\%$). In general, the share of floatable crystals increased by 14% (from 47 to 61%). Attention is drawn to the fact that, at low doses of electromagnetic irradiation ($t_{treat} \leq 30$ s), there was a significant increase in the flotation activity of diamonds from 47% (in the original state without HPEMP treatment) to 56%. Analysis of the experimental findings showed that the maximum content of hydrophobic floatable diamonds was achieved after $t_{treat} \sim 30$ s of the preliminary pulsed treatment. The share of hydrophilic

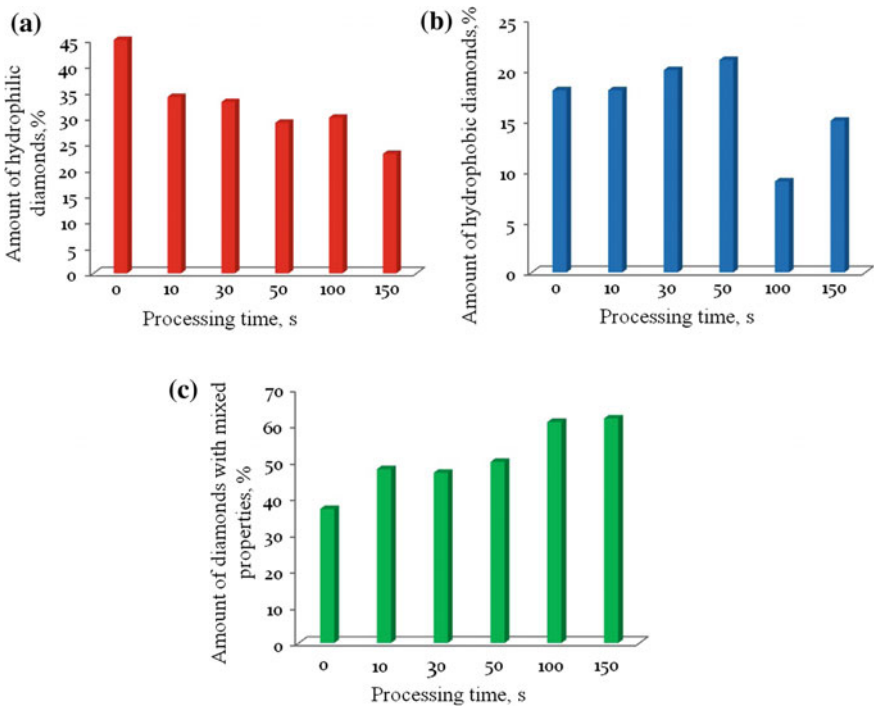

Fig. 7.5 Dependences of the distribution in collection of hydrophilic **a** hydrophobic **b** and mixed properties **c** diamonds on the HPEMP processing time

non-floatable diamonds significantly reduced after $t_{treat} \sim 10 - 30$ s of HPEMP treatment, indicating the advisability of the short pulsed energy impacts ($t_{treat} \cong 30$ s) to achieve controllable changes in the chemical-structural state of the surface, physico-chemical and flotation properties of diamond crystals.

7.4 Conclusions

As a result of the comprehensive studies, carried out with the application of state-of-the-art precision physical and chemical analysis methods, the mechanism was described and the main stages (phases) were identified of the controlled changes in the composition of the functional surface layer, chemical-structural and process (technological, namely, flotation) properties of diamonds. After a short electropulse treatment (stage 1, $t_{treat} \sim 10 - 30$ s), detachment, fracturing, and partial removal of films of secondary mineral phases occurred on the surface of natural diamonds, which caused an increase in the hydrophobicity and floatability of the crystals. After a prolonged treatment of diamond crystals (stage 2,

$t_{treat} \sim 30 - 150$ s), due to the oxidation of the surface layer (with the formation of hydroxyl and/or carbonyl groups), hydroxylation of the diamond surface was observed, causing a decrease in the hydrophobicity of crystals with an initially clean surface. The obtained experimental data confirm the theoretical possibility and efficiency of using pulsed energy impacts to intensify the flotation of diamonds in the processing of diamond kimberlites.

For the first time ever, the effect of increasing the concentration of B2-defects in crystals of natural diamonds with a relatively high concentration of nitrogen in the aggregated form (NB $\sim$35–65%) as a result of the non-thermal action of high-voltage nanosecond pulses was demonstrated. Together with this, the electropulse treatment of diamonds did not cause a significant change in the concentration and distribution of nitrogen centers in the crystals.

Acknowledgements This work was supported by the RF President's grant for the state support of leading scientific schools of the Russian Federation, Academician V.A. Chanturia's School NSh-7608.2016.5.

References

1. V.A. Chanturiya, I.Zh. Bunin, J. Min. Sci. **43**(3), 311 (2007)
2. V.A. Chanturiya, K.N. Trubetskoy, S.D. Viktorov, I.Zh. Bunin, *Nanoparticles in Geological Materials Destruction and Extraction Processes* (IPKON RAS, Moscow, 2006). (in Russian)
3. A.J. Swart, *Geochemistry—Earth's System Processes*, ed. by D. Panagiotaras (INTECH Open Access Publisher, 2012), p. 457
4. A.N. Didenko, B.V. Zverev, A.V. Prokopenko, Trans. Russian Akad. Sci. **403**(2), 19 (2005)
5. V.A. Chanturiya, Y.V. Gulyaev, V.D. Lunin, I.Zh. Bunin, V.A. Cherepenin, V.A. Vdovin, A. V. Korzhenevsky, Trans. Russian Akad. Sci. **366**(5), 680 (1999)
6. V.A. Chanturiya, K.V. Godun, Y.G. Zhelyabovskii, B.E. Goryachev, Gornyi Zhurnal. **3**, 67 (2015). (in Russian)
7. V.A. Chanturiya, B.E. Goryachev, *Modern Technologies of Complex Processing of Mineral Raw Materials* (Ore & Metals, Moscow, 2008), p. 151 (in Russian)
8. V.A. Chanturiya, Y.V. Gulyaev, I.Zh. Bunin, V.A. Vdovin, A.V. Korzhenevsky, V.D. Lunin, V.A. Cherepenin, Trans. Russian Akad. Sci. **379**(3), 372 (2001)
9. V.A. Chanturiya, Y.V. Gulyaev, I.Zh. Bunin et al., J. Min. Sci. **37**(4), 427 (2001)
10. I.Zh. Bunin, N.S. Bunina, V.A. Vdovin, P.S. Voronov, Y.V. Gulyaev, A.V. Korzhenevsky, V.D. Lunin, V.A. Chanturiya, V.A. Cherepenin, *Bull. Russian Acad. Sci.: Phys*. **65**(12), 1950 (2001)
11. I.Zh. Bunin, Theoretical Fundamentals of Nanosecond Electromagnetic Impulse Effects on Disintegration and Exposure of Finely Dispersed Mineral Complexes and Precious Metal Recovery from Ores, Dr. Tech. Sci. thesis, Moscow, 2009 (in Russian)
12. V.A. Chanturiya, I.Zh. Bunin, M.V. Ryazantseva, L.O. Filippov, Miner. Process. Extr. Metall. Rev. **32**(2), 105 (2011)
13. V.A. Cherepenin, Phys. Usp. **49**(10), 1097 (2006)
14. I.Zh. Bunin, V.A. Chanturiya, N.E. Anashkina, M.V. Ryazantseva, E.V. Koporulina, In: *Advanced Materials—Techniques, Physics, Mechanics and Applications. Springer Proceedings in Physics*, vol. 193, ed. by I.A. Parinov, S.-H. Chang, M.A. Jani (Springer, Heidelberg, New York, Dordrecht, London, 2017), p. 37

15. I.Zh. Bunin, V.A. Chanturiya, N.E. Anashkina, M.V. Ryazantseva, J. Min. Sci. **51**(4), 799 (2015)
16. V.G. Minenko, V.I. Bogachev, Miner. Process. **1–2**, 36 (1999). (in Russian)
17. Y.L. Orlov, *Morphology of Diamond* (Nauka, Moscow, 1973). (in Russian)
18. N.N. Zinchuk, V.I. Koptil, *Typomorphism of Diamonds of the Siberian Platform* (Nedra, Moscow, 2003). (in Russian)
19. G.B. Bokiy, G.N. Bezrukov, YuA Klyuev, A.M. Naletov, V.I. Nepsha, *Natural and Synthetic Diamonds* (Nauka, Moscow, 1986). (in Russian)
20. L.A. Kazytsyn, N.B. Kupletskaya, *Use of UV, IR and NMR–Spectroscopy in Organic Chemistry* (Higher Education, Moscow, 1971). (in Russian)
21. I.I. Plyusnina, *Infrared Spectra of Silicates* (Moscow State University Press, Moscow, 1967)
22. N.E. Anashkina, G.K. Khachatryan, *Ores and Metals*, vol. 3 (Publishing House of Central Research Institute of Geological Exploration for Base and Precious Metals, Moscow, 2015), p. 70 (in Russian)
23. T. Evans, I. Kiflawi, W. Luyten, G. van Tendeloo, G.S. Woods, Proc. R. Soc. Lond. Ser. A **449**, 295 (1995)
24. E.V. Sobolev, *Nitrogen Centers and Growth of Natural Diamond Crystals, in Problems in the Petrology of the Earth's Crust and Upper Mantle* (Nauka, Novosibirsk, 1978). (in Russian)
25. G.K. Khachatryan, *Ores and Metals* vol. 4 (Publishing House of Central Research Institute of Geological Exploration for Base and Precious Metals, Moscow, 2009), p. 73 (in Russian)
26. A.E. Alekseevskii, YuI Osipov, AYa. Vil' et al., Phys. Solid State **43**(1), 145 (2001)
27. Y.S. Lee, T.H. Cho, B.K. Lee et al., J. Fluor. Chem. **120**(2), 99 (2003)
28. W. Dai, P. Ke, A. Wang, Vacuum **85**(8), 792 (2011)
29. V.I. Nefedov, *X-Ray Photoelectron Spectroscopy of Chemical Compounds: A Reference Book* (Chemistry, Moscow, 1984). (in Russian)
30. S.D. Gardner, C.S. Singamsetty, G.L. Booth et al., Carbon **33**(5), 587 (1995)
31. A.F. Azevedo, J.T. Matsushima, F.C. Vicentin et al., Appl. Surf. Sci. **255**(13), 6565 (2009)
32. S. Petrick, C. Benndorf, Diam. Relat. Mater. **10**(3), 519 (2001)
33. V.A. Zakrevskii, N.T. Sudar, Phys. Solid State **47**(5), 961 (2005)

Chapter 8
Diffusion Method of Steel Boriding Without Formation of Iron Borides

Yuri F. Migal and Vladimir I. Kolesnikov

Abstract A new method of strengthening of steel surfaces based on the diffusion saturation of surface layers by boron atoms is proposed. In contrast to the known method of chemical heat treatment (CHT), where boriding of the steel surface is carried out at high temperatures, in this case the surface is treated at temperatures below 800 °C. The advantage of this approach is that iron borides do not appear on the steel surface. Such compounds strengthen the surface and in the same time increase its fragility, which can lead to the destruction of the surface when rapidly changing the mechanical action on the metal. In this article, we consider the possibility to create a new surface boriding technology without formation of iron borides. Three variants of this technology are proposed.

8.1 Introduction

The treatment of steel surface is the most important step for improving the mechanical properties of steel. One of the ways of this procedure is a chemical heat treatment (CHT). Here we consider a certain variant of the CHT, namely boriding. It was proposed by Chizhevski [1] in 1915, and today it is one of the most reliable and widely used methods of steel surface treatment. Within this method, the surface is saturated by boron at high temperatures. The main effect of the CHT boriding is stipulated by appearance of iron borides FeB and Fe_2B on the surface [2, 3]. Exactly these compounds provide high strength and wear resistance of steel parts. Unfortunately, the CHT boriding has an essential fault: after such treatment, the steel surface becomes more fragile. In a number of cases (for example, under shock loads), this type of boriding becomes unsuitable.

Our task is to achieve a stable but not fragile surface by changing the way of boriding.

Y. F. Migal (✉) · V. I. Kolesnikov
Rostov State Transport University, 2, pl. Rostovskogo Strelkovogo Polka Narodnogo Opolcheniya, Rostov-on-Don 344038, Russia
e-mail: ymigal@mail.ru

I. A. Parinov et al. (eds.), *Advanced Materials*, Springer Proceedings in Physics 207, https://doi.org/10.1007/978-3-319-78919-4_8

8.2 Interaction of Boron with Grain Boundaries in Iron: Quantum Chemical Simulation

We are based on earlier studies of the phenomenon of grain boundary segregation in iron. The essence of the matter is that impurity and alloying elements located within the metal can go onto the surface of metal grains and weaken or strengthen the bonds between grains and, as a result, affect the overall strength of the metal. Studying this phenomenon by a simple method in the 1980s, Seah [4, 5] showed which elements harden the steel, and which soften it.

To prove this, he used empirical data on the enthalpy of sublimation of various elements on *free* iron surface. He suggested that the greater the enthalpy of sublimation of some element on the surface of steel is, the stronger this element connects the grains to each other inside steel. Despite the simplicity of this approach, the results correspond with the experimental data on a qualitative level. This fact indicates that in this case the strength of the chemical bonds between atoms of the elements and the metal surface (external or internal) is of decisive importance.

However, Seah's approach seems to be simplified, and more precise models are required. We investigated the problem at the atomic level [6, 7]. We applied various models simulating grain boundaries in iron. There was a cluster model among them in which sets of 30 atoms were used, and a periodic slab model in which the cells of the crystal structure were considered.

One of the variants of the slab model we applied is shown in Fig. 8.1. The boundary between grains is represented in the top part of the figure as a set of atomic layers. The intermediate layer consists of atoms of impurity or alloying elements. Above this layer and below it there are layers of iron atoms. We considered the iron layers corresponding to surfaces with Miller indices (100) and (110).

By using quantum chemical methods, based on the DFT approach [8], we calculated the binding energy of this system. The calculations were carried out by using the ADF software package [9]. Then we considered the disintegration of the system into two parts: an upper part containing only iron layers, and a lower part containing iron layers and an impurity layer. The energy E_d required for the disintegration was calculated as the difference between the energy of the entire complex and the total energy of its two parts.

The results of calculation of the energy, required for the disintegration of the system, are shown in Fig. 8.2. The data for cluster and slab models, obtained in [10, 11] for elements of the first five periods, are presented. The results for elements of the sixth period are given in [12].

We can see from the figure that there is a periodic dependence of the decohesion energy of segregation complexes on the atomic number of the impurity element, and this fact obviously corresponds to the Periodic Law. In addition, it is important that details of the dependence are similar for all used models. These facts increase the reliability of the obtained results.

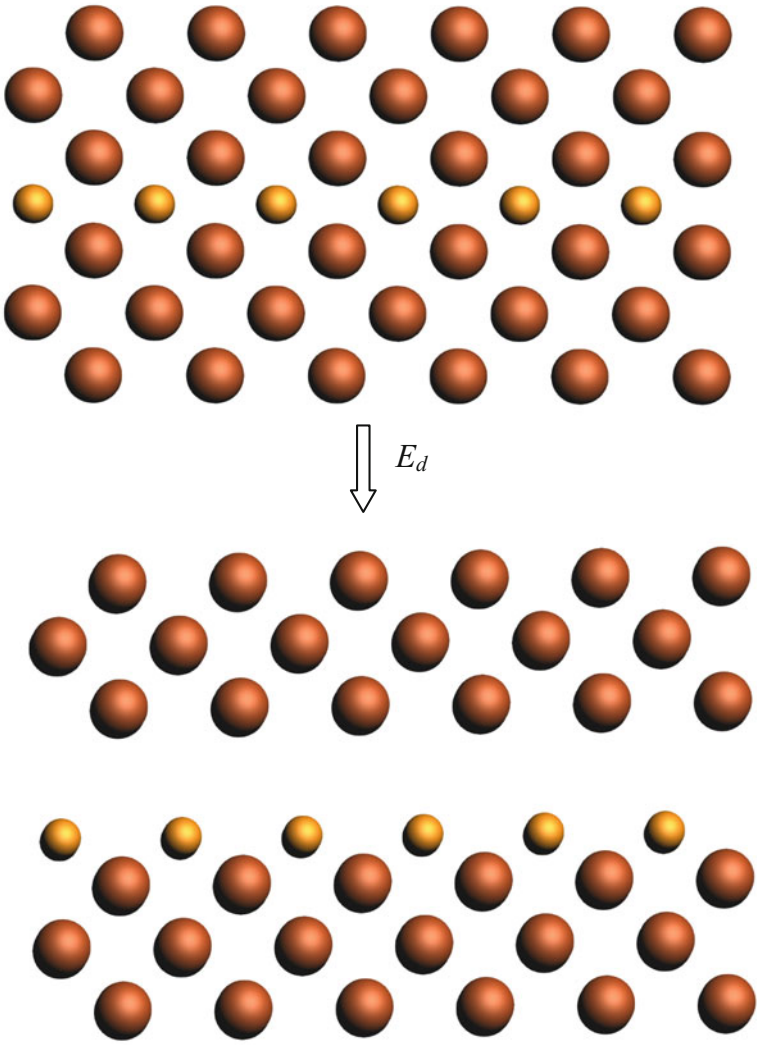

Fig. 8.1 Grain boundary model with (100) surface and its disintegration into two parts

Here the most important question is: which elements have a high binding energy with iron, comparable to the binding energy in pure iron, and which elements have a low energy. Elements with a higher binding energy strengthen iron, elements with a lower energy soften it. Analysis shows that the first group of the Periodic Table consists of elements that soften iron. These include alkali metals, copper, silver, etc. Sulfur, phosphorus, and zinc are also softening elements. Strengthening elements include boron, transition elements, zirconium, niobium, molybdenum. The

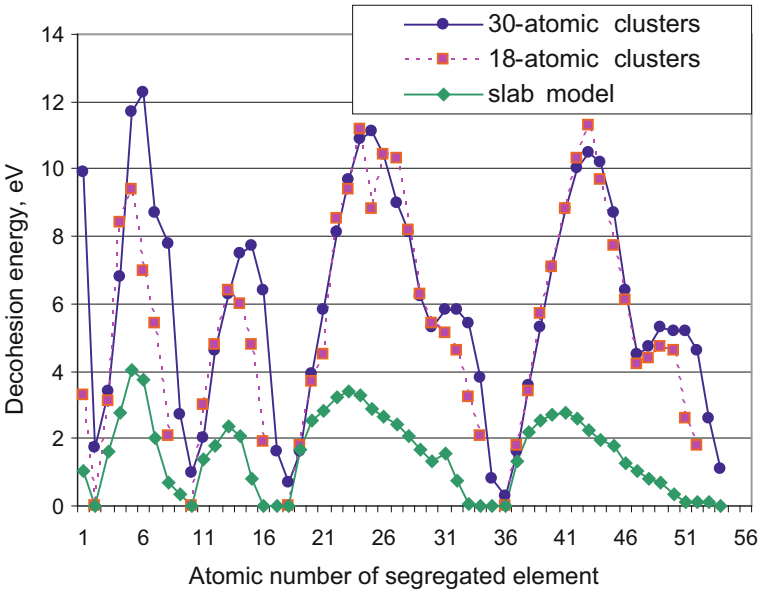

Fig. 8.2 The decohesion energy of segregation complexes containing impurity (segregated) atoms from the first five periods of the periodic table. Energy for slab models is calculated per one cell

obtained results are in qualitative agreement with the results of Seah [4] and known experimental information [13].

In this context, boron deserves special attention. This element is slightly soluble in the bulk of grains [14], so it is located on the surface of grains. Since binding energy of boron with grain surface is relatively high, it displaces atoms with low binding energies, including atoms of sulfur and phosphorus, from the surface. Due to this, the boron, introduced into the surface layers of iron, even in small amounts can substantially strengthen the surface of iron.

The property of boron to harden steel is well known in metallurgy. Steel grades containing boron in small quantities are widely used. The interval of optimal concentrations is 0.001–0.0025% [15]. Dissolved boron in steels significantly changes their properties, in particular, increases their wear resistance. It is important that the presence of boron in them is not associated with an increase in fragility. This defect is characteristic mainly for borated steel *surfaces*, due to the appearance of iron borides. In this connection, the task arises to change the surface boriding technology to reduce the degree of fragility of the samples.

8.3 Methods of Introducing Boron into Steel Surface Layers

The above theoretical reasoning served for us as the base for practical steps in given direction. With this background, we proposed several options for the diffusion introducing of boron into steel surface layers. These include: (i) boriding in a muffle furnace; (ii) a method simulating the action of a brake pad on the surface of a railway wheel; (iii) low-temperature putting of a boron layer on the surface, accompanied by diffusion of boron into the surface.

Below we consider some details of these options.

8.3.1 Boriding in Muffle Furnace

Our study of the furnace boriding process confirmed that iron borides appear on the surface only at a sufficiently high temperature, at 800 °C and above. At lower temperatures, iron borides do not arise. In connection with this, we have chosen a limitation on temperature values for furnace boriding. Its maximum value should not exceed 750 °C. As the process of diffusion at such temperatures slows drastically down, our operating range was chosen to be quite narrow: 700–750 °C, and the boriding time was 25 h or more (instead of 4 h in the standard CHT method). As a starting material for boriding, we used a mixture of boron + boron carbide + alumina + ammonium chloride.

The next problem after boriding was to fix the appearance of boron within the surface layer of the test samples. It turned out that the boron concentration in this case is so small that it can not be fixed by standard methods of X-ray and Auger electron spectroscopy. Indeed, since boron atoms are located mainly in the form of a monoatomic layer on the grain boundary, and the size of the grains themselves is about of a micrometer, the percentage of boron is extremely low.

A quite reliable method for detecting such concentrations is mass spectrometry. However, to study our samples in this way the composition should be homogeneous in all volume of the test sample. In our case, since boron is located only in a narrow surface layer with a thickness of about 20 μm, the application of the mass spectrometry method is ineffective.

At present, the adequate method for detecting such concentrations is an X-ray electron microscopy with a wave dispersion microanalysis. Exactly this method is usually used to study the type of compounds in samples after CHT boriding. The investigation carried out with the help of this method has allowed us to fix the presence of boron in our samples. Figure 8.3 shows the distribution of boron and carbon in samples that have been processed at 700 and 730 °C for 25 h.

The so-called solid solution of boron, which is exactly the state of boron in the steel, we are trying to get, is observed in the area highlighted in Fig. 8.3. It is important to emphasize that in these samples, there were no iron borides. Thus, we

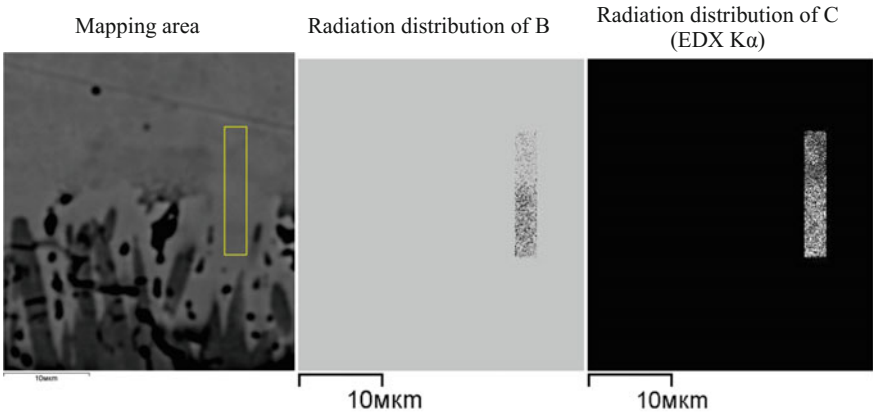

Fig. 8.3 Results of WDS mapping of sample, which has been boronized at temperature of 730 °C for 25 h

can state that in our study, as iron borides are absent, the boron was recorded in the steel surface layers. Presumably, the boron atoms are located on the boundaries of the metal grains.

At present, we study the mechanical and tribological characteristics of the obtained samples with a borated surface.

8.3.2 Simulating the Action of Brake Pad on the Surface of Railway Wheel

Another way of boriding we study is based on the process simulating the influence of brake shoes on a steel wheel surface. Our previous studies of the interaction between a brake shoe and a wheel demonstrated the possibility of the diffusion of the elements of brake pad into the surface layers of the wheel.

We investigated this phenomenon using the Auger electron spectroscopy (AES), which is known as a method that allows us to study directly the phenomenon of grain boundary segregation. By using the AES, the elemental composition at grain boundaries of steel of a railway wheel, decommissioned due to numerous typical defects of its working surface, was investigated. The studied clefts were mainly passed along grain boundaries. The samples tested were cut from various defective areas of the surface (dents, etc.), from the already separated fragments, as well as from sections of the wheel at different depths.

Atoms of various elements, including alloying elements C, Cu, Mn, Cr, Si, impurities P, S, and also Ba, Zn, Ca, K were detected on the surfaces of defective areas and on clefts. The reasons for the appearance of these elements on the rolling surface of the wheel are different. Atoms of barium and zinc are contained in fillers

of polymeric composite brake pad, which base is a hydrocarbon binder. Atoms of potassium and calcium belong to the elements of the environment. Silicon is a part of the material of the wheel, and also presents in the environment.

The main result is that a number of elements, containing in brake pads, were transferred to the surface layers of the wheel during the working process [2]. It is also important that segregation of the atoms of impurity elements take place at grain boundaries located on the clefts. Due to this, the concentration of these elements in the investigated layers exceeds their volume content by a factor of tens.

With this background, it is possible to use the following way of boriding the steel surface. When manufacturing a part simulating a brake shoe, we introduce boron-containing compounds into its composition. Then, as we make a braking contact of this part with the test sample, the atoms of hardening elements will diffuse from the part into metal and ultimately harden the surface layer of metal. High temperature and pressure occurring in the tribo-contact will contribute to this process.

Such a way of boriding is being tested now.

8.3.3 Low-Temperature Putting of Boron Layer on the Surface

The above ways of surface boriding assume an active impact on the surface. The necessity of such an impact is connected with the fact that boron particles should overcome a certain barrier, existing on the surface, and making it difficult for the boron atoms to enter the surface layers of the steel. A typical example of such a barrier is the oxide layer on the steel surface. To overcome the barrier, the surface should be preliminarily cleaned, and a relatively high temperature and atomization of boron from its compounds are needed. The high temperature activates the processes of passage of boron atoms. Atomization of boron is required because a polyatomic complex containing boron atoms has a large cross-sectional area and, accordingly, a low probability of penetration into the metal.

As an alternative to methods involving active action on the surface, we consider a method of boron putting that does not require high temperatures and atomization of boron from its compounds. One of options is an electron-beam evaporation of boron for ion-plasma synthesis of coatings in the vacuum region of pressures [16]. In this scheme, a vacuum chamber with a working pressure range of 2–10 Pa is used. An electron beam, produced by a plasma source, impacts the material from the boron and evaporates it.

As a result, beam plasma, which includes boron and molecules of residual atmosphere, is generated in the chamber. This plasma is then deposited on a specially prepared flat sample from the selected material and creates a layer of small thickness on it. Under such conditions, the boron atoms diffuse into the surface

layer on metal surface purified from the oxides. In this way, it is possible to borate the steel surface under low temperature conditions.

Now we test the samples, obtained in this way.

8.4 Conclusion

Based on theoretical ideas about the nature of the distribution of boron in the surface layers, the possibility of creating a technology for boriding the surface of steel without the formation of iron borides has been considered. Three methods of boriding have been analyzed. We expect that the development of such technology will allow us to increase the wear resistance of the steel surface, without increasing its fragility.

Acknowledgements This work was supported by the Russian Science Foundation (RSCF) (grant No. 16-19-10467, provided to the Rostov State Transport University).

References

1. N.P. Chizhevski, J. Rus. Metall. Soc. **4**(19), 645 (1915) (in Russian)
2. H. Kunst, B. Haase, J.C. Malloy, K. Wittel, M.C. Nestler, A.R. Nicoll, U. Erning, G. Rauscher, *Ullmann's Encyclopedia of Industrial Chemistry* (Wiley-VCH, Weinheim, 2006)
3. A. Matuschka, in *Boronizing* (Hanser, Munich, 1980), 97pp
4. M.P. Seah, Acta Metall. **28**, 955 (1980)
5. D. Briggs, M.P. Seah, *Practical Surface Analysis by Auger and X-ray Photoelectron Spectroscopy* (Wiley, Chichester, 1990)
6. Y.F. Migal, in *Anti-Abrasive Nanocoatings: Current and Future Applications*, ed. by M. Aliofkhazarei (Woodhead Publishing Ltd., Cambridge, 2015), p. 385
7. Y.F. Migal, V.I. Kolesnikov, I.V. Kolesnikov, Comput. Mater. Sci. **111**, 503 (2016)
8. W. Kohn, A.D. Becke, R.G. Parr, J. Phys. Chem. **100**, 129 (1996)
9. G. te Velde, F.M. Bickelhaupt, S.J.A. van Gisbergen, C.F. Guerra, E.J. Baerends, J.G. Snijders, T. Ziegler, J. Comput. Chem. **22**, 931 (2001)
10. V.I. Kolesnikov, A.T. Kozakov, Y.F. Migal, J. Frict. W. **31**(1), 11 (2010)
11. V.I. Kolesnikov, Y.F. Migal, I.V. Kolesnikov, E.S. Novikov, Dokl. Phys. Chem. **464**, 194 (2015)
12. Y.F. Migal, V.I. Kolesnikov, in: *Advanced Materials—Techniques, Physics, Mechanics and Applications*, ed. by I.A. Parinov, S.-H Chang, M.A. Jani. Springer Proceedings in Physics (Springer, Cham, 2017), p. 65
13. E.P. DeGarmo, J.T. Black, R.A. Kohser, *Materials and Processes in Manufacturing*, 10th edn. (Wiley, New Jersey, 2007)
14. W.R. Thomas, G.M. Leak, Nature **176**, 29 (1955)
15. Y.-L. Gao, X.-X. Xue, H. Yang, Acta Metall. Sin. (Engl. Lett.) **28**, 931 (2015)
16. Y.G. Yushkov, A.V. Tyunkov, E.M. Oks, D.B. Zolotukhin, J. Appl. Phys. **120**, 23302 (2016)

Chapter 9
Effect of Process Parameters on Shrinkage of Acrylonitrile Butadiene Styrene Parts Fabricated by 3D Printing Process

Sukhdeep Singh, Rituraj Rajpoot, Vansh Bedi, Sandeep Vats and Vineet Srivastava

Abstract 3D Printing is one of the preferred rapid manufacturing techniques where parts are built by fusion of layers. For a functional prototype, the part should have high accuracy especially for aerospace and rapid tooling applications. Shrinkage is one of the major factors, which influence the accuracy of the 3D Printing parts. The amount of shrinkage encountered is found to be governed by the process parameters during processing and the properties of the build materials. In the present work, the relationship between shrinkage and the process parameters namely layer thickness, head speed and length of the part has been investigated for X direction laying using Acrylonitrile Butadiene Styrene (ABS) as the build material. Response surface methodology has been used to plan the experiments. A model has been developed for estimating the shrinkage of the parts. Length of the part and layer thickness was found to be the most important parameters effecting shrinkage of the parts. Further, it has been found that shrinkage tends to increase with increase in length of the part and decreases with increase in layer thickness and head speed.

9.1 Introduction

In the last three decades [1], additive manufacturing technology has shown a massive growth rate and also a great prospective for the future development. The reassuring future of this technology has a strong effect on the industries. The first additive method was invented by Kodama [2] in 1981, which fabricated 3-dimensional plastic model. In his work, Kodama presented the use of photo-hardening polymer and UV light exposure through masked pattern. Since then the evolution of additive manufacturing has been huge. Berman et al. [3]

S. Singh · R. Rajpoot · V. Bedi · S. Vats · V. Srivastava (✉)
Department of Mechanical Engineering, Thapar Institute of Engineering & Technology, Patiala 147004, Punjab, India
e-mail: vineet.srivastava@thapar.edu

I. A. Parinov et al. (eds.), *Advanced Materials*, Springer Proceedings in Physics 207, https://doi.org/10.1007/978-3-319-78919-4_9

explained this evolution in three phases that are industrial designing and prototyping phase; direct digital manufacturing or rapid tooling phase; and the phase where consumer owns the technique just like a traditional desktop printer.

3D printing is a more identified name of additive manufacturing these days. It can be defined as the process in which the three dimensional part is produced by depositing the material in a layer-by-layer fashion [4]. It is being used in various fields, for instance in medical science to print artificial human teeth and bones [5]; in industries to create moulds for manufacturing assembly components [5]; in aerospace industry to fabricate large flexible structural parts and load-bearing parts [6] and in architecture to fabricate architectural design models [7].

3D printing not only makes production appropriate on any level but also has an exceptional flexibility [1]. Only confine is that very few polymers are compatible with the 3D printing platforms due to particular properties, desired for a suitable print [4]. While even with the existing polymer materials there are countable conflicts such as shrinkage, uncertain voids, low shear strength etc. The motivation behind our study is to deal with these conflicts, specifically linear shrinkage as it is well-known that manufacturing industries and many more applications highly relies on dimensional accuracy. As discussed by Wang et al. [8], several researchers have now worked on the study of shrinkage in order to obtain an accurate prototype. Most of the studies cover stereo lithography, selective laser sintering and FDM processes. At first, Jacobs [9] in 1992 systematically investigated the processing accuracy in SL process. Jacobs examined the accuracy in terms of distortions and warpage. Subsequently, Lu et al. [10] in 1995 investigated the effect of altered laser power settings and layer pitches on shape stability of parts in SL processes using UV laser scanning. Huang et al. [11] also discussed shrinkage compensation in SL process by optimizing build parameters such as exposure time, light intensity and layer thickness.

In SLS, Yang et al. [12] proposed test pieces in X, Y and Z axes for compensation of distortions. They used Taguchi method and suggested a set of basic equations used as scale factors to adapt shrinkage rate. Pandey and Raghunath [13] also used Taguchi method in their work to evaluate the effect of process parameters such as laser power, beam speed, hatch spacing, part bed temperature and scan length on shrinkage in SLS process. Kumar and Gupta [14] extended the work on shrinkage compensation in SLS by optimizing scale factors using pattern search tool and genetic algorithms.

In finite deposition modelling, Dao et al. [15] evaluated shrinkage compensation factor for Stratasys FDM 1650 to improve dimensional accuracy using Christmas-Tree methodology. Gregorian et al. [16] also evaluated shrinkage compensation factor for FDM 1650 built by Stratasys but with a different user part or CAD model. Song et al. [17] as well discussed dimensional accuracy in FDM in the result of extruder's position error and shape deformation, induced by processing error. While an extent of work it has already been done to deal with shrinkage in various 3D printing techniques, there is still some space to be worked out in finite filament modelling in author's knowledge by altering the process parameters.

FFM technique uses the fundamentals of fused deposition modelling with name being the only difference. It can be defined as a process, in which a regular supply of molten filament of desired material is provided by an extruder to form layers on the bed/platform, thus producing a part required [18]. FFM, being very less exposed to shrinkage evaluation, is the highlight of the experimentation, performed and presented in this paper. Flash-Forge [19] Creator Pro 3D, which employs FFM technique, has been used to carry out the experimentation.

9.1.1 Research Purpose

This paper intends to study the effect of process parameters as well as to discuss the reasons behind linear shrinkage in parts, fabricated by FFM. Shrinkage can be due to perspective reasons such as rate of cooling, length of specimen, layer thickness, speed of the extruder and orientation. Different models are generated with different sets of process parameters, selected from the perspective reasons based upon their controllability and significance.

9.1.2 Research Scope

Flash-Forge creator pro 3D is capable of working on four materials [19] namely ABS, PLA, HIPS and PVA. However, acrylonitrile butadiene styrene (ABS) and polylactic acid (PLA) are the most used materials for extrusion due to their dimensional stability and low extrusion temperature. Conversely, to be more specific regarding the test specimen, out of two, the study has been performed taking ABS as a prior material for evaluation.

9.2 Experimental Equipments

9.2.1 Design

(i) Solid modeling software: PTC Creo Parametric Student Version Release 13.0 [20]
(ii) Slicing software: Simplify 3D
(iii) Design of Experiment software: MiniTab 7.0.

9.2.2 Specification of Printer

Flash-Forge [19] Creator Pro 3D has been used for production of test model. It is dual extruder printer with a precision of 2.5 microns on Z-axis and 11 microns on X/Y axis. It provides a range of 100—400 microns for layer thickness variation. It has a maximum build dimension of 8.9″ × 5.9″ × 5.7″ with a nozzle diameter of 0.4 mm. The overall chamber size of the printer is 12.59″ × 18.38″ × 15″ (Fig. 9.1).

9.2.3 Measuring Equipment

Absolute Digimatic Calliper 500 series [20] by Mitutoyo™ is used for linear measurement of the produced test model. The specifications of the equipment are given in the Table 9.1.

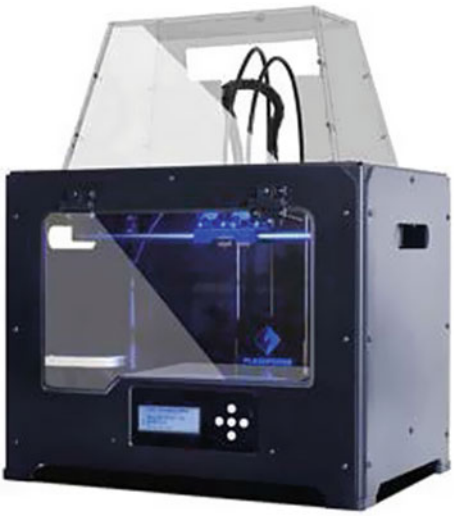

Fig. 9.1 Illustration of apparatus/printer flash-forge creator pro 3D

Table 9.1 Specification of measuring instrument Absolute Digimatic Calliper 500 series

Accuracy (excluding quantization error) (mm)	±0.02
Repeatability (mm)	±0.01
Resolution (mm)	±0.01

9.2.4 Filament

(i) Material: ABS—Industrial grade
(ii) Filament type: Spool of 1.75 mm diameter.

9.3 Research Method

9.3.1 Part Production Methodology

Test models are designed in Creo Parametric and consequently generating an STL file with an ASCII conversion format. Chord Height and angle control for each test model are precise to be 0.040825 and 0°, respectively. The STL files are then processed in Simplify 3D for repairing hence controlling the process parameters. Subsequently generating slice information and conversion into printer compatible format that is .x3d.

Throughout the evaluation, the orientation of test model is constrained to 90° about *y*-axis as shown in Fig. 9.2. The infill percentage is set to 70% for a rectilinear pattern with 30% of outline overlap. Platform and extruder temperature being predetermined are set to 115 and 230 °C, respectively for the purpose of decent adhesion. Numbers of top and bottom solid layers, both are set to 3 with outline direction of inside-out to provide respectable strength to persist the contraction during measurements. All the pre-settings have been done to cope with conflicts like warpage/curling. All the parts are manufactured with an initial pre-heating time of 5–10 min.

9.3.2 Experimental Procedure

The linear shrinkage of a part produced is governed by a large number of interactive variables. However, to facilitate the experimental work only three controllable variables are considered namely layer thickness, head speed and length of the model. The experiments have been conducted keeping these factors at various levels. The range of each factor has been selected, based on the capabilities of the machine. For the purpose of easy experimentation, Minitab 7.0 has been used for a proper design of experiments. Surface response design methodology has been specifically chosen to design the experiment. The process parameters with chosen levels are given in Table 9.2.

The range of layer thickness is so chosen for the reason being to produce an appropriate part for assessment. For a lower range of layer thickness would have harmed the purpose of study as it would have increased the build time subsequently compensating the effect generated due to increase in head speed in some cases. The

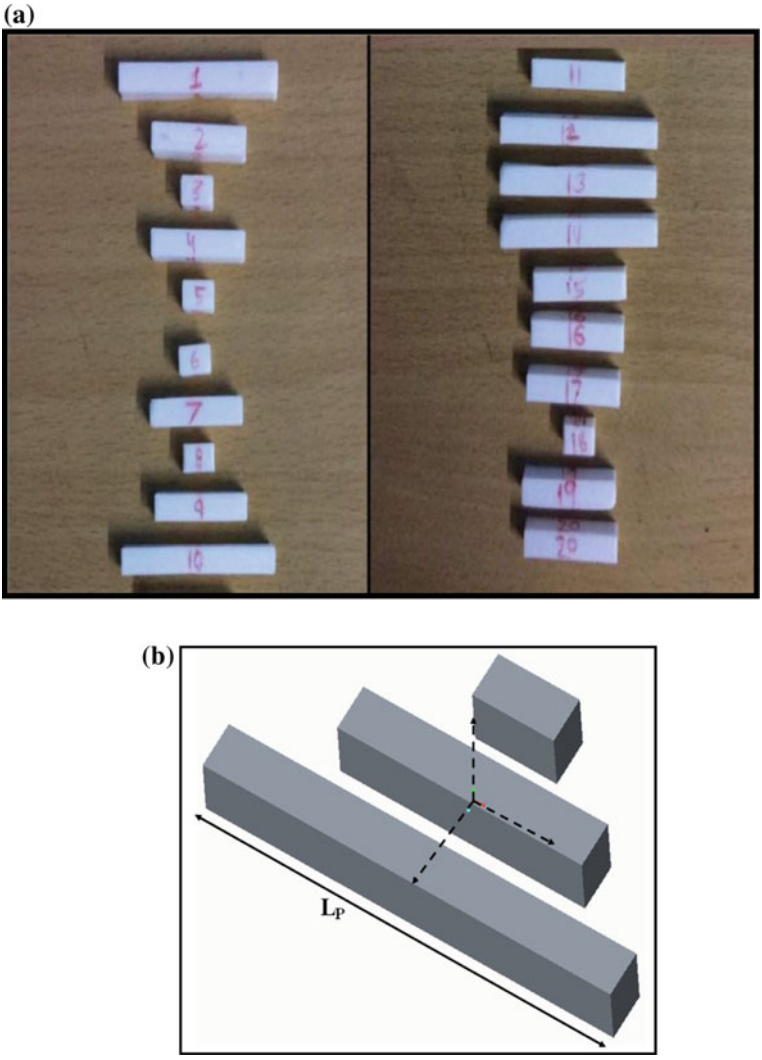

Fig. 9.2 **a** Produced test specimens, **b** CAD model of test specimens

Table 9.2 Selected process parameters with levels

Factors	Units	Levels		
		−1	0	1
Layer thickness	mm	0.20	0.22	0.24
Length	mm	10	30	50
Head speed	mm/s	3000	3200	3400

levels of length of part are so chosen to neglect the effect of shrinkage due to naked curling. Head speed being one of major factor increase the build and subsequently providing more time for part to cool while in the chamber, has been given a wider range comparatively to encounter and include the non-linearity in the trend.

9.3.3 Shrinkage Measurement

Linear shrinkage is measured by comparing the model's dimension with the produced prototype dimension as per the given definition, where δ represents linear shrinkage.

$$\delta = L_{Original} - L_{Prototype}. \tag{9.1}$$

Total four readings of every produced part have been taken using the measuring equipment to improve the accuracy of experimentation. Average of the readings is computed to come up with a single value of shrinkage for each experimental model. Measured responses of linear shrinkage for each experiment are present in Table 9.3.

Table 9.3 Linear shrinkage values for each experiment

Expt. no.	LNX	LT	HS	SHX
1	50	0.24	3400	0.41
2	30	0.22	3200	0.30
3	10	0.2	3400	0.05
4	30	0.22	3200	0.27
5	10	0.24	3400	0.06
6	10	0.2	3000	0.02
7	30	0.2	3200	0.31
8	10	0.24	3000	0.02
9	30	0.22	3200	0.19
10	50	0.2	3000	0.59
11	30	0.22	3400	0.23
12	50	0.2	3400	0.48
13	50	0.22	3200	0.44
14	50	0.24	3000	0.38
15	30	0.22	3000	0.33
16	30	0.24	3200	0.28
17	30	0.22	3200	0.28
18	10	0.22	3200	0.08
19	30	0.22	3200	0.33
20	30	0.22	3200	0.23

$$\delta = \frac{\delta 1 + \delta 2 + \delta 3 + \delta 4}{4}. \tag{9.2}$$

9.4 Result and Discussion

A model for SHX (Linear shrinkage) is obtained by analyzing the data presented in Table 9.3, and is given below as (9.3) after eliminating all the insignificant parameters:

$$\begin{aligned} \mathbf{SHX} = {} & 2.05 + (0.0486 \times LNX) - (25.2 \times LT) + (0.00023 \times HS) \\ & - (0.000059 \times LNX \times LNX) + (25.6 \times LT \times LT) \\ & - (0.0875 \times LNX \times LT) - (0.000005 \times LNX \times HS) \\ & + (0.00469 \times LT \times HS) \end{aligned} \tag{9.3}$$

ANOVA was used to check the adequacy of the developed model. The analysis revealed that the model is adequate and lack of fit (p-value: 0.554) is insignificant. Main effect plots for SHX are displayed in Fig. 9.3. Adjusted R-square value (91.70) and predicted R-square value (74.53) of the model was found at par to indicate shrinkage stochastically.

It can be observed that the shrinkage increases with increase in length. This effect can be explained using the principle of thermal expansion and contraction. As

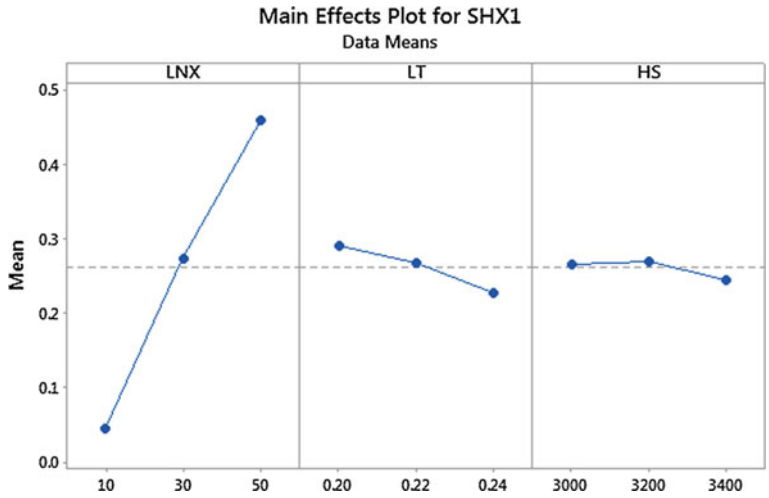

Fig. 9.3 Main effect plots for linear shrinkage; where LNX is Length of specimen, LT is Layer thickness and HS stands for Head speed

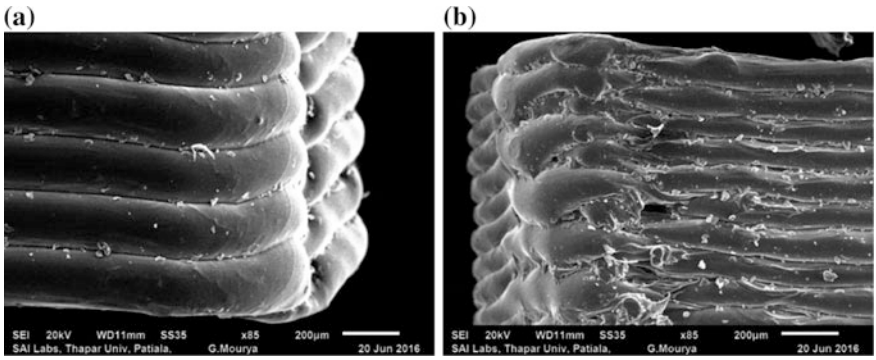

Fig. 9.4 SEM micrographs showing the effects of shrinkage at **a** length of 10 mm **b** length of 50 mm

the heat transferred to the workpiece, it elongates in the direction of the heat flow. However as the workpiece is plastic material, on cooling, molecular rearrangement occurs which makes it more brittle due to high thermal coefficients of expansion. This results in higher shrinkage as the length increases, which is further evident from the SEM images given in Fig. 9.4.

The effect of head speed on shrinkage is insignificant because the shrinkage values vary around the mean. As the head speed increases, the rate of deposition of materials also increases. As a result, the heat remains entrapped in the layer because before it is dissipated, a new layer gets deposited. Consequently, no significant shrinkage is observed.

With increase in layer thickness, shrinkage decreases, which can be observed from Fig. 9.3. This may be due to that together with layer thickness the cross-sectional area also increases. These results in more heat absorption capacity as well as enhancement of the heat transfer, hence, establishing thermal equilibrium and concluding a lower shrinkage.

9.5 Conclusion

In this work, a study regarding shrinkage of linear parts has been successfully performed by correlating length, layer thickness and head speed. A mathematical model has been developed, which correlates the part shrinkage with the process parameters. It was observed that shrinkage increased with increase in length of the part, however it decreased with increase in layer thickness and head speed. Further, it has been found that length of the part is the most predominant factor, which influences shrinkage.

References

1. B. Lu, D. Li, X. Tian, Engineering **1**(1), 85 (2015)
2. H. Kodama, Rev. Sci. Instrum. **52**(11), 1770 (1981)
3. B. Berman, Bus. Horiz. **55**(2), 155 (2012)
4. A.R.T. Perez, D.A. Roberson, R.B. Wicker, J. Fail. Anal. Prev. **14**(3), 343 (2014)
5. A. Sutradhar et al., Comput. Biol. Med. **52**, 8 (2014)
6. *General Electric Company. Advanced manufacturing is reinventing the way we work* (2014). http://www.ge.com/stories/advanced-manufacturing
7. G. Cesaretti et al., Acta Astronaut. **93**, 430 (2014)
8. W.L. Wang et al., Mater. Design **17**(4), 205 (1996)
9. P.F. Jacobs, *Rapid Prototyping and Manufacturing: Fundamentals of Sereolithography*. Society of Manufacturing Engineers (1992)
10. L. Lu et al., Mater. Res. Bull. **30**(12), 1561 (1995)
11. Q. Huang et al., IIE Trans. **47**(5), 431 (2015)
12. H.-J. Yang, P.-J. Hwang, S.-H. Lee, Int. J. Mach. Tools Manuf **42**(11), 1203 (2002)
13. N. Raghunath, P.M. Pandey, Int. J. Mach. Tools Manuf **47**(6), 985 (2007)
14. A. Gupta, P.S. Kumar, Optimization of scale factors in shrinkage compensations in SLS using pattern search tool and genetic algorithm. Power (w) 36(36):36
15. Q. Dao et al., Comput. Appl. Eng. Educ. **7**(3), 186 (1999)
16. A. Gregorian et al., *Solid Freeform Fabrication Proceedings* (2001)
17. S. Song et al., *Automation Science and Engineering (CASE),* In 2014 IEEE international conference on. IEEE (2014)
18. S. Saini, V.G. Srivastava, G.S.G. Saini., *Statistical Modeling and Optimization of Dimensional Accuracy for Solidified Polylactic Acid Parts Fabricated by Fused Filament Modeling Process*. Thesis (2016)
19. *Flash-Forge Creator Pro 3D*, http://www.flashforge-usa.com/shop/flashforge-new-creator-pro-dual-extrusion-3d-printer.html
20. *PTC Creo 2.0 Student Edition-Quick Installation Guide,* https://support.ptc.com/WCMS/files/153998/en/Install_Creo2_Student.pdf
21. *Mitutoyo™- Absolute Digimatic Calliper 500 Series*, http://ecatalog.mitutoyo.com/ABSOLUTE-Digimatic-Caliper-Series-500-with-Exclusive-ABSOLUTE-Encode-Technology-C1381.aspx

Chapter 10
Molecular Dynamics Simulations to Design Novel Solvents for Deep Desulfurization

Dinara Gapeyenko, Prashant Jamwal and Dhawal Shah

Abstract For the last decade, deep eutectic solvents (DESs), novel solvents have attracted a lot of attention due to their favorable properties such as a low melting point, non-toxicity and low-cost. In this work, a combination of tetrabutylammonium chloride (TBAC), polyethylene glycol (PEG-200), and ferric chloride ($FeCl_3$) at a molar ratio of 4:1:0.05, a metallic based deep eutectic solvent is analyzed using molecular dynamics simulation. The analysis reveals the interactions between the components of DES, which might lead to the formation of the DES, i.e., strong depression in the melting point as compared to the individual component. Further, the solvent was also tested for fuel desulfurization using molecular simulations. For the analysis, *n*-octane was chosen as fuel with ~2000 ppm of dibenzothiophene and the results suggest strong absorption of sulfur compounds by the DES.

10.1 Introduction

Petroleum products play a significant role in daily life. However, it is not a secret that those products carry lot of polluting compounds, which have been removed in an environmentally friendly way. Production of diesel, in particular, with low content of sulfur became one of the significant challenges for the petroleum industry. Legislation of majority countries in the world requires decreasing the allowable limit of sulfur concentration in fuels and middle distillates to as low as 10 ppm and beyond [1]. The conventional method of sulfur content reduction is hydrodesulfurization (HDS) process. However, the process has its own drawbacks, such as use of elevated temperatures 300–400 °C, high pressure varying from 30 to 130 atm., consumption of huge amount of hydrogen, and, complicated aromatic-sulfur compounds such as dibenzothiophene (DBT) and thiophene (TP) cannot be totally extracted [2]. These shortcomings of HDS method have pushed towards development of alternative

D. Gapeyenko · P. Jamwal · D. Shah (✉)
School of Engineering, Nazarbayev University, Astana, Kazakhstan
e-mail: dhawal.shah@nu.edu.kz

I. A. Parinov et al. (eds.), *Advanced Materials*, Springer Proceedings in Physics 207, https://doi.org/10.1007/978-3-319-78919-4_10

desulfurization techniques, amongst which the most promising development is towards the use of extractive process by suitable solvents.

Recently, several ionic liquids have been suggested to work efficiently to extract sulfur-based compounds from diesel. However, ionic liquids, because of their difficult synthesis, high cost, and questionable toxicity have not been commercialized [3]. On the other hand, more recent focus has been on development of deep eutectic solvents (DESs) for extractive desulfurization. DESs are considered as greener replacement to ionic liquids. A typical DES consists of at least one hydrogen bond accepter and one hydrogen bond donor, which results in a mixture with lower melting temperatures than their individual components [4]. Deep eutectic solvents have a number of beneficial properties such as low vapor pressure, good solubility and also they can be easily recovered by anti-solvents like methanol or ethanol. Moreover, DES is considered as non-flammable, non-toxic, biodegradable and relatively cheap [5]. Considering these favorable properties, several applications of DESs have emerged recently, including the use of DESs to complete removal of thiophenic compounds from diesel.

In this work, we used molecular dynamics simulations and primarily focused on the formation mechanisms of a DES that has been proposed as an efficient solvent to extract the refractory compounds from model oils [6]. Later, we also explore the intermolecular interaction between the DESs, diesel, and thiophenic compounds to understand the extraction process. In particular, we used a combination of tetrabutylammonium chloride (TBAC), polyethylene glycol (PEG-200), and $FeCl_3$ at a ratio of 4:1:0.05 as DES and octane was used as to model diesel. The following mixture had been reported to extract thiophenic compounds with an efficiency ranging from 81 to $\sim$100%, even at very low concentrations and room temperatures [6]. In our simulations, we used dibenzothiophene (DBT) representing the sulfur compound. The simulations were done at 25 °C and 1 bar. In the following, we present our simulation methodology, formation dynamics of the DES, and its interactions with the octane and DBT molecules.

10.2 Simulation Methodology

Gromacs 5.0 package was used to perform all-atom molecular dynamics simulation for the DES. Optimized coordinates and forcefield parameters for tetrabutyl ammonium (TBA) ion and PEG-200 were taken from Automated Topology Builder (ATB) database (Fig. 10.1). The interaction parameters for Fe^{+3} ion was taken from Lin et al. [7]. All other parameters were taken according to the gromos54a7 forcefield. Simulations were started using a low-density box, $15 \times 15 \times 15$ nm^3, and the number of molecules were inserted according to specified molar ratio of 4:1:0.05. Specifically, we used 400 molecules of tetrabutylammonium, 415 molecules of chloride, 100 molecules of polyethylene glycol and finally, 5 molecules of iron were added. In addition, octane (911 molecules) was used as to model diesel and DBT (2 molecules) was used to mimic 2000 ppm of sulfur content in oil.

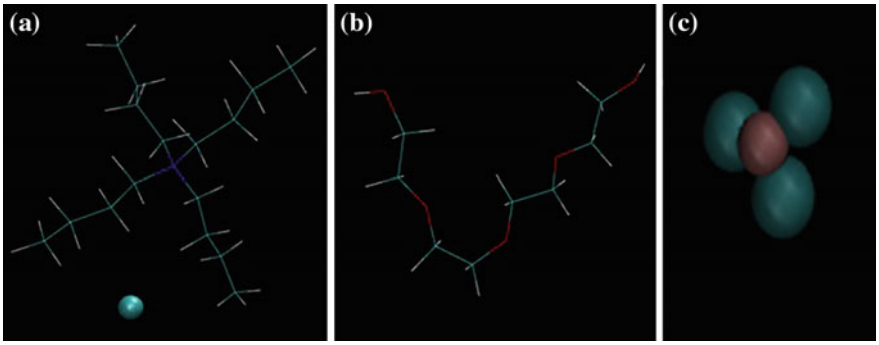

Fig. 10.1 Molecular structure modeled via VMD tool: **a** TBA ion with Cl ion shown separately, **b** PEG-200, **c** $FeCl_3$

Forcefield parameters from octane and DBT were also taken from the ATB server. Several systems, as shown in Table 10.1, were designed to systematically explore the mechanism(s) of DES formation and the sulfur extraction process.

After creating the initial geometry with the molecules, we performed energy minimization and further NVT-equilibration and NPT-equilibration for 0.2 ns at 298 K and 1 bar was performed. The simulations were put to run for 10 ns and only the last 2 ns were taking for the equilibrium analysis. During this simulation, LINCS constraint algorithm was applied for all the bonds. For Coulomb and Lennard-Jones (LJ) short-range interactions, 1.5 nm cut-off was applied. Particle Mesh Ewald summation method was used to calculate long-range interactions with 0.16 nm grid spacing and fourth-order interpolation. The modified Berendsen coupling method was used for temperature parameter and kept the system constant at 298 K, while pressure parameter was running under Parrinello-Rahman coupling method with 1 bar constant pressure. Periodic boundary conditions were during all simulation steps. After the simulation was completed, Visual Molecular Dynamics (VMD) tool was applied to extract the radial distribution functions and visual models of running systems. All other analysis was performed using Gromacs package.

10.3 Results and Discussion

Our first aim in this work is to explore the formation mechanism of the DES, i.e. to understand the strong depression in the freezing point observed from the molecular point of view. We begin our analysis with comparing systems 1 and 2 as mentioned in Table 10.1. We determined the radial distribution functions (rdfs) between different components of the DES. The rdfs show the measure of probability for an atom being at the distance r from the reference atom. Nitrogen atom of the TBA ion, and central oxygen atom of the PEG molecules were chosen as reference to determine the rdfs.

Table 10.1 Number of molecules used in simulation for different systems simulated. The temperature and pressure of all systems were kept constant at 298 K and 1 bar

System No.	Number of molecules of					
	TBA^+	Cl^-	Fe^{+3}	PEG	Octane	DBT
1	400	400	–	–	–	–
2	400	415	5	100	–	–
3	–	–	–	–	911	2
4	400	415	5	100	911	2

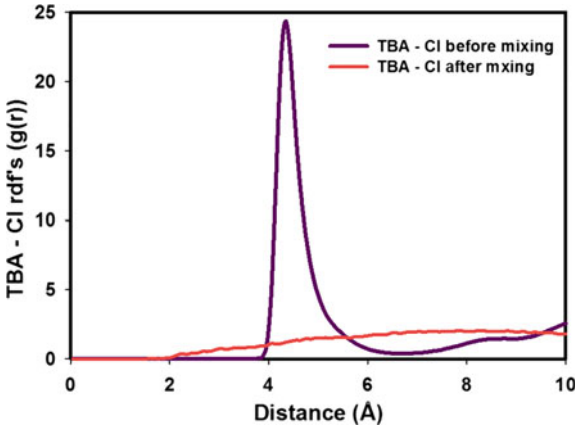

Fig. 10.2 Radial distribution functions for TBA-Cl system before and after mixing

Figure 10.2 shows the rdfs between the central nitrogen atom of the TBA ion with the chloride ion before and after mixing with $FeCl_3$ & PEG, i.e., system 1 and system 2 according to Table 10.1. From this figure, it can be seen that before mixing the first Cl ion appears at distance of 4.35 Å from the central nitrogen atom with a peak of 25. However, after mixing the interaction force decreased significantly, which can be explained by the fact that TBA ion started to interact with PEG molecule as shown in Fig. 10.3. It is also important to highlight that after mixing the distance between nitrogen atom and chloride ion decreases with very low peak. The strong decrease in the strength of interactions between the TBA and Cl ions probably causes the strong depression the melting point of the DES.

Moreover, we also calculated the total interaction energies (sum of LJ and Coloumbic energies) between TBA and Cl ions before mixing was compared with total energy of DES. Figure 10.4 clearly shows that interaction energy of TBAC system is higher than the DES system, which also indicates the depression in the melting point as observed in the DES.

Furthermore, we analyze systems 3 and 4, to evaluate the effectiveness of DES in sulfur extraction from the fuel. Figure 10.5 compares the interaction energy between DBT and *n*-octane before mixing with DES and interaction energy

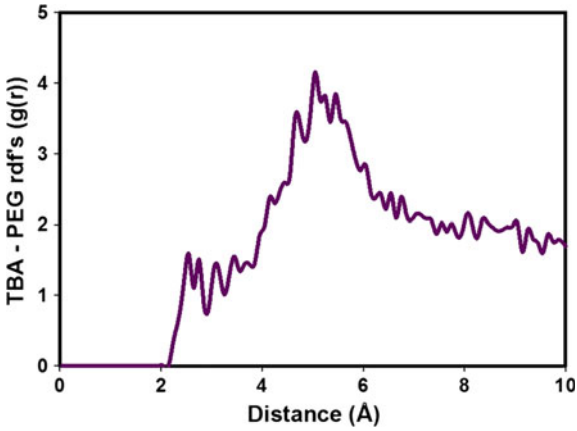

Fig. 10.3 Radial distribution function between the TBA ion and PEG system

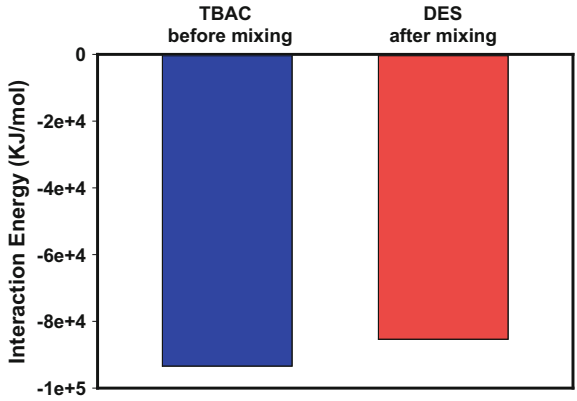

Fig. 10.4 Interaction energy profile for TBAC and DES systems

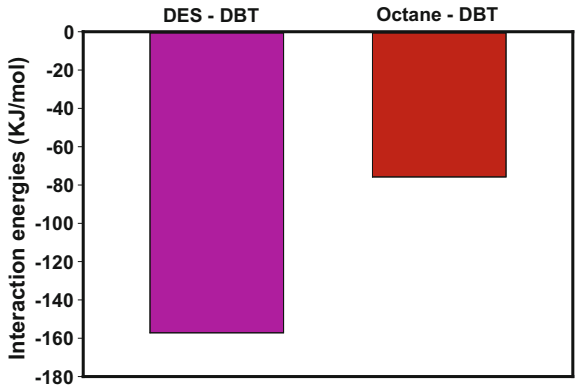

Fig. 10.5 Interaction energy profile for DBT-octane and DBT-DES system

between DBT and DES after mixing fuel with deep eutectic solvents. The results show that DES captures the DBT molecules because DBT-DES system has approximately twice the energy in comparison with the DBT-octane system.

10.4 Conclusion

This research was aimed to understand the molecular interaction occurring in the metallic deep eutectic solvent. Our results with TBAC:PEG:$FeCl_3$ at 4:1:0.05 molar ratio under 25 °C and 1 bar show that each individual chemical compound initially has a very strong interaction energy, however, after mixing let to a decrease in the total interaction energy. Moreover, to check its sulfur extraction abilities, DES was put with model fuel (*n*-octane) with 2000 ppm DBT concentration and we observed that all sulfur molecules were captured by solvents. However, further analysis needs to be carried to develop details insights into the systems.

References

1. L. Hao, M. Wang, W. Shan, C. Deng, W. Ren, Z. Shi, H. Lu, J. Hazard. Mater. **339**, 216 (2017)
2. H.F.M. Zaid, C.F. Kait, M.I.A. Mutalib, Fuel **192**, 10 (2017)
3. J. Li, H. Xiao, X. Tang, M. Zhou, Energy Fuels **30**, 5411 (2016)
4. S.E.E. Warrag, C.J. Peters, M.C. Kroon, Curr. Opin. Green Sustain. Chem. **5**, 55 (2017)
5. M. Hayyan, A.M. Alakrach, A. Hayyan, M.A. Hashim, H.F. Hizaddin, ACS Sustain. Chem. Eng. **5**, 1854 (2017)
6. C. Li, J. Zhang, Z. Li, J. Yin, Y. Cui, Y. Liua, G. Yanga, Green Chem. **18**, 3789 (2016)
7. W. Lin, W.J. Welsh, W.R. Harris, Inorg. Chem. **33**, 884 (1994)

Part II
Physics of Advanced Materials

Chapter 11
Laser-Induced Engineering of Surface Structures and Properties on Oxygen-Adsorbed TiC(111) Surface: First-Principles Calculations

V. V. Ilyasov, B. C. Meshi, D. K. Pham, Ch. V. Nguyen, O. M. Holodova, T. P. Zhdanova, I. V. Ershov, N. V. Prutsakova and I. G. Popova

Abstract In this chapter, we used the density functional theory (DFT) to systematically investigate the electron structure and elastic moduli of oxygen-adsorbed O/Ti_xC_y(111) surface affecting its potential reconstructions with laser. For the first time we studied within the density functional theory framework the local atomic and electron structures of potential O/Ti_xC_y(111) surface configurations as well as their thermodynamic and elastic properties. A considerable rearrangement has been established in the local atomic structure of O/TiC(111) surface depending upon the degree of its coverage with atomic oxygen in FCC stacking position. We have demonstrated that the distance between adsorbate and TiC(111) surface decreased with the increase of its coverage with oxygen. Additionally, the effect of oxygen adsorbed on the Ti_xC_y(111) surface on the electronic properties in its different reconstructions has been also studied. The results showed that a correlation between the energy level of flat bands in the −5.1 eV and −5.7 eV energy regions was responsible for the doublet of singular peaks corresponding to partial densities of oxygen 2*p* electrons, and the bond energy and adsorption energy of oxygen atom in non-stoichiometric O/TiC_y(111) systems. Effective charges of titanium and carbon atoms surrounding the oxygen adatom in various reconstructions have been identified. We have established charge transfer from titanium atom to oxygen and carbon atom,s determined by the reconstruction of local atomic and electron structures and correlating with their electronegativity values and chemisorption processes. Calculated values of elastic moduli for the upper part of ultrathin O/TiC

V. V. Ilyasov (✉) · B. C. Meshi · D. K. Pham · O. M. Holodova · T. P. Zhdanova
I. V. Ershov · N. V. Prutsakova · I. G. Popova
Don State Technical University, Rostov-on-Don, Russia
e-mail: viily@mail.ru

Ch.V. Nguyen
School of Mechanical Engineering, Le Quy Don Technical University, Hanoi, Vietnam

I. A. Parinov et al. (eds.), *Advanced Materials*, Springer Proceedings in Physics 207, https://doi.org/10.1007/978-3-319-78919-4_11

(111) and O/Ti_xC_y(111) layers correlate well with experimental findings and other theoretical results. Potential mechanisms for laser nanostructuring of titanium carbide surface have been suggested.

11.1 Introduction

Surface properties of ultrathin titanium carbide (TiC) films remain in the focus of attention owing to their extraordinary physical properties, such as high thermal and electric conductivity, high hardness, durability [1–3]. Stoichiometric TiC has plain B1 crystal structure. However, TiC films typically contain vacancies both in the titanium sublattice and carbon sublattice [4]. In order to understand the physical properties of such materials, it is necessary to investigate the atomic behavior of the TiC crystals [5]. There are many ways to modulate the surface properties of TiC materials, one of the most used methods is the laser surface nanostructuring [6], which includes melting, cooling, and crystallization [7, 8]. In order to adjust these methods exactly, we can modulate the energy density and laser pulse duration. Recently, numerical experimental and theoretical investigations on the structural properties of the TiC(111) surface showed that the TiC(111) surface with Ti-terminated is the polar surface [9–11].

Currently, from He^+ ion scattering spectroscopy, Souda et al. [12] showed that when an oxygen was adsorbed on the TiC(111) surface, the (1×1) and $(\sqrt{3} \times \sqrt{3})$ *R*30 types of atomic structures were formed. Additionally, it was shown that at room temperature the TiC(111)-(1 × 1)-O structure is stable [13], whereas it reconstructed to TiC(111)-$(\sqrt{3} \times \sqrt{3})$ *R*30-O form, when the temperature heated up to 1000 °C [13, 14]. The results also indicated that the positions in the face-centered cubic (FCC) arrangement can be occupied by adsorbed oxygen atoms [14].

As above-mentioned, reconstructions of TiC(111) atomic surface are manifested in the electron spectrum of titanium and carbon subsystems, and also in the elastic constants and moduli of the top layer similarly to the O/TiC(001) system [15]. Recently, Marques et al. [4] by using a three-dimensional (3D) model of bulk TiC crystal have studied the effect of an oxygen atom on the structural, electronic and mechanical properties of TiC_xO_y structure. They indicated that the lattice parameters and elastic constants of the TiC_xO_y system decrease with increasing oxygen content. Edamoto et al. have studied the electronic state of oxygen adsorbed on a TiC surface by using angle-resolved photoemission electron microscopy [13]. In comparison with the $2p_z$ orbital, it was shown that for chemisorption processes the $2p_{x,y}$ orbitals of oxygen atom are the most essential for the TiC surface. The atomic, electronic and thermodynamic properties of adsorption of atoms in the three first periods on the TiC(111) surface have been also investigated from first principles calculations [11]. By using DFT method, Wang et al. also investigated the structural and electronic properties of TiC(110) surface [5].

Up-to-date, the electronic and elastic properties of oxygen-adsorbed TiC(111) surface with distributed Ti and C vacancies has not yet been studied thoroughly. Thus, in this work we focus on the electronic and elastic properties of the O/Ti_xC_y(111) system upon thermal action using DFT method from first principles calculations.

11.2 Model and Method

Theoretical study of the O/TiC(111) system is based on three-dimensional periodic slab model. Titanium-terminated supercell consisting of 2 × 2 unit cells arranged within a plane (111) was used. Figure 11.1a demonstrates a fragment of the TiC (111) slab, in Fig. 11.1b potential positions of the oxygen atom are shown. We have studied 6 various configurations of oxygen atom positions on a TiC(111) slab: A—Oxygen atom situated above the Ti atom of the top layer; B—Oxygen atom situated above the Ti atom of the third layer (FCC hollow); C—Oxygen atom situated on carbon atom of second layer (HCP hollow); D—Oxygen atom situated in the bridge site; A_{vak}—Oxygen atom situated above the surface vacancy of the Ti atom in top layer; C_{vak}—Oxygen atom situated above the vacancy of the carbon atom in second layer.

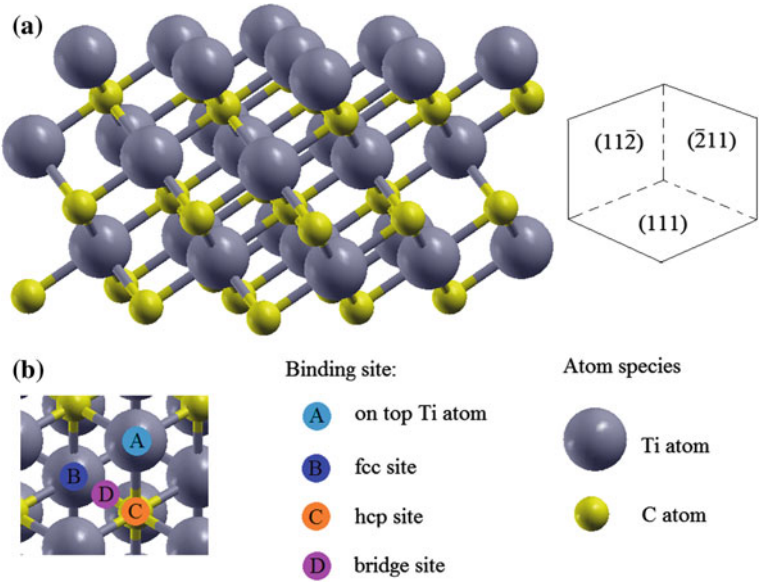

Fig. 11.1 TiC(111) surface model (**a**) and binding positions of oxygen atom (**b**) on TiC(111) surface, top view

FCC hollow position (in our case, B) is known [11] to be a relatively stable binding site for O atom on TiC(111) surface. Therefore, we have performed calculations for oxygen in B position for the coverage range from 1/9 to a complete monolayer. All coverage values of $\Theta = 0.11, 0.22, 0.33, 0.44, 0.55$ and 1.0 were calculated based on the (111) plane of a (2×2) TiC supercell. In particular, $\Theta = 0.33$ coverage corresponds to the TiC(111)-$(\sqrt{3} \times \sqrt{3})$ $R30$-O reconstruction, while the coverage $\Theta = 1.0$ corresponds to the TiC(111)-(1×1)-O structure.

TiC(111) slab represents six non-equivalent alternating Ti and C layers in the [111] direction. Vacuum gap of 12 Å excluded any interactions between the slab translations in the [111] direction. In this study self-consistent calculations were carried, based on the density functional theory (DFT) within pseudopotential method (Quantum Espresso code) [16]. Exchange and correlation were taken into account using PBEsol functionals (GGA approximation) [17, 18]. The plane waves expansion cutoff energy of 400 eV was used. The convergence test for the surface energy and interplanar distance confirmed the cutoff energy of 400 eV and a $3 \times 3 \times 1$ Monkhorst-Pack grid were sufficient [19]. The SCF unit cell total energy convergence was at least 10^{-6} Ry/cell. To describe the interaction between valence electrons and the core, Vanderbilt ultrasoft pseudopotentials were used. The pseudopotentials were generated using Troullier-Martins scheme [20]. The following electronic configurations were used: Ti—[Ar]$3d^2 4\ s^2$, O—[He]$2s^2 2p^4$, C—[He]$2s^2 2p^2$. [Ar] and [Ne] were considered as core states.

The effective charges were estimated on the oxygen atom as well as on the surface Ti and C nearest atoms in six O-adsorbed O/Ti_xC_y(111) models using Löwdin population analysis [21].

Elastic properties of the O/Ti_xC_y(111) and O/TiC(111) systems were theoretically studied using Elastic program [22], based on DFT total energy calculations for deformed crystal structures. Elastic constants $c_{i,j}$ determine the crystal response to applied external forces and characterize the bulk modulus B, as well as Young's modulus E, shear modulus G, and Poisson's ratio υ [23]. Cubic systems are usually represented by 3 independent elastic constants c_{11}, c_{12}, and c_{44} [3]. Elastic constants were calculated using the stress-strain approximation, based on generalized Hooke's law. The Voigt-Reuss-Hill (VRH) approximation was used to estimate bulk modulus B, shear modulus G, and Young's modulus E. The approximation provides the best estimation of mechanical properties of polycrystalline materials based on elastic constants and the formulas in [22, 23].

11.3 Results and Discussion

11.3.1 Energy and Atomic Structure of Oxygen-Adsorbed $Ti_xC_y(111)$ Surfaces

To study the electron structure and elastic moduli of O-adsorbed O/Ti_xC_y(111) surface, relaxation of two upper atomic layers (Ti, C) of a TiC slab with adsorbate was made. Initially, the O atom was placed in the binding sites (Fig. 11.1) at the distance of 2 Å from the TiC(111) surface. Two lower atomic layers of the 2D O/Ti_xC_y(111) system considered "frozen". Relaxation was carried out until the total force in the system reduced to 0.001 eV/Å. Atomic structures of a three-layer slab with oxygen in various configurations of the O/Ti_xC_y(111) and O/TiC(111) systems after relaxation are shown in Fig. 11.2. Table 11.1 offers the calculated parameters of atomic structures, including the lengths of bonds d_{Ti-O} and d_{Ti-C} between the oxygen atom and its nearest neighbors, vertical distances: d_0—between the adsorbate and the first Ti layer, d_1—between the first Ti layer and C layer, d_2—between the C layer and the third Ti layer, total energy of the substrate with oxygen E_{tot}, total energy of the original substrate surface E_{ref} for oxygen binding sites on the surface of TiC(111) and Ti_xC_y(111) slabs. It also contains some known theoretical and experimental findings correlating with the data of this DFT calculation.

Analysis of Table 11.1 shows that the processes of oxygen chemisorption result in considerable rearrangement of the local atomic structure of O/Ti_xC(111) and O/TiC_y(111) surfaces in comparison with O/TiC(111). For the FCC hollow binding site, we have performed calculations of coverage with atomic oxygen ranging from 1/9 to a complete monolayer. Table 11.2 offers calculated parameters of atomic structures for all coverage values of $\Theta = 0.11, 0.22, 0.33, 0.44, 0.55$, and 1.0, including vertical distances d_0, d_1, and d_2, pointed in Table 11.1, adsorption energy E_{ads}, the effective charge on the oxygen atom and the nearest Ti and C atoms. It also contains some known findings correlating with the data of these DFT calculations.

Analysis of Table 11.2 allows one to observe a considerable rearrangement in the local atomic structure of O/TiC(111) surface depending upon the degree of its coverage with atomic oxygen. In particular, the distance between adsorbate and (111) surface decreases with the increase of its coverage with oxygen. Atomic structure reconstruction may be caused by charge transfer from Ti atoms to C atoms, resulting in stronger electrostatic interaction between Ti and C atoms. Changes in the d_1 and d_2 distances in various atomic configurations of the O/TiC (111) surface depending on its coverage with oxygen are of specific interest. Calculation results in Table 11.2 demonstrate that the increase of oxygen coverage is followed by an increase of the distance between the layers of Ti and C atoms in the surface layers to d_1 = 1.314 Å with a simultaneous decrease of the distance d_2 = 1.244 Å (at $\Theta = 1.0$).

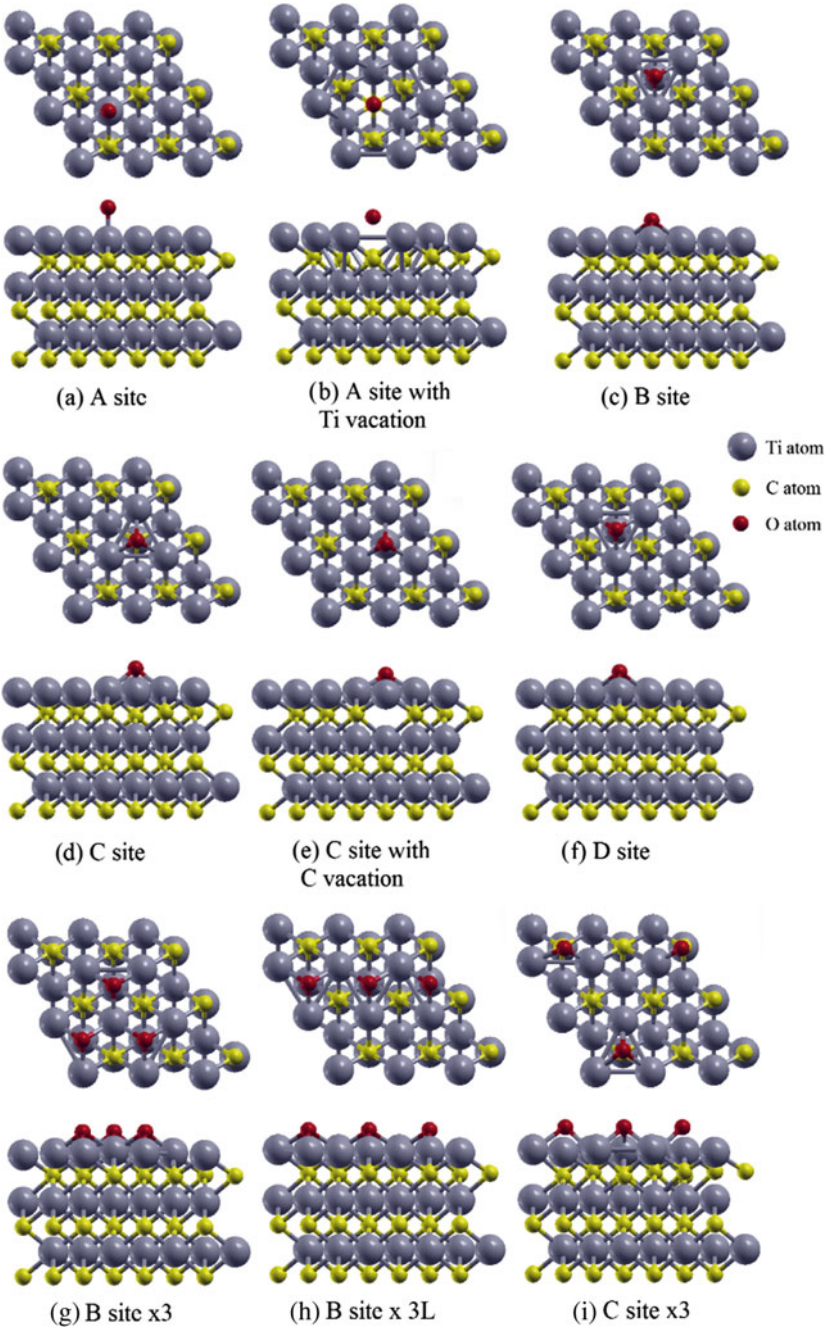

Fig. 11.2 Supercells of the atomic structure surface (**a**, **c**, **d**, **f**) in the O/TiC(111) system, **b**, **e** the O/Ti_xC_y(111) system, and **g**–**i** the 3-O/TiC(111) system after relaxation (side and top views)

Table 11.1 Bond lengths d_{Ti-O} and d_{Ti-C}, vertical distance d_O between the oxygen atom and TiC (111) surface, distances d_1 and d_2 between layers of Ti and C atoms in three surface layers, total energy E_{tot} of the surface with oxygen, total energy E_{ref} of the original surface

Phase (O-atom position)	d_{Ti-O} (Å)	d_{Ti-C} (Å)	d_O (Å)	d_1 (Å)	d_2 (Å)	E_{tot}	E_{ref}
						Ry	
TiC(111)	–	–	–	1.041 1.010 [11] 0.87 [24]	1.354 1.388 [11]	–	−3456.5663
O/TiC (A)	1.71	2.09	1.709	1.037	1.356	−3488.7557	−3456.5663
O/TiC (B)	1.97	2.06	1.105	1.069	1.349	−3488.9248	−3456.5663
O/TiC (C)	2.01	2.09	1.214	1.065	1.347	−3488.8641	−3456.5663
O/TiC (D)	1.97	2.06	1.105	1.069	1.347	−3488.9249	−3456.5663
O/TiC(A–Ti_{vac})	3.13	1.99	1.057	1.053	1.346	−3371.6716	−3339.7200
O/TiC(C–C_{vac})	1.94	2.12	0.971	1.064	1.344	−3477.3891	−3445.0028

Table 11.2 Distance d_O between oxygen atoms and TiC(111) surface, distances d_1 and d_2 between the layers of Ti and C atoms in three surface layers, adsorption energy E_{ads}, effective charge on the oxygen atom and nearest Ti and C atoms in the B position (FCC site) at various coverage degrees

Degree of oxygen coverage	d_O (Å)	d_1 (Å)	d_2 (Å)	E_{ads} (eV/atom)	Effective charge		
					Ti	C	O
0.11	1.105	1.069	1.349	−10.68	1.05 1.34 [11]	−1.09 −1.68 [11]	−0.78 −1.17 [11]
0.22	1.089	1.097	1.338	−10.60	1.06	−1.11	−0.78
0.33	1.072	1.119	1.329	−10.47	1.07	−1.07	−0.78
0.44	1.055	1.147	1.319	−10.42	1.09	−1.10	−0.77
0.55	1.028	1.172	1.311	−10.34	1.23	−1.12	−0.76
1.0	0.894 0.891 [11]	1.314 1.314 [11]	1.244 1.253 [11]	−9.93 −8.12 [11]	1.42	−1.13	−0.73

We should note that coverage increase from $\Theta = 0.11$ to $\Theta = 1.0$ insignificantly affects the adsorption energy value. The highest adsorption energy was found at the coverage degree of $\Theta = 0.11$ reaching $E_{ads} = -10.68$ eV/atom. In that position the effective charge accumulated by the O atom was −0.78e, titanium atom +1.05e, carbon atoms −1.09e. The adsorption energy at the coverage degree of $\Theta = 1.0$ reached $E_{ads} = -9.93$ eV/atom, which is 1.2 times higher than the data in [11].

11.3.2 Electron Structure of Oxygen-Adsorbed $Ti_xC_y(111)$ Surfaces

The noted rearrangement of local atomic structure significantly affects the electronic energy spectrum of titanium, carbon and oxygen surface atoms in the $O/Ti_xC_y(111)$ systems examined above. Calculation of the band structure of these systems, demonstrated in Fig. 11.3, reveals dependence upon the local atomic structure, and corresponds to the metallic type. Total and partial densities of electron states, also shown in Fig. 11.3, characterize the peculiarities of chemical bond with adsorbed oxygen atom on (111) TiC surface. We should note hybridization occurring between 2*p* orbitals of oxygen and carbon atoms and 3*d* orbitals of titanium atoms. It is indicated by matching of the energy peaks of occupied states in O, C, and Ti atoms (Fig. 11.3).

Several features should be noted in the band spectrum of non-stoichiometric $O/Ti_xC(111)$ configuration in position A shown in Fig. 11.3a. In particular, the hybridization of oxygen 2*p* orbitals with titanium 3*d* orbitals results in the formation of a broad +(1.9–2.3) eV peak of unoccupied electronic states in O/Ti_xC (111). The +0.07 eV peak of the total density of states (Fig. 11.3a) is formed predominantly by unsaturated bonds of oxygen, carbon and titanium surface atoms of the $O/Ti_xC_y(111)$ system. The peak at the Fermi level is mainly formed by contributions from 3*d* states of the surface Ti atoms with a small contribution of 2*p* states of carbon and oxygen atoms. The peak of total DOS is present in all

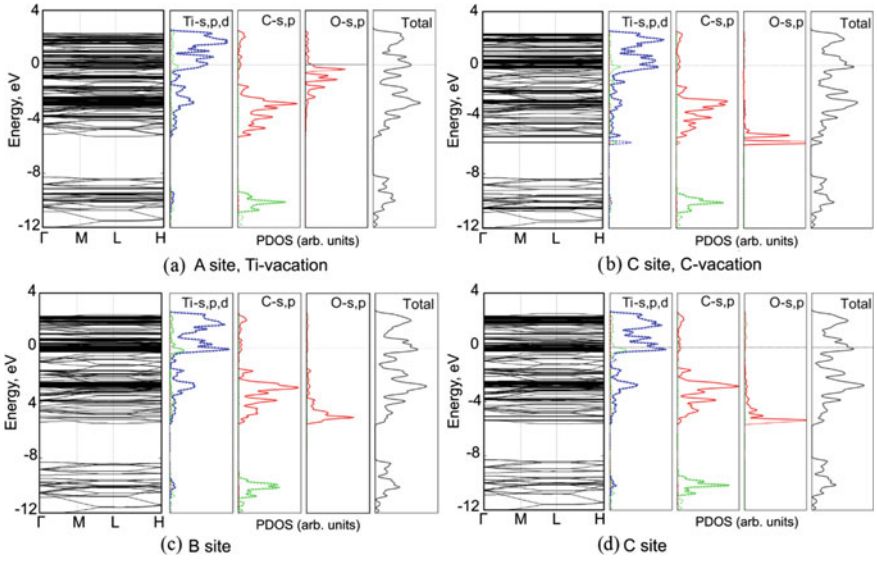

Fig. 11.3 DFT calculation of the band spectrum, partial DOS for Ti, C and O atoms, and total DOS in the binding sites on (111) surface: **a**, **b** O/Ti_xC_y, **c** O/TiC (FCC site), **d** O/TiC (HCP site); partial DOS: s—green, p—red, d—blue, total DOS—black

surface configurations of TiC(111) with and without adsorbate, which have been studied. Bonding states are associated with a strong covalent interaction, characterized by hybridization of Ti_{3d}–$C_{2}p$ atomic orbitals in the −2.5 to −3.8 eV energy interval, and defining the main properties of adsorbing titanium carbide surface. Modification of local atomic structure induced by non-stoichiometry and atomic oxygen adsorption results in a change of the electronic structure. In particular, the electron spectrum is characterized by Ti_{3d}–C_{2p}–O_{2p} hybridization in the energy intervals of 0 to −0.7 eV and −1.5 to −2.3 eV, which is manifested in the band structure and partial DOS in Fig. 11.3a. Statistical weight of partial states should be noted for the electrons participating in hybridization of Ti_{3d}–C_{2p}–O_{2p} orbitals. Analysis of Fig. 11.3a shows that the overlapping regions between 2*p* orbitals of atomic oxygen and Ti_{3d} and C_{2p}-orbitals are insignificant, in agreement with low value of the O atom adsorption energy (−5.14 eV/atom). The latter should be related to the absence of partial states of oxygen in the −2.5 to −3.8 eV energy region, representing the main part of occupied partial states of Ti and C atoms. Comparison of the electronic structure of this atomic configuration with the stoichiometric system O/TiC(111) reveals a different picture. In particular, the overlapping regions between 2*p*-orbitals of atomic oxygen and Ti_{3d} and C_{2p}-orbitals are significant, in agreement with higher value of the O atom adsorption energy in the Ti-top position.

Electronic structure has some new features in case of non-stoichiometric O/TiC_y(111), where O atom takes up the position above the C atom vacancy in the second layer of the slab (Fig. 11.3b). In that configuration bond length amounts d_{O-Ti} = 1.94 Å, which determines a strong chemical bonding between the O atoms and their nearest Ti neighbors. In particular, the energy of chemical bond of O atom on TiC_y(111) surface amounts E_{coh} = 5.7 eV. We refer the estimation of bond energy E_{coh} with the positions of two sharp peaks corresponding to the O_{2p} states in the −5.1 and −5.7 eV interval of energies (Fig. 11.3b). The main part of partial DOS of C and Ti atoms lies in the −1.9 to −3.7 eV interval of energies; it characterize the main properties of the O/TiC_y(111) system. This energy region is represent by a wide band of partial densities of states of Ti and C. The −4.5 to −5.7 eV interval of energies presents mixing between partial states of O, C, and Ti electrons, which plays major role in formation of the corresponding bond and determines the adsorption energy. The maximum value of the adsorption energy of O atom on non-stoichiometric TiC_y(111) surface amounts E_{ads} = −11.06 eV/atom. The increase of the E_{ads} in this configuration correlates with the existence of flat bands (−5.1 and −5.7 eV) in the band structure and is responsible for the double peaks reflecting the O_{2p} electron states.

We should note that a similar correlation was found in stoichiometric O/TiC (111) system with the O atom in B and C positions (Fig. 11.2c, d). In particular, Fig. 11.3c presents two flat bands in the band structure within the −4.6 to −5.0 eV interval of energies responsible for the partial densities of O_{2p} electrons. In the electronic band structure of the atomic configuration (Fig. 11.2c), these flat bands are located almost in the same energy interval as in the previous configuration (Fig. 11.2e). Hence the adsorption energy of atomic oxygen in that configuration is

high (−10.68 eV/atom). The main feature of the stoichiometric O/TiC(111) electronic structure in position C (Fig. 11.2d) is the correlation similar to the one described above. The band spectrum (Fig. 11.3d) of this configuration features three flat bands with the energy of −4.9, −5.1, and −5.3 eV corresponding to sharp peaks of partial densities of O and C_{2p} electrons. These peaks represent hybridization of C_{2p}–O_{2p} orbitals, with partial mixing of Ti_{3d} orbitals. The main part of partial DOS of C and Ti atoms is into −2.1 to −4.9 eV energy interval. This energy interval reveals hybridization between C_{2p}–Ti_{3d} orbitals of C and Ti atoms. The −2.1 to −4.9 eV interval of energies presents a small mixing of partial states of O, C, and Ti electrons, which is caused by adsorption. Average value of the bond energy for O atom in position C is E_{coh} = 5.2 eV, correlating with high adsorption energy (−9.85 eV/atom).

Figure 11.4a–c demonstrate typical peculiarities of the electron structure of a O/TiC(111) system, where three O atoms occupy position B (or C), forming triangular and trimeric clusters on the surface (see Fig. 11.2g–i). In particular, bond length in the triangular configuration is d_{O-Ti} = 1.96 Å; the fact determines a tight chemical bond between the atoms of oxygen and their nearest titanium neighbors. Among other factors, the chemical bond energy of oxygen atom on TiC(111) surface is E_{coh} = 5.2 eV. We associate the estimate of bond energy E_{coh} with the position of main peak reflecting the states of oxygen 2*p* electrons in the −5.2 eV energy region (Fig. 11.4a).

The main part of partial DOS of carbon and titanium atoms is into −1.5 to −3.3 eV interval of energies; it determines the basic properties of the 3-O/TiC(111) system. The energy of −2.8 eV exhibits hybridization between C_{2p}–Ti_{3d} orbitals. Mixing between partial states of O, C, and Ti electrons into −3.5 to 5.4 eV interval of energies plays a decisive role in forming of the corresponding chemical bond and adsorption energy. A comparison was performed between the electron spectrum of total oxygen DOS in triangular configuration with a similar spectrum in the configuration with a single oxygen atom (Fig. 11.3c) in the same binding site. Analysis has shown that the rearrangement in the atomic structure of 3-O/TiC(111) surface noted above is manifested in a change in the electron energy spectrum of the system. In particular, the maximum positions and the shape of peaks for the energies of −1.8, −2.8, and −5.2 eV indicate strengthening of the chemical bond between carbon, titanium, and oxygen atoms. The shift in the energy is $\Delta E = 0.1-0.6$ eV.

In the trimeric configuration (Fig. 11.2h) average length of the bond between oxygen atom and its nine nearest neighbors is d_{O-Ti} = 1.98 Å. The energy of the hybridized ground state of C_{2p}–Ti_{3d} electrons is −2.6 eV, which is 0.2 eV higher than in triangular configuration in the same FCC position. In our opinion, position of the major peak of oxygen 2*p* electrons in the −(4.0–5.0) eV interval of energies shown in Fig. 11.4b determines the character and intensity of chemical bond between the oxygen atoms and TiC(111) film surface. In this configuration, the Ti–O chemical bond is largely ionic, as indicated by the shape of the electron energy spectrum in Fig. 11.4b. In a triangular cluster (Fig. 11.2i), formed by oxygen atoms on TiC(111) surface in HCP positions, the average length of the bond between the

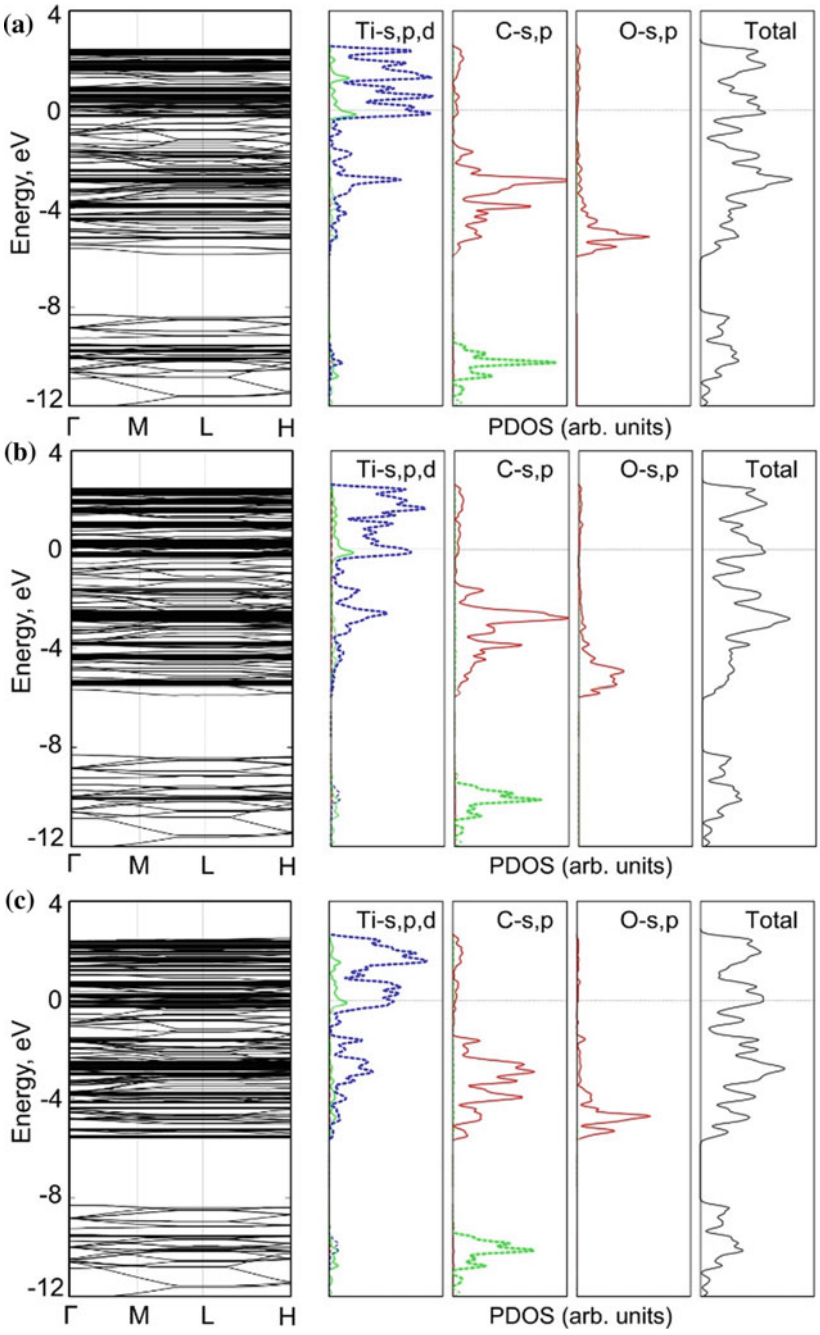

Fig. 11.4 DFT calculations of the band spectrum, partial DOS for Ti, C and O atoms, and total DOS on (111) surface: **a** 3-O/TiC (triangle, FCC site), **b** 3-O/TiC (trimer, FCC site), **c** 3-O/TiC (triangle, HCP site); partial DOS: s—green, p—red, d—blue, total DOS—black

oxygen atom and its nine nearest neighbors is d_{O-Ti} = 2.02 Å. Energies of the hybridized ground state of C_{2p}–Ti_{3d} electrons in this atomic structure configuration and in the configuration in Fig. 11.2g appear to be identical. However, in this configuration (Fig. 11.2i) the Ti–O chemical bond is largely covalent, as indicated by the shape of the electron energy spectrum in Fig. 11.4c. The electron energy spectrum contains three maxima in the −(3.5–5.6) eV interval of energies of the total DOS curve, which in our opinion determine the character and intensity of the chemical bond between the oxygen cluster and TiC(111) film surface.

11.3.3 Elastic Properties of the O/Ti_xC_y(111) Surface

In the present work we have shown that adsorption of atomic O on the non-ideal Ti_xC_y(111) surfaces in different binding positions results in considerable change of the local atomic structure and the band structure as well as total energy of the O/Ti_xC_y(111) systems. Analysis of Tables 11.1 and 11.2 additionally shows that the bond length d_{Ti-C} in 2D lattice of Ti_xC_y(111) demonstrates dependence upon the position of oxygen on the surface under study. It can be assumed that by variation of the bond length d_{Ti-C} we can control elastic properties of the O/Ti_xC_y(111) and O/TiC(111) systems. In this section we employed DFT total energy calculations of deformed structures and Elastic software [22] in order to study the elastic properties of reconstructed TiC(111) surfaces. We have calculated elastic moduli: bulk modulus B, Young's modulus E, shear modulus G, and Poisson ratio υ, which are essential properties of mechanical and dynamic characteristics of crystals [2]. First of all, we calculated elastic constants c_{11}, c_{12}, and c_{44}, which were used to calculate elastic moduli. The latter satisfies the conditions of mechanical stability for cubic systems in accordance with [23]:

$$c_{11} > 0, \quad c_{44} > 0, \quad c_{11} - c_{12} > 0, \quad c_{11} + 2c_{12} > 0. \tag{11.2}$$

Elastic constants for the reconstructed TiC surfaces under study are present in Table 11.3. For comparison we also provide elastic constants for an ultrathin 2D TiC(111) slab and a 3D TiC crystal.

The first column of Table 11.3 contains atomic configurations ordered from the top down depending on the length d_{Ti-C} of the Ti–C bond provided in the second column. For calculation of elastic constants, we used the parameters of a simulated unit cell (column 3) equal to doubled length d_{Ti-C} of the Ti–C bond in the atomic configurations under consideration. For the bond length d_{Ti-C}, we used its value between three top Ti and C layers. In order to find the average bond length d_{Ti-C}, we used 40 pairs of Ti and C atoms. Calculated elastic constants c_{11}, c_{12}, and c_{44} characterize the entire reconstructed top layer (comprising three monolayers, i.e. two Ti monolayers and one C monolayer) of ultrathin TiC(111) band with atomic oxygen coverage of 0.11 ML. These elastic constants were used to calculate the

Table 11.3 Average bond length, d_{Ti-C} (Å); lattice parameter a (Å); elastic constants c_{11}, c_{12}, c_{44} (GPa); elastic moduli B, G, E (GPa); Poisson's ratio υ for the top layer in various atomic configurations of the O/Ti_xC_y(111), O/TiC(111), 2D TiC(111), 2D TiC(001) systems, and in a TiC crystal

Site	d_{Ti-C} (Å)	a (Å)	C_{11}	C_{12}	$C_{11}-C_{12}$	C_{44}	B	G	E	υ
			GPa							
O/TiC(A)	2.150	4.300	593.7	122.3	471.4	193.5	279.4	209.4	502.6	0.20
O/TiC(B)	2.153	4.306	564.4	120.4	444.0	187.9	268.4	200.8	482.3	0.20
O/TiC(C)	2.152	4.304	567.9	120.6	447.3	188.5	267.7	201.9	484.7	0.20
O/TiC(D)	2.152	4.304	567.9	120.6	447.3	188.5	267.7	201.9	484.7	0.20
O/Ti_xC(A, Ti_{vak})	2.142	4.284	605.5	122.6	472.9	195.5	283.5	212.8	510.56	0.20
O/TiC_x(C, C_{vak})	2.150	4.300	575.6	120.9	454.7	189.9	272.5	204.1	489.9	0.20
2D TiC(111)	2.139	4.278	615.8	123.4	482.4	197.5	287.5	215.8	520.2	0.20
2D TiC(001) [15]	2.155	4.310	557.4	119.8	437.7	186.5	265.65	198.82	477.38	0.20
3D TiC(theory)	2.165	4.330	522.2	117.8	404.4	179.9	252.56, 251.4 [3]	188.51, 205.7 [3]	452.65, 481.4 [3]	0.20, 0.181 [3]
3D TiC(test)	2.165	4.33 [23]	500 [25]	113 [25]	387 [25]	178.3 [25]	242.0 [25]	182 [25]	437 [26]	0.199 [26]

bulk modulus B, Young's modulus E, shear modulus G, and Poisson's ratio υ, summarized in Table 11.3.

Analysis of the data in Table 11.3 allows one to note some peculiarities. In particular, elastic constants c_{11}, c_{12}, c_{44}, bulk modulus B, Young's modulus E, shear modulus G, decrease with the increase of the bond length $d_{\mathrm{Ti-C}}$ between Ti and C atoms. Dependence of elastic constants and elastic moduli upon the length $d_{\mathrm{Ti-C}}$ of the bond between Ti and C atoms is illustrated in Fig. 11.5. The largest change is exhibited by the elastic constant c_{11} and Young's modulus E, the smallest change is typical of the c_{12} elastic constant (see Fig. 11.5a). Poisson's ratio υ does not change for these atomic configurations, remaining at $\upsilon = 0.20$ and matching the υ coefficient value for ultrathin 2D TiC(111) band and a 3D TiC crystal.

In our opinion, the elastic constants and elastic moduli in Table 11.3 can characterize elastic properties of the surface, affected by laser radiation. It is appropriate to summarize the potential physical mechanisms of nanostructuring, based on the previous results. Let us consider the pristine 3D TiC crystal, characterized by the lattice parameter $a = 4.330$ Å, which corresponds to the Ti–C bond length $d_{\mathrm{Ti-C}} = 2.165$ Å. This bond length is characteristic of the equilibrium crystal structure of 3D TiC, which we accept as the reference for the $d_{\mathrm{Ti-C}}$ bond length values. Left part contains atomic configurations, corresponding to smaller bond lengths and higher values of the elastic moduli (see Fig. 11.5b). Total energy of Ti-terminated stoichiometric 2D TiC(111) is −3456.5663 Ry after relaxation.

The state corresponds to the smallest bond length $d_{\mathrm{Ti-C}} = 2.139$ Å and to maximum values of elastic moduli (see Table 11.3). The results of our similar calculation for TiC (001) surface are also provided here. A comparison was performed between the values of elastic moduli B, G, and E for (111) and (001) stoichiometric 2D TiC surfaces. Analysis has shown that elastic moduli B, G, and E of Ti-terminated (111) surface exceed the corresponding moduli for (001) surface by 21.85, 16.98, and 42.82 GPa, respectively.

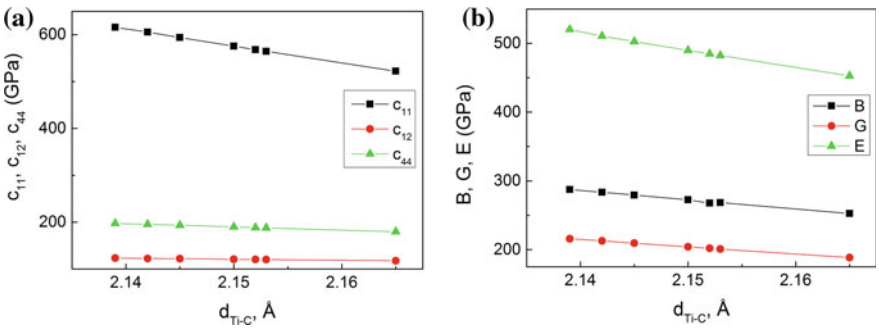

Fig. 11.5 Dependence of elastic constants (**a**) and elastic moduli (**b**) upon the length of the Ti–C bond in atomic configurations of O/Ti_xC_y(111), O/TiC(111), TiC(111) systems, and in a TiC crystal

The processes of titanium carbide nanostructuring with laser in the air may involve different mechanisms of surface reconstruction forming new material properties. Submicrometer structures are known [27] to appear on the surface in two cases—in the mode below the ablation threshold when melt is present in the affected area, and in the ablation mode, characterized by removal of surface fragments. This paper is devoted to the first case, which is typically characterized by the presence of a molten pool. According to the theoretical findings of [28], carbon atoms evaporate several times faster than titanium atoms. Therefore, carbon atoms will be ejected from the molten pool more often than titanium atoms. In our view, crystallization of TiC(111) surface may result in vacancies, which can appear both in the carbon and the titanium sublattices. The number of carbon vacancies at that must be higher than the number of titanium vacancies. In this connection, the following mechanism of surface reconstruction appears to be most probable (*first mechanism*): carbon atoms may be "ejected" from the surface melt layer creating a vacancy in the second layer from the (111) surface top. An oxygen atom may take up a position above such vacancy (see Fig. 11.2e). As DFT calculation has demonstrated, the process is accompanied with a decrease of the Ti–C bond length to $d_{\mathrm{Ti-C}}$ = 2.150 Å for surface atoms. According to Fig. 11.5b, this bond length value corresponds to higher values of elastic moduli relatively to a titanium carbide crystal. The increase in the values of elastic moduli for the O/TiC_y(001) configuration reaches 8% compared with a 3D TiC crystal. The effect can be viewed as a nanostructuring process. In that case total energy of the calculated cell in the O/TiC_y(001) system decreases to −3477.3891 Ry, indicating preference of this process in terms of energy. It should also be noted that the adsorption energy for atomic oxygen in this configuration has maximum value (−11.06 eV/atom) among the examined reconstructions. In particular, the chemical bond energy of the oxygen atom in the O/TiC_y(001) atomic configuration is E_{coh} = 5.7 eV, indicating the presence of a tight chemical bond.

Second mechanism: during laser evaporation of a surface titanium atom one can observe a reconstruction of the local O/Ti_xC(111) atomic structure, where the oxygen atom occupies the position above the titanium vacancy of the first layer (see Fig. 11.2b). In that configuration the averaged length of the Ti–C bond reached $d_{\mathrm{Ti-C}}$ = 2.142 Å for surface atoms. The increase in the values of elastic moduli for the O/Ti_xC(111) configuration is over 12% relatively to a 3D TiC crystal. The effect can also be viewed as a nanostructuring process. In this case, total energy of the calculated cell for a O/Ti_xC(111) system increases to −3371.6716 Ry, as determined by nonstoichiometry following from the loss of the titanium atom during laser evaporation. In this configuration the adsorption energy of atomic oxygen turned out to be minimal (−5.14 eV/atom) in the O/TiC(111) system. In particular, the chemical bond energy of the oxygen atom in the O/Ti_xC(111) atomic configuration is E_{coh} = 2.3 eV, indicating the presence of a chemical bond.

Third mechanism: an oxygen atom has accidentally appeared in a position above carbon atom (HCP hollow) in the second (111) surface layer. The bond length $d_{\mathrm{Ti-O}}$ is 2.01 Å. That atomic configuration (Fig. 11.2d) is characterized by an averaged length of the Ti–C bond of $d_{\mathrm{Ti-C}}$ = 2.09 Å for surface atoms. The increase in the

values of elastic moduli for the O/TiC(111) configuration is over 6%, which can be considered as a nanostructuring effect. Total energy of the O/TiC(111) system is −3488.8641 Ry. The oxygen atom adsorption energy in this configuration is E_{ads} = −9.85 eV/atom.

Fourth mechanism: an oxygen atom, which has accidentally appeared in a bridge binding site (see Fig. 11.2f), forms a sufficiently stable atomic configuration. The length of the bridge forming bond is d_{O-Ti} = 1.97 Å. The energy of the oxygen atom adsorption on TiC(001) surface in the bridge binding site is E_{ads} = −10.68 eV/atom. That configuration is characterized by an averaged length of the Ti–C bond of d_{Ti-C} = 2.06 Å for surface atoms. The increase in the values of elastic moduli for the O/TiC(111) configuration reaches 6%. Total energy of the O/TiC(111) system is −3488.9249 Ry.

Fifth mechanism: an oxygen atom, which has appeared in a position above a titanium atom, forms a TiO_x oxide with the bond length d_{Ti-O} = 1.71 Å. At such distance chemisorption processes can occur and result in creation of a TiO_x compound, as confirmed in [28]. That configuration is characterized by an averaged length of the Ti–C bond d_{Ti-C} = 2.15 Å for surface atoms, and an increase in the values of elastic moduli by over 10%. Total energy of the O/TiC(111) system in this configuration is −3488.7557 Ry.

11.4 Conclusion

In the present work the ab initio calculations based on the density functional theory were performed and the Lagrangian elasticity theory (within the framework of ElaStic) was applied in order to study the local atomic structure, thermodynamic, electronic, and elastic properties of non-stoichiometric O/Ti_xC_y(111) systems in different surface reconstructions. Nine possible reconstructions of TiC surface were considered. The reconstructions were simulated by placement of atomic oxygen on the surface, simulating potential laser reconstructions of the surface.

It has been demonstrated that adsorption of atomic oxygen upon nonideal Ti_xC_y(001) surfaces in different binding positions results in considerable reordering of the local atomic structure and the band spectrum. The rearrangement determines the total energy of generated configurations. For the first time a correlation between the energy level of flat bands in the −5.1 and −5.7 eV energy regions was established, responsible for the double singular peaks of partial densities of oxygen 2*p* electrons, and the bond energy E_{coh} of O atom in non-stoichiometric O/TiC_y(111) systems. In this configuration, the main part of partial DOS of C and Ti atoms is in the −1.9 to −3.7 eV interval of energies. This feature determines the basic properties of the O/TiC_y(111) system. The −4.5 to −5.7 eV interval of energies shows mixing between partial states of O, C, and Ti electrons, which plays a decisive role in forming of the corresponding chemical bond and adsorption energy. The revealed correlation plays an important role in the understanding of the chemical bond character and oxygen atom adsorption onto a non-stoichiometric

TiC(111) surface. DFT-based calculations established a considerable rearrangement in the local atomic structure of O/TiC(111) surface depending upon the degree of its coverage with atomic oxygen. We have demonstrated that the distance between adsorbate and TiC(111) surface decreases with the increase of coverage with oxygen. In our view, atomic structure reconstruction may be caused by charge transfer from Ti atoms to C atoms, resulting in stronger electrostatic interaction between Ti and C atoms.

In the present work, the effective charges of Ti and C atoms surrounding the oxygen adatom in different reconstructions have been identified. Based on DFT calculations, the charge transfer from Ti to O and C atoms have been established, which is caused, in our opinion, by the reconstruction of atomic and electronic structures; it correlates with the electronegativity of the studied atoms. Investigation of the chemisorption processes is of the greatest interest in case of non-stoichiometric $TiC_y(001)$ with the oxygen atom located above the carbon atom vacancy in the second layer. Relaxation results in oxygen atom substitution in the bridge site to formation of the bond length d_{O-Ti} = 1.94 Å. The oxygen atom in that position accumulates a considerable effective charge of −0.79e. The nearest titanium and carbon atoms accumulate effective charges of +0.92 and −1.12e, respectively. This configuration corresponds to the largest adsorption energy value of E_{ads} = −11.06 eV/atom, which in our opinion is determined by the change in the local atomic structure.

The bond lengths have been established for 40 pairs of Ti and C atoms of three upper layers in six examined O/TiC(111) configurations. We have checked the hypothesis suggesting a relation between elastic moduli and the length of the bond between titanium and carbon atoms, as well as its applicability in order to evaluate elastic properties of a reconstructed top layer of $O/Ti_xC_y(111)$ surface depending upon the position of atomic oxygen thereon. Potential mechanisms for laser nanostructuring of titanium carbide surface have been suggested.

References

1. X. Yuan, L. Cheng, L. Zhang, J. Alloy Compd. **622**, 282 (2015)
2. J. Xiao, B. Jiang, K. Huang, H. Zhu, Comput. Mater. Sci. **88**, 86 (2014)
3. J. Kim, S. Kang, J. Alloy Compd. **528**, 20 (2012)
4. L.S. Marques, A. Fernandes, F. Vaz, M. Ramos, Plasma Processes Polym. **4**, S195 (2007)
5. L. Wang, L.-H. Fang, J.-H. Gong, Trans. Nonferrous Metals Soc. China **22**, 170 (2012)
6. H. Ye, G. Chen, Y. Zhu, S.-H. Wei, Phys. Rev. B **77**, 033302 (2008)
7. C.I. Mikoluzhkii, V.Y. Homich, V.A. Shmakov, V.Y. Yamshikov, Russia Nanotechnol. **11/12**, 65 (2011) (in Russian)
8. V.V. Ilyasov, D.K. Pham, Vestnik of DSTU **14**, 72 (2014). (In Russian)
9. S. Zaima, Y. Shibata, H. Adachi, C. Oshima, S. Otani, M. Aono, Y. Ishizawa, Surf. Sci. **157**, 380 (1985)
10. K.E. Tan, M.W. Finnis, A.P. Horsfield, A.P. Sutton, Surf. Sci. **348**, 49 (1996)
11. C. Ruberto, B.I. Lundqvist, Phys. Rev. B **75**, 235438 (2007)
12. R. Souda, C. Oshima, S. Otani, Y. Ishizawa, M. Aono, Surf. Sci. **199**, 154 (1988)

13. K. Edamoto, A. Mochida, T. Anazawa, T. Itakura, E. Miyazaki, H. Kato, S. Otani, Phys. Rev. B **46**, 7127 (1992)
14. J. Ahn, H. Kawanowa, R. Souda, Surf. Sci. **429**, 338 (1999)
15. V.V. Ilyasov, K.D. Pham, O.M. Holodova, I.V. Ershov, Appl. Surf. Sci. **351**, 433 (2015)
16. P. Giannozzi, S. Baroni, N. Bonini, M. Calandra, R. Car, C. Cavazzoni, D. Ceresoli, G.L. Chiarotti, M. Cococcioni, I. Dabo, J. Phys. Condens. Matter **21**, 395502 (2009)
17. J.P. Perdew, K. Burke, M. Ernzerhof, Phys. Rev. Lett. **77**, 3865 (1996)
18. J.P. Perdew, A. Ruzsinszky, G.I. Csonka, O.A. Vydrov, G.E. Scuseria, L.A. Constantin, X. Zhou, K. Burke, Phys. Rev. Lett. **100**, 136406 (2008)
19. V.V. Ilyasov, D.K. Pham, O.M. Kholodova, Order. Miner. Alloys **1**, 131 (2014)
20. N. Troullier, J.L. Martins, Phys. Rev. B **43**, 1993 (1991)
21. P.-O. Löwdin, *Advances in Quantum Chemistry*, ed. by L. Per-Olov (Academic Press, London, 1970), p. 185
22. R. Golesorkhtabar, P. Pavone, J. Spitaler, P. Puschnig, C. Draxl, ElaStic. Comput. Phys. Commun. **184**, 1861 (2013)
23. Y. Li, Y. Gao, B. Xiao, T. Min, Z. Fan, S. Ma, L. Xu, J. Alloy Compd. **502**, 28 (2010)
24. Y. Liu, Y. Jiang, R. Zhou, J. Feng, J. Alloy Compd. **582**, 500 (2014)
25. J. Holliday, *Advances in X-Ray Analysiss*, vol. 13. (Plenum Press, New York, 1970), p. 136
26. E. Francisco, M. Blanco, G. Sanjurjo, Phys. Rev. B **63**, 094107 (2001)
27. I.N. Zavestovskaya, Quantum Electron. **40**, 942 (2010)
28. J.A. Rodriguez, P. Liu, J. Dvorak, T. Jirsak, J. Gomes, Y. Takahashi, K. Nakamura, J. Chem. Phys. **121**, 465 (2004)

Chapter 12
Density Matrix Method in Atom Theory

Boris V. Bondarev

Abstract In this work, we apply a new variational principle that allows us to find the distribution function of electron in an arbitrary atom. This principle is based on the method of density matrix. Using the density matrix, we found the energy of the electrons in an atom, entropy and thermodynamic potential. The main idea of this article is that all two-electron matrices must be anti-symmetric. This refers to the two-electron Hamiltonian. This applies to Slater two-particle wave function. We found the equation for the distribution function of electrons at the quantum orbits. This equation can be obtained in two cases. In the first case, based on the density matrix of the first order, this equation is obtained only for the distribution function. In the second case two equations are obtained, which include distribution function and correlation function. The distribution function of electrons in the atom is similar to the function of Fermi–Dirac for electrons in a solid. In this work we apply a new approach to calculate the energy levels of electron in an arbitrary atom. This approach is also based on the method of density matrix.

12.1 Introduction

The density matrix is the most general description of the system in quantum mechanics. The state of the system, described by a density matrix, is called mixed. In a particular case, the density matrix can be proportional to the product of two wave functions. In this case the system state is called pure.

The concept of the density matrix was first defined in [1]. Currently, the density matrix is discussed in the books [2, 3] and original papers [4–13]. In [14–20], we apply the calculation method of the energy spectrum of an arbitrary atom, which is called the method of Hartree–Fock. Based on the variational principle, this method uses different combinations of one-electron wave functions that take into account their anti-symmetry. This provides the electrons to be fermions.

B. V. Bondarev (✉)
Moscow Aviation Institute, Volokolamskoye Shosse, 4, Moscow 125871, Russia
e-mail: bondarev.b@mail.ru

I. A. Parinov et al. (eds.), *Advanced Materials*, Springer Proceedings in Physics 207, https://doi.org/10.1007/978-3-319-78919-4_12

Here we apply the method of density matrix to obtain the equation for the distribution of electrons in an arbitrary atom and the stationary Schrodinger equation, in which the Hamiltonian is chosen in a special way. The solution of this equation allows us to find the energy levels of electrons in the atom.

12.2 Statistical Operators

System of identical particles in quantum mechanics is characterized by a hierarchical sequence of statistical operators $\hat{\varrho}^{(1)}, \hat{\varrho}^{(2)}, \hat{\varrho}^{(3)}, \ldots$

We will only need the first two operators of this sequence: $\hat{\varrho}^{(1)}$ and $\hat{\varrho}^{(2)}$. Let q_1 and q_2 be the quantum coordinates that define the state of the two particle of the system. The first of these operators $\hat{\varrho}^{(1)}$ depends only on one of these numbers:

$$\hat{\varrho}^{(1)} = \hat{\varrho}^{(1)}(q). \tag{12.1}$$

Statistical operator $\hat{\varrho}^{(2)}$ depends on these two numbers:

$$\hat{\varrho}^{(2)} = \hat{\varrho}^{(2)}(q_1, q_2). \tag{12.2}$$

Electrons are identical particles. A consequence of the in distinguish ability of the two electrons is the symmetry of the operator $\hat{\varrho}^{(2)}$, i.e.

$$\hat{\varrho}^{(2)}(q_1, q_2) = \hat{\varrho}^{(2)}(q_2, q_1). \tag{12.3}$$

12.3 Density Matrix

The density matrix of any system in quantum mechanics has the form $\varrho_{\alpha\alpha'}$, where α and α' are the quantum numbers defining the state of one particle. The density matrix corresponds to the statistical operator $\hat{\varrho}^{(1)}$. This correspondence is defined by the formula:

$$\varrho_{\alpha\alpha'} = \int \varphi_{\alpha}^{*}(q)\hat{\varrho}^{(1)}(q)\varphi_{\alpha'}(q)dq, \tag{12.4}$$

where $\varphi_{\alpha}(q)$ is a wave function, satisfying the orthonormality condition:

$$\int \varphi_{\alpha}^{*}(q)\varphi_{\alpha'}(q)dq = \delta_{\alpha\alpha'}, \tag{12.5}$$

where $\delta_{\alpha\alpha'}$ is the symbol of Kronecker.

The meaning of the density matrix is that the diagonal elements $\varrho_{\alpha\alpha}$ of this matrix are equal to the probability $w_\alpha = \varrho_{\alpha\alpha}$ to find system in the state α. The probability w_α satisfies the normalization condition for the

$$\sum_\alpha w_\alpha = N, \tag{12.6}$$

here N is the number of particles in the system.

The two-particle operator $\hat{\varrho}^{(2)}$ corresponds to the density matrix $\varrho^{(2)}$:

$$\varrho^{(2)} = \varrho_{\alpha_1\alpha_2,\alpha_1'\alpha_2'}. \tag{12.7}$$

The density matrix in the abbreviated form can be written in any coordinates like this:

$$\varrho^{(1)} = \varrho_{11'}, \quad \varrho^{(2)} = \varrho_{12,1'2'}.$$

Since electrons are fermions, their two-particle density matrix must be anti-symmetric. This means that the equalities are true:

$$\varrho_{12,1'2'} = -\varrho_{21,1'2'} = -\varrho_{12,2'1'} = \varrho_{21,2'1'}. \tag{12.8}$$

The ratio of anti-symmetry can be fulfilled, if two-particle density matrix is approximately equal to

$$\varrho_{12,1'2'} = \varrho_{11'}\varrho_{22'} - \varrho_{12'}\varrho_{21'}. \tag{12.9}$$

One-electron density matrix is associated with two-electron matrix by the expression:

$$\sum_{\alpha_2} \varrho_{12,1'2} = (N-1)\varrho_{11'}. \tag{12.10}$$

Let us sum this expression on α_1. The condition (12.9) gives

$$\sum_{\alpha_1}\sum_{\alpha_2} \varrho_{12,12} = (N-1)\,N. \tag{12.11}$$

12.4 Equation for the Density Matrix of System of Fermions

In [13] we obtained the quantum kinetic equation for a system consisting of identical particles-fermions. This equation can be written as

$$i\hbar\dot{\hat{\varrho}} = \left[\widehat{H}\hat{\varrho}\right] + i\hbar\sum_k\sum_l C_{kl}\left\{\left[\hat{a}_k\hat{\varrho}, \hat{a}_l^+(1-\hat{\varrho})\right] + \left[(1-\hat{\varrho})\hat{a}_k, \hat{\varrho}\hat{a}_l^+\right]\right\}, \quad (12.12)$$

where $\hat{\varrho}$ is the statistical operator of one of the identical particles of the system, $\widehat{H}$ is the Hamiltonian of the system, C_{kl} are the undefined multipliers, $\hat{a}_k$ is the operator. The corresponding equation for the density matrix $\varrho_{\alpha\alpha'} = \varrho_{11'}$ will look as

$$\begin{aligned} i\hbar\dot{\varrho}_{11'} = &\sum_2 (H_{12}\varrho_{21'} - \varrho_{12}H_{21'}) \\ &+ i\hbar/2\sum_2\sum_3 (2\gamma_{12,31'}\varrho_{23} - \gamma_{23,12}\,\varrho_{31'} - \gamma_{31',23}\,\varrho_{12}) \\ &+ i\hbar/2\sum_2\sum_3\sum_4 [\varrho_{12}\varrho_{34}(\gamma_{43,21'} - \gamma_{21',43} - \gamma_{23,41'} + \gamma_{41',23}) \\ &+ \gamma_{12,34} - \gamma_{34,12} - \gamma_{14,32} + \gamma_{32,14})\varrho_{43}\varrho_{21'}], \end{aligned} \quad (12.13)$$

where H_{12} are the matrix elements of the Hamiltonian, and $\gamma_{12,34}$ is a matrix.

Substitute in this equation the diagonal formula:

$$\varrho_{\alpha\alpha'} = w_\alpha\delta_{\alpha\alpha'}, \quad (12.14)$$

where w_α is the probability to detect an electron with quantum state α, $\delta_{\alpha\alpha'}$ is the symbol of Kronecker. Considering the Hamiltonian to be also diagonal

$$H_{\alpha\alpha'} = \varepsilon_\alpha\delta_{\alpha\alpha'}, \quad (12.15)$$

where ε_α is the energy of a particle in a state α, we have the equation:

$$\dot{w}_\alpha = \sum_\beta \left[p_{\alpha\beta}(1-w_\alpha)w_\beta - p_{\beta\alpha}w_\alpha(1-w_\beta)\right]. \quad (12.16)$$

where

$$p_{\alpha\beta} = \gamma_{\alpha\beta,\beta\alpha} = (2\pi/\hbar)\sum_N\sum_M |v_{\alpha N,\beta M}|^2 W_M\delta(\varepsilon_\alpha - \varepsilon_\beta + E_N - E_M) \quad (12.17)$$

is the probability of transition of a system from the state β to the state α per unit of time,

$$W_N = v\,\exp(-\beta E_N) \quad (12.18)$$

is the probability that the medium surrounding the system is in the equilibrium state with quantum numbers N, and E_N is the energy in this state, v is the selection multiplier, $\beta = 1/(k_BT)$ is the inverse temperature; $v_{\alpha N,\beta M}$ are the matrix elements of the interaction of the system with its surroundings. Formula (12.17) is the Fermi Golden rule.

The probability of transition $p_{\alpha\beta}$ can always be represented in the form:

$$p_{\alpha\beta} = p_{\alpha\beta}^{(o)} \mathrm{e}^{-\beta\left(\varepsilon_\alpha - \varepsilon_\beta\right)/2}, \tag{12.19}$$

where

$$p_{\alpha\beta}^{(o)} = p_{\beta\alpha}^{(o)}.$$

The distribution function of electrons w_α can be found by solving (12.16). But there is another way to find this function. This way is the variational principle, which we apply in this work and which is valid only for equilibrium systems.

12.5 Energy of Electrons in Atom, Written with the Help of Statistical Operators

Let us use the expression for the electron energy of an arbitrary atom:

$$E = \int \widehat{H}^{(1)} dq + 1/2 \int \widehat{H}^{(2)} \hat{\varrho}^{(2)} dq_1\, dq_2, \tag{12.20}$$

where

$$\widehat{H}^{(1)} = -\hbar^2/(2\,m)\nabla^2 - Ze^2/r \tag{12.21}$$

is the Hamiltonian of the kinetic energy of the electron and the potential energy of its interaction with the nucleus, Z is the number of electrons in an atom,

$$\widehat{H}^{(2)} = e^2/r_{12} \tag{12.22}$$

is the Hamiltonian of the potential energy of interaction of two electrons, r_{12} is the distance between them.

12.6 Wave Function of One Electron Around Arbitrary Kernel

We introduce an orthonormal system of functions, which describe only one electron, moving around the nucleus:

$$\varphi_\alpha(q) \equiv \phi_s(\boldsymbol{r})\chi_\zeta(\sigma), \tag{12.23}$$

where $q = \{r, \sigma\}$, $\phi_s(\mathbf{r})$ is some wave function of the electron, $\chi_\zeta(\sigma)$ is a spin function, $\alpha = \{s, \zeta\}$ is a set of quantum numbers determining the state of the electron. Function (12.23) satisfies the normalization condition:

$$\int \varphi^*_\alpha(q)\varphi_{\alpha'}(q)dq = \delta_{\alpha\alpha'}. \tag{12.24}$$

Taking into account $q = \{\mathbf{r}, \zeta\}$ the normalization condition can be written as

$$\int \phi^*_s(\boldsymbol{r})\phi_{s'}(r)d\boldsymbol{r} = \delta_{ss'}, \tag{12.25}$$

$$\sum_{\sigma=-1/2}^{1/2} \chi^*_\zeta(\sigma)\chi_{\zeta'}(\sigma) = \delta_{\zeta\zeta'}. \tag{12.26}$$

As a function $\varphi_\alpha(q)$, we use the eigenfunctions of the electron in the atom, which consists of a nucleus and one electron, i.e. this function is a solution of the stationary Schrödinger equation:

$$\widehat{H}^{(1)}\varphi_\alpha = E^{(o)}\varphi_\alpha, \tag{12.27}$$

or in detail

$$\left[-\hbar^2/(2\,m)\nabla^2 - Ze^2/r\right]\varphi_\alpha = E^{(o)}\varphi_\alpha. \tag{12.28}$$

Function $\varphi_\alpha(q)$, which depends on the polar coordinates $\{r, \vartheta, \varphi\}$, has the form:

$$\varphi_\alpha(q) \equiv \phi_s(\boldsymbol{r})\chi_\zeta(\sigma) = R_{nl}(r)Y_{lm}(\vartheta, \varphi)\chi_\zeta(\sigma), \tag{12.29}$$

Parameters

$$\alpha = \{n, l, m, \zeta\}, \quad s = \{n, l, m\}, \tag{12.30}$$

where $n = 1, 2, \ldots$ is the principal quantum number, $l = 0, 1, 2, \ldots, n-1$ is the orbital number, $m = 0, \pm1, \pm2 \ldots, \pm(l-1), \pm l$ is the magnetic quantum number, $R_{nl}(r)$ is the radial function of the absolute value r of the radius-vector $\mathbf{r}$, $Y_{lm}(\vartheta, \varphi)$ is the eigenfunction of the operator of the angular momentum $\mathbf{M}^2$ $(\widehat{\mathbf{M}} = [\widehat{\mathbf{r}}\widehat{\mathbf{p}}])$, which depends on the polar coordinates ϑ and φ. The number α for a fixed number n adopts $2n^2$ different values. Eigenvalue $E^{(o)}$ has the formula

$$E^{(o)}_n = -Z^2 me^4/\left(2\hbar^2 n^2\right) = -Z^2\,R\,\hbar\,/n^2, \tag{12.31}$$

R is a Rydberg constant.

12.7 Matrix Elements of Hamiltonians

The transition from the coordinate representation, usual for Hamiltonians, to some α-representation is performed by means of the orthonormal system of wave functions $\varphi_\alpha(q)$. Knowing these functions, we can calculate the matrix elements of the Hamiltonians by the same formula (12.4):

$$H_{\alpha\alpha'} = \int \varphi^*_\alpha(q)\widehat{H}^{(1)}\varphi_{\alpha'}(q)dq, \tag{12.32}$$

As for the two-electron Hamiltonian $H_{\alpha_1\alpha_2,\alpha'_1\alpha'_2}$, it must be antisymmetric, i.e.

$$H_{12,1'2'} = -H_{21,1'2'} = -H_{12,2'1'} = H_{21,2'1'}. \tag{12.33}$$

So we write it in the form:

$$H_{\alpha_1\alpha_2,\alpha'_1\alpha'_2} = \int \Phi^*_{\alpha_1\alpha_2}\widehat{H}^{(2)}\Phi_{\alpha'_1\alpha'_2}\,dq_1dq_2, \tag{12.34}$$

where $\Phi_{\alpha_1\alpha_2}$ is the Slater two-particle wave function:

$$\Phi_{\alpha_1\alpha_2} = 1/\sqrt{2}\left[\varphi_{\alpha_1}(q_1)\varphi_{\alpha_2}(q_2) - \varphi_{\alpha_1}(q_2)\varphi_{\alpha_2}(q_1)\right]. \tag{12.35}$$

The matrix (7.4) satisfies the normalization condition:

$$\int \Phi^*_{\alpha_1\alpha_2}\Phi_{\alpha'_1\alpha'_2}dq_1\,dq_2 \approx \delta_{\alpha_1\alpha'_1}\delta_{\alpha_2\alpha'_2} - \delta_{\alpha_2\alpha'_1}\delta_{\alpha_1\alpha'_2}. \tag{12.36}$$

This function is taken in order to make the matrix elements of the Hamiltonian $H_{\alpha_1\alpha_2,\alpha'_1\alpha'_2}$ anti-symmetric matrix elements. Substituting this function in (12.34), we get the anti-symmetric matrix:

$$H_{12,1'2'} = 1/2(V_{12,1'2'} - V_{21,1'2'} - V_{12,2'1'} + V_{21,2'1'}), \tag{12.37}$$

where

$$V_{12,1'2'} = \int \varphi^*_{\alpha_1}(q_1)\varphi^*_{\alpha_2}(q_2)e^2/r_{12}\varphi_{\alpha'_1}(q_1)\varphi_{\alpha'_2}(q_2)\,dq_1\,dq_2. \tag{12.38}$$

Let us substitute the function (12.29) in formulas (12.32) and (12.38). Then we will have matrix elements $H_{\alpha\alpha'}$ and $V_{12,1'2'}$ in the form:

$$H_{\alpha\alpha'} = \int \varphi^*_\alpha(q)\widehat{H}^{(1)}\varphi_{\alpha'}(q)dq = \varepsilon^{(o)}_n\int \varphi^*_\alpha(q)\varphi_{\alpha'}(q)\,dq = \varepsilon^{(o)}_n\delta_{\alpha\alpha'}, \tag{12.39}$$

$$V_{12,1'2'} = e^2 \sum_{\zeta_1=-1/2}^{1/2} \chi^*_{\sigma_1}(\zeta_1)\chi_{\sigma'_1}(\zeta_1) \sum_{\zeta_2=-1/2}^{1/2} \chi^*_{\sigma_2}(\zeta_2)\chi_{\sigma'_2}(\zeta_2) \cdot \int \phi^*_{s_1}(\mathbf{r}_1)\phi^*_{s_2}(\mathbf{r}_2)1/|\mathbf{r}_1 - \mathbf{r}_2|\phi_{s'_1}(\mathbf{r}_1)\phi_{s'_2}(\mathbf{r}_2)\mathrm{d}\mathbf{r}_1\mathrm{d}\mathbf{r}_2.$$

Taking into account the conditions of normalization (12.26) of the spin functions, we shall obtain

$$V_{12,1'2'} = e^2\delta_{\sigma_1\sigma'_1}\delta_{\sigma_2\sigma'_2}\int \phi^*_{s_1}(\boldsymbol{r}_1)\phi^*_{s_2}(\boldsymbol{r}_2)1/|\,\boldsymbol{r}_1 - \boldsymbol{r}_2|\phi_{s'_1}(\boldsymbol{r}_1)\phi_{s'_2}(\boldsymbol{r}_2)d\boldsymbol{r}_1\,d\boldsymbol{r}_2. \quad (12.40)$$

We denote the function:

$$\Phi\left(s_1, s_2; s'_1, s'_2\right) = \int \phi^*_{s_1}(\boldsymbol{r}_1)\phi^*_{s_2}(\boldsymbol{r}_2)1/|\,\boldsymbol{r}_1 - \boldsymbol{r}_2|\phi_{s'_1}(\boldsymbol{r}_1)\phi_{s'_2}(\boldsymbol{r}_2)d\boldsymbol{r}_1\,d\boldsymbol{r}_2. \quad (12.41)$$

Now the matrix $V_{12,1'2'}$ will look as follows:

$$V_{12,1'2'} = e^2\delta_{\sigma_1\sigma'_1}\delta_{\sigma_2\sigma'_2}\Phi\left(s_1, s_2; s'_1, s'_2\right). \quad (12.42)$$

12.8 Energy of Electrons in Nucleus Recorded by Means of Density Matrix

The unknown density matrices $\varrho_{\alpha\alpha'}$ and $\varrho_{12,1'2'}$, written in the α-representation, allow us to transform the expression (12.20) to the form:

$$E = \sum_{\alpha,\alpha'} H_{\alpha\alpha'}\varrho_{\alpha'\alpha} + 1/2\sum_{\{\alpha\}} H_{12,1'2'}\varrho_{12,1'2'}, \quad (12.43)$$

where $\{\alpha\} = \alpha_1, \alpha_2, \alpha'_1, \alpha'_2$. Let us express the two-electron matrix through one-electron matrix. Put here the approximate expression (12.8), and obtain

$$E = \sum_{\alpha\alpha'} H_{\alpha\alpha'}\varrho_{\alpha'\alpha} + \sum_{\{\alpha\}} H_{12,1'2'}\varrho_{11'}\varrho_{22'}. \quad (12.44)$$

We assume that the density matrix is diagonal, i.e.

$$\varrho_{\alpha'\alpha} = w_\alpha\delta_{\alpha\alpha'}, \quad (12.45)$$

now the normalization condition is

$$\sum_{\alpha} w_{\alpha} = Z. \tag{12.46}$$

The average energy of the electrons has the form:

$$E = \sum_{\alpha} H_{\alpha\alpha} w_{\alpha} + \sum_{\alpha\beta} H_{\alpha\beta,\alpha\beta} w_{\alpha} w_{\beta}, \tag{12.47}$$

Substituting here the matrix elements of the Hamiltonians:

$$H_{\alpha\alpha'} = \varepsilon_n^{(o)} \delta_{\alpha\alpha'}, \quad H_{\alpha\beta,\alpha\beta} = 1/2(V_{\alpha\beta,\alpha\beta} - V_{\beta\alpha,\alpha\beta} - V_{\alpha\beta,\beta\alpha} + V_{\beta\alpha,\beta\alpha}),$$

obtain

$$E = \varepsilon_n^{(o)} \sum_{\alpha} w_{\alpha} + \sum_{\alpha\beta} \left(V_{\alpha\beta,\alpha\beta} - V_{\beta\alpha,\alpha\beta} \right) w_{\alpha} w_{\beta}. \tag{12.48}$$

We find matrix elements $V_{\alpha\beta,\alpha\beta}$ and $V_{\beta\alpha,\alpha\beta}$, using the formula (12.40):

$$V_{\alpha\beta,\alpha\beta} = e^2 \int \phi_{s_1}^*(\boldsymbol{r}_1) \phi_{s_2}^*(\boldsymbol{r}_2) 1/|\, \boldsymbol{r}_1 - \boldsymbol{r}_2| \phi_{s_1}(\boldsymbol{r}_1) \phi_{s_2}(\boldsymbol{r}_2)\, d\boldsymbol{r}_1\, d\boldsymbol{r}_2, \tag{12.49}$$

here $\alpha = \{s_1, \sigma_1\}$, $\beta = \{s_2, \sigma_2\}$;

$$V_{\beta\alpha,\alpha\beta} = e^2 \delta_{\sigma_1\sigma_2} \int \phi_{s_2}^*(\boldsymbol{r}_1) \phi_{s_1}^*(\boldsymbol{r}_2) 1/|\, \boldsymbol{r}_1 - \boldsymbol{r}_2| \phi_{s_1}(\boldsymbol{r}_1) \phi_{s_2}(\boldsymbol{r}_2)\, d\boldsymbol{r}_1\, d\boldsymbol{r}_2. \tag{12.50}$$

We denote the functions:

$$\Phi(s_1, s_2) = \int |\phi_{s_1}(\boldsymbol{r}_1)|^2 1/|\, \boldsymbol{r}_1 - \boldsymbol{r}_2| \cdot |\phi_{s_2}(\boldsymbol{r}_2)|^2\, d\boldsymbol{r}_1\, d\boldsymbol{r}_2, \tag{12.51}$$

$$\Psi(s_1, s_2) = \int \phi_{s_2}^*(\boldsymbol{r}_1) \phi_{s_1}^*(\boldsymbol{r}_2) 1/|\, \boldsymbol{r}_1 - \boldsymbol{r}_2| \phi_{s_1}(\boldsymbol{r}_1) \phi_{s_2}(\boldsymbol{r}_2)\, d\boldsymbol{r}_1\, d\boldsymbol{r}_2. \tag{12.52}$$

We write the functions:

$$V_{\alpha\beta,\alpha\beta} = e^2 \Phi(s_1, s_2), \quad V_{\beta\alpha,\alpha\beta} = e^2 \delta_{\sigma_1\sigma_2} \Psi(s_1, s_2). \tag{12.53}$$

Thus, we have

$$E = \varepsilon_n^{(o)} \sum_{\alpha} w_{\alpha} + e^2 \sum_{\alpha\beta} \left(\Phi(s_1, s_2) - \delta_{\sigma_1\sigma_2} \Psi(s_1, s_2) \right) w_{\alpha} w_{\beta}. \tag{12.54}$$

12.9 Entropy

Since according to (12.45) the density matrix is diagonal, in this case we can write an approximate expression for the entropy:

$$S = -k_B \sum_{\alpha} \{w_\alpha \ln w_\alpha + (1 - w_\alpha) \ln(1 - w_\alpha)\}. \tag{12.55}$$

Entropy can be more precisely expressed using one- and two-electron density matrix. Only now two-electron matrix must also be diagonal:

$$\varrho_{12,1'2'} = w_{12}(\delta_{11'}\delta_{22'} - \delta_{12'}\delta_{21'}), \tag{12.56}$$

where $w_{\alpha\beta}$ is the probability that of two electrons one is in the state α and the other is in the state β. This probability satisfies the normalization condition:

$$\sum_{\alpha} \sum_{\beta \neq \alpha} w_{\alpha\beta} = Z(Z - 1). \tag{12.57}$$

Now let us write the expression for the entropy in the second approximation:

$$S = -k_B \left[\sum_{\alpha} \sum_{n=0}^{1} w_\alpha^{(n)} \ln w_\alpha^{(n)} + 1/2 \sum_{\alpha} \sum_{\beta \neq \alpha} \sum_{n=0}^{1} \sum_{m=0}^{1} w_{\alpha\beta}^{(nm)} \ln \mu_{\alpha\beta}^{(nm)} \right], \tag{12.58}$$

where

$$w_\alpha = w_\alpha^{(1)}, \quad w_\alpha^{(0)} = 1 - w_\alpha, \tag{12.59}$$

$$w_{\alpha\beta} = w_{\alpha\beta}^{(11)}, \quad w_{\alpha\beta}^{(10)} + w_{\alpha\beta}^{(11)} = w_\alpha^{(1)} u_{\alpha\beta}, \quad w_{\alpha\beta}^{(00)} + w_{\alpha\beta}^{(01)} = w_\alpha^{(0)} u_{\alpha\beta}, \tag{12.60}$$

$$u_{\alpha\beta} = 1 - \delta_{\alpha\beta}, \tag{12.61}$$

$$\mu_{\alpha\beta}^{(nm)} = w_{\alpha\beta}^{(nm)} / \left(w_\alpha^{(n)} w_\beta^{(m)} \right) \tag{12.62}$$

is correlation multiplier.

12.10 Variational Principle

We can now write an expression for the thermodynamic potential:

$$\Omega = E - ST - \mu Z. \tag{12.63}$$

where μ is the chemical potential. Substitution of the expressions (12.54) and (12.55) into this formula gives us the thermodynamic potential in the first approximation:

$$\begin{aligned}\Omega\{w_\alpha\} = \varepsilon_n^{(o)} \sum_\alpha w_\alpha + e^2 \sum_{\alpha\beta} (\Phi(s_1, s_2) - \delta_{\sigma_1\sigma_2}\Psi(s_1, s_2))w_\alpha w_\beta \\ + k_B T \sum_\alpha \{w_\alpha \ln w_\alpha + (1 - w_\alpha)\ln(1 - w_\alpha)\} - \mu \sum_\alpha w_\alpha.\end{aligned} \tag{12.64}$$

Differentiate this function with respect to w_α and equate the resulting expression to zero:

$$\partial\Omega/\partial w_\alpha = 0.$$

We have the equation:

$$\varepsilon_n^{(o)} + 2\,e^2 \sum_\beta (\Phi(s_1, s_2) - \delta_{\sigma_1\sigma_2}\Psi(s_1, s_2))w_\beta + k_B T \ln[w_\alpha/(1 - w_\alpha)] - \mu = 0.$$

Write this non-linear equation as follows:

$$\ln[(1 - w_\alpha)/w_\alpha)] = \beta\left[\varepsilon_n^{(o)} - \mu + 2\,e^2 \sum_\beta (\Phi(s_1, s_2) - \delta_{\sigma_1\sigma_2}\Psi(s_1, s_2))w_\beta\right]. \tag{12.65}$$

The derived equation is very similar to the function of Fermi – Dirac, which gives the distribution of electrons in the crystal. Only here the solution w_α of this equation gives the distribution function of electrons in an arbitrary equilibrium atom at any temperature. This is the sought equation for the distribution function w_α of electrons in the atom. Equation (12.65) should be complemented by the normalization condition:

$$\sum_\alpha w_\alpha = Z. \tag{12.66}$$

12.11 Equations for Distribution Functions and Correlation Functions

The diagonal density matrix of the second order can be conveniently represented in the form:

$$\varrho_{12,1'2'} = w_{12}(\delta_{11'}\delta_{22'} - \delta_{12'}\delta_{21'}), \tag{12.67}$$

where binary probability w_{12} is equal to

$$w_{\alpha\beta} = w_\alpha w_\beta u_{\alpha\beta} + \xi_{\alpha\beta}, \tag{12.68}$$

$u_{\alpha\beta} = 1 - \delta_{\alpha\beta}$, $\xi_{\alpha\beta}$ is the correlation function, which satisfies the conditions:

$$\xi_{\alpha\beta} = \xi_{\beta\alpha}, \quad \xi_{\alpha\alpha} = 0. \tag{12.69}$$

Substitute the density matrix $\varrho_{\alpha\alpha'}$ and $\varrho_{12,1'2'}$ in the formula (12.54) for the electron energy and obtain

$$E = \varepsilon_n^{(o)} \sum_\alpha w_\alpha + \sum_{\alpha\beta} \left(V_{\alpha\beta,\alpha\beta} - V_{\beta\alpha,\alpha\beta}\right)(w_\alpha\, w_\beta u_{\alpha\beta} + \xi_{\alpha\beta}). \tag{12.70}$$

Now express the probability w_α and $w_{\alpha\beta}$ through the probability w_α and correlation function $\xi_{\alpha\beta}$ using the relations (12.59), (12.60) and (12.68). We have

$$w_\alpha^{(1)} = w_\alpha, w_\alpha^{(0)} = 1 - w_\alpha, w_{\alpha\beta}^{(11)} = w_{\alpha\beta} = w_\alpha w_\beta u_{\alpha\beta} + \xi_{\alpha\beta},$$
$$w_{\alpha\beta}^{(10)} = w_\alpha(1 - w_\beta)u_{\alpha\beta} - \xi_{\alpha\beta}, w_{\alpha\beta}^{(00)} = (1 - w_\alpha)(1 - w_\beta)u_{\alpha\beta} + \xi_{\alpha\beta}.$$

Thus, the electron energy and the entropy are the functions of the probability w_α and correlation functions $\xi_{\alpha\beta}$. Substituting these expressions into the formula of the thermodynamic potential, we have

$$\begin{aligned}\Omega\{w_\alpha, \xi_{\alpha\beta}\} = {} & \varepsilon_n^{(o)} \sum_\alpha w_\alpha + \sum_{\alpha\beta} \left(V_{\alpha\beta,\alpha\beta} - V_{\beta\alpha,\alpha\beta}\right)(w_\alpha\, w_\beta u_{\alpha\beta} + \xi_{\alpha\beta}) \\ & + k_B T \left[\sum_\alpha \sum_{n=0}^{1} w_\alpha^{(n)} \ln w_\alpha^{(n)} \right. \\ & \left. + 1/2 \sum_\alpha \sum_{\beta\neq\alpha} \sum_{n=0}^{1} \sum_{m=0}^{1} w_{\alpha\beta}^{(nm)} \ln \mu_{\alpha\beta}^{(nm)} \right] \\ & - \mu \sum_\alpha w_\alpha.\end{aligned} \tag{12.71}$$

Let us differentiate this function with respect to w_α, $\xi_{\alpha\beta}$ and equate the resulting expression to zero:

$$\partial\Omega/\partial w_\alpha = 0, \ \partial\Omega/\partial\xi_{\alpha\beta} = 0.$$

As a result, we have two equations in which the unknowns are the distribution function w_α and the correlation function $\xi_{\alpha\beta}$.

12.12 New Calculation of Energy Levels of Electrons in Atom

Finding the energy levels of electrons in the atom, we can consider their pure state. The pure state, by definition, is such state that the density matrix is equal to the product of the wave functions c_α of the system. Let the statistical operator is equal to

$$\hat{\varrho}^{(1)} = Z\delta(q - q_o), \tag{12.72}$$

where $\delta(q - q_o)$ is the Delta function, q_o = const. According to the formula (12.4), we have

$$\varrho_{\alpha\alpha'} = Z\int \psi^*_\alpha(q)\delta(q - q_o)\psi_{\alpha'}(q)dq = Z\psi^*_\alpha(q_o)\psi_{\alpha'}(q_o) = Zc^*_\alpha c_{\alpha'}, \tag{12.73}$$

where

$$c_\alpha = \psi_\alpha(q_o). \tag{12.74}$$

The numbers c_α satisfy the normalization condition:

$$\sum_\alpha c^*_\alpha c_\alpha = 1. \tag{12.75}$$

In equilibrium, for the pure state, the numbers c_α must satisfy the stationary Schrodinger equation.

We write the average energy of electrons in the pure state. To do this, we substitute the density matrix $\rangle_{\alpha\alpha'} = Z\, c^*_\alpha c_{\alpha'}$ into the formula (12.44) and obtain

$$E = Z\sum_{\alpha\alpha'} H_{\alpha\alpha'}c^*_{\alpha'}c_\alpha = Z(Z-1)\sum_{\{\alpha\}} H_{12,1'2'}c^*_{1'}c_1c^*_{2'}c_2. \tag{12.76}$$

Here we have substituted the exact number Z – 1, which presences in the formula (12.11). If we use formula (12.29), the matrix $H_{\alpha\alpha'}$ is diagonal (12.39), and the matrix $H_{12,1'2'}$ is anti-symmetric (12.37):

$$E = Z\sum_\alpha \varepsilon^{(o)}_n c^*_\alpha c_\alpha + Z(Z-1)\sum_{\{\alpha\}} H_{12,1'2'}c^*_{1'}c_1c^*_{2'}c_2. \tag{12.77}$$

Now we write the equation for numbers c_α. This equation has the form:

$$\varepsilon_n^{(o)} c_\alpha + (Z-1) \sum_{\alpha_1 \alpha_2 \alpha_1'} H_{12,1'\alpha} c_1 c_2 c_{1'}^* = \varepsilon c_\alpha, \tag{12.78}$$

where $\alpha = \{n, l, m, \sigma\}$, ε is an eigenvalue. If we multiply this equation by Z c_α^* and sum it on α, then taking into account (12.75) we get $E = Z\varepsilon$.

The numbers c_α have a lot of values that we will denote by the index $\beta = \{n', l', m', \sigma'\}$:

$$\varepsilon_n^{(o)} c_\alpha^{(\beta)} + (Z-1) \sum_{\alpha_1 \alpha_2 \alpha_1'} H_{12,1'\alpha} c_1^{(\beta)} c_2^{(\beta)} c_{1'}^{(\beta)*} = \varepsilon^{(\beta)} c_\alpha^{(\beta)}. \tag{12.79}$$

If $Z = 1$, then for a hydrogen atom we have $\varepsilon^{(\beta)} = \varepsilon_n^{(o)}$.

At $Z = 2, 3, \ldots$ we must find the matrix $H_{12,1'2'}$. Using formula (12.37) and (12.42), we obtain

$$\begin{aligned} H_{12,1'2'} = 1/2e^2 \Big[& \delta_{\sigma_1\sigma_1'} \delta_{\sigma_2\sigma_2'} \Phi(s_1, s_2; s_1', s_2') - \delta_{\sigma_2\sigma_1'} \delta_{\sigma_1\sigma_2'} \Phi(s_2, s_1; s_1', s_2') \\ & - \delta_{\sigma_1\sigma_2'} \delta_{\sigma_2\sigma_1'} \Phi(s_1, s_2; s_2', s_1') + \delta_{\sigma_2\sigma_2'} \delta_{\sigma_1\sigma_1'} \Phi(s_2, s_1; s_2', s_1') \Big]. \end{aligned} \tag{12.80}$$

Equation (12.79) can be compared with the equation:

$$\varepsilon_n^{(o)} c_\alpha^{(\beta)*} + (Z-1) \sum_{\alpha_1 \alpha_2 \alpha_1'} H_{12,1'\alpha} c_1^{(\beta)*} c_2^{(\beta)*} c_{1'}^{(\beta)} = \varepsilon^{(\beta)} c_\alpha^{(\beta)*}.$$

12.13 Conclusion

For the distribution function w_α in the first approximation, we obtained the nonlinear equation (12.65). If in this equation we put the functions $\Phi(s_1, s_2)$ and $\Psi(s_1, s_2)$ equal to zero, we get the equation:

$$\ln, [1 - w_\alpha)/w_\alpha] = \beta(\varepsilon_n^{(o)} - \mu). \tag{12.81}$$

The solution of this equation is a function: $w_\alpha = w(n)$.

If we calculate the dependence of the functions $\Phi(s_1, s_2)$ and $\Psi(s_1, s_2)$ of their arguments $s_1 = \{n_1, l_1, m_1\}$ and $s_2 = \{n_2, l_2, m_2\}$, then we have the equation for the distribution function:

$$w_\alpha = w(n, l, m, \sigma). \tag{12.82}$$

The solution of (12.79) gives $\varepsilon^{(\beta)} = \varepsilon^{(n,l,m,\sigma)} = \varepsilon^{(n,l,m,\sigma)}$, the spectrum of energies of electrons in an arbitrary equilibrium atom. To solve these problems, we need to use a computer. This hard work requires a young and smart mathematician.

References

1. J. von Neumann, *Mathematical Basis of Quantum Mechanics* (Nauka, Moscow, 1964)
2. K. Blum, *Density Matrix Theory and Application* (Plenum, New York, 1981)
3. B.V. Bondarev, *Density Matrix Method in Quantum Cooperative Process Theory*, 2nd edn. (Sputnik, Moscow, 2013) (in Russian)
4. Y.R. Shen, Phys. Rev. **155**, 921 (1967)
5. M. Grover, R. Silbey, Chem. Phys. **52**, 2099 (1970); **54**, 4843 (1971)
6. A. Kossakowski, Rep. Math. Phys. **3**, 247 (1972)
7. G. Lindblad, Commun. Math. Phys. **48**, 119 (1976)
8. B.V. Bondarev, Phys. A **176**, 366 (1991)
9. B.V. Bondarev, Phys. A **184**, 205 (1992)
10. B.V. Bondarev, Phys. A **183**, 159 (1992)
11. B.V. Bondarev, Phys. A **209**, 477 (1994)
12. B.V. Bondarev, Theor. Mat. Fiz. **100**, 33 (1994)
13. B.V. Bondarev, Vestnik MAI **8**, 61 (2001) (in Russian)
14. D. Hartree, *Calculations of Atomic Structures* (Foreign Literature, Moscow, 1960) (in Russian)
15. D.I. Blokhintsev, *Fundamentals of Quantum Mechanics* (High School, Moscow, 1961) (in Russian)
16. V.A. Fok, *Beginning of Quantum Mechanics, Part IV* (Nauka, Moscow, 1976) (in Russian)
17. J. Slater, *Methods of Self-consistent Field for Molecules and Solids* (Mir, Moscow, 1978) (in Russian)
18. N.F. Stepanov, *Quantum Mechanics and Quantum Chemistry* (Mir, Moscow, 2001) (in Russian)
19. R.M. Aminova, *Foundations of Modern Quantum Chemistry* (Kazan State University Press, Kazan, 2004) (in Russian)
20. A.K. Shiryaev, *Quantum Mechanics and Quantum Chemistry* (Samara State Technical University Press, Samara, 2014) (in Russian)

Chapter 13
Electric Response to Bending Vibrations and Pyroelectric Effect in Unpolarized Ferroelectric Ceramic Plates with Electrodes, Differing in the Magnitude of the Coefficient of Thermal Expansion on Opposite Surfaces

V. P. Sakhnenko, Yu. N. Zakharov, I. A. Parinov, A. G. Lutokhin, E. V. Rozhkov, N. S. Filatova, I. P. Raevski, V. A. Chebanenko, A. V. Pavlenko, L. I. Kiseleva and E. S. Rodinin

Abstract The manufacture of electrode materials by the methods of sintering and cathodic sputtering of metals with different coefficients of linear thermal expansion on opposite surfaces of unpolarized ferroelectric ceramics plates creates stationary gradients of mechanical deformations and stresses in specimens' volume. As a result, an electrical response to the three-point mechanical loading (flexural vibrations at the resonant frequency) and pyroelectric current in the dynamic mode of measurement were observed.

V. P. Sakhnenko · Yu. N. Zakharov (✉) · A. G. Lutokhin · N. S. Filatova
I. P. Raevski · E. S. Rodinin
Physics Research Institute, Southern Federal University,
194, Stachki Ave., Rostov-on-Don 344090, Russia
e-mail: delta-46@mail.ru

I. A. Parinov · E. V. Rozhkov
I. I. Vorovich Mathematics, Mechanics and Computer Science Institute,
Southern Federal University, 8a, Milchakova Str.,
Rostov-on-Don 344090, Russia
e-mail: parinov_ia@mail.ru

V. A. Chebanenko · A. V. Pavlenko · L. I. Kiseleva
Southern Scientific Center of RAS, 41, Chekhova Str.,
Rostov-on-Don 344022, Russia
e-mail: valera.chebanenko@yandex.ru

I. A. Parinov et al. (eds.), *Advanced Materials*, Springer Proceedings
in Physics 207, https://doi.org/10.1007/978-3-319-78919-4_13

13.1 Introduction

It is known that the unipolarity of the switching characteristics in ferroelectric crystals depends on the material and the method of applying of the electrodes. For example, when using liquid electrodes, the unipolarity of the repolarization of $BaTiO_3$ crystals in the fields lower than the coercive one was revealed by studying the motion of 90° boundaries [1]. A switching unipolarity can be obtained by using non-equivalent electrodes (different material or method of application) [2–6]. This unipolarity does not disappear under the long-term action of a strong alternating field as well as after heating above the Curie temperature T_C. In TGS crystals, when using In-Au electrodes, the unipolarity turned out to be greater than the natural one [7, 8]. Investigation of the pyroelectricity in a quasistatic mode revealed two types of pyroelectric current change with temperature. In the first case, the dependence of the pyroelectric current on temperature has the usual form with a maximum in the T_C region (the pyroelectric current flows in the external circuit from the face to the electrode providing the worst repolarization conditions, or the electrode is applied on the crystal face with a large number of defects). In the other case, the pyroelectric current changes its direction near T_C [9, 10]. As a rule, the explanation of the effects of unipolarity is based on the assumption of the existence of a special layer at the surface with a state of polarization that differs from the bulk part of the sample under study. A considerable number of theoretical and experimental studies have been devoted to the proof and confirmation of the relation between a unipolar state and a spatial distribution of polarization in ferroelectrics, covering practically the entire period of the development of the physics of ferroelectricity.

The scope of the present work is an investigation of the unipolarity, caused by a stationary strain gradient in the near-surface regions of non-poled ferroelectric ceramics. This gradient was formed by applying on the opposite surfaces of the samples electrodes from the metals with different values of linear thermal expansion coefficient α^T.

13.2 The Contribution of the Temperature Dependence of the Dielectric Constant to the Pyroelectric Effect

According to thermodynamics in the absence of electric fields [11], the pyroelectric coefficient $\gamma \sim \varepsilon P$, where ε is the dielectric constant and P is the polarization, then the extremum condition of P:

$$\varepsilon \frac{dP}{dT} + P\frac{d\varepsilon}{dT} = 0, \quad \frac{d\varepsilon}{dT} = -\frac{\varepsilon\gamma}{P} > 0, \quad \text{since } \gamma < 0 \tag{13.1}$$

Consequently, the maximum of $\gamma(T)$ is below the maximum of $\varepsilon(T)$ at the site of increase of $\varepsilon(T)$.

The presence of an electric field will lead to an additional relative shift of the maxima $\varepsilon(T)$ and $\gamma(T)$. The source of the electric field can be the external field, contact fields, the unipolarity field, and the field of free charges shielding the polarization. The contribution of the component $Ed\varepsilon/dT$ is usually considered small and is usually not taken into account in the calculations, without making any remarks about the direction of E with respect to the direction of P.

At the same time, the presence of a field of some nature that coincides in direction with P, may even lead to a sign change of $\gamma(T)$. This is due to independence of P and $\varepsilon(T)$, since, if $P(T)$ is a vector, then $\varepsilon(T)$ is the possibility of variations of this vector in magnitude.

An additional contribution to the pyroelectric response arises, since

$$D = \varepsilon\varepsilon_0 E + P, \quad \gamma = \frac{dD}{dT} = E\varepsilon_0 \frac{d\varepsilon}{dT} + \frac{dP}{dT} \tag{13.2}$$

where dE/dT is assumed equal to zero, therefore we neglect changes of E.

In the capacity of E, we can consider the external field, contact fields, the unipolarity field, which manifests itself under changes of P. This contribution can, in dependrnce on the signs of E, dP/dT, $d\varepsilon/dT$ both add up to $\gamma = dP/dT$ and subtract from it. Usually $dP/dT < 0$ and $d\varepsilon/dT > 0$, then the presence of E, coinciding with P, will lead to a decrease of γ. If E is antiparallel to P, then γ will increase. The pyroelectric response can also be determined by the first term of (2), while dP/dT is small.

Not taking into account the contribution of the constituent $\sim E(d\varepsilon/dT)$ to the pyroelectric response is typical for most papers, which leads to an incorrect interpretation of the experimental data. The contribution to the pyroelectric response due to the temperature dependence of the permittivity takes place in all possible cases of investigation. Under certain conditions, this contribution may turn out to be predominant.

13.3 Samples and Experimental Techniques

To investigate responses to bending vibrations, unpolarized plates were manufactured from hot-pressed ferroelectric ceramics PZT-19 with sizes $54 \times 4 \times 0.6$ mm^3, firstly. On one surface of all the plates, the electrode was sintered by the method of reduction of silver nitrate at 730 °C for 30 min. Then 3 types of electrodes were applied to opposite surface: (i) sintering of Ag method; (2) method of cathodic sputtering of Pt and (3) thermal evaporation of monel in a vacuum. The values of linear thermal expansion coefficients α^T for Ag and Pt were 19.5×10^{-6} K^{-1} and 9.2×10^{-6} K^{-1}, respectively.

The scheme and measurement technique using the three-point scheme are given in [12]. Also in [12], studies of the effect of mechanical damage to the electrode surface from Ag prior to sintering were performed. One of the surfaces of the

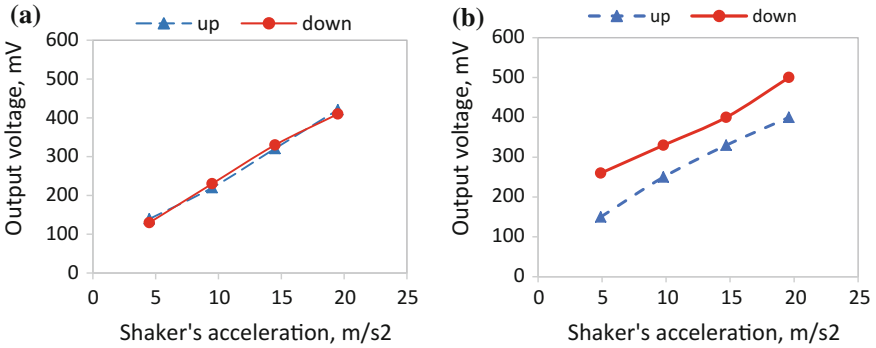

Fig. 13.1 Relationship between electrical response of samples with applied Ag electrodes on both sides to mechanical impact of proof mass 3 g at the resonance frequency and acceleration of the worktable: before (up) and after (down) rotation of the specimens on 180°: **a** equivalent electrode surfaces, **b** one of the surfaces is damaged

sample from PZT-19 with sizes 50 × 4 × 0.7 mm^3 was processed with grinding powders, which had different grain sizes. At the boundary of this surface with bulk of ceramic beam, non-equivalent gradient of mechanical strain and tangential compressive stresses were applied. The results of testing the sample using a three-point loading scheme with a mass of 3.1 g with equivalent surfaces and a sample with one damaged surface are shown in Fig. 13.1.

Figure 13.1a, b show the relationships between the electrical response of specimen and acceleration of worktable. Analysis of Fig. 13.1a shows that after sintering of Ag, electrical polarization stable to cyclic mechanical load is created by static strain gradients at the boundaries of sintered layers with the bulk of ceramics and by tangential compressive stresses in the near-electrode layers.

Figure 13.1b shows a 25% increase in the electrical response (from 0.26 to 0.5 V, depending on the acceleration), when rougher face is located on the opposite side of the proof mass. The difference in the magnitude of the output voltage can account for higher values of residual polaristion of the surface.

This effect was investigated at room temperature in the ferroelectric phase of PZT-19. Most likely, it can occur in a very thin transition layer: border of cermet layer—volumetric, homogeneous bulk of ceramic. Assuming that the thickness of this layer is about 1 μm, it generates on resitive load of 360 kΩ electric potential with the electric field strength up to 50 kV/cm.

Measurements of electrical responses of plates with one Ag and one Pt electrodes to the bending at the resonance frequency, given by the shaker, according to the three-point loading scheme of the attached mass 1 g (Fig. 13.2), showed that their amplitude increased up to 100% when the plate experienced tensile stress on the side of Pt (Fig. 13.2). The measurements were carried out at normal temperature (T_{norm}). For comparison, Fig. 13.1a shows similar responses of a plate with symmetric electrodes from Ag at the fixed value of resistive load. In addition, the

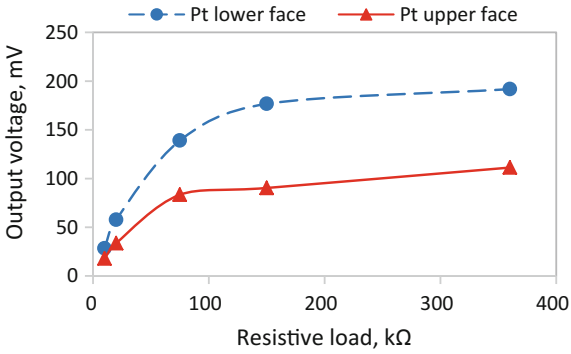

Fig. 13.2 Electrical responses of samples with applied Ag and Pt electrodes to the bending at the resonance frequency

samples were examined using a YE 2730A d_{33} meter. The average d_{33} module was equal to 5×10^{-12} C/N.

The study of pyroelectric effect at the dynamic mode of measurement by sinusoidally modulated thermal radiation has important features. Such an effect leads to periodic changes in the temperature gradient in the interelectrode space of the samples under study. The maximum temperature decreases from the irradiated electrode in the volume at each modulation period. The rotation of a uniformly polarized sample in a holder at 180° should result in a mandatory change in sign of pyroelectric response.

In samples with antiparallel polarization of near-electrode regions, the sign of the pyro-response is preserved. Its amplitudes are proportional to the pyroelectric coefficient in the near-electrode region. Taking this into account, we will consider successively the experimental results for each sample. In addition, the observed unipolarity with electric displacement fields in samples with a stationary deformation gradient in the near-electrode space requires the obligatory consideration of the contribution of the temperature variations of the dielectric constant to the pyroelectric current. Let us consider this in more detail.

The study of unipolarity was carried out with a rectangular sample of the PZT-19 with dimensions $8 \times 3.5 \times 0.72$ mm^3 and electrodes from different metals, applied by technology described above. The pyroelectric effect was investigated in a dynamic mode of measurement at a thermal radiation frequency of 3 Hz. Orthogonal projections of the pyroelectric response in a dynamic mode were recorded with the help of two lock-in nanovoltmeters (Unipan). First, thermal radiation occurred from the one electrode of the sample, then from the other one electrode. According to the measured projections of the pyroelectric response, its modulus was calculated. The coefficient γ was determined by comparing the modulus of the pyroelectric response with the response of the reference sample (PZT-11).

In Figs. 13.3, 13.4 and 13.5, the unit of measurement of the pyroelectric coefficient is $[\gamma] = \text{Cl K}^{-1} \text{ m}^{-2}$, and complex component of the pyroelectric signal voltage U_p is dimensionless.

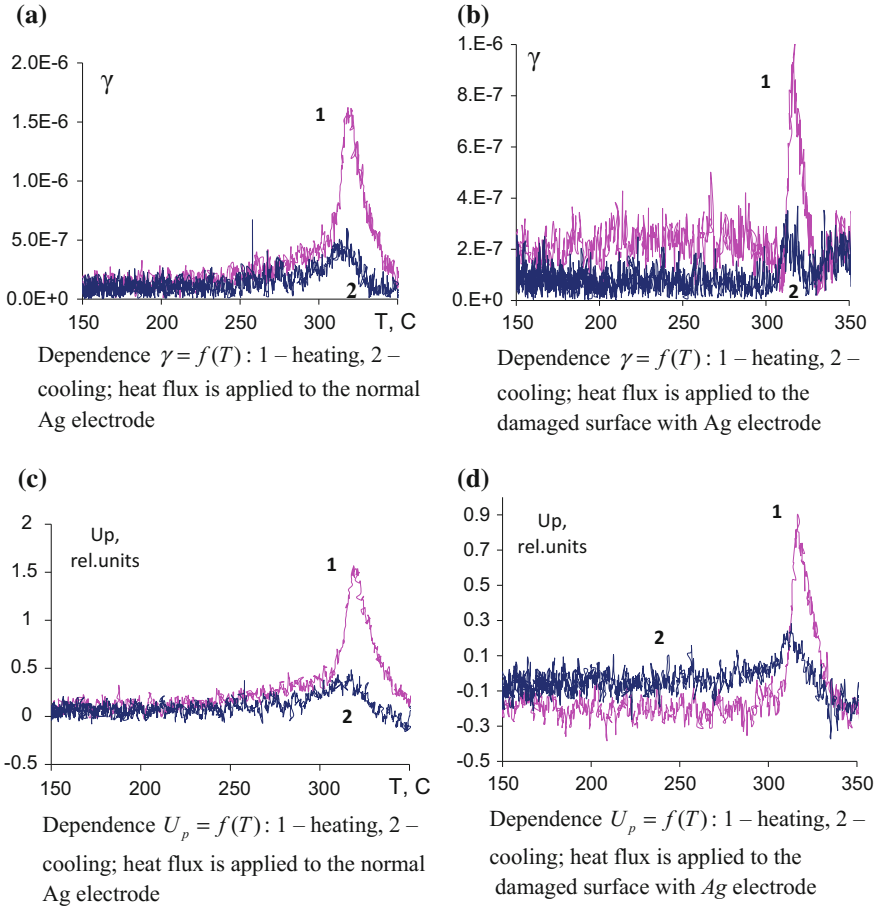

Dependence $\gamma = f(T)$: 1 – heating, 2 – cooling; heat flux is applied to the normal Ag electrode

Dependence $\gamma = f(T)$: 1 – heating, 2 – cooling; heat flux is applied to the damaged surface with Ag electrode

Dependence $U_p = f(T)$: 1 – heating, 2 – cooling; heat flux is applied to the normal Ag electrode

Dependence $U_p = f(T)$: 1 – heating, 2 – cooling; heat flux is applied to the damaged surface with *Ag* electrode

Fig. 13.3 Dependencies of pyroelectric coefficient and complex component of the pyroelectric signal voltage on temperature for sample from PZT-19; one electrode is made from Ag, the other is Ag on a damaged surface

Analysis of the results, shown in Figs. 13.3, 13.4 and 13.5, allows us to draw the following conclusions:

(i) In all the samples studied, when the electrodes were applied, near-surface layers with stationary counter-directed gradients of deformation were formed;

(ii) investigation of the temperature dependences of pyroelectric responses showed that their amplitude is the result of the algebraic summation of signals from each layer;

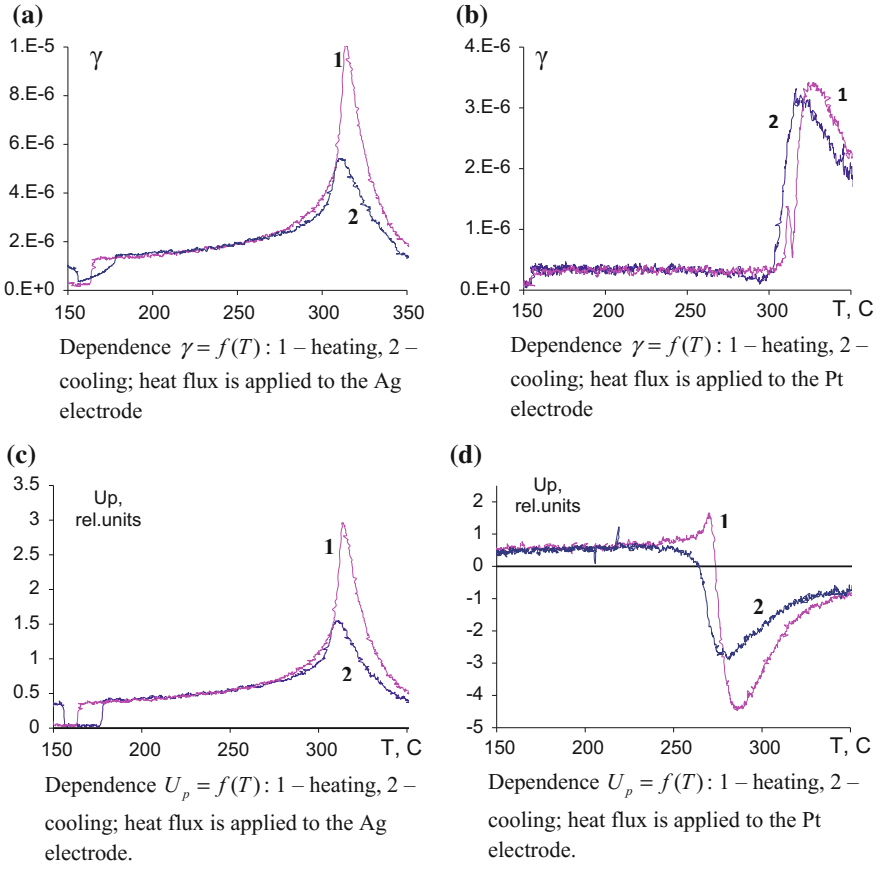

Fig. 13.4 Dependencies of pyroelectric coefficient and complex component of the pyroelectric signal voltage on temperature for sample from PZT-19; one electrode is made from Pt, the other one is Ag

(iii) in the ferroelectric phase for PZT-19 with heating and cooling from 300 °C, the resulting response corresponds to the difference in the pyroelectric coefficients of each layer; at $T > 300$ °C in the paraelectric phase, this response is due to the difference in the quantities of $d\varepsilon/dT$.

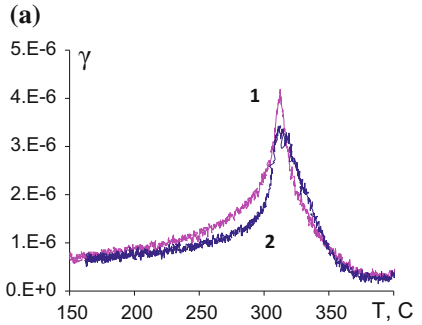

Dependence $\gamma = f(T)$: 1 – heating, 2 – cooling; heat flux is applied to the monel electrode

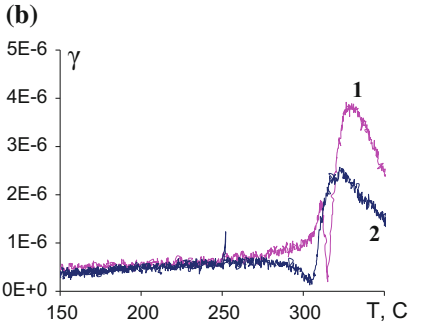

Dependence $\gamma = f(T)$: 1 – heating, 2 – cooling; heat flux is applied to the colloidal graphite electrode

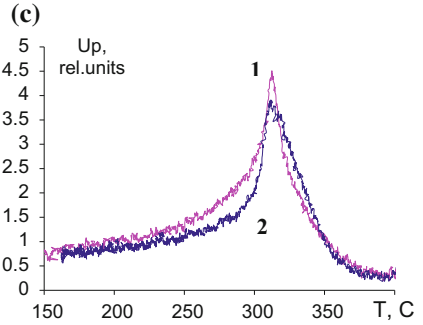

Dependence $U_p = f(T)$: 1 – heating, 2 – cooling; heat flux is applied to the monel electrode.

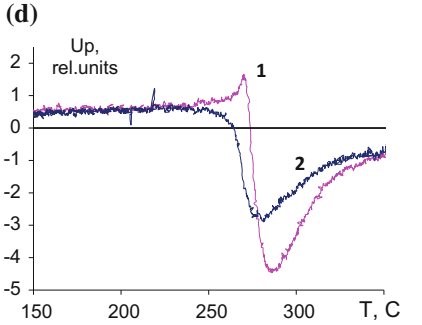

Dependence $U_p = f(T)$: 1 – heating, 2 – cooling; heat flux is applied to the colloidal graphite electrode

Fig. 13.5 Dependencies of pyroelectric coefficient and complex component of the pyroelectric signal voltage on temperature for sample from PZT-19; one electrode is made from monel, the other one is colloidal graphite

13.4 Conclusion

The main results of this study are the detection of thermally stable macroscopic polarization, formed during application of electrodes, and internal electric displacement field, created by stationary strain gradients in the near-electrode layers.

Acknowledgements The work was supported by the Russian Foundation for Basic Research (grants № 16-58-52013MHT_a, 16-08-00740_a).

References

1. I.S. Zheludev, *Physics of Crystalline Dielectrics* (Nauka, Moscow, 1968) (in Russian)
2. E. Fatuzzo, W.J. Merz, *Ferroelectricity* (North-Holland, Amsterdam, 1967)
3. V.A. Meleshina, I.S. Res, Izvestiya. AN SSSR, Ser. Fizich. **4**(28), 740 (1964) (in Russian)
4. V.Z. Borodin, *Influence of External Influences on the Processes of Polarization in Ferroelectric Ceramics of the $BaTiO_3$ Type*. Ph.D. Thesis (Rostov State University Press, Rostov-on-Don, 1962) (in Russian)
5. V.Z. Borodin, S.G. Gakh, V.G. Kuznetsov, O.P. Kramarov, L.M. Berberova, *Piezoelectric Materials and Converters* (Rostov State University Press, Rostov-on-Don, 1969). (in Russian)
6. V.Z. Borodin, S.G. Gakh, O.P. Kramarov, V.G. Kuznetsov, V.V. Yanchich, Electron. Eng. **14** (1), 24 (1969) (in Russian)
7. S.G. Gakh, *Investigation of the Effects of Unipolarity and the Nature of the Unipolar State in $BaTiO_3$ Single Crystals*. Ph.D. Thesis (Rostov State University Press, Rostov-on-Don, 1974) (in Russian)
8. V.A. Koptsik, N.D. Gavrilova, *Izvestiya AN SSSR, Ser. Fizich*. **11**(29), 1969 (1965) (in Russian)
9. M.B. Roytberg, A.Z. Rabinovich, L.I. Pyatigorskaya, Z.I. Shapiro, *Barium Titanate* (Nauka, Moscow, 1973) (in Russian)
10. K.N. Karmen, *Solid State Phys.* **7**(2), 1671 (1960) (in Russian)
11. R. Güttich, in *Procceding of 9th International Symposium on Technical Communication on Photon Detection*, Budapest (1980), p. 347
12. A.N. Soloviev, V.A. Chebanenko, Y.N. Zakharov, E.V. Rozhkov, I.A. Parinov, V.K. Gupta, in *Advanced Materials—Techniques, Physics, Mechanics and Applications*, ed. by I.A. Parinov, S.-H. Chang, M.A. Janiin. Springer Proceedings in Physics, vol. 193 (Springer, Cham, 2017), p. 485

Chapter 14
Structure and Dielectric Properties of Solid Solutions $Bi_{4+x}Sr_{2-x}Ti_xTa_{4-x}O_{18}$ (x = 0.0, 0.5, 1.0, 1.5, 2.0)

Sergei V. Zubkov

Abstract The structure and dielectric properties of a numbers of layered perovskite-like of $Bi_{4+x}Sr_{2-x}Ti_xTa_{4-x}O_{18}$ (x = 0.0, 0.5, 1.0, 1.5, 2.0) oxides with the APs structure have been studied. The temperature dependences of the relative permittivity $\varepsilon/\varepsilon_0$(T) and tangents to the tangential dielectric losses tan δ have been measured. Single-phase and space groups (A21*am*, Z = 36) of the Aurivillius phases (m = 2) have been determined from X-ray powder diffraction data. The relationship between crystal lattice distortions (parameters a, b, c) and the chemical composition of synthesized compounds have been established. The temperature of the second-order phase transition from the paraelectric state to the ferroelectric state varies with the parameter x, respectively. The activation energies have been calculated.

14.1 Introduction

Layered perovskite-like bismuth oxides with the Aurivillius phases (APs) structure have been known for several decades [1–3], but interest to them has been growing due to their potential practical applications. At present time, the number of known APs is equal to several hundred, and continues to increase. The chemical composition of APs described by the general formula $A_{m-1}Bi_2B_mO_{3m+3}$, and their crystal structure consists of alternating $[Bi_2O_2]^{2+}$ layers. Between them there are m perovskite-like $[A_{m-1}B_mO_{3m+1}]^{2-}$, where large-radius A-ions (Bi^{3+}, Ca^{2+}, Y^{3+}, Sr^{2+}, Ba^{2+}, Pb^{2+}, Na^{+}, K^{+}, Th^{4+} and Ln^{3+} (lanthanides)) have the dodecahedral coordination, whereas the B-sites inside oxygen octahedra are occupied with small-radius ions (Ti^{4+}, Nb^{5+}, Ta^{5+}, W^{6+}, Zr^{4+}, Mo^{6+}, Fe^{3+}, Mn^{4+}, Cr^{3+}, Ga^{3+}, etc.).

Unusual physical characteristics of the APs, such as the existence of the ferroelectric state up to high temperatures ($T_c \leq 965$ °C) [4, 5], piezoelectric properties,

S. V. Zubkov (✉)
Scientific Research Institute of Physics, Southern Federal University, Rostov-on-Don, Russia
e-mail: svzubkov61@mail.ru; zubkovsfedu@gmail.com

I. A. Parinov et al. (eds.), *Advanced Materials*, Springer Proceedings in Physics 207, https://doi.org/10.1007/978-3-319-78919-4_14

high ionic conductivity, and so on, allow one to consider these compounds as promising materials for application in electronic devices, operating under extreme conditions. $SrBi_2Nb_2O_9$ and $SrBi_2Ta_2O_9$ based solid solutions are the most studied APs due to perspectives of their application in memory devices (FeRAM) because of its good fatigue properties, low switching voltage and unlimited write/erase cycles [6–16], as multifunctional materials, exhibiting magnetic properties (multiferroics) [17, 18], photoluminescence [19, 20], etc. A priority problem is the optimization of the dielectric characteristics of the APs. Due to the studies of the dependence of these characteristics on various factors are important. In particular, the electrophysical properties of ceramic with the APs structure $(SrBi_2Nb_2O_9)_{1-x}(Bi_3TiNbO_9)_x$ and $SrBi_2(Nb_{1-x}Ta_x)_2O_9$ with $0 \leq x \leq 1$ were earlier studied in the dependence on the ceramic density and grain sizes that are determined by the prehistory of precursors used and their preliminary mechanical activation.

In this chapter, we have investigated the relationship between the structural characteristics and dielectric properties of ceramic with the APs structure $Bi_{4+x}Sr_{2-x}Ti_xTa_{4-x}O_{18}$ (x = 0.0, 0.5, 1.0, 1.5, 2.0) in the dependence of the chemical composition. To perform this study, we measured the temperature dependences the relative permittivity $\varepsilon/\varepsilon_0(T)$ on the temperature, the loss tangent $\tan\delta$, obtained dependences of the permittivity $\varepsilon/\varepsilon_0$ maximum, Curie temperature T_C, unit cell parameters a, b, c, and volume V on concentration x. We have carried out X-ray diffraction investigations, measured the temperature dependences of the dielectric characteristics of new APs in the series $Bi_4Sr_2Ta_4O_{18}$, $Bi_{4.5}Sr_{1.5}Ti_{0.5}Ta_{3.5}O_{18}$, $Bi_5SrTiTa_3O_{18}$, $Bi_{5.5}Sr_{0.5}Ti_{1.5}Ta_{2.5}O_{18}$, $Bi_6Ti_2Ta_2O_{18}$.

14.2 Experimental

Polycrystalline APs samples were synthesized by solid solutions reaction of the corresponding oxides of Bi_2O_3, TiO_2, Ta_2O_5 and carbonate $SrCO_3$. After weighing and preliminary grinding of the starting compounds, the APs synthesis was carried out at a temperature of 870 °C (2 h), then a second grinding and annealing were synthesized at a temperature of 1100 °C (2 h), followed by grinding with the addition of a binder. Before the final firing, samples with a diameter of 9–9.5 mm and a thickness of 1.0–1.5 mm have been pressed, pre-heated at 600 °C for 2 h and were finally burnt at a temperature of 1100 °C (2 h).

To obtain the X-ray powder diffraction spectra, a DRON-3 M diffractometer was used with a GP 13 adapter for powder diffraction and a BSV21 Cu X-ray tube. $CuK\alpha_1,\alpha_2$-radiation was selected from the total spectrum using a Ni filter. The diffraction patterns were measured in the range of 2θ-angles from 10° to 60° with a scan step of 0.04° and an exposure of 20 s per point. The analysis of the profiles of the diffraction patterns, the determination of the positions of the lines, their indexing (*hkl*), and refinement of the unit cell parameters were performed with the PCW 2.4 program [21].

To perform the electric measurements, the samples were pressed as ~1 mm thick discs with 9 mm in diameter, and then Ag–Pd electrodes were deposited on the plane surfaces of the discs. The measurements were carried out using an E7-20 immittance meter in the frequency range 100 kHz–1 MHz at temperatures in the range from room temperature to 930 °C.

14.3 Results and Discussion

The X-ray powder diffraction diagrams of all $Bi_{4+x}Sr_{2-x}Ti_xTa_{4-x}O_{18}$ (x = 0.0, 0.5, 1.0, 1.5, 2.0) solid solutions under study correspond to single phase APs with m = 2 of the orthorhombic system with space group $A21am$ (36) and do not contain additional maxima. It is determined that all the APs obtained crystallize in orthorhombic system with the space group of the unit cell A21*am* (36). The unit cell values are refined on the base of the X-ray diffraction data and the volumes and values of the orthorhombic and tetragonal deformations, calculated on their base, as well as tolerance factors t are given in table form. The tolerance factor was introduced by Goldschmidt [22] as a parameter, determining the geometric variant of the ionic packing in cubic unit cell and characterizing the stability of the cubic structure:

$$t = \frac{R_A + R_O}{\sqrt{2}(R_B + R_O)},$$

R_A and R_B are the cation radii in positions A and B, respectively, R_O is the oxygen ion radius. In this work, the tolerance factor was calculated using the ionic radii by Shannon [23] R_O = 1.40 Å for O^{2-} (coordination number is 6), R_{Sr} = 1.44 Å for Sr^{2+} (coordination number is 12), R_{Ta} = 0.64 Å for Ta^{5+} (coordination number is 6), and R_{Ti} = 0.605 Å for Ti^{4+} (coordination number is 6). The radius of the Bi^{3+} ion, whose coordination number is 12 is not given in [23], and its value is found from the radius of the ion, whose coordination number is 8 by multiplying on the approximating coefficient 1.12, and we obtain R_{Bi} = 1.31 Å for Bi^{3+} (coordination number is 12). The highest stability range of the cubic structures corresponds to the range $0.9 \leq t \leq 1.0$, to which all values of the tolerance factors t are obtained for the APs, synthesized (Fig. 14.1).

The dependence of the unit cell parameters on the parameter x is shown in Fig. 14.2. The change in the unit cell volume in the aforementioned series does not exceed 4%. The changes the parameters of the crystal lattice of the APs $Bi_{4+x}Sr_{2-x}Ti_xTa_{4-x}O_{18}$ are caused by the difference in the radii of the ions in the dodecahedra and octahedra (positions A and B) of the perovskite-like layers, where the Ta^{5+} ions (R_{Ta5+} 0.64 Å [23]) are replaced by the Ti^{4+} with smaller radii (R_{Ti4+} = 0.605 Å [23]) and the Sr^{2+} ions (R_{Sr2+}= 1.44 Å [23]) are replaced by the Bi^{4+} with smaller radii (R_{Bi4+} = 0.1.31 Å [23]). The observed decrease in the unit cell volume is caused only by the decrease in the unit cell parameters a, whereas the

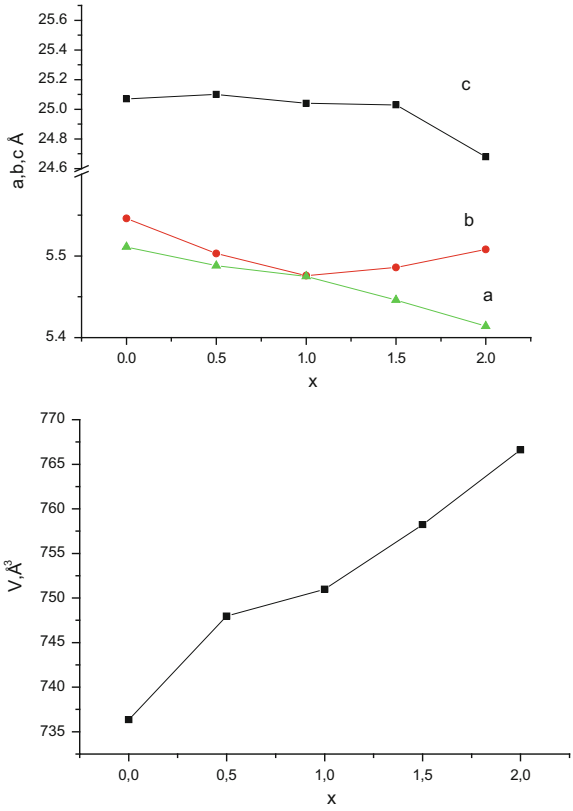

Fig. 14.1 Dependences of parameters a, b, c, volume V of the synthesized compounds $Bi_{4+x}Sr_{2-x}Ti_xTa_{4-x}O_{18}$ (x = 0.0, 0.5, 1.0, 1.5, 2.0) on the parameter x

parameters b, c decrease at concentration x = 0–1.0 and again increase at x = 1.0–2.2 and increases at x = 0.0–0.5 and decreases at concentration x = 0.5–2.0, respectively (Table 14.1).

The orthorhombic distortion Δa calculated based on the experimental lattice parameters is nonlinearly dependent on x as shown in Table 14.2. The orthorhombic distortion of the cell δb (Table 14.2) decreases substantially even at small x as compared to the undoped $Bi_6Ti_2Ta_2O_{18}$. The structure of APs and the degree of its distortion is frequently characterized using the following parameters [24, 25]: the average tetragonal period $a_t = (a_0 + b_0)/2^{3/2}$, the perovskite-like layer thickness $c' = 3c/(8 + 6\ m)$, and the relative distortion of oxygen octahedral along axis c: $\delta c' = (c' - a_t)/a_t$.

It is well-known fact that Curie temperature T_C of APs correlates the values of ionic radii R_A. It was noted that T_C APs decreases with increasing the ionic radius, and the ferroelectric–paraelectric phase transition itself becomes more diffuse [26]. In addition, it was shown in [26] that T_C of AP increases with decreasing tolerance

Table 14.1 Parameters of the crystal lattice: a, b, c, volume V, relative permittivity $\varepsilon/\varepsilon_0$, were measured at frequency of 100 kHz

Compound	a (Å)	b (Å)	c (Å)	V (Å^3)	$\varepsilon/\varepsilon_0$
$Bi_{6.0}$ $Ti_{2.0}Ta_{2.0}O_{18}$	5.414(4)	5.508(6)	24.68(9)	736.3(6)	956
$Bi_{5.5}$ $Sr_{0.5}Ti_{1.5}Ta_{2.5}O_{18}$	5.446(9)	5.486(3)	25.03(1)	747.9(7)	564
$Bi_5SrTiTa_3O_{18}$	5.475(2)	5.476(9)	25.04(4)	750.9(9)	354
$Bi_{4.5}$ $Sr_{1.5}Ti_{0.5}Ta_{3.5}O_{18}$	5.488(4)	5.503(4)	25.10(3)	758.2(3)	450
Bi_4 $Sr_2Ta_4O_{18}$	5.511(2)	5.546(9)	25.07(7)	766.6	400

Table 14.2 Parameters of the orthorhombic δb and tetragonal $\delta c'$ strains; average tetragonal period a_t; tolerance factor t; average thickness of single perovskite layer c_0, Cutie temperature T_C, and activation energy E_a of the samples under study

Compound	a_t (Å)	c_0 (Å)	δb (%)	t	$\delta c'$ (%)	T_C (°C)	E_a (eV)
$Bi_{6.0}$ $Ti_{2.0}Ta_{2.0}O_{18}$	3.861	3.7	1.7	0.951	−4.16	887	0.92/0.6/0.01
$Bi_{5.5}$ $Sr_{0.5}Ti_{1.5}Ta_{2.5}O_{18}$	3.865	3.75	0.71	0.952	−2.975	710	0.8/0.4/0.04
$Bi_5SrTiTa_3O_{18}$	3.872	3.756	0.03	0.954	−2.99	580	0.86/0.3/0.04
$Bi_{4.5}$ $Sr_{1.5}Ti_{0.5}Ta_{3.5}O_{18}$	3.886	3.765	0.2	0.955	−3.11	415	0.66/0.34/0.01
Bi_4 $Sr_2Ta_4O_{18}$	3.909	3.761	0.64	0.957	−3.78	335	0.32/0.55/0.077

factor t and respectively increase structural distortions. Similar dependence is also observed in $Bi_{4+x}Sr_{2-x}Ti_xTa_{4-x}O_{18}$ APs as it is seen in Fig. 14.2. The substitution of Ti^{4+} in the oxygen octahedra does not practically influence on the change in T_C in APs, since the ionic radii of doped cations B are slightly different and do not play a main structural role in polarization processes [27].

Along with the structural studies, we also measured the relative permittivity $\varepsilon/\varepsilon_0(T)$ (Fig. 14.3a, c, e, g, i) and dielectric loss tangent tgδ (Fig. 14.3b, d, f, h, j). Conductivity σ of the APs at various frequencies of 100–1000 kHz and the current activation energy E_a were calculated in various temperature ranges.

As is seen from Fig. 14.3, all temperature dependences $\varepsilon/\varepsilon_0$ (T) (Fig. 14.3) have a clear peak corresponding to the phase transition from the orthorhombic to cubic phase. The Curie temperatures T_C of all the samples were found at this peak position (Table 14.2).

The dependence of T_C on x and t is almost linear, which agrees with the results of R_{Ti4+}, R_{Ta5+} preceding studies [28–30], and it is a further proof that the solid solutions are single phase. However, the value of the permittivity maximum is strongly nonlinear in x. It should be noted that earlier dielectric studies of the solid solutions of this system [28] indicate more pronounced nonlinearity of the above dependence.

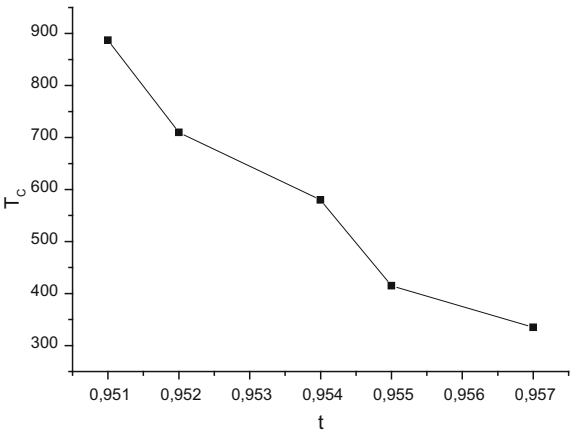

Fig. 14.2 Dependence of the Curie temperature T_C on tolerance factor t for $Bi_{4+x}Sr_{2-x}Ti_xTa_{4-x}O_{18}$ (x = 0.0, 0.5, 1.0, 1.5, 2.0)

Thus, it can be concluded that, in the compounds under study, the structural changes leading to a nonlinear decrease in the orthorhombic distortion with varying the composition influence substantially the value of the permittivity maximum and almost do not influence the Curie temperature that varies linearly over entire concentration range.

The temperature dependences of tanδ (Fig. 14.3b) for the Aurivillius phases under study show a sharp increase in the dielectric loss at high temperatures (>500 °C). This increase is due to a large number of charge carriers, whose concentration increases sharply at high temperatures due to formation of oxygen vacancies. However, the values of tanδ (Fig. 14.3b, d, f, h, j), taken at a certain temperature, e.g., T_C, differ several times for different APs, under study, and this fact indicates different degrees of defects of the crystal structure of the APs.

Based on the dependence of ln σ on $1/kT$, we calculated the activation energy of the charge carriers E_a for the full series of APs (Table 14.2). Figure 14.4 shows a typical ln $\sigma = f(1/kT)$ dependence for $Bi_5SrTi_3TaO_{18}$, and we clearly see that there are three temperature ranges, in which the values of activation energy differ significantly.

This is due to that at high temperatures the dominant charge carrier in the APs represents internal defects, the formation of which requires high activation energies. At low temperatures, the conductivity is mainly due to impurity defects, which have substantially lower activation energies. It should be noted that the activation energies of all $Bi_{4+x}Sr_xTi_{2-x}Ta_{2+x}O_{18}$ (x = 0.0, 0.5, 1.0, 1.5, 2.0) series compounds are close in low-temperature ranges, and this indicates that the conductivity in this range does not change. At the same time, changes occur in the high-temperature region indicating the appearance of new charges carriers.

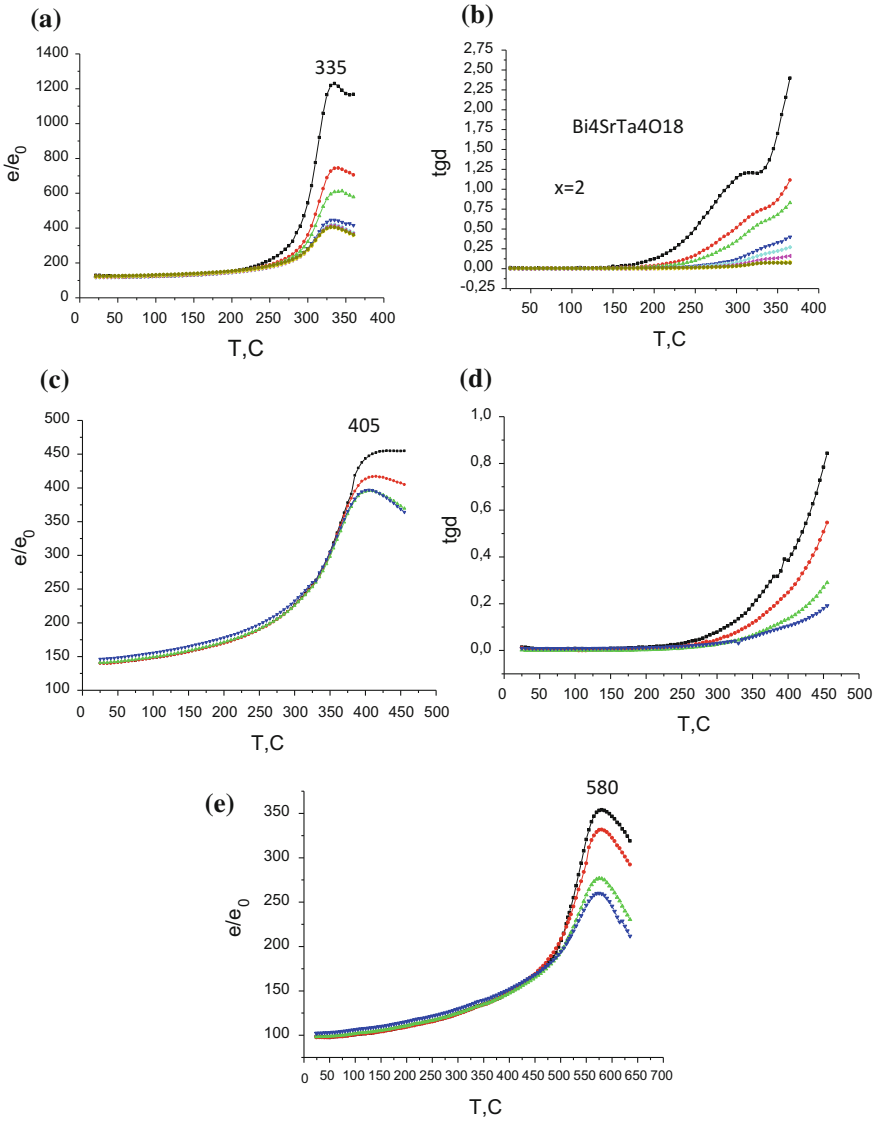

Fig. 14.3 Temperature dependences of the relative permittivity $\varepsilon/\varepsilon_0(T)$ (**a**, **c**, **e**, **g**, **i**) and loss tangent tgδ (**b**, **d**, **f**, **h**, **j**) for $Bi_{4+x}Sr_{2-x}Ti_xTa_{4-x}O_{18}$ (x = 0.0, 0.5, 1.0, 1.5, 2.0)

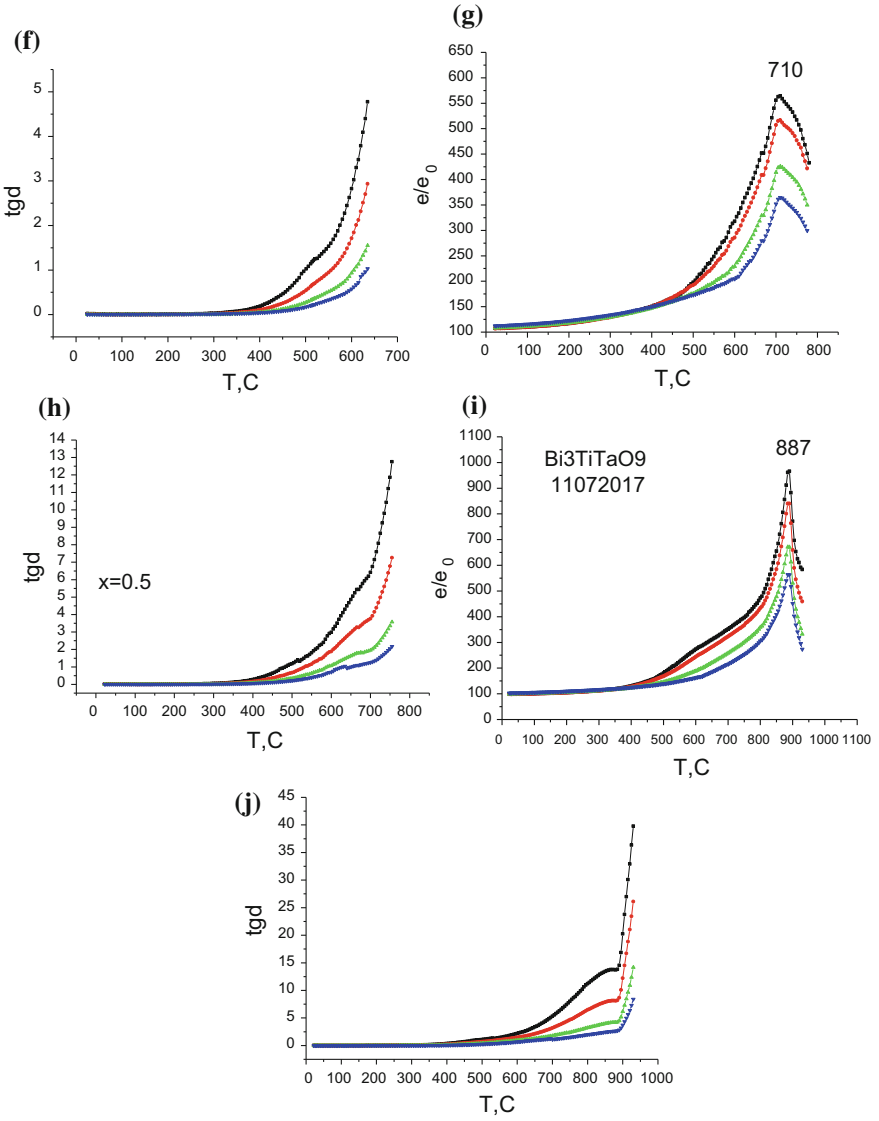

Fig. 14.3 (continued)

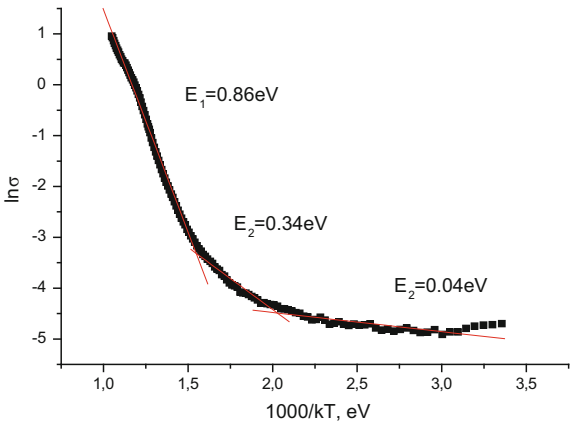

Fig. 14.4 Dependence of ln σ on $1/kT$ for the $Bi_5SrTi_3TaO_{18}$ sample

14.4 Conclusions

The performed structural and dielectric studies of the series of layered perovskite-like oxides $Bi_{4+x}Sr_{2-x}Ti_xTa_{4-x}O_{18}$ (x = 0.0, 0.5, 1.0, 1.5, 2.0) with the APs structure show that the lattice parameter, corresponding to the polar direction, is not deviated from the Vegard's law. The dependence of the orthorhombic distortion on x is non-linear. However, this nonlinearity of the structural parameters does not influence the Curie temperature that varies linearly over entire concentration range. The examination of the specific features of the electrical conductivity of APs demonstrated that all the studied compounds are characterized by several temperature regions with significantly different activation energies, corresponding to the different nature of the charge carriers in these compounds.

Acknowledgements The work was performed with the financial support by the Ministry of Education and Science of the Russian Federation (Project No. 3.5710.2017/8.9).

References

1. B. Aurivillius, Arkiv. Kemi **1**(54), 463 (1949)
2. B. Aurivillius, Arkiv. Kemi **1**(58), 499 (1949)
3. B. Aurivillius, Arkiv. Kemi **2**(37), 512 (1950)
4. S.V. Zubkov, V.G. Vlasenko, J. Phys. Solid State **59**(12), 2325 (2017)
5. S.V. Zubkov, V.G. Vlasenko, V.A. Shuvaeva, J, Phys. Solid State **58**(1), 44 (2016)
6. B.H. Park, B.S. Kang, S.D. Bu, T.W. Noh, J. Lee, W. Jo, Nature **401**, 682 (1999)
7. Y.T. Kim, C.W. Lee, Jpn. J. Appl. Phys. Part 1 **35**, 6153 (1996)
8. C.A. de Araujo, J.D. Cuchlaro, L.D. McMillan, M.C. Scott, J.F. Scott, Nature **374**, 627 (1995)
9. K. Amanuma, T. Hase, Y. Miyasaka, Appl. Phys. Lett. **66**, 221 (1995)
10. D. Ito, T. Yoshimura, N. Fujimura, T. Ito, Appl. Surf. Sci. **138**, 159 (2000)
11. T. Kijima, Y. Fujisaki, H. Ishiwara, J. Appl. Phys. **40**, 2977 (2001)
12. M. Dawber, K.M. Rabe, J.F. Scott, Rev. Mod. Phys. **77**, 1083 (2005)

13. A.P. de Araujo, J.D. Cuchiaro, L.D. Mcmillan, M.C. Scott, J.F. Scott, Nature **374**, 627 (1995)
14. S.B. Majumder, P.S. Dobal, S. Bhaskar, R.S. Katiyar, Ferroelectrics **241**, 287 (2000)
15. Y. Cheol-Hoon, K. Jae-Sun, Y. Soon-Gil, Integr. Ferroelectr. **21**, 475 (1998)
16. X. Chen, J. Xiao, Y. Xue, X. Zeng, F. Yang, P. Su, Ceram. Int. **40**, 2635 (2014)
17. V.G. Vlasenko, V.A. Shuvaeva, S.I. Levchenkov, Ya.V. Zubavichus, S.V. Zubkov, J. Alloys Compd. **610**, 184 (2014)
18. H. Zou, X. Hui, X. Wang, D. Peng, J. Li, Y. Li, X. Yao, J. Appl. Phys. **114**, 223103 (2013)
19. H. Nakajima, T. Mori, S. Itoh, M. Watanabe, Solid State Commun. **129**, 421 (2004)
20. F. Gao, G.J. Ding, H. Zhou, G.H. Wu, N. Qin, D.H. Bao, J. Electrochem. Soc. **158**(5), G128 (2011)
21. W. Kraus, G. Nolze, *Powder Cell for Windows, Version 2.3* (Federal Institute for Materials Research and Testing, Berlin, Germany, 1999)
22. V.M. Goldschmidt, *Geochemisca Veterlun* (Norske Videnkap, Oslo, 1927)
23. R.D. Shannon, Acta Crystallogr. Sect. A. Cryst. Phys. Diffr. Theor. Gen. Crystallogr. **32**, 75 (1976)
24. V.A. Isupov, Zh Neorg, Khim. **39**(5), 731 (1994)
25. V.A. Isupov, Inorg. Mater. **42**(11), 1236 (2006)
26. E. Subbarao, Integr. Ferroelectr. **12**, 33 (1996)
27. Y. Shimakawa, Y. Kubo, Y. Nakagawa, S. Got, T. Kamiyama, H. Asano, F. Izumi, Phys. Rev. B: Condens. Matter **61**, 6559 (2001)
28. B. Jiménez, L. Pardo, A. Castro, P. Millán, R. Jiménez, M. Elaatmani, M. Oualla, Ferroelectrics **241**, 279 (2000)
29. T. Sivakumar, M. Itoh, J. Mater. Chem. **21**, 10865 (2011)
30. D.Y. Suarez, I.M. Reaney, W.E. Lee, J. Mater. Res. **16**, 3139 (2001)

Chapter 15
Structure and Magnetic Properties of $(1 - x)BiFeO_3$–$xPbFeO_3$ Solid Solutions

A. G. Rudskaya, S. P. Kubrin, A. V. Shevchuk, N. M. Teslenko, Yu. V. Kabirov, A. V. Nazarenko, N. M. Novikovsky, M. F. Kupriyanov, D. I. Rudsky, N. B. Kofanova and A. V. Pavlenko

Abstract In this paper, there are presented the studies' results of the structures and magnetic properties of the $(1 - x)BiFeO_3$–$xPbFeO_3$ solid solutions with $x = 0.05$; 0.10; 0.15; 0.20; 0.25; 0.30; 0.50. It has been established that at room temperature in the compositions $x = 0.05$ and $x = 0.10$, there is a rhombohedral phase of $R3c$, in the compositions with $x = 0.15$–0.30 there exists a pseudocubic phase of $Pm\text{-}3m$ and there is a rhombohedral phase of $R\text{-}3c$ in the composition with $x = 0.50$. Using the γ-resonance method, it has been established that the Fe^{3+} ions are present in all the compositions, which corresponds to the non-stoichiometry of the oxygen ions.

15.1 Introduction

Physical properties, such as charge transfer, magnetic and ferroelectric properties in the oxygen-octahedral structures are determined by the presence of *d*-elements in the octahedral oxygen environment. At the same time, the role of the cations occupying cuboctahedral positions in the oxygen-octahedral structures is less defined in the manifested physical properties. Such cations are, as a rule, characterized by *s*-states (Ca, Sr, Ba). Cations with *sp*-states (Pb, Bi) determine *sp*-hybridization of the states in the cation—oxygen systems.

A. G. Rudskaya (✉) · A. V. Shevchuk · Yu. V. Kabirov · M. F. Kupriyanov
D. I. Rudsky · N. B. Kofanova
Department of Physics, Southern Federal University, Rostov-on-Don 344090, Russia
e-mail: arudskaya@yandex.ru

S. P. Kubrin · N. M. Teslenko · N. M. Novikovsky · A. V. Pavlenko
Research Institute of Physics, Southern Federal University, Rostov-on-Don 344090, Russia

A. V. Nazarenko · A. V. Pavlenko
Southern Scientific Centre of Russian Academy of Science, Rostov-on-Don 344006, Russia

I. A. Parinov et al. (eds.), *Advanced Materials*, Springer Proceedings in Physics 207, https://doi.org/10.1007/978-3-319-78919-4_15

The ferroelectric properties of the lead-containing oxides with a perovskite structure are explained by the formation of the asymmetric electron configurations described by the combination of *s*- and *p*-atomic states, which are the characteristic of the Pb atom ($6s^2 6p^2$). It has also been stated that similar possibilities exist for Bi ($6s^2 6p^3$) and Tl ($6s^2 6p$) [1].

An inert 6*s* unshared electron pair in the Bi^{3+} ions (in particular in $BiFeO_3$) is the main reason for the occurrence of ferroelectricity. Such pairs are characterized by high polarizability. Clearly, the appearance of the polarization can be represented as the process of ordering of such electron pairs in one direction. The presence of a number of the magnetic ions [2, 3], such as Cr^{3+}, Mn^{2+}, Mn^{3+}, Mn^{4+}, Fe^{3+}, Fe^{2+}, Co^{3+}, Ni^{2+}, in such structures can additionally lead to the existence of the magnetic properties. In such cases, the compounds and solid solutions are multiferroics.

The combination effects in the structure of the ABO_3 perovskite type of the Bi^{3+} and Pb^{2+} ions in the *A* positions and Fe^{3+}/Fe^{4+} ions in the *B* positions can be observed in $(1 - x)BiFeO_3$–$xPbFeO_3$ solid solutions [4, 5]. Formally, the balance of valencies in $PbFeO_3$ requires either tetravalence of the Fe^{4+} iron ions [2, 6, 7], or the non-stoichiometry in oxygen content [8–11].

Examination of the anion-deficient perovskites with the crystallographic shift of planes on oxygen vacancies shows that in cases of lead-containing compounds (for example, $Pb_2Fe_2O_5$), Pb ions can be displaced from the centers of the cuboctahedral positions of the perovskite structure. It leads to ferroelectric spontaneous polarization, which interacts with the ordering of the magnetic moments of transition cations, such as Fe [12]. Such materials are potential multiferroics.

The results of investigations of the chemical composition, microstructures, structures, and magnetic properties of $(1 - x)BiFeO_3$–$xPbFeO_3$ solid solutions with $x = 0.05$, 0.10, 0.15, 0.20, 0.25, 0.30, 0.50 are presented.

15.2 Samples and Experimental Methods

15.2.1 Solid-Phase Synthesis

Compositions of $(1 - x)BiFeO_3$–$xPbFeO_3$ solid solutions with $0.05 \leq x \leq 0.30$ and the step $\Delta x = 0.05$ and $x = 0.50$ were prepared by the solid-phase synthesis. As initial reagents there were used the oxides of bismuth (Bi_2O_3), iron (Fe_2O_3) and lead (PbO). Before the preparation of the corresponding stoichiometric mixtures, these reagents were checked by the X-ray diffraction analysis. The synthesis of the samples of the $(1 - x)BiFeO_3$–$xPbFeO_3$ system was carried out by the annealing at temperatures $T_1 = 700$ °C (for 3 h) and $T_2 = 750$ °C (for 3 h) after mixing of the stoichiometric mixtures in the ethanol during one hour. The chemical composition of the samples showed that they were characterized by the same ratio of the content of Bi and Pb ions, which was used in the initial oxide mixtures.

15.2.2 Microstructure

Microstructure studies of the samples of the $(1 - x)BiFeO_3$–$xPbFeO_3$ system were performed by scanning laser microscopy using the KEYENCE VK-9700 scanning laser microscope (violet, 408 nm). Images were constructed by confocal microscopy. In this case, the images taken in focus at different depths of the sample were shot sequentially. Anything above or below the focus was cut off by a confocal slit, leaving only the surface which was clear at a given depth. Scanning took place in the interior of the sample in steps of 0.2 μm, after which all the images, obtained at different depths, were "stitched together", forming a clear two-dimensional picture. Samples were measured with an increase of ×1000 and ×3000.

15.2.3 X-ray Spectral Analysis

The chemical composition of the samples was tested on an X-ray fluorescent TXRF spectrometer RFS-001 (MoK_α–radiation) with an Amptek detector with an energy resolution of approximately 180 eV. Registration and processing of X-ray fluorescence spectra was performed in the UniverRS program. A refinement of the content of $PbFeO_3$ for $(1 - x)BiFeO_3$–$xPbFeO_3$ solid solutions was performed using the experimental data of X-ray fluorescence of the Bi and Pb ions [13].

15.2.4 X-ray Diffraction Analysis

All the samples were studied at room temperature by X-ray diffraction on a DRON-3 M diffractometer (CuK_α–radiation, Ni–filter) with Bragg-Brentano focusing ($\theta - 2\theta$). The registration of diffraction profiles was performed in the range of angles $20° \leq 2\theta \leq 60°$ in the step-by-step scanning mode of the sample detector with a step of 0.02 deg and a pulse-recruitment time at each point $\tau = 2$ s. The choice of this range of angles 2θ was due to the fact that it contained the most intense diffraction maxima. The extension of the interval toward the angles 2θ 60° led to the possibility of consideration of the weak maxima of reflections' higher orders when spesified. At the same time, there was a strong overlap of these maxima, which, of course, did not improve the results of refinement of structural parameters. The specification of structural parameters was performed using the computer program PowderCell 2.3.

15.2.5 Mossbauer Spectroscopy

The Mossbauer spectra were measured with a spectrometer MS1104Em. ^{57}Co was used as a source of γ-quanta in the Cr matrix. Model decoding was performed in the program SpecrReah [14]. Isomeric shifts were given with respect to α-Fe.

15.3 Results and Discussion

The chemical composition of the samples, annealed at T_1 = 700 °C and T_2 = 750 °C, showed (Fig. 15.1) that they were characterized by the ratio of the Bi and Pb ion content that was incorporated into the initial oxide mixtures. Figure 15.2 presents the photographs of the microstructures of $(1 - x)BiFeO_3$–$xPbFeO_3$ solid solutions after the synthesis at T_1 = 700 °C (x = 0.50) and after the synthesis at T_2 = 750 °C (x = 0.05, 0.10, 0.15, 0.20, 0.25, 0.30, 0.50). The microstructure of the samples on the chips is basically a mixture of "nano-sized" crystallites (0.5–1 μm). In some samples, there are large crystallites of 4–5 μm size.

In compositions with x = 0.05, 0.30, and 0.50, a noticeable increase in the amount of "large" crystallites is observed with an increase in the annealing temperature. For other compositions with x = 0.10 and x = 0.20, an increase in the annealing temperature does not lead to appreciable changes in the crystallite size.

Figure 15.3 shows the X-ray diffraction profiles of the compositions of $(1 - x)$ $BiFeO_3$–$xPbFeO_3$ solid solutions after the synthesis at T_2 = 750 °C. All diffraction profiles were used to refine the structures of the phases, existing in the samples. Table 15.1 shows the concentrations of the perovskite (C_1), the impurity phases $Bi_2Fe_4O_9$ (C_2), $Bi_{25}FeO_{40}$ (C_3), and Pb_2BiO_4 (C_4).

Table 15.2 presents the structural parameters of the compositions of $(1 - x)$ $BiFeO_3$–$xPbFeO_3$ solid solutions with x = 0.10, 0.15 and 0.50 after their synthesis at T_2 = 750 °C and also shows the refinement results of the atomic parameters for these compositions. Figure 15.4 shows the dependence of the volumes of the unit cells per one formula unit of ABO_3, V_{ABO3} and the existence region at room temperature of rhombohedral phases $R3c$ and R-$3c$ and cubic phases Pm-$3m$. The inset of the figure shows the ratio of the parameters c_H/a_H, where a_H and c_H are the parameters of the elementary cells of the perovskite structure in hexagonal installations. The parameters $\mathbf{a}_H = \mathbf{a}_p + \mathbf{b}_p$ and $\mathbf{c}_H = 2(\mathbf{a}_p + \mathbf{b}_p + \mathbf{c}_p)$, where $\mathbf{a}_p$, $\mathbf{b}_p$ and $\mathbf{c}_p$ are translations of the perovskite structure. It can be seen that after the synthesis at T_2 = 750 °C the compositions with x = 0.05 and x = 0.10 are characterized by the rhombohedral phase $R3c$ and by a decrease in the c_H/a_H with increasing of x with the reducing of the period c_H, which corresponds to a reduction of the spontaneous polarization. It is noteworthy that a region $R3c$ phase exists after the synthesis tapers at T_2 = 750 °C as compared with the area of the initial phase after the synthesis at T_1 = 700 °C. Compositions with x = 0.15–0.30 are characterized by

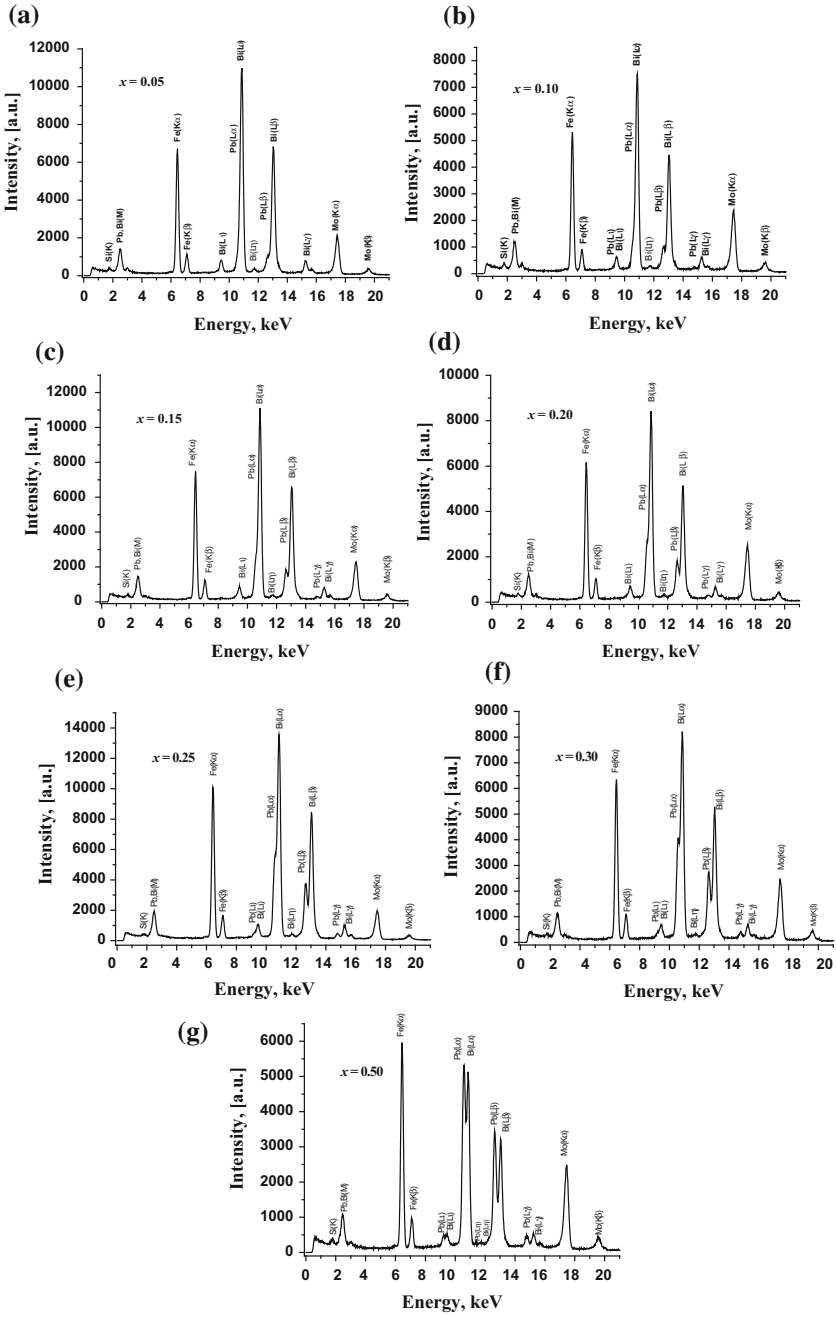

Fig. 15.1 X-ray fluorescence spectra of compositions of $(1 - x)BiFeO_3$–$xPbFeO_3$ solid solutions, prepared at T_2 = 750 °C: **a** x = 0.05; **b** x = 0.10; **c** x = 0.15; **d** x = 0.20; **e** x = 0.25; **f** x = 0.30; **g** x = 0.50

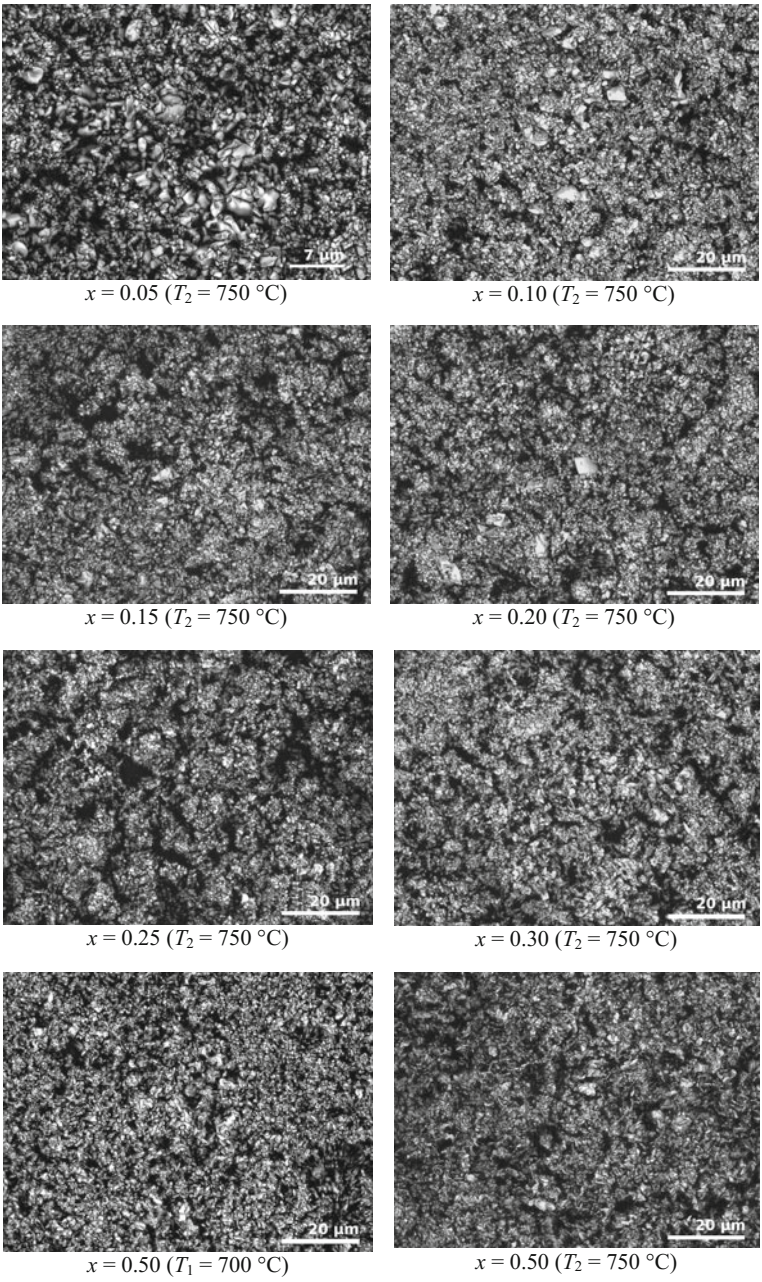

$x = 0.05$ ($T_2 = 750$ °C) $x = 0.10$ ($T_2 = 750$ °C)

$x = 0.15$ ($T_2 = 750$ °C) $x = 0.20$ ($T_2 = 750$ °C)

$x = 0.25$ ($T_2 = 750$ °C) $x = 0.30$ ($T_2 = 750$ °C)

$x = 0.50$ ($T_1 = 700$ °C) $x = 0.50$ ($T_2 = 750$ °C)

Fig. 15.2 Microstructures of the compositions of $(1 - x)BiFeO_3$–$xPbFeO_3$ solid solutions after the synthesis at $T_1 = 700$ °C ($x = 0.50$) and after the synthesis at $T_2 = 750$ °C with $x = 0.05$, 0.10, 0.15, 0.20, 0.25, 0.30, 0.50

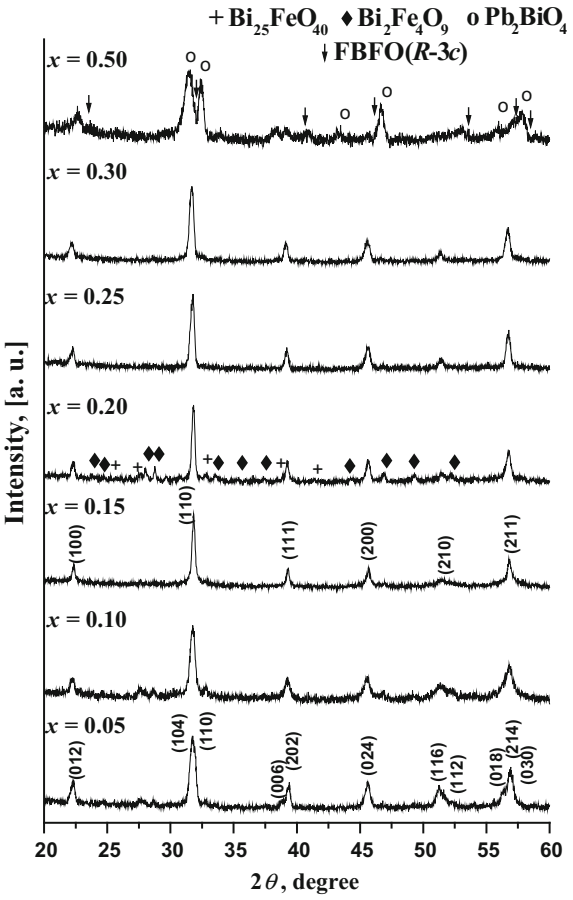

Fig. 15.3 X-ray diffraction profiles of the compositions of $(1 - x)BiFeO_3$–$xPbFeO_3$ solid solutions after the synthesis at T_2 = 750 °C

cubic phases *Pm*-3*m*. The composition with $x = 0.50$ is characterized by the rhombohedral phase *R*-3*c* with the ratio c_H/a_H equal to 2.46. It is noteworthy that there is the contrast of the *R*-3*c* phase from the *R*3*c* phase, consisting in the fact that in this phase the rhombohedral perovskite cell is compressed by the threefold axis unlike the cell stretching along the polar axis in the third order phase *R*3*c*, which is associated with the presence of the spontaneous polarization of the ferroelectric.

The Mossbauer spectra of $(1 - x)BiFeO_3$–$xPbFeO_3$ solid solutions with $x = 0.30$ and $x = 0.50$, measured at room temperature, are shown in Fig. 15.5. The spectra are a superposition of different number of sextets the parameters of which are given in Table 15.3. The parameters of the sextets differ from the parameters of the Mossbauer spectra, measured for $BiFeO_3$ [15, 16]. The isomeric chemical shifts in all spectra correspond to the Fe^{3+} ions [17] in various oxygen environments.

Table 15.1 Phase composition of the samples of $(1 - x)BiFeO_3$–$xPbFeO_3$ solid solutions at room temperature after the sequential synthesis at T_1 = 700 °C and T_2 = 750 °C[a]

T (°C)	x	$(1 - x)$BFO–xPFO C_1 (%)	$Bi_2Fe_4O_9$ C_2 (%)	$Bi_{25}FeO_{40}$ C_3 (%)	Pb_2BiO_4 C_4 (%)
700	0.05	60.0	27.2	12.8	–
	0.10	52.2	33.9	13.9	–
	0.15	76.1	17.3	6.6	–
	0.20	84.8	12.8	2.5	–
	0.25	98.3	–	1.7	–
	0.30	100.0	–	–	–
	0.50	43.6	–	–	56.4
750	0.05	94.2	1.8	4.0	–
	0.10	75.8	17.6	6.6	–
	0.15	97.6	–	2.4	–
	0.20	64.9	20.1	15.0	–
	0.25	97.0	3.0	–	–
	0.30	100.0	–	–	–
	0.50	45.0	–	–	55.0

[a]C_i concentration of phases, determined with accuracy ±0.5%

The sample spectrum of $0.70BiFeO_3$–$0.30PbFeO_3$ (T_1 = 700 °C) consists of three sextets. Sextet *S*1 has an isomer shift of 0.4 mm/s, which corresponds to the Fe^{3+} state in the octahedral environment. A small value of the quadrupole bias ($\varepsilon = -0.08$) indicates a weak distortion of the oxygen octahedra. The magnitude of the isomeric shift of the sextet *S*3 is the characteristic for the Fe^{3+} ions with a coordination number 5, which indicates the presence of an oxygen deficiency. In addition, the high value of the quadrupole displacement indicates strong distortions of the oxygen polyhedra. The component *S*2 is conditioned by the Fe^{3+} ions in the oxygen octahedra. Relatively high, in comparison with the component *S*1, the magnitude of the quadrupole displacement, indicating more significant distortions of the oxygen octahedra, suggests that these octahedra directly border on the oxygen polyhedra of the component *S*3. The difference in the magnitudes of magnetic hyperfine fields on Fe^{57} nuclei is due to several different contributions to the field, conditioned by the following exchange interactions: Fe_{Oct}–O–Fe_{Oct}, Fe_{Oct}–O–Fe_{Pol}, and Fe_{Pol}–O–Fe_{Pol} [18, 19]. Large values of the widths of the Mössbauer spectra are apparently due to inhomogeneities in the oxygen environment of Fe^{3+}. That is, in the samples there are sets of the oxygen octahedra and polyhedra, surrounding the Fe^{3+} ions, each of which is slightly different from the others. Thus, the component represents some «averaged» oxygen octahedron or

Table 15.2 Structural parameters $(1 - x)BiFeO_3$–$xPbFeO_3$ at room temperature, for compositions with $x = 0.10$, 0.15 and 0.50, synthesized at $T_2 = 750$ °C

x		0.10	0.15	0.50
Space group		*R*3*c*	*Pm*-3*m*	*R*-3*c*
a_H (Å)		5.587(3)	–	5.506(3)
c_H (Å)		13.807(4)	–	13.438(4)
a_p (Å)		3.962(3)	3.963(3)	3.889(3)
α (deg)		89.66(2)	90.00	90.14(2)
V_{ABO3} (Å^3)		62.20(2)	62.22(2)	58.81(2)
c_H/a_H		2.47(1)	2.46(1)	2.46(1)
C_p (%)		76.3(5)	97.6(5)	40.9(5)
Bi/Pb	*x* *y* *z*	0 0 1	0 0 0	0 0 0.25
B(Bi/Pb) (Å^2)		0.1	0.15	0.15
Fe	*x* *y* *z*	0 0 0.25	0.5 0.5 0.5	0 0 0
B(Fe) (Å^2)		0.1	0.15	0.15
O	*x* *y* *z*	0.475 0.015 0.955	0 0.5 0.5	0.446 0 0.25
B(O) (Å^2)		0.1	0.05	0.1
R_p (%)		5.4	5.7	6.7
R_{wp} (%)		6.8	7.3	8.4
R_{exp} (%)		0.4	0.5	0.2
$l_{Bi/Pb–O}$		2.287(3)	2.807(3)	2.458(3)
$l_{Bi/Pb–O}$		2.686(3)	–	3.049(3)
$l_{Bi/Pb–O}$		3.040(3)	–	2.762(3)
$l_{Fe–O}$		1.776(2)	1.985(2)	1.967(2)
$l_{Fe–O}$		2.355(2)	–	–
$l_{O–O}$		2.686(3)	2.807(3)	2.801(3)
$l_{O–O}$		2.827(3)	–	2.762(3)
$l_{O–O}$		2.811(3)	–	2.801(3)
$l_{O–O}$		2.936(3)	–	–

polyhedron. A similar picture is observed for the Mossbauer spectrum of the sample $0.70BiFeO_3$–$0.30PbFeO_3$ ($T_2 = 750$ °C).

In the spectra of the samples with $x = 0.50$, another picture is observed. So the component *S*1 has lower values of δ and B_{eff} in comparison with the similar component of the sample $x = 0.30$ ($T_1 = 700$ °C). In addition, *S*1 has a large value

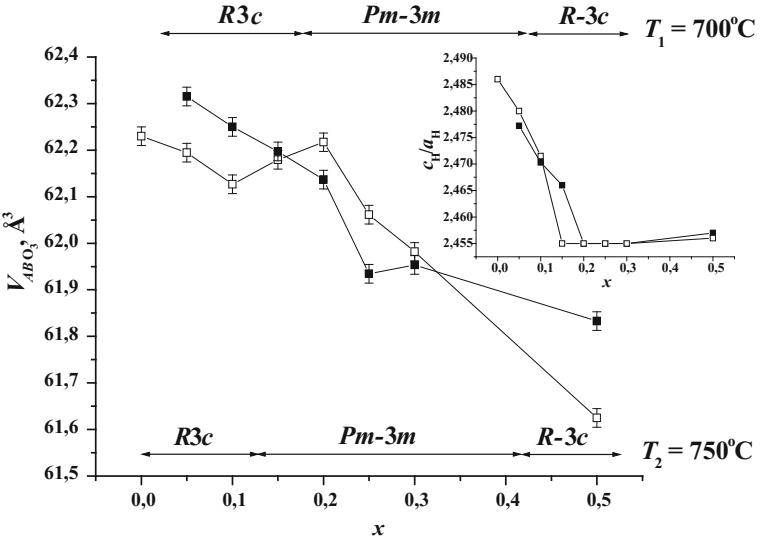

Fig. 15.4 Dependence of the volumes of the unit cells per one formula unit of ABO_3, and the existence region at room temperature of rhombohedral phases *R*3*c* and *R*-3*c* and cubic phases *Pm*-3*m* for $(1 - x)BiFeO_3$–$xPbFeO_3$ solid solutions; the inset of the figure shows the ratio of the parameters c_H/a_H (filled square—T_1 = 700 °C; open square—T_2 = 750 °C)

of ε, which indicates a strong distortion of the oxygen octahedra. All this suggests that this component corresponds to the Fe^{3+} ions in the oxygen octahedra bordering on the oxygen polyhedra with a lower coordination number. Components *S*2, *S*3, *S*4 and *S*5 correspond to the Fe^{3+} ions in the oxygen polyhedra with coordination number 5. Differences between these components are connected mainly with the degree of distortion of the polyhedra. The low B_{eff} values for the components *S*3, *S*4, *S*5 are probably conditioned by the low value of the temperature of the magnetic phase transition.

Thus, the iron ions are only in the Fe^{3+} state in the samples of ceramics $(1 - x)$ $BiFeO_3$–$xPbFeO_3$ (x = 0.30, 0.50), and charge compensation for the replacement of the Bi^{3+} ions by the Pb^{2+} ions occurs through the formation of the oxygen vacancies.

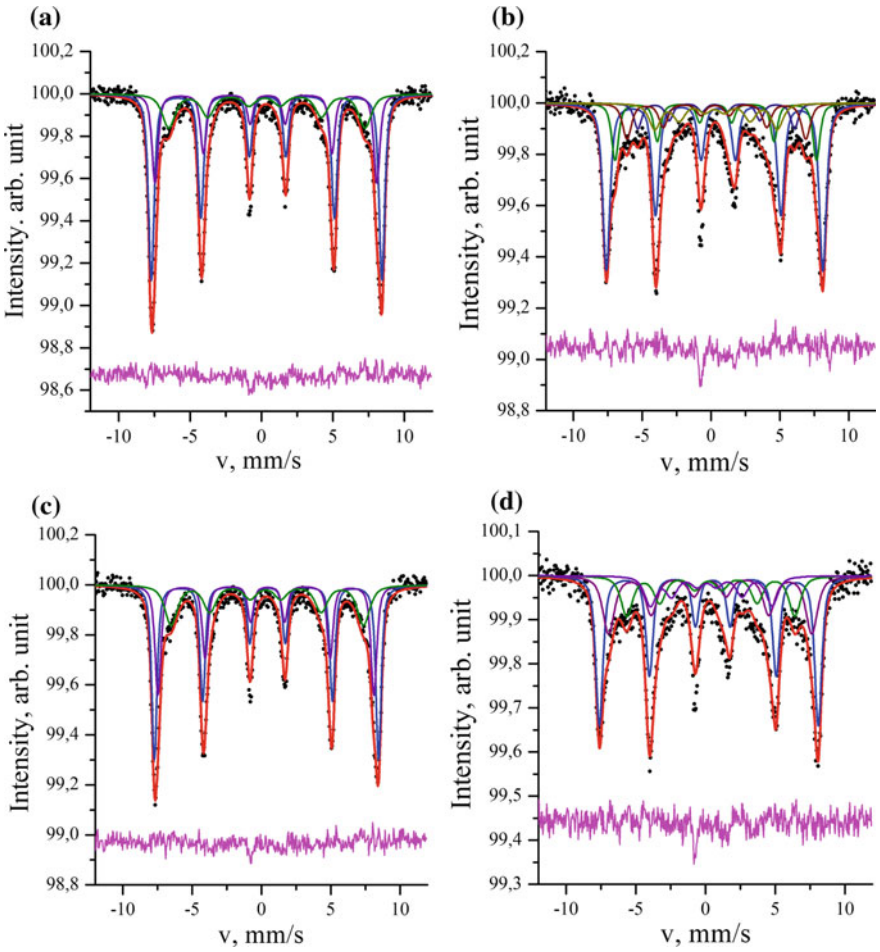

Fig. 15.5 Mossbauer spectra of the $(1 - x)BiFeO_3$–$xPbFeO_3$ ceramic samples, measured at room temperature: **a** $0.70BiFeO_3$–$0.30PbFeO_3$ and **b** $0.50BiFeO_3$–$0.50PbFeO_3$ at $T_1 = 700$ °C; **c** $0.70BiFeO_3$–$0.30PbFeO_3$ and **d** $0.50BiFeO_3$–$0.50PbFeO_3$ at $T_2 = 750$ °C

Table 15.3 Parameters of Mossbauer spectra of the samples of ceramics $(1 - x)BiFeO_3$–$xPbFeO_3$ solid solutions ($x = 0.30$, 0.50), measured at room temperature: δ is the isomeric chemical shift; ε is the quadrupole displacement; B_{eff} is the effective magnetic field on Fe^{57} nuclei; S is the area of the components of the spectrum; G is the width of spectral lines, χ^2 is the Pearson's criterion

Sample		Component	δ (mm/s)	ε (mm/s)	B_{eff} (T)	S (%)	G (mm/s)	χ^2
$T_1 = 700$ °C	$x = 0.30$	*S*1	0.40	−0.08	50.1	52	0.48	1.616
		*S*2	0.37	−0.12	48.2	27	0.51	
		*S*3	0.30	0.16	42.7	21	1.01	
	$x = 0.50$	*S*1	0.39	−0.26	48.8	49	0.62	1.691
		*S*2	0.34	0.01	45.4	18	0.61	
		*S*3	0.34	0.10	40.3	13	0.77	
		*S*4	0.31	0.12	35.3	8	0.65	
		*S*5	0.31	0.10	27.6	12	1.00	
$T_2 = 750$ °C	$x = 0.30$	*S*1	0.40	−0.08	50.1	49	0.50	1.441
		*S*2	0.38	−0.12	48.1	26	0.54	
		*S*3	0.35	0.12	43.0	25	1.18	
	$x = 0.50$	*S*1	0.38	−0.28	48.7	41	0.61	1.335
		*S*2	0.32	0.02	45.3	27	0.99	
		*S*3	0.30	0.16	37.5	18	1.00	
		*S*4	0.30	0.32	27.2	14	1.00	

15.4 Conclusion

The main feature of the structures of $(1 - x)BiFeO_3$–$xPbFeO_3$ solid solutions is that the cubic phase *Pm*-3*m* ($x = 0.15$, 0.20, 0.25, 0.30) is observed at room temperature between *R*3*c* ($x = 0$, 0.05 and 0.10) and *R*-3*c* ($x = 0.50$) after the synthesis at $T_2 = 750$ °C. The presence of a cubic phase at room temperature indicates that the phase transitions in the corresponding compositions occur at lower temperatures.

The Mossbauer study of the compositions of the solid solutions of the $(1 - x)$ $BiFeO_3$–$xPbFeO_3$ system with $T_1 = 700$ °C and $T_2 = 750$ °C has shown that all the iron ions in the solid solution compositions under study are in the Fe^{3+} state. An increase in the concentration of the Pb^{2+} ions leads to the appearance of the oxygen vacancies with Fe^{3+}, and not to the formation of the mixed valence state of $Fe^{3+} \leftrightarrow Fe^{4+}$. The oxygen deficit leads to a decrease in μ_{Fe}, which weakens the magnetic properties of this system.

Acknowledgements This work was supported by the Southern Federal University grant No. VnGr-07/2017-23, by the Ministry of Education and Science of the Russian Federation Projects No. 3.5346.2017/8.9 and by the Russian Foundation for Basic Research grant No. 16-32-60095.

References

1. J.B. Goodenough, J.M. Longo, in *Landolt-Börnstein New Series III*, vol. 4, ed. by K.-H. Hellwege, A.M. Hellwege (Springer, Berlin, 1970), p. 207
2. J.B. Goodenough, J. Zhou, Sci. Technol. Adv. Mater. **16**, 036003 (2015)
3. R. Asih, M. Gufron, D. Darminto, Padjadjaran Inter. Phys. Symp. **1554**, 50 (2013)
4. I.O. Troyanchuk, O.S. Mantytskaya, A.N. Chobot, N.V. Tereshko, Phys. Solid State **51**(10), 2105 (2009) (in Russian)
5. I.O. Troyanchuk, M.V. Bushinsky, D.V. Karpinsky, V. Sirenko, V. Sikolenko, V. Efimov, Eur. Phys. J. B **73**, 375 (2010)
6. T. Tsuchiya, H. Saito, M. Yoshida, T. Katsumata, T. Ohba, Y. Inaguma, T. Tsurui, M. Shikano, Mater. Res. Soc. Symp. Proc. **988**, 0988 (2007)
7. A. Erkişi, E.K. Yıldırım, G. Gökoğlu, Int. J. Mod. Phys. B **28**, 1450205 (2014)
8. J. Hadermann, A.M. Abakumov, I.V. Nikolaev, E.V. Antipov, G. Tendeloo, Solid State Sci. **10**, 382 (2008)
9. M. Wang, G. Tan, Mater. Res. Bull. **46**, 438 (2011)
10. A.M. Abakumov, J. Hadermann, S. Bals, I.V. Nikolaev, E.V. Antipov, G. Tendeloo, Angew. Chem. Int. Ed. **45**, 6697 (2006)
11. I.V. Nikolaev, H. D'Hondt, A.M. Abakumov, J. Hadermann, A.M. Balagurov, I.A. Bobrikov, D.V. Sheptyakov, V.Y. Pomjakushin, K.V. Pokholok, D.S. Filimonov, G. Tendeloo, E.V. Antipov, Phys. Rev. B **78**, 024426 (2008)
12. A.M. Abakumov, J. Hadermann, G. Tendeloo, E.V. Antipov, J. Am. Ceram. Soc. **91**(6), 1807 (2008)
13. A.S. Golofastov, N.M. Novikovsky, V.M. Raznomazov, A.V. Pavlenko, I.A. Verbenko, D.A. Sarychev, L.A. Reznichenko, A.V. Mahiboroda, UPF **4**(1), 32 (2016) (in Russian)
14. M.E. Matsnev, V.S. Rusakov, AIP Conf. Proc. **1489**, 178 (2012)
15. V.S. Pokatilov, V.V. Pokatilov, A.S. Sigov, Phys. Solid State **51**(3), 552 (2009) (in Russian)
16. I.A. Verbenko, Y.M. Gufan, S.P. Kubrin, A.A. Amirov, A.A. Pavelko, V.A. Aleshin, L.A. Shilkina, O.N. Razumovskaya, L.A. Reznichenko, I.A. Osipenko, D.A. Sarychev, A.B. Batdalov, Bull. Russ. Acad. Sci. Phys. **74**, 1141 (2010) (in Russian)
17. F. Menil, J. Phys. Chem. Solids **46**, 763 (1985)
18. A.S. Sigov, V.S. Pokatilov, A.O. Konovalova, V.V. Pokatilov, Dokl. Phys. **58**, 438 (2013) (in Russian)
19. N.L. Huang, R. Orbach, E. Siminek, J. Owen, D.R. Taylor, Phys. Rev. **156**, 383 (1967)

Chapter 16
The Effect of Cr-Doping on the Structure, Dielectric and Magnetic Properties of $BiFeO_3$ and $Pb(Fe_{0.5}Sb_{0.5})O_3$ Multiferroics

S. I. Raevskaya, S. P. Kubrin, A. V. Pushkarev, N. M. Olekhnovich, Y. V. Radyush, V. V. Titov, H. Chen, C.-C. Chou, M. A. Malitskaya, I. P. Raevski, V. V. Stashenko and D. A. Sarychev

Abstract X-ray diffraction and Mössbauer studies of perovskite $BiFe_{1-x}Cr_xO_3$ and $PbFe_{0.5-x}Cr_xSb_{0.5}O_3$ solid solution ceramics, fabricated under high pressure (4–6 GPa) have been carried out. Two morphotropic phase boundaries were revealed in the $BiFe_{1-x}Cr_xO_3$ system: one between rhombohedral (*R3c*) and orthorhombic (*Pbam*) phases at $x \approx 0.5$–0.6 and the other between the orthorhombic (*Pbam*) and monoclinic (*C2/c*) phases at $x \approx 0.9$. It was found out that substitution of Cr^{3+} for Fe^{3+} in $BiFeO_3$ does not lead to the appearance of a low-spin state of Fe^{3+} ions, as was predicted by some first-principles calculations. A composition dependence of the magnetic phase transition temperature for $BiFe_{1-x}Cr_xO_3$ is very similar to that in the solid solutions of $BiFeO_3$ with non-magnetic ions, implying the lack of magnetic exchange between Fe^{3+} and Cr^{3+}. The reason of such behavior seems to be a difference in their electronic configuration. Addition of Cr to $PbFe_{0.5}Sb_{0.5}O_3$ leads to a dramatic lowering and diffusion of the dielectric permittivity maximum and its shift to lower temperatures. Thus, Cr substitution for Fe seems to destroy both ferroelectric and magnetic long-range order in perovskite multiferroics.

S. I. Raevskaya · S. P. Kubrin · V. V. Titov · M. A. Malitskaya · I. P. Raevski (✉)
V. V. Stashenko · D. A. Sarychev
Research Institute of Physics and Faculty of Physics, Southern Federal University, Rostov-on-Don, Russia
e-mail: igorraevsky@gmail.com

A. V. Pushkarev · N. M. Olekhnovich · Y. V. Radyush
Scientific-Practical Materials Research Centre of NAS of Belarus, 220072 Minsk, Belarus

H. Chen
University of Macau, Macau, China

C.-C. Chou
National Taiwan University of Science and Technology, Taipei, Taiwan, China

I. A. Parinov et al. (eds.), *Advanced Materials*, Springer Proceedings in Physics 207, https://doi.org/10.1007/978-3-319-78919-4_16

16.1 Introduction

Multiferroics are the materials that simultaneously possess two or more order parameters, for example, ferroelectric and magnetic, attract much attention nowadays due to the possibility of cross-controlling their magnetic and electrical properties [1, 2]. The most widely studied multiferroic is a perovskite $BiFeO_3$, in which the temperatures of both ferroelectric and magnetic phase transition are well above the room temperature [1–3]. However, applications of $BiFeO_3$, as well as other iron-containing single-phase perovskite multiferroics are limited due to the antiferromagnetic nature of spin ordering in these compounds [2, 3, 4]. Only a quadratic magnetoelectric effect is possible in such materials, its magnitude being much smaller than that of the linear one. While in some multiferroics, for example, in $PbFe_{0.5}Nb_{0.5}O_3$ and its solid solutions with $PbTiO_3$ rather large quadratic magnetoelectric coupling has been reported both in antiferromagnetic and paramagnetic phases [5, 6], its value is still insufficient for applications. It is generally believed that in iron-containing perovskites, magnetic and ferroelectric subsystems are independent. Magnetic properties are provided by Fe^{3+} ions, while ferroelectric properties are due to the dangling bonds of Bi^{3+} or Pb^{2+} [1]. However recently some contribution to the magnetic superexchange via the empty 6*p* states of Pb^{2+}or Bi^{3+} ions was revealed in $PbFe_{0.5}Nb_{0.5}O_3$ and $BiFeO_3$ [7–9]. Thus ion substitutions for both Bi^{3+} (or Pb^{2+}) and Fe^{3+} in Bi- and Pb-containing multiferroics may have a great effect on their magnetic properties.

Several years ago, basing on the first-principles calculations, the possibility of obtaining ferromagnetic properties in $BiFe_{1-x}Cr_xO_3$ solid solutions was predicted [10]. The most attractive properties, according to these calculations, should have a composition with $x = 0.5$. Several years later first-principles calculations reported in [11] have shown that in the composition with $x = 0.5$, four competing phases can be realized: two ferrimagnetic and two ferromagnetic and, in addition, a part of the iron ions may be in a low-spin state. However all the attempts to obtain single-phase perovskite modification of $BiFe_{1-x}Cr_xO_3$ compositions with $x > 0.05$ by a solid-state synthesis at ambient pressure failed [12]. Using a sol-gel synthesis method, perovskite $BiFe_{0.9}Cr_{0.1}O_3$ ceramics were fabricated [13]. This ceramics exhibited magnetic hysteresis loops at room temperature and this fact was interpreted as an evidence of the antiferromagnetic spatial spin-modulated cycloid structure suppression due either to Cr-doping or to the size effect, as the mean grain size (65 nm) of ceramics studied in [13] was close to the cycloid period (62 nm) in $BiFeO_3$ [1–3]. However, one cannot exclude the possibility of the presence of a small amount of ferrimagnetic impurity in these samples. Though the content of this impurity seems to be much lower than the detection limit of the X-ray diffraction or Mössbauer spectroscopy, ferrimagnetic impurity in the antiferromagnetic matrix has a great impact on the magnetic properties of the sample. Such effects have been already reported for $PbFe_{0.5}Nb_{0.5}O_3$, $PbFe_{0.5}Ta_{0.5}O_3$ [14, 15] and $BiFe_{0.5}Cr_{0.5}O_3$ [16] ceramics.

The breakthrough in fabrication of perovskite $BiFe_{1-x}Cr_xO_3$ ceramics was achieved by using the high-pressure synthesis [16, 17]. Studies of $BiFe_{0.5}Cr_{0.5}O_3$ composition revealed that it is not a ferromagnet as was predicted in [10, 11], but rather an antiferromagnet or a spin- glass. Temperature T_M of the magnetic phase transition in this ceramics appeared to be rather low (≈130 K). It is commonly adopted that the value of T_M in iron-containing oxides depends on the number of superexchange Fe^{3+}–O–Fe^{3+} links in their lattice [18, 19]. In $BiFe_{0.5}Cr_{0.5}O_3$ the ordering of Fe^{3+} and Cr^{3+}cations would lower T_M, as such an ordering lowers the number of the Fe^{3+}–O–Fe^{3+} links. While thorough studies of neutron, electron and X-ray diffraction did not find any evidence of superstructure reflexes due to long range ordering of Fe^{3+} and Cr^{3+} in $BiFe_{0.5}Cr_{0.5}O_3$ [16], one cannot exclude the presence of a short range ordering. There are a lot of data of Extended X-ray Absorption Fine Structure (EXAFS), Nuclear Magnetic Resonance (NMR), Raman and acoustic emission studies of complex $Pb\,B'_n\,B''_m\,O_3$ perovskites, showing that the local structure of these compounds differs greatly from the macroscopic one [20–25]. It is well documented that a short-range local ordering of Fe^{3+} and B^{5+} cations in $PbFe^{3+}{}_{0.5}\,B''{}_mO_3$ perovskites (B'' = Nb, Ta, Sb) affects substantially their T_M values [26–34].

The only known perovskite multiferroic of the $Pb\,B'_n\,B''_m\,O_3$ type with a high degree of a long-range ordering of B' and B'' ions is $PbFe_{0.5}Sb_{0.5}O_3$ [26, 27]. $PbFe_{0.5}Sb_{0.5}O_3$ has a ferroelectric transition at about 200 K, while on cooling below $T_M \approx 30$ K, a transition into the antiferromagnetic phase of the I-type occurs [26]. Highly-ordered $PbFe_{0.5}Sb_{0.5}O_3$ exhibits giant low-frequency magnetic susceptibility values at unusually high temperatures (150–250 K), i.e. well above the T_M and it is a magnetic analog of relaxor ferroelectrics [26]. In the explanation of the unique magnetic properties of $PbFe_{0.5}Sb_{0.5}O_3$, a special role is ascribed to the high degree of a long-range ordering of Fe^{3+} and Sb^{5+} cations, because in disordered samples magnetic susceptibility values are much lower [35]. Since the ordering of Fe^{3+} and Cr^{3+} ions is an important condition of appearing of the ferrimagnetic state in $BiFe_{0.5}Cr_{0.5}O_3$ composition [10], it would be interesting to study the effect of Cr-doping on the properties of $PbFe_{0.5}Sb_{0.5}O_3$.

The scope of the present work was to fabricate perovskite $BiFe_{1-x}Cr_xO_3$ and $(1-x)PbFe_{0.5}Sb_{0.5}O_3$–$xPbCr_{0.5}Sb_{0.5}O_3$ solid solution compositions by high pressure synthesis and to study their structure, magnetic and dielectric properties in order to reveal the effect of Cr-doping on the temperatures of ferroelectric and magnetic phase transitions in both $BiFeO_3$ and $PbFe_{0.5}Sb_{0.5}O_3$.

16.2 Experimental

For synthesis of both $BiFe_{1-x}Cr_xO_3$ and $(1-x)PbFe_{0.5}Sb_{0.5}O_3$–$xPbCr_{1/2}Sb_{1/2}O_3$ solid solution compositions, high pure Bi_2O_3, Fe_2O_3, PbO, Sb_2O_5 and Cr_2O_3 were used as starting reagents. These oxides were mixed in a stoichiometric ratio,

ball-milled in ethanol, dried, and pressed into pellets. The pellets were calcined in a closed alumina crucible at 770–950 °C for 2 h and then quenched to room temperature. The pre-synthesized powders were pressed into pellets of 4.5 mm in diameter and about 4 mm height. High-pressure synthesis was performed using an anvil press DO-138A at 900–1400 °C for 1–5 min under the pressure 4–6 GPa. Due to slightly reducing atmosphere in a high-pressure apparatus [35], thus obtained samples usually contained a large number of oxygen vacancies, which are the most easily-formed intrinsic defects in the oxides of the perovskite family [36]. To reduce both the residual mechanical stresses and the concentration of oxygen vacancies, all the samples, obtained by a high-pressure synthesis, were annealed in air at 350–450 °C for 2 h prior to measurements. X-ray diffraction studies of the powdered samples were performed at room temperature using DRON-3 diffractometer and Cu-Kα radiation.

Mössbauer spectra were recorded with the MS-1104Em rapid spectrometer and analyzed using a SpectrRelax software [37]. The temperature was changed in the 12–320 K range using the closed-cycle helium cryostat-refrigerator Janis Ccs-850 (Cryogenics).

16.3 Results and Discussion

X-ray diffraction studies of the single-phase perovskite $BiFe_{1-x}Cr_xO_3$ compositions, synthesized under high pressure, revealed the presence of two concentration phase transitions in this solid solution system (see Fig. 16.1). In the composition range $0 \leq x < 0.6$, the solid solutions have a rhombohedral (*R*3*c*) lattice. In the region $0.6 < x \leq 0.9$, the lattice is orthorhombic (*Pbam*) similar to $PbZrO_3$, $BiFe_{0.5}Sc_{0.5}O_3$, or to the high-pressure modification of $BiFeO_3$ [38]. In the $x > 0.90$ composition range the symmetry is monoclinic (*C*2/*c*), as in $BiCrO_3$. The room-temperature crystal structure of $BiFe_{1-x}Cr_xO_3$ compositions with the *Pbam* symmetry is characterized by the antipolar shifts of Bi^{3+} and O^{2-} ions, corresponding to the antiferroelectric state.

Figure 16.2 shows the room temperature Mössbauer spectra of $BiFe_{1-x}Cr_xO_3$ (x = 0.05, 0.1, 0.2, 0.4 and 0.5) compositions. The parameters of these spectra are listed in Table 16.1. The structure of the $BiFe_{0.95}Cr_{0.05}O_3$ spectrum is similar to that of $BiFeO_3$ [39–41] and consists of two Zeeman sextets. The magnetic hyperfine field values of sextets are $H_1 = H_2 = 495$ kOe for $BiFeO_3$ [39–41] and $H_1 = 483$ kOe and $H_2 = 485$ kOe for $BiFe_{0.95}Cr_{0.05}O_3$. Smaller hyperfine magnetic field values for $BiFe_{0.95}Cr_{0.05}O_3$ as compared to those for $BiFeO_3$ seem to be due to the lower magnetic phase transition temperature T_M in the former composition. The lowering of T_M with the growth of x in the $BiFe_{1-x}Cr_xO_3$ system is confirmed by the results of magnetization versus temperature studies [16, 17]. The presence of two Zeeman sextets in the Mössbauer spectrum of undoped $BiFeO_3$ is usually a fingerprint of a spatial spin-modulated cycloid structure [39, 40].

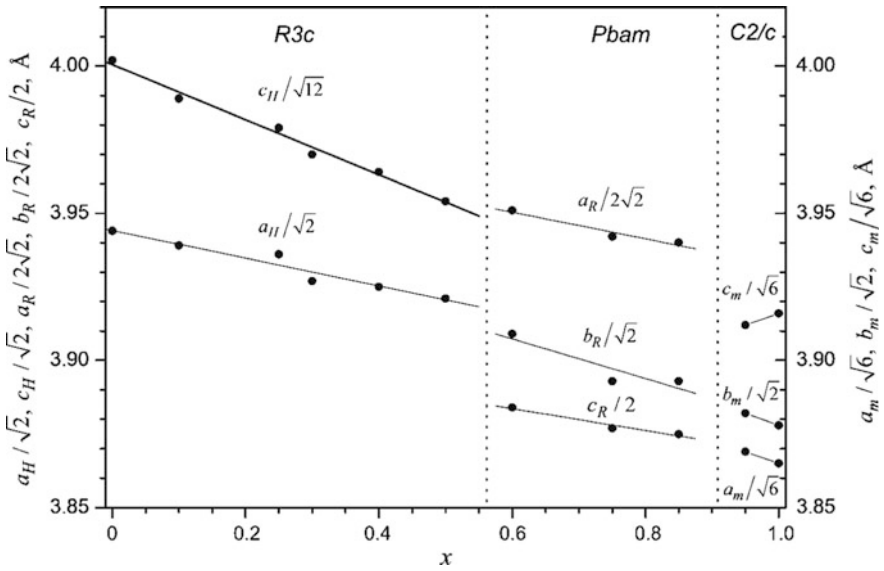

Fig. 16.1 Composition dependence of the lattice parameters for $BiFe_{1-x}Cr_xO_3$ solid solution system

The room temperature Mössbauer spectra of $BiFe_{1-x}Cr_xO_3$ compositions with $x = 0.1$, 0.2, and 0.4 (Fig. 16.2) consist of both Zeeman lines and quadrupole-split lines in the central part of the spectrum. In the case of the samples with $x = 0.1$ and 0.2, the latter lines seem to be related to paramagnetic doublet, corresponding to $Bi_{25}FeO_{39}$ impurity phase [42]. The isomer shift values of the sextets ($\delta \approx 0.38$ mm/s) correspond to Fe^{3+} ions in oxygen octahedron [43]. Both the broadening of the spectral peaks seen as an increase of the line widths, as well as the decrease of the H values (see Table 16.1) for $BiFe_{0.9}Cr_{0.1}O_3$ and $BiFe_{0.8}Cr_{0.2}O_3$ compositions are due to the increase of crystal inhomogeneity and lowering of T_M as a result of Cr^{3+} substitution for Fe^{3+}. The presence of three sextets in Mössbauer spectra of the samples with $x = 0.1$ and 0.2 seems to be due to the Fe^{3+} ions having three types of surrounding. The sextets S1 and S2 with higher H values correspond to the Fe^{3+} ions having a smaller number of Cr^{+3} ions as neighbors. The sextet S3 with the lowest H value arises from Fe^{3+} ions surrounded mainly by Cr^{3+} ions.

The Mössbauer spectrum of $BiFe_{0.6}Cr_{0.4}O_3$ consists of paramagnetic doublet and three Zeeman sextets ($H_1 \approx 490$ kOe, $H_2 \approx 321$ kOe and $H_3 \approx 259$ kOe). The parameters of doublet (isomer shift $\delta \approx 0.4$ mm/s and quadrupole splitting Δ 0.5 mm/s) are close to those typical for iron-containing perovskite compounds [44–50]. The H_1 value of sextet S1 is larger than the values, estimated for $x = 0.1$ and 0.2 samples and is close to H_1 value of undoped $BiFeO_3$ (see Table 16.1). One may suppose that this sextet corresponds to Fe^{3+} ions, which have only Fe^{3+} in its surrounding. The sextets S2 and S3 possess the lower H values as compared to S1

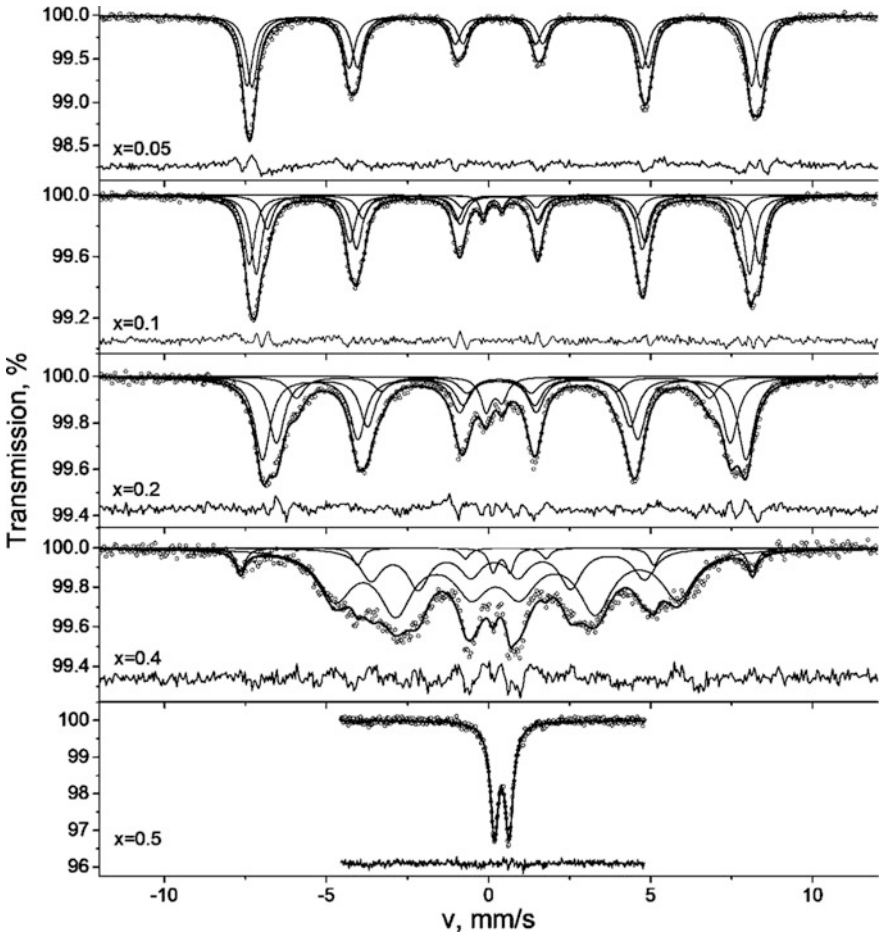

Fig. 16.2 Room temperature ^{57}Fe Mössbauer spectra of $BiFe_{1-x}Cr_xO_3$ solid solution compositions. Symbols present experimental points. Solid line describes the result of fitting; thin lines show the deconvolution of the experimental spectra into sextet and doublet components used for fitting

and seem to correspond to the Fe^{3+} ions, which have different number of Cr^{3+} ions as their neighbors.

The room temperature Mössbauer spectrum of $BiFe_{0.5}Cr_{0.5}O_3$ (Fig. 16.2) is a paramagnetic doublet. Its isomer shift value is $\delta \approx 0.4$ mm/s and is close to δ values of other iron-containing perovskite compounds such as $AFe_{0.5}B_{0.5}O_3$ (A = Pb, Sr; B = Nb, Ta, Sb) [44–50] and $BiFeO_3$ [39, 40]. In [11] basing on the first principles calculations, it was predicted that in $BiFe_{0.5}Cr_{0.5}O_3$ a part of Fe^{3+} ions may be in a low spin state at the normal conditions. Since the δ value ranges of both low- and high spin Fe^{3+} partially overlap [51], the isomer shift value cannot serve as an unambiguous criterion to determine the spin state in this case. However,

Table 16.1 Parameters of room-temperature ^{57}Fe Mössbauer spectra for some $BiFe_{1-x}Cr_xO_3$ solid solution compositions

x	Spectrum component	$\delta \pm 0.02$ (mm/s)	$\varepsilon/\Delta \pm 0.02$ (mm/s)	$H \pm 1$ (kOe)	$A \pm 0.5$ (%)	$G \pm 0.02$ (mm/s)
0.05	S1	0.38	0.16	485	50.4	0.43
	S2	0.38	0.07	483	49.6	0.43
0.1	D	0.12	0.58	–	2.6	0.29
	S1	0.38	0.10	488	35.5	0.40
	S2	0.38	0.06	472	41.2	0.40
	S3	0.38	0.05	451	20.6	0.40
0.2	D	0.17	0.50	–	4.9	0.40
	S1	0.38	0.10	463	45.7	0.58
	S2	0.38	0.07	434	36.3	0.58
	S3	0.38	0.06	388	13.1	0.58
0.4	D	0.40	0.52	–	2.54	0.30
	S1	0.38	0.21	259	26.7	0.80
	S2	0.38	0.17	321	64.3	1.22
	S3	0.38	−0.14	490	6.4	0.35
0.5	D1	0.40	0.46	–	100	0.30

D doublet, *S* sextet, δ isomer shift, ε quadrupole shift, Δ – quadrupole splitting, *H* hyperfine magnetic field on ^{57}Fe nucleus, *A* area of corresponding spectrum components, *G* line width

in $BiFeO_3$ a transition of Fe^{3+} ions from a high-spin state to a low-spin one was observed under high (≈46 GPa) pressure [52]. This transition was accompanied by an increase of quadrupole splitting value (Δ) by two times. The Δ value for our $BiFe_{0.5}Cr_{0.5}O_3$ sample, determined from its Mössbauer spectrum (Fig. 16.2), is about 0.46 mm/s and is close to that of $BiFeO_3$ in the paramagnetic phase under the normal pressure [40]. Thus, both δ and Δ values indicate that in $BiFe_{0.5}Cr_{0.5}O_3$ all Fe^{3+} ions are in the high-spin state.

For estimation of magnetic phase transition temperature T_M, the method of temperature scanning was used. The essence of this method is the measuring of Mössbauer spectrum intensity η within the 0–1.2 mm/s velocity range, normalized to its value at 300 K, in the course of sequential decreasing of the temperature. The appearance of magnetic ordering below T_M causes the transformation of the paramagnet doublet into Zeeman sextet, which is accompanied by a dramatic decrease of η value. The temperature dependence of η for $BiFe_{0.5}Cr_{0.5}O_3$ is presented in Fig. 16.3 (curve 1). One can see that the $\eta(T)$ curve has an abrupt drop at about 250 K. We have shown earlier for several perovskite multiferroics and their solid solutions that such a drop corresponds to T_M [14, 45, 47, 53]. Interestingly the obtained value of T_M is close to $T_M \approx 220$ K, reported for $BiFe_{0.5}Sc_{0.5}O_3$ [54], though Sc is not a magnetic ion. It is worth noting that T_M value for $BiFe_{0.5}Cr_{0.5}O_3$, determined from the magnetization studies, is about 130 K [16]. Such a large difference of T_M values, determined by different methods, is well explained, if one assumes, in accordance with the data of [16], that $BiFe_{0.5}Cr_{0.5}O_3$ is not an antiferromagnet, but rather a spin-glass, and the $\eta(T)$ anomaly corresponds to a spin-glass blocking temperature T_g. Similar difference between T_g values, determined from magnetization and Mössbauer studies, was reported for many spin-glass materials, e.g. $PbFe_{12-x}Cr_xO_{19}$ hexaferrites [55] and some $PbFe_{1/2}Ta_{1/2}O_3$-based [14] and $PbFe_{1/2}Nb_{1/2}O_3$-based [56] solid solutions. Such behavior is caused by the fact that the upper limit of the spin relaxation rates in spin glasses is larger than the characteristic time of Mössbauer effect [57].

Both the decrease of H values and lowering of magnetic phase transition temperature T_M with the increase of Cr concentration in $BiFe_{1-x}Cr_xO_3$ solid solutions imply that Cr^{3+} ions, incorporated into the $BiFeO_3$ lattice, behave similar to nonmagnetic dopants, despite they possess d-electrons. The electron configuration of Cr^{3+} and Fe^{3+} is $3d^3$ and $3d^5$, respectively. The value of the transfer integral for 180

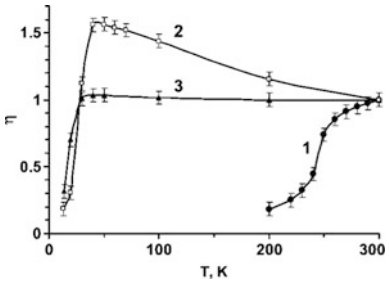

Fig. 16.3 Temperature dependences of η-intensity of Mössbauer spectrum related to its value at 300 K for $BiFe_{0.5}Cr_{0.5}O_3$ (curve 1) and $(1 - x)PbFe_{0.5}Sb_{0.5}O_3$–$xPbCr_{0.5}Sb_{0.5}O_3$ compositions with $x = 0.2$ (curve 2) and $x = 0.4$ (curve 3)

cation—anion—cation magnetic exchange between octahedron-site $3d^3$ and $3d^5$ cations is close or equal to zero [19]. Similar results have been obtained recently for $PbFe_{0.5-x}Cr_xNb_{0.5}O_3$ multiferroic solid solutions [58, 59].

Figure 16.4 shows the Mössbauer spectra of the $(1 - x)PbFe_{0.5}Sb_{0.5}O_3$–$xPbCr_{0.5}Sb_{0.5}O_3$ samples ($x = 0.2$ and 0.4). The parameters of these spectra are listed in Table 16.2. Each spectrum consists of singlet and doublet components. The isomer shift of both singlet and doublet corresponds to Fe^{3+} ions in the octahedral environment [43]. The singlet is characteristic for perovskite-like compounds with a high degree of compositional ordering of the *B*-site cations [27, 29, 50]. The simultaneous presence of the singlet and doublet components in the Mössbauer spectra indicates the presence of both ordered and disordered regions in the samples under study. The area of the singlet (this value approximately corresponds to the degree S of long-range compositional ordering of Fe^{3+} and Sb^{5+} ions [27, 50]) decreases from ≈58 to ≈51% as x grows from 0.2 to 0.4. However the rate of this decrease is much lower than that observed in the $(1 - x)PbFe_{0.5}Sb_{0.5}O_3$–$xPbFe_{0.5}Nb_{0.5}O_3$ solid solution system [50].

Figure 16.5 presents the temperature dependences of the real part of permittivity ε' (panel a) and loss tangent tan δ (panel b) for some $(1 - x)PbFe_{0.5}Sb_{0.5}O_3$–$xPbCr_{0.5}Sb_{0.5}O_3$ compositions, measured at different frequencies. While undoped $PbFe_{0.5}Sb_{0.5}O_3$ has a very high degree of long-range compositional ordering $S \approx 87\%$ [26, 27], its $\varepsilon'(T)$ maximum is rather diffused (Fig. 16.5a). Addition of Cr to $PbFe_{0.5}Sb_{0.5}O_3$ leads to a dramatic lowering and diffusion of the $\varepsilon'(T)$ maximum and its shift to lower temperatures (see Fig. 16.5a and the inset in this panel). Similar character of the evolution of the dielectric properties with the increase of Cr content was observed previously for $(1 - x)PbFe_{0.5}Nb_{0.5}O_3$–$xPbCr_{0.5}Nb_{0.5}O_3$ solid

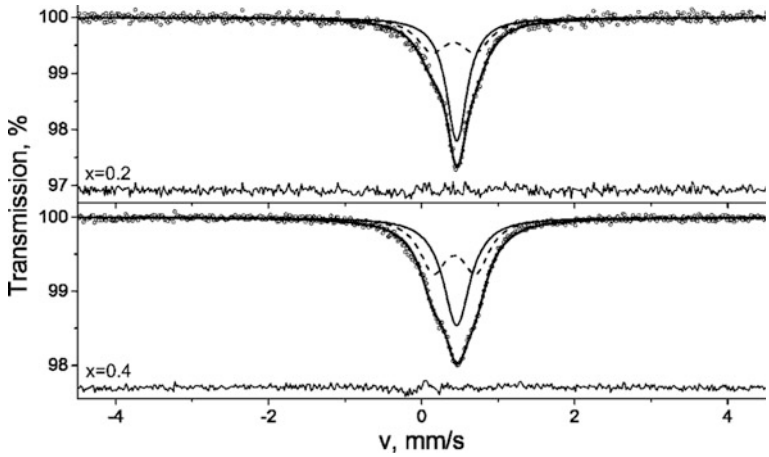

Fig. 16.4 Room temperature ^{57}Fe Mössbauer spectra of $(1 - x)PbFe_{0.5}Sb_{0.5}O_3$–$xPbCr_{0.5}Sb_{0.5}O_3$ solid solution compositions. Symbols correspond to experimental points and solid lines are the result of fitting; thin lines show the deconvolution of the experimental spectra into singlet and doublet components, used for fitting

Table 16.2 Parameters of room-temperature ^{57}Fe Mössbauer spectra for some $(1 - x)PbFe_{0.5}Sb_{0.5}O_3$–$xPbCr_{0.5}Sb_{0.5}O_3$ solid solution compositions

x	Spectrum component	$\delta \pm 0.002$ (mm/s)	$\Delta \pm 0.005$ (mm/s)	$A \pm 2$ (%)	$G \pm 0.008$ (mm/s)
0.2	Singlet	0.462		58	0.320
	Doublet	0.422	0.561	42	0.320
0.4	Singlet	0.464		51	0.368
	Doublet	0.430	0.558	49	0.368

δ isomer shift, Δ quadrupole splitting, A area of corresponding spectrum components, G line width

solution system [58, 59]. As one can see in Fig. 16.6, the rate of the decrease of the $\varepsilon'(T)$ maximum temperature T_m with the increase of the Cr content is very similar for both $(1 - x)PbFe_{0.5}Sb_{0.5}O_3$–$xPbCr_{0.5}Sb_{0.5}O_3$ (line 1) and $(1 - x)PbFe_{0.5}Nb_{0.5}O_3$–$xPbCr_{0.5}Nb_{0.5}O_3$ (line 2) solid solution systems.

It should be noted that besides the $\varepsilon'(T)$ maximum corresponding to a diffused ferroelectric phase transition, in the samples of $(1 - x)PbFe_{0.5}Sb_{0.5}O_3$–$xPbCr_{0.5}Sb_{0.5}O_3$ compositions with $x = 0.4$ and 0.5, there are also high-temperature relaxation maxima of ε' and loss tangent tan δ (Fig. 16.5). The frequency shift of the temperature of the tan $\delta(T)$ maximum obeys the Debye law (see the inset in the panel (b) of Fig. 16.5). Activation energies of relaxation appeared to be 0.31 and 0.33 eV for $(1 - x)PbFe_{0.5}Sb_{0.5}O_3$–$xPbCr_{0.5}Sb_{0.5}O_3$ compositions with $x = 0.4$ and 0.5, respectively. Similar high-temperature Debye-like relaxation has been observed previously both in lead-containing $Pb_2B'NbO_6$ ($B' = Fe, Sc$; $B'' = Nb, Ta$) perovskites [60–64] and lead-free $BaFe_{0.5}Nb_{0.5}O_3$ and $SrTiO_3$ perovskites [65, 66] as well as in some $BiFeO_3$-based [67] and $NaNbO_3$-based [68, 69] solid solutions and

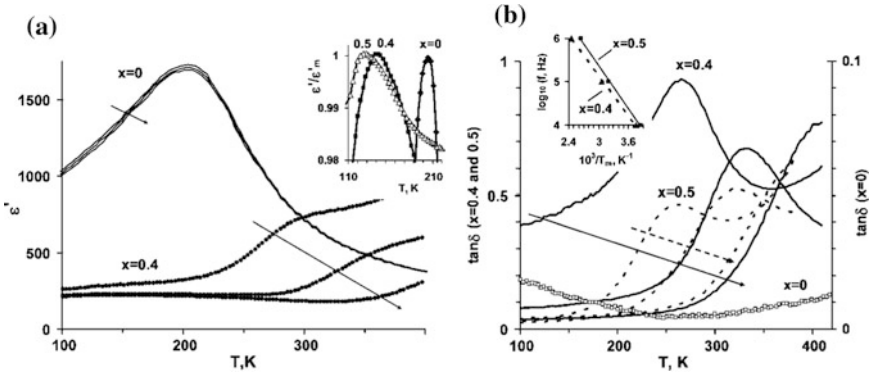

Fig. 16.5 Temperature dependences of the real part of permittivity ε' (**a**) and loss tangent tan δ (**b**) for some $(1 - x)PbFe_{0.5}Sb_{0.5}O_3$–$xPbCr_{0.5}Sb_{0.5}O_3$ compositions, measured at 10^4, 10^5 and 10^6 Hz; the arrows show the direction of the frequency increase; the inset in panel **a** highlights the lowering of the $\varepsilon'(T)$ maximum temperature with the increase of x; the inset in panel **b** shows the Arrhenius plots of the frequency shift for the tan $\delta(T)$ maxima

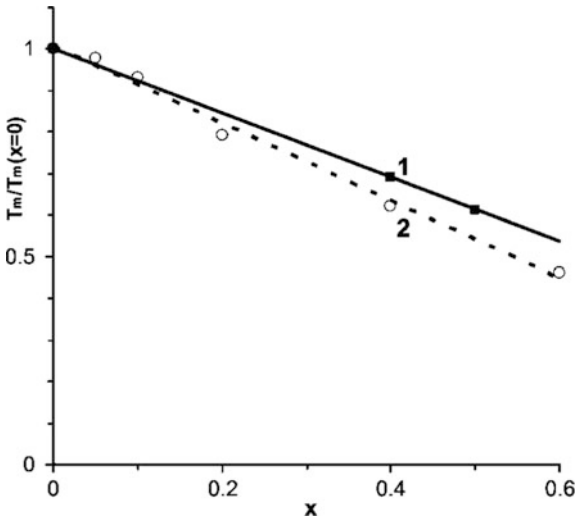

Fig. 16.6 Composition dependence of the temperature T_m of the $\varepsilon'(T)$ maximum related to T_m value at $x = 0$ for $(1 - x)PbFe_{0.5}Sb_{0.5}O_3$–$xPbCr_{0.5}Sb_{0.5}O_3$ (line 1) and $(1 - x)PbFe_{0.5}Nb_{0.5}O_3$–$xPbCr_{0.5}Nb_{0.5}O_3$ (line 2) solid solution systems; the data for the latter system are taken from [58]

was usually attributed to the presence of oxygen vacancies. Activation energies of about 0.3–0.4 eV, i.e. close to that found for $(1 - x)PbFe_{0.5}Sb_{0.5}O_3$–$xPbCr_{0.5}Sb_{0.5}O_3$ ceramic compositions were observed, e.g. in ceramics of Bi-doped $SrTiO_3$ [66], $BaFe_{0.5}Nb_{0.5}O_3$ [65] and $(Pb_{1-x}Ca_x)Fe_{0.5}Nb_{0.5}O_3$ [63]. These values of activation energies correspond well to the energy of the second level of the oxygen vacancy, determined both theoretically [36] and experimentally [70] for a large number of perovskite oxides.

Temperature of magnetic phase transition, determined from the $\eta(T)$ dependence (Fig. 16.3) does not change substantially when Cr is added to $PbFe_{0.5}Sb_{0.5}O_3$. Such stability is typical of spin-glasses, where only a short-range magnetic order occurs.

16.4 Conclusion

X-ray diffraction studies of the single-phase perovskite $BiFe_{1-x}Cr_xO_3$ compositions, synthesized under high (4–6 GPa) pressure, revealed two concentration phase transitions: one between rhombohedral (*R3c*) and orthorhombic (*Pbam*) phases at $x \approx 0.5$–0.6 and the other between the orthorhombic (*Pbam*) and monoclinic (*C2/c*) phases at $x \approx 0.9$.

It was found out that substitution of Cr^{3+} for Fe^{3+} does not lead to the appearance of a low-spin state of Fe^{3+} ions in $BiFe_{0.5}Cr_{0.5}O_3$, as was predicted by some first-principles calculations [11]. A composition dependence of the magnetic phase transition temperature for $BiFe_{1-x}Cr_xO_3$ is very similar to that observed for the solid solutions of $BiFeO_3$ with non-magnetic ions, e.g. in the $BiFe_{1-x}Sc_xO_3$ system [54], implying the lack of magnetic exchange between Fe^{3+} and Cr^{3+}. The reason of such behavior seems to be a difference in their electronic configuration

[19]. Addition of Cr to $PbFe_{0.5}Sb_{0.5}O_3$ leads to a dramatic lowering and diffusion of the dielectric permittivity maximum and its shift to lower temperatures. Thus, Cr substitution for Fe seems to destroy both ferroelectric and magnetic long-range order in perovskite multiferroics.

Acknowledgements This study was partially supported by the Ministry of Education and Science of the Russian Federation (research project 3.5346.2017/BP), Russian Foundation for Basic Research (grant No 16-52-00072_Bel_a), Belarusian Republican Foundation for Basic Research (grant No T16R-079) and Research Committee of the University of Macau (Research & Development Grant for Chair Professor No RDG007/FST-CHD/2012).

References

1. D.I. Khomskii, J. Magn. Magn. Mater. **306**, 1 (2006)
2. A.P. Pyatakov, A.K. Zvezdin, Phys. Usp. **55**, 557 (2012)
3. G. Catalan, J.F. Scott, Adv. Mater. **21**, 2463 (2009)
4. J. Yu, J.H. Chu, Chin. Sci. Bull. **53**, 2097 (2008)
5. V.V. Laguta, A.N. Morozovska, E.I. Eliseev, I.P. Raevski, S.I. Raevskaya, E.I. Sitalo, S.A. Prosandeev, L. Bellaiche, J. Mater. Sci. **51**, 5330 (2016)
6. V.V. Laguta, V.A. Stephanovich, I.P. Raevski, S.I. Raevskaya, V.V. Titov, V.G. Smotrakov, V.V. Eremkin, Phys. Rev. B **95**, 014207 (2017)
7. I.P. Raevski, S.P. Kubrin, S.I. Raevskaya, V.V. Titov, D.A. Sarychev, M.A. Malitskaya, I.N. Zakharchenko, S.A. Prosandeev, Phys. Rev. B **80**, 024108 (2009)
8. I.P. Raevski, S.P. Kubrin, S.I. Raevskaya, S.A. Prosandeev, D.A. Sarychev, M.A. Malitskaya, V.V. Stashenko, I.N. Zakharchenko, Ferroelectrics **398**, 16 (2010)
9. R. De Sousa, M. Allen, M. Cazayous, Phys. Rev. Lett. **110**, 267202 (2013)
10. P. Baettig, N.A. Spaldin, Appl. Phys. Lett. **86**, 012505 (2005)
11. M. Goffinet, J. Iniguez, P. Ghosez, Phys. Rev. B **86**, 024415 (2012)
12. F. Chang, N. Zhang, F. Yang, S. Wang, G. Song, J. Phys. D Appl. Phys. **40**, 7799 (2007)
13. B.-C. Luo, C.-L. Chen, K.-X. Jin, Solid State Commun. **151**, 712 (2011)
14. I.P. Raevski, V.V. Titov, M.A. Malitskaya, E.V. Eremin, S.P. Kubrin, A.V. Blazhevich, H. Chen, C.-C. Chou, S.I. Raevskaya, I.N. Zakharchenko, D.A. Sarychev, S.I. Shevtsova, J. Mater. Sci. **49**, 6459 (2014)
15. M. Puri, S. Bahel, I.P. Raevski, S.B. Narang, J. Magn. Magn. Mater. **407**, 195 (2016)
16. M.R. Suchomel, C.I. Thomas, M. Allix, M.J. Rosseinsky, A.M. Fogg, M.F. Thomas, Appl. Phys. Lett. **90**, 112909 (2007)
17. S.S. Arafat, Chin. Phys. B **23**, 066101 (2014)
18. M.A. Gilleo, J. Phys. Chem. Solids **13**, 33 (1960)
19. J.B. Goodenough, *Magnetism and Chemical Bond* (Interscience Publisher (a division of Wiley), New York, London, 1963), 393pp
20. V.A. Shuvaeva, I. Pirog, Y. Azuma, K. Yagi, K. Sakaue, H. Terauchi, I.P. Raevskii, K. Zhuchkov, M.Y. Antipin, J. Phys.: Condens. Matter **15**, 2413 (2003)
21. K. Kouril, V. Chlan, H. Štepánková, R. Reznícek, K. Ulicná, V.V. Laguta, I.P. Raevski, Acta Phys. Pol. A **127**, 234 (2015)
22. N.S. Druzhinina, Y.I. Yuzyuk, I.P. Raevski, M. El Marssi, V.V. Laguta, S.I. Raevskaya, Ferroelectrics **438**, 107–114 (2012)
23. E. Dul'kin, I.P. Raevski, S.M. Emel'yanov, Phys. Solid State **45**, 158 (2003)
24. E. Dul'kin, E. Mojaev, M. Roth, I.P. Raevski, S.A. Prosandeev, Appl. Phys. Lett. **94**, 252904 (2009)

25. S. Prosandeev, I.P. Raevski, M.A. Malitskaya, S.I. Raevskaya, H. Chen, C.C. Chou, B. Dkhil, J. Appl. Phys. **114**, 124103 (2013)
26. V.V. Laguta, V.A. Stephanovich, M. Savinov, M. Marysko, R.O. Kuzian, N.M. Olekhnovich, A.V. Pushkarev, Y.V. Radyush, I.P. Raevski, S.I. Raevskaya, S.A. Prosandeev, New J. Phys. **16**, 11304 (2014)
27. I.P. Raevski, A.V. Pushkarev, S.I. Raevskaya, N.M. Olekhnovich, Y.V. Radyush, S. P. Kubrin, H. Chen, C.-C. Chou, D.A. Sarychev, V.V. Titov, M.A. Malitskaya, Ferroelectrics **501**, 154 (2016)
28. A.A. Gusev, S.I. Raevskaya, V.V. Titov, V.P. Isupov, E.G. Avvakumov, I.P. Raevski, H. Chen, C.-C. Chou, S.P. Kubrin, S.V. Titov, M.A. Malitskaya, D.A. Sarychev, V.V. Stashenko, S.I. Shevtsova, Ferroelectrics **496**, 231 (2016)
29. I.P. Raevskii, D.A. Sarychev, S.A. Bryugeman, L.A. Reznichenko, L.A. Shilkina, O.N. Razumovskaya, V.S. Nikolaev, N.P. Vyshatko, A.N. Salak, Crystallogr. Rep. **47**, 1012 (2002)
30. M. Maryško, V.V. Laguta, I.P. Raevski, R.O. Kuzian, N.M. Olekhnovich, A.V. Pushkarev, Y. V. Radyush, S.I. Raevskaya, V.V. Titov, S.P. Kubrin, AIP Adv. **7**, 056409 (2017)
31. S.I. Raevskaya, S.P. Kubrin, I.P. Raevski, C.C. Chou, H. Chen, V.V. Titov, M.A. Malitskaya, D.A. Sarychev, I.N. Zakharchenko, Ferroelectrics **509**, 64 (2017)
32. Y.I. Yuzyuk, I.P. Raevski, S.I. Raevskaya, N. Lemee, M.G. Karkut, W. Peng, M. El Marssi, H. Chen, J. Alloy. Compd. **695**, 1821 (2017)
33. S.A. Prosandeev, I.P. Raevski, S.I. Raevskaya, H. Chen, Phys. Rev. B **92**, 220419(R) (2015)
34. A.A. Gusev, S.I. Raevskaya, V.V. Titov, E.G. Avvakumov, V.P. Isupov, I.P. Raevski, H. Chen, C.-C. Chou, S.P. Kubrin, S.V. Titov, M.A. Malitskaya, A.V. Blazhevich, D.A. Sarychev, V.V. Stashenko, S.I. Shevtsova, Ferroelectrics **475**, 41 (2015)
35. V.A. Stephanovich, V. Laguta, M. Marysko, I. Raevsky, N. Olekhnovich, A. Pushkarev, Y. Radyush, S. Raevskaya, R. Kuzian, V. Chlan, H. Štěpánková, Acta Phys. Pol. A **131**, 1534 (2017)
36. S.A. Prosandeev, A.V. Fisenko, A.V. Riabchinski, I.A. Osipenko, I.P. Raevski, N. Safontseva, J. Phys.: Condens. Matter **8**, 6705 (1996)
37. M.E. Matsnev, V.S. Rusakov, AIP Conf. Proc. **1489**, 178 (2012)
38. S.A. Prosandeev, D.D. Khalyavin, I.P. Raevski, A.N. Salak, N.M. Olekhnovich, A.V. Pushkarev, Y.V. Radyush, Phys. Rev. B **90**, 054110 (2014)
39. V.S. Rusakov, V.S. Pokatilov, A.S. Sigov, M.E. Matsnev, T.V. Gubaidulina, JETP Lett. **100**, 463 (2014)
40. A. Sobolev, I. Presniakov, V. Rusakov, A. Belik, M. Matsnev, D. Gorchakov, I. Glazkova, AIP Conf. Proc. **1622**, 104 (2014)
41. A.V. Zalesskii, A.A. Frolov, A.K. Zvezdin, A.A. Gippius, E.N. Morozova, D.F. Khozeev, A. S. Bush, V.S. Pokatilov, J. Exp. Theor. Phys. **95**, 101 (2002)
42. V.M. Denisov, N.V. Belousova, V.P. Zhereb, L.T. Denisova, V.M. Skorikov, J. Siber. Fed. Univ. Chem. **2**, 146 (2012)
43. F. Menil, J. Phys. Chem. Solids **46**, 763 (1985)
44. S.P. Kubrin, S.I. Raevskaya, S.A. Kuropatkina, I.P. Raevski, D.A. Sarychev, Ferroelectrics **340**, 155 (2006)
45. I.P. Raevski, S.P. Kubrin, S.I. Raevskaya, S.A. Prosandeev, M.A. Malitskaya, V.V. Titov, D. A. Sarychev, A.V. Blazhevich, I.N. Zakharchenko, IEEE Trans. Ultrason. Ferroelectr. Freq. Control **59**, 1872 (2012)
46. I.P. Raevski, S.P. Kubrin, S.I. Raevskaya, D.A. Sarychev, S.A. Prosandeev, M.A. Malitskaya, Phys. Rev. B **85**, 224412 (2012)
47. I.P. Raevski, M.S. Molokeev, S.V. Misyul, E.V. Eremin, A.V. Blazhevich, S.P. Kubrin, H. Chen, C.-C. Chou, S.I. Raevskaya, V.V. Titov, D.A. Sarychev, M.A. Malitskaya, Ferroelectrics **475**, 52 (2015)
48. P.D. Battle, T.C. Gibb, A.J. Herod, S.-H. Kim, P.H. Munns, J. Mater. Chem. **5**, 865 (1995)
49. S.I. Raevskaya, V.V. Titov, I.P. Raevski, S.P. Kubrin, H. Chen, C.-C. Chou, D.A. Sarychev, S.I. Shevtsova, M.A. Malitskaya, I.N. Zakharchenko, Ferroelectrics **496**, 213 (2016)

50. I.P. Raevski, N.M. Olekhnovich, A.V. Pushkarev, Y.V. Radyush, S.P. Kubrin, S.I. Raevskaya, M.A. Malitskaya, V.V. Titov, V.V. Stashenko, Ferroelectrics **444**, 47 (2013)
51. Frank J. Berry, David J. Vaughan (eds.), *Chemical Bonding and Spectroscopy in Mineral Chemistry* (Chapman and Hall, New York, London, 1985)
52. I.S. Lyubutin, A.G. Gavriliuk, V.V. Struzhkin, JETP Lett. **88**, 524 (2008)
53. I.P. Raevski, S.P. Kubrin, S.I. Raevskaya, V.V. Stashenko, D.A. Sarychev, M.A. Malitskaya, M.A. Seredkina, V.G. Smotrakov, I.N. Zakharchenko, V.V. Eremkin, Ferroelectrics **373**, 121 (2008)
54. D.D. Khalyavin, A.N. Salak, N.M. Olekhnovich, A.V. Pushkarev, Y.V. Radyush, P. Manuel, I.P. Raevski, M.L. Zheludkevich, M.G.S. Ferreira, Phys. Rev. B **89**, 174414 (2014)
55. G. Albanese, B.E. Watts, F. Leccabue, Castanon S. Diaz, J. Magn. Magn. Mater. **184**, 337 (1998)
56. I.P. Raevski, S.P. Kubrin, V.V. Laguta, M. Marysko, H. Chen, S.I. Raevskaya, V.V. Titov, C.-C. Chou, A.V. Blazhevich, E.I. Sitalo, D.A. Sarychev, T.A. Minasyan, A.G. Lutokhin, Y. N. Zakharov, L.E. Pustovaya, I.N. Zakharchenko, M.A. Malitskaya, Ferroelectrics **475**, 20 (2015)
57. I.A. Campbell, Hyperfine Interact. **27**, 15 (1986)
58. S.I. Raevskaya, S.P. Kubrin, A.V. Pushkarev, N.M. Olekhnovich, Y.V. Radyush, V.V. Titov, M.A. Malitskaya, I.N. Zakharchenko, H. Chen, C.-C. Chou, I.P. Raevski, Ferroelectrics **509**, 40 (2017)
59. A.T. Kozakov, A.G. Kochur, A.V. Nikolskii, I.P. Raevski, S.P. Kubrin, S.I. Raevskaya, V.V. Titov, M.A. Malitskaya, I.N. Zakharchenko, S.I. Shevtsova, J. Mater. Sci. **52**, 10140 (2017)
60. I.P. Raevskii, V.V. Eremkin, V.G. Smotrakov, M.A. Malitskaya, S.A. Bogatina, L.A. Shilkina, Crystallogr. Rep. **47**, 1007 (2002)
61. A.V. Pavlenko, N.A. Boldyrev, L.A. Reznichenko, I.A. Verbenko, G.M. Konstantinov, L.A. Shilkina, Inorg. Mater. **50**, 750 (2014)
62. I.P. Rayevsky, A.A. Bokov, A.S. Bogatin, S.M. Emelyanov, M.A. Malitskaya, O.I. Prokopalo, Ferroelectrics **126**, 191 (1992)
63. M. Puri, S. Bahel, I.P. Raevski, S.B. Narang, J. Mater. Sci. Mater. Electron. **27**, 1077 (2016)
64. V. Bobnar, H. Uršič, G. Casar, S. Drnovšek, Phys. Status Solidi B **250**, 2232 (2013)
65. I.P. Raevski, S.A. Kuropatkina, S.P. Kubrin, S.I. Raevskaya, V.V. Titov, D.A. Sarychev, M. A. Malitskaya, A.S. Bogatin, I.N. Zakharchenko, Ferroelectrics **379**, 272 (2009)
66. C. Ang, Z. Yu, L.E. Cross, Phys. Rev. B **62**, 228 (2000)
67. I.P. Raevski, S.P. Kubrin, S.I. Raevskaya, D.A. Sarychev, J.-L. Dellis, Ferroelectrics **371**, 113 (2008)
68. I.P. Raevski, L.A. Reznitchenko, M.A. Malitskaya, L.A. Shilkina, S.O. Lisitsina, S.I. Raevskaya, E.M. Kuznetsova, Ferroelectrics **299**, 95 (2004)
69. S.I. Raevskaya, L.A. Reznichenko, I.P. Raevski, V.V. Titov, S.V. Titov, J.-L. Dellis, Ferroelectrics **340**, 107 (2006)
70. I.P. Raevski, S.M. Maksimov, A.V. Fisenko, S.A. Prosandeev, I.A. Osipenko, P.F. Tarasenko, J. Phys.: Condens. Matter **10**, 8015 (1998)

Chapter 17
Structural and Dielectric Studies of $PbYb_{1/2}Nb_{1/2}O_3$ Ceramics with the Differing Degree of the Long-Range Compositional Ordering Fabricated by Mechanoactivation

I. P. Raevski, Yu. A. Kuprina, I. N. Zakharchenko, A. A. Gusev, V. P. Isupov, O. A. Bunina, V. V. Titov, S. I. Raevskaya, M. A. Malitskaya, A. V. Blazhevich, S. V. Orlov and E. I. Sitalo

Abstract It was found out that compositional ordering degree S of Yb^{3+} and Nb^{5+} ions in $PbYb_{1/2}Nb_{1/2}O_3$ ceramics and correspondingly both the temperature and diffusion of antiferroelectric phase transition can be varied within a wide range by means of high-energy mechanical activation. In particular, for the first time disordered $PbYb_{1/2}Nb_{1/2}O_3$ ceramics exhibiting relaxor-like dielectric properties was fabricated without the use of any additives. For the most ordered $PbYb_{1/2}Nb_{1/2}O_3$ samples ($S \approx 0.82$), the coexistence of cubic paraelectric and orthorhombic antiferroelectric phases in a temperature range 190–300 °C was revealed.

17.1 Introduction

Ternary perovskite oxides $PbB'_nB''_{1-n}O_3$ (B' = Fe, Sc, In, Yb, Mg; B'' = Nb, Ta, Sb; n = 1/2 or 1/3) and solid solutions on their base exhibiting high dielectric, piezoelectric, electrostrictive, pyroelectric, electrocaloric and magnetoelectric responses, have been widely studied in the last three decades both in ceramic and in

I. P. Raevski (✉) · Yu. A. Kuprina · I. N. Zakharchenko · O. A. Bunina · V. V. Titov
S. I. Raevskaya · M. A. Malitskaya · A. V. Blazhevich · S. V. Orlov · E. I. Sitalo
Research Institute of Physics and Faculty of Physics, Southern Federal University,
344090 Rostov-on-Don, Russia
e-mail: igorraevsky@gmail.com

Yu. A. Kuprina · A. A. Gusev · V. P. Isupov
Institute of Solid State Chemistry and Mechanochemistry, SB RAS,
630128 Novosibirsk, Russia

I. A. Parinov et al. (eds.), *Advanced Materials*, Springer Proceedings
in Physics 207, https://doi.org/10.1007/978-3-319-78919-4_17

the single-crystalline form [1–18]. It was established that an ordering or disordering of the *B*-site cations have a large impact on the properties of these materials [19–22].

The possibility of changing the distribution of the B' and B'' cations over the octahedral sites of the lattice in so-called 1:1 perovskites $PbB^{3+}_{1/2}M^{5+}_{1/2}O_3$ was discovered about 40 years ago [20–22] and is extensively studied up to nowadays, as it has a strong effect on the phase transition temperatures and dielectric properties [20–26]. The degree of such compositional or chemical ordering is characterized by a long-range order parameter (S) which is defined as $S = 2p - 1$, where p is an occupation probability of certain-type ions in their "own" sublattice. Later it was found out that changes in the ordering degree have even larger effect on the temperature T_M of magnetic phase transitions and magnetic properties of $PbFe^{3+}_{1/2}M^{5+}_{1/2}O_3$ (M = Nb, Ta, Sb) perovskites than on their ferroelectric properties [27–36]. This is due to the fact that the ordering of Fe^{3+} and M^{5+}ions changes dramatically the number of the Fe–O–Fe links in the lattice which, in turn, determine the value of T_M [37]. It should be noted that the long-range ordering of Fe^{3+} and M^{5+}ions is observed only in perovskites where M = Sb [30–32, 35], while in niobates and tantalates only a short-range ordering or clustering takes place as is evidenced by the results of nuclear magnetic resonance [38, 39], Raman [40, 41] and Mossbauer [42] studies as well as by first-principles calculations [42, 43].

For a long time the only method of varying the ordering degree in $PbB'_nB''_{1-n}O_3$ perovskites was a long-time annealing at temperatures below the temperature T_{OD} of the order-disorder phase transition [20–22, 44]. However long-time annealing at high temperatures often causes the formation of the parasitic pyrochlore phase due to partial evaporation on PbO. Moreover, when the T_{OD} value is about 1000–1100 °C, the diffusion rate of *B*-cations is too low to achieve large enough changes of the ordering degree. For example, no substantial changes in the S values of the ordered $PbB^{3+}_{1/2}M^{5+}_{1/2}O_3$ (B^{3+}= Yb, Lu, Tm) perovskites have been achieved by annealing. Later a possibility of changing the S values of $PbB'_nB''_{1-n}O_3$ single crystals within certain limits by varying the growth conditions was established [45–48]. But a real breakthrough in changing the compositional ordering degree of the $PbB^{3+}_{1/2}M^{5+}_{1/2}O_3$ perovskites was achieved by using the additions of 1–2 wt% of Li_2CO_3 [49, 50]. This addition forms a liquid phase during sintering of ceramics, which promotes the nucleation of the new centers of crystallization and growth of grains with a new degree of ordering which is equilibrium at sintering temperature. As the diffusion of ions takes place in a melt, the kinetic restrictions typical of the solid-state diffusion can be avoided in this method. Lithium ions are very small and are expected not to incorporate into the lattice but rather to concentrate in the amorphous intergranular phase and/or evaporate during sintering. This assumption is confirmed by the fact that ferroelectric Curie point T_C of the Li-doped disordered perovskite $PbFe_{1/2}Nb_{1/2}O_3$ ceramics shows only a weak if any dependence on the amount of the Li_2CO_3 addition and is close to that of undoped ceramics [51–53]. In contrast to this, T_C of Li-doped $BaTiO_3$ ceramics depends dramatically both on the amount of Li-doping and on the duration of sintering implying that Li substitutes

for Ti and evaporates during sintering [54]. Nevertheless it is no direct evidence that Li does not incorporate into the lattice of $PbB^{3+}_{1/2}M^{5+}_{1/2}O_3$ perovskites.

Some time ago there appeared several reports that mechanical activation stimulates compositional disordering of $PbSc_{1/2}Nb_{1/2}O_3$ [44] and $PbSc_{1/2}Ta_{1/2}O_3$ [55] ceramics. We also observed the disappearing of relaxor properties and increase of T_M in both undoped and Li-doped $PbFe_{1/2}Ta_{1/2}O_3$ (PFT) ceramics, sintered from the mechanoactivated powders [56, 57]. These effects may be also caused by the local order-disorder processes. However in a recent work $PbYb_{1/2}Nb_{1/2}O_3$ (PYN) ceramics sintered from the mechanoactivated powders was reported to possess a sharp permittivity maximum at ≈ 270 °C [58], i.e. its dielectric properties are similar to those of ceramics obtained by usual methods [3, 14, 49, 59].

The scope of the present work was the study of the possibility of fabricating $PbYb_{1/2}Nb_{1/2}O_3$ (PYN) ceramics with differing degree of Yb^{3+} and Nb^{5+} ordering by mechanical activation without using any additions.

17.2 Experimental

$PbYb_{1/2}Nb_{1/2}O_3$ (PYN) ceramics was fabricated using two technological routes. Route I included the preliminary synthesis of the $YbNbO_4$ precursor via a usual solid state synthesis from Yb_2O_3 and Nb_2O_5 at 1000 °C for 4 h and subsequent mechanical activation of the mixture of this precursor with PbO. Route II also included the preliminary synthesis of $YbNbO_4$ precursor, but via the 20 min-long mechanochemical synthesis. In order to compensate PbO losses during sintering, 3 wt% excess of PbO was added in both cases to the nominally stoichiometric compositions. High-energy mechanical activation was carried out using planetary-centrifugal mill AGO-2 under a ball acceleration of 40 g. A mixture of powdered reagents (10 g) was placed into a steel jar together with 200 g of steel balls 8 mm in diameter. After each five minutes of activation, the mill was stopped, the jars were opened, the powder was taken out and homogenized in a mortar, and then it was put back into the jar for further activation. The green samples for sintering in the form of discs 10 mm in diameter and 3 mm—thick were pressed at 1000 kg/cm^2 without a plasticizer. Sintering of the samples placed into a sealed alumina crucible filled with $PbZrO_3$ powder, creating a buffer atmosphere suppressing the PbO evaporation, was carried out in an electric furnace at 800–1100 °C for 2 h. The density of thus obtained ceramics determined by the Archimedes method was about 93–95% of the theoretical one. Analysis of the images of the cleavage surfaces, obtained using Tescan Vega II LMU Scanning Electron Microscope, has shown that the mean grain size was about 2.0–3.5 μm for PYN samples, fabricated by both Route I and Route 2 and sintered at 900–1100 °C. X-ray diffraction (XRD) studies of the powder, obtained by crushing the ceramic samples, were performed using the DRON-7 diffractometer and filtered Co–Kα radiation. Phase control data were collected at room temperature in the 2Θ interval 20°–110°. XRD powder data in the 350–20 °C temperature range were collected

using the Anton Paar HTK 1200 N temperature camera in the cooling mode with the 15 min delay prior to starting measurements at each point. Phase identification and Rietveld quantitative phase analysis were carried out using the PCW software.

Dielectric studies were carried out on the Novocontrol (Alpha-A) impedance analyzer. The electrodes for measurements were deposited by firing on the silver past at 500 °C.

17.3 Results and Discussion

Room-temperature XRD studies of the surface of the as-sintered $PbYb_{1/2}Nb_{1/2}O_3$ (PYN) ceramic samples have shown that all the samples had a perovskite structure. However the splitting of the main perovskite reflections, indicating the orthorhombic distortion of the unit cell, typical of the ordered PYN [3, 5, 14, 49, 58, 59], was observed only for ceramics, obtained via the route I. All the samples obtained via the route II had a pseudocubic perovskite structure with some admixture of the pyrochlore phase. The content of the pyrochlore phase roughly estimated from the ratio of relative intensities of the (222) pyrochlore peak and the (110) perovskite peak [60] was about 15–30%. In contrast to both undoped and Li-doped $PbFe_{1/2}Nb_{1/2}O_3$ ceramics, obtained using mechanoactivation [34, 61, 62], where the pyrochlore phase was formed predominantly in the surface layer of the samples, in all the PYN samples studied the content of this parasitic phase was approximately the same throughout the specimen.

Figure 17.1 shows the temperature dependencies of the real part of permittivity ε' for some PYN samples, sintered from mechanoactivated powders, obtained using different technological routes, activation time τ and sintering temperature T_S. For the samples obtained by the technological route II, variation of both T_S within the 900–1100 °C range and τ within the 10–20 min range, caused comparatively small

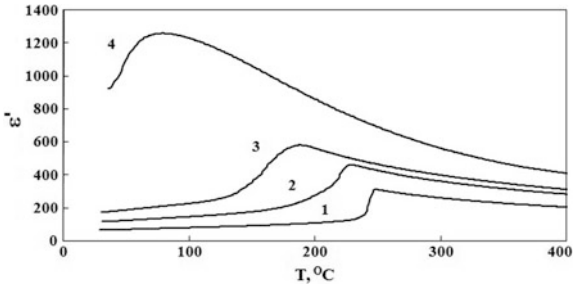

Fig. 17.1 Temperature dependencies of the real part of permittivity ε' measured at 1 MHz for $PbYb_{1/2}Nb_{1/2}O_3$ ceramics, sintered from mechanoactivated powders, obtained using different technological routes, activation time τ and sintering temperature T_S. (1) Route I: τ = 20 min; T_S = 900 °C; (2) route I: τ = 10 min; T_S = 900 °C; (3) route I: τ = 10 min; T_S = 1100 °C; (4) route II; τ = 20 min; T_S = 900 °C

changes of the $\varepsilon'(T)$ maximum temperature T_m usually not exceeding 20 K. In contrast to this, both T_m values and the shape of the ε''(T) maximum for PYN samples, obtained by different routes at the same values of τ (curves 1 and 4) as well as those for the PYN samples obtained by route I at different either τ (curves 1 and 2) or T_S (curves 2 and 3) values differ substantially.

It is well documented that highly-ordered PYN ceramics have a sharp antiferroelectric phase transition at 280–300 °C [3, 5, 14, 49, 58, 59]. Disordering, which has been achieved only for Li-doped PYN, leads to lowering of T_m down to 60–75 °C, accompanied by both growing and diffusion of the $\varepsilon'(T)$ maximum [49, 50]. Thus one can suppose that samples 1, 2 and 3 possess rather high degree of ordering, while the sample 4 is highly-disordered. This supposition is confirmed by the fact that the samples 1, 2 and 3 do not exhibit the frequency dependence of the $\varepsilon'(T)$ maximum, while diffused $\varepsilon'(T)$ maximum of the sample 4 shifts to higher temperatures and becomes lower as the measuring frequency increases (see Fig. 17.2). These results match well the data, obtained for Li-doped PYN ceramics with differing degree of ordering [49, 50].

To achieve a further insight into the origin of the large difference in the properties of PYN ceramic, fabricated using the different conditions, more precise XRD studies of the most ordered and most disordered samples (corresponding to curves 1 and 4 in Fig. 17.1), have been carried out. These samples will be referred further as PYN-o and PYN-d, respectively.

X-ray data for the PYN-o sample at all the temperature points studied, show the common reflections of the simple perovskite structure as well as reflections, indicating the 1:1 ordering of *B*-site ions (Fig. 17.3). Above 290 °C, all X-ray powder patterns of the PYN-o sample were indexed on the basis of cubic unit cell with the lattice constant $a = 2a_0$, were index 0 denotes the parameter of primitive perovskites cell. At 350 °C the value of cubic lattice constant is $a = 8.346(2)$ Å.

Below 290 °C, the additional reflections are found (Fig. 17.3), which can be attributed to the doubling of the diagonal of the unit cell in the high-temperature phase. This result is well consistent with the PYN structural model [59], suggesting

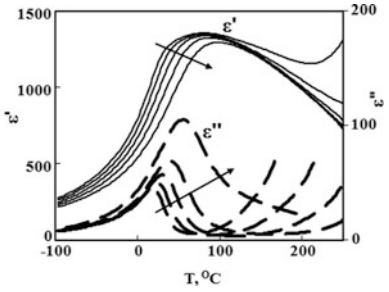

Fig. 17.2 Temperature dependences of the real part of permittivity ε' and imaginary part of permittivity ε'' measured at 10^2, 10^3, 10^4, 10^5, 10^6 Hz for the disordered PYN sample, fabricated via the route II at $\tau = 20$ min and $T_S = 900$ °C; the arrows show the direction of the frequency increase

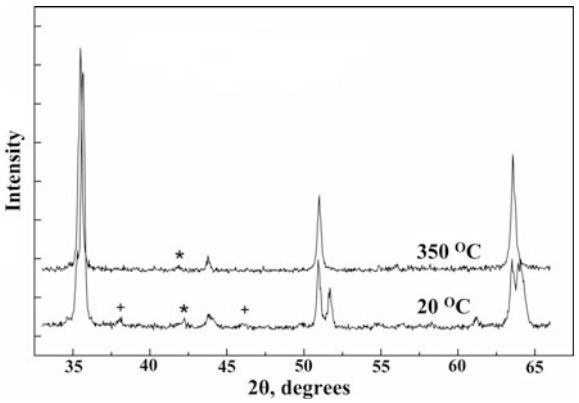

Fig. 17.3 XRD patterns for the PYN-o sample at 350 and 20 °C; two types of superstructural reflections are shown: the reflections corresponding to antiparallel Pb^{2+} shifts in [110] direction are marked by crosses; asteriks show the reflection, testifying the 1:1 compositional ordering of *B*-cations

the antiparallel shifts of Pb^{2+} ions, causing the antiferroelectric behavior of the ordered PYN. Low-temperature X-ray data were indexed on the base of the orthorhombic unit cell with lattice parameters:

$$\bar{a} = (\bar{a}_0 + \bar{b}_0); \quad \bar{b} = 4(\bar{a}_0 + \bar{b}_0); \quad \bar{c} = 2\bar{c}_0,$$

where index 0 stays for the parameters of the primitive perovskite cell. At room temperature a = 5.911(2) Å, b = 23.476(2) Å, c = 8.218(2) Å.

In the vicinity of the antiferroelectric phase transition, reflections of the cubic phase show deformations, which are supposed to result from the presence of a small amount of the low-temperature orthorhombic phase. To clarify the temperature range of the phase coexistence, the Rietveld quantitative phase analysis was carried out. At all temperatures two phases were used as the reference data: orthorhombic *Pbmn* (D_{2h}^{16}) for antiferroelectric ordered PYN [59] and cubic *Fm*3 *m* (O_h^5) for the ordered paraelectric phase. At the Rietveld cycles, lattice constants for both phases as well as their concentrations were refined. The best reliability factors R at all temperatures did not exceed 10% and the phase concentrations were determined with the accuracy not worse than 1%. Temperature dependence of lattice constants, obtained as a result of quantitative Rietveld analysis, is shown in Fig. 17.4. To plot lattice constants of the cubic and orthorhombic phases in one scale, normalization to the primitive perovskite cell was used. Normalized parameters shown in Fig. 17.4, are: $a_n = a/\sqrt{2}$; $b_n = b/(4\sqrt{2})$; $c_n = c/2$ for the orthorhombic phase and $a_n = a/2$ for the cubic phase.

In the temperature range 300–350 °C, the best result of fitting corresponds to 100% of the cubic phase. At 350 °C the long-range ordering, degree S was estimated according to [59]:

$$S^2 = (I_{111}/I_{200})_{exp.}/(I_{111}/I_{200)calc},$$

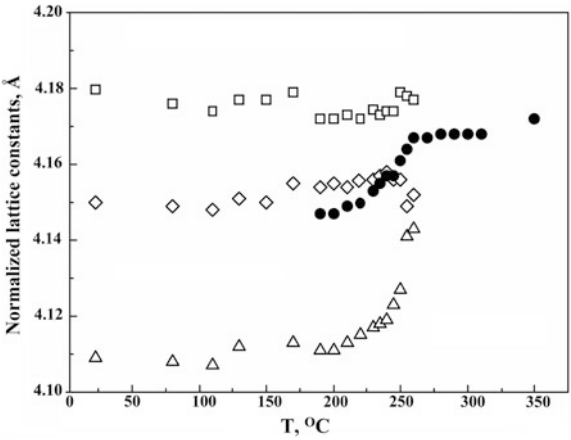

Fig. 17.4 Temperature dependence of the normalized lattice constants for the ordered PYN-o sample; open symbols indicate the parameters of the orthorhombic phase and rhomboids denote $a_n = a/\sqrt{2}$; squares show $b_n = b/(4\sqrt{2})$ and triangles correspond to $c_n = c/2$; closed circles indicate the normalized cubic lattice parameter, $a_n = a/2$

where I_{exp} denotes the measured X-ray intensities of the 111 and 200 reflections of the PYN-o sample; I_{calc} are the calculated intensities for PYN with fully 1:1 ordered ($S = 1$) Yb^{3+} and Nb^{5+} cations. The results for the PYN-o sample give $S = 0.82$ at 350 °C, so testifying the high degree of compositional ordering.

Below 190 °C the best refinement results were obtained for the single orthorhombic phase. In the 190–290 °C temperature range, the best Rietveld result ($R < 10\%$) corresponds to the coexistence of the cubic and orthorhombic phases (Fig. 17.5). Attempts of data minimization with the zero content of either cubic or

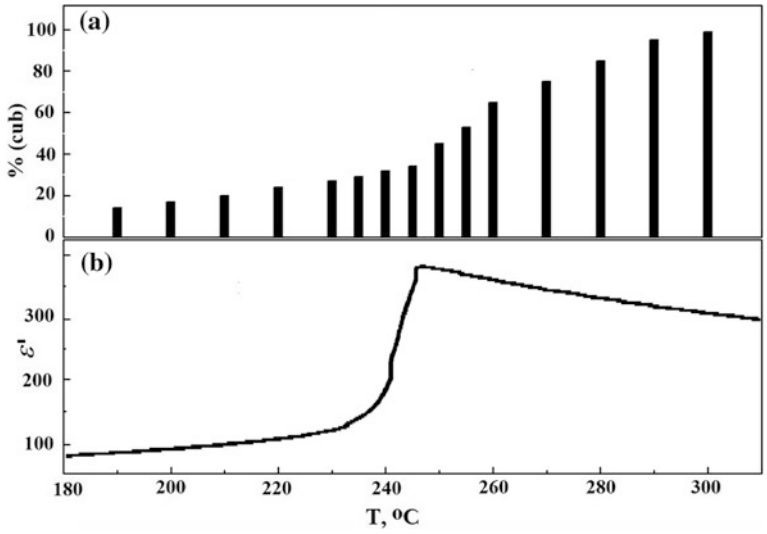

Fig. 17.5 Temperature dependencies of the relative concentration of the cubic phase (**a**) and the real part of dielectric permittivity, measured at 1 MHz (**b**) for the most ordered PYN-o sample

orthorhombic phase have led to significantly worse data convergence. Above 260 °C the lattice parameters of orthorhombic phase could not be determined with the appropriate accuracy because of the low intensities of the corresponding superstructure reflections.

Lowering of the unit cell symmetry in the PYN-o sample is followed by the dielectric anomaly (Fig. 17.5). Dielectric measurements show the abrupt change of the real part of dielectric permittivity ε' in the vicinity of 250 °C. This temperature range corresponds to the cubic phase concentration of about 30–40% that is close to the percolation threshold. One can see some jerks on the $\varepsilon'(T)$ curve, which may be due to the presence of the regions with different values of the long-range ordering degree S. According to the $S^2 - T$phase diagram, plotted in [49], PYN samples with $S = 0.82$ should have $T_m \approx 250$ °C, in good agreement with the data shown in Fig. 17.5.

XRD patterns of the disordered $PbYb_{1/2}Nb_{1/2}O_3$ sample, PYN-d, show the formation of simple perovskite phase without any traces of the antiferroelectric or compositional ordering (Fig. 17.6). Additional reflections were defined as the pyrochlore $Pb_{1.45}Nb_2O_{6.26}$ [63] phase. At the first approach of Rietveld quantitative phase analysis the primitive perovskite $Pm3\ m$ (O_h^7) and pyrochlore $Pb_{1.45}Nb_2O_{6.26}$ [63] were used as the reference phases. At the Rietveld minimization cycles, lattice constants for both phases as well as their concentrations were refined. The best reliability factors R at all temperatures did not exceeded 10% and the phase concentrations were determined with the accuracy not worse than 1%. As a result, the concentration of PYN (perovskite) phase was found equal to 75%.

Since the pyrochlore impurity phase contains only lead and niobium, the presence of additional ytterbium-containing impurity phase can be assumed. The absence of corresponding XRD reflections can be explained by the presence of the Yb_2O_3 impurity [64], its reflexes being superimposed on the $Pb_{1.45}Nb_2O_{6.26}$ ones. So at the second Rietveld approach the presence of all the three above-mentioned reference phases was tested. Results have shown no affect of additional Yb_2O_3

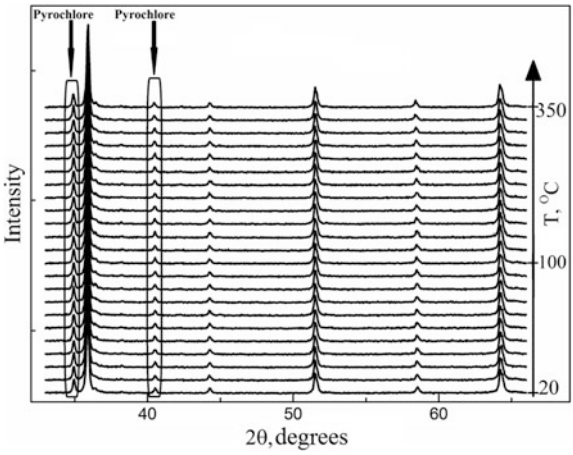

Fig. 17.6 X-ray diffraction data for the disordered PYN-d sample in the temerature range 20–350 °C; rectangles mark the reflections of the pyrochlore phase

impurity on the PYN lattice parameters and concentration. The final result for phase concentrations is 75% for PYN (perovskite), 23% for $Pb_{1.45}Nb_2O_{6.26}$ pyrochlore and 2% for Yb_2O_3. So, according to the results of Rietveld quantitative phase analysis, the concentrations of perovskite and total impurity phases in the PYN-d sample do not vary at changing the temperature.

Figure 17.7 shows the temperature dependence of the lattice parameter a for the disordered PYN-d sample. No changes of the cubic symmetry on cooling from 500 °C down to 20 °C were found. However, in the 60–100 °C temperature range the $a(T)$ curve shows a plateau. This anomaly may indicate the structural phase transition. It is worth noting that just in this temperature range the temperature dependence of the real part of permittivity ε' of the PYN-d sample has a maximum (Fig. 17.2).

As was already mentioned above, the PYN-d sample exhibits a relaxor-like dielectric behavior (Fig. 17.2), i.e. the temperature dependencies of both the real part of permittivity ε' and imaginary part of permittivity ε'' have diffused maxima, which become lower and shift to higher temperatures as the measuring frequency f grows. One of the most characteristic features of relaxors is a non-Debye character of dielectric relaxation. Figure 17.8a shows that for the PYN-d sample studied, the increase of T_m with the frequency f does not follow the Arrhenius law, implying the non-Debye character of relaxation, but is well fitted with the empirical Vogel–Fulcher relation:

$$f = f_0 \exp[-W/k(T_m - T_0)],$$

where f_0 is an attempt frequency, W is the activation energy and T_0 is the Vogel–Fulcher temperature, which is usually defined as the temperature of the polar nanoregions freezing and transition into the dipole-glass state [11, 65, 66]. Though nowadays it is believed that the Vogel–Fulcher-type behavior is not necessarily related to the relaxation freezing [67], the Vogel–Fulcher scaling remains a

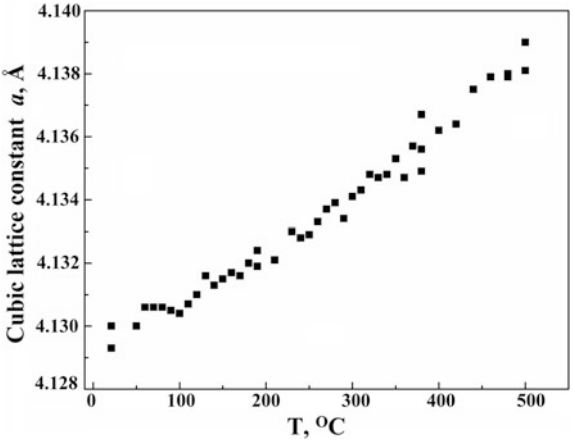

Fig. 17.7 Temperature dependence of the cubic lattice constant for the disordered PYN-d sample

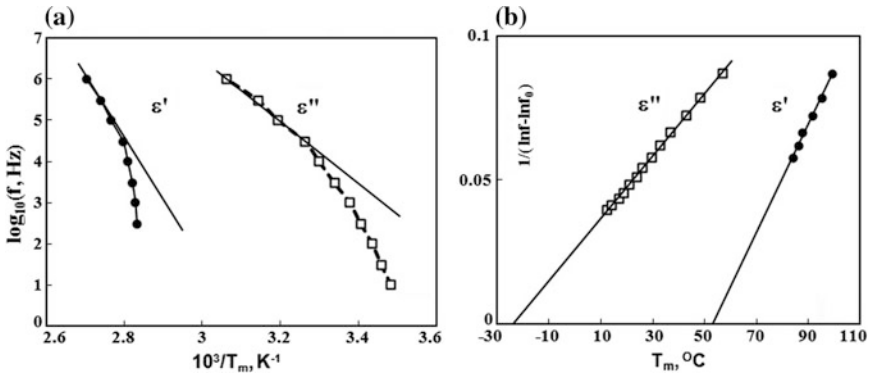

Fig. 17.8 **a** Nonlinear dependences of the temperatures of $\varepsilon'(T)$ and $\varepsilon''(T)$ maxima on frequency f in the Arrhenius coordinates for disordered PYN ceramics, illustrating the non-Debye character of relaxation; **b** dependences of $(\ln f_0 - \ln f)^{-1}$ on T_m for the same sample as in the panel (**a**), illustrating the applicability of the Vogel–Fulcher relation for fitting the frequency shift of both $\varepsilon'(T)$ and $\varepsilon''(T)$ maxima

convenient tool for comparing the properties of different relaxors. For the PYN-d sample studied, $f_0 = 2 \times 10^{10}$ Hz, $T_0 \approx 55$ °C and $E_0 \approx 0.035$ eV for the $\varepsilon'(T)$ maximum while for the $\varepsilon''(T)$ maximum $T_0 \approx -25$ °C and $E_0 \approx 0.084$. It is worth noting that for single crystals and ceramics of the classical relaxor $PbMg_{1/3}Nb_{2/3}O_3$ and its solid solutions T_0, values for both real and imaginary parts of permittivity are nearly the same [65, 68, 69]. However, for solid solutions of antiferroelectric $NaNbO_3$ exhibiting relaxor-like dielectric properties, T_0, values for the $\varepsilon''(T)$ maximum are much lower than those for the $\varepsilon'(T)$ [70], as in the case of the PYN-d sample.

Though the most disordered PYN samples, obtained in the present work (Fig. 17.1, curve 4 and Fig. 17.2) are contaminated by the parasitic pyrochlore phase, the maximal values of permittivity are somewhat higher than those reported for the Li-doped disordered PYN ceramics, fabricated by usual methods [49, 50]. To estimate quantitatively diffusion of the $\varepsilon'(T)$ maxima of the disordered PYN ceramics, obtained in the present work and in [49, 50], we used the parameter W2/3 M–H, defined as the difference between T_m and the temperature, where ε' reaches 2/3 of the maximum value from the high-temperature side of the $\varepsilon'(T)$ peak. This parameter is widely used for estimation of the diffusion of the $\varepsilon'(T)$ maximum in relaxors and ferroelectrics with a diffuse phase transition having different composition and structure [7, 34, 56, 71–77]. For PYN-d sample the value of W2/3 M–H appeared equal to ≈ 160 K, while for the most disordered Li-doped PYN sample, sintered at 1074 °C [49], it is ≈ 65 K. Larger diffusion of the $\varepsilon'(T)$ maximum as compared to similar ceramics, obtained by usual method, has been already reported for ferroelectric ceramics, fabricated using mechanical activation [56, 62, 78]. This difference was attributed to higher concentration of defects, appearing in the course of mechanical activation. In our case additional

sources of the $\varepsilon'(T)$ maximum diffusion may be the admixture of the parasitic pyrochlore phase, having low
ε' values [60] and spatial inhomogeneities in the compositional ordering degree, observed in both single crystals and ceramics of the $Pb_2B'B''O_6$ (B' = Fe, Sc, In; B'' = Nb, Ta) perovskites [79–81].

Besides the $\varepsilon'(T)$ maximum at ≈ 70 °C, in the PYN-d sample a high-temperature relaxation $\varepsilon'(T)$ maximum is observed above ≈ 400 °C (Fig. 17.9). The frequency shift of the temperature of these maximum linearizes in the Arrhenius coordinates (see the inset in Fig. 17.9), i.e. it obeys the Debye law. Activation energy of relaxation appeared equal to 1.45 eV. Similar high-temperature Debye-like relaxation was observed previously in a large number of perovskites, both lead-containing ($PbB'_{1/2}B''_{1/2}O_3$ (B' = Fe, Sc; B'' = Nb, Ta) [23, 82–84]), and lead-free ($BaFe_{1/2}Nb_{1/2}O_3$, $SrTiO_3$ [85, 86]), as well as in solid solutions (e.g. $BiFeO_3$-based [87] and $NaNbO_3$-based [88, 89]). This relaxation was usually attributed to the presence of oxygen vacancies being the most easily-formed intrinsic point defects in perovskites [90, 91]. Activation energies of about 1.5 eV, i.e. close to that found for PYN-d sample, were observed, e.g. in Bi-doped $SrTiO_3$ [86] and in (Pb, Ca)$Fe_{1/2}Nb_{1/2}O_3$ [83] solid solution ceramics. This relaxation seems to correspond to a long-range motion of the doubly-ionized oxygen vacancies [86].

It should be noted that in the present work mechanical activation was carried out using steel balls and jars. So one could expect that a small amount of iron from a milling media incorporates into the processed powder. This is indeed so, because

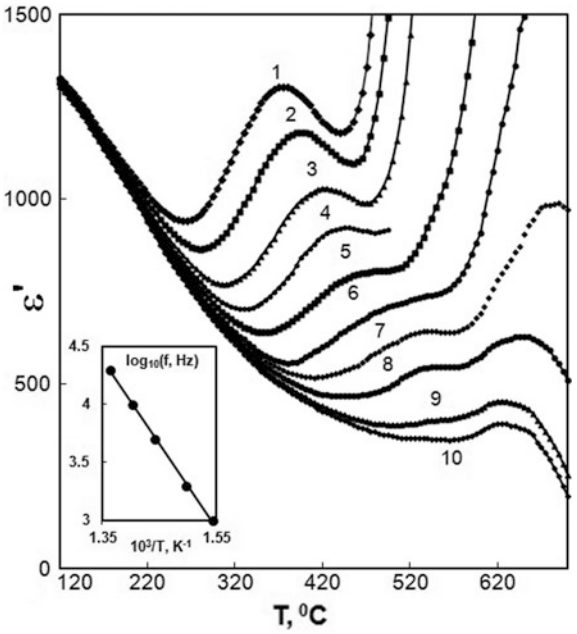

Fig. 17.9 $\varepsilon'(T)$ curves for disordered PYN-d ceramic sample measured at different frequencies f (Hz): (1) 10^3, (2) 2×10^3, (3) 5×10^3, (4) 10^4, (5) 2×10^4, (6) 5×10^4, (7) 10^5, (8) 2×10^5, (9) 5×10^5, (10) 10^6; the inset shows Arrhenius plot of the frequency shift for the high-temperature relaxation maximum

the color of the samples studied is not a yellowish, typical of PYN ceramics fabricated by usual methods, but rather a brownish. The amount of iron, incorporated during mechanical activation usually does not exceed 1 wt% [78]. Even if one assume, as it was done in [78], that all this iron incorporates into the crystal lattice and forms $(1 - x)Pb(Yb_{1/2}Nb_{1/2})O_3 - xPb(Fe_{1/2}Nb_{1/2})O_3$ (PYN—PFN) solid solution, the concentration of PFN in this solutions would not exceed 12 mol%. PYN—PFN solid solutions have been already studied [92] and it was established that in this system T_m lowers and the $\varepsilon'(T)$ maximum diffuses as the concentration of PFN increases. However, composition 0.88PYN—0.12PFN has a sharp and frequency independent $\varepsilon'(T)$ maximum at $\approx$ 150 °C [92], i.e. substantially higher than T_m value of the PYN-d sample (Figs. 17.1 and 17.2). Moreover, one could expect that the powders, activated for a longer time, should contain larger amount of iron. In contrast to this expectation the PYN sample, fabricated via the route I at τ = 20 min (Fig. 17.1, curve 1) has much higher T_m than the samples, fabricated via the same route at τ = 10 min (Fig. 17.1, curves 2 and 3). Thus one may conclude that the changes of T_m as well as diffusion of the $\varepsilon'(T)$ maximum, observed for PYN samples, fabricated using mechanical activation method, are due to the changes in compositional ordering degree of Yb^{3+} and Nb^{5+} ions rather than due to formation of the PYN—PFN solid solution as a result of incorporating of iron from the milling media.

17.4 Summary

High-energy mechanical activation makes it possible to obtain ceramics of disordered $Pb(Yb_{1/2}Nb_{1/2})O_3$ (PYN) without the use of any additives. The degree of compositional ordering of the Yb^{3+} and Nb^{5+} ions and, accordingly, the temperature and diffusion of the antiferroelectric phase transition in PYN ceramics can be changed within wide limits by varying the duration of the mechanical activation, starting materials (oxides or preliminary synthesized precursors) and sintering temperature.

Acknowledgements This work was supported in part by the Ministry of Education and Science of the Russian Federation (research project No. 3.1649.2017/4.6) and by the Russian Foundation for Basic Research (grant No. 17-03-01293_a).

References

1. A. Sternberg, L. Shebanovs, J.Y. Yamashita, M. Antonova, M. Livinsh, Ferroelectrics **241**, 51 (2000)
2. E.I. Sitalo, I.P. Raevski, A.G. Lutokhin, A.V. Blazhevich, S.P. Kubrin, S.I. Raevskaya, YuN Zakharov, M.A. Malitskaya, V.V. Titov, I.N. Zakharchenko, IEEE Trans. Ultrason. Ferroelect. Freq. Contr. **58**, 1914 (2011)

3. V.A. Isupov, Ferroelectrics **289**, 131 (2003)
4. V.V. Shvartsman, A.L. Kholkin, I.P. Raevski, S.I. Raevskaya, F.I. Savenko, A.S. Emelyanov, J. Appl. Phys. **113**, 187208 (2013)
5. A. Kania, J. Cryst. Growth **310**, 2767 (2008)
6. Y.N. Zakharov, S.I. Raevskaya, A.G. Lutokhin, V.V. Titov, I.P. Raevski, V.G. Smotrakov, V. V. Eremkin, A.S. Emelyanov, A.A. Pavelko, Ferroelectrics **399**, 20 (2010)
7. I.P. Raevski, V.V. Titov, M.A. Malitskaya, E.V. Eremin, S.P. Kubrin, A.V. Blazhevich, H. Chen, C.-C. Chou, S.I. Raevskaya, I.N. Zakharchenko, D.A. Sarychev, S.I. Shevtsova, J. Mater. Sci. **49**, 6459 (2014)
8. E. Dul'kin, I.P. Raevski, S.M. Emel'yanov, Phys. Solid State **45**, 158 (2003)
9. E. Dul'kin, E. Mojaev, M. Roth, I.P. Raevski, S.A. Prosandeev, Appl. Phys. Lett. **94**, 252904 (2009)
10. S.I. Raevskaya, YuN Zakharov, A.G. Lutokhin, A.S. Emelyanov, I.P. Raevski, M.S. Panchelyuga, V.V. Titov, S.A. Prosandeev, Appl. Phys. Lett. **93**, 042903 (2008)
11. S. Prosandeev, I.P. Raevski, M.A. Malitskaya, S.I. Raevskaya, H. Chen, C.C. Chou, B. Dkhil, J. Appl. Phys. **114**, 124103 (2013)
12. S. Zhang, F. Li, J. Appl. Phys. **111**, 031301 (2012)
13. E.I. Sitalo, YuN Zakharov, A.G. Lutokhin, S.I. Raevskaya, I.P. Raevski, M.S. Panchelyuga, V.V. Titov, L.E. Pustovaya, I.N. Zakharchenko, A.T. Kozakov, A.A. Pavelko, Ferroelectrics **389**, 107 (2009)
14. N. Yasuda, H. Inagaki, Japan. J. Appl. Phys. **5**, L2050 (1991)
15. V.I. Aleshin, I.P. Raevski, J. Alloys Compnds **587**, 138 (2014)
16. V.V. Laguta, A.N. Morozovska, E.I. Eliseev, I.P. Raevski, S.I. Raevskaya, E.I. Sitalo, S.A. Prosandeev, L. Bellaiche, J. Mater. Sci. **51**, 5330 (2016)
17. D.A. Sanchez, N. Ortega, A. Kumar, G. Sreenivasulu, R.S. Katiyar, J.F. Scott, D.M. Evans, M. Arredondo-Arechavala, A. Schilling, J.M. Gregg, J. Appl. Phys. **113**, 074105 (2013)
18. V.V. Laguta, V.A. Stephanovich, I.P. Raevski, S.I. Raevskaya, V.V. Titov, V.G. Smotrakov, V.V. Eremkin, Phys. Rev. B **95**, 014207 (2017)
19. Y. Yamashita, K. Harada, Y. Hosono, S. Natsume, N. Ichinose, Jpn. J. Appl. Phys. **37**, 5288 (1998)
20. C.G.F. Stenger, F.L. Scholten, A.J. Burggraaf, Solid State Commun. **32**, 989 (1979)
21. N. Setter, L.E. Cross, J. Appl. Phys. **51**, 4356 (1980)
22. A.A. Bokov, I.P. Rayevsky, Ferroelectric **90**, 125 (1989)
23. A.A. Bokov, I.P. Raevskii, V.G. Smotrakov, Fizika Tverd Tela. **26**, 2824 (1984)
24. P.K. Davies, H. Wu, A.Y. Borisevich, I.E. Molodetsky, L. Farber, Annu. Rev. Mater. Res. **38**, 369 (2008)
25. V.A. Shuvaeva, I. Pirog, Y. Azuma, K. Yagi, K. Sakaue, H. Terauchi, I.P. Raevskii, K. Zhuchkov, MYu. Antipin, J. Phys. Condens. Matter. **15**, 2413 (2003)
26. A.A. Bokov, N.P. Protsenko, Z.-G. Ye, J. Phys. Chem. Sol. **61**, 1519 (2000)
27. I.P. Raevskii, D.A. Sarychev, S.A. Bryugeman, L.A. Reznichenko, L.A. Shilkina, O.N. Razumovskaya, V.S. Nikolaev, N.P. Vyshatko, A.N. Salak, Crystallogr. Rep. **47**, 1012 (2002)
28. S.P. Kubrin, S.I. Raevskaya, S.A. Kuropatkina, I.P. Raevski, D.A. Sarychev, Ferroelectrics **340**, 155 (2006)
29. I.P. Raevski, S.P. Kubrin, S.I. Raevskaya, S.A. Prosandeev, D.A. Sarychev, M.A. Malitskaya, V.V. Stashenko, I.N. Zakharchenko, Ferroelectrics **398**, 16 (2010)
30. V.V. Laguta, V.A. Stephanovich, M. Savinov, M. Marysko, R.O. Kuzian, N.M. Olekhnovich, A.V. Pushkarev, YuV Radyush, I.P. Raevski, S.I. Raevskaya, S.A. Prosandeev, New J. Phys. **16**, 11304 (2014)
31. I.P. Raevski, N.M. Olekhnovich, A.V. Pushkarev, Y.V. Radyush, S.P. Kubrin, S.I. Raevskaya, M.A. Malitskaya, V.V. Titov, V.V. Stashenko, Ferroelectrics **444**, 47 (2013)
32. I.P. Raevski, A.V. Pushkarev, S.I. Raevskaya, N.M. Olekhnovich, Y.V. Radyush, S. P. Kubrin, H. Chen, C.-C. Chou, D.A. Sarychev, V.V. Titov, M.A. Malitskaya, Ferroelectrics **501**, 154 (2016)

33. A.A. Gusev, S.I. Raevskaya, V.V. Titov, V.P. Isupov, E.G. Avvakumov, I.P. Raevski, H. Chen, C.-C. Chou, S.P. Kubrin, S.V. Titov, M.A. Malitskaya, D.A. Sarychev, V.V. Stashenko, S.I. Shevtsova, Ferroelectrics **496**, 231 (2016)
34. A.A. Gusev, S.I. Raevskaya, I.P. Raevski, V.P. Isupov, E.G. Avvakumov, S.P. Kubrin, H. Chen, V.V. Titov, T.A. Minasyan, C.-C. Chou, S.V. Titov, M.A. Malitskaya, Ferroelectrics **496**, 250 (2016)
35. M. Maryško, V.V. Laguta, I.P. Raevski, R.O. Kuzian, N.M. Olekhnovich, A.V. Pushkarev, YuV Radyush, S.I. Raevskaya, V.V. Titov, S.P. Kubrin, AIP Adv. **7**, 056409 (2017)
36. S.I. Raevskaya, S.P. Kubrin, I.P. Raevski, C.-C. Chou, H. Chen, V.V. Titov, M.A. Malitskaya, D.A. Sarychev, I.N. Zakharchenko, Ferroelectrics **509**, 64 (2017)
37. M.A. Gilleo, J. Phys. Chem. Sol. **13**, 33 (1960)
38. V.V. Laguta, J. Rosa, L. Jastrabik, R. Blinc, P. Cevc, B. Zalar, M. Remskar, S.I. Raevskaya, I. P. Raevski, Mater. Res. Bull. **45**, 1720 (2010)
39. K. Kouril, V. Chlan, H. Štepánková, R. Reznícek, K. Ulicná, V.V. Laguta, I.P. Raevski, Acta Phys. Polonica A. **127**, 234 (2015)
40. N.S. Druzhinina, YuI Yuzyuk, I.P. Raevski, M. El Marssi, V.V. Laguta, S.I. Raevskaya, Ferroelectrics **438**, 107 (2012)
41. Y.I. Yuzyuk, I.P. Raevski, S.I. Raevskaya, N. Lemee, M.G. Karkut, W. Peng, M. El Marssi, H. Chen, J. Alloys Compd. **695**, 1821 (2017)
42. I.P. Raevski, S.P. Kubrin, S.I. Raevskaya, D.A. Sarychev, S.A. Prosandeev, M.A. Malitskaya, Phys. Rev. B. **85**, 224412 (2012)
43. S.A. Prosandeev, I.P. Raevski, S.I. Raevskaya, H. Chen, Phys. Rev. B. **92**, 220419(R) (2015)
44. H. Uršič, A. Benčan, G. Dražič, G. Esteves, J.L. Jones, T.-M. Usher, T. Rojac, S. Drnovšek, M. Deluca, J. Jouin, V. Bobnar, G. Trefalt, J. Holc, B. Malič, J. Mater. Chem. C. **3**, 10309 (2015)
45. A.A. Bokov, I.P. Raevsky, V.G. Smotrakov, S.M. Zaitsev, Kristallografiya **32**, 1301 (1987)
46. I.P. Raevski, S.A. Prosandeev, S.M. Emelyanov, F.I. Savenko, I.N. Zakharchenko, O.A. Bunina, A.S. Bogatin, S.I. Raevskaya, E.S. Gagarina, E.V. Sahkar, L. Jastrabik, Ferroelectrics **53**, 475 (2003)
47. I.P. Raevskii, V.V. Eremkin, V.G. Smotrakov, M.A. Malitskaya, S.A. Bogatina, L.A. Shilkina, Crystallogr. Rep. **47**, 1007 (2002)
48. I.P. Raevski, S.A. Prosandeev, S.M. Emelyanov, V.G. Smotrakov, V.V. Eremkin, I.N. Zakharchenko, S.I. Raevskaya, E.S. Gagarina, F.I. Savenko, E.V. Sahkar, Ferroelectrics **298**, 267 (2004)
49. A.A. Bokov, V.Y. Shonov, I.P. Rayevsky, E.S. Gagarina, M.F. Kupriyanov, J Phys. Condens Matter. **31**, 5491 (1993)
50. I.P. Raevski, V.Y. Shonov, M.A. Malitskaya, E.S. Gagarina, V.G. Smotrakov, V.V. Eremkin, Ferroelectrics. **235**, 205 (1999)
51. D. Bochenek, P. Kruk, R. Skulski, P. Wawrzała, J. Electroceram. **26**, 8 (2011)
52. I.P. Raevskii, S.T. Kirillov, M.A. Malitskaya, V.P. Filippenko, S.M. Zaitsev, L.G. Kolomin, Inorg. Mater. **24**, 217 (1988)
53. A.V. Pavlenko, N.A. Boldyrev, L.A. Reznichenko, I.A. Verbenko, G.M. Konstantinov, L.A. Shilkina, Inorg. Mater. **50**, 750 (2014)
54. J.M. Haussonne, G. Desgardin, P.H. Bajolet, B. Raveau, J. Am. Ceram. Soc. **66**, 801 (1983)
55. X. Gao, J. Xue, J. Wang, Mater. Sci. Eng. B **99**, 63 (2003)
56. A.A. Gusev, S.I. Raevskaya, V.V. Titov, E.G. Avvakumov, V.P. Isupov, I.P. Raevski, H. Chen, C.-C. Chou, S.P. Kubrin, S.V. Titov, M.A. Malitskaya, A.V. Blazhevich, D.A. Sarychev, V.V. Stashenko, S.I. Shevtsova, Ferroelectrics **475**, 41 (2015)
57. M. Savinov, P. Bednyakov, S.I. Raevskaya, A.A. Gusev, V.P. Isupov, I.P. Raevski, V.V. Titov, H. Chen, S.A. Kovrigina, C.-C. Chou, T.A. Minasyan, M.A. Malitskaya, Ferroelectrics **509**, 80 (2017)
58. C. Cochard, F. Karolak, C. Bogicevic, O. Guedes, P.-E. Janolin, Adv. Mater. Sci. Eng. **2015**, 408101 (2015)
59. J.R. Kwon, W.K. Choo, J. Phys. Condens Matter. **3**, 2147 (1991)

60. I.P. Raevski, S.P. Kubrin, S.A. Kovrigina, S.I. Raevskaya, V.V. Titov, A.S. Emelyanov, M.A. Malitskaya, I.N. Zakharchenko, Ferroelectrics **397**, 96 (2010)
61. A.A. Gusev, I.P. Raevski, E.G. Avvakumov, V.P. Isupov, Sci. Sinter. **48**, 283 (2016)
62. A.A. Gusev, I.P. Raevski, E.G. Avvakumov, V.P. Isupov, S.I. Raevskaya, H. Chen, V.V. Titov, C.-C. Chou, S.P. Kubrin, S.V. Titov, M.A. Malitskaya, Ferroelectrics **475**, 61 (2015)
63. F. Beech, W.M. Jordan, C.R.A. Catlow, A. Santoro, B.C.H. Steele, J. Solid State Chem. **77**, 322 (1988)
64. M. Mitric, B. Antic, M. Balanda, D. Rodic, M.L. Napijaolo, J. Phys. Cond. Matter **9**, 4103 (1997)
65. D. Viehland, S. Jang, L.E. Cross, M. Wuttig, Phil. Mag. B. **64**, 335 (1991)
66. I.P. Raevski, V.V. Eremkin, V.G. Smotrakov, E.S. Gagarina, M.A. Malitskaya, Phys. Solid State **42**, 161 (2000)
67. A.A. Bokov, Z.-G. Ye, J. Adv. Dielectrics. **2**, 1241010 (2012)
68. I.K. Bdikin, J. Gracio, D.A. Kiselev, I.P. Raevski, S.I. Raevskaya, S.A. Prosandeev, A.L. Kholkin, J. Appl. Phys. **110**, 052002 (2011)
69. F. Chu, I.M. Reaney, N. Setter, Ferroelectrics **151**, 343 (1994)
70. S.I. Raevskaya, L.A. Reznitchenko, V.V. Titov, I.P. Raevski, M.A. Malitskaya, I.N. Zakharchenko, J.-L. Dellis, Ferroelectrics **371**, 63 (2008)
71. I.P. Raevski, S.P. Kubrin, V.V. Laguta, M. Marysko, H. Chen, S.I. Raevskaya, V.V. Titov, C.-C. Chou, A.V. Blazhevich, E.I. Sitalo, D.A. Sarychev, T.A. Minasyan, A.G. Lutokhin, YuN Zakharov, L.E. Pustovaya, I.N. Zakharchenko, M.A. Malitskaya, Ferroelectrics **475**, 20 (2015)
72. C. Lei, A.A. Bokov, Z.-G. Ye, J. Appl. Phys. **101**, 084105 (2007)
73. S.I. Raevskaya, A.G. Lutokhin, A.M. Pugachev, I.P. Raevski, V.V. Titov, YuN Zakharov, D. V. Suzdalev, E.M. Panchenko, S.A. Prosandeev, Ferroelectrics **440**, 59 (2012)
74. A.T. Kozakov, A.G. Kochur, A.V. Nikolskii, I.P. Raevski, S.P. Kubrin, S.I. Raevskaya, V.V. Titov, M.A. Malitskaya, I.N. Zakharchenko, S.I. Shevtsova, J. Mater. Sci. **52**, 10140 (2017)
75. S.I. Raevskaya, V.V. Titov, I.P. Raevski, A.G. Lutokhin, YuN Zakharov, VYu. Shonov, A.V. Blazhevich, E.I. Sitalo, H. Chen, C.-C. Chou, S.A. Kovrigina, M.A. Malitskaya, Ferroelectrics **475**, 31 (2015)
76. J. Zhai, H. Chen, C.-C. Chou, S.I. Raevskaya, S.A. Prosandeev, I.P. Raevski, J. Alloys Compounds. **509**, 6113 (2011)
77. S.I. Raevskaya, S.P. Kubrin, A.V. Pushkarev, N.M. Olekhnovich, YuV Radyush, V.V. Titov, M.A. Malitskaya, I.N. Zakharchenko, H. Chen, C.-C. Chou, I.P. Raevski, Ferroelectrics **509**, 40 (2017)
78. Z. Branković, G. Branković, V. Vukotić, R. Tararam, J.A. Varela, Metall. Mater. Trans. A **39**, 875 (2008)
79. A.A. Bokov, M.A. Malitskaya, I.P. Raevskii, VYu. Shonov, Fizika Tverdogo Tela. **32**, 2488 (1990)
80. A.S. Bogatin, A.A. Bokov, I.P. Rayevsky, V.P. Filippenko, Ferroelectrics **118**, 232 (1990)
81. I.P. Raevski, S.P. Kubrin, S.I. Raevskaya, V.V. Stashenko, D.A. Sarychev, M.A. Malitskaya, M.A. Seredkina, V.G. Smotrakov, I.N. Zakharchenko, V.V. Eremkin, Ferroelectrics **373**, 121 (2008)
82. I.P. Rayevsky, A.A. Bokov, A.S. Bogatin, S.M. Emelyanov, M.A. Malitskaya, O.I. Prokopalo, Ferroelectrics **126**, 191 (1992)
83. M. Puri, S. Bahel, I.P. Raevski, S.B. Narang, J. Mater. Sci. Mater. El. **27**, 1077 (2016)
84. V. Bobnar, H. Uršič, G. Casar, S. Drnovšek, Phys. Status Solidi B **250**, 2232 (2013)
85. I.P. Raevski, S.A. Kuropatkina, S.P. Kubrin, S.I. Raevskaya, V.V. Titov, D.A. Sarychev, M. A. Malitskaya, A.S. Bogatin, I.N. Zakharchenko, Ferroelectrics **379**, 272 (2009)
86. C. Ang, Z. Yu, L.E. Cross, Phys. Rev. B. **62**, 228 (2000)
87. I.P. Raevski, S.P. Kubrin, S.I. Raevskaya, D.A. Sarychev, J.-L. Dellis, Ferroelectrics **371**, 113 (2008)
88. I.P. Raevski, L.A. Reznitchenko, M.A. Malitskaya, L.A. Shilkina, S.O. Lisitsina, S.I. Raevskaya, E.M. Kuznetsova, Ferroelectrics **299**, 95 (2004)

89. S.I. Raevskaya, L.A. Reznichenko, I.P. Raevski, V.V. Titov, S.V. Titov, J.-L. Dellis, Ferroelectrics **340**, 107 (2006)
90. S.A. Prosandeev, A.V. Fisenko, A.V. Riabchinski, I.A. Osipenko, I.P. Raevski, N. Safontseva, J. Phys. Condens. Matter. **8**, 6705 (1996)
91. I.P. Raevski, S.M. Maksimov, A.V. Fisenko, S.A. Prosandeev, I.A. Osipenko, P.F. Tarasenko, J. Phys. Condens. Matter. **10**, 8015 (1998)
92. B.J. Kuh, D.C. Choi, W.K. Choo, Ferroelectrics **223**, 187 (1999)

Chapter 18
Third-Order Fuchs Elastic Constants and the Pressure Derivatives of the Second-Order Elastic Constants for Compressed Ne and Ar in the Model of Deformable Atoms

Ievgen Ie. Gorbenko, Elena P. Troitskaya, Ekaterina A. Pilipenko, Ilya A. Verbenko and Yuriy I. Yurasov

Abstract The theoretical ab initio investigation of the elastic properties of the compressed rare-gas crystals is carried out in a model of deformable and polarizable atoms, taking into account the many-body interaction and quadrupole interaction. The analytical expressions for the Fuchs elastic moduli have been obtained from the equations of lattice vibrations in the long-wave approximation. The derivatives of the second-order Fuchs elastic moduli with respect to the pressure and corresponding third-order Fuchs elastic moduli were calculated in the wide pressure range. It has been shown that values for the pressure derivatives of the second-order Fuchs elastic moduli were in good agreement with the experiment at zero pressure and the results of the empirical calculations of other authors.

18.1 Introduction

Investigation of second-order elastic constants and other related elastic properties under pressure [1–7] is an important tool for studying the behavior of solids under extreme conditions. Elastic constants of higher-orders were a subject of extensive

Ie. Ie. Gorbenko (✉)
Lugansk Taras Shevchenko National University, Lugansk, Ukraine
e-mail: e_g81@mail.ru

E. P. Troitskaya · E. A. Pilipenko
Donetsk A.A. Galkin Physics and Technology Institute, Donetsk, Ukraine

I. A. Verbenko · Y. I. Yurasov
Research Institute of Physics, Southern Federal University, Rostov-on-Don, Russia

Y. I. Yurasov
Southern Scientific Centre RAS, Rostov-on-Don, Russia

I. A. Parinov et al. (eds.), *Advanced Materials*, Springer Proceedings in Physics 207, https://doi.org/10.1007/978-3-319-78919-4_18

study for several last decades and estimated in the earlier works [3, 8–11] predominantly for ionic crystals.

A series of works [12–18] is devoted to studying elastic moduli of stressed crystals. Equations for the derivatives of adiabatic and isothermal elastic moduli with respect to the stress tensor for the initially stressed crystal of the arbitrary symmetry are deduced. The proposed methods of obtaining the derivatives with respect to the stress tensor and the relations between different elastic moduli may be applied to the elastic moduli of higher order. The theory developed by authors may by basis for the experimental static determination of the third-order elastic moduli of crystals with different types of chemical bonds and symmetry. Some results of these studies are given in the monography [19].

For rare-gas crystals (RGC) numerous theoretical [20–28] studies of the second- and third-order elastic moduli at high pressures were performed with the use ab initio methods and model potentials. The first attempts to incorporate many-body effects into the energetic calculations of RGC were made by Axilrod and Teller [29].

To study the lattice dynamics of RGC, Lehri and Verma [23] developed a three-body interaction model incorporating varied induced dipoles. Using this model as a basis, they calculated the second- and third-order Brugger elastic moduli of RGC at $p = 0$ in two variants [24]: (1) using the experimental first derivative of the bulk elastic modulus with respect to the pressure (dB/dp) and (2) approximating the three-body potential with the exponential function proposed by Cochran [30]. The other four model parameters were estimated from three second-order elastic moduli and an equilibrium condition. Using this potential in the second variant including the energetic contribution of zero-point oscillations (the Lundqvist potential), the first- and second-order derivatives of the bulk elastic and two shear moduli with respect to the pressure were calculated for crystals of the Ne–Xe series at $p = 0$ [31].

The three-body Lundqvist potential [32] was also used by Gupta and Goyal [28] to obtain the expressions for the second- and third-order Brugger elastic moduli and the first-order derivatives of the bulk and shear moduli with respect to the pressure. In [28], the values of third-order elastic constants for Ne to 100 GPa and Ar to 75 GPa are computed. The authors note that the obtained results are interesting and may be helpful in understanding the elastic behavior of all series of Ne–Xe over a wide pressure range.

In [7] value of isothermal bulk modulus B and its first-order pressure derivative $B' = dB/dp$ for solid crystals Ne, Ar, Cu, Al, LiH, and MgO were obtained as a compression function. The studies were carried out on the base of well-known empirical equations of states, such as Birch-Murnaghan (see [4] and references there), Vinet et al. [33], Shanker et al. [34], Poirier and Tarantola [35], and Hama and Suito [36] with help of the formulation, developed by Stacey [5]. The parameters, proposed by Hama and Suito [36], were used as input data for B_0, B'_0, and B''_0.

The lattice dynamics theory developed by K. B. Tolpygo was successfully applied to describe the properties of alkali-halide crystals, semiconductors, and dielectrics [37–42] at zero pressure. The consideration of the deformable electron shells of atoms in the Tolpygo approach takes into account the response of the

system of crystal electrons to the oscillations of nuclei. In the classical version of the Tolpygo theory, the force parameters, expressed in terms of the first- and second-order derivatives of the short-range potential $V_{sr}(r^{ll'})$, the deformation parameters of the electron shells, and the Van der Waals parameter C, were obtained by fitting to the experimental phonon dispersion curves at $p = 0$. The non-empirical version of this theory (see [43] and references there) permits one to analyze different properties of RGC from first principles with the use only of the wave functions of the ground and excited states of atoms.

In the previous works [44–50], the nonempirical version of the quantum mechanical model of deformable and polarizable atoms was used as a basis to perform the quantitative study of the Birch elastic moduli and the Cauchy relation for the entire Ne–Xe series over a wide pressure range. It has been shown that the observed deviation from the Cauchy relation $\delta(p)$ for each crystal resulted from two competing interactions, namely, many-body interaction and quadrupole interaction, which exhibited as a quadrupole deformation in the electron shells of atoms upon the displacements of nuclei. The presented ab initio calculated pressure dependences of the Birch elastic moduli $\mathcal{B}_{ij}(p)$ and $\delta(p)$ are in good agreement with the experiment.

In this work, the second-order Fuchs elastic moduli B_{ij}, their pressure derivatives dB_{ik}/dp, and corresponding third-order Fuchs moduli B_{ikl} are studied for compressed crystals Ne and Ar.

18.2 Elastic Properties of Compressed Crystals

When studying the elastic properties of a stressed crystal, it is necessary to use the theory of finite deformations [51, 52]. In the presence of stress, elastic moduli are classified into types of the free energy expansion coefficients $C_{ikl\ldots}$ (Brugger-type moduli):

$$C_{\alpha\beta\ldots\gamma\delta}(T) = \frac{1}{N\Omega}\frac{\partial^n F(u,T)}{\partial u_{\alpha\beta}\ldots\partial u_{\gamma\delta}}\bigg|_{\bar{u}=0} \tag{18.1}$$

and the proportionality coefficients in the Hookes law for a stressed crystal $\mathcal{B}_{ikl\ldots}$ (Birch-type moduli):

$$\sigma_{ik}(x) = \mathcal{B}_{iklm}(x)\varepsilon_{lm}. \tag{18.2}$$

The Brugger moduli $C_{\alpha\beta\gamma}$ are commonly applied, but it is sometimes more convenient to use the deformation parameters γ_i, which have an obvious physical meaning. The parameters γ_i are introduced such that they vanish upon the disappearance of deformation, and the deformations corresponding to them are isotropic compression (γ_1), uniaxial compressions (γ_2 and γ_3), and shears (γ_4, γ_5, and γ_6). If a unit cell contains several atoms, the parameters γ_7, γ_8, … describe the relative displacement of these atoms upon the deformation of a crystal.

The derivative of the free energy $F(\gamma)$ with respect to the parameters $\gamma_1 - \gamma_6$ determines the Fuchs-type elastic moduli as

$$B_{i\ldots l} = \frac{1}{\Omega}\left(\frac{\partial^n F(\gamma)}{\partial\gamma_i \ldots \partial\gamma_l}\right)_{\gamma=0}, \tag{18.3}$$

where γ_i is expressed through the distortion tensor $u_{\alpha\beta}$ (see, e.g., [19]).

The behavior of a compressed crystal will further be described with these second-order moduli B_{ik}, their pressure derivatives dB_{ik}/dp, and corresponding third-order moduli B_{ikl}.

We have the relations between the second-order moduli of Fuchs B_{ij}, Brugger C_{ij}, and Birch $\mathcal{B}_{ij}$ in a stressed crystal $(p \neq 0)$:

$$B_{11} = \frac{1}{3}(C_{11} + 2C_{12}) + \frac{1}{3}p; \quad C_{11} = B_{11} + \frac{4}{3}B_{33} + p; \tag{18.4}$$

$$B_{33} = \frac{1}{2}(C_{11} - C_{12}) - p; \quad C_{12} = B_{11} - \frac{2}{3}B_{33} - p; \tag{18.5}$$

$$B_{44} = C_{44} - p; \quad C_{44} = B_{44} + p. \tag{18.6}$$

The bulk modulus is

$$B = (C_{11} + 2C_{12})/3 = B_{11} - \frac{1}{3}p. \tag{18.7}$$

The shear modulus is

$$C' = (C_{11} - C_{12})/2 = B_{33} + p. \tag{18.8}$$

The Birch moduli are expressed as

$$\mathcal{B}_{\alpha\beta\gamma\vartheta} = C_{\alpha\beta\gamma\vartheta} - p\left(\delta_{\alpha\gamma}\delta_{\beta\vartheta} + \delta_{\alpha\vartheta}\delta_{\beta\gamma} - \delta_{\alpha\beta}\delta_{\gamma\vartheta}\right), \tag{18.9}$$

$$\mathcal{B}_{11} = B_{11} + \frac{4}{3}B_{33} = C_{11} - p, \tag{18.10}$$

$$\mathcal{B}_{12} = B_{11} - \frac{2}{3}B_{33} = C_{12} + p, \tag{18.11}$$

$$\mathcal{B}_{44} = B_{44} = C_{44} - p. \tag{18.12}$$

The Brugger-type moduli C_{ij} depend on p, and B_{ij} can be composed only of the Birch moduli $\mathcal{B}_{ij}$, which are immediately measured in ultrasonic experiments in the case of a cubic CI crystal. The ignoring of this circumstance leads to confusion in the numerical values of the elastic moduli of stressed crystals.

18.3 Calculation Results for the Second-Order Fuchs Elastic Moduli

In the previous works [47–49], the pressure dependences of the Birch elasticity moduli $\mathcal{B}_{ij}$ and the deviations from the Cauchy relation $\delta(p)$ were calculated for the entire series of compressed RGC with consideration for many-body interaction and electron shell deformation in the quadrupole approximation. Good agreement between theoretical and experimental results $\delta(p)$ has shown the adequacy of the developed theory and the model used to calculate the parameters [44–46].

From the equations for vibrations (see [43] and references therein) and the long-wave approximation [1], we can express the second-order Fuchs moduli B_{ij} through the obtained parameters as [18, 52]

$$\begin{aligned} B_{11} &= \frac{e^2}{6a^4}[2G - H - 2F + 2E - V_t - 2.710107D]; \\ B_{33} &= \frac{e^2}{8a^4}\left[G + 4H + 8F + 2E - 2V_q + V_t - 0.231934D\right]; \\ B_{44} &= \frac{e^2}{4a^4}\left[G + 2H + 4F - 8V_q + V_t - 0.52494D\right]. \end{aligned} \tag{18.13}$$

Here, $H = H_0 + \delta H$, $G = G_0 + \delta G$, $H_0(r_0)$ and $G_0(r_0)$ are the first- and second-order derivatives of the pair short-range repulsion potential $V_{sr}(r^{ll'})$ for the equilibrium distances between the first neighbors $(r_0 = a\sqrt{2})$; δH and δG are the three-body corrections leading to the eccentricity of pair interaction, F and E are the pair short-range forces between the second neighbors, $F = H_0(2a)$, $E = G_0(2a)$; V_t and V_q are the parameters of three-body interaction and quadrupole interactions, respectively, and D characterizes van der Waals interaction (the table of calculated parameters for different compression see, e.g., in [49]).

Fuchs moduli (18.13) can be expressed as

$$\begin{aligned} B_{ij} &= B_{ij}^0 + B_{ij}^t + B_{ij}^q; \\ B_{11}^t &= \frac{1}{3}K(p)[2\delta G - \delta H - V_t], \quad B_{11}^q = 0, \; K(p) = \frac{e^2}{2a^4}, \\ B_{33}^t &= \frac{1}{4}K(p)[\delta G + 4\delta H + V_t], \quad B_{33}^q = K(p)\left[-\frac{1}{2}V_q\right], \\ B_{44}^t &= \frac{1}{2}K(p)[\delta G + 2\delta H + V_t], \quad B_{44}^q = K(p)\left[-4V_q\right], \end{aligned} \tag{18.14}$$

where B_{ij}^0 are the Fuchs moduli with the pair potential in models M1, M3, and M5 and were determined in our earlier work [18]. The short-range component of the repulsion potential is calculated by the precise formula for the quadratic correction W_2 (see [53]) $V_{sr} = E^{(0)} + W_2(S^n)$ in model M5 and in the approximation S^2 in other models M3 and M1. Moreover, the van der Waals constant

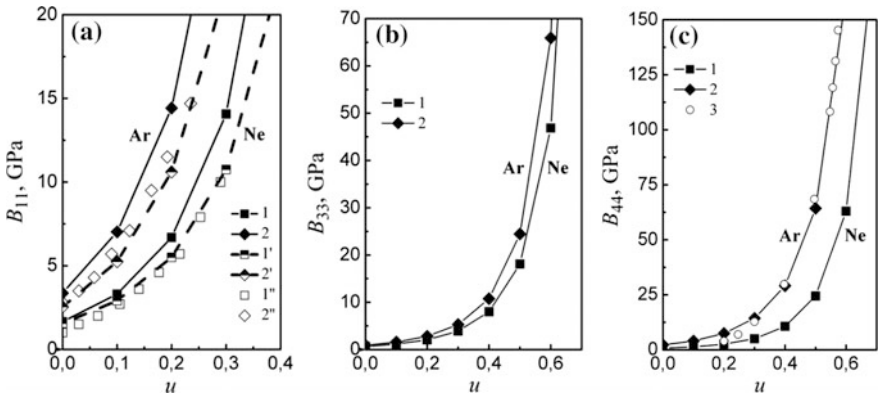

Fig. 18.1 Pressure dependence of the second-order Fuchs elastic moduli **a** B_{11}, **b** B_{33}, and **c** B_{44} for (1) Ne and (2) Ar: (1, 2) calculation of B_{11} in this work with consideration for three-body and quadrupole interactions as $B_{11} = B_{11}^0 + B_{11}^t + B_{11}^q$ (18.14), where B_{11}^0 is determined by model M3, (1′) calculations on the basis of B_{11}^0 in model M5 for Ne, (2′) calculations on the basis of B_{11}^0 in model M1 for Ar, (1″, 2″, 3) experiment [54, 55]

$C \to C(1 - A\exp(-\beta r))$ in models M3 and M5 is predefined, and the "second" neighbors are taken into account in the calculations of short-range forces [18]. In the simplest model M1, $A = \beta = 0$ and only the first neighbors are taken into consideration.

The results of calculating the Fuchs moduli B_{ij} with consideration for three-body and quadrupole interactions in dependence on the compression $u = \Delta V/V_0$ ($\Delta V = V_0 - V(p)$, where V_0 is the volume at $p = 0$), for Ne and Ar are shown in Fig. 18.1 [54, 55]. As can be seen from Fig. 18.1a, c, the agreement between experimental B_{11} [54], B_{44} [55] and its theoretical values is good and depends on the model, selected to calculate the pair potential. Thus, it is advisable to select model M5 [18] as a basis for Ne and M1 for Ar. The deviations of theory (calculation based on models M3 and M5) from the experiment can be observed to exhibit a certain trend: the theoretical modulus B_{11} lies slightly above the experimental curves for light RGC.

The dependence of the shear modulus B_{33} on the compression has the same character as $B_{11}(u)$ (Fig. 18.1b).

Let us note that the linear pressure dependence typical for $\mathcal{B}_{ij}^0(p)$ and B_{ij}^0 is violated when three-body interaction and quadrupole interactions are taken into account at a high pressure [18, 47].

18.4 Third-Order Fuchs Elastic Moduli

Higher-order elastic moduli contain higher-order coordinate derivatives (higher than second order ones) of the cohesive energy. Due to a rapid variation of the interatomic potential with distance, the third-order Fuchs elastic moduli B_{ikl} are much higher than the second-order elastic moduli B_{ik} and can serve as a good applicability test for one or other theory. In the case of a cubic CI crystal, there exist one first-order modulus ($B_1 = -p$), three second-order moduli B_{ik}, and six third-order moduli B_{ikl} (see, e.g., [19], p. 51). The three moduli B_{111}, B_{133}, and B_{144} can be found from the measurements (calculations) of dB_{ik}/dp at $p = 0$, with which they are related as

$$\begin{aligned} B_{111} &= -B\left(\frac{dB_{11}}{dp} + 1\right); \\ B_{133} &= C' - B\frac{dB_{33}}{dp}; \\ B_{144} &= \frac{1}{3}C_{44} - B\frac{dB_{44}}{dp}, \end{aligned} \tag{18.15}$$

where B and C' are determined by (18.7) and (18.8);

$$\frac{dB_{11}}{dp} = \frac{dB}{dp} + \frac{1}{3}; \quad \frac{dB_{33}}{dp} = \frac{dC'}{dp} - 1; \quad \frac{dB_{44}}{dp} = \frac{dC_{44}}{dp} - 1. \tag{18.16}$$

Table 18.1 contains the first-order derivatives, calculated by us in the model of deformable atoms with consideration for three-body interactions for the bulk elastic and shear moduli with respect to the pressure dB_{ik}/dp, the third-order Fuchs elastic moduli B_{ikl} (18.15) at $p = 0$, the results of some other authors [24, 28], and the experimental data [56].

To compare our results of calculations for B_{ikl} with the results of calculations for C_{ikl} from the work [24], we have engaged the following relationships valid at $p = 0$ (see, e.g., [19], p. 51):

$$\begin{aligned} B_{111} &= -B + \frac{1}{9}(C_{111} + 6C_{112} + 2C_{123}); \\ B_{133} &= B + \frac{4}{3}C' + \frac{1}{6}(C_{111} + C_{123}); \\ B_{144} &= B + \frac{2}{3}C_{44} + \frac{1}{3}(C_{144} + 2C_{166}). \end{aligned} \tag{18.17}$$

As can be seen from the Table 18.1, our calculation of dB/dp is in very good agreement with the experimental data [56] for Ar (error, $\sim 3\%$) and in slightly worse agreement with them for Ne. The results of calculations [24, 28] based on the empirical Lundqvist potential very poorly agree with the experiment [56] in

Table 18.1 Derivatives of the bulk elastic modulus dB/dp and the shear elastic moduli dC'/dp and dC_{44}/dp with respect to the pressure and the third-order Fuchs elastic moduli B_{111}, B_{133}, and B_{144} for Ne and Ar crystals at $p = 0$[a]

RGS	Theory	a (Å)	dB/dp exp.	dB/dp	γ (%)	dC'/dp	dC_{44}/dp	B_{111} (GPa)	B_{133} (GPa)	B_{144} (GPa)
Ne	Present calculation	2.231	7 [56]	5.862	16	2.804	3.295	−11.88	−2.304	−3.548
	Lehri and Verma [24]	2.227		10.2 –	46	2.63 (2.23)	8.45 (7.65)	−12.475 (−8.85)	−2.422 (−1.06)	−7.131 (−6.23)
	Gupta and Goyal [28]	2.227		6.66	5	1.91	6.10	–	–	–
Ar	Present calculation	2.656	7 [56]	7.247	3	2.383	4.774	−28.91	−3.747	−11.97
	Lehri and Verma [24]	2.656		8.9 –	27	2.03 (1.79)	7.02 (6.53)	−29.822 (−24.01)	−5.167 (−3.057)	−15.617 (−14.16)
	Gupta and Goyal [28]	2.656		7.74	11	1.8	5.81	–	–	–

[a]The results of Lehri and Verma [24] using the experimental values of dB/dp [56] in their calculations are given in parentheses. The relative error is $\gamma = \left|\frac{(dB/dp)^{\exp} - (dB/dp)^{theor}}{(dB/dp)^{\exp}}\right| \cdot 100\%$

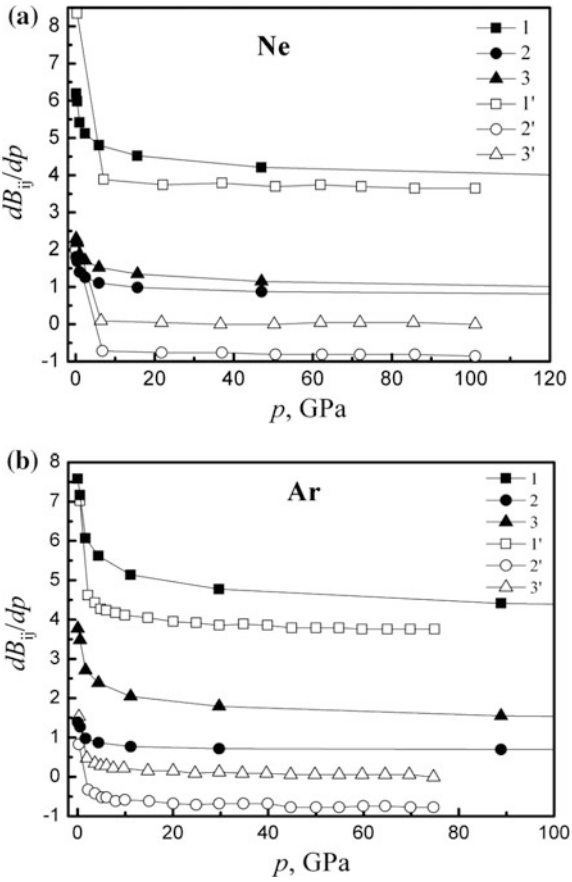

Fig. 18.2 Pressure dependences of the second-order Fuchs elastic moduli derivatives (1) dB_{11}/dp, (2) dB_{33}/dp, and (3) dB_{44}/dp with respect to the pressure for **a** Ne and **b** Ar: (1–3) calculation of dB_{ij}/dp in present paper, (1′–3′) calculation of dB_{ij}/dp by (18.16), using dB/dp, dC'/dp and dC_{44}/dp, obtained in the work [24]

comparison with our data. Unfortunately, there are no experimental data for the derivatives of two shear moduli with respect to the pressure, and the results of our calculations appreciably differ from the results of other authors, especially for dC_{44}/dp. The third-order elastic moduli B_{ikl}, determined by the derivatives of the second-order elastic moduli with respect to the pressure dB_{ik}/dp, show the same behavior. Our calculations of B_{111} demonstrate the best agreement (at a precision to 5%) with the calculations, performed by Lehri and Verma [24] in the second variant, described in the introduction. Our calculation of B_{133} for light RGC fits within the range between the calculations [24] performed in two different models, but is slightly lower for B_{144}.

The values of dB_{ik}/dp for Ne and Ar are plotted as functions of the pressure in Fig. 18.2 and Table 18.2. For comparison, we have also given the corresponding calculation performed in the work [28] for dB_{ik}/dp through dC_{ik}/dp (18.16) on the base of the three-body Lundqvist potential [32]. In both cases, all the three values of dB_{ik}/dp descend with an increase in pressure to 15–25 GPa corresponding to the compression u = 0.4–0.5 for Ne and Ar.

Table 18.2 Derivatives of the bulk elastic modulus dB/dp and the shear elastic moduli dC'/dp and dC_{44}/dp with respect to the pressure and the third-order Fuchs elastic moduli B_{111}, B_{133}, and B_{144} for Ne and Ar crystals in a wide pressure range

u	p (GPa)	dB/dp		dB/dp	dC'/dp	dC_{44}/dp	B_{111} (GPa)	B_{133} (GPa)	B_{144} (GPa)
		[33]	[7]						
Ne									
0.0	0.126	8.4	7.61	5.862	2.804	3.295	−11.580	−2.102	−3.410
0.1	0.396	6.836	6.26	5.647	2.692	3.179	−22.145	−3.821	−6.337
0.2	0.998	5.898	5.43	5.080	2.402	2.873	−40.802	−5.857	−10.739
0.3	2.402	5.235	4.82	4.787	2.257	2.707	−81.178	−10.357	−20.160
0.4	5.911	4.712	4.34	4.472	2.107	2.522	−170.77	−18.631	−39.237
0.5	15.644	4.261	3.92	4.187	1.985	2.345	−393.81	−36.549	−82.600
0.6	47.049	3.843	3.54	3.878	1.871	2.145	−1027.0	−77.674	−188.98
0.7	174.86	3.424	3.15	3.529	1.772	1.909	−3237.4	−188.76	−483.42
0.8	952.78	2.967	2.73	3.131	1.699	1.632	-14309	−575.15	−1456.3
Ar									
0.0	0.016	7.8	7.07	7.247	2.383	4.774	−28.864	−3.723	−11.948
0.1	0.507	6.407	5.87	6.830	2.269	4.481	−55.948	−6.618	−22.348
0.2	1.650	5.544	5.1	5.734	1.975	3.711	−98.036	−9.066	−34.569
0.3	4.358	4.926	4.54	5.286	1.871	3.388	−190.180	−15.376	−62.397
0.4	11.127	4.433	4.09	4.803	1.768	3.044	−383.832	−26.148	−114.45
0.5	29.705	4.008	3.69	4.440	1.718	2.791	−853.552	−51.935	−233.41
0.6	88.875	3.614	3.33	4.078	1.693	2.550	−2152.13	−120.99	−532.78
0.7	328.95	3.22	2.97	3.731	1.711	2.327	−6713.58	−378.81	−1481.9
0.8	1842.9	2.792	2.57	3.392	1.771	2.099	-31342.5	−1901.4	−5916

As can be seen from Fig. 18.2, our calculations and the calculations [28] are in the best agreement for the pressure dependences of dB_{11}/dp and dB_{44}/dp in the worst agreement for dB_{33}/dp.

As we mentioned in the Introduction, a method for calculating isothermal bulk moduli B and their pressure derivatives dB/dp for several crystals was presented in [7]. Calculations for Ne and Ar crystals were performed at different compressions based on several empirical equations of state [4, 33–36]. In order to make a comparison of our results and calculations of the pressure derivative dB/dp, associated with the Vinet equation of state [33], we use the expressions given in [7] as

(i) for the Vinet equation of state: $p = 3B_0x^{-2}(x-1)\exp[\eta(1-x)]$;
(ii) for isothermal bulk modulus: $B = B_0x^{-2}[1+(\eta+1)(1-x)]\exp[\eta(1-x)]$;
(iii) for pressure derivative of isothermal bulk modulus: $\frac{dB}{dp} = \frac{1}{3}\left[\frac{x(1-\eta)+2\eta x^2}{1+(\eta x+1)(1-x)} + \eta x+2\right]$, where $\eta = \frac{3}{2}(B_0'-1), x = \left(\frac{V}{V_0}\right)^{1/3}$.

In contrast to the authors of [7], we have fitting parameters (bulk modulus B_0 $(p=0)$ and its pressure derivative B_0' at $p=0$, which are determined by acoustic experiments (at low pressure) presented by Vinet et al. [33], namely, for Ne: B_0 = 1.08, $B_0' = 8.4$, and for Ar: B_0 = 2.834, $B_0' = 7.8$. As can be seen from Table 18.2 the value of dB/dp calculated by us from the Vinet equation of state and by the authors of [7] (for Ne and Ar crystals) differ from each other, the difference is of the order of 9%. The pressure derivative from the bulk modulus dB/dp, calculated by us with taking into account the three-particle interaction and quadrupole interaction are in good agreement with the empirical calculations [7, 33]. If we compare the calculated values dB/dp with the available experiment data at $p=0$, presented in Table 18.1, we can say that the calculation of [7] is close to the experiment in light RGC, and the present calculation is close to the experiment [56] for Ar crystal.

18.5 Conclusion

When analyzing the elastic properties of compressed rare-gas crystals, we have paid rather great attention to the comparison of our calculations for pressure derivative of bulk modulus with experiment data at $p=0$ [56], and with empiric calculations [7, 24, 28] in a wide pressure range. It should be noted that the results of calculation of the isothermal bulk modulus (B) and its pressure derivative (dB/dp) given in [7], in our opinion, are not correct, since the authors used the parameters of the Hama–Suito equation of state [36]. The accuracy of the results [7] is limited applicability of the five empirical equations of states.

A troubling thing in the work [24] is a great difference between the results of calculations performed for dC_{ik}/dp and C_{ikl} in two variants. The variant closer to our data is the second one, in which the three-body interaction parameter is

determined by the Cochran exponential formula [30]. In any case, the moduli B_{111} are close to our results, though their first-order derivative of the bulk elastic modulus with respect to the pressure dB/dp poorly agrees with the experiment.

Good agreement obtained by us for dB/dp with the available experimental data [56] at $p = 0$ and an adequate description of Zener elastic anisotropy $A_Z(p)$ [50] and, especially, the deviations from the Cauchy relation $\delta(p)$ [43, 48, 49] allows us to make a conclusion in favor of the predictive value of calculations for the elastic, dynamic, and thermodynamic properties of compressed RGC in the model of deformable and polarizable atoms on the base of the nonempirical short-range potential.

Acknowledgements The work was supported by the Ministry of Education and Science of the Russian Federation in projects Nos. 3.6371.2017/8.9, 3.6439.2017/8.9 (the basic part of the state task) and grant of Russian Foundation for Basic Research No. 17-08-01724. The study had been performed with equipment of the Collective center of using "Electro-magnetic, Electromechanical and Thermal Properties of Solids", Research Institute of Physics, Southern Federal University.

References

1. M. Born, K. Huang, *Dynamical Theory of Crystal Lattices* (Oxford University Press, Oxford, 1954)
2. M.P. Tosi, Solid State Phys. **16**, 1 (1964)
3. G.R. Barsch, Z.P. Chang, J. Appl. Phys. **39**, 3276 (1968)
4. F. Birch, J. Geophys. Res. **57**, 227 (1952)
5. F.D. Stacey, J. Phys.: Condens. Matter **11**, 575 (1999)
6. M. Kumar, High Temp.-High Pressures **31**, 221 (1999)
7. S. Gaurava, B.S. Sharma, S.B. Sharma, S.C. Upadhyaya, Phys. B **322**, 328 (2002)
8. G.R. Barsch, J. Appl. Phys. **39**, 3780 (1967)
9. R.C. Hollinger, G.R. Barsch, J. Phys. Chem. Solids **37**, 845 (1976)
10. V.K. Garg, D.S. Puri, M.P. Verma, Phys. Status Solidi **87**, 401 (1978)
11. K.P. Thakur, J. Phys. Chem. Solids **41**, 465 (1980)
12. E.V. Zarochentsev, S.M. Orel, V.N. Varyukhin, Phys. Status Solidi (a) **52**, 455 (1979)
13. E.V. Zarochentsev, S.M. Orel, V.N. Varyukhin, Phys. Status Solidi (a) **53**, 75 (1979)
14. E.V. Zarochentsev, S.M. Orel, Phys. Status Solidi (a) **57**, 137 (1980)
15. E.V. Zarochentsev, S.M. Orel, A.Yu. Yakovets, Phys. Status Solidi (a) **94**, 515 (1986)
16. E.V. Zarochentsev, S.M. Orel, I.V. Kochergin, Phys. Status Solidi (a) **95**, 105 (1986)
17. E.V. Zarochentsev, S.M. Orel, Yu.V. Stepanchuk, Phys. Status Solidi (a) **116**, 295 (1989)
18. E.V. Zarochentsev, V.N. Varyukhin, E.P. Troitskaya, V.V. Chabanenko, E.E. Horbenko, Phys. Status Solidi (b) **243**(12), 2672 (2006)
19. V.G. Bar'yakhtar, E.V. Zarochentsev, E.P. Troitskaya, *Theory of Adiabatic Potential and Atomic Properties of Simple Metals* (Gordon & Breach, London, 1999)
20. T. Tsuchiya, J. Kawamura, J. Chem. Phys. **114**, 10086 (2001)
21. T. Tsuchiya, J. Kawamura, J. Chem. Phys. **116**, 2121 (2002)
22. T. Tsuchiya, J. Kawamura, J. Chem. Phys. **117**, 5859 (2002)
23. S. Lehri, M.P. Verma, Phys. Status Solidi (b) **92**, 363 (1979)
24. S. Lehri, M.P. Verma, Phys. Status Solidi (b) **98**, 789 (1980)
25. A.L. Karasevskii, W.B. Holzapfel, Phys. Rev. B **67**, 224301 (2003)
26. M. Aoki, T. Kurokawa, J. Phys.: Condens. Matter **19**, 236228 (2007)

27. E. Pechenic, I. Kelson, G. Makov, Phys. Rev. B **78**, 134109 (2008)
28. S. Gupta, S.C. Goyal, Sci. China Ser. D Earth Sci. **52**, 1599 (2009)
29. B.M. Axilrod, E. Teller, J. Chem. Phys. **11**, 299 (1943)
30. W. Cochran, CRC Crit. Rev. Solid State Sci. **2**, 1 (1971)
31. S. Gupta, S.C. Goyal, J. Phys. Chem. Sol. **64**, 1125 (2003)
32. M.P. Verma, R.K. Singh, Phys. Status Solidi (b) **33**, 769 (1969)
33. P. Vinet, J.H. Rose, J. Ferrante, J.R. Smith, J. Phys.: Condens. Matter **1**, 1941 (1989)
34. J. Shanker, S.S. Kushwah, P. Kumar, Phys. B **239**, 337 (1997)
35. J.-P. Poirier, A. Tarantola, Phys. Earth Planet. Inter. **109**, 1 (1998)
36. J. Hama, K. Suito, J. Phys.: Condens. Matter **8**, 67 (1996)
37. I.G. Zaslavskaya, K.B. Tolpygo, Ukr. Fiz. Zh. **1**, 226 (1956)
38. Z.A. Demidenko, T.I. Kucher, K.B. Tolpygo, Sov. Phys. Solid State **3**, 1803 (1961)
39. Z.A. Demidenko, K.B. Tolpygo, Sov. Phys. Solid State **3**, 2493 (1961)
40. K.B. Tolpygo, E.P. Troitskaya, Sov. Phys. Solid State **13**, 939 (1971)
41. K.B. Tolpygo, Phys. Status Solidi (b) **56**, 591 (1973)
42. O.N. Bolonin, K.B. Tolpygo, Sov. Phys. Solid State **15**, 1124 (1973)
43. E.P. Troitskaya, Ie.Ie. Gorbenko, E.A. Pilipenko, Low Temp. Phys. **42**, 411 (2016)
44. E.P. Troitskaya, V.V. Chabanenko, I.V. Zhikharev, Ie.Ie. Gorbenko, Phys. Solid State **53**, 1634 (2011)
45. E.P. Troitskaya, V.V. Chabanenko, I.V. Zhikharev, Ie.Ie. Gorbenko, E.A. Pilipenko, Phys. Solid State **54**, 1254 (2012)
46. E.P. Troitskaya, V.V. Chabanenko, I.V. Zhikharev, Ie.Ie. Gorbenko, E.A. Pilipenko, Phys. Solid State **55**, 389 (2013)
47. E.P. Troitskaya, V.V. Chabanenko, E.A. Pilipenko, I.V. Zhikharev, Ie.Ie. Gorbenko, Phys. Solid State **55**(11), 2335 (2013)
48. V.N. Varyukhin, E.P. Troitskaya, V.V. Chabanenko, Ie.Ie. Gorbenko, E.A. Pilipenko, Phys. Status Solidi (b) **251**(4), 774 (2014)
49. V.N. Varyukhin, E.P. Troitskaya, Ie.Ie. Gorbenko, E.A. Pilipenko, V.V. Chabanenko, Phys. Status Solidi (b) **252**, 709 (2015)
50. Ie.Ie. Gorbenko, E.P. Troitskaya, E.A. Pilipenko, Phys. Solid State **59**, 132 (2017)
51. F.D. Murnaghan, *Finite Deformation of an Elastic Solid* (Wiley, New York, 1951)
52. D. Wallace, Solid State Phys. **25**, 301 (1970)
53. E.V. Zarochentsev, E.P. Troitskaya, Phys. Solid State **43**, 1345 (2001)
54. M.S. Anderson, C.A. Swenson, J. Phys. Chem. Sol. **36**, 145 (1975)
55. H. Shimizu, H. Tashiro, T. Kume, S. Sasaki, Phys. Rev. Lett. **86**, 4568 (2001)
56. C.A. Swenson, in *Rare Gas Solids*, vol. 11, ed. by M.L. Klein, J.A. Venables (Academic Press, New York, 1977), p. 863

Chapter 19
The Investigation of Photoelectrical and Optoacoustic Properties of ZnO—Ferroelectric Structure

Leonid V. Grigoryev, Alex F. Kraychko, Anatoly V. Mikhailov, Vachyslav G. Nefedov and Oleg V. Shakin

Abstract Currently, the direction of integrated photoelectronics is actively developing, dedicated to the creation of UV photodetectors. In this regard, photosensitive acoustoelectronic amplifiers to incident UV radiation can compete with classical photodetectors, such as photodiodes. The relevance of studying the interaction of UV radiation with charge carriers in structures with surfactants is due to the possibility of creating on its base thermostable sensors and radiometers of the UV range.

19.1 Introduction

Currently, the investigation of the structural, luminescent, photovoltaic and opto-acoustic properties of the semiconductor-ferroelectric structures on the base of zinc oxide (ZnO) has attracted great attention of researchers. This is due to the possibility of creating high-speed solid-state ultraviolet (UV) radiation sensors for integrated optical information processing systems [1, 2]. These UV radiation sensors are necessary for constructing optical sensor monitoring networks on their base, for example, radiation-hazardous objects on which there is an explosive atmosphere (hydrogen–oxygen, methane–air, gas–dust, etc.). The necessity of studying photoelectric processes in structures containing a ZnO thin film on the

L. V. Grigoryev
Optoinformatic Technologies and Materials Department,
ITMO University, St. Petersburg, Russia

L. V. Grigoryev (✉) · A. F. Kraychko · V. G. Nefedov · O. V. Shakin
Radioelectronics and Optoelectronics System Department, Saint-Petersburg State University of Aerospace Instrumentation, St. Petersburg, Russia
e-mail: lvgrigoryev@oi.ifmo.ru

A. V. Mikhailov
Optical Technology Department, Optical Research Institute, St.Petersburg, Russia

I. A. Parinov et al. (eds.), *Advanced Materials*, Springer Proceedings in Physics 207, https://doi.org/10.1007/978-3-319-78919-4_19

surface of various active dielectric wafers is also due to the possibility of creating a highly sensitive photosensor in a solid-state optocoupler operating in the UV range. This optocoupler will be suitable for replacing the existing system "solid-state scintillator—photoelectric multiplier".

19.1.1 Research Purpose

The paper presents the results of investigating structural properties, photoconductivity and photoluminescence processes, as well as the optical-acoustic properties of ZnO–$LiTaO_3$ and ZnO–$LiNbO_3$ thin-film structures.

19.2 Manufacture of Sample

Thin-film structures of ZnO–$LiTaO_3$ and ZnO–$LiNbO_3$ were manufactured on the surface of polished plates of $LiTaO_3$ and $LiNbO_3$. Previously, all ferroelectric substrates were cleaned of organic contaminants in polar and nonpolar solvents, then they were washed in de-ionized water before the spraying operation. To clean the traces of contamination and to increase the adhesion of the deposited film from ZnO, the surfaces of the ferroelectric wafers used were ion bombarded. The thin film of ZnO on the substrate surface was formed by the method of reactive ion-plasma deposition [3]. The target for ion-plasma formation of the layer was a high-purity Zn disk. Sputtering occurred in an oxygen-argon plasma at a constant current of the magnetron. As a result of ion-plasma deposition, a thin film of ZnO with a thickness of 1.5–1.2 μm was formed on the substrate surface.

19.3 Result and Discussion

X-ray diffraction investigation were carried out on a DRON-3M diffractometer with CuKα = 1.542 Å radiation, the anode voltage of the X-ray tube was 25 kV. The measurement was carried out in the Bragg range of angles 2θ from 20 to 60° with step Δ2θ = 0.05°. The time for accumulation of pulses at the measurement point was 10 s. Diffractograms of ZnO films in ZnO–$LiTaO_3$ and ZnO–$LiNbO_3$ structures, synthesized by ion plasma beam deposition, are shown in Fig. 19.1.

The semiconductor film ZnO on ferroelectric substrates has a low density of structural defects, located at the interface of the ferroelectric-zinc oxide. The diffractograms (Figs. 19.1a, b) show a high-intensity diffraction peak characteristic of hexagonal ZnO (002), indicating the structural perfection of the synthesized thin films and the presence of a distinguished axial texture in the direction of the axis perpendicular to the substrate surface [4]. Reactive ion-plasma deposition of the

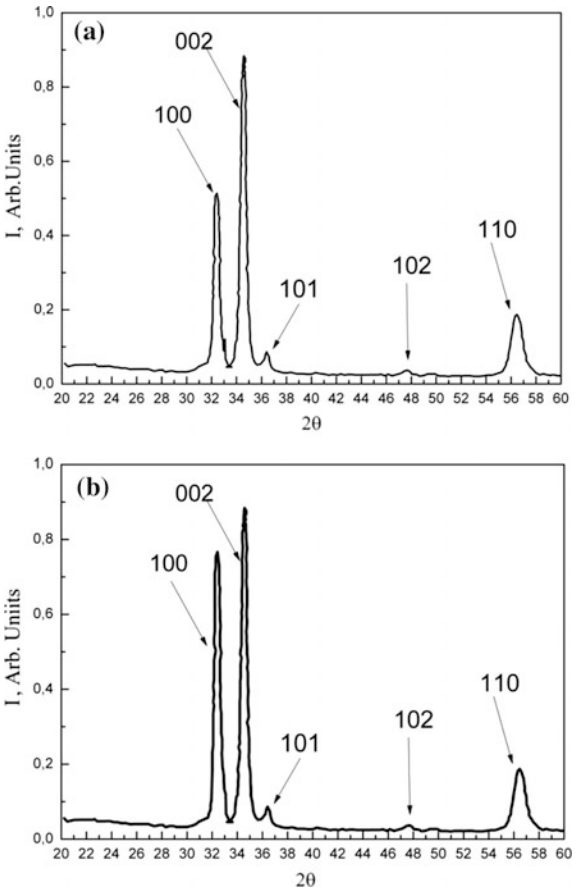

Fig. 19.1 X-ray diffractogram of ZnO films in $ZnO–LiTaO_3$, **a** and $ZnO–LiNbO_3$, **b** structures

thin-film ZnO layer on various ferroelectric substrates shows a change in the intensity of the diffraction maxima responsible for the (100) direction. The formed thin-film ZnO layer on $LiNbO_3$ substrate did not lead to a shift in the diffraction maxima (002) and (100) as compared to the position of similar maxima on the diffractograms of $ZnO–LiTaO_3$ structures. The intensity of the maximum responsible for the (002) direction becomes larger in the $ZnO–LiNbO_3$ structures compared to the analogous peak in the $ZnO–LiTaO_3$ diffractograms pattern. The greatest intensity of diffraction maxima (002) is in the $ZnO–LiNbO_3$ structure, which also indicates the greatest perfection of the synthesized ZnO layer on this structure. There are no shifts in the positions of the maxima on the diffractograms, which can be explained by the absence of an increase in the interplanar distance in ZnO arising in the synthesis of ZnO film on $LiNbO_3$ substrates and to a lesser extent on $LiTaO_3$ substrates. According to X-ray diffraction analysis, all synthesized ZnO films have a nanocrystalline structure. The crystalite sizes in the thin-film ZnO layer of the structure "ZnO-ferroelectric", calculated by the Selyakov-Scherrer

formula [4], did not exceed 16 nm. Comparison of the literature data on the character of the X-ray diffraction patterns of ZnO films, synthesized by the high-frequency (HF) magnetron sputtering of the ZnO target [5], with above results of X-ray diffraction analysis, shows correlation in the character of the diffraction patterns in all cases. A joint analysis of the shape of the X-ray diffractograms of films, synthesized by the methods of ion-plasma sputtering and HF magnetron sputtering, shows the absence of diffraction maxima (100), (101), (102), (110) on X-ray diffraction patterns of the samples, produced by the HF magnetron sputtering. The average sizes of ZnO nanocrystals, synthesized by both methods, are practically equivalent.

Investigation of the photoluminescence properties of the structures was carried out on a Perkin Elmer LS50B fluorescent spectrometer at room temperature, and the wavelength of the exciting radiation was 320 nm. The photoluminescence spectra (PL) of the structures under study are shown in Fig. 19.2. The intensity of photoluminescence is given in relative units of sensitivity of the Perkin Elmer LS50B fluorimeter.

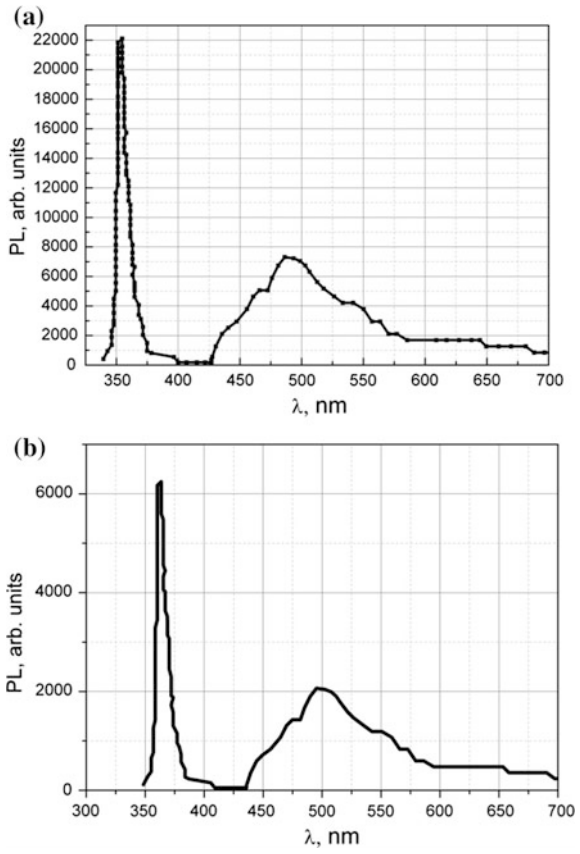

Fig. 19.2 PL spectra of $ZnO–LiTaO_3$, **a** and $ZnO–LiNbO_3$, **b** structures

All spectra contain a narrow intense luminescence band, located in the UV region, the maximum of which lies in the spectral band of 350–380 nm. The maximum of the luminescence band of the ZnO–$LiTaO_3$ structure is at a wavelength of 358 nm, the half-width is 15 nm. The maximum of the photoluminescence band for the ZnO layer deposited on the $LiNbO_3$ surface corresponds to a wavelength of 365 nm and a half-width of 16 nm, which coincides with the literature data on the photoluminescence of the ZnO layer. The intensities of this UV band differ significantly in comparison with each other. The intensity of the UV luminescence band of the ZnO–$LiTaO_3$ sample exceeds by 3.95 times the intensity of a similar UV photoluminescence band observed in the ZnO–$LiNbO_3$ structure. In addition, in the ZnO–$LiNbO_3$ structure, the UV photoluminescence band is shifted to the long-wavelength region in comparison with the analogous photoluminescence band in the ZnO–$LiTaO_3$ structure. Such a ratio of the intensities of the photoluminescence bands of the samples can be explained as follows: the process responsible for intense photoluminescence in the UV range of the spectrum is the recombination of exactions in the bulk of a semiconductor ZnO film [6, 7]. This is supported by the position of narrow photoluminescence bands of all the investigated structures in the UV range of the spectrum and their similarity to the exaction of photoluminescence band in the ZnO film [7].

The significantly different intensity of UV luminescence bands suggests that the concentration of exactions in the semiconductor layer in the ZnO–$LiTaO_3$ and ZnO–$LiNbO_3$ structures is significantly different. The intensity of the photoluminescence band of the ZnO–$LiTaO_3$ structure in the UV range exceeds by 3.95 times the intensity of the similar photoluminescence band, which suggests the largest concentration of exactions in the volume of the ZnO semiconductor film in this type of samples. In favor of this fact says, that the activation energy of optical traps lies into range from 3.26 to 3.33 eV. In the structures of ZnO–$LiTaO_3$, ZnO–$LiNbO_3$, broad luminescence bands being in the blue-green region of the visible spectral range and having different peak half-widths and peak intensities are observed. In the structure of ZnO–$LiTaO_3$, the intensity of the wide photoluminescence band is less than the intensity of the narrow UV band of photoluminescence by approximately 3.4 times. The maximum of the band is at a wavelength of 480 nm and has a half-width of 105 nm. The intensity of the broad photoluminescence band of the ZnO–$LiTaO_3$ structure is the largest of the experimental structures and exceeds the intensity of a similar band for the ZnO–$LiNbO_3$ structure by 3.5 times. The maximum of the wide photoluminescence band for the ZnO–$LiNbO_3$ structure is at a wavelength of 500 nm, and the half-width is 120 nm. The peak photoluminescence band in the blue-green region of the spectrum of the investigated ZnO-ferroelectric structures has an asymmetric form with respect to the position of the maximum. In this case, there is a region of smooth decrease in intensity, which may be due to the luminescence of optically active defects with an activation energy from 2.53 to 1.87 eV. Optically active defects responsible for photoluminescence in this spectral range include oxygen vacancies, which form during reactive ion-plasma synthesis of ZnO thin film. The activation energy of optically active defects and the spectral position of wide maxima have a correlation with the literature data [6, 7].

The difference in the intensities of broad photoluminescence bands can be due to different concentration of oxygen vacancies in the volume of ZnO thin film, formed in reactive ion-plasma synthesis. The highest concentration of vacancies in oxygen is observed in the ZnO layer of the ZnO–$LiTaO_3$ structure. The investigation of the spectral dependences of the photoconductivity currents was carried out on the apparatus, described in [8].

Measurements of the photoconductivity currents were performed in the spectral range from 220 to 460 nm by using a nanovoltmeter with a voltage source (Keithley 6487) at room temperature. For these measurements, the samples were placed in a fore vacuum cryostat and pumped to a pressure not exceeding 0.5 Pa. Figure 19.3 shows the spectral dependences of the photoconductivity currents of the investigated structures.

Analysis of the spectral dependences of the photoconductivity of the investigated structures indicates a different intensity of the photostimulated current, flowing through the layer zinc oxide. The magnitude of the maximum photoconductivity current in the ZnO–$LiTaO_3$ structure exceeds the maximum value of the

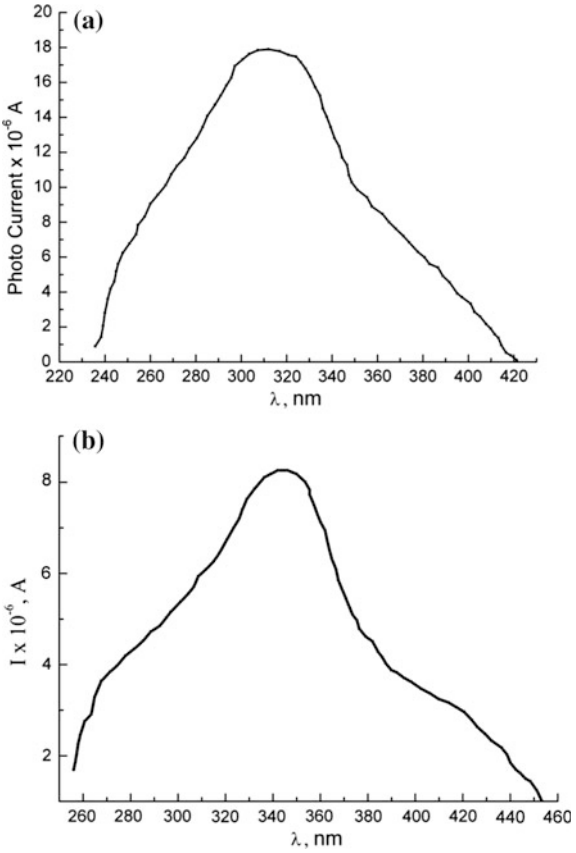

Fig. 19.3 Photoelectrical current in ZnO–$LiTaO_3$, **a** and in ZnO–$LiNbO_3$, **b** structures

photostimulated current, recorded in the ZnO–$LiNbO_3$ structure by 2.25 times. The maximum photoconductivity of the ZnO–$LiTaO_3$ structure is at 310 nm. The maximum photoconductivity of the ZnO–$LiNbO_3$ structure is at 345 nm. The shift in the maximum photosensitivity of the ZnO–$LiTaO_3$ structure to the short-wavelength region compared to the photosensitivity of single-crystal ZnO can be explained by the effect of the electric field, induced by the ferroelectric in the near-surface region of the semiconductor. This shift in the maximum of the spectral sensitivity is due to the contribution of the surface conductivity at the semiconductor—ferroelectric interface and the resonance absorption of UV radiation in the volume of the semiconductor layer. The magnitude of the electric field at the semiconductor—ferroelectric interface is larger for the ZnO–$LiTaO_3$ structure, which also leads to an increase in the Pula-Fraenkel conductivity and, ultimately, leads to a greater photosensitivity of the structure compared to ZnO–$LiNbO_3$.

To investigation the optical-acoustic properties of the ZnO film, the pulsed laser optoacoustic spectroscopy technique was used [9–11]. The laser radiation incident on the surface of a solid can excite both surface acoustic waves (SAW) and bulk acoustic waves [9]. We chose the generation conditions corresponding to the excitation of surface acoustic waves. For this purpose, the incident UV radiation was selected, which is completely absorbed in the zinc oxide layer and a laser source SAW having a one-dimensional configuration was formed by means of a cylindrical lens. The laser radiation incident on the absorbing surface of the zinc oxide was in the form of a strip elongated along the surface of the ZnO film, and the acoustic wave propagated along the surface of the semiconductor film perpendicular to the light strip. We assume that the absorbing medium is structurally homogeneous and has an optic absorption coefficient α. The intensity of light in incident laser radiation can be described by the function: $I(t) = I_0 f(t)$. In this approach, the laser-stimulated thermo-optical excitation of an acoustic wave is described by equations [9, 10]:

$$\frac{\partial^2 \phi}{\partial t^2} - c_0^2 \frac{\partial^2 \phi}{\partial x^2} = -\left[\frac{\alpha c_0^2 \beta}{\rho c_p}\right] I_0 \exp[-\alpha x f(t)]; \tag{19.1}$$

$$v = \text{grad}\, \varphi,$$

where φ is the scalar potential of the velocity field, β is the temperature coefficient of medium expansion, v is the vibrational velocity of the particles of the medium, c_0 is the speed of sound in the medium, c_p is the specific heat at constant pressure, ρ is the density of medium.

To solve (19.1), we used the spectral method, proposed in [9–11]. The experimentally measurement value is the pressure, which in a plane acoustic wave is defined as

$$\frac{v(t)}{c_0} = \frac{p(t)}{\rho c_0^2}. \tag{19.2}$$

To excite the acoustic signal, we used He–Cd laser radiation at the fundamental mode wavelength of 325 nm. The pulse duration of the laser radiation was 8–10 ns. The energy in the pulse did not exceed 1.3 mJ. An electro-optical modulator was used. The transverse distribution of the intensity of the laser radiation before incidence on the cylindrical lens was close to Gaussian, the radius of the beam was 1.5 mm. The scheme for the installation of pulsed laser optoacoustic spectroscopy is given in [12]. Since the ZnO layer is piezoelectric and semiconductor material, the recording of ZnO propagating surface acoustic waves was carried out using a system of planar interdigital electrodes made of aluminum sputtered on to the zinc oxide surface. Registration of the ultrasonic waveform of the SAW was carried out using a digital oscilloscope Keysight DSO4104A. The time dependence of the pressure $p(\tau)$, taking into account the diffraction effect in a traveling acoustic wave (SAW), emitted into the zinc oxide layer can be described by the expression [9–11]:

$$p(\tau) = p_d(\tau) + \omega_d \int_0^{\tau} p_d(x)dx, \tag{19.3}$$

where $\omega_d = 2c_0L^2/a^2$ is the frequency of a wave with diffraction length of L, a is the radius of the acoustic beam, coinciding with the radius of the laser beam, c_0 is the speed of sound in zinc oxide, $p_d(\tau)$ is the experimentally recorded profile of optoacoustic pressure pulse.

When $p(\tau)$ is registered, the time moment $\tau = 0$ corresponds to the arrival of the front of the ultrasonic signal, excited by the incident laser pulse to the second SAW receiver. Figure 19.4 shows the profile of the leading edge of the probing optoacoustic signal.

Based on the experimental data of optical-acoustic spectroscopy, the optical absorption coefficient α in the thin film ZnO was calculated, the value of which was $\alpha = 49.2\ \mathrm{m}^{-1}$. Comparing the obtained value of α with the literature data on the optical properties of single-crystal and polycrystalline thin ZnO films, it is seen that the optical absorption coefficient for thin zinc oxide films lies in the range from $\alpha = 49.8\ \mathrm{m}^{-1}$ for films obtained by magnetron sputtering [5, 6], to $\alpha = 46.4\ \mathrm{m}^{-1}$ for films obtained by the sol-gel method [2]. In this regard, the optical absorption coefficient, measured by the optical-acoustic method, correlates with the values of α, obtained by other authors from the method of joint analysis of transmission and reflection spectra of the zinc oxide layer. The error in measuring the optical absorption coefficient α by an optoacoustic method directly depends on the error in measuring the time dependence of the pressure at the front of the acoustic probing signal. When using a 12-bit analog-to-digital conversion of the sounding acoustic signal, used for digitization, the total measurement error did not exceed 3%. To create a model of a solid-state UV optocoupler, a photosensitive acoustoelectronic

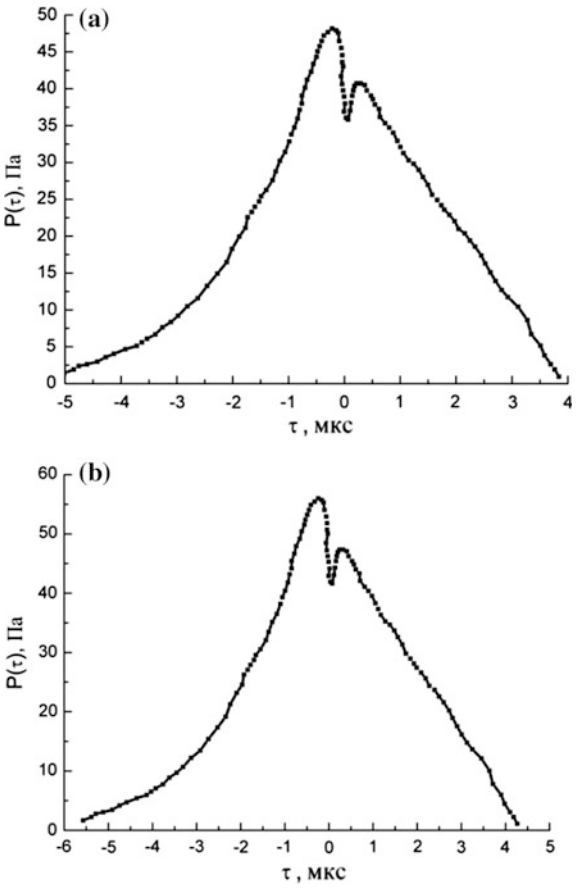

Fig. 19.4 Acoustic signals in ZnO layer of ZnO–$LiTaO_3$, **a** and ZnO–$LiNbO_3$, **b** structures

amplifier was chosen, with a receiving surface and a medium for forming a SAW from a thin ZnO film. The choice in favor of the acoustoelectronic amplifier and the rejection of the sensor in the form of a photodiode from ZnO was due to two factors. First, the output signal of an acoustoelectronic amplifier, in contrast to a photodiode, is practically independent of the temperature change. Second, the output signal of the acoustoelectronic amplifier has a frequency modulation, which increases the noise immunity of the UV sensor. To investigate the spectral sensitivity of a UV solid-state optocoupler, a photosensitive acoustoelectronic amplifier was formed on the surface of a ZnO layer and consisted of two interdigital probes (Al) from Al and a sensor pad of zinc oxide between them. The scheme for measuring the dependence of the frequency shift of the output signal of an acoustoelectronic amplifier in the UV range of the spectrum was similar to given in [13]. As a source of UV radiation, we used a light source on a xenon lamp and a high-aperture monochromator MDR-12. With the help of a mirror condenser, the light spot collimated purely over the area of the receiving sensor, without the

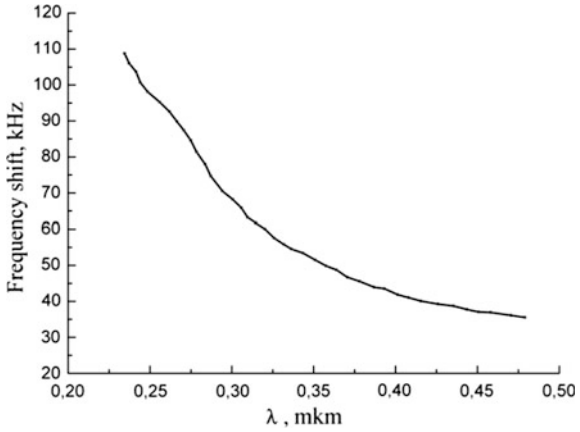

Fig. 19.5 Frequency shift at output signal of acoustoelectrical amplifier in UV spectral range

exposure of the interdigital electrodes. To view the frequency shift of SAW sygnal was used a two-channel digital oscilloscope Keysight DSO4104A. The dependence of the frequency shift of the output signal of the acoustoelectronic amplifier, in the UV range of the spectrum, is shown in Fig. 19.5.

From the spectral dependence of the frequency shift, it is seen that in the range of the maximum spectral sensitivity of the investigated structures (300–350 nm), the frequency shift is in the range 50–70 kHz. It should be noted that spreading a useful signal is not difficult, either with the help of narrow-band analog filters, or with the help of digital filter.

19.4 Conclusion

The conducted investigation has shown the possibility of creating a UV sensor with a output frequency based on a photosensitive acoustoelectronic amplifier. The maximum spectral sensitivity of the ZnO–$LiTaO_3$ and ZnO–$LiNbO_3$ structures lies in the range 310–350 nm. The magnitude of the frequency shift in the range of the highest spectral sensitivity of the investigated structures (310–350 nm) belongs to the range 50–70 kHz. The formation of a UV radiation sensor, based on the ZnO-ferroelectric structure in the integrated optical structure, will allow the creation of sensor systems on a crystal with fully optical control.

Acknowledgements This work was supported by the Russian Foundation for Basic Research (grant No. 16-07-00237).

References

1. T.V. Blank, U.A. Goldenberg, Semiconductors **37**(9), 1025 (2003)
2. C.L. Wei, Y.E. Chen, C.C. Cheng et al., Thin Solid Films **518**(11), 3059 (2010)
3. L.V. Grigoryev, V.G. Nefedov, O.V. Shakin, A.V. Mikhailov, E.N. Eliseev, J. Opt. Technol. **82**(5), 66 (2015)
4. A.A. Rusakov, A.A. Русаков, *Radiography of Metals* (Atomizdat, Moscow, 1977) (in Russian)
5. C. Gumus, O.M. Ozkedid, H. Kovak, Y. Ufuktepe, J. Optoelectron. Adv. Mater. **8**(1), 299 (2006)
6. A.N. Gruzintsev, V.T. Volkov, K. Barthow, Semiconductors **36**(6), 741 (2002)
7. A.A. Serdobincev, O.A. Kiriasova, A.G. Veselov, Semiconductor **42**(4), 496 (2008)
8. L.V. Grigoryev, S.O. Solomin, D.A. Poaykov, V.P. Veiko, A.V. Mikhailov, J. Opt. Technol. **85**(7), 51 (2016)
9. A.A. Karabutov, M.P. Matrosov, N.B. Podymova, V.A. Pyzh, Sov. Phys. Acoust. **37**(2), 311 (1991)
10. L.V. Burmistrova, O.V. Rudenko, A.V. Cherpetskya, Sov. Phys. Acoust. **28**(5), 655 (1978)
11. A.A. Karabutov, N.B. Podymova, V.S. Letokhov, Appl. Phys. B **63**, 545 (1996)
12. L.V. Grigoryev, M.A. Mazurov, V.G. Nefedov, O.V. Shakin, A.V. Mikhailov, J. Opt. Technol. **84**(2), 71 (2017)
13. W.-C. Tsai, H. Kao, K.-H. Liao, Y.-H. Liu et al., Opt. Express **23**(3), 2187 (2015)

Chapter 20
Structural Features and Optical Properties of Lithium Niobate Crystals

Nikolay V. Sidorov, Mikhail N. Palatnikov, Natalya A. Teplyakova, Alexander V. Syuy and Dmitry S. Shtarev

Abstract The behavior of the band gap, photorefractive and electroconductive properties depending on the composition, structural features and the defect state of $LiNbO_3$ crystals, nominally pure and doped, obtained both in a single and in different growing technologies, are studied by a set of methods.

20.1 Introduction

Lithium niobate single crystal ($LiNbO_3$) belongs to one of the most important materials of electronic engineering, the physical properties of which can be substantially controlled by its composition [1–3]. The optical homogeneity of crystals is directly related to structural ordering, largely determined by the growing method [4] and relates to one of the fundamental problems of modern materials science. The presence of optical inhomogeneities leads to a change in the physical parameters of the crystals, such as electro-optical coefficients, the refractive index, the absorption coefficient, etc. The presence of optical inhomogeneities in crystals leads to the appearance of regions with biaxiality [5]. All the above deviations of the physical parameters of lithium niobate single crystals lead to incorrect operation of optoelectronic devices, which are made on the base of these crystal. The chemical composition, physico-chemical parameters of the charge and starting materials for the synthesis of charge have a determining effect on the production of crystals with

N. V. Sidorov (✉) · M. N. Palatnikov · N. A. Teplyakova
I.V. Tananaev Institute of Chemistry and Technology of Rare Elements and Mineral Raw Materials of the Kola Science Center of the Russian Academy of Sciences, 26 a, Akademgorodok, Apatity, Murmansk 184209, Russia
e-mail: sidorov@chemy.kolasc.net.ru

A. V. Syuy · D. S. Shtarev
Far Eastern State Transport University, 47, Seryshev Str., Khabarovsk 680021, Russia

D. S. Shtarev
Y.A. Kosygin Institute of Tectonics and Geophysics of Far East Department of Russian Academy of Science, 65, Kim Y. Chen Str., Khabarovsk 680000, Russia

I. A. Parinov et al. (eds.), *Advanced Materials*, Springer Proceedings in Physics 207, https://doi.org/10.1007/978-3-319-78919-4_20

a high degree of structural units, ordering similar to those of stoichiometric composition [6–9]. Fine features of the cation sublattice ordering in lithium niobate crystals are already formed at the stage of charge preparation.

In the lithium niobate crystal, in addition to deep electron traps, created by point photorefractive centers (mainly by Nb_{Li} defects—Nb^{5+} ions, located at Li^{+} ions sites within a perfect structure of stoichiometric composition), there are many small traps that affect the effect of photoinduced change in refractive indices (photorefraction effect, optical damage) and electrical properties [3, 10, 11]. In addition, lithium niobate is a phase of variable composition, which, by doping and variation of stoichiometry, both radically change the properties and subtly control the physical characteristics of the crystal [1, 3]. The number of Nb_{Li} defects and small electron traps depends on the crystal composition [3]. In nominally pure crystals with an increase in the R = Li/Nb ratio, the number of deep electron traps (Nb_{Li} defects) decreases, but at the same time the number of defects in the form of small electron traps increases [3, 12].

When the laser radiation is applied to a ferroelectric $LiNbO_3$ crystal, a spatial separation of the charge occurs as a result of photoexcitation processes (drift and electron diffusion) and an internal electric field arises that leads to a photoinduced change in the refractive indices at the location of the radiation [1, 3, 12, 13]. In the $LiNbO_3$ crystal, the photovoltaic mechanism is the predominant photorefraction mechanism. The value of the photovoltaic field is much larger than the value of the diffusion field [3, 12, 13]. In addition, under the action of laser radiation, Rayleigh photoinduced light scattering (PILS) occurs on static and dynamic (fluctuating) defects with changed refractive index, induced by laser radiation [14, 15]. In this case, the value of the electro-optic effect determines the angle of the PILS indicatrix opening. Photoinduced light scattering in the $LiNbO_3$ crystal occurs predominantly along the polar Z axis [14, 15]. The magnitude and speed of PILS development are determined by the photorefractive sensitivity and speed of photorefractive record of information in electro-optical crystals [15, 16]. The magnitude of the photorefraction effect, photo- and electrical conductivity in the $LiNbO_3$ crystal widely vary depending on the composition [3, 14–22]. In this case, the band gap width must change. The band gap for a nominally pure congruent crystal is 3.72 eV. This is close to the value characteristic for wide-gap semiconductors [13, 16, 23]. By reducing the band gap width, we can approximate the $LiNbO_3$ crystal properties to semiconductor crystals, which allows us to develop materials with cross effects.

In this paper, we have investigated a series of congruent crystals, doped with cations Mg^{2+}(0.35 wt%), Zn^{2+}(2.05), B^{3+}(0.12), Gd^{3+}(0.26, 0.44, 0.51), Y^{3+}(0.46), Gd^{3+}(0.23):Mg^{2+}(0.75), Mg^{2+}(0.86):Fe^{3+}(0.0036), Ta^{5+}(1.13):Mg^{2+}(0.01), Y^{3+}(0.24):Mg^{2+}(0.63), Er^{3+}(3.1), nominally pure stoichiometric lithium niobate crystal ($LiNbO_{3stoich}$). We also studied congruent crystals, grown from a charge, obtained using cyclohexanone $LiNbO_{3cong}$(CHN) as an extractant, as well as from a charge, obtained using cyclohexanone and dimethylamides of carboxylic acids as extractants, $LiNbO_{3cong}$(CHN + DCA).

The investigated crystals have low effect of photorefraction and are promising materials for frequency converters, electro-optical modulators and shutters, optical

materials with micron and submicron periodic structures. Double doping is perspective for obtaining of crystals with increased optical damage resistance.

20.2 Method

Growth of $LiNbO_3$ single crystals was carried out by the Czochralski method in the air atmosphere [7]. The dopant was introduced directly into the melt in the form of the corresponding oxide with impurities less than 10^{-4} wt%. We have used the lithium niobate charge, produced in I.V. Tananaev Institute of Chemistry and Technology of Rare Elements and Mineral Raw Materials of the Kola Science Center of the Russian Academy of Sciences; the technology is described in the work [24]. Stoichiometric crystals were grown from the melt with 58.6 mol% Li_2O. The growth of congruent crystals was made from a charge of a congruent composition (48.6 mol% Li_2O), synthesized from different initial components: niobium pentoxide obtained using cyclohexanone as an extractant (a charge of CHN) and niobium pentoxide obtained using dimethylamides of carboxylic acid (charge CHN + DCA) as an extractant [3, 25]. In the first case ($LiNbO_{3cong}$(CHN) crystals), we have used the CHN charge, and in the second case ($LiNbO_{3cong}$(CHN + DCA) crystals), we have used mixed in a certain proportion CHN charge and CHN + DCA charge. The crystal growing process is described in detail in [3]. Crystalline samples for the studies had the form of rectangular parallelepipeds measuring $\sim 7 \times 6 \times 5$ mm^3 (± 2 mm) with ribs coinciding in direction with the crystal-physical axes *X*, *Y*, *Z*, where the *Z*-axis is the polar axis of the crystal. The edges of the parallelepipeds were thoroughly polished.

The determination of the absorption edge was carried by MDR-41 monochromator. To determine the band gap width, the transmission spectrum of the crystal was recorded. According to the obtained dependence of the intensity of radiation passing through the crystal an inverted spectrum (absorption spectrum) was constructed. The source of radiation was a deuterium lamp. The obtained absorption spectrum in the decreasing linear part of the curve was approximated by a straight line before crossing with the abscissa axis. The intersection point of this line and the abscissa axis is the wavelength corresponding to the absorption edge of the crystal. The width of the band gap was determined by the formulae $E = hc/\lambda$, where λ is the wavelength corresponding to the absorption edge, h is the Planck constant, and c is the speed of light in a vacuum. The error of determining the edge of the absorption edge is ± 1.0 nm.

PILS was excited by a laser Nd:YAG (MLL-100), $\lambda_o = 532$ nm, $I \sim 6.29$ W/cm^2. The scattered radiation falls on a semitransparent screen placed behind the crystal, and is recorded by a digital video camera. The experimental setup and the procedure for determining the PILS indicatrix are described in detail in [15, 26]. In PILS experiments, the laser beam is directed along the *Y*-axis, and the intensity vector **E** of the electric field of the laser radiation is parallel to the polar *Z*-axis of the crystal. The values of the intensities of the photovoltaic and diffusion electric fields, as well as

the induced birefringence in view of the Selmeyer formulae, were determined in the investigated crystals by the parameters of the PILS indicatrix. The installation and methods for determining of the electro-optical coefficients by the interference method and the photoelectric fields are described in detail in the works [27–31]. The error in calculating the photoelectric fields under the experimental conditions is 5–10%. The method of conoscopic studies is described in [32–34]. The laser radiation was used Nd:YAG (MLL-100) (λ_o = 532.0 nm, intensity up to 3.54 W/cm^2). In the PILS experiments and in conoscopic studies, the sample was mounted on a movable two-coordinate optical stage, which made it possible to obtain a number of PILS and conoscopic pictures corresponding to different sections of the sample. The conoscopic picture is recorded on a translucent screen by a digital camera.

The Raman spectra were excited with a 514.5 nm band of the Spectra Physics argon laser (model 2018-RM) and recorded with a Horba Jobin Yvon T64000 spectrograph using a confocal microscope. In this case, Raman spectra were excited by low-power radiation ($P < 3$ mW) to exclude the effect of the photorefraction effect on the spectrum. All spectra are recorded at a resolution of 1.0 cm^{-1} at room temperature. Spectra processing is performed using the Horiba LabSpec 5.0 and Origin 8.1 software package. The error of determining the frequencies, widths and band intensities is ±1.0, ±3.0 cm^{-1} and 5%, respectively.

20.3 Result and Discussion

Table 20.1 demonstrates the results of calculating the band gap width from the absorption spectra of $LiNbO_3$ crystals of different compositions, the values of the photoelectric fields (photovoltaic $\mathbf{E}_{PV}$ and diffusion $\mathbf{E}_D$), and the angle of the PILS indicatrix. In the series of studied crystals the photoelectric fields and the effect of photorefraction (induced birefringence) are minimal for crystals $LiNbO_3$:Er(3.1 wt%), $LiNbO_3$:Gd(0.23 wt%):Mg(0.75), $LiNbO_3$:Y(0.46 wt%), lithium niobate crystal of stoichiometric composition ($LiNbO_{3stoich}$) and maximal for crystal $LiNbO_3$:Mg (0.35 wt%) (Table 20.1). Note that the photoelectric fields and the magnitude of the induced birefringence were determined taking into account the geometric dimensions of the crystals, their orientation in the optical scheme and at the same value of the scattered radiation angle ~6°. We took into account that most of the crystals under study had a clearly reduced photorefraction effect and the largest angle of PILS indicatrix deviation hardly reached 15°. Only in the $LiNbO_{3stoich}$ crystal, the angle of PILS indicatrix reached 56°, with the maximum photovoltaic field ~7.5 kV/cm.

It can be seen from the obtained data that the band gap width for the studied crystals is in the range 3.25–3.84 eV. Crystals of $LiNbO_3$:B(0.12 wt%), $LiNbO_3$:Gd(0.26 wt%) have the smallest width of the band gap as well as crystals with double doping $LiNbO_3$:Fe(0.0036 wt%):Mg(0.86), $LiNbO_3$:Ta(1.13 wt%):Mg (0.011), Table 20.1. Crystals $LiNbO_3$:Gd(0.23 wt%):Mg(0.75) and $LiNbO_3$:Zn

Table 20.1 Photoelectric parameters of the PILS and the of band gap width of lithium niobate crystals at t = 25 °C

Crystal	λ_g (nm)	ΔE_g (eV)	λ = 532 nm, $I \sim$ 6.29 W/cm^2		
			E_{pv} (V/cm)	E_D (V/cm)	$\Delta n\ 10^{-5}$
[a]$LiNbO_3$:Gd(0.23 wt%):Mg (0.75)	323.8	3.84 ± 0.012	3800	745	5.3
[a]$LiNbO_3$:Zn(2.05 wt%)	323.0	3.83 ± 0.012	4770	75	5.6
[a]$LiNbO_{3cong}$	334.2	3.72 ± 0.011	5620	104	6.7
[a]$LiNbO_3$:Er(3.1wt%)	335.2	3.71 ± 0.011	4400	81	5.2
[a]$LiNbO_3$:Mg(0.35 wt%)	341.0	3.65 ± 0.011	7405	295	9.0
$LiNbO_3$:Y(0.24 wt%):Mg (0.63)	342.2	3.63 ± 0.011	5440	98	6.5
$LiNbO_3$:Y(0.46 wt%)	346.4	3.59 ± 0.01	4340	237	5.3
$LiNbO_{3stoich}$	360.0	3.48 ± 0.01	3178	1360	5.3
$LiNbO_3$:B(0.12 wt%)	380.0	3.27 ± 0.009	5374	99	6.4
[a]$LiNbO_3$:Gd(0.26 wt%)	380.0	3.27 ± 0.009	–	–	–
[a]$LiNbO_3$:Fe(0.0036 wt%): Mg(0.86)	382.4	3.25 ± 0.009	4655	127	5.6
$LiNbO_3$:Ta(1.13 wt%):Mg (0.01)	380.0	3.27 ± 0.009	6052	115	7.1

[a]For these crystals the PILS indicatrix does not develop at $I \sim$ 6.29 W/cm^2

(2.05 wt%) have the greatest width, Table 20.1. In the congruent crystal ($LiNbO_{3cong}$), the width of the band gap is close to the maximum (3.72 eV). In this case, the electrical conductivity of a congruent crystal is $\approx 10^{-16}$–10^{-15} $(\Omega \cdot cm)^{-1}$ [35, 36], the conductivity in the directions along the polar Z-axis is much lower than the conductivity perpendicular to the axis [35, 36]. The stoichiometric crystal, according to our data, is characterized by an average value of the band gap width (3.48 eV). Data on the electrical conductivity of the stoichiometric crystal were not found by us. Thus, the composition of the lithium niobate crystal, which affects the features of its secondary structure [3, 10], significantly affects the width of the band gap, the electrical conductivity and the photoelectric fields. Note that for weakly colored crystals $LiNbO_3$:Fe(0.0036 wt%):Mg(0.86) and $LiNbO_3$:Er(3.1 wt%), the absorption bands of the doping element can influence the absorption bands of the crystal [37–39]. Moreover, the closer the corresponding absorption bands to the edge of fundamental absorption is, the stronger is this influence.

Thus, for the studied crystals, a correlation is observed in the values of the band gap, the magnitude of the photoelectric fields, the magnitudes and time dependence of the PILS parameters, the type of conoscopic figures and Raman spectra, Figs. 20.1 and 20.2; Tables 20.1 and 20.2. The defects with electrons, localized on them, are responsible for effect of photorefraction in a $LiNbO_3$ crystal. The main defects in a nominally pure crystal are Nb^{5+} cations, located at the sites of Li^+ cations in a perfect structure (Nb_{Li}), and defects in the form of shallow electron

traps [3, 10–13]. Moreover, the greater the value of R = Li/Nb is, the less the Nb_{Li} defects present in the crystal, but the more defects in the form of shallow electron traps present in the crystal [3, 10, 12]. From the data obtained, it is also seen that the higher photoelectric fields are created in the crystal, the greater the effect of photorefraction is and the farther the PILS indicatrix stretches. At the same time, the induced birefringence increases, this manifests in conoscopic figures.

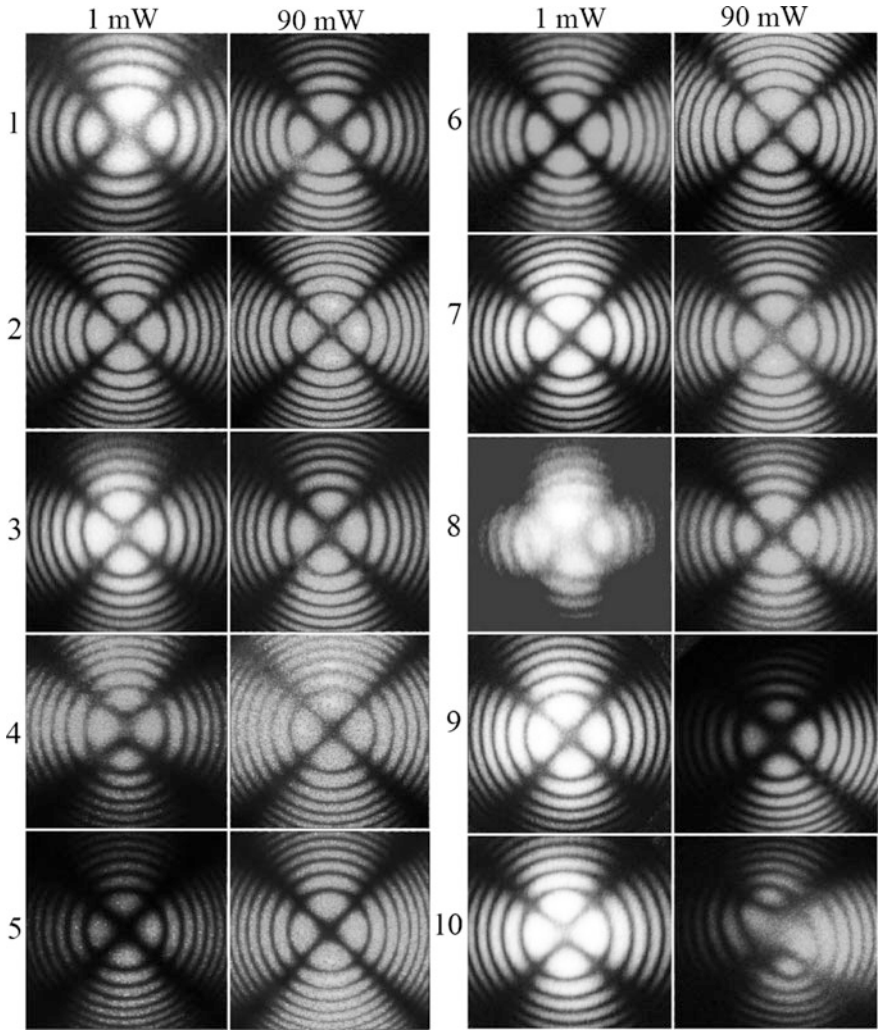

Fig. 20.1 Conoscopic figures of lithium niobate crystals, power of laser radiation: ~1 mW (**a**); ~90 mW (**b**): 1. $LiNbO_3$:Gd(0.51 wt%), 2. $LiNbO_3$:Mg(0.35 wt%), 3. $LiNbO_3$:Gd(0.23 wt%):Mg(0.75), 4. $LiNbO_3$:Zn(2.05 wt%), 5. $LiNbO_3$:Er(3.1 wt%), 6. $LiNbO_3$:Fe(0.0036 wt%):Mg(0.86). 7. $LiNbO_3$:B(0.12 wt%), 8. $LiNbO_3$:Ta(1.13 wt%):Mg(0.011), 9. $LiNbO_3$:Y(0.46 wt%), 10. $LiNbO_3$:Y(0.24 wt%):Mg(0.63)

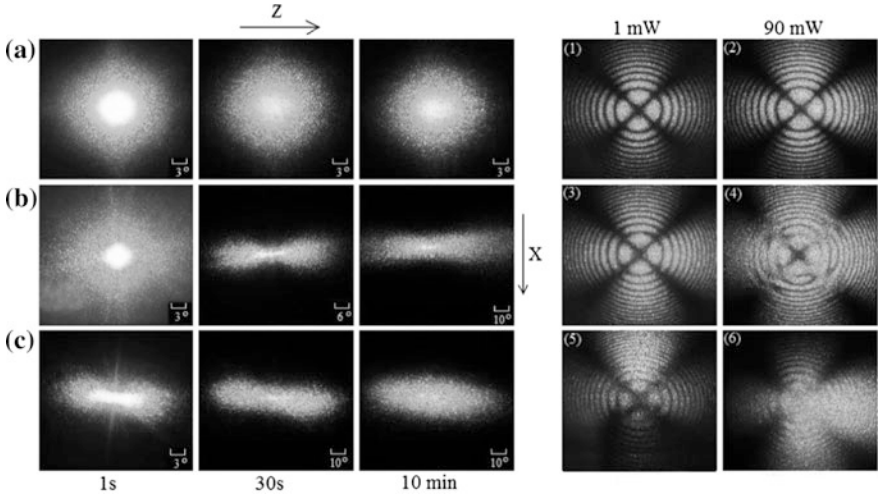

Fig. 20.2 PILS figures of crystals: **a** $LiNbO_{3cong}$(CHN); **b** $LiNbO_{3cong}$(CHN + DCA); **c** $LiNbO_{3stoich}$. λ_0 = 532 nm, I = 6.29 W/cm^2; conoscopic figures of crystals: (1), (2) $LiNbO_{3cong}$(CHN); (3), (4) $LiNbO_{3cong}$(CHN + DCA); (5), (6) $LiNbO_{3stoich}$; λ_0 = 532 nm, I = 0.039 and 3.54 W/cm^2

Figures 20.1 and 20.2 demonstrate conoscopic figures of the studied crystals. When the crystals are irradiated with 1 mW radiation, the conoscopic figures reflect the state of structural defectiveness of the crystal (determined by the composition and crystal growing conditions) in the absence of the photorefraction effect. When laser radiation of power P = 90 mW (λ = 532 nm, d = 1.8 mm) excites conoscopic figures, defects, induced by laser radiation is additionally manifested.

On conoscopic figures of crystals $LiNbO_{3cong}$, $LiNbO_3$:Gd(0.51 wt%), $LiNbO_3$:Mg(0.35 wt%), $LiNbO_3$:Gd(0.23 wt%):Mg(0.75), $LiNbO_3$:Zn(2.05 wt%), $LiNbO_3$:Er(3.1 wt%), $LiNbO_3$:Fe(0.0036 wt%):Mg(0.86), excited by laser radiation of 90 mW, no additional distortions were observed, in comparison with the conoscopic figures obtained at the radiation power of 1 mW (λ = 532 nm, d = 1.8 mm), Figs. 20.1(1–6) and 20.2(1, 2). For these crystals, there was no disclosure of the PILS indicatrix, Table 20.1.

Conoscopic figures of $LiNbO_{3cong}$ crystals, as well as $LiNbO_3$:Mg(0.35 wt%), $LiNbO_3$:Er(3.1 wt%), Figs. 20.1(2, 5) and 20.2(1, 2) correspond to practically perfect conoscopic figures of a uniaxial optically inactive crystal. It is type of figures, which testify the optical homogeneity of the samples and a good optical quality.

Conoscopic figures of lithium niobate crystals $LiNbO_3$:Gd(0.51 wt%), $LiNbO_3$:Gd(0.23 wt%):Mg(0.75), $LiNbO_3$:Zn(2.05 wt%), $LiNbO_3$:Ta(1.13 wt%):Mg(0.011), $LiNbO_3$:Y(0.24 wt%):Mg(0.63), Fig. 20.1(1, 3, 4, 8, 10) contain typical features of biaxial crystals, namely deformation of isochromes and “Maltese cross” with its clarification and rupture into two parts in the center of the field of view.

Table 20.2 The frequencies (ν) and widths (*S*) of the bands in the Raman spectra of single crystals $LiNbO_3$ of different compositions in scattering geometries $Y(ZZ)\overline{Y}(A_1(TO))$ and $Y(ZX)\overline{Y}(E(TO))$ at t = 25 °C

$LiNbO_{3stoich}$		$LiNbO_{3cong}$		$LiNbO_3$:Zn (2.05 wt%)		$LiNbO_3$:B (0.12 wt%)		$LiNbO_3$:Y (0.24):Mg (0.63 wt%)		$LiNbO_3$:Y (0.46 wt%)		$LiNbO_3$:Gd (0.44 wt%)	
ν	*S*	ν	*S*	ν	*S*	ν	*S*	ν	*S*	ν	*S*	ν	*S*
A_1(TO)													
253	21	252	30	259	24	255	24	251	32	254	30	252	32
277	11	276	12	280	16	277	14	275	13	273	14	275	13
333	8	332	10	335	14	333	11	331	10	330	12	331	9
632	20	631	25	624	31	629	23	631	26	632	29	632	26
E(TO)													
156	7	156	12	154	16	155	9	151	11	152	12	148	11
240	9	240	11	238	16	240	10	236	11	237	12	234	11
268	10	268	14	266	32	270	13	264	12	264	14	261	14
324	10	324	13	326	18	324	14	321	15	322	20	318	15
371	17	371	23	371	30	370	26	368	24	368	28	365	24
434	10	434	14	437	15	432	11	432	14	434	16	429	12
576	16	576	15	579	31	576	33	578	22	578	27	576	23
632[a]	31	626	25	631	35	626	46	616	83	622	95	627	50

[a]band with frequency ~630 cm^{-1}; A_1(TO) is appeared in the Raman spectrum in the scattering geometry $Y(ZX)\overline{Y}$, in which E(TO) phonons are active, due to the effect of photorefraction

In this case, the isochromes have the form of ellipses. The "Maltese Cross" is divided into two parts with their shift in the direction from the center, corresponding to the direction of deformation of the optical indicatrix of the crystal. When the laser radiation power is increased to 90 mW, the signs of anomalous optical biaxiality on crystal conoscopic figures $LiNbO_3$:Gd(0.51 wt%), $LiNbO_3$:Zn(2.05 wt %) and $LiNbO_3$:Ta(1.13 wt%):Mg(0.011), Fig. 20.1(1, 4, 8) decrease. The conoscopic figures of these crystals become less deformed, which is obviously related to the "healing" of defects in crystals by the laser radiation.

On the conoscopic figures of crystals $LiNbO_{3stoich}$, $LiNbO_3$:B(0.12 wt%), $LiNbO_3$:Ta(1.13 wt%):Mg(0.011), $LiNbO_3$:Y(0.46 wt%), $LiNbO_3$:Y(0.24 wt%):Mg(0.63), for which the PILS indicatrix was revealed, Table 20.1, with an increase in the laser radiation power up to 90 mW, additional anomalies appear that are absent in the conoscopic figures at 1 mW. It is obviously associated with the appearance of defects induced by laser radiation in the crystal structure. Especially strong deformation of conoscopic figures with increasing in laser radiation power is characteristic for crystals $LiNbO_{3stoich}$ and $LiNbO_3$:Y(0.24 wt%):Mg(0.63), Figs. 20.1(10) and 20.2(6) for which a rapid disclosure of the PILS indicatrix is characteristic, Table 20.1. The appearance of an anomalous optical biaxiality with increasing in the laser radiation power is probably connected with the existence of local regions in a crystal with birefringence.

For crystals $LiNbO_{3cong}$, $LiNbO_3$:Gd(0.51 wt%), $LiNbO_3$:Mg(0.35 wt%), $LiNbO_3$:Gd(0.23 wt%):Mg(0.75), $LiNbO_3$:Zn(2.05 wt%) even at a relatively high intensity of the exciting radiation ($I \sim 6.29$ W/cm^2) photorefractive response is absent, the PILS indicatrix is not revealed, but only circular scattering is observed on static structural defects. The scattering figure does not change in time and retains a shape close to the circle throughout the experiment. At the same time for crystals $LiNbO_{3stoich}$, $LiNbO_3$:B(0.12 wt%), $LiNbO_3$:Ta(1.13 wt%):Mg(0.011), $LiNbO_3$:Y (0.46 wt%), $LiNbO_3$:Y(0.24 wt%):Mg(0.63) a photorefractive response is characteristic of crystals, Table 20.1, and the disclosure of the PILS indicatrix is observed with the appearance of a pronounced three-layered speckle structure that significantly changes over time. In this case, energy is transferred from the central region of the PILS figure (the region of the laser beam incidence) to the scattered radiation. For crystals $LiNbO_{3stoich}$, $LiNbO_3$:B(0.12 wt%), $LiNbO_3$:Ta(1.13 wt%):Mg(0.011), PILS images opened for $\sim$60 s, and they transform with time into an oval ("comet") shape from the round shape (first seconds of excitation), and then take the form of an asymmetric "eight" oriented along the polar axis of the crystal. In the positive direction of the polar axis, coinciding with the direction of the spontaneous polarization vector, a larger "petal" of the figure "eight" develops, and in the negative direction, the smaller one. For this group of crystals, the gradual transfer of energy of different layers of the PILS figure in the direction of the polar axis of the crystal is also characteristic over time. For crystals $LiNbO_3$:Y(0.46 wt%) and $LiNbO_3$:Y(0.24 wt%):Mg(0.63), the disclosure of the PILS indicatrix is much faster than the rest of the crystals during the first second of irradiation of the crystal by laser radiation. It is noteworthy that for crystals $LiNbO_{3stoich}$, $LiNbO_3$:B(0.12 wt%), $LiNbO_3$:Ta(1.13 wt%):Mg(0.011), $LiNbO_3$:Y(0.46 wt%), $LiNbO_3$:Y(0.24 wt%):

Mg(0.63), difference is less in comparison with other crystals, the band gap width, the strongest photorefractive response is observed and the PILS indicatrix reveals the greatest opening, Table 20.1.

Table 20.2 shows the values of some Raman bands widths of crystals $LiNbO_{3stoich}$, $LiNbO_{3cong}$, $LiNbO_3$:B(0.12 wt%), $LiNbO_3$:Y(0.46 wt%), $LiNbO_3$:Y (0.24 wt%):Mg(0.63), $LiNbO_3$:Gd(0.44 wt%), $LiNbO_3$:Zn(2.05 wt%), corresponding to fundamental vibrations A_1(TO) and E(TO) type symmetry, occurring, respectively, along and perpendicular to the polar axis of the crystal. It can be seen that the smallest values of the width of the majority of bands have the Raman spectrum of crystals $LiNbO_{3stoich}$ and $LiNbO_3$:B(0.12 wt%), and the largest values for the spectrum of the crystal $LiNbO_3$:Zn(2.05 wt%). Moreover, the strongest dependences of the widths on the crystal composition are characteristic for bands with frequencies 630 A_1(TO) and 576 cm^{-1} (E(TO)), corresponding, respectively, to the completely symmetric and doubly degenerate vibrations of the oxygen atoms of the octahedra O_6. Unusual is that the band with frequency 576 cm^{-1} has the largest width in the spectrum of the crystal $LiNbO_3$:B(0.12 wt%), in comparison with other studied crystals, Table 20.2. This can be explained by the fact that non-metallic cations B^{3+} practically do not enter the structure of the crystal $LiNbO_3$, but they structure the melt, thus affecting the structural features and optical properties of the crystal. With a content of about 1.2 mol% B_2O_3 in the melt, in the crystal there will be only $\sim 4 \times 10^{-4}$ mol% B_2O_3, which corresponds to the concentration of uncontrolled trace of numerous cationic impurities in the crystal $LiNbO_3$ (Zr, Mo, Ca, Fe, Ti, Si et al.) [7–9, 24].

According to the Raman tensor in the spectrum in the scattering geometry $Y(ZX)\overline{Y}$, only bands, corresponding to oscillations of the E (TO) type of symmetry, should be present [3]. However, in the Raman spectra of all the studied crystals, owing to the presence of the photorefraction effect, there is a band with frequency ~ 630 cm^{-1}, which corresponds to the totally symmetric vibrations of oxygen octahedra of the A_1 type of symmetry. By measuring the intensity of the "forbidden" band with frequency 630 cm^{-1}, it is possible to estimate the magnitude of the photorefractive effect [3]. At the same time, the width of this band, as well as the band width with frequency 576 cm^{-1} (E(TO)), indicates a degree of distortion of oxygen octahedra O_6. Table 20.2 shows that the minimum band width with frequency ~ 630 cm^{-1} is observed for a crystal $LiNbO_{3stoich}$, characterized by the most ordered cation sublattice, but a high photorefraction effect. Band width with frequency ~ 630 cm^{-1} in the spectrum of crystals $LiNbO_{3stoich}$, $LiNbO_3$:B(0.12 wt%), $LiNbO_3$:Y(0.46 wt%), $LiNbO_3$:Y(0.24 wt%):Mg(0.63), for which there was a disclosure of the PILS indicatrix, Table 20.1, increases, in comparison with the width in the spectrum of the crystal $LiNbO_{3cong}$, Table 20.2. However, the increase in width occurs not in proportion to the increase in the opening angle of the PILS indicatrix, Tables 20.1 and 20.2. The greatest angle of disclosure of the PILS indicatrix is observed for a crystal $LiNbO_{3stoich}$, Table 20.1, and the largest band width with frequency ~ 630 cm^{-1} for crystal $LiNbO_3$:Y(0.46 wt%), Table 20.2. In addition, the width of this band in the Raman spectrum of crystals $LiNbO_3$:Gd(0.44 wt%) and

$LiNbO_3$:Zn(2.05 wt%) is broader than in the spectrum of the crystal $LiNbO_{3stoich}$, Table 20.2. This is because the contribution to the width of the band with frequency $\sim 630\ cm^{-1}$ is brought not only by the effect of photorefraction, but also by the degree of distortion of the oxygen octahedra of the crystal, which depends on the composition. The distortion of oxygen octahedra is influenced, first of all, by differences in the ionic radii of the doping cations and ions Li^+, Nb^{5+}, the nature of the bonds, formed by cations with oxygen ions, as well as the particular order in the location of the basic and doping cations and vacancies along the polar axis.

Usually single crystals of congruent composition (R = Li/Nb = 0.946) are applied. At the same time, for the production of materials with submicron periodically polarized domain structures, perfected lithium niobate single crystals of stoichiometric composition (Li/Nb = 1) have a significant advantage in comparison with congruent crystals because they have a significantly lower (five times or more) coercive field [6]. However, stoichiometric crystals grown from a melt with 58.6 mol% Li_2O are characterized by a high inhomogeneity of the refractive index along the growth axis, and also, much higher than the congruent crystal effect of photorefraction (optical damage) [3, 6, 12, 26, 40]. In addition, the considerable heterogeneity of the composition along the length of the monocrystal, arising during the growth process, makes it difficult to grow stoichiometric crystals of sufficiently large size [1, 3], suitable for industrial manufacturing of optical elements. Congruent single crystals have a high constancy of the refractive index along the growth axis [1, 3].

Figure 20.2 demonstrates PILS figures and conoscopic pictures of a stoichiometric single crystal $LiNbO_{3stoich}$ and congruent single crystals grown from a charge of various geneses. Single crystals of congruent composition are grown from a charge, obtained using cyclohexanone as an extractant — $LiNbO_{3cong}$(CHN), as well as from the charge, obtained using cyclohexanone and dimethylamides of carboxylic acids as extractants — $LiNbO_{3cong}$(CHN + DCA) [3]. Laser conoscopy methods and PILS do not give direct information about the features of the internal structure of crystals and defects that determine their photorefractive properties, but they allow obtaining preliminary information on optical homogeneity and photorefractive properties of crystals, which is important at the stage of development of technology for growing lithium niobate crystals.

PILS, arising on spatial microdefects with a laser (static) or fluctuating refractive index, changed under the influence of laser radiation, causes a strong destruction of the laser beam in the crystal and is an interfering factor for the generation and transformation of radiation [14, 15]. The shape and features of the speckle structure of the PILS indicatrix depend on the features of the structure of the crystal, the state of its defectiveness, and also on the polarization of the radiation and the geometry of the experiment [14, 15].

For crystal $LiNbO_{3cong}$(CHN) even after irradiation for 10 min by laser radiation with a power density 6.29 W/cm^2, the PILS indicatrix is not disclosed, but only circular scattering is observed on static structural defects, Fig. 20.2a. It should be noted that the central layer of the speckle structure of the crystal $LiNbO_{3cong}$(CHN)

PILS, Fig. 20.2a, corresponding to the cross-section of the laser beam, disappears almost completely within the first 30 s after the beginning of the irradiation of the crystal, then reappears.

At the same time, crystals $LiNbO_{3cong}$(CHN + DCA) and $LiNbO_{3stoich}$ PILS figures vary considerably over time, Fig. 20.2b, c. Indicatrix of PILS froms a rounded shape with time is transformed first into an oval ("comet") shape, and then takes the form of an asymmetric "eight", oriented along the polar axis of the crystal. For these crystals, the gradual shift of the intensity of different layers of the PILS figure in the direction of the polar axis of the crystal is also characteristic over time, Fig. 20.2b, c. For the crystal $LiNbO_{3stoich}$ indicatrix of PILS is revealed in the first seconds of irradiation, Fig. 20.2c. The opening angle of the PILS is 66° and 56° for crystals $LiNbO_{3cong}$(CHN + DCA) and $LiNbO_{3stoich}$, respectively.

Often a congruent charge of lithium niobate [3] leads to appearance of a slightly greenish or yellowish-greenish color in single crystals. The presence of the color can limit the possibility of single crystals application for optical devices that require optical perfection of the material. The appearance of color is due to the appearance in the crystal of cluster defects in the form of molecular complexes on the base of intrinsic and impurity defectiveness. This defectiveness is partly laid down at the stage of preparation of the initial niobium pentoxide by extraction [3]. It is possible to obtain perfectly colorless (water white) $LiNbO_3$ crystals using a mixture of charge synthesized from niobium pentaoxides produced with the help of different extractants: carboxylic acid amides and cyclohexanone. Apparently, the use of lithium niobate charge, mixed in a certain proportion of different genesis, leads to compensation of defect formation mechanisms and to the absence of visible color of the crystal. Comparative studies of crystals, grown from one type of charge,—$LiNbO_{3cong}$ (CHN) and from the mixture—$LiNbO_{3cong}$(CHN + DCA) showed significantly higher optical homogeneity, as well as an absolute visual colorlessness (water white) in crystals, grown from a mixture of charge, synthesized from niobium pentaoxides, produced by various extractants [3]. In addition, for the crystal $LiNbO_{3cong}$(CHN + DCA) the fundamental absorption edge is essentially shifted to the region of short wavelengths in comparison with the crystal $LiNbO_{3cong}$(CHN) [41], which means it has a substantially larger optical transparency window. The latter indicates a higher degree of structural perfection of congruent crystals $LiNbO_{3cong}$(CHN + DCA), apparently, approaching the degree of structural perfection of crystals of stoichiometric composition $LiNbO_{3stoich}$.

It was established in [14] that small electronic traps can form in structurally imperfect lithium niobate crystals. In such crystals, the contribution of the energy of the electronic subsystem to the total energy of the crystal is high [23]. At the same time, the photorefractive effect is noticeably reduced due to an increase in the efficiency of the eradicative recombination of photo-excited carriers without their capture to deep levels. The reasons for this are that when the crystal is illuminated by the laser radiation, there are two competing processes. On the one hand, with an increase in the degree of structural perfection in the crystal, the number of charged defects and associated deep trapping levels in the band gap decreases, on the other hand, the number of small traps ("sticking levels" [14]) decreases and, accordingly,

decreases the probability of eradicative recombination photoexcited carriers. The main part of the photoelectrons is captured by the existing deep traps. Consequently, uncompensated internal electric fields that affect the refractive index and determine the photorefractive properties of the crystal become larger. This, apparently, explains the greater effect of photorefraction in more structurally perfect crystals $LiNbO_{3stoich}$ and $LiNbO_{3cong}$(CHN + DCA) in comparison with the crystal $LiNbO_{3cong}$(CHN), Fig. 20.2.

The optical homogeneity of the crystals was investigated by laser conoscopy at laser power densities (I) (λ_o = 532 nm) 0.039 и 3.54 W/cm^2, Fig. 20.2.

For the crystal $LiNbO_{3cong}$(CHN), standard conoscopic pictures of a uniaxial crystal of high optical quality are observed, Fig. 20.2(1, 2). On the background of concentric rings-isochromes, the branches of the "Maltese cross", formed by two isogyres of minimum intensity, intersect at the center of the field of view, perpendicular to each other and coincide with the transmission axes of the polarizer and analyzer.

Crystal $LiNbO_{3cong}$(CHN + DCA) conoscopic figures at radiation power density 0.039 W/cm^2 have a standard shape, corresponding to a uniaxial crystal, and consist of a contrasting black "Maltese cross", which is superimposed on concentric rings-isochromes, centered at the exit point of the optical axis, coinciding with the center of the "Maltese cross". The "Maltese Cross" retains the minimum intensity within the entire field of view, Fig. 20.2(3). When the power density of the laser radiation is increased to 3.54 W/cm^2 was also obtained a conoscopic figure, corresponding to a uniaxial crystal, Fig. 20.2(4), but it is much more deformed than the conoscopic figure at 0.039 W/cm^2, Fig. 20.2(3). There is a decrease in the contrast and clarity of the image, there is a significant violation of the circular symmetry of the rings-isochromes, there is marked pairing, discontinuities, dislocations and inconsistencies with isochromes, when crossing the "Maltese cross" branches, Fig. 20.2(4). Significant deformation of the conoscopic patterns with increasing laser radiation power density from 0.039 to 3.54 W/cm^2 for the crystal $LiNbO_{3cong}$(CHN + DCA) is probably due to this crystal is characterized by a significant photorefractive response, Fig. 20.2b.

Figure 20.2(5, 6) demonstrates conoscopic patterns of the crystal $LiNbO_{3stoich}$. As with small (0.039 W/cm^2), and with a large (3.54 W/cm^2) power density of laser radiation, the conoscopic patterns are significantly deformed. On both conoscopic crystal figures $LiNbO_{3stoich}$ there are signs of anomalous optical biaxiality, in which there is a deformation of the optical indicatrix of the crystal in the vertical direction, corresponding to the direction of the shift of the "Maltese cross" parts. In this case, the isochromes are stretched in the direction of displacement of the fragments of the cross and take the form of ellipses. Each ring-isochrome, being a line of the same phase shift, corresponds to a cone of rays with the same angle of incidence when the axis of the conical radiation beam coincides with the optical axis of the crystal. Such anomalies of conoscopic figures indicate a significant optical inhomogeneity of the crystal $LiNbO_{3stoich}$. The increase in the power of laser radiation, Fig. 20.2(6), leads to a decrease in the overall contrast and sharpness of the image, as well as to a noticeable "blurring" of the branches of the "Maltese cross". Significant distortion of

conoscopic patterns for a crystal $LiNbO_{3stoich}$, when the power density of the laser radiation is increased to 3.54 W/cm^2 is apparently due to the presence of a significant photorefractive response, Fig. 20.2c.

By the interference method, using the technique described in [27], the electro-optical coefficients are determined, which for a crystal $LiNbO_{3stoich}$ amounted to r_{22} = 6.4 pm/V and $r_e = n_0^3 r_{13} - n_e^3 r_{33}$ = 19.3 pm/V, for a congruent crystal $LiNbO_{3cong}$(CHN + DCA) amounted to r_{22} = 6.5 pm/V and $r_e = n_0^3 r_{13} - n_e^3 r_{33}$ = 29.3 pm/V. According to the literature, r_e for crystal $LiNbO_{3cong}$(CHN) amounted to 17–19 pm/V. Thus, it can be stated that the crystals $LiNbO_{3cong}$(CHN + DCA) have significantly higher electro-optical properties than crystals $LiNbO_{3cong}$(CHN).

20.4 Conclusion

Absorption spectra, Raman spectra and PILS figures were researched for $LiNbO_3$ crystals nominally pure and doped with cations: Mg^{2+}(0.35 wt%), Zn^{2+}(2.05), B^{3+}(0.12), Gd^{3+}(0.26, 0.44, 0.51), Y^{3+}(0.46), Gd^{3+}(0.23):Mg^{2+}(0.75), Mg^{2+}(0.86):Fe^{3+}(0.0036), Ta^{5+}(1.13):Mg^{2+}(0.01), Y^{3+}(0.24):Mg^{2+}(0.63), Er^{3+}(3.1). It is established that the position and character of the behavior of the absorption edge of lithium niobate crystals depends on the type of the dopant. The width of the band gap of crystals is calculated from the parameters of the absorption edge. It is shown that the width of the band gap depends on the state of the defect structure of the crystals, which determines the magnitude of the photorefraction effect. The smaller width of the band gap is observed in crystals $LiNbO_{3stoich}$, $LiNbO_3$:B(0.12), $LiNbO_3$:Ta(1.13):Mg(0.011), $LiNbO_3$:Y(0.46), $LiNbO_3$:Y(0.24):Mg(0.63). In these crystals, a photorefractive response is present and the PILS indicatrix is revealed, when irradiated with laser radiation of λ_0 = 476.5 nm and the radiation intensity $I \sim 8.49$ W/cm^2. In the crystals $LiNbO_{3stoich}$, $LiNbO_3$:Y(0.46 wt%), $LiNbO_3$:Y(0.24):Mg(0.63), the disclosure of the PILS indicatrix occurs very quickly, during the first second of irradiation of the crystal by laser radiation. In Raman spectra of these crystals, a significant broadening of the bands, corresponding to vibrations of cations, located in octahedral void spaces, and vibrations of the oxygen octahedra of the A_1(TO) and E(TO) symmetry type is revealed, indicating an increased disorder in the structural units of crystals. The optical homogeneity and photorefractive properties of stoichiometric and congruent lithium niobate crystals, grown from the charge of different genesis are investigated. It is shown that for crystals $LiNbO_{3cong}$(CHN) at a power density of laser radiation up to 6.29 W/cm^2 the PILS indicatrix is not disclosed, but only circular scattering is observed on static structural defects. For crystals $LiNbO_{3cong}$(CHN + DCA) and $LiNbO_{3stoich}$ the PILS indicatrix is fully revealed within a minute from the beginning of irradiation with laser radiation, the opening angle is 66° and 56°, respectively. Investigation of optical homogeneity of crystals by laser conoscopy showed a sufficiently high

optical quality of crystals $LiNbO_{3cong}$(CHN) and $LiNbO_{3cong}$(CHN + DCA). On both $LiNbO_{3stoich}$ crystals conoscopic figures, obtained for small (0.039 W/cm^2) and large (3.54 W/cm^2) power density of laser radiation has signs of anomalous optical biaxiality. Crystal $LiNbO_{3cong}$(CHN + DCA) is more optically homogeneous than $LiNbO_{3stoich}$, but at the same time it has a great effect of photorefraction and substantially higher electro-optical properties than the crystal $LiNbO_{3cong}$(CHN).

References

1. Y.S. Kuzminov, *Electro-optical and Nonlinear-optical Lithium Niobate Crystal* (Nauka, Moscow, 1987) (in Russian)
2. G.G. Gurzadyan, V.G. Dmitriev, D.N. Nikogosyan, *Nonlinear Optical Crystals. Properties and Applications in Quantum Electronics* (Radio and Communication, Moscow, 1991) (in Russian)
3. N.V. Sidorov, T.R. Volk, B.N. Mavrin, V.T. Kalinnikov, *Lithium Niobate: Defects, Photorefraction, Vibrational Spectra, Polaritons* (Nauka, Moscow, 2003) (in Russian)
4. S.V. Mikhlyaev, *Mater. Electron. Eng.* (2), 32 (2013)
5. V.V. Krishtop, M.N. Litvinova, V.G. Efremenko, V.I. Stroganov, A.V. Syuy, A.V. Denisov, O.S. Grunsky, Opt. J. **73**(12), 84 (2006)
6. M.N. Palatnikov, N.V. Sidorov, *Oxide Electronics and Functional Properties of Transition Metal Oxides* (NOVA Sience Publishers, New York, 2014), p. 31
7. M.N. Palatnikov, I.V. Biryukova, N.V. Sidorov, A.V. Denisov, V.T. Kalinnikov, P.G.R. Smith, V.Y. Shur, J. Cryst. Growth **291**, 390 (2006)
8. M.N. Palatnikov, I.V. Biryukova, S.M. Masloboeva, O.V. Makarova, D.V. Manukovskaya, N.V. Sidorov, J. Cryst. Growth **386**, 113 (2014)
9. M.N. Palatnikov, S.M. Masloboeva, I.V. Biryukova, O.V. Makarova, N.V. Sidorov, V.V. Efremov, J. Inorg. Chem. **59**(3), 318 (2014)
10. N.V. Sidorov, M.N. Palatnikov, V.T. Kalinnikov, *Influence of the Secondary Structure on Optical Properties of Ferroelectric Crystals of Lithium Niobate with Low Photorefractive Effect.* Proc. KSC RAS. Chemistry and Materials. Apatity (2015) (in Russian)
11. A.A. Blistanov, V.M. Lyubchenko, A.N. Goryunova, Kristallographija **43**(1), 86 (1998)
12. T. Volk, M. Wohlecke, *Lithium Niobate. Defects, Photorefraction and Ferroelectric Switching* (Springer, Berlin, 2008)
13. M. Lines, A. Glass, *Ferroelectrics and Related Materials* (Mir, Moscow, 1981) (in Russian)
14. V.V. Obukhovsky, *Processes of Photorefractive Scattering of Light in Crystals*, Ph.D. Thesis, Kiev, 1989 (in Russian)
15. V.A. Maksimenko, A.V. Syui, Y.M. Karpets, *Photoinduced Processes in Lithium Niobate Crystals* (Fizmatlit, Moscow, 2008) (in Russian)
16. S.G. Odulov, M.S. Soskin, A.I. Khizhnyak, *Lasers on Dynamic Gratings* (Nauka, Moscow, 1990) (in Russian)
17. A.S. Pritulenko, A.V. Yatsenko, S.V. Evdokimov, Kristallographija **60**(2), 293 (2015)
18. A.V. Yatsenko, S.V. Yevdokimov, A.S. Pritulenko, D.Y. Sugak, I.M. Solskii, Phys. Solid State **54**, 2231 (2012)
19. A. Weidenfelder, J. Shi, P. Fielitz, G. Borchardt, K.D. Becker, H. Fritze, Solid State Ion. **225**, 26 (2012)
20. A.A. Bulycheva, *Electrical Conductivity and Electron-hole Processes in Lithium Niobate Crystals Heavily Doped with Magnesium Oxide*, PhD Thesis, Tomsk, 2005 (in Russian)

21. K.K. Wong, *Properties of Lithium Niobate* (INSPEC, The Institution of Engineers, London, 2002)
22. A.A. Blistanov, V.V. Geraskin, A.V. Khretinina, *Izv. High Schools. Mater. Electron. Eng.* (1), 28 (1998)
23. V.M. Fridkin, *Ferroelectrics–Semiconductors* (Nauka, Moscow, 1976) (in Russian)
24. M.N. Palatnikov, N.V. Sidorov, I.V. Biryukova, O.B. Shcherbina, V.T. Kalinnikov, *Perspekt. Mater.* (2), 93 (2011) (in Russian)
25. M.N. Palatnikov, N.V. Sidorov, V.T. Kalinnikov, *Ferroelectrical Solid Solutions Based on Oxyde Compounds of Niobium and Tantalum: Synthesis, Research of Structure Order and Physical Characteristics* (Nauka, Saint-Petersburg, 2001) (in Russian)
26. N.V. Sidorov, E.A. Antonycheva, A.V. Syui, M.N. Palatnikov, Kristallographija **55**(6), 1079 (2010)
27. A.V. Syuy, E.O. Kile, in *Proceedings of SPIE. Aisa-Pacific Conference on Fundamental Problems of Opto- and Microelectronics*, 101761N (2016). https://doi.org/10.1117/12.2268233
28. M. Goulkov, M. Imlau, Th Woike, Phys. Rev. **77**, 235110 (2008)
29. A.V. Syuy, N.V. Sidorov, A.Y. Gaponov, V.I. Panfilov, M.N. Palatnikov, Opt. Spectrosc. **114** (5), 845 (2013)
30. A.V. Syuy, N.V. Sidorov, A.Y. Gaponov, M.N. Palatnikov, V.G. Efremenko, Optik **124**, 5259 (2013)
31. A.V. Syui, N.V. Sidorov, M.N. Palatnikov, D.S. Shtarev, E.A. Antonycheva, A.Y. Gaponov, K.A. Chekchonin, Opt. J. **82**(5), 71 (2015)
32. N.V. Sidorov, O.Y. Picoul, A.A. Kruk, N.A. Teplyakova, A.A. Yanichev, M.N. Palatnikov, Opt. Spectrosc. **118**(2), 273 (2015)
33. N.V. Sidorov, O.Y. Picoul, N.A. Teplyakova, A.A. Kruk, M.N. Palatnikov, *Perspekt. Mater.* (4), 70 (2014) (in Russian)
34. O.Y. Pikoul, N.V. Sidorov, M.N. Palatnikov, O.V. Makarova, *J. Mod. Phys.* (4), 12 (2013)
35. I.S. Akhmadullin, V.A. Golenishchev-Kutuzov, S.A. Migachev, S.P. Mironov, Fiz.Tverd. Tela **40**(7), 1307 (1998)
36. I.F. Kanaev, V.K. Malinovsky, DAN USSR **266**(6), 137 (1982)
37. N.V. Sidorov, A.A. Gabain, A.A. Yanichev, I.N. Efremov, I.V. Biryukova, M.N. Palatnikov, Opt. Spectrosc. **118**(2), 283 (2015)
38. N.V. Sidorov, M.N. Palatnikov, A.A. Kruk, A.A. Yanichev, O.V. Makarova, N.A. Teplyakova, O.Y. Pikoul, Opt. Spectrosc. **116**(2), 298 (2014)
39. M.N. Palatnikov, I.V. Biryukova, O.B. Shcherbina, N.V. Sidorov, O.V. Makarova, N.A. Teplyakova, Kristallographija **61**(6), 999 (2016)
40. F. Jermann, M. Simon, E. Krätzig, *J. Opt. Soc. Am.* (12), 2066 (1995)
41. N.A. Teplyakova, N.V. Sidorov, M.N. Palatnikov, A.V. Syuy, D.S. Shtarev, Inorg. Mater. **53**(11), 1189 (2017)

Chapter 21
Interfacial Microstructures and Characterization of the Titanium—Stainless Steel Friction Welds Using Interlayer Technique

Muralimohan Cheepu, V. Muthupandi, D. Venkateswarlu, B. Srinivas and Woo-Seong Che

Abstract The joints of dissimilar metals and alloys are increasing demand as essential parts of aerospace, nuclear and cryogenic applications. One of the greatest challenges for design engineers is to develop and implement fast and cost-effective industrial procedures to join titanium with stainless steel and aluminum. Regardless of the welding conditions, such high specific properties of the metal combinations cannot be fusion welded in conventional method, because of the formation of highly brittle intermetallic compounds in the fusion zone. However, solid-state joining processes, friction-welding process contemplated to offer the highest potential for successful joining of bimetallic components. The friction welding techniques are highly efficient and it has the advantage of far greater weldability and reduces the risk of interfacial reaction. In the present investigation, microstructure formation at the interfaces of friction welds between titanium and stainless steel with and without interlayer are discussed. The formation of fragile intermetallic compounds like Fe–Ti and Cr–Ti are completely avoided between the titanium and stainless steel by introducing of interlayer material. The interlayer material successfully controlled the undesirable compounds from the weld interface and

M. Cheepu (✉) · W.-S. Che
Department of Mechatronics Engineering, Kyungsung University, Busan 48434, Republic of Korea
e-mail: muralicheepu@gmail.com

V. Muthupandi
Department of Metallurgical and Materials Engineering, National Institute of Technology Tiruchirappalli, Tiruchirappalli 620015, Tamil Nadu, India

D. Venkateswarlu
Department of Mechanical Engineering, Marri Laxman Reddy Institute of Technology and Management, Hyderabad 500043, Telangana, India

B. Srinivas
Department of Mechanical Engineering, MVGR College of Engineering, Vizianagaram 535005, Andhra Pradesh, India

I. A. Parinov et al. (eds.), *Advanced Materials*, Springer Proceedings in Physics 207, https://doi.org/10.1007/978-3-319-78919-4_21

developed a new weld interface. The new microstructure formation at weld interface enhanced the final properties of the titanium to stainless friction welds.

21.1 Introduction

In contemporary years, it is necessary to develop various materials utilizing for different applications such as advanced structural and construction industries. Manufacturing engineer challenges and continuously looking forward to shifting or modifying the currently available novel materials to the metal matrix composites and the combination of various compounds for obtaining metallurgical joints as like conventional materials [1]. It needs to be understand the microstructure properties and to build the modern synthesis compounds to enhance the properties and its optimization levels for essential weld interfaces of the joints between compound and other designed materials. The currently developed bulk materials or synthesis compounds of the welded joints in particular challenging to prevent the brittle intermetallic compounds, which are, have a tendency to form at the weld interfaces when the joints produced through conventional fusion welding processes [2]. The combination of dissimilar alloys such as steel to aluminum (Al), magnesium (Mg) to aluminum and titanium (Ti) to stainless steel (SS) are more prone to have brittle intermetallic formation under conventional welding processes. Every dissimilar materials combination has difficulties for achieving strong joints to utilize their benefits completely. The most challenging and very high scope to develop the applications of the dissimilar materials combination is titanium and austenitic stainless steel. The dissimilar combination of titanium to stainless steel couple is used in chemical, aerospace and biomedical applications [3].

The demand for these materials combination owes to demand for properties of one of the material such as titanium, which has low density, high melting point, adept corrosion resistance and high strength to weight ratio make this material suitable for chemical industry, structural, medium energy and medium temperature applications [1, 4, 5]. However, titanium alone is not sufficient to withstand the higher loads, where the multiple thicknesses of plates are desirable, due to the drawback of their strength weakening at elevated temperatures. Because of this, its demand increasing presently for conjoining the functional properties of titanium with the other materials, which has almost similar properties of stainless steel, becomes a structural support material. The joints between titanium and its alloys to structural steels demands for several applications. The highest demand has been obtain especially for the dissimilar combination of austenitic stainless steels to Ti alloys, which are extensively used in nuclear, petrochemical, aerospace and cryogenic industries [6–9]. However, the joining of stainless steel to titanium using conventional fusion welding techniques has been ascertained ineffective as it will cause to the construction of undesirable secondary phases in the weld zone, which will weaken the joint properties. There are many reasons behind the welding of titanium to stainless steel by conventional welding methods and are became

challenging due to the high reactivity nature of titanium with nitrogen and oxygen at elevated temperatures [10], and the formation of brittle intermetallic compounds of CrTi, Fe_2Ti and FeTi in the fusion zone [11]. In addition, the substantial differences in their thermo-physical properties like heat transfer, thermal expansion coefficient, melting temperatures, low solubility and chemical compositions possibly will acquaint with large residual stresses in the weld interface [1, 12]. Chen et al. [13], have been studied the laser welding of titanium to stainless steel with different pulse shapes and observed the formation of FeTi, Fe_2Ti and Ti-rich intermetallic compounds. These intermetallic compounds are highly brittle and causing weldments to crack spontaneously, due to its highest hardness, which is recorded as more than 1300 HV [14], and thermal mismatch between both of the substrates. Therefore, minimizing the formation of brittle intermetallic phases is the key factor to comprehending the reliable and quality joints.

The solid-state joining methods are feasible solutions to overcome these difficulties between the dissimilar joining methods. These are attributed to the solid solubility action of Fe in α-Ti very limited range at room temperature. Using the solid state welding methods, different combinations of materials were joined successfully compared to the conventional welding methods [15–18]. Also the dissimilar combination of titanium to stainless steel couple was joined by various solid state welding methods, such as brazing [19], diffusion bonding process [20], friction welding [21], explosive welding [22], friction stir welding [23]. The results of these methods achieved better joint quality and up to some extent of controlling the formation of intermetallic compounds, compared to the conventional fusion welding methods. Furthermore, drawbacks of their process duration, low productivity and high operational cost leads in restricted for few applications and very limited joint configurations. Friction welding process has gained much importance among these solid state welding processes, and its applications are widely used in several industries [24–26]. Friction welding is unlike other welding methods and to make the joints, required heat is generated because of the relative motion between two materials faying surfaces continuous rubbing without melting of the weld interface. It is well developed process and extensively used for dissimilar and similar combinations without any difficulties [21]. Friction welding method involves in three types such as direct drive, inertia drive and linear friction welding methods. For all the applications, most commonly used one is direct drive, which is run by motor at constant speed. The important process variables of friction welding is heating pressure, heating time, upset time, upset pressure and rotational speed, which control the necessary heat and pressure for welding [4]. Among these variables, rotational speed is very less effective and its range can be used widely, when the heating duration and load are suitably controlled. The heat input also can be easily controlled with the rotational speed, the lower heat input obtained at higher rotational speed, which is most suitable to weld heat sensitive materials [27]. Other than process variables, the strength of the welds also effects by surface roughness of the faying surface of the materials, in particular for dissimilar combinations. The surface smoothness is not so critical for similar combinations due to their equal amount of deformation on both sides of the materials. Whereas, the

amount of flash and degree of deformation for dissimilar combination is differs greatly, especially the combination of titanium to stainless couples has much more difference in deformation on titanium side higher than the stainless steel side. Hence the surface roughness of the one of the hardest materials is crucial and need to be smoothened as like as other material surface smoothness [28]. The selection of process parameters is very important to control the maximum temperature at the joint interface, which is very crucial for dissimilar joints to confine the residual stresses and melting of the substrates and subsequent formation of hard intermetallic phases. The weld interface temperatures of 1425 °C for dissimilar combination of mild steel to stainless steel were identified using infrared rays [29]. The surface stresses are highest at the weld centerline and the distribution of strain during welding are influenced through the pressure acting on the joints initial stage and final stage of the pressures. The joint strength of the direct joining of friction welds between titanium (grade 2) and 304 stainless steel is almost similar to strength of the titanium base metal. Whereas the joints obtained very poor ductility and bending angle and joint failure took place at weld interface [30]. Some researchers have reported that the comparison studies of titanium to 321 stainless steel using friction welding and brazing (using silver-based Bag-19 fillers). The strength of the brazed joints is poorer than the friction welded joints and the joint failure in the weld interface. Whereas, the joint failure in friction welds is titanium base metal could be due to the formation of thinner intermetallic compounds layer at the weld interface [31].

However, the direct joining of titanium to stainless steel using friction-welding method was not affordable to control the formation of reaction zones completely at the weld interface to obtain the reliable joints. Consequently, to acquire the quality joints in recent years direct joining was comprehended by adding an interlayer metal to avert the metallurgical reactions during friction welding process. Ochi et al. [32] joined the dissimilar materials of 2017 aluminum to carbon steel with aluminum insert metals using friction welds. The strength of the joints drastically improved and joint strength depended on the remaining insert metal thickness at the weld interface. The joint failure occurred along the insert metal and carbon steel interface due to the reactions of the alloying elements during welding. In the same year, Lee et al. [33] reported the influence of copper interlayer metal on the joint characteristics of the friction welding of TiAl to AISI 4140 structural steel combination. The copper insert metal acted as a buffer layer at the weld interface and aid to stress relief the joints, therefore its prevent the crack formation at the interface. However, at the weld interface of insert metal copper and TiAl, it was observed the formation of two types of intermetallic phases like $AlCu_2Ti$ and $TiCu_4$. In addition, at the peripheral region of the welds between insert metal copper and TiAl, $AlCu_2Ti$ and $TiCu_4$ thick reaction zones were composed. In later years, Maldonado et al. [34] investigated the formation of intermetallic compounds during friction welding process of 6061 (T6) aluminum alloy metal matrix composite and AISI 304 stainless steel. The microstructure analysis revealed the mutual interaction of the insert metal silver with the aluminum, produced the circular shaped silver nanoparticles with the dimensions of 10 to 20 nm and the formation of Ag_3Al

intermetallic compounds in the weld interface. Whereas, there are very few studies conducted on friction welding of titanium to stainless steel using interlayer material. Correspondingly, aluminum insert metal [4, 35] has been used for titanium to stainless steel couple to avoid the formation of brittle intermetallic compounds, and therefore improving the mechanical properties of the joints. Ashfaq et al. [36] reported the friction welding of 304 stainless steel to titanium using tantalum, nickel and vanadium interlayers. The strength of the joints significantly improved in the range from 89 to 94% of titanium base metal strength and the joint failure occurred along the interface. The interlayer materials of tantalum and vanadium are extruded out from the weld interface during welding due to their poor thermal conductivity and less tensile strength. Most recently Muralimohan et al. [37] have been used the nickel interlayer technique for friction welding of 304 stainless steel to titanium. The brittle intermetallic compounds of FeTi, Fe_2Ti and CrTi have been completely avoided by using nickel interlayer. The joint strengths of the interlayer welds are improved compared to the direct joints.

However, most of the studies on titanium to stainless joining using nickel interlayer technique are available in diffusion bonding, brazing and laser welding processes. The reason for considering nickel as a interlayer material is due to its excellent erosion resistance, and it can form an restrained solid solution with the iron, and the Ni–Ti metallic phases contains a higher plasticity. Moreover, the dissimilar combination of titanium to stainless steel which has applications at higher temperatures are recognized the joints nickel interlayer material has the better performance compared to the copper, aluminum and silver interlayer materials [38]. He et al. [39] and Kundu et al. [40] have been extensively studied the diffusion bonding of 304 stainless steel to Ti using nickel interlayer and its effect on microstructure formation and mechanical properties. The width of discrete reaction layer changes with the increasing in processing temperature, and the weld interface between Ti and Ni interlayer contains the Ti_2Ni, TiNi and Ni_3Ti intermetallic compounds. The growth of the reaction zones therefore increases the intermetallic compounds regions and leads to faster growth of secondary phases at the weld interface considered, having close relation with the processing temperature, duration of the bonding, reacting layers growth velocity and activation energy of the growth of the reacting layers [41]. However, the friction welding process temperature and welding time is very less compared to other welding processes, hence the formation of reaction layers are excepting to be thinner and growth of the intermetallic compounds is slower. In the present investigation, dissimilar combination of titanium to stainless steel couples are joined using nickel interlayer to characterize the interfacial microstructures, reaction zones at weld interface and its effects on joint properties. It is also observed that the feasibility of the Ni interlayer as barrier between titanium and stainless to avoid the direct contact of the two substrates. The metallurgical compatibility of Ni as an insert metal between titanium and stainless, and its diffusion characteristics with Ti and Fe at the weld interface during friction welding process and formation of intermixing zones are studied.

21.1.1 Research Purpose

The present study focuses on the introducing of nickel interlayer technique for joining of titanium to stainless steel, using friction welding to evaluate the interface microstructure characteristics, formation of reaction zone and its width, and intermetallic compounds therefore their effect on joint properties. Moreover, the feasibility of using nickel interlayer for friction welds and analyses of the optimum thickness of the nickel interlayer to obtain the reliable joints and its effect on the producing of reaction zones along the joint interface are discussed.

21.1.2 Research Scope

In this study, we consider the following circumscriptions of the problem:

- The joining materials are commercially pure titanium and 304 austenitic stainless steel
- Nickel interlayer material, used as barrier between the two substrates
- The thickness of the Ni interlayer, varied to find optimum thickness
- Continuous drive friction welding method, used for this study
- Scanning electron microscope (SEM) analysis, and Electron probe micro-analyzer (EPMA)
- Fractography analysis of the tensile failure surfaces
- X-ray diffraction analysis for the tensile fracture samples.

21.2 Research Method

21.2.1 Materials and Samples Preparation

Dissimilar combinations of the materials were used in the present study of 304 austenitic stainless steel (304 SS) and commercially pure titanium (Cp–Ti) rods of 100 mm in long with the diameter of 16 mm. Chemical composition of the substrates (Table 21.1) and their tensile and hardness properties at room temperature (Table 21.2) are provided. The faying surfaces of all the samples of mating faces were machined to flattened shape and polished using as per the metallographic technique up to the size of 0.1 μm of diamond slurry polishing before welding. The surface roughness of the both the materials maintained equal with the average value of 0.1 μm.

As reported by Fuji et al. [28], the mechanical properties of the friction welded joints were affected by surface roughness of the faying surfaces of the joining dissimilar materials. It is also helps in melting surfaces of the joint interface region

Table 21.1 Chemical compositions of the elements of substrates used in this study (wt%)

304 stainless steel	Ni	Cr	Mn	C	Si	Fe
	8.37	18.15	1.64	0.08	0.38	Balance
Cp-Titanium	O	Fe	H	C	N	Ti
	0.18	0.03	0.015	0.08	0.03	Balance

Table 21.2 Mechanical properties of two substrates at room temperature

Substrates	YS (MPa)	UTS (MPa)	Elongation (%)	Hardness ($Hv_{0.5}$)
Cp-Titanium	284	435	37	169
304 stainless steel	242	536	64	286

for mutual chemical reactions. The main challenging issue of using interlayers in friction welding is how to insert the interlayer materials in between the rotating members. With facing these challenges, authors were recognized a new approach of inserting interlayers with the electrodeposition coating over the one of the substrates of stainless steel which is more compatible with the nickel interlayer. The necessary precautions were taken before electrodeposition of the interlayer with the proper cleaning of the samples with alcohol to remove contamination surfaces. Then finally the samples were thoroughly cleaned with running water to make a good adhesion with nickel interlayer using optimum process conditions of temperature and current density. The deposited samples were once again was washed with acetone solution and are dried in air to prevent it from organic contamination of grease, oil, etc.

21.2.2 Friction Welding Procedure and Process Parameters

Friction welding was carried out between titanium and electrodeposited nickel interlayer coating on the stainless steel members. Titanium rod was fixed in the stationary chuck and the stainless steel rod fixed in the rotating chuck as illustrated in Fig. 21.1a. It is the concept that from the forcible viewpoint titanium is softer than the stainless steel therefore to avoid the excessive deformation on titanium side, it was chosen to fix on stationary side. To achieve the quality joints in friction welding, using of optimum welding conditions is very important. In this study, friction welding conditions were chosen through the trial and error method for achieving the optimum welding conditions. The range of process parameters values were initially adopted from the previous research reports, which were used for direct joining of titanium to stainless steel [37]. However, these welding conditions are ineffective to form the strong joints for the friction welding of 304 stainless steel to titanium with nickel interlayer. Hence, the welding conditions are developed for interlayer welds after testing of various experiments, thus the welding conditions of

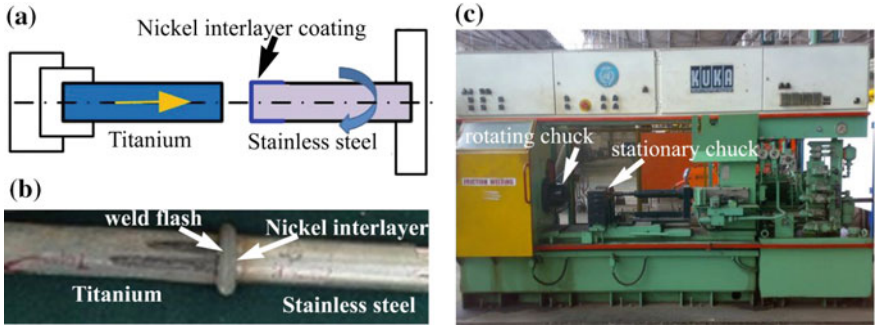

Fig. 21.1 **a** Schematic view illustrates the friction welding samples setup and welding procedure, **b** photograph of the friction welding of 304 stainless steel to titanium with Ni interlayer joint, and **c** friction welding machine setup, used in the present study

direct joints were different from the indirect joints (with nickel interlayer). For joining of indirect joints, involved in two interfaces, they are should be heated with the rubbing action of the mating surfaces. Therefore, it needs much higher amount of heat to produce the reliable joints with interlayer. The dissimilar combination with nickel interlayer welds was carried out using welding condition of heating time of 1–6 s, heating pressure of 160–180 MPa, upset time of 5 s, upset pressure of 120–180 MPa and spindle speed of 1125 rpm. For the initial trial welds suggested, the heating time and upset pressure values had strong influence on the joint properties. To avoid the reaction zones at the weld interface and consideration of joint quality, welds were produced with the minimum heat input conditions. The resulted friction welding of titanium to stainless with nickel interlayer joint is depicted in Fig. 21.1b. Weld flash was formed around the interface uniformly in circular shape, and mostly it is extruded out from the titanium rod.

21.2.3 Friction Welding Equipment

Friction welding process was carried out using continuous drive friction welding made of KUKA 15/20 kW model and a capacity of 150 kN machine, exhibited in Fig. 21.1c. In this machine, the flexible individual setting of spindle speeds can vary to values of 1125, 1500, 2250 and 3000 rpm. The rotational spindle speed was selected, based on the materials physical properties to control the heat input of the welds. It is also possible preset the desire major process conditions of heating time, heating pressure, upset time, upset pressure, brake delay time, upset delay time and feed rate could be selected as required for the joining members. In the present study, a constant welding speed was used and the other parameters are discussed in the previous section.

21.2.4 Microstructure Characterization

The diametrically cut cross-sections of the samples for microstructure characterization was prepared from the welded joints. The cross-sections of the samples were mounted and polished for examine the joint interfaces at titanium and stainless steel sides as per the metallographic procedure. To reveal the microstructure features, titanium side was etched with Kroll's reagent and the stainless steel substrate side used 10% oxalic acid solution for electrolytically etching. For the characterization analysis of the microstructure observations of the welds, we used (HITACHI S-3000H) scanning electron microscope (SEM) and optical microscope (OM). To identify the chemical composition, the reaction zones across the weld interfaces were analyzed with SEM to point the regions and energy dispersive X-ray spectroscopy (EDAX) attachment in line scan mode and Electron probe micro-analyzer (EPMA) in spot scan and line scan mode. After the tensile tests, the failure surfaces were characterized under the SEM to investigate the failure modes and fracture paths. In addition, the intermetallic phases formation across the joint interface were distinguished through Bruker D8 advance X-ray diffraction with the considerations of Cu target with the operation conditions of 40 kV, 30 mA current and 0.058 (=2θ) step size, and 20–80° scanning range was used.

21.2.5 Microhardness Tests

The friction weld joints were diametrically cut with the length of sample consisting base metal and weld interfaces. Vickers microhardness tester of Zwick 3212 was used to analyze the hardness of the joints across the interfaces and base metal. During hardness measuring, 500 g of load and 15 s test duration was selected to make indentations over the microstructures. Then the diagonal shape of the indentation measurements was calculated to plot the graphs. The hardness men surations were selected at the weld center and periphery regions of the joints.

21.2.6 Tensile Testing

Friction welded samples were machined according to the metallic tensile tests samples ASTM E8 standard [42], to assess the mechanical properties of the joints. The weld flash was removed from the joints by machining process and testing was carried out using computerized universal testing machine of TFUC-400 (India). The tensile testing of the samples was acquitted at room temperature of 26 °C and 3 mm/min cross head speed. To maintain the accuracy of the strength of the joints, four samples were tested for each of conditions and average of the four values were considered for the joint strength.

21.3 Result and Discussion

21.3.1 Macrostructure Analysis and Interlayer Joining Phenomena in Friction Welds

In friction welding process, controlling the parameters are main factors to decide the bonding between the welds, joint interface formation and the formation of weld flash. Figure 21.1b depicted the circular shaped with uniform width of material, which is extruded out at the joint interface as a weld flash. It is observed the difference in flash formation between friction welding of direct joints and joints with interlayer inter station. The friction welding conditions for interlayer addition welds should have higher values compared to the without interlayer. The required heat for the joints during welding was producing by rubbing action of the two mating surfaces [26]. After the inserting of Ni interlayer between 304 SS and Ti, the joint consists of three bodies and it needs more heat to melt and bonding the two interfaces (Ti/Ni and Ni/304 SS) over the direct joints (Ti/304 SS). The welding conditions for three bodies joining were developed with the optimization and experimental evaluation of the welds. The variation in wide range of welding conditions of heating time and upset pressure exhibited the significant effect on strength of the joints and formation of the joint interface. The macrostructures of the interface of the welds at center and periphery regions shows significant variation, and are illustrated in Fig. 21.2. The radius (r) of the rods is linked with the linear velocity (v) of the rods, angular velocity (ω) and speed rotation (n) with the relationship of $v = r\omega$, where ($\omega = n\pi$). In most of the conditions, the value of v remains zero at center part of the joint, and keeps increasing towards periphery of the joint. However, it can be varied with the change in welding conditions, therefore with the frictional rubbing action and heat generation and interface formation (as shown in Fig. 21.2a, b). The weld flash was increasing with increasing heating time and upset pressure and titanium side amount flash increased. Then, 304 SS side did not deform while the Ti deformed with increasing heating time. However, the transferred Ti at the periphery region on 304 SS side did not increase due low temperature in this region (see Fig. 21.2b).

21.3.2 Interfacial Microstructure Characterization

The microstructures of the cross-section of the joints, consisting of base metal and weld interface, are depicted in Fig. 21.3. Titanium had a very fine equiaxed grains microstructure adjacent to the weld interface in several widths, and beyond that the grain sizes coarsening observed. The formation grain refinement is due to the presence of dynamic recrystallization zone, which is affected by plastic deformation during welding. Whereas, there is evidence of grain refinement on stainless side and a small region of strain hardening has been occurred at the vicinity of the joint

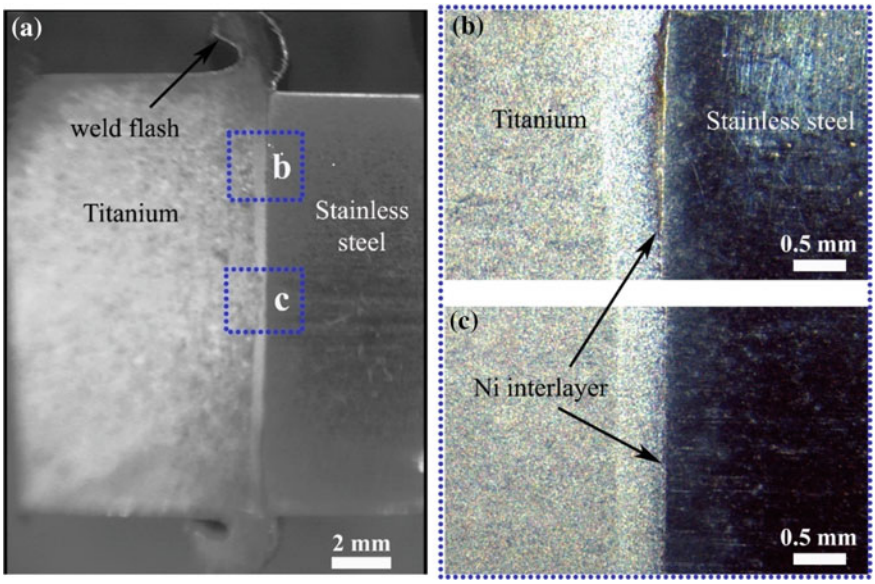

Fig. 21.2 **a** Macrograph of the cross-section of friction welded joint, enlarged views of the joint macrostructures are marked in two different locations of **b** periphery region, and **c** center region of the welds

interface. Outside this area, the matrix had the austenite phase microstructure of grains with the mechanical twinning boundary. Friction welded joint interface of the peripheral region and central region evinced the interfacial regions of titanium and nickel interaction zone. Whereas, there are no interaction zones, formed between the stainless steel and nickel interlayer. The microstructure features clearly indicated the defect-free interface formation with the uniform width of intermixing zone at the central region. On the contrary, a small number of microlevel cracks formed in intermixing zone of the titanium/nickel interlayer interface at periphery region. The difference in these two regions of microstructure formation (Fig. 21.2b, c), micrographs of which give the evidence of microstructures owing to the variation of relative velocity region, which starts from zero at central region to extreme value of 3 m/s at the peripheral region of the weld joint [43].

The dark etched regions at the joints interface in Ti side was composed of the intermixing region of Ti and Ni interlayer. To make the detailed analysis of the interfacial microstructures, the higher magnification of this region is illustrated in Fig. 21.4. The interface between Ni interlayer and stainless steel had smooth interface without any formation of reaction zones. Whereas, the Ti/Ni interlayer interface shows the formation of three distinct interfacial reaction zones in titanium side due to the solid-state reaction. The unattached microstructure adjacent to the Ni interlayer indicates as region I, the combined dark and white etched zone with the fine grains and lath like structure shows the region II, and the region III is dark

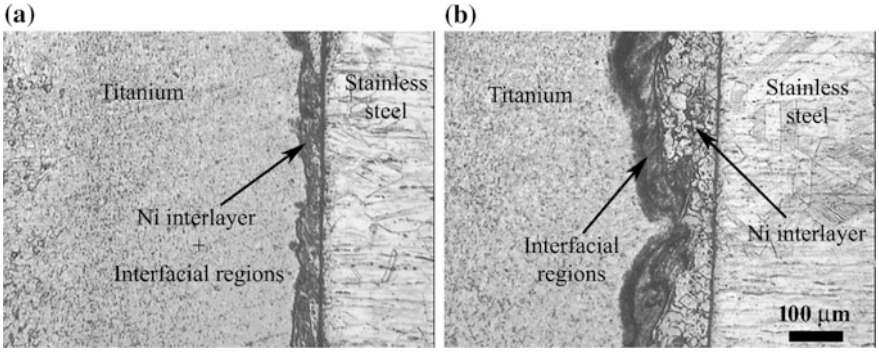

Fig. 21.3 Microstructures of the Ni interlayer cross-section of the joints, showing the remnant thickness of interlayer and width of interfacial areas at **a** central and **b** periphery regions

etched region in the titanium matrix side spread with several microns higher than other two regions. The diffusion zone at the Ti/Ni interlayer reacts faster due to the changes in Ti physical properties. Below 882 °C titanium comprises α (hcp) + β (bcc) dual phase structure, which can transforms to β-titanium, when the temperature reaches over the β-transition temperature. On the contrary, nickel and stainless steel has the same crystal structure (fcc) and the total diffusion of Fe in Ni is restricted to some extent. Whereas, the nickel atoms can easily travel deep into the Ti matrix compared to the Ti into the Ni lattice due to its more open crystallographic structure [44]. Hence, the migration of atoms occurs between Ni and Ti during upset stage of the friction welding with the influence of axial direction of pressure and heat acting on the joint interface. It also observed that the interfacial regions and its width in joint interface significantly changing with the upset pressure and heating time. As mentioned earlier in friction welding process, formation of the joint has dependent on the proper selection of the welding conditions. With reference to that, the linear dependence of the interfacial reaction zones and thickness of these zones is directly proportional to the square root of its welding heating time and deduces that the growth of interaction between two materials reaction zone is induces by diffusion mechanism [26]. The interfacial reaction zones tend to form intermetallic compounds according to the reaction binary phase diagram of Ti–Ni, the possible reactions between Ti–Ni couple mainly Ti_2Ni, $TiNi_3$ and TiNi type intermetallic compounds. However, these reaction zones are need to conform through microchemcial analysis. The similar interfacial reaction zones with thin multi-layers are also characterized by diffusion bonding couples with Ni interlayer [38, 39]. However, the thickness of these interfacial reaction regions, which are very thin in friction welding over diffusion bonding, is almost below the half of the thickness of diffusion bonding interface reaction zones. It is observed that the higher magnification of the interfacial region microstructures at periphery region revealed the presence of defects with appearing with circular shape dark etched regions.

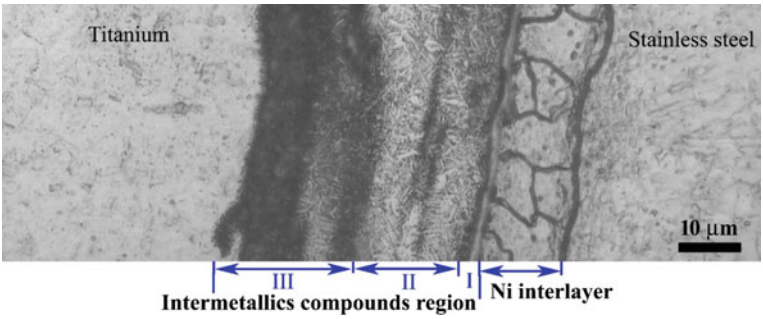

Fig. 21.4 Interfacial regions of microstructure showing the formation of intermetallic compounds between titanium matrix and Ni interlayer material

21.3.3 Microchemical Analysis and Intermetallic Compounds Formation

In order to identify the interfacial microstructure interaction, mixing zones (as shown in Fig. 21.4) are characterized by revealing the formation of intermetallic phases using EPMA line scan analysis across the joint interface. Figure 21.5 clearly illustrates the elemental concentration profiles of Ti, Fe and Ni across the weld interface and substrates. Interfacial reaction zones in Fig. 21.4 demonstrate that the concentration profiles drastically vary between these zones. It is clearly indicating that the Ni deeply migrated into Ti matrix and vice versa. The concentration of Ti at Ni interlayer regions is slightly migrated and gradually decreasing, whereas it has highest concentration at region I almost similar to base metal concentration. Suddenly, it is dropped down to 20 from 90 wt% in region II, where the Ni

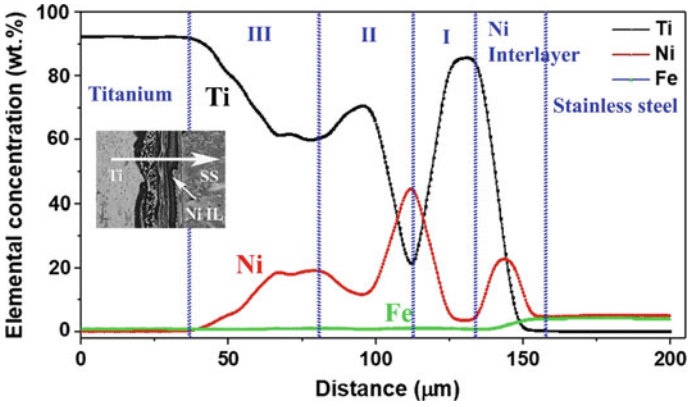

Fig. 21.5 EPMA line scan analysis across the joint interface depicting the interaction of Fe, Ti and Ni concentration profiles variance in interfacial regions and Ni interlayer

concentration drastically increases to 48 wt%. In region III again, the Ti concentration profile raises to 76 wt% and Ni dropped down to 18 wt%.

The EPMA analysis distinctly designated the migration of Ni atoms deeply into Ti lattice. The Ti lattice initially allowed the Ni atoms (region I and II) to migrate on a certain distance and then suddenly it stopped their growth in region III. By adding a β–stabilizer, the dissemination of Ni atoms can stabilizes the Ti (bcc phase) at high temperature. During cooling of the weld interface, this temperature transforms from eutectoid temperature to ambient temperature, that affirms the enhancing of the bcc phase growth, comprising of two-phase microstructure with the α-Ti and Ti_2Ni [37, 45]. Obviously, the EPMA concentration profiles on 304 SS side do not show any interaction zones formation; it is also evident from the joint interface microstructures, shown in Figs. 21.3 and 21.4.

As stated earlier, the dark circular shape regions in the intermixing zone and interfacial regions, analyzed through SEM-EDAX spot scan analysis to identify their elemental concentration, are shown in Fig. 21.6. The intermixing zone, adjacent to the titanium matrix, locates in dark region of point p2, consisting of Ni (18.65–26.84 wt%), and Ti (bal.), and is identified as Ti_2Ni intermetallic phase at the Ti–Ni binary phase diagram [46]. Whereas, the point p3 of region II is enriched with the Ni (73.87–78.24 wt%), and Ti (bal.) is responsible for the $TiNi_3$ phases [47]. The corresponding EDAX spectrum of p3 is depicted in Fig. 21.3b, which shows the intensity of the elements concentration. The EDAX point of p4 also indicates the Ti_2Ni phase, which is formed in the region I with concentration of Ni (22.35–28.05 wt%). Whereas the interfacial region close to the Ni interlayer (EDAX points of p5 as shown in Fig. 21.6a) revealed the TiNi phases with Ti (45.89–52.12 wt%) and Ni (51.41–47.88 wt%). The EDAX spot analysis points, that p1, p7 and p8 are the base substrates of Ti, Ni and 304 SS, respectively. On the other hand, the Ni/304 SS interfaces show the good metallurgical bonding between the Ni and 304 SS. Both EPMA and EDAX elemental analysis clearly represented the absence of intermixing zones and smooth transition of the profiles. It is identified that the diffusion of Ni atoms into stainless lattice has very significant quantity of Ni (16.56–24.98 wt%) and Fe (bal.) and is not enough to form any reaction phases, as evidence of microstructure formation. However, the brittle phases of Fe–Ti and Cr–Ti type intermetallic compounds are not formed [11, 46], and these are completely obviated from the joint interface. The thickness of the interfacial reaction zones can be bounded to such a low quantity using the novel technique of using interlayers. Therefore, the mechanical properties of the joints also improved expressively over the direct joints.

21.3.4 Mechanical Properties and Fractography Analysis

The hardness profiles of the joints are taken across the cross-section of the joints of base metal and weld interface. The highest hardness peak is obtained at weld interface between Ti–Ni interface, and it is caused by the formation of intermetallic

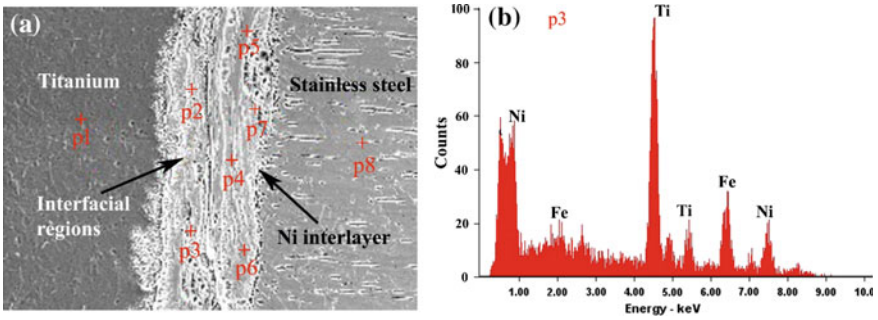

Fig. 21.6 SEM-EDAX spot scan analysis of the interfacial regions and Ni interlayer at the joint interface to distinguish the intermixing zones and interlayer: **a** SEM image with the selected points, and **b** EDAX point X-ray spectrum of the point p3

compounds. The hardness values were obtained within the formed three interfacial regions. As evident from the interfacial microstructure, hardness values also distributed according to their nature of intermetallic phases. However, there is such a high hardness as like as of Fe–Ti phases, which clearly indicated that, these hard intermetallic compounds were avoided with Ni barrier. The Ni interlayer joints tensile strength achieved higher value than the without Ni interlayer joints.

The maximum strength of direct welded joints is 228 MPa, whereas the Ni interlayer joints attains highest strength of 321 MPa, which is the highest strength of two times over the diffusion bonding joints with different interlayer materials [48, 49]. The interfacial microstructures formation has direct influence on the strength of the joints, as the heating time increases thickness of interfacial reaction zones reduces and the transferring of Ti at periphery region to 304 SS side increases, therefore the strength of the joints gradually improves. Evidently, the microstructure characterization of the fracture surfaces showed the joint failure under tensile stress was along the Ti–Ni phases at the joint interface [50], whereas the direct

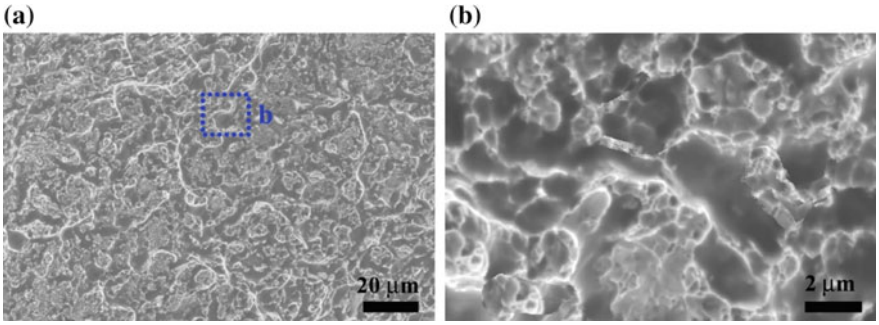

Fig. 21.7 Fracture morphologies of the joints across the Ti/Ni interface: **a** fracture surface on Ti side, **b** magnified view of the indicated region

joints fracture took place along the Fe–Ti brittle phases. The fracture surfaces of the joints belong to mixed mode of ductile and brittle failure, as exhibited in Fig. 21.7. The XRD analysis of the fracture surfaces also shows the presence of Ti_2Ni, $TiNi_3$ and TiNi phases that is in good agreement with the microstructure features and mechanical properties of the joints.

21.4 Conclusion

Friction welding of dissimilar metals such as commercially pure titanium and 304 stainless steel are joined successfully with the insertion metal technique of using nickel interlayer material. The thickness of the Ni interlayer at joint interface was studied extensively to optimize the remaining thickness for obtaining maximum tensile strength of joints and minimum width of the interfacial regions. The microstructure characterization of the Ni interlayer joints over direct joints evoked that the jointing of Ti to 304 SS with Ni interlayer will be an ascertained for fabrication of several dissimilar combinations that cannot be joined due to their hapless welding characteristics. The tensile strength of the Ni interlayer joints achieved the highest strength, compared to the case of the absence of Ni interlayer joints between Ti and 304 SS. Newly welding conditions are evolved for joining of Ti to 304 SS with Ni interlayer with the coveted strength and microstructural formation. The joint interface owing to the friction contained the several widths of three different types of interfacial regions. The interfacial regions are comprises of ductile phases such as Ti_2Ni, $TiNi_3$ and TiNi type intermetallic compounds. The elemental composition, analyzed by the techniques of EPMA and EDAX analysis, corroborated the various interfacial regions at the Ti/Ni interface. The crack initiated at Ti/Ni interface, where the intermetallic compounds were formed, and the fractures surfaces demonstrated the mixing mode of brittle and ductile failure.

References

1. J. Song, A. Kostka, M. Veehmayer, D. Raabe, Mater. Sci. Eng. A **528**, 2641 (2011)
2. M.H. Tsai, J.W. Yeh, Mater. Res. Lett. **2**, 107 (2014)
3. A. Astarita, M. Curioni, A. Squillace, X. Zhou, F. Bellucci, G.E. Thompson, K.A. Beamish, Mater. Corros. **66**, 111 (2015)
4. C.H. Muralimohan, V. Muthupandi, K. Sivaprasad, Int. J. Mater. Res. **105**, 350 (2014)
5. M.M. Cheepu, V. Muthupandi, S. Loganathan, Mater. Sci. Forum **710**, 620 (2012)
6. I. Tomashchuk, D. Grevey, P. Sallamand, Mater. Sci. Eng. A **622**, 37 (2015)
7. M. Fazel-Najafabadi, S.F. Kashani-Bozorg, A. Zarei-Hanzaki, Mater. Des. **32**, 1824 (2011)
8. C.H. Muralimohan, V. Muthupandi, Adv. Mater. Res. **794**, 351 (2013)
9. J.G. Lee, S.J. Hong, M.K. Lee, C.K. Rhee, J. Nucl. Mater. **395**, 145 (2009)
10. I. Tomashchuk, P. Sallamand, H. Andrzejewski, D. Grevey, Intermetallics **19**, 1466 (2011)
11. C.H. Muralimohan, V. Muthupandi, K. Sivaprasad, Procedia Mater. Sci. **5**, 1120 (2014)
12. S.A.A.A. Mousavi, P.F. Sartangi, Mater. Sci. Eng. A **494**, 329 (2008)

13. H.C. Chen, G. Bi, B.Y. Lee, C.K. Cheng, J. Mater. Process. Technol. **231**, 58 (2016)
14. G. Bykovskiy, I.V. Tkachenko, Avtom. Svarka **9**, 414 (1987)
15. K. Kimapong, T. Watanabe, Weld. J. **10**, 277 (2004)
16. C.H. Muralimohan, S. Haribabu, Y.H. Reddy, V. Muthupandi, K. Sivaprasad, J. Adv. Mech. Eng. Sci. **1**(1), 57 (2015)
17. H. Shi, S. Qiao, R. Qiu, X. Zhang, H. Yu, Mater. Manuf. Process. **27**, 1366 (2012)
18. C.H. Muralimohan, S. Haribabu, Y.H. Reddy, V. Muthupandi, K. Sivaprasad, Procedia Mater. Sci. **5**, 1107 (2014)
19. X. Yue, P. He, J.C. Feng, J.H. Zhang, F.Q. Zhu, Mater. Charact. **59**, 1721 (2008)
20. S. Kundu, S. Sam, S. Chatterjee, Mater. Des. **32**, 2997 (2011)
21. H.C. Dey, M. Ashfaq, A.K. Bhaduri, P.K. Rao, J. Mater. Process. Technol. **209**, 5862 (2009)
22. S.A.A.A. Mousavi, Mater. Des. **30**, 459 (2009)
23. M. Fazel-Najafabadi, S.F. Kashani-Bozorg, A. Zarei-Hanzaki, Mater. Des. **31**, 4800 (2010)
24. K.H. Rafi, J.G.D. Ram, G. Phanikumar, P.K. Rao, Mater. Des. **31**, 2375 (2010)
25. E.P. Pokataev, Y.P. Trykov, Weld. Inter. **15**, 827 (2001)
26. M. Cheepu, M. Ashfaq, V. Muthupandi, Trans. Indian Inst. Met. **70**, 2591 (2017)
27. J.W. Elmer, D.D. Kautz, in: *Fundamentals of frictionwelding*, *ASM Handbook*, vol. 6, 10th edn. (1993), p. 150
28. A. Fuji, T.H. North, K. Ameyama, M. Futamata, Mater. Sci. Technol. **8**, 219 (1992)
29. S.A.A.M. Akbari, A.K. Rahbar, Mater. Sci. Forum **580–582**, 335 (2008)
30. U.K. Mudali, B.M.A. Rao, K. Shanmugam, R. Natarajan, B. Raj, J. Nucl. Mater. **321**, 40 (2003)
31. S.W. Baek, W.B. Lee, J.M. Koo, C.Y. Lee, S.B. Jung, Mater. Sci. Forum **580–582**, 423 (2008)
32. H. Ochi, K. Ogawa, Y. Yamamoto, Y. Suga, Weld. J. **83**, 36 (2004)
33. W.-B. Lee, Y.-J. Kim, S.-B. Jung, Intermetallics **12**, 671 (2004)
34. C. Maldonado, A. Medina-Flores, L. Bejar-Gomez, A. Ruız, Rev. Mex. Fis. **55**, 130 (2009)
35. M. Cheepu, V. Muthupandi, B. Srinivas, K. Sivaprasad, in *Techno-Societal 2016,* ed. by P. M. Pawar, B. P. Ronge, R. Balasubramaniam, S. Seshabhattar, vol. 73. (Springer, Cham, 2018), p. 709
36. M. Ashfaq, K.P. Rao, H.K. Rafi, B.S. Murty, H.C. Dey, A.K. Bhaduri, Prakt. Metallogr. **48**, 188 (2011)
37. C.H. Muralimohan, M. Ashfaq, R. Ashiri, V. Muthupandi, K. Sivaprasad, Metall Mater. Trans. A. **47**, 347 (2016)
38. S. Kundu, S. Chatterjee, Mater. Sci. Technol. **23**, 1167 (2007)
39. P. He, J. Zhang, R. Zhou, X. Li, Mater. Character. **43**, 287 (1999)
40. S. Kundu, M. Ghosh, S. Chatterjee, ISIJ Int. **44**, 1882 (2004)
41. S. Kundu, S. Chatterjee, Mater. Sci. Technol. **22**, 1201 (2006)
42. *ASTM E8/E8M-16a, Standard Test Methods for Tension Testing of Metallic Materials* (ASTM International, West Conshohocken, PA, 2016)
43. R.A. Bell, J.C. Lippold, D.R. Adolphson, Weld. Res. Suppl. **11**, 325 (1984)
44. M. Ghosh, S. Chatterjee, Mater. Sci. Eng. A **358**, 152 (2003)
45. J.L. Li, L.P. Huo, F.S. Zhang, J.T. Xiong, W.Y. Li, Mater. Sci. Forum **620–622**, 399 (2009)
46. T.B. Massalski, *Binary Alloy Phase Diagrams*, 2nd edn. (ASM International, Materials Park, 1996)
47. S. Chatterjee, T.A. Abinandanan, K. Chattopadhyay, Mater. Sci. Eng. A **490**, 7 (2008)
48. S. Kundu, S. Chatterjee, J. Mater. Sci. **42**, 7906 (2007)
49. A. Elrefaey, W. Tillmann, J. Mater. Process. Technol. **209**, 2746 (2009)
50. S. Kundu, S. Sam, S. Chatterjee, Mater. Sci. Eng., A **560**, 288 (2013)

Part III
Mechanics of Advanced Materials

Chapter 22
New Mathematical and Finite Element Models with Dissipations for Multiferroic Media with Voids

Gerardo Iovane and Andrey V. Nasedkin

Abstract In this chapter, for modeling magnetoelectric or piezomagnetoelectric media and transducers, the special mathematical model, which generalize the model of the magnetoelectric material with dissipation, and the Cowin-Nunziato approach for the elastic and piezoelectric media with voids are proposed. Using these models for magnetoelectric bodies with voids or pores, the effective moduli of porous magnetoelectric composite material could be defined more precisely. In this theory the mechanical displacements, electric and magneticic potentials and porosity change function are the main unknown functions. On the base of this model, we have obtained the setting of the generalized continual formulations for magneto-electric solids with voids or porous and numerical approximation in the general and reduced statements. We have studied the mathematical properties of the eigenfrequencies and eigenvectors for magnetoelectric solids with voids for different mechanical, electric, magnetic and "porous" boundary conditions, including the contact type boundary conditions. We have established some properties of changes of the eigenfrequencies with changes of the boundary conditions and material moduli. For numerical analysis of magnetoelectric solids with voids, we have obtained the finite element approximations with symmetric quasi-definite matrices.

G. Iovane (✉)
Department of Computer Science, University of Salerno,
84084 Fisciano, SA, Italy
e-mail: giovane@unisa.it

A. V. Nasedkin
I. I. Vorovich Institute of Mathematics, Mechanics and Computer Science,
Southern Federal University, 8a, Milchakova Street, 344090 Rostov-on-Don, Russia
e-mail: nasedkin@math.sfedu.ru

I. A. Parinov et al. (eds.), *Advanced Materials*, Springer Proceedings
in Physics 207, https://doi.org/10.1007/978-3-319-78919-4_22

22.1 Introduction

New active magnetoelectric and piezoelectric composite materials exhibit very effective characteristics for many applications. For example, porous piezoelectric ceramics have low acoustic impedance, extended frequencies bandwidth, and higher efficiency than standard dense piezoceramics. In this regard, the use of porous piezocomposite materials enables to improve considerably the main parameters of ultrasonic piezoelectric devices [1–3]. Two-phase piezomagneto-electric composites including the piezomagnetic and piezoelectric phases demonstrate the capacity to mutual transformation of magnetic and electric energies, while each separate phase does not have such ability. The contemporary magnetoelectric composite materials have high effectiveness of the magnetoelectric transformation, sufficiently high temperatures of phase transitions and long technological resource [4, 5]. Mathematical and computer analyses of such composite multiferroic materials of complicated internal structure enable to simulate and predict some their important properties.

It is necessary to note also, that obtained in a result of sintering of ceramic powders the conventional dense piezoceramic material is actually a weakly porous medium, and its density differs from the density of a solid piezoceramics approximately in 2%. The application of special theories is promising for modeling materials with low porosity. A special elastic theory for materials with voids has been proposed by Nunziato and Cowin in [6, 7]. For piezoelectric materials this approaches has been develop in [8] for general theoretical aspect, in [9–12] for cases of modal, harmonic and transient problems, and in [13] for nanodimensional problems, in which the size effects were modeled by the theory of surface effects.

In this paper, we use special mathematical models and finite element approximations for investigations of various problems for magnetoelectric solids with voids and taking into account the coupled damping effects. The formulations of problems include mechanical contact boundary conditions with plane rigid punches and electric boundary conditions for open-circuited and short-circuited electrodes. The similar approaches have been investigated in [14, 15] for the corresponding piezoelectric problems, in [16–18] for elastic solids with voids without piezoelectric properties, and also in [9–13] for piezoelectric solids with voids.

This chapter is organized as follows. We present the formulation of non-stationary boundary problems for magnetoelectric solids with voids in Sect. 22.2; whereas we derive the generalized or week formulation in Sect. 22.3. In Sect. 22.4, we give the week formulation for harmonic and modal problems and we demonstrate the way for generation of the reduced formulations. The mathematical properties of the eigenfrequencies and eigenvectors are described in Sect. 22.5. Also in Sect. 22.5, we formulate some theorems about changes of the eigenfrequencies with modifications of the boundary conditions and physical properties.

Section 22.6 is devoted to the finite element techniques for numerical solving the non-stationary, harmonic and modal problems. Some concluding remarks are presented in Sect. 22.7.

22.2 Mathematical Formulation of the Problem for Magnetoelectric Solid with Voids

Let $\Omega \in \mathrm{R}^3$ be a bounded domain; $\Gamma = \partial\Omega$ is the boundary of the region Ω; $\mathbf{n}(\mathbf{x})$ is the external unit surface normal to Γ; $\mathbf{x} = \{x, y, z\} = \{x_1, x_2, x_3\}$ is the vector of spatial coordinates; t is the time. We will suppose that the volume Ω is the union of a finite number of sets, star-shaped with respect to any balls contained in them, and Γ is a Lipschitz boundary of class C^1.

We will consider magnetoelectric (piezomagnetoelectric) medium with voids or with very small porosity, where the porosity is simulated by the Cowin-Nunziato model with memory effect for the equilibrated intrinsic body forces [6–8]. Let $\mathbf{u} = \mathbf{u}(\mathbf{x}, t)$ denote the displacement vector; $\varphi = \varphi(\mathbf{x}, t)$ is the function of electric potential; $\phi = \phi(\mathbf{x}, t)$ is the function of magnetic potential; $\psi = \psi(\mathbf{x}, t)$ is the porosity change function from the reference state. By the first three functions, we determine the second-order strain tensor $\boldsymbol{\varepsilon}$, the electric fields vector $\mathbf{E}$, and the magnetic fields vector $\mathbf{H}$:

$$\boldsymbol{\varepsilon} = [\nabla\mathbf{u} + (\nabla\mathbf{u})^{\mathrm{T}}]/2, \quad \mathbf{E} = -\nabla\varphi, \quad \mathbf{H} = -\nabla\phi, \tag{22.1}$$

In the framework of the linear theory, we accept the following constitutive equations for magnetoelectric solids with voids:

$$\boldsymbol{\sigma} = \mathbf{c} : (\boldsymbol{\varepsilon} + \beta_d\dot{\boldsymbol{\varepsilon}}) - \mathbf{e}^{\mathbf{T}} \cdot \mathbf{E} - \mathbf{h}^{\mathbf{T}} \cdot \mathbf{H} + \mathbf{P}\psi, \tag{22.2}$$

$$\mathbf{D} + \varsigma_d\dot{\mathbf{D}} = \mathbf{e} : (\boldsymbol{\varepsilon} + \varsigma_d\dot{\boldsymbol{\varepsilon}}) + \boldsymbol{\kappa} \cdot \mathbf{E} + \boldsymbol{\alpha} \cdot \mathbf{H} - \mathbf{g}\psi - \mathbf{G} \cdot \nabla\psi, \tag{22.3}$$

$$\mathbf{B} + \gamma_d\dot{\mathbf{B}} = \mathbf{h} : (\boldsymbol{\varepsilon} + \gamma_d\dot{\boldsymbol{\varepsilon}}) + \boldsymbol{\alpha}^{\mathrm{T}} \cdot \mathbf{E} + \boldsymbol{\mu} \cdot \mathbf{H} - \mathbf{q}\psi - \mathbf{Q} \cdot \nabla\psi, \tag{22.4}$$

$$\mathbf{p} = \mathbf{G} \cdot \mathbf{E} + \mathbf{Q} \cdot \mathbf{H} + \mathbf{A} \cdot \nabla\psi, \quad g = -\mathbf{P} \cdot (\boldsymbol{\varepsilon} + \lambda_d\dot{\boldsymbol{\varepsilon}}) - \mathbf{g} \cdot \mathbf{E} - \mathbf{q} \cdot \mathbf{H} - \xi\psi, \tag{22.5}$$

where $\boldsymbol{\sigma}$ is the stress tensor of the second order; $\mathbf{D}$ is the dielectric displacement vector or the electric flux density vector; $\mathbf{B}$ is the magnetic flux density vector; $\mathbf{p}$ is the equilibrated stress vector; g is the intrinsic equilibrated body force; $\mathbf{c} = \mathbf{c}^{E,H,\psi}$ is the tensor of elastic stiffness moduli of the fourth order; $\mathbf{e} = \mathbf{e}^{H,\psi}$ is the tensor of piezoelectric moduli of the third order; $\mathbf{h} = \mathbf{h}^{E,\psi}$ is the tensor of magnetostriction moduli of the third order; $\boldsymbol{\kappa} = \boldsymbol{\kappa}^{S,H,\psi} = \boldsymbol{\varepsilon}^{S,H,\psi}$ is the tensor of dielectric permittivity moduli of the second order; $\boldsymbol{\alpha} = \boldsymbol{\alpha}^{S,\psi}$ is the tensor of magnetoelectric coupling coefficients of the second order; $\boldsymbol{\mu} = \boldsymbol{\mu}^{S,E,\psi}$ is the tensor of magnetic permeability

moduli of the second order; $\mathbf{P} = \mathbf{P}^{E,H}$, $\mathbf{G} = \mathbf{G}^{S,H}$, $\mathbf{Q} = \mathbf{Q}^{S,E}$, $\mathbf{A} = \mathbf{A}^{S,E,H}$, $\mathbf{g} = \mathbf{g}^{S,H}$, $\mathbf{q} = \mathbf{q}^{S,E}$ and $\xi = \xi^{S,E,H}$ are the constitutive tensor, vector and scalar values characterizing the porous properties; $\beta_d \geq 0$, $\zeta_d \geq 0$, $\gamma_d \geq 0$ and $\lambda_d \geq 0$ are the damping factors; $(\ldots)^{\mathrm{T}}$ is the operation of transposition, and $(\ldots) : (\ldots)$ is the double inner product operation. The upper indexes indicate at which constant fields the corresponding moduli were calculated. Thus, the upper index S denotes the strain, E and H denote the electric and magnetic fields, ψ denotes the porosity change function.

In the case of the transient problem for a magnetoelectric solid with voids, structural, electric, magnetic and porosity-dependent damping and without porous inertia effect, we have the system that includes the momentum equation, the quasi-electrostatic equation, the quasi-magnetostatic equation and the equation for porosity change

$$\nabla \cdot \boldsymbol{\sigma} + \rho \mathbf{f} = \rho(\ddot{\mathbf{u}} + \alpha_d \dot{\mathbf{u}}), \quad \nabla \cdot \mathbf{D} = \sigma_\Omega, \quad \nabla \cdot \mathbf{B} = 0, \tag{22.6}$$

$$\nabla \cdot \mathbf{p} + g + \rho\, l + \lambda_d \rho\, \dot{l} = 0. \tag{22.7}$$

Here, ρ is the density of the material; $\mathbf{f}$ is the mass forces vector; α_d is the one more non-negative damping factor; σ_Ω is the bulk density of electric charges; l is the extrinsic equilibrated body force.

In model (22.1)–(22.7) for the magnetoelectric solid with voids, we accept a generalized Rayleigh damping similarly to [11–16], which is appropriate for various applications.

For piezoelectric material with voids ($\mathbf{h} = 0$, $\boldsymbol{\alpha} = 0$, $\mathbf{q} = 0$, $\mathbf{Q} = 0$), equation system (22.1)–(22.7) is reduced to the form from [12, 19], and for elastic material with voids (when in additional to the previously conditions, $\mathbf{e} = 0$, $\mathbf{g} = 0$, $\mathbf{G} = 0$), system (22.1)–(22.7) is reduced to the form from [16–18]. When in (22.3), (22.4) $\zeta_d = 0$, $\gamma_d = 0$, then for the magnetoelectric media without voids ($\mathbf{P} = 0$, $\mathbf{g} = 0$, $\mathbf{G} = 0$, $\mathbf{q} = 0$, $\mathbf{Q} = 0$), we have usual model with the mechanical attenuation, which is used in many well-known finite element packages (used for piezoelectric and elastic media). It is true that, when $\zeta_d = 0$, $\gamma_d = 0$, by virtue of the coupled effect between mechanical, electric and magnetic fields, the structural damping will be also extended into the electric and magnetic fields. More complex model (22.2)–(22.5) extends the Kelvin's model to the case of coupled electric fields, magnetic fields and porosity change fields for magnetoelectric solids with voids.

We assume that the density $\rho(\mathbf{x})$ is the piecewise-continuous function, and $\exists\, \rho_0 > 0$: $\rho(\mathbf{x}) \geq \rho_0$. The other moduli in (22.2)–(22.5) are piecewise-smooth together with its first derivatives and have the usual symmetry properties: $c_{ijkl} = c_{jikl} = c_{ijlk} = c_{klij}$, $e_{ikl} = e_{ilk}$, $h_{ikl} = h_{ilk}$, $\kappa_{kl} = \kappa_{lk}$, $\mu_{kl} = \mu_{lk}$, $\alpha_{kl} = \alpha_{lk}$, $A_{ik} = A_{ki}$, $P_{ik} = P_{ki}$, $G_{ik} = G_{ki}$, $Q_{ik} = Q_{ki}$. Moreover, for the positive definiteness of the potential energy for the magnetoelectric material with voids the following inequality must be hold for $\forall\, \boldsymbol{\varepsilon}^{\mathrm{T}} = \boldsymbol{\varepsilon}$, $\mathbf{E}$, $\mathbf{H}$, ψ, $\mathbf{b}$:

$$\boldsymbol{\varepsilon}^{\mathrm{T}} : \mathbf{c} : \boldsymbol{\varepsilon} + \xi\psi^2 + 2\mathbf{P}^{\mathbf{T}} : \boldsymbol{\varepsilon}\,\psi + \mathbf{b}^{\mathbf{T}} \cdot \mathbf{A} \cdot \mathbf{b} + \mathbf{E}^{\mathbf{T}} \cdot \boldsymbol{\kappa} \cdot \mathbf{E} + \mathbf{H}^{\mathbf{T}} \cdot \boldsymbol{\mu} \cdot \mathbf{H} + 2\mathbf{E}^{\mathbf{T}} \cdot \boldsymbol{\alpha} \cdot \mathbf{H} \geq W_0(\boldsymbol{\varepsilon}^{\mathrm{T}} : \boldsymbol{\varepsilon} + \psi^2 + \mathbf{b}^{\mathbf{T}} \cdot \mathbf{b} + \mathbf{E}^{\mathbf{T}} \cdot \mathbf{E} + \mathbf{H}^{\mathbf{T}} \cdot \mathbf{H}) \tag{22.8}$$

where $W_0 > 0$ is a positive constant.

The mechanical, electric, magnetic, "porous" boundary conditions and the initial conditions should be attached to the system (22.6), (22.7) with (22.1)–(22.5).

To specify the mechanical boundary conditions, we suppose that the boundary Γ is subdivided into two parts Γ_σ and Γ_u ($\Gamma = \Gamma_\sigma \cup \Gamma_u$). We suggest that on the boundary Γ_σ the mechanical surface load vector $\mathbf{p} = \mathbf{p}(\mathbf{x}, t)$ is defined, i.e.

$$\mathbf{n} \cdot \boldsymbol{\sigma} = \mathbf{p}; \quad \mathbf{x} \in \Gamma_\sigma. \tag{22.9}$$

On Γ_u we will consider the non-standard contact boundary conditions with plane rigid stamps (punches) [9, 12, 14, 17]. Suppose that $\Gamma_u = \cup_i \Gamma_{ui}$; $i = 0, 1, 2, \ldots, L$; $\Gamma_{u0} \neq \wedge$, Γ_{ui} do not border each other; among Γ_{ui} there are l number of plane areas ($i \in J_p = \{1, 2, \ldots, l\}$) in friction-free contact with massive rigid stamps and $L + 1 - l$ number of areas with prescribed displacements $\mathbf{u} = \mathbf{u}_\Gamma$ ($i \in J_r = \{0, l+1, l+2, \ldots, L\}$). We connect with area Γ_{ui}, $i \in J_p$ the local coordinate system $O_\xi^{(i)} \xi_1^{(i)} \xi_2^{(i)} \xi_3^{(i)}$ so that the axis $\xi_3^{(i)}$ has the direction of external surface normal $\mathbf{n}$ at the point $O_\xi^{(i)}$; and the axes $\xi_1^{(i)}$ and $\xi_2^{(i)}$ coincide with the principal inertia axes for the stamp with number i. In accordance with the above, we assume the following boundary conditions on Γ_{ui}:

$$\mathbf{n} \cdot \mathbf{u} = \sum_{k=0}^{2} \alpha_{ik}^u \xi_k^{(i)}, \quad (\xi_0^{(i)} = 1), \quad \mathbf{x} \in \Gamma_{ui}, \quad i \in J_p, \tag{22.10}$$

$$\int_{\Gamma_{ui}} \xi_p^{(i)} \mathbf{n} \cdot \boldsymbol{\sigma} \cdot \mathbf{n}\, d\Gamma = (-\ddot{\alpha}_{ip}^u - \alpha_d \dot{\alpha}_{ip}^u) M_p^{(i)} + P_{ip}, \quad p = 0, 1, 2, \ \ i \in J_p, \tag{22.11}$$

$$\mathbf{n} \cdot \boldsymbol{\sigma} - (\mathbf{n} \cdot \boldsymbol{\sigma} \cdot \mathbf{n})\,\mathbf{n} = 0, \quad \mathbf{x} \in \Gamma_{ui}, \ \ i \in J_p, \tag{22.12}$$

$$\mathbf{u} = \mathbf{u}_{\Gamma i}, \mathbf{x} \in \Gamma_{ui}, \Gamma_{u0} \neq \wedge, \ \ i \in J_r, \tag{22.13}$$

where in (22.10), (22.11) the summation by repeating indexes i and p is absent; α_{i0}^u is the displacement of the stamp with number i along normal; $\alpha_{i1}^u = -\theta_2^{(i)}$, $\alpha_{i2}^u = \theta_1^{(i)}$ are the stamp rotation angles with respect to axes $\xi_2^{(i)}$ and $\xi_1^{(i)}$, respectively; $M_0^{(i)}$ is the stamp mass; $M_1^{(i)} = J_{\xi_2^{(i)} \xi_2^{(i)}}$, $M_2^{(i)} = J_{\xi_1^{(i)} \xi_1^{(i)}}$ are the inertia moments of stamp; P_{i0} is the force and P_{i1}, P_{i2} are the moments, acting on the stamp with number i; $\mathbf{u}_{\Gamma i} = \mathbf{u}_{\Gamma i}(\mathbf{x}, t)$ are the determined displacement functions on Γ_{ui}, $i \in J_r$.

To formulate the electric boundary conditions we assume that Γ is also subdivided into two subsets Γ_D and Γ_φ ($\Gamma = \Gamma_D \cup \Gamma_\varphi$).

The surface Γ_D does not contain electrodes, and on Γ_D the surface density of electric charge σ_D is given as

$$\mathbf{n} \cdot \mathbf{D} = -\sigma_D; \quad \mathbf{x} \in \Gamma_D. \tag{22.14}$$

The part Γ_φ itself is subdivided into $M+1$ sub-domains $\Gamma_{\varphi j}$ $(j \in J_{eo} \cup J_{es})$, $J_{eo} = \{1, 2, \ldots, m\}$, $J_{es} = \{0\} \cup \{m+1, m+2, \ldots, M\}$, $\Gamma_{\varphi 0} \neq \wedge$, which are not border each other, and which are coated by infinitely thin electrodes. On these surfaces we define the following boundary conditions:

$$\varphi = \Phi_j(t); \quad \mathbf{x} \in \Gamma_{\varphi j}, \ j \in J_{eo}, \tag{22.15}$$

$$\int\limits_{\Gamma_{\varphi j}} \mathbf{n} \cdot \mathbf{D}\, d\Gamma = -Q_j, \dot{Q}_j = \pm I_j, \ j \in J_{eo}, \tag{22.16}$$

$$\varphi = V_j(t), \mathbf{x} \in \Gamma_{\varphi j}, \ \Gamma_{\varphi 0} \neq \wedge, \ j \in J_{es}, \tag{22.17}$$

where the values Φ_j, Q_j, V_j depend only on time t; Q_j is the cumulative electric charge on electrode $\Gamma_{\varphi j}$, and the signs "$\pm$" in (22.17) depend on the selected direction of the current I_j in the external electric circuit.

By (22.15), (22.16) on m electrode surfaces the electric potentials Φ_j are initially unknown, but the total electric charges Q_j or currents I_j on each electrode are defined. On the remaining $M+1-m$ electrode surfaces the electrical voltages V_j are known.

It is important to emphasize that Φ_j in (22.15) and V_j in (22.17) are independent from the space coordinates $\mathbf{x}$, and therefore, the electrodes are equipotential surfaces. Note also, that the integral relation (22.16) is similar to the contact mechanical condition for massless rigid stamps $\left(M_p^{(i)} = 0\right)$.

For homogeneous boundary conditions on the electrodes $\Gamma_{\varphi j}$ with $Q_j = 0$ in (22.16) and with $V_j = 0$ in (22.17), these surfaces are called the open-circuited electrodes and the short-circuited electrodes, respectively.

Further, on the full surface Γ, we assume homogeneous magnetic boundary condition:

$$\mathbf{n} \cdot \mathbf{B} = 0, \quad \mathbf{x} \in \Gamma. \tag{22.18}$$

Since the magnetic potential is determined within a constant, then we can define its value for an arbitrary point $\mathbf{x}_0 \in \Gamma$ of the boundary, for example:

$$\phi(\mathbf{x}_0) = 0. \tag{22.19}$$

For the "porous" boundary condition we suppose that the surface Γ is also divided into two regions: $\Gamma_{\psi 0}$ and $\Gamma_{\psi n}$ $(\Gamma = \Gamma_{\psi 0} \cup \Gamma_{\psi n})$. On the part $\Gamma_{\psi 0}$ we take the homogeneous Dirichlet condition:

$$\psi = 0; \quad \mathbf{x} \in \Gamma_{\psi 0}, \tag{22.20}$$

and on $\Gamma_{\psi n}$ we assume the homogeneous Neumann condition:

$$\mathbf{n} \cdot \mathbf{p} = 0; \quad \mathbf{x} \in \Gamma_{\psi n}, \tag{22.21}$$

where the boundary condition (22.21) in real situations is usually absent.

We also suppose that the domains Γ_σ, Γ_{ui}, Γ_D, $\Gamma_{\varphi j}$, $\Gamma_{\psi 0}$ and $\Gamma_{\psi n}$ have Lipshitz boundaries of class C^1.

For non-stationary problems we assume also the initial conditions in the form:

$$\mathbf{u}(\mathbf{x}, +0) = \mathbf{u}_*(\mathbf{x}), \dot{\mathbf{u}}(\mathbf{x}, +0) = \mathbf{r}_*(\mathbf{x}); \mathbf{x} \in \Omega, \tag{22.22}$$

where $\mathbf{u}_*$ is the vector of initial displacement and $\mathbf{r}_*$ is the vector of initial velocity of the solid's points $\mathbf{x}$.

Formulae (22.1)–(22.22) represent a statement of the linear boundary problems with the generalized Rayleigh damping for magnetoelectric solid with voids.

22.3 Week Problem Formulations

Let us transfer from the statement (22.1)–(22.22) of the transient problems for magnetoelectric solids to their weak (generalized) formulations.

At the beginning we define on Ω the function spaces for the fields $\mathbf{u}$, φ, ϕ and ψ. Let H^0_ρ be the space of vector-functions $\mathbf{u} \in \mathrm{L}_2$ in which the scalar product is defined as $(\mathbf{v}, \mathbf{u})_{\mathrm{H}^0_\rho} = \int_\Omega \rho\, \mathbf{v}^{\mathrm{T}} \cdot \mathbf{u}\, d\Omega$, where here and below the transpose operation $(\ldots)^{\mathrm{T}}$ is complemented by the complex conjugation operation for the steady-state oscillation problems and for modal problems discussed in further.

For the vector-functions $\mathbf{u} \in \mathrm{C}^1$ satisfying homogenous boundary conditions (22.13) on Γ_{ui}, $i \in J_r$, and (22.10) for arbitrary α^u_{ik} on Γ_{ui}, $i \in J_p$, we define the scalar product: $(\mathbf{v}, \mathbf{u})_{\mathrm{H}^1_{ul}} = \int_\Omega (\nabla \mathbf{v})^{\mathrm{T}} : (\nabla \mathbf{u})\, d\Omega$. The closure of set of these vector-functions in the norm generated by the scalar product $(\mathbf{v}, \mathbf{u})_{\mathrm{H}^1_{ul}}$ will be designated by H^1_{ul}, where the index l indicates the number of rigid massive punches, described by the boundary conditions (22.10)–(22.12).

For functions $\varphi \in \mathrm{C}^1$ satisfying boundary conditions (22.15) for arbitrary Φ_j on $\Gamma_{\varphi j}$, $j \in J_{eo}$, and homogenous boundary conditions (22.17) on $\Gamma_{\varphi j}$, $j \in J_{es}$, we define the scalar product: $(\chi, \varphi)_{\mathrm{H}^1_{\varphi m}} = (\chi, \varphi)_{\mathrm{H}^1_s}$, where $(\chi, \varphi)_{\mathrm{H}^1_s} = \int_\Omega (\nabla \chi)^{\mathrm{T}} \cdot \nabla \varphi\, d\Omega$. The closure of set of these functions in the norm, generated by the scalar product $(\chi, \varphi)_{\mathrm{H}^1_{\varphi m}}$, will be designated by $\mathrm{H}^1_{\varphi m}$, where the index m indicates the number of boundary conditions (22.15).

We define the scalar products on the set of field functions $\phi \in \mathrm{C}^1$, $\psi \in \mathrm{C}^1$, satisfying (22.19), (22.20), respectively: $(\eta, \phi)_{\mathrm{H}^1_\phi} = (\eta, \phi)_{\mathrm{H}^1_s}$, $(\varsigma, \psi)_{\mathrm{H}^1_\phi} = (\varsigma, \psi)_{\mathrm{H}^1_s}$. The closures of sets of these functions in the norms, generated by the introduced scalar products, will be designated by H^1_ϕ, H^1_ψ, respectively.

Finally we introduce the function spaces Q_{ul}, $\mathrm{Q}_{\varphi m}$, Q_ϕ and Q_ψ as $\mathrm{Q}_{ul} = \mathrm{L}_2(S_t;\ \mathrm{H}^1_{ul})$, $\mathrm{Q}_{\varphi m} = \mathrm{L}_2(S_t;\ \mathrm{H}^1_{\varphi m})$, $\mathrm{Q}_\phi = \mathrm{L}_2(S_t;\ \mathrm{H}^1_\phi)$, $\mathrm{Q}_\psi = \mathrm{L}_2(S_t;\ \mathrm{H}^1_\psi)$, where $S_t = [0, T]$, and for Banach space B with norm $\|.\|_B$, the function space $\mathrm{L}_2(S_t; B)$ is the space of (class) functions $t \to f(t)$, $t \in S_t$, $f(t) \in B$, with $\int_0^T \|f(t)\|^2_B\, dt = \|f\|^2_{\mathrm{L}_2(S_t;B)} < \infty$.

We will present the functions $\mathbf{u}$ and φ in the transient problem (22.1)–(22.20) in the form:

$$\mathbf{u} = \mathbf{u}_0 + \mathbf{u}_b, \quad \varphi = \varphi_0 + \varphi_b, \tag{22.23}$$

where $\mathbf{u}_0$, φ_0 satisfy homogeneous mechanical and electric boundary conditions and $\mathbf{u}_b$, φ_b satisfy corresponding heterogeneous boundary conditions, i.e.

$$n_j u_{0j} = \sum_{k=0}^{2} \alpha^{u0}_{ik}\, \xi^{(i)}_k,\ n_j u_{bj} = \sum_{k=0}^{2} \alpha^{ub}_{ik}\, \xi^{(i)}_k,\ \ \alpha^{u0}_{ik} + \alpha^{ub}_{ik} = \alpha^{u}_{ik},\ \ \mathbf{x} \in \Gamma_{ui},\ \ i \in J_p, \tag{22.24}$$

$$u_{0j} = 0,\ u_{bj} = u_{\Gamma ij},\ \ \mathbf{x} \in \Gamma_{ui},\ \ \Gamma_{u0} \neq \wedge,\ \ i \in J_r, \tag{22.25}$$

$$\varphi_0 = \Phi_{0j},\ \varphi_b = \Phi_{bj},\ \ \Phi_{0j} + \Phi_{bj} = \Phi_j,\ \ \mathbf{x} \in \Gamma_{\varphi j},\ \ j \in J_{eo}, \tag{22.26}$$

$$\varphi_0 = 0,\ \varphi_b = V_j,\ \ \mathbf{x} \in \Gamma_{\varphi j},\ \ \Gamma_{\varphi 0} \neq \wedge,\ \ j \in J_{es}, \tag{22.27}$$

and therefore,

$$\mathbf{u}_0 \in \mathrm{Q}_{ul},\ \varphi_0 \in \mathrm{Q}_{\varphi m},\ \ \varphi_b \in \mathrm{Q}_{\varphi M}. \tag{22.28}$$

To transfer to the generalized or weak solution we scalar multiply the equation of motion (22.6) by some vector-function $\mathbf{v}(\mathbf{x}) \in \mathrm{H}^1_{ul}$, the second equation (22.6) by some function $\chi(\mathbf{x}) \in \mathrm{H}^1_{\varphi m}$, the last equation (22.6) by some function $\eta(\mathbf{x}) \in \mathrm{H}^1_\phi$, and (22.7) by some function $\varsigma(\mathbf{x}) \in \mathrm{H}^1_\psi$. By integrating the obtained equalities over volume Ω and using integration by parts, granting the formulated boundary conditions, we get the generalized or weak setting of transient problem for magnetoelectric solid with voids, using the introduced functional spaces.

Definition The quadruple of functions $\{\mathbf{u} = \mathbf{u}_0 + \mathbf{u}_b, \varphi = \varphi_0 + \varphi, \phi, \psi\}$, where $\mathbf{u}_0$, $\mathbf{u}_b$, φ_0, φ_b satisfy (22.24)–(22.28), $\mathbf{u}_0 \in \mathrm{Q}_{ul}$, $\varphi_0 \in \mathrm{Q}_{\varphi m}$, $\phi \in \mathrm{Q}_\phi$, $\psi \in \mathrm{Q}_\psi$, are the generalized or weak solution of transient problem for the magnetoelectric solid with voids, if the following integral relations are satisfied:

$$\widetilde{\rho}(\mathbf{v},\ddot{\mathbf{u}}_0)+d(\mathbf{v},\dot{\mathbf{u}}_0)+c(\mathbf{v},\mathbf{u}_0)+e(\varphi_0,\mathbf{v})+h(\phi,\mathbf{v})+p(\mathbf{v},\psi)=L_u(\mathbf{v}), \quad (22.29)$$

$$-e(\chi,\mathbf{u}_0+\zeta_d\dot{\mathbf{u}}_0)+\kappa(\chi,\varphi_0)+\alpha(\chi,\phi)+g(\chi,\psi)=L_\varphi(\chi)+\zeta_d\frac{\partial}{\partial t}\widetilde{L}_\phi(\chi), \quad (22.30)$$

$$-h(\eta,\mathbf{u}_0+\gamma_d\dot{\mathbf{u}}_0)+\alpha(\varphi_0,\eta)+\mu(\eta,\phi)+q(\eta,\psi)=L_\phi(\eta)+\gamma_d\frac{\partial}{\partial t}\widetilde{L}_\phi(\eta), \quad (22.31)$$

$$p(\mathbf{u}_0+\lambda_d\dot{\mathbf{u}}_0,\varsigma)-g(\varphi_0,\varsigma)-q(\phi,\varsigma)+a(\varsigma,\psi)=L_\psi(\varsigma)+\lambda_d\frac{\partial}{\partial t}\widetilde{L}_\psi(\varsigma), \quad (22.32)$$

for $\forall t\in S_t$; $\mathbf{v}\in \mathrm{H}^1_{ul}$, $\chi\in \mathrm{H}^1_{\varphi m}$, $\eta\in \mathrm{H}^1_{\phi}$, $\varsigma\in \mathrm{H}^1_{\psi}$, and the initial conditions (22.20) are also hold.

Here we introduce the bilinear forms and linear functionals:

$$\widetilde{\rho}(\mathbf{v},\mathbf{u})=(\mathbf{v},\mathbf{u})_{H^0_\rho}+\sum_{i=1}^{l}\sum_{k=0}^{2}\alpha^v_{ik}\alpha^u_{ik}M^{(i)}_k, \quad (22.33)$$

$$c(\mathbf{v},\mathbf{u})=\int_\Omega \boldsymbol{\varepsilon}^{\mathrm{T}}(\mathbf{v}):\mathbf{c}:\boldsymbol{\varepsilon}(\mathbf{u})\,d\,\Omega, \quad e(\varphi,\mathbf{v})=-\int_\Omega \mathbf{E}^{\mathrm{T}}(\varphi)\cdot\mathbf{e}:\boldsymbol{\varepsilon}(\mathbf{v})\,d\,\Omega, \quad (22.34)$$

$$h(\phi,\mathbf{v})=-\int_\Omega \mathbf{H}^{\mathrm{T}}(\phi)\cdot\mathbf{h}:\boldsymbol{\varepsilon}(\mathbf{v})\,d\,\Omega, \quad p(\mathbf{v},\psi)=-\int_\Omega \boldsymbol{\varepsilon}^{\mathrm{T}}(\mathbf{v}):\mathbf{P}\psi\,d\,\Omega, \quad (22.35)$$

$$\kappa(\chi,\varphi)=\int_\Omega \mathbf{E}^{\mathrm{T}}(\chi)\cdot\boldsymbol{\kappa}\cdot\mathbf{E}(\varphi)\,d\,\Omega, \quad \alpha(\chi,\phi)=\int_\Omega \mathbf{E}^{\mathrm{T}}(\chi)\cdot\boldsymbol{\alpha}\cdot\mathbf{H}(\phi)\,d\,\Omega, \quad (22.36)$$

$$\begin{aligned} g(\chi,\psi)&=\int_\Omega(\nabla\chi^{\mathrm{T}}\cdot\mathbf{G}\cdot\nabla\psi+\nabla\chi^{\mathrm{T}}\cdot\mathbf{g}\phi)\,d\,\Omega,\\ q(\eta,\psi)&=\int_\Omega(\nabla\eta^{\mathrm{T}}\cdot\mathbf{Q}\cdot\nabla\psi+\nabla\eta^{\mathrm{T}}\cdot\mathbf{q}\phi)\,d\,\Omega, \end{aligned} \quad (22.37)$$

$$d(\mathbf{v},\mathbf{u})=\alpha_d\widetilde{\rho}(\mathbf{v},\mathbf{u})+\beta_d c(\mathbf{v},\mathbf{u}), \quad a(\varsigma,\psi)=\int_\Omega(\nabla\varsigma^{\mathrm{T}}\cdot\mathbf{A}\cdot\nabla\psi+\xi\eta\phi)\,d\,\Omega, \quad (22.38)$$

$$L_u(\mathbf{v})=L_{fp}(\mathbf{v})-\widetilde{\rho}(\mathbf{v},\mathbf{u}_b)-d(\mathbf{v},\mathbf{u}_b)-c(\mathbf{v},\mathbf{u}_b)-e(\varphi_b,\mathbf{v}), \quad (22.39)$$

$$L_{fp}(\mathbf{v}) = \int\limits_{\Omega} v_i f_i \, d\Omega + \int\limits_{\Gamma_\sigma} v_i p_i \, d\Gamma + \sum_{i=1}^{l} \sum_{k=0}^{2} \alpha_{ik}^{v} P_{ik}, \tag{22.40}$$

$$L_{\varphi}(\chi) = \widetilde{L}_{\varphi}(\chi) + e(\chi, \mathbf{u}_b + \zeta_d \dot{\mathbf{u}}_b) - \kappa(\chi, \varphi_b), \tag{22.41}$$

$$\widetilde{L}_{\varphi}(\chi) = \int\limits_{\Omega} \chi \sigma_{\Omega} \, d\Omega + \int\limits_{\Gamma_D} \chi \sigma_D \, d\Gamma + \sum_{j=1}^{m} X_j Q_j, \tag{22.42}$$

$$L_{\phi}(\eta) = h(\eta, \mathbf{u}_b + \zeta_d \dot{\mathbf{u}}_b) - \alpha(\varphi_b, \eta), \tag{22.43}$$

$$L_{\psi}(\varsigma) = \widetilde{L}_{\phi}(\varsigma) - p(\mathbf{u}_b + \lambda_d \dot{\mathbf{u}}_b, \varsigma) + g(\varphi_b, \varsigma), \quad \widetilde{L}_{\phi}(\varsigma) = \int\limits_{\Omega} \varsigma \rho l \, d\Omega, \tag{22.44}$$

where α_{ik}^{v} are the values from (22.10) for vector-function $\mathbf{v} \in \mathrm{H}_{ul}^{1}$ and X_j are the values from (22.15) for function $\chi \in \mathrm{H}_{\varphi m}^{1}$.

From this weak formulation of transient problem, it is easy to obtain the weak setting of static problem, eigenvalue (modal) problem and steady-state oscillation (harmonic) problem for magnetoelectric body with voids.

22.4 Steady-State Oscillation and Modal Problems

When all external loads, specifying pressures, forces, charges, displacements and potentials, change over time according to the same steady-state oscillation law, $\exp[j\omega t]$, we can find the solution in the identical forms: $\mathbf{u} = \widetilde{\mathbf{u}}(\mathbf{x}) \exp[j\omega t]$, $\varphi = \widetilde{\varphi}(\mathbf{x}) \exp[j\omega t]$, $\phi = \widetilde{\phi}(\mathbf{x}) \exp[j\omega t]$, $\psi = \widetilde{\psi}(\mathbf{x}) \exp[j\omega t]$. Then, as it is obvious from (22.29) to (22.32), we have the system of integral relations for the amplitude functions $\widetilde{\mathbf{u}}$, $\widetilde{\varphi}$, $\widetilde{\phi}$ and $\widetilde{\psi}$:

$$-\omega^2 \widetilde{\rho}(\mathbf{v}, \mathbf{u}_0) + j\omega d(\mathbf{v}, \mathbf{u}_0) + c(\mathbf{v}, \mathbf{u}_0) + e(\varphi_0, \mathbf{v}) + h(\phi, \mathbf{v}) + p(\mathbf{v}, \psi) = L_u(\mathbf{v}) \tag{22.45}$$

$$-(1 + j\omega \zeta_d) e(\chi, \mathbf{u}_0) + \kappa(\chi, \varphi_0) + \alpha(\chi, \phi) + g(\chi, \psi) = L_{\varphi}(\chi) + j\omega \zeta_d \widetilde{L}_{\varphi}(\chi), \tag{22.46}$$

$$-(1 + j\omega \gamma_d) h(\eta, \mathbf{u}_0) + \alpha(\varphi_0, \eta) + \mu(\eta, \phi) + q(\eta, \psi) = L_{\phi}(\eta) + j\omega \gamma_d \widetilde{L}_{\phi}(\eta), \tag{22.47}$$

$$(1 + j\omega \lambda_d) p(\mathbf{u}_0, \varsigma) - g(\varphi_0, \varsigma) - q(\phi, \varsigma) + a(\varsigma, \psi) = L_{\psi}(\varsigma) + j\omega \lambda_d \widetilde{L}_{\psi}(\varsigma), \tag{22.48}$$

where the symbol $\{\dot{\cdot}\}$ for amplitude quantities is absent, $\mathbf{u}_0 \in \mathrm{H}^1_{ul}$, $\varphi_0 \in \mathrm{H}^1_{\varphi m}$, $\phi \in \mathrm{H}^1_{\phi}$, $\psi \in \mathrm{H}^1_{\psi}$.

The resonance frequencies $f_k = \omega_k/(2\pi)$ for magnetoelectric solid with voids can be defined from the solution of the generalized eigenvalue (modal) problem, which can be obtained from (22.45)–(22.48), if we suppose $d(\mathbf{v}, \mathbf{u}_0) = 0$, $\alpha_d = \beta_d = \zeta_d = \gamma_d = \lambda_d = 0$,
$L_u(\mathbf{v}) = L_\varphi(\chi) = \widetilde{L}_\varphi(\chi) = L_\phi(\eta) = \widetilde{L}_\phi(\eta) = L_\psi(\varsigma) = \widetilde{L}_\psi(\varsigma) = 0$, i.e. without damping effect and without all inhomogeneous loads

$$-\omega^2 \widetilde{\rho}(\mathbf{v}, \mathbf{u}) + c(\mathbf{v}, \mathbf{u}) + e(\varphi, \mathbf{v}) + h(\phi, \mathbf{v}) + p(\mathbf{v}, \psi) = 0, \tag{22.49}$$

$$-e(\chi, \mathbf{u}) + \kappa(\chi, \varphi) + \alpha(\chi, \phi) + g(\chi, \psi) = 0, \tag{22.50}$$

$$-h(\eta, \mathbf{u}) + \alpha(\varphi, \eta) + \mu(\eta, \phi) + q(\eta, \psi) = 0, \tag{22.51}$$

$$p(\mathbf{u}, \varsigma) - g(\varphi, \varsigma) - q(\phi, \varsigma) + a(\varsigma, \psi) = 0, \tag{22.52}$$

where $\mathbf{u} = \mathbf{u}_0$, $\varphi = \varphi_0$, since $\mathbf{u}_b = 0$, $\varphi_b = 0$ for homogeneous boundary conditions.

Problem (22.49)–(22.52) is an eigenvalue problem, in which the unknown quantities are the eigenvalues $\lambda = \omega^2$ and eigenfunctions $\mathbf{u}$, φ, ϕ and ψ, giving a non-trivial solution.

We can transform the systems of (22.29)–(22.32), (22.45)–(22.48), (22.49)–(22.52) by serial eliminations of the functions ψ, ϕ and φ. Thus, for modal problem (22.49)–(22.52), we can realize the following operations similarly to [9, 12, 14, 17] for elastic and piezoelectric solids.

Note that the forms $\widetilde{\rho}(\mathbf{v}, \mathbf{u})$, $c(\mathbf{v}, \mathbf{u})$, $\kappa(\chi, \varphi)$, $\mu(\eta, \phi)$ and $a(\varsigma, \psi)$ are bilinear, symmetrical and positive defined in the function spaces L_2, H^1_{ul}, $\mathrm{H}^1_{\varphi m}$, H^1_{ϕ} and H^1_{ψ}, respectively, whereas the forms $e(\varphi, \mathbf{v})$, $h(\phi, \mathbf{v})$, $p(\mathbf{v}, \psi)$, $\alpha(\chi, \phi)$, $g(\chi, \psi)$ and $q(\eta, \psi)$ are only bilinear.

Since for arbitrary fixed $\mathbf{u} \in \mathrm{H}^1_{ul}$, $\varphi \in \mathrm{H}^1_{\varphi m}$, $\phi \in \mathrm{H}^1_{\phi}$ and $\psi \in \mathrm{H}^1_{\psi}$ the forms $p(\mathbf{u}, \varsigma)$, $g(\varphi, \varsigma)$, $q(\phi, \varsigma)$ and $a(\varsigma, \psi)$ are linear bounded functionals in H^1_{ψ}, by Riesz theorem [20] the elements $p\mathbf{u}$, $g\varphi$, $q\phi$, $a\psi \in \mathrm{H}^1_{\psi}$ unique exist such that for $\forall\, \varsigma \in \mathrm{H}^1_{\psi}$ the following equations hold:

$$\begin{gathered} p(\mathbf{u}, \varsigma) = (p\mathbf{u}, \varsigma)_{\mathrm{H}^1_{\psi}}, \quad g(\varphi, \varsigma) = (g\varphi, \varsigma)_{\mathrm{H}^1_{\psi}}, \quad q(\phi, \varsigma) = (q\phi, \varsigma)_{\mathrm{H}^1_{\psi}}, \\ a(\varsigma, \psi) = (\varsigma, a\psi)_{\mathrm{H}^1_{\psi}}. \end{gathered} \tag{22.53}$$

Obviously, the elements $p\mathbf{u}$, $g\varphi$, $q\phi$, $a\psi$ are linear operators acting from the space H^1_{ul} into the space H^1_{ψ}, from $\mathrm{H}^1_{\varphi m}$ into H^1_{ψ}, from H^1_{ϕ} into H^1_{ψ}, and from H^1_{ψ} into H^1_{ψ}, respectively, and for $a\psi$ an inverse operator exists. Therefore, from (22.52) to (22.53) we have

$$a\psi = -p\mathbf{u} + g\varphi + q\phi, \psi = -P\mathbf{u} + G\varphi + Q\phi, P = a^{-1}p, G = a^{-1}g, Q = a^{-1}q, \tag{22.54}$$

where the linear bounded operators P, G and Q act from H^1_{ul} into H^1_{ψ}, from $\mathrm{H}^1_{\varphi m}$ into H^1_{ψ}, and from H^1_{ϕ} into H^1_{ψ}, respectively.

Using (22.53), (22.54) we can reduce the system (22.49)–(22.52) to the form:

$$\hat{c}(\mathbf{v},\mathbf{u}) + \hat{e}(\varphi,\mathbf{v}) + \hat{h}(\phi,\mathbf{v}) = \omega^2\hat{\rho}(\mathbf{v},\mathbf{u}), \tag{22.55}$$

$$-\hat{e}(\chi,\mathbf{u}) + \hat{\kappa}(\chi,\varphi) + \hat{\alpha}(\chi,\phi) = 0, \tag{22.56}$$

$$-\hat{h}(\eta,\mathbf{u}) + \hat{\alpha}(\varphi,\eta) + \hat{\mu}(\eta,\phi) = 0, \tag{22.57}$$

where

$$\hat{c}(\mathbf{v},\mathbf{u}) = c(\mathbf{v},\mathbf{u}) - a(P\mathbf{v},P\mathbf{u}), \quad \hat{e}(\varphi,\mathbf{v}) = e(\varphi,\mathbf{v}) + a(P\mathbf{v},G\varphi), \tag{22.58}$$

$$\hat{h}(\phi,\mathbf{v}) = h(\phi,\mathbf{v}) + a(P\mathbf{v},Q\phi), \quad \hat{\kappa}(\chi,\varphi) = \kappa(\chi,\varphi) + a(G\chi,G\varphi), \tag{22.59}$$

$$\hat{\alpha}(\chi,\phi) = \alpha(\chi,\phi) + a(G\chi,Q\phi), \quad \mu(\eta,\phi) = \mu(\eta,\phi) + a(Q\eta,Q\phi). \tag{22.60}$$

Note that for transformation of the system (22.49)–(22.52) to (22.55)–(22.57) the following chains of formulas were used:

$$p(\mathbf{v},\psi) = (p\mathbf{v},\psi)_{\mathrm{H}^1_{\psi}} = (aa^{-1}p\mathbf{v},\psi)_{\mathrm{H}^1_{\psi}} = a(P\mathbf{v},\psi).$$

After excluding the porosity change function ψ, we have the system (22.55)–(22.57) with (22.58)–(22.60), which describes the natural oscillations of magnetoelectric solid with altered piezomagnetoelectric properties. Note, that the forms $\hat{c}(\mathbf{v},\mathbf{u})$, $\hat{\kappa}(\chi,\varphi)$ and $\hat{\mu}(\eta,\phi)$ are positive defined in H^1_{ul}, $\mathrm{H}^1_{\varphi m}$ and H^1_{ϕ}, respectively, because the potential energy of material (22.8) is positive defined. Then we can continue the reduction of system (22.55)–(22.57) by eliminating the magnetic potential ϕ.

Similarly, by Riesz theorem for fixed $\mathbf{u} \in \mathrm{H}^1_{ul}$, $\varphi \in \mathrm{H}^1_{\varphi m}$ and $\phi \in \mathrm{H}^1_{\phi}$ the elements $\hat{h}\mathbf{u}$, $\hat{\alpha}\varphi$, $\hat{\mu}\phi \in \mathrm{H}^1_{\phi}$ exist, are unique, and for $\eta \in \mathrm{H}^1_{\phi}$ we have $\hat{h}(\eta,\mathbf{u}) = (\hat{h}\mathbf{u},\eta)_{\mathrm{H}^1_{\phi}}$, $\hat{\alpha}(\varphi,\eta) = (\eta,\hat{\alpha}\varphi)_{\mathrm{H}^1_{\phi}}$, $\hat{\mu}(\eta,\phi) = (\eta,\hat{\mu}\phi)_{\mathrm{H}^1_{\phi}}$. Then, $\hat{h}\mathbf{u}$, $\hat{\alpha}\varphi$ and $\hat{\mu}\phi$ are linear operators acting from H^1_{ul} into H^1_{ϕ}, from $\mathrm{H}^1_{\varphi m}$ into H^1_{ϕ} and from H^1_{ϕ} into H^1_{ϕ}, respectively, and an inverse operator exists for $\hat{\mu}\phi$. Therefore, we obtain $\hat{\mu}\phi = \hat{h}\mathbf{u} - \hat{\alpha}\varphi$, $\phi = \hat{H}\mathbf{u} - \hat{A}\varphi$, $\hat{H} = \hat{\mu}^{-1}\hat{h}$, $\hat{A} = \hat{\mu}^{-1}\hat{\alpha}$, where the operators $\hat{H}$ and $\hat{A}$ are linear bounded and act from H^1_{ul} into H^1_{ϕ}, and from $\mathrm{H}^1_{\varphi m}$ into H^1_{ϕ}, respectively. So, we obtain from (22.55)–(22.57) the following reduced system:

$$\widetilde{c}(\mathbf{v},\mathbf{u})+\widetilde{e}(\varphi,\mathbf{v}) = \omega^2\hat{\rho}(\mathbf{v},\mathbf{u}), \tag{22.61}$$

$$-\widetilde{e}(\chi,\mathbf{u})+\widetilde{\kappa}(\chi,\varphi)=0, \tag{22.62}$$

where

$$\widetilde{c}(\mathbf{v},\mathbf{u})=\hat{c}(\mathbf{v},\mathbf{u})+\hat{\mu}(\hat{H}\mathbf{v},\hat{H}\mathbf{u}), \tag{22.63}$$

$$\widetilde{e}(\varphi,\mathbf{v})=\hat{e}(\varphi,\mathbf{v})-\hat{\mu}(\hat{A}\varphi,\hat{H}\mathbf{v}), \quad \widetilde{\kappa}(\chi,\varphi)=\hat{\kappa}(\chi,\varphi)-\hat{\mu}(\hat{A}\chi,\hat{A}\varphi), \tag{22.64}$$

Finally, for fixed $\mathbf{u}\in \mathrm{H}^1_{ul}$ and $\varphi\in \mathrm{H}^1_{\varphi m}$ the unique elements $\widetilde{e}\mathbf{u}$, $\widetilde{\kappa}\varphi\in \mathrm{H}^1_{\varphi m}$ exist, that for all $\chi\in \mathrm{H}^1_{\varphi m}$ we have $\widetilde{e}(\chi,\mathbf{u})=(\chi,\widetilde{e}\mathbf{u})_{\mathrm{H}^1_{\varphi m}}$, $\widetilde{\kappa}(\chi,\varphi)=(\chi,\widetilde{\kappa}\varphi)_{\mathrm{H}^1_{\varphi m}}$, where the linear bounded operators $\widetilde{e}\mathbf{u}$ and $\widetilde{\kappa}\varphi$ act from H^1_{ul} into $\mathrm{H}^1_{\varphi m}$ and from $\mathrm{H}^1_{\varphi m}$ into $\mathrm{H}^1_{\varphi m}$, respectively, and there is an inverse for the operator $\widetilde{\kappa}\varphi$. Thus, $\widetilde{\kappa}\varphi=\widetilde{e}\mathbf{u}$, $\varphi=\breve{A}\ \mathbf{u}$, $\breve{A}=\widetilde{\kappa}^{-1}\widetilde{e}$, at that the operator $\breve{A}$, acting from H^1_{ul} into $\mathrm{H}^1_{\varphi m}$, is linear bounded. This allows us to transform the system (22.61), (22.62) with (22.63), (22.64) to the final reduced form:

$$\breve{c}(\mathbf{v},\mathbf{u})=\omega^2\widetilde{\rho}(\mathbf{v},\mathbf{u}), \tag{22.65}$$

where

$$\breve{c}(\mathbf{v},\mathbf{u})=\widetilde{c}(\mathbf{v},\mathbf{u})+\widetilde{\kappa}(\breve{A}\,\mathbf{v},\breve{A}\,\mathbf{u}) \tag{22.66}$$

Definition The set of quantities $(\omega^2,\ \mathbf{u}\in \mathrm{H}^1_{ul},\ \varphi\in \mathrm{H}^1_{\varphi m},\ \phi\in \mathrm{H}^1_{\phi},\ \psi\in \mathrm{H}^1_{\psi})$ is a week solution of modal problem for magnetoelectric body with voids, if (22.65) satisfies for $\forall\,\mathbf{v}\in \mathrm{H}^1_{ul}$, or which is equivalent, (22.61), (22.62) hold for $\forall\,\mathbf{v}\in \mathrm{H}^1_{ul}$, $\forall\,\chi\in \mathrm{H}^1_{\varphi m}$, or (22.55)–(22.57) hold for $\forall\,\mathbf{v}\in \mathrm{H}^1_{ul}$, $\forall\,\chi\in \mathrm{H}^1_{\varphi m}$, $\forall\,\eta\in \mathrm{H}^1_{\phi}$, or (22.49)–(22.52) hold for $\forall\,\mathbf{v}\in \mathrm{H}^1_{ul}$, $\forall\,\chi\in \mathrm{H}^1_{\varphi m}$, $\forall\,\eta\in \mathrm{H}^1_{\phi}$, $\forall\,\varsigma\in \mathrm{H}^1_{\psi}$.

Similarly, we can obtain the reduced formulations for the transient problem (22.29)–(22.32) and for the harmonic problem (22.45)–(22.48).

22.5 Spectral Properties and Some Theorems About Resonance Frequencies

Note that the form $c(\mathbf{v},\mathbf{v})+\kappa(\chi,\chi)+\mu(\eta,\eta)+a(\varsigma,\varsigma)+2p(\mathbf{v},\varsigma)+2\alpha(\chi,\eta)$, concerned to the form $\breve{c}(\mathbf{v},\mathbf{v})$ from (22.66), is positive defined, that is provided by the energy conditions (22.8). Then we introduce the energy function space H^1_c. This space is the closure of the set of vector function $\mathbf{u}\in \mathrm{C}^1$, that satisfy boundary

conditions (22.10) and (22.13) with $\mathbf{u}_{\Gamma i} = 0$, in the norm generated by the scalar product (22.66). Following [21, 22], we can establish that the energy space H_c^1 is equivalent to H_{ul}^1, and from the complete continuity of the embedding operator from H_{ul}^1 into H_ρ^0 the next theorems follow.

Theorem 22.1 *The operator equation (22.65) has a discrete real spectrum* $0 < \omega_1^2 \le \ldots \le \omega_k^2 \le \ldots$; $\omega_k^2 \to \infty$ *as* $k \to \infty$, *and the system of eigenvectors* $\mathbf{u}^{(k)}$ *is orthogonal and complete in the spaces* H_ρ^0 *and* H_c^1.

Theorem 22.2 *There is a minimax Courant—Fisher principle:*

$$\omega_k^2 = \max_{\mathbf{w}_1, \mathbf{w}_2, \ldots, \mathbf{w}_{k-1} \in \mathrm{H}_{ul}^1} \left[\min_{\substack{\mathbf{v} \ne 0, \mathbf{v} \in \mathrm{H}_{ul}^1 \\ \breve{\rho}(\mathbf{v}, \mathbf{w}_i) = 0; i = 1, 2, \ldots, k-1}} R(\mathbf{v}) \right],$$

where $R(\mathbf{v}) = \breve{c}(\mathbf{v}, \mathbf{v}) / \breve{\rho}(\mathbf{v}, \mathbf{v})$ *is the Rayleigh quotient.*

These theorems can be proved using analogous arguments as for elastic problems with replacement of the forms c and ρ by $\breve{c}$ *and* $\breve{\rho}$ [22].

Following [9, 12, 14, 17], we can investigate the changing of the eigenfrequencies (natural frequencies) when some parameters of the problem (22.49)–(22.52) or (22.65) change. We will directly indicate these modifications in the formulations of the next theorems, and the variables related to the changes will be marked by subscripts *lm* or by an asterisk. Meanwhile, the parameters that are not specified in the theorems are assumed identical for the original and modified problems.

We call problem (22.49)–(22.52) or (22.65) the *lm*-problem, to emphasize the presence of l Γ_{ui}; $i = 0, 1, 2, \ldots, l$, in contact with punches and m regions $\Gamma_{\varphi j}$, $j = 0, 1, 2, \ldots, m$, coated by open-circuited electrodes.

We consider two *lm*- and *pm*-problems, which differ solely in the number l and p of contacting parts Γ_{ui} in (22.10)–(22.12). We emphasize that the outer input data in the *lm*- and *pm*-problems are assumed to be the same.

Theorem 22.3 *If* $0 \le l < p \le L$, *than* $\omega_{lmk}^2 \ge \omega_{pmk}^2$ *for* $\forall k$, *i.e. the kth eigenfrequency* ω_{lmk} *of lm-problem is not less than kth eigenfrequency* ω_{pmk} *of pm-problem.*

Note that under the conditions of Theorem 22.3, the boundary Γ_u has not change. When passing from *lm*-problem to *pm*-problem, we change only the conditions of fixed boundary by the conditions of contact with punches on the parts of Γ_{ui}.

We now consider two similar *lm*- and *ln*-problems, which differ solely in the number m and n open-circuited electrodes of $\Gamma_{\varphi j}$ in (22.15)–(22.17).

Theorem 22.4 *If* $0 \leq m < n \leq M$, *than* $\omega_{lmk}^2 \leq \omega_{lnk}^2$ *for* $\forall k$, *i.e. the kth eigenfrequency* ω_{lmk} *of lm-problem is not greater than kth eigenfrequency* ω_{lnk} *of ln-problem.*

Theorem 22.5 *If for two problems the rigidly constrained boundaries and the contact boundaries with the punches are such that* $\Gamma_u \supseteq \Gamma_{*u}$, $\Gamma_{ui} \supseteq \Gamma_{*ui}$, $i = 0, 1, 2, \ldots, L$, *than we have* $\omega_k^2 \geq \omega_{*k}^2$ for $\forall k$.

Theorem 22.6 *If the stiffness moduli, the piezoelectric moduli, the magnetostriction moduli, the constants characterizing the properties of porosity, the densities and the mass characteristics of the punches for two problems are such that* $\tilde{c}_{lm}(\mathbf{v}, \mathbf{v}) \geq \tilde{c}_{lm*}(\mathbf{v}, \mathbf{v})$, $\widetilde{\rho}(\mathbf{v}, \mathbf{v}) \leq \widetilde{\rho}_*(\mathbf{v}, \mathbf{v})$ *for* $\forall \mathbf{v} \in \mathrm{H}_{ul}^1$, *then* $\omega_k^2 \geq \omega_{*k}^2$ *for* $\forall k$.

Theorem 22.7 *If for two problems the electrode-coated surfaces are such that* $\Gamma_\varphi \supseteq \Gamma_{*\varphi}$, $\Gamma_{\varphi j} \supseteq \Gamma_{*\varphi j}$, $j = 0, 1, 2, \ldots, M$, *than we have* $\omega_k^2 \leq \omega_{*k}^2$ *for* $\forall k$.

Theorem 22.8 *If the dielectric permittivity moduli, the magnetoelectric coupling coefficients and the magnetic permeability moduli for two problems are such that* $\kappa(\chi, \chi) + \mu(\eta, \eta) + 2\alpha(\chi, \eta) \geq \kappa_*(\chi, \chi) + \mu_*(\eta, \eta) + 2\alpha_*(\chi, \eta)$ *for* $\forall \chi \in \mathrm{H}_{\varphi m}^1$, $\eta \in \mathrm{H}_{\phi}^1$, *then* $\omega_k^2 \leq \omega_{*k}^2$ *for* $\forall k$.

Theorem 22.9 *If the "porous" Dirichlet boundaries for two problems are such that* $\Gamma_{\psi 0} \supseteq \Gamma_{*\psi 0}$, *than* $\omega_k^2 \geq \omega_{*k}^2$ *for* $\forall k$.

Theorem 22.10 *If the porous diffusion coefficients for two problems are such that* $a(\varsigma, \varsigma) \geq a_*(\varsigma, \varsigma)$ *for* $\forall \varsigma \in \mathrm{H}_{\psi}^1$, *then* $\omega_k^2 \geq \omega_{*k}^2$ *for* $\forall k$.

Note that the proofs of these theorems are similar to presented in [9].

It is interesting to compare the results of Theorems 22.3–22.10. If we replace on certain regions of Γ_{ui} the rigid fixed boundary conditions (22.13) by the contact conditions (22.10)–(22.12), then by Theorem 22.3 the eigenfrequencies can only become smaller.

Contrariwise, if on certain regions of $\Gamma_{\varphi j}$ we change the boundary conditions for the zero electric potential (22.17) by the contact type electric boundary conditions (22.15), (22.16) for open-circuited electrodes, then by Theorem 22.4 the eigenfrequencies can only become greater.

By Theorems 22.5 and 22.6, the eigenfrequencies can only become smaller, if the surfaces of fixed boundaries Γ_u or of the contact boundaries Γ_{ui} reduce, if the stiffness moduli specific decrease, or if the density and the mass characteristics of the punches increase.

On the other hand, according to Theorems 22.7 and 22.8, the eigenfrequencies can only increase if the electrode-coated surfaces Γ_φ and $\Gamma_{\varphi j}$ reduce or if the set of electric and magnetic moduli specific diminishes.

In the result, from Theorems 22.3, 22.5, 22.6 and 22.4, 22.7, 22.8 we can conclude that a resembling modifications in the mechanical and electric boundary conditions or in elastic and magnetoelectric moduli lead to contrary change for the eigenfrequencies.

However, according to Theorems 22.9 and 22.10, the eigenfrequencies can only decrease if the boundary $\Gamma_{\psi 0}$ reduces or if the porous diffusion coefficients specific diminish. Then, from Theorems 22.5, 22.6 and 22.9, 22.10, we can draw a conclusion that a resembling modifications in the mechanical and porous boundary conditions or in the stiffness moduli and in the constitutive porous constants lead to identical change for the eigenfrequencies.

22.6 Finite Element Approaches

We can solve the problems (22.29)–(22.32), (22.45)–(22.48), (22.49)–(22.52) for magnetoelectric solids with voids using the routine finite element approaches. Let Ω_h be a volume with finite element mesh: $\Omega_h \subseteq \Omega$, $\Omega_h = \cup_k \Omega^{e\,k}$, where Ω^{ek} is the individual finite element, k is the element number. On the domain boundary $\Gamma_h = \partial\Omega_h$ we introduce the boundaries $\Gamma_{h\sigma}$, Γ_{hu}, Γ_{hui} etc., which will be the approximations of the corresponding boundaries Γ_σ, Γ_u, Γ_{ui} etc. Then, on Ω_h we can introduce the function spaces H^1_{hul}, $\mathrm{H}^1_{h\varphi m}$, $\mathrm{H}^1_{h\phi}$, $\mathrm{H}^1_{h\psi}$ and Q_{hul}, $\mathrm{Q}_{h\varphi m}$, $\mathrm{Q}_{h\phi}$, $\mathrm{Q}_{h\psi}$ analogously to the function spaces from Sect. 22.3.

We will find the approximate solution $\{\, \mathbf{u}_{h0} \approx \mathbf{u}_0,\ \varphi_{h0} \approx \varphi_0,\ \phi_h \approx \phi,\ \psi_h \approx \psi \,\}$ of transient problem (22.29)–(22.32) in the following form:

$$\mathbf{u}_{h0}(\mathbf{x},t) = \mathbf{N}_u^{\mathrm{T}}(\mathbf{x}) \cdot \mathbf{U}(t), \quad \varphi_{h0}(\mathbf{x},t) = \mathbf{N}_\varphi^{\mathrm{T}}(\mathbf{x}) \cdot \mathbf{\Phi}(t), \tag{22.67}$$

$$\phi_h(\mathbf{x},t) = \mathbf{N}_\phi^{\mathrm{T}}(\mathbf{x}) \cdot \mathbf{M}(t), \quad \psi_h(\mathbf{x},t) = \mathbf{N}_\psi^{\mathrm{T}}(\mathbf{x}) \cdot \mathbf{\Psi}(t). \tag{22.68}$$

Here, $\mathbf{N}_u$ is the matrix of the finite element shape functions for the displacements; $\mathbf{N}_\varphi$, $\mathbf{N}_\phi$, $\mathbf{N}_\psi$ are the vectors of the finite element shape functions for the electric potential, for the magnetic potential, and for the porosity changes; $\mathbf{U}(t)$, $\mathbf{\Phi}(t)$, $\mathbf{M}(t)$, $\mathbf{\Psi}(t)$ are the vectors of the nodal displacements, the nodal electric potential, the nodal magnetic potential, and the nodal porosity changes, respectively. All finite element shape functions form the basis in the appropriate finite-dimensional spaces $\mathrm{V}^t_{hul} \subseteq \mathrm{Q}_{hul}$, $\mathrm{V}^t_{h\varphi m} \subseteq \mathrm{Q}_{h\varphi m}$, $\mathrm{V}^t_{h\phi} \subseteq \mathrm{Q}_{h\phi}$ and $\mathrm{V}^t_{h\psi} \subseteq \mathrm{Q}_{h\psi}$, for non-stationary problem or in the finite-dimensional spaces $\mathrm{V}_{hul} \subseteq \mathrm{H}^1_{hul}$, $\mathrm{V}_{h\varphi m} \subseteq \mathrm{H}^1_{h\varphi m}$, $\mathrm{V}_{h\phi} \subseteq \mathrm{H}^1_{h\phi}$, and $\mathrm{V}_{h\psi} \subseteq \mathrm{H}^1_{h\psi}$, for steady-state oscillation problems. Then, for non-stationary problem: $\mathbf{u}_{h0} \in \mathrm{V}^t_{hul}$, $\varphi_{h0} \in \mathrm{V}^t_{h\varphi m}$, $\phi_h \in \mathrm{V}^t_{h\phi}$, $\psi_h \in \mathrm{V}^t_{h\psi}$. Here, in (22.67), (22.68) for harmonic and modal problems $\mathbf{U}$, $\mathbf{\Phi}$, $\mathbf{M}$ and $\mathbf{\Psi}$ are the constant vectors.

Then, the projecting functions $\mathbf{v}$, χ, η and ς can be present in finite-dimensional spaces V_{hul}, $\mathrm{V}_{h\varphi m}$, $\mathrm{V}_{h\phi}$ and $\mathrm{V}_{h\psi}$, respectively, by the formulae:

$$\mathbf{v}(\mathbf{x}) = \mathbf{N}_u^* \cdot \delta\mathbf{U}, \quad \chi(\mathbf{x}) = \mathbf{N}_\varphi^* \cdot \delta\mathbf{\Phi}, \quad \eta(\mathbf{x}) = \mathbf{N}_\varphi^* \cdot \delta\mathbf{M}, \quad \psi(\mathbf{x}) = \mathbf{N}_\psi^* \cdot \delta\mathbf{\Psi}. \tag{22.69}$$

Substituting approximations (22.67)–(22.69) into the problem (22.29)–(22.32) and using (22.33)–(22.44) for Ω_h, we obtain

$$\widetilde{\mathbf{M}}_{uu} \cdot \ddot{\mathbf{U}} + \widetilde{\mathbf{C}}_{uu} \cdot \dot{\mathbf{U}} + \mathbf{K}_{uu} \cdot \mathbf{U} + \mathbf{K}_{u\varphi} \cdot \mathbf{\Phi} + \mathbf{K}_{u\phi} \cdot \mathbf{M} + \mathbf{K}_{u\psi} \cdot \mathbf{\Psi} = \mathbf{F}_u, \tag{22.70}$$

$$-\mathbf{K}_{u\varphi}^{\mathrm{T}} \cdot (\varsigma_d \dot{\mathbf{U}} + \mathbf{U}) + \mathbf{K}_{\varphi\varphi} \cdot \mathbf{\Phi} + \mathbf{K}_{\varphi\phi} \cdot \mathbf{M} + \mathbf{K}_{\varphi\psi} \cdot \mathbf{\Psi} = \varsigma_d \mathbf{F}_\varphi^t + \mathbf{F}_\varphi, \tag{22.71}$$

$$-\mathbf{K}_{u\phi}^{\mathrm{T}} \cdot (\gamma_d \dot{\mathbf{U}} + \mathbf{U}) + \mathbf{K}_{\varphi\phi}^{\mathrm{T}} \cdot \mathbf{\Phi} + \mathbf{K}_{\phi\phi} \cdot \mathbf{M} + \mathbf{K}_{\phi\psi} \cdot \mathbf{\Psi} = \gamma_d \mathbf{F}_\phi^t + \mathbf{F}_\phi, \tag{22.72}$$

$$\mathbf{K}_{u\psi}^{\mathrm{T}} \cdot (\lambda_d \dot{\mathbf{U}} + \mathbf{U}) - \mathbf{K}_{\varphi\psi}^{\mathrm{T}} \cdot \mathbf{\Phi} - \mathbf{K}_{\phi\psi}^{\mathrm{T}} \cdot \mathbf{M} + \mathbf{K}_{\psi\psi} \cdot \mathbf{\Psi} = \lambda_d \mathbf{F}_\psi^t + \mathbf{F}_\psi. \tag{22.73}$$

For transient problem it is need to add the initial conditions:

$$\mathbf{U}(0) = \mathbf{U}_*, \quad \dot{\mathbf{U}}(0) = \mathbf{V}_*, \tag{22.74}$$

which can be obtain from the continual conditions (22.22).

In (22.70)–(22.73) $\widetilde{\mathbf{M}}_{uu} = \mathbf{M}_{uu} + \mathbf{M}_p$, $\widetilde{\mathbf{C}}_{uu} = \mathbf{C}_{uu} + \alpha_d \mathbf{M}_p$, $\mathbf{M}_p$ is the matrix of mass characteristics for the punches, $\mathbf{M}_{uu} = \sum^a \mathbf{M}_{uu}^{ek}$, $\mathbf{C}_{uu} = \sum^a \mathbf{C}_{uu}^{ek}$, $\mathbf{K}_{uu} = \sum^a \mathbf{K}_{uu}^{ek}$, $\mathbf{K}_{u\varphi} = \sum^a \mathbf{K}_{u\varphi}^{ek}$ etc., $\sum^a$ is the operation of element matrix ensembling, and the element matrices have the forms:

$$\mathbf{M}_{uu}^{ek} = \int\limits_{\Omega^{ek}} \rho \mathbf{N}_u^e \cdot \mathbf{N}_u^{e\mathrm{T}} d\Omega, \quad \mathbf{C}_{uu}^{ek} = \alpha_d \mathbf{M}_{uu}^{ek} + \beta_d \mathbf{K}_{uu}^{ek}, \tag{22.75}$$

$$\begin{gathered} \mathbf{K}_{uu}^{ek} = \int\limits_{\Omega^{ek}} \mathbf{S}_u^{e\mathrm{T}} \cdot \mathbf{c} \cdot \mathbf{S}_u^e d\Omega, \quad \mathbf{K}_{u\varphi}^{ek} = \int\limits_{\Omega^{ek}} \mathbf{S}_u^{e\mathrm{T}} \cdot \mathbf{e}^{\mathrm{T}} \cdot \mathbf{S}_\varphi^e d\Omega, \\ \mathbf{K}_{u\phi}^{ek} = \int\limits_{\Omega^{ek}} \mathbf{S}_u^{e\mathrm{T}} \cdot \mathbf{h}^{\mathrm{T}} \cdot \mathbf{S}_\phi^e d\Omega, \end{gathered} \tag{22.76}$$

$$\mathbf{K}_{u\psi}^{ek} = \int\limits_{\Omega^{ek}} \mathbf{S}_u^{e\mathrm{T}} \cdot \mathbf{P}\, \mathbf{N}_\psi^{e*} d\Omega, \quad \mathbf{K}_{\varphi\varphi}^{ek} = \int\limits_{\Omega^{ek}} \mathbf{S}_\varphi^{e\mathrm{T}} \cdot \boldsymbol{\kappa} \cdot \mathbf{S}_\varphi^e d\Omega, \quad \mathbf{K}_{\varphi\phi}^{ek} = \int\limits_{\Omega^{ek}} \mathbf{S}_\varphi^{e\mathrm{T}} \cdot \boldsymbol{\alpha} \cdot \mathbf{S}_\phi^e d\Omega \tag{22.77}$$

$$\mathbf{K}_{\varphi\psi}^{ek} = \int\limits_{\Omega^{ek}} \left[\mathbf{S}_\varphi^{e\mathrm{T}} \cdot \mathbf{G} \cdot \mathbf{S}_\psi^e + \mathbf{S}_\varphi^{e\mathrm{T}} \cdot \mathbf{g}\, \mathbf{N}_\psi^{e\mathrm{T}} \right] d\Omega, \quad \mathbf{K}_{\phi\phi}^{ek} = \int\limits_{\Omega^{ek}} \mathbf{S}_\phi^{e\mathrm{T}} \cdot \boldsymbol{\mu} \cdot \mathbf{S}_\phi^e d\Omega, \tag{22.78}$$

$$\mathbf{K}^{ek}_{\phi\psi} = \int\limits_{\Omega^{ek}} \left[\mathbf{S}^{eT}_{\phi}\cdot\mathbf{Q}\cdot\mathbf{S}^{e}_{\psi} + \mathbf{S}^{eT}_{\phi}\cdot\mathbf{q}\,\mathbf{N}^{eT}_{\psi}\right]d\Omega, \quad \mathbf{K}^{ek}_{\psi\psi} = \int\limits_{\Omega^{ek}} \left[\mathbf{S}^{eT}_{\psi}\cdot\mathbf{A}\cdot\mathbf{S}^{e}_{\psi} + \xi\,\mathbf{N}^{e}_{\psi}\,\mathbf{N}^{eT}_{\psi}\right]d\Omega, \tag{22.79}$$

$$\mathbf{S}^{e}_{u} = \mathbf{L}(\nabla)\cdot\mathbf{N}^{eT}_{u}, \quad \mathbf{S}^{e}_{\varphi} = \nabla\mathbf{N}^{eT}_{\varphi}, \quad \mathbf{S}^{e}_{\phi} = \nabla\mathbf{N}^{eT}_{\phi}, \quad \mathbf{S}^{e}_{\psi} = \nabla\mathbf{N}^{eT}_{\psi}, \tag{22.80}$$

$$\mathbf{L}^{\mathrm{T}}(\nabla) = \begin{bmatrix} \partial_1 & 0 & 0 & 0 & \partial_3 & \partial_2 \\ 0 & \partial_2 & 0 & \partial_3 & 0 & \partial_1 \\ 0 & 0 & \partial_3 & \partial_2 & \partial_1 & 0 \end{bmatrix}, \tag{22.81}$$

where $\mathbf{N}^{e}_{u}$, $\mathbf{N}^{e}_{\varphi}$, $\mathbf{N}^{e}_{\phi}$, $\mathbf{N}^{e}_{\psi}$ are the matrices and the vectors of element shape functions, determinated on individual finite elements.

In (22.75)–(22.81), we use vector-matrix denotations for the material moduli. Thus, $\mathbf{c}$ is the 6×6 matrix of elastic stiffness moduli; $\mathbf{e}$ and $\mathbf{h}$ is the 3×6 matrices of piezoelectric and magnetostriction moduli, respectively; $\mathbf{P} = \{P_{11}, P_{22}, P_{33}, P_{23}, P_{13}, P_{12}\}$; $c_{\alpha\beta} = c_{ijkl}$, $e_{i\beta} = e_{ikl}$, $h_{i\beta} = h_{ikl}$; $\alpha,\beta = 1,\ldots,6$; $i,j,k,l = 1,\ 2,\ 3$; and the following correspondence law between indices takes place: $\alpha \leftrightarrow (ij)$, $\beta \leftrightarrow (kl)$, $1 \leftrightarrow (11)$, $2 \leftrightarrow (22)$, $3 \leftrightarrow (33)$, $4 \leftrightarrow (23) \equiv (32)$, $5 \leftrightarrow (13) \equiv (31)$, $6 \leftrightarrow (12) \equiv (21)$.

Here, the vectors of right-hand sides of (22.71)–(22.73) are determined from (22.39) to (22.44) and (22.69).

It is important to note, that the matrix properties positive defined follow from the energy inequality obtained from (22.8) to (22.70)–(22.73)

$$\exists W_h > 0, \forall\,\mathbf{U},\boldsymbol{\Phi},\mathbf{M},\boldsymbol{\Psi}: \quad \mathbf{U}^{\mathrm{T}}\cdot\mathbf{K}_{uu}\cdot\mathbf{U} + 2\mathbf{U}^{\mathrm{T}}\cdot\mathbf{K}_{u\psi}\cdot\boldsymbol{\Psi} + 2\boldsymbol{\Phi}^{\mathrm{T}}\cdot\mathbf{K}_{\varphi\phi}\cdot\mathbf{M}$$
$$+\boldsymbol{\Phi}^{\mathrm{T}}\cdot\mathbf{K}_{\varphi\varphi}\cdot\boldsymbol{\Phi} + \mathbf{M}^{\mathrm{T}}\cdot\mathbf{K}_{\phi\phi}\cdot\mathbf{M} + \boldsymbol{\Psi}^{\mathrm{T}}\cdot\mathbf{K}_{\psi\psi}\cdot\boldsymbol{\Psi} \geq W_h(\mathbf{U}^{\mathrm{T}}\cdot\mathbf{U} + \boldsymbol{\Phi}^{\mathrm{T}}\cdot\boldsymbol{\Phi} + \mathbf{M}^{\mathrm{T}}\cdot\mathbf{M} + \boldsymbol{\Psi}^{\mathrm{T}}\cdot\boldsymbol{\Psi}).$$

We also note that for integrating by time the Cauchy problem (22.70)–(22.74), it is convenient to use the Newmark method in a alternative formulation without the calculation of velocities and accelerations in the time steps, similarly to [15, 18]. In these approaches we can reduce the system (22.70)–(22.73) by eliminating the degrees of freedom $\boldsymbol{\Phi}$, $\mathbf{M}$ and $\boldsymbol{\Psi}$. The results of such operations will be more compact, if $\beta_d = \gamma_d = \zeta_d = \lambda_d$.

For the case of zero essential boundary conditions with $\beta_d = \gamma_d = \zeta_d = \lambda_d$, we can use the mode superposition method for solving non-stationary and harmonic problems. This circumstance is an important justification for choosing the accepted method of damping account with the terms with coefficients β_d, γ_d, ς_d and λ_d in (22.2)–(22.5), (22.7).

Note that similarly to [15, 18], we can apply an effective algorithms with quasi-definite symmetric matrices [23] for solving (22.70)–(22.73) in the cases of transient, harmonic, modal problems and the problems of interaction between magnetoelectric bodies with voids and acoustic medium [19]. The basic finite

element procedures (rotations of material coordinate systems, settings of the essential boundary conditions, etc.) can also be realized in symmetrical forms.

22.7 Concluding Remark

In this chapter for investigations of electroelastic (piezoelectric) and magneto electroelastic (magnetoelectric) materials with voids and devices from these materials the original mathematical and finite element models are suggested, which extend the models of the piezoelectric solid with coupled attenuation properties and the Cowin-Nunziato model for solids with voids. In this generalized model, we consider the field functions of mechanical displacements, electric potential, magnetic potential and the porosity change function. The mathematical model contains the momentum equations of continuum mechanics, the quasi-electrostatic equation, the quasi-magnetostatic equation and the equation for change of porosity, and also the corresponding mechanical, electric, magnetic and porous boundary and initial conditions.

On the base of these models, we have formulated the statements of the initial-boundary problems for magnetoelectric solids with voids. We have derived the continual weak (generalized) statements in the original extended and truncated forms and finite element systems with quasi-definite symmetric matrices typical for various problems with a saddle operator. We have also established the mathematical properties of the eigenfrequencies and eigenvectors for multiferroic solids with voids for different types of the boundary conditions, including the mechanical and electric boundary conditions of contact types. We have proved that the spectrum for the eigenvalue problem for bounded magnetoelectric solids with voids is real and discrete and the eigenvector system is orthogonal and complete in the corresponding energetic spaces. A minimax Courant—Fisher principle is constructed, which is similar to the well-known variational principle for the elastic and electroelastic problems. On the base of variational statements, the properties of an increase or a decrease in the eigenfrequencies, when the mechanical, electric, magnetic and porous boundary conditions and the material moduli change, are proved.

It was established that the same type changes of mechanical and magnetoelectric boundary conditions and changes of stiffness moduli and dielectric or magnetic moduli lead to the reverse changes in the eigenfrequencies. Conversely, the modifications of the porous material properties and of the porous boundary conditions lead to the analogous changes for the eigenfrequencies as well as the similar changes of mechanical material properties and boundary conditions.

A set of finite element schemes with quasi-definite symmetric matrices is suggested for finding approximate solutions of non-stationary, harmonic, modal and static problems for piezomagnetoelectric materials with voids.

Acknowledgements The research of second author was supported by the Ministry of Education and Science of the Russian Federation, project No. 9.1001.2017/PCh.

References

1. E. Ringgaard, F. Lautzenhiser, L.M. Bierregaard, T. Zawada, E. Molz, Materials **8**(12), 8877 (2015)
2. A.N. Rybyanets, I.E.E.E. Trans, Ultrason. Ferroelectr. Freq. Control **58**, 1492 (2011)
3. V. Yu Topolov, C.R. Bowen, *Electromechanical Properties in Composites Based on Ferroelectrics* (Springer, London, 2009), p. 202
4. C.-W. Nan, M.I. Bichurin, S. Dong, D. Viehland, G. Srinivasan, J. Appl. Phys. **103**, 031101 (2008)
5. H. Palneedi, V. Annapureddy, S. Priya, J. Ryu, Actuators **5**(1), 9 (2016)
6. S.C. Cowin, J.W. Nunziato, J. Elast. **13**, 125 (1983)
7. J.W. Nunziato, S.C. Cowin, Arch. Ration. Mech. Anal. **72**, 175 (1979)
8. M. Ciarletta, E. Scarpetta, Mech. Res. Commun. **23**, 1 (1996)
9. G. Iovane, A.V. Nasedkin, Appl. Math. Model. **34**(1), 60 (2010)
10. G. Iovane, A.V. Nasedkin, Appl. Math. Model. **34**(1), 47 (2010)
11. G. Iovane, A.V. Nasedkin, in: *Proceedings Of The Tenth International Conference On Computational Structures Technology, CST-2010, Valencia, Spain, 14–17 Sept 2010*. Ed. by B.H.V. Topping, J.M. Adam, F.J. Pallarés, R. Bru, M.L. Romero (Civil-Comp Press, Stirlingshire, UK, 2010), p. 282
12. G. Iovane, A.V. Nasedkin, in *Advanced Nano- and Piezoelectric Materials and their Applications*, ed. by I.A. Parinov (Nova Science Publishers, New York, 2014), p. 145
13. G. Iovane, A.V. Nasedkin, in: *Methods of Wave Dynamics and Mechanics of Composites for Analysis of Microstructured Materials and Metamaterials. Ser. Advanced Structured Materials*, vol 59, ed. by M.A. Sumbatyan (Springer, Singapore, 2017), p. 221
14. A.V. Belokon, A.V. Nasedkin, J. Appl. Math. Mech. (PMM) **60**, 145 (1996)
15. A.V. Nasedkin, in *Piezoceramic Materials and Devices*, ed. by I.A. Parinov (Nova Science Publishers, New York, 2010), p. 177
16. G. Iovane, A.V. Nasedkin, in: *Proceedings of the Eighth International Conference on Computational Structures Technology, CST-2006, Las Palmas de Gran Canaria, Spain, 12–15 Sept 2006,* ed. by B.H.V. Topping, G. Montero, R. Montenegro (Civil-Comp Press, Stirlingshire, UK, 2006), p. 234
17. G. Iovane, A.V. Nasedkin, Comput. Math Appl. **53**(5), 789 (2007)
18. G. Iovane, A.V. Nasedkin, Comput. Struct. **87**(15–16), 981 (2009)
19. G. Iovane, A.V. Nasedkin, J. Coupled Syst. Multiscale Dyn. **1**(3), 393 (2013)
20. F. Riesz, B. Szokefalvi-Nagy, *Functional Analysis* (Dover, New York, 1990)
21. A.V. Belokon, I.I. Vorovich, *Actual Problems in the Mechanics of Deformable Media* (Izv. Dnepropetr. Gos. Univ, Dnepropetrovsk, 1979) (in Russian)
22. S.G. Mikhlin, *Variational Methods in Mathematical Physics* (Pergamon Press, Oxford, 1964)
23. M. Benzi, G.H. Golub, J. Liesen, Acta Numerica **14**, 1 (2005)

Chapter 23
Nonlocal Nonlinear Analysis of Composites

P. Raghu, Anna A. Nasedkina, Andrey V. Nasedkin, A. Rajagopal and B. Saswata

Abstract In this work, we present the behaviour of laminated composite plates, subjected to a static bending load under the influence of varying value of material length scale parameters. Reddy's (J Appl Mech 51:745, 1984 [1]) third order shear deformation theory (TSDT) is used, which describes the kinematics accurately. The geometric nonlinearity, which prevails under the effect of large deformations, is accounted using von Karman nonlinear strains. Finite element model is developed using four-noded rectangular conforming element. Tangent stiffness matrix is derived to implement Newton Raphson method. The concept of non-locality is adopted from the works of Eringen and Edelen (Int J Eng Sci 10:233, 1972 [2]). Parametric study has been conducted to investigate the effect of non-locality and non-linearity on the behaviour of laminated composites.

23.1 Introduction

The classical continuum theories have been used for decades to solve different kinds of boundary value problems. This approach assumes the material is continuously distributed and homogeneous at macroscale. At smaller length scales, it is proven that the material possesses in homogeneities and is not continuously distributed. The experimental results also suggest that conventional continuum approach is in adequate to model the material at smaller length scale such as

P. Raghu · A. Rajagopal (✉)
Civil Engineering Department, Indian Institute of Technology Hyderabad, Sangareddy, India
e-mail: rajagopal@iith.ac.in

A. A. Nasedkina · A. V. Nasedkin
I. I. Vorovich Institute of Mathematics, Mechanics and Computer Science, Southern Federal University, Rostov-on-Don, Russia

B. Saswata
Material Science and Metallurgical Engineering, Indian Institute of Technology Hyderabad, Sangareddy, India

I. A. Parinov et al. (eds.), *Advanced Materials*, Springer Proceedings in Physics 207, https://doi.org/10.1007/978-3-319-78919-4_23

nanoscale. At nanoscale, the materials' spatial dimensions are comparable to the internal characteristic lengths such as grain distance in which case the classical continuum analysis ceases to provide the accurate results. The other deficiencies of classical theory include negligence of microstructural size effect [3], mesh dependent results [4], singularity at crack tip [5]. Hence, the continuum descriptions must be enriched to obviate these discrepancies. The nonlocal approach is proven to overcome these discrepancies. The term nonlocal in nonlocal theories refers to the long range inter atomic that are taken into account in the constitutive relations. Eringen and Edelen [2] first gave the relationship between the local and nonlocal stress tensor through a Kernel function. This Kernel function depends on the internal and external characteristic lengths of the material. John et al. [6] first applied the nonlocal concept to structural mechanics applications. Jirásek et al. [7] explained how the classical theories can be enriched to deal with problems of size effects in microscale elasto-plasticity. Recently Reddy [8] gave the reformulated Euler-Bernouli, Timoshenko beam theories using nonlocal theories. Aydogdu [9] and Adhikari et al. [10] employed nonlocal models to investigate the small-scale effect on elastic rods.

Applications of laminated composite plates range from aerospace industry to sports industry. Accurate analysis is of paramount importance for effective utilizing the material strength and for the safe design. Since laminated composite plates possess low value of shear modulus, compared to Young's modulus, shear deformations are going to play significant effect on their behavior. Hence the correct description of kinematics is necessary to predict the response of the composites accurately. Classical theory does not account for the shear deformations hence cannot be used to analyze thick plates. On the other hand, first order shear deformation theory (FSDT) [11] takes into account shear deformation in a simple way that it needs shear correction factor. Whereas Reddy's TSDT [1] expands the displacement field up to third order, it gives the quadratic variation of transverse shear strains and shear stress. This kinematic description avoids the need for shear correction factor. Classical continuum theory takes into account exclusively the bulk, neglecting the contributions from the surface of the deformable body. However, surface effects predominantly affect the material behavior. Raghu et al. [12] presented the analytical solutions for laminated composite plates using nonlocal third-order shear deformation theory of Reddy considering surface stress effects. Preethi et al. [13] studied the effect of non-locality and non-linearity on the bending and free vibration behavior of rotating nanocantilever beams using finite element method. Mahmoud et al. [14] studied the effect of both non-locality and surface effects on the behavior of nanobeams using finite element method. Recently Barretta et al. [15] transfer the effect of non-locality on the viscoelastic functionally graded nanobeams, subjected to torsion. Ebrahimi et al. [16] used non-local strain gradient theory for the analysis of wave propagation in nanoplates.

23.2 Eringen's Nonlocal Model

In non-local theory, the effect of neighborhood is taken into account via the constitutive relations. The stress at a reference point is functional of strain at all neighboring points. The non-local and local stress tensor are related by an attenuating Kernel function. Eringen proposed a constitutive model that expresses the nonlocal stress tensor $\boldsymbol{\sigma}^{\mathrm{nl}}$ at point x as

$$\boldsymbol{\sigma}^{\mathrm{nl}} = \int \mathrm{K}(|x'-x|, \tau)\boldsymbol{\sigma}(x')dx', \tag{23.1}$$

where $\boldsymbol{\sigma}(x)$ is the classical macroscopic stress tensor at a point x and $\mathrm{K}(|x' - x|, \tau)$ is the Kernel function, which is normalized over the volume of the body represents the nonlocal modulus. $|x' - x|$ is the non-local distance and τ is the material constant that depends on the internal and external characteristic length.

As Hooke law, we have:

$$\boldsymbol{\sigma}(x) = \mathbf{C}(x) : \epsilon(x), \tag{23.2}$$

where ϵ is the strain tensor $\mathbf{C}$ is the fourth order elasticity tensor. Equations (23.1) and (23.2) together form the nonlocal constitutive equation for Hookean solid. Equation (23.1) can be represented equivalently in differential form as

$$(1-\tau^2 l^2 \nabla^2)\boldsymbol{\sigma}^{\mathrm{nl}} = \boldsymbol{\sigma}, \tag{3}$$

where $\tau = (e_0 a)^2/l^2$, e_0 is a material constant and a and l are internal and external characteristic lengths, respectively. In general, ∇^2 is the three dimensional Laplace operator. The nonlocal parameter μ can be taken as $\mu = \tau^2 l^2$.

23.3 Third-Order Shear Deformation Theory

In the third-order shear deformation theory (TSDT) of Reddy [1] the assumptions of the straightness and normality of the transverse normal after deformation are relaxed by expressing the displacements as cubic functions of thickness coordinate. Consequently, the transverse shear strains and shear stresses vary quadratically through the thickness of the laminate and avoid the need for shear correction factor. Here the Reddy's third-order theory is reformulated to account for the nonlocal effect. These nonlocal laminated plate theories allow for the small-scale effect, which becomes significant, when dealing with micro- and nano-plate like structures [8].

23.3.1 Displacement Field

The displacement field of Reddy's third order theory [1] is developed in such a way that the in-plane displacements are expanded up to the third degree of the thickness coordinate. This definition results in quadratic variation of shear strains and hence the shear stress. The transverse displacement is independent of thickness coordinate because it is assumed a transverse normal is inextensible:

$$u(x,y,z) = u_0(x,y) + z\phi_x - (4z^3/3h^2)(\phi_x + \partial w_0/\partial x); \tag{23.4}$$

$$v(x,y,z) = v_0(x,y) + z\phi_y - (4z^3/3h^2)(\phi_y + \partial w_0/\partial y); \tag{23.5}$$

$$w(x,y,z) = w_0(x,y), \tag{23.6}$$

where u_0, v_0, w_0 are the in-plane displacements of a point on the mid plane (i.e. $z = 0$); ϕ_x, ϕ_y denote the rotations of the transverse normal line at mid plane ($\phi_x = \partial u/\partial z$ and $\phi_y = \partial v/\partial z$). The total thickness of the laminate is given by h.

23.4 Equilibrium Equations

The non-local governing equations for TSDT can be derived, using the principle of virtual displacements and (3). They can be derived as follows:

$$\frac{\partial N_{xx}}{\partial x} + \frac{\partial N_{xy}}{\partial y} = 0; \tag{23.7}$$

$$\frac{\partial N_{xy}}{\partial x} + \frac{\partial N_{yy}}{\partial y} = 0; \tag{23.8}$$

$$\begin{aligned} &\frac{\partial \overline{Q_x}}{\partial x} + \frac{\partial \overline{Q_y}}{\partial y} + \frac{\partial}{\partial x}\left(N_{xx}\frac{\partial w_0}{\partial x} + N_{xy}\frac{\partial w_0}{\partial y}\right) + \frac{\partial}{\partial y}\left(N_{xy}\frac{\partial w_0}{\partial x} + N_{yy}\frac{\partial w_0}{\partial y}\right) \\ &\quad + c_1\left(\frac{\partial^2 P_{xx}}{\partial x^2} + 2\frac{\partial^2 P_{xy}}{\partial x \partial y} + \frac{\partial^2 P_{yy}}{\partial y^2}\right) = -q(1 - \mu\nabla^2) \end{aligned} \tag{23.9}$$

$$\frac{\partial \overline{M_{xx}}}{\partial x} + \frac{\partial \overline{M_{xy}}}{\partial y} - \overline{Q_x} = 0; \tag{23.10}$$

$$\frac{\partial \overline{M_{xy}}}{\partial x} + \frac{\partial \overline{M_{yy}}}{\partial y} - \overline{Q_y} = 0, \tag{23.11}$$

where

$$\overline{M_{\alpha\beta}} = M_{\alpha\beta} - c_1 P_{\alpha\beta}, \overline{Q_\alpha} = Q_\alpha - c_2 R_\alpha, c_1 = \frac{4}{3h^2}, c_2 = 3c_1; \tag{23.12}$$

$$\begin{Bmatrix} N_{\alpha\beta} \\ M_{\alpha\beta} \\ P_{\alpha\beta} \end{Bmatrix} = \int_{-\frac{h}{2}}^{\frac{h}{2}} \sigma_{\alpha\beta} \begin{Bmatrix} 1 \\ z \\ z^3 \end{Bmatrix} dz, \begin{Bmatrix} Q_\alpha \\ R_\alpha \end{Bmatrix} = \int_{-\frac{h}{2}}^{\frac{h}{2}} \sigma_{\alpha z} \begin{Bmatrix} 1 \\ z^2 \end{Bmatrix} dz. \tag{23.13}$$

23.5 Finite Element Model

The weak form for each governing equation can be derived and the finite element model is developed after substituting the displacement approximations in the weak form. The weak form suggests that the primary degree of freedom of Reddy's TSDT should be $u, v, w, \frac{\partial w}{\partial x}, \frac{\partial w}{\partial y}, \frac{\partial^2 w}{\partial x \partial y}, \phi_x, \phi_y$. The approximations for each of the primary degrees of freedom are as follows:

$$u \approx \sum_{j=1}^{m} U_j(t)\psi_j(x, y); \tag{23.14}$$

$$v \approx \sum_{j=1}^{m} V_j(t)\psi_j(x, y); \tag{23.15}$$

$$w \approx \sum_{j=1}^{m} \Delta_j(t)\phi_j(x, y); \tag{23.16}$$

$$\phi_x \approx \sum_{j=1}^{m} X_j(t)\psi_j(x, y); \tag{23.17}$$

$$\phi_y \approx \sum_{j=1}^{m} Y_j(t)\psi_j(x, y); \tag{23.18}$$

The Δ here denotes $(w, \frac{\partial w}{\partial x}, \frac{\partial w}{\partial y}, \frac{\partial^2 w}{\partial x \partial y})$ at each node of the finite element. Substitution of (23.14)–(23.18) in the weak forms of the governing equations will yield the discretized weak form as follows:

$$\begin{bmatrix} K^{11} & K^{12} & K^{13} & K^{14} & K^{15} \\ K^{21} & K^{22} & K^{23} & K^{24} & K^{25} \\ K^{31} & K^{32} & K^{33} & K^{34} & K^{35} \\ K^{41} & K^{42} & K^{43} & K^{44} & K^{45} \\ K^{51} & K^{52} & K^{53} & K^{54} & K^{55} \end{bmatrix} \begin{Bmatrix} U \\ V \\ \Delta \\ X \\ Y \end{Bmatrix} = \begin{Bmatrix} F^1 \\ F^2 \\ F^3 \\ F^4 \\ F^5 \end{Bmatrix}. \tag{23.19}$$

It is seen that (23.19) is non-linear in nature. To solve it, the Newton Raphson method is used. The tangent stiffness matrix can be derived using the below formula [17]:

$$T_{ij}^{\alpha\beta} = \frac{\partial R_i^{\alpha}}{\partial \Delta_j^{\beta}} = K_{ij}^{\alpha\beta} + \sum_{k=1}^{n} \frac{\partial K_{ik}^{\alpha\gamma}}{\partial \Delta_j^{\beta}} \Delta_k^{\gamma} - \frac{\partial F_i^{\alpha}}{\partial \Delta_j^{\beta}}. \tag{23.20}$$

23.6 Numerical Results

In this section, numerical examples are presented to investigate the effect of both nonlinearity and nonlocality on the behavior of laminated composite structure, subjected to transverse sinusoidal loading. The effect of *a/h* ratio and the integration rule is also presented. Different types of boundary conditions such as SS-1 and SS-2 are considered. A four-noded rectangular element is used in all examples. The tolerance value of error is fixed as 10^{-3}. The deflection is calculated at the center of the plate and non-dimensionalized as follows:

$$\overline{w} = \frac{w\left(\frac{a}{2}, \frac{b}{2}, 0\right) E_2 h^3}{q_0 a^4}. \tag{23.21}$$

Here q_0 is the intensity of transverse load and a, b, h are the length, width and thickness of the plate respectively. The following material properties typical of graphite epoxy composite laminate are used in all examples:

$$E_1/E_2 = 25, G_{12}/E_2 = 0.6, G_{23}/E_2 = 0.25, G_{12} = G_{13}, \upsilon_{12} = 0.25, \upsilon_{12} = \upsilon_{13}.$$

23.6.1 Boundary Conditions

Two kinds of boundary conditions are considered for the analysis, namely SS-1 (simply supported-1) and SS-2. Figures 23.1 and 23.2 show the SS-1 and SS-2 boundary conditions, respectively.

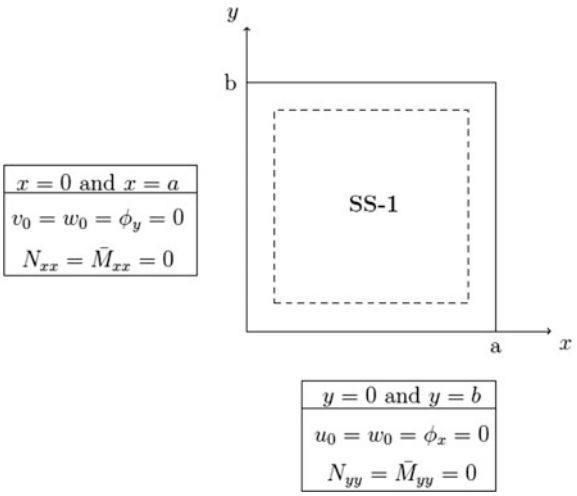

Fig. 23.1 SS-1 boundary conditions

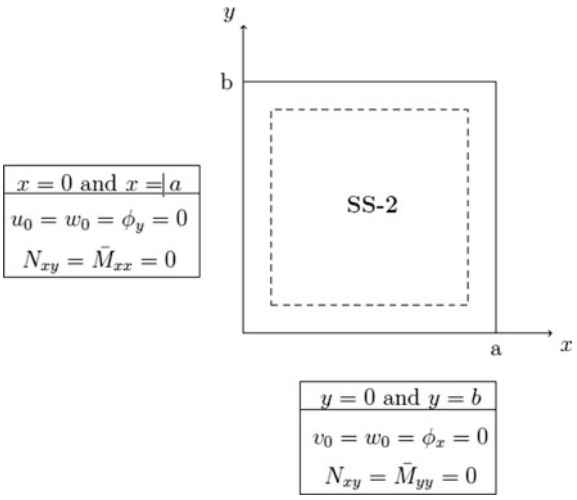

Fig. 23.2 SS-2 boundary conditions

23.6.2 Example 1

A four-layered plate of the orientation (0/90/0/90) with each layer having equal thickness is considered in this example. Both SS-1 and SS-2 boundary conditions are considered. The intensity of the sinusoidal load is considered as one.

Tables 23.1 and 23.2 show the non-dimensionalised deflection values with increasing values of nonlocal parameter for SS-2 and SS-1 boundary conditions. respectively. It has been clearly observed that the deflection value increases as the

Table 23.1 Effect of length scale parameter and integration rule on the non-dimensionalized deflection of SS-2 anti-symmetric cross-ply laminate

a/h	Source	$\overline{w}(\mu = 0)$	$\overline{w}(\mu = 1)$	$\overline{w}(\mu = 3)$	$\overline{w}(\mu = 5)$
10	4 by 4 (F)	0.57911	0.6934	0.922	1.1506
	4 by 4 (S)_	0.5859	0.7016	0.9329	1.16
	4 by 4 (R)	0.5895	0.7058	0.9385	1.1712
20	4 by 4 (F)	0.4531	0.5426	0.7215	0.9003
	4 by 4 (S)_	0.4632	0.5546	0.7375	0.9204
	4 by 4 (R)	0.4639	0.5554	0.7385	0.9217

F full integration, *S* selective integration, *R* reduced integration

Table 23.2 Effect of length scale parameter and integration rule on the non-dimensionalized deflection of SS-1 anti-symmetric cross-ply laminate

a/h	Source	$\overline{w}(\mu = 0)$	$\overline{w}(\mu = 1)$	$\overline{w}(\mu = 3)$	$\overline{w}(\mu = 5)$
10	4 by 4 (F)	0.7206	0.8628	1.1473	1.4317
	4 by 4 (S)_	0.7281	0.8719	1.1593	1.4468
	4 by 4 (R)	0.7342	0.8791	1.1690	1.4588
20	4 by 4 (F)	0.5	0.5987	0.7961	0.9935
	4 by 4 (S)_	0.5093	0.6098	0.8109	1.0119
	4 by 4 (R)	0.5104	0.6111	0.8126	1.0141

Table 23.3 Effect of nonlinearity and nonlocality on $\overline{w}$ of (45/−45) plate with SS-2 boundary conditions (4 by 4 mesh with selective integration is used)

Load value	Nonlinear		Linear	
	$\mu = 0$	$\mu = 1$	$\mu = 0$	$\mu = 1$
0.0125	0.0053	0.0058	0.0093	0.0111
0.05	0.0101	0.0108	0.0372	0.0446
0.1	0.0132	0.0142	0.0744	0.0891
0.5	0.0237	0.0253	0.3722	0.4457
1.0	0.03	0.0321	0.7445	0.8914

value of μ increases. It can also be observed that the effect of integration rule has very less effect on the value of the deflection. Therefore, there is no shear locking. As the value of *a/h* increases, the deflection decreases for the same value of μ.

23.6.3 Example 2

In this example, a two-layered plate of the orientation (45/−45) with each layer having equal thickness is considered in this example. SS-2 boundary conditions are considered. The intensity of the sinusoidal load is considered as one.

Table 23.3 shows the value of deflection with increasing load and increasing value of nonlocal parameter. As expected, the values of deflections both in the nonlinear and linear cases are closer in the initial ranges of load values. Again, it is observed that the deflection value increases as the value of μ increases for the given value of load.

23.7 Conclusions

The finite element formulation for the analysis of laminated composite plates is developed and implemented by using the third-order shear deformation theory and Eringen's nonlocality. It has been observed that the nonlocality and geometric nonlinearity have significant effect on the behavior of laminated composite plates.

Acknowledgements The authors would like to acknowledge the financial support of Indian-Russian Collaborative project grant from DST—RFBR (DST/INT/RFBR/IDIR/P-11/2016 and RFBR 16-58-48009 IND_omi).

References

1. J.N. Reddy, J. Appl. Mech. **51**, 745 (1984)
2. A.C. Eringen, D.G.B. Edelen, Int. J. Eng. Sci. **10**, 233 (1972)
3. Z.P. Bažant, M.D. Isaac, L. Zhengzhi, Trans. ASME **118**, 317 (1996)
4. Z.P. Bažant, J. Milan, Am. Soc. Civil Eng. **128**, 11 (2002)
5. Z. Zhen-Gong, H. Jie-Cai, D. Shan-Yi, Int. J. Solids Struct. **36**, 3891 (1999)
6. P. John, R.B. George, P.M. Richard, Int. J. Eng. Sci. **128**, 305 (2003)
7. M. Jirásek, Acta Polytech. **44**, 16 (2004)
8. J.N. Reddy, Int. J. Eng. Sci. **45**, 288 (2007)
9. M. Aydogdu, Phys. E **41**, 861 (2009)
10. S. Adhikari, T. Murmu, M.A. McCarthy, Phys. E **59**, 33 (2014)
11. R.D. Mindlin, ASME J. Appl. Mech. **18**, 31 (1951)
12. P. Raghu, K. Preethi, A. Rajagopal, J.N. Reddy, Compos. Struct. **139**, 13 (2016)
13. K. Preethi, P. Raghu, A. Rajagopal, J. N. Reddy, Mech. Adv. Mater. Struct. **1** (2017)
14. F. Mahmoud, M.A. Eltaher, A.E. Alshorbagy, E.I. Meletis, J. Mech. Sci. Technol. **26**, 3555 (2012)
15. R. Barretta, L. Feo, R. Luciano, Compos. B Eng. **72**, 217 (2015)
16. F. Ebrahimi, M.R. Barati, A. Dabbagh, Int. J. Eng. Sci. **107**, 169 (2016)
17. J.N. Reddy, *An Introduction to Nonlinear Finite Element Analysis* (Oxford University Press, Oxford, 2015)

Chapter 24
Comparative Study of Cantilever Carbon Nanotube with Carbon Nanotube System

Swati Agrawal, Brijesh Kumar Singh, Vipul Gupta, V. K. Gupta and P. K. Kankar

Abstract Carbon nanotube (CNT) is the allotrope of carbon, which resembles a rolled up graphite sheet capped with a fullerene molecule. One such system is achieved by using intermediate material (such as polymers) between two nanotubes. This idea enabled the path for simplest nanotube system i.e. a double single walled carbon nanotube system (DSWNTS) which has two single walled carbon nanotubes, attached together by a continuous elastic medium. In this study, we investigated the comparison between the performance of a single walled carbon nanotube (SWCNT) and a DSWNTS. The governing equations are derived using modified couple stress theory (MCST) based on vibrational principle approach. Transverse deflection due to point load at the end of the cantilever is calculated using the finite element simulations and are compared with the analytical solution. Such a comparative study can be a base to understand the behaviour of CNT systems clearly and to know their feasibility to be used for sophisticated applications.

24.1 Introduction

Since the discovery of rolled up honeycomb lattice of carbon atoms i.e. carbon nanotube (CNT) in 1991 by Iijima [1], it has drawn focus of nano area researchers due to their characteristic physical properties and potential applications. Extensive research in both theoretical and experimental aspects of CNTs is continued up-to-date. The elastic properties in graphite and CNTs are produced by three kinds of forces between carbon atoms. The atomic forces consist of α-bonding and π-bonding forces between interlayer carbon-carbon bonds and weak interlayer attraction.

S. Agrawal (✉) · B. K. Singh · V. Gupta · V. K. Gupta · P. K. Kankar
Machine Dynamics and Vibrations Laboratory, Mechanical Engineering Discipline, PDPMIIITDM, Jabalpur, India
e-mail: swatiagrawal.iit@gmail.com

I. A. Parinov et al. (eds.), *Advanced Materials*, Springer Proceedings in Physics 207, https://doi.org/10.1007/978-3-319-78919-4_24

Lau and Hui [2] and Thostenson et al. [3] have presented a compressive review on production, physical properties recent advances and applications of CNTs and their composites. The atomic structure, morphology, fabrication, characterization, mechanical properties and mechanics of CNTs are reported. Dresselhaus et al. [4] have reviewed and presented fundamental parameters of CNTs along with the basic relation governing these parameters and typical numerical values of these parameters. Lu [5] used an empirical force constant model to investigate elastic properties of CNTs. The elastic properties of single walled carbon nanotubes (SWCNTs) were insensitive to the radius, chirality, and number of walls.

The finite element (FE) models for various cases of SWCNT are discussed in literature [6–14]. Most of the analyses about modified and degenerated CNTs were discussed in a review [15] to highlight the continuous advancements in the field. All the above stated applications exploit the in depth knowledge of static as well as dynamic behaviour of CNTs. The experiments, which can best describe the behaviour and response to various physical entities of such nano-structures are actually time and cost intensive. Operating with small size precisely is very difficult. To complement this shortage, a lot of discrete and continuum models are being designed. Numerical solution techniques may be quantum molecular mechanics, theoretical calculations (ab initio), Monte Carlo, and molecular dynamics (MD) simulation methods. MD simulation method [16] has attracted much attention due to accuracy and realistic results but the errors made in numerical integration cannot be eliminated entirely. All this needs too much computational cost, time and data bundle. Continuum modelling is, therefore, best and most adopted so as to overcome all above mentioned difficulties [17, 18]. Classical continuum theories are good for structures at macro or micro scale because there is no provision to consider the small length scale effect. There have been many non-classical theories, which consider the size effect but authors find modified couple stress theory (MCST) to be the best due to only one small scale parameter and symmetric couple stress tensor [19]. Significant research has been reported to study the nano/micro structures, oriented to various applications, including sensing [20–22]. An important and promising direction to enhance the electronic properties and the sensing characteristics is to use intermediate materials between two carbon nanotubes. Such a combination is known as complex nanotube system, which may have any arrangement. One of them was given by Murmu and Adhikari [23], known as double single walled carbon nanotube system (DSWNTS), in which two SWCNTs are connected in parallel by an elastic medium. Natural frequency was studied in this study using nonlocal theory.

None of the papers are found by authors, which present a clear comparison between the transverse deflection (static analysis) of SWCNT and DSWNTS obtained by FE simulation and that obtained by analytical method. More specifically, no one has used MCST for this purpose. The primary purpose of the work presented here is to fill this gap. The present study focuses on the deflection behaviour of cantilever type SWCNT and DSWNTS. In the process of analytical analysis, SWCNTs are considered as continuous Euler Bernoulli beams of circular cross-section. In DSWNTS, two SWCNTs are assumed to be separated by

distributed vertical transverse springs. Governing equation for static analysis is derived and transverse deflection is plotted. The same is done using FE simulation and results are compared. The paper also presents the FE model for both the cases.

24.2 Problem Statement

The study presented here is a combination of nanotubes DSWNTS (Fig. 24.1), which is assumed equivalent to double nano beam system (DNBS) [24]. In DSWNTS, two single walled carbon nanotubes (SWCNT-1 and SWCNT-2) of the same mass (m), length (L), density (ρ) and bending rigidity (EI) are coupled with an elastic medium filled between them. The elastic medium is considered as number of vertically distributed springs. The equivalent stiffness of elastic medium

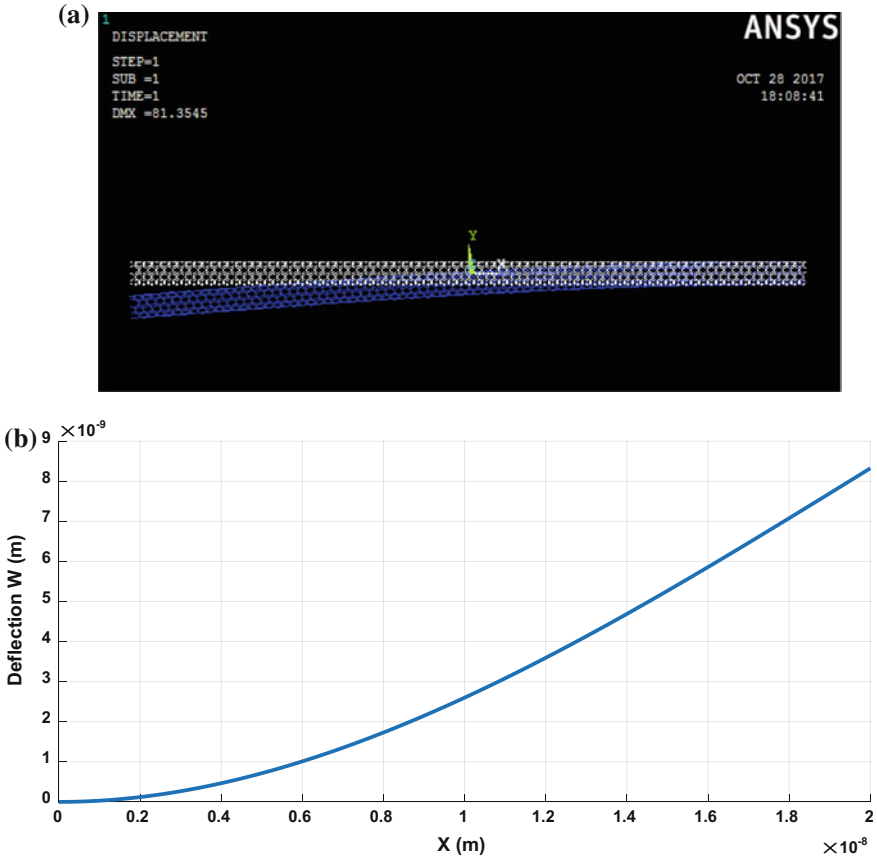

Fig. 24.1 Transverse deflection in SWCNT: **a** ANSYS simulation, **b** analytical method

is given as K. The nanotubes are considered equivalent to Euler Bernoulli beams. The transverse displacements are denoted by w_1 and w_2, respectively.

The Cartesian coordinate system (x, y, z) is taken for the modelling, where x-axis is coincident with the centroidal axis of the undeformed nanobeam, z-axis is the axis of symmetry and y-axis is neutral axis. If u, v and w are the components of displacement vector $\mathbf{u}$ in x, y and z directions, then:

$$u = -z\psi(x) \quad v = 0 \quad w = w(x) \tag{24.1}$$

where, ψ is the angle of rotation of x-axis and is given by

$$\psi \approx \frac{dw(x)}{dx} \tag{24.2}$$

The system is analysed using MCST to consider the effect of the small size. The MCST is explained in the following section together with mathematical modelling.

24.3 Mathematical Model

Yang et al. [19] were the first to propose the idea of MCST in 2002. According to it, for a three dimensional linear elastic body of volume Ω, the strain energy density function is written as

$$U = \frac{1}{2}\int_{\Omega} \left(\sigma_{ij}\varepsilon_{ij} + m_{ij}\gamma_{ij}\right) d\Omega \tag{24.3}$$

It is a function of stress and strain both conjugated with strain and curvature, respectively. Here, σ_{ij} is the generalized hook's law in tensorial/indicial form, ε_{ij} is the strain tensor, m_{ij} represents the deviatoric part of couple stress tensor and γ_{ij} represents the symmetric curvature tensor. These terms have obvious meanings as described in [20]. Here, the term m_{ij} contains the material length scale parameter, l.

Using (24.3), the strain energy density function is calculated by substituting stress, strain, couple stress tensor and curvature tensor in it. It may be seen in literature [20] that for a SWCNT, the governing equation is given by [20] to find out the transverse deflection u, in case of free vibration:

$$\left(\mathrm{EI} + \mu A l^2\right)\frac{d^4 w}{dx^4} = 0 \tag{24.4}$$

The term $\left(\mathrm{EI} + \mu A l^2\right)$ depicts the effect of non-classical theory.

For a DSWNTS, the strain energy density function is written as

$$U = -\frac{1}{2}\int_{x=0}^{L} M_{c_1}\frac{d^2w_1}{dx^2}dx - \frac{1}{2}\int_{x=0}^{L} M_{c_2}\frac{d^2w_2}{dx^2}dx + \frac{1}{2}K(w_1 - w_2)^2 \tag{24.5}$$

where,

$$M_{c_i} = M_{x_i} + Y_{xy_i} = -\left(EI + \mu A l^2\right)\frac{\partial^2 w_i}{\partial x^2} \tag{24.6}$$

The external forces do the work in the absence of body couple and body forces is given by

$$W = \int_{x=0}^{L} q(x)w_1(x)dx + \int_{x=0}^{L} q(x)w_2(x)dx \tag{24.7}$$

Applying the minimum potential energy principle, the governing equation of motion for DSWNTS is:

$$\left(\mathrm{EI} + \mu A l^2\right)\frac{d^4w}{dx^4} + 2Kw = 0 \tag{24.8}$$

The boundary conditions at the two ends of a cantilever SWCNT and DSWNTS are given as

$$\frac{dw}{dx} = 0; \quad at\ x = L \tag{24.9a}$$

$$w = 0; \quad at\ x = L \tag{24.9b}$$

$$\frac{d^2w}{dx^2} = 0; \quad at\ x = 0 \tag{24.9c}$$

$$\frac{d^3w}{dx^3} = -P; \quad at\ x = 0 \tag{24.9d}$$

The idea of solving the two governing equations for a cantilever case is caused by that the cantilever type beams possess the better sensing characteristics. It is so because it can be work in various environments like vacuum, liquid or air. Moreover, it possesses high sensitivity, fast response times and direct transduction without the need for any labels. The solutions of (24.4) and (24.8) draw the static responses of the system for SWCNT and DSWNTS, respectively. This is achieved by using method of separation of variables.

24.4 Finite Element Model

A three-dimension (3D) FE model of SWCNTs was proposed by Tserpes and Papanikos [6]. They investigated the influence of tube wall thickness, diameter and chirality on the elastic moduli of SWCNTs. The choice of wall thickness affects the Young's modulus significantly. The elastic moduli of the SWCNTs increased as the tube diameter increases. The FE model proposed here may be used for studying the mechanical behaviour of CNTs and CNT-based systems. Kirtania and Chakraborty [7] evaluated the coefficient of thermal expansion, Young's modulus and shear modulus of graphene sheet and SWCNTs using FE method. They reported the increase in the Young's modulus of graphene sheet with the increase in the size of the graphene sheet. Based on molecular mechanics for predicting mechanical behaviours of SWCNTs, Lu and Hu [8] developed an improved 3D FE model of armchair, zigzag and chiral SWCNTs. They investigated the effects of diameters, chirality and wall thickness on elastic stiffness of SWCNTs. FE modelling of SWCNT was also presented [9–11] in different ways. There are some studies on the fracture behaviour of isolated CNT in literatures [12–14] on the nano scale. Tserpes et al. [12] proposed atomistic-based progressive fracture model for simulation of the mechanical performance of SWCNTs. FE analysis of defective SWCNT has been performed by applying axial tension. Fracture mechanism in CNT-reinforced composites was briefly discussed by Thostenson and Chou [13]. The study of SWCNT based on a rod model including in-plane cross-sectional deformation is also done [14]. The FE analysis of CNTs and its spring system i.e. their mechanical properties are discussed. In this section, FE modelling of SWCNT and DSWNTS is performed with the help of shape functions and weighted residual method.

24.4.1 Evaluation of Shape Functions

Boundary conditions for both SWCNT and DSWNTS of cantilever type can be given by (24.9a)–(24.9d). The first two boundary conditions of equation (24.9a, b) enforce zero slope and zero displacement at fixed end, respectively, and the last two boundary conditions of equation (24.9c, d) prescribe zero bending moment and load at free end.

For calculating the value of shape functions for both SWCNT and DSWNTS, a trial function is assumed so that it should be differentiable at least four times:

$$w(x) = a + bx + cx^2 + dx^3 \tag{24.10}$$

where u_1 stands for deflection at free end i.e.

$$at\ x = 0;\ w = w_1 \tag{24.11a}$$

where θ_1 stands for angle of deflection at free end i.e.

$$at \;\; x = 0; \;\; \theta = \theta_1 \tag{24.11b}$$

where w_2 stands for deflection at fixed end i.e.

$$at \;\; x = L; \;\; w = w_2 \tag{24.11c}$$

where θ_2 stands for angle of deflection at fixed end i.e.

$$at \;\; x = L; \;\; \theta = \theta_2 \tag{24.11d}$$

Evaluating the value of constants a, b, c, and d in terms of w_1, w_2, θ_1 and θ_2 by substituting the boundary condition (24.11a)–(24.11d) and again substituting it in (24.10). After substituting and separating the coefficients of w_1, w_2, θ_1 and θ_2, shape functions for SWCNT and DSWNTS are obtained as

$$w(x) = N_1 w_1 + N_2 \theta_1 + N_3 w_2 + N_4 \theta_2 \tag{24.12}$$

where

$$N_1 = 1 - \frac{3x^2}{L^2} + \frac{2x^3}{L^3} \tag{24.13a}$$

$$N_2 = x - \frac{2x^2}{L} + \frac{x^3}{L^2} \tag{24.13b}$$

$$N_3 = \frac{3x^2}{L^2} - \frac{2x^3}{L^3} \tag{24.13c}$$

$$N_4 = -\frac{x^2}{L} + \frac{x^3}{L^2} \tag{24.13d}$$

24.4.2 Evaluation of Weak Form of FE Model

Now, the weak form of the FE model is present for both SWCNT and DSWNTS. When an integral function is solved instead of solving a differential equation of the problem; it is known as weak form. The integral function contains the differential equations. Solving an integral function is much easier than solving a differential function.

Moreover, the differential equation of system poses conditions that must be satisfied by the solution, hence it is called strong form. On the other hand, the integral equation states that those conditions need to be satisfied in an average sense, hence it is called weak form. Following section presents the weak form for FE model of SWCNT.

Let $u(x)$ is the presumed trial function and let $W(x)$ is the weighting function. By using (24.1), the weighted residual equation can be written as

$$\int_0^L W(x)\left[\left(\mathrm{EI}+\mu A l^2\right)\frac{d^4w}{dx^4}\right]dx=0 \tag{24.14}$$

By integrating (24.8), following equations are obtained

$$\left[\left(\mathrm{EI}+\mu A l^2\right)\frac{d^3w}{dx^3}W(x)\right]_0^L-\int_0^L\frac{dW(x)}{dx}\left[\left(\mathrm{EI}+\mu A l^2\right)\frac{d^3w}{dx^3}\right]dx=0 \tag{24.15}$$

$$[-P\,.\,W(x)]_0^L-\int_0^L\frac{dW(x)}{dx}\left[\left(\mathrm{EI}+\mu A l^2\right)\frac{d^3w}{dx^3}\right]dx=0 \tag{24.16}$$

$$\left[-\frac{dW(x)}{dx}\left(\mathrm{EI}+\mu A l^2\right)\frac{d^2w}{dx^2}\right]_0^L+\int_0^L\frac{d^2W(x)}{dx^2}\left[\left(\mathrm{EI}+\mu A l^2\right)\frac{d^2w}{dx^2}\right]dx=[P\,.\,W(x)]_0^L \tag{24.17}$$

After applying the essential boundary condition (24.9a)–(24.9d) in (24.14), weak form can be obtained as

$$\int_0^L\frac{d^2W(x)}{dx^2}\left[\left(\mathrm{EI}+\mu A l^2\right)\frac{d^2w}{dx^2}\right]dx=[P\,.\,W(x)]_0^L \tag{24.18}$$

The weighting functions can be written as

$$W_1=1-\frac{3x^2}{L^2}+\frac{2x^3}{L^3} \tag{24.19a}$$

$$W_2=x-\frac{2x^2}{L}+\frac{x^3}{L^2} \tag{24.19b}$$

$$W_3=\frac{3x^2}{L^2}-\frac{2x^3}{L^3} \tag{24.19c}$$

$$W_4=-\frac{x^2}{L}+\frac{x^3}{L^2} \tag{24.19d}$$

After substituting the weighting functions one by one in (24.18), final FE model for SWCNT can be obtained as

$$\left(\mathrm{EI}+\mu Al^2\right)\begin{bmatrix} \frac{12}{L^3} & \frac{6}{L^2} & -\frac{12}{L^3} & \frac{6}{L^2} \\ \frac{6}{L^2} & \frac{4}{L} & -\frac{6}{L^2} & \frac{2}{L} \\ -\frac{12}{L^3} & -\frac{6}{L^2} & \frac{12}{L^3} & -\frac{6}{L^2} \\ \frac{6}{L^2} & \frac{2}{L} & -\frac{6}{L^2} & \frac{4}{L} \end{bmatrix}\begin{bmatrix} w_1 \\ \theta_1 \\ w_2 \\ \theta_2 \end{bmatrix} = \begin{bmatrix} P \\ 0 \\ 0 \\ 0 \end{bmatrix} \tag{24.20}$$

Now, the weak form FE model of DSWNTS is constructed in this portion. Let $u(x)$ is the presumed trial function and let $W(x)$ is the weighting function. By using (24.8), the weighted residual equation can be written as

$$\int_0^L W(x)\left[\left(\mathrm{EI}+\mu Al^2\right)\frac{d^4u}{dx^4}+2kw\right]dx=0 \tag{24.21}$$

$$\left[\left(\mathrm{EI}+\mu Al^2\right)\frac{d^3w}{dx^3}W(x)\right]_0^L-\int_0^L\frac{dW(x)}{dx}\left[\left(\mathrm{EI}+\mu Al^2\right)\frac{d^3w}{dx^3}\right]dx+2k\int_0^L W(x)wdx=0 \tag{24.22}$$

$$\begin{aligned}&[-P\,.\,W(x)]_0^L-\int_0^L\frac{dW}{dx}\left[\left(\mathrm{EI}+\mu Al^2\right)\frac{d^3w}{dx^3}\right]dx\\&+2k\int_0^L W(x)wdx=0\end{aligned} \tag{24.23}$$

$$\begin{aligned}&\left[-\frac{dW(x)}{dx}\left(\mathrm{EI}+\mu Al^2\right)\frac{d^2w}{dx^2}\right]_0^L+\int_0^L\frac{d^2W(x)}{dx^2}\left[\left(\mathrm{EI}+\mu Al^2\right)\frac{d^2w}{dx^2}\right]dx\\&+2k\int_0^L W(x)wdx=[P\,.\,W(x)]_0^L\end{aligned} \tag{24.24}$$

After applying the essential boundary condition (24.3) in (24.24), weak form can be obtained as

$$\int_0^L\frac{d^2W}{dx^2}\left[\left(\mathrm{EI}+\mu Al^2\right)\frac{d^2w}{dx^2}\right]dx+2k\int_0^L W(x)wdx=[P.W(x)]_0^L \tag{24.25}$$

Then weighting functions can be written as

$$W_1 = 1 - \frac{3x^2}{L^2} + \frac{2x^3}{L^3} \tag{24.26a}$$

$$W_2 = x - \frac{2x^2}{L} + \frac{x^3}{L^2} \tag{24.26b}$$

$$W_3 = \frac{3x^2}{L^2} - \frac{2x^3}{L^3} \tag{24.27}$$

$$W_4 = -\frac{x^2}{L} + \frac{x^3}{L^2} \tag{24.28}$$

After substituting the weighting functions from (24.28) one by one in (24.25), the final FE model for DSWNTS can be obtained as

$$\left[\left(\mathrm{EI} + \mu A l^2\right)\begin{bmatrix} \frac{12}{L^3} & \frac{6}{L^2} & -\frac{12}{L^3} & \frac{6}{L^2} \\ \frac{6}{L^2} & \frac{4}{L} & -\frac{6}{L^2} & \frac{2}{L} \\ -\frac{12}{L^3} & -\frac{6}{L^2} & \frac{12}{L^3} & -\frac{6}{L^2} \\ \frac{6}{L^2} & \frac{2}{L} & -\frac{6}{L^2} & \frac{4}{L} \end{bmatrix} + 2k\begin{bmatrix} \frac{13L}{35} & \frac{11L^2}{210} & \frac{9L}{70} & -\frac{13L^2}{420} \\ \frac{11L^2}{210} & \frac{L^3}{105} & \frac{13L^2}{420} & -\frac{L^3}{140} \\ \frac{9L}{70} & \frac{13^2}{420} & \frac{13L}{35} & -\frac{11L^2}{210} \\ -\frac{13L^2}{420} & -\frac{L^3}{140} & -\frac{11L^2}{210} & \frac{L^3}{105} \end{bmatrix}\right]\begin{bmatrix} w_1 \\ \theta_1 \\ w_2 \\ \theta_2 \end{bmatrix} = \begin{bmatrix} P \\ 0 \\ 0 \\ 0 \end{bmatrix} \tag{24.29}$$

24.5 Finite Element Simulation

The covalent bonds among the carbon atoms of a CNT help to form a hexagonal lattice. All the bonds possess a specific bond angle and a bond length in space. These atomic bonds constrain the displacement of the carbon atoms, caused by any external force. So, the interaction among the bonds causes the resultant deformation of the CNT. Here, CNTs are considered as space-frame structures. In this process, bonds as assumed as load carrying members and atoms are considered as joints of connecting members. The mechanical behaviour of CNTs can be analysed using structural mechanics methods. The ANSYS commercial FE code is used to develop three-dimension FE model. The bonds are modelled as 3D elastic element BEAM188 of ANSYS. BEAM188 is a uniaxial element, which is able to deal with axial, bending and torsion related solution capabilities. The six degrees of freedom at each node comprise of three translations and three rotations, each about nodal x, y and z-axes. Together with nodes, element is defined by two dimensions, two moments of inertia, and material properties and cross-section area of the element.

The constitutional element of CNT is a hexagon, which is considered as space-frame based structural element while simulating. The same process is adopted to simulate entire CNT. The element length of each C–C bond is considered as L_e. The coordinates of the carbon atoms are used by FE model to create the nodes and beam elements are generated by appropriate connection of the node. Initially, one beam element per bond was used to compare the stiffness matrices. However, convergence tests showed that there is not much variation in the result, if more elements are used. The size of the FE model has 1620 elements for the armchair CNT of chirality (5, 5) and length L = 20 nm.

24.6 Result and Discussion

24.6.1 SWCNT

The maximum transverse deflections in cantilever SWCNT are represent in Fig. 24.1a, b. The properties of armchair SWCNT of chirality (5, 5) are taken as length of SWCNT = 20 nm, radius of 0.34 nm, elastic modulus of 1TPa, poisons ratio of 0.3 and density of 2300 kg/m^3. Under a point load of 1 nN at the free end of SWCNT, it is found out as 8.1 nm. This is ANSYS simulation result, represented in Fig. 24.1a. For the same SWCNT, the analytical solution, presented in Fig. 24.1b, gives the transverse deflection at free end equal to 8.32 nm. Obviously, the analytical and simulation results show a good agreement.

24.6.2 DSWNTS

The transverse deflection of a cantilever type DSWNTS is present in Fig. 24.2. It has two SWCNTs connected in parallel with the same properties as given in Sect. 24.6.1. The result of ANSYS simulation, shown in Fig. 24.1a, is compared with that of analytical results shown in Fig. 24.1b. Under point load of 1 nN at the free end, the transverse deflection of DSWNTS is obtained as 2.51 nm. With the same load, the analytical value turns out as 3.28 nm.

Even a better comparison can be drawn if the results from FE model, presented in Sect. 24.4, are evaluated. It is so because this FE model considers the CNTs as Euler–Bernoulli beam, similar to analytical method; whereas FE simulation studies the CNT directly without considering it as a beam. It can be deduced here that, analytical method to derive the governing equation using MCST is quite efficient for analysing the nanosystems.

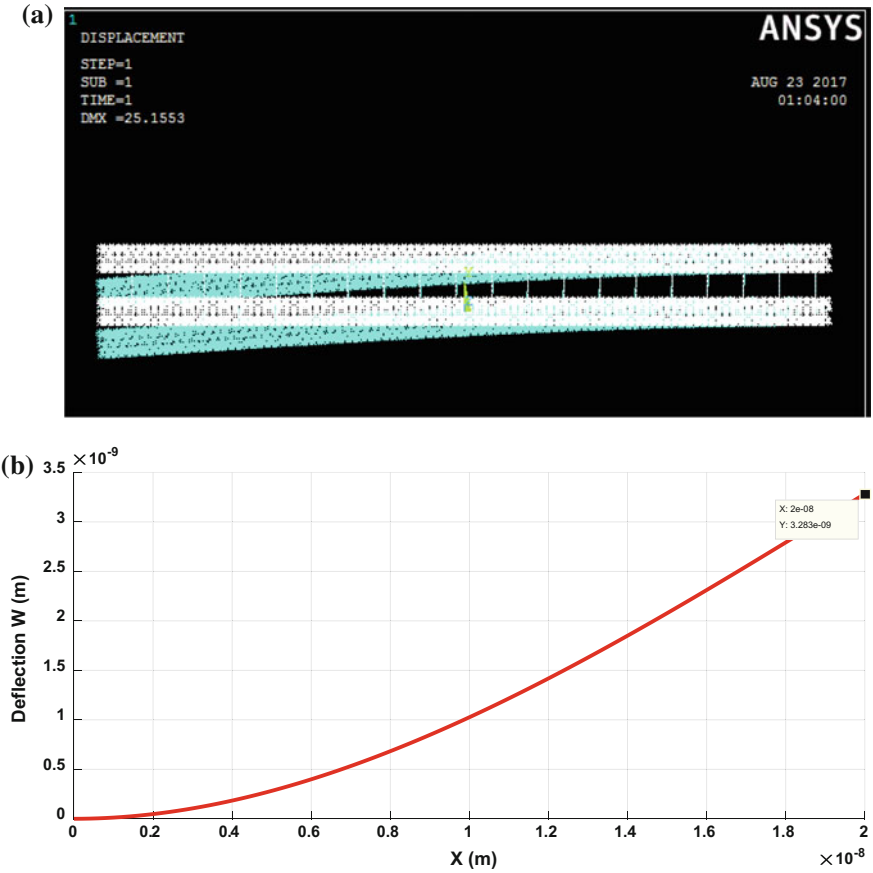

Fig. 24.2 Transverse deflection in DSWNTS: **a** ANSYS simulation, **b** analytical method

24.7 Conclusions

In the work presented, a mathematical model to study transverse deflection of SWCNT and DSWNTS is developed. Finite element model is presented for the same model. SWCNT and DSWNTS are modelled using nanotube modelling software and studied using ANSYS. The results show a good agreement between analytical and ANSYS simulation results. The transverse deflection in the case of SWCNT is more as compared to DSWNTS. This implies that SWCNT will have lesser resonating frequency as compared to that of DSWNTS. It means DSWNTS is a better design as a resonator, to be opted for biosensor. This model is useful to design a biosensor, to be operated anywhere for judging the presence of any bio-molecules. This analytical model might be useful for further static analysis of other similar numerical or experimental models. This can be further extended for dynamic analysis.

References

1. S. Iijima, Nature **34**, 56 (1991)
2. K.T. Lau, D. Hui, Compos. B **33**(4), 263 (2002)
3. E.T. Thostenson, Z. Ren, T.W. Chou, Compos. Sci. Technol. **61**(13), 1899 (2001)
4. M.S. Dresselhaus, G. Dresselhaus, R. Saito, Carbon **33**(7), 883 (1995)
5. J.P. Lu, Phys. Rev. Lett. **79**(7), 1297 (1997)
6. K.I. Tserpes, P. Papanikos, Compos. B **36**(5), 468 (2005)
7. S. Kirtania, D. Chakraborty, J. Reinf. Plast. Compos. **26**(15), 1557 (2007)
8. X. Lu, Z. Hu, Compos. B **43**(4), 1902 (2012)
9. J.H. Rangel, W. Brostow, V.M. Castano, Polimery **58**(4), 276 (2013)
10. C. Fang, A. Kumar, S. Mukherjee, J. Appl. Mech. **78**, 034502 (2011)
11. X.L. Gao, K. Li, Int. J. Solid Struct. **40**, 7329 (2003)
12. K.I. Tserpes, P. Papanikos, S.A. Tsirkas, Compos. B **37**(7–8), 662 (2006)
13. E.T. Thostenson, T.W. Chou, in *Fracture of Nano and Engineering Materials and Structures*, ed. by E.E. Gdoutos (Springer, Dordrecht, 2006), p. 95
14. C. Fang, A. Kumar, S. Mukherjee, Int. J. Solids Struct. **50**(1), 49 (2013)
15. S.I. Yengejeh, S.A. Kazemi, A. Ochsner, Compos. B **86**, 95 (2016)
16. H.A. Wu, Z.H. Sun, Q. Cheng, X.X. Wang, J. Phys. Conf. Ser. **61**, 1266 (2007)
17. M. Mir, A. Hosseini, G.H. Majzoobi, Comput. Mater. Sci. **43**, 540 (2008)
18. C. Li, T.W. Chou, Int. J. Solids Struct. **40**(10), 2487 (2003)
19. D.C.C. Lam, F. Yang, A.C.M. Chong, J. Wang, P. Tong, J. Mech. Phys. Solids **51**(8), 1477 (2003)
20. S.K. Park, X.L. Gao, J. Micromech. Microeng. **16**, 2355 (2006)
21. S.K. Park, X.L. Gao, Z. Angew, Math. Phys. (ZAMP) **59**, 904 (2008)
22. M. Mohandes, A.R. Ghasemi, in *Proceedings of the Institution of Mechanical Engineers*, *Part C: Journal of Mechanical Engineering Science* (2016), p. 1
23. T. Murmu, M.A. McCarthy, S. Adhikari, J. Appl. Phys. **111**, 113511 (2012)
24. T. Murmu, S. Adhikari, J. Appl. Phys. **108**, 083514 (2010)

Chapter 25
On Free Vibration Analysis of FGPM Cylindrical Shell Excited Under d_{15} Effect

Sandeep Kumar Parashar and Amit Gahlaut

Abstract Piezoelectric vibrating shell is the major component of the various equipments related to mechanical, nuclear, aeronautical and aerospace engineering. Shells especially exhibit certain effects that are not present in beams or even in plates. Analysis of vibrational characteristics of functionally graded piezoelectric circular cylindrical shell is quit complex than beams and plates. This is because the coupling of vibration of shell between the three directions can no longer be neglected. Dynamic analysis of FGPM continuum is quite complex, due to the synchronization of electric and mechanical terms. Closed form solution for complex FGPM model by analytical method is quite a tedious task. Approximation method provides an alternate path for solving such kind of problems. Paper contains free vibration analysis of a full three dimensional FGPM cylindrical shell model excited under d_{15} effect. Shear piezoelectric coupling coefficient d_{15} is much higher than the other piezoelectric coefficients d_{31} or d_{33}. Rayleigh–Ritz, an approximation method, is used to obtain the eigenvectors and eigenfrequencies for FGPM cylindrical shell. Orthogonal polynomial functions are used with Rayleigh–Ritz method to formulate the linear eigenvalue problem. Higher order polynomials are generated by Gram–Schmidt method. MATLAB 2015a Symbolic Toolbox is used for calculation and obtained solution is validated using commercial finite element software COMSOL Multiphysics 2014.

25.1 Introduction

Piezoelectricity is a direct conversion of mechanical load to electric field and vice versa. Various class and categories of piezoelectric materials are available at present. Rochelle salt, tourmaline, topaz and quartz are some natural piezoelectric crystals. These have low scale conversion capacity. For enhancing the strength and

S. K. Parashar · A. Gahlaut (✉)
Mechanical Engineering Department, Rajasthan Technical University, Kota, Rajasthan, India
e-mail: agahlaut333@gmail.com

I. A. Parinov et al. (eds.), *Advanced Materials*, Springer Proceedings in Physics 207, https://doi.org/10.1007/978-3-319-78919-4_25

capabilities of piezoelectric effect, many crystals are synthesized in laboratories. Artificial crystals provide better control over the energy conversion rate. Lead Zirconate Titanate (PZT), Langasite ($La_3Ga_5SiO_{14}$) and Barium Titanate ($BaTiO_3$) are some famous artificial piezoelectric materials.

At present, piezoelectricity belongs to the second biggest application field of dielectric materials, just after semiconductors. Nowadays, pure piezoelectric materials have limited use in the engineering applications because of conflicting property requirements. Functionally graded technique is used for enhancing the smartness of the components such as automotive sensors, foetal heart monitors, hydrophones, ultrasonic actuators etc. Wide range of application of the FGPM makes it more promising field and has attracted many scholars working on it.

In the past, various methodologies were adopted to analyze the vibration phenomenon of cylindrical shell such as, Love's first approximation theory, Donnell's approximate theory, Flügge's theory, Reissner's linear theory of thin shell, Sander's first-order approximation theory, Lur'ye-Flugge-Byrne second-order approximation theory, finite element method, Fourier series expressions, differential quadrature method and power series expansion approach. In majority of above mentioned traditional methodologies, different kind of assumptions are adopted to simplify the equations of the motion so that the complexity can be reduced. Consequently, the results obtained have limited validity, reliability and accuracy due to restriction, imposed on behaviour of model by such assumptions. Utility of these results have limited application domain for some specific geometrical restrictions and boundary conditions. Attributing to these facts, a full three-dimensional model of FGPM cylindrical shell is being formulated in the present work.

In the present work, Rayleigh–Ritz, an approximate method is used to obtain the eigenvectors and eigenfrequencies for functionally graded piezoelectric cylindrical shell. Bhat [1] introduced the orthogonal polynomial in Rayleigh–Ritz method for vibration analysis of simple plate structure and got sumptuous level of accuracy. Rayleigh–Ritz method, by orthogonalization of the polynomials using Gram-Schmidt process shows numerically stable process, high convergence rate and precise solution for the higher modes. Orthogonal polynomial function satisfying geometric boundary conditions are used here with Rayleigh–Ritz method to formulate the linear eigenvalue problem.

25.2 Modeling

In this section, first, the linear constitutive relations are obtained in cylindrical coordinate system for FGPM cylindrical shell. Then, kinetic and potential energy expressions are derived and further utilized in Rayleigh–Ritz formulation. Let

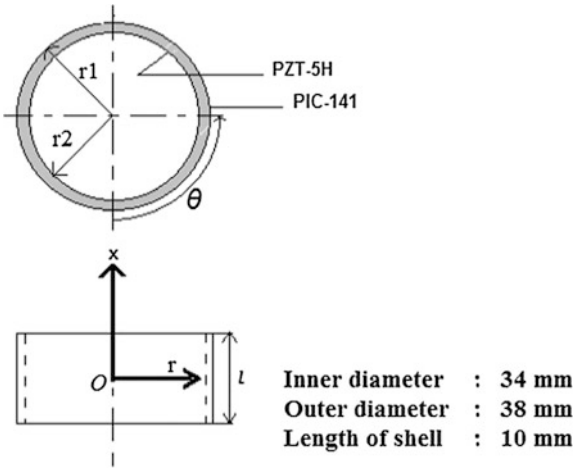

Fig. 25.1 Axially polarized FGPM cylindrical shell

displacement in r, θ and z directions be $u(r, \theta, z, t)$, $v(r,\theta, z, t)$, and $w(r, \theta, z, t)$, respectively. In Fig. 25.1, indices r or 1 are used for radial direction while θ or 2 for circumferential direction and z or 3 represents axial direction.

25.2.1 Linear Constitutive Equations

The linear constitutive relations [2] in the case of direct piezoelectric effect for functionally graded piezoelectric materials can be written as

$$\{T\} = \left[C^E\right]\{S\} - [e]^T\{E\} \quad \text{and} \quad \{D\} = [e]\{S\} + \left[\varepsilon^S\right]\{E\}. \tag{25.1}$$

In the case of converse piezoelectric effect linear constitutive relations can be expressed as

$$\{S\} = \left[s^E\right]\{T\} - [d]^T\{E\} \quad \text{and} \quad \{D\} = [d]\{T\} + \left[\varepsilon^T\right]\{E\}. \tag{25.2}$$

where T, C, S, e, E, D and ε represent stress vector (N/m^2), stiffness coefficient matrix (N/m^2), strain vector, piezoelectric constants (C/m^2), electric field vector (V/m), electric displacement vector (C/m^2) and dielectric constants (C/V m) respectively. Notations are adopted from the IEEE standards on piezoelectricity [2].

In three-dimensional cylindrical coordinate system, for FGPM cylindrical shell, (25.2) in matrix form can be written as

$$\begin{bmatrix} s_1 \\ s_2 \\ s_3 \\ s_4 \\ s_5 \\ s_6 \end{bmatrix} = \begin{bmatrix} s_{11}^E(r) & s_{12}^E(r) & s_{13}^E(r) & 0 & 0 & 0 \\ s_{12}^E(r) & s_{11}^E(r) & s_{13}^E(r) & 0 & 0 & 0 \\ s_{13}^E(r) & s_{13}^E(r) & s_{33}^E(r) & 0 & 0 & 0 \\ 0 & 0 & 0 & s_{44}^E(r) & 0 & 0 \\ 0 & 0 & 0 & 0 & s_{44}^E(r) & 0 \\ 0 & 0 & 0 & 0 & 0 & s_{66}^E(r) \end{bmatrix} \begin{bmatrix} T_1 \\ T_2 \\ T_3 \\ T_4 \\ T_5 \\ T_6 \end{bmatrix} + \begin{bmatrix} 0 & 0 & d_{31}(r) \\ 0 & 0 & d_{31}(r) \\ 0 & 0 & d_{33}(r) \\ 0 & d_{15}(r) & 0 \\ d_{15}(r) & 0 & 0 \\ 0 & 0 & 0 \end{bmatrix} \begin{bmatrix} E_1 \\ E_2 \\ E_3 \end{bmatrix}; \tag{25.3}$$

$$\begin{bmatrix} D_1 \\ D_2 \\ D_3 \end{bmatrix} = \begin{bmatrix} 0 & 0 & 0 & 0 & d_{15}(r) & 0 \\ 0 & 0 & 0 & d_{15}(r) & 0 & 0 \\ d_{31(r)} & d_{31}(r) & d_{33}(r) & 0 & 0 & 0 \end{bmatrix} \begin{bmatrix} T_1 \\ T_2 \\ T_3 \\ T_4 \\ T_5 \\ T_6 \end{bmatrix} + \begin{bmatrix} \varepsilon_{11}^T(r) & 0 & 0 \\ 0 & \varepsilon_{11}^T(r) & 0 \\ 0 & 0 & \varepsilon_{33}^T(r) \end{bmatrix} \begin{bmatrix} E_1 \\ E_2 \\ E_3 \end{bmatrix}. \tag{25.4}$$

Superscripts E and T stand for constant electric field and constant stress, respectively. Here stiffness coefficients, piezoelectric coefficients, dielectric coefficients and density all are the functions of radius r. Material properties are graded continuously in the radial direction according to the power law distribution from inner to outer surfaces of cylindrical shell.

$$\chi(r) = (\chi_0 - \chi_i)\left(\frac{r - r_i}{r_0 - r_i}\right)^n + \chi_i. \tag{25.5}$$

In the above expression, χ_0 and χ_i are the properties of the outer and inner surfaces, respectively, r is the radius of the cylindrical shell and n is the power law index. Stiffness coefficients, piezoelectric coefficients, dielectric coefficients and density all vary with the same rule as expressed in (25.5).

25.2.2 Kinematic Relations

For shear mode of excitation, the kinematic relations between strain S and displacements $u(r, \theta, z, t)$, $v(r, \theta, z, t)$ and $w(r, \theta, z, t)$ in radial, circumferential and axial directions, respectively, are given by

$$\begin{gathered} S_r = \frac{\partial u}{\partial r}; \quad S_\theta = \frac{1}{r}\frac{\partial v}{\partial \theta} + \frac{u}{r}; \quad S_z = \frac{\partial w}{\partial z}; \quad S_{\theta z} = \frac{1}{r}\frac{\partial w}{\partial \theta} + \frac{\partial v}{\partial z}; \\ S_{zr} = \frac{\partial u}{\partial z} + \frac{\partial w}{\partial r}; \quad S_{r\theta} = \frac{\partial v}{\partial r} + \frac{1}{r}\frac{\partial u}{\partial \theta} - \frac{v}{r} \end{gathered} \tag{25.6}$$

The electric field E in terms of the electric potential $\phi(r, \theta, z, t)$ is given by

$$E_r = -\frac{\partial \phi}{\partial r}; \quad E_\theta = -\frac{1}{r}\frac{\partial \phi}{\partial \theta}; \quad E_z = -\frac{\partial \phi}{\partial z}. \tag{25.7}$$

25.2.3 Energy Expression

The kinematic energy expression for FGPM cylindrical shell can be written as

$$\int_V T dV = \frac{1}{2}\int_V \rho(r) \times \left(\dot{u}^2 + \dot{v}^2 + \dot{w}^2\right) dV, \tag{25.8}$$

where $\rho(r)$ is density variation of piezoelectric material from inner to outer surface according to power law expression in FGPM cylindrical shell and dot $[\cdot]$ denotes the derivative with respect to the time. Here ω stands for angular frequency and V indicates volumetric integration.

Conventionally, electric enthalpy H is defined through

$$T_p = \frac{\partial H}{\partial S_p}; \quad D_i = -\frac{\partial H}{\partial E_i}. \tag{25.9}$$

Here H is termed as electric enthalpy even if it contains mechanical, electrical and coupling terms [3]. Mason [4] suggested the name electric enthalpy and later it became standard in piezoelectric literature. For the FGPM cylindrical shell one can obtain

$$H = \frac{1}{2}\left(T_r S_r + T_\theta S_\theta + T_z S_z + T_{\theta z} S_{\theta z} + T_{zr} S_{zr} + T_{r\theta} S_{r\theta} - D_r E_r - D_\theta E_\theta - D_z E_z\right) \tag{25.10}$$

Substituting (25.1) into (25.10), the electric enthalpy density can be expressed as

$$H = \frac{1}{2}\left[C_{11}^{E}(r)\right]S_r^2 + \frac{1}{2}\left[C_{11}^{E}(r)\right]S_\theta^2 + \left[C_{12}^{E}(r)\right]S_\theta S_r + \left[C_{13}^{E}(r)\right]S_z S_r + \left[C_{13}^{E}(r)\right]S_z S_\theta + \frac{1}{2}\left[C_{33}^{E}(r)\right]S_z^2 + \frac{1}{2}\left[C_{44}^{E}(r)\right]S_{zr}^2 + \frac{1}{2}\left[C_{44}^{E}(r)\right]S_{\theta z}^2 + \frac{1}{2}\left[C_{66}^{E}(r)\right]S_{\theta r}^2 - [e_{31}(r)]S_r E_z - [e_{31}(r)]S_\theta E_z - [e_{33}(r)]S_z E_z - [e_{15}(r)]S_{zr} E_r - [e_{31}(r)]S_{\theta z} E_\theta - \frac{1}{2}\left[\varepsilon_{11}^{S}(r)\right]E_r^2 - \frac{1}{2}\left[\varepsilon_{11}^{S}(r)\right]E_\theta^2 - \frac{1}{2}\left[\varepsilon_{33}^{S}(r)\right]E_z^2 \tag{25.11}$$

Now using strain displacement relations, (25.6) and electric field expression from (25.7) the electric enthalpy for FGPM cylindrical shell can be expressed as

$$\begin{aligned}\int_V H dV = \int_Z \int_\theta \int_r \Bigg(& \frac{1}{2r^2}\left[C_{11}^{E}(r)\right]u^2 + \frac{1}{2}\left[C_{11}^{E}(r)\right]\left(\frac{\partial u}{\partial r}\right)^2 + \frac{1}{r^2}\left[C_{11}^{E}(r)\right]u\left(\frac{\partial v}{\partial \theta}\right) \\ & + \frac{1}{2r^2}\left[C_{11}^{E}(r)\right]\left(\frac{\partial v}{\partial \theta}\right)^2 + \frac{1}{r}\left[C_{12}^{E}(r)\right]u\left(\frac{\partial u}{\partial r}\right) + \frac{1}{r}\left[C_{12}^{E}(r)\right]\left(\frac{\partial u}{\partial r}\right)\left(\frac{\partial v}{\partial \theta}\right) \\ & + \left[C_{13}^{E}(r)\right]\left(\frac{\partial u}{\partial r}\right)\left(\frac{\partial w}{\partial z}\right) + \frac{1}{r}\left[C_{13}^{E}(r)\right]\left(\frac{\partial v}{\partial \theta}\right)\left(\frac{\partial w}{\partial z}\right) + \frac{1}{r}\left[C_{13}^{E}(r)\right]u\left(\frac{\partial w}{\partial z}\right) \\ & + \frac{1}{2}\left[C_{33}^{E}(r)\right]\left(\frac{\partial w}{\partial z}\right)^2 + \frac{1}{2}\left[C_{44}^{E}(r)\right]\left(\frac{\partial u}{\partial z}\right)^2 + \left[C_{44}^{E}(r)\right]\left(\frac{\partial u}{\partial z}\right)\left(\frac{\partial w}{\partial r}\right) \\ & + \frac{1}{2}\left[C_{44}^{E}(r)\right]\left(\frac{\partial v}{\partial z}\right)^2 + \frac{1}{2}\left[C_{44}^{E}(r)\right]\left(\frac{\partial w}{\partial r}\right)^2 + \frac{1}{2r^2}\left[C_{44}^{E}(r)\right]\left(\frac{\partial w}{\partial \theta}\right) \\ & + \frac{1}{r}\left[C_{44}^{E}(r)\right]\left(\frac{\partial v}{\partial z}\right)\left(\frac{\partial w}{\partial \theta}\right) + \frac{1}{2r^2}\left[C_{66}^{E}(r)\right]v^2 + \frac{1}{r}\left[C_{66}^{E}(r)\right]\left(\frac{\partial u}{\partial \theta}\right)\left(\frac{\partial v}{\partial r}\right) \\ & - \frac{1}{r^2}\left[C_{66}^{E}(r)\right]\left(\frac{\partial u}{\partial \theta}\right)v + \frac{1}{2r^2}\left[C_{66}^{E}(r)\right]\left(\frac{\partial u}{\partial \theta}\right)^2 + \frac{1}{2}\left[C_{66}^{E}(r)\right]\left(\frac{\partial v}{\partial r}\right)^2 \\ & - \frac{1}{r}\left[C_{66}^{E}(r)\right]v\left(\frac{\partial v}{\partial r}\right) + \frac{1}{r}[e_{31}(r)]u\left(\frac{\partial \phi}{\partial z}\right) + \frac{1}{r}[e_{31}(r)]\left(\frac{\partial v}{\partial \theta}\right)\left(\frac{\partial \phi}{\partial z}\right) \\ & + [e_{31}(r)]\left(\frac{\partial u}{\partial r}\right)\left(\frac{\partial \phi}{\partial z}\right) + \frac{1}{r}[e_{15}(r)]\left(\frac{\partial v}{\partial z}\right)\left(\frac{\partial \phi}{\partial \theta}\right) + [e_{33}(r)]\left(\frac{\partial w}{\partial z}\right)\left(\frac{\partial \phi}{\partial z}\right) \\ & + [e_{15}(r)]\left(\frac{\partial u}{\partial z}\right)\left(\frac{\partial \phi}{\partial r}\right) + [e_{15}(r)]\left(\frac{\partial w}{\partial r}\right)\left(\frac{\partial \phi}{\partial r}\right) + \frac{1}{r^2}[e_{15}(r)]\left(\frac{\partial w}{\partial \theta}\right)\left(\frac{\partial \phi}{\partial \theta}\right) \\ & - \frac{1}{2}\left[\varepsilon_{11}^{S}(r)\right]\left(\frac{\partial \phi}{\partial r}\right)^2 - \frac{1}{2r^2}\left[\varepsilon_{11}^{S}(r)\right]\left(\frac{\partial \phi}{\partial \theta}\right)^2 - \frac{1}{2}\left[\varepsilon_{33}^{S}(r)\right]\left(\frac{\partial \phi}{\partial z}\right)^2 \Bigg) r dr d\theta dz. \end{aligned} \tag{25.12}$$

25.3 Rayleigh–Ritz Method

Bhat [1] introduced the orthogonal polynomial function in Rayleigh–Ritz method to calculate the natural frequencies for free edged rectangular plate. The same method is used for piezoceramic beam and annular plate-type problems by Parashar et al. [5]. Anubhav et al. [6] extended this method to find the natural frequencies for piezoceramic cylindrical shell. Here, above mentioned method is used to obtain the eigenvectors and eigenfrequencies for FGPM cylindrical shell excited under d_{15} effect.

Assume displacement parameters u, v, w and electric potential ϕ as

$$\begin{aligned} u(r,\theta,z,t) &= U(r,\theta,z)\sin\omega t;\\ v(r,\theta,z,t) &= V(r,\theta,z)\sin\omega t;\\ w(r,\theta,z,t) &= W(r,\theta,z)\sin\omega t;\\ \phi(r,\theta,z,t) &= \Phi(r,\theta,z)\sin\omega t. \end{aligned} \tag{25.13}$$

By substituting above relations into (25.8), we get maximum kinetic energy terms as

$$T_{max} = \frac{1}{2}\omega^2 \int_V \rho(r) \times \left(U^2 + V^2 + W^2\right) dV. \tag{25.14}$$

Similarly one can easily obtain maximum electric enthalpy terms after substituting (25.13) into (25.12). The displacement amplitudes U, V, W and the electric potential Φ for the free vibrations of functionally graded piezoelectric may be expressed as

$$\begin{aligned} U &= \{\Psi_1(r,\theta,z)\}^T \{P\}_{(a+1)(b+1)\times 1};\\ V &= \{\Psi_2(r,\theta,z)\}^T \{Q\}_{(i+1)(j+1)\times 1};\\ W &= \{\Psi_3(r,\theta,z)\}^T \{R\}_{(e+1)(f+1)\times 1}; \end{aligned}$$

and

$$\Phi = \{\Psi_4(r,\theta,z)\}^T \{L\}_{(p+1)(q+1)\times 1}, \tag{25.15}$$

where $\{P\}$, $\{Q\}$, $\{R\}$ and $\{L\}$ are the unknown coefficient while $\{\Psi_1\}$, $\{\Psi_2\}$, $\{\Psi_3\}$ and $\{\Psi_4\}$ are

$$\begin{aligned}
\{\Psi_1\}_{(a+1)(b+1)\times 1} &= \left(\{\alpha\}\{\beta\}^T\right)^S \cos(n\theta);\\
\{\Psi_2\}_{(i+1)(j+1)\times 1} &= \left(\{\delta\}\{\gamma\}^T\right)^S \sin(n\theta);\\
\{\Psi_3\}_{(e+1)(f+1)\times 1} &= \left(\{\lambda\}\{\mu\}^T\right)^S \cos(n\theta);\\
\{\Psi_4\}_{(p+1)(q+1)\times 1} &= \left(\{\xi\}\{\zeta\}^T\right)^S \cos(n\theta).
\end{aligned} \tag{25.16}$$

Stacks operator $(.)^S$ is used for mapping the matrix into the column vector [7]. Here n stands for the number of nodal diameter; $\alpha_a(r)$, $\beta_b(z)$, $\gamma_i(r)$, $\delta_j(z)$, $\lambda_m(r)$, $\mu_n(z)$, $\zeta_r(r)$ and $\xi_s(z)$ are polynomial functions (a, b, i, j, m, n, r, s = 0, 1, 2, …) satisfying the geometrical boundary conditions and can be expressed as

$$\begin{aligned}
\{\alpha(r)\} &= [\alpha_0, \alpha_1, \ldots, \alpha_a]^T;\\
\{\beta(z)\} &= [\beta_0, \beta_1, \ldots, \beta_b]^T;\\
\{\delta(r)\} &= [\delta_0, \delta_1, \ldots, \delta_i]^T;\\
\{\gamma(z)\} &= [\gamma_0, \gamma_1, \ldots, \gamma_j]^T;\\
\{\lambda(r)\} &= [\lambda_0, \lambda_1, \ldots, \lambda_e]^T;\\
\{\mu(z)\} &= [\mu_0, \mu_1, \ldots, \mu_f]^T;\\
\{\xi(r)\} &= [\xi_0, \xi_1, \ldots, \xi_p]^T;
\end{aligned}$$

and

$$\{\zeta(z)\} = [\zeta_0, \zeta_1, \ldots, \zeta_q]^T. \tag{25.17}$$

For a free-free hollow FGPM cylinder the starting function for each of these ones is simply a constant term. Gram-Schmidt process is used to obtain higher order functions [1]. The starting functions for displacements U, V and W are constant terms for free-free boundary conditions.

$$\alpha_0 = \beta_0 = \delta_0 = \gamma_0 = \lambda_0 = \mu_0 = const \tag{25.18}$$

If the FGPM cylinder is used as an actuator then an external electric field is prescribed at the boundaries with electrodes (i.e. at $r = r_1, r_2$). For the free vibrations, it is appropriate here to assume that the electric potential in the piezoelectric vanishes at the boundaries [3]. Hence, electrodes are considered to be short-circuited in the present case (i.e. $\phi = 0$ at $r = r_1, r_2$). For the side of the FGPM shell (i.e. at $z = -l/2, l/2$) without electrodes, since the dielectric constant of the air is negligible in comparison to the dielectric constant of the piezoelectric material, the surface charge density is assumed to be zero. Hence for the electric potential, satisfying the electric boundary conditions, we have

$$\xi_0 = const; \quad \zeta_0 = r^2 - (r_1 + r_2)r + r_1 r_2. \tag{25.19}$$

The higher order functions are obtained using Gram-Schmidt process [1] as

$$\beta_1 = (r - J_1)\beta_o(r); \tag{25.20}$$

$$\beta_i = (r - J_i)\beta_{i-1}(r) - G_i\beta_{i-2}(r), \tag{25.21}$$

where J_i and G_i are calculated as

$$J_i = \frac{\int_{r_1}^{r_2} r\sigma(r)\beta_{i-1}^2(r)dr}{\int_{r_1}^{r_2} \sigma(r)\beta_{i-1}^2(r)dr}; \tag{25.22}$$

$$G_i = \frac{\int_{r_1}^{r_2} r\sigma(r)\beta_{i-1}(r)\beta_{i-2}(r)dr}{\int_{r_1}^{r_2} \sigma(r)\beta_{i-2}^2(r)dr}. \tag{25.23}$$

Here weighting function $\sigma(r)$ is assumed as unity. In the case of $\alpha_0(x)$, $\delta_i(x)$, $\lambda_m(x)$ and $\xi_r(x)$, the interval is from $-l/2$ to $l/2$. MATLAB 2015 Symbolic Toolbox is used for calculation of higher order polynomials. As order of polynomials increases, accuracy level of obtained results also improves. For higher order polynomials more computations are required. Computation time directly relates with the hardware capabilities.

25.3.1 Expressions for Maximum Kinetic and Potential Energies

After substituting (25.15) into (25.14), we get modified expression for maximum kinetic energy as

$$T_{max} = \frac{1}{2}\omega^2 \int_V \rho(r) \times \left(\{P\}^T\{\Psi_1\}\{\Psi_1\}^T\{P\} + \{Q\}^T\{\Psi_2\}\{\Psi_2\}^T\{Q\} + \{R\}^T\{\Psi_3\}\{\Psi_3\}^T\{R\}\right)dV \tag{25.24}$$

and after substituting the expressions of U, V, W and ϕ from (25.15) into (25.12), maximum electrical enthalpy expression can be expressed as

$$
\begin{aligned}
H_{max} = \int_Z \int_\theta \int_r \Bigg(& \frac{1}{2r^2}\left[C^E_{11}(r)\right]\{P\}^T\{\Psi_1\}\{\Psi_1\}^T\{P\} + \frac{1}{2}\left[C^E_{11}(r)\right]\{P\}^T\{\Psi_{1,r}\}\{\Psi_{1,r}\}^T\{P\} \\
& + \frac{1}{r^2}\left[C^E_{11}(r)\right]\{P\}^T\{\Psi_1\}\{\Psi_{2,\theta}\}^T\{Q\} + \frac{1}{2r^2}\left[C^E_{11}(r)\right]\{Q\}^T\{\Psi_{2,\theta}\}\{\Psi_{2,\theta}\}^T\{Q\} \\
& + \frac{1}{r}\left[C^E_{12}(r)\right]\{P\}^T\{\Psi_1\}\{\Psi_{1,r}\}^T\{P\} + \frac{1}{r}\left[C^E_{12}(r)\right]\{P\}^T\{\Psi_{1,r}\}\{\Psi_{2,\theta}\}^T\{Q\} \\
& + \left[C^E_{13}(r)\right]\{P\}^T\{\Psi_{1,r}\}\{\Psi_{3,z}\}^T\{R\} + \frac{1}{r}\left[C^E_{13}(r)\right]\{P\}^T\{\Psi_1\}\{\Psi_{3,z}\}^T\{R\} \\
& + \frac{1}{r}\left[C^E_{13}(r)\right]\{Q\}^T\{\Psi_{2,\theta}\}\{\Psi_{3,z}\}^T\{R\} + \frac{1}{2}\left[C^E_{33}(r)\right]\{R\}^T\{\Psi_{3,z}\}\{\Psi_{3,z}\}^T\{R\} \\
& + \frac{1}{2}\left[C^E_{44}(r)\right]\{P\}^T\{\Psi_{1,z}\}\{\Psi_{1,z}\}^T\{P\} + \left[C^E_{44}(r)\right]\{P\}^T\{\Psi_{1,z}\}\{\Psi_{3,r}\}^T\{R\} \\
& + \frac{1}{2}\left[C^E_{44}(r)\right]\{Q\}^T\{\Psi_{2,z}\}\{\Psi_{2,z}\}^T\{Q\} + \frac{1}{2}\left[C^E_{44}(r)\right]\{R\}^T\{\Psi_{3,r}\}\{\Psi_{3,r}\}^T\{R\} \\
& + \frac{1}{2r^2}\left[C^E_{44}(r)\right]\{R\}^T\{\Psi_{3,\theta}\}\{\Psi_{3,\theta}\}^T\{R\} + \frac{1}{r}\left[C^E_{44}(r)\right]\{Q\}^T\{\Psi_{2,z}\}\{\Psi_{3,\theta}\}^T\{R\} \\
& + \frac{1}{2r^2}\left[C^E_{66}(r)\right]\{Q\}^T\{\Psi_2\}\{\Psi_2\}^T\{Q\} + \frac{1}{r}\left[C^E_{66}(r)\right]\{P\}^T\{\Psi_{1,\theta}\}\{\Psi_{2,r}\}^T\{Q\} \\
& - \frac{1}{r^2}\left[C^E_{66}(r)\right]\{P\}^T\{\Psi_{1,\theta}\}\{\Psi_2\}^T\{Q\} + \frac{1}{2r^2}\left[C^E_{66}(r)\right]\{P\}^T\{\Psi_{1,\theta}\}\{\Psi_{1,\theta}\}^T\{P\} \\
& + \frac{1}{2}\left[C^E_{66}(r)\right]\{Q\}^T\{\Psi_{2,r}\}\{\Psi_{2,r}\}^T\{Q\} - \frac{1}{r}\left[C^E_{66}(r)\right]\{Q\}^T\{\Psi_2\}\{\Psi_{2,r}\}^T\{Q\} \\
& + \frac{1}{r}[e_{31}(r)]\{P\}^T\{\Psi_1\}\{\Psi_{4,z}\}^T\{L\} + \frac{1}{r}[e_{31}(r)]\{Q\}^T\{\Psi_{2,\theta}\}\{\Psi_{4,z}\}^T\{L\} \\
& + [e_{31}(r)]\{P\}^T\{\Psi_{1,r}\}\{\Psi_{4,z}\}^T\{L\} + \frac{1}{r}[e_{15}(r)]\{Q\}^T\{\Psi_{2,z}\}\{\Psi_{4,\theta}\}^T\{L\} \\
& + [e_{33}(r)]\{R\}^T\{\Psi_{3,z}\}\{\Psi_{4,z}\}^T\{L\} + [e_{15}(r)]\{P\}^T\{\Psi_{1,z}\}\{\Psi_{4,r}\}^T\{L\} \\
& + [e_{15}(r)]\{R\}^T\{\Psi_{3,r}\}\{\Psi_{4,r}\}^T\{L\} + \frac{1}{r^2}[e_{15}(r)]\{R\}^T\{\Psi_{3,\theta}\}\{\Psi_{4,\theta}\}^T\{L\} \\
& - \frac{1}{2}\left[\varepsilon^S_{11}(r)\right]\{L\}^T\{\Psi_{4,r}\}\{\Psi_{4,r}\}^T\{L\} - \frac{1}{2r^2}\left[\varepsilon^S_{11}(r)\right]\{L\}^T\{\Psi_{4,\theta}\}\{\Psi_{4,\theta}\}^T\{L\} \\
& - \frac{1}{2}\left[\varepsilon^S_{33}(r)\right]\{L\}^T\{\Psi_{4,z}\}\{\Psi_{4,z}\}^T\{L\}\Bigg) r dr d\theta dz.
\end{aligned}
\tag{25.25}
$$

Now after taking the derivatives of maximum energy expression from (25.24) and (25.25) with respect to unknown coefficients $\{P\}$, $\{Q\}$, $\{R\}$ and $\{L\}$, we get

$$
\left\{\frac{\partial T_{max}}{\partial coeff}\right\} = \omega^2 \int_V \rho(r) \left(\begin{bmatrix} \{\Psi_1\}\{\Psi_1\}^T & & & \\ & \{\Psi_2\}\{\Psi_2\}^T & & \\ & & \{\Psi_3\}\{\Psi_3\}^T & \\ & & & [zeros] \end{bmatrix} \right) dV \begin{Bmatrix} P \\ Q \\ R \\ L \end{Bmatrix};
\tag{25.26}
$$

$$\left\{\frac{\partial H_{max}}{\partial coeff}\right\} = \int_V \left(\begin{bmatrix} [\Gamma_{mech}] & [\Gamma_{piezo}] \\ [\Gamma_{piezo}]^T & [\Gamma_{dielectric}] \end{bmatrix} \right) dV \begin{Bmatrix} P \\ Q \\ R \\ L \end{Bmatrix}. \tag{25.27}$$

Details of the matrices Γ_{piezo}, $\Gamma_{dielectric}$ and Γ_{mech} are given in Appendix A. In (25.27), diagonal matrix contains the zero value corresponds to coefficient $\{L\}$. It generates the singularity in the matrix. Guyan reduction method [3] is used for removing the singularity and reduced form equation for eigenvalue problem is expressed as

$$\left[[\Gamma] - \omega^2[M]\right] \begin{Bmatrix} P \\ Q \\ R \end{Bmatrix} = 0, \tag{25.28}$$

where

$$[\Gamma] = \int_V \left([\Gamma_{mech}] - [\Gamma_{piezo}][\Gamma_{dielectric}]^{-1}[\Gamma_{piezo}]^T \right) dV; \tag{25.29}$$

$$[M] = \int_V \rho(r) \left(\begin{bmatrix} \{\Psi_1\}\{\Psi_1\}^T & & \\ & \{\Psi_2\}\{\Psi_2\}^T & \\ & & \{\Psi_3\}\{\Psi_3\}^T \end{bmatrix} \right) dV. \tag{25.30}$$

After calculating the eigenvalues and eigenvectors from the reduced eigenvalue problem, coefficients $\{L\}$ are calculated as

$$\{L\} = -[\Gamma_{dielectric}]^{-1}[\Gamma_{piezo}]^T \begin{Bmatrix} P \\ Q \\ R \end{Bmatrix}. \tag{25.31}$$

25.4 Numerical Results

FGPM cylindrical shell has inner radius 17 mm, outer radius 19 mm and length 10 mm. It is assumed that inner surface is made of purely PZT-5H material and outer of PZT-2 material and properties vary from inner to outer surface according to power law expression as expressed in (25.5). Material parameters of PZT-5H and PZT-2 are listed in Table (25.1).

Table 25.1 Material parameters of PZT-5H and PZT-2 materials [8]

Material parameters	Values for PZT-5H	Values for PZT-2
ρ (kg/m^3)	7500	7600
C_{11}^E (N/m^2)	1.272×10^{11}	1.348×10^{11}
C_{12}^E (N/m^2)	8.021×10^{10}	6.788×10^{10}
C_{13}^E (N/m^2)	8.467×10^{10}	6.808×10^{10}
C_{33}^E (N/m^2)	1.174×10^{11}	1.133×10^{11}
C_{44}^E (N/m^2)	2.298×10^{10}	2.222×10^{10}
e_{31} (C/m^2)	−6.622	−1.816
e_{33} (C/m^2)	23.240	9.050
e_{15} (C/m^2)	17.034	9.778
$\varepsilon_{11}^S/\varepsilon_o$	1704.4	504.1
$\varepsilon_{33}^S/\varepsilon_o$	1433.6	270.1

25.4.1 Convergence Study

First four natural frequencies for free-free FGPM cylindrical shell with zero-, one-, two- and three-nodal diameters are listed in Tables 25.2, 25.3, 25.4 and 25.5, respectively. For all the calculations, power law index n is assumed as unity. It can be observed that convergence rate for natural frequencies are very high, and sufficient level of convergence is achieved with the six polynomials in both axial and radial directions. For higher number of polynomials, more calculations are required and highly configured hardware is needed.

Table 25.2 Convergence study for mode with zero-nodal diameter

No. of polynomials	f_1 (kHz)	f_2 (kHz)	f_3 (kHz)	f_4 (kHz)
3	37.780	38.677	74.264	168.14
4	37.761	38.643	71.163	152.61
5	37.668	38.643	65.948	135.98
6	37.668	38.643	65.704	135.04

Table 25.3 Convergence study for mode with one-nodal diameter

No. of polynomials	f_1 (kHz)	f_2 (kHz)	f_3 (kHz)	f_4 (kHz)
3	3.929	21.987	37.430	45.409
4	3.912	21.932	37.373	45.332
5	3.904	21.932	37.265	45.332
6	3.904	21.932	37.256	45.332

Table 25.4 Convergence study for mode with two-nodal diameter

No. of polynomials	f_1 (kHz)	f_2 (kHz)	f_3 (kHz)	f_4 (kHz)
3	11.513	25.309	38.662	63.922
4	11.418	25.214	38.293	63.916
5	11.385	25.214	38.187	63.913
6	11.382	25.214	38.148	63.913

Table 25.5 Convergence study for mode with three-nodal diameter

No. of polynomials	f_1 (kHz)	f_2 (kHz)	f_3 (kHz)	f_4 (kHz)
3	21.137	26.914	43.753	81.098
4	20.889	26.809	42.914	78.864
5	20.816	26.807	42.854	72.854
6	20.810	26.807	42.783	72.690

25.4.2 Validation

At present, no solution is available in literature for free vibration analysis of FGPM cylindrical shell excited under d_{15} effect. Hence the results, obtained using Rayleigh–Ritz method, are validated with finite element software COMSOL Multiphysics.

Table 25.6 presents the comparison of calculated natural frequencies with FEA results. Present results have close agreements with the results of FEA software. Figure 25.2 shows the mode shapes with zero- and one-nodal diameters.

25.4.3 Mode Shapes

The eigenvectors $\{P\}$, $\{Q\}$ and $\{R\}$ are calculated by solving (25.28). Coefficient $\{L\}$ is obtained after substituting values of eigenvectors in (25.31). Equations (25.15) provide mode shapes by putting the values of $\{P\}$, $\{Q\}$, $\{R\}$ and $\{L\}$. Figure 25.3 displays the mode shapes at various natural frequencies for

Table 25.6 Comparison between Rayleigh–Ritz method and COMSOL multiphysics results

Nodal diameter	Natural frequency (Hz) Rayleigh–Ritz	Natural frequency (Hz) COMSOL multiphysics	Difference (%)
0	37,668	37,865	0.52
1	21,932	22,050	0.53
2	25,214	25,381	0.66
2	68,913	68,565	0.50
4	29,124	29,210	0.29

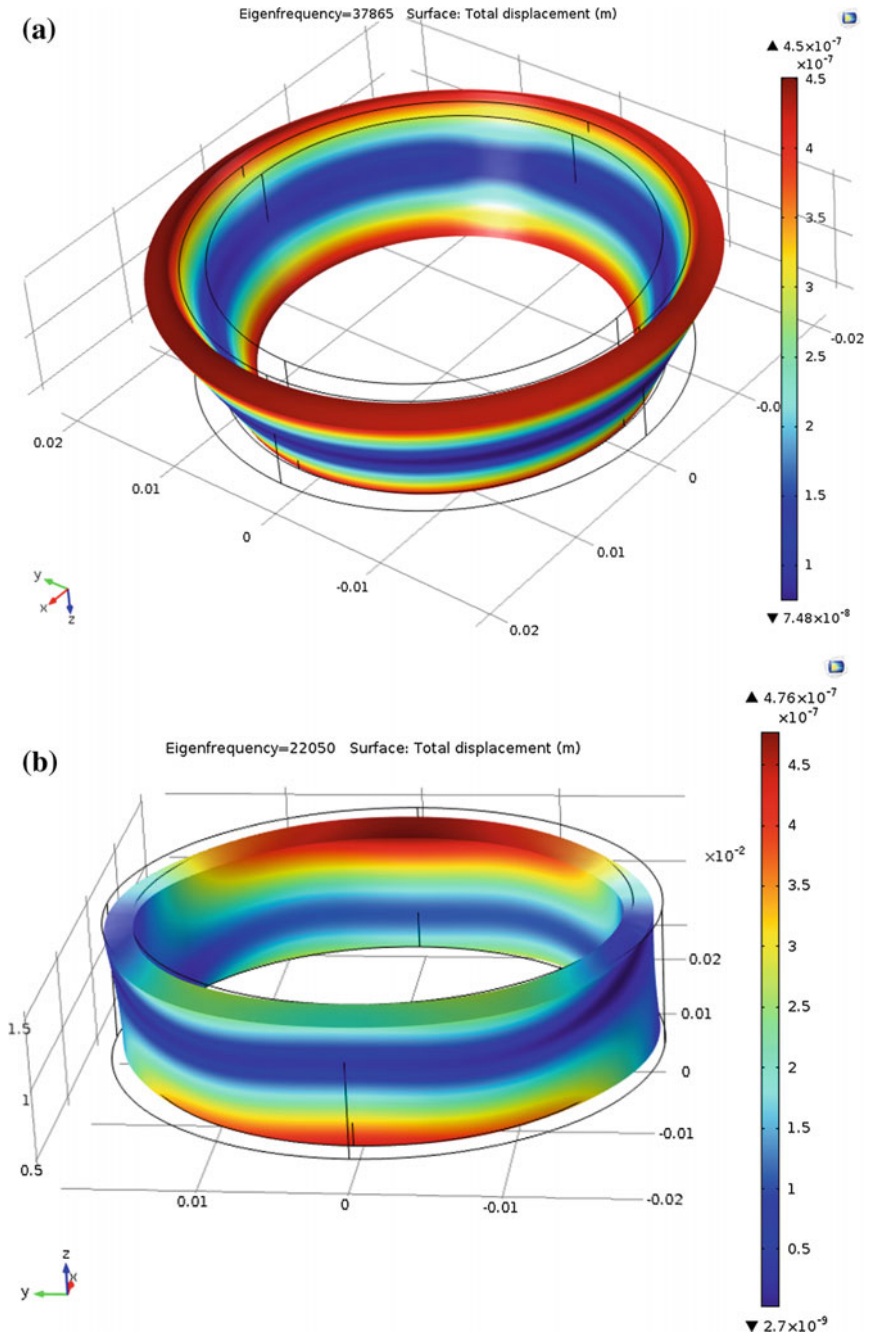

Fig. 25.2 Mode shapes of FGPM cylindrical shell using COMSOL multiphysics: **a** at 37.86 kHz and **b** at 22.05 kHz with zero- and one-nodal diameters, respectively

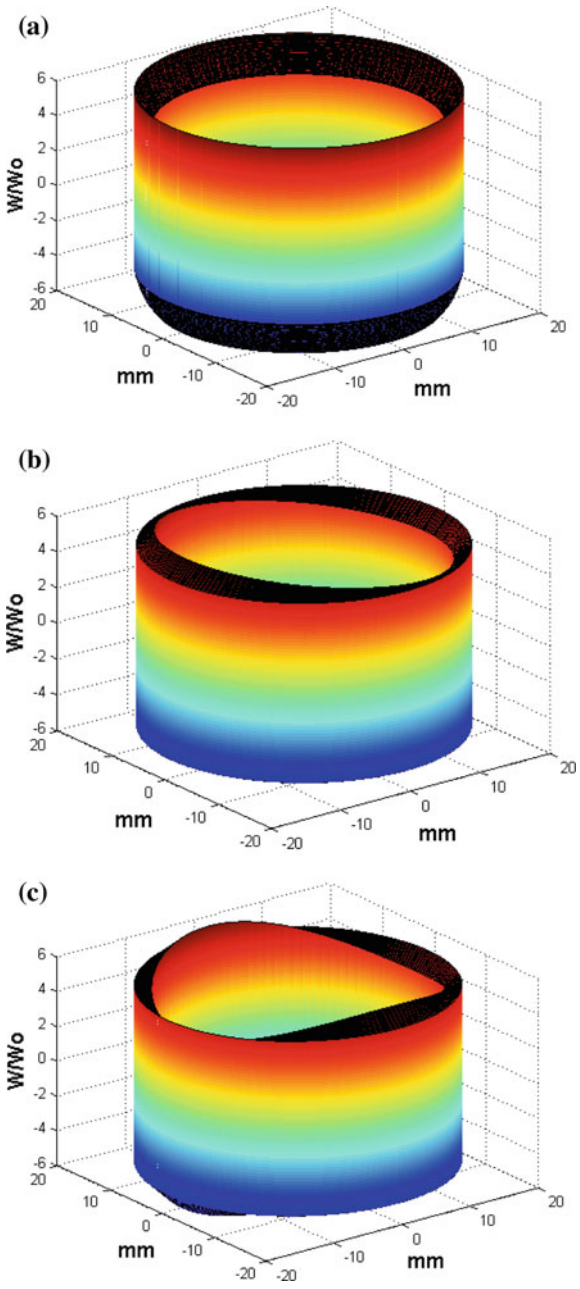

Fig. 25.3 Mode shapes of FGPM cylindrical shell using Rayleigh–Ritz method: **a** at 37.668 kHz with zero-nodal diameter, **b** at 21.932 kHz with one-nodal diameter and **c** at 25.214 kHz with two-nodal diameter

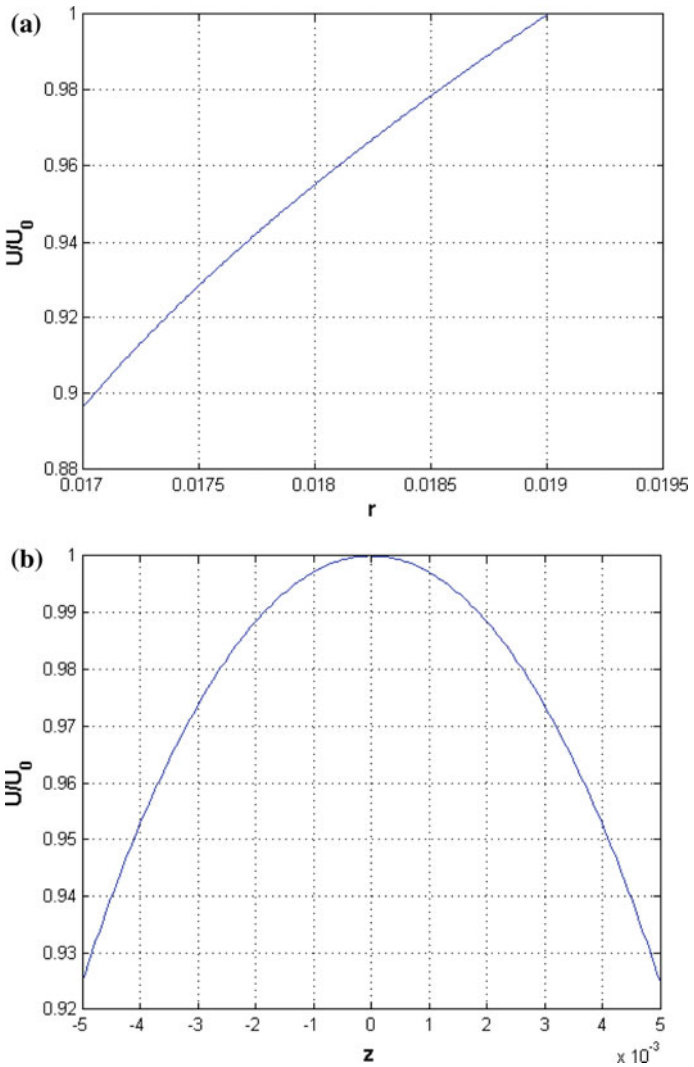

Fig. 25.4 Normalized variation of radial displacement U along thickness and length at 21.932 kHz

different nodal diameters. Only axial deformation is considered during plotting of these mode shapes because radial and circumferential displacements for such a thin cylindrical shell is not so prominent. The displacement values are scaled here to aid visualization.

Variation of normalized displacement parameters along with thickness and length is plotted in Figs. 25.4, 25.5, 25.6 and 25.7 at 21.932 kHz. Sinusoidal variation can be noticed for electric potential Φ along the length. It is an important

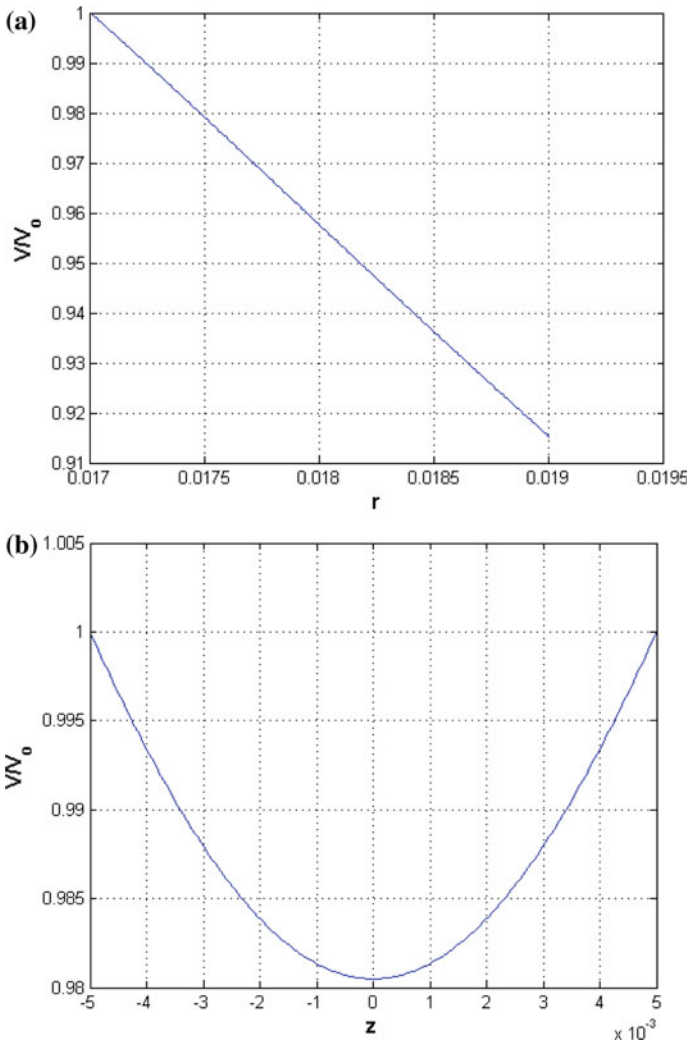

Fig. 25.5 Normalized variation of circumferential displacement V along thickness and length at 21.932 kHz

observation because similar behaviour has been observed in the case of pure piezoceramic beam [3] and is used to obtain reduced order model.

Variation of normalized natural frequency with d/D ratio and L/D ratios are also presented in Figs. 25.8 and 25.9, respectively. In the case of d/D ratio, curves in Fig. 25.8 for all diameters from one- to four-nodal have decreasing nature. However, for zero-nodal diameter, the curve has entirely different behaviour and increases as d/D ratio increases. While for L/D ratio (see Fig. 25.9), as ratio increases normalised natural frequency also increases for all the nodal diameters.

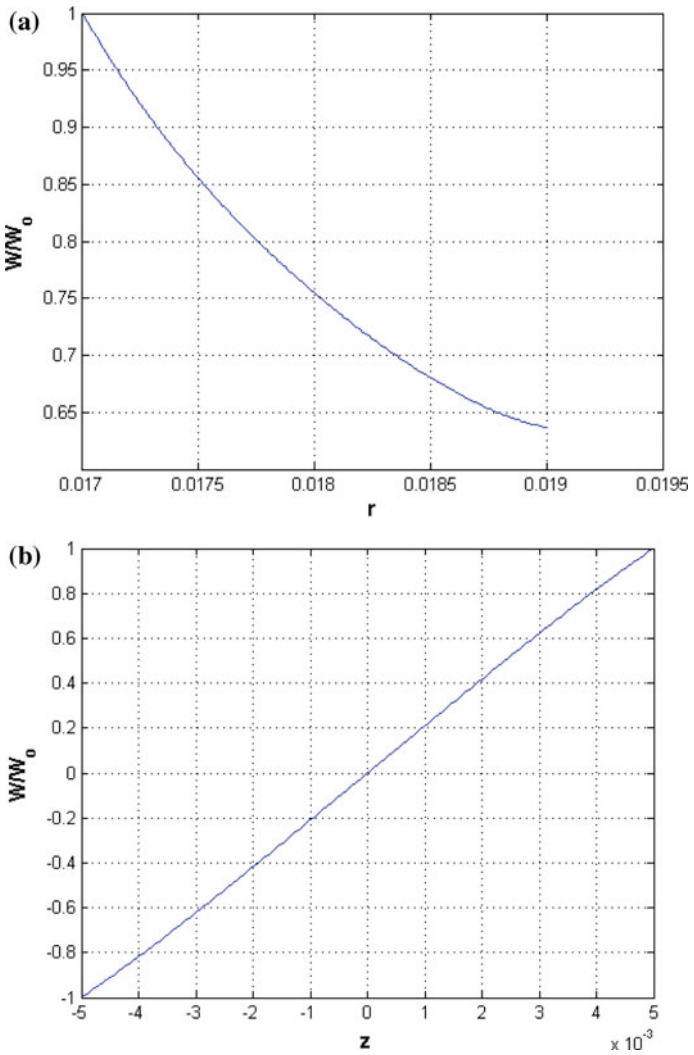

Fig. 25.6 Normalized variation of axial displacement W along thickness and length at 21.932 kHz

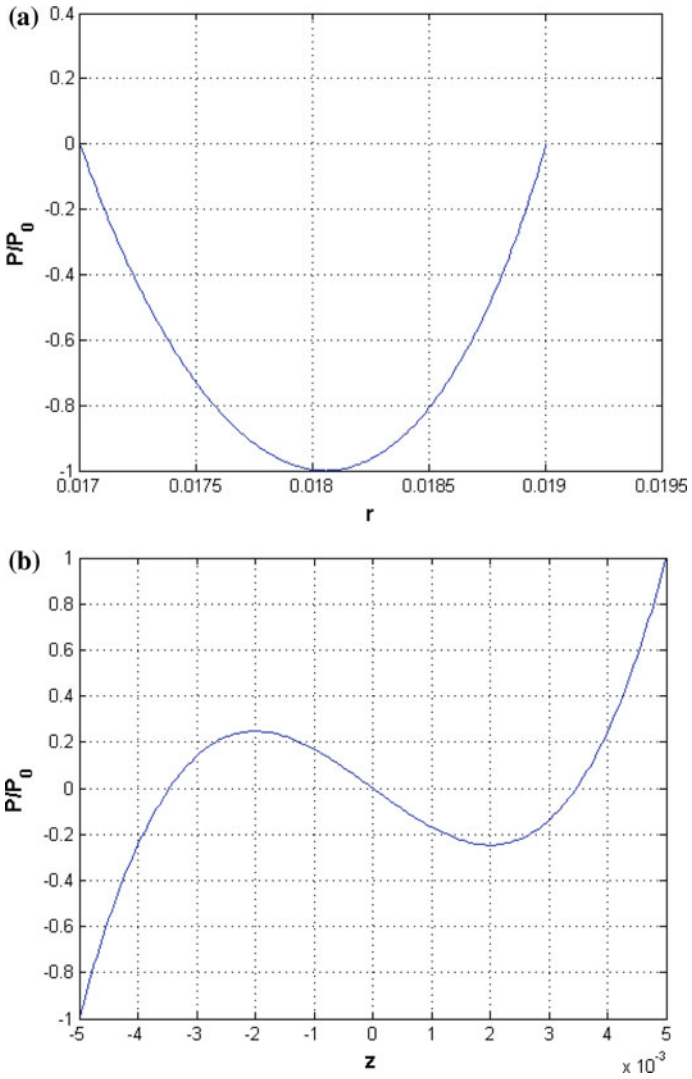

Fig. 25.7 Normalized variation of electric potential Φ along thickness and length at 21.932 kHz

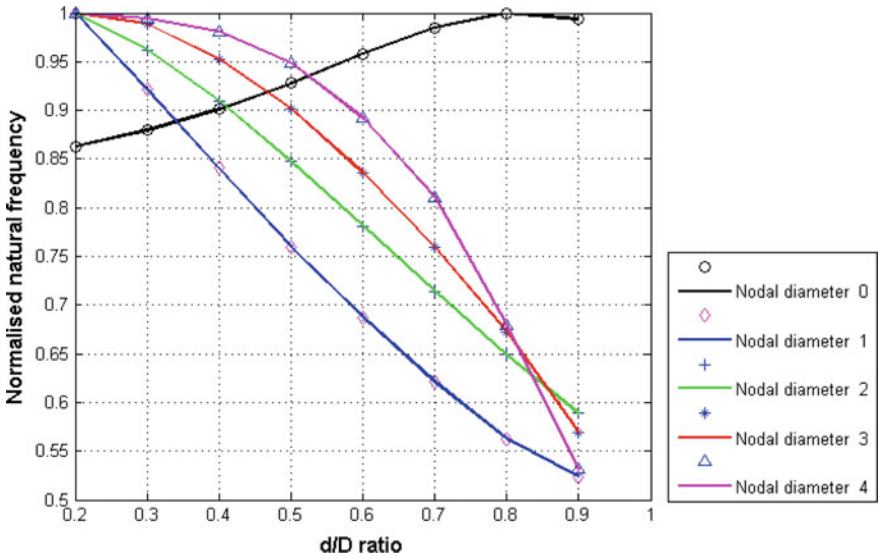

Fig. 25.8 *d/D* ratio versus normalized first natural frequency for different nodal diameters

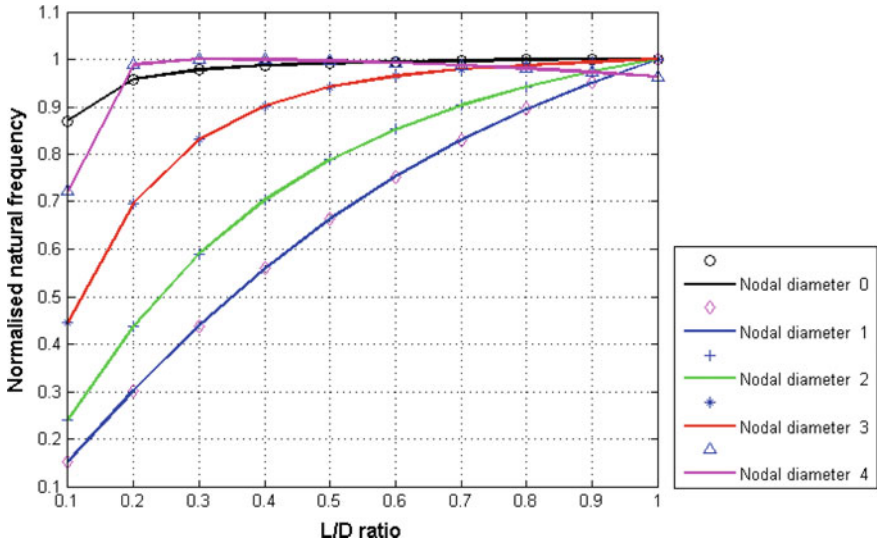

Fig. 25.9 *L/D* ratio versus normalized first natural frequency for different nodal diameters

25.5 Conclusion

In present work, free vibration behaviour of FGPM cylindrical shell excited under d_{15} effect has been analysed. The linear constitutive relations are obtained in cylindrical coordinate system for FGPM cylindrical shell. Then, kinetic energy and electric enthalpy expressions are derived and further utilized in the Rayleigh–Ritz formulation. The Rayleigh–Ritz method is used for calculating the eigenfrequencies and eigenvalues for FGPM cylindrical shell. Convergence study is carried out for the first four natural frequencies with various nodal diameters. From the present results, it can easily be concluded that the Rayleigh–Ritz method provides fairly accurate results, which have close agreement with FEA software's results. Variation of normalised natural frequency with *d*/*D* and *L*/*D* ratios are also presented here. Variation of displacements along radius and length are also plotted.

Model is solved for free–free boundary conditions only. A detailed analysis for other boundary conditions and comparison with present case will be the subject of future scope. Application of this model in sensors and instrumentation field has a bright future and also a challenging field for researchers.

Appendix 1

Expressions for the matrices Γ_{piezo}, $\Gamma_{dielectric}$ and Γ_{mech} are given below:

$$\Gamma_{piezo} = \begin{bmatrix} [e_{31}(r)]\{\Psi_{1,r}\}\{\Psi_{4,z}\}^T + \frac{1}{r}[e_{31}(r)]\{\Psi_1\}\{\Psi_{4,z}\}^T + [e_{15}(r)]\{\Psi_{1,z}\}\{\Psi_{4,r}\}^T \\ \frac{1}{r}[e_{31}(r)]\{\Psi_{2,\theta}\}\{\Psi_{4,z}\}^T + \frac{1}{r}[e_{15}(r)]\{\Psi_{2,z}\}\{\Psi_{4,\theta}\}^T \\ [e_{33}(r)]\{\Psi_{3,z}\}\{\Psi_{4,z}\}^T + + [e_{15}(r)]\{\Psi_{3,r}\}\{\Psi_{4,r}\}^T + \frac{1}{r^2}[e_{15}(r)]\{\Psi_{3,\theta}\}\{\Psi_{4,\theta}\}^T \end{bmatrix}$$

$$\Gamma_{dielectric} = \left[-\left[\varepsilon^S_{11}(r)\right]\{\Psi_{4,r}\}\{\Psi_{4,r}\}^T - \frac{1}{r^2}\left[\varepsilon^S_{11}(r)\right]\{\Psi_{4,\theta}\}\{\Psi_{4,\theta}\}^T - \left[\varepsilon^S_{33}(r)\right]\{\Psi_{4,z}\}\{\Psi_{4,z}\}^T \right]$$

$$\Gamma_{mech} = \begin{bmatrix} \frac{1}{r^2}\left[C_{11}^E(r)\right]\{\Psi_1\}\{\Psi_1\}^T & \frac{1}{r^2}\left[C_{11}^E(r)\right]\{\Psi_1\}\{\Psi_{2,\theta}\}^T & \frac{1}{r}\left[C_{13}^E(r)\right]\{\Psi_1\}\{\Psi_{3,z}\}^T \\ +\frac{2}{r}\left[C_{12}^E(r)\right]\{\Psi_1\}\{\Psi_{1,r}\}^T & +\frac{1}{r}\left[C_{12}^E(r)\right]\{\Psi_{1,r}\}\{\Psi_{2,\theta}\}^T & +\left[C_{13}^E(r)\right]\{\Psi_{1,r}\}\{\Psi_{3,z}\}^T \\ +\left[C_{11}^E(r)\right]\{\Psi_{1,r}\}\{\Psi_{1,r}\}^T & -\frac{1}{r^2}\left[C_{66}^E(r)\right]\{\Psi_{1,\theta}\}\{\Psi_2\}^T & +\left[C_{44}^E(r)\right]\{\Psi_{1,z}\}\{\Psi_{3,r}\}^T \\ +\left[C_{44}^E(r)\right]\{\Psi_{1,z}\}\{\Psi_{1,z}\}^T & +\frac{1}{r}\left[C_{66}^E(r)\right]\{\Psi_{1,\theta}\}\{\Psi_{2,r}\}^T & \\ +\frac{1}{r^2}\left[C_{66}^E(r)\right]\{\Psi_{1,\theta}\}\{\Psi_{1,\theta}\}^T & & \\ \frac{1}{r^2}\left[C_{11}^E(r)\right]\{\Psi_{2,\theta}\}\{\Psi_1\}^T & \frac{1}{r^2}\left[C_{11}^E(r)\right]\{\Psi_{2,\theta}\}\{\Psi_{2,\theta}\}^T & \frac{1}{r}\left[C_{13}^E(r)\right]\{\Psi_{2,\theta}\}\{\Psi_{3,z}\}^T \\ +\frac{1}{r}\left[C_{12}^E(r)\right]\{\Psi_{2,\theta}\}\{\Psi_{1,r}\}^T & +\left[C_{44}^E(r)\right]\{\Psi_{2,z}\}\{\Psi_{2,z}\}^T & +\frac{1}{r}\left[C_{44}^E(r)\right]\{\Psi_{2,z}\}\{\Psi_{3,\theta}\}^T \\ -\frac{1}{r^2}\left[C_{66}^E(r)\right]\{\Psi_2\}\{\Psi_{1,\theta}\}^T & +\frac{1}{r^2}\left[C_{66}^E(r)\right]\{\Psi_2\}\{\Psi_2\}^T & \\ +\frac{1}{r}\left[C_{66}^E(r)\right]\{\Psi_{2,r}\}\{\Psi_{1,\theta}\}^T & +\left[C_{66}^E(r)\right]\{\Psi_{2,r}\}\{\Psi_{2,r}\}^T & \\ & -\frac{1}{r}\left[C_{66}^E(r)\right]\{\Psi_2\}\{\Psi_{2,r}\}^T & \\ \frac{1}{r}\left[C_{13}^E(r)\right]\{\Psi_{3,z}\}\{\Psi_1\}^T & \frac{1}{r}\left[C_{13}^E(r)\right]\{\Psi_{3,z}\}\{\Psi_{2,\theta}\}^T & \left[C_{44}^E(r)\right]\{\Psi_{3,r}\}\{\Psi_{3,r}\}^T \\ +\left[C_{13}^E(r)\right]\{\Psi_{3,z}\}\{\Psi_{1,r}\}^T & +\frac{1}{r}\left[C_{44}^E(r)\right]\{\Psi_{3,\theta}\}\{\Psi_{2,z}\}^T & +\left[C_{33}^E(r)\right]\{\Psi_{3,z}\}\{\Psi_{3,z}\}^T \\ +\left[C_{44}^E(r)\right]\{\Psi_{3,r}\}\{\Psi_{1,z}\}^T & & +\frac{1}{r^2}\left[C_{44}^E(r)\right]\{\Psi_{3,\theta}\}\{\Psi_{3,\theta}\}^T \end{bmatrix}$$

References

1. R.B. Bhat, J. Sound Vibr. **102**, 493 (1985)
2. *IEEE Std.*, *IEEE Standard on Piezoelectricity* (The Institute of Electrical and Electronics Engineers, New York, 1987)
3. S.K. Parashar, U.V. Wagner, P. Hagedorn, J. Sound Vibr. **285**(4), 989 (2005)
4. W.P. Mason, B. Hans, Phys. Today **4**, 23 (1951)
5. S.K. Parashar, U.V. Wagner, P. Hagedorn, Nonlinear Dyn. **37**(3), 181 (2004)
6. S.K. Parashar, A. Kumar, Arch. Appl. Mech. **85**(5), 641 (2015)
7. A. Graham, *Kronecker Products and Matrix Calculus: With Applications* (Wiley, NY, 1982), p. 130
8. M.W. Hooker, *Properties of PZT-Based Piezoelectric Ceramics Between −150 and 250 °C* (NASA Langley Research Center, Hampton, 1998)

Chapter 26
Applied Theory of the Vibration of Inhomogeneously Polarized Axisymmetric Bimorph Piezoelements

Arkadiy Soloviev, Pavel Oganesyan, Pavel Romanenko, Le Van Duong and Olga Lesnjak

Abstract Piezoelectric generators (PEG) are effective for energy harvesting in machines vibrating elements. Using inhomogenously polarized piezoelements in PEG allows one to increase its output characteristics (output electric potential and output power). The paper considers piezoelements, which are circular multilayer plates (bimorphs), consisting of piezoceramic layers with inhomogeneous polarization (in thickness and in radial direction). Such a method of polarization makes it possible to use a piezomodule d_{33} for bending vibrations, which is significantly larger than piezomodule d_{31}. PEG optimization can be performed on the base of mathematical modeling of the process. Linear electroelastic theory, implemented in ACELAN and ANSYS software, was used as mathematical model. Moreover, the applied theory of axisymmetric bending vibrations with a piecewise constant polarization was created. In the applied theory, hypotheses about the distribution of displacements and electric potential along the thickness of the piezoelectric element have been adopted. System of ordinary differential equations and boundary conditions for steady bending vibrations for deflection and electric potential, depending on the radial coordinate, has been formulated. A series of calculations was performed in which resonance frequencies, antiresonance and output characteristics of PEG were determined depending on the design parameters.

A. Soloviev (✉) · O. Lesnjak
Department of Theoretical and Applied Mechanics, Don State Technical University, Rostov-on-Don, Russia
e-mail: solovievarc@gmail.com

P. Oganesyan · P. Romanenko
I. I. Vorovich Mathematics, Mechanics and Computer Sciences Institute, Southern Federal University, Rostov-on-Don, Russia

L. Van Duong
Department of Mechanical Engineering and Energy, Transportation Le Quy Don Technical University, Ha Noi, Vietnam

I. A. Parinov et al. (eds.), *Advanced Materials*, Springer Proceedings in Physics 207, https://doi.org/10.1007/978-3-319-78919-4_26

26.1 Introduction

Simulation of the performance of PEG energy harvesting devices can be carried out on the base of finite element modeling in computer software such as ACELAN, ANSYS, etc. Experimental and numerical studies of PEG of stack and bimorph types are discussed in [1–4]. The ACELAN software implemented the possibility of calculating the process of polarization of piezoelectric elements based on the theory developed in [5]. The use of inhomogeneously polarized piezoelements in the bimorph type of PEG significantly increases its output characteristics [6]. In [7–10], a method for inhomogeneous polarization of rectangular bimorph piezoelements was developed and an applied theory of calculating its cylindrical bending vibrations for piecewise constant polarization was constructed. In this paper we consider axisymmetric vibrations of a bimorph piezoelement in the form of a multilayer circular disk with piezoceramic layers are partially covered with electrodes and are inhomogeneously polarized, with circular and annular regions with a thickness polarization (they are covered with electrodes along one flat face) and an electrically-connected annular section between them with radial polarization (Fig. 26.1).

26.1.1 Research Purpose

The efficiency of PEG with the shape of a bimorph circular plate with axisymmetric bending vibrations is studied. The piezoceramic layer of the transducer has an inhomogeneous polarization.

26.1.2 Research Scope

At this study, we consider the following frameworks of the problem:

(i) Inhomogeneous polarization creation technology and PEG design;
(ii) Applied theory of flexural axisymmetric vibrations of PEG;

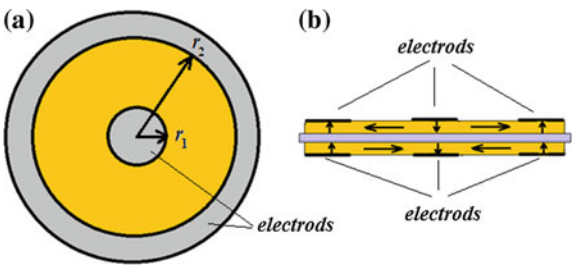

Fig. 26.1 **a** Piezoelectric element top view, axial section, **b** polarization scheme

(iii) Finite element modeling of PEG with an inhomogeneously polarized piezoelement;
(iv) Numerical and analytical calculation of the output characteristics of the power harvesting device;
(v) Optimization of the structural characteristics of PEG for obtaining its greatest efficiency.

26.2 Research Method

26.2.1 Continuous Formulation of the Problem

The mathematical model of flexural steady vibrations of a bimorph circular plate can be reduced to the boundary problem of electro-elasticity, which consists of a system of differential equations [11, 12].

We assume that the following constitutive equations are satisfied (piezoelectric medium is $\Omega_j = \Omega_{pk}$):

$$\rho_{pk}\ddot{\mathbf{u}} + \alpha_{dj}\rho_j\dot{\mathbf{u}} - \nabla\cdot\boldsymbol{\sigma} = \mathbf{f}_j; \quad \nabla\cdot\mathbf{D} = 0, \tag{26.1}$$

$$\boldsymbol{\sigma} = \mathbf{c}_j^E\cdot\cdot(\boldsymbol{\varepsilon} + \beta_{dj}\dot{\boldsymbol{\varepsilon}}) - \mathbf{e}_j^T\cdot\mathbf{E}; \quad \mathbf{D} + \varsigma_d\dot{\mathbf{D}} = \mathbf{e}_j\cdot\cdot(\boldsymbol{\varepsilon} + \varsigma_d\dot{\boldsymbol{\varepsilon}}) + \mathfrak{э}_j^S\cdot\mathbf{E}, \tag{26.2}$$

$$\boldsymbol{\varepsilon} = (\nabla\mathbf{u} + \nabla\mathbf{u}^T)/2; \quad \mathbf{E} = -\nabla\varphi, \tag{26.3}$$

where $\rho(x, t)$ is the continuous function of coordinates (density); $\mathbf{u}(x)$ is the displacement vector-function; $\boldsymbol{\sigma}$ is the stress tensor, $\mathbf{f}$ are the mass forces vector; $\mathbf{D}$ is the electric induction vector; $\mathbf{c}_j^E$ is the elastic constant tensor; $\mathbf{e}_j$ is the tensor of piezoelectric constants; $\boldsymbol{\varepsilon}$ is the strain tensor; $\mathbf{E}$ is the electric field vector; $\varphi(x)$ is the electric potential function; $\mathfrak{э}_j^S$ is the dielectric permittivity tensor; α_{dj}, β_{dj}, ζ_d are non-negative damping coefficients, and the other symbols are the standard designations for theory of electroelasticity with the exception of index "j", corresponding to area Ω_j. (For elastic media $\Omega_j = \Omega_e$, the piezomodules $\mathbf{e}_j$ are equal to zero.)

For the media $\Omega_j = \Omega_{em}$ with pure elastic properties, only stress fields would be considered. Similar (26.1)–(26.3) and constitutive relationships are used, neglecting electric fields and piezoelectric connectivity effects. Equations (26.1)–(26.3) are added to the mechanical and electrical boundary conditions, as well as the initial conditions in the case of non-stationary problem. Numerical modeling of devices that can be described with (26.1)–(26.3) are performed using finite element method.

The boundary conditions are divided into mechanical and electrical. In particular, for an electrode (S_e), included in external circuit, besides the condition of constancy of the electric potential, which presents itself unknown function in this case, it is necessary to add the condition, defining electric current passes through this electrode:

$$\int_{S_e} \dot{D}_m ds = I. \tag{26.4}$$

In addition to previous equations, all material properties are handled as functions of coordinates:

$$\rho_k = \rho_{pk}(x); \quad \mathbf{c}_j^E = \mathbf{c}_j^E(x); \quad \boldsymbol{\varepsilon}_{\mathbf{a}j}^S = \boldsymbol{\varepsilon}_{\mathbf{a}j}^S(x); \quad \mathbf{e}_j^T = \mathbf{e}_j^T(x), \tag{26.5}$$

where we have

$$g = g^i + |P|(g^a - g^i), \text{ for tensors } \mathbf{c}_j^E \text{ and } \mathfrak{d}_j^S; \text{ and } g = |P|g^a, \text{ for tensor } \mathbf{e}_j^T. \tag{26.6}$$

Here g are corresponding tensor components, i points isotropic state, a points anisotropic state. Tensor of piezoconstants $\mathbf{e}_j^T$ will be zero for isotropic bodies. In previous paper [4], we presented specific modules of ACELAN software for describing, presenting and modeling the non-homogeneous polarization.

The matrices of elastic constants, piezoelectric constant and permittivity have the corresponding forms for regions with transverse polarization, respectively:

$$\begin{bmatrix} c_{11} & c_{12} & c_{13} & 0 & 0 & 0 \\ c_{12} & c_{11} & c_{13} & 0 & 0 & 0 \\ c_{13} & c_{13} & c_{33} & 0 & 0 & 0 \\ 0 & 0 & 0 & c_{44} & 0 & 0 \\ 0 & 0 & 0 & 0 & c_{44} & 0 \\ 0 & 0 & 0 & 0 & 0 & \frac{1}{2}c_{11} - \frac{1}{2}c_{12} \end{bmatrix}; \quad \begin{bmatrix} 0 & 0 & e_{31} \\ 0 & 0 & e_{31} \\ 0 & 0 & e_{33} \\ 0 & e_{15} & 0 \\ e_{15} & 0 & 0 \\ 0 & 0 & 0 \end{bmatrix}; \quad \begin{bmatrix} g_{11} & 0 & 0 \\ 0 & g_{11} & 0 \\ 0 & 0 & g_{33} \end{bmatrix}. \tag{26.7}$$

For regions with polarization in radial direction, we have another forms:

$$\begin{bmatrix} c_{33} & c_{13} & c_{13} & 0 & 0 & 0 \\ c_{13} & c_{11} & c_{12} & 0 & 0 & 0 \\ c_{13} & c_{12} & c_{11} & 0 & 0 & 0 \\ 0 & 0 & 0 & \frac{1}{2}c_{11} - \frac{1}{2}c_{12} & 0 & 0 \\ 0 & 0 & 0 & 0 & c_{44} & 0 \\ 0 & 0 & 0 & 0 & 0 & c_{44} \end{bmatrix}; \quad \begin{bmatrix} e_{33} & 0 & 0 \\ e_{31} & 0 & 0 \\ e_{31} & 0 & 0 \\ 0 & 0 & 0 \\ 0 & 0 & e_{15} \\ 0 & e_{15} & 0 \end{bmatrix}; \quad \begin{bmatrix} g_{33} & 0 & 0 \\ 0 & g_{11} & 0 \\ 0 & 0 & g_{11} \end{bmatrix}. \tag{26.8}$$

26.2.2 Technology of Piezoelements Polarization

Polarization of the piezoelement is performed in two stages using technological electrodes on the lower surface, which are removed after the second stage. Calculation of the residual polarization field is conducted in the finite element software ACELAN [7]. Figure 26.2 shows half of the axial section of the upper piezoceramic disk and two polarization stages: the first stage involves transverse polarization of the regions, covered by the electrodes (Fig. 26.2a), and the second stage involves polarization in radial direction of the section between them (Fig. 26.2b).

The lower piezoceramic disk is polarized in a similar way to the circuit, shown in Fig. 26.2 ($-V_0$ is replaced on $+V_0$).

26.2.3 Applied Theory of Flexural Axisymmetric Vibrations of PEG

Under the assumption of Kirchhoff-Love hypotheses for mechanical quantities and a single normal, the angle of inclination of the normal ϑ, radial and circular deformation, expressed through the deflection $U_z = U_z(r)$ of the median surface, takes the form, respectively:

$$\vartheta = -\frac{dU_z(r)}{dr}, \quad \varepsilon_r = -\frac{d^2U_z(r)}{dr^2}z, \quad \varepsilon_t = -\frac{1}{r}\frac{dU_z(r)}{dr}z. \tag{26.9}$$

Electrical potential distribution in parts with transverse polarization is found as

$$\varphi(r,\theta,z) = V_p\frac{z}{2h}\left(1-\frac{2z}{h}\right) + V_m\frac{z}{2h}\left(1+\frac{2z}{h}\right) + \Phi(r)\left(1-\frac{4z^2}{h^2}\right). \tag{26.10}$$

where h is the plate thickness; V_m, V_p are the electrical potentials on the upper and lower electrodes, respectively.

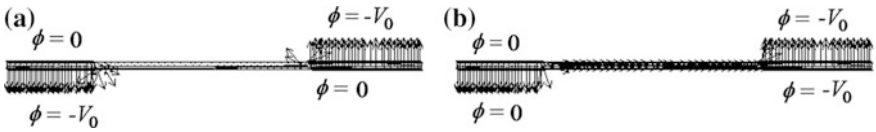

Fig. 26.2 First (**a**) and second (**b**) stages of piezoelement polarization

In a ring with polarization in radial direction, we have:

$$\varphi(r,\theta,z) = \Phi(r). \tag{26.11}$$

System of differential equations for areas with transverse polarization for a two-layer piezoactive bimorph for deflection $U_z = U_z(r)$ and the electric potential of the mid-surface $\Phi = \Phi(r)$ will take the forms:

$$\frac{d^4U_z}{dr^4}D + 2D\frac{1}{r}\frac{d^3U_z}{dr^3} - D\frac{1}{r^2}\frac{d^2U_z}{dr^2} + D\frac{1}{r^3}\frac{d^2U_z}{dr^2} - F\frac{d^2\Phi}{dr^2} - F\frac{1}{r}\frac{d\Phi}{dr} - \omega^2\rho h U_z = p(r); \tag{26.12}$$

$$\frac{d^2\Phi}{dr^2} - 3G\frac{d^2U_z}{dr^2} - G\frac{1}{r}\frac{dU_z}{dr} + H(-V_m + V_p - 4\Phi) = 0, \tag{26.13}$$

where $H = 3\frac{c_{33}g_{33}+e_{33}^2}{h^2 g_n c_{33}}$, $F = \frac{2h}{3}\frac{(c_{13}e_{33}-c_{33}e_{31})}{c_{33}}$, $G = \frac{c_{13}e_{33}-c_{33}e_{31}}{2g_{11}c_{33}}$, ω is the angular frequency of vibration.

Internal mechanical (M_r is the moment, Q_r is the transverse force) and electrical (φ is the electric potential, D_r is the electric induction) factors are expressed as

$$\begin{aligned} M_r &= -D\left(\frac{d^2U_z}{dr^2} + \frac{1}{r}\frac{dU_z}{dr}\right) - \frac{h^3}{18}(-V_m + V_p - 4\Phi)H; \\ Q_r &= -D\left(\frac{d^3U_z}{dr^3} + \frac{1}{r}\frac{d^2U_z}{dr^2} - \frac{1}{r}\frac{dU_z}{dr}\right) - J\frac{d\Phi}{dr}; \end{aligned} \tag{26.14}$$

$$\varphi = \frac{1}{12}(-V_m + V_p + 8\Phi); \quad D_r = -\frac{2}{3}g_{11}\frac{d\Phi}{dr}, \tag{26.15}$$

where $J = \frac{2}{3}h\frac{(c_{33}e_{15}-c_{13}e_{33}+c_{33}e_{31})}{c_{33}}$.

For a region with longitudinal polarization, the system of differential equations corresponding to the system (26.11), (26.12) has the form:

$$D_1\frac{d^4U_z}{dr^4} + 2D_1\frac{1}{r}\frac{d^3U_z}{dr^3} - D_2\frac{1}{r^2}\frac{d^2U_z}{dr^2} + D_2\frac{1}{r^3}\frac{dU_z}{dr} - F_1\frac{d^3\Phi}{dr^3} - F_2\frac{1}{r}\frac{d^2\Phi}{dr^2} - \omega^2\rho h U_z = p(r); \tag{26.16}$$

$$K\frac{d^2\Phi}{dr^2} + L\frac{d^3U_z}{dr^3} - N\frac{1}{r}\frac{d^2U_z}{dr^2} + N\frac{1}{r^2}\frac{dU_z}{dr} = 0; \tag{26.17}$$

where

$$D_1 = \frac{h^3}{12}\frac{(c_{11}c_{33} - c_{13}^2)}{c_{11}}; \quad D_2 = \frac{h^3}{12}\frac{(c_{11}^2 - c_{12}^2)}{c_{11}}; \quad F_1 = \frac{h^2}{4}\frac{(c_{11}e_{33} - c_{13}e_{31})}{c_{11}};$$
$$N = \frac{h}{4}\frac{(c_{12}e_{31} - c_{11}e_{31})}{c_{11}}; \quad F_2 = \frac{h^2}{4}\frac{(2c_{11}e_{33} - c_{13}e_{31} + c_{12}e_{31} - 2c_{13}e_{31})}{c_{11}};$$
$$K = \frac{(c_{11}g_{33} + g_{31}^2)}{c_{11}}; \quad L = \frac{h}{4}\frac{(c_{11}e_{33} - c_{13}e_{31})}{c_{11}}.$$

Internal mechanical and electrical factors are expressed as

$$M_r = -D_1\frac{d^2U_z}{dr^2} - D_3\frac{1}{r}\frac{dU_z}{dr} + F_1\frac{d}{dr}\Phi;$$
$$Q_r = -D_1\frac{d^3U_z}{dr^3} - D_1\frac{1}{r}\frac{d^2U_z}{dr^2} + D_2\frac{1}{r^2}\frac{dU_z}{dr} + F_1\frac{d^2\Phi}{dr^2} + F_3\frac{1}{r}\frac{d\Phi}{dr}; \tag{26.18}$$

$$\varphi = \Phi(r); \quad D_r = \frac{1}{h}F_1\frac{d^2U_z}{dr^2} + N\frac{1}{r}\frac{dU_z}{dr} - K\frac{d}{dr}\Phi, \tag{26.19}$$

where

$$D_3 = -\frac{h^3}{12}\frac{(c_{11}c_{13} - c_{12}c_{13})}{c_{11}}, F_3 = \frac{h^2}{4}\frac{(c_{11}e_{33} - c_{13}e_{31} - c_{11}e_{31} + c_{12}e_{31})}{c_{11}}.$$

The boundary conditions and congruence conditions have the forms:

for $r = 0$:
$\vartheta = 0$ and in the absence of concentrated force or inertial mass, we have
$Q_r = 0$ from (26.14) and $D_r = 0$ from (26.13);
for $r = r_i$, $i = 1, 2$, we have congruence of parts with different polarizations.

The conditions for continuity of deflections U_z, angles ϑ, moments and transverse forces, we obtain from (26.14) and (26.18), electric potential and electrical induction are found from (26.15) and (26.19).

26.3 Results and Discussion

26.3.1 Static Load

Next, the efficiency of a uniformly and inhomogeneously polarized PEG is compared. The thickness of the piezolayers (from PZT-4) is equal to 0.2 mm, the radius is 19 mm, the thickness of the steel plate, on which they are pasted, equals 0.1 mm. The load is a uniform pressure with intensity of 1 kPa. For piecewise constant polarization, the dimensions of the electrodes vary.

Table 26.1 Static load

No.	Type of PEG and sizes of electrodes (mm)	Deflection at the center (mm)	Output potential (V)
1	Uniform polarization	0.5×10^{-3}	0.85
2	Inhomogeneous polarization $r_1 = 3$, $r_2 = 6$	0.54×10^{-3}	13.82
3	Inhomogeneous polarization $r_1 = 2$, $r_2 = 7$	0.58×10^{-3}	21.4
4	Inhomogeneous polarization $r_1 = 1$, $r_2 = 8$	0.62×10^{-3}	28.3

Table 26.1 presents the results of calculation of deflection and output potential for PEG with homogeneous polarization (No. 1) and for different electrode sizes (Nos. 2–4).

26.3.2 Steady-State Vibrations

Steady-state vibrations of the PEG at the first antiresonance frequency are considered. The shape of the vibrations, with the distribution of the axial displacement, is shown in Fig. 26.3a, the distribution of the electrical potential for homogeneous polarization (No. 1 in Table 26.2) is shown in Fig. 26.3b, and for the inhomogeneous polarization (No. 3 in Table 26.2), it is shown in Fig. 26.3c.

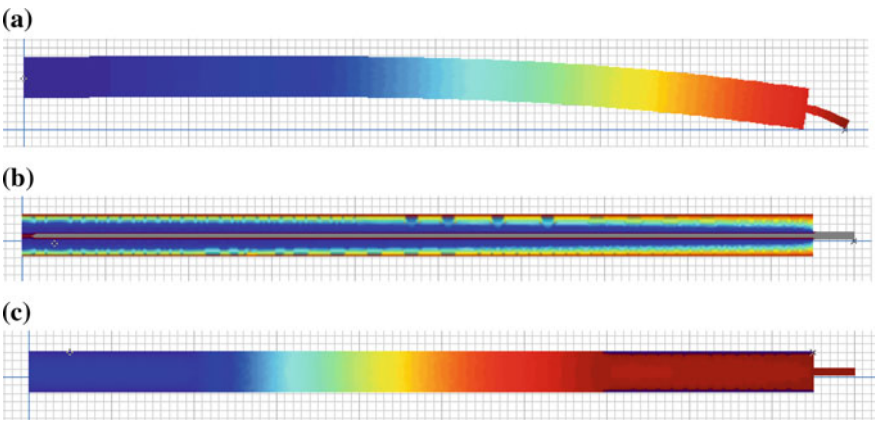

Fig. 26.3 Distributions of deflection (**a**) and electric potential (**b**) at homogeneous polarization, (**c**) inhomogeneous polarization

Table 26.2 Harmonic analysis

No.	Type of PEG and sizes of electrodes (mm)	Antiresonance frequency (kHz)	Deflection at the center (mm)	Output potential (V)
1	Uniform polarization	4.528	2.34×10^{-3}	37.8
2	Inhomogeneous polarization $r_1 = 3$, $r_2 = 6$	4.350	2.51×10^{-2}	617
3	Inhomogeneous polarization $r_1 = 2$, $r_2 = 7$	4.200	2.66×10^{-2}	939
4	Inhomogeneous polarization $r_1 = 1$, $r_2 = 8$	4.095	2.77×10^{-2}	1221

Table 26.2 shows the calculation results for the first antiresonance frequency: the deflection at the center and the output potential for PEG with homogeneous polarization No. 1 and for different electrode sizes Nos. 2–4.

26.4 Conclusion

An applied theory of axisymmetric vibrations of PEG with a piecewise constant polarization is constructed. The results of the calculations show the significant efficiency of PEG with regions of polarization in radial direction, when generating an output potential in comparison with PEG with homogeneous polarization of piezoceramic layers. It is shown that the output potential increases with the growth of the region with polarization in radial direction. There is a limiting size of this section, which can be efficiently polarized. So, it is possible to make several such sections of a given size to create an effective device.

Acknowledgements This research was performed into framework of financing RFBR grant number 16-01-00354A.

References

1. A.N. Solovyev, L.V. Duong, Int. J. Appl. Mech. **8**(3), 1650029 (2016)
2. L.V. Duong, M.T. Pham, V.A. Chebanenko, A.N. Solovyev, C.V. Nguyen, Int. J. Appl. Mech. **9**(6), 1750084 (2017)
3. A.N. Soloviev, I.A. Parinov, L.V. Duong, C.C. Yang, S.H. Chang, J.C.Y. Lee, in *Physics and Mechanics of New Materials and Their Applications*, ed. by I.A. Parinov, S.-H. Chang (Nova Science Publishers, New York, 2013), 147pp

4. V.A. Akopyan, I.A. Parinov, Y.N. Zakharov, V.A. Chebanenko, E.V. Rozhkov, in *Advanced Materials—Studies and Applications*, ed. by I.A. Parinov, S.H. Chang, S. Theerakulpisut (Nova Science Publishers, New York, 2015), 417pp
5. A.V. Belokon, A.S. Skaliukh, *Mathematical Modeling of Irreversible Processes of Polarization* (FizMatLit, Moscow, 2010), 328pp (in Russian)
6. A.S. Skaliukh, A.N. Soloviev, P.A. Oganesyan, Ferroelectrics **483**(1), 95 (2015)
7. A.N. Soloviev, P.A. Oganesyan, A.S. Skaliukh, in *Advanced Materials—Studies and Applications*, ed. by I.A. Parinov, S.H. Chang, S. Theerakulpisut (Nova Science Publishers, New York, 2015), 169pp
8. A.O. Vatulian, I.P. Getman, N.B. Lapnitskaya, Appl. Mech. **27**(10), 101 (1991)
9. A.O. Vatul'yan, A.A. Rynkova, J. Appl. Mech. Tech. Phys. **42**(1), 164 (2001)
10. A.N. Soloviev, P.A. Oganesyan, A.S. Skaliukh, Le V. Duong, V.K. Gupta, I.A. Panfilov, in *Advanced Materials—Techniques, Physics, Mechanics and Applications*, vol. 193, Springer Proceedings in Physics, ed. by A. Parinov, S.-H. Chang, M.A. Jani (Springer Cham, Heidelberg, New York, Dordrecht, London, 2017), 473pp
11. A.V. Belokon, V.A. Eremeyev, A.V. Nasedkin, A.N. Solov'yev, J. Appl. Math. Mech. **64**(3), 367 (2000)
12. A.V. Belokon, A.V. Nasedkin, A.N. Solov'yev, J. Appl. Math. Mech. **66**(3), 481 (2002)

Chapter 27
Propagation and Attenuation of Elastic Guided Waves in Laminate Fiber-Reinforced Composite Plates

Artem Eremin, Eugen Zimmermann and Rolf Lammering

Abstract Elastic guided wave phenomenon in modern fiber-reinforced laminates is a complex mechanical process. Along with the amplitude and dispersion directivity of source-induced wave fields conditioned by the microscopic material anisotropy, the effects originating from the microstructure of fibrous composites play a non-neglectable role. Among such features are the wave attenuation due to the polymer matrix viscosity and the continuous mode conversion phenomenon originating from the severe difference between matrix/fiber mechanical properties. Possessing remarkable intensity, these features should be accounted for in ultrasonic non-destructive testing and structural health monitoring systems for the reliable operation. In this work, we investigate their influence on guided wave propagation in unidirectional laminates experimentally and numerically. In the computational model, viscosity driven attenuation is addressed through the complex stiffness matrix, and semi-analytical integral approach is employed for parametric analysis of source-induced guided wave dispersion properties and transient propagation. To handle the continuous mode conversion effect, the concept of spatially varying material properties and the finite element method are used. Experimental measurements are performed for piezoelectrically excited guided waves with scanning laser Doppler vibrometry technique.

A. Eremin (✉)
Institute for Mathematics, Mechanics and Informatics, Kuban State University, 149, Stavropolskaya Street, Krasnodar 350040, Russia
e-mail: eremin_a_87@mail.ru

A. Eremin · E. Zimmermann · R. Lammering
Institute of Mechanics, Helmut-Schmidt-University/University of the Federal Armed Forces, 85, Holstenhofweg, 22043 Hamburg, Germany
e-mail: eugen.zimmermann@hsu-hh.de

I. A. Parinov et al. (eds.), *Advanced Materials*, Springer Proceedings in Physics 207, https://doi.org/10.1007/978-3-319-78919-4_27

27.1 Introduction

Fiber-reinforced polymer (FRP) composite materials are widely adopted for structural components in modern applications due to their remarkable strength and stiffness properties and possibilities of weight reduction, which makes them being the main among objectives of research efforts in the fields of Non-Destructive Testing (NDT) and Structural Health Monitoring (SHM) [1, 2]. Among the approaches to integrity evaluation of prolonged thin-walled constructions manufactured from composites with NDT/SHM systems, ultrasonic guided waves (GWs) are recognized as an efficient solution, allowing for the detection of possible damage and used for the continuous diagnostics of material degradation.

Effective implementation of GW-based methods requires rigorous experimental investigations, extensive computer simulations and reliable parametric analysis of wave phenomena, taking into account a possible complexity of structure mechanical properties. The latter is especially important for FRP laminates, characterized by fiber-induced anisotropy of elastic properties and non-neglectable wave damping resulting from polymer-based matrix [3]. Another distinctive feature, observed in fibrous composites, is the "continuous mode conversion" (CMC) phenomenon [4, 5]. It is conditioned by the complex material microstructure, i.e., severe difference in mechanical properties of fibers and polymer matrix, which induces a spatial variation of mechanical properties. This phenomenon is pronounced by the occurrence of the fundamental anti-symmetrical wave A0 inside and immediately after the wave packets corresponding to the symmetrical one (S0) passes everywhere through the structure. These properties have a strong effect on GW propagation and, therefore, should be adequately addressed in mathematical and computer models and considered, when interpreting measured wave signals.

In the current contribution, the results of theoretical and experimental investigations of the influence of viscoelastic material behavior and CMC phenomenon on GWs in unidirectional laminates are present and discussed. Evaluation of GW dispersion properties (complex wave numbers and energy velocities) and computer simulation of transient GW propagation are realized in the context of general 3D elastodynamics of viscoelastic laminate anisotropic homogeneous structures through integral equation based asymptotic solutions for forced GWs [6]. Continuous mode conversion is reproduced for the plane waves propagating along the composite principal axis, assuming the spatial variation of material Young's modulus and density in the form of a two-dimensional random field with exponential covariance function [7]. Corresponding numerical implementation is achieved with the Karhunen-Loeve expansion (KLE) and spectral finite element method (FEM). The attenuation of piezoelectrically induced GWs and arising CMC phenomenon in the considered laminate are experimentally quantified with a non-contact 1D scanning laser Doppler vibrometer (SLDV).

27.2 Guided Waves in Viscoelastic Anisotropic Waveguide

If the time harmonic motion $\mathbf{u}(\mathbf{x},\omega)e^{-i\omega t}$, $\mathbf{u}=(u_x,u_y,u_z)$, $\mathbf{x}=(x,y,z)$ of a plate-like traction-free anisotropic waveguide $D=\{(x,y,z):|x|,|y|<\infty,-H<z<0\}$ is considered (Fig. 27.1), linear viscoelasticity can be modeled by assuming complex components in the material's stiffness matrix: $\widetilde{C}=C-i\eta$, where C and η are real-valued frequency-independent (hysteretic model [8]) 6×6 matrixes. The components of $\widetilde{C}$ might be determined directly from experiments, e.g., utilizing ultrasonic interferometry methods [9], or, alternatively, parametrically expressed through the C-matrix elements [10]. In the case of a transversely isotropic elastic layer with its symmetry axis (fiber alignment direction) coinciding with the x-axis, the following relations are suggested:

$$\widetilde{C}_{ii}=C_{ii}/(1+ip\sqrt{C_{55}/C_{ii}}),\ i=1,5;\quad \widetilde{C}_{ii}=C_{ii}/(1+ip\beta\sqrt{C_{55}/C_{ii}}),\ i=2,4$$
$$\widetilde{C}_{12}=(C_{12}+C_{55})/(1+ip\sqrt{C_{55}/C_{ii}})-\widetilde{C}_{55}. \tag{27.1}$$

Here parameter p is the damping factor, and β is the additional coefficient employed for the attenuation enhancement in the direction orthogonal to the symmetry axis.

Assuming that the structure is excited by a load $\mathbf{q}(\mathbf{x},\omega)e^{-i\omega t}$, $\mathbf{q}=(q_x,q_y,q_z)$, localized at the top surface $z=0$ of the waveguide (the time-harmonic factor $e^{-i\omega t}$ is further omitted), the integral Fourier transform F_{xy} over the horizontal spatial variables x, y could be applied to derive the explicit solution of the considered boundary value problem in terms of inverse Fourier two-fold path integral. With the polar coordinates (r,φ) and (α,γ), introduced in spatial and Fourier domains, respectively, it takes the form:

$$\mathbf{u}(\mathbf{x})=\frac{1}{4\pi^2}\int_{\Gamma_+}\int_0^{2\pi}K(\alpha,\gamma,z)\mathbf{Q}(\alpha,\gamma)e^{-i\alpha r\cos(\gamma-\varphi)}d\gamma\alpha d\alpha, \tag{27.2}$$

where $K=F_{xy}[k]$ and $\mathbf{Q}=F_{xy}[\mathbf{q}]$ are Fourier symbols of the Green's matrix $k(\mathbf{x})$ and the contact stress vector $\mathbf{q}(x,y)$ (the notation of [6, 11] is employed). Since

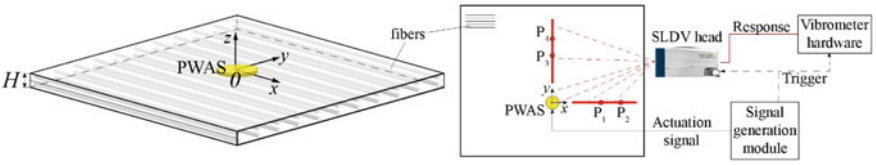

Fig. 27.1 Geometry of the problem (left) and the schematic representation of the experimental setup

the poles of the matrix K elements are now complex values with positive imaginary part, the integration path Γ_+ goes in the complex plane directly along the real semi-axis $\mathrm{Re}\,\alpha \geq 0$, $\mathrm{Im}\,\alpha = 0$. With the residue technique and the stationary phase method, the relations (27.1) is reduced to the asymptotic expansions in terms of quasi-cylindrical guided waves $\mathbf{u}_n$:

$$\begin{aligned} \mathbf{u}(\mathbf{x}) &= \sum_{n=1}^{N_r} \mathbf{u}_n(\mathbf{x}) + O((\zeta_n r)^{-1}), \quad \zeta_n r \to \infty; \\ \mathbf{u}_n(\mathbf{x}) &= \sum_{m=1}^{M_n} \mathbf{a}_{nm}(\varphi, z) e^{i s_{nm} r} / \sqrt{\zeta_n r}. \end{aligned} \tag{27.3}$$

Here $s_{nm} = s_n(\gamma_{nm})$ are the complex wave numbers of the GWs $\mathbf{u}_n$; γ_{nm} are the stationary points of the phase functions, $\hat{s}_n(\gamma) = \mathrm{Re}[\zeta_n(\gamma + \varphi + \pi/2)] \sin\gamma$, that is $\hat{s}_n'(\gamma_{nm}) = 0$; N_r is the number of poles ζ_n closest to the real axis; M_n is the number of stationary points γ_{nm} of the n-th phase function $\hat{s}_n$; amplitude factors $\mathbf{a}_{nm}$ are expressed via the residues of the product $K\mathbf{Q}$ from the real poles $\zeta_n(\gamma_{nm})$. Each term in the second sum of the (27.3) is a cylindrical guided wave (CGW), specified in the radial observation direction φ by the complex wave number $s_{nm}(\varphi)$ and wave length $\lambda_{nm} = 2\pi/\mathrm{Re}\, s_{nm}$. In the case of lossy media, the conventional relation for group velocities $c_{g,nm}(\varphi) = d\omega/ds_{nm}$ has no physical meaning, therefore, energy velocities $c_{e,nm}$ are used to characterize the speed of propagating wave packets. They are expressed in the following form [12]:

$$c_{e,nm}(\varphi) = \frac{\langle \mathbf{e} \cdot \mathbf{n}_\varphi \rangle_H}{\langle \mathrm{K} + \Pi \rangle_H}, \tag{27.4}$$

where the brackets $\langle .. \rangle_H$ denote the average over the waveguide thickness, symbol "$\cdot$" is for scalar product of complex-valued vectors, $\mathbf{e}(z)$ is the time-averaged Umov-Poynting vector, $\mathbf{n}_\varphi$ stands for the unit vector along the observation direction φ; K and Π are time-averaged kinetic and potential energy:

$$\mathrm{K} = \frac{\rho\omega^2}{4}(\mathbf{u}, \mathbf{u}), \quad \Pi = \frac{1}{4}\mathrm{Re}(\boldsymbol{\varepsilon}, \boldsymbol{\sigma})$$

and the six-component strain and stress vectors $\boldsymbol{\varepsilon}$ and $\boldsymbol{\sigma}$ are obtained from the corresponding tensors by means of the Voigt notation. Since (27.4) is derived within the plane wave assumption, the displacement vector is rewritten as follows

$$\mathbf{u}_{nm}(\mathbf{x}) = \mathbf{a}_{nm}(\varphi, z) \exp[-i\varsigma_{nm}(x\cos(\gamma_{nm}) + y\sin(\gamma_{nm}))],$$

and the terms $\mathbf{a}_{nm}(\varphi, z), \varsigma_{nm}, \gamma_{nm}$ are taken from (27.2).

After numerical testing of the proposed computational model over the results from [13, 14], it has been adopted for experimental carbon FRP sample with unidirectional $[0°]_4$ lay-up of prepregs. The dimensions of the specimen are

$1000 \times 1000 \times 1.12\ \text{mm}^3$; the material density is $1482\ \text{kg/m}^3$ and the elastic properties in the principal directions of material symmetry are the following (in GPa) [15]: $C_{11} = 117.2$, $C_{22} = 10.2$, $C_{12} = 4.7$, $C_{44} = 2.79$, $C_{55} = 3.51$.

Preliminarily, the parameters p and β from (27.1) have been estimated to fit the frequency dependences of the attenuation factor $\chi(f)$ ($\omega = 2\pi f$, f [Hz] is dimensional frequency) measured along the material principal axis. It is directly related to the imaginary part of the complex wave number s_{nm} and is calculated through the relation:

$$\chi(f) = \frac{1}{d}\ln\left|\frac{v_z(\mathbf{x}_1, f)}{v_z(\mathbf{x}_2, f)}\right|, \quad d = |\mathbf{x}_2 - \mathbf{x}_1|,$$

where $v_z(\mathbf{x}_{1,2}, f)$ is the spectrum of the measured out-of-plane velocities $v_z(t)$ at surface points $\mathbf{x}_1$ and $\mathbf{x}_2$. To minimize the beam spreading effect, the GW excitation has been performed with a couple of elongated rectangular piezoelectric wafer active sensors (PWAS) of dimensions $30 \times 10 \times 0.25\ \text{mm}^3$ (further referred as RA), aligned either along the x or y direction. The actuators are adhesively attached to the structure and are driven with transient voltages in the form of sine-windowed two-cycle sinus tone bursts for a range of several central frequencies f_c. The location of measurement points $\mathbf{x}_1$ and $\mathbf{x}_2$ is chosen in such a way that the wave packets, corresponding to S0 and A0 modes, are well separated and, therefore, attenuation factors $\chi_{S0}(f)$ and $\chi_{A0}(f)$ might be estimated. The obtained results are summarized in Fig. 27.2, where markers stand for the experimental data and solid lines show $\text{Im}\, s_{nm}$ curves for $p = 0.07$ and $\beta = 2.5$.

To reveal the importance of taking into consideration the material viscosity, measured velocities $v_z(t)$ are compared with theoretical data, computed for the described lossy model and for the ideally elastic structure. Small circular PWAS of radius R = 3 mm and thickness 0.25 mm is used for GW generation, and the tone burst with $f_c = 180\,\text{kHz}$ is applied to the actuator. Due to the relatively small thickness of the actuator, the arising contact stresses $\mathbf{q}(\mathbf{x}, \omega)$ are approximated with the pin-force model [16], i.e., by ring delta-like distribution of surface radial tension. Wave patterns at the points $P_1(80\,\text{mm}, 0)$, $P_2(130\,\text{mm}, 0)$, $P_3(0, 80\,\text{mm})$ and $P_4(0, 130\,\text{mm})$ are shown in Fig. 27.3 in the normalized form. While for the

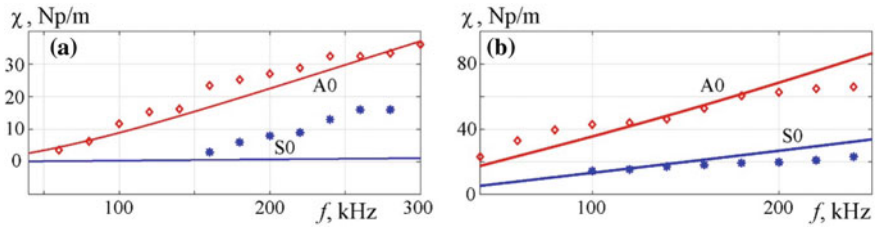

Fig. 27.2 Experimental (markers) and computed (solid lines) attenuation of fundamental S0 and A0 modes for propagation direction along (**a**) and perpendicular (**b**) to the fiber alignment

propagation direction along the fiber alignment (points P_1 and P_2) the influence of viscosity is marginal, the attenuation of A0 mode in the perpendicular direction is substantial and could not be neglected, i.e., at the point P_4 antisymmetric wave is almost indistinguishable from the measurement noise. On the other hand, in the considered frequency range up to the first cut-off frequency of the lossless, anisotropic waveguide GW dispersion curves are almost insensitive to the damping. The latter is illustrated in Fig. 27.4, where the relative difference between group velocities of fundamental modes evaluated for the ideally elastic structure and energy velocities calculated for the same waveguide with attenuation is plotted.

27.3 Continuous Mode Conversion in Unidirectional Laminate

If an intact waveguide with homogeneous macroscopic mechanical properties is considered (either isotropic or anisotropic), no mode conversion could be observed in the computations (theoretical results in Fig. 27.3 serving as an example). Therefore, possible spatial fluctuation of elastic moduli conditioned by complex material microstructure, should be taken into account, e.g., by describing them as second order random fields [17, 18]. Numerical treatment of wave propagation problem in such a case is usually performed in the FEM framework.

SLDV visualization of piezoelectrically excited fundamental Lamb waves in unidirectional FRP samples reveals that for a broad frequency range, CMC phenomenon is primarily detected, when S0 mode travels along the material horizontal principal axes (x and y axes in Fig. 27.1) [5]. Since plane wave motion is possible for these two directions, in the current simulations, the initial three-dimensional problem is reduced to a plane-strain statement for two laminates with lay-ups [0°] and [90°]. It corresponds to the wave propagation along and perpendicular to the fiber alignment

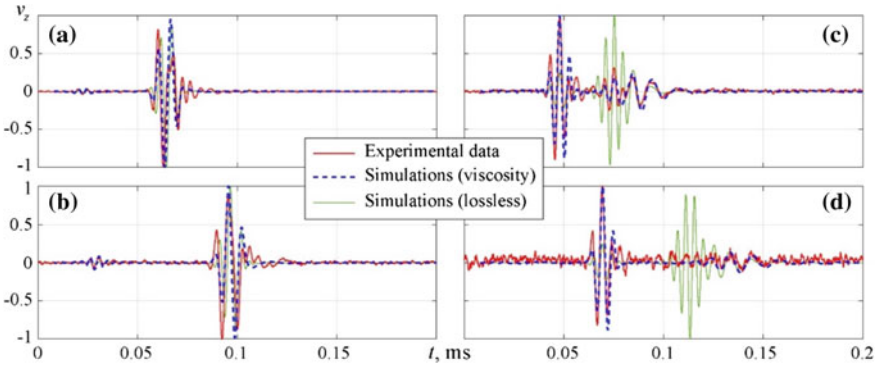

Fig. 27.3 Normalized measured and computed time histories of out-of-plain velocities at surface points P_1, P_2, P_3 and P_4 (subplots from (**a**) to (**d**), respectively)

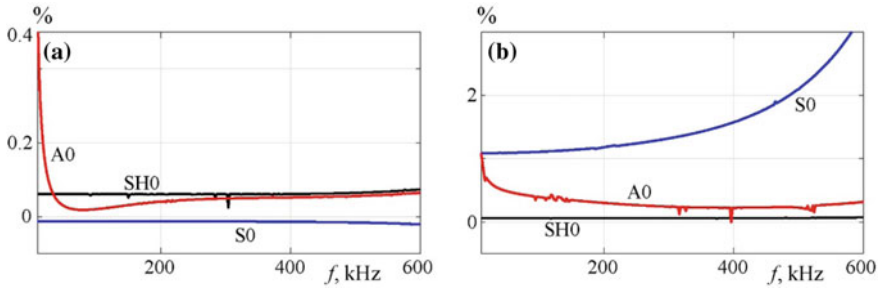

Fig. 27.4 Relative discrepancy (in percents) between group velocities of fundamental modes (lossless waveguide) and energy velocities (waveguide with viscosity) for propagation direction along fiber alignment (**a**) and in the perpendicular one (**b**)

respectively. The waveguides are occupying the finite domain $\widetilde{D} = \{\mathbf{x} = (x, z) : |x| < A,\ -H < z < 0\}$, $A = 500$ mm, $H = 1.12$ mm, and the transient oscillations are initiated by shear point forces $\mathbf{q}(\mathbf{x}, t) = \mathrm{m} f(t)\{\delta(x \pm a), 0\}$, $a = 5$ mm, simulating the PWAS action and being located symmetrically on top and bottom specimen surfaces so that only S0 mode is initially excited (Fig. 27.5). Function $f(t)$ is a sine-windowed two-cycle sinus tone burst. The structure is discretized with 8×4 nodes spectral finite elements (100 in x-direction and 4 for the vertical one) and Newmark method is used for time integration.

Proceeding from the real-valued stiffness matrix C of a transversally isotropic material described above (viscosity is now omitted) to a set of five engineering constants, it is further supposed that parameter E_2 (Young's modulus in the direction perpendicular to fiber alignment) and the density ρ exhibit spatial stochastic variation. The reason for this choice consists in that S0 dispersion properties for unidirectional laminates in the considered frequency range are affected only by these parameters. The Young's modulus E_1 has a constant value. The reason is that the Young's modulus of carbon fibers in the longitudinal direction is almost two orders of magnitude higher that the corresponding parameter for the polymer matrix. Therefore, even being present, the fluctuations in fiber alignment do not introduce considerable scattering in the global Young's modulus E_1 of the unidirectional composite [19]. Applying KLE, the following expansions for E_2 and ρ are obtained [17]:

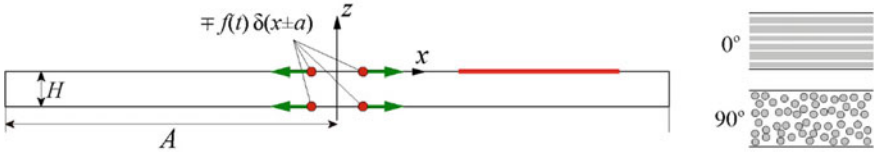

Fig. 27.5 Schematic view of the FEM model and stacking sequences of the investigated laminates

$$E_2(\mathbf{x},\theta) \approx \overline{E}_2\left(1+\sigma_{E_2}\sum_{n=1}^{N_{KL}}\sqrt{\lambda_n}\xi_n(\theta)f_n(\mathbf{x})\right)$$
$$\rho(\mathbf{x},\theta) \approx \overline{\rho}\left(1+\sigma_{\rho}\sum_{n=1}^{N_{KL}}\sqrt{\lambda_n}\eta_n(\theta)f_n(\mathbf{x})\right). \tag{27.5}$$

Here $\overline{E}_2 = 8.05\,\text{GPa}$ and $\overline{\rho} = 1482\,\text{kg/m}^3$ are the mean values of corresponding parameters, $\sigma_{E_2} = 0.2$ and $\sigma_{\rho} = 0.05$ are standard deviations, $N_{KL} = 1000$ is the number of preserved terms in KLE, $\xi_n(\theta)$ and $\eta_n(\theta)$ are uncorrelated random variables, θ is the element of a sample space. Deterministic quantities λ_n and $f_n(\mathbf{x})$ represent the eigenvalues and eigenfunctions of the random field covariance function, which is assumed to have the exponential form:

$$\hat{C}(\mathbf{x}_1,\mathbf{x}_2) = \sigma^2 e^{-\frac{|x_1-x_2|}{b_x}-\frac{|z_1-z_2|}{b_z}},$$

and, since the problem domain $\widetilde{D}$ is a rectangular, have closed analytical expressions [7]. The quantities $b_x = 3\,\text{mm}$ and $b_z = 1.12\,\text{mm}$ are the correlation distances in the x- and z-direction, respectively. They specify the decay of the mutual influence of two locations of the random field and, therefore, control the necessary number of terms in KLE. The particular choice of values for b_x and b_z is conditioned, respectively, by the minimum A0 wavelength in the frequency range considered and the waveguide thickness. Expansions (27.5) cause the analogous decomposition of the stiffness and mass matrices of the FEM scheme. Generating a set of independent Gaussian variables with zero mean and unit variance $\xi_n(\theta_0)$, $\eta_n(\theta_0)$, $n = 1,\ldots,N_{KL}$ for a particular realization θ_0 allows assembling these matrices, and the implementation of the time integration scheme becomes possible.

It should be noted that since the stiffness matrices of the considered 2D waveguides are obtained from the global matrix C, which now implicitly depends on $E_2(\mathbf{x},\theta)$ through the inverse of the compliance matrix, the stochastic fluctuation of this Young's modulus would affect elastic properties of both specimens and might influence on calculated wave patterns.

To visualize the CMC phenomenon and to provide qualitative comparison of the numerical and experimental results, out-of-plane velocities $v_z(\mathbf{x},t)$ are computed and measured at a set of points on the specimen surface (depicted as red lines in Figs. 27.1 and 27.5), post-processed with Hilbert transform, and combined to the B-scan plots (Fig. 27.6 for the tone burst excitation at $f_c = 240\,\text{kHz}$). These surfaces are the time-amplitude data of each observation point with distance r between it and PWAS center on the horizontal axis and time on the vertical one. In the experiments GWs are excited by elongated rectangular piezoactutors (type RA) aligned along the material principal axes to follow approximately the plain wave assumption of the computational model. The primary wave packages of fundamental modes reveal themselves as oblique thick lines with various inclination

angle, and the CMC phenomenon is pronounced as spurious spots following S0 mode propagation. As expected, its intensity is stronger for the propagation direction perpendicular to the fiber alignment, which is also observed in the numerical simulations. Oblique lines in the upper part of the subplot (a) stand for the waves reflected from the boundaries of the computational domain.

Since the out-of-plane velocities of the converted (secondary) A0 and the incident S0 waves might be of the same order of magnitude, the question arises how such energy losses would affect the dispersion properties of the fundamental symmetric wave. Its importance is caused by the high potential of S0 mode utilization for reliable and fast estimation of Young's moduli of the FRP sample [15].

Applying two-dimensional Fourier transform over spatial and temporal coordinates to the simulated signals acquired for B-scans, frequency-wave number representation is obtained (Fig. 27.7a for the [90°] composite sample with simulated CMC), and wave numbers of normal modes are becoming visible. Plotting theoretical dispersion curves for the same waveguide but with deterministic elastic properties readily proves that the spurious motion relates to A0 mode, since the location of strong local peaks almost coincide with its wave number curve. It is also visible that at higher frequencies the trajectory of local maxima for S0 wave starts deviating quite sufficiently from the theoretical curve. This behavior is illustrated in Fig. 27.7c where S0 phase velocity dispersion curves obtained with the semi-analytical technique and from FEM simulations are compared. Additionally, in Fig. 27.7b analogous values for [0°] laminate are provided. Though both FEM-based curves do not coincide directly with the theoretical one, they fluctuate regularly around it.

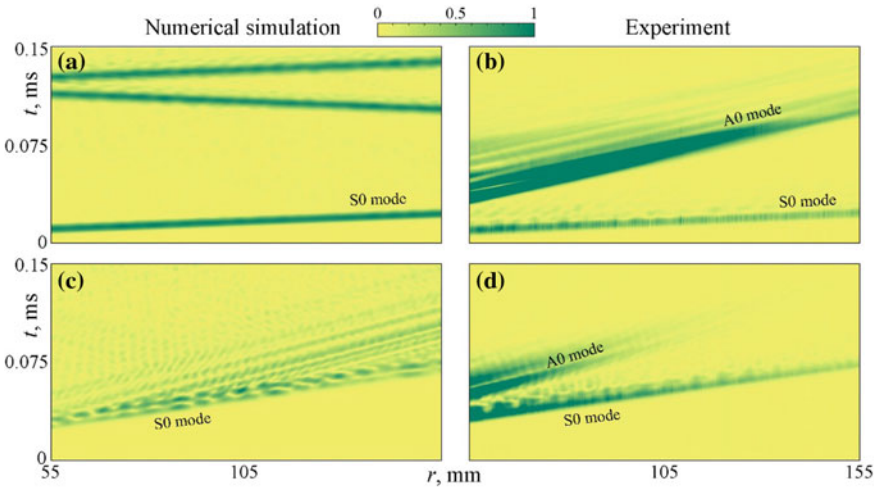

Fig. 27.6 Theoretical (**a**, **c**) and experimental (**b**, **d**) B-scans of the composite specimen surface along fiber alignment direction (**a**, **b**) and in the perpendicular direction (**c**, **d**); in each subplot the data are normalized to the highest observed amplitude of the primary S0 mode

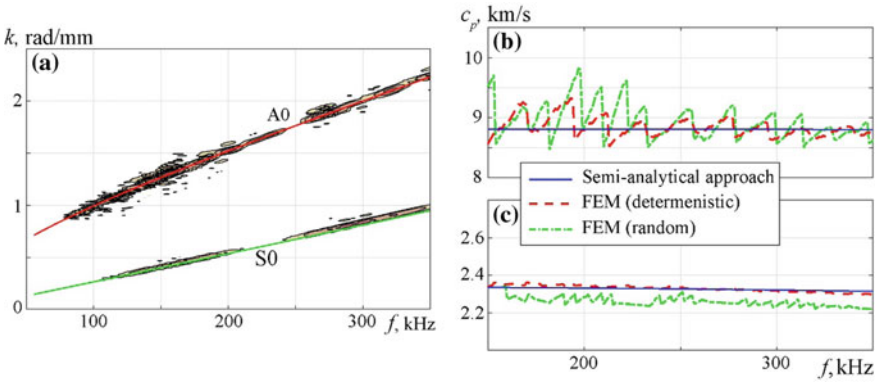

Fig. 27.7 Influence of the simulated CMC phenomenon on GW dispersion properties; wave number-frequency plot for the [90°] laminate with CMC being considered (**a**); phase velocities of fundamental S0 mode for [0°] (**b**) and [90°] (**c**) samples

27.4 Conclusions

The influence of viscoelastic material behavior and CMC phenomenon on elastic GWs in unidirectional FRP laminates has been investigated both theoretically and experimentally. It is shown that although viscosity driven wave attenuation should be taken into account for the adequate simulation of amplitude decay of propagating GWs, especially in the direction perpendicular to the fiber alignment, its effect on GW dispersion properties in the frequency range of fundamental modes is inessential. It is also illustrated that the CMC effect, observed, at first, experimentally, could be adequately qualitatively represented with the FEM-based computational model assuming random spatial distribution of material elastic properties. Parametric analysis within the developed approach reveals the possible non-zero impact of CMC on dispersion curves of fundamental symmetric wave.

Acknowledgements This work is partly funded by the Ministry of Education and Science of the Russian Federation (Project No. 9.1022.2017/4.6) and Russian Foundation for Basic Research jointly with Krasnodar Regional Administration (Project No. 16-41-230744).

References

1. V. Giurgiutiu, *Structural Health Monitoring of Aerospace Composites*, 1st edn. (Elsevier Academic Press, New York, 2015)
2. R. Lammering, U. Gabbert, M. Sinapius, T. Schuster, P. Wierach, *Lamb-Wave Based Structural Health Monitoring in Polymer Composites* (Springer Cham, 2017)
3. R. Chandra, S.P. Singh, K. Gupta, Compos. Struct. **46**, 41 (1999)
4. C. Willberg, S. Koch, G. Mook, J. Pohl, U. Gabbert, Smart Mater. Struct. **21**, 075022 (2012)
5. B. Hennings, R. Lammering, Compos. Struct. **151**, 142 (2016)

6. E. Glushkov, N. Glushkova, A. Eremin, J. Acoust. Soc. Am. **129**(5), 2934 (2011)
7. R.G. Ghanem, P.D. Spanos, *Stochastic Finite Elements: A Spectral Approach* (Springer, New York, 1991)
8. R. Lakes, *Viscoelastic Materials* (Cambridge University Press, 2010)
9. M. Castaings, B. Hosten, T. Kundu, NDT&E Int. **33**, 377 (2000)
10. A.K. Mal, S. Lih, J. Appl. Mech. **59**(4), 878 (1992)
11. E. Glushkov, N. Glushkova, A. Eremin, R. Lammering, J. Acoust. Soc. Am. **135**(1), 154 (2014)
12. B.A. Auld, *Acoustic Fields and Waves in Solids*, vol. 1 (Wiley, 1973)
13. G. Neau, Lamb waves in anisotropic viscoelastic plates: study of the wave fronts and attenuation. Ph.D. thesis, University Bordeaux, Bordeaux (2003)
14. I. Bartoli, A. Marzani, F.L. di Scalea, E. Viola, J. Sound Vib. **295**, 685 (2006)
15. A.A. Eremin, E.V. Glushkov, N.V. Glushkova, R. Lammering, Compos. Struct. **125**, 458 (2015)
16. V. Giurgiutiu, J. Intell. Mater. Syst. Struct. **16**, 291 (2005)
17. E. Zimmermann, A. Eremin, R. Lammering, GAMM-Mitteilungen **41** (2018) (accepted)
18. E. Zimmermann, A. Eremin, R. Lammering, in *Proceedings of the 11th International Workshop on Structural Health Monitoring* (Stanford, USA, 2017), p. 94
19. D.F. Adams, S.W. Tsai, J. Compos. Mater. **3**(3), 368–381 (1969)

Chapter 28
Modelling of Elastic Wave Propagation Through Damaged Interface via Effective Spring Boundary Conditions

Mikhail V. Golub, Anders E. Boström and Olga V. Doroshenko

Abstract The present work deals with the application of spring boundary conditions in order to describe elastic wave propagation in composites with damaged interfaces. Dynamic behaviour of the damaged zone is described by means of a distribution of micro-cracks and introduction of spring boundary conditions, where stresses are proportional to the jump in displacement along the damaged interface and the proportionality factor is the distributed spring stiffness. The stiffness in the spring boundary conditions is determined from the equivalence of the transmission coefficients for these two models. As a result, the normal and tangential components of the spring stiffness tensor depend on the concentration of the defects, their typical size and elastic properties of the contacting materials. The three-dimensional problem with elastic wave scattering by a random or periodic distribution of rectangular microcracks is considered, the latter with a boundary integral equation method. The transmission through the damaged interface with random and periodic distribution of rectangular cracks is compared with a good correspondence giving confidence that the models are appropriate.

28.1 Introduction

Elastic wave scattering by delaminations and debondings is of considerable importance for ultrasonic non-destructive evaluation and structural health monitoring, where ultrasound is widely used to detect interfacial damage [1]. A precursor to destruction of a sample of a composite material is usually the formation of a set

M. V. Golub (✉) · O. V. Doroshenko
Institute for Mathematics, Mechanics and Informatics,
Kuban State University, Krasnodar, Russian Federation
e-mail: m_golub@inbox.ru

A. E. Boström
Division of Dynamics, Department of Applied Mechanics,
Chalmers University of Technology, Göteborg, Sweden

I. A. Parinov et al. (eds.), *Advanced Materials*, Springer Proceedings
in Physics 207, https://doi.org/10.1007/978-3-319-78919-4_28

of microcracks, which are simulated as a stochastic or as a periodic distribution of micro-defects. Detection of internal inhomogeneities and identification of their parameters, particularly detecting internal and interfacial defects by non-destructive testing requires the presence of effective mathematical models describing the diffraction of elastic waves by such damage. Domains containing distribution of microdefects can be modelled as a set of cracks [2, 3] or with the help of special boundary conditions [4]. Wave diffraction by a single crack can be modelled using numerical [5] and semi-analytical methods [6]. If imperfect contact or a partially debonded interface is considered, then modified approaches should be applied [7].

The present work deals with the application of spring boundary conditions in order to describe elastic wave propagation in layered composites with damaged interfaces. Dynamic behaviour of the damaged zone is described by means of a random distribution of micro-cracks and introduction of the spring boundary conditions, which point on the jump in displacement along the damaged interface, and the proportionality factor is the distributed spring stiffness. The stiffness for the spring boundary conditions is determined from the equivalence of transmission coefficients for these two models. As a result, the normal and tangential components of the spring stiffness tensor depend on the concentration of defects, their typical size and elastic properties of the contacting materials. Wave scattering by a random distribution of rectangular cracks is simulated, using the ensemble average. The latter allows consideration of the random distribution array of micro-cracks, based on the solution of the problem for a single rectangular crack. Wave scattering by a periodic array of interface rectangular cracks is also considered, using a boundary integral equation method. The transmission through the damaged interface is simulated by a random or periodic distribution of cracks.

28.2 Spring Boundary Conditions and Random Distribution of Rectangular Cracks

Consider an interface with a random distribution of rectangular cracks at the interface, located between two dissimilar half-spaces V_j, $j = 1, 2$, see Fig. 28.1. The half-spaces are determined by the following material properties: densities ρ_j, Lamé constants λ_j and μ_j. Wave velocities v_{js} are also used; here subscript s corresponds to the longitudinal $(s = \mathrm{L})$ and transversal $(s = \mathrm{T})$ waves. The displacement vector $\boldsymbol{u}_j$ obeys the Lamé equation, written in terms of wave numbers $k_{js} = \omega / v_{js}$:

$$k_{j\mathrm{L}}^{-2} \nabla \nabla \cdot \boldsymbol{u}_j - k_{j\mathrm{T}}^{-2} \nabla \times \left(\nabla \times \boldsymbol{u}_j \right) + \boldsymbol{u}_j = 0.$$

The distribution is assumed translationally invariant, and all the cracks are of the same size. The wave interaction between the cracks is neglected by assuming small cracks compared to the wavelength. The density of cracks is defined as

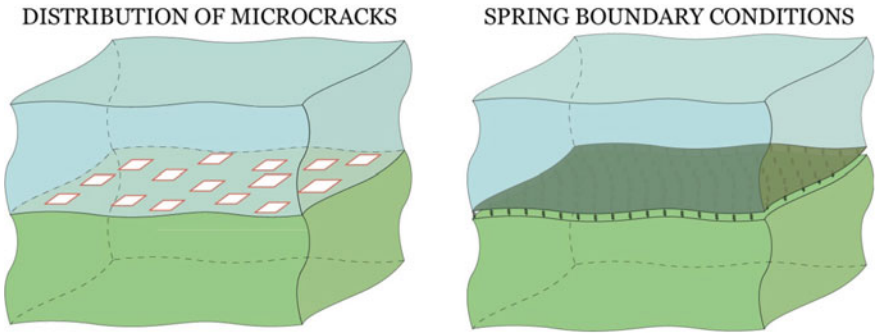

Fig. 28.1 Geometry of the problem: damaged interface

$C = S_{\text{dam}}/S_{\text{total}}$, where in a three-dimensional case, S_{dam} is the damaged area and S_{total} is the total area of the considered surface. Then the ensemble average technique can be applied for the construction of the scattered field, which is represented in the form of plane waves in a far-field zone from the interface [8, 9]. The Betty-Rayleigh reciprocal theorem is applied along a rectangular contour with the interface in the centre to two elastodynamic states [9]: incident and scattered wave-fields $\boldsymbol{u}^{\text{in}}$ and $\boldsymbol{u}^{\text{sc}}$. The ensemble average of the scattered field has the following representation:

$$\left\langle \boldsymbol{u}_s^{\text{sc}} \right\rangle = \begin{cases} P_s^- \, \mathrm{e}^{-\mathrm{i}\, k_{1s} x_3}, & x_3 < 0, \\ P_s^+ \, \mathrm{e}^{\mathrm{i}\, k_{2s} x_3}, & x_3 > 0. \end{cases}$$

The integrals along parts of the contour, which are orthogonal to the interface, cancel each other. Finally, the total transmission coefficient for the distribution of crack in the case of incident longitudinal $(s = \mathrm{L})$ and transversal $(s = \mathrm{T})$ waves becomes:

$$\widetilde{T}_s = T_s^- + P_s^+ = T_s^- \left(1 - \frac{1}{2} \boldsymbol{p}_s \, \Delta \overline{\boldsymbol{u}}_s \right). \tag{28.1}$$

Here $\boldsymbol{p}_s$ is the polarization vector and $\Delta \overline{\boldsymbol{u}}_s$ is average COD for all the cracks, which is calculated as

$$\Delta \overline{\boldsymbol{u}}_s = \frac{1}{S_\Omega} \iint\limits_\Omega \Delta \, \boldsymbol{u}_s(x_1, \, x_2) \mathrm{d}x_1 x_2 \tag{28.2}$$

in the case of cracks of equal size, where S_Ω is the area of a single crack. The random distribution of cracks is then compared with the distributed spring model, where the damaged interface is described via spring boundary conditions. These boundary conditions demand that the stresses are continuous, while the displacement jump is proportional to the stresses:

$$\boldsymbol{\tau}_1(\boldsymbol{x}) = \boldsymbol{\tau}_2\boldsymbol{x} = \boldsymbol{\kappa}\cdot(\boldsymbol{u}_1 - \boldsymbol{u}_2). \tag{28.3}$$

Here $\boldsymbol{\kappa}$ is a three-by-three matrix, $\boldsymbol{\tau}_j$ is the vector of normal and tangential stress components. The elements of the stiffness matrix $\boldsymbol{\kappa}$ are calculated by a comparison of transmission coefficients for the random distribution of cracks and for the spring model. According to this procedure a normally incident incoming longitudinal wave is used to determine the stiffness matrix component $\kappa_{33} = \kappa_{\mathrm{L}}$. The incoming incident plane wave in a three-dimensional case has the following representation:

$$\mathbf{u}_s = \begin{cases} \mathbf{p}_s\left(\mathrm{e}^{\mathrm{i}k_{1s}x_3} + \hat{R}_s\mathrm{e}^{-\mathrm{i}k_{1s}x_3}\right), & x_3 < 0 \\ \mathbf{p}_s\hat{T}_s\mathrm{e}^{\mathrm{i}k_{2s}x_3}, & x_3 > 0 \end{cases}$$

where the amplitude reflection and transmission coefficients depend on wave number and spring stiffness as

$$\begin{aligned} \hat{R}_s &= \frac{\mathrm{i}\,k_{1s}c_{1s}k_{2s}c_{2s} + \kappa_s(k_{1s}c_{1s} - k_{2s}c_{2s})}{\mathrm{i}\,k_{1s}c_{1s}k_{2s}c_{2s} + \kappa_s(k_{1s}c_{1s} + k_{2s}c_{2s})}, \\ \hat{T}_s &= \frac{2\,\kappa_s\,k_{1s}c_{1s}}{\mathrm{i}\,k_{1s}c_{1s}k_{2s}c_{2s} + \kappa_s(k_{1s}c_{1s} + k_{2s}c_{2s})}. \end{aligned} \tag{28.4}$$

At the next step, plane wave diffraction by a rectangular interface crack ($\Omega = \{|x_1| \le l_1, |x_2| \le l_2, x_3 = 0\}$) is considered. Incident wave-field is calculated, assuming $\boldsymbol{\kappa} = 0$ in (28.3). The total wave-field is the superposition of the incident field $\boldsymbol{u}^{\mathrm{in}}$ in the absence of the crack and the wave-field scattered by the crack $\boldsymbol{u}^{\mathrm{sc}}$. The wave-field, scattered by an interface rectangular crack Ω, can be represented as the Fourier integrals [9]:

$$\boldsymbol{u}_j^{\mathrm{sc}} = \frac{1}{4\,\pi^2}\iint\limits_{\Gamma_1\Gamma_2} \mathbf{K}_j(\alpha_1,\ \alpha_2\ x_3)\cdot\boldsymbol{Q}(\alpha_1,\ \alpha_2)\cdot\mathrm{e}^{-\mathrm{i}(\alpha_1 x_1 + \alpha_2 x_2)}\mathrm{d}\alpha_1\mathrm{d}\alpha_2, \tag{28.5}$$

where the Fourier transform $\boldsymbol{Q}(\alpha_1,\ \alpha_2)$ of the traction vector $\boldsymbol{\tau}^{\mathrm{sc}}(x_1, x_2, 0)$ at the interface is related with the Fourier transform of the unknown COD $\Delta\boldsymbol{u} = \boldsymbol{u}(x_1, x_2, 0^-) - \boldsymbol{u}(x_1, x_2, 0^+)$ as follows:

$$\begin{aligned} \boldsymbol{Q}(\alpha_1, \alpha_2) &= \mathbf{L}(\alpha_1, \alpha_2)\cdot\Delta\boldsymbol{U}(\alpha_1, \alpha_2), \\ \mathbf{L}(\alpha_1, \alpha_2) &= [\mathbf{K}_{\boldsymbol{I}}(\alpha_1, \alpha_2) - \mathbf{K}_{\boldsymbol{2}}(\alpha_1, \alpha_2)]^{-1}. \end{aligned}$$

Substitution of the integral representation for $\boldsymbol{\tau}^{\mathrm{sc}}$ into the boundary condition (28.3) gives the following boundary integral equation:

$$\frac{1}{4\,\pi^2}\iint\limits_{\Gamma_1\Gamma_2} \mathbf{L}(\alpha_1, \alpha_2)\cdot\Delta\boldsymbol{U}(\alpha_1, \alpha_2)\cdot\mathrm{e}^{-\mathrm{i}(\alpha_1 x_1 + \alpha_2 x_2)}\,\mathrm{d}\alpha_1\mathrm{d}\alpha_2 = -\boldsymbol{\tau}^{\mathrm{in}}(\boldsymbol{x}). \tag{28.6}$$

To discretize the integral equation (28.6), the COD is expanded into series:

$$\Delta \boldsymbol{u} = \sum_{k_1=0}^{\infty} \sum_{k_2=0}^{\infty} \boldsymbol{c}_{k_1 k_2} p_{k_1}(x_1/l_1) \cdot p_{k2}(x_2/l_2), \tag{28.7}$$

where the Chebyshev polynomials of the second kind are used as basis functions. The one-dimensional Fourier transforms of basis functions are

$$P_k(\alpha\, l) = \pi\, \mathrm{i}\, (k+1) \frac{J_{k+1}(\alpha\, l)}{\alpha}.$$

The unknown coefficients $\boldsymbol{c}_{k_1 k_2}$ in (28.7) can be found applying the Bubnov–Galerkin scheme to the integral equation (28.6), which leads to the system of linear algebraic equations

$$\sum_{k_1=0}^{\infty} \sum_{k_2=0}^{\infty} \mathbf{A}_{k_1 k_2 k_1' k_2'} \boldsymbol{c}_{k_1 k_2} = \boldsymbol{f}_{k_1' k_2'}, \tag{28.8}$$

$$\mathbf{A}_{k_1 k_2 k_1' k_2'} = \frac{1}{4\,\pi^2} \iint\limits_{\Gamma_1 \Gamma_2} \mathbf{L}(\alpha_1, \alpha_2) \cdot P_{k_1}(\alpha_1\, l_1) P^*_{k_1'}\left(\alpha_1^*\, l_1\right) P_{k_2}(\alpha_2\, l_2) P^*_{k_2'}\left(\alpha_2^*\, l_2\right) \mathrm{d}\alpha_1 \mathrm{d}\alpha_2,$$

$$\boldsymbol{f}_{k_1' k_2'} = -\int\limits_{\Omega} \boldsymbol{\tau}^{\mathrm{in}}(x_1, x_2, 0) \cdot p_{k_1' k_2'}(x_1, x_2) \mathrm{d}x_1 \mathrm{d}x_2.$$

The kernel of the integral equation (28.6) can be expanded as follows:

$$\mathbf{L}(\alpha_1, \alpha_2) = \alpha_1 \mathbf{L}_1 + \alpha_2 \mathbf{L}_2 + \widetilde{\mathbf{L}}(\alpha_1, \alpha_2)$$

Keeping one term in the expansion (28.7) and taking into account that

$$\iint\limits_{\Gamma_1 \Gamma_2} \widetilde{\mathbf{L}}(\alpha_1, \alpha_2) \cdot P_{k_1}(\alpha_1 l_1) P^*_{k_1'}\left(\alpha_1^*\, l_1\right) P_{k_2}(\alpha_2\, l_2) P^*_{k_2'}\left(\alpha_2^*\, l_2\right) \mathrm{d}\alpha_1 \mathrm{d}\alpha_2 \to 0$$

As $l_m k_{js} \to 0$, an asymptotic solution for single rectangular crack can be obtained. Indeed, the matrices in the system (28.8) can be derived in the analytic form:

$$\mathbf{A}^{as}_{0000} = \frac{8\, l_1}{3\, \pi} \begin{pmatrix} \frac{m_1}{m_1^2 - m_3^2} & 0 & 0 \\ 0 & \frac{1}{m_2} & 0 \\ 0 & 0 & \frac{m_1}{m_1^2 - m_3^2} \end{pmatrix} + \frac{8\, l_2}{3\, \pi} \begin{pmatrix} \frac{1}{m_2} & 0 & 0 \\ 0 & \frac{m_1}{m_1^2 - m_3^2} & 0 \\ 0 & 0 & \frac{m_1}{m_1^2 - m_3^2} \end{pmatrix}$$

$$m_1 = \left(\frac{\lambda_1 + 2\mu_1}{\mu_1(\lambda_1 + \mu_1)} + \frac{\lambda_2 + 2\mu_2}{\mu_2(\lambda_2 + \mu_2)}\right), \quad m_2 = \left(\frac{1}{\mu_1} + \frac{1}{\mu_2}\right),$$
$$m_3 = \frac{1}{2}\left(\frac{1}{\lambda_1 + \mu_1} - \frac{1}{\lambda_2 + \mu_2}\right).$$

A similar trick was also used for a distribution of circular cracks in [10]. Asymptotic solution for longitudinal and two transverse waves, polarized along axes x_1 and x_2, are given by the following expressions, respectively:

$$\mathbf{u}_{\mathrm{P}} = \begin{pmatrix} 0 \\ 0 \\ c_{\mathrm{P}} \end{pmatrix} \sqrt{1 - \frac{x_1^2}{l_1^2}} \sqrt{1 - \frac{x_2^2}{l_2^2}}, \quad c_{\mathrm{P}} = \frac{3\,\pi^3 l_1 l_2 f_1 \left(m_1^2 - m_3^2\right)}{32 m_1 (l_1 + l_2)},$$
$$\mathbf{u}_{\mathrm{SV}} = \begin{pmatrix} c_{\mathrm{SV}} \\ 0 \\ 0 \end{pmatrix} \sqrt{1 - \frac{x_1^2}{l_1^2}} \sqrt{1 - \frac{x_2^2}{l_2^2}}, \quad c_{\mathrm{SV}} = \frac{3\,\pi^3 l_1 l_2 f_2 \left(m_1^2 - m_3^2\right) m_2}{32\left(\left(m_1^2 - m_3^2\right) l_1 + m_1 m_2 l_2\right)}, \quad (28.9)$$
$$\mathbf{u}_{\mathrm{SH}} = \begin{pmatrix} 0 \\ c_{\mathrm{SH}} \\ 0 \end{pmatrix} \sqrt{1 - \frac{x_1^2}{l_1^2}} \sqrt{1 - \frac{x_2^2}{l_2^2}}, \quad c_{\mathrm{SH}} = \frac{3\,\pi^3 l_1 l_2 f_2 \left(m_1^2 - m_3^2\right) m_2}{32\left(\left(m_1^2 - m_3^2\right) l_2 + m_1 m_2 l_1\right)}$$

$$f_s = \frac{2\,\mathrm{i}\,k_{1s} c_{1s} k_{2s} c_{2s}}{k_{1s} c_{1s} + k_{2s} c_{2s}}.$$

To determine the spring stiffness κ_s the expression (28.4) for $\hat{T}_s$ should be set equal to the amplitude transmission coefficient for the random distribution of cracks $\widetilde{T}$ given by the relation (28.1). Using the asymptotic solution for a single rectangular crack (28.9), the average COD gives

$$\kappa_{\mathrm{P}} = \frac{512\, m_1 (l_1 + l_2)}{3\pi^5 C \left(m_1^2 - m_3^2\right) l_1 l_2} - \frac{f_1}{2},$$
$$\kappa_{\mathrm{SV}} = \frac{512\left(\left(m_1^2 - m_3^2\right) l_1 + m_1 m_2 l_2\right)}{3\pi^5 C m_2 \left(m_1^2 - m_3^2\right) l_1 l_2} - \frac{f_2}{2}, \quad (28.10)$$
$$\kappa_{\mathrm{SH}} = \frac{512\left(\left(m_1^2 - m_3^2\right) l_2 + m_1 m_2 l_1\right)}{3\pi^5 C m_2 \left(m_1^2 - m_3^2\right) l_1 l_2} - \frac{f_2}{2}.$$

28.3 Periodic Array of Rectangular Cracks

Periodic distribution of cracks is a special case, which has been attentively studied, e.g. [11–13]. Of particular interest for this paper is a doubly periodic array of rectangular cracks $\Omega_{j_1 j_2}$, placed at the interface in a square lattice. The cracks are of

equal size, their centres are situated in the plane $x_3 = 0$ at the square lattice, based on two vectors $\boldsymbol{g}_1$ and $\boldsymbol{g}_2$ ($|\boldsymbol{g}_1| = |\boldsymbol{g}_2| = s$). The geometry is shown in Fig. 28.2. Let us denote a reference cell as

$$G_{00} = \{\boldsymbol{x} | (x_1, x_2, 0) = \beta_1 \boldsymbol{g}_1 + \beta_2 \boldsymbol{g}_2, |x_3| < \infty\}, \quad \beta_i \in [-1/2, 1/2].$$

The interface can be divided into a doubly periodic array of the unit-cells:

$$G_{j_1 j_2} = \{\boldsymbol{y} | \boldsymbol{y} = \boldsymbol{x} + j_1 \boldsymbol{g}_1 + j_2 \boldsymbol{g}_2\}, \quad \boldsymbol{x} \in G_{00}.$$

The centres of the cracks are situated at the points:

$$\chi_{j_1 j_2} = \left(\alpha_1^{j_1 j_2}, \alpha_2^{j_1 j_2}, 0\right), \quad a_1^{j_1 j_2} = s j_1, \quad a_2^{j_1 j_2} = s j_2.$$

The total wave-field can be represented as a sum of incident a wave-field $\boldsymbol{u}^{\text{in}}$ and scattered by each cracks $\Omega_{j_1 j_2}$ wave-fields $\boldsymbol{u}^{\text{sc}} = \sum_{j_1, j_2 = -\infty}^{\infty} \boldsymbol{u}_{j_1, j_2}^{\text{sc}}$. The periodicity of the array of rectangular cracks implies that

$$\boldsymbol{u}^{\text{sc}}(x_1,\ x_2,\ x_3) = \boldsymbol{u}^{\text{sc}}(x_1 - s j_1,\ x_2 - s j_2,\ x_3), \quad j_1, j_2 \in Z. \tag{28.10}$$

Of course, the relation (28.10) is valid for the COD, $\Delta \boldsymbol{u}$, so that the Fourier transform of the total COD is written as

$$\Delta \boldsymbol{U}(\alpha_1, \alpha_2) = \sum_{j_1, j_2 = -\infty}^{\infty} \Delta \boldsymbol{U}_{j_1, j_2}(\alpha_1, \alpha_2) = \sum_{j_1, j_2 = -\infty}^{\infty} \Delta \boldsymbol{U}_{00}(\alpha_1, \alpha_2) \cdot \mathrm{e}^{-\mathrm{i}\left(\alpha_1 a_1^{j_1 j_2} + \alpha_2 a_2^{j_1 j_2}\right)}. \tag{28.11}$$

Substitution of the representation (28.11) into the boundary integral equation (28.6) gives the following boundary integral equation, written in terms of the COD at the reference crack:

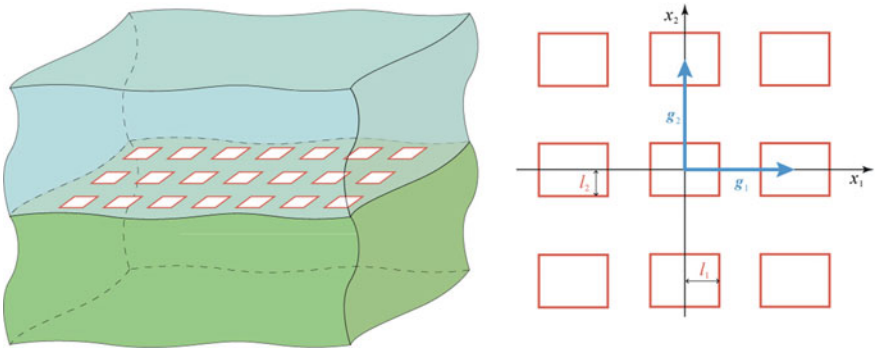

Fig. 28.2 Geometry of the problem: periodic array of rectangular cracks

$$\frac{1}{4\pi^2}\sum_{j_1,j_2=-\infty}^{\infty}\iint_{\Gamma_1\Gamma_2}\mathbf{L}(\alpha_1,\alpha_2)\cdot\Delta\mathbf{U}_{00}(\alpha_1,\alpha_2)\cdot e^{-i\left(\alpha_1 d_1^{j_1 j_2}+\alpha_2 d_2^{j_1 j_2}\alpha_1 x_1+\alpha_2 x_2\right)}d\alpha_1 d\alpha_2 = -\boldsymbol{\tau}^{\text{in}}(\mathbf{x}). \tag{28.12}$$

The kernel of the integral equation (28.12) is evaluated using the relation between an exponential series and a sum of Dirac delta functions δ:

$$\sum_{j=-\infty}^{\infty} e^{i\beta j} = \sum_{j=-\infty}^{\infty}\delta\left(\frac{\beta}{2\pi}-j\right).$$

Finally, the integral equation (28.12) is reduced to a system of linear algebraic equations in the same manner as system (28.8) has been obtained for a single rectangular crack.

28.4 Numerical Analysis

Let us analyse the influence of crack density and sizes on the wave transmission through interfaces with a random and periodic distribution of rectangular cracks. Information about wave-fields can be illustrated by the energy flux vector $\boldsymbol{e}$ (Umov-Poynting vector) [14, 15]:

$$e_j = \frac{\omega}{2}\text{Im}\left(\sigma_{ij}\,u_j^*\right).$$

For further analysis the energy transmission coefficient η^+ is introduced as the ratio of the time-averaged energy E^+, transmitted through a single unit-cell cross-section in the presence of the array of cracks to the energy E^0, transferred by the incident wave-field. In the same way, the energy reflection coefficient η^- is defined.

Figures 28.3, 28.4, 28.5, 28.6, 28.7, 28.8, 28.9 and 28.10 demonstrate the energy reflection and transmission coefficients $\eta^{\pm}$ for longitudinal and transverse waves, scattered by random and periodic distributions of square cracks of different sizes. We study two pairs of materials: identical (aluminium/aluminium) and dissimilar (aluminium/copper). Material properties are given in Table 28.1.

A good coincidence between the energy reflection and transmission coefficients $\eta^{\pm}$ for random and periodic distributions can be seen at lower frequencies both for identical and dissimilar media. Periodic organization of the cracks leads to cut-off frequencies, which can be observed as peaks in the plots. Of course, the number of cut-off frequencies is greater for dissimilar materials, this gives more rugged lines.

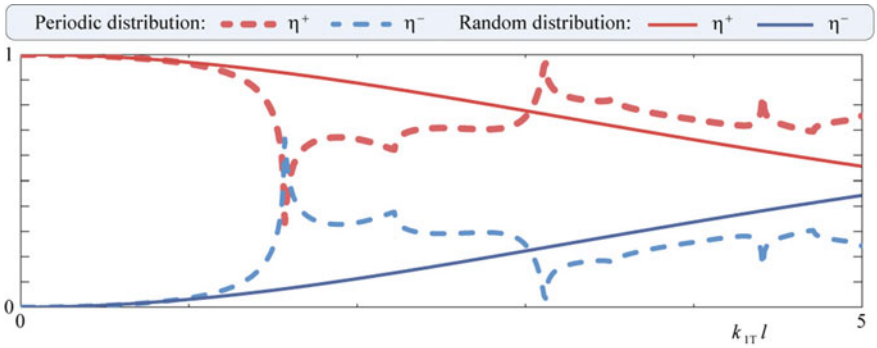

Fig. 28.3 Energy reflection and transmission coefficients $\eta^{\pm}$ for longitudinal wave, scattered by random and periodic distributions of square cracks ($l_1 = l_2 = 0.25\,\mathrm{s}$); aluminium/aluminium

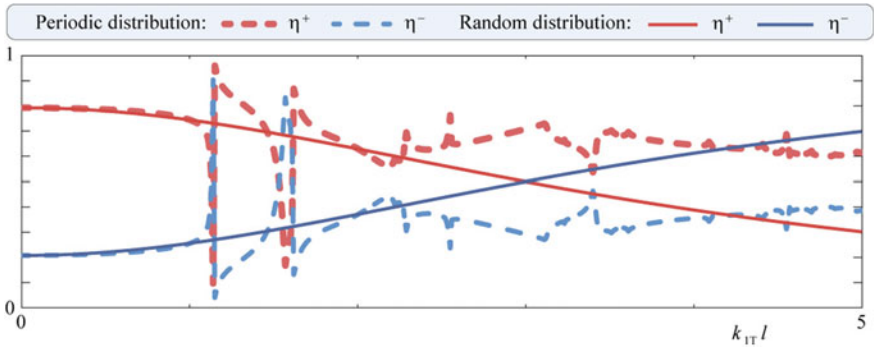

Fig. 28.4 Energy reflection and transmission coefficients $\eta^{\pm}$ for longitudinal wave, scattered by random and periodic distributions of square cracks ($l_1 = l_2 = 0.25\,\mathrm{s}$); aluminium/copper

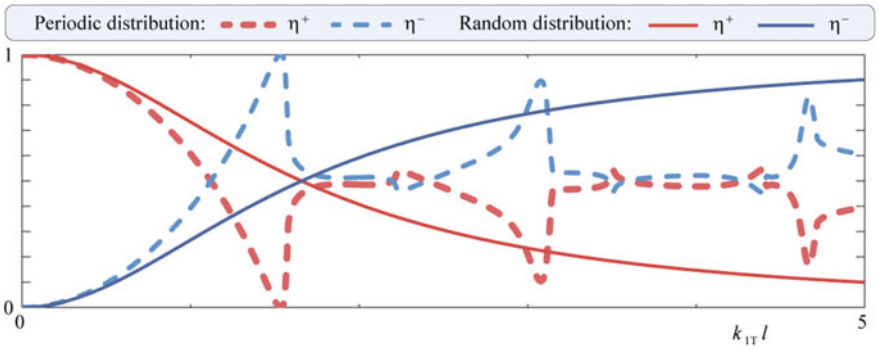

Fig. 28.5 Energy reflection and transmission coefficients $\eta^{\pm}$ for longitudinal wave, scattered by random and periodic distributions of square cracks ($l_1 = l_2 = 0.375\,\mathrm{s}$); aluminium/aluminium

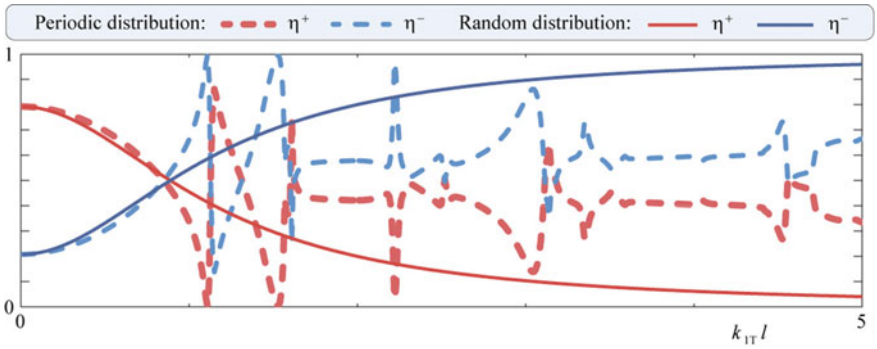

Fig. 28.6 Energy reflection and transmission coefficients $\eta^{\pm}$ for longitudinal wave, scattered by random and periodic distributions of square cracks ($l_1 = l_2 = 0.375\,\mathrm{s}$); aluminium/copper

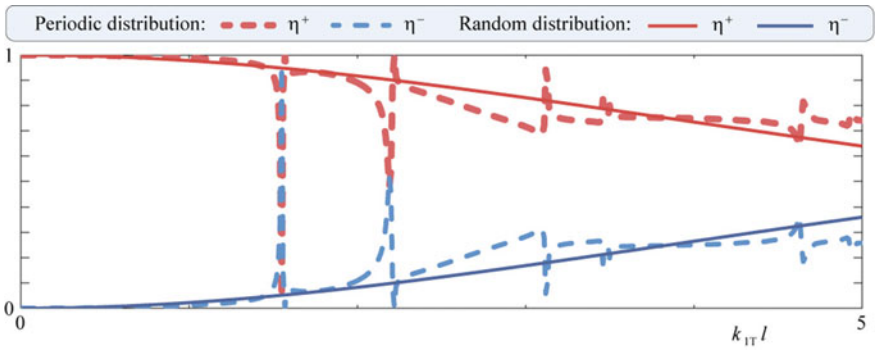

Fig. 28.7 Energy reflection and transmission coefficients $\eta^{\pm}$ for transverse wave, scattered by random and periodic distributions of square cracks ($l_1 = l_2 = 0.25\,\mathrm{s}$); aluminium/aluminium

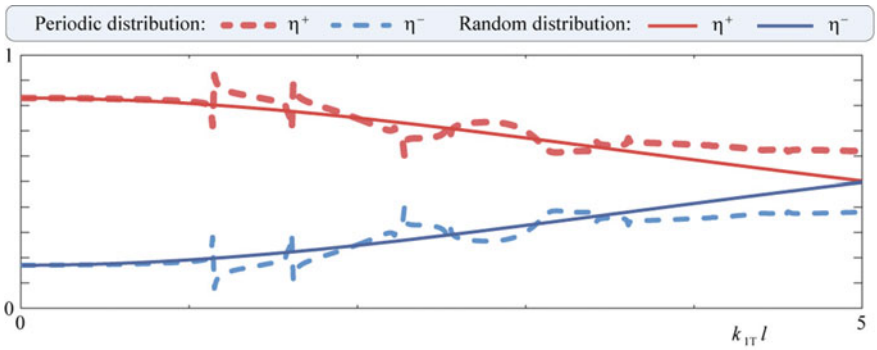

Fig. 28.8 Energy reflection and transmission coefficients $\eta^{\pm}$ for transverse wave, scattered by random and periodic distributions of square cracks ($l_1 = l_2 = 0.25\,\mathrm{s}$); aluminium/copper

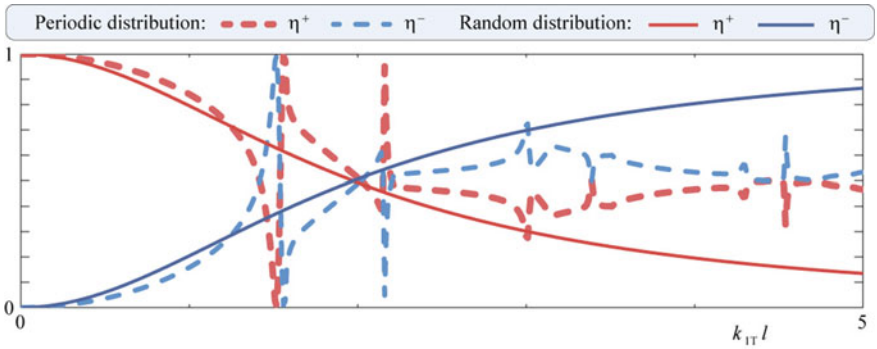

Fig. 28.9 Energy reflection and transmission coefficients $\eta^{\pm}$ for transverse wave, scattered by random and periodic distributions of square cracks ($l_1 = l_2 = 0.375$ s); aluminium/aluminium

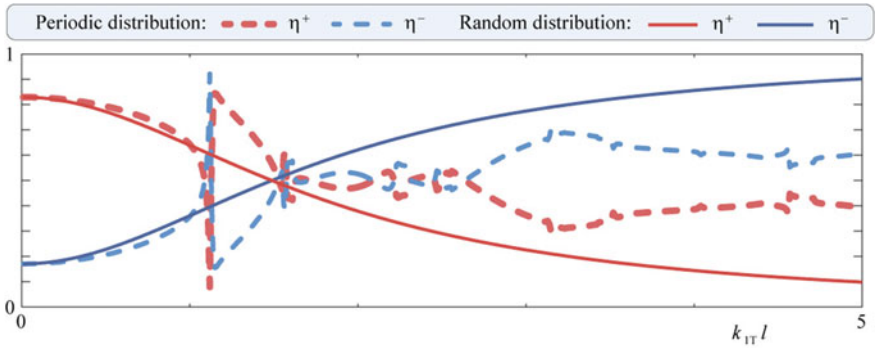

Fig. 28.10 Energy reflection and transmission coefficients $\eta^{\pm}$ for transverse wave, scattered by random and periodic distributions of square cracks ($l_1 = l_2 = 0.375$ s); aluminium/copper

Table 28.1 Material properties

No	Material	Longitudinal wave velocity, v_L (m/s)	Transverse wave velocity, v_T (m/s)	Density, ρ (kg/m^3)
1	Aluminium	6420	3040	2700
2	Copper	5010	2270	8930

Reflection of a transverse wave by periodic and random distributions compared to longitudinal wave is similar (cf. Figs. 28.7 and 28.8). Corresponding values of the energy reflection and transmission coefficients $\eta^{\pm}$ have very similar values in a much wider frequency range.

Crack densities $C = 0.25$ and $C = 0.5625$ for distributions are considered here, corresponding plots for the coefficients $\eta^{\pm}$, are depicted in Figs. 28.3, 28.4, 28.5,

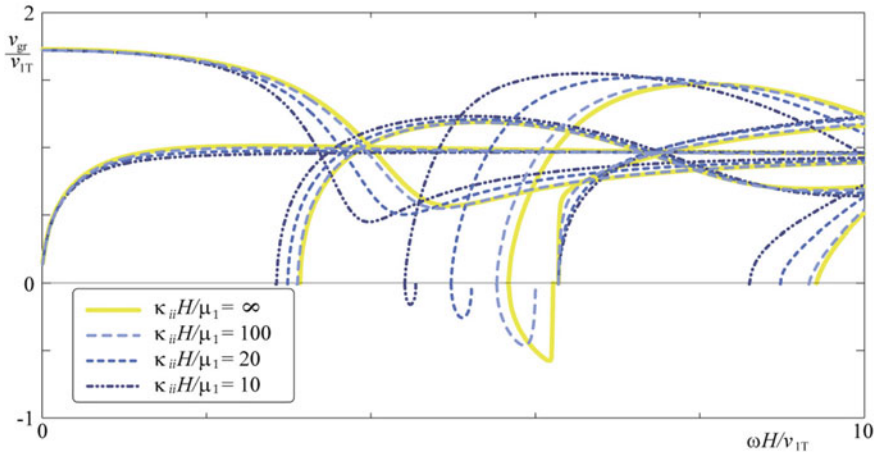

Fig. 28.11 Group velocities of Lamb waves in aluminium plate with distribution of damage situated at the middle of the plate $(h_1 = h_2)$

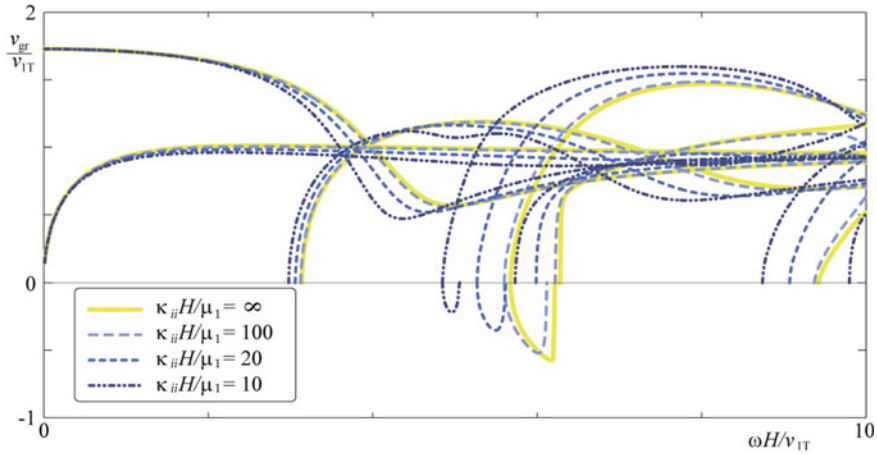

Fig. 28.12 Group velocities of Lamb waves in aluminium plate with distribution of damage, situated far from the middle of the plate $(h_1 = 3h_2)$

28.6, 28.7, 28.8, 28.9 and 28.10 for both kinds of incoming waves. It can be concluded that transmission through a damaged interface modelled by a random and periodic distribution of cracks is in good agreement for lower values of the crack density C for both identical and dissimilar media.

To demonstrate the application of the spring boundary conditions for different ultrasonic applications, consider two layered elastic plates with damaged interfaces. Thicknesses of two sub-layers with contact, described by the spring boundary

conditions (28.3), are denoted h_1 and h_2. Group velocities of Lamb waves in two damaged plates are depicted in Figs. 28.11 and 28.12 for different values of spring stiffness and two different ratios between thickness ($h_1 = h_2$ and $h_1 = 3h_2$). If adhesion between layers decreases (κ_{ii} decreases at the same time), then the cut-off frequencies shift to lower frequencies and group velocities become smaller. This information can be employed for damage or adhesion identification [16].

28.5 Conclusion

The main goal of the present paper is to derive simple, explicit expressions for the spring constants, (28.10), that can be used to model interface damage. This is accomplished by first solving for a single rectangular interface crack and then using ensemble averaging techniques. Results, obtained with these spring constants, are also compared to results for a periodic distribution of cracks and for small interface cracks (compared to the wavelengths) the two approaches give very similar results.

These distributed spring constants should be of value, when interface damage is investigated by ultrasound. They could, for example, be used to investigate the scattering by a finite damaged interface or to see the influence on the phase and group velocities, when a long part of an interface is damaged.

Acknowledgements The work is supported by the Russian Science Foundation (Project 17-11-01191), which is gratefully acknowledged.

References

1. I. Solodov, J. Bai, G. Busse, J. Appl. Phys. **113**, 223512 (2013)
2. D.A. Sotiropoulos, J.D. Achenbach, J. Nondestr. Eval. **7**, 123 (1988)
3. M. Kachanov, Adv. Appl. Mech. **30**, 259 (1994)
4. J.-M. Baik, R.B. Thompson, J. Nondestr. Eval. **4**, 177 (1984)
5. S. Gopalakrishnan, A. Chakraborty, D.R. Mahapatra, *Spectral Finite Element Method: Wave Propagation, Diagnostics and Control in Anisotropic and Inhomogeneous Structures* (Springer-Verlag London Limited, 2008), 449pp
6. Y.V. Glushkov, N.V. Glushkova, A.V. Yekhlakov, J. Appl. Math. Mech. **66**(1), 141 (2002)
7. A. Boström, G.R. Wickham, J. Nondestr. Eval. **10**, 139 (1991)
8. M.V. Golub, A. Boström, Wave Motion **48**(2), 105 (2011)
9. E. Glushkov, N. Glushkova, J. Comput. Acoust. **9**, 889 (2001)
10. M.V. Golub, O.V. Doroshenko, A. Boström, Int. J. Solids Struct. **81**, 141 (2016)
11. V. Mykhas'kiv, I. Zhbadynskyi, C. Zhang, J. Math. Sci. **203**, 114 (2014)
12. M.Y. Remizov, M.A. Sumbatyan, Math. Mech. Solids **22**, 1 (2017)
13. M.V. Golub, O.V. Doroshenko, Math. Mech. Solids, December (2017)
14. E. Glushkov, J. Appl. Math. Mech. **47**, 70 (1983)
15. V. Babich, A. Kiselev, *Elastic Waves. A High-Frequency Theory* (BHV-Petersburg, 1981) (in Russian)
16. Y. Ishii, S. Biwa, J. Acoust. Soc. Am. **141**, 1099 (2017)

Chapter 29
Wave Energy Evaluation for Ultrasonic Air-Coupled Material Characterization

O. A. Miakisheva, E. V. Glushkov and N. V. Glushkova

Abstract Ultrasonic non-destructive evaluation and material characterization involve the processing of the acquired data on the basis of efficient computer models both for transducer generated beams and scattered wave fields. The simulation of wave processes in coupled source-structure environments is also beneficial for the design and optimization of such non-destructive inspection systems. The present work deals with the development of analytically based, and so cost-effective, simulation tools for ultrasonic probing of fluid-immersed elastic plates, using contactless (air-coupled) transducers. Explicit integral representations for the generated and scattered wave fields have been obtained, using the Fourier transform technique. In the far field, the bulk acoustic waves and guided elastic waves are described by asymptotic representations, derived from those path integrals as the contribution of phase saddle points and residues from the integrand's poles. The present study is focused on the source energy partition among the generated waves of different types and among different directions of wave propagation. The dependence of the total source energy and its parts on the frequency and source distance to the plate is illustrated by numerical examples.

29.1 Introduction

The determination of effective elastic moduli is a classical problem of structural mechanics. Ordinarily, the mechanical properties are determined by experimental methods that have a destructive invasive nature. For example, even to predict material parameters on the basis of high precision experimental measurements and computer simulation of vibration eigenfrequencies and eigenmodes [1], one has to cut out a test sample from the inspected plate. On the other hand, non-destructive prediction of elastic constants is possible on the basis of ultrasonic techniques that

O. A. Miakisheva (✉) · E. V. Glushkov · N. V. Glushkova
Institute for Mathematics, Mechanics and Informatics, Kuban State University, Krasnodar, Russia
e-mail: miakisheva.olga@gmail.com

I. A. Parinov et al. (eds.), *Advanced Materials*, Springer Proceedings in Physics 207, https://doi.org/10.1007/978-3-319-78919-4_29

utilize bulk waves and guided waves (GWs) [2, 3]. The GW-based methods use sensing devices implemented into the engineering structure under investigation [4, 5]. There are two basic GW-based approaches for the identification of effective elastic moduli. First, identification is achieved through the minimization of an objective function, defining some metric between the experimentally measured and theoretically calculated GW characteristics [6–9]. The second approach is based on the evaluation of a direct dependence of wave numbers or group velocities on the material constants [10–14].

The methods and systems of non-destructive evaluation and material characterization are increasingly used for structural health monitoring (SHM) of safety-critical engineering constructions such as aircrafts, pipelines, nuclear storages, etc. The SHM technologies of elastic constant prediction are based on the GW excitation and registration by a comparatively sparse net of piezoelectric wafer active sensors (PWAS) [15]. Along with the nets of permanently attached PWASs, non-contact (air-coupled) transducers are also widely used both for excitation and for registration of bulk and guided waves in plate samples immersed in an acoustic environment (air or fluid). Not infrequently, the air-coupled transducers (ACTs) are regarded as a cheaper alternative to the laser Doppler vibrometry (LDV). To optimize the operation of ACT-based systems, it is useful to develop effective mathematical and computer models for the simulation of wave processes underlying their work.

The interaction of incident acoustic waves, generated by an ultrasound transducer with a multilayered plate, immersed in acoustic fluid, excites GWs propagating over the plate and in the adjacent environment. These travelling waves re-radiate the wave energy into the environment in the course of their propagation, becoming actually leaky guided waves. Modern commercial finite-element packages are quite sufficient for the simulation of such wave processes but their use is often too expensive. Alternatively, analytically based computer models can provide a fast parametric analysis and better insight into the wave structure. That is why, we have been developing the models that are based on the explicit integral and asymptotic representations for the point-source solutions of the corresponding boundary value problems (BVP) for the coupled source-fluid-plate structures as a whole (i.e., on the Green's functions of such structures). The present paper deals with the parametrical analysis of the total wave energy, emitted by a source, located in the fluid at a certain distance to the inspected plate and its partition among the excited GWs and transmitted through and reflected from the plate bulk waves.

29.2 Mathematical Framework and General Solution Scheme

A steady-state time-harmonic oscillation $\mathbf{u}(\mathbf{x})\mathrm{e}^{-i\omega t}$, where $\mathbf{u} = (u_x, u_y, u_z)$, $\mathbf{x} = (x, y, z)$, of an elastic layer of thickness h, immersed in acoustic fluid is under

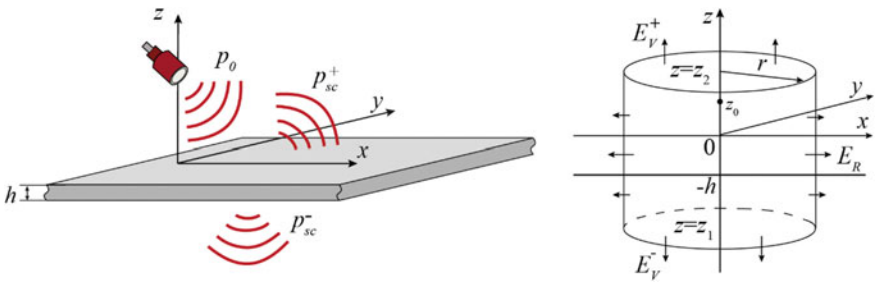

Fig. 29.1 Ultrasonic sounding by an air-coupled transducer (left); lateral cylindrical and horizontal plane surfaces for the calculation of energy fluxes E_R and $E_V^{\pm}$, respectively (right)

consideration (Fig. 29.1, left). The displacement vector $\mathbf{u}$ obeys the full set of 3D Navier–Lamé equations:

$$(\lambda+\mu)\nabla \mathrm{div}\mathbf{u} + \mu\Delta\mathbf{u} + \rho\omega^2\mathbf{u} = 0, \tag{29.1}$$

where λ and μ are Lamé constants, and ρ is the density of the layer; hereinafter, the time-harmonic factor $\mathrm{e}^{-i\omega t}$ is conventionally omitted.

Acoustic pressure $p(\mathbf{x})$ in the surrounding liquid satisfies the Helmholtz equation:

$$\Delta p + \kappa_0^2 p = \delta(\mathbf{x}-\mathbf{x}_0), \tag{29.2}$$

where $\kappa_0 = \omega/c_0$ is a wave number, and c_0 is a sonic velocity. Dirac's delta function models a monopole source located in the upper half-space at a point $\mathbf{x}_0 = (0,0,z_0)$. The pressure $p(\mathbf{x})$ can be represented as a sum of the direct source field $p_0(\mathbf{x})$ and the scattered field $p_{sc}(\mathbf{x})$. The spherical body waves radiated by the point source are described by the classical fundamental solution of the Helmholtz equation:

$$p_0 = -\frac{1}{4\pi R}\mathrm{e}^{i\kappa_0 R}, \quad R = |\mathbf{x}-\mathbf{x}_0|, \tag{29.3}$$

while the scattered field p_{sc} is unknown.

The total field $p(\mathbf{x}) = p_0(\mathbf{x}) + p_{sc}(\mathbf{x})$ and the vertical displacement component $u_z = \frac{1}{\omega^2\rho_0}\frac{\partial p}{\partial z}$ are continuous at the fluid-solid interfaces: $z=0$ and $z=-h$. These interface boundary conditions are augmented by the radiation conditions at infinity following from the principle of limiting absorption.

The application of the Fourier transform F_{xy} with respect to the horizontal coordinates x and y allows one to obtain explicit integral representation of the BVP solution. The unknown fields $p_{sc}^{\pm}$ and $\mathbf{u}$ are expressed in terms of their Fourier

symbols $P_{sc}^{\pm} = F_{xy}[p_{sc}^{\pm}]$ and $\mathbf{U} = F_{xy}[\mathbf{u}]$ (here and further, plus and minus are for the acoustic half-spaces $z \geq 0$ and $z \leq -h$, respectively):

$$p_{sc}^{\pm}(\mathbf{x}) = F_{xy}^{-1}[P_{sc}^{\pm}]\frac{1}{4\pi^2}\int\limits_{\Gamma_1}\int\limits_{\Gamma_2} P_{sc}^{\pm}(\alpha, z)\mathrm{e}^{-i(\alpha_1 x + \alpha_2 y)}d\alpha_1 d\alpha_2, \tag{29.4}$$

$$\mathbf{u}(\mathbf{x}) = F_{xy}^{-1}[\mathbf{U}]\frac{1}{4\pi^2}\int\limits_{\Gamma_1}\int\limits_{\Gamma_2} K_3(\alpha, z)\mathrm{Q}(\alpha)\mathrm{e}^{-i(\alpha_1 x + \alpha_2 y)}d\alpha_1 d\alpha_2. \tag{29.5}$$

Here $\alpha = (\alpha_1, \alpha_2)$ is the vector of Fourier parameters, K_3 is the third column of the Green's matrix for the two-layered half-space $z \leq 0$ (elastic layer $-h \leq z \leq 0$ underlain by the fluid $z \leq -h$) in the conventional notations of [16]. Its three components can be expressed via two functions $T(\alpha, z)$ and $R(\alpha, z)$, which depend only on the radial variable $\alpha = |\alpha| = \sqrt{\alpha_1^2 + \alpha_2^2}$:

$$K_3 = \begin{pmatrix} -i\alpha_1 T \\ -i\alpha_2 T \\ R \end{pmatrix};$$

$Q = F_{xy}[q]$ is the Fourier symbol of the interface load q that can be explicitly expressed via the Fourier symbol of the source field p_0 at the interface $z = 0$:

$$Q = \frac{2\sigma_0 P_0}{\omega^2 \rho_0 R - \sigma_0}, \quad P_0 = -\frac{\mathrm{e}^{-\sigma_0 z_0}}{2\sigma_0}, \quad \sigma_0 = \sqrt{\alpha^2 + \kappa_0^2}.$$

The Fourier symbol of the scattered pressure field $P_{sc}^{\pm}$ can be written in the form $P_{sc}^{\pm} = P^{\pm}(\alpha)\mathrm{e}^{\mp\sigma_0(z \pm z_0)}$. The integration paths Γ_1 and Γ_2 go along the real axes, rounding the real poles ζ_n of the integrand in accordance with the principle of limiting absorption. Here and further, we use the formulas and notations of [16–18].

By using the polar coordinates: $x = r\cos\varphi$; $y = r\sin\varphi$; $\alpha_1 = \alpha\cos\gamma$; $\alpha_2 = \alpha\sin\gamma$, double integrals (29.4) and (29.5) are reduced to the one-fold path integrals:

$$p_{sc}^{\pm}(r, z) = \frac{1}{2\pi}\int\limits_{\Gamma} P_{sc}^{\pm}(\alpha, z)J_0(\alpha r)\alpha d\alpha, \tag{29.6}$$

$$u_r(r, z) = -\frac{1}{2\pi}\int\limits_{\Gamma} T(\alpha, z)Q(\alpha)J_1(\alpha r)\alpha^2 d\alpha, \tag{29.7}$$

$$u_z(r, z) = \frac{1}{2\pi}\int\limits_{\Gamma} R(\alpha, z)Q(\alpha)J_0(\alpha r)\alpha d\alpha, \tag{29.8}$$

where J_0 and J_1 are the Bessel functions and $\alpha = |\alpha|$. The contour Γ goes along the real semi-axis $\mathrm{Re} \geq 0$. The application of the residue technique to these path integrals yields far-field asymptotic representations of the excited wave fields in terms of cylindrical guided waves propagating in the lateral direction:

$$\mathbf{u}(r,z) = \sum_{i=1}^{N} \mathbf{a}_n(z) H_0^{(1)}(\zeta_n r)\zeta_n \quad \text{and} \quad p_{\mathrm{sc}}^{\pm}(r,z) = \sum_{i=1}^{N} b_n^{\pm}(z) H_0^{(1)}(\zeta_n r)\zeta_n, \tag{29.9}$$

where

$$\mathbf{a}_n = \frac{i}{2}\mathrm{res} K_3(\partial/\partial x, \partial/\partial y, z)\Big|_{\alpha=\zeta_n} Q(\zeta_n),\ b_n^{\pm} = \frac{i}{2}\mathrm{res} P_{\mathrm{sc}}^{\pm}(\alpha, z)\Big|_{\alpha=\zeta_n},$$

and ζ_n are real and nearly real poles of the integrands in (29.6)–(29.8) that play the role of wave numbers in GW representations (29.9).

Wave fields, generated by a real dimensional (non-point) transducer, can be represented via the convolution of the point-source solution (Green's function) with a load $\varphi(\mathbf{x})$ distributed over the area of its radiating element. Such a distribution simulates its action on the surrounding acoustic medium. In the case of a horizontal circular radiating area of radius a, the source is modeled by an axially symmetric distribution $\varphi(\mathbf{x}) = \varphi(r)$, $r = \sqrt{x^2 + y^2}$, and the convolution is analytically brought to the path integrals of the same form as in (29.6)–(29.8) but with the additional factor:

$$\Phi(\alpha) = F_{xy}[\varphi] = 2\pi a J_1(a\alpha)/\alpha$$

in the integrands.

Hereinafter, the numerical results are presented in the dimensionless form. The thickness h, shear wave velocity c_s, and density ρ of the plate are taken as three basic variables. In these variables, the dimensionless parameters for a steel plate immersed in water are as follows: P-wave velocity $c_p = 1.85$, $c_s = 1$, $\rho = 1$, and $h = 1$ in the elastic plate; $c_0 = 0.47$ and $\rho_0 = 0.125$ in the surrounding fluid. The dimensionless angular frequency $\omega = 2\pi f h/c_s$, where f is dimensional frequency.

Figure 29.2 shows dispersion curves of GWs propagating in a fluid-loaded plate with such dimensionless parameters: solid and dashed lines are for the real and imaginary parts of their complex wave numbers ζ_n, i.e. for $\mathrm{Re}\zeta_n$ and $\mathrm{Im}\zeta_n$, respectively.

The real parts of these dispersion curves are not too different from the dispersion curves of classical Lamb waves in a free elastic plate. The appearance of imaginary parts (dashed lines, see also Fig. 29.3) indicates the transformation of Lamb waves into leaky waves. In addition to the leaky Lamb waves, two Schotler–Stoneley guided waves appear in the liquid close to the immersed plate [19, 20]. In Fig. 29.2, their pure real dispersion curves are conventionally denoted as A and S (antisymmetric and symmetric Scholter–Stoneley waves). These waves propagate

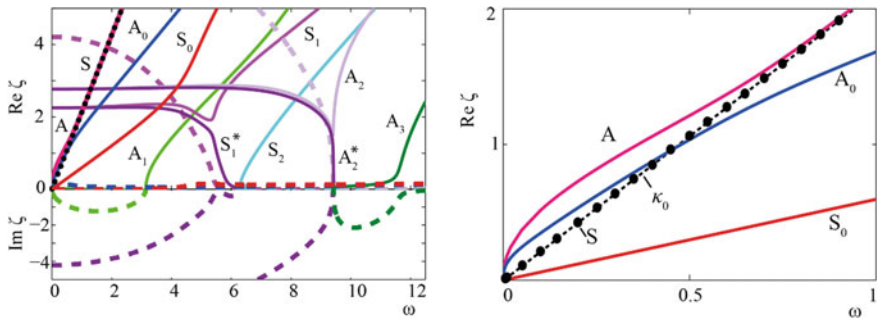

Fig. 29.2 Real (solid lines) and imaginary (dashed lines) parts of the complex dispersion curves for steel plate immersed in water (left); zoomed-in cutout with purely real curves of Scholte–Stoneley modes *A* and *S* (right)

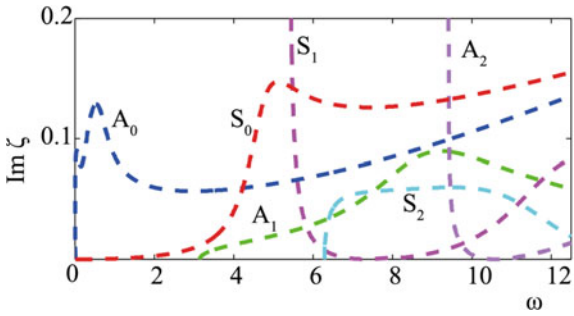

Fig. 29.3 Zoomed-in imaginary parts $\mathrm{Im}\zeta_n$ of the dispersion curves of leaky Lamb waves in Fig. 29.2

with almost the same phase velocity as bulk acoustic waves in the fluid (the corresponding dispersion curves in Fig. 29.2 are pressed to the asymptote $\kappa_0 = \omega/c_0$).

Small dissipation, specified by the imaginary parts of the wave numbers ζ_n of former Lamb waves (Fig. 29.3), is due to the wave energy re-radiation into the fluid in the course of GW propagation over the plate. As the result, leaky Lamb waves cannot carry the wave energy received from the source to infinity. On the contrary, the Scholter–Stoneley waves with pure real wave numbers transport the wave energy along the plate to infinity.

Thus, the energy emitted by the source into acoustic fluid with an immersed elastic plate is transported to infinity upward and downward by the reflected and transmitted bulk waves $p_{sc}^{\pm}$ and laterally along the plate by Scholter–Stoneley guided waves. Figure 29.4 gives an example of the typical pattern of energy stream lines, which visualize the trajectories of time-averaged energy fluxes from a circular transducer of radius $a = 2.5$. Ordinarily, only a few close to the central axis stream lines go directly through the plate, the others either turn laterally depicting winding trajectories of energy transfer along the plate with the excited GWs or turn upward being reflected from the plate. To obtain the quantitative characteristics of the source energy partition among these waves, we use the formulae given in the next section.

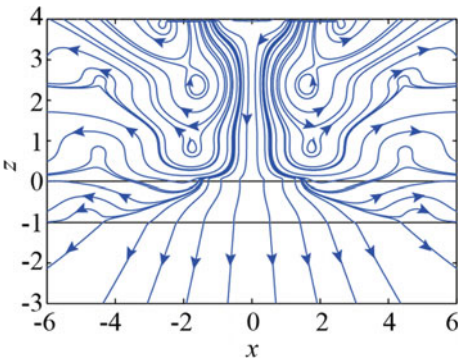

Fig. 29.4 Example of energy stream lines for a circular transducer: $a = 2.5$, $z_0 = 4$, and $\omega = 1$

29.3 Energy Fluxes

The expression for the time-averaged energy E_0, radiated by a point source into a fluid-loaded structure has been presented and numerically validated in [18] and the earlier papers cited therein. The energy conservation law has been checked for the energy fluxes going through spherical surfaces of various radii centered at the source point. On the other hand, the side and end surfaces of a closed cylinder (Fig. 29.1, right) are also of interest for the evaluation of energy fluxes. To maintain the energy balance, we equal the sum of the amounts of energy, transferred by the waves of different types through these surfaces

$$E_c = E_V^- + E_V^+ + E_R,$$

to the source power E_0. Here, E_V^- (transmitted energy) and E_V^+ (reflected energy) are time-averaged amounts of the wave energy, carried by the transmitted and reflected acoustic waves through the upper and lower horizontal plane surfaces $z = z_1$ and $z = z_2$, respectively (see Fig. 29.1, right); E_R is the energy flux, carried by GWs (more precisely, only by Scholter–Stoneley waves) through the lateral cylindrical surface of arbitrary radius $r = \sqrt{x^2 + y^2} \gg 1$, enclosed between the planes $z = z_1$ and $z = z_2$.

The energy flux through a horizontal plane $z = const$ can be calculated as the integral of the normal component e_z of the Umov-Poynting vector of energy density $\mathbf{e} = (e_r, e_z)$:

$$E_z = \iint_{-\infty}^{+\infty} e_z dx dy. \tag{29.10}$$

In the acoustic fluid,

$$e_z = \frac{1}{2\omega\rho_0}\mathrm{Im}[p'_z p^*].$$

The asterisk denotes here the complex conjugation. Integral representations (29.4) and (29.6) allow us to bring (29.10) for the energy fluxes through the planes $z = z_1$ and $z = z_2$ to the forms:

$$E_V^- = \frac{1}{4\pi\omega\rho_0}\mathrm{Im}\int_\Gamma \sigma_0|P_{sc}^-|^2\alpha d\alpha, \quad z < -h, \text{ and} \tag{29.11}$$

$$E_V^+ = -\frac{1}{4\pi\omega\rho_0}\mathrm{Im}\int_\Gamma \sigma_0|P_0 + P_{sc}^+|^2\alpha d\alpha, \quad z > z_0. \tag{29.12}$$

The energy flux E_R through the lateral surface of the cylinder is calculated as

$$E_R = \int_{z=z_1}^{z=z_2}\int_0^{2\pi} e_r(r,\varphi,z)rd\varphi dz = 2\pi\int_{z=z_1}^{z=z_2} e_r(r,z)rdz, \tag{29.13}$$

where

$$e_r = \begin{cases} \frac{\omega}{2}\mathrm{Im}[\tau_{rr}u_r^* + \tau_{rz}u_z^*], & -h < z < 0, \\ \frac{1}{2\omega\rho_0}\mathrm{Im}\left[\frac{\partial p_{sc}^{\pm}}{\partial r}p_{sc}^{\pm *}\right], & z \geq 0 \text{ and } z \leq -h. \end{cases}$$

The numerical tests have shown that, indeed, within the model developed, the power balance $E_0 = E_c$ holds for any horizontal planes $z_1 > z_0$ and $z_2 < -h$, and large enough radius $r \gg 1$ of the side cylindrical surface. In more details, the examples of energy partitions are given in the next section.

29.4 Energy Balance and Numerical Examples

In the current paper, we confine ourselves to illustrating and discussing numerical examples for an isotropic steel plate immersed in water. The plots in Figs. 29.5, 29.6, 29.7, 29.8, 29.9 and 29.10 are for a monopole point source, while Fig. 29.11 is for a non-point air-coupled transducer. We have compared the power energy and the sum of energy fluxes, transmitted through the lateral and end surfaces of the closed cylinder (Fig. 29.1, right) for the three source distances: $z_0 = 1$, 2, and 4, selected for the verification examples. The curves E_0 (solid lines) and E_c (circle markers) in Fig. 29.5 confirms that the energy balance holds for any of them.

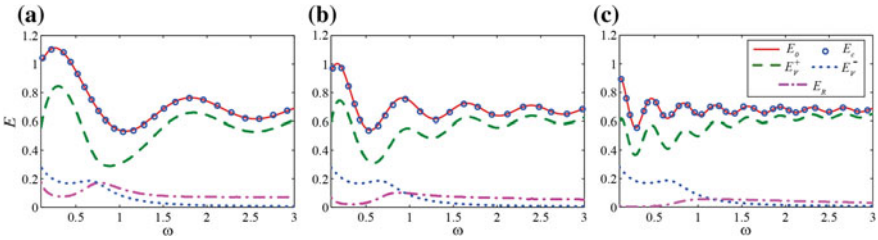

Fig. 29.5 Check of the energy balance: frequency dependencies of the source energy E_0 (solid lines), total energy flux through the closed cylindrical surface E_c (markers), and its parts E_V^+ (dashed lines), E_V^- (dot lines), and E_R (dash-dot lines) through the upper, lower and lateral surfaces of the cylinder for various source distances: **a** $z_0 = 1$, **b** $z_0 = 2$, **c** $z_0 = 4$

Moreover, Fig. 29.5 illustrates the energy distribution among the directions of radiation. The main part of the source energy E_0 reflects from the plate surface $z = 0$ and goes to infinity through the upper plane $z = z_1$ (the curves E_V^+ in the figure). While a much smaller part of the source energy passes through the plate with the bulk waves (E_V^-) and goes through the lateral surface with the Scholter–Stoneley waves (E_R).

Figure 29.6 depicts the partition of the Scholter–Stoneley wave energy between A and S modes. One can see that at low frequencies the main part of this energy is transferred by the A mode while at higher frequencies the energy of both modes becomes practically equal.

Figure 29.7 shows the transverse profiles (dependence on z) of the horizontal component $e_r(z)$ of the energy density vector, calculated separately for the modes A and S. The profiles are shown for three fixed frequencies $\omega = 0.5$ (left column), $\omega = 1$ (middle column), and $\omega = 2$ (right column) and the same source distances as above. For those frequencies, the energy of mode A is greater than that of mode S as in Fig. 29.6. One can see that although, at low frequencies, a considerable part of the A mode energy flows inside the plate, with increasing frequency the overwhelming majority of energy flows outside the plate, in the adjacent fluid, concentrating at the fluid-solid interfaces.

To understand general rules of energy partitions, Figs. 29.8, 29.9 and 29.10 depict the total source energy and its constituents as functions of two variables: frequency ω and distance z_0. For convenience, all these amounts are normalized to the value of the point-source energy in the unbounded acoustic space, $E_\infty = 1/(8\pi c_0 \rho_0)$. In this way, the level-line patterns of these figures display: $\hat{E}_0 = E_0/E_\infty$, $\hat{E}_V^+ = E_V^+/E_\infty$, $\hat{E}_V^- = E_V^-/E_\infty$, $\hat{E}_A = E_A/E_\infty$, and $\hat{E}_S = E_S/E_\infty$. Note that the scales in these figures are different.

Figure 29.8 shows the normalized total energy $\hat{E}_0(\omega, z_0)$ of the point source. Its pattern is featured by the alternating concave bands of local maxima and minima of the source power. In the plots of Fig. 29.5, this alternation appears as wave-like frequency dependences for fixed distances z_0. Figure 29.9 depicts the normalized

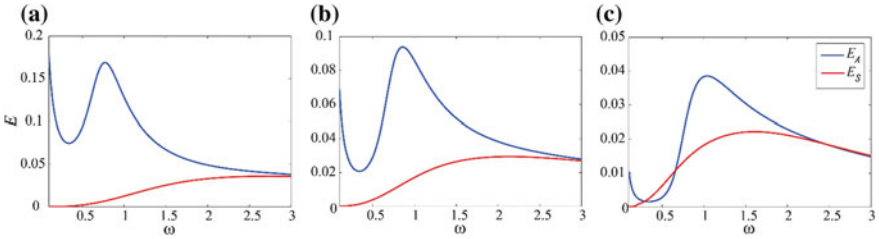

Fig. 29.6 Energy fluxes E_A and E_S carried out to infinity by A and S Scholter–Stoneley modes (two parts of E_R in Fig. 29.5) for the same source distances as in Fig. 29.5

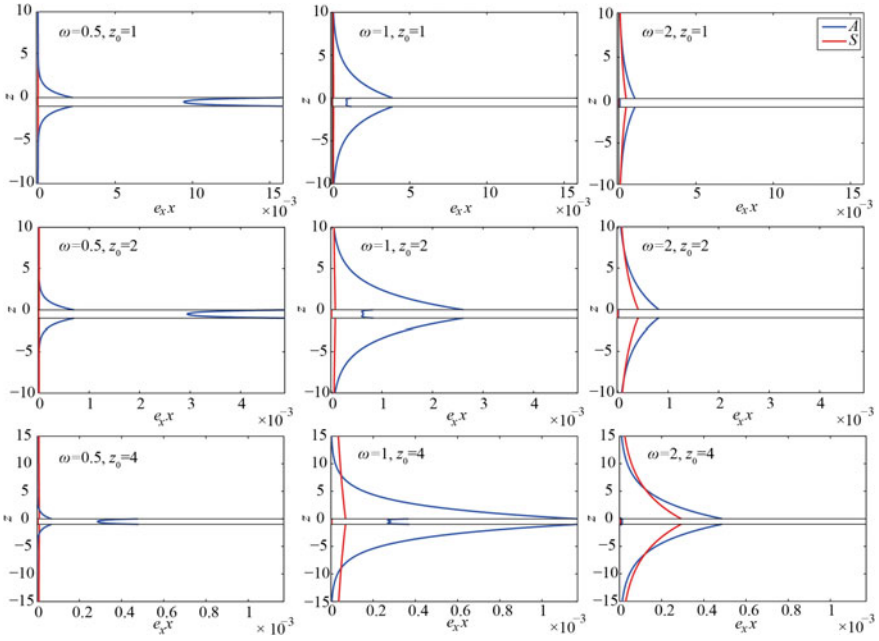

Fig. 29.7 Vertical profiles of energy density $e_r(r,z)r$ [integrands in (29.13)] for A and S modes

amounts of energy $\hat{E}{}_V^-$ and $\hat{E}{}_V^+$, transferred through the lower and upper horizontal planes $z = z_1$ (transmitted) and $z = z_2$ (reflected), respectively. It demonstrates that the most part of source energy reflects from the plate surface $z = 0$ and only small part transmits through the plate with any distance z_0, especially at higher frequencies. Figure 29.10 shows the normalized energy $\hat{E}_A$ (left) and $\hat{E}_S$ (right), i.e. the summands of the normalized GW energy E_R, carried through the lateral surface of the cylinder by A and S modes.

To estimate the effect of transducer dimension on the energy emission and partition, Fig. 29.11 presents the same energy characteristics as in Fig. 29.5c, but

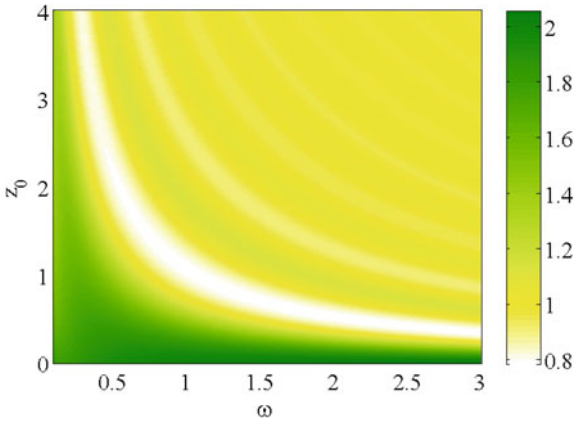

Fig. 29.8 Normalized source energy $\hat{E}_0$ as a function of ω and z_0

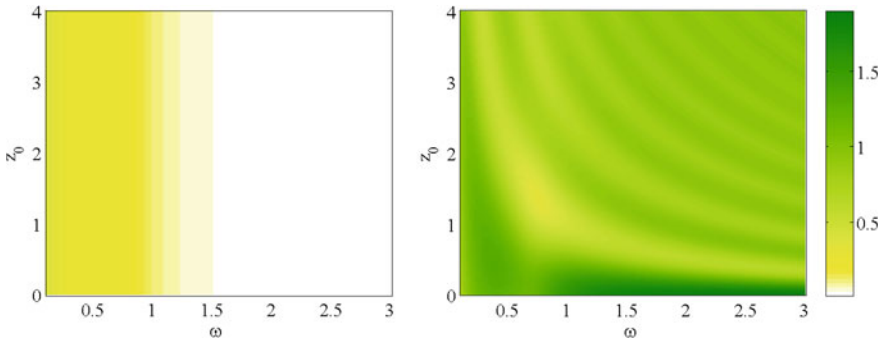

Fig. 29.9 The same as in Fig. 29.8 for the transmitted wave energy $\hat{E}_V^-$ (left) and reflected wave energy $\hat{E}_V^+$ (right)

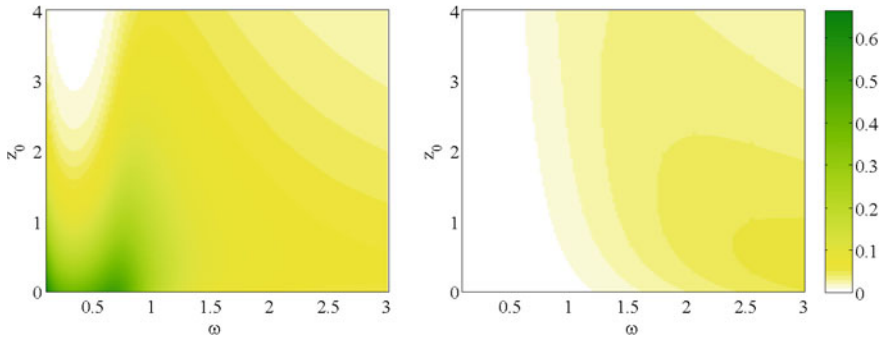

Fig. 29.10 The same as in Fig. 29.8 for the normalized energy fluxes $\hat{E}_A$ (left) and $\hat{E}_S$ (right), carried laterally by the GW modes *A* and *S*

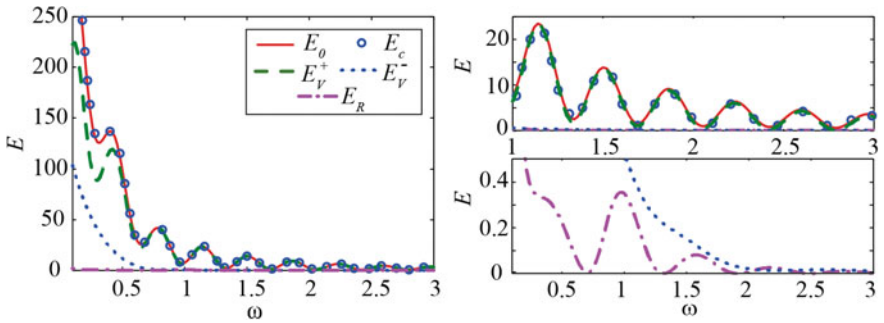

Fig. 29.11 The same as in Fig. 29.5c but for air-coupled transducer of radius $a = 2.5$ at the distance $z_0 = 4$ (left); and zoomed-in cutouts of these plots (right)

for the air-coupled transducer with the same radius $a = 2.5$ and distance $z_0 = 4$ as in Fig. 29.4. The power emitted by such a transducer into the medium is tens of times greater than the point source power in Fig. 29.5c. The reflected energy E_V^+ is much greater than the transmitted energy E_V^-, and E_R is the smallest.

29.5 Conclusion

The analytically based computer model for the fluid-loaded elastic plate has been developed on the base of explicit integral and asymptotic representations for the generated and scattered wave fields. The numerical examples confirm the fulfillment of the energy balance within the model framework. Numerical examples illustrate general regularities of the source energy spatial distribution as well as its partition among the excited bulk and guided waves depending on the source location and frequency.

Acknowledgements The work is supported by the Russian Science Foundation (Project No. 17-11-01191).

References

1. P.S. Frederiksen, J. Compos. Mater. **31**(4), 360 (1997)
2. M. Kersemans, A. Martens, N. Lammens et al., Exp. Mech. **54**(6), 1121 (2014)
3. W.P. Rogers, Res. Nondestr. Eval. **6**, 185 (1995)
4. F. Li, H. Murayama, K. Kageyama et al., Sensors **9**(5), 4005 (2009)
5. G. Liu, W. Ma, X. Han, Comput. Methods Appl. Mech. Eng. **191**(33), 3543 (2002)
6. A. Marzani, L. De Marchi, J. Intell. Mater. Syst. Struct. **24**(17), 2135 (2013)
7. A.B. Spencer, K. Worde, W.J. Staszewski et al., Shock. Vib. **19**(5), 1027 (2012)
8. S. Ha, F.K. Chang, Smart. Mater. Struct. **19**(2), 025006 (2010)

9. Z. Tian, L. Yu, J. Intell. Mater. Syst. Struct. **25**(9), 1107 (2014)
10. A. Raghavan, C.E.S. Cesnik, Smart. Mater. Struct. **16**(2), 355 (2007)
11. H. Gravenkamp, C. Song, J. Prager, J. Sound Vib. **331**(11), 2543 (2012)
12. J. Vishnuvardhan, C.V. Krishnamurthy, K. Balasubramaniam, Smart. Mater. Struct. **16**(5), 1650 (2007)
13. K. Lasn, A. Klauson, F. Chati et al., Mech. Compos. Mater. **47**, 435 (2011)
14. A.A. Eremin, E.V. Glushkov, N.V. Glushkova, R. Lammering, Compos. Struct. **125**, 449 (2015)
15. L. Yu, V. Giurgiutiu, JOM **64**(7), 814 (2012)
16. I.I. Vorovich, V.A. Babeshko, *Dynamic Mixed Problems of Elasticity for Non-classical Areas* (Nauka, Moscow, 1979). (in Russian)
17. E.V. Glushkov, N.V. Glushkova, O.A. Miakisheva, in *Proceedings of the International Conference Days on Diffraction* (2015), p. 107
18. E.V. Glushkov, N.V. Glushkova, O.A. Miakisheva, in *Proceedings of the International Conference Days on Diffraction* (2016), p. 166
19. M.F.M. Osborne, S.D. Hart, J. Acoust. Soc. Am. **17**, 1 (1945)
20. J.-P. Sessarego, J. Sagéloli, C. Gazanhes, H. Überall, J. Acoust. Soc. Am. **101**(1), 135 (1997)

Chapter 30
Three-Dimensional Boundary-Element Modeling of Transversal Vibrations of a Poroelastic Plate

Leonid Igumnov, Igor Vorobtsov and Andrey Petrov

Abstract The problem of the effect of a transversal harmonic load on a poroelastic rectangular plate in a 3D formulation is considered. The poroelastic continuum is described using Biot's mathematical model. The material is assumed to consist of a solid phase constituting an elastic form-defining skeleton and carrying most of the loading, and a liquid phase filling the pores. Dynamic equations of the poroelastic medium are written for unknown functions of displacement of the elastic skeleton and pore pressure of the filling material. The boundary-value problem is analyzed using a direct approach of the boundary integral equation (BIE) method. Relations for transversal displacement as a function of frequency have been obtained. For a posteriori analysis of the boundary-element poroelastic solution, boundary-element computations for drained and undrained models of the material are given.

30.1 Introduction

Studying dynamic processes in poroelastic materials, as well as parts and structural elements made of them, gains considerable attention because of their wide use in modern technologies. Special attention of the researching community is paid to mechanical vibrations of poroelastic bodies of simple geometries, such as beams, plates etc. Such structural elements are used in automotive and aircraft industries because of their acoustic absorptivity.

The results of modeling the dynamic response of elastic isotropic, orthotropic and functionally graded plates, obtained using numerical and analytical approaches, are widely covered in scientific literature. Reviews of Liew et al. [1], Noor [2], Reddy [3] and Tessler et al. [4] contain detailed information on such studies. Poroelastic formulations are used much more rarely. To solve this kind of problems, adequate mathematical, methodological and the related software provision is

L. Igumnov · I. Vorobtsov · A. Petrov (✉)
Research Institute for Mechanics, National Research Lobachevsky State University of Nizhni Novgorod, Nizhni Novgorod, Russia
e-mail: andrey.petrov@mech.unn.ru

I. A. Parinov et al. (eds.), *Advanced Materials*, Springer Proceedings in Physics 207, https://doi.org/10.1007/978-3-319-78919-4_30

required. Even with considerable simplifications, use of a model of a liquid-saturated porous material substantially complicates the computational scheme of the boundary-value problem as compared with an elastic or viscoelastic formulation. A poroelastic formulation makes it possible to account for liquid flows into or out of any regions formed by pores. This account is especially important, when analyzing wave processes, because a contribution of the dynamic behavior of the liquid alters their picture drastically.

The solution of the problem of vibrations of a simply supported plate, obtained on the base of classical Kirchhoff's theory, using defining relations of Biot's poroelastic medium [5, 6], are presented by Theodorakopoulos and Beskos [7]. A similar formulation, but for the case of incompressible components of a poroelastic medium, is used by Leclaire et al. [8]. Vibrations of a poroelastic plate under harmonic loading, using asymptotic series expansion in combination with the finite-element methodology, are analyzed by Nagler and Schanz [9]. At the same time, the results of boundary-element computations in a 3D formulation for similar problems in scientific literature are absent.

30.2 Mathematical Model

The constitutive equations for a poroelastic medium in terms of stress according to works by Biot can be formulated as follows:

$$\sigma_{ij} = 2G\varepsilon^s_{ij} + \left(K - \frac{2}{3}G\right)\varepsilon^s_{kk}\delta_{ij} - \alpha\delta_{ij}p, \tag{30.1}$$

where K and G are the elastic moduli of the porous material, p is the porous pressure of the filling material. Coefficient α is determined as

$$\alpha = 1 - \frac{K}{K^s}, \tag{30.2}$$

where K^s is bulk modulus of the skeleton grains. The stress tensor components of the solid body are ε^s_{ij}. The kinematic relations, in the assumption of small strain gradients, have the following form:

$$\varepsilon^s_{ij} = \frac{1}{2}\left(u^s_{i,j} + u^s_{j,i}\right), \tag{30.3}$$

where u^s_i are solid body displacements.

In addition to net stress σ_{ij}, change of the liquid volume per unit of initial volume is introduced as

$$\zeta = \alpha\varepsilon_{kk}^{s} + \frac{\varphi^2}{R}p, \tag{30.4}$$

where porosity is designated as+

$$\varphi = \frac{V^f}{V}, \tag{30.5}$$

The parameter characterizing the relation between the solid body and the liquid:

$$R = \frac{\varphi^2 K^f K^{s2}}{K^f(K^s - K) + \varphi s(K^s - K^f)} \tag{30.6}$$

In (30.5), V^f is the volume of interconnected pores in a specimen with volume V, in (30.6), K^f is the bulk modulus of the liquid. Change of the liquid is described by the continuity equation:

$$\dot{\zeta} + q_{i,i} = 0. \tag{30.7}$$

In (30.7), the notion of specific flow, or filtration vector is introduced as

$$q_i = \varphi(\dot{u}_i^f - \dot{u}_i^s). \tag{30.8}$$

where u_i^f is displacement of the liquid. To describe liquid transfer, a dynamic version of Darcy law is used:

$$q_i = -\kappa\left(p_{,i} + \frac{\rho_a}{\varphi}(\ddot{u}_i^f - \ddot{u}_i^s) + \rho_f \ddot{u}_i^f\right), \tag{30.9}$$

where κ is permeability, ρ_f is density of the filling material. To describe the dynamic interaction between the liquid and the skeleton, Biot introduced an additional density:

$$\rho_a = C\varphi\rho_f, \tag{30.10}$$

where C is a coefficient depending on the pore geometry and excitation frequency. In what follows, the coefficient C is taken equal to 0.66.

Transformation into Laplace region makes it possible to write an expression for q_i, keeping in mind (30.8) and (30.9), as follows:

$$\hat{q}_i = -\frac{\kappa\rho_f\varphi^2 s^2}{\beta}\frac{1}{s^2\rho_f}(\hat{p}_{,i} + s^2\rho_f\hat{u}_i^s), \quad \beta = \varphi^2 s + s^2\kappa(\rho_a + \varphi\rho_f) \tag{30.11}$$

Symbol «^» denotes Laplace transform with complex variable s. The momentum balance equation for a mixture is formulated in Biot's work. Dynamic equilibrium, with the account of (30.11), is defined as:

$$\hat{\sigma}_{ij,j} + \hat{F}_i + s^2 \rho \hat{u}_i^s = \beta(\hat{p}_{,i} - s^2 \rho_f \hat{u}_i^s) \tag{30.12}$$

where $\rho = \rho_s(1-\varphi) + \varphi\rho_f$, ρ_s is density of the skeleton grains, $\hat{F}_i$ is volume force density.

The differential equation system in Laplace representations for displacements $\hat{u}_i^s$ and pore pressure $\hat{p}$ in the absence of volume forces has the following form:

$$G\hat{u}_{i,jj}^s + \left(K + \frac{1}{3}G\right)\hat{u}_{j,ij}^s - (\alpha - \beta)\hat{p}_{,i} - s^2(\rho - \beta\rho_f)\hat{u}_i^s = 0, \tag{30.13}$$

$$\frac{\beta}{s\rho_f}\hat{p}_{,ii} - \frac{\varphi^2 s}{R}\hat{p} - (\alpha - \beta)s\hat{u}_{i,i}^s = 0,\ \mathbf{x} \in \Omega,\ \Omega \subset R^3. \tag{30.14}$$

A generalized displacement vector and a generalized force vector are additionally introduced as

$$\mathbf{u}(\mathbf{x}, s) = (\hat{u}_1^s, \hat{u}_2^s, \hat{u}_3^s, \hat{p}), \tag{30.15}$$

$$\mathbf{t}(\mathbf{x}, s) = (\hat{t}_1, \hat{t}_2, \hat{t}_3, \hat{q}), \tag{30.16}$$

where $\hat{t}_i = \hat{\sigma}_{ij}n_i$, and $\hat{q} = q_i n_i$, n_i are components of the vector of the normal to the boundary of region Ω.

Equations (30.13) and (30.14), supplemented with boundary conditions:

$$\mathbf{u}(\mathbf{x}, s) = \tilde{\mathbf{u}}, \quad \mathbf{x} \in \boldsymbol{\Gamma}^{\mathbf{u}}, \tag{30.17}$$

$$\mathbf{t}(\mathbf{x}, s) = \tilde{\mathbf{t}}, \quad \mathbf{x} \in \boldsymbol{\Gamma}^{\boldsymbol{\sigma}}, \tag{30.18}$$

where $\boldsymbol{\Gamma}^{\mathbf{u}}$ is the Dirichlet's boundary and $\boldsymbol{\Gamma}^{\boldsymbol{\sigma}}$ is the Neumann's boundary, fully describe the boundary problem in the representations of the 3D isotropic dynamic theory of poroelasticity.

30.3 BIE and Boundary-Element Methodology

Boundary-value problem (30.13)–(30.18) is solved using the direct boundary-element method (BEM), based on a combined use of integral Laplace transform and BIE's of the 3D isotropic theory of poroelasticity:

$$\mathbf{C}(\mathbf{y})\mathbf{u}(\mathbf{y},s)+\int_{\Gamma}\mathbf{T}(\mathbf{x},\mathbf{y},s)\mathbf{u}(\mathbf{x},s)d\Gamma=\int_{\Gamma}\mathbf{U}(\mathbf{x},\mathbf{y},s)\mathbf{t}(\mathbf{x},s)d\Gamma,\quad \mathbf{x},\mathbf{y}\in\Gamma, \tag{30.19}$$

where $\mathbf{U}(\mathbf{x},\mathbf{y},s)$ and $\mathbf{T}(\mathbf{x},\mathbf{y},s)$ are matrices of fundamental and singular solutions, respectively, $\mathbf{x}$ is an integration point, $\mathbf{y}$ is an observation point. The values of the coefficients of matrix $\mathbf{C}$ are defined by the geometry of boundary Γ. A procedure for obtaining BIE's, based on the weighted residual method can be found in [10]. Some of the problems of the arising kernels of BIE's are discussed in [11].

Equation (30.19) comprise singular integrals in the sense of Cauchy, which are quite difficult to compute. Use of the boundary properties of retarded potentials makes it possible, based on [12], to write down a regular representation of (30.19):

$$\int_{\Gamma}\big(\mathbf{T}(\mathbf{x},\mathbf{y},s)\mathbf{u}(\mathbf{x},s)-\mathbf{T}^{0}(\mathbf{x},\mathbf{y})\mathbf{u}(\mathbf{y},s)-\mathbf{U}(\mathbf{x},\mathbf{y},s)\mathbf{t}(\mathbf{x},s)\big)d\Gamma=0,\quad \mathbf{x},\mathbf{y}\in\mathit{\Gamma}, \tag{30.20}$$

where $\mathbf{T^0}(\mathbf{x},\mathbf{y})$ is singularity matrix. Using (30.20), it is possible to construct a boundary-element solution of the BIE.

In the result of spatial discretization, boundary Γ is represented with a set of K_E quadrangular eight-node boundary elements. The geometry of each element E_k is defined by biquadratic functions of form N_m [13] and the global coordinates of nodes $\mathbf{x}_m^k$, related as

$$\mathbf{x}(\xi)=\sum_{m=1}^{8}N_m(\xi)\mathbf{x}_m^k,\ k=1..K \tag{30.21}$$

where $\xi=(\xi_1,\xi_2)\in[-1,\ 1]^2$ are local coordinates. According to correlated interpolation model [14], displacements are described using bilinear elements with the related bilinear functions of form $R_l(\xi)$, and surface generalized forces are described with constant boundary elements:

$$\mathbf{u}(\xi)=\sum_{l=1}^{4}R_l(\xi)\mathbf{u}_l^k, \tag{30.22}$$

$$\mathbf{t}(\xi)=\mathbf{t}^k, \tag{30.23}$$

where $\mathbf{u}_m^k$ and $\mathbf{t}^k$ are nodal values of displacements and tractions, respectively, over element E_k.

A discrete representation of BIE's written at the nodes of the approximation of boundary functions $\mathbf{y}^i$, using the collocation method and accounting for (30.21)–(30.23), is of the following form:

$$\sum_{k=1}^{K_E}\sum_{m=1}^{4}\Delta\mathbf{T}_{mi}^{k}\mathbf{u}_{m}^{k}=\sum_{k=1}^{K}\Delta\mathbf{U}_{mi}^{k}\mathbf{t}^{k}, \tag{30.24}$$

$$\Delta\mathbf{U}_{mi}^{k}=\int_{-1}^{1}\mathbf{U}(\mathbf{x}^{k}(\xi),\mathbf{y}^{i},s)J^{k}(\xi)d\xi, \tag{30.25}$$

$$\Delta\mathbf{T}_{mi}^{k}=\int_{-1}^{1}[R_{m}(\xi)\mathbf{T}(\mathbf{x}^{k}(\xi),\mathbf{y}^{i},s)-\mathbf{I}\cdot\mathbf{T}^{0}(\mathbf{x}^{k}(\xi),\mathbf{y}^{i})]J^{k}(\xi)d\xi, \tag{30.26}$$

where $\mathbf{I}$ is unit matrix, J^k is Jacobean of the local coordinates into global ones.

The elements of matrices $\Delta\mathbf{U}_{mi}^{k}$, $\Delta\mathbf{T}_{mi}^{k}$ are computed using numerical integration schemes chosen depending on the kind of integral (nonsingular or singular). Nonsingular integrals arise, when the collocation point does not belong to the element. Here, standard Gaussian-type formula are used in combination with a hierarchical subdivision of the elements [15]. Singular integrals arise, when the collocation point belongs to the element being integrated over. In this case, new local coordinates are introduced, making it possible to eliminate a singularity in the integrand and to use Gaussian integration.

30.4 Numerical Example

Consider a poroelastic impermeable rectangular 4.0 × 4.0 × 0.2 m^3 plate. The poroelastic skeleton is assumed to be rigidly fixed along the sides of the plate, and a normal harmonic force with the amplitude of 500 Pa is assumed to act on the upper surface (Fig. 30.1a). The center of the global coordinate system coincides with the center of the plate. The geometry of the problem and the loading mode make it possible to use a quarter of the boundary-element mesh (Fig. 30.1b). The mesh consists of 880 square boundary elements.

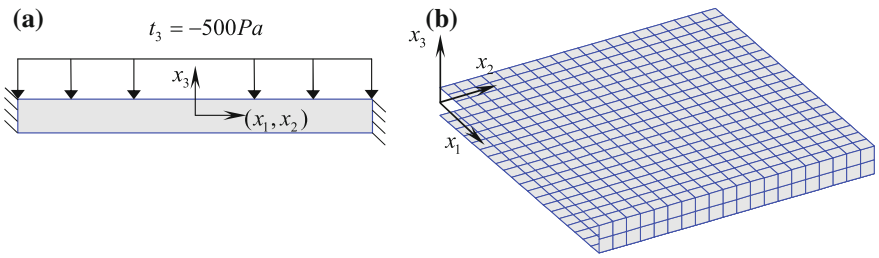

Fig. 30.1 Schematic representation of the problem (**a**) and the boundary-element mesh (**b**)

In computations according to the poroelastic material model, parameters of water-saturated sand are used (Table 30.1). Two limiting cases of deformation of a two-phase medium—drained and undrained [16, 17]—are also considered. Figure 30.2 shows diagrams of displacement u_3 as function of ω at point with coordinates $x_1 = x_2 = 0, x_3 = 0.1$, and a comparison for the three models. Substantial difference in the behavior of the solution is observed for ω close to the eigen-frequencies: the vertical displacements in the solutions for drained and undrained models of the material are higher than the corresponding displacements in the poroelastic solution. This feature demonstrates the effect of the filling moving inside the pores. For $\omega \in [0, 50]$, the poroelastic solution lies between the solutions,

Table 30.1 Material data

Parameter	Poroelastic	Elastic drained	Elastic undrained
Bulk modulus $K[\mathrm{N/m^2}]$	8×10^9	8×10^9	1.6×10^{10}
Shear modulus $G[\mathrm{N/m^2}]$	6×10^9	6×10^9	6×10^9
Density $\rho[\mathrm{kg/m^3}]$	2458	2458	2458
Solid bulk modulus $K^s[\mathrm{N/m^2}]$	3.6×10^9	–	–
Fluid bulk modulus $K^f[\mathrm{N/m^2}]$	3.3×10^9	–	–
Fluid density $\rho_f[\mathrm{kg/m^3}]$	1000	–	–
Porosity $\varphi[-]$	0.19	–	–
Permeability $\kappa[\mathrm{m^4/(N\ s)}]$	1.9×10^{-7}	–	–

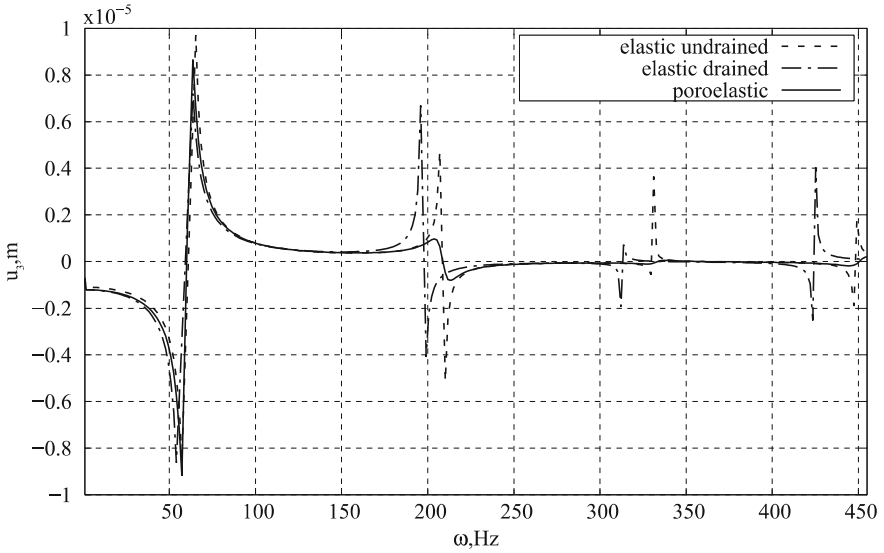

Fig. 30.2 The posteriori evaluation of the poroelastic solution according to elastic material models

obtained using the drained and undrained models, but as the frequency increases, the undrained solution tends to describe the dynamic response of the two-phase porous plate better.

The displacement u_3 in dependence on the frequency ω for different values of the porosity is present in Fig. 30.3. It is observed that u_3 increases when approaching the eigenfrequency.

The BIE method is used for computing unknown generalized displacements or tractions along boundary Γ of random region Ω. The solution inside the region is obtained based on a generalized Somigliana formula:

$$\mathbf{u}(\mathbf{y}, s) = \int_{\Gamma} \mathbf{U}(\mathbf{x}, \mathbf{y}, s)\mathbf{t}(\mathbf{x}, s)d\Gamma - \int_{\Gamma} \mathbf{T}(\mathbf{x}, \mathbf{y}, s)\mathbf{u}(\mathbf{x}, s)d\Gamma, \quad \mathbf{x} \in \Gamma, \mathbf{y} \in \Omega. \tag{30.27}$$

Table 30.2 depicts displacements and pore pressure in the points with coordinates $(x_1, x_2) = (0.1, 0.0)$ for $\omega = 100$ Hz.

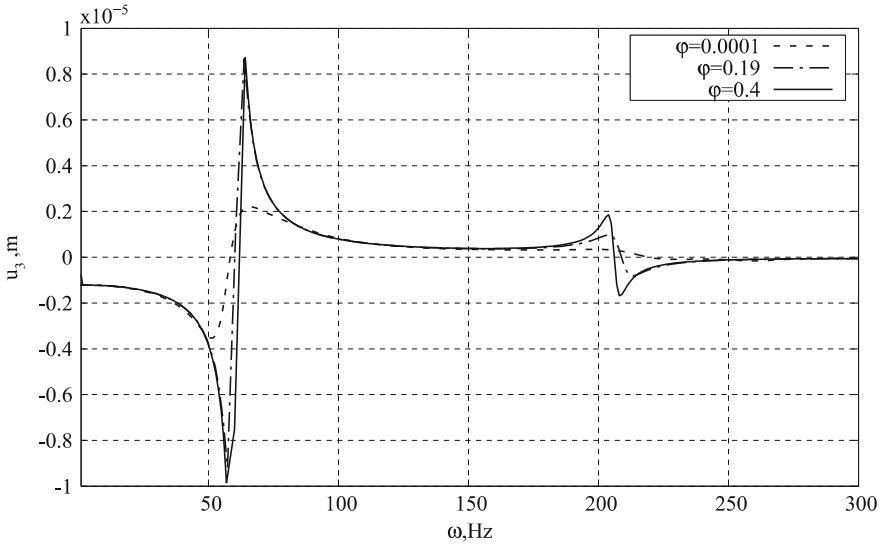

Fig. 30.3 Effect of porosity φ on displacement u_3

Table 30.2 Generalized displacements in external points of the plate

x_3	u_1[m]	u_2[m]	u_3[m]	u_4[N/m^2]
0.1	9.56523×10^{-8}	-2.19245×10^{-11}-	7.41139×10^{-6}	-5.33455×10^{3}
0.05	4.72488×10^{-8}	-8.46398×10^{-12}	7.43937×10^{-6}	-3.77777×10^{3}
-0.05	-4.72697×10^{-8}	8.46578×10^{-12}	7.44041×10^{-6}	3.99567×10^{3}
-0.1	-9.56741×10^{-8}	2.19376×10^{-11}	7.41345×10^{-6}	5.55240×10^{3}

30.5 Conclusion

A mathematical model of a boundary-value problem of the 3D dynamic poroelastic theory using integral Laplace transform is presented. The description of the mathematical model of a fully saturated porous medium is based on Biot's model with four basic functions. The boundary-element modeling methodology is described. The problem on normal harmonic force, acting on the upper plane of a rectangular 3D plate is solved. Diagrams of transversal displacements of the plate as a function of frequency are present. The boundary-element poroelastic solution is assessed using the drained and undrained models of a two-phase porous medium. A pronounced effect of the behavior of the filling pores on the dynamic response of the plate is noted. Results of computing unknown fields in internal points of the plate are given.

Acknowledgements The research was carried out under the financial support of the Russian Science Foundation (project No. 16-19-10237).

References

1. K.M. Liew, Y. Xiang, S. Kitipornchai, J. Sound Vib. **180**(1) (1995)
2. A.K. Noor, AIAA J. **11**(7) (1973)
3. J.N. Reddy, Shock Vib. Dig. **22**(7) (1990)
4. A. Tessler, E. Saether, T. Tsui, *Journal of Sound and Vibration.* **179**(3) 1995
5. M.A. Biot, J. Acoust. Soc. Am. **28**(2) (1956)
6. M.A. Biot, J. Acoust. Soc. Am. **34**(9A) (1962)
7. D.D. Theodorakopoulos, D.E. Beskos, Acta Mech. **103**(1–4) (1994)
8. P. Leclaire, K.V. Horoshenkov, A. Cummings, J. Sound Vib. **247**(1) (2001)
9. L. Nagler, M. Schanz, Arch. Appl. Mech. **80**(10) (2010)
10. M. Schanz, *Wave Propagation in Viscoelastic and Poroelastic Continua* (Springer, Berlin, 2001), 170pp
11. A.V. Amenitsky, A.A. Belov, L.A. Igumnov, I.S. Karelin, Probl. Strength Plast. **71** (2009)
12. V.G. Bazhenov, L.A. Igumnov, *Boundary Integral Equations and Boundary Element Methods in Treating the Problems of 3D Elastodynamics with Coupled Fields* (PhysMathLit, Moscow, 2008), 351pp (in Russian)
13. L.A. Igumnov, S.Y. Litvinchuk, A.N. Petrov, A.A. Ipatov, in *Advanced Materials—Manufacturing, Physics, Mechanics and Applications*, ed. by I.A. Parinov, S.-H. Chang, V.Y. Topolov. Springer Proceedings in Physics, vol. 175 (Springer, Cham, 2016), p. 505
14. R.V. Goldshteyn, *Boundary Integral Equations Method: Numerical Aspects and Application in Mechanics* (Mir, Moscow, 1978), 183pp (in Russian)
15. J.C. Lachat, J.O. Watson, Int. J. Numer. Methods Eng. **10**(5) (1976)
16. E. Detournay, A.H.D. Cheng, in *Comprehensive Rock Engineering: Principles, Practice and Projects*, ed. by C. Fairhurst (Pergamon Press, Oxford, 1993), p. 113
17. K. Terzaghi, R.B. Peck, G. Mesri, *Soil Mechanics in Engineering Practice*, 3rd edn. (Wiley, New York, 1996), 529pp

Chapter 31
Comparative Study on Progressive Damage Models for Composites

K. S. S. Reddy, Anna A. Nasedkina, Andrey V. Nasedkin, B. Saswata and A. Rajagopal

Abstract The evolution of damage in laminated fiber reinforced composites is a complex phenomenon, which involves interaction of different modes of failure like fiber breakage, matrix cracking, fiber-matrix debonding and delamination. In the present work the effect of fiber volume fraction and different damage mechanisms such as fiber breakage, fiber-matrix debond and matrix cracks on the effective properties of unidirectional fiber-reinforced composites is predicted based on a micromechanical analysis. The material properties are calculated using a three-dimensional micromechanical representative volume element (RVE). A finite element based progressive damage model is developed to predict failure behavior of a laminate in respective load-constraint conditions. The proposed model also helps to determine where and how failure occurs first and how the damage evolves. Hashin's and Puck's failure models are used for laminated composite plates of various stacking sequences and their respective numerical results are compared. The influences of the failure criteria and material degradation model are studied through a numerical analysis. The case studies considered vary from a unidirectional laminate with a hole, laminates with single bolt lap joint.

K. S. S. Reddy (✉) · A. Rajagopal
Department of Civil Engineering, Indian Institute of Technology Hyderabad, Hyderabad, India
e-mail: suryashekar.komirelly@gmail.com

A. A. Nasedkina · A. V. Nasedkin
I. I. Vorovich Institute of Mathematics, Mechanics and Computer Science, Southern Federal University, Rostov-on-Don, Russia

B. Saswata
Department of Materials Science and Metallurgical Engineering, Indian Institute of Technology Hyderabad, Hyderabad, India

I. A. Parinov et al. (eds.), *Advanced Materials*, Springer Proceedings in Physics 207, https://doi.org/10.1007/978-3-319-78919-4_31

31.1 Introduction

Composite materials are the materials, which have strong fibers surrounded by a weak matrix material. The matrix serves to transmit the load to the fibers and also distribute the fibers. The bondage between fibers and matrix is created while manufacturing and this has fundamental influence on the mechanical properties of the composite material. The evaluation of effective properties of composite materials is of great importance in engineering design and application. Two approaches are considered in obtaining the global properties of composites: (i) micro mechanical analysis and (ii) macro mechanical analysis. The material is considered as a homogeneous orthotropic continuum in micromechanical analysis and the study is at the level of fiber and matrix. The overall behavior of the composite is determined by knowing the properties of the fiber and matrix using unit cell technique. Murari and Upadhay [1, 2] have developed a damage model by considering the effect of different damage modes and fiber volume fraction on effective properties based on the RVE analysis. Harish et al. [3] found the homogenized properties for unstrengthen masonry and also strengthened masonry using CFRP (inserted in bed joints) with help of modified rule of mixture. Bhalchandra et al. [4] compared the properties of transversely isotropic lamina using method of cells and composite cylinder assemblage. Wu et al. [5] explained the method of applying periodic boundary conditions using finite element analysis. Gay [6] and Jones [7] gave the constitutive equations for different types of materials.

Mechanically fastened joints are used in complex structures as they can be easily disassembled without damage and avoid surface preparation for joining. The only dependence on the materials is the strength of the materials at the joint location. For instance, if the materials are weak in compression, the compressive force, excreted by bolts and nuts, could lead the materials to deform. Moreover, if the materials are not strong in shear, screws may not hold. Strong and durable composite joints are crucial for the structural members made of composite laminates. It is difficult to analyze the joint behavior of the composites because of its anisotropic and heterogeneous nature compared to isotropic materials. The load carried by each fastener increases accordingly as the efficiency of the structure increases because of the better design of joints thereby increasing the probability of failure. Therefore, for damage-tolerant design it is difficult to assess the stresses around the fasteners holes. The presence of unknown contact stresses and contact region between the fastener and the laminate makes the analysis of a pin-loaded hole considerably more complex than that of a traction-free hole. For reliable strength evaluation and failure prediction it is essential to accurately predict the stress distribution along the hole edge. Progressive damage analysis is important to calculate the maximum load capacity of a joint under an overload situation and to understand the failure process [8].

There have been more recent works on progressive failure or damage analysis of composites. A comparison between failure theories and experimental results is given in [9, 10]. A modified maximum stress failure criterion is proposed in [11].

A three-dimensional failure criterion for laminates is proposed in [12]. The effect of fasteners on mechanical behavior of lap joints is studied in [13].

31.2 Modeling and Analysis Methods

31.2.1 Micromechanical Analysis

In a lamina there can be several micro damage mechanisms that are possible. In this study, only three types of damage mechanisms are present. They are: (i) fiber breaking (due to σ_{11}), (ii) fiber-matrix debonding (due to σ_{12} and σ_{13}) and (iii) matrix cracks (due to σ_{22} and σ_{33}). In the present study, the fiber breaking is represented by a centrally located crack in the fiber. The strong interface is assumed and fiber-matrix debonding is modeled by a complete debonding. A linear elastic analysis is conducted for various lengths of the crack in the depth direction, with maximum length equal to the cell length, l. The fiber-matrix debonding can grow either due to σ_{12} or σ_{13}, in the direction along the fiber. The matrix cracks are represented as radial cracks, whose growth is assumed to be along the fiber. All the damage modes assumed are shown in Fig. 31.1.

31.2.1.1 Definition of Damage Parameters

Fiber break: $d_1 = 0$ (no fiber break); $d_1 = 1$ (complete fiber break).

Fiber-matrix debond: $d_2 = \frac{2\pi R_f l_d}{2\pi R_f l} = \frac{l_d}{l}$

Matrix cracks: $d_3 = \frac{2\pi R_f l_d}{2\pi R_f l} = \frac{l_d}{l}\,\frac{2\left(l-D_f\right)l_c}{2\left(l-D_f\right)l} = \frac{l_c}{l}$

where l_d and l_c are the length of debonding and length of matrix cracks, respectively. The range of damage variables, considered for the current study, is from 0.2 to 0.8.

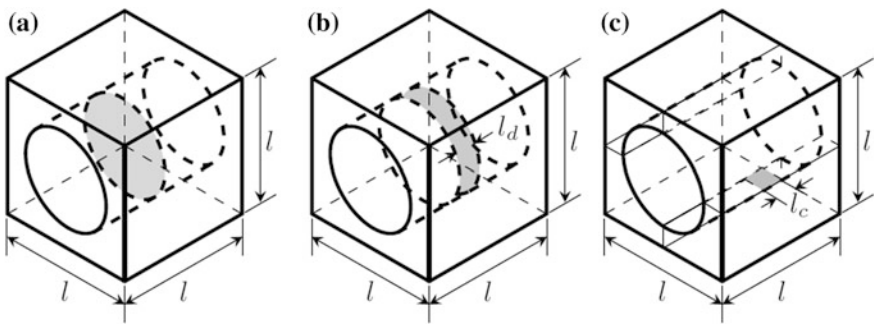

Fig. 31.1 **a** Fiber breakage. **b** Fiber-matrix debond. **c** Matrix cracks

31.2.1.2 Evaluation of Effective Properties of Composites

The finite element software package ANSYS is used to evaluate the effective properties of composite. The program is written in APDL (ANSYS Parametric Design Language), using three-dimensional structural solid element SOLID186 to determine elastic properties, which is defined by 20 nodes having three translational degrees of freedom. The stress strain relation for a transversely isotropic material whose properties are isotropic in one of its planes and the stiffness tensor is represented as

$$\begin{pmatrix} \bar{\sigma}_{11} \\ \bar{\sigma}_{22} \\ \bar{\sigma}_{33} \\ \bar{\sigma}_{23} \\ \bar{\sigma}_{13} \\ \bar{\sigma}_{12} \end{pmatrix} = \begin{pmatrix} C_{11} & C_{12} & C_{12} & 0 & 0 & 0 \\ C_{12} & C_{22} & C_{23} & 0 & 0 & 0 \\ C_{12} & C_{23} & C_{22} & 0 & 0 & 0 \\ 0 & 0 & 0 & \frac{C_{22}-C_{23}}{2} & 0 & 0 \\ 0 & 0 & 0 & 0 & C_{66} & 0 \\ 0 & 0 & 0 & 0 & 0 & C_{66} \end{pmatrix} \begin{pmatrix} \bar{\varepsilon}_{11} \\ \bar{\varepsilon}_{22} \\ \bar{\varepsilon}_{33} \\ \bar{\varepsilon}_{23} \\ \bar{\varepsilon}_{13} \\ \bar{\varepsilon}_{12} \end{pmatrix}$$

The elastic properties of the material are computed once the components of the transversely isotropic stiffness tensor are known as given below:

Longitudinal modulus:

$$E_{11} = C_{11} - \frac{2C_{12}^2}{(C_{22} + C_{23})}$$

Transverse modulus:

$$E_{22} = \frac{\left[C_{11}(C_{22} + C_{23}) - 2C_{12}^2\right](C_{22} - C_{23})}{\left(C_{11}C_{22} - C_{12}^2\right)}$$

Poisson's ratio:

$$v_{12} = \frac{C_{12}}{(C_{22} + C_{23})}, \quad v_{23} = \frac{C_{11}C_{23} - C_{12}^2}{C_{11}C_{22} - C_{12}^2}$$

Shear modulus:

$$G_{12} = \frac{E_{11}}{2(1 + v_{12})}, \quad G_{23} = \frac{E_{22}}{2(1 + v_{23})}$$

31.2.1.3 Boundary Conditions for Evaluation of Elastic Properties

Composites can be represented as a periodic array of the RVEs. Hence, periodic boundary conditions are applied to the RVE models, which implies that each RVE in the composite has the same deformation mode without any separation or overlap

between the neighboring RVEs after deformation. The average stress is calculated as follows

$$\bar{\sigma}_{ij} = \frac{1}{V}\int_{V} \sigma_{ij} V^{e}$$

where $\bar{\sigma}_{ij}$ is the average stress, σ_{ij} is the stress in each element, V is the total volume of the RVE and V^{e} is the volume of each element.

31.2.2 Macromechanical Analysis

Progressive failure analysis (PFA) is a numerical procedure, which involves repetitive solutions of equilibrium during the growth of cracks, flaws or voids. Once the damage criterion is satisfied, further loading will cause the reduction of stiffness coefficients. It is a challenging task to predict the strength and failure mechanism because of the heterogeneity and anisotropic nature of composites. Since the prediction of strength and failure mechanism by conducting sufficient tests are time consuming and very expensive, predictive tools such as finite element method (FEM) are getting wide acceptance [14]. However, there are few disadvantages of using finite element analysis. One of the major problems encountered while performing analysis using finite element analysis is mesh sensitivity. Results from FEA tend to vary with the size of mesh, where the damage/stress concentration/change in properties tend to be more focused and concentrated, when the element size is decreased [15]. This makes the analysis slightly unreliable. The mesh size, used for both Hashin and Puck criteria is same thereby, the error due to mesh sensitivity also remains same in both cases. The phenomenon of stiffness degradation of composite laminates under continuous load is an important response to the damage initiation and evolution and this is a key principle for progressive failure analysis.

In the present work, we adopt Hashin's and Puck's failure criteria on different laminate configurations. A progressive damage model is thus formulated and implemented, considering both the theories in a finite element framework. A comparative study on accuracy of the two theories is performed, to understand the differences in detailed prediction of constituent mode of failure, distribution of load-deflection and stress–strain curves. A parametric study is thus performed by considering different lay-up sequence of laminates together with different structures, which include unidirectional laminate, laminated plate with a hole and a single-bolt lap joint.

31.2.2.1 Hashin's Failure Criterion

Hashin's failure criterion involves more than one stress component to evaluate the different failure modes, indicating that the stresses interact with each other to cause failure. These criteria were developed for unidirectional polymeric composites. Usually Hashin's criteria are implemented in two-dimension classical lamination approach for point stress calculations with ply discounting as the material degradation model [16]. Hashin's criteria involve four failure modes and failure indices are related to fiber and matrix failures. The maximum stress criteria are used for transverse normal stress component for analyzing three-dimension problems. The failure modes included in Hashin's criteria are as follows:

i. *Fiber failure under tensile load*, $(\sigma_{xx} \geq 0)$

$$\left(\frac{\sigma_{xx}}{X_T}\right)^2 + \frac{\left(\sigma_{xy}\right)^2 + \left(\sigma_{xz}\right)^2}{S_{xy}^2} = \begin{cases} \geq 1 & \textit{failure}; \\ < 1 & \textit{no failure}. \end{cases}$$

ii. *Fiber failure under compressive load*, $(\sigma_{xx} < 0)$

$$\left(\frac{\sigma_{xx}}{X_C}\right)^2 = \begin{cases} \geq 1 & \textit{failure}; \\ < 1 & \textit{no failure}. \end{cases}$$

iii. *Matrix failure under tensile load*, $(\sigma_{yy} + \sigma_{zz} > 0)$

$$\frac{\left(\sigma_{yy} + \sigma_{zz}\right)^2}{Y_T^2} + \frac{\sigma_{yz}^2 - \sigma_{yy}\sigma_{zz}}{S_{xz}^2} + \frac{\sigma_{xy}^2 + \sigma_{xz}^2}{S_{xy}^2} = \begin{cases} \geq 1 \textit{ failure}; \\ < 1 \textit{ no failure}. \end{cases}$$

iv. *Matrix failure under compressive load*, $(\sigma_{yy} + \sigma_{zz} < 0)$

$$\left[\left(\frac{Y_C}{2S_{yz}}\right)^2 - 1\right]\left(\frac{\sigma_{yy} + \sigma_{zz}}{Y_C}\right) + \frac{\left(\sigma_{yy} + \sigma_{zz}\right)^2}{4S_{yz}^2} + \frac{\sigma_{yz}^2 - \sigma_{yy}\sigma_{zz}}{S_{yz}^2} + \frac{\sigma_{xy}^2 + \sigma_{xz}^2}{S_{xy}^2} = \begin{cases} \geq 1 & \textit{failure}; \\ < 1 & \textit{no failure}. \end{cases}$$

v. *Fiber-matrixshear-out*, $(\sigma_{xx} < 0)$

$$\left(\frac{\sigma_{xx}}{X_C}\right)^2 + \left(\frac{\sigma_{xy}}{S_{xy}}\right)^2 + \left(\frac{\sigma_{xz}}{S_{xz}}\right)^2 = \begin{cases} \geq 1 & \textit{failure}; \\ < 1 & \textit{no failure}. \end{cases}$$

Here σ_{ij} represent the stress components. The parameters X_T, Y_T represent the allowable tensile strengths along the principal material directions, whereas X_C, Y_C represent the allowable compressive strengths. Further, S_{xy}, S_{xz} and S_{yz} represent allowable shear strengths along the respective principal material directions. Hashin's criterion assumes a quadratic interaction between the tractions acting on a plane of failure by calculating the angle of fracture for an element.

31.2.2.2 Puck's Failure Criterion

The fiber failure and inter-fiber failure in a unidirectional composite are identified by Puck's criterion. Fiber failure gives two different physical modes and inter-fiber failure gives three different physical modes [17]. Puck's failure criteria are listed below:

i. *Fiber Failure due to tension*

$$\frac{1}{R_{\parallel}^{t}}\left[\sigma_1 - \left(v_{\perp\parallel} - v_{\perp\parallel f} m_{\sigma f}\frac{E_{\parallel}}{E_{\parallel f}}\right)(\sigma_2+\sigma_3)\right] \geq 1$$

ii. *Fiber Failure due to compression*

$$\frac{1}{-R_{\parallel}^{c}}\left[\sigma_1 - \left(v_{\perp\parallel} - v_{\perp\parallel f} m_{\sigma f}\frac{E_{\parallel}}{E_{\parallel f}}\right)(\sigma_2+\sigma_3)\right] \geq 1$$

iii. *Inter Fiber Failure*: *Mode A*

$$\sqrt{\left(\frac{\tau_{21}}{S_{21}}\right)^2 + \left(1 - p_{\perp\parallel}\frac{Y_T}{S_{21}}\right)^2\left(\frac{\sigma_2}{Y_T}\right)^2} + p_{\perp\parallel}\frac{\sigma_2}{S_{21}} = 1 - \left|\frac{\sigma_1}{\sigma_{1D}}\right|$$

iv. *Inter Fiber Failure*: *Mode B*

$$\frac{1}{S_{21}}\left(\sqrt{\tau_{21}^2 + \left(p_{\perp\parallel}\sigma_2\right)^2} + p_{\perp\parallel}\sigma_2\right) = 1 - \left|\frac{\sigma_1}{\sigma_{1D}}\right|$$

v. *Inter Fiber Failure*: *Mode C*

$$\left[\left(\frac{\tau_{21}}{2(1+p_{\perp\perp})S_{21}}\right)^2 + \left(\frac{\sigma_2}{Y_C}\right)^2\right]\frac{Y_C}{-\sigma_2} = 1 - \left|\frac{\sigma_1}{\sigma_{1D}}\right|$$

where $R_{\parallel}^{t,c}$ is the fiber parallel strength in tension or compression; σ_1 is the longitudinal stress in fiber direction; σ_2 and σ_3 are the transverse stresses to fiber direction; $v_{\perp\parallel}$ is the major Poisson's ratio of the lamina; $v_{\perp\parallel f}$ is the major Poisson's

ratio of the fiber; $E_{\|}$ is the longitudinal modulus of the lamina parallel to the fibers; $E_{\|f}$ is the longitudinal modulus of the fibers; $m_{\sigma f}$ is a magnification factor for the transverse stress in the fibers, which assumes the typical values of 1.3 for glass fiber and 1.1 for carbon fiber composites; Y_T, Y_C are the tensile and compressive strengths of the unidirectional layer transverse to the fiber direction; $p_{\perp\perp}, p_{\perp\|}$ are the slopes for stress plane fracture envelope; S_{21} is the shear strength of a unidirectional layer transverse and parallel to the fiber direction; τ_{21} is the shear stress of a unidirectional layer in the elastic symmetry direction (the first subscript indicates the direction normal to the plane on which the shear stresses acting; the second subscript indicates the direction of the shear force); f_w is the weakening factor due to the degrading influence of high σ_1 stresses; $R^A_{\perp\perp}$ is the fracture resistance of the action plane against its fracture due to transverse/transverse shear stressing and σ_{1D} is the stress value for linear degradation.

31.3 Results and Discussion

31.3.1 Micromechanical Analysis

The concentration of stress in the RVE for different loading conditions are shown below. The initiation damage is likely to occur in these areas of stress concentrations (see Figs. 31.2, 31.3 and 31.4).

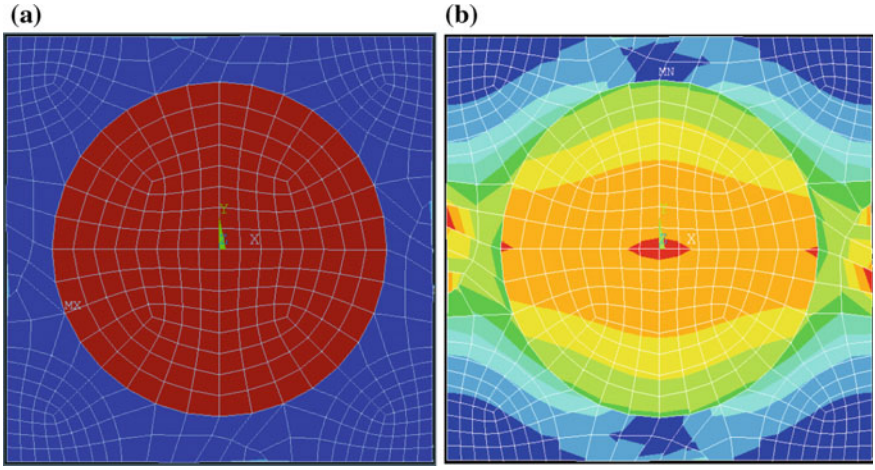

Fig. 31.2 Stress concentration in the RVE. **a** $\varepsilon_{11} = 1$. **b** $\varepsilon_{22} = 1$

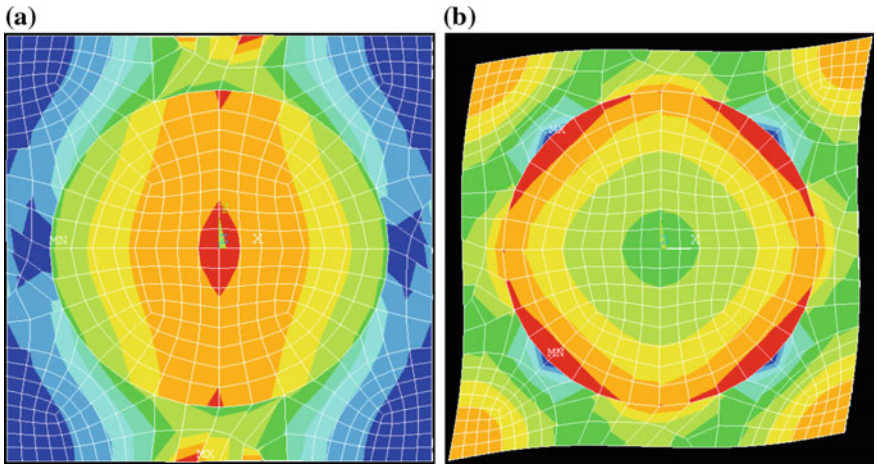

Fig. 31.3 Stress concentration in the RVE. **a** $\varepsilon_{33} = 1$. **b** $\varepsilon_{23} = 1$

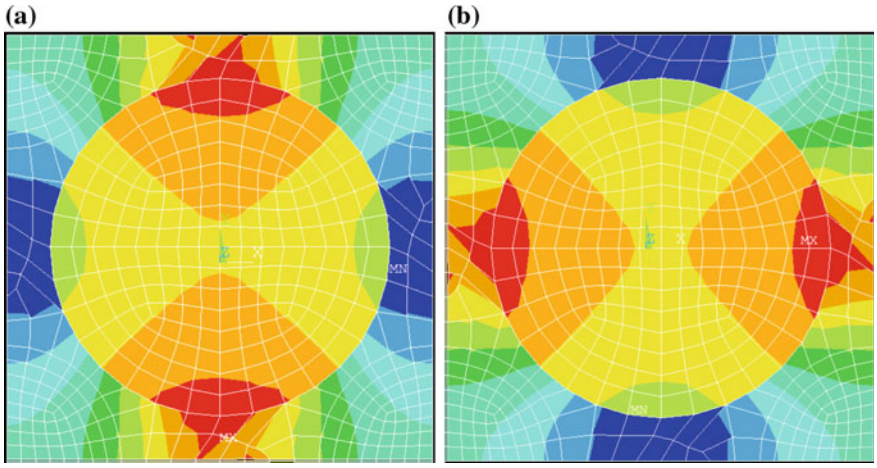

Fig. 31.4 Stress concentration in the RVE. **a** $\varepsilon_{13} = 1$. **b** $\varepsilon_{12} = 1$

31.3.1.1 Effect of Variation of Fiber Volume Fraction on Effective Properties

The effect of perturbation of fiber volume fraction on the effective properties is studied by conducting a series of numerical experiments on an undamaged unit-cell RVE with different fiber volume fractions (see Fig. 31.5).

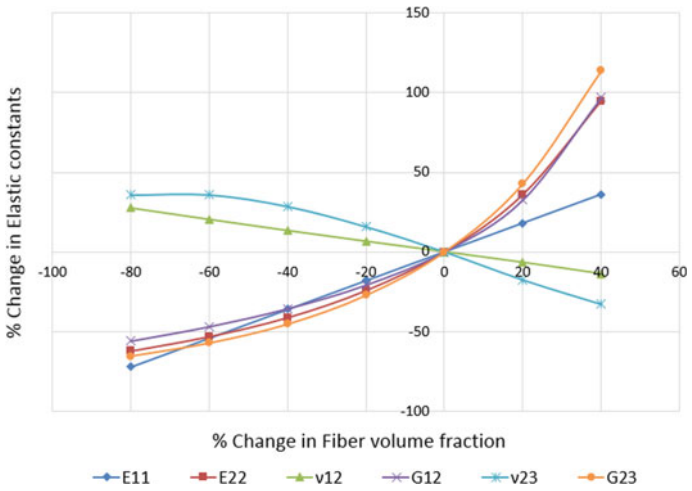

Fig. 31.5 Effect of fiber volume fraction on the effective properties

31.3.1.2 Effect of Damage on Effective Properties

The effect of damage on the effective properties is studied by conducting a series of numerical experiments on the unit-cell RVE at the reference volume fraction with different damage modes and sizes (see Figs. 31.6, 31.7 and 31.8).

31.3.2 Macromechanical Analysis

In unidirectional symmetric laminate $0°/0°/0°/0°$, when it follows Hashin's criteria, the elements that undergo tension around the hole (element along the line of action) fracture due to matrix failure caused by compression, where as the elements

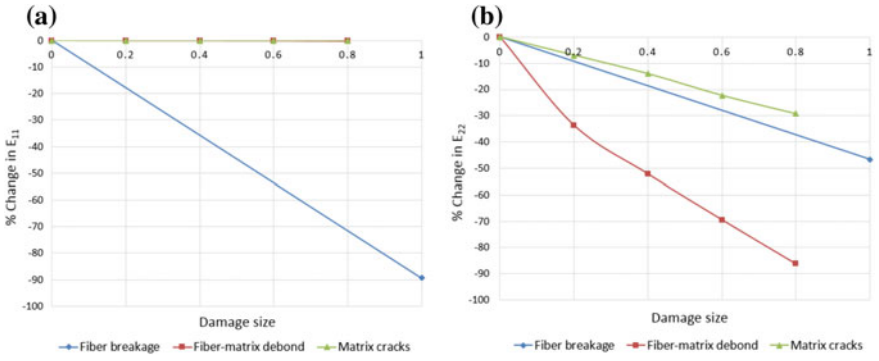

Fig. 31.6 Effect of damage modes on **a** longitudinal modulus and **b** transverse modulus

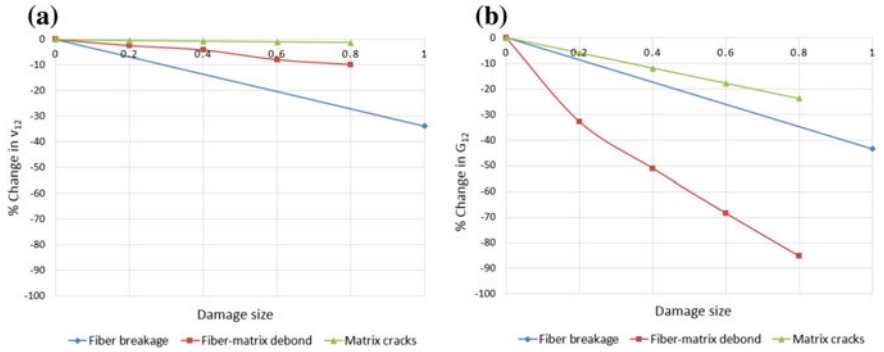

Fig. 31.7 Effect of damage modes on in-plane **a** Poisson's ratio and **b** shear modulus

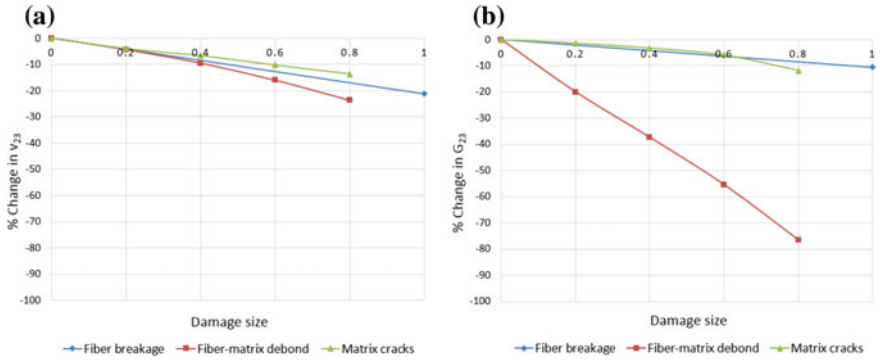

Fig. 31.8 Effect of damage modes on out-of-plane **a** Poisson's ratio and **b** shear modulus

that are transverse to the line of action fracture due to fiber failure caused by compression. The elements, which are not near the proximity of the hole, fracture due to fiber failure caused by tension. When the Puck criterion for failure is used, the distribution of failure differs vastly. The elements that are in proximity to the hole fracture due to inter fiber failure (mode A and mode C). The elements away from the hole again fracture due to fiber failure in tension as shown in Fig. 31.9.

In unidirectional antisymmetric cross ply laminate $0°/90°/0°/90°$, when it follows Hashin's criteria, the elements that undergo tension around the hole (element along the line of action) fracture due to matrix failure caused by compression, where as the elements that are transverse to the line of action fracture due to fiber failure caused by compression. Failure shear out and fiber failure in tension is also observed in regions away from the hole region as shown in Fig. 31.10. When Puck criterion for failure is adopted we observe a different distribution of failure. The elements that are in proximity to the hole region fracture due to the inter fiber failure (mode C along the loading direction and in mode A in the transverse direction). At regions away from the hole very little fiber failure in tension is observed together with inter fiber failure of mode A type as shown in Fig. 31.10.

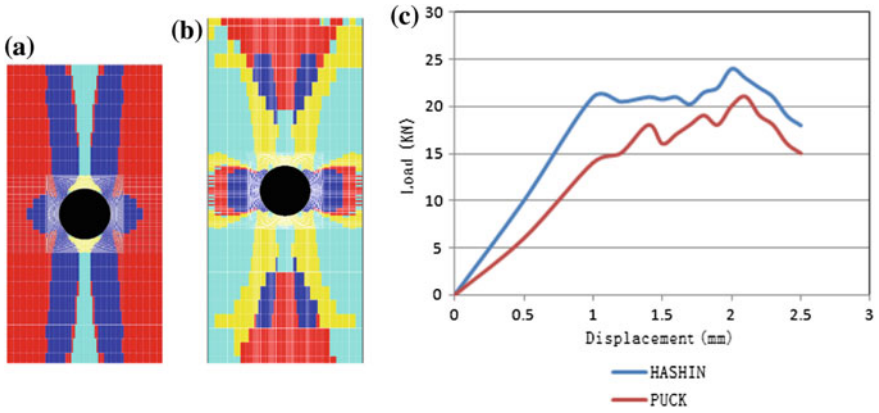

Fig. 31.9 **a** Hashin's failure, **b** Puck's failure and **c** load-displacement plot for symmetric laminate $0°/0°/0°/0°$

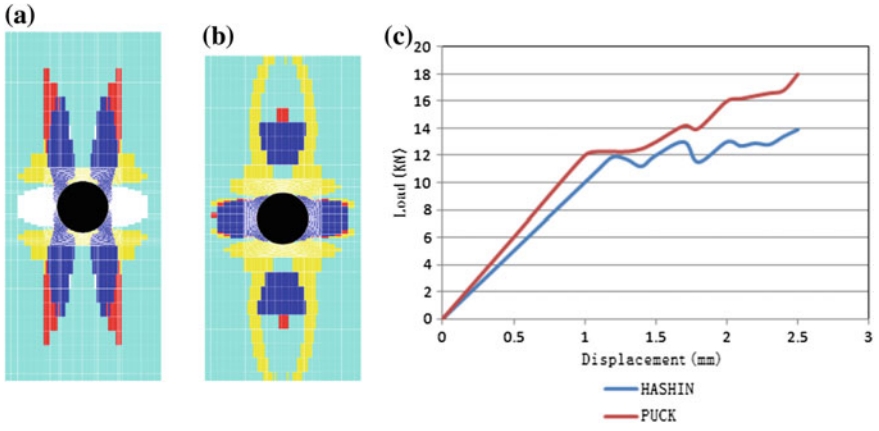

Fig. 31.10 **a** Hashin's failure, **b** Puck's failure and **c** load-displacement plot for antisymmetric laminate $0°/90°/0°/90°$

In unidirectional symmetric cross ply laminate $0°/90°/90°/0°$, when it follows Hashin's criteria, the elements that undergo tension around the hole (element along the line of action) fracture due to matrix failure caused by compression, where as few elements that are transverse to the line of action fracture due to fiber failure, attributed to fiber shear out. Rest of the elements in the proximity to the hole region fracture due to matrix failure in tension as shown in Fig. 31.11. In regions away from hole region, fiber failure in tension and shear out, matrix failure in tension and matrix failure in compression are also observed (see Fig. 31.11). When Puck's criterion for failure is adopted we observe a different distribution of failure. The elements that are in proximity to the hole region fracture due to the inter fiber failure

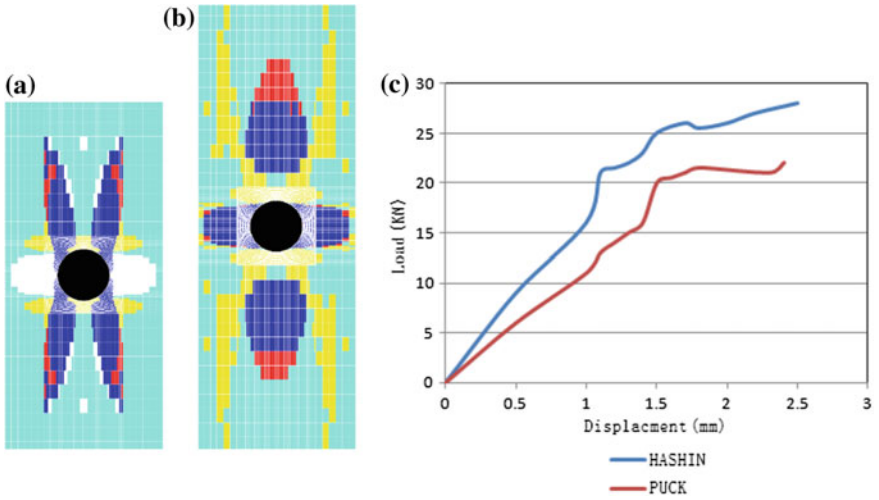

Fig. 31.11 **a** Hashin's failure, **b** Puck's failure and **c** load-displacement plot for symmetric laminate $0°/90°/90°/0°$

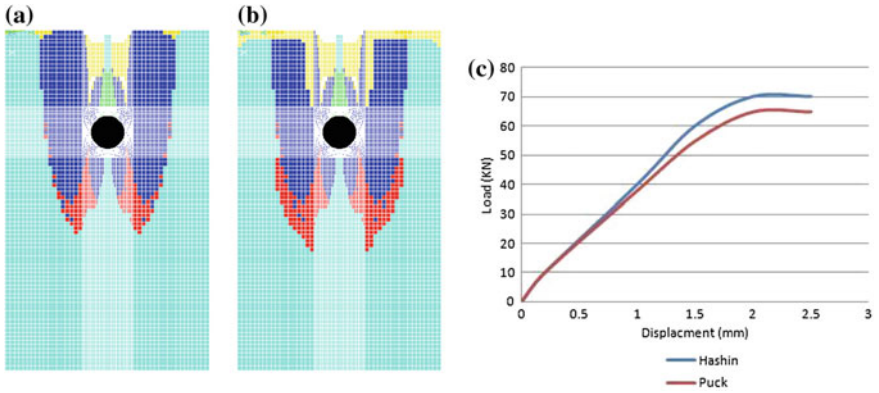

Fig. 31.12 **a** Hashin's failure, **b** Puck's failure and **c** load-displacement plot for lap joint

(mode C along the loading direction and in mode A in the transverse direction). At regions away from the hole very little fiber failure in tension is observed togther with inter fiber failure of mode A type as shown in Fig. 31.11.

In lap joint, both Puck's criterion and Hashin's criterion show similar distribution of failure (see Fig. 31.12), where deformation largely occurs due to matrix failure caused by tension, significant failure is also observed due to fiber failure caused by compression. There are matrix failure due to compression, fiber matrix shear out and fiber failure due to tension, when Hashin's criterion is adopted. When Puck's criterion is adopted, damage occurs largely due to IFF (mode A), significant

failure is also observed due to fiber failure caused by compression, IFF (mode C), fiber failure caused by tension, IFF (mode B). Failure is mainly observed only in the lap region. Both fixed strap and pulling strap show the same pattern of failure.

31.4 Conclusion

The elastic moduli are increasing and Poisson's ratio is decreasing with increase in fiber volume fraction. Longitudinal modulus is severely affected by fiber breakage. It is reduced by 90% (approx.) at 0.5 fiber volume fraction. All the effective properties are significantly affected except the longitudinal modulus in case of fiber–matrix debonding. E_{22}, G_{12} and G_{23} are reduced by 80% (approx.) by fiber-matrix debonding at 0.5 fiber volume fraction. The effect of matrix cracks is not significant on any of the properties.

Progressive damage modelling of composite laminates can be employed to get detailed and accurate failure analysis of a composite laminate structure (this is validated by experimental results also). It is observed that except for a few cases, both Hashin and Puck criteria work very well with the PDM technique in detecting, where an element failure occurs. It is also observed from both distribution of failure and plots of load-displacement and stress-strain that Hashin's failure criterion can be adopted to get an overall damage information, i.e., main failure reason can be spotted and the structure can be designed accordingly. However, to get a detailed analysis of where and how damage in individual constituent occurs, Puck's criterion works best to predict the distribution of failure.

Acknowledgement The authors would like to acknowledge the financial support of Indo Russian Collaborative project grant from DST-RFBR vide project number from DST side DST/INT/RFBR/IDIR/P-11/2016 and vide project number from RFBR 16-58-48009 IND_omi.

References

1. V. Murari, C. Upadhyay, Micromechanics based ply level material degradation model for unidirectional composites. Compos. Struct. (Elsevier). **94**, 671–680 (2012)
2. V. Murari, C. Upadhyay, Micromechanics based diffuse damage model for unidirectional composites. Compos. Struct. (Elsevier). **96**, 419–432 (2013)
3. L. Harish, A. Rajagopal, *Computational Homogenization and Failure Modeling of Periodic Composites*. Master Thesis, Indian Institute of Technology Hyderabad (2012)
4. S.A. Bhalchandra, Y. Shiradhonkar, S.S. Daimi, Comparison of properties of transversely isotropic lamina using method of cells and composite cylinder assemblage. Int. J. Adv. Sci. Technol. SERSC **64**, 43–58 (2014)
5. W. Wu, J. Owino, *Applying Periodic Boundary Conditions in Finite Element Analysis*. SIMULIA Community Conference (2014)
6. D. Gay, S.V. Ho, S.W. Tsai, *Composite Materials Design and Applications* (CRC Press LLC, 2003)

7. R.M. Jones, *Mechanics of Composite Materials* (Taylor & Francis, 1998)
8. U.P. Jabir, *Damage Prediction in Fiber Reinforced Composites* (Indian Institute of Technology, Hyderabad, 2013)
9. A.S. Kaddour, M.J. Hinton, Maturity of 3d failure criteria for fiber reinforced composites: Comparison between theories and experiments: Part b of wwfe-ii. J. Compos. Mater. **47**(6–7), 925–966 (2013)
10. E.A. Alexandros, K. Christoph, P.P. Theodore, Mechanical behavior of glass/epoxy tubes under combined static loading. part ii: Validation of FEA progressive damage model. Compos. Sci. Technol. **69**(13), 2248–2255 (2009)
11. Z. Libin, Q. Tianliang, Z. Jianyu, A.S. Ramanand, Modified maximum stress failure criterion for composite joints. J. Compos. Mater. **47**(23), 2995–3008 (2013)
12. G. Catalanotti, P.P. Camanho, A.T. Marques, Three-dimensional failure criteria for fiber-reinforced laminates. Compos. Struct. **95**, 63–79 (2013)
13. Q. Tianliang, Z. Libin, Z. Jianyu, Fastener effects on mechanical behaviors of double-lap composite joints. Compos. Struct. **100**, 413–423 (2013)
14. J. Meisam, C. Gergely, R.W. Michael, Numerical modeling of the damage modes in ud thin carbon/glass hybrid laminates. Compos. Sci. Technol. **94**, 39–47 (2014)
15. P.F. Liu, Z.P. Gu, Y.H. Yang, X.Q. Peng, A nonlocal finite element model for progressive failure analysis of composite laminates. Compos. B Eng. **86**, 178–196 (2016)
16. Z. Hashin, Failure criteria for unidirectional fiber composites. J. Appl. Mech. **47**(2), 329–334 (1980)
17. P. Giovanni, P.V. Nils, T.E. Andreas, *Numerical Analyses of Low Velocity Impacts on Composite. Advanced Modelling Techniques*. In Proceedings of the SIMULIA Customer Conference_2012, (2012)

Chapter 32
Numerical Study of Crack Initiation in Surface Hardened Ti_6Al_2V Alloy Based on the Residual Stress Analysis

A. N. Savkin, D. S. Denisevich, V. P. Bagmutov, I. N. Zakharov and A. A. Sedov

Abstract In this study, a three-dimensional (3D) finite element model of residual stresses after thermo-force surface hardening is developed. Numerical solution of the coupled thermo-mechanical problem is considered. A mathematical model of the phase transition, based on a complex analysis of calculated data on the dynamics of temperature fields and continuous cooling temperature diagram is developed. The mechanical part of the model accounts for the thermoviscoplastic behavior of the material coupled with martensitic phase transformation. The simulated results for titanium alloy Ti_6Al_2V are present, non-uniform distribution of residual stresses and potential cracking zones is determined.

32.1 Introduction

The surface treatment techniques that combine several types of treatments, including high-powered heat and pressure treatments is a well-known method for improving mechanical properties of metals and alloys [1]. At the same time thermo-force loading often leads to crack initiation, which is closely connected to the residual stress distribution [2]. Residual stresses have been studied intensively in the past years a lot of research has been carried out on its magnitude and distribution during different technological processes [3–5]. However, few works have dealt with the investigation of non-uniform residual stresses formation, influenced by phase transition. Experimental study of such distribution for thin surface layers by X-Ray diffraction method can be very hard and sometimes even impossible. In this case, numerical simulation is only available tool to optimize the

A. N. Savkin (✉) · D. S. Denisevich · V. P. Bagmutov · I. N. Zakharov · A. A. Sedov
Department of Strength of Materials, Volgograd State Technical University, Volgograd, Russia
e-mail: fpik@vstu.ru

I. A. Parinov et al. (eds.), *Advanced Materials*, Springer Proceedings in Physics 207, https://doi.org/10.1007/978-3-319-78919-4_32

hardened areas location. The objective of this study is investigation of residual stresses in case of Ti_6Al_2V alloy after thermo-force surface treatment in order to prevent the possibility of cracking in the heat-affected zones.

32.2 Mathematical Model

In this paper, we consider the simulation of contact thermo-force treatment by alternating current [1] in 3D case, based on the coupled solution of the next equations:

(i) balance of linear momentum;
(ii) balance of energy;
(iii) phenomenological equation of martensitic phase transition kinetics.

32.2.1 Governing Equations and Basic Assumptions

We assume large deformations and consider together the balance law of momentum without inertial term and balance law of energy with coupled terms in explicit form as

$$\nabla \cdot \boldsymbol{\sigma} + \mathbf{f} = \mathbf{0}, \tag{32.1}$$

$$\nabla \cdot (\boldsymbol{\lambda} \cdot \nabla T) + Q_{\mathrm{J}} + Q_{\mathrm{L}} + Q_{\mathrm{D}} = \mathrm{c}\rho\dot{T}, \tag{32.2}$$

where ∇ is the nabla-operator in actual configuration of deformable body; σ is the Cauchy stress tensor; $\mathbf{f}$ is the body force vector; $\boldsymbol{\lambda}$ is the conductivity tensor; c is the specific heat capacity; ρ is the density of the material; T is the temperature; Q_J is the Joule heating; Q_L is the latent heat; Q_D is the heat dissipation under plastic deformation.

Governing equations are complemented by initial and boundary conditions for thermal and mechanical parts of model [1] (Fig. 32.1) (32.3)–(32.5).

Contact tool is taken as absolutely-rigid ellipsoidal die. In addition to the mechanical boundary conditions, we assume well-known in contact mechanics Hertz–Signorini conditions for the frictionless contact. Also at the infinity and at the initial time, displacements and stresses are zero:

$$\begin{aligned} &\boldsymbol{\sigma} \cdot \mathbf{n} = \mathbf{0}, && \Gamma \notin \Gamma_{\mathrm{c}} \\ &\boldsymbol{\sigma} \cdot \mathbf{n} = \mathbf{t}_{\mathrm{c}}, \quad \int\limits_{\Gamma_{\mathrm{c}}} \mathbf{t}_{\mathrm{c}} \mathrm{d}\Gamma = \mathbf{f}_{\mathrm{ext}}, && \Gamma \in \Gamma_{\mathrm{c}} \\ &g_{\mathrm{n}} \geq 0, \ \sigma_{\mathrm{n}} \geq 0, \ g_{\mathrm{n}}\sigma_{\mathrm{n}} = 0, \end{aligned} \tag{32.3}$$

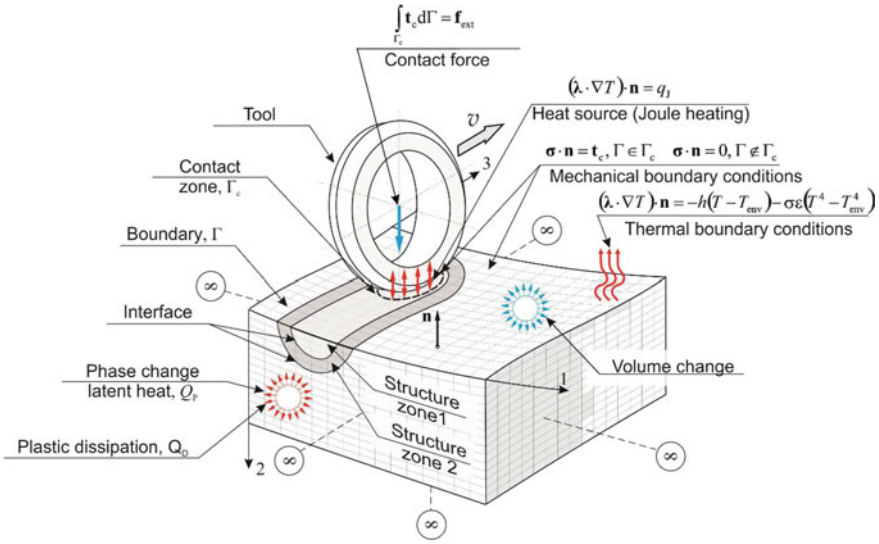

Fig. 32.1 Heterogeneous body phase change problem with thermo-force contact loading

where $\mathbf{n}$ is the unit normal vector; $\mathbf{f}_{ext}$ is the external load, applied to the tool; $\mathbf{t_c}$ is the contact traction vector; g_n is the gap function; $\sigma_n = \mathbf{t}_c \cdot \mathbf{n}$ is the contact pressure.

Due to the small curvature of the surface and the local character of the contact, the calculation area is considered as a half-space with subregions, which has different thermo-physical properties. These zones correspond to the metal with different microstructure, which forms after thermo-force treatment (for example, fragments with the martensitic structure and the base metal, zones 1 and 2 in Fig. 32.1). Their current position is determined at each calculation step from the solution of the coupled problem.

In the contact zone between rigid die and flexible half-space acts uniformly distributed surface heat source q. Temperature at the initial time T^0 and at the infinite T^∞ is taken equal to the environment temperature T_{env}. To consider heat losses, both thermal radiation and convective transfer are taken into account:

$$\left.\begin{array}{l} (\boldsymbol{\lambda} \cdot \nabla T) \cdot \mathbf{n} = -h(T - T_{cp}) - (T^4 - T_{env}^4), \quad \Gamma \in \Gamma_c \\ q = q(t), \quad T^0 = T_{env}, \quad T^\infty = T_{env}, \end{array}\right\} \tag{32.4}$$

where h is a convective heat transfer coefficient; σ is a Stefan–Boltzmann constant; ε is the heat emissivity. According to the Joule law, we consider heat source for the impulse thermo-force treatment (alternating current) as

$$q(t) = 2kUI \sin^2(2\pi\nu t), \tag{32.5}$$

where I is a effective current value; U is a effective value of contact voltage; k is a coefficient that takes into account heat exchange between tool and half-space; v is the current frequency.

32.2.2 Phase Change Phenomena

Mathematical model of phase change during thermal impact of titanium pseudo-α-alloy Ti_6Al_2V includes simulation of the phase transformation $\alpha \rightarrow \beta$ upon heating and $\beta \rightarrow \alpha'(\alpha'')$ (martensitic) transformation during cooling process based on continuous cooling temperature diagram analysis [6].

For the current time step at the considered point martensite start and finish temperatures as well as the phase composition of the alloy can be defined through the thermokinetic diagram as a function of the cooling rate (Fig. 32.2). Due to the high growth rate of martensite during the transformation (close to the speed of sound), it is commonly assumed that the transformation occurs instantaneously. In this case, the kinetics of the martensitic phase change can be well defined by empirical Koistinen–Marburger equation [6]:

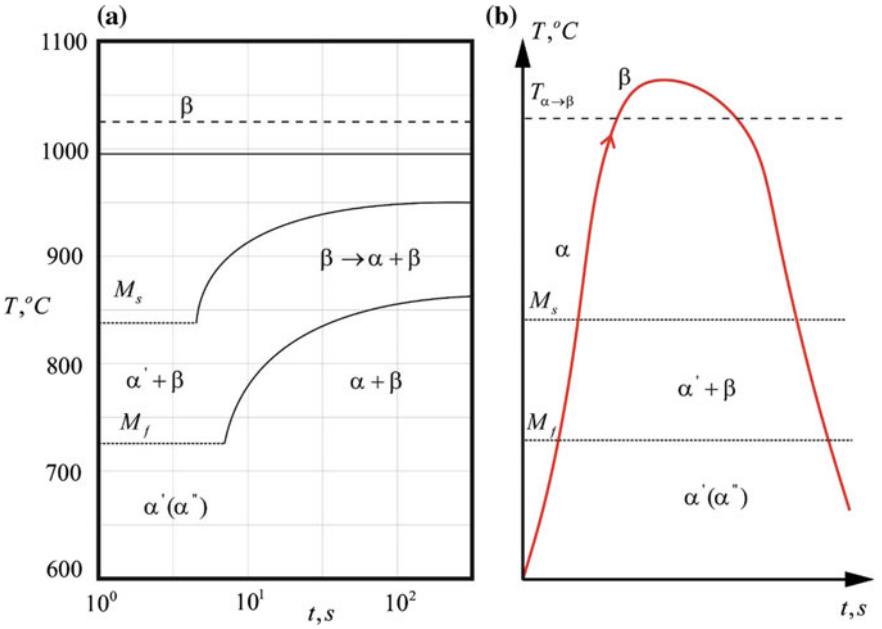

Fig. 32.2 Continuous cooling diagram **a** and an example of the thermal cycle of Ti_6Al_2V alloy **b** (α, α′, α″ are the stable and metastable phases, formed during the decay β-phase in the process of continuous cooling M_s, M_f are the temperatures of martensite transformation start and finish; $T_{\alpha\rightarrow\beta}$ is the $\alpha \rightarrow \beta$ temperature transformation) [6]

$$\zeta = 1 - \exp(-b(M_s - T)), \tag{32.6}$$

where ζ is the martensite volume fraction, M_s is the martensite start temperature, b is a empirical coefficient (b = –0.05 for Ti_6Al_2V).

In case of high-speed heat treatment processes, heat rate dependence of critical temperatures should be taken into account. For titanium alloys, as the heating rate increases, temperature transformation $T_{\alpha\to\beta}$ increase can be observed due to the suppression of the β phase growth, the phase transition is carried out only by the formation of new nuclei in the high temperature range. Maximum increase around 90 °C can be observed at the heat rate about 10^5–10^7 °C/s [7].

32.3 Finite Element Solution

Balance of energy equation is solved via standard weak form of Galerkin finite element method. The solution of the nonlinear thermal problem is performed using Picard iterations in combination with simple relaxation formula.

Mechanical analysis is carried out using updated Lagrangian formulation with the presence of additional contact term. The regularization of the received variational inequality is performed using penalty approach for unilateral contact between a rigid die and a flexible half-space. The constitutive equations, used in this work, is based on the additive decomposition of the rate of deformation tensor into the sum of elastic, plastic and volume change parts, respectively:

$$\mathbf{D} = \mathbf{D}^{\mathrm{e}} + \mathbf{D}^{\mathrm{p}} + \mathbf{D}^{\mathrm{d}}, \tag{32.7}$$

$\mathbf{D} = \frac{1}{2}(\nabla \otimes \mathbf{v} + \nabla \otimes \mathbf{v}^{\mathrm{T}})$ is the rate of deformation tensor; $\mathbf{D} = \left(\alpha \mathrm{T} + \frac{1}{3}\delta_{\mathrm{p}}\zeta\right)\mathbf{1}$ is the volume change part of rate of deformation tensor; α is a thermal expansion coefficient; δ_{p} is the volume change of phase transformation; $\mathbf{1} = \delta^{ij}\mathbf{e}_i \otimes \mathbf{e}_j$ is the second order unit tensor; $\delta^{ij} = \delta_{ij}$ is the Kronecker delta.

Stress–strain relationship is introduced via hypoelastic law within the framework of the Jaumann rate of the Cauchy stress tensor, according to the principle of material objectivity:

$$\boldsymbol{\sigma} = {}^4\mathbf{C} : \left(\mathbf{D} - \mathbf{D}^{\mathrm{p}} - \mathbf{D}^{\mathrm{d}}\right) + {}^4\mathbf{C}^{\mathrm{rot}} : \mathbf{W}, \tag{32.8}$$

where $\boldsymbol{\sigma}$ is the full time derivative of Cauchy stress tensor; ${}^4\mathbf{C} = (\lambda + (2/3)\mu)\mathbf{1} \otimes \mathbf{1} + 2\mu\,{}^4\mathbf{1}_{\mathrm{dev}}$ is the forth order elasticity tensor; ${}^4\mathbf{C}^{\mathrm{rot}} = 1/2\left(\sigma^{il}\delta^{jk} + \sigma^{jl}\delta^{ik} -\right.$

$\sigma^{ik}\delta^{jl} - \sigma^{jk}\delta^{il})\mathbf{e}_i \otimes \mathbf{e}_j \otimes \mathbf{e}_k \otimes \mathbf{e}_l$ is the forth order tensor, which represents rotational effect of Cauchy stress tensor; λ, μ are Lame constants; ${}^4\mathbf{1}^{\text{dev}} = {}^4\,1 - \frac{1}{3}\mathbf{1} \otimes \mathbf{1}$ is the fourth order unit deviatoric tensor; ${}^4\mathbf{1} = 1/2\left[\delta^{ik}\delta^{jl} + \delta^{il}\delta^{jk}\right]\mathbf{e}_i \otimes \mathbf{e}_j \otimes \mathbf{e}_k \otimes \mathbf{e}_l$ is the fourth order unit tensor.

Integration algorithm of constitutive equations, implemented in this work, is based on standard return mapping scheme and Hughes–Winget algorithm. We used von-Mises yield function with isotropic hardening in combination with Johnson–Cook material model in order to take into account thermoviscoplastic effect:

$$\sigma(e^{\text{p}}, e^{\text{p}}, T) = \left[A + B(e^{\text{p}})^n\right]\left[1 + C\left(ln\frac{e^{\text{p}}}{e_0}\right)^p\right]\left[1 - \left(\frac{T - T_{\text{env}}}{T_{\text{f}} - T_{\text{env}}}\right)^m\right], \qquad (32.9)$$

T_{f} is the fusion temperature; A, H, C, n, m, p are material constants. The solution of the mechanical part nonlinear problem is carried out using the Newton–Raphson method.

32.4 Calculation Results

32.4.1 Temperature Fields and Microstructure

Thermal cycles at different distances from the surface (0, 0.25, 0.5 and 0.75 mm) during thermo-force treatment in case of titanium pseudo-alpha-alloy Ti_6Al_2V are shown in Fig. 32.3 (effective current $I = 400$ A, processing speed $\upsilon = 1.23$ m/min).

The temperature influence on the material is quite complex, different points of the material can pass several times the stage of hardening and hardening (Fig. 32.3, 1). The maximum temperature almost reaches melting point, but is local and rapidly decreases. The depth of the hardened zone, corresponding to quenching, is of the order of 0.2 mm. The maximum cooling rate is around $T = (1.2 - 1.5) \times 10^5\,^{\circ}\text{C/s}$.

32.4.2 Residual Stresses

Based on the developed model, an analysis of residual stresses during surface thermo-mechanical processing of titanium pseudo-alpha alloys is considered. Figure 32.4 shows residual stress distribution at the surface after thermo-force treatment. From the figure, it can be seen that residual stress distribution has periodic non-uniform structure with zones of stresses which repeats microstructure fragmentation. Maximum value of the tensile stress in quasistationary region reaches 350 MPa

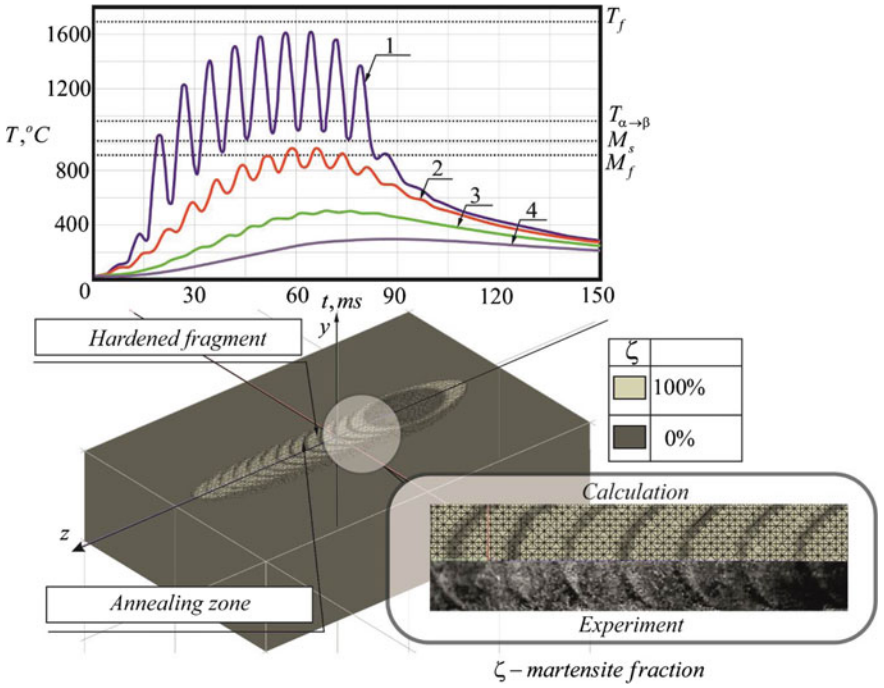

Fig. 32.3 Thermal cycle and microstructure of Ti_6Al_2V alloy surface during processing at a rate of $\upsilon = 1.23$ m/min

and the same time in the comprehensive region is about 295 MPa at the distance of about 0.5 mm from the center of treatment direction axis. From main stress analysis, it is determined that hardened zones mainly correspond closely to comprehensive region of stresses in comparison with annealing zones, which corresponds to tensile region of stresses.

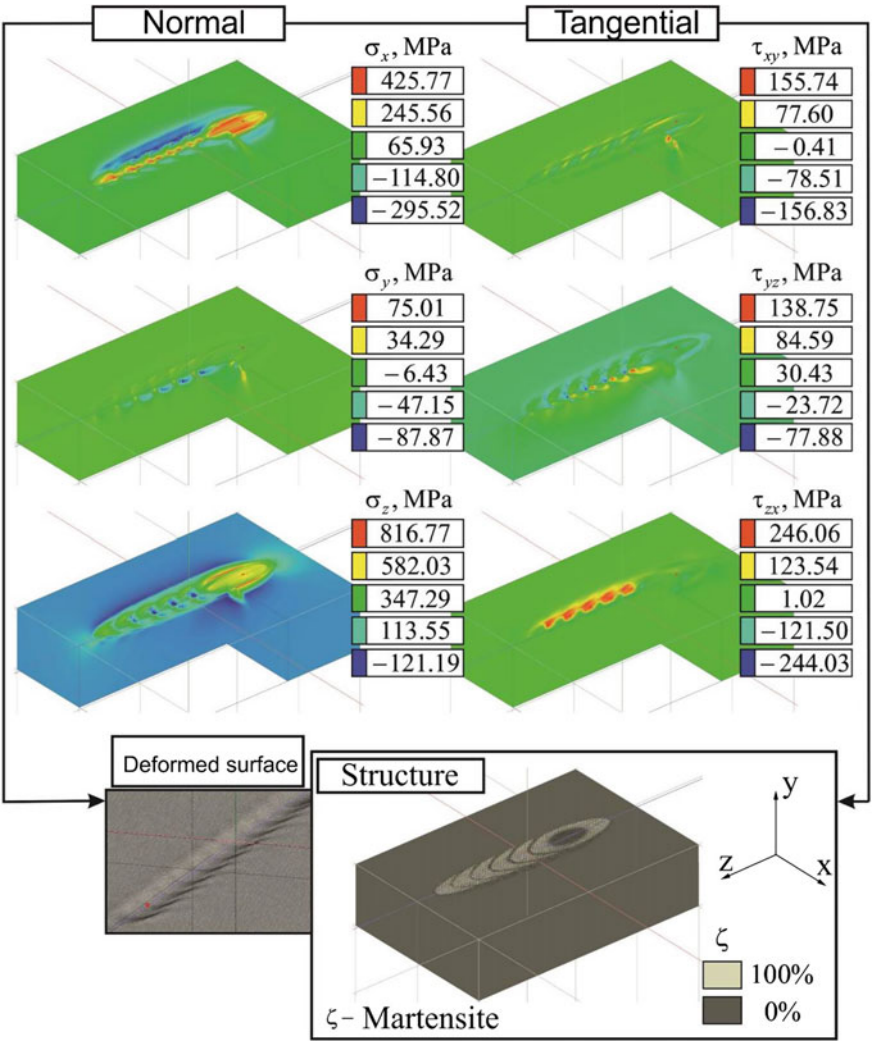

Fig. 32.4 Calculated residual stress distribution

32.5 Conclusions

Finite element model of thermo-force heat treatment is developed. Temperature cycles and residual stress distribution, obtained from the simulation, which is based on thermo-mechanical model, coupled with phase transition problem, are presented. From the simulated results the following conclusions can be drawn:

(i) The temperature distributions after heat source passes are unsteady in nature. Cyclic thermal impact on the surface of titanium alloy Ti_6Al_2V forms periodic microstructure;
(ii) high temperatures, which is observed during thermo-force treatment, leads to formation of plastic zone near the contact region;
(iii) residual stress distribution have the same periodic fragmentation as microstructure with highly tensile regions corresponds to annealing zones, which can lead to crack initiation.

Acknowledgements The reported study was funded by Grant of the President of the Russian Federation MK-943.2017.85/954-17, and RFBR according to the research projects Nos. 17-08-01648 and 17-08-01742 A.

References

1. V.P. Bagmutov, V.I. Vodop'yanov, I.N. Zakharov, A.I. Gorunov, D.S. Denisevich, Rus. Metall. (Metally) **2013**(9), 712 (2013)
2. V.P. Bagmutov, V.I. Vodop'yanov, I.N. Zakharov, D.S. Denisevich, Rus. Metall. (Metally) **2016**(7), 663 (2016)
3. F. Kong, R. Kovacevic, J. Mater. Process. Technol. **210**, 941 (2010)
4. A. De, T. Deb Roy, Sci. Technol. Weld. Join. **6**(3), 204 (2011)
5. F. Kong, J. Ma, R. Kovacevic, J. Mater. Process. Technol. **211**, 1102 (2011)
6. C. Şimşir, C.H. Gür, Turk. J. Eng. Environ. Sci. **32**, 85 (2008)
7. A.I. Gordienko, A.A. Shipko. *Structural and Phase Transformations in Titanium Alloys at Quick Heating*, ed. by M.N. Bodiako (Science and Technique, Minsk, 1983), 336pp (in Russian)

Chapter 33
Modeling of Contact Stresses for Condition Monitoring Using Finite-Element Method and Semi-analytical Approach

Evgenia V. Kirillova, Wolfgang Seemann and Maria S. Shevtsova

Abstract In this article, three different models simulating the wave propagation in an infinite isotropic structure are compared. The first semi-analytical model is based on the Fourier transform and Galerkin method for the calculation of the occurring contact stresses, when the function of displacements in the contact area is specified. The wave fields excited by this model are compared to the results calculated for a finite element (FE) model of an isotropic layer during the steady-state analysis. The structure is loaded by the given displacements in the contact zone. According to the third approach, the effect of the actuator is approximated by a pin-force model. This problem is simulated using the FE formulation as well. In both FE models, the infinite boundary conditions are simulated using the perfectly matched layers (PML). The efficiency of the presented approaches is assessed by comparing the obtained results.

33.1 Introduction

Damages in composite structures, such as delaminations, voids or inclusions, considerably diminish the strength of the whole system. Guided waves are extensively used in condition monitoring [1, 2], structural health monitoring [3, 4] and nondestructive control of engineering systems made of composite materials. The Condition Monitoring (CM) method makes it possible to take into account high-frequency waves with the short wave lengths and is thus suitable for the

E. V. Kirillova (✉) · M. S. Shevtsova
RheinMain University of Applied Sciences, Kurt-Schumacher-Ring 18, 65197 Wiesbaden, Germany
e-mail: evgenia.kirillova@hs-rm.de

M. S. Shevtsova
e-mail: maria.shevtsova@hs-rm.de

W. Seemann
Karlsruhe Institute of Technology, Kaiserstrasse 10, 76131 Karlsruhe, Germany

I. A. Parinov et al. (eds.), *Advanced Materials*, Springer Proceedings in Physics 207, https://doi.org/10.1007/978-3-319-78919-4_33

detection of small-size defects. It starts with using permanently installed sensors, which help to collect data about the current state of the structure. Then the collected data are used for the subsequent analysis of changes in the condition of a structural component while it is in operation. Condition monitoring enables to describe the present state of the considered structural component and indicates the deviation of the collected data from standard parameters, thus, the deterioration of a component can be predicted in the early stages.

Nowadays, a large number of methods for excitation and measurement of elastic waves exists. However, the method based on the use of piezoelectric elements remains the most frequently used [3–5], due to the small size and exceedingly low weight of the elements. Piezoelectric sensors and actuators can be installed onto the structure or embedded inside; they do not require high production costs and can also be used simultaneously for sensing and actuating the response of the structure [6]. When an electric charge or a voltage is applied to the structure, the piezoelectric element and the structure interact electromechanically, then longitudinal deformations appear in the piezo element and lead to the vibrations of the elastic surface. The investigations of the interaction between a piezoelectric sensor or an actuator and the elastic structure showed that the occurring contact shear stresses concentrate at the edge of the contact area [6, 7]. This explains the use of simplified models describing the effect of contact stresses by means of concentrated forces (pin-force models) applied in the opposite directions to the boundaries of the contact zone [4, 8, 9]. Such models can be applied for isotropic structures [10] as well as for structures with anisotropic characteristics [11]. However, most of the simplified models do not take into account the interaction between the actuators and the host structure.

The purpose of this paper is to analyze the wave excitation in an isotropic infinite layer using three different approaches and to estimate the validity ranges of these methods. According to the first method, the interaction between the structure and the piezoelectric element is described with the help of integro-differential equations. The unknown contact stresses occuring in the contact area are calculated using the Galerkin method [9]. In the second approach, the considered isotropic structure is loaded by the given displacements in the contact zone and the displacement field is obtained by means of a steady-state analysis performed in the FE package COMSOL Multiphysics. The third approach describes the effect of a thin actuator using the pin-force model. This problem is simulated and solved by the FE package as well. For both FE models the absorbing boundary condition is described by means of perfectly matched layers (PMLs). The occuring wave fields are analyzed at different angular frequencies.

33.2 Mathematical Formulation of the Model

An isotropic infinite waveguide of thickness h (see Fig. 33.1), which occupies the volume $D = \{(x, z)| - \infty < x < \infty; -h \le z \le 0\}$ is considered. The oscillations of

the considered layer are excited by a thin piezoelectric actuator bonded on the upper surface in the region $[-a, a]$. The time dependency is assumed harmonic in the form $e^{-i\omega t}$, where ω is an angular vibration frequency. This coefficient is omitted hereinafter. Lame's equations for the steady-state harmonic vibrations can be written in compact form:

$$L\mathbf{u} + \rho\omega^2\mathbf{u} = 0 \tag{33.1}$$

where ρ is the mass density and $\mathbf{u}$ is the displacement field. The upper and bottom surfaces are free of stress and the contact between the layer and the actuator is assumed frictionless:

$$\sigma_z|_{z=0} = 0, \tag{33.2}$$

$$\tau_{xz}|_{z=0} = \begin{cases} q(x), & |x| < a \\ 0, & |x| > a \end{cases}, \tag{33.3}$$

$$u|_{z=0} = f(x), \quad |x| < a\,, \tag{33.4}$$

where u is the first component of $\mathbf{u}$, $q(x)$ is the unknown contact stress and $f(x)$ is the function of the horizontal displacement of the actuator.

The aim of this study is to determine the displacement field $\mathbf{u}$, caused by the harmonic vibrations of a piezoelectric patch, bonded on the upper surface of the considered strip. In order to calculate the unknown displacement field, three different methods are applied. The first approach, which is based on the Fourier transform and Galerkin method and described in details in [9], is implemented in Matlab. The second considered method is based on the simplified model commonly used in engineering calculations [4, 8]. According to this approach, the action of the patch can be approximated by two oppositely directed delta-functions, applied at the boundary points of the contact area. Simulation of this model is realized by FE package COMSOL Multiphysics. According to the third model, an isotropic layer of a finite length is actuated by a thin actuator. Two perfectly matched layers (PMLs) on the sides of the layer imitate the absorbing boundary condition and help

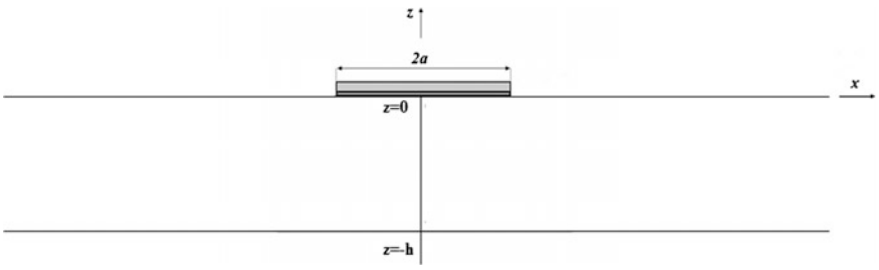

Fig. 33.1 Scheme of the loaded structure

to simulate the open boundaries. The displacement field in the contact area is specified by known function of coordinate x. An unknown wave-field is obtained by carrying out the frequency response analysis performed in COMSOL Multiphysics as well. The aforementioned approaches are described in more detail below.

33.3 Semi-analytical Solution and Galerkin Method

The formulated problem (33.1)–(33.4) is solved using an approach based on the use of integral representations of the wave fields that are used jointly with the conditions of a contact between an elastic structure and an actuator of small thickness. When this approach is used, the considered problem can be reduced to a boundary value problem for a system of integro-differential equations with respect to the unknown stresses occurring in the contact zone. When the unknown contact stresses are calculated, the wave fields in the considered system are calculated using integral representations [9].

The Fourier transform with respect to the spatial coordinate x is applied to (33.1)–(33.3) with Fourier variable α, and the solution of the initial problem is written as follows

$$\mathbf{u}(x,z) = \frac{1}{2\pi}\int_{\Gamma} \mathbf{K}(\alpha,z)\mathbf{Q}(\alpha)e^{-i\alpha x}d\alpha, \tag{33.5}$$

where $\mathbf{K}$ and $\mathbf{Q}$ are the Fourier transforms of the Green's matrix and of the unknown contact stresses, respectively. As the contact stresses are assumed to act in x-direction, $\mathbf{q}$ has only one component, $q(x)$. In accordance with the limiting absorption principle [12] the integration contour Γ goes in the complex plane α along the real axis deviating when traversing the poles of Fourier transform $\mathbf{K}$ of the Green's matrix $\mathbf{k}$. According to the boundary condition (33.4), the integral equation (33.5) is transformed for the first component of $\mathbf{Q}$ into the form:

$$\frac{1}{2\pi}\int_{\Gamma} K_{11}(\alpha,0)Q(\alpha)e^{-i\alpha x}d\alpha = f(x), \tag{33.6}$$

where $Q(\alpha) = \int_{-\infty}^{\infty} q(x)e^{i\alpha x}dx$ and K_{11} is the first element of $\mathbf{K}$, thus

$$\frac{1}{2\pi}\int_{\Gamma} K_{11}(\alpha,0)\int_{-\infty}^{\infty} q(\xi)e^{i\alpha\xi}d\xi e^{-i\alpha x}d\alpha = f(x). \tag{33.7}$$

The integral equation (33.7) is solved with respect to the unknown function using the Galerkin method [9], when the correct solution $q(x)$ is approximated by a solution $q_N(x)$, composed of linearly independent basis functions $\varphi_i(x)$ in L_2:

$$q(x) \approx q_N(x) = \sum_{i=1}^{N} C_i \varphi_i(x). \tag{33.8}$$

The solution (33.8) depends on the unknown parameters C_i, where $\varphi_i(x)$ is a system of linearly independent basis functions in L_2 for $i = 1, N,\ \Delta x = 2a/N,\ x_i = -a + (i - 0.5)\Delta x$.

For $i = 2, N - 1$, we have

$$\varphi_i(x) = \begin{cases} 1 - |(x - x_i)/\Delta x|,\ x \in [x_{i-1}; x_{i+1}] \\ 0,\ x \notin [x_{i-1}; x_{i+1}] \end{cases}. \tag{33.9}$$

For i = 1 and i = N the basis functions have the forms:

$$\varphi_1(x) = \begin{cases} 2 \cdot (x_1 - x)/\Delta x,\ x \in [-a; x_1] \\ 0,\ x \notin [-a; x_1] \end{cases} \tag{33.10}$$

and

$$\varphi_N(x) = \begin{cases} 2 \cdot (x - x_N)/\Delta x,\ x \in [x_N; a] \\ 0,\ x \notin [x_N; a] \end{cases}, \tag{33.11}$$

respectively. The unknown coefficients C_i are determined by solving the linear algebraic system, obtained by projection of the unknown function q in L_2 on the system of the basis functions φ_i:

$$(\mathrm{K}q_N - f, \varphi_i)_{\mathbf{L}_2} = 0,\ i = 1, \ldots, N. \tag{33.12}$$

Once the coefficients C_i are calculated, the wave field $u(x, z)$ could be obtained in each point. Numerical calculations are performed using two different types of basis functions. The first type is described by (33.9)–(33.11). In order to take into account the root singularities of contact stresses near the boundaries of the contact zone between the considered structure and the actuating patch, we performed calculations using basis functions with the already given singularity as well:

$$q_N(x) = \frac{1}{\sqrt{a^2 - x^2}} \cdot \sum_{i=1}^{N} C_i \varphi_i(x). \tag{33.13}$$

In order to estimate the convergence rate of the approximated functions of contact stresses $q_N(x)$ to a correct solution $q(x)$, we specify the function of displacements in the contact area:

$$f(x) = u_{\max} \cdot x/a, \tag{33.14}$$

where $u_{\max} = 10^{-4}$, and check the error by gradually increasing the number of basis functions.

All the numerical calculations are performed for the structure with dimensionless parameters. Material properties are described by density $\rho = 1$ and Lame parameters $\lambda = 1.5$ and $\mu = 1$. A half-length of the contact area and the thickness of the considered layer are equal to $a = 1$ and $h = 1$, respectively. Non-dimensional angular frequency is calculated using the formula:

$$\omega = f_r \cdot h \cdot 2\pi/c_s, \tag{33.15}$$

where $c_s = \sqrt{\mu/\rho}$ is the S-wave velocity and f_r is the dimensional angular frequency in Hz. In Fig. 33.2 the contact stresses, obtained using both kinds of basis functions, are presented. Numerical calculations are performed for the three different frequency ranges: $f_r \in [0; 5]$, $f_r \in [5; 100]$ and $f_r \in [100; 200]$ kHz. All the results of the numerical calculations are presented in the dimensional form for the convenience of subsequent comparison with the results of the FE-models. Analysis of the obtained contact stresses and displacement fields shows that for the two first considered frequency ranges, the required number of basis functions is lower than for the third range. Considering the frequencies $f_r \leq 100$ kHz, the number of basis functions $N = 70$ is used for the functions described by (33.9)–(33.11) and $N = 50$ in the case of basis functions, described by (33.13); $N = 100$ and $N = 120$ for the third considered frequency range.

In Fig. 33.3 the displacement fields across the right half of the contact zone, calculated for $f_r = 50$ kHz, are presented. These displacements are compared to the specified function of displacement (33.14).

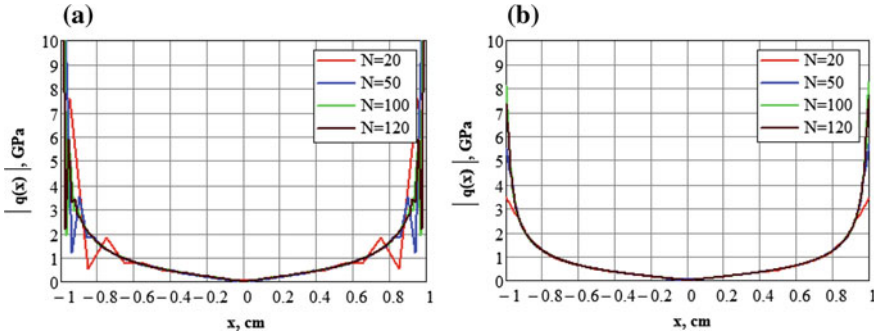

Fig. 33.2 Contact stresses, obtained without (**a**) and with (**b**) account of the singularity for angular frequency $f_r = 50$ kHz and calculated using Galerkin method

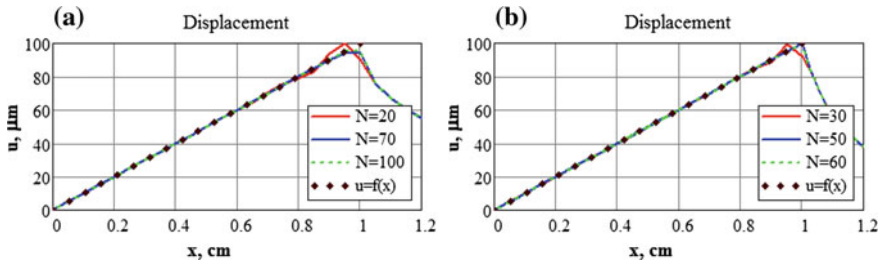

Fig. 33.3 Displacement fields without (**a**) and with (**b**) account of the singularity

The numerical error is calculated in accordance with the formula:

$$\varepsilon = \sum_{i=1}^{N_x} |f(x_i) - u_N(x_i)|/N_x. \tag{33.16}$$

Here N_x and N are the number of points and intervals, used for the calculation of the integral (33.7), and the number of basis functions, respectively. Figure 33.4 shows a convergence estimate, calculated using the basis functions of both types (33.9)–(33.11) and (33.13). It is apparent that the use of the weight functions accelerates the convergence.

33.4 Finite Element Problem Formulation

Finite element models of an isotropic layer, actuated in two different ways, are simulated with FE package Comsol Multiphysics. Let us consider a steel layer S of the thickness $h = 0.01$ m and length $l = 1$ m (Fig. 33.5). A part of the upper surface $x \in [-a; a]$, when $a = 0.01$ m, is considered as a contact zone. Elastic

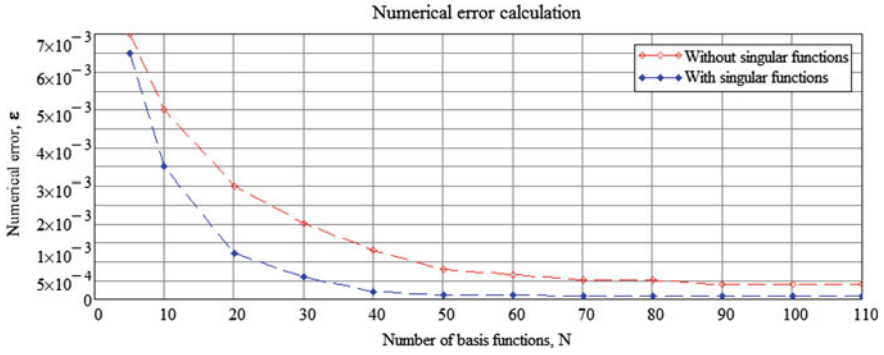

Fig. 33.4 Numerical error, calculated for angular frequency $f_r = 50$ kHz

properties of the layer are taken as mass density ρ = 7850 kg/m^3, Poisson's ratio ν = 0.3 and Young's modulus E = 200 GPa.

In order to simulate a reflectionless boundary condition, an artificial absorbing subdomain S_1 or a perfectly matched layer (PML) of a finite length l_1 = 0.1 m is used. Two identical PMLs are placed on the edges of the region S. For all subdomains elastic properties are taken equal, the only difference is that the PML-properties of the considered isotropic subdomain S are disabled, whereas for the side-subdomains an absorbing in x-direction is specified. In both models, the side surfaces of PMLs are fixed. All other boundaries, except the contact area on the upper surface, are assumed to be free.

The difference between the considered FE-models can be explained by two different types of loading excitation. According to the first model, a function of displacement (33.14) with $u_{\max} = 1 \times 10^{-4}$m is specified on the contact surface $x \in [-a; a]$. Thereby the displacement field in the contact area is assumed to be known, and the occurring contact stresses in this zone as well as the wave-field out of the contact surface must be calculated.

In the second model, contact stresses appearing under the actuating patch on the surface $x \in [-a; a]$ are described by means of a simplified approach. According to this model, the bonding between the thin piezoelectric patch and the waveguide is assumed to be ideal and the shear stress distribution along the actuator's surface can be expressed using two Dirac delta-functions:

$$\tau_{xz}|_{z=0}(x) = a\tau_0[\delta(x-a) - \delta(x+a)], \tag{33.17}$$

where $a\tau_0$ is the pin force applied at the boundary points $x = \pm a$ of the contact area [4, 8].

For both models, the frequency response analysis is used to calculate the response of the considered structure about steady-state oscillatory excitation. Using the parametric solver, the displacement fields at different angular frequencies can be obtained. In our research, we consider the frequency range $f_r \in [5; 200]$ kHz.

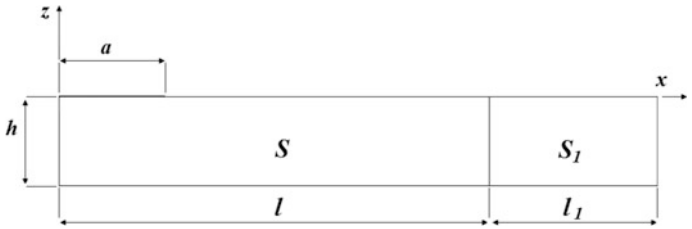

Fig. 33.5 Half of the simulated structure

33.5 Simulation Results and Analysis

Contact stresses appearing in the contact area as well as the displacement fields in actuated isotropic structures are calculated using both semi-analytical and FE-approaches. The obtained results are compared at different angular frequencies. Figure 33.6 presents the comparison of the contact stresses calculated on the upper surface of the considered structure by the aforementioned methods. Figure 33.6a corresponds to the angular frequency $f_r = 5$ kHz. It is apparent that all three

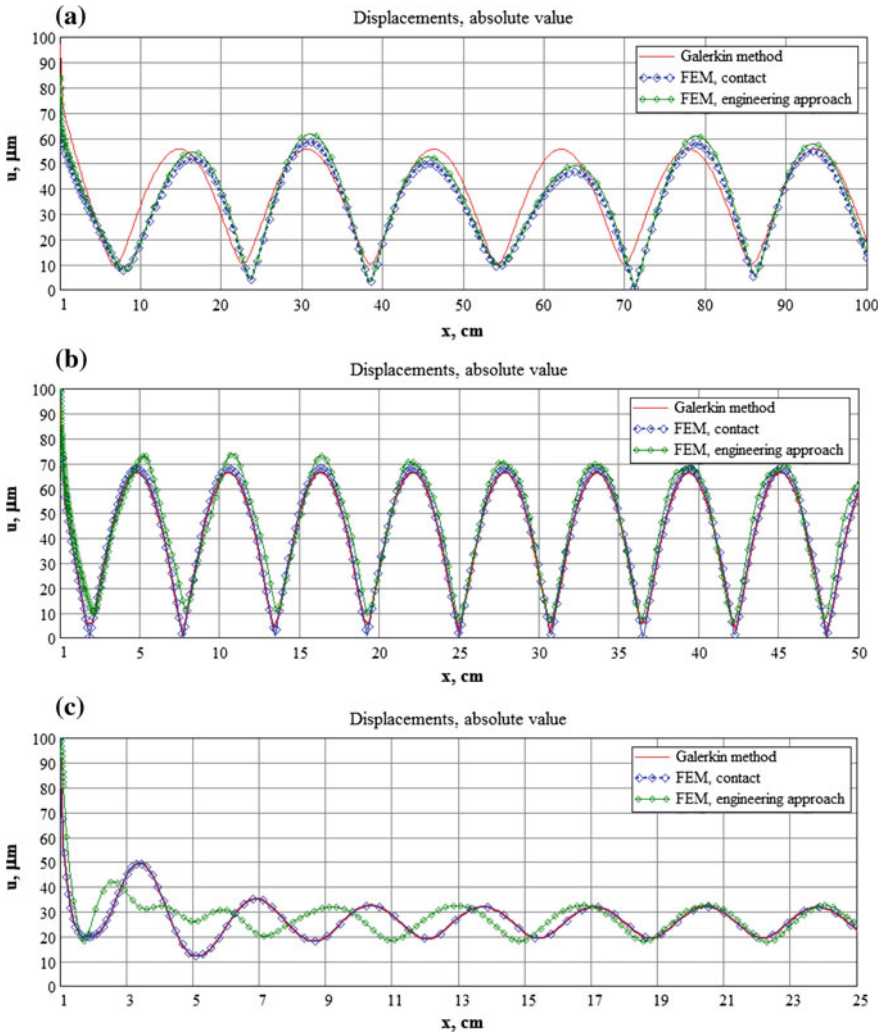

Fig. 33.6 Comparison of the wave-fields, obtained by the implemented methods for f_r = 5 kHz (**a**), f_r = 50 kHz (**b**) and f_r = 150 kHz (**c**)

methods give very close results and the error does not exceed 5–10% across the whole surface. In Fig. 33.6b, the calculated displacements for the angular frequency $f_r = 50\,\text{kHz}$ are present. The error does not exceed 2–3% for all the methods. The worst results are obtained for the higher frequency $f_r = 150\,\text{kHz}$. It can be seen from Fig. 33.6c that the simplified engineering approach gives a displacement field similar to the other two methods only in the far field, when the results are not in good agreement close to the contact area.

33.6 Conclusion

Calculated wave fields occurring in a thin infinite isotropic layer, described using three different actuation methods, are presented in this work. Comparison of the obtained results shows that all the applied methods can be effectively used in the frequency range $f_r \in [0; 100]\,\text{kHz}$. In this range, the FE-models and the semi-analytical approach give comparable results for lower frequencies $f_r \in [0; 5]\,\text{kHz}$ with the difference in displacement fields less than 5–10% and 2–3% for $f_r \in [5; 100]\,\text{kHz}$. It can be concluded that the accurate preliminary adjustment of the finite element mesh is required. It is shown that the efficiency of engineering approach decreases with increasing frequency. The wave field, obtained by this method for $f_r \in [100; 150]\,\text{kHz}$, differs significantly from the results corresponding to the other approaches near the vibration source. The results' discrepancy decreases with distance from the contact zone. The results, obtained by the FE-model of the contact problem, are in a good agreement with the semi-analytical results across the whole considered frequency range. However, it is required to substantially refine the FE-mesh with increasing frequency, which has no significant effect during the analysis of steady-state vibrations, but can lead to considerable time and computational costs for transient analysis. The integration approach shows good efficiency for the whole considered frequency range.

Acknowledgements This research was supported by the German Federal Ministry of Education and Research (BMBF), Grant No. 03FH009IX5 and grant of the Russian Foundation for Basic Research No. 16-08-52013-MNT_a.

References

1. Ch. Sheng, Zh Li, L. Qin, Procedia Eng. **15**, 142 (2011)
2. K.I. Salas, C.E.S. Cesnik, Smart Mater. Struct. **19**(1), 25pp (2009)
3. K. Diamanti, C. Soutis, Prog. Aerosp. Sci. **46**, 342 (2010)
4. V. Giurgiutiu, Intell. Mater. Syst. Struct. **16**(4), 291 (2005)
5. W. Ostachowicz, P. Kudela, P. Malinowski, T. Wandowski, Mech. Syst. Signal Process. **23**, 1805 (2009). M.A. Trindade*, J. Intell. Mater. Syst. Struct.* **18** (2007)
6. E.F. Crawley, J. Luis, AIAA J. **25**, 1373 (1987)

7. V. Giurgiutiu, A.N. Zagrai, J. Intell. Mater. Syst. Struct. **11**, 959 (2000)
8. E.V. Glushkov, N.V. Glushkova, A.A. Evdokimov, Ch. Zhang, Phys. Procedia **70**, 945 (2015)
9. E.V. Kirillova, W. Seemann, M. Shevtsova, in *Advanced Materials. Techniques, Physics, Mechanics and Applications*, Springer Proceedings in Physics, vol. 193, ed. by I.A. Parinov, S.-H. Chang, M.A. Jani (Springer, Cham, Heidelberg, New York, Dordrecht, London, 2017), p. 501
10. A. Raghavan, C.E.S. Cesnik, Smart Mater. Struct. **14**, 1448 (2005)
11. A. Karmazin, E. Kirillova, W. Seemann, P. Syromyatnikov, in *Proceedings IMECE* (2010)
12. V. Babeshko, E. Glushkov, Z. Zinchenko, *Dynamics of Inhomogeneous Linearly Elastic Media* (Nauka, Moscow, 1989) (in Russian)

Chapter 34
Contact Interaction for Bodies of Complex Shape Taking into Account Wear

M. I. Chebakov, S. A. Danilchenko and A. A. Lyapin

Abstract Into framework of the linear theory of elasticity, the problem of the thermoelastic contact interaction of the brake disk and the pads studied. In the contact zone, the process of heat generation is realized due to friction forces. The friction coefficient is adopted as a function of temperature on the base of experimental data. The wear amount is calculated on the base of Archard model taking into account the dependency of model parameters on temperature. A number of calculation experiments is performed for various materials of braking pad.

34.1 Introduction

In the process of work of various technological joints and moving elements of machines and mechanisms, inevitable wear of friction surfaces occurs. The result is a change in the shape and size of the mechanical components, which leads to a disruption in the operation of the devices and brings the failure time closer. There are many methods to reduce the wear of parts based on the use of lubricants and antifriction coatings. However, studying the mechanics of the interaction of elastic bodies with regard to wear is still an important problem.

Wear is a process of some continuous loss of material from the surface of the elastic body due to contact with other bodies. It is associated with complex phenomena involving both mechanical interaction [1, 2], physical and chemical phenomena in the contact zone [3, 4]. The phenomenon of wear on contacting surfaces is attracting the attention of researchers for a long time. The most proven mathematical model of mechanical wear on the surfaces of elastic bodies is the Archard model [5], which characterizes the wear value as a function of contact pressure, sliding speed and a certain wear coefficient. This model is used in the study of contact interaction within the linear theory of elasticity and correlates well with experimental data [6–9].

M. I. Chebakov (✉) · S. A. Danilchenko · A. A. Lyapin
Southern Federal University, Rostov-on-Don, Russia
e-mail: michebakov@yandex.ru

I. A. Parinov et al. (eds.), *Advanced Materials*, Springer Proceedings in Physics 207, https://doi.org/10.1007/978-3-319-78919-4_34

In such technological joints as the systems of braking, the wear proves most obviously because of the large amount of work of friction forces. Moreover, the presence of high sliding speeds of the contact surfaces leads to a significant heating of the contact zone. In such cases, it becomes necessary to study the wear amount of the contacting bodies taking into account the dependence on the temperature field. It is known that the coefficient of friction changes with increasing or decreasing temperature [10, 11]. Consequently, the wear value will vary under different temperature conditions.

In the present work, an investigation of the contact interaction of elastic bodies in sliding, releasing of heat from friction, taking into account the wear of friction surfaces was made.

34.2 Formulation of Problem

In a cylindrical coordinate system $O\rho\varphi z$ the elastic disc ($R_d^i \le \rho \le R_d^o$; $0 \le \varphi \le 2\pi$; $0 \le z \le h_d$) rotates counterclockwise about an axis Oz with a constant angular velocity of rotation ω_z. On the surface of disk ($R_d^i \le \rho \le R_d^o$; $0 \le \varphi \le 2\pi$; $z = h_d$) the braking pad in the form of the sector of a disk ($R_k^i \le \rho \le R_k^o$; $0 \le \varphi \le \pi/3$; $h_d \le z \le h_d + h_k$) is located. It is loaded with a normal uniformly distributed force P (Fig. 34.1). The inner ($\rho = R_d^i$; $0 \le \varphi \le 2\pi$; $0 \le z \le h_d$) and outer ($\rho = R_d^o$; $0 \le \varphi \le 2\pi$; $0 \le z \le h_d$) side surfaces of the disc that do not interact with the pad are stress-free. The lower boundary ($R_d^i \le \rho \le R_d^o$; $0 \le \varphi \le 2\pi$; $z = 0$) is fixed along the axis Oz. Between the disc and the pad, Coulomb friction with a coefficient k is given.

The study includes the solution of two problems: the nonstationary thermoelastic contact problem of pressing the brake pad against a rotating brake disc and the problem of wear of the friction surfaces of the bodies under study, taking into account the previously obtained temperature fields. In the result of the work of

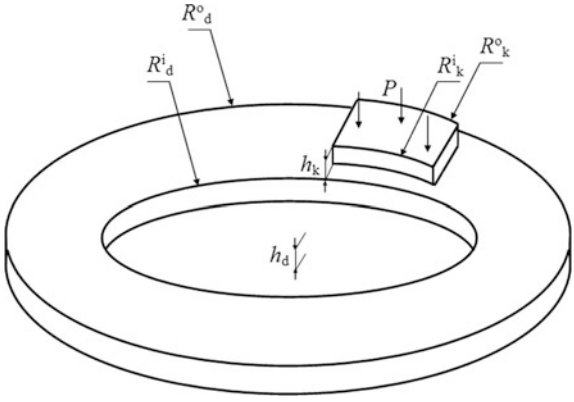

Fig. 34.1 Geometry of the problem

frictional forces in the contact zone, the bodies begin to warm up, which is simultaneously taken into account in the form of an adjustment of the friction coefficient on the base of experimental data on its temperature dependence.

To solve the problems, the finite element method and the special software complex ANSYS were used. For each task, the solution was carried out in two stages. At the first stage, the static contact problem of the theory of elasticity was solved concerning the pressing of an elastic pad into an elastic disc. At the second stage, for task 1, the non-stationary problem of pressing the braking pad into a rotating disc was considered for friction and heat generation; for task 2, the non-stationary problem of pressing the braking pad into a rotating disc was considered for friction and wear. It is assumed that the wear rate of the disc is small in comparison with the wear rate of the braking pad. Therefore, to reduce the time of calculations, the wear of the disc was not taken into account.

The Archard model, which simulates the process of wear of friction surfaces is represented as

$$w = \frac{K}{H} P^m v_{rel}^n, \tag{34.1}$$

where, w is the displacement of the points of the contact surface in the direction of wear, K is a wear coefficient, H is the material hardness, P is the contact pressure, v_{rel} is the relative sliding speed of the contacting surfaces, m, n are the some parameters characterizing the dependence of the wear value on the contact pressure or the relative velocity.

34.3 Results

Calculations were made for a steel disc and three different pad materials. In both problems, the same geometric parameters (Table 34.1), physical-mechanical and thermophysical properties of materials (Table 34.2), disk rotation speed and load were used.

Angular rotation speed $\omega_z = 10$ rps, stress $P = 0.1$ MN, rotation time $t = 5$ s.

Table 34.3 shows the friction coefficient values for selected materials as a function of temperature. For the task 1 the value of 20 °C was used. After the calculation, the dependence of the heating temperature of the pad on time was determined. These results were compared with the data in Table 34.3, after which

Table 34.1 Geometric parameters of the problem

Parameter	Value for disk	Value for pad
Inner radius (m)	$R_d^i = 0.12$	$R_k^i = 0.14$
Outer radius (m)	$R_d^o = 0.22$	$R_k^o = 0.2$
Thickness (m)	$h_d = 0.02$	$h_k = 0.02$

Table 34.2 Material properties of disc and pads

Parameter	Steel	Cast iron	Phenylon	TIIR 300
Density ρ (kg/m^3)	7826	7100	1350	2100
Elastic modulus E (GPa)	200	100	3.2	5
Poisson's ratio	0.3	0.3	0.3	0.36
Thermal conductivity Λ (W/(m K))	48	54	0.3	1.4
Coefficient of thermal expansion α (K^{-1})	1.19×10^{-5}	0.95×10^{-5}	3.9×10^{-5}	3.9×10^{-5}
Specific heat C (J/(kg K))	437	480	1860	1480

the friction coefficient was plotted against time. This dependence was used in the calculation in problem 2.

The values of wear resistance coefficients for selected materials are present in Table 34.4. The indices m and n and formula (34.1) were taken equal to 1.

From the plot shown in Fig. 34.2, it can be seen that the maximum heating temperature of the base of the pad from cast iron and TIIR 300 is almost the same. It should be noted that the pads from cast iron heat has more uniform temperature, while the pad from TIIR 300 has a sharp temperature jump after $t = 4.5$ s. At the initial stage (until $t = 3$ s), the value of temperature and the heating pattern of the pad from a phenylon coincide with the pad from TIIR 300. However, with a further increase in the rotation time, it does not experience such a sharp temperature rise. The maximum value is much lower than that of the pad from cast iron and TIIR 300.

Denote lines $\rho = (R_k^o - R_k^i)/2,\ 0 \le \varphi \le \pi/3,\ z = h_d\ (i = 1)$ and $R_k^i \le \rho \le R_k^o$; $\varphi = \pi/6$; $z = h_d\ (i = 2)$ as l_1 and l_2. Figure 34.3 presents wear and contact pressure along lines l_i, $i = 1, 2$ at different times for the pad from cast iron.

From the results obtained, it follows that on the sole of the pad in the direction of movement of the disk (along the line $\rho = (R_k^o - R_k^i)/2,\ 0 \le \varphi \le \pi/3,\ z = h_d$) contact pressures and wear are significantly reduced, while along the line $R_k^i \le \rho \le R_k^o,\ \varphi = \pi/6,\ z = h_d$ the changes are insignificant. Thus, wear from the inner radius to the outer radius of the pad is almost uniform. Similar changes are also characteristic for the pads from phenylon and TIIR 300 (Figs. 34.4 and 34.5).

With increasing rotation time for the shoe from cast iron, the following picture is observed: the contact pressures at the boundary $\varphi = 0$, $\rho = R_k^o$ decrease and at the boundary $\varphi = \pi/3$, $\rho = R_k^i$ they increase.

Table 34.3 Dependence of friction coefficients of materials on temperature

Material of pad	Temperature value (°C)			
	20	50	100	150
Cast iron	0.4	0.4	0.39	–
Phenylon	0.38	0.38	0.39	0.4
TIIR 300	0.41	0.43	0.46	0.47

Table 34.4 Values of the coefficient of wear resistance

Material of pad	Coefficient of wear resistance l
Cast iron	4×10^{-13}
Phenylon	3.9×10^{-13}
TIIR 300	4.1×10^{-13}

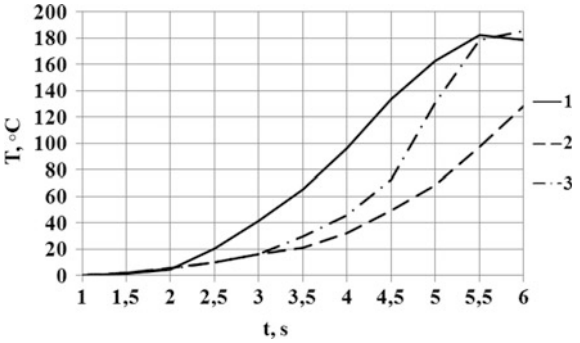

Fig. 34.2 Heat curves of the sole of the braking pad made of cast iron (1), phenylon (2) and TIIR 300 (3)

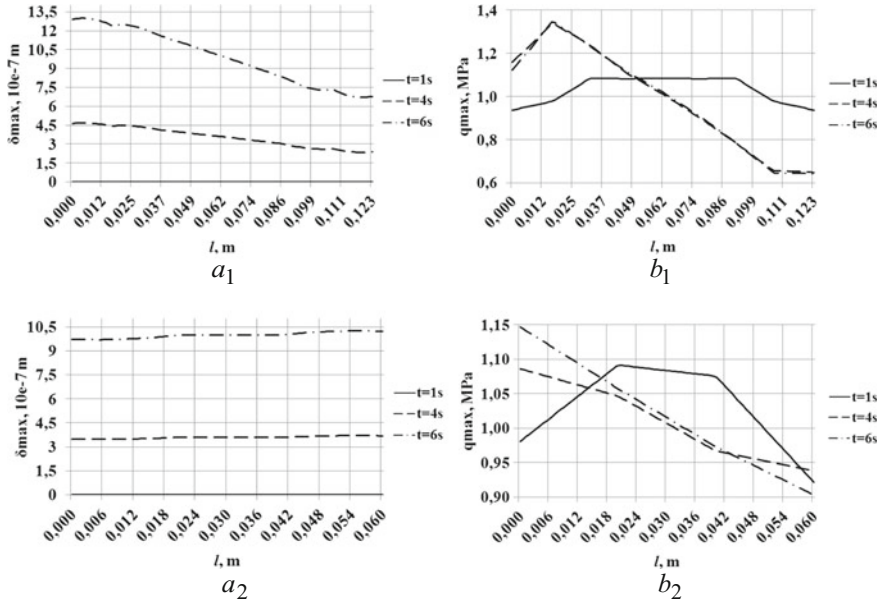

Fig. 34.3 Wear (a_i) and contact pressure (b_i) along lines l_i, $i = 1, 2$, at different times for the pad from cast iron

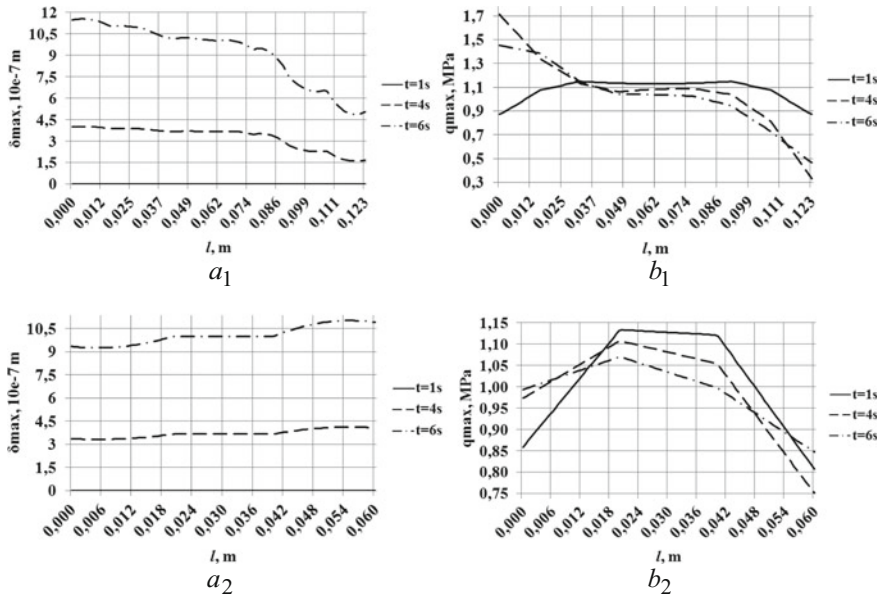

Fig. 34.4 Wear (a_i) and contact pressure (b_i) along lines l_i, $i = 1, 2$, at different times for the pad from phenylon

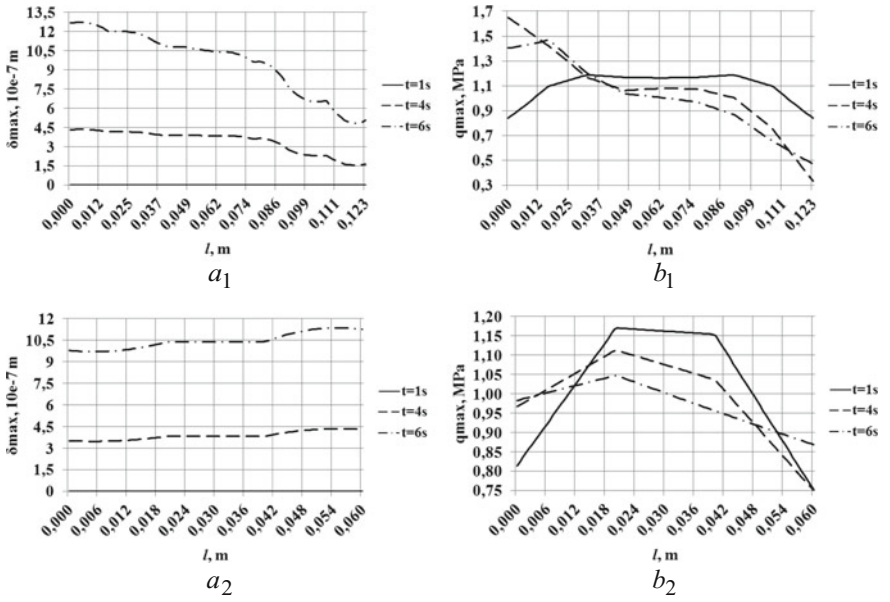

Fig. 34.5 Wear (a_i) and contact pressure (b_i) along lines l_i, $i = 1, 2$, at different times for the pad from TIIR 300

For pads from phenylon and TIIR 300, changes in contact pressures at the boundaries have a slightly different character. The difference lies in the fact that the contact pressures on the boundary $\rho = R_k^o$ with time also increase.

It can be seen from Figs. 34.4 and 34.5 that the plots of wear and contact pressure changes for pads from phenylon and TIIR 300 have a similar appearance, but differ in their values. The maximum wear values for the pad from TIIR 300 are higher.

34.4 Conclusion

Computational experiments have shown that, depending on the material used, the distribution of contact stresses and temperatures on the contact surfaces can vary significantly. This fact leads to uneven wear and requires analysis in each specific case. The complexity of the geometry of the elements of the brake systems requires additional analysis of the degree and magnitude of the heating, as well as the forecast of the wear resistance of the structure.

Acknowledgements This work is supported by the Ministry of Education and Science of the Russian Federation (project number BCH 0110-11/2017-48) and the Russian Foundation for Basic Research (project number 16-08-00852a).

References

1. M. Gee, J. Nunn, Wear **376–377**, Pt. B, 1866 (2017)
2. T. Dyck, P. Ober-Wörder, A. Bund, Wear **368–369**(Suppl. C), 390 (2016)
3. A. Sethuramiah, R. Kumar, in *Modeling of Chemical Wear*, ed. by A. Sethuramiah, R. Kumar (Elsevier, Oxford, 2016), p. 161
4. L. Wang, P. Zhou, Y. Yan et al., Int. J. Mach. Tools Manuf. **120**(Suppl. C), 61 (2017)
5. J. Archard, J. Appl. Phys. **24**(8), 981 (1953)
6. T. Telliskivi, Wear **256**(7), 817 (2004)
7. M.A. Cremona, B. Liu, Y. Hu et al., Reliab. Eng. Syst. Safety **154**(Suppl C), 49 (2016)
8. C.R. A'vila da Silva, G. Pintaude, Tribol. Int. **41**(6), 473 (2008)
9. M.I. Chebakov, S.A. Danilchenko, A.A. Lyapin, Izvestiya VUZov of North-Caucasus region. Nat. Sci. **2**, 32 (2017) (in Russian)
10. I.V. Kolesnikov, S.A. Danilchenko, E.M. Kolosova, M.I. Chebakov, A. A. Lyapin Transp. Probl. **11**(3), 73 (2016)
11. V.I. Kolesnikov, M.I. Chebakov, I.V. Kolesnikov, A.A. Lyapin, in *Advanced Materials: Manufacturing, Physics, Mechanics and Applications*, ed. by I. A. Parinov, S.-H. Chang, V.Y. Topolovin. Springer Proceedings in Physics, vol. 175 (2016), p. 527

Chapter 35
Model of Composite Wear with Abrasive Particles

Alexey Shpenev

Abstract Composite materials show as high mechanical properties (strength and rigidity) as high tribological characteristics (heat resistance and wear resistance). In this study, we model the fibrous composite friction process that involves fiber tips break-off and abrasive particles wear, which is typical for aircraft brake disks based on carbon-carbon composites. We define the influence of matrix and fiber parameters on wear resistance of composite material.

35.1 Introduction

Composite materials are increasingly used in engineering as the base for various friction joints. Thus, in contrast to the theory of strength and fracture of the composites, the theory of friction and wear of composites is much less developed. The first steps in describing the wear of heterogeneous materials were undertaken by Khrushchev and Babichev [1]. They proposed a hypothesis of equal linear wear rates for different materials that make up the composite in the process of steady friction ("Equal Wear" ("EW") mode). Together with the assumption of a linear dependence of the wear rate on the contact pressure, it is possible to obtain a formula which describes the wear resistance of the composite material, known as the "rule of mixture." Later, this model was improved by Goryacheva et al. [2], taking into account the nonlinear character of the dependence of the wear rate on the contact pressure and elastic deformations of the surface. This approach describes real composite materials wear resistance upper limit, since it does not take into account the processes of destruction and degradation of the heterogeneous structure of the composite (fiber peeling off the matrix, dying reinforcing particles, etc.). Phenomenological approach, taking into account the processes of composite material structure destruction during wear, was proposed by Zum-Gahr. This approach is based on the assumption of contact pressure uniform distribution in the

A. Shpenev (✉)
A. Yu. Ishlinsky Institute for Problems in Mechanics RAS, Moscow, Russia
e-mail: kel-a-kris@list.ru

I. A. Parinov et al. (eds.), *Advanced Materials*, Springer Proceedings in Physics 207, https://doi.org/10.1007/978-3-319-78919-4_35

composite material frictional surface (“Equal Pressure” (“EP”) mode) and allows obtaining a formula which describes the lower limit of the composite wear resistance (“inverse rule of mixture”) [3]. The rule of mixture and the inverse rule of mixture give a very wide range in which the wear resistance of real composite materials rests, and these models do not take into account the specific mechanisms of material failure in the wear process. The methods of modeling the composite failure mechanisms during friction have been developed by Dharan et al. for fiber composites [4] and for particles filled materials [5]. These approaches do not take into account the process of surface stresses redistribution between the phases of the composite in the process of wear and the abrasive action of particles arising from the composite surface destruction.

In technical applications, abrasive particles often plays important role in wear process of friction joints containing composite materials. In particular, this situation occurs in aviation braking systems, based on carbon-carbon composite discs. Materials, based on carbon fibers and carbonized pitch carbon matrix when worn, give relatively hard particle material of the fibers, which make a significant contribution to the wear of brake disks [6].

Like many other composites, based on tough fibers and a relatively soft matrix, the wear of such materials is unsteady and cyclic. The process of wear involves the fact that due to uneven wear the more rigid and wear-resistant fiber starts to rise above the friction surface, after what its tip breaks off and the process begins again. In this study, we build a model of the composite wear by abrasive particles taking into account pressure redistribution between matrix and fiber surfaces and fiber tips break-offs.

35.2 Problem Statement

The fibrous composite slides over the surface of a flat rigid half-space with a velocity V (Fig. 35.1). The fibers of the composite are located along the normal to the friction surface; the surfaces are pressed against each other with an average specific load P. The contacting surfaces are separated by rigid spherical particles of diameter D and of concentration on the friction surface N_a. The contact between the particle and the surface occurs according to the plastic scenario, the indentation of the particle is assumed equal to the geometric intersection of the sphere with the friction surface, and the pressure in the contact surface of the particle and the body is equal to the hardness of the body [7].

According to Zhao and Rabinovich, the volume wear amount ΔG, caused by the single particle, is proportional to the projection of the intersection of the particle and the surface into which it is embedded on a plane perpendicular to the slip direction with a coefficient, depending on the “attack angle” of the particle θ (Fig. 35.2) [7, 8]:

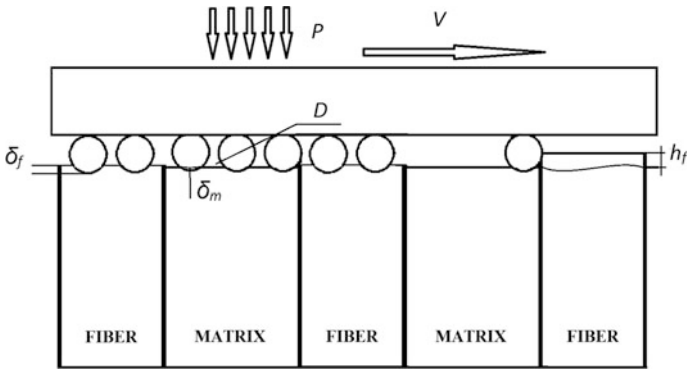

Fig. 35.1 Contact diagram

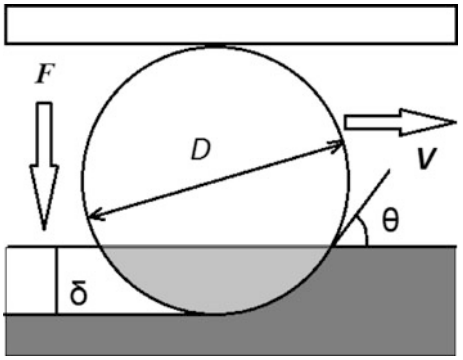

Fig. 35.2 The process of particle indentation into a worn surface

$$\Delta G = KVt\delta\sqrt{\delta D}; \quad K = \frac{3}{\pi}\tan\theta = \frac{3}{\pi}\frac{\sqrt{\delta D - \delta^2}}{D/2 - \delta}; \tag{35.1}$$

$$\Delta G = \frac{3}{\pi}Vt\frac{\delta^2\sqrt{D}\sqrt{D-\delta}}{D/2-\delta}, \tag{35.2}$$

where δ is the indentation of the particle into the material, D is the diameter of the particle, V is the slip velocity. From (35.1) and (35.2) we obtain the average linear wear rate of the surface of the fibers u_f and matrix u_m:

$$u_{f/m} = \frac{d\Delta G}{dt}N_a = \frac{3}{\pi}\frac{V}{2}N_a\frac{\delta_{f/m}^2\sqrt{D}\sqrt{D-\delta_{f/m}}}{D/2-\delta_{f/m}}. \tag{35.3}$$

The normal force, arising in the contact between the particle and the fiber surface F_f (matrix surface F_m), is:

$$F_{f/m} = \frac{H_{f/m}\pi D\delta_{f/m}}{2}. \tag{35.4}$$

The averaged pressure on the fiber surface p_f and matrix surface p_m is obtained as

$$p_{f/m}(t) = F_{f/m}N_a = H_{f/m}\pi D\delta_{f/m}(t)N_a. \tag{35.5}$$

From (35.5) we obtain the indentation of a particle into the fiber surface δ_f and the matrix surface δ_m:

$$\delta_{f/m}(t) = \frac{p_{f/m}(t)}{H_{f/m}\pi DN_a} \tag{35.6}$$

Substituting (35.6) into (35.3) we obtain:

$$u_{\substack{f\\m}}(\mathrm{t}) = \frac{3}{\pi}\frac{V}{2}N_a\frac{\left(\frac{p_{\substack{f\\m}}(t)}{H_{\substack{f\\m}}\pi DN_a}\right)^2\sqrt{D}\sqrt{D-\frac{p_{\substack{f\\m}}(t)}{H_{\substack{f\\m}}\pi DN_a}}}{D/2-\frac{p_{\substack{f\\m}}(t)}{H_{\substack{f\\m}}\pi DN_a}}. \tag{35.7}$$

Far from the contact surface, the distribution of normal stresses in the components of the fibrous composite will be determined by the hypothesis of equal deformations:

$$\begin{cases} P = v\sigma_f^{\infty} + (1-v)\sigma_m^{\infty} \\ \varepsilon^{\infty} = \frac{\sigma_f^{\infty}}{E_f} = \frac{\sigma_m^{\infty}}{E_m} \end{cases} \tag{35.8}$$

where σ_f^{∞} is the normal stress in the fiber (σ_m^{∞} is in the matrix), ε^{∞} are the normal deformation far from the contact surface; E_f is Young's modulus of fiber, (E_m of matrix), P is averaged contact pressure on the surface of the composite (Fig. 35.3).

According to the "shear-lag" model of composite materials [9], the distribution of axial normal stresses near the fiber end can be described by the equation:

$$\frac{d\sigma_f}{dz} = \frac{2\tau}{r};\ \sigma_f\big]_{z=0} = p_f;\ \sigma_f\big]_{z=L} = \sigma_f^{\infty}, \tag{35.9}$$

where τ is the shear stress in the fiber/matrix interface; r is the radius of the fiber; L is the length of region, where matrix slips over fiber surface. Therefore:

$$L(t) = r\frac{p_f(t) - \sigma_f^{\infty}}{2\tau}. \tag{35.10}$$

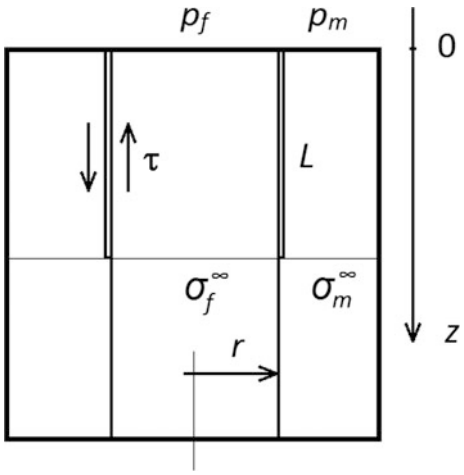

Fig. 35.3 Detachment of the matrix from the fibers in the process of friction surface destruction

From (35.10) and equilibrium conditions, we obtain:

$$p_f(t) = \sigma_f^\infty + \frac{2\tau L(t)}{r}; \tag{35.11}$$

$$p_m(t) = \frac{P - v p_f(t)}{1 - v}. \tag{35.12}$$

Taking into account that particle indentation into composite surface is relatively small we can assume that, under load, the surfaces of the fiber and matrix are practically at the same level. Thus, we can obtain the difference in the levels of the fiber and matrix without load h_f at each instant in the form:

$$\begin{aligned} h_f(t) &= \int_0^L \big(\varepsilon_f(z) - \varepsilon_m(z)\big)dz = L\left[\frac{\sigma_f^\infty + p_f(t)}{2E_f} - \frac{\sigma_m^\infty + p_m(t)}{2E_m}\right] \\ &= 2\frac{L(t)^2\tau}{r}\left(\frac{1}{E_f} + \frac{v}{E_m(1-v)}\right), \end{aligned} \tag{35.13}$$

where ε_f and ε_m are the normal strains of the fiber and matrix in the z-direction in the vicinity of the contact surface.

Now let us consider the dynamic process of the fiber elevation growth above the matrix surface, starting from the flat (polished) surface of the composite ($h_f = 0$) and resulting from the different wear rates of the fiber and matrix. As was mentioned above, fiber tip elevation is considered in unloaded state. The magnitude of the elevation can be defined as the integral of the difference between the linear wear rates of the fiber and the matrix:

$$h_f(t) = \int_0^t \left(u_m - u_f\right)dt \Rightarrow \frac{dh_f}{dt} = u_m - u_f. \tag{35.14}$$

Initially, $t = 0$: $h_f = 0$; $p_f = \sigma_f^\infty$; $p_m = \sigma_m^\infty$. Subsequently h_f value increases until it reaches a critical value h_{cr}, then the tip of the fiber breaks off and the process starts from the beginning.

From (35.13), we obtain:

$$L(t) = \sqrt{\frac{rh_f(t)}{2\tau\left(\frac{1}{E_f} + \frac{v}{E_m(1-v)}\right)}}. \tag{35.15}$$

Substituting (35.15) into (35.11) we obtain:

$$p_f(t) = \sigma_f^\infty + \sqrt{\frac{2\tau h_f(t)}{r\left(\frac{1}{E_f} + \frac{v}{E_m(1-v)}\right)}} \tag{35.16}$$

Substituting (35.16) into (35.12) we obtain:

$$p_m(t) = \frac{P - v\left(\sigma_f^\infty + \sqrt{\frac{2\tau h_f(t)}{r\left(\frac{1}{E_f} + \frac{v}{E_m(1-v)}\right)}}\right)}{1 - v}. \tag{35.17}$$

Substituting (35.16) and (35.17) into (35.7) and then (35.7) into (35.14) one can obtain a differential equation of the form (it is too cumbersome for direct recording):

$$\frac{dh_f}{dt} = F\left(h_f\right) \tag{35.18}$$

After solving it by the finite differences method, we have a model of the evolution of the fiber from the onset of wear, to its breaking off after reaching the critical value h_{cr} (Fig. 35.4). Then the process will start again. The mean linear wear rate of the composite would be:

$$u = \frac{\int_0^{T_*} u_m(t)dt}{T_*} = \frac{\int_0^{T_*} u_f(t)dt + h_{cr}}{T_*}, \tag{35.19}$$

where T_* is the period of fiber elevation growth before fiber breakage.

If the fiber tip break-off does not occur, fiber and matrix wear rates come to asymptotic equilibrium; fiber elevation growth tends to zero and composite friction

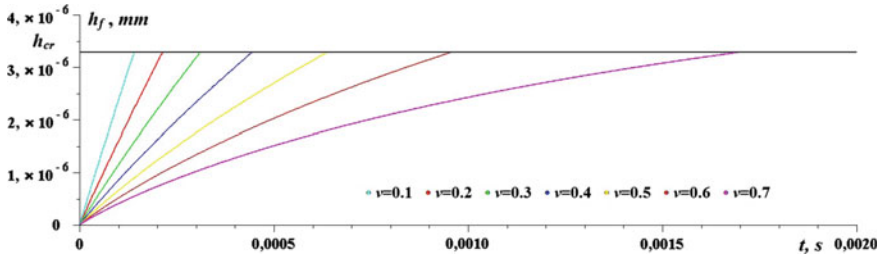

Fig. 35.4 Fiber tip elevation h_f versus time t for different volume fiber concentration v

process comes to equal wear mode (upper boundary of the composite wear resistance). In this case, the composite wear rate and fiber elevation will be equal:

$$u^* = \frac{3}{\pi}\frac{V}{2}N_a\frac{\delta^2\sqrt{D}\sqrt{D-\delta}}{D/2-\delta}; \quad \delta = \frac{P}{\pi D N_a\left[vH_f + (1-v)H_m\right]}; \tag{35.20}$$

$$h_f^* = \frac{P^2 r}{2\tau}\left(\frac{1}{E_f} + \frac{v}{E_m(1-v)}\right)\left(\frac{1}{v + \frac{E_m}{E_f}(1-v)} - \frac{1}{v + \frac{H_m}{H_f}(1-v)}\right)^2. \tag{35.21}$$

35.3 Result and Discussion

Figure 35.5 shows the dependence of the average wear rate of composite material on the volume concentration of the fibers for the "EW" mode and for the mode of breaking off the fiber tips. Expectedly fibers tip, breaking off wear mode, shows greater wear rate but the difference tends to zero, when the fiber concentration tends to zero and unity. Figure 35.6 shows the dependence of the average wear rate on the magnitude of the critical fiber elevation above the matrix at which the fiber tip breaks. Reduction of the critical value (and, consequently, the size of fiber fragments in our assumptions) causes an increase in the average wear rate. This is due to the fact that in the limit as h_{cr} tends to zero, the friction of the material switches to the "EP" wear mode, since the redistribution of pressures does not occur during the wear process (fiber tip that begins to elevate immediately breaks off). At the same time, the "EP" mode, as mentioned above, is the lower limit of the wear resistance of the composite. When h_{cr} tends to a possible maximum h_f^*, the wear rate of the composite decreases, but remains significantly higher than the wear rate in the EB mode.

Calculations were made for values, typical for aircraft brake disks, based on carbon-carbon composites properties:

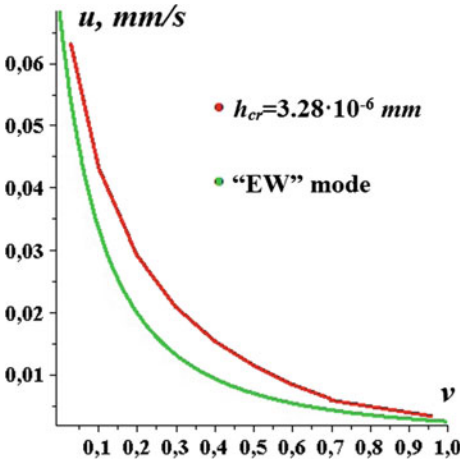

Fig. 35.5 Composite linear wear rate u versus volume fiber concentration v for "equal wear mode" (green) and tip break-off process (red)

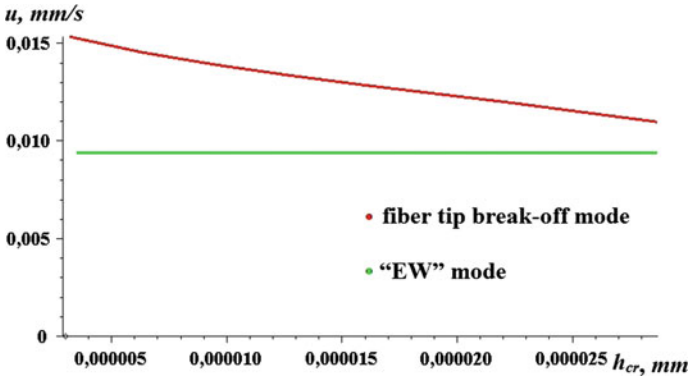

Fig. 35.6 Composite linear wear rate u versus critical fiber tip elevation h_{cr} for "equal wear mode" (green) and tip break-off process (red)

E_f = 500 GPa
E_m = 150 GPa
H_f = 1 GPa
H_m = 0.2 GPa
$r = 10^{-2}$ mm
$\tau = 10^{-4}$ GPa
$P = 5 \cdot 10^{-2}$ GPa
V = 10 mm/s
$D = 5 \times 10^{-5}$ mm
$N_a = 4 \times 10^{8}$ mm^{-1}

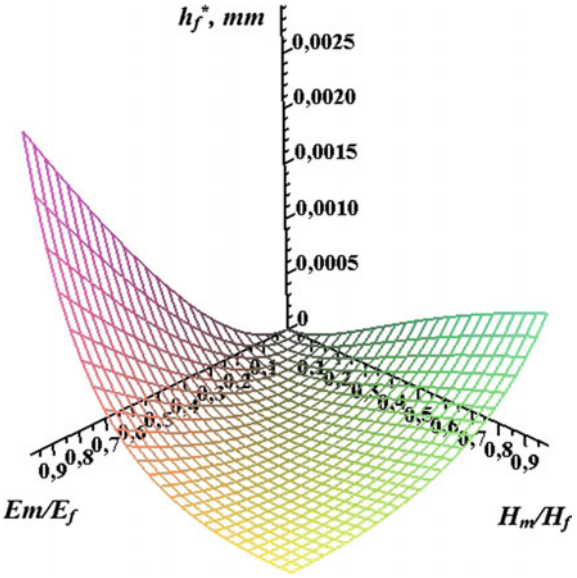

Fig. 35.7 Maximum fiber tip elevation h_f^* versus matrix to fiber hardness and stiffness quotient

35.4 Conclusion

The process of fiber tips breaking off during friction significantly increases the wear rate of the composite material, reducing its tribological characteristics. In this case, the regulation of the fragments size can only reduce the composite wear rate to a limited extent. The most promising method of increasing the composite wear resistance is the fiber tips breaking off process termination and switching the friction to "EW" mode. The most obvious way to achieve this is to reduce (ideally up to zero) the maximum possible elevation of the fiber tip over the matrix h_f^* by adjusting the properties of the composite. Figure 35.7 shows the dependence of h_f^* on the properties of fiber and matrix. As follows from the plot and from the formula (35.21), at $H_m/H_f = E_m/E_f$, the value of the maximum fiber elevation is zeroed, which automatically means access to "EW" mode. Since it is possible for carbon materials to adjust both the toughness and rigidity over a wide range sufficiently independently due to heat treatment conditions, this way to increase the wear resistance of carbon-carbon composites could be widely used.

Acknowledgements The work was financially supported by the Federal Agency of Scientific Organizations (Reg. No. AAAA-A17-117021310379-5), and partially supported by Russian Foundation for Basic Research (project No. 17-58-52030).

References

1. M.M. Khruschov, Wear **28**, 69 (1974)
2. I.G. Goryacheva, E.V. Torskaya, J. Friction Wear **13**(1), 185 (1992) (in Russian)
3. K.H. Zum-Gahr, in *International Conference on Wear of Materials*, ed. by K.C. Ludema (American Society of Material Engineering, Vancouver, 1985), p. 793
4. B. Yen, C.K.H. Dharan, Wear **195**, 123 (1996)
5. Gun Y. Lee, C.K.H. Dharan, R.O. Ritchie, Wear **252**, 322 (2002)
6. A.G. Shpenev, A.M. Kenigfest, A.K. Golubkov, Advanced materials—manufacturing, physics, mechanics and applications, in *Springer Proceedings in Physics*, vol. 175, ed. by I.A. Parinov, S.-H. Chang, V.Y. Topolov (Springer, Cham, 2016), p. 551
7. Y. Zhao, L. Chang, Wear **252**, 220 (2002)
8. E. Rabinowicz, *Friction and Wear of Materials*, 2nd edn. (Wiley, New York, 1995)
9. T.W. Clyne, Mater. Sci. Eng. A **122**, 183 (1989)

Chapter 36
Study of Physical, Mechanical and Tribological Properties of Nanocomposites Based on Oil-Filled Polymers

P. G. Ivanochkin, S. A. Danilchenko, E. S. Novikov and D. S. Manturov

Abstract Oilynit (oleaginous polymer) is a multifunctional, universal wear inhibitor of tribosystems. It is an oil-filled polymer characterized by intellect: the ability of dynamically adjustment of its own functional properties at friction. The paper contains the comparative studies of physical, mechanical and tribological characteristics of two types of antifriction self-lubricating polymer composite materials, developed in Rostov State Transport University under the Maslyanit trade mark. The study of physical and mechanical properties of composites (microhardness, modulus of elasticity, elastic recovery) was carried out by the nanoindentation method on NanoTest 600, a special set-up for determining physical and mechanical properties of the materials. Tribological tests were carried out at a fixed sliding speed and a stepped loading on the friction machine of Amsler type by a "finger-roller" scheme.

36.1 Introduction

The creation of non-lubricated friction units with a large operating lifetime and minimal friction losses is an urgent task of the contemporary mechanical engineering. At present, Russian industry suffers from a lack of structural materials of its own production for friction units operating under severe conditions (sliding bearings, face seals, piston rings, etc.). In some cases, non-ferrous metals and alloys are used for such purposes. At the same time, these materials have a number of significant drawbacks when used in friction units. They are a large labor-intensive and material-intensive production, operation and repair, insufficiently high

P. G. Ivanochkin (✉) · S. A. Danilchenko · E. S. Novikov · D. S. Manturov
Rostov State Transport University, Rostov-on-Don, Russia
e-mail: ivanochkin_p_g@mail.ru

S. A. Danilchenko
Southern Federal University, Rostov-on-Don, Russia

I. A. Parinov et al. (eds.), *Advanced Materials*, Springer Proceedings in Physics 207, https://doi.org/10.1007/978-3-319-78919-4_36

antifriction properties, a relatively high consumption of lubricants and inability to work under conditions of dry friction, insufficient leak tightness, relatively low resistance to fracture due to fatigue, etc.

One of the most promising directions of creating materials with controlled properties is the use of antifriction self-lubricating polymer composites [1–3]. A composite is a multicomponent system, each component of which has its own functional purpose and ensures the development of a certain property. Simultaneous operation of all composite components in combination with effects arising from friction on their surfaces can be accompanied by a synergistic effect and lead to an improvement of the corresponding properties of the material.

One of the most up-and-coming methods of creating polymer composite materials with new or improved properties is the introduction of diverse types of nanomodified fillers and nanodimensional additives into the polymer matrix [2, 4–9]. The properties of composite materials with nanodimensional additives differ significantly from composites with macrodispersed fillers due to the developed surface and high surface activity [10–12].

It is economically expedient to create composite materials based on such polymers that are characterized by their production capacities, for instance, aromatic polyamide phenylone. Phenylone (Phenylone C-2) is a linear heterocyclic copolymer whose macromolecule's stem nucleus contains amide group –HNCO–, connected with phenyl fragments on both sides. It is obtained by emulsion polycondensation of metaphenylenediamine with isophthalic and terephthalic acid dichlorides in the ratio 3:2. In friction units, Phenylone C-2 has a load-bearing capacity up to 25 MPa and withstands operating temperatures up to 250 °C.

Phenylone occupies a special place among the polymers due to the relatively high deformation and strength parameters, high wear resistance, chemical resistance to aggressive media, and stability of a shape in a wide temperature range. However, the possibility of using this material in friction units is limited due to a sufficiently high coefficient of friction [13]. Our previous studies were devoted to the investigation of the influence of the type and percentage of certain nanofillers to the aromatic polyamide Phenylone C-2 on the physical, mechanical, and tribological properties of antifriction composites, based on Phenylone, created for work at unlubricated friction [14, 15].

The given paper depicts the possibility of creating oil-filled composites, based on the obtained materials. It is necessary to mention that Federal State Unitary Enterprise Special Design and Technological Bureau «Orion» have been long and successfully carrying out researches of oil-filled composites. Moreover, there was created a whole set of self-lubricating polymer materials of «Maslyanit» trademark [16–18].

Maslyanit is a multifunctional, universal wear inhibitor of tribosystems. It is an oil-filled polymer characterized by intellect: the ability of dynamical adjustment of their own functional properties at friction, expressed in the ability to clad selectively the most worn areas of the friction surface under the influence of friction energy, initiating physical and chemical processes of primary and secondary adjustment of the structure of its polymer matrix. Materials of this class can generally be regarded

as three-component systems, consisting of a polymeric binder, a plasticizer and multifunctional additives-fillers.

Hence, the paper contains the results of the carried out comparative studies of physical, mechanical, and tribological properties of antifriction self-lubricating polymer composite material, «Maslyanit-GM» and materials, developed at Rostov State Transport University.

36.2 Tribolical Tests of Oil-Filled Nanocomposite Materials

The oil-filled composite materials were obtained by saturating the previously acquired composite based on Phenylone C-2 [1] with oils of PFPE (perfluoropolyether) and PMPS (polymethylphenylsiloxane) at a temperature of 200 °C for 2–2.5 h at different pressures.

The tribological tests were carried out at a speed 0.3 m/s and loadings 209, 310, 420, 520, 620, 720, 820, 920, 1020 N on the friction machine of Amsler type by a «finger-roller» scheme. Table 36.1 presents the measurement results of the mass wear of samples according to the test outcomes.

Table 36.1 Mass wear of samples during testing

The name of the sample	Wear (g)
Maslyanit of SDTB «Orion»	0.007
Phenylone + Arimid 5% + Fluoroplastic 10%	0.050
Phenylone + Arimid 5% + Fluoroplastic 10%, PFPE oil	0.055
Phenylone + Arimid 5% + Fluoroplastic 10%, PMPS oil	0.048
Phenylone + Arimid 10% + Fluoroplastic 20% + aerosil 5%	0.130
Phenylone + Arimid 10% + Fluoroplastic 20% + aerosil 5%, PFPE oil	0.043
Phenylone + Arimid 10% + Fluoroplastic 20% + aerosil 5%, PMPS oil	0.132
Phenylone + Arimid 5% + Fluoroplastic 20% + spinel 3%	0.024
Phenylone + Arimid 5% + Fluoroplastic 20% + spinel 3%, PFPE oil	0.022
Phenylone + Arimid 5% + Fluoroplastic 20% + spinel 3%, PMPS oil	0.114
Phenylone + Arimid 5% + Fluoroplastic 20% + serpentinite3%	0.035
Phenylone + Arimid 5% + Fluoroplastic 20% + serpentinite 3%, PFPE oil	0.029
Phenylone + Arimid 5% + Fluoroplastic 20% + serpentinite 3%, PMPS oil	0.035
Phenylone + Arimid 5% + Fluoroplastic 10%, PFPE oil, 10 atm.	0.033
Phenylone + Arimid 10% + Fluoroplastic 20% + aerosil 5%, PFPE oil, 10 atm.	0.092
Phenylone + Arimid 5% + Fluoroplastic 10%, PMPS oil, 10 atm.	0.059
Phenylone + Arimid 10% + Fluoroplastic 20% + aerosil 5%, PMPS oil, 10 atm.	0.083
Phenylone + Arimid 5% + Fluoroplastic 10%, PFPE oil, 5 atm.	0.041
Phenylone + Arimid 10% + Fluoroplastic 20% + aerosil 5%, PFPE oil, 5 atm.	0.078
Phenylone + Arimid 5% + Fluoroplastic 10%, PMPS oil, 5 atm.	0.177

As specified by the obtained data, «Maslyanit» samples by SDTB «Orion» made of polyamide 6 have the greatest abrasion resistance. Moreover, the best results were obtained while introducing PFPE oil into the composites. The introduction of PMPS oil, on the contrary, led to the increasing of samples wear.

The friction coefficient of the samples was determined during the set of tribological tests. Some of the obtained results are present in Fig. 36.1, 36.2, 36.3 and 36.4.

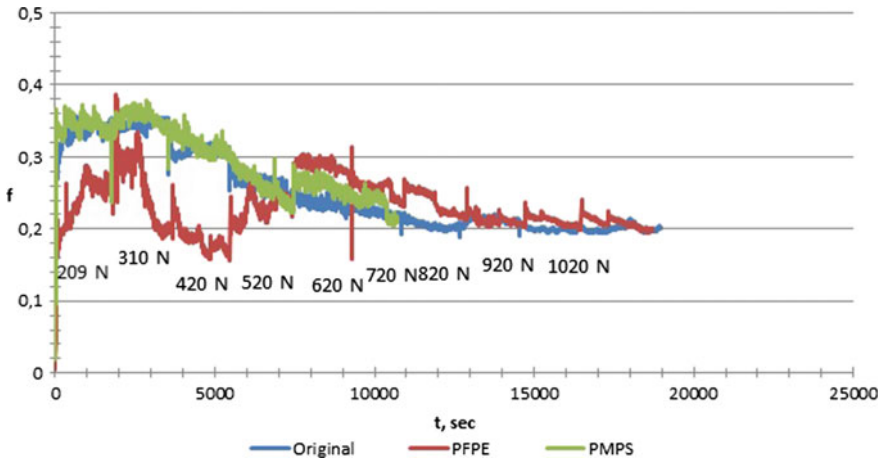

Fig. 36.1 Plots of the coefficient of friction of samples at $V = 0.3$ m/s: Phenylone + Arimid 5% + Fluoroplastic 10%

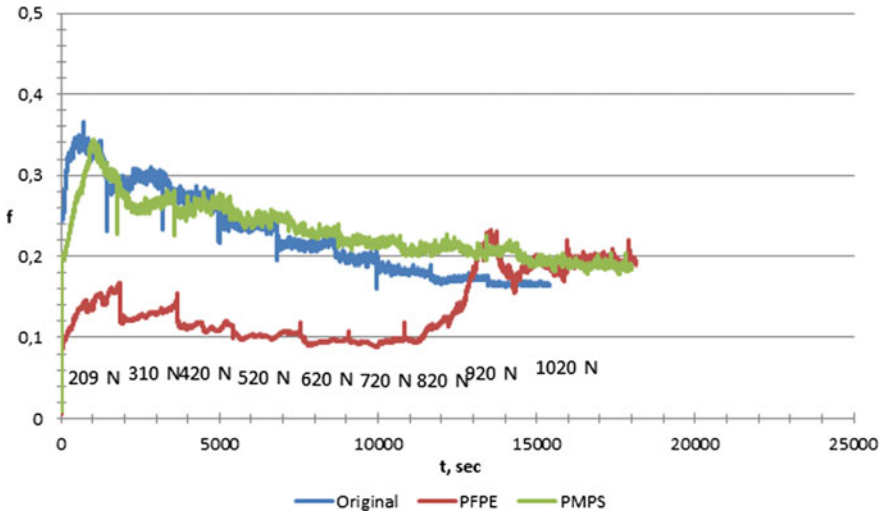

Fig. 36.2 Plots of the coefficient of friction of samples at $V = 0.3$ m/s: Phenylone + Arimid 10% + Fluoroplastic 20% + aerosil 5%

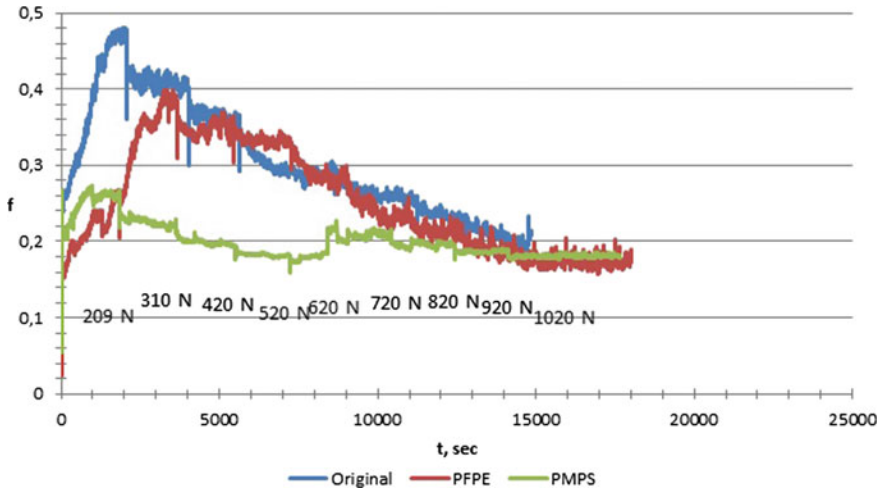

Fig. 36.3 Plots of the coefficient of friction of samples at $V = 0.3$ m/s: Phenylone + Arimid 5% + Fluoroplastic 20% + spinel 3%

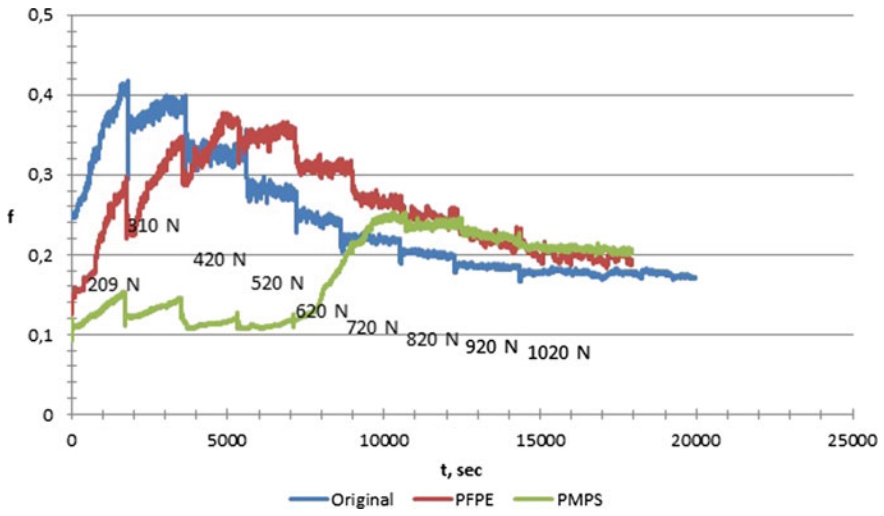

Fig. 36.4 Plots of the coefficient of friction of samples at $V = 0.3$ m/s: Phenylone + Arimid 5% + Fluoroplastic 20% + serpentinite 3%

Based on the gained results, it can be concluded that the oil introduction into the composite material has a positive effect. However, the introduction PFPE oil resulted in a significant reduction of the friction coefficient practically in the entire loading range only in composites with aerosil. PMPS oil, on the contrary, strengthened the antifriction effect in the load range of 209–720 N in samples

containing spinel and serpentine. The minimum value of the coefficient of friction equal to 0.1, obtained for «Maslyanit» samples by SDTB «Orion» made of polyamide 6, was attained at the lowest loads of 209 and 310 N. Further increase of loads led to a sharp increase of the friction coefficient up to 0.5.

36.3 Determination of Physical and Mechanical Properties of Oil-Filled Nanocomposite Materials

The determination of physical and mechanical properties of the studied materials was performed according to the procedure described in [14] using the NanoTest 600 set-up. To implement such an experiment, according to the test methodology, there were pre-made the samples. A piece of material with a size of $10 \times 10 \times 1.5$ mm^3 was cut with the automatic high-precision cutting machine Briliant 221, then at a temperature of 180 °C and a pressure of 11 MPa, it was pressed into a "pellet" in Opal 460, a fully automated press for hot-pressing. Bakelite was used as the basis for pressing. The obtained samples were ground with a single disk grinding and polishing machine Sapphir 550. After this procedure, the fragments of the material were extracted from press forming. Grinding was performed to reduce the surface roughness of the test sample and thereby reduce its effect on the final indentation results.

The procedure of nanoindentation consisted of 40 shots for each prepared sample. All shots were divided into 5 columns. The distance between the shots in the same column was 50 μm. The distance between the columns was also equal to 50 μm. The same maximum force of indentation was set as 150 mN and rate of rise and the rate of load is relieving was set as 0.2 mN/s in each "loading–unloading" cycle.

Time lag of the indenter in the static position at the maximum load was set to 5 s to determine the creep degree of the material. While unloading, when the value of the applied force was reduced to 20 mN, the temperature drift with 60 s pause was set to exclude the possibility of the temperature effect on the final results. "*P*–*h*" diagram depicting the load depending on the penetration depth of an indenter was built and maintained for each cycle of "loading–unloading".

Based on the measurement results there was made a table for each sample. Such values as the maximum depth of indenter penetration, microhardness H, modulus of elasticity E, ratio H/E and H^3/E^2, coefficient of elastic recovery for each individual injection. Emanated from the given tables, we created a summary table containing the averaged values of these properties (see Table 36.2).

As it follows from Table 36.2, samples Phenylone C-2 + 5% Arimid + 10% Fluoroplastic in PFPE oil, manufactured without pressure and at a pressure of 5 atmospheres, Phenylone C-2 + 10% Arimid + 20% Fluoroplastic + 5% Aerosil in PFPE and PMPS, manufactured under pressure of 10 atmospheres, got the highest physical and mechanical properties.

Table 36.2 Averaged values of physical and mechanical properties of the samples

Sample	Micro-hardness H (GPa)	Modulus of elasticity E (GPa)	H/E	H^3/E^2	Coefficient of elastic recovery
Phenylone + Arimid 5% + Fluoroplastic 20% + spinel 3%, PFPE oil	0.226	3.958	0.057	0.000756	0.184
Phenylone + Arimid 5% + Fluoroplastic 20% + spinel 3%, PMPS oil	0.238	3.789	0.063	0.000958	0.209
Phenylone + Arimid 5% + Fluoroplastic 10%, PFPE oil, 10 atm.	0.239	3.368	0.072	0.001240	0.237
Phenylone + Arimid 5% + Fluoroplastic 20% + serpentinite 3%, PMPS oil	0.242	3.987	0.061	0.000907	0.204
Phenylone + Arimid 5% + Fluoroplastic 10%, PMPS oil	0.243	2.796	0.087	0.001894	0.283
Phenylone + Arimid 5% + Fluoroplastic 20% + serpentinite 3%, PFPE oil	0.246	3.842	0.064	0.001030	0.218
Phenylone + Arimid 5% + Fluoroplastic 10%, PMPS oil, 5 atm.	0.252	3.401	0.074	0.001405	0.254
Phenylone + Arimid 10% + Fluoroplastic 20% + aerosil 5%, PMPS oil, 5 atm.	0.258	4.287	0.060	0.000960	0.21
Phenylone + Arimid 10% + Fluoroplastic 20% + aerosil 5%, PFPE oil	0.259	3.744	0.069	0.001279	0.236
Phenylone + Arimid 5% + Fluoroplastic 10%, PMPS oil, 10 atm.	0.262	2.914	0.090	0.002158	0.3
Phenylone + Arimid 10% + Fluoroplastic 20% + aerosil 5%, PMPS oil	0.265	3.954	0.067	0.001213	0.237
Phenylone + Arimid 10% + Fluoroplastic 20% + aerosil 5%, PFPE oil, 5 atm.	0.267	3.481	0.077	0.001600	0.271
Phenylone + Arimid 5% + Fluoroplastic 10%, PFPE oil	0.278	3.317	0.086	0.002057	0.302

(continued)

Table 36.2 (continued)

Sample	Micro-hardness H (GPa)	Modulus of elasticity E (GPa)	H/E	H^3/E^2	Coefficient of elastic recovery
Phenylone + Arimid 10% + Fluoroplastic 20% + aerosil 5%, PFPE oil, 10 atm.	0.283	3.668	0.077	0.001721	0.286
Phenylone + Arimid 5% + Fluoroplastic 10%, PFPE oil, 5 atm.	0.297	3.607	0.083	0.002035	0.309
Phenylone + Arimid 10% + Fluoroplastic 20% + aerosil 5%, PMPS oil, 10 atm.	0.327	4.559	0.072	0.001702	0.288

In addition, it can be concluded that the pressure increases when manufacturing samples generally led to an increase of the mechanical properties of the resulting composites.

Furthermore, we compared the values of the microhardness and modulus of elasticity of the studied samples and Maslyanit by Experimental Design Bureau «Orion» . The microhardness value of the given Maslyanit is 0.168 GPa, and the modulus of elasticity is 2.492 GPa. Hence, the conducted comparison demonstrated that the values of mechanical properties of the obtained composites are much higher (up to two times) than of the selected Maslyanit.

To assess the way the oil introduction affects physical and mechanical properties of the materials, the values, presented in Table 36.2, were differentiated with the measurement data of samples, prepared without the oils. The results for such samples are partially described in [14, 15]. The differentiation showed that the microhardness and modulus of elasticity of oil-filled composites are reduced by 20–25%. In addition, the oil introduction also led to an increase of the value range of physical and mechanical properties, i.e. to greater heterogeneity of the material. However, we cannot make an unambiguous conclusion about the use of which of the selected oils leads to a greater decrease of mechanical properties.

Since the value H/E characterizes the ability of a material to change its size and shape during deformation, it can be used to evaluate the wear resistance of materials at friction. Based on the obtained results, it can be stated that the wear resistance of oil-filled composites decreases while introducing PMPS oil and remains at the same level or increases slightly while introducing PFPE oil.

36.4 Conclusion

The conducted researches allow drawing a conclusion about the change of physical, mechanical, and tribological properties of oil-filled polymer composite materials with a matrix based on Phenylone C-2, depending on the used nanofillers and oil.

The introduction of PFPE oil led to a significant decrease of the coefficient of friction practically in the entire loading range only in composites containing aerosil. At the same time introduction of PMPS oil, in contrast, strengthened the antifriction effect of the samples, containing spinel and serpentine.

The results of tribological tests correlate well with the studies of the physical and mechanical properties of the developed composites.

On the base of these results, it can be concluded, which composition is most suitable for use in non-lubricated friction units.

Acknowledgements This work is supported by the Russian Science Foundation under grant 14-29-00116 and performed in the Rostov State Transport University.

References

1. Y.K. Mashkov, Z.N. Ovchar, MYu. Baybaratskaya, *Polymer Composite Materials in Tribotechnics* (Nedra, Moscow, 2004) (in Russian)
2. S.V. Avdeychick et al., *Nanocomposite Engineering Materials: Experience in Development and Application*, ed. by V.A. Struk (Grodno State University Press, Grodno, 2006) (in Russian)
3. F.G. Lovshenko et al., *New Resource-Saving Technologies and Composite Materials* (Energoatomizdat, Gomel, 2004) (in Russian)
4. A.M. Kochnev, S.S. Galibeev, *Modification of Polymers* (Kazan State Technological University Press, Kazan, 2008) (in Russian)
5. A.A. Okhlopkova, A.V. Vinigradova, L.S. Pinchuk, *Plastics Filled with Ultradisperse Inorganic Compounds* (Institute of Mechanics of Metal—Polymer Systems of National Academy of Sciences of Belorussia, Gomel, 1999) (in Russian)
6. I.V. Gorynin, Nanocomposites: advantages and prospects. Technopolis **XXI**, 20 (2006) (in Russian)
7. A.I. Sviridenok, A.V. Kravtsevich, S.I. Mikulich, in *Perspective Materials and Technologies*, ed. by V.V. Klubovych (Vitebsk State Technical University Press, Vitebsk, 2013), p. 113 (in Russian)
8. H. Gleiter, Mater. Sci. Forum **189–190**, 67 (1995)
9. A.A. Okhlopkova, O.A. Andrianova, S.N. Popov, *Modification of Polymers by Ultradispersed Compounds* (Yakutsk Branch of the Siberian Branch of the Russian Academy of Sciences, Yakutsk, 2003) (in Russian)
10. S.V. Avdeychick, V.A. Liopo, A.A. Ryskulov, *Introduction to the Physics of Nanocomposite Engineering Materials* (Grodno State Agrarian University, Grodno, 2009) (in Russian)
11. A.A. Okhlopkova, P.N. Petrova, O.V. Gogoleva, Wear Friction **30**(5), 500 (2009) (in Russian)
12. S.S. Pesetskiy, S.P. Bogdanovich, N.K. Myshkin, Wear Friction **28**(5), 500 (2007) (in Russian)

13. A.I. Burya, E.V. Tkachenko, O.P. Chigvintseva, Composite materials: international scientific and technical digest. Dnepropetrovsk State Agrarian Univ. Dnepropetrovsk **3**(1), 4 (2009) (in Russian)
14. P.G. Ivanochkin, S.A. Danilchenko, E.S. Novikov, Proc. Eng. **150**, 520 (2016)
15. V.I. Kolesnikov, P.G. Ivanochkin, N.A. Myasnikova, S.A. Danilchenko, Ph.V. Myasnikov, in *Proceedings of the 2016 International Conference "Physics, Mechanics of New Materials and Their Applications*, ed. by I.A. Parinov, S.-H. Chang, M.A. Jani (Nova Science Publishers, New York, 2017), p. 121
16. A.A. Kutkov, *Wear-Resistant and Antifriction Coatings* (1976) (in Russian)
17. P.D. Derlugyan, V.T. Loginov, A.S. Sukhov, I.D. Derlugyan, Izvestiya VUZov. North-Caucasian Reg. Tech. Sci. **3**, 61 (1987) (in Russian)
18. P.D. Derlugyan, V.A. Lenivtsev, Izvestiya VUZov. North-Caucasian Reg. Tech. Sci. **2**, 9 (2004) (in Russian)

Chapter 37
The Study of Tribological Properties of Composites Based on Phenylone and Hybrid Filler

I. V. Kolesnikov, N. A. Myasnikova, D. S. Manturov and Ph. V. Myasnikov

Abstract The paper conveys the creation principles of hybrid composites for friction units, based on binder Phenylone C-2, filled with modified polytetrafluoroethylene and inorganic nanoadditives, natural minerals, dispersed to a colloidal state. The optimal methods for modifying the fillers surface were selected in order to improve the adhesion strength at the components interface and to improve the properties of composite materials. The conducted tribological tests and morphological studies made it possible to optimize nanocomposites composition. It is shown that the dispersity increase of the filler leads to an improvement of tribocontact characteristics. Spectroscopic studies of the triboconjugation surface confirmed that the frictional film, formed on the friction surface, imparts high wear resistance and good antifriction properties to the friction unit.

37.1 Introduction

The current stage of mechanical engineering development is characterized by tightening the requirements for used tribotechnical materials. The present-day level of the mechanical engineering development dictates contradictory requirements to the structural elements of the crucial friction units. These requirements consist in solving the problem of optimizing their construction while ensuring the maximum tribological stability and preserving the minimum mass of the mobile elements. The mentioned requirements can be fulfilled by the use of new composite polymer materials that are more technologically efficient under the given conditions of friction and wear of mechanical systems.

The use of polymers as a matrix of composite materials of antifriction purposes is determined by the low friction coefficient in comparison with metals, high specific strength, and resistance to many liquid and gaseous media that are corrosive to metals. However, the expansion of the polymers use is possible only by modi-

I. V. Kolesnikov · N. A. Myasnikova · D. S. Manturov (✉) · Ph. V. Myasnikov
Rostov State Transport University, Rostov-on-Don, Russia
e-mail: manturovds@rgups.ru

I. A. Parinov et al. (eds.), *Advanced Materials*, Springer Proceedings in Physics 207, https://doi.org/10.1007/978-3-319-78919-4_37

fying the properties of known types of polymers. The most accessible and acceptable type of modification is the creation of composite materials, which are a multicomponent system capable of changing the initial properties of the polymer [1–3]. One of the most promising areas in the development of polymer composite materials is the creation of hybrid composites, the materials that include three or more components. These materials allow solving a number of problems that cannot be eliminated using mono-reinforced composites.

The paper is aimed to the developing, studying the properties and defining the optimal composition of new polymer composite materials, based on the heat-resistant aromatic polyamide Phenylone C-2.

Phenylone C-2 is a linear heterocyclic copolymer, whose macromolecule's stem nucleus contains amide group −HNCO−, connected with phenyl fragments on both sides. In friction units, phenylone C-2 has a load-bearing capacity up to 25 MPa and withstands operating temperatures up to 250 °C. Arimid fiber (Arimid 29.4 Tex) in an amount of 10–20 wt% and carbonic hydrogen-cellulose fibers in an amount of 30–40% wt% were selected as reinforcing fillers, while the powder of F4 MB polytetrafluoroethylene (copolymer of tetrafluoroethylene with hexafluoropropylene) in an amount of 10–20 wt% was used an antifriction filler.

In tribotechnical practice one of the most promising ways of targeted selection of nanoadditives for polymer composites is the use of natural minerals dispersed to a colloidal state. This direction is based on the ability of some elements to form chemical compounds of coordination type under friction or special external conditions. We detected a whole class of natural materials, nonmetallic ones, the wastes of domestic mining industries that being introduced in small amounts into polymers (up to 5 wt%) can increase the tribological properties of the friction unit.

Such minerals are minerals of the silicate class: magnesium hydrosilicates (layered structure) and mixed oxides (spinel type structure). Nanodimensional additives (40–100 nm) were introduced into the composite for improving its properties. Hence, there were introduced nanodimensional additives of spinel (iron, manganese, magnesium, and chromium), serpentinites, fulerene soot, modified graphite. The concentration of nanoadditives does not exceed 1.5–3 wt%. Moreover, as the filler dispersity increases, it is possible to minimize the degree of polymer matrix filling with the filler, in which its strength and wear resistance grow without increasing the modulus of elasticity, roughness and coefficient of friction.

37.2 Result and Discussion

37.2.1 Methods of Testing and Research of Nanocomposites at Tribocontact

The nanodimensional components were obtained with the *Netzsch* MicroCer Bead Mill. The grinding process (40–50 nm) and dispersion there leads to the effect of

mechanical activation, i.e. the change in the energy state of the material in the grinding process. The particle size, obtained by grinding in a bead mill, was analyzed using CPS Model DC24000 analyzer, which measures the distribution of particle size (in the range from 10 to 400 nm) with centrifugal sedimentation in optically clear spinning disc filled with fluid. It allows conducting measurements with high accuracy, resolution, and reproducibility. The use of nanodimensional particles as additives promotes the formation of new compounds in the surface layer, characterized by a low coefficient of friction and increased wear resistance.

Some optimal methods for modifying the filler surface were selected to enhance the adhesive strength at the interface between components and to improve the properties of composite materials [4]. In the result of the plasma-chemical modification of the surface, a change in the chemical composition and structure of the surface layers was revealed [5], while the properties and composition of the main bulk of the material remained unchanged. Studies of the chemical structure of the modified polymers surface or their fillers were carried out using IR-Fourier spectroscopy of MFTIR. Spectrum analysis provides information about the component composition of the sample surface.

In the FTIR spectra of MFTIR for F4 MB samples treated with a low-temperature glow discharge plasma, there are bands specific for double bonds and conjugated double bonds of RFCF = CF_2, RFCF = CO, C_2F_3O (1400–1750 $см^{-1}$), as well as for CH_2 and CH_3 (550–700 $см^{-1}$). It leads to an increase of fluoroplastic adhesive ability to polymer binders. In addition, when calculating the adhesion bond, for example, magnesium spinel and modified fluoroplastic, in which part of $–C_2F_4–$ links are replaced with $–C_2F_3O–$ links, it turned out that the values of both chemical and van der Waals interactions are much higher than for unmodified ones. The energy of fluoroplastic – spinel chemical bond is 0.39 and 1.76 eV for unmodified and modified ones respectively, i.e. in 4.5 times larger [6]. Due to that, the processes of structure formation initiate and the mechanism of its crystallization changes [7]. Thus, there were obtained hybrid fillers with well-bound components.

The comparative tribological tests were carried out without external lubrication and with a discretely varying load (in the ranges of 209, 310, 420, 520, 620, 720, 820, 920, 1020 N) on the friction machine AI-5018 by a «finger-roller» scheme in order to assess the wear resistance of the composite material at a constant specific pressure. During the entire test time there was a continuous record of the moment of friction force on the lower shaft of the machine. After the end of the test, weight wear was measured.

Moreover, tribological tests were carried out on the end type friction machine «finger-flat disk» constructed in the laboratory. It is able to simulate the thrust sliding bearing at different loadings (from 0.3 to 10 MPa) and in a wide range of sliding speed (from 0.1 to 10 m/s).

The results of the tribological test are present in Tables 37.1 and 37.2.

Table 37.1 Weight wear of the tested composite materials at a sliding speed of 0.4 m/s and test time of 2 h («finger-roller» friction scheme), the roughness of the metal counterbody after friction

Material	Wear (g)	Coefficient of friction	Roughness R_a (μm)
Phenylone C-2	0.0458	0.4–0.34	0.513
Phenylone C-2 + F4 MB (10%)	0.0627	0.28–0.25	0.626
Phenylone C-2 + Arimid-T (10%)	0.0321	0.36–0.32	0.548
Phenylone C-2 + F4 MB (10%) + serpentinite (3%)	0.0323	0.24–0.22	0.565
Phenylone C-2 + F4 MB (10%) + spinel (3%)	0.0318	0.20–0.16	0.476
Phenylone C-2 + silver graphite (5%)	0.0311	0.19–0.16	0.467
Phenylone C-2 + Arimid-T (5%) + thermally expanded graphite (10%)	0.0291	0.21–0.15	0.433
Phenylone C-2 + Arimid-T (5%) + F4 MB (10%) + spinel (3%)	0.0297	0.22–0.19	0.439

Table 37.2 Average linear wear of polymer samples on the end type friction machine at load of 1 MPa, sliding speed of 0.5 m/s and test time of 2 h

Tested samples	Average linear wear (mm)
Phenylone C-2	0.43
Phenylone C-2 + 10% F4 MB	0.46
Phenylone C-2 + 10% Arimid-T	0.37
Phenylone C-2 + 10% F4 MB + 3% serpentinite	0.245
Phenylone C-2 + 10% F4 MB + 3% spinel	0.22
Phenylone C-2 + 10% thermally expanded graphite + 5% Arimid-T	0.15

There is an almost complete agreement between the results on the friction coefficients and the correlation of the weight and linear wear of the same composites with different tribological conjunction methods. The best results were obtained for the compositions of Phenylone C-2 + F4 MB (10%) + serpentine (3%) and, especially, for Phenylone C-2 + F4 MB (10%) + spinel (3%). It was studied the nanomodified additives effect to the composites with various nanodimensional additives, on the microrelief of the friction surface and the surface state of the metal counterbody after friction (using the surface analysis system of the interference microscope—the optical profilometer "NewView-600"). This study showed that the surface roughness value correlates with the value of the weight wear, obtained at friction by the "finger-roller" scheme (Table 37.1).

37.2.2 Study of Frictionally Transferred Phenomenon Under Influence of Nanodimensional Additives

The study of anti-friction tribopolymer film on the surface of the disk after tribomating on the end friction machine was conducted by studied by FTI method of MFTIR spectroscopy at Nicolet 380 spectrophotometer. It helped to research the influence of various factors on the formation of anti-friction tribopolymer film. These factors include changes in the test conditions, the addition of various fillers and nanoadditives to the test material. As noted above the formation of transferred film is the result of the interaction between the polymer and the metal surface. The transferred film is characterized by various thicknesses on the sample area. In transferred film often there are fragments of polymer molecules, formed in the result of the destruction of polymer composite, products of molecular oxidation, particles of the metal counterbody that are in the chemical bond with the molecular fragments of the polymer, etc. Each friction surface prepared for tests is like a shear or snapshot of the friction process at the time moment, at a certain load and relative sliding velocity. If the film thickness on tribocontact is comparable with the information depth of analysis method (0.1–3 μm), then using the infrared spectra, obtained from a large area, it is possible to view the presence of the transferred film on the tribomating surface, its composition and structural properties. The sequence of output of composite component in the transferred film, the destruction processes of polymer molecules, i.e. natural and broken bonds of atoms in the polymer molecule, etc. are reflected in these spectra.

The conclusions about these processes can be made by comparing the intensity and the energy position of the spectra lines, obtained from the friction surfaces with the spectra of initial polymer compositions. The presence and condition of the frictionally transferred film at friction with various tested composites studied under different loads and tribomating times were evaluated, based on analytical lines in the FTIR spectra of the friction surfaces.

The analysis of the obtained data shows that there is formation of a stable frictionally transferred film on the steel disk surface while tribomating the tested composite material based on Phenylone C2 for the period of 5 h at a load of 1 MPa. The introduction of nanoadditives in an amount of 1.5–3% into the initial composite leads to a significant increase of the intensity of the absorption bands (1000–1200 $см^{-1}$), i.e. increase the thickness of the film. The formation of the frictional film depends not only on the presence and concentration of nanoadditives, but also on their size. Creating composites, we selected nanoadditives with the maximum distribution of the particles sizes of 40 and 100 nm.

Figure 37.1 demonstrates FTIR spectra of the frictionally transferred films on a steel disk while tribomating with composites based on Phenylone C2.

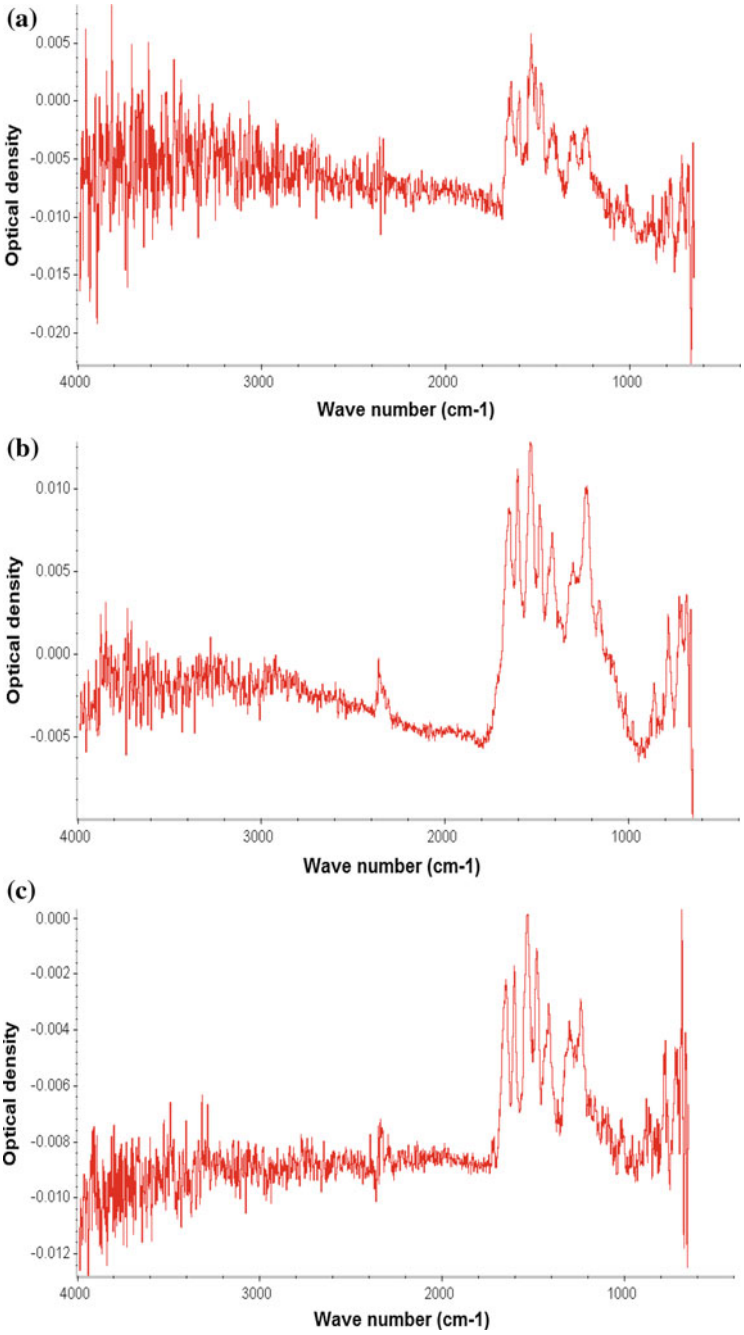

Fig. 37.1 FTIR spectra of the frictionally transferred filmson a steel disk while tribomating with composites based on Phenylone-C2: **a** phenylone C2 + 10% F4 MB, **b** Phenylone C2 + 10% F4 MB + 3% spinel Mn (40 nm), **c** Phenylone C2 + 10% F4 MB + 3% spinel Mn (100 nm)

37.3 Conclusion

The results of tribological tests and studies of the tribocontact surface allow revealing influence regularities of functional additives on the structural state of the surface layers at the nanoscale and tribophysical properties of tribosystem. It is shown the increasing of filler dispersion improves conditions of friction film formation at the tribocontact, which significantly improves tribological properties and reduces the friction coefficient up to 0.15–0.18.

Based on the above-mentioned facts we examined the possibility of regulating the wear of tribocontact surface with the selection of specific complex nanodimensional additives in composite materials and formulated the development and technology principles of creating nanocomposite polymer materials of a tribotechnical purpose. The obtained results allowed pointing out the most promising hybrid fillers to polymer composites and nanoadditives that contribute to the formation of frictionally transferred films at tribocontact.

Acknowledgements This work is supported by the Russian Science Foundation under grant 14-29-00116 and performed in Rostov State Transport University.

References

1. A.E. Mironov, I.A. Toder, J. Friction Wear **34**(5), 374 (2013)
2. S.V. Panin, L.A. Kornienko, L.R. Ivanova, S. Piriyaon, S.V. Shil'ko, Y.M. Pleskachevskii, V. M. Orlov, J. Friction Wear **32**(3), 199 (2011)
3. A.I. Burya, O.A. Naberezhnaya, V.I. Kolesnikov, N.A. Myasnikova, in *Proceedings of the XIII Russian-Chinese Symposium on New Materials and Technologie* (2015), p. 468 (in Russian)
4. V.I. Kolesnikov, Y.F. Migal, N.A. Myasnikov, A.I. Burya, F.V. Myasnikov, O. P. Chigvintseva, Vestnik RGUPS **4**, 9 (2011) (in Russian)
5. V.V. Serafimovich, V.A. Shelestova, P.N. Grakovich, in *Abstracts of the International Scientific Conference on Polymer Composites, Coatings, Films* (2003), p. 107 (in Russian)
6. V.I. Kolesnikov, YuF Migal, I.V. Kolesnikov, N.A. Myasnikova, Vestnik RGUPS **4**, 14 (2014) (in Russian)
7. A.A. Okhlopkova, S.A. Sleptsova, P.N. Petrova, S.N. Popov, Russ. J. Gen. Chem. **79**(3), 686 (2009)

Chapter 38
Polarizable Models in Molecular Dynamics for Identification of Effective Properties

A. N. Soloviev, R. U. Gruzdev, C.-Y. Jenny Lee, Hsiao-Wen Tin and C.-C. Yang

Abstract The importance of mathematical modeling of modern materials is emerged due to high cost of test samples and dependence of created samples on pre-modeling. Today scientists tend to develop such research methods that describe test samples as accurately as possible. In this chapter, we describe two highly-effective methods of molecular dynamics (MD): (i) Fluctuating charge method and (ii) Effective moduli method. The first one is used for modeling of polarization effect by combining charge equilibration with electronegativity principle. The second one is used in mechanics for identification of homogeneous materials and composites properties. Computational experiments were performed using the LAMMPS software. Test sample is a nanorod of zinc oxide. It was built on wurtzite basis cell with 8 basis atoms. COMB3 potential was chosen for its accuracy and capability of taking into account polarization effect. The sample is divided into 3 parts: loading area, "computational" area and fixation area. Our goal was to identify its piezoelectric effective constants and we used the next experiment: first we performed relaxation of the sample and then continued research with relaxation/loading periods. After each relaxation/loading stage, we computed piezoelectric effective constant using effective moduli method and after all stages were studied, we analyzed all results. We also investigated three different sizes of

A. N. Soloviev
Don State University, Rostov-on-Don, Russia

A. N. Soloviev (✉) · R. U. Gruzdev
Southern Federal University, Rostov-on-Don, Russia
e-mail: solovievarc@gmail.com

R. U. Gruzdev
e-mail: rgruzd91@gmail.com

C.-Y. Jenny Lee · C.-C. Yang
Department of Microelectronics Engineering, National Kaohsiung Marine University, Kaohsiung, Taiwan

H.-W. Tin
National Kaohsiung Marine University, Kaohsiung, Taiwan

I. A. Parinov et al. (eds.), *Advanced Materials*, Springer Proceedings in Physics 207, https://doi.org/10.1007/978-3-319-78919-4_38

the sample to detect size effect. Results of computational experiments are given in tables and diagrams and correspond to other experiments in this area. Effective constant value tends to the value of this constant for crystal with increasing the sample size, demonstrating the expected size effect.

38.1 Introduction

Molecular dynamics method is a computer simulation method for studying physical movements of atoms and molecules, and presents thus a type of *N*-body simulation. With some assumptions, it is capable to take into account polarization effect. Fluctuating charge method of LAMMPS software has shown good results, both in accuracy and computational time [1]. Zinc oxide (ZnO) nanorods of different configurations are point of interest in this paper. ZnO was chosen due to its unique properties: for example, piezoelectricity in textile fibers coated in ZnO have been shown capability to fabricate "self-powered nanosystems" with everyday mechanical stress from wind or body movements [2, 3].

Main idea of numerical experiments is to apply periods of loading/relaxation to the sample and after period of relaxation to compute efficient piezoconstant. Boundary conditions and averaging rules were grounded on effective moduli method.

By investigating samples of different sizes, we expect to calculate values of piezoconstants and detect size effect.

38.1.1 Research Purpose

We study size effect and applicability of effective moduli method for nano-scale samples with complex parameters, included into the model.

38.1.2 Research Scope

At this study, we consider following framework of the problem:

(i) the sample is ZnO nanorod;
(ii) investigation of size effect and identification of effective properties;
(iii) first relaxation duration is 30 ps;
(iv) alteration of loading/relaxation period duration to 20 ps.

38.2 Research Method

Firstly, we built ZnO sample on the wurtzite basis cell with 8 atoms:

$$a_1 = (4.34, 0, 0); \quad a_2 = (0, 7.51, 0); \quad a_3 = (0, 0, 7.08);$$
$$b_1 = (0, 0, 0); \quad b_2 = (0.5, 0.5, 0); \quad b_3 = \left(\frac{1}{3}, 0, 0.5\right); \quad b_4 = \left(\frac{5}{6}, 0.5, 0.5\right);$$
$$b_5 = (0, 0, 0.625); \quad b_6 = (0.5, 0.5, 0.625); \quad b_7 = \left(\frac{1}{3}, 0, 0.125\right); \quad b_8 = \left(\frac{5}{6}, 0.5, 0.125\right),$$

where a_i are basis vectors of elementary cell and b_i are basis coordinates of atoms in LAMMPS notation. By using the ZnO basis cell (see Fig. 38.1), we built three samples (see Table 38.1):

The structure of investigated sample is presented in Fig. 38.2.

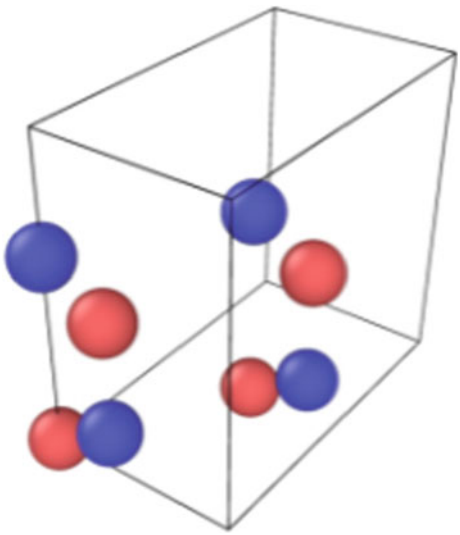

Fig. 38.1 ZnO basis cell

Table 38.1 Parameters of model samples

Rod number	Number of atoms	Sizes along the axes (Å)		
		x	y	z
1	1080	9.747	8.441	156.18
2	3000	16.245	14.068	156.18
3	5880	22.743	19.696	156.18

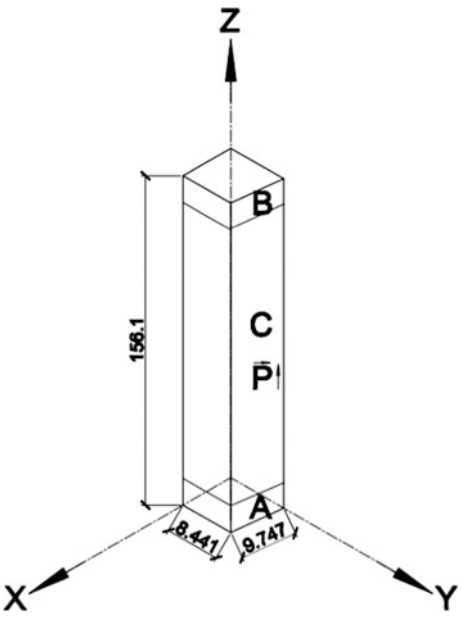

Fig. 38.2 Structure of investigated sample: A is fixation area, B is loading area, C is identification area, ***P*** is polarization vector

Since molecular dynamics simulations operate with interaction potentials, COMB3 potential was chosen for this study [4]. The total energy of a system of atoms is given as

$$E_T = \sum_i \left[E_i^{\text{self}}(q_i) + \sum_{j>i} \left[E_{\text{ij}}^{\text{short}}(r_{\text{ij}}, q_i, q_j) + E_{\text{ij}}^{\text{Coul}}(r_{\text{ij}}, q_i, q_j) \right] + E^{\text{polar}}(q_i, r_{\text{ij}}) + E^{\text{vdW}}(r_{\text{ij}}) + E^{\text{barr}}(q_i) + E^{\text{corr}}(r_{\text{ij}}, \theta_{\text{jik}}) \right],$$

where E_i^{self} is the self-energy of atom i (including atomic ionization energies and electron affinities), $E_{\text{ij}}^{\text{short}}$ is the bond-order potential between atoms i and j, $E_{\text{ij}}^{\text{Coul}}$ is the Coulomb interaction, E^{polar} is the polarization term for organic systems, E^{vdW} is the van der Waals energy, E^{barr} is the charge barrier function, and E^{corr} are the angular correction terms. Decision on using certain potential is critically important point of any MD simulation. We had chosen COMB3 potential due to several its advantages. First, it is a potential, which takes into account charges (LAMMPS variable charge potential family) and hence is suitable for simulation of polarization effects. Second, it supports the electronegativity equalization method [5] and hence is available for modeling of polarization effect by combining charge equilibration with electronegativity principle. The COMB3 potential is still under development; new versions arise with refined parametrization and new modeled materials. The current state of studying the COMB3 potential is described in Table 38.2.

Table 38.2 Current state of the investigation of COMB3 potential [6]: F—fully optimized; M—only optimized for dimer molecule; P—in progress

	O	Cu	N	C	H	Ti	Zn	Zr
O	F	F	F	F	F	F	F	F
Cu	F	F	P	F	F	P	F	P
N	F	P	F	M	F	P	P	P
C	F	F	M	F	F	M	M	M
H	F	F	F	F	F	M	M	F
Ti	F	P	P	M	M	F	P	P
Zn	F	F	P	M	M	P	F	P
Zr	F	P	P	M	F	P	P	F

First, 30 ps relaxation time period is considered to obtain initial state of the sample. After that, we use series of 20 ps loading/relaxation time periods for identification of piezo-constant.

The idea of effective moduli method consists of conduction of experiments with specific initial and boundary conditions for obtaining material properties:

$$\varepsilon_{11} \neq 0 \Rightarrow c_{11}^{E_{\text{eff}}} = \frac{\langle \sigma_{11} \rangle}{\varepsilon_{11}};\ c_{12}^{E_{\text{eff}}} = \frac{\langle \sigma_{22} \rangle}{\varepsilon_{11}};\ c_{13}^{E_{\text{eff}}} = \frac{\langle \sigma_{33} \rangle}{\varepsilon_{11}};\ e_{31}^{\text{eff}} = \frac{\langle D_3 \rangle}{\varepsilon_{11}};$$
$$\varepsilon_{33} \neq 0 \Rightarrow c_{33}^{E_{\text{eff}}} = \frac{\langle \sigma_{33} \rangle}{\varepsilon_{33}};\ c_{13}^{E_{\text{eff}}} = \frac{\langle \sigma_{11} \rangle}{\varepsilon_{33}} = \frac{\langle \sigma_{22} \rangle}{\varepsilon_{33}};\ e_{33}^{\text{eff}} = \frac{\langle D_3 \rangle}{\varepsilon_{33}};$$
$$\varepsilon_{23} \neq 0 \Rightarrow c_{44}^{E_{\text{eff}}} = \langle \sigma_{33} \rangle / 2\varepsilon_{23};\ e_{15}^{\text{eff}} = \langle D_2 \rangle / 2\varepsilon_{23};$$
$$E_1 \neq 0 \Rightarrow e_{15}^{\text{eff}} = -\langle \sigma_{13} \rangle / E_1;\ \varepsilon_{11}^{S_{\text{eff}}} = \langle D_1 \rangle / E_1;$$
$$E_3 \neq 0 \Rightarrow e_{31}^{\text{eff}} = -\langle \sigma_{11} \rangle / E_3 = -\langle \sigma_{22} \rangle / E_3;\ e_{33}^{\text{eff}} = -\langle \sigma_{33} \rangle / E_3;\ \varepsilon_{33}^{S_{\text{eff}}} = \langle D_3 \rangle / E_3;$$
$$\langle \rangle = \frac{1}{\Omega} \int ()\, d\Omega.$$

38.3 Results

After series of experiments, the next material constants were obtained (Table 38.3):

The size effect, estimated by modeling e_{33} pirzoconstant, is present in Fig. 38.3.

Table 38.3 Summary of experiments' results

Elastic modules (GPa)		Piezoconstant	
C_{11}	219	Rod number	e_{33}
C_{12}	120	1	2.21
C_{13}	104	2	1.98
C_{33}	230	3	1.88
C_{44}	51		
C_{55}	44	**Bulk crystal**	1.4

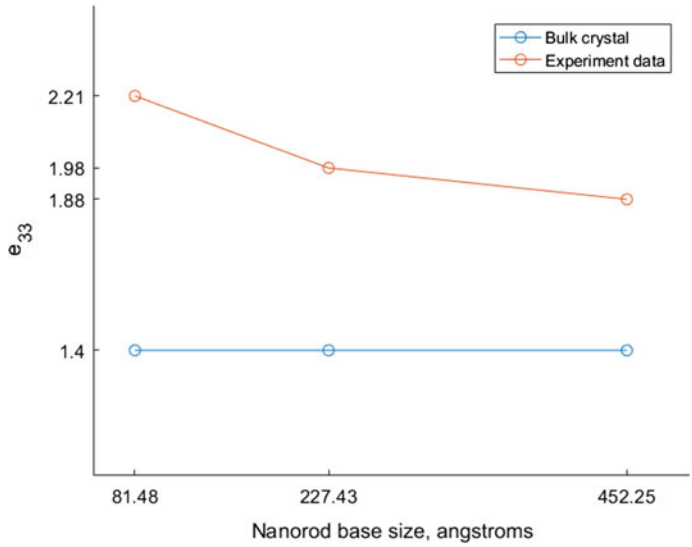

Fig. 38.3 Size effect for e_{33} pirzoconstant

38.4 Discussion and Conclusion

COMB3 potential showed good results in identification of both elastic and piezoelectric properties, corresponding to results of similar studies. The highest value of piezoconstant e_{33} is derived from the smallest sample and vice versa for the largest one. From these results, it is proved that piezoconstant tends to its bulk value, demonstrating the expected size effect.

Developed by one of the authors ACELAN (ACoustic and ELectrical ANalysis) software [7, 8] allows ACELAN-COMPOS module to work in the multiscale framework [9].

Figure 38.4 demonstrates a possibility to add almost any MD model or algorithm to ACELAN. Restrictions are related to the chosen MD solver. The nearest-future task is to add models for nanotubes modeling and atomistic finite element method framework [10].

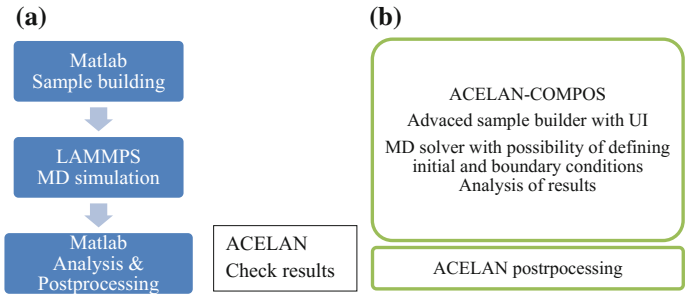

Fig. 38.4 ACELAN-COMPOS workflow: **a** current research (any algorithm/model could be added into ACELAN), **b** final version of ACELAN software

Acknowledgements This study is supported by RFBR grant No. 16-08-52013 MNT_a.

References

1. S. Plimpton, J. Comp. Phys. **117**, 1 (1995)
2. K. Brandon, *Piezoelectric Nanowires Turn Fabric Into Power Source*. Wired News. Condé Net. (2008)
3. Y. Qin, X. Wang, Z.L. Wang, Nature **451**(7180), 809 (2008)
4. T. Liang, T.-R. Shan, Y.-T. Cheng, B.D. Devine, M. Noordhoek, Y. Li, Z. Lu, S.R. Phillpot, S.B. Sinnott, Mat. Sci. Eng. **R 74**, 255 (2013)
5. S.W. Rick, S.J. Stuart, Rev. Comput. Chem. **18**, 89 (1999)
6. Pair_style comb command. (n.d.). http://lammps.sandia.gov/doc/pair_comb.html
7. A.V. Belokon, V.A. Eremeyev, A.V. Nasedkin, A.N. Solovyev, J. Appl. Math Mech. **64**(3), 367 (2000)
8. A.V. Belokon, A.V. Nasedkin, A.N. Solovyev, J. Appl. Math. Mech. **66**(3), 481 (2002)
9. Y. Efendiev, T.Y. Hou, *Multiscale Finite Element Methods. Theory and Applications. Surveys and Tutorials in the Applied Mathematical Sciences*, vol. 4 (Springer, New York, 2008)
10. H.A. Wu, G.R. Liu, X. Han, X.X. Wang, Chaos, Solitons Fractals **30**(4), 791 (2006)

Chapter 39
Evaluation of Mechanical Properties of the Two-Layer Coating Using Nanoindentation and Mathematical Modeling

E. V. Sadyrin, B. I. Mitrin, L. I. Krenev, A. L. Nikolaev and S. M. Aizikovich

Abstract The mechanical properties of the NiO–Ni two-layer coating, deposited by magnetron sputtering, on the Si substrate from the series of experiments on nanoindentation were investigated. A comparison of the experimental results with the results, obtained using the mathematical model that takes into account the internal structure of the coating was conducted. The effect of thin surface oxide film on the effective Young's modulus of the coating during nanoindentation was demonstrated.

39.1 Introduction

Deposition of thin films and coatings on surfaces of parts can significantly change the physical and mechanical properties of the details without affecting their volume. This is achieved owing to the combination of the properties of the materials constituting the coating. On the one hand, the synthesis of modern coatings is aimed at creating thinner coatings, and, on the other hand, at constructing coatings of more complex structure, such as composite (multilayer or functionally graded) coatings [1]. Coatings deposition can largely improve wear and erosion resistance, durability, protection against abrasion and corrosion, increase thermal and chemical stability, reduce friction coefficient of the construction, instrumental and other materials.

However, the adoption of composite materials into various industries is limited due to lack of research, certification and diagnostic methods of their properties, which require the development of new characterization methods. Implementation of

E. V. Sadyrin (✉) · B. I. Mitrin · L. I. Krenev · S. M. Aizikovich
Don State Technical University, Rostov-on-Don, Russia
e-mail: rainesquall@icloud.com

A. L. Nikolaev · S. M. Aizikovich
Southern Federal University, Rostov-on-Don, Russia

I. A. Parinov et al. (eds.), *Advanced Materials*, Springer Proceedings in Physics 207, https://doi.org/10.1007/978-3-319-78919-4_39

nanoindentation as a set of methods, using precise local force, applied to the material with simultaneous recording of the deformation response at nanometer resolution [2], is becoming common for these tasks. Nanoindentation is actively used to evaluate mechanical properties of single layer [3, 4] and multilayer coatings [4–7].

Nonetheless, the methodology for determining the mechanical characteristics of coatings by means of nanoindentation is not developed enough. The interpretation of the experimental results, even for homogeneous materials is associated with the need to consider a number of factors, namely: roughness and coating thickness, temperature drift, imperfect geometry of the indenter, the structural features of the material, etc. [8]. Layered coating study is complicated by the fact that the elastic properties vary by depth. In the interface between the layers, there may be a significant change of the elastic properties. The correct interpretation of the results of the layered coating indentation is only possible by methods developed on the base of mathematical models that take into account the peculiarities of the coating internal structure.

The aim of the present study is to investigate the mechanical properties of the magnetron sputtered NiO–Ni two-layer coating on the Si substrate. During the research, a series of experiments on nanoindentation was held. The comparison of the experimental results with the results, calculated using a mathematical model, which take into account the peculiarities of the internal structure of the coating, is made.

39.2 Sample Preparation

A monocrystalline Si plate was selected as a coating substrate. Before coatings deposition, the substrate was prepared in several stages by holding it in baths with the following liquids:

(i) reagent grade acetone, brought to boil,
(ii) H_2O_2, brought to boil and then cooled,
(iii) CH_3COOH, diluted with distilled water by volume of 1: 1,
(iv) deionized water,
(v) solution of 2% HF,
(vi) deionized water.

The coating was deposited by using a DC magnetron sputtering unit BH-2000 M at the voltage of 470–520 V and the constant current of 35 mA. Before the deposition, the pressure of $\sim 2 \times 10^{-5}$mbar was created in the vacuum chamber. After that, the argon admission to a pressure of $\sim 2.2 \times 10^{-1}$ mbar was held. Deposition time was 44.5 min. The distance from the target to the sample was 65 mm. Magnetron sputtering allows one to obtain the coating of high purity and homogeneity (even on large surfaces) with strong adhesion to the substrate [9]. Before the deposition,

the substrate was partially masked for the subsequent evaluation of the mechanical characteristics of the substrate.

As a result, the NiO–Ni two-layer coating was obtained. On the difference in height between the deposited coating and the substrate (which was covered with a mask), the total thickness of the coating was determined by using a Contour Elite K (Bruker, USA) 3D optical microscope (Fig. 39.1). The total thickness was ~300 nm.

To obtain the thickness of the NiO oxide thin film, the ion beam etching by using a scanning electron microscope (SEM) was carried out. As a result, the thickness of NiO film was ~50 nm (Fig. 39.2). Thus, thickness of Ni layer was ~250 nm.

The values of the mechanical characteristics of the materials, constituting the coating, were obtained from available references and preliminary experiments. These values are shown in Table 39.1 (if the reference is not pointed, this characteristic was obtained from preliminary experiments).

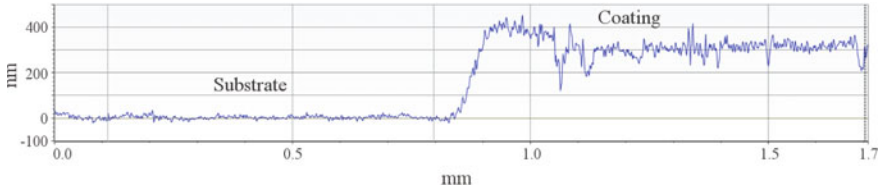

Fig. 39.1 NiO–Ni coating thickness determination

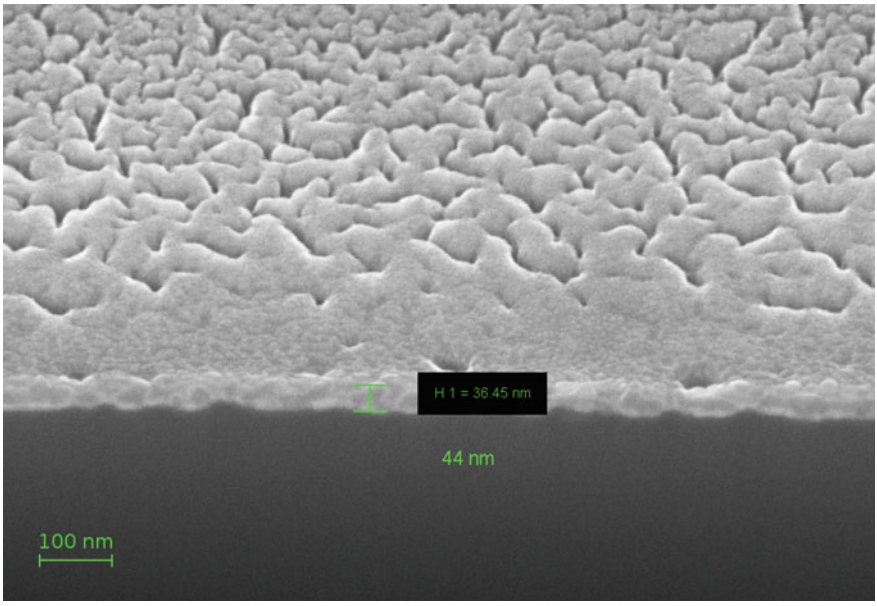

Fig. 39.2 NiO layer thickness determination

Table 39.1 Mechanical characteristics of the materials, constituting the coating

Material	Young's modulus E (GPa)	Poisson's ratio (ν)
NiO	90 [10]	0.21 [11]
Ni	203 ± 7 [12, 13]	0.31 [13]
Si	145.7 ± 2.3	0.22 [14]

It should be noted that moduli of elasticity of the materials, constituting the coating is significantly different: NiO and Ni differ in 2.2 times, Ni and Si substrate differ in 1.4 times.

39.3 Micro-Geometry Characteristics

Using an atomic force microscope (AFM) Nanoeducator (NT-MDT, Russia), the following microgeometrical characteristics of the Si substrate were obtained:

(i) maximum roughness height R_t not exceeding 25.1 nm,
(ii) average roughness R_a not exceeding 3.71 nm (Fig. 39.3).

After that, the same characteristics were obtained for the coating:

(i) maximum roughness height R_t not exceeding 18.7 nm,
(ii) average roughness R_a not exceeding 3.2 nm (Fig. 39.4).

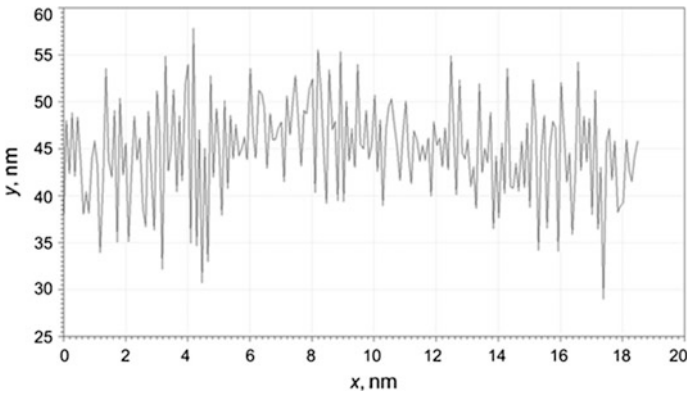

Fig. 39.3 Si-substrate surface profile

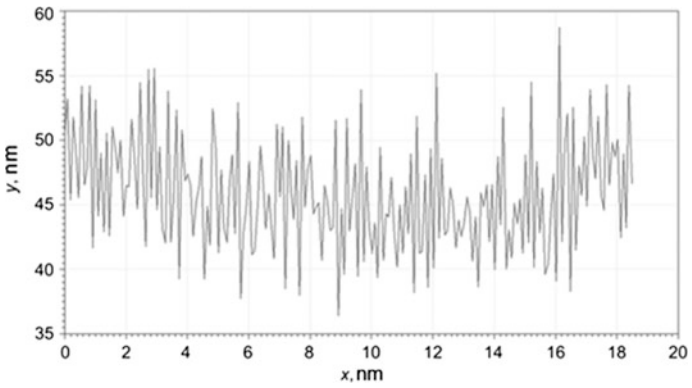

Fig. 39.4 Coating surface profile

39.4 Theory

To achieve the aims of the present research, we consider the dependence of the value of the effective Young's modulus on the indentation contact depth [2] as

$$E = \left(1 - \nu^2\right)\left(\frac{1}{E_r} - \frac{1 - \nu_i^2}{E_i}\right)^{-1}, \tag{39.1}$$

where ν and ν_i are the Poisson's ratios of the material under test and the indenter respectively; E_i is the Young's modulus of indenter; E_r is the reduced indentation modulus. The reduced modulus E_r can be calculated from the formula:

$$E_r = \frac{S\sqrt{\pi}}{2\beta\sqrt{A_c}}, \tag{39.2}$$

where A_c is the projected area of the print on the plane normal to the pressing force; S is contact stiffness; β is adjusting coefficient, proposed by King [15] to account for the influence of the shape of the indenter on the contact stiffness in elastic contact of material with rigid non-spherical indenters (for Berkovich indenter $\beta = 1.034$ [16]). The experimental values of the effective Young's modulus were determined by using the Oliver and Pharr method [2] from the analysis of the unloading part of the force—displacement curve.

Due to the spherical blunting of the Berkovich indenter tip, it is possible to use a spherical indenter mathematical model for the simulation of indentation at small depths. For the theoretical calculation of the Young's modulus as a function of indentation depth, we apply the solution of the elasticity theory for contact problem on the penetration of a rigid spherical indenter into an elastic coating inhomogeneous by depth. The coating is coupled with a homogeneous elastic half-space [17].

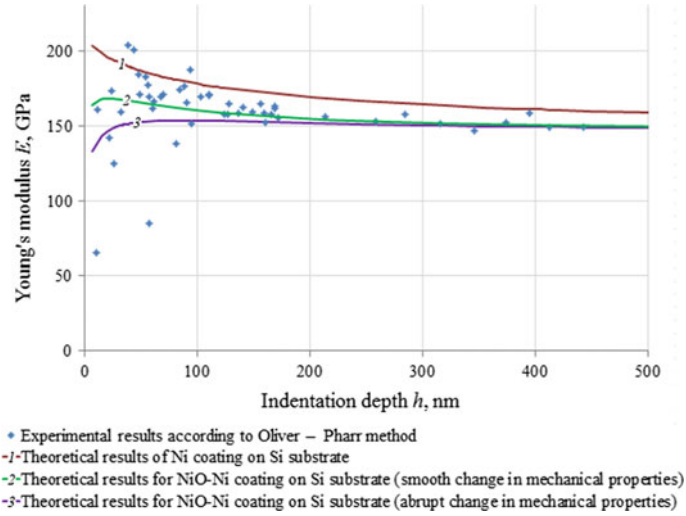

Fig. 39.5 Comparison of experimental and theoretical results

On the base of assumptions about the rigidity and the spherical shape of indenter, we selected for modeling results: $E_r = E$ and $\beta = 1$.

Theoretical curves, demonstrating dependence of Young's modulus on contact depth for the elastic spherical indenter, which penetrates into Ni–Si and NiO–Ni–Si structures, are shown in Fig. 39.5.

39.5 Experimental Details and Results

For the experimental investigation of the mechanical properties of coating, a Nano Test 600 (Micro Materials, UK) for nanoindentation testing was used. During all the experiments, a functional block "Nanotest", allowing one to apply the load from 0.01 mN up to 500 mN, was connected. The device was equipped with a chamber, in which the temperature is kept constant (during all the experiments it was equal to 27.5 °C). The test unit was situated on the antivibration table with an air bag. In all the experiments, the Berkovich indenter with the diamond tip was used. Radius of curvature of the indenter tip was $\sim$100 nm.

Experiments were conducted with the load range from 0.1 up to 75 mN. "Loading—holding—unloading" time was equal to 30 s for each of the stages. The approach speed of the indenter to surface was 20 nm/s. Special experimental mode was applied for the registration of the thermal drift. This mode comprises the hold period of the indenter for 60 s under the constant load at the beginning of the loading and at the end of the unloading. Correction of the thermal drift was performed by using the software of the nanoindentation test unit.

The values of effective Young's modulus, depending on the contact depth, obtained in the each experiment are plotted in Fig. 39.5 with dots. The dependences of the effective Young's modulus on the contact depth for the elastic spherical indenter, penetrating into Ni–Si (curve 1) and NiO–Ni–Si (curve 2 and 3) structures, are demonstrated. The curve 3 is plotted for abrupt change of the mechanical properties between NiO and Ni layers, while the curve 2 corresponds to smooth change of the mechanical properties between these layers.

Analysis of the experimental and theoretical results allows one to establish the following:

(i) smooth change of the mechanical properties between NiO and Ni layers (curve 3), taken into account in mathematical modeling, better corresponds to the experimental data; the results, presented below, relate to this case;
(ii) theoretical dependences for the Ni and NiO–Ni coatings differs significantly throughout the load range;
(iii) experimental results correspond to the theoretical curve for the NiO–Ni coating; it confirms the hypothesis about the influence of the oxide film on the indentation experiment results;
(iv) the effective values of Young's modulus (both experimental and theoretical for NiO–Ni coating), depending on the indentation depth, may differ significantly from the values for Ni. In this case, application of the standard approach, namely indentation to a depth of $\leq 10\%$ on the coating thickness (ISO 14577—1:2015), will lead to the erroneous results in determining the elastic modulus of the Ni coating.

39.6 Conclusions

Theoretical calculations and experimental results have shown that the presence of the thin oxide film significantly affects the deformation response of the coating. Studying the coating structure and mathematical modeling of indentation process is crucial for accurate determination of the mechanical properties of thin coatings by means of nanoindentation. It is important with viewpoint of the possibility that an oxide film might form on the sample (particularly in experiments at elevated temperatures [18]).

Acknowledgements This work was supported by the Russian Foundation for Basic Research grants Nos. 15-07-05820-a, 17-08-01253-a and the Russian Ministry of Education and Science (grant No. 9.1481.2017/4.6). Aizikovich S. M. acknowledges the Russian Ministry of Education and Science for grant No. 9.4761.2017/6.7 in the framework of Government Assignment. Authors appreciate Vinitskaya A.M. for providing English language help. The AFM study and nanoindentation of the sample were conducted in the Collective Resource Center of REC "Materials" of DSTU (http://nano.donstu.ru). The sample preparation and coating deposition were performed in the Scientific and Research Laboratory of Nanomaterials in the I. I. Vorovich Mathematics, Mechanics and Computer Sciences Institute of the Southern Federal University.

References

1. S.M. Aizikovich, V.M. Alexandrov, A.S. Vasiliev, L.I. Krenev, I.S. Trubchik. *Analytical Solutions of Mixed Axisymmetric Problems for Functionally-Graded Media*, (Fizmatlit, Moscow, 2011), 192pp (in Russian)
2. Yu.I. Golovin. *Nanoindentation and Its Possibilities*, (Mashinostroenie, Moscow, 2009), 312 pp (in Russian)
3. T.H. Fang, S.R. Jian, D.S. Chuu, Appl. Surf. Sci. **228**(1), 365 (2004)
4. I.G. Goryacheva, E.V. Torskaya, Y.V. Kornev, I.N. Kovalyova, N.K. Mishkin, Frict. Wear **36** (3), 262 (2015). (in Russian)
5. O.V. Kudryakov, V.N. Varavka, Inorg. Mater. **51**(15), 1508 (2015)
6. V.N. Varavka, O.V. Kudryakov, A.V. Ryzhenkov, In: *Piezoelectrics and Nanomaterials: Fundamentals, Developments and Applications*. ed. by I.A. Parinov, (Nova Science Publishers, New York, 2015), p. 105
7. O.V. Kudryakov, V.N. Varavka, V.V. Ilyasov, J. Phys: Conf. Ser. **857**, 1 (2017)
8. Yu.V. Kornev, O.V. Boyko. *Vestnik of Lobachevsky State University of Nizhni Novgorod*. **2** (4), 473 (2011) (in Russian)
9. S. Swann, Phys. Technol. **19**, 67 (1988)
10. J.E. Keem, J.M. Honig. *Selected Electrical and Thermal Properties of Undoped Nickel Oxide* [CINDAS Report], **52**, 72pp. (1970)
11. M.A. James, F.C. Voogt, O.C. Rogojanu, L. Niessen, S.S. Saxena, W. Eerenstein, T. Hibma, G.A. Sawatzky, Bullt. Stefan Univ. **11**(15), 359 (1999)
12. M.E. Dritz, *Properties of Elements*, (Metallurgia, Moscow, 1985), 672pp (in Russian)
13. J.M. Gere, S.P. Timoshenko, *Mechanics of Materials*. (PWS Pub. Co., Boston, 1997), 912pp
14. J. Dolbow, M. Gosz, Mech. Mater. **23**, 311 (1996)
15. R.B. King, Int. J. Sol. Struct. **23**(12), 1657 (1987)
16. W.C. Oliver, G.M. Pharr, J. Mater. Res. **7**(6), 1564 (1992)
17. S.M. Aizikovich, V.M. Alexandrov, I.S. Trubchik, L.I. Krenev, Dokl. Phys. **53**(1), 29 (2008)
18. E.V. Sadyrin, L.I. Krenev, B.I. Mitrin, I.Y. Zabiyaka, S.M. Aizikovich, S.O. Abetkovskaya, In: *Proceedings of the 2015 International Conference on Physics and Mechanics of New Materials and Their Applications*, 2016, eds. by I.A. Parinov, S.-H. Chang, V.Y. Topolov (Nova Science Publishers, New York, 2016), p. 331

Part IV
Applications of Advanced Materials

Chapter 40
Benchmark Analysis of a Helmholtz Resonator for Estimating Acoustic Metamaterial Properties

Karisma Mohapatra and D. P. Jena

Abstract Acoustic metamaterial gets significant attention due to possibility in control, direct and manipulate sound waves. Various metamaterial models have been proposed mostly for air medium, however applicable to water medium for cloaking purpose. Control of the various forms of sound waves is possible with a negative refractive index material, mostly accomplished through bulk modulus and density of the material. However, in case of acoustic metamaterial, the shapes and structures play vital role in accomplishing the same. Present research focuses in analysing the most known acoustic structure, Helmholtz resonator, to estimate the metamaterial properties such as effective mass density and effective bulk modulus. The transfer matrix of Helmholtz resonator is used to extract the scattering matrix, which is subsequently used to estimate the effective bulk modulus and effective mass density. Next, a finite element analysis (FEA) has been carried out using two-load boundary condition to estimate the transfer matrix, validated against experimental results. In a similar manner, the effective mass density and effective bulk modulus have been extracted and validated against analytical results. Moreover, two Helmholtz resonators separated with a known duct have been analysed to evaluate the applicability of transfer matrix method in estimating acoustic metamaterial properties. All analytical results have been validated against numerical results for air medium.

40.1 Introduction

Metamaterial is a recent trend in material science, in general, is not available in nature due to its uncommon material properties in an effect can manipulate the conventional laws of physics. If we talk about specifically acoustic metamaterial, we can say that using such materials the sound wave gets manipulated as an

K. Mohapatra · D. P. Jena (✉)
Industrial Acoustics Laboratory, Department of Industrial Design,
National Institute of Technology, 769008 Rourkela, India
e-mail: jenad@nitrkl.ac.in

I. A. Parinov et al. (eds.), *Advanced Materials*, Springer Proceedings
in Physics 207, https://doi.org/10.1007/978-3-319-78919-4_40

outcome bending and twisting phenomena can be introduced. Metamaterials can be classified with zero or negative refractive index. The refractive index can be controlled by controlling the effective mass density or effective bulk modulus or both in case of acoustic metamaterial. Various acoustic metamaterial patterns have been introduced and reported till date to demonstrate the possibilities of such phenomena which is really uncommon in nature [1–10].

In present work, the possibilities of estimating acoustic metamaterial properties from electro-acoustic modelling is investigated [1]. In line with the objective, the most classical acoustic filter such as a Helmholtz resonator has been taken for analysis. First the analytical technique has been used to estimate the transfer matrix followed by extraction of effective mass density and effective bulk modulus [1, 4]. Subsequently, an array of Helmholtz resonator, specifically, two different Helmholtz resonators separated by a duct have been analysed. The report demonstrates the potential of analytical modelling, potential of numerical modelling of the experiment defined by ASTM E2611 to extract the transfer matrix which is subsequently used in estimating the metamaterial properties. However, it can be noticed that the acoustic metamaterial properties such as negative bulk modulus and negative mass density are estimated by using transfer matrix, which is very essential to extract transmission and reflection coefficient.

40.1.1 Research Purpose

The present research aims to extract the reflection and transmission coefficients of a Helmholtz resonator using analytical or transfer matrix method. The estimated reflection and transmission coefficients will be used to extract the effective mass density and effective bulk modulus. The estimated results will be judged against the numerical results.

40.1.2 Research Scope

At this study, we consider the following observations of the problem:

(i) benchmarking of Helmholtz resonator;
(ii) extracting the metamaterial properties such as effective mass density and effective bulk modulus;
(iii) Helmholtz resonator and two Helmholtz resonators separated by a duct have been investigated by analytically, numerically and experimentally.

40.2 Analytical Modelling

Helmholtz resonator is a kind of classical acoustic filter, more specifically a passive acoustic band stop filter, which is modelled analytically with electro-acoustic modelling theory using the empirical model to estimate the lumped acoustic impedance of the resonator [1]. In general, it is essential to get transfer matrix of any acoustic filter to estimate corresponding acoustic properties. As the focus of the work is to understand the behaviour of a Helmholtz resonator from metamaterial prospective, we first try to model the resonator of a given dimension. The analytically extracted transfer matrix is subsequently used to estimate the acoustic transmission loss of the given resonator and two resonators separated by a duct. Mathematically, the corresponding transfer matrix for resonators, shown in Fig. 40.3c, b, can be written as

$$\begin{cases} TM^1 = TM_{duct-1} \times TM_{HR-1} \times TM_{duct-2} \\ TM^2 = TM_{duct-1} \times TM_{HR-1} \times TM_{duct-2} \times TM_{HR-2} \times TM_{duct-3} \end{cases} \tag{40.1}$$

The transfer matrix of any acoustic duct (TM_{duct}) in liner acoustics can be modelled using duct radius (d_r), and duct length (l_r). In a similar fashion, the lumped system can also be modelled for any Helmholtz resonator, TM_{HR}, using the geometrical parameters such as cavity volume (V_c), neck radius (r_n), and length (l_n). Mathematically it can be written [1–3] as

$$TM_{duct} = \begin{bmatrix} \cos(kl_r) & -j\,Y_r \sin(kl_r) \\ -j/Y_r \sin(kl_r) & \cos(kl_r) \end{bmatrix}, \quad \text{where} \quad Y_r = c/\pi d_r^2, \tag{40.2}$$

and

$$TM_{HR} = \begin{bmatrix} 1 & 0 \\ Z_{HR}^{-1} & 1 \end{bmatrix}, \quad \text{where} \quad \begin{cases} Z_{HR} = j\left\{ w\frac{l_{eq}}{S_n} - \frac{c^2}{wV_c} \right\} + \frac{w^2}{\pi c^2} \\ leq = l_n + 1.7r_n, \text{(neglecting thickness)} \end{cases} \tag{40.3}$$

In above expressions, w is the frequency in radian, c is the speed of sound and k is the wave number.

40.3 Extraction of Metamaterial Properties

Now, using aforementioned electro-acoustic modelling, the transfer matrix of any acoustic filter can be presented as mentioned below. The upper subscript '1' and '2' stands for two different acoustic filter configurations, shown in Fig. 40.3c, b:

$$TM^1 = \begin{bmatrix} TM_{11}^1 & TM_{12}^1 \\ TM_{21}^1 & TM_{22}^1 \end{bmatrix}, \quad \text{and} \quad TM^2 = \begin{bmatrix} TM_{11}^2 & TM_{12}^2 \\ TM_{21}^2 & TM_{22}^2 \end{bmatrix} \tag{40.4}$$

The effective acoustic metamaterial properties such as acoustic impedance (Z_{eff}) and refractive index (n_{eff}) can be extracted using reflection coefficient of the acoustic filter (R) and transmission coefficient of the filter (T) as mentioned below [4]:

$$\begin{cases} K_{eff}/K_0 = n_{eff}/Z_{eff}, \quad and \quad \rho_{eff}/\rho_0 = n_{eff}Z_{eff} \\ Z_{eff} = \frac{r}{1-2R+R^2-T^2}, \quad \text{and,} \quad n_{eff} = \frac{-j\log x + 2\pi m}{kd}, \\ \text{where} \quad r = \pm\sqrt{(R^2 - T^2 - 1)^2 - 4T^2}, x = \frac{1-R^2+T^2+r}{2T} \end{cases} \tag{40.5}$$

In order to extract the aforementioned properties, the reflection coefficient (R) and transmission coefficient (T) are essential which can be extracted from the corresponding transfer matrix using below mathematical relations [5]:

$$R = \frac{T_{11} - \rho c T_{21}}{T_{11} + \rho c T_{21}}, \quad \text{and} \quad T = \frac{2e^{jkd}}{T_{11} + T_{12}/\rho c + \rho c T_{21} + T_{22}} \tag{40.6}$$

The transmission loss can be estimated as

$$TL = 20 \log 10\left(\frac{1}{T}\right) \tag{40.7}$$

40.4 Numerical Modelling

From design prospective numerical modelling is essential, particularly, from industrial prospective. In line with this, first a Helmholtz resonator configuration is taken from literature for analysis as shown in Fig. 40.1a [6]. The modelling and analysis has been carried out in COMSOL platform, which is a boundary element method (BEM) based software. The analyses, mimicking two source experiment ASTM E2611, have been carried. The sound pressure from four different microphone positions (m_1 to m_4 mentioned in Fig. 40.1 have been used to extract the corresponding transfer matrix following ASTM E2611 standard. The perfectly matched layer (PML) has been used at outlet to simulate the non-reflecting boundary condition).

The corresponding results such as real part of effective mass density ratio and effective compressibility ratio, extracted using aforementioned equations, are shown in Fig. 40.2. It can be noted that if outlet is modelled by applying characteristic acoustic impedance, $Z_{air} = \rho c$, as boundary conditions, the same fact also is observed. Analysing results, it can be concluded that the analytical result agrees adequately with numerical result. So now we can do further analyses using above

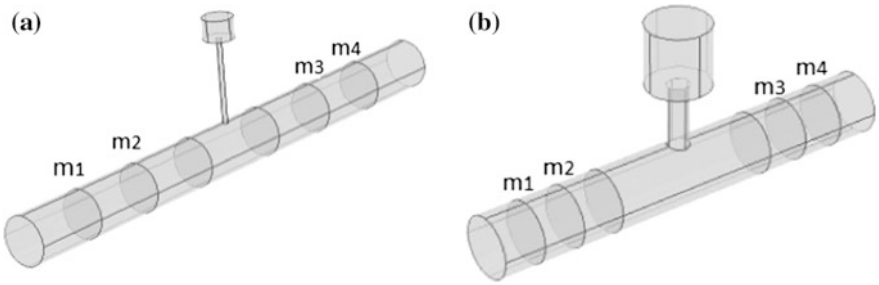

Fig. 40.1 Numerical model of Helmholtz resonators; **a** Helmholtz resonator from literature [6], and **b** experimental Helmholtz resonator

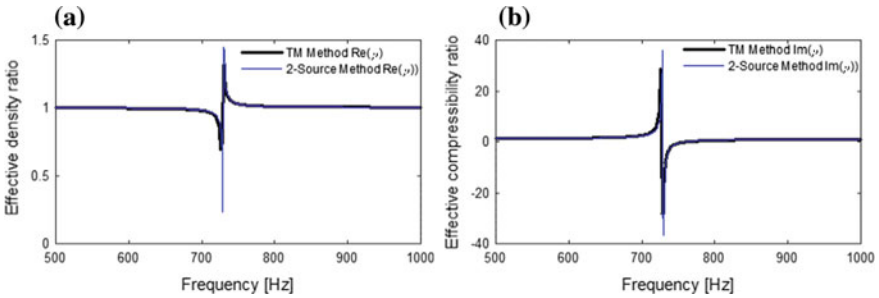

Fig. 40.2 **a** Effective mass density ratio, and **b** effective compressibility ratio of Helmholtz resonator [6]

said technique to understand the response of a single Helmholtz resonator and two Helmholtz resonators, separated by a duct, in detail from acoustic metamaterial point of view.

40.5 Experiment

So as to authenticate the analytical modelling, subsequently, a Helmholtz resonator and two Helmholtz resonators, separated by a duct, have been fabricated using 3D printing for experimental investigation as shown below in Fig. 40.3. The neck radius, neck length, and cavity radius of Helmholtz resonators are 5, 30, and 15 mm, respectively. However, the cavity length of smaller one is 30 mm and the larger one is 37.5 mm and the duct length attached to each resonator is 80 mm, where the resonator is mounted on the mid of the duct. The experiments have been conducted with a B&K© make transmission loss tube and corresponding results against analytical results have been shown in Fig. 40.4. From experiments, the potential of transfer matrix method again gets re-established through adequate agreement with experimental results, which motivate us for further investigation.

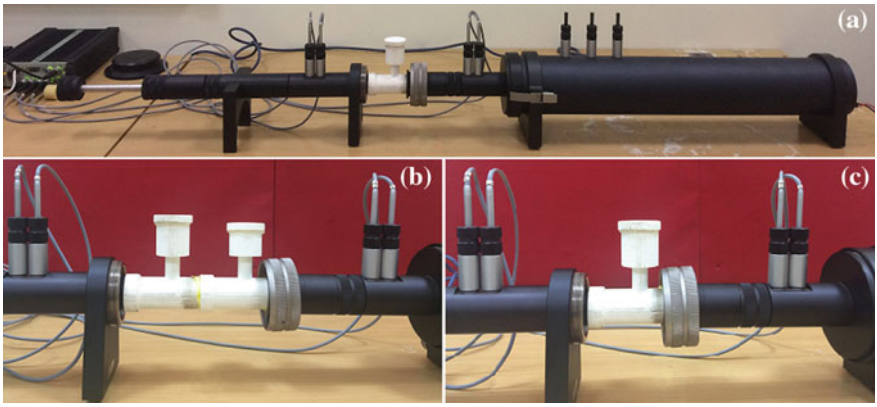

Fig. 40.3 Experimental test setup; **a** B&K© make transmission loss tube, **b** two Helmholtz resonators, separated by a duct, and **c** single Helmholtz resonator, fitted in test setup (the experiments have been carried out at IIT Bhubaneswar)

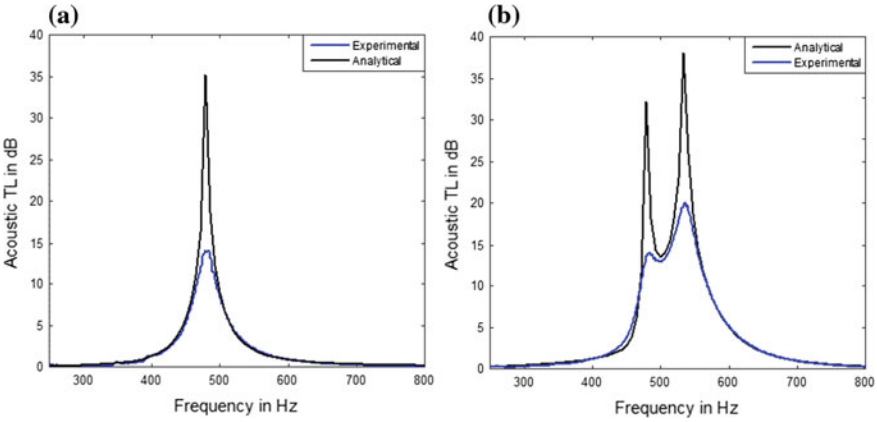

Fig. 40.4 Acoustic transmission loss of Helmholtz resonators; **a** single Helmholtz resonator, **b** two Helmholtz resonators, separated by a duct

40.6 Results and Discussion

Now, the objective is to understand the possibilities of estimating effective material properties of a Helmholtz resonator and an array using linear electro-acoustic modelling. Accordingly, first the transfer matrix of the single Helmholtz resonator has been estimated. The transmission and reflection coefficients have been extracted using aforementioned (40.6).

Subsequently, those coefficients have been used in (40.5) for estimating the effective material properties. In a similar fashion, the numerical model as discussed

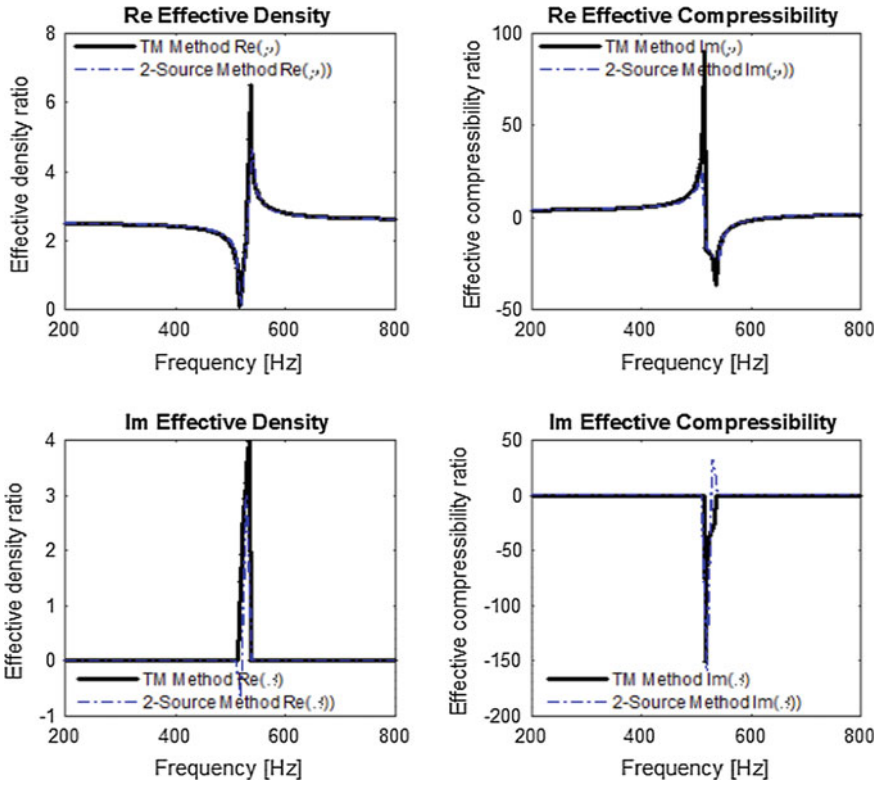

Fig. 40.5 Effective metamaterial properties of a single Helmholtz resonator ("Re" stands for real part and "Im" stands for imaginary part)

earlier has been analysed to estimate the transfer matrix using two source conditions. The numerically extracted transfer matrix has also been processed using aforesaid equations to estimate the effective material properties. The corresponding results have been shown in Fig. 40.5.

In a similar fashion, the array of Helmholtz resonators has also been analysed. The corresponding analytical and numerical results have been shown in Fig. 40.6. From above analyses, it can be noticed that in the case of single Helmholtz resonator, the real part of compressibility only gets negative in resonant frequency. However, in the case of array the real part of both effective mass and compressibility get negative. The effect may be justified with the phenomena of resonance considering the array as a single meta-atom.

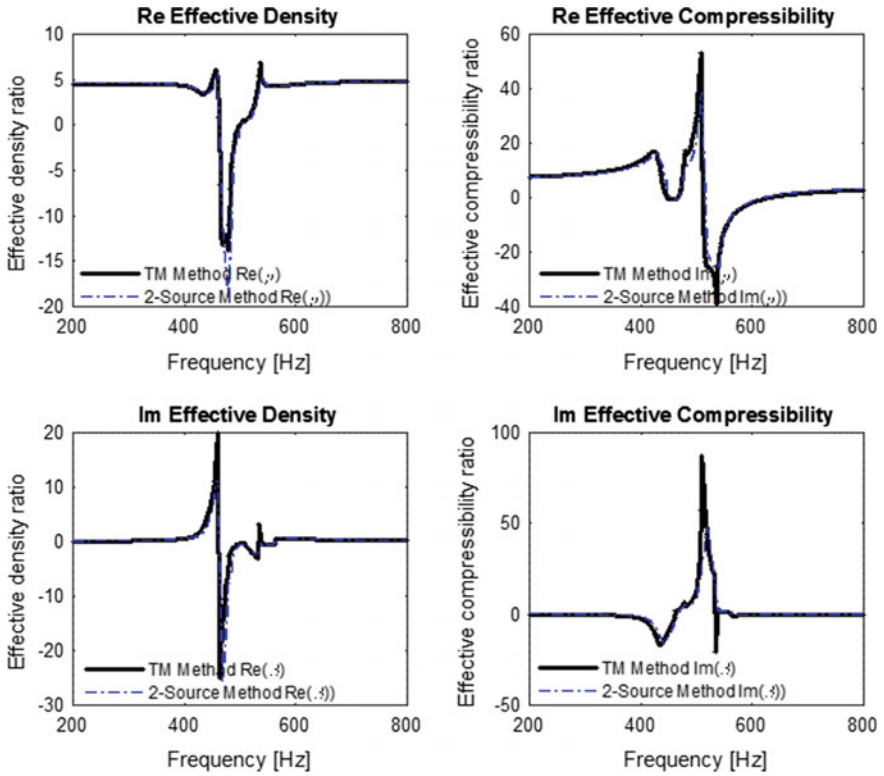

Fig. 40.6 Effective metamaterial properties of two Helmholtz resonators, separated by a duct ("Re" stands for real part and "Im" stands for imaginary part)

40.7 Conclusion

From experimental analyses, it is re-established that the linear acoustic modelling can be used to extract almost accurate transfer matrix of an acoustic filter. Moreover, it can be noticed that the corresponding transfer matrix can be used to extract the transmission and reflection coefficient to estimate the effective acoustic metamaterial properties such as effective mass density and effective compressibility or bulk modulus. The numerical and analytical results agree to each other adequately. The above report also may be perceived that the layers of acoustic metamaterial is possible to model using corresponding transfer matrix, based on linear electro-acoustic modelling theory, if the impedance of the meta-atom is known. Last but not the least, the potential of numerical technique, mimicking experiment of two source method defined by ASTM E2611, has been demonstrated to be effective in estimating the effective metamaterial properties in case of unknown metamaterial which is essential from industrial design prospective.

Acknowledgements Authors want to acknowledge their gratitude to IIT Bhubaneswar and Prof. S.N. Panigrahi for providing facilities for analyses and executing experiments. Authors also want to acknowledge the Funding source NRB-380/MAT/16-17 and SERB- ECR/2016/001131.

References

1. M.L. Munjal, *Acoustics of Ducts and Mufflers*, 2nd edn. (Wiley, Hoboken, NJ, 2014)
2. D.R. Smith, D.C. Vier, T.H. Koschny, C.M. Soukoulis, Phys. Rev. E **71**, 036617 (2005)
3. *Handbook of Noise and Vibration Control*, ed. by M.J. Crocker (Wiley, Hoboken, NJ, 2007)
4. V. Fokin, M. Ambati, C. Sun, X. Zhang, Phys. Rev. B **76**, 144302 (2007)
5. ASTM E2611, *Standard Test Method for Measurement of Normal Incidence Sound Transmission of Acoustical Materials Based on the Transfer Matrix Method* (2009)
6. N. Cselyuszka, Novel metamaterial structures for non-conventional propagation of acoustic waves, Ph.D. thesis, University of Novi Sad Faculty of Technical Sciences Novi Sad (2015)
7. S.A. Cummer, J. Christensen, A. Alù, Nat. Rev. Mater. **1**, 16001 (2016)
8. Z. Liu, X. Zhang, Y. Mao et al., Science **289**, 1734 (2000)
9. M. Ambati, N. Fang, C. Sun, X. Zhang, Phys. Rev. B **75**, 195447 (2007)
10. J. Li, C.T. Chan, Phys. Rev. E **70**, 055602(R) (2004)

Chapter 41
Thermoelectric Converter Based on Metal–Dielectric–Semiconductor–Metal Structures and Its Experimental Investigation

G. Ya. Karapetyan and I. A. Parinov

Abstract The thermoelectric converter of field-effect transistor type, based on metal–dielectric–semiconductor–metal (MDSM) structures, is proposed, in which a thermal energy transforms into the potential energy of a charged gate capacitor. Experiments with field-effect transistors in a circuit with diodes were performed upon the action on the circuit a sinusoidal electric signal with bias. The excess of the power, released to the elements of the circuit, over the power consumption by tens of percents was obtained, which in a whole confirms the correctness of the proposed concept of the conversion of heat into electricity.

41.1 Introduction

The state of the art in the field of thermoelectric conversion is described in the reviews [1, 2], in which the principle of thermoelectric conversion is not questioned and assumes mandatory presence a heater and a refrigerator. From this principle of thermoelectric conversion it follows that the presence of thermal conductivity substantially reduces the efficiency of the thermoelectric conversion, since some of the heat passes unhindered from the hot end to the cold end, without being converted to electric energy.

For many decades until the end of the last century, the properties of thermoelectric materials on the dimensionless quality parameter ZT were at the level of ~ 1, which corresponds to efficiency of about 5% when used in practical devices. The main reserve for further increase in ZT is the decrease in the thermal conductivity of the material. In this direction, the most active research has been conducted recently. Physically, this means that it is possible to create in a solid such heterogeneities that would be effective for phonon scattering, reducing their mean

G. Ya. Karapetyan (✉) · I. A. Parinov
I. I. Vorovich Institute of Mathematics, Mechanics and Computer Sciences, Southern Federal University, 344090 Rostov-on-Don, Russia
e-mail: jorichkaka@yandex.ru

I. A. Parinov et al. (eds.), *Advanced Materials*, Springer Proceedings in Physics 207, https://doi.org/10.1007/978-3-319-78919-4_41

free path and, consequently, thermal conductivity, and at the same time, practically do not affect the scattering of charge carriers, would not change their mobility, and hence the electrical conductivity. The creation of materials with strong phonon scatterers is based on the filling of interstices (micropores) of the initial crystal—matrix by heavy atoms, the effective radius of which is smaller than the micropore radius. It ensures their weak coupling with the matrix and the appearance of large anharmonicity of local oscillation modes. This makes it possible to improve the transformation of the heat flux into electrical energy in the manufacture of branches of the thermal element of *p*- and *n*-types in the form of solid solutions containing magnesium, silicon, lead, and barium, and also one or more additional alloying materials [3]. Thanks to careful selection of the concentrations of these impurities, it was possible to obtain an extremely small value of the thermal conductivity, equal to 0.002 W/(cm K). This is reasonably expected to lead to an increase in the thermoelectric quality index ZT to a level of the order of 3 at room temperature.

As noted in [1, 2], thermoelectric studies attracted a significant attention only with the advent of new concepts and theories aimed at controlling the transfer of electrons and phonons in nanostructures and bulk materials. For example, it was shown in [4] that double quantum dots can be used in thermoelectric generators using different quantum dots as *n*- and *p*-branches. The research of quantum points was also performed in [5, 6]. For example, it was shown in [7] that in pores with a size of 20 nm in SiGe crystals, it was possible to increase the value of ZT to 1.4, while pores of about 1 μm size almost do not affect the thermal conductivity of the crystals. In [8], nanoporous graphene was considered, in which it was possible to significantly reduce the thermal conductivity to 0.9 W/(m K), i.e. reduce thermal conductivity by 5000 times.

The results of modern studies of thermoelectric converters show that it is possible to obtain electric energy not only in the presence of a temperature difference, but also in its absence. For example, a thermoelectric transducer, based on samarium sulphide, was proposed in [16], which started to generate a voltage at uniform heating above 150 °C (without creating a temperature gradient). At the same time, it cooled absorbing heat from environment. With this purpose, a gradient of samarium ion concentration was created in the samarium sulphide crystal perpendicular to the electrodes on which the voltage was measured. Such a generator produced an electric voltage in the form of short pulses, the occurrence of which took place randomly. This process did not allow the summation of the values of electrical voltages of several connected in series converters and thereby one to increase their summary power.

Recently, papers [9, 10] have also appeared, in which an AC design was proposed for a thermoelectric cooler that had not a hot end; it only works for cooling. However, it can work only at helium temperatures, where superconductivity of aluminum is possible, which is a significant drawback. Thus, above discussion shows, that at present all thermoelectric converters use a temperature difference for their work. Those converters that can work without the presence of temperature difference (gradient) either do not allow us to obtain the necessary power, or operate at very low temperatures.

The proposed in the paper thermoelectric transducer based on MDSM structures will also operate without a temperature difference, but at room temperatures and above. Moreover, it will produce a constant voltage or in the form of periodic pulses, which will allow the summation of voltages from several such converters to increase power. Therefore, it has a significant novelty and can make a great contribution to the scientific foundations of thermoelectric conversion. It can be argued that the thermoelectric transducer proposed by us, to some extent, simulates the situation that occurs in a single-electron cooler: electrons carry heat from the semiconductor substrate during the discharge–charging cycle of the gate capacitor.

41.2 Main Conception

The semiconductor thermoelectric converter of the field-effect transistor type, based on metal–dielectric–semiconductor–metal (MDSM) structures (see Fig. 41.1), was proposed in [11–13]. It should generate a voltage not in the form of random pulses, but in the form of a constant or alternating voltage with a stable phase. This allows one to summarize the generated voltages and increase electric power. These studies showed that during charging a gate capacitor by using an external battery, the thermal energy, absorbed at the junction "bottom electrode–semiconductor substrate", converts into the potential energy of the charged capacitor. The electric

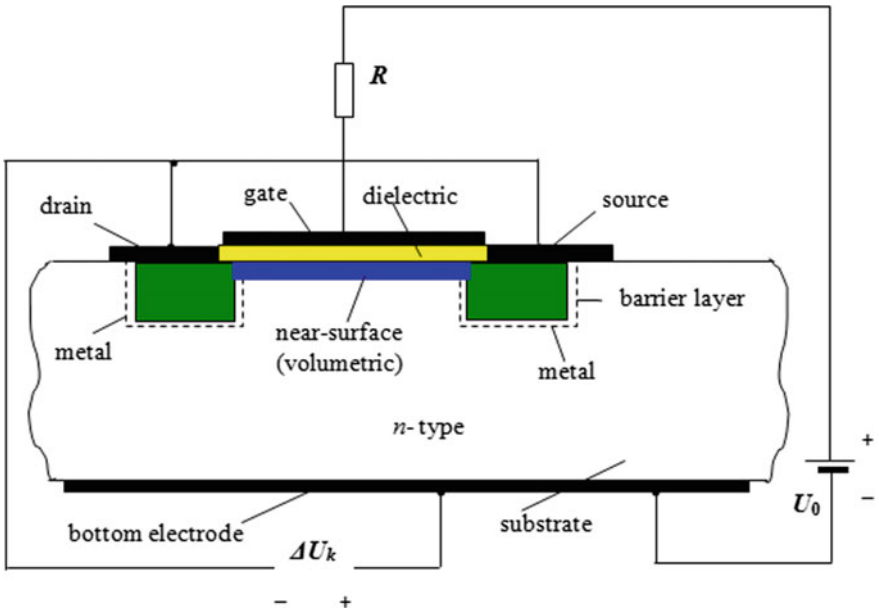

Fig. 41.1 MDSM structure

potential of a near-surface charge is equal to the electric potential of the semiconductor substrate (see Fig. 41.1). The concentration of electrons in the near-surface charge is far higher than into volume of the substrate.

The electric potential of the near-surface charge should be greater than the voltage U_0 of the battery charging the gate capacitor by the value of the potential barrier $U_k = (E_c - E_F)/e$. Here E_c is the energy at the bottom of the conduction band, E_F is the Fermi energy and e is the charge of electron. This is due to electrons overcome the potential barrier by absorbing the thermal energy at the junction "bottom electrode–substrate" (Fig. 41.1). Therefore, the energy of a charged capacitor is greater than the energy, obtained from the battery, by an amount $C_g U_0 U_k$ (where C_g is the capacitance of the gate capacitor) [12]. In this case, the potential of the near-surface charge is not U_0, but $U_0 + U_k$. Then the bottom of the conduction band in the near-surface charge will be disposed at the same level as in the semiconductor volume (Fig. 41.2). At the same time, the electron concentration in the near-surface charge will be far higher than in the bulk of the semiconductor.

Since the electron concentration depends on the difference between the bottom of the conduction band, and it is larger when the difference is lower [14], but the bottom of the conduction band does not bend, then this leads to the fact that the Fermi level in the near-surface charge zone is bent (Fig. 41.2). Therefore, this Fermi level of the near-surface charge differs from the Fermi level in the semiconductor substrate and, correspondingly, from the Fermi level in the bottom electrode. The latter level is equal to the Fermi level in the substrate due to thermodynamic equilibrium. In the area of the near-surface charge, the conditions are not satisfied for thermodynamic equilibrium, but only for electrostatic one, which does not coincide with the thermodynamic equilibrium. It leads to above-mentioned bending the Fermi level (see Fig. 41.2) [13].

The electric potential of the bottom electrode (see Fig. 41.1) differs from the potential of the semiconductor substrate by the magnitude of the potential barrier, which electrons overcome during the passing from metal into semiconductor. Then an electric potential difference equal to the potential barrier arises between the

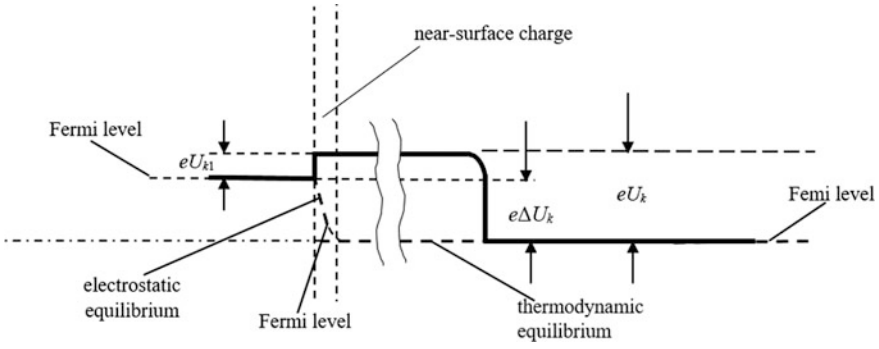

Fig. 41.2 Energy chart of near-surface charge in MDSM structure, presented in Fig. 41.1

near-surface charge and the bottom electrode. The inequality of the Fermi levels shows that it creates a source of electromotive force (EMF), in which there is always an electric potential difference and an inequality of the Fermi levels at the electrodes. However, in the above-mentioned works, the processes, which arise at the junction of the near-surface charge with the electrodes, joined to it (Fig. 41.1), are not explained. It makes these works logically incomplete with an unclear possibility of practical application.

The following question arises. Is it possible to join a metallic electrode to a near-surface charge by preserving the arisen electric potential difference, at least in part? It is not between the near-surface charge and the bottom electrode, but between the electrodes, one of which is the bottom electrode and the other is the electrode, joined to the near-surface charge. To answer this question, we consider two cases.

Case 1. Let the metallic electrode, joined to the near-surface charge, does not form a barrier layer with a semiconductor substrate, that is can freely exchange charge carriers with the substrate and near-surface charge, simultaneously. Before charging the gate capacitor, the Fermi level in this electrode coincides with the Fermi level in the substrate. After charging the capacitor, near-surface charge forms, in which the Fermi level is bent [13]. This charge is joined to the electrodes, joined to the drain and source (see Fig. 41.1). Since the junction area with the substrate will be far larger than the junction area with the near-surface charge and metal is able to exchange freely charge carriers with the substrate, the Fermi level in the main part of the metal will not change. In the region of junction with the near-surface charge, a transition region is formed in the near-surface charge. In this region, the Fermi level will vary smoothly from the Fermi level in the substrate to the Fermi level in the near-surface charge. It is clear that in this case, the electric potential difference between the electrode, joined to the near-surface charge, and the bottom electrode will be absent. It is caused by that, what an electric potential difference arises in the transition region between the near-surface charge and the electrode. It will have the opposite sign in respect to the potential barrier between the bottom electrode and the substrate. Then the electrons, passing through the transition region into the electrode, will give away an additional energy that they acquire during the transition from metal to semiconductor, overcoming the potential barrier. So, neither the voltage source nor the cooler cannot be created in this way.

Case 2. Let the metallic electrode, joined to the near-surface charge, forms a barrier layer with a semiconductor substrate, as initially suggested in [11]. In this case, before charging the gate capacitor, the Fermi level in the electrode is equal to the Fermi level in the substrate. However, because of the presence of the barrier layer, the electrode cannot freely exchange carriers with the substrate. By charging the capacitor, near-surface charge forms, in which the electrons are in a degenerate state, and this charge is joined to the electrode (see Fig. 41.1). Therefore, the electrode can freely exchange electrons with the near-surface charge, but no with the substrate. Then the Fermi level of this electrode becomes equal to the Fermi level of the near-surface charge, at least for a while, until there is an exchange of

electrons between the electrode and the substrate. An electric potential difference arises at the junction "electrode–near-surface charge". However, this electric potential difference U_{k1} (potential barrier) is much less than the electric potential difference between the bottom electrode and the substrate, since the concentration of electrons in the near-surface charge is much higher. Then the electric potential difference between the electrodes, joined to the near-surface charge, and the bottom electrode will be $\Delta U_k = U_k - U_{k1}$, where U_k is the electric potential difference between the substrate and the bottom electrode (see Figs. 41.1 and 41.2).

Thus, an electric potential difference forms between the electrode, joined to the near-surface charge, and the bottom electrode. These electrodes have different Fermi levels and it allows one to consider the resulting electric potential difference as a source of EMF. In this case, the heat, released at the junction "electrode–surface charge Q_2" at discharging the gate capacitor, is far less than the heat, absorbed at the junction "bottom electrode–substrate Q_1" at its charging. It takes place, since the potential barrier between the electrode and the near-surface charge is much less than the potential barrier between the bottom electrode and the substrate.

Let us perform charging–discharging of the gate capacitor in the MDSM structure into range of voltages, at which the near-surface charge is joined to the metal regions all the time. Then, after each process of charging, the transition layer, formed due to possible carriers exchange between the metal regions and the substrate, will disappear. This will take place because after each process of charging, the gate capacitor will acquire an additional energy due to the absorption of heat at the junction "bottom electrode–substrate". In the result, it will restore the electric potential of the near-surface charge in a whole gate region and lead to the disappearance of the transition layer. The near-surface charge is always joined to the electrode during process of charging–discharging the gate capacitor. Therefore, the electrode can quickly exchange electrons with a near-surface charge and their Fermi levels equalize. The time of the electron exchange between the electrode and the substrate is far longer because of the presence of a barrier layer. Therefore, the electrode will be recharged always to the electric potential of substrate (if carrier exchange occurs and a transition region is formed as in Case 1). The energy, required for this recharging, will be generated at the junction "bottom electrode–substrate".

We now discharge the gate capacitor through the resistor R before the exchange of charges between the metal regions and the substrate. Then, not only the energy, acquired from the voltage source, but also the energy, obtained during the absorption of heat at the junction "bottom electrode–substrate", will be released on the capacitor minus the energy, released at the junction "metal region–drain/source". As noted above, the latter energy is much lesser than the energy, absorbed at the junction "bottom electrode–substrate". Then during the charge–discharge cycle of the gate capacitor, the MDSM structure will cool down and convert the absorbed heat into electrical energy. This will occur even at exchanging charge carriers between the metal regions and the substrate. During the charge carriers

exchange between the drain/source and the bottom electrode, through the resistor, the current will pass, which shorts circuit of electrodes. This current will restore after each charging the gate capacitor. Thus, the MDSM structure will operate as a voltage source and a cooler or only as a cooler, if there is an exchange of charges between the metal regions and the substrate.

In experiment, we have studied field-effect transistors, which presented also MDSM structures. However, in the field-effect transistors, the barrier layer, formed between *p*-regions and *n*-type substrate, disappears only between the near-surface charge and the *p*-regions. However, it remains between the substrate and the *p*-regions, joined to the near-surface charge (see Fig. 41.3) in the regime of strong inversion, when a negative electric potential is applied to the gate. The barrier layer does not disappear also between the near-surface charge and the *p*-regions in the saturation regime, when a positive potential is applied to the gate. This leads to a sharp increase in the electric resistance between the bottom electrode and the connected in parallel drain and source, since a *p*-*n* junction forms between them, in which the current passes in the direction of the junction "substrate–drain/source".

The area of the *p*-*n* junction is much larger than in dot diodes. Therefore, it will have reverse currents of the order of several fractions of the microampere. During charging and discharging the gate capacitor, the current passes through this junction, when a voltage dropping at the junction "substrate–drain/source" exceeds 0.4 V [11, 15]. Therefore, during charging–discharging cycle of the gate capacitor of field-effect transistor, current will pass through the junctions "bottom electrode–substrate" and "near-surface charge–drain/source" and heat will absorb or release. However, because of the bending of the Fermi level (since the *p*-regions are isolated from the substrate and cannot freely exchange charges with it for at least some time), the amount of heat, absorbed in the region of the near-surface charge, can exceed the amount of heat released. This will lead to cooling the transistor and converting the absorbed heat into electrical energy. In this case, at the charging–discharging cycle of the gate capacitor, a greater energy should be released on the electrical circuit elements than consumed one from the voltage source, which charges the gate capacitor. Such experiments were described in [12].

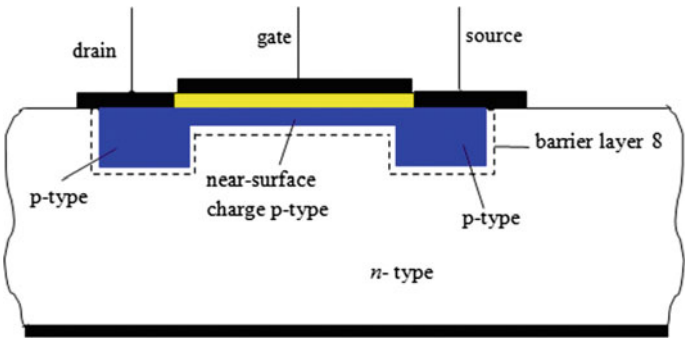

Fig. 41.3 Field-effect transistor is the MDSM structure

In work [11], measurements were carried out in the saturation regime and the values of output power, exceeding the power consumption by 1–7%, were obtained for charging–discharging cycle of the gate capacitor. In work [15], measurements, using the same cycle, were carried out in the regime of strong inversion and an excess over the consumed power was obtained not less than 10%. In these studies, a parallel connection of 10 field-effect transistors KP304A (2N4268) was used to provide a total gate capacitance (90 pF), which was much larger than a capacitance of the touched probe (5 pF). It was performed in order to minimize the effect of the touched probe on the measurement results. The voltages of the power supplies U_0 and U were higher than the threshold value, at which the drain and source were always joined to the near-surface charge. Since the parameters of the transistors were differed from each other, this could lead to a decrease in the ratio of the output power to the consumed one in comparison with the measurements, carried out for a single transistor. The touched probe for the single transistor had a capacitance smaller than the gate capacitance (9 pF). Therefore, the measuring circuit for one transistor was investigated (see Fig. 41.4).

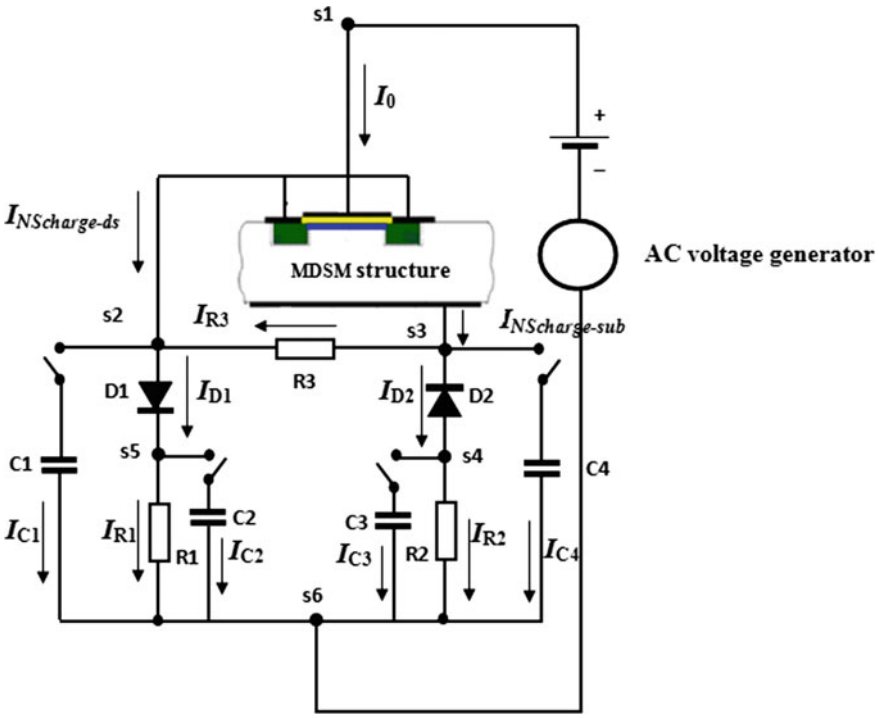

Fig. 41.4 Measurement electric scheme

41.3 Description of Experiment

Using diodes D219A (DR482) in this electric scheme allowed instead of charging–discharging cycle of the gate capacitor one to apply to the circuit a sinusoidal voltage with a bias up to +12 V to obtain a mode of strong inversion or saturation in the transistor.

The values of voltage in the circuit were measured at points s1, s2, …, s6 with respect to point s0, using a digital oscilloscope V-421. The measured voltage was applied to the oscilloscope by using a touched probe (NR-9060), which had an input resistance of 10 MΩ and an input capacitance of 23 pF. To take into account the influence of the touched probe, the measuring circuit was designed so that capacitors with a capacity of 23 pF were joined to all measurement points s1, s2,…, s6. For measurements at the point si, the capacitor Ci (i = 0, 1, …, 4) was disjoined and instead of it a touched probe with the same capacitance was joined. Therefore, the operation of the circuit was not disturbed when the touched probe was joined. The capacitance C0 (connected in parallel to the source of alternating voltage and the source of direct bias) had practically no effect on the operation of the circuit, and therefore was not taken into account in the calculations, although it was joined to the circuit during the measurement. Since resistors R1 and R2 had resistance equal to 10 kΩ, and the touch probe resistance was 10 MΩ (10^3 times greater), the influence of the probe resistance on the operation of the circuit could be neglected. Thus, by measuring in this scheme, the touched probe did not affect the operation of the circuit and results, obtained during the measurement. The oscilloscope had a scan of 1024 points (k = 0; 1; 2; …; 1023), and a frequency of alternative sine signal was f = 597 kHz. At the same time, the number of the considered points per a period of oscillation T was j_{max} = 168. The measurements at each point were averaged based on the results of 10^4 measurements, which minimized the effect of random hindrances. These hindrances significantly decreased upon summation and had almost no effect on the accuracy of the measurements.

The results were processed by using the MathCaD-14 software, which allowed one to determine the currents and powers in the circuit by using the voltage measurements. The voltages and currents in the circuit were designed as follows:

$U_{R1} = U_{s5} - U_{s0}$ is the voltage on the resistor R1 and the capacitor C2;
$U_{R2} = U_{s4} - U_{s0}$ is the voltage on the resistor R2 and the capacitor C3;
$U_{R3} = U_{s3} - U_{s2}$ is the voltage on the resistor R3;
$U_{C1} = U_{s5} - U_{s0}$ is the voltage on the capacitor C1;
$U_{C4} = U_{s4} - U_{s0}$ is the voltage on the capacitor C4;
$U_{D1} = U_{s2} - U_{s5}$ is the voltage on the left diode D1;
$U_{D2} = U_{s2} - U_{s4}$ is the voltage on the right diode D2;
$U_{12} = U_{s1} - U_{s2}$ is the voltage between gate and the connected in parallel drain and source;
$U_{13} = U_{s1} - U_{s3}$ is the voltage between gate and substrate;
$U_0 = U_{s1} - U_{s0}$ is the voltage on the voltage source (DC-voltage and AC-voltage);

$I_{C1} = C_1 \frac{U_{R1_{k+1}} - U_{R1_k}}{dt}$ is the current passing through the capacitor C1, $dt = 1/(j_{\max} \cdot f)$;
$I_{C2} = C_2 \frac{U_{R2_{k+1}} - U_{R2_k}}{dt}$ is the current passing through the capacitor C2;
$I_{C3} = C_3 \frac{U_{R3_{k+1}} - U_{R3_k}}{dt}$ is the current passing through the capacitor C3;
$I_{C4} = C_4 \frac{U_{C4_{k+1}} - U_{C4_k}}{dt}$ is the current passing through the capacitor C4;
$I_{R1} = \frac{U_{R1}}{R_1}$ is the current passing through the resistor R1;
$I_{R2} = \frac{U_{R2}}{R_2}$ is the current passing through the resistor R2;
$I_{R3} = \frac{U_{R3}}{R_3}$ is the current passing through the resistor R3;
$I_{D1} = I_{R1} + I_{C2}$ is the current passing through the left diode D1;
$I_{D2} = I_{R2} + I_{C3}$ is the current passing through the right diode D2;
$I_{sub} = I_{C3} + I_{C4} + \frac{U_{R2}}{R_1} + \frac{U_{R3}}{R_3}$ is the current passing through the junction "substrate–bottom electrode";
$I_{d-s} = I_{C1} + I_{C2} + \frac{U_{R1}}{R_1} + \frac{U_{R3}}{R_3}$ is the current passing through the connected in parallel drain and source;
$I_0 = I_{C1} + I_{R1} + I_{C2} + I_{R2} + I_{C3} + I_{C4}$ is the current passing through the gate of transistor.

Numerical calculation of the derivative leads to the appearance of noise on the time dependences of the current, which could lead to errors in the calculation of power (see Fig. 41.5). Therefore, by using the MathCaD-14 software, the obtained dependences were smoothed with help of the built-in smoothing function based on the Gaussian function *ksmooth* (z, I_{Ci}, b), where $b = 4$ is the width of the window of smoothing (see Fig. 41.6).

It is seen that the noise is decreased sharply after smoothing. In this case, the periodicity of the functions is retained. Average value of the power on resistors during the oscillation period on the resistors is determined as average value over the

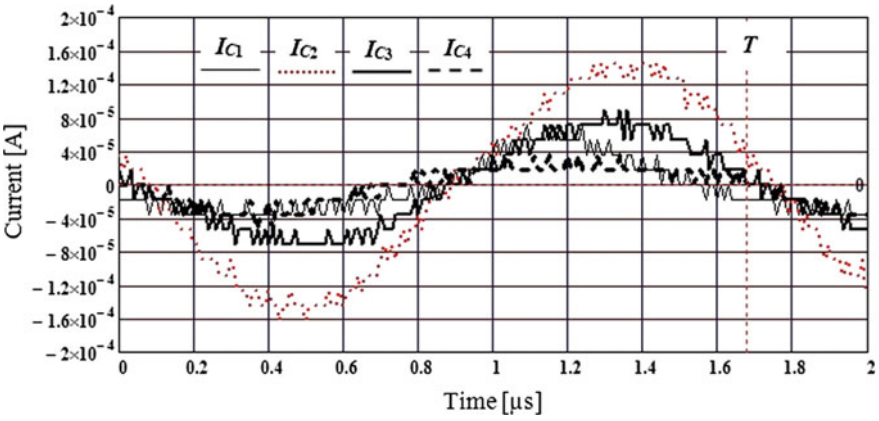

Fig. 41.5 Time dependences of currents passing through capacitors, $T = 1/f$ is the oscillation period

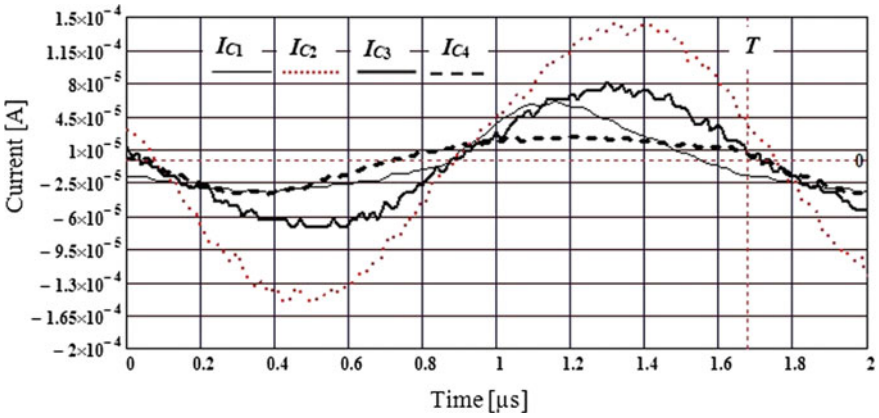

Fig. 41.6 Time dependences of currents passing through capacitors after smoothing, $T = 1/f$ is the oscillation period

oscillation period T of the power, released on the resistors (R1, R2), diodes (D1, D2) and capacitors (C1, C2, C3, C4). It can be written in discrete form as

$$Int(S) = \frac{1}{2j_{\max}} \sum_{j=1}^{j_{\max}-1} (2S_j) + \frac{1}{2j_{\max}} (S_0 + S_{j\max}); j_{\max} = 1024 \frac{T}{t_{1023}}, \qquad (41.1)$$

where values of S_j are defined by the following expressions:

$S_j = \frac{(U_{R1_j})^2}{R_1}$ for mean power on the resistor R1; $W_{R1} = Int\ (S_j)$ is the power on the resistor R1;

$S_j = \frac{(U_{R2_j})^2}{R_2}$ for mean power on the resistor R2; $W_{R2} = Int\ (S_j)$ is the power on the resistor R2;

$S_j = I_{C1_j} U_{C1_j}$ for mean power on the capacitor C1; $W_{C1} = Int\ (S_j)$ is the power on the capacitor C1;

$S_j = I_{C2_j} U_{C2_j}$ for mean power on the capacitor C2;

$W_{C2} = Int\ (S_j)$ is the power on the capacitor C2;

$S_j = I_{C3_j} U_{C3_j}$ for mean power on the capacitor C3;

$W_{C3} = Int\ (S_j)$ is the power on the capacitor C3;

$S_j = I_{C4_j} U_{C4_j}$ for mean power on the capacitor C4;

$W_{C4} = Int\ (S_j)$ is the power on the capacitor C4;

$S_j = \left(\frac{U_{R1_j}}{R_1} + I_{C2_j}\right) U_{D1_j}$ for mean power on the left diode D1;

$W_{D1} = Int\ (S_j)$ is the power on the left diode D1;

$S_j = \left(\frac{U_{R2_j}}{R_2} + I_{C3_j}\right) U_{D2_j}$ for mean power on the right diode D2;

$W_{D2} = Int\ (S_j)$ is the power on the right diode D2;

$S_j = \left(I_{C1_j} + I_{C2_j} + \frac{U_{R1_j}}{R_1} - \frac{U_{R3_j}}{R_3}\right) U_{12_j}$ for mean power at the junction "gate–drain/source";
$W_{12} = Int\ (S_j)$ is the power at the junction "gate–drain/source";
$S_j = \left(I_{C3_j} + I_{C4_j} + \frac{U_{R2_j}}{R_2} - \frac{U_{R3_j}}{R_3}\right) U_{13_j}$ for mean power at the junction "gate–substrate";
$W_{13} = Int\ (S_j)$ is the power at the junction "gate–substrate";
$S_j = I_{0_j} U_{0_j}$ for the mean power, consumed from the voltage source;
$W_0 = Int\ (S_j)$ is the consumed power.

The source of the bias DC takes value of about ± 12 V. In this case, the near-surface charge is either in the saturation mode, or in the strong inversion mode and the capacitance of the gate capacitor (C_g) is almost independent of the voltage applied to the gate. Therefore, if we know the current, passing through the gate, and the capacitance of the gate capacitor, it is possible to determine the voltage between the near-surface charge and the gate as

$$U_{Cg_k} = \frac{T}{C_g j_{\max}} \sum_{j=0}^{k} I_{0_j} + A,$$

where A is a constant, selected from the condition that average value of U_{Cg} per period is equal to the constant component of the voltage, applied to the circuit (the voltage of source of the bias DC in Fig. 41.4).

For the mean power, released at the junction "near-surface charge–drain/source", we have

$$S_j = \left(I_{C1_j} + I_{C2_j} + \frac{U_{R1_j}}{R_1} - \frac{U_{R3_j}}{R_3}\right)\left(U_{12_j} - U_{Cg_j}\right).$$

Then $W_{NScharge-1} = Int\ (S_j)$ is the power, released at the junction "near-surface charge–drain/source".

For the mean power, released at the junction "near-surface charge–substrate", we have

$$S_j = \left(I_{C3_j} + I_{C4_j} + \frac{U_{R2_j}}{R_2} - \frac{U_{R3_j}}{R_3}\right)\left(U_{13_j} - U_{Cg_j}\right).$$

Then $W_{NScharge-2} = Int\ (S_j)$ is the power, released at the junction "near-surface charge–substrate".

For the mean power, released at the junction "gate–near-surface charge", we have

$$S_j = I_{0_j} U_{Cg_j}.$$

Then W_{Cg}= *Int* (S_j) is the power, released at the junction "gate–near-surface charge".

Figures 41.7 and 41.8 show the measured dependences of voltages and currents, respectively, on the circuit elements.

The calculated values of power, based on formula (41.1), are defined as

$W_{R1} = 5.61\times10^{-6}$ W, $W_{R2} = 1.25\times10^{-5}$ W, $W_{C1} = -5.189\times10^{-7}$ W,
$W_{C2} = -1.014\times10^{-7}$ W,
$W_{C3} = -2.263\times10^{-7}$ W, $W_{C4} = -2.198\times10^{-6}$ W, $W_{D1} = 2.834\times10^{-7}$ W,
$W_{D2} = 1.749\times10^{-6}$ W,
$W_{12} = -2.006\times10^{-5}$ W, $W_{13} = 1.328\times10^{-8}$ W, $W_0 = 1.889\times10^{-5}$ W,
$W_{13} + W_{12} = -6.782\times10^{-6}$ W.

The ratio of the sum of the powers on the elements of the circuit to the power consumed is defined

(i) without taking into account the near-surface charge as

$$\frac{W_{R1} + W_{R1} + W_{C1} + W_{D1} + W_{D2} + W_{C2} + W_{C3} + W_{C4} + W_{12} + W_{13}}{W_0} = 1.0009;$$

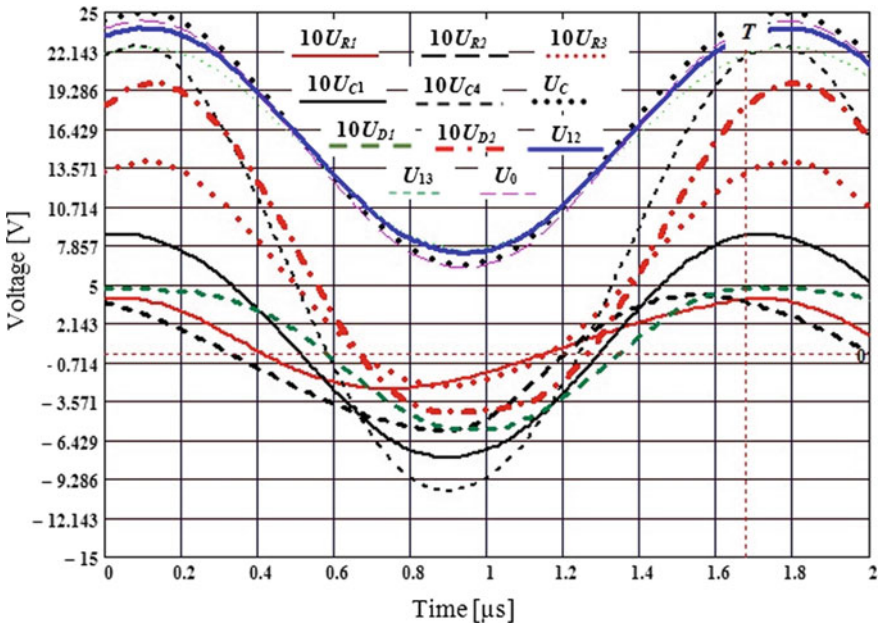

Fig. 41.7 Measured dependences of voltages on the circuit elements, $T = 1/f$ is the oscillation period

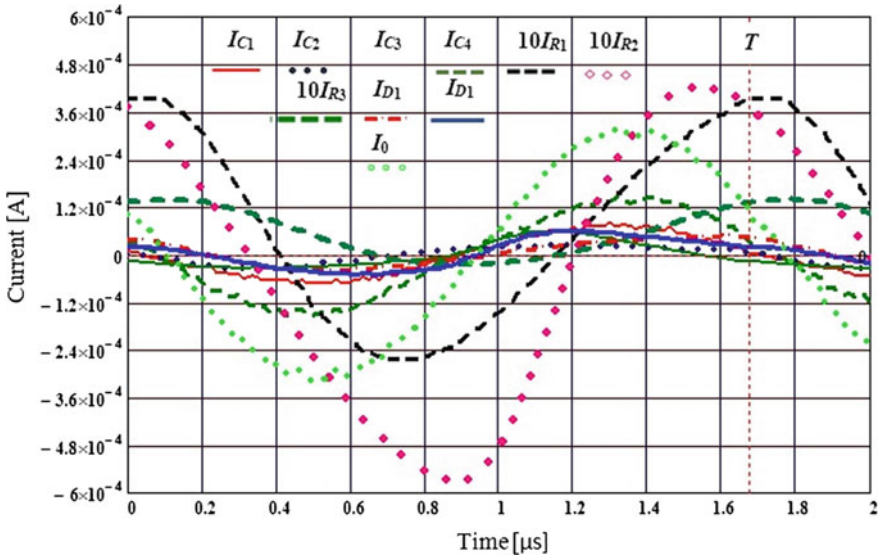

Fig. 41.8 Measured dependences of currents on the circuit elements, $T = 1/f$ is the oscillation period

(ii) with account of the near-surface charge as

$$\frac{W_{R1} + W_{R1} + W_{C1} + W_{D1} + W_{D2} + W_{C2} + W_{C3} + W_{C4} + W_{12} + W_{13} + W_{NScharge-1} + W_{NScharge-2} + W_{Cg}}{W_0} = 1.0009.$$

It is seen that both ratios are close to 1 (differ from 1 in the fourth significant digit after the decimal point), which confirms the law of energy conservation for this electric scheme. Moreover, during measurements, the law of charge conservation was fulfilled. This means that the total current, passing through the resistors R1 and R2, had not a DC component or this component did not exceed the measurement accuracy (not more than 1%). Measurement of the currents, passing via these resistors, showed that the DC components of these currents had the opposite signs and differed in the third significant digit after the decimal point (not more than 1%). The DC components of these currents were determined by using formula (41.1), where the following expressions were used for the function S_j:

$$S_j = \frac{U_{R1_j}}{R_1} \quad \text{and} \quad S_j = \frac{U_{R2_j}}{R_2}.$$

The total power, consumed at the junctions "near-surface charge–substrate" and "near-surface charge–drain/source" is equal to $W_{NScharge-1} + W_{NScharge-2} + W_{Cg} = -6.782 \times 10^{-6}$ W; both values of $W_{NScharge-1}$ and $W_{NScharge-2}$ are negative. At the

same time, as can be seen from the last expression, W_{Cg}= 2.862 × 10^{-5} W > 0, i.e. on the gate capacitor there are losses in contrast to the capacitors C1 and C2.

It is interesting to note that $U_{Cg_{max}} > U_{0_{max}}$, because $U_{Cg_{max}}$ = 9.27 V and $U_{0_{max}}$ = 9.07 V, i.e. the gate voltage on the capacitor exceeds the voltage, applied to the gate.

41.4 Discussion of Results

We note that the power, released on resistors and diodes, exceeds the consumed power by 52%:

$$\frac{W_{R1} + W_{R1} + W_{C1} + W_{D1} + W_{D2}}{W_0} = 1.52.$$

It takes place because of the negative total power at the junctions 1–2 and 1–3 due to the bending of the Fermi level under the action of an external field in the gate region [16]. Thus, the values of power at the junctions "gate–drain/source" and "gate–substrate" are negative. This result is explained by that in the field-effect transistor, besides the junctions "near-surface charge–substrate" and "near-surface charge–drain/source", there is also a *p-n* junction, at which heat absorption or generation can also take place. In a state of equilibrium, when the voltage on gate is zero, the junctions "substrate–bottom electrode" and "near-surface charge–drain/source" have one polarity, but the *p-n* junction has another polarity, and they cancel out one of other. However, when the voltage is applied to the gate, the Fermi level bends in the near-surface charge and the equilibrium is violated. This leads to the appearance of an uncompensated EMF and the absorption of environment heat in one of these junctions. Since the voltages are alternative, the Fermi levels will also vary with time, which leads to a change in the phase shift between the corresponding currents and voltages (see Fig. 41.9) in the regions of the junctions "near-surface charge–bottom electrode" and "near-surface charge–drain/source".

In turn, it leads to that what mean values of power at these junctions become negative. Then, at these junctions, heat is consumed (cooling occurs) from environment and then converted into the potential energy of the gate capacitor. Then the energy of this capacitor becomes larger compared to the value, which it can acquire from a voltage source. So, in the process of the capacitor charging and discharging, a greater energy is released on the circuit elements compared to the consumed energy from the voltage source by the amount of the heat energy, absorbed from environment.

At power of heat consumption equal to approximately 7 μW, a transistor KP304 with a mass of 1 g will cool with a rate of 10^{-5} K/s, if we assume that the transistor and its housing are manufactured of silicon. Then the transistor, when completely insulated, is cooled by 0.1 K during 10^4 s. However, full insulation of the transistor is impossible. Therefore, the heat flux from outside to such an insulated transistor

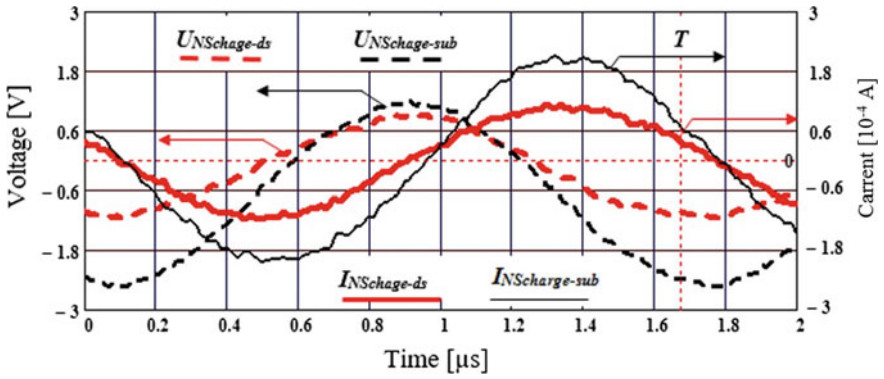

Fig. 41.9 Time dependences of voltage and current at the junctions "near-surface charge–bottom electrode" $U_{NScharge\text{-}sub}$, $I_{NScharge\text{-}sub}$ (black curves) and "near-surface charge–drain/source", $U_{NScharge\text{-}ds}$, $I_{NScharge\text{-}ds}$ (red curves), $T = 1/f$ is the oscillation period

during above-mentioned time may exceed the heat absorption in the transistor and the decrease in its temperature will not exceed the measurement error limits. In spite of this, the reliability of the measurements is confirmed by the fulfillment of the law of energy conservation and the law of charge conservation for the proposed circuit (Fig. 41.4). As noted above, the value at each point was averaged on the base of 10^4 measurements that minimized the effects of random hindrances, which at summing up, were reduced substantially and almost did not affect the measurement accuracy that also confirmed the reliability of the measurements.

In respect to the negative capacities, resulting on the capacitors C1, C2, C3 and C4, this phenomenon can be explained by the fact that the energy, consumed at the transistor junctions "substrate–bottom electrode", "*n*-area–*p*-area" and "drain–source", in any way was stored on the capacitors. It is more likely, since the law of conservation of energy in the circuit is carried out only at the negative powers on the capacitors.

41.5 Conclusion

Thus, the conducted experiment shows that this circuit produces an electric power that exceeds 52% the power, consumed from the voltage source, by consuming heat from the environment. For transistor KP304, this power, consumed from the environment, is equal to 7 μW. This confirms in a whole the correctness of our concept [11–13] of the conversion of thermal energy into electrical one. The absorbed power will be significantly increased, if MDSM structure is not fabricated in the form of a field-effect transistor, but in accordance with the proposed concept. In this case, the proposed thermoelectric converter presents itself a MDSM structure, manufactured on a silicon plate. On a low-resistive silicon plate (with a

specific conductivity of 0.01 Ω cm or less), a 10 μm layer with a conductivity of at least 1 Ω cm is created with following manufacture of a MDSM structure. The electric resistance between the near-surface charge and the low-resistive part of the plate will be approximately 10 Ω, if sizes of the MDSM structure are equal to 0.1×0.1 mm^2. Resistance of the near-surface charge will be equal to 100 Ω, and an electron concentration is close to the electron concentration in metal at its thickness of 50 Å, a length of 100 μm and a width of 100 μm. Thus, the resistance of the system "bottom electrode–near-surface charge" will be 110 Ω for such a MDSM structure. At a capacitor area of 0.01 mm^2 and a dielectric coating thickness of 0.1 μm with $\varepsilon = 50$–100 and a voltage of $U_0 = 5$ V, the electron concentration in the near-surface charge can reach $(2.7 \pm 5) \times 10^{19}$ cm^{-3}. This is quite enough for staying electrons in the degenerate state in the near-surface charge, in order to the barrier layer disappeared and the near-surface charge joined to the metal electrodes.

At a square of 1 cm^2, 10^4 MDSM structures could be placed. If they are connected in parallel, the resistance of the system "bottom electrode–near-surface charge" will be 10^4 times smaller and equal to 0.011 Ω. The total capacity of the connected in parallel 10^4 MDSM structures can be estimated as 1 μF. Then at a generator frequency of 100 kHz, it will be easy to create an operating current of about 1 A. In this case, the voltage dropping at an internal resistance of 0.011 Ω will be equal to 0.011 V, which is one order of magnitude smaller than $\Delta U_k = U_k - U_{k1} = 0.1$ V [12], but the consumed thermal power will be equal to $1 \text{ A} \times 0.1 \text{ V} = 0.1$ W. Thus, we can obtain 0.1 W of the absorbed heat power with a square of 1 cm^2, and up to 100 W with a square of 10^3 cm^2, which is quite acceptable for many applications. The consumed heat will be converted in the MDSM structure into the potential energy of the charged capacitor, and be released on the resistor R (Fig. 41.1). If rectifiers are used as these resistors, then obtained electricity can be used for the power supply of generator. It will significantly reduce the energy consumed or even eliminate its consumption.

Acknowledgements This study has been performed at partial financial support of the Russian Foundation for Basic Research (grant No. 16-08-00740). I. A. Parinov acknowledges financial support of the Russian Ministry of Education and Sciences into framework of the "Organization of Scientific Research" Government Assignment.

References

1. J.-C. Zheng, Front. Phys. China **3**, 269 (2008)
2. A.V. Dmitriev, I.P. Zvyagin, Phys. Usp. **53**, 789 (2010)
3. M. Nicolau, *International Application.* WO03023871 (A2) (2003)
4. S. Donsa, S. Andergassen, K. Held, Phys. Rev. B **89**, 12503 (2014)
5. D. Wasserman, S.A. Lyon, M. Hadjipanayi, A. Maciel, J.F. Ryan, Appl. Phys. Lett. **83**, 5050 (2003)
6. H. Zhang, Y. Liu, X. Ye, Y. Chen, J. Appl. Phys. **114**, 244308 (2013)
7. H. Lee, D. Vashaee, D.Z. Wang, M.S. Dresselhaus, Z.F. Ren, G. Chen, J. Appl. Phys. **107**, 094308 (2010)

8. P. Thiyagarajan, M.-W. Oh, J.-C. Yoon, J.-H. Jang, Appl. Phys. Lett. **105**, 033905 (2014)
9. J.P. Pekola, F. Giazotto, O.-P. Saira, Phys. Rev. Lett. **98**, 037201 (2007)
10. O.-P. Saira, M. Meschke, F. Giazotto, A.M. Savin, M. Mottonen, J.P. Pekola, Phys. Rev. Lett. **99**, 027203 (2007)
11. L.S. Lunin, G.Y. Karapet'yan, V.G. Dneprovskii, V.F. Kataev, Tech. Phys. **58**, 1619 (2013)
12. G.Y. Karapetyan, V.G. Dneprovski, I.A. Parinov, in: *Advanced Materials. Studies and Applications,* ed. by I.A. Parinov, S.-H. Chang, S. Theerakulpisut (Nova Science Publishers, 2015), p. 209
13. G.Y. Karapetyan, V.G. Dneprovski, I.A. Parinov, G. Parchi, in: *Advanced Materials: Manufacturing, Physics, Mechanics and Applications*, Springer Proceedings in Physics, vol. 175, ed. by I.A. Parinov, S.-H. Chang, V.Y. Topolov (2016), p. 329
14. K. Seeger, in: *Semiconductor Physics*, Chapter: Semiconductor Statistics (Springer, 1989), p. 34
15. V.A. Akop'yan, G.Y. Karapet'yan, Meas. Tech. **59**, 979 (2016)
16. V.M. Egorov, V.V. Kaminskii, M.M. Kazanin, S.M. Soloviev, A.V. Golubkov, Tech. Phys. Lett. **39**, 650 (2013)

Chapter 42
Finite Element Analysis of Cymbal Transducer from Porous Piezoceramics PZT-4 with Various Material Properties

Andrey V. Nasedkin, Anna A. Nasedkina and Amirtham Rajagopal

Abstract The chapter deals with the finite element modeling of the disk piezoelectric transducer with cymbal-shaped end-caps. Under radial oscillations of piezoceramic disk this transducer generates axial oscillations with large amplitude thanks to more flexible metal end-caps. One of the factors contributing to the efficiency of transformating radial displacement into axial is the value of the transverse piezomodulus of the piezoceramic material. As it was recently found, porous piezoceramic with fully metallized pore surfaces exhibits a growth of the transverse piezomodulus with the porosity growth unlike ordinary piezoceramics, where the transverse piezomodulus decreases under the growth of porosity. This work investigates the oscillations of the cymbal piezoelectric transducer with the disk made of porous piezoceramic with fully metallized pore surfaces for various percentage of porosity. The results of the numerical experiments have confirmed the prospects of using new types of piezoceramic materials for a cymbal transducer.

42.1 Introduction

Flextensional piezoelectric transducers are widely used in modern sensors, actuators and emitters. The flextensional class V piezoelectric transducer comprises two types of transducers, namely, moonie and cymbal [1]. In standard forms, moonie and

A. V. Nasedkin · A. A. Nasedkina (✉)
I. I. Vorovich Institute of Mathematics, Mechanics and Computer Science,
Southern Federal University, 8a, Milchakova Street,
344090 Rostov-on-Don, Russia
e-mail: aanasedkina@sfedu.ru

A. V. Nasedkin
e-mail: nasedkin@math.sfedu.ru

A. Rajagopal
Department of Civil Engineering, Indian Institute of Technology,
502205 Hyderabad, India
e-mail: rajagopal@iith.ac.in

I. A. Parinov et al. (eds.), *Advanced Materials*, Springer Proceedings
in Physics 207, https://doi.org/10.1007/978-3-319-78919-4_42

cymbal transducers are three-layer constructions, where a piezoceramic disk is sandwiched between two more flexible metal end-caps in the form of disks with moon-shaped cavities (Fig. 42.1a) or truncated conical plates (cymbals) (Fig. 42.1b). The main feature of moonie and cymbal transducers is the ability to generate sufficiently large vertical displacements of the end-caps under radial or planar oscillations of piezoceramic disk.

The first transducer with such feature was the moonie transducer described in [2]. The original design of the moonie transducer was improved and analyzed in [3, 4]. New cymbal transducer was suggested in [5, 6]. The cymbal transducer has demonstrated high efficiency, and this fact has increased interest to its further investigation. For example, some reviews and general analysis of cymbal transducers can be found in [7, 9]. An influence of the geometrical dimensions of cymbal transducer on the coefficient of electromechanical transformation was analyzed in [10–14]. In [15–17] the performance of the cymbal transducer in acoustic medium was studied. The strength of the disk in the places of the end-caps gluing was investigated in [12, 18]. At present, research on cymbal transducers and their high-tech applications is still actual (see [19–21] and other works).

As it was shown in [2], an effective longitudinal piezomodule d_{33}^s is a linear combination of the longitudinal piezomodulus d_{33} and the transverse piezomodulus d_{31} of piezoceramic material, i.e. $d_{33}^s = G_1 d_{33} - G_2 d_{31}$, where G_1, G_2 are non-negative multipliers that depend on geometrical dimensions of various parts of the cymbal. Thus, the effectiveness of electromechanical transformation can be increased not only by varying the dimensions of the construction but also by choosing special piezoelectric material for the transducer, which has high values of the piezomoduli d_{33} and $|d_{31}|$. Recent results on computer simulation of porous piezoceramic materials with metallized pore surfaces [22–24] have shown that under the growth of porosity such materials exhibit growth of the piezomoduli d_{33} and $|d_{31}|$. Moreover, for a porous material the acoustic impedance is smaller than for analogous dense material. Therefore, using porous materials for piezoelectric transducers in acoustic applications results in better generation of waves into external medium [25, 26].

The reasons provided above have determined the research directions for this work. The chapter describes the problem setting, the finite element model of the cymbal transducer and the technologies of numerical experiments. Numerical results of simulation give opportunity to analyze the effectiveness of exciting the axial displacements on the top surface of the end-caps under electric influence depending on the material moduli of a piezoceramic with metallized pore surfaces.

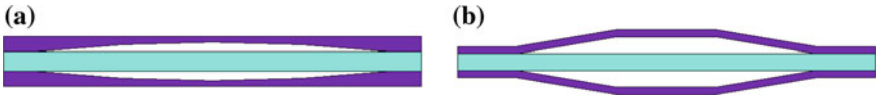

Fig. 42.1 Cross-sections of moonie (**a**) and cymbal (**b**) transducers

42.2 Mathematical Formulation of the Problem and Finite Element Simulation for the Cymbal Transducer

The object of this study is an axisymmetric cymbal piezoelectric transducer consisting of a piezoelectric disk and two metal cymbal-shaped end-caps bonded to the top and bottom of the disk. Due to the axial symmetry of the structure, we consider a meridional section S of the transducer in a cylindrical coordinate system $Orz\theta$ (Fig. 42.2). Let us introduce the following notations: R_p is the radius of the piezoceramic disk, h_p is the thickness of the piezoceramic disk, r_1 is the maximal radius of the cavity, r_2 is the minimal radius of the cavity, h_c is the height of the cavity along the axis of symmetry, h_m is the thickness of the metal end-cap.

We consider that the piezoceramic disk is made of porous piezoceramic PZT-4 which is polarized along the z-axis. Further, we will consider other types of porous materials for the disk, both ordinary and with metallized pore surfaces [22–24].

Let us consider that the lower $\left(\Gamma_{\varphi 1} = \left\{0 \le r \le R_p,\ z = -h_p/2\right\}\right)$ and the upper $\left(\Gamma_{\varphi 2} = \left\{0 \le r \le R_p,\ z = h_p/2\right\}\right)$ end faces of the piezoelectric disk are electrodeposited, and the side surface $r = R_p$ (Γ_D) is free from stress and electrodes. We also adopt that along its annular surfaces $\{r_1 \le r \le R_p,\ z = \pm h_p/2\}$ the piezoelectric disk is rigidly glued to the metal cymbal end-caps. On the rest of the boundaries the end-caps are considered to be stress-free except for the points $\left\{r = R_p,\ z = \pm(h_p/2 + h_m)\right\}$, in which we assume zero axial displacements u_z. These conditions imitate fixation of the transducer in certain housing. For the meridional section it is also necessary to adopt the conditions of symmetry along the axis $z = 0$.

In order to analyze the transducer we consider the equations of electroelasticity. Under steady-state oscillations $\exp(i\omega t)$ with the frequency $f = \omega/(2\pi)$ for the amplitude values of the functions of displacement $\mathbf{u}(\mathbf{x})$ and electric potential $\varphi(\mathbf{x})$ in Cartesian coordinate system, these equations can be written in the form:

$$\mathbf{L}^*(\nabla) \cdot \mathbf{T} = -\omega^2 \mathbf{u}, \quad \nabla \cdot \mathbf{D} = 0, \tag{42.1}$$

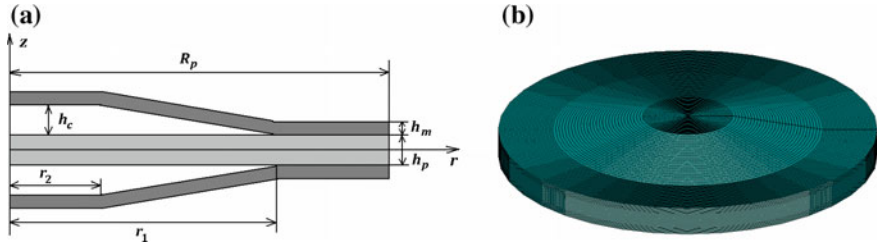

Fig. 42.2 Geometry of the meridional section (**a**) and 3D expansion of the finite element mesh (in different scales) (**b**)

$$\mathbf{T} = (1 + iQ_d^{-1})\mathbf{c}^E \cdot \mathbf{S} - \mathbf{e}^* \cdot \mathbf{E}, \quad \mathbf{D} = \mathbf{e} \cdot \mathbf{S} + \boldsymbol{\varepsilon}^S \cdot \mathbf{E}, \tag{42.2}$$

$$\mathbf{S} = \mathbf{L}(\nabla) \cdot \mathbf{u}, \quad \mathbf{E} = -\nabla\varphi, \tag{42.3}$$

$$\mathbf{L}^*(\nabla) = \begin{bmatrix} \partial_1 & 0 & 0 & 0 & \partial_3 & \partial_2 \\ 0 & \partial_2 & 0 & \partial_3 & 0 & \partial_1 \\ 0 & 0 & \partial_3 & \partial_2 & \partial_1 & 0 \end{bmatrix}, \quad \nabla = \begin{Bmatrix} \partial_1 \\ \partial_2 \\ \partial_3 \end{Bmatrix}. \tag{42.4}$$

Here ρ is the density; $\mathbf{T} = \{\sigma_{11}, \sigma_{22}, \sigma_{33}, \sigma_{23}, \sigma_{13}, \sigma_{12}\}$ is the array of the stress tensor components σ_{ij}; $\mathbf{D}$ is the electric induction vector; $\mathbf{S} = \{\varepsilon_{11}, \varepsilon_{22}, \varepsilon_{33}, 2\varepsilon_{23}, 2\varepsilon_{13}, 2\varepsilon_{12}\}$ is the array of the strain tensor components ε_{ij}; $\mathbf{E}$ is the electric field stress vector; $\mathbf{c}^E$ is the 6×6 matrix of elastic stiffness measured at constant electric field; $\mathbf{e}$ is the 3×6 matrix of piezomoduli; $\boldsymbol{\varepsilon}^S$ is the 3×3 matrix of dielectric permittivities, measured at constant strain; Q_d is the mechanical quality factor for the frequency independent way of taking damping into account; $(\ldots)^*$ is the transposition operation for the matrices and vectors.

When $\mathbf{e} = 0$ the electroelasticity problem (42.1)–(42.4) can be divided into independent equations of the elasticity theory and quasi-electrostatics, which can be used to describe the oscillations of elastic bodies. In this case, if the dielectric permittivities of the piezoceramic are much greater than the dielectric permittivities of the elastic bodies contacting with the piezoceramic, then the equations of quasi-electrostatics can be omitted for the elastic bodies. In the problem under consideration, the piezoceramic disk contacts with metal end-caps through a layer of glue. Therefore for the piezoceramic disk we can consider equations of electroelasticity (42.1)–(42.4), and for the end-caps we can adopt the equations of elasticity following from (42.1) to (42.4) when $\mathbf{e} = 0$.

In an axisymmetric problem $\mathbf{u} = \mathbf{u}(r, z)$, $\varphi = \varphi(r, z)$, hence, system of (42.1)–(42.4) can be presented in a cylindrical coordinate system $Orz\theta$. In order to formulate the boundary-value problem for this system, we should add mechanical and electric boundary conditions at the boundary: $\Gamma = \partial S$.

As almost the entire boundary Γ is stress-free, we can adopt the following condition for all its parts Γ_σ, except for the fixation points and the axis of symmetry:

$$\mathbf{p}_\sigma = \mathbf{L}^*(\mathbf{n}) \cdot \mathbf{T}, \quad \mathbf{p}_\sigma = 0, \quad \mathbf{x} \in \Gamma_\sigma, \tag{42.5}$$

where $\mathbf{n}$ is the vector of external unit vector normal to the boundary.

At the points $\Gamma_u = \{r = R_p, z = \pm(h_p/2 + h_m)\}$ condition (42.5) must be substituted by the sliding contact condition:

$$u_z = 0, \quad p_{\sigma r} = 0, \quad \mathbf{x} \in \Gamma_u, \tag{42.6}$$

Electric boundary conditions are independent from mechanical conditions. Therefore, they could be set only on the boundary of the piezoelectric disk.

The side surface of the disk Γ_D does not contain electrodes, hence we can adopt

$$\mathbf{n}^* \cdot \mathbf{D} = 0, \quad \mathbf{x} \in \Gamma_D. \tag{42.7}$$

We set zero electric potential on one of the electrodes, for example on $\Gamma_{\varphi 1}$

$$\varphi = 0, \quad \mathbf{x} \in \Gamma_{\varphi 1}. \tag{42.8}$$

On the second electrode $\Gamma_{\varphi 2}$, we can consider two types of electric external influence. In the first case, on $\Gamma_{\varphi 2}$ we set the potential V, which changes according to the harmonic law:

$$\varphi = V, \quad \mathbf{x} \in \Gamma_{\varphi 2}. \tag{42.9}$$

(Here we consider the problem for the amplitude values of displacements and electric potential. Consequently, the multiplier $\exp(i\omega t)$ can be omitted everywhere).

In the second case, the electrode $\Gamma_{\varphi 2}$ is powered by electric current generator with the amplitude value of electric current I or by electric charge with the amplitude value of electric charge Q. Hence we can set the following boundary conditions:

$$\varphi = \Phi, \quad \mathbf{x} \in \Gamma_{\varphi 2}, \tag{42.10}$$

$$\int\limits_{\Gamma_{\varphi 2}} \mathbf{n}^* \cdot \mathbf{D}\, d\Gamma = -Q, \quad I = \pm j\omega Q, \quad \mathbf{x} \in \Gamma_{\varphi 2}, \tag{42.11}$$

where the value of Φ is unknown, but does not depend on $\mathbf{x}$ on $\Gamma_{\varphi 2}$. The integral by $\Gamma_{\varphi 2}$ should be calculated in cylindrical coordinate system, and the sign "±" in (42.11) is chosen in accordance with the accepted direction of the current I in the electric circuit.

In order to solve problems (42.1)–(42.9) or (42.1)–(42.8), (42.10), (42.11) numerically, we will use the finite element method. Let us make transition to the weak statements of these problems and apply the technique of finite element approximations [27–30]. Let us introduce $\Omega_h = S_h \cup [0, 2\pi]$, where S_h is a region occupied by the corresponding finite element mesh, $S_h \subseteq S$, $S_h = \cup_k S^{ek}$, where S^{ek} is a separate finite element with the number k. For the problem of steady-state oscillations we will search the approximate solution $\{\mathbf{u}_h \approx \mathbf{u},\ \varphi_h \approx \varphi\}$ in the form

$$\mathbf{u}_h(r, z) = \mathbf{N}_u^*(r, z) \cdot \mathbf{U}, \quad \varphi_h(r, z) = \mathbf{N}_\varphi^*(r, z) \cdot \mathbf{\Phi}, \tag{42.12}$$

where $\mathbf{N}_u^*$ is the matrix of the basis (shape) functions for the displacements; $\mathbf{N}_\varphi^*$ is the row-vector of the basis functions for the electric potential; $\mathbf{U}$, $\mathbf{\Phi}$ are the vectors of nodal amplitudes for the displacements and electric potential, respectively.

In accordance with standard finite element technique, we approximate the continual weak formulation of the piezoelectric problem in finite-dimensional spaces that correspond to the basis functions $\mathbf{N}_u^*$ and $\mathbf{N}_\varphi^*$ [27–30]. Substituting (42.12) and similar expressions for projection functions into the weak formulation of the piezoelectric problem in Ω_h, we get the following finite element system:

$$-\omega^2 \mathbf{M}_{uu} \cdot \mathbf{U} + (1 + iQ_d^{-1}) \mathbf{K}_{uu} \cdot \mathbf{U} + \mathbf{K}_{u\varphi} \cdot \mathbf{\Phi} = \mathbf{F}_u, \tag{42.13}$$

$$-\mathbf{K}_{u\varphi}^* \cdot \mathbf{U} + \mathbf{K}_{\varphi\varphi} \cdot \mathbf{\Phi} = \mathbf{F}_\varphi, \tag{42.14}$$

where $\mathbf{M}_{uu}$ is the mass matrix, $\mathbf{K}_{uu}$ is the stiffness matrix, $\mathbf{K}_{u\varphi}$ is the matrix of piezoelectric coupling, $\mathbf{K}_{\varphi\varphi}$ is the matrix of dielectric permittivity, $\mathbf{F}_u$, $\mathbf{F}_\varphi$ are the vectors of generalized nodal forces and electric charges, resulting from taking inhomogeneous external influences into account.

Using (42.13), (42.14) we can formulate eigenvalue problems for $Q_d^{-1} = 0$, $\mathbf{F}_u = 0$, $\mathbf{F}_\varphi = 0$. Other problems of interest are the problem of finding electric resonance frequencies f_{rm} for electrical boundary (42.7)–(42.9) with $V = 0$ and the problem of finding electric antiresonance frequencies f_{ak}, when instead of condition (42.9) the condition of free electrode (42.10), (42.11) with zero electric charge $Q = 0$ is used. The solution of these two problems enables us to determine electrically active frequencies [28–30], for which the values f_{rm} and f_{am} with the same number k are significantly different. For such frequencies we can calculate the dynamic coefficients of electromechanical coupling, $k_{dm} = \sqrt{1 - f_{rm}^2 / f_{am}^2}$.

42.3 Input Data for Numerical Experiments

We take the same geometrical dimensions of the cymbal transducer as in [15]: R_p = 6.3 mm, h_p = 0.5 mm, r_1 = 4.5 mm, r_2 = 1.5 mm, h_c = 3.3 mm, h_m = 0.22 mm. For the metal end-caps we adopt material properties of brass as an isotropic material with the density $\rho_m = 8400\,\mathrm{kg/m^3}$, the Young's modulus $E_m = 9.5 \times 10^{10}\,\mathrm{N/m^2}$ and the Poisson's ratio $\nu_m = 0.35$.

For the piezoelectric disk, we will consider three types of porous piezoceramics PZT-4. For the first case, we adopt that the PZT-4 piezocearmic has closed porosity of stochastic structure. To calculate the effective moduli, we will use the approaches described in [22–24]. Specifically, in order to determine the full set of effective moduli $c_{\alpha\beta}^{E\mathrm{eff}}$, $e_{i\alpha}^{\mathrm{eff}}$ and $\varepsilon_{ij}^{S\mathrm{eff}}$ for the representative volume in the finite element software ANSYS, it is necessary to solve five static problems of electroelasticity with various linear by $\mathbf{x}$ essential boundary conditions for the displacements and electric potential.

A representative volume Ω for the porous piezoceramic composite was built as a regular cubic finite element mesh according to the following algorithm. At the beginning, a basic cubic cell with the dimensions $l_c \times l_c \times l_c$ was generated. In the

center of this cell we set the main cubic finite element with the edge l_p, expressed by the coefficient k_p and the length l_c of the cell side: $l_p = k_p l_c$. This cubic element was uniformly surrounded by 26 hexahedral finite elements to fulfill the basic cell. Then the basic cell of 27 hexahedral finite elements was duplicated n_c times along three coordinate axes. The resulting structure was an array $L \times L \times L$ $(L = n_c l_c)$ consisting of n_c^3 basic cells. Then, depending on the input porosity p_s, the random number generator was used to select N_p central finite elements of the cells, and their material properties were modified to the properties of pores. The value N_p was calculated by the formula $N_p = \left[p_s \left(n_c/k_p\right)^3\right]$, where $[\ldots]$ is the integer part of a number. The real porosity in this case was equal to $p = N_p (k_p/n_c)^3 \approx p_s$.

The described algorithm allows us to obtain the representative volume of porous piezoelectric material with closed porosity of partly stochastic structure. In this representative volume, N_p elements are pores Ω_{pi}, all faces $\Gamma_{pi} = \partial\,\Omega_{pi}$ of which are in full contact with the boundaries of the neighboring elements of the composite material. All elements were set as piezoelectric finite elements SOLID5 with an option of piezoelectric analysis. The skeleton elements and the pore elements differ only by their material properties. The calculations for this and two other cases were performed for the same geometrical dimensions: $L = 500\,\mu\text{m}$, $n_c = 10$, $k_p = 0.9$. For such dimensions the pore edges were equal to $l_p = k_p L/n_c = 45\,\mu\text{m}$.

The results of the effective moduli calculation for the porous piezoceramics PZT-4 with various porosities are summarized in Table 42.1.

In the second case, we consider porous piezoceramic with fully metallized pore surfaces where the thickness of the metal layer is negligibly small. This case differs from the previous one by the boundary condition of free electrodes (42.10), (42.11) with $Q = 0$ instead of (42.7) and by substitution of $\Gamma_{\varphi 2}$ by Γ_{pi}. These conditions will be repeated N_p times $\left(i = 1, 2, \ldots, N_p\right)$, i.e. for every pore the boundary conditions (42.10), (42.11) are satisfied separately. The results of the effective moduli computation for this case under different porosities are provided in Table 42.2.

In the third case, we continue to study porous piezoceramic with fully metallized pore surfaces, taking into account the metal layer of the pore covering. We assume that the thickness of the layer is uniform for all pore surfaces and is equal to $h_s = 1\,\mu\text{m}$. The material for the metal layer is nickel with the density $\rho_s = 8800\,\text{kg/m}^3$, the Young's modulus $E_s = 20.4 \times 10^{10}\,\text{N/m}^2$ and the Poisson's ratio $\nu_s = 0.28$. In the computer model for the third case in addition to the boundary conditions of free electrodes, we cover the pore surfaces by shell elastic finite elements.

It is important to note that for this case we take large enough value of the shell elements thickness: $h_s = 1$ μm. For such thickness value the mass fraction of metal on the pore boundaries with respect to the mass of piezoceramics in the representative volume equals 2.24% for the porosity $p = 0.1$ and 6.14% for the porosity $p = 0.5$ [23].

Table 42.1 Effective moduli of ordinary porous piezoceramics PZT-4

p (%)	0	5	10	15	20	25	30	35	40
ρ (kg/m^3)	7500	7125	6750	6375	6000	5625	5250	4875	4500
$c_{11}^{E\mathrm{eff}}$ (10^{10} N/m^2)	13.9	12.42	11.19	9.94	8.91	7.90	7.08	6.09	5.40
$c_{12}^{E\mathrm{eff}}$ (10^{10} N/m^2)	7.78	6.74	5.86	5.05	4.35	3.73	3.22	2.69	2.31
$c_{13}^{E\mathrm{eff}}$ (10^{10} N/m^2)	7.74	6.38	5.52	4.71	4.03	3.41	2.90	2.42	2.02
$c_{33}^{E\mathrm{eff}}$ (10^{10} N/m^2)	11.5	10.20	9.09	8.05	7.13	6.29	5.51	4.88	4.23
$c_{44}^{E\mathrm{eff}}$ (10^{10} N/m^2)	2.56	2.38	2.18	2.01	1.82	1.62	1.46	1.31	1.14
e_{33}^{eff} (C/m^2)	15.1	14.17	13.27	12.37	11.45	10.60	9.63	8.92	8.01
e_{31}^{eff} (C/m^2)	−5.2	−4.64	−4.16	−3.69	−3.26	−2.83	−2.47	−2.05	−1.76
e_{15}^{eff} (C/m^2)	12.7	11.73	10.83	9.87	8.96	8.05	7.22	6.40	5.59
$\varepsilon_{11}^{S\mathrm{eff}}/\varepsilon_0$	730	694	659	623	588	552	519	475	442
$\varepsilon_{33}^{S\mathrm{eff}}/\varepsilon_0$	635	604	573	540	508	472	439	405	368

Table 42.2 Effective moduli of porous piezoceramics PZT-4 with pore surface metallization, described by the boundary conditions of free electrodes

p (%)	0	5	10	15	20	25	30	35	40
ρ (kg/m^3)	7500	7125	6750	6375	6000	5625	5250	4875	4500
$c_{11}^{E\mathrm{eff}}$ (10^{10} N/m^2)	13.9	12.25	10.86	9.63	8.49	7.56	6.64	5.80	5.04
$c_{12}^{E\mathrm{eff}}$ (10^{10} N/m^2)	7.78	6.58	5.57	4.74	3.98	3.36	2.78	2.34	1.93
$c_{13}^{E\mathrm{eff}}$ (10^{10} N/m^2)	7.74	6.29	5.38	4.56	3.84	3.26	2.73	2.27	1.88
$c_{33}^{E\mathrm{eff}}$ (10^{10} N/m^2)	11.5	10.15	9.05	7. 96	7.01	6.20	5.47	4.76	4.15
$c_{44}^{E\mathrm{eff}}$ (10^{10} N/m^2)	2.56	2.37	2.18	2.00	1.82	1.63	1.45	1.30	1.14
e_{33}^{eff} (C/m^2)	15.1	13.48	12.15	10.77	9.58	8.56	7.67	6.74	5.92
e_{31}^{eff} (C/m^2)	−5.2	−5.90	−6.36	−6.83	−7.15	−7.41	−7.57	−7.74	−7.80
e_{15}^{eff} (C/m^2)	12.7	11.88	11.07	10.28	9.42	8.59	7.74	6.93	6.19
$\varepsilon_{11}^{S\mathrm{eff}}/\varepsilon_0$	730	771	808	847	890	933	976	1025	1064
$\varepsilon_{33}^{S\mathrm{eff}}/\varepsilon_0$	635	660	682	705	725	741	755	770	783

As it can be seen from Tables 42.1, 42.2, 42.3, the pore surface metallization significantly changes the material properties of the piezoceramic material [23].

Specifically, the stiffness moduli decrease with the increase of porosity for all considered cases. Moreover, for the pore surface metallization case the presence of the equipollency condition (42.10), (42.11) alone gives slightly larger decrease compared to the case of ordinary porous piezoceramic. Naturally, when we take into account the stiffness of the metallized pore surfaces, it leads to smaller decrease of the effective stiffness with the growth of porosity p. At the same time, the effective moduli of dielectric permittivities for ordinary porous piezoceramic decrease with the growth of porosity (Table 42.1), while the effective moduli of dielectric permittivities of porous piezoceramic with metallized pore surfaces, on

Table 42.3 Effective moduli of porous piezoceramics PZT-4 with pore surface metallization described by the boundary conditions of free electrodes and shell elements

p (%)	0	5	10	15	20	25	30	35	40
ρ (kg/m^3)	7500	7182	6868	6550	6236	5918	5600	5286	4968
$c_{11}^{E\text{eff}}$ (10^{10} N/m^2)	13.9	12.67	11.57	10.57	9.69	8.86	8.08	7.37	6.74
$c_{12}^{E\text{eff}}$ (10^{10} N/m^2)	7.78	6.82	5.99	5.24	4.61	4.03	3.52	3.06	2.66
$c_{13}^{E\text{eff}}$ (10^{10} N/m^2)	7.74	6.54	5.77	5.07	4.47	3.92	3.42	3.00	2.61
$c_{33}^{E\text{eff}}$ (10^{10} N/m^2)	11.5	10.51	9.65	8.84	8.12	7.45	6.83	6.31	5.78
$c_{44}^{E\text{eff}}$ (10^{10} N/m^2)	2.56	2.41	2.26	2.12	1.98	1.84	1.71	1.59	1.44
e_{33}^{eff} (C/m^2)	15.1	13.86	12.74	11.69	10.68	9.78	8.91	8.24	7.48
e_{31}^{eff} (C/m^2)	−5.2	−5.73	−6.15	−6.49	−6.80	−7.02	−7.23	−7.30	−7.45
e_{15}^{eff} (C/m^2)	12.7	11.99	11.29	10.58	9.89	9.20	8.52	7.82	7.09
$\varepsilon_{11}^{S\text{eff}}/\varepsilon_0$	730	766	802	841	878	916	955	996	1040
$\varepsilon_{33}^{S\text{eff}}/\varepsilon_0$	635	656	677	696	715	732	747	757	769

the contrary, increase with the porosity growth (see Tables 42.2 and 42.3). In this case, taking stiffness into account leads to slightly lesser growth of the dielectric permittivities. The behaviour of piezomodi is even more interesting. Indeed, in the case of ordinary porous piezoceramic, the piezomoduli e_{33}^{eff} and e_{31}^{eff} decrease with the increase of porosity. However, for both cases of a piezoceramic with metallized pore surfaces the piezomoduli e_{33}^{eff} also decrease with the growth of p, and they do it notably faster than in the first case. Meanwhile, the piezomoduli e_{31}^{eff} in the second and third cases increase with the growth of porosity.

Considerable difference in the behavior of material moduli from Tables 42.1, 42.2, 42.3 in the case of pore surface metallization causes differences in the behavior of other moduli of piezoceramic. Since for an ordinary piezoceramic the piezomodulus d_{33}^{eff} almost does not depend on the porosity p, and the piezomodulus $|d_{31}^{\text{eff}}|$ decreases with the growth of porosity p, then taking into account the pore surface metallization leads to the growth of both moduli d_{33}^{eff} and $|d_{31}^{\text{eff}}|$. This growth becomes more significant when decreasing the metal thickness on the pore surfaces. Thus, we can expect that the use of porous piezoceramic with metallized pore surfaces and the porosity change will have a significant impact on the efficiency of the cymbal transducer.

42.4 Numerical Results

Finite element simulation of a cymbal transducer was implemented in ANSYS finite element package using technique described in [28, 30]. Study of resonance frequencies under steady-state oscillations was performed in two steps. At the first step, the values of the first electrically active resonance and anti-resonance

frequencies were obtained. In all computations, we used regular mesh consisting of quadrilateral elements PLANE13 with piezoelectric properties and elastic elements PLANE182, both with additional option of axial symmetry. The whole transducer construction in the meridional section was divided in quadrilateral areas, which were meshed in 29 finite elements along its length, whereas along its thickness there were 6 elements for metal end-caps and 12 elements for piezoelectric disk. This mesh ensured sufficient accuracy of computations with respect to the further finite element mesh refinement.

Figure 42.3 illustrates the dependence of the first electric resonance frequency $f_{r1}^{(i)}$, the first electric antiresonance frequency $f_{a1}^{(i)}$, and the coefficient of electromechanical coupling $k_{d1}^{(i)}$ on porosity. Here and after the superscript in the brackets denotes the number of the material properties set from Tables 42.1, 42.2, 42.3. Namely, number 1 indicates the curves corresponding to the results for ordinary porous piezoceramic. Number 2 indicates the curves, corresponding to the results for porous piezoceramic with pore surface metallization, described by the boundary conditions of free electrodes. Number 3 is related to the results for porous piezoceramic with pore surface metallization, described by the boundary conditions of free electrodes and shell elements. In Fig. 42.3a, solid lines denote the values of electric resonance frequencies, and dash lines denote the values of electric antiresonance frequencies. Mode shapes at the first two most electrically active resonance frequencies for ordinary porous piezoceramic are shown in Fig. 42.4. Here $f_{r1}^{(1)} = 34.98\,\text{kHz}$ in Fig. 42.4a, and $f_{r1}^{(2)} = 225.2\,\text{kHz}$ in Fig. 42.4b. Moreover, for this case there are two intermediate less electrically active resonance frequencies with the coefficients of electromechanical coupling equal to 0.018 and 0.024.

As it can be seen in Fig. 42.3a, the values of resonance and antiresonance frequencies decrease with the growth of porosity for all three cases of porous piezoceramics. However, the character of the relative decrease of resonance and antiresonance frequencies for various cases of piezoceramic is significantly different. This difference affects the dependences of the electromechanical coupling coefficients on porosity (Fig. 42.3b). As it can be seen, for the case of ordinary

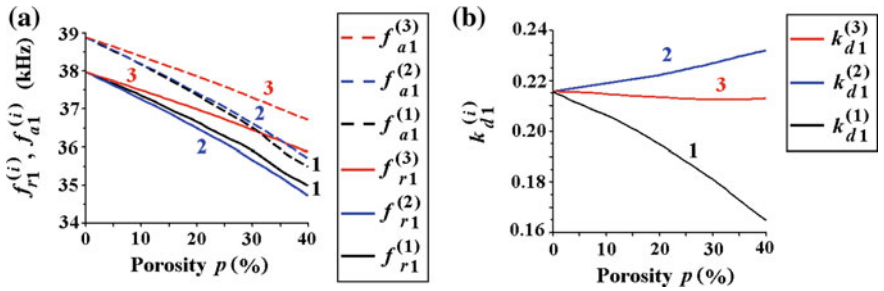

Fig. 42.3 The first electrically active resonance and antiresonance frequencies (**a**) and the coefficient of electromechanic coupling (**b**)

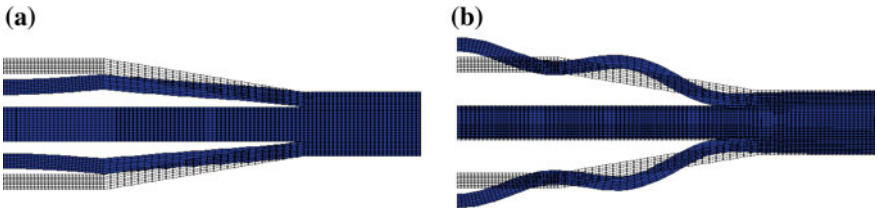

Fig. 42.4 Mode shapes at the first two most electrically active resonance frequencies

piezoceramic the first resonance frequencies become electrically less active ($k_{d1}^{(1)}$ decreases) with the growth of porosity. However, the coefficient $k_{d1}^{(2)}$ increases with the growth of p for the case of piezoceramic with pore surface metallization described by the boundary conditions of free electrodes (case 2), whereas for the third case, when the thickness of the metal layer is taken into account, the coefficient $k_{d1}^{(3)}$ almost does not change with the growth of porosity. Thus, we can conclude that the pore surface metallization enhances electrical activity of resonance frequencies.

In order to obtain amplitude-frequency characteristics at steady-state oscillations for a fixed frequency range $[f_{beg}, f_{end}]$ for various porosity and various types of porous piezoceramics, we solve problems (42.13), (42.14) dividing the frequency range into three parts $\left[f_{beg}, f_{r1}^{(i)}\right]$, $\left[f_{r1}^{(i)}, f_{a1}^{(i)}\right]$, $\left[f_{a1}^{(i)}, f_{end}\right]$. Such approach ensures that calculations of steady-state oscillations will be performed at resonance frequencies in their vicinities, and therefore the amplitude-frequency characteristics will be obtained with sufficient accuracy. For numerical experiments, the ends of the frequency range were taken as $f_{beg} = 34\,\text{kHz}$; $f_{end} = 40\,\text{kHz}$; and the frequency step Δf was varied depending on the range length from 10 to 20; the quality factor was uniform for the whole construction and equal to $Q_d = 1000$.

For the analysis we consider the amplitude-frequency characteristics $w_p^{(i)} = |u_z|_p^{(i)}$ of axial displacement at the upper central point $\{r = 0,\ z = h_p/2 + h_c + h_m\}$ and radial displacement $u_p^{(i)} = |u_r|_p^{(i)}$ at the central point $\{r = R_p,\ z = 0\}$ of the side surface of the transducer. As previously, the superscript in the brackets denotes the number of the material properties set of piezoceramics from Tables 42.1, 42.2, 42.3, and additional index $i = 0$ corresponds to the material of dense piezoceramic. Moreover, the lower index p denotes the porosity value at which the computations are performed (p = 40% and p = 20%).

Some computational results are shown in Figs. 42.5 and 42.6. The curve numbers 1–3 refer to the same cases of porous piezoceramics as in Fig. 42.3. Solid curves with numbers 1–3 were obtained for materials with 40% porosity and dash curves were obtained for materials with 20% porosity. Green curves with number 0 indicate the results obtained for the dense piezoceramic PZT-4.

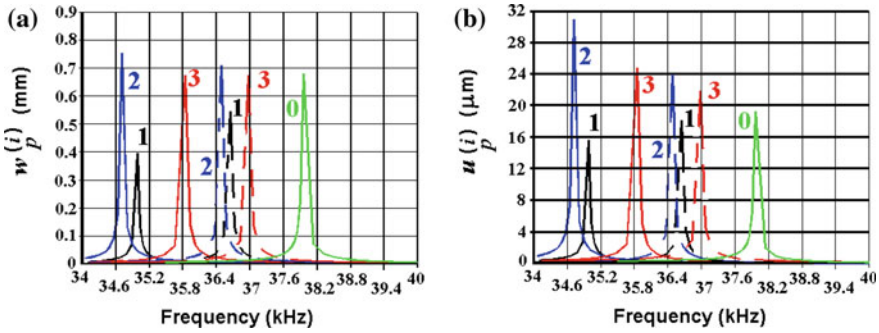

Fig. 42.5 Deflection at the top center point **a** and axial displacement at the side surface **b** for the problem with given electric potential

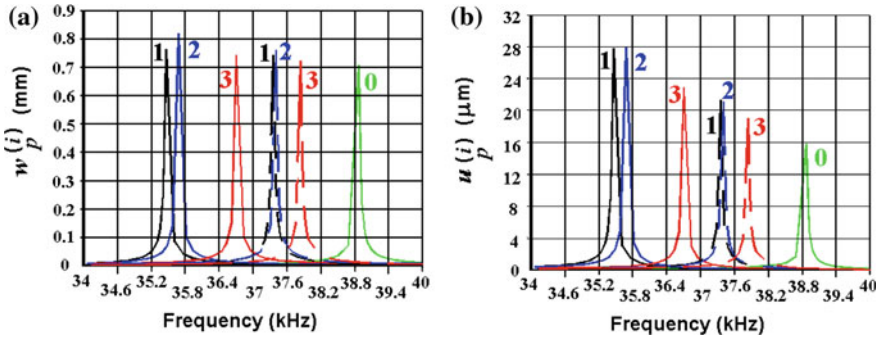

Fig. 42.6 Deflection at the top center point **a** and axial displacement at the side surface **b** for the problem with given electric charge

The amplitude-frequency characteristics in Figs. 42.5 and 42.6 were received for various electrical influences. Figure 42.5 corresponds to the problem with a given oscillating potential difference of the amplitude $V = 100$ V, whereas Fig. 42.6 corresponds to the problem with a given electric charge of the amplitude $Q = 0.25 \times 10^{-6}$ C at one electrode and grounded other electrode. As it can be seen from Figs. 42.5 and 42.6, the dependences on porosity for the maximal amplitudes of displacements in these two problems are significantly different. The porosity type also considerably affects the amplitude values. As it is usually observed [28], for the problems with given potential difference, the maximal amplitudes are obtained at the frequencies of electric resonances, whereas for the problems with given electric charge, the frequencies of electric antiresonances give maximal amplitudes.

In the case of ordinary porous piezoceramic (case 1), when we set the potential differences at the electrodes, the amplitudes of displacements at resonance frequencies decrease with the growth of porosity. We note that the amplitudes of axial displacements decrease faster than the amplitudes of radial displacements. For

porous piezoceramic with infinitely thin metallized pore surfaces (case 2), the maximal values of axial displacements grow weakly with the porosity increase, whereas the maximal axial displacements grow much faster. In the case of porous piezoceramic with sufficiently thick metal covering of the pore surfaces (case 3) the maximal amplitudes of axial displacements almost do not depend on porosity, while the maximal amplitudes of radial displacements also grow with the porosity growth, but less intensively than in the case 2.

The difference in the maximums of axial displacements become less noticeable when the oscillations of the cymbal transducer are excited by electric charge (Fig. 42.6). Here for all three cases the maximal displacements slightly increase with the growth of porosity. As it took place for the previous problem, the maximal increase is observed for case 2. In the same manner for all three cases the maximal amplitudes of radial displacements increase with the growth of porosity. The increase in the amplitudes of both axial and radial displacements is minimal for the third case with thick metal layer of the pore surface covering.

We note that in all cases at the first resonance frequencies the axial displacements in central end areas of the transducer are in order of magnitude greater compared to the radial displacements of its side surfaces. Thus, the cymbal transducer at the first resonance frequency efficiently generates axial oscillations. Moreover, the use of porous piezoceramic with the pore surfaces, covered by a very thin layer of metal, excites oscillations in the most effective way. Taking into account smaller acoustic impedance of porous piezoceramic in comparison with ordinary dense piezoceramic, we can conclude that piezoceramic materials of such type are very perspective for use as active materials for the acoustic waves transducers.

42.5 Concluding Remarks

Using numerical simulation, we have analyzed a cymbal piezoelectric transducer, consisting of piezoceramic disk with two metal end-caps. As active material of the transducer we considered both ordinary porous piezoceramic and porous piezoceramic with fully metallized pore surfaces according to technology described in [31].

In the first part of this study, we presented numerical results of the effective properties calculation for such microporous piezoceramic materials. This investigation was based on a complex approach, which included the effective moduli method for the mechanics of composites, the simulation of representative volumes, the finite element solution of the set of static problems of the piezoelectricity theory with special boundary conditions, and the postprocessing of computation results. To simulate the metallization on the boundaries of pores with piezoceramic matrix, we used the boundary conditions of free electrodes and elastic shell finite elements. The results of the numerical experiments on solving the homogenization problems with the help of ANSYS finite element package enabled us to estimate the influence of the pore surface metallization on the values of the effective moduli of piezoelectric

materials, which were obtained by the method of micro- or nanoparticles transportation into ceramic skeletons [31].

The second part contained the analysis of a cymbal transducer with the piezoelectric disk made of different types of piezoceramics PZT-4. We have considered four types: (i) dense piezoceramic, (ii) ordinary porous piezoceramic, (iii) porous piezoceramic with porous surfaces, covered by infinitely thin layer of metal, and (iv) porous piezoceramic with porous surfaces, covered by metallized layer with sufficiently great thickness. For every simulation case for the material of piezoelectric disk, we adopted suitable effective material moduli of porous piezoceramic PZT-4 obtained previously. Then we have built solid and finite element models of the considered cymbal transducer in an axisymmetric statement. Numerical computation was performed in ANSYS finite element software using scripts in APDL language. The simulation results allowed us to calculate the first electrically active resonance frequencies and to carry out the harmonic analysis of axial and radial vibrations of the transducer near to resonance frequencies. The computation results have shown that the axial vibrations at the first electrically active resonance frequency are the largest for the cymbal transducer made of porous piezoceramic with the pore surfaces, covered by infinitely thin layer of metal with maximal percentage of porosity. Thus, we can conclude that microporous piezoceramics with metallized pore surfaces have perspective properties for practical applications.

By changing the geometrical dimensions, the piezoceramic porosity and the structure of the pore surface metallization, along with the fixing boundary conditions, it is possible to vary the parameters of the transducer within a fairly wide range and obtain optimal performance in various ultrasound and piezotechnical applications.

Acknowledgements This research was performed in the framework of the Indian-Russian DST-RFBR Collaborative project with DST grant number DST/INT/RFBR/IDIR/P-11/2016 and RFBR grant number RFBR 16-58-48009 IND_omi.

References

1. K.D. Rolt, J. Acoust. Soc. Amer. **87**, 1340 (1990)
2. Q.C. Xu, S. Yoshikawa, J.R. Belsick, R.E. Newnham, IEEE Trans. Ultrason. Ferroelectr. Freq. Control **38**, 634 (1991)
3. W.Y. Shin, W.H. Shin, I.A. Aksay, J. Am. Ceramic Soc. **80**, 1073 (1997)
4. K. Onitsuka, A. Dogan, Q. Xu, S. Yoshikawa, R.E. Newnham, Ferroelectrics **156**, 37 (1994)
5. A. Dogan, *Flextensional "Moonie and Cymbal" Actuators*. Ph.D. Thesis, The Pennsylvania State University, University Park, PA, 362 p. (1994)
6. A. Dogan, K. Uchino, R.E. Newnham, I.E.E.E. Trans, Ultrason. Ferroelectr. Freq. Control **44**, 597 (1997)
7. A. Dogan, K. Uchino, R.E Newnham, In: *Piezoelectric Materials: Advances in Science, Technology and Applications*. NATO Science Series 3, eds. by C. Galassi, M. Dinescu, K. Uchino, M. Sayer, vol. 76, (Springer, Dordrecht, 2000), p. 357

8. R.E. Newnham, J. Zhang, R. Meyer, In: *ISAF 2000. Proceedings* of the *XII IEEE International Symposium* on *Applications of Ferroelectrics*, vol. **1**, (2000), p. 29
9. P. Ochoa, J.L. Pons, M. Villegas, J.F. Fernandez, Sens. Actuators, A **132**, 63 (2006)
10. J.F. Fernandez, A. Dogan, J.T. Fielding, K. Uchino, R.E. Newnham, Sens. Actuators, A **65**, 228 (1998)
11. W. Lina, L. Denghua, W. Min, J. Meijian, J. Weijun, Integr. Ferroelectr. **80**, 297 (2006)
12. P. Ochoa, M. Villegas, J.F. Fernandez, Ferroelectrics **273**, 315 (2002)
13. E.A. Uzgur, A. Dogan, R.E. Newnham, Key Eng. Mater. **206–213**(2), 1297 (2002)
14. L. Wang, D. Li, M. Wu, M. Jia, W. Ju, Integr. Ferroelectr. **80**, 297 (2006)
15. S. Guo, W. Li, L. Sang, C. Sun, X.-Z. Zhao, Integr. Ferroelectr. **78**, 103 (2006)
16. Z. Li, A. Huang, G. Luan, J. Zhang, Ultrasonics **44**, e759 (2006)
17. J.F. Tressler, W. Cao, K. Uchino, R.E. Newnham, IEEE Trans. Ultrason. Ferroelectr. Freq. Control **45**(5), 1363 (1998)
18. P. Ochoa, J.L. Pons, M. Villegas, J.F. Fernandez, J. Eur. Ceram. Soc. **27**, 1143 (2007)
19. F. Bejarano, A. Feeney, R. Wallace, H. Simpson, M. Lucas, Ultrasonics **72**, 24 (2016)
20. A. Moure, M.A. Izquierdo Rodríguez, S.H. Rueda, A. Gonzalo, F. Rubio-Marcos, D.U. Cuadros, A. Pérez-Lepe, J.F. Fernández, Energy Convers. Manag. **112**, 246 (2016)
21. G. Yesner, M. Kuciej, A. Safari, A. Jasim, H. Wang, A. Maher, In: *2016 Joint IEEE International Symposium on the Applications of Ferroelectrics, European Conference on Application of Polar Dielectrics, and Piezoelectric Force Microscopy Workshop (ISAF/ECAPD/PFM*), *Darmstadt, Germany,* 21–25 Aug 2016. IEEE Conference Publication (2016)
22. A.V. Nasedkin, A.A. Nasedkina, A.N. Rybyanets, In: *Proceedings of the 2016 International Conference on "Physics, Mechanics of New Materials and Their Applications*", eds. by I.A. Parinov, S.-H. Chang, M.A. Jani (Nova Science Publishers, New York, 2017), p. 385
23. A. Nasedkin, A. Nasedkina, A. Rybyanets, Ferroelectrics **508**, 100 (2017)
24. A.V. Nasedkin, A.A. Nasedkina, A.N. Rybyanets In: *Poromechanics VI. Proceedings of* the *Sixth Biot Conference* on *Poromechanics,* Paris, France. 9–13 July 2017, eds. by M. Vandamme, P, Dangla, J.-M. Pereiram, S. Ghabezloo (Publ. ASCE, Reston, Virginia, USA, 2017), p. 724
25. E. Ringgaard, F. Lautzenhiser, L.M. Bierregaard, T. Zawada, E. Molz, Materials **8**(12), 8877 (2015)
26. A.N. Rybyanets, IEEE Trans. Ultrason. Ferroelectr. Freq. Control **58**, 1492 (2011)
27. M. Kaltenbacher, *Numerical Simulation of Mechatronic Sensors and Actuators: Finite Elements for Computational Multiphysics* (Springer, Berlin, Heidelberg, New York, 2015)
28. A.V. Nasedkin, *Modeling of Piezoelectric Transducers in ANSYS* (SFedU Press, Rostov-on-Don, 2015). (in Russian)
29. A.V. Nasedkin, In: *Piezoceramic Materials and Devices*, ed. by I.A. Parinov (Nova Science Publishers, New York, 2010), p. 177
30. A.V. Nasedkin, A.A. Nasedkina, *Finite Element Modeling of Coupled Problems: Textbook* (SFedU Press, Rostov-on-Don, 2015)
31. A.N. Rybyanets, A.A. Naumenko, In: *Physics and Mechanics of New Materials and Their Applications*, eds by I.A. Parinov, S.-H. Chang (Nova Science Publishers, New York, 2013), p. 3

Chapter 43
Mathematical Modelling of Stepped Beam Energy Harvesting Using Euler–Bernoulli's Theory

S. K. Prajapati, V. K. Gupta and S. Mukherjee

Abstract Energy harvesting with cantilever beam is the most commonly used method for small electrical input devices like sensors etc. Uniform cantilever beam with no concentrated mass at the end produces less energy than the beam with concentrated mass at end. In this paper, instead of addition of the tip mass, single step beam with no concentrated mass is studied. Stepped beam with less stiff end as fixed end, given excitation at the base showing better results than the uniform beam with base excitation at the fixed end in form of transmissibility function. Frequency response function (FRF) has been plotted for voltage output, current and power, showing good results than the uniform beam. While comparing the results between the uniform beam and stepped beam the total mass kept equal.

43.1 Introduction

Smart materials like piezoelectric materials are immerged as a source of energy among various non-conventional sources of energy. Piezoelectric material converts mechanical energy into electrical energy by the electromechanical coupling [1]. Energy harvesting using unimorph cantilever beam with piezoelectric material, limited to use for small input power electronics and MEMS devices. Energy harvesting by using uniform cross-section cantilever beam is studied by many researchers. Exciting the base of harvester, based on different theories, namely lumped mass, Euler–Bernoulli, Rayleigh and Timoshenko, and studied for the output power has been done. Erturk et al. [2] discussed issues, related to uniform beam harvester modeling. They explained that, single degree of freedom models have inaccuracy in results and can be corrected either by addition of large proof mass or by the correction factor [3, 4]. They proposed that by distributed parameters the lumped mass results can be corrected. In the solution, excitation was not

S. K. Prajapati · V. K. Gupta · S. Mukherjee (✉)
PDPM Indian Institute of Information Technology, Design and Manufacturing, Jabalpur 482005, India
e-mail: sujoy@iiitdmj.ac.in

I. A. Parinov et al. (eds.), *Advanced Materials*, Springer Proceedings in Physics 207, https://doi.org/10.1007/978-3-319-78919-4_43

restricted to harmonic excitation [5]. Proportional damping has been presented by them on the base of closed form expression for electrical power output.

Erturk et al. [4] presented the energy harvesting model, based on Euler–Bernoulli's assumptions, and gave analytical solution for bimorph cantilevered harvester model for series and parallel connections to piezoelectric layers. They experimentally validated the bimorph cantilever model with and without tip mass. They presented single-mode analytical express-ions for the voltage output and deflection FRFs. Fakhzan et al. [6] experimentally validated the analytical model for cantilever beam harvester with and without tip mass for multi-mode FRFs for voltage output and tip deflection. As the Euler–Bernoulli beam theory neglects the rotary inertia and shear effects, it gives the simplified formulations, whereas the Timoshenko beam theory includes both the effects. Dietl et al. [7] had given exact formulation for voltage output and tip deflection, based on the Timoshenko beam theory. They compared with the Euler–Bernoulli beam model and concluded that it over predicts the results for voltage output and tip displacement. The results for very long Euler–Bernoulli beam are equivalent to the Timoshenko beam, which was further proved by Wang [8], who used spectral finite element method for comparison between two models.

To increase the power output, many researchers have done some modifications to their harvester model. Jagannathan et al. [9] proposed two modifications, first, voltage inversion method in which voltage was in phase with current, which increases power by 50% in series inversion. Second, the use of tapered cantilever beam over rectangular cantilever beams increases power by 3 times. Ayed et al. [10] used variable width of cantilever harvester, varied either linearly or quadratically with respect to position. They used Euler–Lagrange equation and enhanced power density at low frequency of excitation. Annapureddy et al. [11] introduced cavity along the width of harvester, which increased the strain hence power and output voltage increased up to 1.75 times. Guan et al. [12] used H-shaped proof mass for cantilever harvester, which provided large rotary inertia. They experimentally and using FEM analysis verified their results. Sang et al. [13] splits harvester beam into beams with small width. They found that on single splitting power increased by 2.45 times and on two splitting power increased by 2.76 times compared to beam without splitting. Splitting decreases the damping of beam, which increases the vibration amplitude hence power. Dayou et al. [14] experimentally verified the analytical solution of harvester with split width.

Levinson [15] presented the expressions for the natural frequency for stepped string and stepped beam by the continuity condition at the junction of two sections. Exact solution for frequency equation, given by Jang et al. [16], they compared to theoretical solution with finite element method (FEM) for different end conditions of the stepped beam. Rosa [17] calculated natural frequency equations for the Euler–Bernoulli stepped beam with elastic end condition. Naguleswaran [18] used three types of stepped beams, first, beam with step in width, second, beam with step in thickness and third, circular beam with step in diameter with similar cross-section. For all the types of beam model frequency equation was developed for different end conditions. Bhattacharyya et al. [19] gave an analytical solution for

the frequency equation for single step change stepped beam for free-free end condition and they verified theoretical model experimentally. Wickenheiser [20] used a piezo-electric cantilevered beam with variable cross-sections, multiple discontinuity with lumped mass and angle between the steps provided. Equation of motion and eigen-function was derived and experimentally validated. Vaz et al. [21] presented the modes shapes of the Euler–Bernoulli beam with multiple step changes theoretically and validated experimentally.

In this paper, unimorph stepped cantilever beam harvester of rectangular cross-section is studied. Harvester is excited at the fixed base in the form of translation and small rotation which is not restricted to be harmonic. As per the Euler–Bernoulli's assumptions relative tip displacement of the stepped beam for transverse vibration is derived. Both types of damping, namely internal (strain-rate damping) and external (viscous-air damping) are considered. For better comparison with uniform beam harvester, mass of stepped beam kept equal to uniform beam. Moment of inertia of the both the model are different. Expression for relative transmissibility function and voltage, current and power FRFs are derived. FRFs are plotted against the excitation frequency for different load resistances.

43.2 Stepped Beam Model

43.2.1 Relative Tip Displacement of the Harvester

Stepped cantilever unimorph beam, shown in Fig. 43.1, consists of two sections AB and BC. The less stiff end (end A) of the harvester is fixed and given excitation at that end considering no restriction to be harmonic in nature. The excitation is combination of translation $g(t)$ and small rotation $h(t)$. Assuming as thin beam enables to neglect the effect of rotary inertia and shear deformation hence Euler–Bernoulli formulation can be performed. The harvester is unimorph in which piezo-electric layer is on the substrate layer. The flexural stiffness of section AB of the beam is going to affect by the configuration of layers of the harvester.

The transverse deflection at the free end of the beam is given by $w(x, t)$. Two sections AB and BC with different cross-sections of the stepped beam junction at the B. The undamped equation of motion for the section AB of the beam is given as [22]

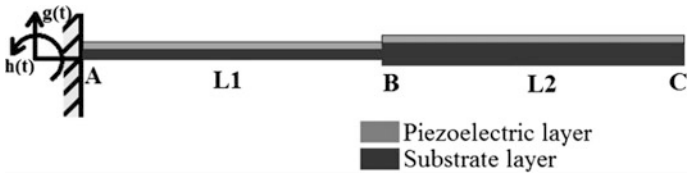

Fig. 43.1 Unimorph stepped cantilever beam harvester with base excitation

$$Y_1 I_1 \frac{\partial^4 w_1(x,t)}{\partial x_1^4} + m_1 \frac{\partial^2 w_1(x,t)}{\partial t^2} = 0 \tag{43.1}$$

where $Y_1 I_1$ is equivalent bending stiffness (Y is the Young's modulus and I is the moment of inertia) and m_1 is the mass per unit length of section AB of the stepped beam with PZT layer cross-section. There are two types of damping involved namely strain rate damping and air-viscous damping. The damped equation of motion is written as

$$Y_1 I_1 \frac{\partial^4 w_1(x,t)}{\partial x_1^4} + C_{s,1} I_1 \frac{\partial^5 w_1(x,t)}{\partial x_1^4 \partial t} + C_{a,1} \frac{\partial w_1(x,t)}{\partial t} + m_1 \frac{\partial^2 w_1(x,t)}{\partial t^2} = 0 \tag{43.2}$$

where C_a is viscous air damping coefficient due to air displaced near the beam and C_s is strain rate damping coefficient due to internal friction in the beam. Both of the damping considered satisfies the proportional damping criteria, so they are convenient for the modal response analysis of the beam. The absolute transverse displacement is given as [4]

$$w(x,t) = w_{rel}(x,t) + w_b(x,t) \tag{43.3}$$

where $w_{rel}(x,t)$ is the relative transverse deflection and $w_b(x,t)$ is the base motion. The base motion is combination of transverse base motion and small rotation as shown in Fig. 43.1. Equation (43.2) can be rewritten as

$$\begin{aligned} E_1 I_1 \frac{\partial^4 w_{1,rel}(x,t)}{\partial x_1^4} + C_{s,1} I_1 \frac{\partial^5 w_{1,rel}(x,t)}{\partial x_1^4 \partial t} + C_{a,1} \frac{\partial w_{1,rel}(x,t)}{\partial t} \\ + m_1 \frac{\partial^2 w_{1,rel}(x,t)}{\partial t^2} = -C_{a,1} \frac{\partial w_{1,b}(x,t)}{\partial t} - m_1 \frac{\partial^2 w_{1,b}(x,t)}{\partial t^2} \end{aligned} \tag{43.4}$$

The solution of (43.1) for space can be written as

$$\mathrm{X}_1(x_1) = \mathrm{C}_1 \sin\beta_1 \mathrm{x}_1 + \mathrm{C}_2 \cos\beta_1 \mathrm{x}_1 + \mathrm{C}_3 \sinh\beta_1 \mathrm{x}_1 + \mathrm{C}_4 \cosh\beta_1 \mathrm{x}_1 \tag{43.5}$$

where β_1 is dimensionless frequency parameter roots of characteristics equation at frequency ω, and given as

$$\beta_1^4 = \frac{m_1 \omega^2}{Y_1 I_1} \tag{43.6}$$

The solution of (43.4) is given as [22]

$$w_{rel}(x,t) = \sum_{r=1}^{\infty} \varnothing_r(x) \eta_r(t) \tag{43.7}$$

where $\varnothing_r(x)$ is eigen-function and $\eta_r(t)$ is modal coordinate of the beam at r-th mode. Now applying the boundary conditions to (43.5) as

$$\begin{gathered}\text{Deflection,} \quad X_1(x_1 = 0) = 0 \\ \text{Slope,} \quad X_1'(x_1 = 0) = 0 \\ \mathrm{X_1}(x_1) = \mathrm{C_1}(\sin\beta_1 \mathrm{x_1} - \sinh\beta_1 \mathrm{x_1}) + \mathrm{C_2}(\cos\beta_1 \mathrm{x_1} - \cosh\beta_1 \mathrm{x_1})\end{gathered} \tag{43.8}$$

Similarly, considering the section BC of the stepped beam, the equation of the motion can be given as

$$Y_2 I_2 \frac{\partial^4 w_2(x,t)}{\partial x_2^4} + m_2 \frac{\partial^2 w_2(x,t)}{\partial t^2} = 0 \tag{43.9}$$

and the solution for the above equation is

$$\mathrm{X_2}(x_2) = \mathrm{C_5}\sin\beta_2 \mathrm{x_2} + \mathrm{C_6}\cos\beta_2 \mathrm{x_2} + \mathrm{C_7}\sinh\beta_2 \mathrm{x_2} + \mathrm{C_8}\cosh\beta_2 \mathrm{x_2} \tag{43.10}$$

Here $\mathrm{X_2}(x_2)$ is the normal mode of the section BC at natural frequency ω and

$$\beta_2^4 = \frac{m_2 \omega^2}{Y_2 I_2} \tag{43.11}$$

As it can be seen from Fig. 43.1, the B is the junction point of two sections, namely AB and BC. At this junction, beam must satisfy the continuity conditions, which are given by following equations:

$$\text{Deflection,} \, \mathrm{X_1}(x_1 = L_1) = \mathrm{X_2}(x_2 = 0) \tag{43.12a}$$

$$\text{Slope,} \, X_1'(x_1 = L_1) = X_2'(x_2 = 0) \tag{43.12b}$$

$$\text{Bending moment,} \, Y_1 I_1 X_1''(x_1 = L_1) = Y_2 I_2 X_2''(x_2 = 0) \tag{43.12c}$$

$$\text{Shear force,} \, Y_1 I_1 X_1'''(x_1 = L_1) = Y_2 I_2 X_2'''(x_2 = 0) \tag{43.12d}$$

where "′" represents the differentiation with respect to position x. Applying above conditions to (43.8) and (43.10) implies as follows

$$\mathrm{C_1}(\sin\beta_1 \mathrm{L_1} - \sinh\beta_1 \mathrm{L_1}) + \mathrm{C_2}(\cos\beta_1 \mathrm{L_1} - \cosh\beta_1 \mathrm{L_1}) = \mathrm{C_6} + \mathrm{C_8} \tag{43.13a}$$

$$\beta_1(\mathrm{C_1}(\cos\beta_1 \mathrm{L_1} - \cosh\beta_1 \mathrm{L_1}) - \mathrm{C_2}(\sin\beta_1 \mathrm{L_1} + \sinh\beta_1 \mathrm{L_1})) = \beta_2(\mathrm{C_5} + \mathrm{C_7}) \tag{43.13b}$$

$$Y_1 I_1 \beta_1^2(\mathrm{C_1}(\sin\beta_1 \mathrm{L_1} + \sinh\beta_1 \mathrm{L_1}) + \mathrm{C_2}(\cos\beta_1 \mathrm{L_1} + \cosh\beta_1 \mathrm{L_1})) = Y_2 \mathrm{I_2} \beta_2^2(\mathrm{C_6} - \mathrm{C_8}) \tag{43.13c}$$

$$Y_1 I_1 \beta_1^3 (C_1(\cos\beta_1 L_1 - \cosh\beta_1 L_1) - C_2(\sin\beta_1 L_1 - \sinh\beta_1 L_1)) = Y_2 I_2 \beta_2^3 (C_5 - C_7) \tag{43.13d}$$

Solve above equations such that the constants C_5, C_6, C_7 and C_8 can be expressed via constants C_1 and C_2:

$$C_5 = C_1 \cos\beta_1 L_1 - C_2 \sin\beta_1 L_1,$$

$$C_6 = C_1 \sin\beta_1 L_1 + C_2 \cos\beta_1 L_1$$

$$C_7 = -C_1 \cosh\beta_1 L_1 - C_2 \sinh\beta_1 L_1,$$

$$C_8 = -C_1 \sinh\beta_1 L_1 - C_2 \cosh\beta_1 L_1$$

Substituting the above values in (43.10), the normal mode function can be simplified as

$$\begin{aligned} X_2(x_2) = {} & C_1(\cos(\beta_1 L_1)\sin(\beta_2 x_2) + \sin(\beta_1 L_1)\cos(\beta_2 x_2) \\ & - \cosh(\beta_1 L_1)\sinh(\beta_2 x_2) - \sinh(\beta_1 L_1)\cosh(\beta_2 x_2)) \\ & + C_2(-\sin(\beta_1 L_1)\sin(\beta_2 x_2) + \cos(\beta_1 L_1))\cos(\beta_2 x_2) \\ & - \sinh(\beta_1 L_1)\sinh(\beta_2 x_2) - \cosh(\beta_1 L_1)\cosh(\beta_2 x_2)) \end{aligned} \tag{43.14}$$

The boundary conditions for cantilever beam harvester at the free end C which is given by

$$\text{Bending moment,} \quad E_2 I_2 X_2''(x_2 = L_2) = 0 \tag{43.15a}$$

$$\text{Shear force,} \quad E_2 I_2 X_2'''(x_2 = L_2) = 0 \tag{43.15b}$$

Applying above boundary conditions to (43.14), implies:

$$\begin{aligned} & Y_2 I_2 \beta_2^2 (C_1(-\cos(\beta_1 L_1)\sin(\beta_2 L_2) - \sin(\beta_1 L_1)\cos(\beta_2 L_2) \\ & -\cosh(\beta_1 L_1)\sinh(\beta_2 L_2) - \sinh(\beta_1 L_1)\cosh(\beta_2 L_2)) \\ & - C_2(\sin(\beta_1 L_1)\sin(\beta_2 L_2) - \cos(\beta_1 L_1)\cos(\beta_2 L_2) \\ & - \sinh(\beta_1 L_1)\sinh(\beta_2 L_2) - \cosh(\beta_1 L_1)\cosh(\beta_2 L_2))) = 0 \end{aligned} \tag{43.16a}$$

$$\begin{aligned} & Y_2 I_2 \beta_2^3 (C_1(-\cos(\beta_1 L_1)\cos(\beta_2 L_2) + \sin(\beta_1 L_1)\sin(\beta_2 L_2) \\ & - \cosh(\beta_1 L_1)\cosh(\beta_2 L_2) - \sinh(\beta_1 L_1)\sinh(\beta_2 L_2)) \\ & + C_2(\sin(\beta_1 L_1)\cos(\beta_2 L_2) + \cos(\beta_1 L_1)\sin(\beta_2 L_2) \\ & - \sinh(\beta_1 L_1)\cosh(\beta_2 L_2) - \cosh(\beta_1 L_1)\sinh(\beta_2 L_2))) = 0 \end{aligned} \tag{43.16b}$$

Above equations can also be written in simplified form as

$$Y_2 I_2 \beta_2^2 (C_1 z_1 + C_2 z_2) = 0 \tag{43.17a}$$

$$Y_2 I_2 \beta_2^3 (C_1 z_3 + C_2 z_4) = 0 \tag{43.17b}$$

For characteristic or frequency equation, the determinant of the coefficients C_1 and C_2 must be equals to zero:

$$\begin{vmatrix} z_1 z_2 \\ z_3 z_4 \end{vmatrix} = 0 \Rightarrow z_1 z_4 - z_2 z_3 = 0 \tag{43.18}$$

Equation (43.18) will give the frequency equation, whose roots will give the natural frequency of the stepped beam harvester. Since β_1 and β_2 are the functions of natural frequency and natural frequency of the stepped beam is the function of material properties of the beam, it can be calculated from (43.11).

From (43.14) [22], C_2 can be eliminated and normal mode function will have only one constant i.e. C_1, which is calculated by the orthogonality condition of the beam. The normal mode function at r-th mode is given as

$$\begin{aligned} \varnothing_r(x) = \sqrt{\frac{1}{m_2 L_2}} [&(\cos(\beta_1 L_1)\sin(\beta_2 x_2) + \sin(\beta_1 L_1)\cos(\beta_2 x_2) \\ &- \cosh(\beta_1 L_1)\sinh(\beta_2 x_2) - \sinh(\beta_1 L_1)\cosh(\beta_2 x_2)) \\ &- \sigma_r(-\sin(\beta_1 L_1)\sin(\beta_2 x_2) + \cos(\beta_1 L_1)\cos(\beta_2 x_2) \\ &- \sinh(\beta_1 L_1)\sinh(\beta_2 x_2) - \cosh(\beta_1 L_1)\cosh(\beta_2 x_2))] \end{aligned} \tag{43.19}$$

where σ_r is given as

$$\sigma_r = \frac{\begin{pmatrix} -\cos(\beta_1 L_1)\sin(\beta_2 L_2) - \sin(\beta_1 L_1)\cos(\beta_2 L_2) - \\ \cosh(\beta_1 L_1)\sinh(\beta_2 L_2) - \sinh(\beta_1 L_1)\cosh(\beta_2 L_2) \end{pmatrix}}{\begin{pmatrix} \sin(\beta_1 L_1)\sin(\beta_2 L_2) - \cos(\beta_1 L_1)\cos(\beta_2 L_2) - \\ \sinh(\beta_1 L_1)\sinh(\beta_2 L_2) - \cosh(\beta_1 L_1)\cosh(\beta_2 L_2) \end{pmatrix}}$$

Above eigen-function is valid only for the Euler–Bernoulli's stepped cantilever beam with no load condition at the free end irrespective of fixed end. The eigen-function also satisfies the orthogonality condition can be given as

$$\begin{aligned} \int_{x_2=0}^{L_2} m_2 \varnothing_s(x)\varnothing_r(x)dx &= \delta_{rs} \\ \int_{x_2=0}^{L_2} E_2 I_2 \varnothing_s(x) \frac{\partial^4 \varnothing_r(x)}{\partial x_r^4} dx &= \omega_r^2 \delta_{rs} \end{aligned} \tag{43.20}$$

where δ_{rs} is Kronecker's delta, defined as one for $i = j$ and zero for $i \neq j$ and ω_r is the undamped natural frequency at r-th mode given as

$$\omega_r = (\beta_2 L_2)_r^2 \sqrt{\frac{E_2 I_2}{m_2 L_2^4}} \tag{43.21}$$

Solution of following ordinary differential equation gives the model response function of the stepped beam:

$$\frac{d^2\eta_r(t)}{dt^2} + (2\zeta_r\omega_r)\frac{d\eta_r(t)}{dt} + \omega_r^2\eta_r(t) = f_r(t) \tag{43.22}$$

where

$$2\zeta_r\omega_r = \frac{c_s\omega_r^2}{Y} + \frac{c_a}{m} \tag{43.23}$$

Here ζ_r is overall damping constant, which includes both the damping effect, i.e. strain rate damping and air-viscous damping, shown in the equation. The strain rate damping coefficient is proportional to structural stiffness and viscous air damping is proportional to mass per unit length. From (43.22), modal forcing function $f_r(t)$ is given by

$$f_r(t) = -m\left(\gamma_r^w \frac{d^2g(t)}{dt^2} + \gamma_r^\theta \frac{d^2h(t)}{dt^2}\right) - c_a\left(\gamma_r^w \frac{dg(t)}{dt} + \gamma_r^\theta \frac{dh(t)}{dt}\right) \tag{43.24}$$

where $g(t)$ is the translation and $h(t)$ is the rotation at the base and m is the mass per unit length of the beam and

$$\begin{aligned} \gamma_r^w &= \int_{x_2=0}^{L_2} \varnothing_r(x)dx \\ \gamma_r^\theta &= \int_{x_2=0}^{L_2} x\varnothing_r(x)dx \end{aligned} \tag{43.25}$$

Harvester is assumed as thin beam, so we can neglect rotation term, then $h(t) = 0$. We solve (43.22), using zero initial condition (Duhamel integral) and neglecting air-viscous damping $\left(\zeta_r^a\right)$ effect by assuming it has very less effect to overall damping effect. Then the model response function can be given as

$$\eta_r(t) = \frac{(m\omega^2)}{\omega_r^2 - \omega^2 + i2\zeta_r\omega_r\omega}\gamma_r^w Y_0 e^{i\omega t} \tag{43.26}$$

Solution of the beam is given by (43.7), which is the function of the eigen-function and model response function. Substituting their values in the equation, the tip displacement of the beam at $x_2 = L_2$ is given as

$$\begin{aligned} w(\mathrm{L}_2, t) = Y_0 e^{i\omega t} \sum_{i=1}^{\infty} \Bigg(\sqrt{\frac{1}{m_2 L_2}} [(\cos(\beta_1 L_1)\sin(\beta_2 \mathrm{L}_2) \\ + \sin(\beta_1 L_1)\cos(\beta_2 L_2) - \cosh(\beta_1 L_1)\sinh(\beta_2 \mathrm{L}_2) \\ - \sinh(\beta_1 L_1)\cosh(\beta_2 \mathrm{L}_2) - \sigma(-\sin(\beta_1 \mathrm{L}_1)\sin(\beta_2 L_2) \\ + \cos(\beta_1 L_1)\cos(\beta_2 L_2) - \sinh(\beta_1 L_1)\sinh(\beta_2 L_2) \\ - \cosh(\beta_1 L_1)\cosh(\beta_2 \mathrm{L}_2))] \Bigg) \left(\gamma_r^w \frac{(m\omega^2)}{\omega_r^2 - \omega^2 + i2\zeta_r\omega_r\omega} \right) \end{aligned} \tag{43.27}$$

Relative transmissibility function is defined as the ratio of amplitude of tip displacement to amplitude of base displacement. It is a dimensionless parameter, which can be plotted against the ratio of the excitation frequency, given on its base, to the natural frequnecy of the stepped beam harvester. For comparison with uniform beam model [4, 5] for stepped beam relative transmissibility is given as

$$\begin{aligned} T_{rel}^{EB} = \sum_{i=1}^{\infty} \Bigg(\sqrt{\frac{1}{m_2 L_2}} [(\cos(\beta_1 L_1)\sin(\beta_2 \mathrm{L}_2) + \sin(\beta_1 L_1)\cos(\beta_2 \mathrm{L}_2) \\ - \cosh(\beta_1 L_1)\sinh(\beta_2 \mathrm{L}_2) - \sinh(\beta_1 L_1)\cosh(\beta_2 \mathrm{L}_2)) \\ - \sigma(-\sin(\beta_1 \mathrm{L}_1)\sin(\beta_2 L_2) + \cos(\beta_1 L_1)\cos(\beta_2 \mathrm{L}_2) \\ - \sinh(\beta_1 L_1)\sinh(\beta_2 L_2) \\ - \cosh(\beta_1 L_1)\cosh(\beta_2 \mathrm{L}_2))] \Bigg) \left(\gamma_r^w \frac{(m\omega^2)}{\omega_r^2 - \omega^2 + i2\zeta_r\omega_r\omega} \right) \end{aligned} \tag{43.28}$$

Figure 43.2 shows the results of the relative transmissibility function for the stepped beam and uniform beam harvester. Geometrical and electromechanical properties taken for the stepped harvester are present in Table 43.1. The results are compared with the uniform beam, given by Erturk [4], according to that comparison made, which is shown in Fig. 43.2. We consider the equivalent mass of the stepped beam to the uniform beam, comparing the transmissibilty function at $\zeta = 0.01$ of both the beam models, at which $\Omega \cong 1$ shows the maximum peak.

The value of relative transmissibility for the stepped beam at resonance is 337.6 and for uniform beam is 78.27. The relative transmissibility of stepped beam harvester is by 3.41 times more than the uniform beam harvester. The plot is drawn between the relative transmissibility modulus and ratio (Ω) of the excitation

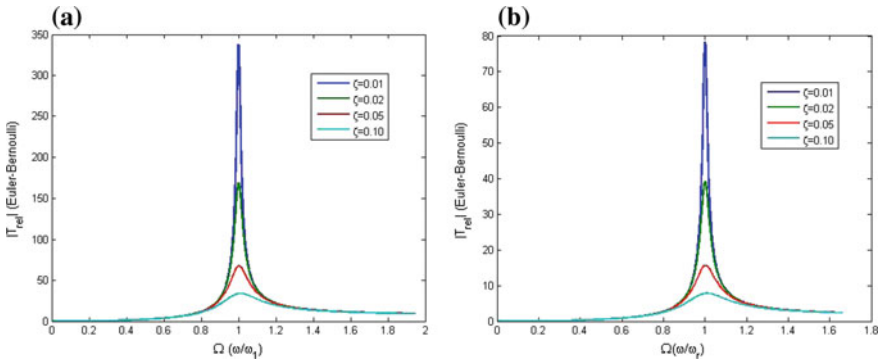

Fig. 43.2 Relative transmissibility function for stepped beam **a** and uniform beam **b** harvester model

Table 43.1 Geometrical and electromechanical properties taken for the stepped harvester

Parameters	Values
Length of each section, $L_1 = L_2$ (mm)	34
Width of the beam, b (mm)	9
Thickness of piezoelectric layer, h_p (mm)	0.5
Thickness of substrate section AB, h_{1s} (mm)	0.5
Thickness of substrate section BC, h_{2s} (mm)	1.0
Young's modulus of substrate, Y_s (GPa)	200
Young's modulus of piezoelectric, Y_p (GPa)	70.92
Piezoelectric constant, d_{31}(pm/V)	−290
Permittivity, ϵ_{33}^s (nm/V)	27.22
Density of piezoelectric, ρ_p (kg/m^3)	7600
Density of substrate, ρ_s (kg/m^3)	8000

frequency to first natural frequency for different damping ratio values (ζ = 0.01, 0.02, 0.05, 0.1). As the relative transmissibility is function of the ζ also so that as its value increases the relative transmissibility peak decreases accordingly.

43.2.2 Power Output from the Harvester

Considering Fig. 43.1, excited at the base, electrical output across the piezoelectric in form of voltage is calculated here. The configuration has the series connection of the electric circuit. The circuit is connected through the resistances of different values (from 100 Ω to 1 MΩ) and output in form of voltage is taken out. We consider the constitutive equation of the piezoelectric and electric displacement given as [1]

$$D_3 = d_{31} T_1 + \epsilon_{33}^T E_3 \tag{43.29}$$

where 1 and 3 correspond to x- and y-axis, respectively, d_{31} is the piezoelectric constant, T_1 is the stress in x-direction, ϵ_{33}^T is the permittivity at constant stress and E_3 is the electric field. Substitution of stress, $T_1 = S_1 Y_p$, and replacement on the permittivity at constant strain and electric field $E_3 = -v(t)/h_p$ in (43.29), give:

$$D_3 = d_{31} Y_p S_1 - \epsilon_{33}^s \frac{v(t)}{h_p} \tag{43.30}$$

where S_1 is the strain, and at any position x in the piezoelectric layer, it is given as

$$S_1 = -h_{pc} \frac{d^2 w(x,t)}{dx^2} \tag{43.31}$$

where h_{pc} is the distance between centre of the piezoelectric layer and substrate layer and $w(x, t)$ is the tip displacement of the beam end. Then (43.30) is re-written as

$$D_3 = -d_{31} Y_p h_{pc} \frac{d^2 w(x,t)}{dx^2} - \epsilon_{33}^s \frac{v(t)}{h_p} \tag{43.32}$$

The electric charge, $q(t)$, collected by the electrode, is integration of the electric displacement over the electrode area, which can be given as

$$q(t) = \int D_3 \cdot n \cdot dA = -\int \left(d_{31} Y_p b h_{pc} \frac{d^2 w(x,t)}{dx^2} + \epsilon_{33}^s b \frac{v(t)}{h_p} \right) dx \tag{43.33}$$

where n is unit normal outward the piezoelectric layer and dA is area of electrode. The current is electric charge per unit time and by Ohm's law voltage is load resistance into current.

$$I(t) = \frac{dq(t)}{dt}, v(t) = R_l . I(t) \tag{43.34}$$

$$v(t) = -R_l \left[\int \left(d_{31} Y_p b h_{pc} \frac{d^3 w(x,t)}{dx^2 dt} dx + \frac{\epsilon_{33}^s b L}{h_p} \frac{dv(t)}{dt} \right) \right] \tag{43.35}$$

where R_l is the load resistance and $\epsilon_{33}^s bL/h_p$ is the capacitance of the piezoelectric layer, which is generally connected to the load resistance as it stores the energy. Here voltage generated is function of motion of the beam. Substituting (43.7) to above equation, we get

$$\epsilon_{33}^{s} bLh_p \frac{dv(t)}{dt} + \frac{v(t)}{R_l} = -\int_0^L d_{31} Y_p b h_{pc} \sum \frac{d^2 \varnothing_r(x)}{dx^2} \frac{d\eta_r(t)}{dt} dx \tag{43.36}$$

$$\frac{dv(t)}{dt} + \frac{h_p}{\epsilon_{33}^{s} bL} \frac{v(t)}{R_l} = -\sum \frac{d\eta_r(t)}{dt} \frac{h_p d_{31} Y_p h_{pc}}{\epsilon_{33}^{s} L} \frac{d\varnothing_r(x)}{dx} \tag{43.37}$$

$$\frac{dv(t)}{dt} + \frac{1}{\tau} v(t) = \sum \frac{d\eta_r(t)}{dt} \varphi_r \tag{43.38}$$

where τ is the time constant and φ_r is given at $x = L_2$ as

$$\varphi_r = -\frac{h_p d_{31} Y_p h_{pc}}{\epsilon_{33}^{s} L_2} \frac{d\varnothing_r(x)}{dx} \tag{43.39}$$

We substitute $v(t) = V_0 e^{i\omega t}$ in the above equation and solve the RHS of (43.39), which is differential equation, then (43.38) can be written as

$$i\omega V_0 e^{i\omega t} + \frac{1}{\tau} V_0 e^{i\omega t} = \sum_{r=1}^{\infty} \varphi_r \frac{d}{dt} \left(\frac{(m\omega^2 - i\omega c_a)}{\omega_r^2 - \omega^2 + i2\zeta_r \omega_r \omega} \gamma_r^w Y_0 e^{i\omega t} \right) \tag{43.40}$$

By considering overall damping is less and neglecting the effect of the air-viscous damping in (43.40), it can be re-written as

$$i\omega V_0 e^{i\omega t} + \frac{1}{\tau} V_0 e^{i\omega t} = \sum_{r=1}^{\infty} \varphi_r \left(\frac{(im\omega^3)}{\omega_r^2 - \omega^2 + i2\zeta_r \omega_r \omega} \gamma_r^w Y_0 e^{i\omega t} \right) \tag{43.41}$$

43.2.2.1 FRF of Output Voltage

The frequency response function (FRF) of the voltage is given by the ratio of output voltage to base acceleration in terms of [V s^2/m] as

$$\frac{v(t)}{\omega^2 Y_0 e^{i\omega t}} = \frac{1}{\left(i\omega + \frac{1}{\tau}\right)} \sum_{r=1}^{\infty} \varphi_r \left(\frac{im\omega \gamma_r^w}{\omega_r^2 - \omega^2 + i2\zeta_r \omega_r \omega} \right) \tag{43.42}$$

Figure 43.3 shows the FRF of output voltage (43.42) at different frequencies for various load resistances. The output voltage increases when load resistance increases. The maximum value is obtained at first (natural frequency) mode of vibration then at second mode and third mode. First mode frequency is equal to 159.5 Hz, at which FRF has the peak value of the voltage 19.35 V s^2/m. For all three modes of vibration, peak is obtained at 1 MΩ, i.e. at this value of resistance, the output voltage is maximum.

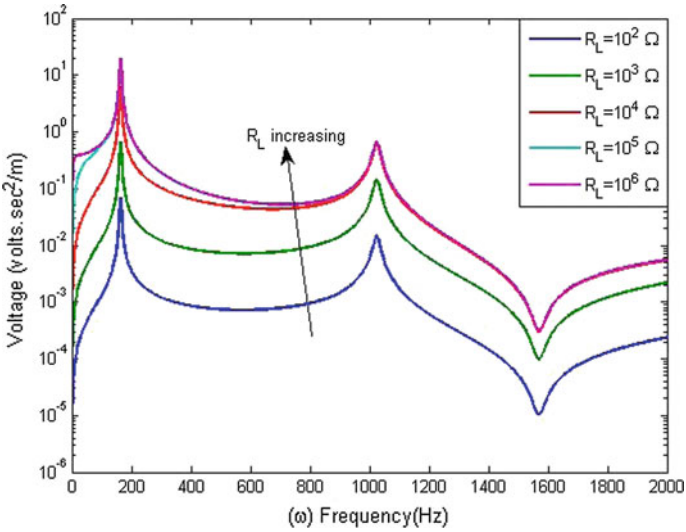

Fig. 43.3 FRF of output voltage for stepped beam harvester at different load resistances

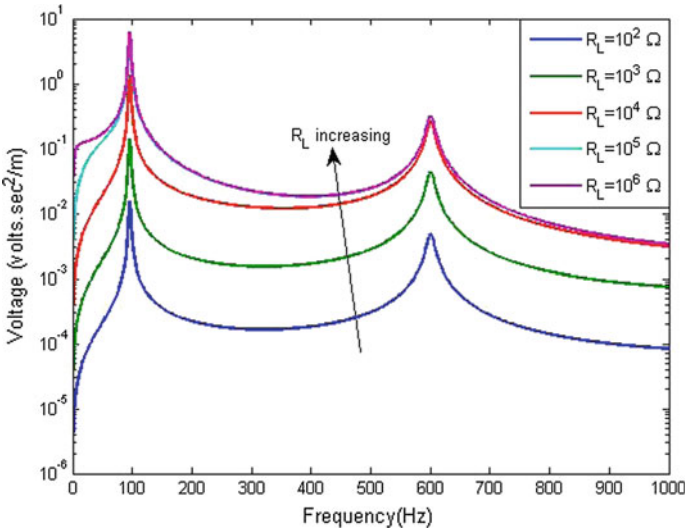

Fig. 43.4 FRF of output voltage for uniform beam harvester at different load resistances

Figure 43.4 shows the FRF of output voltage of the uniform beam having maximum value 6.243 V s^2/m at 96 Hz. The stepped beam harvester produces approximate 3.04 times more voltage than the uniform beam harvester.

It is known that if load resistance is less, then the regime is close to short circuit condition and if value of load resistance is higher, then it is close to open circuit

condition. Here among all load resistances, the value of 100 Ω is lower one means gives the short circuit condition and the value of 1 MΩ is higher one gives the open circuit condition to the circuitry arrangement made for the output voltage. In this case, there is not such a difference between the short circuit and open circuit in frequency for any of the modes, which can be seen in Fig. 43.3. In Fig. 43.3, it can be clearly seen that the FRF of output voltage is independent of the circuit condition of harvester for any of the mode shapes. All load resistances shows peak in the FRF of output voltage at the same frequency.

43.2.2.2 FRF of Output Current

The equation for the FRF of output current is given by dividing the FRF of output voltage ((43.42)) by load resistance, which gives:

$$\frac{I(t)}{\omega^2 Y_0 e^{i\omega t}} = \frac{1}{R_l\left(i\omega + \frac{1}{\tau}\right)} \sum_{r=1}^{\infty} \varphi_r \left(\frac{im\omega\gamma_r^w}{\omega_r^2 - \omega^2 + i2\zeta_r\omega_r\omega} \right) \tag{43.43}$$

Figure 43.5 shows the FRF of output current (43.43) at different frequencies for various load resistances. Due to the current has reciprocal effect of load resistance and it can be seen in Fig. 43.5, the output current decreases with the increase of load resistance. The FRF of output current also shows that at first mode of vibration, the output current is more for lower load resistance value in contrast to the FRF of output voltage.

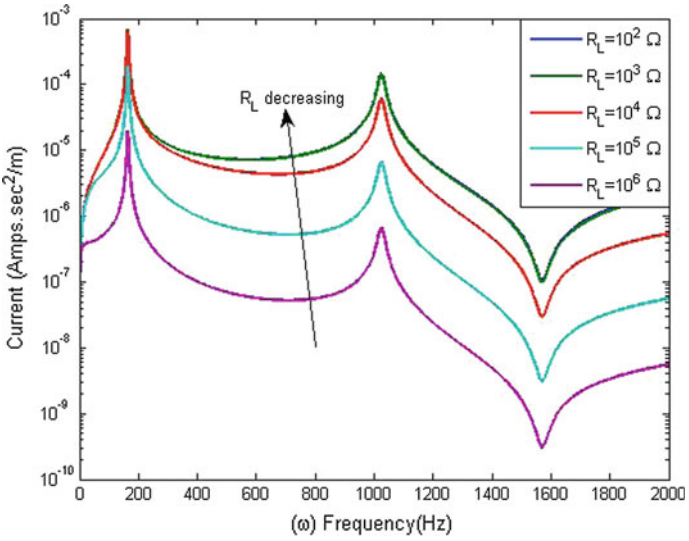

Fig. 43.5 FRF of output current for different values of load resistance

It also shows absence of the effect of short circuit and open condition in frequency at any of the modes. At 1569 Hz, an anti-resonance can be seen between the second and third modes, showing the lowest value of the current with no effect of circuit condition. The same as Fig. 43.4, It also shows, at first mode of vibration, the output current is maximum followed by second mode and so on. From the plot, it can be concluded that for maximal output current, the load resistance should be minimal.

43.2.2.3 FRF of Output Power

Power, produced by any electrical circuit, is product of the voltage and current. The expression for the output power is obtained by multiplying (43.42) and (43.43). Expression for the FRF of output power is given as

$$\frac{P(t)}{\omega^2 Y_0 e^{i\omega t}} = \frac{1}{R_l}\left(\frac{1}{\left(i\omega + \frac{1}{\tau}\right)}\sum_{r=1}^{\infty}\varphi_r\left(\frac{im\omega\gamma_r^w}{\omega_r^2 - \omega^2 + i2\zeta_r\omega_r\omega}\right)\right)^2 \tag{43.44}$$

In Fig. 43.6, higher value of output power is obtained at the first mode, when load resistance is equal to 100 KΩ. In the case of the FRF of output voltage at 1 MΩ and the FRF of output current at 100 Ω, the peak values were obtained at first mode followed by other modes. For the second and third modes, the peak values were obtained at 10 KΩ. Due to the power is product of current and voltage, then this variation of the peak value due to load resistance is occurred. In similar manner,

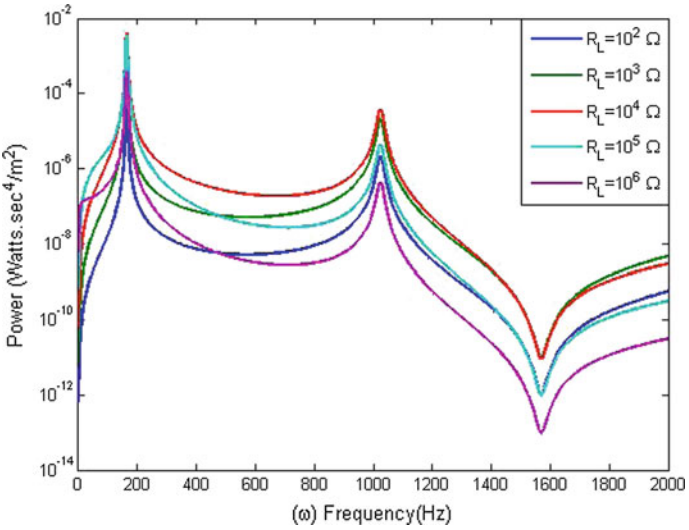

Fig. 43.6 Power FRF at different values of load resistance

lower output power at first mode is found at the 100 Ω whether for the second and third modes, it is attained at 1 MΩ. An anti-resonance exists also at 1569 Hz, showing the least output power at this frequency as it was in Fig. 43.5.

In this plot also there is not such a difference in short circuit and open circuit conditions. For both the cases there is not change in frequency value, which shows the change, connected with these conditions. In Fig. 43.6, it can be clearly seen that one curve intersects another showing the same value of power output at certain frequency for different load resistances.

43.3 Conclusions

In this chapter, the expressions are derived on the base of the Euler–Bernoulli's assumptions for tip displacement and relative transmissibility function. The base excitation is given to the harvester in the form of translation and small rotation. For modal response function, damping due to strain rate and air damping is considered. For the tip displacement of the stepped beam, eigen-function and natural frequency of the stepped beam is calculated. Mass of the stepped beam is kept equal to the uniform beam then results can be compared. Relative transmissibility function is for the stepped beam harvester, compared with the uniform beam model, and it demonstrate the value in 61 times greater than in the uniform beam.

Expressions for the output voltage, current and power have been derived and FRF were plotted for each of them. These FRF were obtained in the dependence on the frequency between 1 and 2000 Hz at different load resistance, changing from 100 Ω to 1 MΩ. The FRF plots found are independent of short circuit or open circuit conditions. The output current and power FRF showed anti-resonance at 1569 Hz and all FRFs showed resonance frequency at 163 Hz. The output voltage, produced by the stepped beam, is approximately 3 times greater than in the uniform beam model.

References

1. D.J. Leo, *Engineering Analysis of Smart Material System* (Wiley, Hoboken, NJ, 2007)
2. A. Erturk, D.J. Inman, Smart Mater. Struct. **17**, 065016 (2008)
3. A. Erturk, D.J. Inman, Smart Mater. Struct. **18**, 025009 (2009)
4. A. Erturk, D.J. Inman, J. Intell. Mater. Syst. Struct. **19**(11), 1311 (2008)
5. A. Erturk, D.J. Inman, J. Vib. Acoust. **130**, 041002 (2008)
6. M.N. Fakhzan, A.G.A. Muthalif, Mechatronics **23**(1), 61 (2013)
7. J.M. Dietl, A.M. Wickenheiser, E. Garcia, Smart Mater. Struct. **19**, 055018 (2010)
8. G. Wang, J. Intell. Mater. Syst. Struct. **24**(2), 226 (2012)
9. S. Mehraeen, K. Corzine, Energy harvesting using piezoelectric materials and high voltage scavenging circuitry and high voltage scavenging circuitry, Faculty Research & Creative Works, Paper 827, Missouri University of Science and Technology (2008)
10. S. Ben Ayed, A. Abdelkefi, F. Najar, J. Intell. Mater. Syst. Struct. **25**(2), 174 (2014)

11. A.R. Reddy, M. Umapathy, D. Ezhilarasi, G. Uma, J. Vib. Acoust. **22**(13), 3057 (2014)
12. Q.C. Guan, B. Ju, J.W. Xu, Y.B. Liu, Z.H. Feng, J. Intell. Mater. Syst. Struct. **24**(9), 1059 (2015)
13. C.M. Sang, J. Dayou, W.Y.H. Liew, Int. J. Precis. Eng. Manuf. **14**(12), 2149 (2013)
14. J. Dayou, J. Kim, J. Im, L. Zhai, Smart Mater. Struct. **24**(4), 45006 (2015)
15. M. Levinson, J. Sound Vib. **49**(1–2), 287 (1976)
16. S.K. Jang, C.W. Bert, J. Sound Vib. **130**(2), 342 (1989)
17. Rosa M.A. De, J. Sound Vib. **173**(4), 563 (1994)
18. S. Naguleswaran, J. Sound Vib. **252**(4), 751 (2002)
19. M.A. Koplow, A. Bhattacharyya, B.P. Mann, J. Sound Vib. **295**(1–2), 214 (2006)
20. A.M. Wickenheiser, J. Intell. Mater. Syst. Struct. **24**(6), 729 (2012)
21. J.D.C. Vaz, Junior J.J. de Lima, J. Vib. Control **22**(1), 193 (2014)
22. S.S. Rao, *Mechanical Vibration*, Fifth Edition (Pearson, 2010)

Chapter 44
The Effect of Operating Frequency and Needle Diameter on Performance of Piezoelectric Micropump

Rakesh Kumar Haldkar, Tanuja Sheorey and Vijay Kumar Gupta

Abstract In recent years, there is an increasing interest in development of micropumps for various applications in the chemical, medical and biomedical fields. Various researchers have tried to design and develop micropumps to handle small and accurate quantity of fluid. This paper focuses on the analysis of a piezoelectric actuator based micropump. Fluid is sucked inside the micropump by actuation of piezoelectric bimorph. Due to motion of bimorph, back pressure is generated inside the pump, causing the fluid to flow. Simulations are performed using ANSYS 12.1® at an applied voltage of 20 V and varying operating frequency. The simulation results show that the performance of micropump in terms of flow rate is a function of bimorph deflection, which depends on applied frequency. Effect of microneedle diameter and applied frequency on flow rate has been analyzed and discussed.

44.1 Introduction

In recent years, there is an increasing interest in development of micropumps for various applications especially in the field of bio-fluidic and micro-fluidic. Various researchers have tried to design and develop micropumps to handle small and accurate quantity of fluid due to the requirements of the applications such as microelectronic cooling, miniature biochemical analysis system, and biomedical [1–3]. Some of the potential applications in biomedical field are drug delivery for diabetic and cancer patients [4, 5]. Beside other mechanisms, piezoelectric actuated micropumps are gaining attention of the researchers. Flow analysis in micropump with deferent shapes of microneedle has been analyzed by Haldkar et al. [6, 7].

In this paper effect of variation of operating frequency and diameter of microneedle has been analyzed. For the purpose, simulations are performed in ANSYS®

R. K. Haldkar (✉) · T. Sheorey · V. K. Gupta
Mechanical Engineering Displine, PDPM Indian Institute of Information Technology Design and Manufacturing, Jabalpur 482004, India
e-mail: rakeshh@iiitdmj.ac.in

I. A. Parinov et al. (eds.), *Advanced Materials*, Springer Proceedings in Physics 207, https://doi.org/10.1007/978-3-319-78919-4_44

software. Experiment has been performed on piezoelectric bimorph to validate simulation results, related to frequency and amplitude. Further, analysis is carried out on flow of fluid inside the micropump at varying applied frequency, using the FSI boundary condition.

44.2 Modeling of Micropump

Piezoelectric micropump consists of piezoelectric bimorph actuator, micropump chamber and microneedle as shown in Fig. 44.1. This micropump is modeled in the ANSYS 12.1® software and analyzed. The micropump consists of pump chamber in which fluid is to be collected, piezoelectric bimorph actuator for pumping actuation and a microneedle through which fluid will be sucked. Inner diameter of pump chamber is 20 mm, depth is 2 mm and microneedle length is 15 mm considered.

44.2.1 Piezoelectric Bimorph Actuator

The piezoelectric bimorph actuator works, based on the application of sinusoidal voltage and its frequency. On application of sinusoidal voltage, upper piezoelement contracts/expands and the lower piezoelement expands/contract, resulting in bending motion of the piezoelectric bimorph. The bending direction changes as the

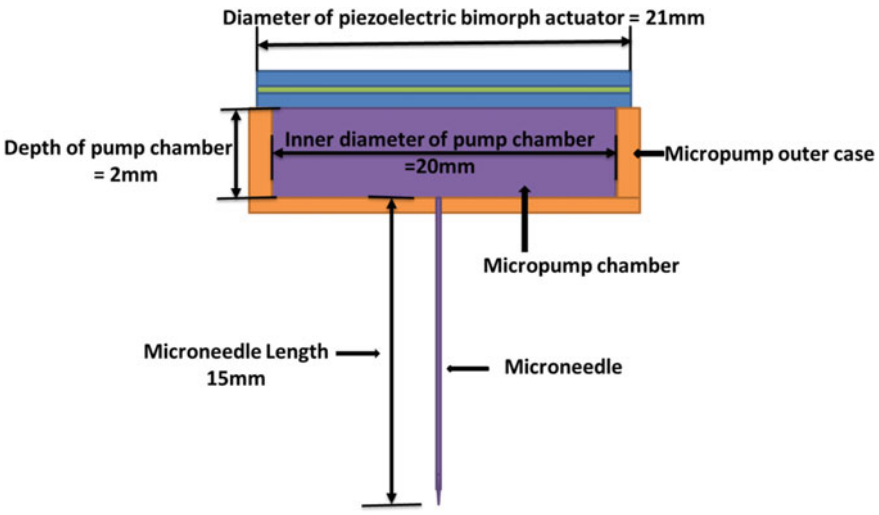

Fig. 44.1 Sketch diagram of micropump

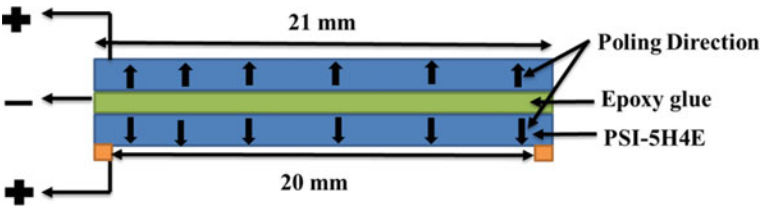

Fig. 44.2 Dimensions of piezoelectric actuator

voltage direction changes. This creates suction and pressure inside the pump chamber. Piezoelectric bimorph is made of PSI-5H4E and glued with epoxy glue. Dimension details of the piezoelectric bimorph are shown in Fig. 44.2 and material properties are summarized in Tables 44.1 and 44.2.

Analysis was carried out on the piezoelectric bimorph actuators. For modeling piezoelectric bimorph actuator in ANSYS®, symmetry was explored and analysis was carried out on half-domain. For meshing SOLID226 (Twenty node tetrahedron) element has been used for the piezoelectric bimorph actuator and SOLID186 (Twenty node tetrahedron) element for the epoxy glue. Figure 44.3 shows finite element model of the actuator on which analysis has been carried out. Figure 44.4 shows the first mode actuation of the piezoelectric bimorph actuator. Corresponding

Table 44.1 Piezoelectric material properties (PSI-5H4E)

Compliance matrix for PSI-5H4E

$$\mathbf{S_E} = \begin{vmatrix} 16.5 & -4.78 & -8.45 & 0 & 0 & 0 \\ -4.78 & 16.5 & -8.45 & 0 & 0 & 0 \\ -8.45 & -8.45 & 20.7 & 0 & 0 & 0 \\ 0 & 0 & 0 & 43.5 & 0 & 0 \\ 0 & 0 & 0 & 0 & 43.5 & 0 \\ 0 & 0 & 0 & 0 & 0 & 42.6 \end{vmatrix} \times 10^{-12}\ \mathrm{m^2/N}$$

Piezoelectric coefficient matrix

$$\mathbf{d} = \begin{vmatrix} 0 & 0 & 0 & 0 & 920 & 0 \\ 0 & 0 & 0 & 920 & 0 & 0 \\ -320 & -320 & 650 & 0 & 0 & 0 \end{vmatrix} \times 10^{-12}\ \mathrm{C/N}$$

Relative permittivity

$$\varepsilon_T/\varepsilon_0 \begin{vmatrix} 3800 & 0 & 0 \\ 0 & 3800 & 0 \\ 0 & 0 & 3800 \end{vmatrix}, \quad \varepsilon_0 = 8.854 \times 10^{-12}\ \mathrm{F/M}$$

Density: 7800 kg/m^3

Table 44.2 Epoxy glue properties

Material	Density (kg/m^3)	Young's modulus (GPa)
Epoxy glue	1400	2.478

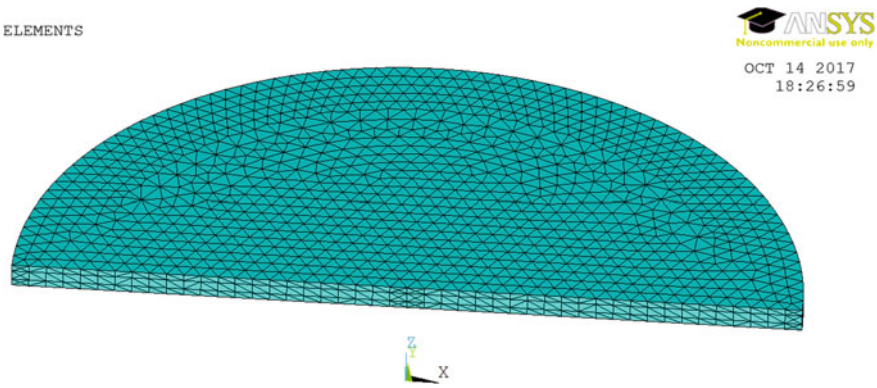

Fig. 44.3 FEA model of piezoelectric actuator

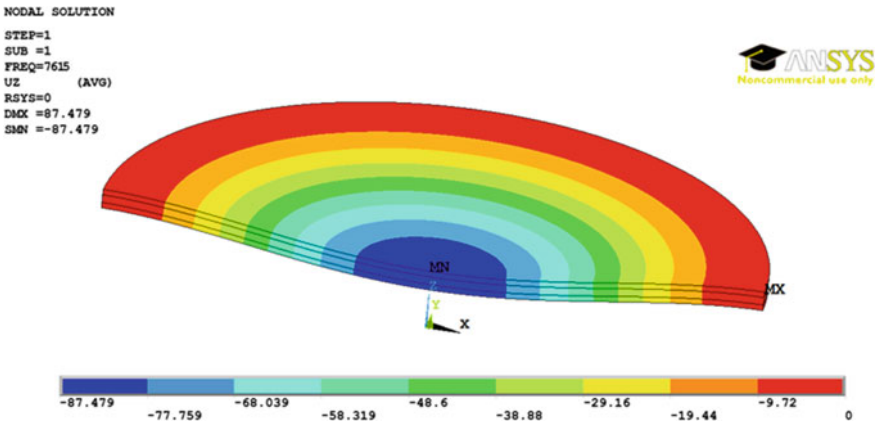

Fig. 44.4 First natural frequency

natural frequency is observed as 7615 Hz. Harmonic analysis has been carried out at an applied voltage of 20 V and maximum amplitude is observed as 29 μm at 7615 Hz frequency as shown in Fig. 44.5. Transient simulations are carried out by giving actuation voltage as given in (44.1).

$$\text{Applied voltage} = 20\ \sin(2\pi ft), \tag{44.1}$$

where f is the applied frequency, t is the run time for actuator.

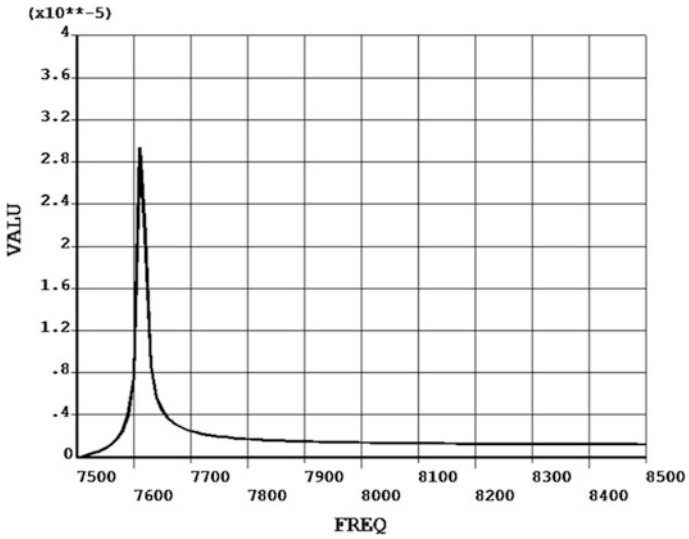

Fig. 44.5 Amplitude versus frequency

44.2.2 Fabrication of Piezoelectric Bimorph Actuator

Piezoelectric bimorph actuator was fabricated with two sheets of 21 mm diameter and 0.196 mm thickness of piezoelectric (PSI-5H4E) material. Both piezoelectric sheets are glued with epoxy glue as shown in Fig. 44.2. The effective diameter of piezoelectric bimorph actuator was 20 mm and Outer ring was 0.5 mm. Outer ring of the piezoelectric bimorph actuator was fixed with the micropump outer case. Fabricated piezoelectric actuator with micropump chamber is shown in Fig. 44.6.

44.2.3 Experimental Procedure

Experiment was conducted by supplying 20 V with power supply. Sinusoidal signal was obtained by function generator and supplied to the amplifier. Amplifier was used to amplify the current. The voltage from amplifier was supplied to the micropump. Laser Vibrometer (Polytec PDV100®) was used to measure the amplitude of piezoelectric actuator and recorded in PC through the interface. Line diagram of the experimental procedure is shown in Fig. 44.7.

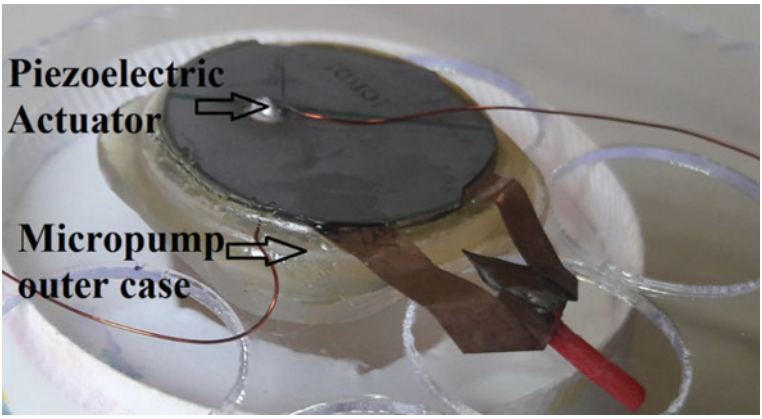

Fig. 44.6 Piezoelectric actuator with micropump outer case

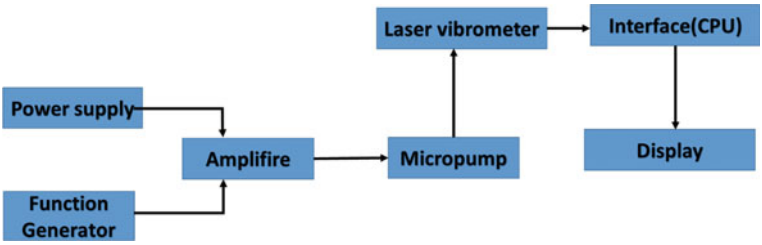

Fig. 44.7 Line diagram of experimental procedure

44.2.4 Experimental Setup

Figure 44.8 shows experimental setup for measuring piezoelectric actuator amplitude. Laser Virbrometer (Polytec PDV100®) is used to measure amplitude of the piezoelectric bimorph actuator at 20 V. Amplitude of 20.870 μm was measured and is shown in Fig. 44.9.

Experimental and simulation results are summarized in Table 44.3. A difference of 4.2% was observed in natural frequency and 28% in amplitude. This may be due to the errors during the fabrication process in terms of gluing and boundary conditions. In simulation, perfect gluing and rigidly fixed boundary conditions have been considered, which could not be achieved in the experiment. After building the confidence between experiment and simulation results, further analysis was carried by performing the simulations only.

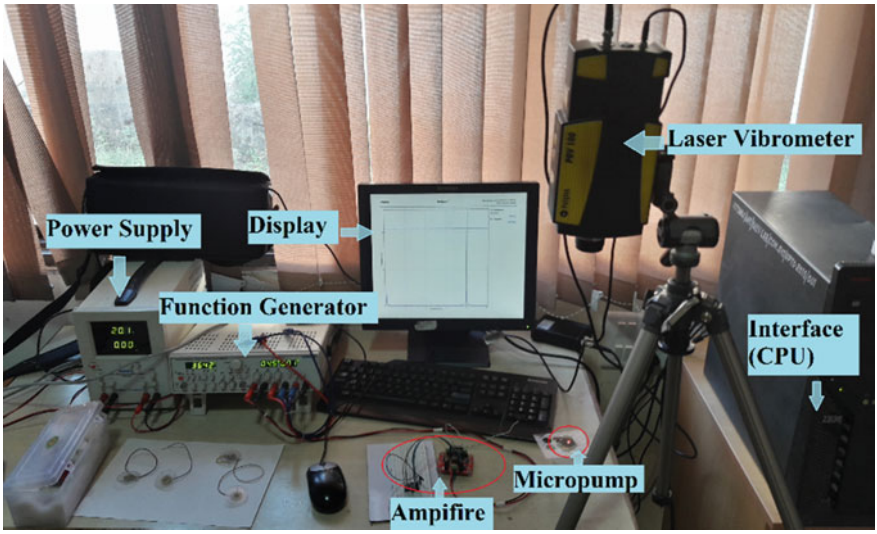

Fig. 44.8 Experimental setup

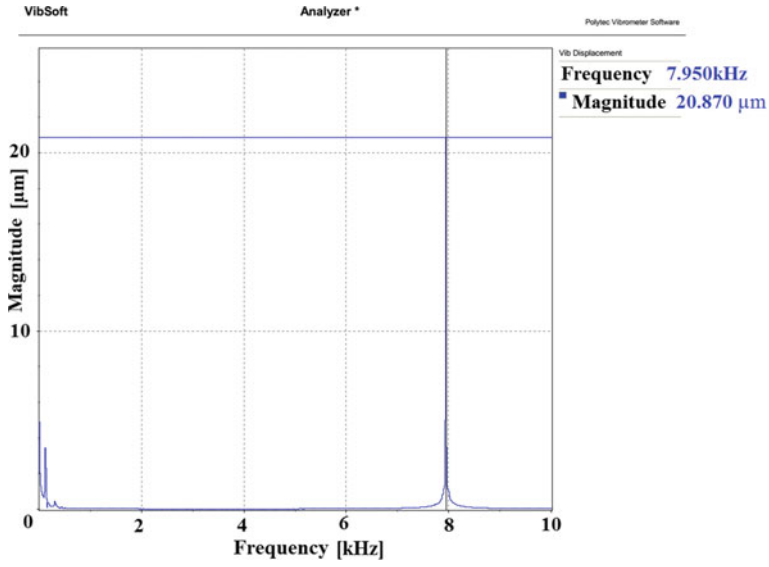

Fig. 44.9 Amplitude and frequency, measured by laser vibrometer

Table 44.3 Comparison between experimental and simulation results

Name	Experimental	Simulation
Natural frequency (Hz)	7950	7615
Amplitude (µm)	20.87	29.0

44.3 Simulation of Micropump with Variable Microneedle Size

Micropump consists of outer case, microneedle and micropump chamber as shown in Fig. 44.1. The micropump is modeled in the ANSYS® software. Finite element model of outer case and fluid chamber are shown in Fig. 44.10. Circular microneedle has 15 mm length and 200 µm diameter. SOLID186 and FLUID143 elements were used to mesh outer case and micropump chamber (including microneedle), respectively.

Fig. 44.10 FEA model: **a** micropump outer case and **b** micropump chamber

44.3.1 Boundary Conditions

For the analysis, boundary conditions were imposed on the finite element model. All boundary conditions are shown in Fig. 44.11 and summarized here.

(i) *Opening condition*

As the piezoelectric bimorph moves up, suction starts, resulting in flow of fluid in the microneedle. When piezoelectric bimorph moves downward, a part of the sucked volume may flow out through microneedle. Hence opening boundary condition was applied at the inlet of the microneedle. At the inlet of microneedle, pressure was considered as 100 kPa corresponding to human blood pressure.

(ii) *Wall condition*

The flow of fluid is restricted due to solid surface at the bottom and the peripheral wall of the micropump chamber. Hence, wall condition is applied at these places.

(iii) *Symmetry condition*

Only half of the domain is used for the flow analysis. Symmetry condition has been applied along the central plane of symmetry.

(iv) *Interface condition*

FSI boundary condition was applied at the interface of fluid region and piezoelectric bimorph actuator. Under this condition, fluid region tries to follow the shape of the piezoelectric bimorph actuator.

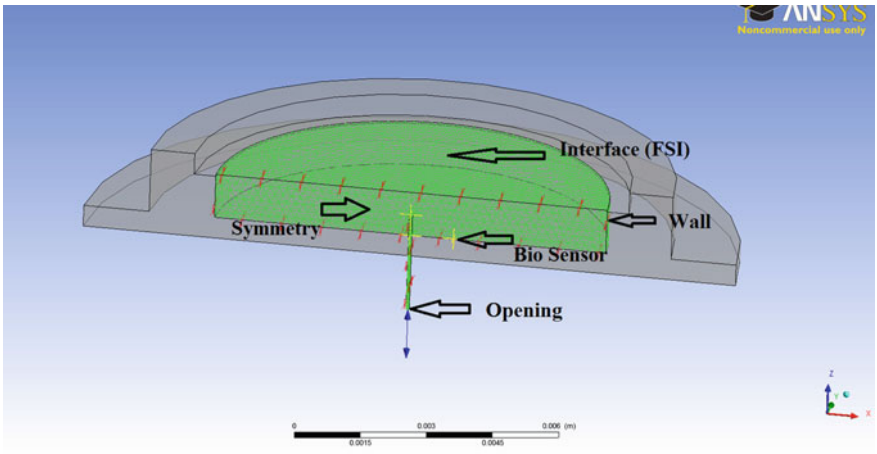

Fig. 44.11 Boundary conditions

44.3.2 Results and Discussion

Figure 44.12 shows monitor points A and B inside the pump chamber. Point A is 1 mm above the microneedle and point B is at 1 mm radial distance from the microneedle (biosensor point). A voltage of 20 V was applied to the piezoelectric bimorph actuator. At natural frequency, maximum pressure inside the micropump is observed as 3 MPa, and average velocity is observed as 3.5 mm/s at monitor point B. Figure 44.13 shows velocity vector and velocity streamline plots. Figure 44.14 shows variation of the velocity with time. After a short initialization time, flow is seen accumulating and reaches to almost a constant average velocity of 3.5 mm/s at approximately 1.8 ms.

44.3.3 Effect of Microneedle Diameter

Different cases are considered by varying microneedle diameter from 100 to 400 µm. Applied voltage (20 V) and frequency (7615 Hz) were constant in each simulation. Results are summarized in Table 44.4. It can be observed that when microneedle diameter decreases, pressure and velocity inside the micropump chamber increases.

44.3.4 Effect of Applied Frequency

Effect of applied frequency was observed by fixing the microneedle diameter as 200 µm. Applied frequency varied from 100 to 7615 Hz (natural frequency). Results are summarized in Table 44.5. It can be observed that when applied frequency increases, pressure inside the micropump chamber and hence velocity increases.

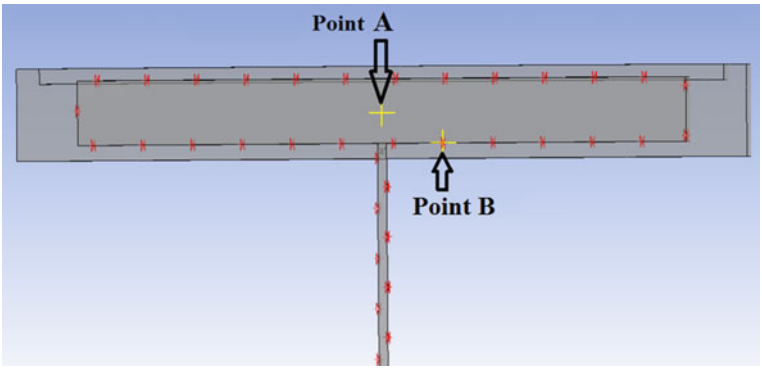

Fig. 44.12 Monitors points

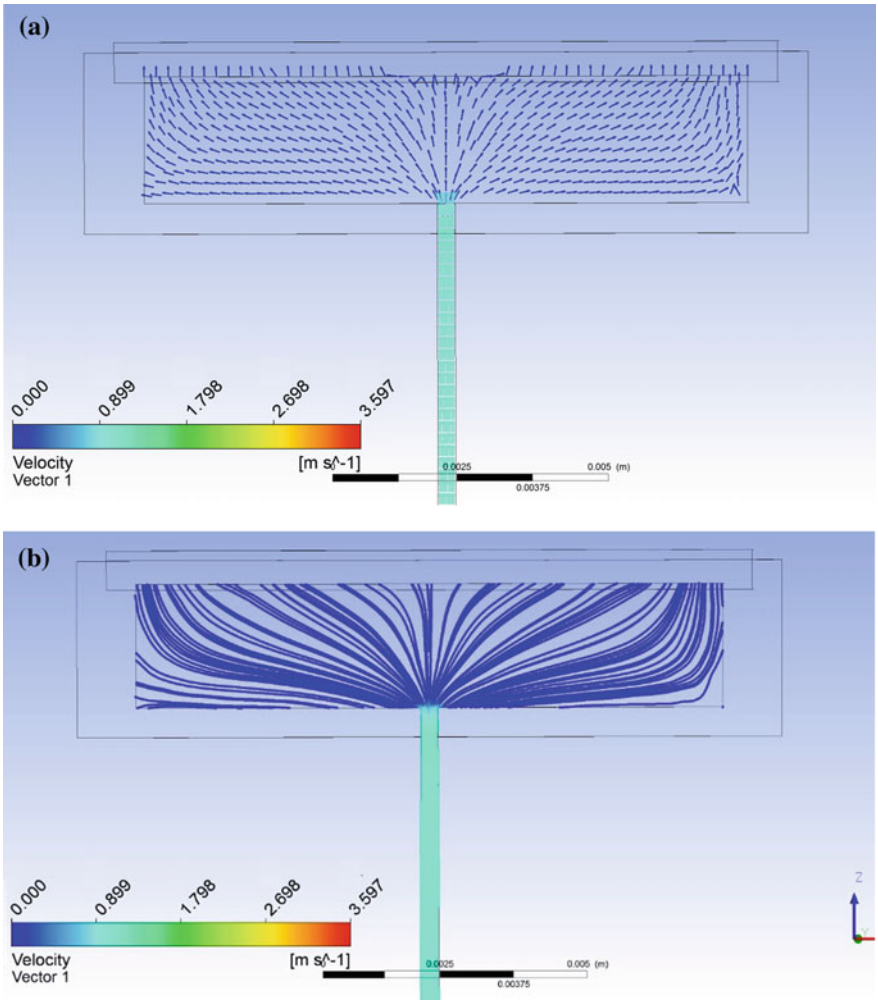

Fig. 44.13 Velocity vector (**a**) and velocity streamline (**b**)

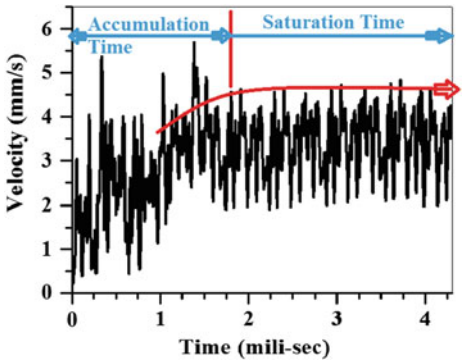

Fig. 44.14 Velocity at biosensor point

Table 44.4 Effect of microneedle diameter

Microneedle diameter (μm)	Pressure (MPa)	Velocity (biosensor point) (mm/s)
400	0.5	0.8
300	1.5	2.1
200	3	3.5
100	5	5.2

Table 44.5 Effect of frequency

Applied frequency (Hz)	Pressure (kPa)	Velocity (mm/s) (at biosensor point)
100	1.98	0.020
135	2.1	0.025
500	200	0.080
1000	900	0.2
5000	2000	1
7615 (NF)	3000	1.5

44.4 Conclusion

Study began with comparison of experimental and simulation results of piezoelectric bimorph actuator. A 4.3% difference in natural frequency may be considered insignificant. Further investigations were conducted on electro—solid—fluid numerical model. The effects of microneedle diameter and actuation frequency on flow were observed. With increase in applied frequency, pressure inside the micropump increases. With the increase in the diameter of the microneedle, pressure and velocity inside the pump decrease. Thus, selection of an optimum value of microneedle diameter and applied frequency plays crucial role for the desired flow from the micropump.

References

1. P. Woias, Sens. Actuators B **105**, 22 (2005)
2. N.-C. Tsai, C.-Y. Sue, Sens. Actuators A **134**, 555 (2007)
3. K. Tsuchiya, N. Nakanishi, Y. Uetsuji, E. Nakamachi, Biomed. Microdevice **7**(4), 347 (2005)
4. F. Amirouche, Y. Zhou, T. Johnson, Microsyst. Technol. **15**, 647 (2009)
5. A. Nisar, N. Afzulpurkar, B. Mahaisavariya, A. Tuantranont, Sens. Actuators B **130**, 917 (2008)
6. B. Wang, X. Chu, E. Li, L. Li, Ultrasonics **44**, e643 (2006)
7. R.K. Haldkar, V.K. Gupta, T. Sheorey, J. Mech. Sci. Technol. **31**(6), 2933 (2017)

Chapter 45
Coded Control of Piezoactuator Nano- and Microdisplacement for Mechatronics Systems

Sergey M. Afonin

Abstract In the present chapter, the influence of the rigidity of piezoactuator and the load rigidity on the mechanical and control characteristics of the multilayered piezoactuator for the longitudinal, transverse and shear piezoeffect in the case of the parallel and coded control are considered. The effects of the parameters of the multilayered sectional piezoactuator and the load on its static and dynamic characteristics are determined. For calculation of the control systems for the nano- and microdisplacement, the transfer functions of the multilayered piezoactuator with parallel and coded control are obtained.

45.1 Introduction

The piezoactuator solves problems of the precise adjustment in the microelectronics and the nanotechnology, the compensation of the temperature and gravitational deformations, the atmospheric turbulence by the wave front correction [1–12]. The investigation of static and dynamic characteristics of the multilayered piezoactuator of the nano- and micrometric movements as the control object is necessary for the calculation of the piezoactuator for control systems of the nano- and micrometric displacement. The structural design of the multilayered piezoactuator from PZT ceramic depends on the manufacture technology. The multilayered piezoactuator for the longitudinal piezoeffect is made as the compound piezoelectric converter, from the separate piezoelectric plates, elastically compressed, the stack type or the block piezoelectric converter from the piezoplates sintered using silver paste, the compound piezoelectric converter from piezoelectric stacks with elastic reinforcement, the multilayered piezoelectric converter glued from piezoelectric plates, or the multilayered piezoelectric converter with layers deposited using the thin film or the thick film technologies. The problems of providing precision of the control

S. M. Afonin (✉)
Department of Intellectual Technical Systems, National Research University of Electronic Technology (MIET), Moscow, Russia
e-mail: eduems@mail.ru

I. A. Parinov et al. (eds.), *Advanced Materials*, Springer Proceedings in Physics 207, https://doi.org/10.1007/978-3-319-78919-4_45

systems for the deformation of the multilayered piezoactuator of the nano- and micrometric movements in the case of the parallel and coded control are topical [4–8]. The solution of these problems requires the determination of mechanical and control characteristics of the piezoactuator. In the case of the parallel control, all piezolayers (piezoplates) in the multilayered piezoactuator are connected in parallel.

The application of the multilayer sectional piezoactuator with the coded control makes it possible to efficiently use the electromechanical digital-analog conversion for the nano- and microdisplacement. In the case of the coded control, the piezolayers in the piezoactuator are connected in parallel in each section and the control voltage is supplied to each section via the multiplexer. The number of the piezolayers in the section is equal to the power of 2, i.e., 1, 2, 4, 8, 16, and so on. In order to calculate deformation of the multilayered piezoactuator for the control system, it is necessary to take into account the specific features of its mechanical and control characteristics in the case of the parallel and coded control. The main parameter of the external load of the piezoactuator is the load rigidity, i.e., the ratio of the force of the elastic reaction of the load to the value of the load deformation. The mechanical and control (adjusting) characteristics of the multilayered piezoactuator for the longitudinal, transverse and shear piezoeffect in the case of the parallel and coded control are obtained. By solving the matrix equation with allowance for the corresponding equations of the piezoelectric effect, the boundary conditions on loaded working surfaces of the multilayered piezoactuator, the strains along the coordinate axes are constructed by the transfer functions of the multilayered piezoactuator.

45.2 Problem Statement

Let us consider the static and dynamic characteristics, the control characteristics and the transfer functions for the longitudinal, transverse and shear piezoeffect in the case of the parallel and coded control of the multilayered piezoactuator [5, 11, 12]. We take into account the features of the mechanical and control characteristics in the code control when calculating the deformation of the multilayer piezoactuator in the control system. Let us consider the mechanical and control characteristics of the multilayer piezoactuator under the code control for various structural designs.

The ratio of the magnitude of the elastic load response force to the strain load value is the main parameter of the external load of the piezoactuator presenting the rigidity of the load. We obtain the total deformation of the multilayer piezoactuator with code control in the form of the sum of the deformations of individual sections of the piezoactuator when the voltage and deformation of the multilayer piezoactuator are applied to them under the action of the load force. When designing the control systems for nanotechnology equipment, the actual effects of the load rigidity on the mechanical and control characteristics of the multilayer piezoactuator under code control are of interest. When using the multilayer sectional piezoactuator with the longitudinal, transverse or shear piezoelectric effect with code control, we

obtain nano- and microdisplacements proportional to the control code for the electromechanical digital-to-analog converter. The multilayer sectional piezoactuator is used for code control of sections (Fig. 45.1) for nano- and micromanipulators in the nanotechnology equipment. In the multilayer sectional piezoactuator there are N sections with the number n_k of the piezolayers in the kth section. Accordingly, the sections of the piezoactuator are mechanically connected in series, however electrically isolated. The piezolayers in the section are electrically connected in parallel and mechanically in series.

In general, the equation of the inverse piezoeffect [3–5] for the multilayered piezoactuator has the following form

$$S_i = d_{mi}E_m + s_{ij}^E T_j, \tag{45.1}$$

where S_i is the relative deformation of the multilayered piezoactuator along the axis i, T_j is the mechanical tension in the actuator in the axis j of the multilayered piezoactuator, E_m is the electric field strength in the actuator along the axis m, s_{ij}^E is the elastic compliance with E = const, d_{mi} is the piezomodule, $i, j = 1, 2,\ldots, 6$; $m = 1, 2, 3$ are the indices.

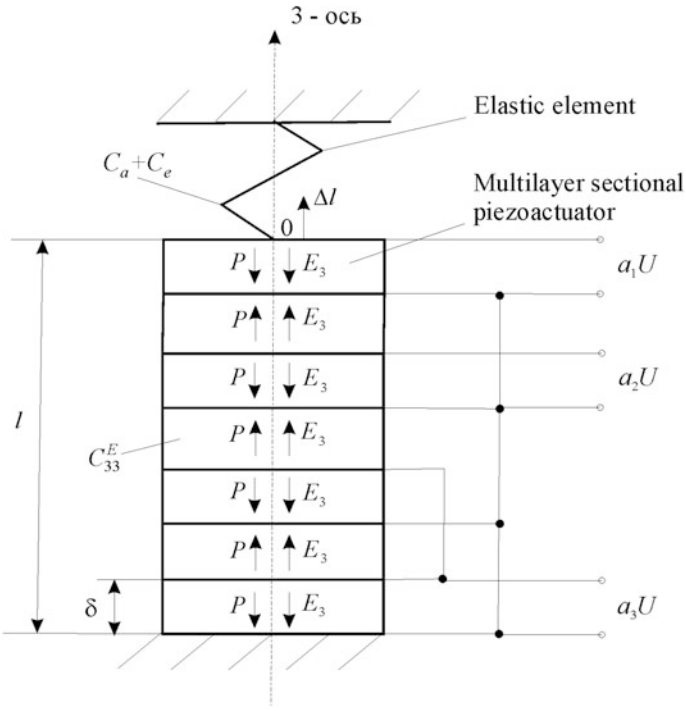

Fig. 45.1 Kinematic scheme of multilayer sectional piezoactuator with longitudinal piezoeffect at elastic load

Accordingly, the equation of the multilayered piezoactuator inverse piezoeffect [3–5] with the longitudinal piezoeffect of the multilayered piezoactuator has the form

$$S_3 = d_{33}E_3 + s_{33}^E T_3, \tag{45.2}$$

where S_3 is the relative deformation of the multilayered piezoactuator along axis 3, $T_3 = -F/S_0$ is the mechanical tension in the multilayered piezoactuator in the axis 3, F is the force, S_0 is the cross-section area of the piezoactuator, $E_3 = U/\delta$ is the electric field strength in the piezolayer along the axis 3, δ is the thickness of the piezolayer, $l = n\delta$ is the length of the multilayered piezoactuator, n is the number of the piezolayers, s_{33}^E is the elastic compliance with E = const, U is the voltage at the electrodes of the piezolayer, d_{33} is the longitudinal piezomodule.

The equation of the inverse piezoeffect [3–5] for the transverse piezoeffect of the multilayered piezoactuator has the form

$$S_1 = d_{31}E_3 + s_{11}^E T_1, \tag{45.3}$$

where S_1 is the relative deformation of the multilayered piezoactuator along axis 1, T_1 is the mechanical tension in the multilayered piezoactuator in the axis 1, E_3 is the electric field strength in the piezolayer along the axis 3, s_{11}^E is the elastic compliance with E = const, d_{31} is the transverse piezomodule.

The equation of the inverse piezoeffect [3–5] for the shear piezoeffect of the piezoactuator has the form

$$S_5 = d_{15}E_1 + s_{55}^E T_5, \tag{45.4}$$

where S_5 is the relative shear deformation of the multilayered piezoactuator, T_5 is the mechanical shear tension of the multilayered piezoactuator, E_1 is the electric field strength in the piezolayer along the axis 1, s_{55}^E is the elastic compliance with E = const, d_{15} is the shear piezomodule.

Let us consider the multilayer sectional piezoactuator in Fig. 45.1 consisting of n piezolayers (piezoplates), united in N sections, with the longitudinal piezoeffect, which has n_k number of piezolayers in the kth section

$$n_k = 2^{k-1}, \tag{45.5}$$

length of the kth section

$$l_k = 2^{k-1}\delta. \tag{45.6}$$

where k = 1, 2,…, N, and N is the number of sections, $l_1 = \delta$ is the length of the first section of the piezoactuator; δ is thickness of the piezolayer.

Hence, from (45.5) and (45.6), we obtain the total length of the multilayer sectional piezoactuator with the longitudinal piezoeffect (Fig. 45.1)

$$l = \sum_{k=1}^{N} l_k = (2^N - 1)\delta. \tag{45.7}$$

From (45.1) and (45.7) we obtain the maximum displacement of the multilayer sectional piezoactuator with a longitudinal piezoeffect and the connection of N sections in the form

$$\Delta l_{\max_N} = d_{33}(2^N - 1)U = d_{33}nU \tag{45.8}$$

where $n = 2^N - 1$ is the number of the piezolayers in the multilayer sectional piezoactuator.

45.3 Construction of the Static Characteristics of the Multilayered Piezoactuator

We obtain the static characteristics of the multilayer sectional piezoactuator when the binary code is fed to the input of the voltage switch and the voltage is connected from the outputs of the switch to the piezoactuator section. Accordingly, we receive the displacement of the multilayer sectional piezoactuator with the longitudinal piezoeffect as

$$\Delta l = \sum_{k=1}^{N} a_k \Delta l_k; \tag{45.9}$$

$$U_k = a_k U,$$

where $a_k \in \{0;\ 1\}$ are digits of the binary code, U_k is voltage on kth section of the piezoactuator.

From (45.6) and (45.9) we have

$$\Delta l = \sum_{k=1}^{N} a_k d_{33} 2^{k-1} U = d_{33}\left(\sum_{k=1}^{N} a_k 2^{k-1}\right)U. \tag{45.10}$$

Let us consider the mechanical and control characteristics of the multilayer sectional piezoactuators with the code control under the longitudinal piezoeffect. From (45.2), (45.9) and (45.10), we obtain the equation of the mechanical static characteristic of the multilayer piezoactuator with the longitudinal piezoeffect and the code controlled voltage

$$\Delta l = d_{33}\left(\sum_{k=1}^{N} a_k 2^{k-1}\right)U - s_{33}^{E} Fl/S_0 = d_{33}\left(\sum_{k=1}^{N} a_k 2^{k-1}\right)U - F/C_{33}^{E}, \quad (45.11)$$

where $C_{33}^{E} = S_0/\left(s_{33}^{E} l\right)$ is the rigidity of the multilayer sectional piezoactuator with the longitudinal piezoeffect.

Hence, we have the equation of the mechanical static characteristic in the form

$$\Delta l = \Delta l_{3\max}(1 - F/F_{3\max}), \quad (45.12)$$

$$\Delta l_{3\max} = d_{33} n_s U, \quad F_{3\max} = \frac{d_{33} n_s U S_0}{s_{33}^{E} l}, \quad n_s = \sum_{k=1}^{N} a_k 2^{k-1},$$

where $\Delta l_{3\max} = d_{33}\left(\sum_{k=1}^{N} a_k 2^{k-1}\right)U$ is the maximum displacement along the axis 3, $F_{3\max} = \frac{d_{33}\left(\sum_{k=1}^{N} a_k 2^{k-1}\right)US_0}{s_{33}^{E} l}$ is the maximum force along the axis 3, where n_s is the number of the piezolayers of the multilayer piezoactuator connected to the voltage source.

The control (adjustment) characteristic of the multilayer sectional piezoactuator with the longitudinal piezoeffect and the elastic load (Fig. 45.1), taking into account (45.2) and (45.11), has the following form

$$\Delta l = \frac{d_{33}\left(\sum_{k=1}^{N} a_k 2^{k-1}\right)U}{1 + \frac{C_a + C_e}{C_{33}^{E}}} \quad (45.13)$$

or

$$\Delta l = \frac{(d_{33} l_1/\delta)\left(\sum_{k=1}^{N} a_k 2^{k-1}\right)U}{1 + \frac{C_a + C_e}{C_{33}^{E}}}, \quad (45.14)$$

where $l_1 = \delta$ is the length of the 1st section of the multilayer sectional piezoactuator, C_a is the rigidity of the reinforcing element (amplifying element), C_e is the rigidity of the load.

Accordingly, the adjustment characteristic of the multilayer sectional piezoactuator with the longitudinal (Fig. 45.1), transverse or shear piezoeffect and the elastic load has the form

$$\Delta l = k_c U, \quad (45.15)$$

where k_c is the transmission coefficient of the piezoactuator under the code control

$$k_c = \begin{cases} \dfrac{(d_{33} l_1/\delta)\sum_{k=1}^{N} a_k 2^{k-1}}{1+\frac{C_a+C_e}{C_{33}^E}}; \\ \dfrac{(d_{31} l_1/\delta)\sum_{k=1}^{N} a_k 2^{k-1}}{1+\frac{C_a+C_e}{C_{11}^E}}; \\ \dfrac{(d_{15} l_1/\delta)\sum_{k=1}^{N} a_k 2^{k-1}}{1+\frac{C_a+C_e}{C_{55}^E}}. \end{cases}$$

In general, the transmission coefficient of the multilayer sectional piezoactuator under the code control

$$k_c = \frac{(d_{mi} l_1/\delta)\left(\sum_{k=1}^{N} a_k 2^{k-1}\right)}{1+\frac{C_a+C_e}{C_{ij}^E}}, \tag{45.16}$$

where $l_1 = \delta, h, b$ is the length of the 1st section of the piezoactuator, d_{mi} is the piezomodule, $C_{ij}^E = S_0/\left(s_{ij}^E l\right)$ is the rigidity of the piezoactuator.

Accordingly, the transmission coefficient of the multilayer piezoactuator under the parallel control has the form

$$k_c = \frac{d_{mi} l/\delta}{1+(C_a+C_e)/C_{ij}^E}. \tag{45.17}$$

The adjustment characteristic of the multilayer sectional piezoactuator under the code control with the elastic load has the form

$$\Delta l = \frac{(d_{mi} l_1/\delta)\left(\sum_{k=1}^{N} a_k 2^{k-1}\right)U}{1+(C_a+C_e)/C_{ij}^E}. \tag{45.18}$$

45.4 Construction of Transfer Functions and Dynamic Characteristics of the Multilayered Piezoactuator

We obtain the expression for the transfer function [4, 5, 7, 8, 11] of the multilayer piezoactuator with parallel control and the elastic-inertial load at one rigidly fixed edge of the multilayer piezoactuator and the longitudinal piezoelectric effect at $m \ll M$ in the form

$$W(p) = \frac{\Xi(p)}{U(p)} = \frac{d_{33} n}{\left[1+(C_a+C_e)/C_{33}^E\right]\left(T_{33}^2 p^2 + 2T_{33}\xi_{33} p + 1\right)}, \tag{45.19}$$

$$l = n\delta, \quad T_{33} = \sqrt{\frac{M}{C_a + C_e + C_{33}^E}}, \quad \xi_{33} = \frac{\alpha l^2 C_{33}^E}{3c^E \sqrt{M\left(C_a + C_e + C_{33}^E\right)}}$$

where m is the mass of the multilayer piezoactuator; M is the mass of the load; T_{33}, ξ_{33} are the time constant and the coefficient attenuation, respectively, for the longitudinal piezoeffect of the multilayer piezoactuator and the elastic-inertial load.

From (45.13) and (45.19) we have, under code control and longitudinal piezoelectric effect, the transfer function of the multilayer sectional piezoactuator for the elastic-inertial load for $m \ll M$ in the following form

$$W(p) = \frac{\Xi(p)}{U(p)} = \frac{(d_{33} l_1/\delta) \sum_{k=1}^{N} a_k 2^{k-1}}{\left(1 + \frac{C_a + C_e}{C_{33}^E}\right)\left(T_{33}^2 p^2 + 2T_{33}\xi_{33} p + 1\right)}. \tag{45.20}$$

Hence, for the length of the 1st section $l_1 = \delta$, we have the transfer function

$$W(p) = \frac{\Xi(p)}{U(p)} = \frac{d_{33} \sum_{k=1}^{N} a_k 2^{k-1}}{\left(1 + \frac{C_a + C_e}{C_{33}^E}\right)\left(T_{33}^2 p^2 + 2T_{33}\xi_{33} p + 1\right)}.$$

In the general form, with the code control, taking into account (45.14) and (45.19), we obtain the transfer function of the multilayer sectional piezoactuator for the elastic-inertial load for $m \ll M$ in the form

$$W(p) = \frac{\Xi(p)}{U(p)} = \frac{(d_{mi} l_1/\delta)\left(\sum_{k=1}^{N} a_k 2^{k-1}\right)}{\left(1 + \frac{C_a + C_e}{C_{ij}^E}\right)\left(T_{ij}^2 p^2 + 2T_{ij}\xi_{ij} p + 1\right)}, \tag{45.21}$$

$$T_{ij} = \sqrt{\frac{M}{C_a + C_e + C_{ij}^E}}, \quad \xi_{ij} = \frac{\alpha l^2 C_{ij}^E}{3c^E \sqrt{M\left(C_a + C_e + C_{ij}^E\right)}},$$

where T_{ij}, ξ_{ij} are the time constant and the coefficient attenuation, respectively, of the multilayer sectional piezoactuator and the elastic-inertial load.

Taking into account (45.15), (45.20), (45.21), the transient response of the multilayer sectional piezoactuator under the elastic-inertial load is written in the generalized form

$$\xi(t) = k_c U_0 h(t) = \xi_0 h(t), \tag{45.22}$$

where k_c is the transmission coefficient, U_0 is the amplitude of the voltage, $h(t)$ is the normalized transient response of the piezoactuator, ξ_0 is the steady displacement value.

In general, the steady displacement value (steady-state displacement) of the multilayer sectional piezoactuator under the code control is defined as

$$\xi_0 = \frac{(d_{mi} l_1/\delta)\left(\sum_{k=1}^{N} a_k 2^{k-1}\right) U_0}{1 + \frac{C_a + C_e}{C_{ij}^E}}, \tag{45.23}$$

where the corresponding parameters of the multilayer piezoactuator for the longitudinal piezoelectric effect: $l_1 = \delta$ and with the indices $mi = 33$, $ij = 33$, for the transverse piezoelectric effect: $l_1 = h$ and with the indices $mi = 31$, $ij = 11$, for the shear piezoelectric effect: $l_1 = b$ and with the indices $mi = 15$, $ij = 55$.

Hence, we have the expression for $h(t)$ of the dynamic characteristic in the form normalized transient response of the multilayer sectional piezoactuator under the code control

$$h(t) = 1 - \frac{e^{-\frac{\xi_{ij} t}{T_{ij}}}}{\sqrt{1 - \xi_{ij}^2}} \sin\left(\beta_{ij} t + \varphi_{ij}\right), \tag{45.24}$$

where the parameters

$$\beta_{ij} = \frac{\sqrt{1 - \xi_{ij}^2}}{T_{ij}}, \quad \varphi_{ij} = \operatorname{arctg}\left(\frac{\sqrt{1 - \xi_{ij}^2}}{\xi_{ij}}\right).$$

The effects of the parameters of the multilayer sectional piezoactuator and the elastic load on the static and dynamic characteristics of the piezoactuator are obtained. The transfer functions of the multilayered piezoactuator with the parallel and coded control are determined for the control systems of the nano- and microdisplacement for the mechatronics systems.

45.5 Conclusion

The analytical solution of the static and dynamic characteristics of the multilayered piezoactuator are constructed. The transfer functions of the multilayered piezoactuator with the parallel and coded control are received for the nano- and microdisplacement of the mechatronics systems. The characteristics of the multilayer piezoactuator with the parallel and coded control are received using its physics parameters, namely the rigidity and the mass of the load. The expressions for the displacements of the multilayered piezoactuator for the longitudinal, transverse and shear piezoeffect in the case of the parallel and coded control are obtained.

The transfer functions of the multilayered sectional piezoactuator with coded control are obtained from the transfer functions of the multilayer piezoactuator with

parallel control, taking into account the features of the deformations and the transmission coefficient of the multilayer sectional piezoactuator under the code control. The static and dynamic characteristics of the multilayer sectional piezoactuator are determined taking into account its physical properties and the elastic-inertial load.

References

1. J. Schultz, J. Ueda, H. Asada, *Cellular Actuators* (Butterworth-Heinemann Publisher, Oxford, 2017), 382pp
2. K. Uchino, *Piezoelectric Actuator and Ultrasonic Motors* (Kluwer Academic Publisher, Boston, MA, 1997), 347pp
3. *Physical Acoustics: Principles and Methods. Vol.1. Part A. Methods and Devices,* ed. by W. Mason (Academic Press, New York, 1964), 515pp
4. S.M. Afonin, Structural-parametric model and transfer functions of electroelastic actuator for nano- and microdisplacement, in *Piezoelectrics and Nanomaterials: Fundamentals, Developments and Applications*, ed. by I.A. Parinov (Nova Science Publisher Inc., New York, 2015), pp. 225–242
5. S.M. Afonin, *Doklady Math.* **74**(3) (2006)
6. S.M. Afonin, *J. Comput. Syst. Sci. Int.* **45**(2) (2006)
7. S.M. Afonin, *Doklady Phys*. **53**(3) (2008)
8. S.M. Afonin, *Doklady Math*. **73**(2) (2006)
9. S.M. Afonin, *Russ. Eng. Res*. **36**(6) (2016)
10. S.M. Afonin, *J. Comput. Syst. Sci. Int*. **54**(3) (2015)
11. S.M. Afonin, *Mech Solids*. **44**(6) (2009)
12. S.M. Afonin, *Russ. Eng. Res*. **32**(7–8) (2012)

Chapter 46
Fiberization and Reuse of Slag for High Added Value and Its Application

Chang Wook Park and Yun Hae Kim

Abstract The slag is divided into large blast furnace slag and steel slag to more than 470 million tons emissions in Korea. Much of the blast furnace slag is a trend that recycled material for cement is recognized as a new resource from waste. This material can replace the currently used industrial fibers (glass, basalt, carbon fibers). Slag fibers have economic and environmental benefits because of the waste recycling. Fibers, produced by mixing various slag, have a chemical composition similar to that of basalt fibers. It is anticipated that this will be possible as alternative fibers for basalt fibers that can overcome price competitiveness while protecting natural resources. As a result of measuring the tensile strength in this study, the average is measured to be over 3000 MPa. Therefore, it is expected to be applicable in industrial applications.

46.1 Introduction

Domestic steel-making slag is produced annually 20 million tons or more. Generally, in the process of producing 1 ton of steel, from 100 to 500 kg of steel-making slag is generated. For example, Fe–Ni slag is generated more than 1 million tons per year and fly ash, which is an industrial by-product, is generated 1.3 million tons annually, based on one thermal power plant. The generated slag is dumped into the yard and cools and coagulates in the atmosphere with a large amount of water-proof. The solidified clay of slag is recycled as raw material for cement, but some are buried and processed affected by market conditions. However, it is difficult to create high value-added product or use as a raw material. Therefore, there is a need for a new method different from the application to low value-added

C. W. Park · Y. H. Kim (✉)
Department of Material Engineering, Korea Maritime and Ocean University, Busan, Korea
e-mail: yunheak@kmou.ac.kr

I. A. Parinov et al. (eds.), *Advanced Materials*, Springer Proceedings in Physics 207, https://doi.org/10.1007/978-3-319-78919-4_46

industries and the recovery of metals or resources from existing single-composition waste resources. Therefore, a new recycling method could be presented through the combination of various process by-products [1–4].

Representative industrial fibers such as carbon fiber, glass fiber, and basalt fiber have been applied to various industrial fields. Carbon fibers have many advantages such as tensile strength, elasticity and corrosion resistance, but they are disadvantageous in that they are expensive. Glass fiber is applied to many industrial fields because of cheap price, but work environment and health problem are serious. So much effort is being made to replace them [5–8]. Basalt fibers have been developed for the replacement of glass fibers. Currently, much research is underway to replace glass fiber, but basalt fiber raw materials are undervalued compared to glass fibers in terms of its originality of natural resources and low competitiveness of price. Fibers produced by mixing various slags have a chemical composition similar to that of basalt fibers. It is anticipated that this will be possible as alternative fibers for basalt fibers that can overcome price competitiveness while protecting natural resources [9–11].

In this study, basic characteristics of fiber and spinning process of slag fiber through raw material analysis were studied.

46.1.1 Research Purpose

We studied the applicability of slag fiber to industrial through the analysis of basic characteristics, spinning process characteristics, and fiber properties.

46.1.2 Research Scope

At this study, we consider the following issues:

- Analysis of composition of slag
- Characteristics of raw materials
- Vitreous raw material
- Fly ash content ration (wt%): 40–60
- Spinning temperature: 1150–1247 °C
- Single fiber diameter (μm): 18.54–33.43
- Winding speed (m/s): 23.36–38.94
- Weight reduction rate: (wt%): 0.01–0.05
- Single fiber tensile strength (MPa): 1960–4176.

46.2 Research Method

46.2.1 Raw Materials

First of all, it is necessary to find a suitable component system to which the slag fibers can be spinned through the combination of Fe–Ni slag, converter slag and fly ash slag. The suitable component system can have a composition of basicity similar to that of commercially available basalt so as to have conditions similar to those of basalt fiber. For the analysis of suitable component system, XRF analysis was performed and TG/DTA was used to investigate the high temperature characteristics of each raw material.

To investigate the chemical resistance, the raw materials were immersed into 37.5 wt% of barium chloride, 22.37 wt% of hydrochloric acid, 20 wt% of sodium hydroxide and 98 wt% of sulfuric acid for 24 h, respectively. After that, the weight changes were compared and analyzed.

46.2.2 Spinning

Generally, a spinning system needs an industrial furnace with a high heat capacity as the base material of the slag is melted at a temperature above 1300 °C. It also requires precise controls of heating rate, temperature and diameter of the fiber. In this study, a feasible lab scale spinning system, which meets above requirements, has been designed. The designed spinning system consists of three parts: furnace, bushing, and winding part.

The spinning system has been designed considering the fact that the compounded slag is mainly composited with SiO_2 with high amounts of other compounds such as of Al_2O_3. The furnace part can raise the temperature up to maximum of 1600 °C, and the refractory of the furnace has been crafted with heat resisting and insulating materials that is frictionless and thermostable at high temperature. Figure 46.1 (a) presents the components of the furnace part, and (b) depicts the actual furnace part in lab scale.

As this is the most core construction of this spinning system, the bushing is made with alloy of Pt–Rh. The design includes two holes, based on the lab scale. Also, this part is designed thermostatically, in order to prevent hardening and clogging of the bushing entrance. Figure 46.2 (a) shows the design specification of bushing, and (b) the actual bushing part of this design.

Winding system is consisted of two bobbins and a guide, and has a speed control capacity of 0–6000 rpm. This part has been designed to wind a superfine fiber of 6–24 μm diameter without breaking it. Also, when a fixed amount of fiber is winded, the bobbin will shift automatically, allowing further winding. Figure 46.3 (a) shows the design specification of winder, and (b) the actual winding part of this design. Slag spinning machine part is present in Fig. 46.4 and the process of spinning is shown in Fig. 46.5.

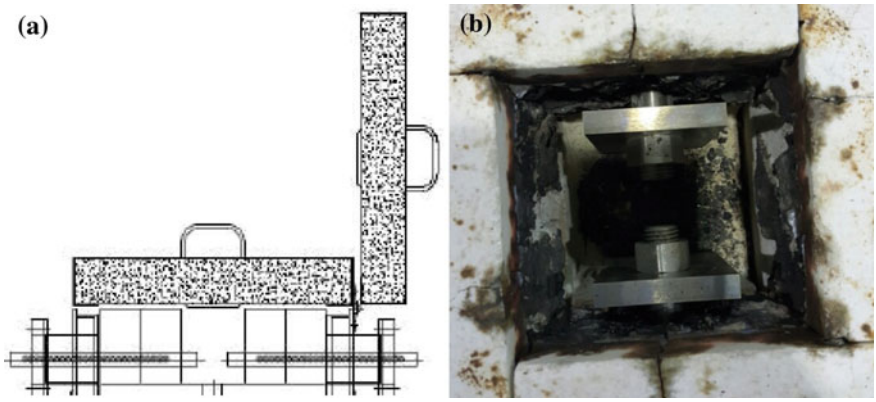

Fig. 46.1 Furnace part

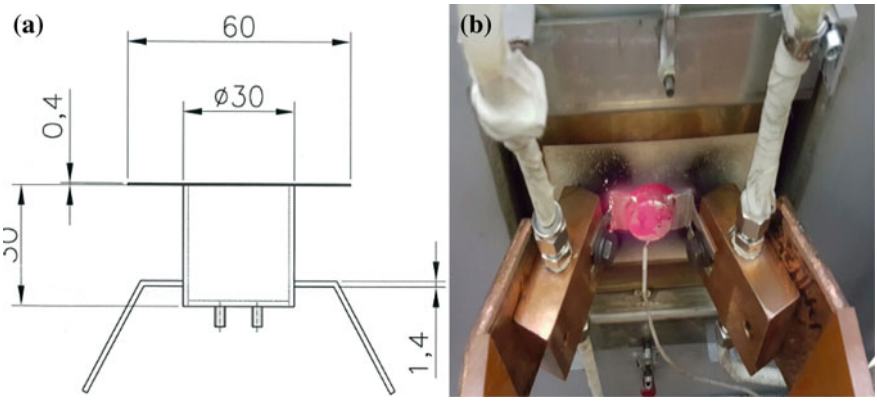

Fig. 46.2 Bushing part

46.2.3 Single Fiber Tensile Test

There are two experimental measurement methods in Short Fiber Tensile Strength; ASTM D 3822 and ASTM D 4018. ASTM D 3822 is a method of preparing every strand of specimen by separating spun fibers and then using paper as a frame (Fig. 46.6). In this method, a tensile test is conducted at 1.0 mm/min in a small tensile tester. At least 50 data are required because the data error is large. Therefore, the short fiber tensile strength was tested by ASTM D 4018 instead of ASTM D 3822. All the filaments were washed using the acetone in order to clean the fiber surface. Tensile strength was tested by ASTM D 4018 strand tensile test. This test is to fabricate specimens with fiber bundles. Orientation of the fiber is in one direction and the fiber content is produced as a 40–50 wt%. Since tensile

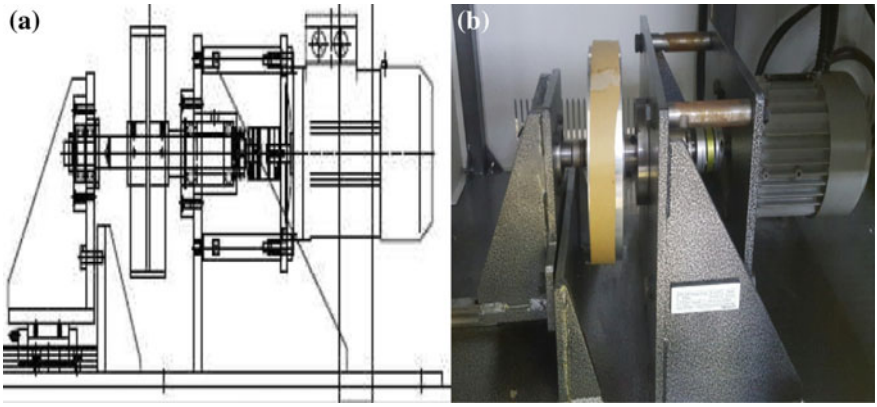

Fig. 46.3 Winding part

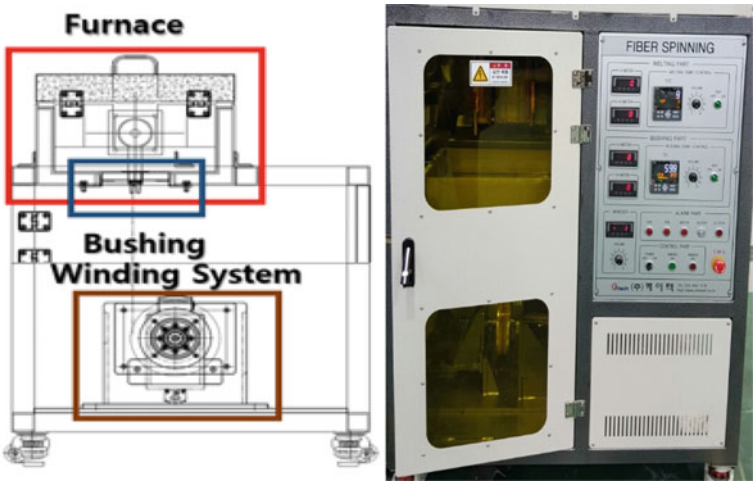

Fig. 46.4 Slag spinning machine part

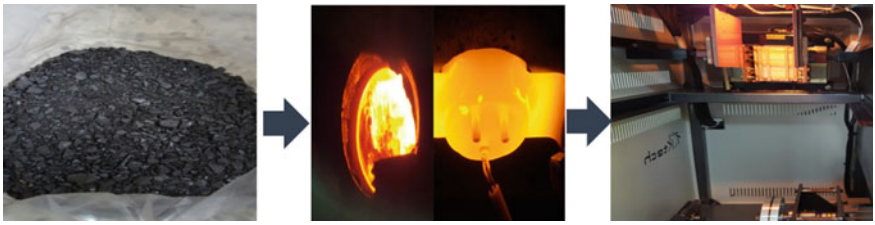

Fig. 46.5 Process of spinning

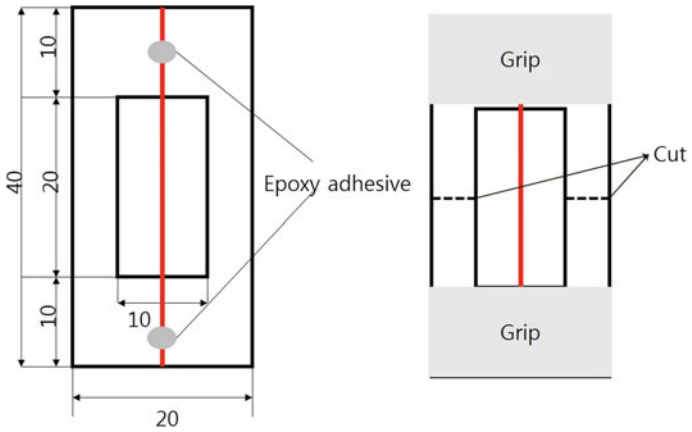

Fig. 46.6 Schematic of single fiber tensile test (ASTM D 3822)

strength of resin is very small compared to fiber, tensile strength was calculated by ignoring resin. Figure 46.7 shows a schematic of the ASTM D 4018 specimen.

$$M_{\mathrm{UL}} = W_1/L \tag{46.1}$$

M_{UL} is the mass per unit length, g/m (46.2)

W_1 is the mass of the specimen, g (46.3)

L is the length of the specimen, m (46.4)

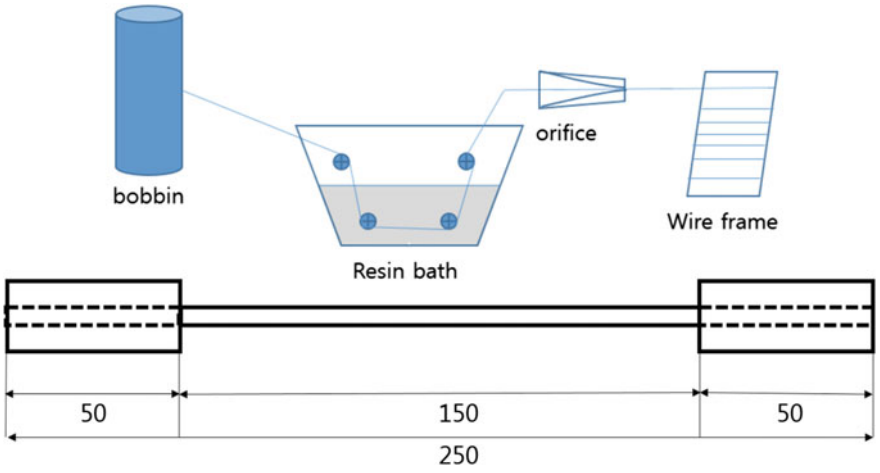

Fig. 46.7 Schematic of ASTM D 4018 specimen

$$\text{Tensile strength (MPa)} = A \times P \times \rho_f / M_{\text{UL}} \tag{46.5}$$

$$P \text{ is the maximum load, measured in tensile test, N} \tag{46.6}$$

$$\rho_f \text{ is the fiber density, g/m}^3 \tag{46.7}$$

$$A \text{ is an unit conversion factor } (=1, \text{ if load in N}) \tag{46.8}$$

46.3 Result and Discussion

46.3.1 Raw Material

The composition of the compounded slag closely resembles that of basalt rock. Therefore, the ideal composition of the raw material for spinning would require compositing the chemical compounds similar to that of the basalt fiber. Table 46.1 shows the components that affects the fiberization of basalt compounds for spinning continuous fiber.

Table 46.2 presents the composition of the slag compounds using XRF analysis. Upon comparing the composition of the basalt and the compounded slag, it can be concluded both compositions are appropriate for manufacturing a continuous fiber.

X-ray diffraction (XRD) analysis was used to confirm vitreous raw material. In Fig. 46.8, it can be observed that there is no peak line, which means this material is clearly vitreous. If the crystallinity of the raw material is confirmed during fiber spinning, it is impossible to spin the long fibers continuously. It is important to produce an amorphous raw material because a short circuit occurs at the portion where crystallinity is confirmed. When cooling slowly over several hours after

Table 46.1 Fiberization of basalt compounds for spinning continuous fiber

SiO_2 (%)	Al_2O_3 (%)	FeO + Fe_2O (%)	CaO (%)	MgO (%)	TiO_2 (%)	MnO (%)	Na_2O (%)	K_2O (%)
47–56	14–19	7–15	8–11	3.5–10	0.2–2.0	3.5–10	1.5–6.0	–

Table 46.2 Slag compounds, studied by using XRF analysis

	SiO_2 (%)	Al_2O_3 (%)	FeO + Fe_2O (%)	CaO (%)	MgO (%)
Furnace slag	15.41	3.02	23.34	36.45	5.03
Fe–Ni slag	55.50	2.60	7.99	0.55	30.70
Fly ash	61.68	21.89	4.72	4.45	1.29
Slag (40:25:25)	45.70	12.81	15.21	9.52	13.90
Slag (50:25:25)	51.49	17.47	11.21	8.28	6.49
Slag (60:25:25)	54.68	17.56	9.48	8.15	3.48

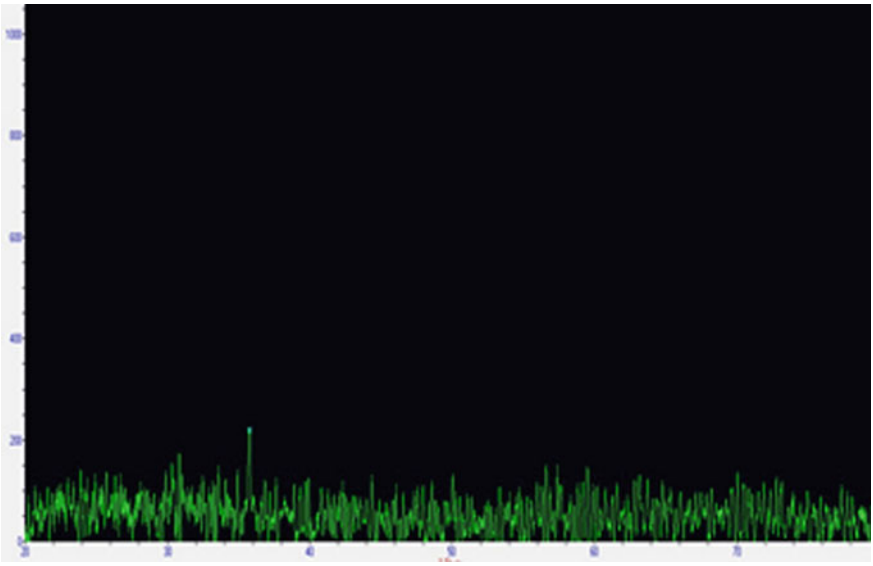

Fig. 46.8 XRD analysis of slag

melting, much of the spinning raw material becomes crystalline. When it is cooled at the RT condition, the temperature of the melt is rapidly reduced, but some parts of the melt are partially crystallized. When it is under water cooling condition, rapid cooling is achieved, and amorphous raw materials can be formed as a whole (see Fig. 46.9).

TG/DTA analysis was performed to analyze the thermal decomposition of the compounded slag. Both basalt and the compounded slag had similar thermal decomposition behaviors. Basalt had melting point of 1258 °C, Tg of 813 °C, approximately. The compounded slag had melting point around 1325 °C, which was about 80 °C higher than the Basalt, and Tg of 838 °C. Figure 46.10 presents TG/DTA analysis chart.

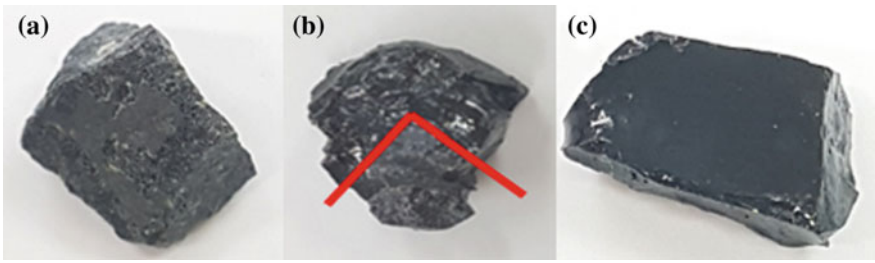

Fig. 46.9 **a** Cooling in furnace, **b** cooling in air, **c** cooling in water

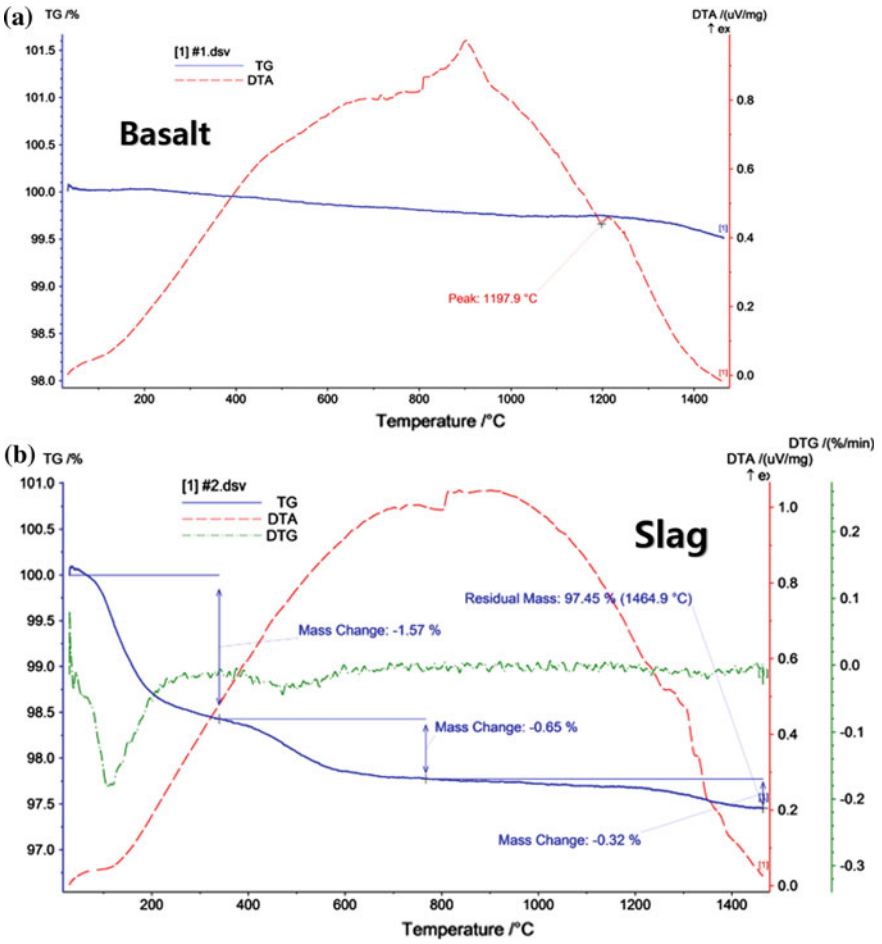

Fig. 46.10 **a** High-temperature characteristics of basalt **b** and slag

Analysis of the chemical resistance of the raw materials revealed that there was almost no weight change in the acid and base environment. After immersing for 24 h, the following results were obtained and the chemical resistance was considered to be excellent: a mass reduction of 0.05% at 37.5 wt% barium chloride; 0.02% at 22.37 wt% hydrochloric acid; 0.01% at 20 wt% sodium hydroxide; 0.04% at 98 wt% sulfuric acid (see Table 46.3).

Table 46.3 Slag compounds, studied by using XRF analysis

	Before weight (g)	After weight (g)	Mass reduction (%)
$BaCl_2$	50	49.975	0.05
HCl	50	49.99	0.02
NaOH	50	49.995	0.01
H_2SO_4	50	49.98	0.04

46.3.2 Spinning

The slag fibers were kept at 1150, 1200 and 1220 °C for one hour, respectively, so that the raw materials could receive heat sufficiently. This allowed the spinning to occur at the appropriate spinning temperature. The higher the amount of fly ash, the higher the spinning temperature (Fig. 46.11) as the content of SiO_2 increased. The slag fibers were produced between 1150 and 1245 °C and winding speed was 9.73–16.22 m/s. The diameter of the fibers was measured to be about 18–30 μm (see Fig. 46.12; Table 46.4). It could be produced on average 1244 °C, 416 RPM, 19.78 μm. Unstable spinning conditions are not uniform because the composition ratio of slag is slightly different and the viscosity of the melt is also different.

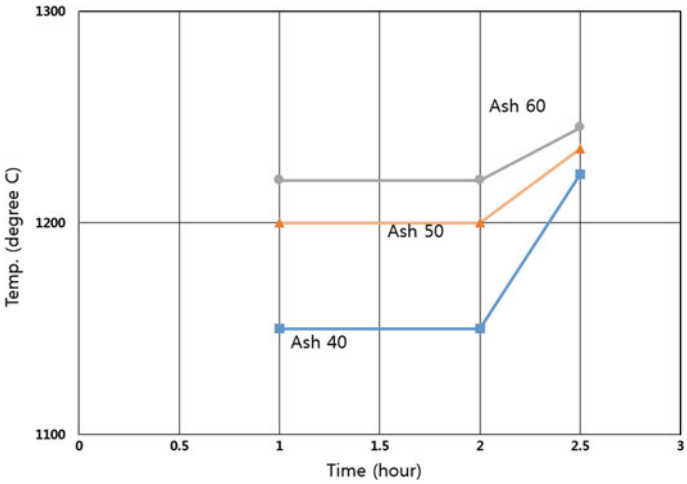

Fig. 46.11 Comparison of spinning temperature with fly ash content

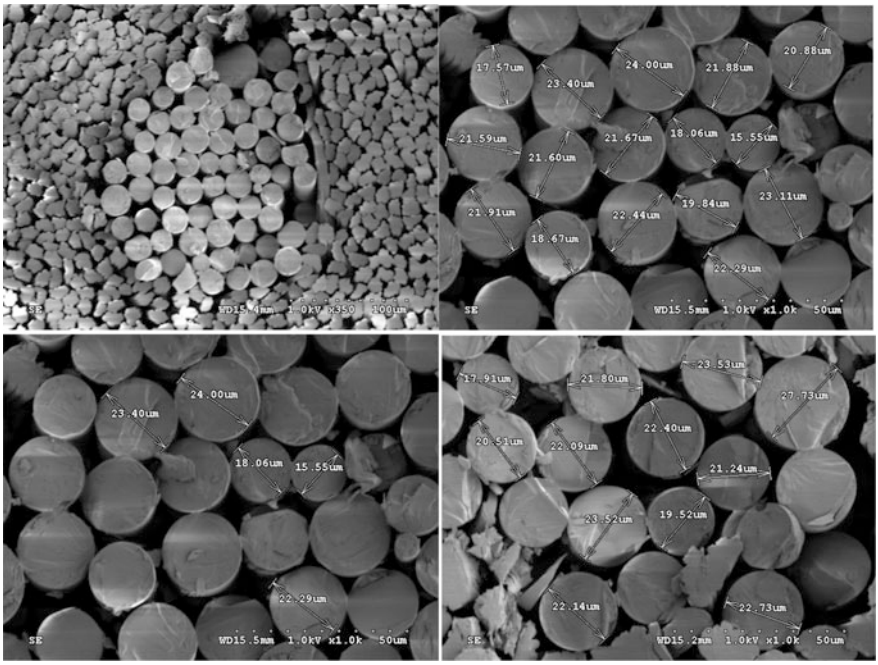

Fig. 46.12 Diameter of slag fiber, studied by using FESEM

Table 46.4 Slag compounds, studied by using XRF analysis

Fly ash: Furnace: Fe–Ni	Spinning temperature (°C)	Winding speed (m/s)	Diameter (μm)
40:25:25	1150	9.93	32.63
	1180	Fail	Fail
	1155	10.01	25.46
	1167	Fail	Fail
	1152	8.24	28.32
50:25:25	1223	16.22	20.34
	1220	15.84	24.45
	1221	15.48	25.01
	1224	16.04	22.34
	1220	16.43	18.54
60:25:25	1245	6.49	32.20
	1250	7.04	31.73
	1245	6.58	32.45
	1247	6.50	33.43
	1247	6.49	32.51

Fig. 46.13 Specimen of tensile strength

46.3.3 Single Fiber Tensile Test

Single-fiber tensile specimens were prepared as shown in Fig. 46.13, using the ASTM D 4018 standard. The tensile strength test results for each case are shown in Fig. 46.14. In case of slag fiber, containing 40 wt% of fly ash, the results were not obtained except for two non-spinning cases. There was a significant difference in tensile strength, depending on the composition ratio. The average tensile strength of fibers with fly ash of 50 wt% (see Fig. 46.15) showed the best tensile strength values of 3959 MPa, which is the average value of three specimens. However, its value was at least 3215 MPa and at most 4746 MPa, which showed a large

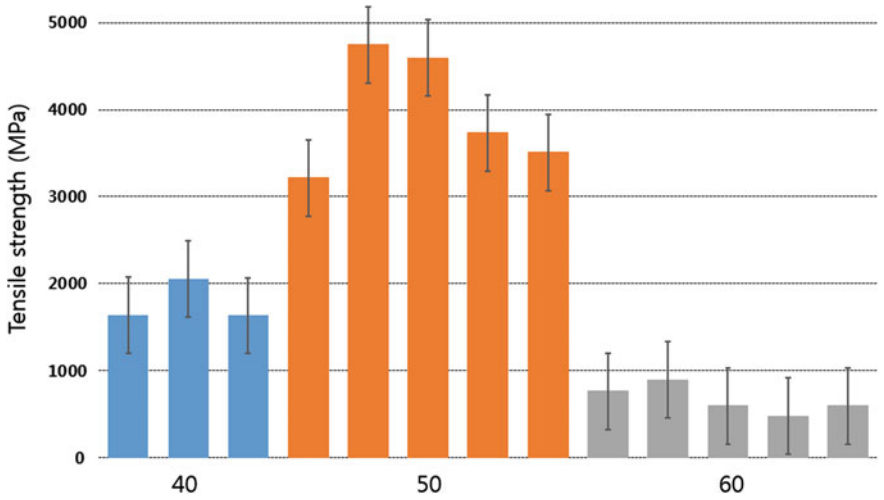

Fig. 46.14 Comparison of tensile strength with fly ash content

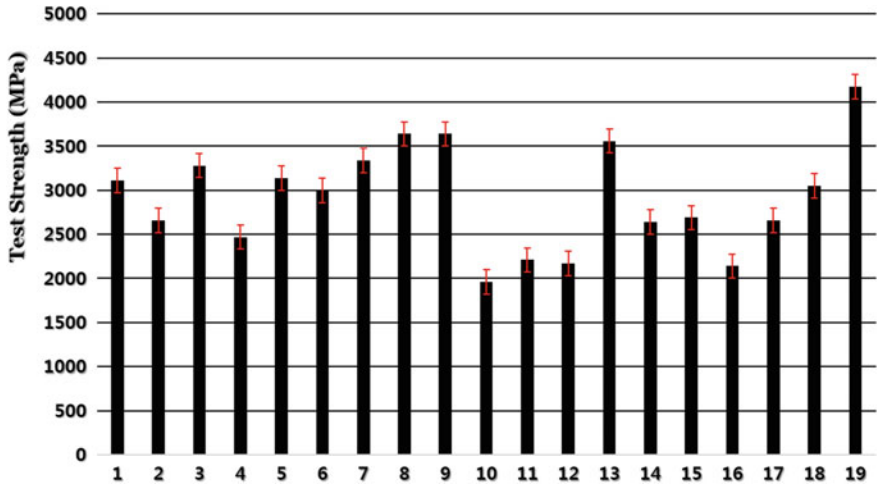

Fig. 46.15 Tensile strength (fly ash 50 wt%)

difference of 1500 MPa. Next, fiber, containing 40 wt% of fly ash spinned 3 times in 5 running times, but the average tensile strength was 1778 MPa. Fiber, containing 60 wt% of fly ash, showed the lowest tensile strength of 595 MPa. In case of spinning of slag fiber, containing 60 wt% of fly ash, the diameter was large (see Table 46.5) and the content of SiO_2 was large due to the high viscosity of the melt.

Table 46.5 Slag fiber compounds, studied by using XRF analysis

Spinning temperature (°C)	Winding speed (m/s)	Diameter (μm)
1175	38.94	16.8
1240	25.96	20.8
1240	29.20	20.5
1243	23.36	19.8
1243	24.66	19.8
1243	23.36	19.5
1245	29.20	20.8
1245	29.85	20.5
1245	25.96	19.8
1245	25.96	18.5
1245	27.26	18.5
1250	26.61	20.5
1250	25.96	20.5
1250	26.61	19.8
1260	25.96	20.5
1260	25.96	18.2
1270	24.66	22.7

46.4 Conclusion

In this study, the new production technology and estimation of the quality of fibers using slag is established. The study verifies the applicability of slag fibers to industrial fibers.

(i) The composition of the slag compounds is studied by using XRF analysis. The composition of the slag fiber closely resembles that of basalt fiber.
(ii) Through XRD analysis, it can be observed that there is no peak line, which means this material is clearly vitreous.
(iii) basalt had melting point of 1258 °C, Tg of 813 °C, approximately, and the compounded slag had melting point around 1325 °C, which was about 80 °C higher than the basalt, and Tg of 838 °C.
(iv) Analysis of the chemical resistance of the raw materials revealed that there was almost no weight change in the acid and base environment. This resistance is very excellent because almost no change in weight.
(v) The higher the amount of fly ash, the higher the spinning temperature as the content of SiO_2 increased. The slag fibers were produced between 1150–1245 °C and winding speed was 9.73–16.22 m/s. The diameter of the fibers was measured to be about 18–30 μm. It could be produced at average 1244 °C, 416 RPM, 19.78 μm. Unstable spinning conditions are not uniform because the composition ratio of slag is slightly different and the viscosity of the melt is also different.

(vi) The average tensile strength of fibers with fly ash of 50 wt% showed the best tensile strength values of 3959 MPa, which is the average value of three specimens. However, its value was at least 3215 MPa and at most 4746 MPa, which showed a large difference of 1500 MPa.

Acknowledgements This work is financially supported by the Ministry of Trade, Industry and Energy (MOTIE) through the fostering project of Industry—University Convergence District.

References

1. S. Bernard, M. Weinmann, P. Gerstel, P. Miele, F. Aldinger, J. Mater. Chem. **5**, 289 (2005)
2. S.S. Garrido, L.C. Pardini, in: *14 Congresso Brasileiro de Engenharia e Ciencia Dos. Materiais e 7 Congresso Brasileiro de Microscopia de Materiais—CBECIMAT*, **2000**, São Pedro (2000)
3. H.J. Kim, H.W. Yang, K.J. Jeon, Y. Huh, *A Novel Method for Melt Spinning of Mineral Fibers* (2009)
4. Ya.V. Lipatov, S.I. Gutnikov, M.S. Manylov, E.S. Zhukovskaya, B.I. Lazoryak, Mater. Des. **73**, 60 (2015)
5. B. Ozturk, F. Arslan, S. Ozturk, Tribol. Int. **40**(1), 37 (2007)
6. H.J. Park, S.M. Park, J.W. Lee, G.C. Roh, J.K. Kim, Compos. Res. **23**(3), 43 (2010)
7. R. Parnas, M. Shaw, Q. Liu. *Basalt Fiber Reinforced Polymer Composites*. The New England Transportation Consortium, Project No. 03-7—NETCR63 (2007)
8. G.L. Sheldon, Platin. Met. Rev. **21**, 18 (1977)
9. J. Sim, C.W. Park, D.Y. Moon, Compos. B Eng. **36**(6), 504 (2005)
10. B. Wei, H. Cao, Shenhua Song, Mater. Des. **31P**, 4244 (2010)
11. Y.K. Kim, J.R. Lee, H.J. Jang, *Composites Research*, p. 189, 01 Nov 1999

Chapter 47
Mineral Additives from Technogenic Raw Materials

N. I. Buravchuk, O. V. Guryanova, M. A. Jani and E. P. Putri

Abstract Description of the material composition and active components of ash-slag wastes and burnt mine rocks as hydraulic additives is given. The results of the evaluation of the activity of such additives are present. The influence of fine-disperse hydraulic additives on hardening processes and the formation of the structure and properties of cement stone, containing fly ash and burnt mine rocks is estimated.

47.1 Introduction

The economic part of the concept of stable development implies the optimal use of natural resources and the use of efficient technologies, the creation of environmentally friendly products, minimization, processing and elimination of wastes [1]. In this context, the utilization of technogenic raw materials acquires a comprehensive character and becomes part of the modern economic worldview. Among the generated and accumulated wastes, the secondary products of the coal and fuel industries are the most numerous [2–4]. However, the instability of the chemical-mineralogical composition and properties of ashes of heat electric stations (HESs), as well as many other technogenic materials [5, 6], restrains their use in the manufacture of concrete due to significant fluctuations in the properties of the products obtained on their base. For the effective utilization of technogenic wastes, a fundamentally new approach [7, 8] is required for their elimination. It requires expenditures to create an information database on wastes, sanitary and hygienic

N. I. Buravchuk (✉) · O. V. Guryanova
I. I. Vorovich Mathematics, Mechanics and Computer Sciences Institute,
Southern Federal University, Rostov-on-Don, Russia
e-mail: burav@math.rsu.ru

M. A. Jani · E. P. Putri
University of 17 Agustus 1945 Surabaya, Surabaya, Indonesia

E. P. Putri
Khon Kaen University, Khon Kaen, Thailand

I. A. Parinov et al. (eds.), *Advanced Materials*, Springer Proceedings
in Physics 207, https://doi.org/10.1007/978-3-319-78919-4_47

assessment, and development of methods for their applications. The use of ash-slag mixtures and mine rocks in the building materials industry is one of the strategic ways to decide the environmental problem in improving the environment in the zones of operation of HESs and in the regions with a developed coal industry [9]. The number of such regions includes the Rostov region of Russia, on the territory of which there are significant reserves of coal and facilities for the heat and power industry.

47.1.1 Research Purpose

The purpose of the research is to study the properties and composition of burnt mine rocks and ash-slag wastes for use as mineral hydraulic additives in the technology of binders, concretes and mortars.

47.1.2 Research Scope

In the chapter, we study the next issues:

(i) the composition and properties of ash-slag wastes and burnt mine rocks;
(ii) the ways to increase the activity of ash and slag wastes and burnt mine rocks;
(iii) the processes of hardening the binder with the additives of ash-slag wastes and burnt mine rocks;
(iv) the formation mechanisms of structureStructure and properties of cement stone with additives of ash-slag wastes and burnt mine rocks.

47.2 Research Method

The object of research was burnt mine rocks and ash-slag wastes accumulated in dumps at the area of the Rostov region.

Analytical and laboratory studies were performed to obtain information on the chemical and material composition of the raw materials. activity and physical-mechanical properties. The results of the studies make it possible to determine the directions of the using the such additives. The analysis of the effect of ash additives and burnt rock on hardening, structure formation and properties of cement stone is carried out.

47.3 Results and Discussion

47.3.1 Features of Mineral Composition

The objects of study of this work are burnt mine rocks and ash-slag wastes (ash of dry selection and with slag mixture). In several papers, the authors observed that the ash and slag are largely identical to that of natural mineral raw materials on the chemical-mineralogical, granulometric and phase-mineralogical composition [9–13]. However, the conditions for the formation of these materials are different. Burnt rocks are formed during prolonged self-burning of carbonaceous rocks, which occurs in waste pits, namely the cone-shaped dumps near coal mines at temperatures of 600–1000 °C. Under the influence of atmospheric oxygen, spontaneous burn out of organic substances and sulfur takes place, which continues dozens of years. In burnt rocks, the content of carbonaceous impurities does not exceed 5.0%. Ash-slag waste is a product of burning coal in boiler furnaces at temperatures above 1000 °C, up to 1700 °C. The chemical composition of the raw materials used is shown in Table 47.1.

The chemical compositions of ash samples and burnt rocks are mainly oxides of silicon, aluminum and iron. The chemical compositions of the wastes are semiacid materials, with high content of coloring oxides. The phase-mineralogical and chemical composition of ash and burnt rocks is determined mainly by the content of the mineral substances of carbonaceous rocks and fuel and also the changes that it undergoes in the process of high-temperature treatment, namely annealing in dumps or in the boilers of HESs.

At the annealing temperature, the mineral part of the fuel is undergone transformations, associated with dehydration, dissociation, oxidation, polymorphic changes, interaction in the solid phase, in the melt, and amorphization. These factors affect the properties, the degree of activation and reactivity of the final products of thermal treatment, namely burnt rocks and ash-slag wastes.

The carbonaceous rocks depositions are composed mainly of mudstones, siltstones, sandstones and limestones. Four types of dumps are distinguished: sandy, sandy-clayey, clayey and calcareous-sandy-clayey. The clayey type of mine dumps dominates at the area of the Rostov region.

Table 47.1 Chemical composition of mineral raw materials

Material	The content of oxides (wt%)									
	SiO_2	Al_2O_3	Fe_2O_3	CaO	MgO	SO_3	Na_2O	K_2O	P_2O_5	Loss on ignition
Fly ash	54.80	23.45	5.13	4.96	1.86	0.52	0.97	1.13	0.93	6.25
Ash-slag waste	53.31	21.42	7.83	5.10	1.97	0.95	1.23	1.87	0.54	5.78
Burnt mine rock	56.00	22.41	7.04	2.45	1.46	1.24	1.98	2.27	0.35	4.80

In the mineral part of solid fuel, as in the original mine rocks, clay minerals predominate. The most characteristic type of clay minerals in coal seams is kaolinite ($Al_2O_3 \cdot 2SiO_2 \cdot 2H_2O$).

In the ash and burnt rock, there are the main groups of substances: crystalline, amorphous and organic. The amorphous part of the ashes is a glass phase and an amorphous clay substance.

Mineral composition of fly ash is described by Fig. 47.1.

Mineral composition of burnt mine rock is described by Fig. 47.2.

The mineral composition of burnt rocks and ash contains crystalline minerals: quartz and its modifications, iron in the form of magnetite and hematite, a clay substance represented by hydromica with an admixture of kaolinite and chlorite:

(i) β-SiO_2 with d = 3.35; 2.29; 2.12; 1.82; 1.67 Å;
(ii) β-cristobalite with d = 2.81; 2.53; 2.49; 1.59; 1.54 Å;
(iii) γ-tridymite with d = 4.29; 3.21; 2.81; 2.49 Å;
(iv) γ-Al_2O_3 with d = 2.70; 2.45; 2.29; 1.97 Å;
(v) mullite with d = 2.20; 1.69; 1.59 Å.

When burning in the waste dump or combustion in the boiler furnaces, the dehydration and amorphization of clayey matter and the formation of the following phases are occurred [14]:

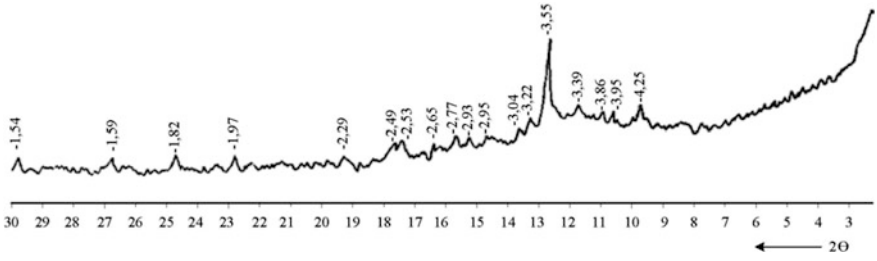

Fig. 47.1 X-ray pattern of fly ash

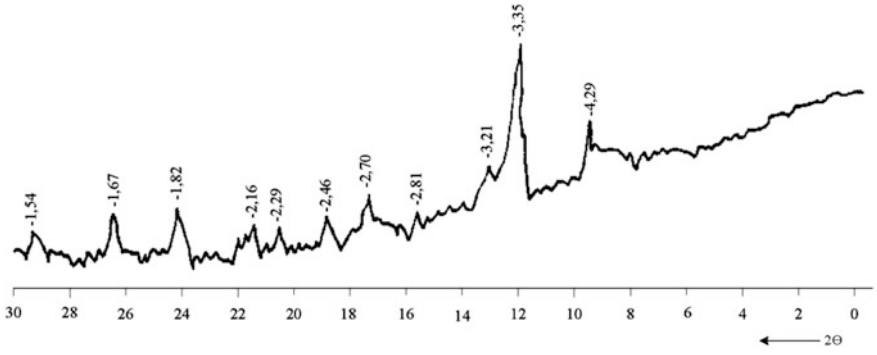

Fig. 47.2 X-ray pattern of burnt mine rock

(i) metakaolinite is not fully dehydrated and amorphous clay substance, which retains a distorted crystal lattice and is capable to hydration;
(ii) an amorphous, but not caked substance, characterized by a highly developed surfaceSurface and consisting mainly of fine mechanical mixture of amorphous silica and alumina;
(iii) sintered and partially vitrified substance, having a much smaller specific surfaceSurface area.

High specific surface area and the greatest hydraulic activity characterize the first phase. The metakaolinite, which has a large specific surface, reacts actively with calcium hydroxide at ordinary temperatures to form calcium hydrosilicates and hydrogelenite according to the reaction:

$$Al_2O_3 \cdot 2SiO_2 + 3Ca(OH)_2 + (n+5)H_2O = 2CaO \cdot Al_2O_3 \cdot SiO_2 \cdot 8H_2O + CaO \cdot SiO_2 \cdot H_2O$$

With a decrease in the specific surface and partial vitrification of amorphous products of high-temperature treatment of clay minerals, it is reduced the hydraulic activity of the components of burned rocks, ashes and slag.

Along with the clay substance, sandstone is also exposed to pyroprocesses, which presents itself cemented grains of quartz. In the burning process, quartz, having undergone a number of transformations, returns to the low-temperature modification of the β-quartz, but with a broken structural lattice. The existing ferruginous impurities also undergo changes under the influence of burning processes and pass into forms with greater activity. Thus, the main active components of burnt rocks, ash and slag, capable to further interaction are metakaolinite, as well as SiO_2, Al_2O_3, Fe_2O_3, in which the burning process violates the structure of the original minerals. The presence of these components is associated with a violation of the crystal lattice of clay minerals under thermal influences and the appearance of a certain energy potential in thermo-modified products. This new state of matter causes the ability of burnt rocks and ashes to hydrate and absorb lime from the solution. Unlike ashes, burnt rocks contain a considerable amount of clayey, ferruginous and siliceous hydraulic components. Burnt mine rocks show the properties of active clay, and ash has characteristics of a medium-active silicate-ferruginous additive. The most active component of ashes and slag is the vitrified substance and the glass phase. The activity of the ashes is mainly due to the presence of the glass phase.

In the studied ash-slag wastes, glassy phase is contained in a minor amount. As ash and burning rocks do not contain calcium oxide in the free form, therefore, when mixed with water they do not harden. However, in combination with binders (lime, cement), they exhibit characteristic properties of puzzolana. At the usual temperatures, they are able to bind calcium hydroxide to form insoluble compounds capable to hydraulic hardening. The latent hydraulic activity of burnt rocks and ash-slag wastes causes their use as hydraulic additives in binders, concretes and

mortars mixed with lime or cement. Methods for assessing the activity of the additives, exhibiting the properties of pozzolana, are as follows:

(i) setting the time deadline for a binder (normal density dough), consisting of additives, hydrated lime and gypsum not later than 7 days after mixing;
(ii) setting the time deadline on the base of resistance to water the binder within 3 days of presence in water the samples, containing additive, when blurring is not detected;
(iii) setting the time deadline on the base of the compressive strength of the heat-treated samples of the binder, containing additives (compressive strength should be not less than 3 MPa);
(iv) setting the time deadline on the base of ability to absorb dye from solution.

It is objectively possible to estimate the hidden activity of mineral additives according to the degree of their involvement in the pozzolanic reaction with the calcium hydroxide, generated by the hydrolysis of cement.

47.3.2 Kinetics of Involving the Additives in Reaction of Cement with Calcium Hydroxide

Figure 47.3 shows comparative assessment of the involvement of ash or burnt rock in reaction with calcium hydroxide. This technique allows comparative assessment of the activity of pozzolanic additives. Activity is estimated according to the degree (ρ) of involvement of the additive in the reaction. It is expressed as a ratio of the mass of the additives, which entered into reaction, to the mass of all introduced additives. From the data obtained, it follows that the pozzolanic reaction begins at a fairly early

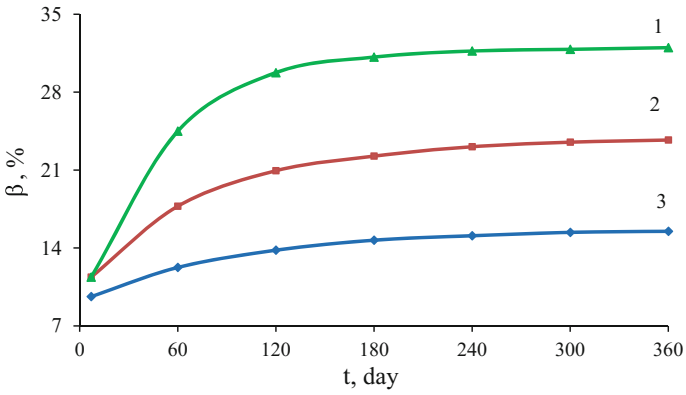

Fig. 47.3 Kinetics of the involvement of additives in the reaction with calcium hydroxide: 1—milled burnt mine rock with a specific surface of 600 m^2/kg; 2—ash of dry selection with a specific surface of 350 m^2/kg; 3—ash waste with a specific surface of 200 m^2/kg

Table 47.2 Assessment of the quality of additives from technogenic raw materials

No.	Composition, atomic weight (%)		Strength at compression at the age of 7 days (MPa)		The state of the samples after 3 days of water saturation	
	Fly ash	Burnt rock	Fly ash	Burnt rock	Fly ash	Burnt rock
1	70	30	8.6	7.4	The blurring of the samples was not detected, the clearness of their sides remains	
2	60	40	7.5	6.8		
3	50	50	6.3	5.1		
4	40	60	5.2	4.8		
5	30	70	4.1	3.4		

age, but a noticeable amount of the additives is involved in the reaction after 7 days. Then, there is a slow increase in the amount of reacted ash or burnt rock. The data obtained are consistent with the dispersity of the additives and features of their amorphous phases, exhibiting pozzolanic activity. From these data, it follows that fine-milled burnt mine rock (curve 1) is more actively involved in the process of hydration. The burnt rock is composed mainly of amorphization clayey matter, and this is the main reason for its active involvement in the pozzolanic reaction. The influence of the pozzolanic effect increases with increasing specific surface of the additives (curves 2 and 3). This is due to improved physico-chemical activity along with chemical one due to the extremely developed surface of the particles.

It is known that with increasing specific surface of the material, its sorption and chemical activity are increased. This is especially evident in inorganic binders. The increase in dispersity of binders accelerates and qualitatively changes the processes of hydration and hardening. It should be noted that a more complete involvement of the additives in pozzolanic reaction causes the intense binding of calcium hydroxide, which enhances the hydrolysis of the silicates of the cement and leads to a further increase in the degree of hydration. This affects the structure and properties of the solidified material. The simplest method for assessing the quality of various types of mineral additives is the ability of treated binders, containing additives and having strength at the age of 7 days, to withstand water resistance tests after 3 days of water saturation. The results of the evaluation of the quality of additives from burnt rock and fly ash at different ratios with cement are given in Table 47.2.

47.3.3 Effect of Co-grinding of Mixture of Fly Ash and Burnt Rock with Alkaline Additives on the Specific Surface of Mineral Additives from Technogenic Raw Materials

Figure 47.4 shows the change in the specific surface area of a mixture of ash and burnt rock, in a ratio of 1:1, at co-grinding with an alkali-containing additive. As

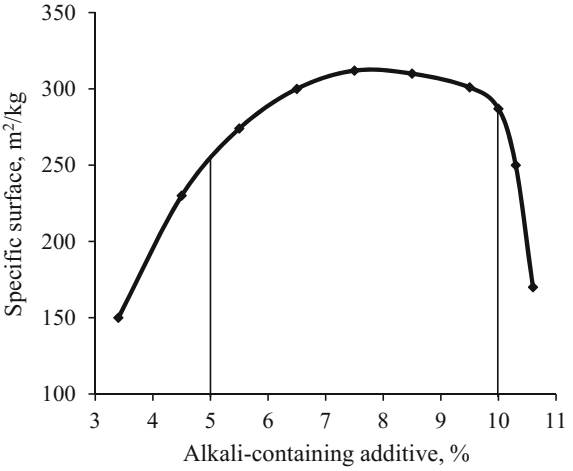

Fig. 47.4 Change in the specific surface of the additive composition (fly ash: burnt rock = 1:1)

such an additive, solid wastes of the spent electrolyser solution of sodium hydroxide production are taken.

It was experimentally proved that the specific surface of hydraulic additives from ash-slag wastes and burnt mine rocks should be at least 500 m^2/kg. This conclusion agrees with the authors' statement [16] that the optimum dispersity of the additive to cement should exceed the dispersity of the cement by 120–200 m^2/kg.

The activity of the mineral additives was evaluated at adsorption of dye methylene blue [17]. Characteristic of adsorption activity is the change in the optical density of the dye (initial concentration) to treatment with a dye and after treatment (the final concentration of dye): $\Delta D = D_1 - D_2$, where D_1 is the density of the dye initial concentration before treatment of mineral supplements, and D_2 is the density of the dye after treatment of mineral supplements.

The comparative determinations of the adsorption capacity of the original fly ash and burnt rock and their mixture and after mixed grinding with an alkaline additive confirm the increase in adsorption activity by more than 3.2 times (Table 47.3).

It follows from the data given that fly ash is more active in comparison with a burnt rock. However, the ability to activate in a burnt rock is more pronounced than that of fly ash. The greatest effect of activation was observed in a mixture of fly ash and burnt rock. Obviously, there is a synergistic effect, which is confirmed by increased values of ΔD for a mixture of ash and rock.

Table 47.3 Adsorption activity of mineral additives (ΔD)

Physical condition of mineral additives	Estimation of adsorption activity, ΔD		
	Fly ash	Burnt rock	$\frac{\text{Fly ash}}{\text{Burnt rock}}$ = 1:1
Original	0.031	0.022	0.05
After grinding	0.071	0.062	0.09
After mixed grinding with alkaline additive	0.13	0.11	0.16
Increase in adsorption activity, times	4.19	5.0	3.2

47.3.4 *Effect of Co-grinding of Mixture of Fly Ash and Burnt Rock with Alkaline Additive on Adsorption Activity of Mineral Additive from Technogenic Raw Materials*

Figure 47.5 shows the change in the adsorption activity of a mineral additive containing fly ash and burnt rock in a 1:1 ratio.

From Figs. 47.4 and 47.5, it follows that when co-grinding ash or rocks with an alkaline additive, optimum values of their specific surface and adsorption activity are achieved with an alkaline additive content from 5 to 10%.

The processes of hardening binders with hydraulic additives have not yet been fully studied and are characterized by the complexity and variety of the interactions of the mixture of components with water [18, 19], in which there are clinker part, amorphous clay substance, glass phase, silica in the form of pozzolana and other active ingredients.

Activated fly ash or burnt mine rocks is involved in the hardening of cement. Additives ash and milled burnt mine rocks affect the process of structure formation of cement stone [9], which is divided into three periods: (i) an induction is immediately after mixing the cement paste with water; (ii) a coagulation, defined by a grasp and (iii) the period of solidification and formation of the condensation-crystallization and crystal structure.

The kinetics of the growing the cement stone strength in a mixture with ash during the initial hardening period can be characterized by a change in the plastic strength of the cement paste in time, and in later periods, directly by the compressive strength of the samples of cement-ash stone.

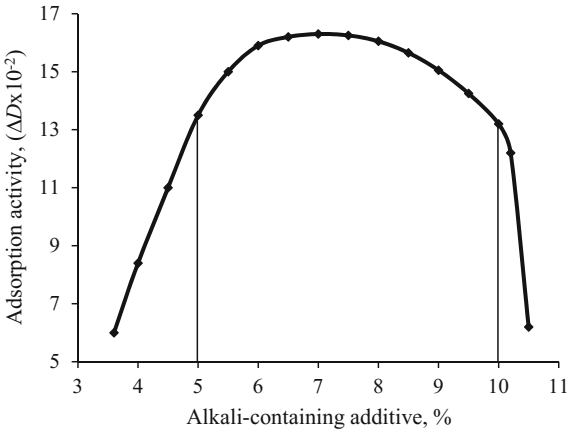

Fig. 47.5 Change of the adsorption activity of the mixture of fly ash and burnt rocks in the ratio of 1:1 in grinding with alkali-containing additive

47.3.5 *Kinetics of Hardening of Binder with Mineral Additive from Fly Ash*

Figure 47.6 shows the kinetics of hardening of cement stone and cement-ash mixture, in which 20% of cement with respect to control sample is replaced by ash.

It should be noted that the nature of hardening cement-ash mixture is not fundamentally different from the strength of cement stone. The only difference is in the quantitative values of the plastic strength and the compressive strength of the samples under consideration and the duration of the periods of structuring. For the cement-ash mixture, a slow increase in strength is characteristic, both at the initial period (Fig. 47.6a) and at the subsequent hardening (Fig. 47.6b, c). During the first day, it is almost impossible to evaluate the plastic strength of a cement mixture. The initial period of structure formation finishes approximately on the second day. Further, the structure is hardened, but with lesser intensity than in the control

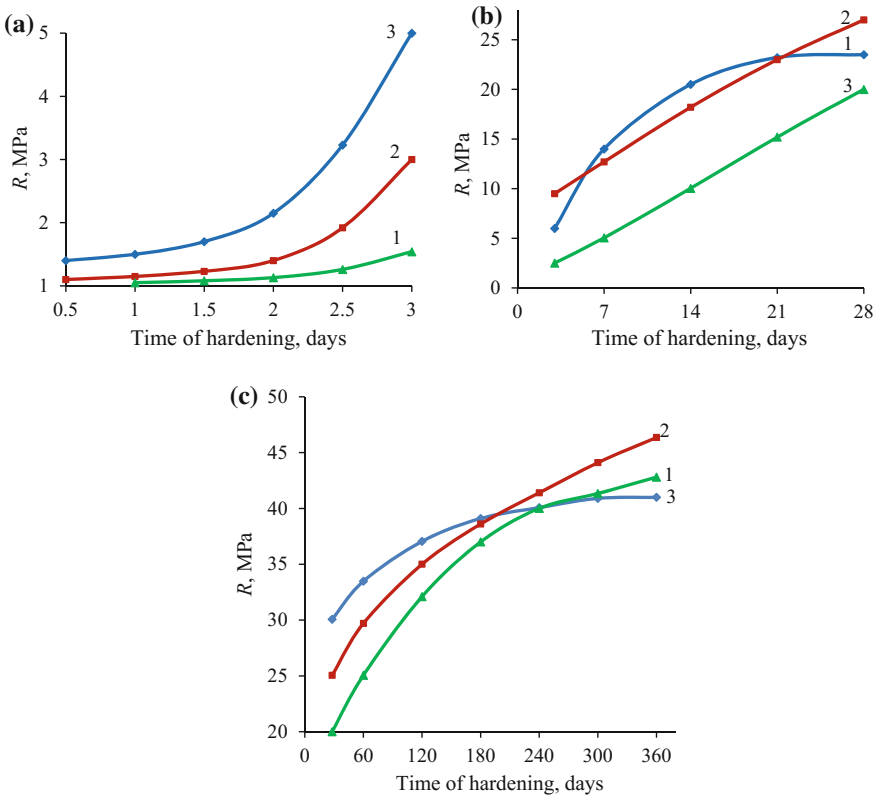

Fig. 47.6 Kinetics of hardening of binders: **a** the initial period; **b** 28 days of hardening; **c** long period: 1—cement: fly ash = 80:20 (wt%); 2—the same, with the addition of $CaCl_2$; 3—cement (control sample)

sample. In the control sample, a period of the stabilization of strength growth begins since about 10 days. Cement-ash mixture does not reach this period up to 28 days and the strength growth of these mixtures is ongoing. Additives of hardening accelerators not significantly change the nature of processes of structure formation, changing only the quantitative characteristics. One of the characteristics of additives, exhibiting the properties of pozzolans is the slow growth of hardness in the mixture with cement at the initial period and the continuation of the strength growth for a long time (Fig. 47.6c). Thus, for binders, hardening under natural conditions, the replacement of part of cement with ash leads to a lower strength in early age. With the time, the difference in the strength of pure cement binders and binders with ash gradually decreases, and in late dates of hardening (over 90 days) binders with ash not only acquire strength equal to the strength of cement without additives, but even exceed it. This is clearly illustrated by the data presented in Fig. 47.6.

Dispersity plays a positive role in forming the structure and properties of the mixtures, containing hydraulic additives (fly ash or milled burnt mine rocks). Fine particles are distributed between the coarse additives, increasing the specific surface area of the system and defining the effect of fine powders [20]. Increasing in the strength of artificial stone is due to the formation of new structures at hydration. The formation of hydrates is mainly due to surface reactions. On the developed surface similar to a substrate, the nuclei of new structure are deposited. At the initial period, the hardening effect of addition of ash or burning rocks is mostly physical in nature. New structures arise in the form of gels. Weak intermolecular bonds between particles are characteristic of coagulation-type structures. With the time, the pozzolanic properties of additives begin to appear in the binding of calcium hydroxide, formed during the hydration of clinker minerals. Hardening of artificial stone leads to an increase in the crystallization of the new structures. In addition to the gel, the hydration products are represented by crystallized low-basic hydrosilicates. The structures of the coagulation type are converted into reinforced condensation-crystallization fibrous structures. Felt weave patterns of needle crystals are also formed. The products of hardening fill the pores and microcracks increasing the contacts of particles. This is a long-time process, therefore, for systems containing hydraulic additives, it is characteristic that the strength increases after reaching the design one. The low strength of the artificial stone with the additions of fly ash or burnt rock is compensated by a higher strength in the later periods of hardening. The ultimate strength can exceed the design strength by 2–3 times.

The active constituents of the additions of fly ash or burnt rock bind free lime, forming during the hydration of cement. So, for example, after 6 months, an artificial mixture of cement with ash may contain 1.8–2.2 times less free calcium hydroxide than a pure cement mixture. Therefore, materials on mixed binders are more resistant to aggressive environments than materials, based on a cement binder. Comparative tests of such materials on corrosion resistance were carried out by keeping in a 5% solution of sodium sulfate for 2 years. In the composition of the binder, the content of finely milled burnt mine rocks was 50%.

In pure cement samples, there is a violation of the integrity of the sample and a gradual decrease in strength until destruction at the end of the test period.

47.3.6 State of the Samples of Cement Stone, Based on Pure Cement Binding and with the Addition of Burnt Rock After Corrosion Test

From Fig. 47.7, it is followed that in the samples with the additives of burnt rocks, external destruction is not observed.

47.3.7 Influence of Mineral Additives of Fly Ash on the Structure of Cement Stone

Figure 47.8 shows the microstructure of the cement stone with addition of fly ash. With increasing storage time in the aggressive solution is the increase of the strength coefficient of resistance for these samples by the end of the test exceeded the unit. Ash or burnt mine rocks participates in cement hardening with the formation of low-basic hydrosilicates, which have increased strength and durability. As a result, all potential possibilities of cement are used and the coefficient of its use is increased. When this binder is hardened, an optimal dense and more durable cement stone structure is created, contributing to the formation of a dense, strong, weather- and corrosion-resistant cement stone with a reduced consumption of cement clinker.

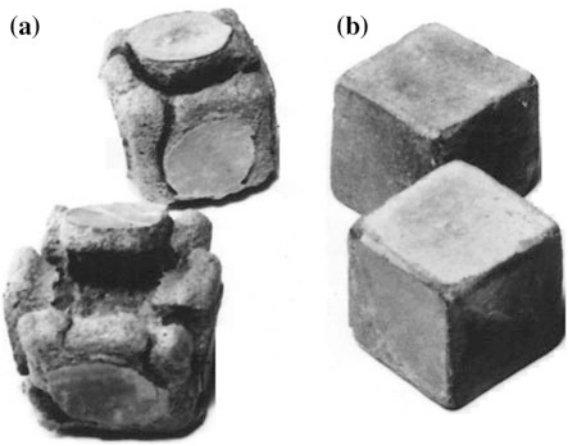

Fig. 47.7 Samples of cement stone after the test for corrosion resistance: **a** pure cement samples, **b** samples, containing 50% of fine-disperse burnt rocks

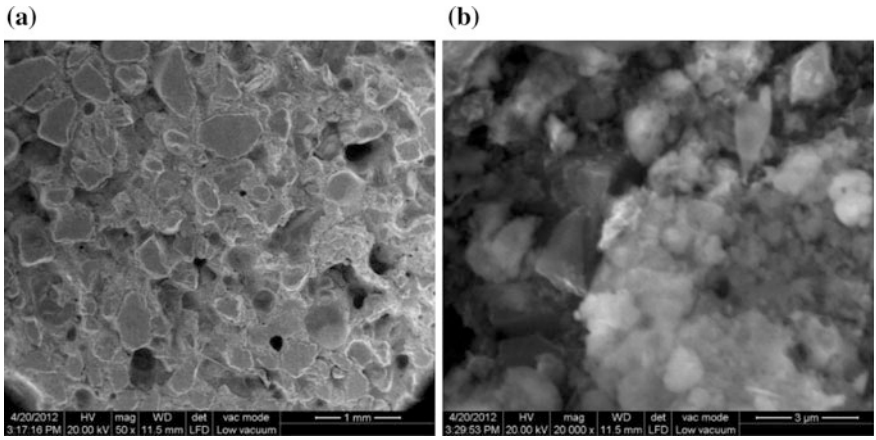

Fig. 47.8 Microstructure of cement stone, containing fly ash: **a** increase is 50×; resolution is 1 mm; **b** increase is 20,000×; the resolution is 3 µm

Corrosion resistance of a binder with hydraulic additives is explained by the fact that in the presence of fine-disperse ash or burned rock, the formation of hydrosulfoaluminate takes place at the initial stage of hardening, when the structure of the cement stone is still mobile and does not cause an increase in the osmotic pressure. In the future, the formation of ettringite, which can lead to the destruction of the stone, does not occur due to the lack of free calcium hydroxide in the solution. Moreover, in aggressive media, components of ash or burned rock are primarily active being in a metastable state. Later, cementing substances may fracture. The compounds, formed under the influence of an aggressive medium, are retained on the surface of the particles and prevent penetration of the aggressive solution deeply into the interior. The increased density of cement stone with mineral additives of ash-slag waste and burned mine rocks causes its high strength, minimal shrinkage, reduced heat generation, crack resistance, resistance to temperature differences and the influence of aggressive media.

47.4 Conclusion

Fine-disperse ash-slag wastes and burnt mine rocks as products of thermal effects exhibit the properties of hydraulic additives. In a mixture with Portland cement, the pozzolanic activity of these additives promotes an increase in the degree of hydration of clinker minerals and an increase in the number of cementing substances and contacts of force interactions. These additional hydrate compounds fill the microcracks and pores and dense the structure of the cement stone. The strength of cement stone increases with lower presence of clinker minerals.

Such additives are recommended for using in the manufacture technology of binders, concretes and mortars. The use of such additives allows one to economy the consumption of clinker minerals at simultaneous improving the construction and technical properties and performance characteristics of building composites. The results of the studies are confirmed by the practice of using ash-slag wastes and burned mine rocks.

Acknowledgements This research was carried out within the framework of financing of the Ministry of Education and Science of the Russian Federation for the project No. BCH0110-11/2017-20.

References

1. The Declaration of Rio de Janeiro on Environment and Development, *14 June 1992*. http://www.un.org/ru
2. L.I. Dvorkin, O.L. Dvorkin, *Building Materials from Waste Industry* (Phoenix, Rostov-on-Don, 2007) (in Russian)
3. M.Ya. Shpirt, *Waste Management of Production and Processing of Solid Fuels* (Nedra, Moscow, 1991) (in Russian)
4. M.J. Shpirt, A.V. Ruban, Y.V. Itkin, *Rational Use of Waste Production and Processing of Coal* (Nedra, Moscow, 1990) (in Russian)
5. E.I. Evtushenko, Vestnik V. G. Shukhov Belgorod State Tech. Univ. **8** (2004)
6. V.S. Lesovik, E.I. Evtushenko. Izvestiya VUZov. Build. **12** (2002) (in Russian)
7. V.I. Solomatov, *Build. Mater. Equip. Technol. XXI Century* **1** (2000) (in Russian)
8. V.S. Lesovik, *Problems of Building Material Sciences and New Technologies* (Belgram, Belgorod, Pt 5, 1997) (in Russian)
9. N.I. Burachuk, K.I. Rut'kov, in *Processing and Use of Waste Production and Combustion of Solid Fuel* (North-Caucasus Scientific Center of Higher School Press, Rostov-on-Don, 1997) (in Russian)
10. V.Z. Abdrakhimov, E.S. Abdrahimova, Izvestiya VUZov. Build. **1** (2006) (in Russian)
11. V.G. Lemeshev, S.V. Petrov, Izvestiya VUZov. Build. **5** (2002) (in Russian)
12. M.I. Wheneva, E.B, Khobotova. Vestnik Kharkov Nat Univ Chem. **18**(41) (2010) (in Russian)
13. N.I. Buravchuk, *Resource-Saving in Technology of Building Materials* (Southern Federal University Press, Rostov-on-Don, 2009) (in Russian)
14. A.V. Volzhensky, V.I. Burov, B.N. Vinogradov et al., *Concretes and Products from Slag and Ssh Materials* (Stroyizdat, Moscow, 1969) (in Russian)
15. V.P. Kuzmin, Build. Mater. **7** (2006); *Technolog*—Appendix to the Build. Mater. **5** (2006) (in Russian)
16. E.G. Velichko, G.S. Belyakova, Build. Mater. **3** (1966) (in Russian)
17. G.I. Knigina, Izvestiya North-Caucasus Sci. Center High School. Build. Architect. **2** (1962) (in Russian)
18. V.V. Vlasov, Izvestiya VUZov. Build. **5** (1997)
19. E.M. Chernyshev, E.I. Dyachenko, Izvestiya VUZov. Build. **3** (1996) (in Russian)
20. F.M. Li, *Chemistry of Cement and Concrete* (Stroyizdat, Moscow, 1961) (in Russian)

Chapter 48
Treatment of Dioxin-Contaminated Soil by Organic Waste Co-composting System

C. Lin, A. Kaewlaoyoong, C. T. Vu and W. Y. Huang

Abstract Food waste collected from kitchen leftovers and dinner tables were applied to co-composting dioxin-contaminated soils. The initial TEQ of the soil was 6048 ng-TEQ/kg dry wt, which was 6 times higher than the limit standard of 1000 ng-TEQ/kg dry wt issued by Taiwan EPA. It then decreased quickly by around 50% to 2934 ng-TEQ/kg dry wt at the 7 days. Though about 70% of PCDD/Fs had successfully degraded with co-composting approach after 49 days, the final TEQ value of 1604 ng-TEQ/kg dry wt remained higher than the standard limit of dioxins in soil (1000 ng-TEQ/kg dry wt). Subsequent attempts to bring the final TEQ value down to the standard limit are required. Nevertheless, this study has successfully demonstrated an enhanced thermophilic biodegradation approach to degrade dioxins. And the operation of the biological treatment is believed more robust and easier to operate in comparing to other traditional approaches while dealing with mesophiles.

48.1 Introduction

The remediation of dioxin [polychlorinated dibenzo-*p*-dioxins (PCDDs) and polychlorinated dibenzofurans (PCDFs)] contaminated site, where once was a large pentachlorophenol production area, has always attracted widespread public attention in Taiwan [1]. Bioremediation approaches have been reported to be environmentally friendly, creating less or no secondary pollutants, energy-efficient, and most importantly cost-efficient. Co-composting, a biological treatment approach for

C. Lin (✉) · C. T. Vu · W. Y. Huang
Department of Marine Environmental Engineering, National Kaohsiung Marine University, Kaohsiung 81157, Taiwan
e-mail: ctlin@webmail.nkmu.edu.tw

A. Kaewlaoyoong
Department of Safety Health and Environmental Engineering, National Kaohsiung First University of Science and Technology, Kaohsiung 82445, Taiwan

I. A. Parinov et al. (eds.), *Advanced Materials*, Springer Proceedings in Physics 207, https://doi.org/10.1007/978-3-319-78919-4_48

organic contaminant degradation, has been successfully employed in our previous study to handle diesel-contaminated soil [2]. Several studies have reported that dioxin-contaminated soil could successfully be degraded in laboratory scale co-composting [3–5]. Food waste, a common kitchen organic waste, can be considered as effective carbon and energy source for composting process. Co-composting, which includes the addition of readily available wastes (or bulking agents), relies mainly on the catabolic ability of naturally occurring microorganisms. Appropriate control parameters, e.g. moisture content, pH, temperature, nutrients, oxygen feeding and ratio of bulking agents determine the efficiency of co-composting process [2].

Successful composting degradation approaches of polychlorinated biphenyls (PCBs) [6] and polycyclic aromatic hydrocarbons (PAHs) [2] provide a reliable technical feasibility support for this study of co-composting on highly dioxin-contaminated field soil. Further, to our best knowledge, most organic contaminant degradation composting studies have been conducted in laboratory-scale set-up models with simulated contaminated soil materials [6], which in fact cast doubt on the success of pilot and field-scale setups.

This study was designed to assess the feasibility of co-composting approach on remediating highly dioxin-contaminated field soil in a pre-pilot scale composting setup. The correlation between the degradation efficiency and control parameters (temperature, moisture, pH and odorous NH_3) was identified. The results of this study serve as a foundation for larger scale applications of composting in the degradation of PCDD/Fs.

48.2 Materials and Methods

Dioxin standard solutions were obtained from Sigma-Aldrich (Missouri, USA) with 17 dioxin compounds mixed in solvent nonane. Other chemicals and reagents satisfied standards for laboratory use.

Food waste, used for co-composting experiment, contained discarded dairy products, grains, bread, fruits, vegetables, red meat, seafood and kitchen waste [7]. The ingredient composition was approximately estimated to be 50% of meat carcass or gizzard wastes from fresh market, 35% of vegetables, and 15% of others. This ratio was used in our previous study of co-composting degradation of diesel-contaminated soil [8]. Fresh food waste was shredded into fractions (<5 mm diameter). Sawdust was used to adjust the moisture content of the compost mixture [9]. Mature compost was added to enrich the microbial population and to enhance fermentation processes. The bioreactor (Fig. 48.1) (0.2 m^3, 0.7 m in height and 0.45 in width) was packed with 45 kg wet wt of food waste, 5 kg of sawdust, 15 kg of mature compost, and 15 kg dry wt of highly dioxin-contaminated field soil. The reactor was laid inside a greenhouse and daily-operated aeration rate (at 8.48 vvm) adjustment by a mechanical mixer placed inside. Representative compost (100 g dry wt) was sampled after the experimental setup and every 7 day.

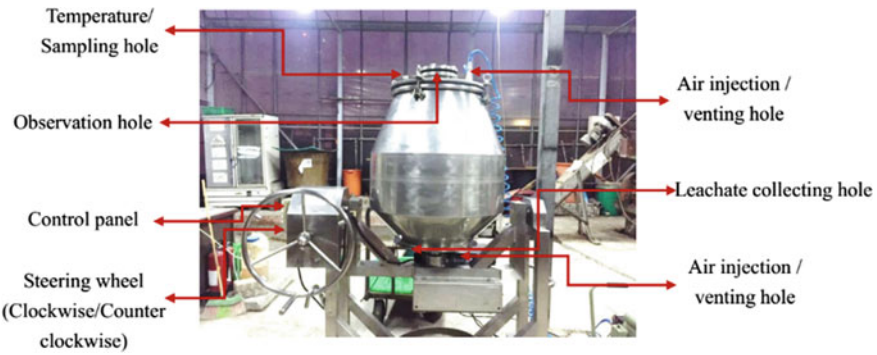

Fig. 48.1 Bioreactor appearance and operational functions

USEPA SW-846 Test 8280B method [10] integrated with Taiwan NIEA method M801.13B [11] were adopted for the sample preparation and PCDD/Fs analysis. Agilent 6890N Gas Chromatography coupled with Agilent 5973N Mass Spectrometry (Agilent Technologies, Avondale, PA, USA) were used in this study. All studies are performed by the Selective Ion Monitoring (SIM) mode. Calibration curve's average response factors was <20% (or $R^2 > 0.990$). Midpoint recovery was 100 ± 20% for OCDD and OCDF, and 100 ± 25% for other species. Blanks showed non-detected PCDD/F concentrations. Sample duplicates showed relative percent difference (RPD) less than 20%.

48.3 Results and Discussion

48.3.1 Variations in Control Parameters

Temperature and moisture variations are shown in Fig. 48.2. Moisture content was adjusted to be 30–50% throughout with some exceptions from days 47–49 (55.6–56.5%) due to the dry surrounding conditions. The temperature rose substantially from the beginning 28.4–56 °C on day 1 and continue climbing to more than 70 °C on day 10 and remained until day 15 prior to dropping to the ambient temperature on day 21. It should be noted that the temperature of the co-composting dramatically rose to 50 °C (thermophilic stage) on day 1, indicating that bioactivity was not inhibited by the dioxin content (approximately 6000 ng TEQ/kg dry wt). Thermophilic stage has been reported to favor organic degradation due to benefiting the development of organisms [8]. Therefore, we tried to maintain this stage by adding food waste (15 kg each) on days 21 and 35, when the temperature reached ambient condition. Three stages of thermophilic stages during the co-composting are shown in Fig. 48.2. Generally, this approach was successful as right after the food waste addition, temperature profile showed about 70 °C. However, due to

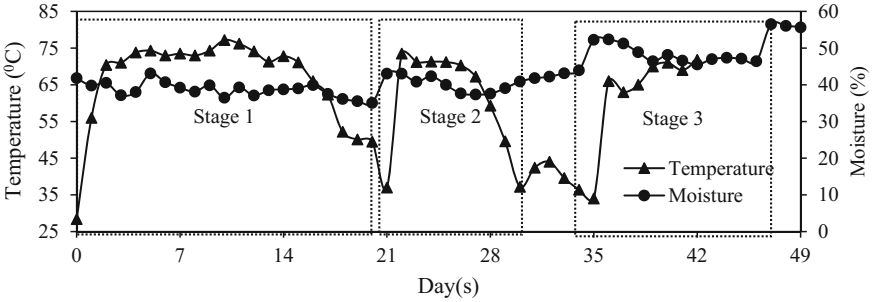

Fig. 48.2 Temperature and moisture profile of co-composting process

the effect of cold environment during the winter, thermophilic stage could not resist too long.

After three days, pH value rose from 5.7 to 7.28 (neutral) and remained constant at about 8.0 during thermophilic periods. This is in accordance with other studies of aerobic co-composting and neutral pH value (5.5–8.5) is reported to facilitate the development aerobic microbial community [4].

48.3.2 Dioxin Degradation

The initial TEQ of the soil was 6048 ng-TEQ/kg dry wt, which was 6 times higher than the limit standard of 1000 ng-TEQ/kg dry wt issued by Taiwan EPA. It then decreased by around 50% to 2934 ng-TEQ/kg dry wt after 7 days. This degradation rate was very high at 444.85 ng-TEQ/kg dry wt/day. This period was, when the temperature rose rapidly to reach thermophilic stage, where the microbial activity was higher than any other stages of the composting process. In addition, high temperature favors the activated energy breakdown of organic compounds [8]. Then, though showing fluctuation, the general trend of dioxin TEQ profile was going down (1604 ng-TEQ/kg dry wt) on day 49, indicating the success of our effort to maintain thermophilic period. This stage was more of the maturation stage. Dioxin degradation at this stage should be less significant [4]. The fact that TEQ values fluctuated slightly should be attributed to the variability of sampling. Maturation stage was when microbial activity was slowing down adversely affected the catabolic ability [4]. The final TEQ value after 49-day incubation period was 1604 ng-TEQ/kg dry wt, which remained higher than the standard limit of dioxins in soil (1000 ng-TEQ/kg dry wt). Therefore, we have devised subsequent studies attempting to bring the final TEQ value down to the standard limit. However, about 70% of PCDD/Fs had been successfully degraded with co-composting approach in this study. Further enhanced monitored natural attenuation (MNA) could also be feasible with the residual microbial dynamics.

Acknowledgements This work was financially supported the Center of Environmental Analysis Services (CEAS) at National Kaohsiung Marine University, Kaohsiung, Taiwan. The authors acknowledge the contribution of CEAS laboratory members for the energetic participation during the experimental setup, the sample collection and analysis. We would like to thank Mrs. Wen-Ming Mao for her technical assistance in instrumental analysis and Dr. Wen-Yen Huang for providing the soil material.

References

1. W.Y. Chen, J.H. Wu, S.C. Lin, J.E. Chang, J. Hazard. Mater. **312**, 159 (2016)
2. S. Covino, T. Fabianova, Z. Kresinova, M. Cvancarova, E. Burianova, A. Filipova, J. Voriskova, P. Baldrian, T. Cajthaml, J. Hazard. Mater. **301**, 17 (2016)
3. S. Kaiya, S. Utsunomiya, S. Suzuki, N. Yoshida, H. Futamata, T. Yamada, A. Hiraishi, Microbes and Environ. **27**, 127 (2012)
4. T. Narihiro, S. Kaiya, H. Futamata, A. Hiraishi, J. Biosci. Bioeng. **109**, 249 (2010)
5. N. Yoshida, N. Takahashi, A. Hiraishi, Appl. Environ. Microbiol. **71**, 4325 (2005)
6. I. Siebielska, R. Sidelko, Chemosphere **126**, 88 (2015)
7. C. Lin, Biores. Technol. **99**, 7651 (2008)
8. C.T. Lin, D.S. Sheu, T.C. Lin, C.M. Kao, D. Grasso, Environ. Eng. Sci. **29**, 117 (2012)
9. Y.T. Chang, T. Lo, H.L. Chou, Y.F. Laio, C.C. Lin, H.T. Chen, Int. Biodeterior. Biodegrad. **113**, 228 (2016)
10. U.S. EPA, SW-846 Test Method 8280B: Polychlorinated Dibenzo-p-Dioxins (PCDDs) and Polychlorinated Dibenzofurans (PCDFs) by High-Resolution Gas Chromatography/ Low-Resolution Mass Spectrometry (HRGC/LRMS). Hazardous Waste Test Methods, Office of Solid Waste, Washington, DC (2007)
11. NIEA Taiwan, Method M801.13B: Dioxins and furans analysis method by Gas Chromatography/High Resolution Mass Spectrometry (GC/HRMS). National Institute of Environmental Accreditation (NIEA), Zhongli City, Taiwan, R.O.C. (2014)

Chapter 49
Study of Bio-Composites to Search and Characterize Suitable Material for Human

Elsen Ronando, Muaffaq Achmad Jani, Ery Sadewa and Yudha Wrahatnala

Abstract Bio-composite materials are very varied and have some different characteristics depending on the applications. Bio-composite materials that can be adapted with human characteristic are one of challenging in the current research. In this paper, we conduct a survey of bio-composite materials based on the compatibility of human properties. Here we also are focused on the quality and the material properties with more cost efficient and environment-friendly. Pioneering the research for material properties are used in the field of Prosthetics. Data was processed from various physical tests on the characteristics of composite materials, spe-cifically polypropylene matrix with agricultural filler. An in-depth analysis of bio-composite materials describe them in detail, by fabricating bio-composite experimentally by compression molding method, then samples were tested by mechanical testing afterwards. The result shows that polypropylene with corncob filler has the highest mechanical properties, 21.1 MPa of tensile strength, 37.5 MPa of flexural strength, and 9% of tensile elongation. This result is compared with standard composite materials for prosthetics and it seems the bio-composite material are promising further research and provides a new direction of materials that is correlates with human properties.

49.1 Introduction

Bio-composite is a material consisting natural fibers as reinforcement and polymer as its matrix. Nowadays, bio-composite are widely used in several applications. It is due bio-composite materials have several advantages, such as reducing weight, easy to recycle, and easily formed. Therefore, bio-composites materials are very important to be developed.

Bio-composite materials that can be improved with human properties are one of the things that need to be advanced. Paper [1] proposed natural fibers for leg

E. Ronando (✉) · M. A. Jani · E. Sadewa · Y. Wrahatnala
University of 17 Agustus 1945, Surabaya, Indonesia
e-mail: elsen.ronando@untag-sby.ac.id

I. A. Parinov et al. (eds.), *Advanced Materials*, Springer Proceedings in Physics 207, https://doi.org/10.1007/978-3-319-78919-4_49

prosthetic, such as kenaf and corncob. Their research proposed indicated that natural fibers have a good quality with the advantages of cheaper and easily recycled. Paper [2] also evaluated bio-composite material from natural fiber for prosthetics, like ramie, banana, and kenaf fiber with plant-oil based resin. While paper [3] was focused on kenaf composite for designing prosthetic, bio-composites researches that adapted with human properties are also widely applied in biomedicine [4, 5]. Moreover, several studies were still less talked about mechanical properties, which has an important role to improve the quality of material.

This research studies a bio-composite material that suitable for human properties. Thus, we evaluate the mechanical properties and apply results for prosthetic hand. Moreover, here we also consider other aspects of material determination, as follows easily available materials and affordable prices [6].

One of composite materials for matrix in prosthetics is polypropylene, which has good physical and mechanical properties [7]. Based on this, we use polypropylene as matrix in our research. As reinforcement, we evaluate three composite materials with the reason of facility to get and cheap, such as corncob, bottom ash, and bamboo fiber.

Compression molding method is applied to evaluate the mechanical performance in our experiments. There are three observations in our focus as follows, tensile strength, flexural strength, and tensile elongation. The results then are compared to obtain the best results.

49.1.1 Research Purpose

The objective of this research is to search bio-composite material that can be adapted with human properties. The bio-composite materials thus are applied for prosthetic hand. The mechanical properties, such as tensile strength, flexural strength, and tensile elongation, are discussed.

49.1.2 Research Scope

- The material is bio-composite;
- Testing conducted are tensile strength, flexural strength, and tensile elongation;
- Pause between each testing is equal to 5 min.

Fig. 49.1 Tensile machine used to measure tensile strength, flexural strength, and tensile elongation

49.2 Research Method

Firstly, we combine polypropylene one by one with corncob, bottom ash, and bamboo fiber by heating 800 °C until melt. Then, we perform a combination between polypropylene–corncob, polypropylene–bottom ash, and polypropylene–bamboo fiber. Tensile strength, flexural strength, and tensile elongation are evaluated for each combination by using compression molding method as it is illustrated in Fig. 49.1.

49.3 Results and Discussion

The results of testing can be seen in Fig. 49.2.

From Fig. 49.2 we can see that polypropylene–corncob has tensile strength with 21.1 MPa, flexural strength with 37.5 MPa, and elongation percentage 9%. For polypropylene–bottom ash, tensile strength is 15 MPa, flexural strength is 30 MPa, and elongation percentage 7%. Polypropylene–bamboo fiber has the results: tensile strength with 10.3 MPa, flexural strength with 26.8 MPa, and elongation percentage 5%. The highest testing results demonstrate polypropylene–corncob with 21.1 MPa tensile strength, 37.5 MPa flexural strength, and 9% elongation. It means that polypropylene–corncob has a good comparative strength for prosthetic hand.

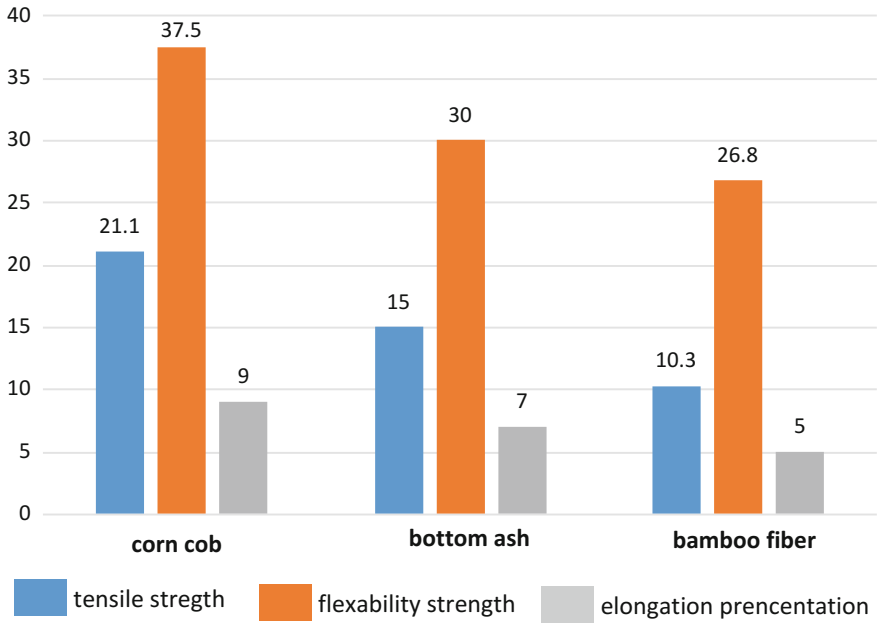

Fig. 49.2 Results of testing

Although polypropylene–corncob shows a good result, yet several conditions for testing phase are need to be observed. Thus, it can influence the results of testing. Another bio-composite materials also still need to be evaluated combining with polypropylene.

49.4 Conclusion

Based on our experiments, we propose the combination of polypropylene with corncob filler as bio-composite material for prosthetics hand. It can be showed that polypropylene with corncob filler has the best result of mechanical properties, as follows 21.1 MPa of tensile strength, 37.5 MPa of flexural strength, and 9% of tensile elongation. With the results, bio-composite material proposed is a suitable material for human properties.

For the future work, we will analyses the feature of suitable bio-composite material for human, especially prosthetic hand. Further, we will develop a machine learning system for validating the analysis result in reality and prediction of the optimal characteristics of bio-composite materials. Thus, we will evaluate the material performance.

Acknowledgements This research was performed into framework of the International Conference on Physics and Mechanics of New Materials and Their Applications (PHENMA) 2017 in Jabalpur, India.

References

1. R. Che Me, R. Ibrahim, P.M. Tahir, Alam Cipta **5**(1), 136 (2012)
2. R.N.M. Chowdary, A Study Rep. **4**(9), 2343 (2013)
3. M.H. Nurhanisah, N. Saba, M. Jawaid, M. Paridah, *Green Biocomposites, Green Energy and Technology* (Springer, Cham, 2017), p. 127
4. D. Chandramohan, K. Marimuthu, Int. J. Adv. Med. Sci. Appl. Res. **1**(1), 9 (2011)
5. S. Ramakrishna, J. Mayer, E. Wintermantel, K.W. Leong, Compos. Sci. Technol. **61**(9), 1189 (2001)
6. N. Abilash, M. Sivapragash, Int. J. Appl. Innov. Eng. Manage. **2**(1), 53 (2013)
7. T.T. Verhoeff, P.A. Poetsma, L. Gasser, H. Tung, Prosthet. Orthot. Int. **23**, 249 (1999)

Chapter 50
The Application of Bottom Ash Reinforced Aluminum Metal Matrix Composite for Motorcycle Disc Brake

Maula Nafi, Muaffaq A. Jani, Retno Hastijanti, Ivan A. Parinov and Shun-Hsyung Chang

Abstract Metal matrix composite (MMC) from aluminum matrix and bottom ash reinforcement is now developed as a part of automotive, in this case a motorcycle disc brake. Motorcycle disc brake is fabricated by aluminum matrix and bottom ash reinforced composite, and then performed T6 heat treatment. Squeal noise testing is being tested afterward with 600, 700, and 800 rpm and weight variation of 3, 4, and 5 kg. The result shows that composite Al–bottom ash composite has a highest number of sequel noise of 100.7 dB, compared with original motorcycle disc brake, the sequel noise is 76.8 dB. So there will be chances of improvements in Al–bottom ash composite in fabrication. The variation of 600 rpm and 3 kg weight shows the best squeal noise of 75 dB. Hardness testing with Rockwell F method is performed to analyze mechanical properties of the disc brake. The result shows the hardness of Al–bottom ash composite is 80.6 HRF, compared to the original disc brake 59.2 HRF. In a whole, Al–bottom ash composite has good mechanical and thermal properties, so that it can be advanced as a spare part of automotive, especially motorcycle disc brake.

50.1 Introduction

Disc brakes are one type of brake widely used in modern vehicle braking systems. The appearance of noise during braking is done like groan, judder, moan and squeal still a problem in the braking system. Noises emerging due to obstacles to braking system support components such as discs, brake pads and calipers [1]. One type of sound that is very disturbing is the sound squeal (sound shrill), which has a fre-

M. Nafi (✉) · M. A. Jani · R. Hastijanti
University of 17 Agustus 1945, Surabaya, Indonesia
e-mail: maula.nafi@untag-sby.ac.id

I. A. Parinov
Southern Federal University, Rostov-on-Don, Russia

S.-H. Chang
National Kaohsiung Marine University, Kaohsiung, Taiwan

I. A. Parinov et al. (eds.), *Advanced Materials*, Springer Proceedings in Physics 207, https://doi.org/10.1007/978-3-319-78919-4_50

quency above 1000 Hz. This sound comes from an unstable brake smile today that also disturbs the calm as well. To avoid the negative effect of vibration, then in the early stages it is required to develop vibration shock model that can interfere with the performance of the brake.

A disc brake has been manufactured by using aluminum matrix composite with reinforcement of bottom ash coal [2]. Metal matrix composites are combined of two or more materials, where metal is used as a matrix and ceramic is used commonly as the reinforcement. Aluminum is selected as the matrix due to its low weight, good fabrication properties and cheapness. With the development of composite, aluminum can be combined with ceramics to get better physical and mechanical properties [3], so that it can be applied as automotive parts.

T6 heat treatment is commonly used in aluminum alloy fabrication. The purpose of this heat treatment is to increase the mechanical properties, especially strength and hardness. It consists of three main steps: solution treatment, quenching and artificial aging.

This research conducted an experiment of squeal noise testing to a disc brake, manufactured from Al–bottom ash composite under T6 heat treatment. The result would be compared to an original disc brake.

50.1.1 Research Purpose

The objective of this research is to understand the effect of using rpm and weight variation to the squeal noise of Al–bottom ash disc brake. It also would be a feasibility study of Al–bottom ash composites application in automotive parts.

50.1.2 Research Scope

- The material is Al–bottom ash composite
- Testing conducted are squeal noise and hardness
- Solution treatment: at 540 °C for 6 h
- Artificial aging: 180 °C for 6 h
- Variation of rpms: 600, 700, and 800 rpms
- Variation of load/weight: 3, 4, and 5 kg
- Pause between each squeal noise testing: 5 min.

50.2 Research Method

Firstly, Al–bottom ash composite is fabricated using the method of stir casting. Aluminum would be heated until melt in 700 °C, then it is stirred while insert powder of bottom ash little by little. The temperature is kept at 700 °C, and kept stirred until the bottom ash mixed properly with the molten Al. Then we pour the molten metal in the mold.

Machining process is performed to fabricate a disc brake by using CNC machine. Then T6 heat treatment is executed in a muffle furnace. Hardness test is conducted for three specimens, namely: original disc brake, Al–bottom ash disc brake without T6, and Al–bottom ash disc brake with T6. The hardness testing is used Rockwell F testing because it is purposed for annealed copper alloy, aluminum alloy and soft sheet metals [4]. Braking and squeal testing are then conducted by using the natural model (see Fig. 50.1) and tools (see Fig. 50.2).

The squeal noise testing is started by adjusting the speed control for the motor. The rotation of tire, measured by digital tachometer, exactly corresponds to 600, 700, and 800 rpm. After rotating performed steadily, load is given to the brake lever so that the braking starts until squealing. Squeal noise is measured by sound level meter and all three specimens are tested the same way.

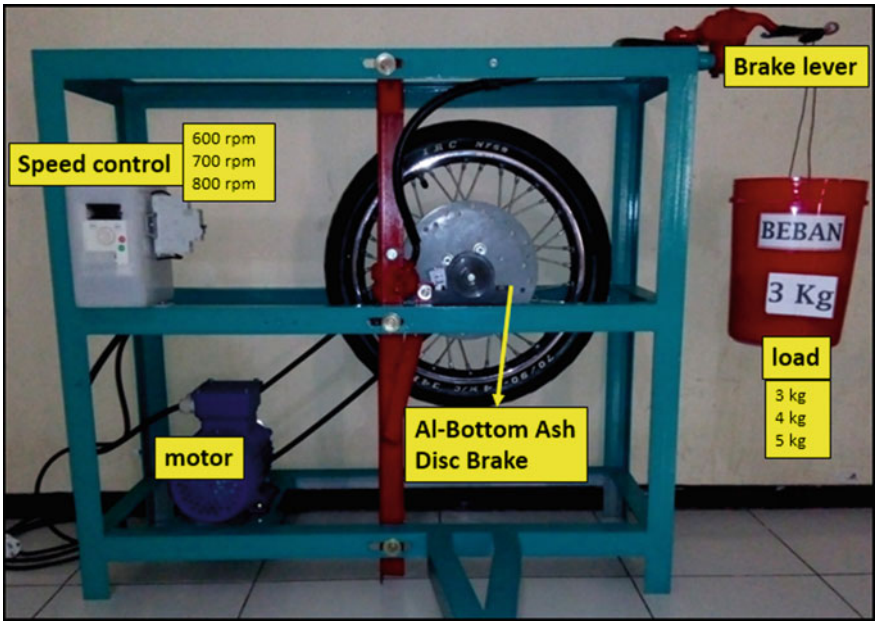

Fig. 50.1 Model to execute squeal noise testing

Sound level meter Thermo laser Digital tachometer

Fig. 50.2 Tools used to measure squeal noise, rpm, and temperature

50.3 Results and Discussion

The results of hardness testing are present in Table 50.1.

From the hardness results in Table 50.1, basically Al–bottom ash disc brake has higher value of hardness, compared to the original disc brake. There is growth of hardness value because of T6 heat treatment and Al–bottom ash became harder after T6 heat treatment. From viewpoint of these results for mechanical properties, we can conclude that Al–bottom ash is a well alternative for disc brake because it has higher hardness value.

The results of squeal noise testing can be seen in Fig. 50.3. From Fig. 50.3 we can see that original disc brake has squeal noise of 76.8 dB. For Al–bottom ash disc brake, the squeal noises are varied with changing considered parameters. The case of 800 rpm and 3 kg load demonstrates the loudest squeal noise, 100.7 dB. The lowest squeal noise of 75 dB is gotten for the case of 600 rpm and 3 kg load. This result is better than the original disc brake. It means that by using squeal noise test results, we can conclude that at specific values of rpm and loads, Al–bottom ash composite is a good alternative material for disc brake.

The faster the rotation and the heavier the load, squealing is getting noisier. However, at rotation of 800 rpm, the squealing noise is decreasing at loads of 4 and 5 kg. We can conclude that there are optimum values of rotation speed and load. Therefore, we assume to conduct more experiments with more variations of parameters to fill existing gap.

Table 50.1 Hardness testing results

Specimen	Hardness (HRF)
Original disc brake	59.2
Al–bottom ash without T6	75.4
Al–bottom ash with T6	80.6

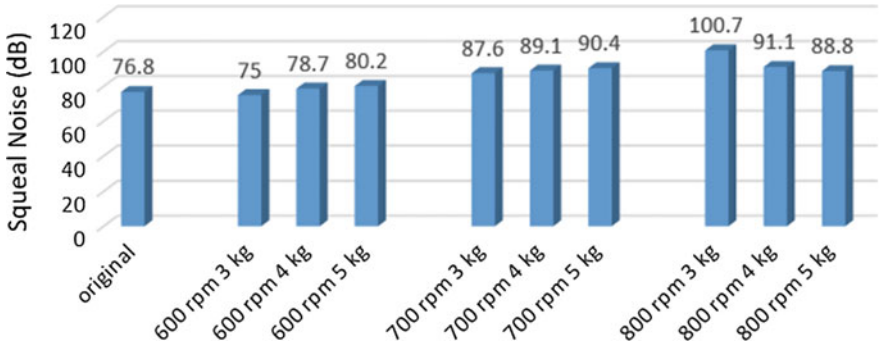

Fig. 50.3 Results of squeal noise testing

50.4 Conclusion

From above experiments, we can make the following conclusions:

(i) There is significant difference in hardness between Al–bottom ash and original disc brake: Al–bottom ash is harder than the original disc brake;
(ii) T6 heat treatment affects the hardness number of Al–bottom ash: Al–bottom ash disc brake with T6 heat treatment has a higher number of hardness compared to Al–bottom ash without T6;
(iii) The case of 300 rpm and 3 kg in squeal noise testing demonstrates lesser noisy than squeal noise at original disc brake;
(iv) Al–bottom ash is suitable and feasible composite as an alternative material for disc brake.

Acknowledgements This research was performed into International Conference on Physics and Mechanics of New Material and Their Applications (PHENMA-2017) in Jabalpur, India.

References

1. M. Rusli, M. Okuma, in *Squeal Noise Analysis in Mechanical Structure with Friction*, ed. by E. K. Mueller (VDM Verlag, Saarbrücke, 2010)
2. H. Seputro, B. Prastio, M. Abdulrahim, in *Abstracts and Schedule of the 2016 International Conference on "Physics and Mechanics of New Materials and Their Applications" (19–22 July 2016, Surabaya, Indonesia)*, ed. by M.A. Jani, I.A. Parinov, S.-H. Chang (UNTAG Press, Surabaya, 2016), p. 71
3. K. Ulhas, G.B. Annigeri, V. Kumar, Mater. Today Proc. **4**(2), 1140 (2017)
4. T.A. Costa, M. Dias, L.G. Gomes, O.L. Rocha, A. Garcia, J. Alloy Compd. **683**, 485 (2016)

Index

I. A. Parinov et al. (eds.), *Advanced Materials*, Springer Proceedings in Physics 207, https://doi.org/10.1007/978-3-319-78919-4